

Process Technology Proceedings, 12

High Pressure Chemical Engineering

Edited by
Ph. Rudolf von Rohr
and
Ch. Trepp



Elsevier

High Pressure Chemical Engineering

Process Technology Proceedings

- Vol. 1** Multi-Phase Flow and Heat Transfer III (Proceedings of the Third Multi-Phase Flow and Heat Transfer Symposium-Workshop, Miami Beach, Florida, U.S.A., April 18-20, 1983), edited by T.N. Veziroğlu and A.E. Bergles (Parts A and B)
- Vol. 2** Industrial Crystallization (Proceedings of the 9th Symposium on Industrial Crystallization, The Hague, The Netherlands, September 25-28, 1984), edited by S.J. Jančić and E.J. de Jong
- Vol. 3** Supercritical Fluid Technology, edited by J.M.L. Penninger, M. Radosz, M.A. McHugh and V.J. Krukoniš
- Vol. 4** Flocculation in Biotechnology and Separation Systems (Proceedings of the International Symposium on Flocculation in Biotechnology and Separation Systems, San Francisco, California, U.S.A., July 28-August 1, 1986), edited by Y.A. Attia
- Vol. 5** Preconcentration and Drying of Food Materials (Thijssen Memorial Symposium-Proceedings of the International Symposium on Preconcentration and Drying of Foods, Eindhoven, The Netherlands, November 5-6, 1987), edited by S. Bruin
- Vol. 6** Industrial Crystallization 87 (Proceedings of the 10th Symposium on Industrial Crystallization, Bechyne, Czechoslovakia, September 21-25, 1987), edited by J. Nývlt and S. Žáček
- Vol. 7** Interfacial Phenomena in Biotechnology and Materials Processing (Proceedings of the International Symposium on Interfacial Phenomena in Biotechnology and Materials Processing, Boston, Massachusetts, U.S.A., August 3-7, 1987), edited by Y.A. Attia, B.M. Moudgil and S. Chander
- Vol. 8** Gas Separation Technology (Proceedings of the International Symposium on Gas Separation Technology, Antwerp, Belgium, September 10-15, 1989), edited by E.F. Vansant and R. Dewolfs
- Vol. 9** Computer Applications in Chemical Engineering (Proceedings of the European Symposium on Computer Applications in Chemical Engineering, ComChem '90, The Hague, The Netherlands, May 7-9, 1990), edited by H.Th. Bussemaker and P.D. Iedema
- Vol. 10** Computer-Oriented Process Engineering (Proceedings of COPE-91, Barcelona, Spain, October 14-16, 1991), edited by L. Puigjaner and A. Espuña
- Vol. 11** Separation Technology (Proceedings of the Third International Symposium on Separation Technology, Antwerp, Belgium, August 22-27, 1993), edited by E.F. Vansant
- Vol. 12** High Pressure Chemical Engineering (Proceedings of the 3rd International Symposium on High Pressure Chemical Engineering, Zürich, Switzerland, October 7-9, 1996), edited by Ph. Rudolf von Rohr and Ch. Trepp

Process Technology Proceedings, 12

High Pressure Chemical Engineering

Proceedings of the 3rd International Symposium on High Pressure Chemical Engineering, Zürich, Switzerland, October 7-9, 1996

Edited by

Ph. Rudolf von Rohr

and

Ch. Trepp

Institut für Verfahrens- und Kältetechnik, ETH Zentrum, Zürich, Switzerland



1996

ELSEVIER

Amsterdam - Lausanne - New York - Oxford - Shannon - Tokyo

Elsevier Science B.V.
Sara Burgerhartstraat 25
P.O. Box 521, 1000 AM Amsterdam, The Netherlands

ISBN 0-444-82475-8

©1996 Elsevier Science B.V. All rights reserved.

No part of this publication may be reproduced, stored in a retrieval system or transmitted in any form or by any means, electronic, mechanical, photocopying, recording or otherwise without the prior written permission of the publisher, Elsevier Science B.V., Copyright & Permissions Department, P.O. Box 521, 1000 AM Amsterdam, The Netherlands.

Special regulations for readers in the USA - This publication has been registered with the Copyright Clearance Center Inc. (CCC), 222 Rosewood Drive, Danvers, MA 01293, USA. Information can be obtained from the CCC about conditions under which photocopies of parts of this publication may be made in the USA. All other copyright questions, including photocopying outside the USA, should be referred to the copyright owner, Elsevier Science B.V., unless otherwise specified.

No responsibility is assumed by the Publisher for any injury and/or damage to persons or property as a matter of products liability, negligence or otherwise, or from use or operation of any methods, products, instructions or ideas contained in the material herein.

This book is printed on acid-free paper.

Printed in the Netherlands

Preface

During the annual Meeting of the EFCE-Working Party "High pressure technology" held October 8, 1993, at Kaiseraugst, Switzerland, under the chairmanship of the late Prof. Helmut Tiltscher, it was decided to hold the 3rd International Symposium on High Pressure Chemical Engineering on October 7 - 9, 1996 at ETH in Zurich. Here, the Institute of Process Engineering and Cryogenics (Profs Rudolf von Rohr and Trepp) have taken on the task of organizing the meeting.

The two previous conferences were held in 1984 and 1990 in Erlangen, Germany, at a University with considerable impact on the promotion of this emerging technology in industry. Following the Erlangen tradition the Zurich symposium is also subdivided in three major sections, namely

- Chemical reaction engineering
- Separation processes and phase equilibria
- Plant, apparatus, machinery, measurements, control

From the contributions offered, the papers section of the scientific committee has chosen a number of more than 60 as oral and about an equal number for poster presentations. This volume contains the text of all contributions (oral and posters) which have reached us in time, except the four invited papers.

R.R. Emst:	NMR, a powerful tool for the investigation of molecules and materials at high and ambient pressure
P. G. Debenedetti:	Materials processing with supercritical fluids
C. Suter:	Competing through technology
G. Vetter:	High pressure machinery - a permanent challenge for engineers

For these an other form and way of publication will be used.

We are grateful to the lead scientists of this conference, experts in the area, for their contributions in coordinating the evaluation of contributed papers and maintaining the high quality of research papers in these proceedings. We especially acknowledge the professional help of reviewers from all over the world for selection of papers and suggestions for improvement of the content of accepted papers published in the proceedings.

Finally, we greatly appreciate the cooperation provided by Drs Huub Manten-Werker of Elsevier Science Publishers B.V. for her preparation of these fine proceedings in a very timely manner.

The Editors

Scientific Committee

- Prof. Ch. Trepp (CH), Chairman
- Prof. A. Baiker (CH)
- Prof. A. Bertucco (I)
- Prof. G. H. Brunner (D)
- Prof. P. G. Debenedetti (USA)
- Mr. M. Gehrig (D)
- Dr. K. W. Hutchenson (USA)
- Prof. I. Kikic (I)
- Dr. L. A. Kleintjens (NL)
- Prof. Z. Knez (SLO)
- Dr. J. Krekel (D)
- Dr. E. Lack (A)
- Prof. A. Laurent (F)
- Prof. A. Merbach (CH)
- Prof. S. Peter (D)
- Dr. K. Steiner (CH)
- Prof. G. Vetter (D)
- Prof. W. K. Yuan (PRC)

Organizing Committee

Members of the Organizing Committee
(Institute of Process Engineering and Cryogenics ETHZ):

- Prof. Dr. Ph. Rudolf von Rohr, Chairman
- Prof. Dr. Ch. Trepp
- Dr. W. Dörfler
- M. Weber
- H. Brandenberger
- E. Phasuk
- R. Zuercher
- S. Haferl
- M. Lustenberger

Table of Contents

Preface	v
Scientific Committee, Organizing Committee	vi

A: Chemical Reaction Engineering

Enhancing the Activity of Solid Acid Catalysts with Supercritical Reaction Media: Experiments and Theory B. SUBRAMANIAM, D.M. GINOSAR, University of Kansas, Lawrence	3
Influence of Chain Architecture on High-Pressure Copolymer Solution Behaviour: Experiments and Modeling S.-H. LEE, M.A. MCHUGH, John Hopkins University, Baltimore	11
Hardening of Fats and Oils in Supercritical Carbon Dioxide T. TACKE, S. WIELAND, P. PANSTER, Degussa AG, Hanau	17
The Importance of Surfactants for Polymerizations in Carbon Dioxide D.E. BETTS, J.B. MCCLAIN, J.M. DE SIMONE, The University of North Carolina, Chapel Hill	23
Integration of Indirect Electrochemistry and Separation by Supercritical Fluids U. LEFFRANG, U. GALLA, H. SCHMIEDER, Forschungszentrum Karlsruhe, Karlsruhe	31
CSTR-System for Kinetic Investigation for Hydrogenation Reactions A.G. ZWAHLEN, F.Hoffmann-La Roche AG, Basel A. BERTUCCO, Università di Padova, Padova	37
Hydrogenation at Supercritical Conditions M. HÄRRÖD, Chalmers University of Technology, Göteborg P. MØLLER, Aarhus	43
Application of RESS to Several Low Molecular Weight Compounds P. SUBRA, Université Paris XIII, Villateneuse P. DEBENEDETTI, Princeton University, Princeton	49
Wet Oxidation of Organics under Near-Critical Conditions E. PONGRATZ, S. PETER, Friedrich-Alexander Universität, Erlangen G. HÄRTEL, C. FREESE, Freiberg Universität, Freiberg	55

Oxidation of Organic Material in Supercritical Water and Carbon Dioxide	
H. GOLDACKER, J. ABELN, M. KLUTH, A. KRUSE, H. SCHMIEDER, G. WIEGAND, Forschungszentrum Karlsruhe GmbH, Karlsruhe	61
Clean Chemistry in Supercritical Fluids	
M. POLIAKOFF, S.M. HOWDLE, M.W. GEORGE, Nottingham University, Nottingham	67
Use of Metallocene Catalysts in the Polymerization under High Pressure	
G. LUFT, Universität Darmstadt, Darmstadt	73
Integration of Lipase Catalysis and Product Separation in Supercritical Carbon Dioxide	
H. GUNNLAUGSDOTTIR, B. SIVIK, University of Lund, Lund	79
Supercritical Carbon Dioxide as a Medium for Enzymatically Catalyzed Reaction	
M. HABULIN, V. KRMEJ, Z. KNEZ, University of Maribor, Maribor	85
Synthesis of N,N-Dimethylformamide by Heterogeneous Catalytic Hydrogenation of Supercritical Carbon Dioxide	
O. KRÖCHER, R.A. KÖPPEL, A. BAIKER, Eidg. Technische Hochschule, Zürich	91
Photooxidation Reactions in Supercritical Carbon Dioxide	
S. KODA, Y. OSHIMA, J. OTOMO, T. EBUKURO, University of Tokyo, Tokyo	97
Enzymatic Reaction in Supercritical Carbon Dioxide Internal Mass Transfer Limitation	
P. BERNARD, D. BARTH, LTCA-ENSIC, Nancy	103
Supercritical Carbon Dioxide Aided Catalyst Design, its Characterization and Behaviour in Reacting Environments	
S.G. SUNOL, Z. TOSYALI, A.K. SUNOL, University of South Florida, Tampa	109
Enzymatic Catalysis in Supercritical Carbon Dioxide: Effect of Water Activity	
H. MICHOR, R. MARR, T. GAMSE, Technische Universität Graz, Graz	115
Behaviour of a Cooled Wall Reactor for Supercritical Water Oxidation	
M.J. COCERO, J.L. SORIA, O. GANADO, R. GONZÁLEZ, F. FERNANDEZ-POLANCO, Universidad de Valladolid, Valladolid	121
Enzyme Catalyzed Reactions, Enantioselectivity and Stability under High Hydrostatic Pressure	
O. GUTHMANN, R. SCHWERDTFEGER, A. RIEKS, G. ANTRANIKIAN, V. KASCHE, G. BRUNNER, Technische Universität Hamburg-Harburg, Hamburg	127

Kinetic Study of the Titanium Tetraisopropoxide Decomposition in Supercritical Isopropanol V. GOURINCHAS-COURTECUISE, K. CHHOR, J.F. BOCQUET, C. POMMIER, Université Paris XIII, Villetaneuse	133
Enantioselective Hydrogenation in Supercritical Fluids. Limitations of the Use of Supercritical Carbon Dioxide. B. MINDER, T. MALLAT, A. BAIKER, Eidg. Technische Hochschule, Zürich	139
Investigation of Various Zeolite Catalysts under Supercritical Conditions F. NIU, H. HOFMANN, Universität Erlangen-Nürnberg, Erlangen	145
Coking Mechanism of Zeolite for Supercritical Fluid Alkylation of Benzene Y. GAO, Y.-F. SHI, Z.-N. ZHU, W.-K. YUAN East China University of Science and Technology, Shanghai	151
Model and Simulation of Supercritical Water Oxidation G. PETRICH, J. ABELN, H. SCHMIEDER, Forschungszentrum Karlsruhe, Karlsruhe	157
Degradation Processes in Sub- and Supercritical Water (SCWO) TH. HIRTH, G. BUNTE, N. EISENREICH, H. KRAUSE, R. SCHWEPPE, S. JÄHNKE Fraunhofer Institut, Pfinztal	163
 B: Separation Processes and Phase Equilibria	
Determination of the Volumetric Gas-Liquid Mass Transfer Coefficients at Pressures up to 5 MPa M. BICHARI, C. ROIZARD, A. LAURENT, N. MIDOUX, CNRS-ENSIC-INPL, Nancy	169
Cloud-Point Curves in Ethylene-Acrylate-Poly(ethylene-co-acrylate) Systems M. BUBACK, M. BUSCH, H. DIETZSCH, T. DRÖGE, K. LOVIS, Georg-August-Universität, Göttingen	175
Continuous Extraction of Contaminated Soil with Supercritical Water A. FIRUS, G. BRUNNER, Technische Universität Hamburg-Harburg, Hamburg	179
Supercritical Fluid Extraction of a High-Ash Brazilian Mineral Coal S.R.P. ROCHA, J.V. OLIVEIRA, Federal University of Santa Catarina, Santa Catarina S.G. D'AVILA, UNICAMP	185

Interaction of Density, Viscosity and Interfacial Tension in Counter-current Extraction with Near-Critical Fluids S. PETER, Universität Erlangen-Nürnberg, Erlangen	191
The Heat Transfer to Supercritical Carbon Dioxide in Tubes with Mixed Convection T. WALISCH, M. MÜLLER, W. DÖRFLER, Ch. TREPP, Eidg. Technische Hochschule, Zürich	199
Porocritical Fluid Extraction: A New Technique for Continuous Extraction of Liquids with Near-Critical Fluids M. SIMS, J. ROBINSON, A. J. DENNIS, Marc Sims SFE, Berkeley.	205
Crystallization under Gas Pressure H. FREUND, R. STEINER, Friedrich-Alexander Universität, Erlangen	211
Formation of Biocompatible Polymer Microspheres for Controlled Drug Delivery by a Supercritical Antisolvent Technique A. BERTUCCO, P. PALLADO, Università di Padova, Padova L. BENEDETTI, Fidia Advanced Biopolymers, Abano Terme	217
Powder Generation from Polyethyleneglycols with Compressible Fluids E. WEIDNER, R. STEINER, Technische Universität Erlangen-Nürnberg, Erlangen Z. KNEZ, University of Maribor, Maribor	223
Regeneration of Loaded Supercritical Carbon Dioxide with Activated Carbon I. REISS, A. SCHLEUSSINGER, S. SCHULZ, Universität Dortmund, Dortmund	229
A New Mixing Rule for Accurate Prediction of High Pressure Vapor-Liquid Equilibria of Gas/Large n-Alkane Systems C. ZHONG, H. MASUOKA, Hiroshima University, Higashi-Hiroshima	235
High Pressure Multiphase Equilibria in the Ternary System Carbon-Dioxide-Water-1-Propanol T. ADRIAN, G. MAURER, Universität Kaiserslautern, Kaiserslautern	241
Extraction of Spray-Particles with Supercritical Fluids R. EGGERS, P. JAEGER, Technische Universität Hamburg-Harburg, Hamburg H. WAGNER, Unilever Research Laboratory, Vlaardingen	247
Application of Supercritical Fluid Extraction for Spices and Herbs with Pressures up to 800 bar E. LACK, H. SEIDLITZ, NATEX GesmbH, Ternitz	253
High Pressure Investigations on the Solubility of Synthetic and Natural Dyestuffs in Supercritical Gases by VIS-Spectroscopy up to 180 MPa C.B. KAUTZ, D. TUMA, G.M. SCHNEIDER, Ruhr-Universität, Bochum	259

Modeling Solubility of Biological Compounds in Supercritical Fluids

E. NEAU, S. GARNIER, Université de Luminy, Aix-Marseille

P. ALESSI, A. CORTESI, I. KIKIC, University of Trieste, Trieste 265

High Pressure Treatment of Vegetables

R. STUTE, CPC-Europe Cons. Foods Ltd., Heilbronn

M.N. ESHTIAGI, S. BOGUSLAWSKI, D. KNORR, Universität Berlin, Berlin 271

Partitioning of Carbohydrates in the Three-Phase Region of Systems Containing Carbon Dioxide, Water and a Modifier at High Pressure

O. PFOHL, G. BRUNNER, Technische Universität Hamburg-Harburg, Hamburg

R. DOHRN, Bayer AG, Leverkusen 277

The Fractionation of High Molecular Weight Alkane Mixtures with Supercritical Fluids

I. NIEUWOUDT, University of Stellenbosch, Stellenbosch 283

Separation of Multicomponent Mixtures of Fatty Acid Ethyl Esters from Fishoil by Countercurrent SFE

C. TIEGS, K. STEINER, F. Hoffmann-La Roche AG, Basel

V. RIHA, G. BRUNNER, Universität Hamburg-Harburg, Hamburg 291

Cocoa Butter Fractionation with Supercritical Carbon Dioxide

C. BERTOLI, Nestlé S.A., Lausanne

A.R. BHASKAR, S.S.H. RIZVI, Cornell University, Ithaca 297

Fractionation of Citrus Oil by Cyclic Adsorption Process in Supercritical Carbon Dioxide

M. SATO, M. GOTO, A. KODAMA, N. TANOUE, T. HIROSE,

Kumamoto University, Kumamoto 303

Gas Anti-Solvent Fractionation of Natural Products

O.J. CATCHPOLE, S. HOCHMANN, S.R.J. ANDERSON,

Industrial Research Ltd., Lower Hutt 309

Separation of Metals from Simulated Mixed Waste Streams through Hydrothermal Crystallization in Supercritical Water

R.L. SMITH, JR., P. ATMAJI, Y. HAKUTA, T. ADSCHIIRI, K. ARAI,

Tohoku University, Sendai 315

Thermal Swing Adsorption in Supercritical Fluids

B.D. MIERAU, A.K. SUNOL, University of South Florida, Tampa 321

Monte Carlo Simulation for Distribution Equilibrium between Supercritical Fluid and Slit Pores

T. SHIGETA, T. NITTA, Osaka University, Osaka 327

Removal of Xanthines from Cacao J. SEBALD, J. SCHULMEYER, M. GEHRIG, Hopfen-Extraktion HVG Barth, Raiser & Co., Nürnberg	333
Solubilities and Phase Equilibria for the System Furfural-CH ₃ COOH-H ₂ O and Supercritical Carbon Dioxide T. GAMSE, R. MARR, Technische Universität Graz, Graz F. FRÖSCHL, M. SIEBENHOFER, VTU Engineering, Graz	339
Supercritical Fluid Extraction of Polar Nitrogen Containing Substances M. NIEHAUS, U. TEIPEL, G. BUNTE, H. KRAUSE, W. WEISWEILER Fraunhofer Institut, Pfinztal	345
Solubility of Solids in Supercritical Fluids Using Equations of State - Excess Gibbs Free Energy Models C.V. FILHO, Petrobras S.A., Bahia G.M.N. COSTA, Universidade Federal da Bahia, Bahia	351
Supercritical Fluid Extraction of Medicinal Plants B. SIMANDI, M. OSZAGYAN, E. RONYAI, J. FEKETE, Technical University of Budapest, Budapest A. KERY, E. LEMBERKOVICS, Semmelweis University of Medicine, Budapest I. MATHE, Albert Szent-Györgyi Medical University, Szeged E. HETHELYI, Caola Ltd., Budapest	357
Kinetics of Extraction of Macroporous Solid Bodies with a Dense Gas F. STÜBER, M.A. LARRAYOZ, F. RECASENS, Universitat Politècnica de Catalunya, Barcelona	363
Solids Formation by Rapid Expansion of Supercritical Solutions P. GERBER, U. TEIPEL, H. KRAUSE, Fraunhofer Institut, Pfinztal	369
Solubility, Extraction and Modification of Polymer and Polymer Additives in Supercritical Carbon Dioxide L. MERZ, O. MUTH, Fraunhofer Institut, Pfinztal	373
Design of Experiments for Thermodynamic Model Discrimination Applied to Phase Equilibria at High Pressures C. DARIVA, J.V. OLIVEIRA, Federal University of Santa Catarina, Santa Catarina E. CASSEL, Federal University of Rio de Janeiro, Rio de Janeiro	379
Predictive Quasilattice Equation of State for Unified High Pressure Phase Equilibria of Pure Fluids and Mixtures S.J. YOO, H.Y. SHIN, K.-P. YOO, Sogang University, Seoul C.S. LEE, Korea University, Seoul W. ARLT, Technische Universität Berlin, Berlin	385
Static and Dynamic Light Scattering Test of Polymer Particles Formation Process in Supercritical Fluid D.YU. IVANOV, R. TUFEU, A.V. SOLOVIEV, Université Paris XIII, Villetaneuse	389

Resolution of Ibuprofen and cis-Chrysanthemic Acid by Supercritical Fluid Extraction

S. KESZEL, B. SIMANDI, E. FOGASSY, J. SAWINSKY, CS. NIKLOS, R. LOVAS

Technical University of Budapest, Budapest 393

Extraction of Useful Components from Herbs Using Supercritical Carbon Dioxide: Experimental Findings and Data Modelling

R. SANTOS, T. LU, L. SCHLIEPER, M.B. KING, University of Birmingham, Birmingham

J. BASTOS, Universidade do Porto, Porto 399

Application of a Generalized Van der Waals Equation of State to Several Nonpolar Mixtures at High Pressures

N. VAN NHU, Technische Universität München, Garching

U.K. DEITERS, Universität Köln, Köln 405

High-Pressure Phase Equilibria Data of Systems Containing Limonene, Linalool and Supercritical Carbon Dioxide

S.A.B. VIEIRA DE MELO, P. PALLADO, A. BERTUCCO, G.B. GUARISE,

Università di Padova, Padova 411

High-Pressure Extraction of Cork with Carbon Dioxide and 1,4-Dioxane

A.S. REIS MACHADO, M. NUNES DA PONTE, Universidade Nova de Lisboa, Lisboa

A.M. MIRANDA, H. PEREIRA, Universidade Técnica de Lisboa, Lisboa 417

Supercritical Carbon Dioxide Desorption of Organics from Activated Carbon and Zeolite

G. VALLÉE, D. BARTH, LTCA-ENSIC, Nancy 423

A New Efficient Fractionation Process: The Simulated Moving Bed with Supercritical Eluent

J.Y. CLAVIER, R.M. NICLOUD, M. PERRUT, SEPAREX, Champigneulle 429

Experimental Measurement of Clathrate Phase Equilibria Containing Carbon Dioxide, Methane, Phenol and p-Cresol

H. LEE, J.-H. YOON, S.-P. KANG,

Korea Advanced Institute of Science and Technology, Taejeon 435

Three Phase Flash Calculation under High Pressure Using Continuous Thermodynamics Method

Z. CHENG_HAI, C.-L. LI, East China University, Shanghai

X. Fang, Fushun Research, Fushun 441

Representation of the Ternary System Carbon Dioxide-Water-Methanol

E. RAUZY, F. SABLAYROLLES, C. RÉBUFA, C. BERRO,

Faculté des Sciences de Luminy, Marseille 445

Calculation of High-Pressure Phase Equilibria Involving Light Gases J. KOHLBRUCH, U.K. DEITERS, Universität Köln, Köln	451
The Study of High Pressure - High Temperature Interaction between Co-Base Melts and Diamond Powders A.A. BOCHECHKA, V.G. GARGIN, A.A. SHULZHENKO, National Academy of Sciences of Ukraine, Kiev	457
Extraction of Ethanol from Fermentation Broth Using Supercritical Carbon Dioxide A. GÜVENÇ, Ü. MEHMETOĞLU, A. ÇALIMLI, University of Ankara, Ankara	463
Solubility Calculation of Solid Compounds in Supercritical Carbon Dioxide by a Group-Contribution Method L. BARNA, J.-M. BLANCHARD, INSA de Lyon, Villeurbanne E. RAUZY, C. BERRO, Faculté des Sciences de Luminy, Marseille	469
Extraction of Alkaloids From <i>Lupinus albus</i> sp. Using Compressed Carbon Dioxide. F.J. CAETANO, M.G. BERNARDO-GIL, Universidade de Lisboa, Lisboa M.L. BEIRAO DA COSTA, Cien. e Tecn. de Alimentos-ISA, Lisboa	475
The Phase Separation of Water + Methyl-di(n-amy)lphosphynoxide at Pressures up to 230 MPa M.Z. FAIZULLIN, V.P. SKRIPOV, Ural Division of Russian Academy of Sciences , Ekaterinburg	481
Scale-Up of a Supercritical Extraction Unit for the Deacidification of Olive Oil P.J. CARMELO, P.J. PEREIRA, Universidade Nova de Lisboa, Oeiras P.C. SIMOES, M. NUNES DA PONTE, Universidade Nova de Lisboa, Monte da Caparica	487
Gas-Liquid Mass Transfer in High Pressure Trickle-Bed Reactors: Experiments and Modelling M. CASSANELLO, Universidad de Buenos Aires, Buenos Aires F. LARACHI, Laval University, Québec A. LAURENT, G. WILD, N. MIDOUX, CNRS ENSIC INPL, Nancy	493
Influence of Mechanical Stresses on Phase Transitions of Polydimethylsiloxane and Diacetate Cellulose Solutions E.V. RUSINOVA, S.A. VSHIVKOV, Ural State University, Ekaterinburg	499
Adsorption Properties of Synthesized Diamond as a Function of Microdoping of the Solution-Melt Systems G.P. BOGATYREVA, A.V. ANREYEV, V.L. GYAZDOVSKAYA, V.N. Bakul Institut for Superhard Materials, Kiev	503

Impregnation of Porous Supports with Active Substances by Means of Supercritical Fluids

C. MAGNAN, C. BAZAN, F. CHARBIT, G. CHARBIT, Université d'Aix-Marseille, Marseille
J. JOACHIM, Laboratoire de Pharmacie Galénique Industrielle Marseille, Marseille 509

Solubility of Technical Oils in Supercritical Carbon Dioxide

N. DAHMEN, H. SCHMIEDER, J. SCHÖN, H. WILDE,
Forschungszentrum Karlsruhe, Karlsruhe 515

Separation of Non-Volatile Components by Expansion with High-Pressure Gases

B. BUNGERT, G. SADOWSKI, W. ARLT, Technische Universität Berlin, Berlin
R. TIPPL, Technische Universität Graz, Graz 519

Mathematical Models for Supercritical Extraction of Oregano

"*Origanum virens* L."

M.M. ESQUIVEL, C.L. DE SOUSA, M.A. RIBEIRO, M.G. BERNARDO-GIL,
Instituto Superior Técnico, Lisboa 525

Searching Prodrug Substances from Natural Resources by Supercritical Carbon Dioxide Extraction and Bioassay Tests

Y.H. CHOI, E.J. PARK, J.S. LEE, J. KIM, Seoul National University, Seoul
M.J. NOH, E.S. CHOI, K.P. YOO, Sogang University, Seoul 531

Extraction of Brominated Flame Retardents with Supercritical Carbon Dioxide

G. BUNTE, TH. HÄRDLE, H. KRAUSE, E. MARIOTH
Fraunhofer Institut, Pfinztal 535

C: Plant, Apparatus, Machinery, Measurements, Control

A Method for the Determination of Pressure Dependence of Liquid-Liquid Phase Behaviour in High Viscous Systems

H. LENTZ, U. MICHEL, Universität Siegen, Siegen
L.A. KLEINTJENS, DSM Research, Geleen 541

An Experimental Method to Determine the Sorption and Swelling Behaviour of Solids at High Pressures

C.A. LOCKEMANN, TH. RIEDE, P. MAGIN, BASF AG, Ludwigshafen 547

UV/vis Biochemical Spectroscopy under High Pressure

C. BALNY, J.-L. SALDANA, R. LANGE, INSERM, Montpellier
M.J. KORNBLATT, J.A. KORNBLATT, Concordia University of Canada 553

A High Pressure Combustion Cell Based on Numerical Flow Simulation and Reaction Zone Radiation Modelling B. MICHELFELDER, M. WEINDEL, W. ECKL, N. EISENREICH, M.M. HERMANN, Fraunhofer Institut, Pfinztal B. NOLL, ESG GmbH, Baden-Baden	559
Required Fuel Contents for Sewage Disposal by means of Supercritical Wet Oxidation (SCWO) in a Pilot Plant Containing a Wall Cooled Hydrothermal Burner (WCHB) M. WEBER, CH. TREPP, Eidg. Technische Hochschule, Zürich	565
Low Pulsation Design of Piping Systems for High Pressure Reciprocating Pumps S. NOTZON, URACA-Pumpenfabrik GmbH + Co. KG, Bad Urach	575
Dyeing of Poly(Ethylene Terephthalate) Fibers in Supercritical Carbon Dioxide E. BACH, E. Cleve, E. Schollmeyer, Deutsches Textilforschungszentrum Nord-West, Krefeld	581
Research with Modular Laboratory and Pilot Equipment in the Field of Supercritical Fluid Processing R. SIEBER, B. ZEHNDER, Sitec Sieber Engineering AG , Maur	587
High Pressure-Process-Diaphragm Pumps: Application and Technical Requirements E. SCHLÜCKER, W. HORN, LEWA, Leonberg	593
Hermetical Canned Motor Centrifugal Pumps in High-Pressure Processes R. KRÄMER, R. NEUMAIER, Hermetic-Pumpen GmbH, Gundelfingen	599
Multistage High Pressure Mixer-Settler System W. PIETZONKA, CH. TREPP, Eidg. Technische Hochschule, Zürich	609
Energetical Optimization of Supercritical Fluid Extraction Processes U. SIEVERS, Fachhochschule Hamburg, Hamburg	615
A New Design of a Multi-Purpose Plant for Extraction of Liquids with Supercritical Fluids O. BECKER, E. WEIDNER, R. STEINER, Universität Erlangen-Nürnberg, Erlangen	621
Safety in Supercritical Operations J.Y. CLAVIER, M. PERRUT, SEPAREX, Champigneulles	627
Endurance Prediction of Thickwalled High Pressure Components under Corrosion Fatigue Conditions G. VETTER, L. DEPMEIER, Universität Erlangen-Nürnberg, Erlangen	633

Extrapolation from Pilot Plant to Industrial Scale SFE : A Case Study J.Y. CLAVIER, W. MAJEWSKI, M. PERRUT, SEPAREX, Champigneulle	639
Design Rules for the Wallcooled Hydrothermal Burner (WHB) H.L. LA ROCHE, M. WEBER, CH. TREPP, Eidg. Technische Hochschule, Zürich	645
High Pressure Cell Heaters for Diamond Synthesis A.I. BORIMSKY, V.B. VOLKOV, P.A. NAGORNY, National Academy of Sciences of Ukraine, Kiev	651
Interfacial Tension Measurements Between α -Tocopherol and Carbon Dioxide at High Pressures M. MOSER, W. PIETZONKA, CH. TREPP, Eidg. Technische Hochschule, Zürich	655
Detection of Nitroaromatic Compounds Dissolved in Liquid and Supercritical Carbon Dioxide by UV-VIS Spectroscopy S. LÖBBECKE, G. BUNTE, TH. HÄRDLE, H. KRAUSE Fraunhofer-Institut, Pfinztal	661
Phase Transitions Registration at High Pressures up to 30 GPa V.V. SHCHENNIKOV, A.YU. DEREVSKOV, RAS, Ekaterinburg V.A. SMIRNOV, National Academy of Sciences, Poltava	667
Design and Construction Criteria for Pressure Vessels under Constant and Cyclic Load P. KÖRNER, W. HILLER, UHDE GmbH, Hagen	673
Hydrodynamic Behaviour of Packed Column under High Pressure B. BENADDA, K. KAFOUFI, M. OTTERBEIN, INSA, Villerbanne	679
Supercritical Adsorption and Desorption Measurements using a New Automated Apparatus P. ALESSI, A. CORTESI, I. KIKIC, University of Trieste, Trieste R. KITTEL, Technische Universität Berlin, Berlin	687
A Novel Microwave Autoclave for Automation of High Pressure Chemical Reaction Applications W. LAUTENSCHLAGER, W.G. ENGELHART, M. METZGER, F. VISINONI MLS/Milestone s.r.l., Sorisole	693

Appendix

Author Index	701
Keyword Index	705

This page intentionally left blank

This page intentionally left blank

Enhancing the Activity of Solid Acid Catalysts with Supercritical Reaction Media: Experiments and Theory[@]

Bala Subramaniam⁺ and Daniel M. Ginossar^{*}

Department of Chemical and Petroleum Engineering
University of Kansas, Lawrence, KS 66045-2223, U. S. A.

A detailed mathematical model is presented for describing the coking and isomerization activity of a Pt/ γ -Al₂O₃ catalyst in a tubular reactor. The main reaction is the acid-catalyzed isomerization of 1-hexene ($P_c = 31.7$ bar; $T_c = 231^\circ\text{C}$). Consistent with our experimental observations, the model predicts that (i) near-critical reaction mixtures provide an optimum combination of transport and solvent properties for extracting coke precursors from the catalyst, thereby maximizing isomerization rates and minimizing catalyst deactivation rates; and (ii) the mitigation of feed peroxides and the addition of inert co-solvents significantly reduce oligomer formation in the fluid phase, thereby curtailing the coke formation (i.e., catalyst deactivation) rates.

1. INTRODUCTION

The deactivation of solid acid catalysts, such as those used in reforming and alkylation practice, by coking occurs because the coke precursors that are formed either in the fluid phase or on the catalyst have relatively low volatilities at the operating pressure and temperature. Supercritical media have been shown to offer a unique combination of solvent and transport properties for the *in situ* extraction of coke-forming compounds from porous catalysts. Reported investigations of the supercritical decoking concept are summarized elsewhere [1].

Employing 1-hexene isomerization on a Pt/ γ -Al₂O₃ reforming catalyst as a model reaction system, we showed that isomerization rates are maximized and deactivation rates are minimized when operating with near-critical reaction mixtures [2]. The isomerization was carried out at 281°C, which is about 1.1 times the critical temperature of 1-hexene. Since hexene isomers are the main reaction products, the critical temperature and pressure of the reaction mixture remain virtually unaffected by conversion. Thus, an optimum combination of gas-like transport properties and liquid-like densities can be achieved with relatively small changes in reactor pressure around the critical pressure (31.7 bars). Such an optimum combination of fluid properties was found to be better than either gas-phase or dense supercritical (i.e., liquid-like) reaction media for the *in situ* extraction of coke-forming compounds.

The catalyst activity is determined by the coke extraction rate relative to the coke formation rate. The coke extraction rate is determined by the solubility of the coke compounds in the reaction mixture and the diffusivity of the extracted compounds through the porous catalyst. The coke formation on the catalyst occurs from the hexenes, and more significantly, from hexene oligomers formed in the fluid phase catalyzed by traces of peroxide impurities [3]. A detailed mathematical model is presented here to interpret the results presented in our earlier paper [2] and to develop a better understanding of the underlying physicochemical processes.

[@]Partially supported by the U. S. National Science Foundation (OSR-9255223)

⁺ To whom correspondence concerning this paper should be addressed; bsubramaniam@ukans.edu

^{*}Presently at EG&G Idaho Inc., P. O. Box 1625, Idaho Falls, ID 83415

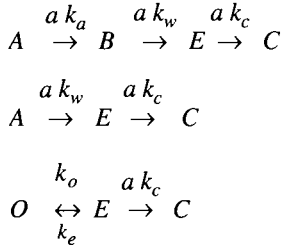
2. MODEL

A single pore (radius r_o , length $2L$) model is employed to describe simultaneous transport, isomerization, coke formation and coke extraction in the Pt/ γ -Al₂O₃ catalyst. The model is a significant improvement over previous efforts summarized in a recent paper [4]. Coke formation on the catalyst is assumed to occur from oligomers formed both in the bulk phase (catalyzed by peroxide impurities) and on the acid sites of the catalyst. The equilibrium distribution of these oligomers between the bulk fluid phase and the catalyst surface depends upon temperature and pressure. At supercritical conditions, more of the oligomers tend to be in the fluid phase while at subcritical conditions the oligomers are more strongly adsorbed on the catalyst. The oligomers adsorbed on the catalyst surface are termed extractable coke (E) and undergo transformation on the acid sites to consolidated coke (C), which is not extractable by the reaction mixture. Thus, the catalyst surface is populated by two species of coke.

The main assumptions relating to coke formation and extraction are:

- Oligomer formation in the bulk fluid phase is instantaneous relative to oligomer adsorption and reaction to form coke. The oligomer distribution (up to tetramers) is approximated (i.e., lumped) by the trimer, 1-octadecene (O).
- The surface oligomers (E) result from 1-hexene (A), hexene isomers (B) and the fluid phase oligomers. The rate constants associated with the formation of the surface oligomers from 1-hexene and the isomer products are identical.
- All coke formation reactions (producing E or C) are first order with respect to the coke precursor concentration.
- The extraction of the surface oligomers from the catalyst is described by an effective desorption rate constant (k_e).

The overall reaction network with multiple pathways for coke (C) formation is as follows:



The mass balances for the main reactant, the oligomer, the extractable coke and the consolidated coke in the catalyst pore are as follows:

$$\frac{\partial}{\partial z} \left(D_a^e \frac{\partial C_a}{\partial z} \right) - a (k_a \rho_c) C_a = 0 \quad (1)$$

$$\frac{\partial}{\partial z} \left(D_o^e \frac{\partial C_o}{\partial z} \right) - a (k_o \rho_c) C_o + (k_e S_a \rho_c / M_w) W_e = 0 \quad (2)$$

$$\frac{\partial W_e}{\partial t} = a (k_w M_w / S_a) (C_a + C_b) + a (k_o M_w / S_a) C_o - k_e W_e - a (k_c \rho_c) W_e \quad (3)$$

$$\frac{\partial W_c}{\partial t} = a (k_c \rho_c) W_e \quad (4)$$

The initial and boundary conditions are:

$$C_a(\pm L, t) = C_a^o; C_o(\pm L, t) = C_o^o \quad (5a)$$

$$\frac{\partial C_a}{\partial z}(0, t) = \frac{\partial C_o}{\partial z}(0, t) = W_e(z, 0) = W_c(z, 0) = 0 \quad (5b)$$

Note that in the hexene balance (eq. 1), the yield of coke is neglected as being insignificant when compared to the yield of the isomers. A linear deactivation function (a) is employed for all surface-catalyzed reactions as follows:

$$a = 1 - \left(\frac{W_e + W_c}{W_s} \right) = 1 - \frac{W_t}{W_s} \quad (6)$$

The reduction in the effective pore radius (r), as coke accumulates, is related to the empty pore radius (r_o), the coke density (ρ_c), and the total coke (W_t) as follows:

$$r^2 = r_o^2 - (2 r_o W_t / \rho_w) \quad (7)$$

Lee *et al.* [5, 6] and Tsai *et al.* [7] employed the following modified version of the Spry-Sawyer correlation to describe restricted diffusion of solutes in γ -Al₂O₃ catalysts:

$$\left(\frac{D_i^e}{D_i^o} \right) = \left(\frac{1 - r_m/r}{1 - r_m/r_o} \right)^p \left(\frac{r}{r_o} \right)^2 \quad (8)$$

where p was found to range from 4.9 to 5.1 at liquid-like conditions, and decreased to 4.4 as the solvent temperature approached its critical value. Since there are no reported correlations of diffusion as a function of density ranging from subcritical to supercritical values, an approximation is used in this work. Eq. (8) was employed altering the value of the exponent p with reaction mixture density (ρ_r) as follows:

$$p = 0 \text{ for } \rho_r \leq 1.0; p = 5.1 (\rho_r - 1) \text{ for } 1.0 < \rho_r \leq 2.0; \text{ and } p = 5.1 \text{ for } \rho_r > 2.0 \quad (9)$$

Thus, at subcritical, gas-like conditions, there is no restricted diffusion. As the density increases beyond the critical point, the extent of pore-diffusion restriction increases.

Erkey and Akgerman [8] reported an adsorption equilibrium constant for naphthalene in alumina pores filled with supercritical CO₂. Analysis shows that this desorption equilibrium constant is simply proportional to the solubility of naphthalene in CO₂ as measured by Tsekhanskaya *et al.* [9]. Hence, the desorption rate constant was estimated from the following type of correlation reported for the naphthalene-ethylene system by Tsekhanskaya *et al.* [9]:

$$\ln(k_e) = k_{ef} (c_1 + c_2 \rho_r) \quad (10)$$

where the parameters c_1 and c_2 were fit to the measured solubility data and k_{ef} was estimated by a fit with our experimental data.

For fixed or chosen values of the parameters, the model equations (eqs. 1-4) along with the initial and boundary conditions (eqs. 5) are solved iteratively by a centered-in-space, forward-in-time, finite difference scheme to obtain (i) the hexene and hexene oligomer concentration profiles in the pore fluid phase, and (ii) the coke (extractable + consolidated) accumulation profile. The effectiveness factor (η) is estimated from the hexene concentration profile as follows:

$$\eta(t) = \frac{D_a^e(L, t) \frac{\partial C_a}{\partial z}(L, t)}{L \rho_c k_a C_a^o} \quad (11)$$

The foregoing effectiveness factor was used to predict temporal hexene isomerization rates (r_{obs}) at the exit of an isothermal tubular reactor as follows:

$$r_{obs} = \frac{F_t}{\omega_c} \left(1 - \exp \left(- \frac{\eta k_a \omega_c C_a^o}{F_t} \right) \right) \quad (12)$$

The reaction rate and adsorption equilibrium constants (k_w , k_o , k_c and k_{ef}) were obtained from a fit of the model simulation results employing a limited number of experimental data. The data used in the model simulations are presented in Table 1. Details of the simulation may be found elsewhere [10]. In the following section, the predicted isomerization rates are compared with experimentally observed isomerization rates reported earlier [2].

Table 1
Parameter values used in the simulations

Variable	Definition	Value	Source
F_t	flow rate of hexene feed to reactor	4.46 (10 ⁻⁷) kg mol/s	(a)
k_a	rate constant for $A \rightarrow B$	0.85 (10 ⁻³) m ³ /kg cat/s	(a)
k_o	rate constant for $O \rightarrow W_e$	0.11 (10 ⁻³) m ³ /kg cat/s	(b)
k_w	rate constant for $A, B \rightarrow W_e$	9.9 (10 ⁻⁷) m ³ /kg cat/s	(b)
k_c	rate constant for $W_e \rightarrow W_c$	1.4 (10 ⁻⁷) m ³ /kg cat/s	(b)
k_{ef}	adsorption equilibrium constant (eq. 12)	0.11	(b)
L	pore length	3.04 (10 ⁻⁴) m	(a)
M_w	molecular weight of coke	252.5 kg/kg mol	(a)
r_o	mean radius of empty pore	32 (10 ⁻¹⁰) m	(a)
ρ_c	bulk density of catalyst	1.2 (10 ³) kg/m ³	(a)
ρ_w	density of coke	1.5 (10 ³) kg/m ³	(a)
S_a	catalyst surface area	174.9 (10 ³) m ² /kg cat	(a)
ω_c	catalyst loading in reactor	1.0 (10 ⁻³) kg	(a)
W_s	coke laydown at total deactivation	2.37 (10 ⁻⁶) kg/m ²	(a)

^ameasured; ^bfitted

3. RESULTS AND DISCUSSION

3.1 Reaction Mixture Density Effects

The simulated and experimental variations of the end-of-run (i.e., 8 hr.) isomerization rates with density are compared in Figure 1. Details of the experiments are provided elsewhere [2, 3]. At subcritical densities, the extraction of coke precursors is insignificant. Hence, an increase in the concentration of the hexene and coke precursors (i.e., oligomers) leads to lower isomerization rates. At near-critical densities, the extraction of coke precursors becomes significant. Hence, the isomerization rate increases. Both the experimental and simulated rates show a decreasing trend when the density is increased from near-critical to supercritical values. This is attributed to pore-diffusion limitations as the fluid changes from gas-like to liquid-like. Above 2.0 ρ_c , the isomerization rate increases with density as the ability of the reaction mixture to extract the coke precursors increases.

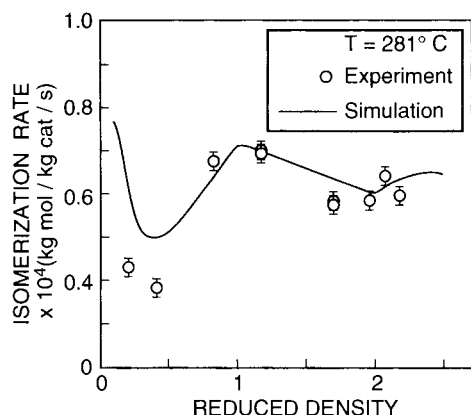


Figure 1. Comparison of experimental and simulated variations of end-of-run (8 hr) isomerization rates with density

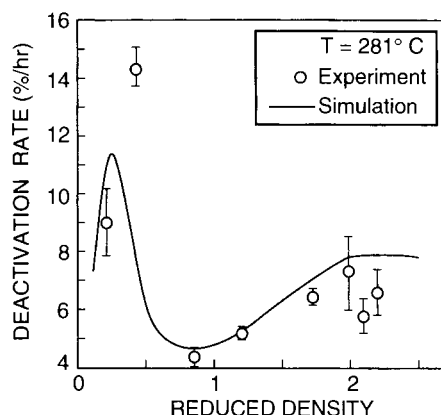


Figure 2. Comparison of experimental and simulated deactivation rates at various reaction mixture densities

A complementary trend is seen in the simulated and experimental end-of-run deactivation rates (defined as the percent decrease in the isomerization rate between six and eight hours into the run). As seen in Figure 2, both the simulated and experimental deactivation rates show an increasing trend with density in the subcritical range, a decreasing trend as the density approaches its critical value, and an increase with density up to $2.0 \rho_c$, above which the deactivation rates are lower.

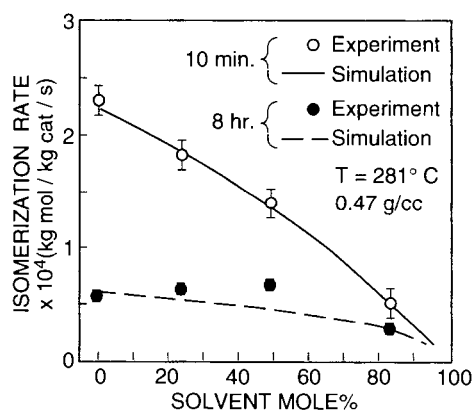


Figure 3. Effect of solvent addition on experimental and simulated initial and end-of-run isomerization rates

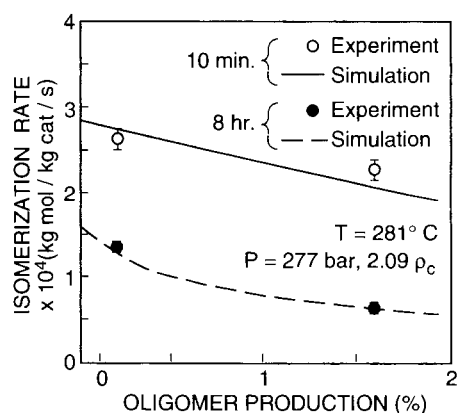


Figure 4. Effect of oligomer production on experimental and simulated initial and end-of-run isomerization rates

3.2 Solvent Effects

By adding an inert co-solvent with the hexene feed, and adjusting the operating pressure such that the reaction mixture density is maintained constant, the coke precursor concentrations can be reduced while maintaining the *in situ* extraction of the extractable coke compounds [3]. However, dilution of the feed with the co-solvent also reduces the isomerization rate. Figure 3

compares simulated initial (i.e., 10 min.) and end-of-run (8 hr.) isomerization reaction rates with experimental results obtained with *n*-pentane as the co-solvent. In all the experiments, the reaction mixture density is maintained constant at $0.47(10^3) \text{ kg/m}^3$. The simulated and experimental initial reaction rates show excellent agreement, decreasing linearly with co-solvent addition, as would be expected for a first-order reaction.

As regards the end-of-run isomerization rates, whereas the experimental results show a maximum at roughly 50 mol% co-solvent, the simulated results show a continuous decrease in isomerization rate with co-solvent addition. This might suggest a higher extent of coke extraction with the *n*-pentane co-solvent relative to that predicted for hexene. Such solvent effects have been reported previously [11]. The model does not account for solvent type and is hence unable to predict co-solvent effect on the solubility of coke precursors.

3.3 Oligomer Effects

The oligomers are formed in the fluid phase, aided by organic peroxide impurities in the feed. Oligomer production increases linearly with reaction mixture density. Experimentally, coke formation was observed to increase when oligomers were added to the reactor feed, decrease when oligomer concentrations were reduced by dilution with an inert co-solvent, and increase with higher oligomer production due to an increase in feed peroxide concentration [3]. The initial and end-of-run isomerization reaction rates obtained from a set of model simulations are compared to experimental results in Figure 4 for runs at 281°C , 277 bar, yielding a reduced density of 2.09. The oligomer production was varied from nearly zero to 2% by increasing the peroxide content in the feed by aeration. The simulated and experimental isomerization rates show excellent agreement, increasing with a decrease in oligomer production.

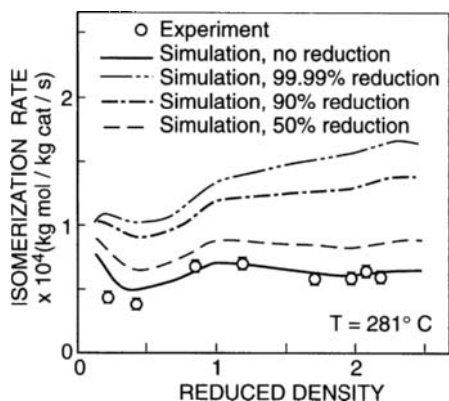


Figure 5. Effect of oligomer reduction on simulated end-of-run isomerization rates

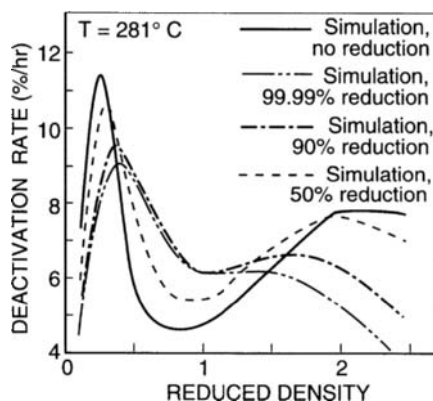


Figure 6. Effect of oligomer reduction on simulated end-of-run deactivation rates

Figure 5 shows the effect of reducing the oligomer production to 50%, 90% and 99.99% of the value obtained with an untreated hexene feed (i.e., without oligomer reduction). The reduction may be achieved by adsorbing the organic peroxides in the feed with activated alumina [12]. With 50% oligomer reduction, the simulated isomerization rates show a similar qualitative trend as the rates with no oligomer reduction. In both these simulations, a rate maximum is observed around the critical density. Despite the similarity in trends, the isomerization rates predicted with 50% oligomer reduction are roughly 30% higher than those with no oligomer reduction. With 90% reduction in oligomer production and beyond, the isomerization rate trends change. Although there is still a minimum in the subcritical region ($0.48 \rho_c$), there is no maximum around the critical density. In all cases, however, an increase in the isomerization rate is accompanied by a decrease in the deactivation rate (Figure 6).

4. CONCLUSIONS

A detailed mathematical model is presented for describing the coking and isomerization activity of a $\text{Pt}/\gamma\text{-Al}_2\text{O}_3$ catalyst in a tubular reactor. The main reaction is the acid-catalyzed isomerization of 1-hexene. Consistent with our earlier experimental results [2, 3], the model predicts that (i) near-critical reaction mixtures provide an optimum combination of transport and solvent properties for extracting coke precursors from the porous catalyst, thereby maximizing isomerization rates and minimizing catalyst deactivation rates; and (ii) the mitigation of feed peroxides and the addition of inert co-solvents significantly reduce oligomer formation in the fluid phase, thereby curtailing the coke formation (i.e., catalyst deactivation) rates. Indeed, as we had reported recently [12], reduction of organic peroxides in the olefinic feed in conjunction with supercritical operation leads to dramatic improvements in catalyst activity. Nearly *steady* catalyst activity at high conversions (roughly 70%) is observed at 281°C, 70 bars and a space velocity of 135 g hexene/h/g cat. We are currently investigating the feasibility of applying the supercritical decoking concept to enhance the activity of solid-acid catalysts for the alkylation of 1-butene with isobutane. If successful, such a process would clearly be an environmentally superior alternative to conventional alkylation technology that employs hazardous liquids such as sulfuric and hydrofluoric acids as catalysts.

NOTATION (partial list; others defined in the main text and in Table 1)

C_i^o	concentration of species i at the pore mouth or in the reactor fluid phase, kmol m^{-3}
C_i	concentration of species i in the fluid phase inside the catalyst pore, kmol m^{-3}
D_i^e	effective diffusivity of species i in the pore at time t , $\text{m}^2 \text{s}^{-1}$
D_i^o	effective diffusivity of species i in the empty pore, $\text{m}^2 \text{s}^{-1}$
k_e	effective desorption rate constant, s^{-1}
r_m	molecular radius of diffusing solute, m
W_c	consolidated coke laydown on catalyst, kg/m^2
W_e	extractable coke laydown on catalyst, kg/m^2

REFERENCES

1. P. E. Savage, S. Gopalan, T. I. Mizan, C. J. Martinio and E. E. Brock, *AIChE J.*, 41 (1995) 1723.
2. D. M. Ginosar and B. Subramaniam, in *Catalyst Deactivation: Stud. in Surf. Sci. and Catal.*, 88, Delmon, B. and G. F. Froment (eds.), Elsevier, Amsterdam, (1994) 327.
3. D. M. Ginosar and B. Subramaniam, *J. Catal.*, 152 (1995) 31.
4. B. J. McCoy and B. Subramaniam, *AIChE J.*, 41 (1995) 317.
5. S. Y. Lee, J. D. Seader, C. H. Tsai, and F. E. Massoth, *Ind. Eng. Chem. Res.*, 30 (1991) 29.
6. S. Y. Lee, J. D. Seader, C. H. Tsai, and F. E. Massoth, *Ind. Eng. Chem. Res.*, 30 (1991) 607.
7. C. H. Tsai, F. E. Massoth, S. Y. Lee and J. D. Seader, *Ind. Eng. Chem. Res.*, 30 (1991) 22.
8. C. Erkey and A. Akgerman, *AIChE J.*, 36 (1990) 1715.
9. Y. V. Tsekhanskaya, M. B. Imotev and E. V. Mushkina, *Russ. J. Phys. Chem.*, 39 (1964) 1173.
10. D. M. Ginosar, Ph. D. Dissertation, University of Kansas, 1994.
11. J. C. Fetzer, J. A. Graham, R. F. Arrendale, M. S. Klee and L. B. Rogers, *Sep. Sci. Tech.*, 16 (1981) 97.
12. M. C. Clark and B. Subramaniam, *Chem. Engng. Sci.*, 51 (1996) 2369.

This page intentionally left blank

Influence of Chain Architecture on High-Pressure Copolymer Solution Behavior: Experiments and Modeling

Sang-Ho Lee and Mark A. McHugh

Department of Chemical Engineering, Johns Hopkins University, Baltimore, Maryland 21218, USA

Phase behavior studies with poly(ethylene-*co*-methyl acrylate), poly(ethylene-*co*-butyl acrylate), poly(ethylene-*co*-acrylic acid), and poly(ethylene-*co*-methacrylic acid) were performed in the normal alkanes, their olefinic analogs, dimethyl ether, chlorodifluoromethane, and carbon dioxide up to 250 °C and 2,700 bar. The backbone architecture of the copolymers as well as the solvent quality greatly influences the solution behavior in supercritical fluids. The effect of cosolvent was also studied using dimethyl ether and ethanol as cosolvent in butane at varying concentrations of cosolvent, exhibiting that the cosolvent effect diminishes with increasing cosolvent concentrations.

1. INTRODUCTION

In the 1960's several extensive investigations were performed on the high-pressure solution behavior of the polyethylene (PE) [1,2]. The high-pressure process is also currently being used to produce polar/nonpolar, ethylene-based copolymers since many catalytic processes fail as the polar comonomer is a poison for the catalyst. Once again, high-pressure phase behavior becomes an important consideration when processing ethylene-based copolymers using techniques formerly developed to produce PE.

Over the past five years we have been investigating the role of backbone architecture on the phase behavior of ethylene-based copolymers in a variety of supercritical fluids [3]. We have studied the phase behavior of poly(ethylene-*co*-methyl acrylate), poly(ethylene-*co*-butyl acrylate), poly(ethylene-*co*-acrylic acid), and poly(ethylene-*co*-methacrylic acid) in many solvents. These copolymers can be distinguished from one another based on their ability to form hydrogen bonds. We have performed systematic phase behavior studies with these random copolymers since the properties of a given copolymer varies with the percent of each constituent in the backbone of the copolymer. Likewise, the properties of the solvents needed to solubilize a given type of copolymer change as a function of copolymer architecture. The solvents that have been investigated include the alkanes, their olefinic analogs, dimethyl ether, chlorodifluoromethane, and carbon dioxide. This wide range of solvents allows us to systematically vary solvent

properties with a given copolymer to determine the type of intermolecular interaction that fixes the location of the cloud-point curve.

In the talk, we present phase behavior data for copolymer-solvent-cosolvent mixtures at temperatures to 300 °C and pressures to 3,000 bar. We also present data on the impact of cosolvents on the phase behavior.

2. EXPERIMENTAL

Cloud points are obtained using a high-pressure, variable-volume cell that has a sapphire window to allow visual observation of the phases. The polymer-solvent mixture is compressed by moving a piston located in the cell. The pressure of the mixture is measured to within ± 3.5 bar; the temperature is measured to within ± 0.4 °C. The mixture inside the cell is viewed on a video monitor using a camera coupled to a borescope placed against the sapphire window. The solution in the cell is mixed with a stir bar activated by an external magnet. Cloud points are repeated at least twice at each temperature and are reproducible to ± 5 bar. The lowest temperature of the cloud-point curves is either the highest operating pressure of the apparatus or the crystallization boundary.

3. RESULTS AND DISCUSSION

A more detailed presentation of experimental data is presented in the talk. Here highlights are given for a few, well-chosen phase diagrams that summarize the effects of solvent quality, polar comonomer, and of cosolvents.

3.1 Poly(ethylene-co-methyl acrylate) (EMA)

Figure 1 shows the phase behavior of EMA_x (the subscript x denotes the molar acrylate content) copolymers in propylene which is slightly more polar than propane [4,5]. The EMA₁₀ curve is at slightly lower pressures than the PE curve since the first few acrylate units interact favorably with the quadrupole of propylene. However, the cloud-point curves shift to higher pressures and temperatures and as the amount of MA units increases to 31 and 41 mol% in the copolymer. EMA₄₁ *does not* dissolve in propane to temperatures of 200 °C and pressures of 2,000 bar, whereas it is readily soluble in propylene.

Figure 2 demonstrates the impact of solvent quality and hydrogen bonding on the solubility of EMA₃₁. Increasing the size of the alkane increases its polarizability and its critical temperature. Hence, the solvent quality increases going from ethane to butane and the cloud-point curves shift to lower temperatures and pressures.

If the size of the solvent molecule is kept constant, but some polarity is added to it, the cloud-point curve shifts to much lower temperatures as shown with ethane and ethylene. Notice that the pressure of the ethylene cloud-point curve is not radically lower than that of the ethane curve since the densities of both solvents are very close to one another at these elevated pressures.

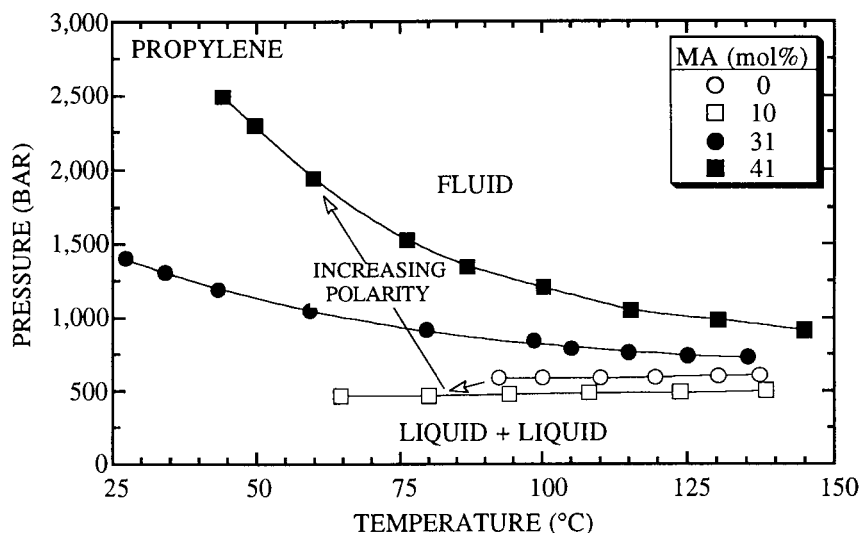


Figure 1. Cloud-point curves for EMA copolymers in propylene [3]. The MA content in the copolymer is given in the legend in the figure.

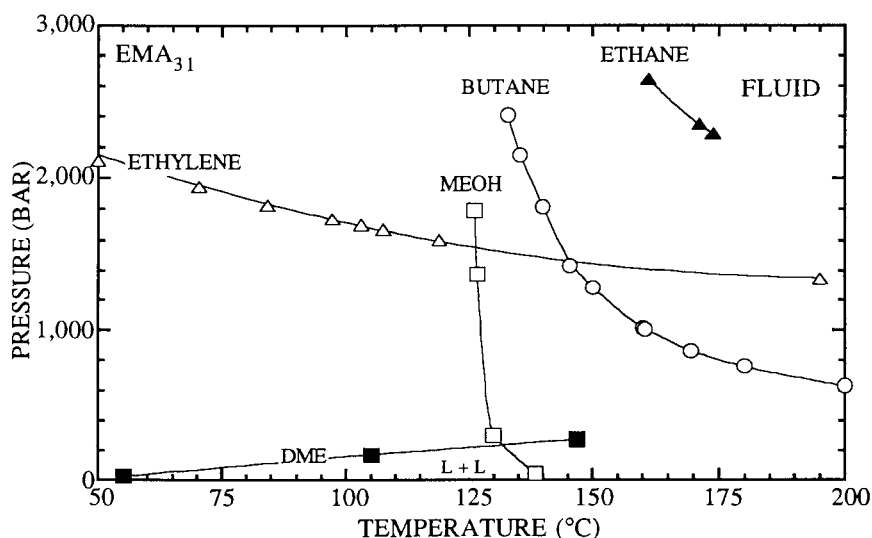


Figure 2. Cloud-point curves for EMA_{31} in a variety of solvents [3].

If the solvent size is again kept essentially constant, but now the solvent can hydrogen bond to the copolymer, very low cloud-point pressures are observed as long as the temperature remains high as shown with ethane compared to methanol. At temperatures below 125 °C, methanol prefers to self-associate

rather than complex with the acrylate groups in the copolymer. Hence, the cloud-point curve increases sharply with pressure indicating that increasing pressure does absolutely nothing to improve solubility. In this case the forces of attraction between the copolymer and solvent are more heavily weighted toward solvent-solvent interactions rather than solvent-copolymer interactions.

Keeping the solvent size essentially constant, but giving it a significant dipole moment has a large effect on the location of the cloud-point curve as shown by comparing the ethane curve with the DME curve. The dipole moment of DME interacts quite effectively with the dipole moment of the acrylate groups. Also, DME does not self-associate as does methanol so that DME remains a high-quality solvent to very low temperatures. Of course, DME is also a better solvent than ethane since it is more dense than ethane. But, as shown with the methanol case, increasing density does not insure solubility.

3.2 Poly(ethylene-co-acrylic acid) (EAA)

Figure 3 demonstrates the impact of solvent quality and hydrogen bonding on the solubility of EAA_{3.9} (the subscript 3.9 denotes the molar acrylate content). Many characteristics of the cloud-point curves of this acid copolymer are similar to those of the acrylate copolymers. For example, in butane, both the acid and acrylate cloud-point pressures are low at high temperatures, where polar and hydrogen bonding interactions are weak. The pressure increases for both copolymer-butane curves as the temperature is decreased as polymer-polymer interactions become more favored. Note that there are only 4 mol% acid groups compared with 31 mol% acrylate groups in the two copolymers. The energy of interaction of two acid groups far outweighs that between two acrylate groups since the acid groups dimerize [7-9].

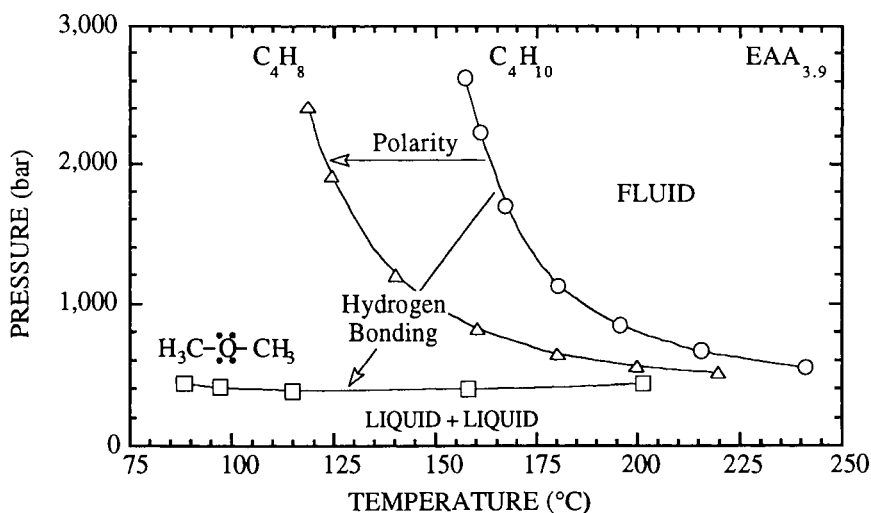


Figure 3. Cloud-point curves for EAA_{3.9} in butane, butene, and dimethyl ether (DME) [3].

If the size of the solvent molecule is kept constant, but polarity is added to it, the cloud-point curve shifts to lower temperatures as shown with butane and butene. In this case butene interacts with the acid groups both through polar interactions and π -acid complexing. Since the interactions are related to the number of groups and the interaction energy, it is likely that the π -acid complex plays a bigger role in shifting the cloud-point curve to lower pressures than does polar interactions because there are so few acid groups. This is not the case with the acrylate copolymers where the concentration of polar groups in the backbone of the copolymer is much higher and butene and methyl acrylate do not form a complex.

Low cloud-point pressures are observed if the solvent is capable of hydrogen bonding to the acid groups in the copolymer. The energy of hydrogen bonding is so strong between an acid and DME that the cloud-point curve is virtually flat at ~ 450 bar over a 125°C range. The cloud-point curve of EAA_{3.9}-DME is shifted by over 2,000 bar relative to those of the C₄ hydrocarbons at moderate temperatures. This indeed is a dramatic example of how the phase behavior shifts as the balance of intermolecular forces changes.

3.3 Poly(ethylene-co-methacrylic acid) (EMAA)-Butane-Cosolvent

Figure 4 shows the impact of ethanol as a cosolvent. Ethanol hydrogen bonds to the methacrylic acid repeat units as well as hydrogen bonding to itself [3,6]. At an ethanol concentration of 15 wt% there are 62 times as many ethanol molecules as compared to methacrylic acid repeat units which suggests that there are more than enough ethanol molecules to saturate the methacrylic acid sites. At 42.4 wt% ethanol, there are now 176 times as many ethanol molecules as compared to methacrylic acid repeat units. The cloud-point curve at this concentration exhibits a sudden increase in pressure at 115°C which suggests that the interchange energy is now dominated by the self association of ethanol that does not favor the formation of a single phase. At 53.5 wt% ethanol the cloud-point curve again exhibits a sudden increase in pressure, but now this pressure increase occurs at 160°C . These two cloud-point curves show that temperature has a large impact on the cloud-point behavior since the temperature will modulate the number of ethanol-acid, acid-acid, and ethanol-ethanol complexes that are formed in solution. The sharp increase in the cloud-point curves results from ethanol-ethanol interactions dominating the interchange energy which promotes the formation of a second phase.

4. CONCLUSIONS

As the amount of polar units in the backbone architecture is increased, copolymer-copolymer polar interactions increase and high temperatures are required to dissolve the copolymer in nonpolar solvents. If the copolymer has a comonomer capable of hydrogen bonding, the solubility in alkane and alkene solvents is dramatically reduced at lower temperatures, where copolymer-copolymer hydrogen bonding is much stronger than other intermolecular interactions. The solubility of copolymers greatly increases in the solvents that

hydrogen bond with the copolymer. In addition, the solubility of a copolymer depends on the temperature which attenuates the specific interactions.

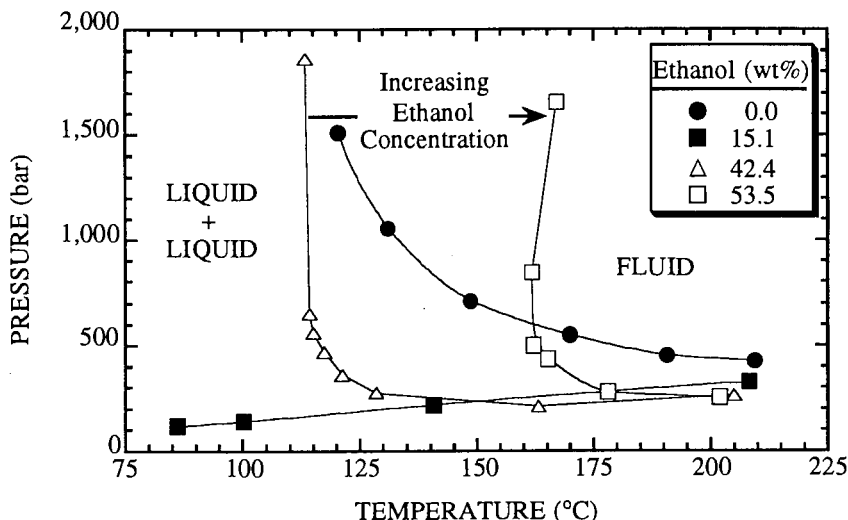


Figure 4. Effect of high concentrations of ethanol on the phase behavior of ~ 5 wt% EMAA_{3.1} in butane [6].

REFERENCES

1. P. Ehrlich and J.J. Kurpen, *J. Poly. Sci.: Part A*, 1 (1963) 3217.
2. R. Koningsveld and A.J. Staverman, *J. Poly. Sci. Part A-2*, 6 (1968) 349.
3. S.-H. Lee, M.A. LoStracco, B.M. Hasch, and M.A. McHugh, *J. Phys. Chem.*, 98 (1994) 4055.; B.M. Hasch,, M.A. Meilchen, S.-H. Lee, and M.A. McHugh, *J. Polym. Sci.: Polym. Phys. Ed.*, 31 (1993) 429; B.M. Hasch, S.-H. Lee, and M.A. McHugh, *Fluid Phase Equilibria*, 83 (1993) 341; M.A. Meilchen, B.M. Hasch, S.-H. Lee, and M.A. McHugh, *Polymer*, 33 (1992) 1922; B.M. Hasch,, M.A. Meilchen, S.-H. Lee, and M.A. McHugh, *J. Polym. Sci.: Polym. Phys. Ed.*, 30 (1991) 1365; M.A. Meilchen, B.M. Hasch, and M.A. McHugh, *Macromolecules*, 24 (1991) 4874; B.M. Hasch, S.-H. Lee, and M.A. McHugh, *J.J. Watkins, and V.J. Krukoni*, *Polymer*, 34 (1993) 2554; M.A. McHugh, *NATO ASI Series E*, Kluwer Academic Publishers, (1994) 599; S.-H. Lee, M.A. LoStracco, and M.A. McHugh, *Macromolecules*, 29 (1996) 1349.
4. R.C. Reid, J.M. Prausnitz, and B.E. Polling, *The properties of gases and liquids*, 4th ed.; McGraw-Hill: New York, 1987; Appendix A.
5. R.L. David, *CRC Handbook of Chemistry and Physics*, 73rd ed.; CRC Press, 1992; Chapter 9.
6. S.-H. Lee and M.A. McHugh, *Polymer*, (1996) in press.
7. M. Buback and F. Mahling, *J. Supercritical Fluids*, 8 (1995), 119.
8. T. R. Earnest, Jr. and W. J. MacKnight, *J. Polym. Sci., Polym. Phys. Ed.*, 16 (1978), 143; *Macromolecules*, 13 (1980), 844.
9. E. P. Otocka and T. K. Kwei *Macromolecules*, 1 (1968), 244.

Hardening of Fats and Oils in Supercritical CO₂

Thomas Tacke, Stefan Wieland and Peter Panster

Degussa AG, Inorganic Chemical Products Division,
Research and Applied Technology Chemical Catalysts and Organosilanes,
P. O. Box 1345, D-63403 Hanau, Germany

ABSTRACT

Selective and complete hardening reactions of fats and oils, free fatty acids and fatty acid esters with hydrogen were carried out continuously in supercritical CO₂ (sc CO₂) with DELOXAN® supported precious metal fixed bed catalysts. Depending on feed and the desired degree of hardening, temperatures between 60 and 160°C, total pressures between 8.0 and 16.0 MPa and space velocities (LHSV) between 5 and 60 h⁻¹ were investigated. We observed up to 6 times higher space time yields in free fatty acid hardening using a DELOXAN® supported 1 wt. % palladium fixed bed catalyst in comparison to trickle bed hardening with an activated carbon supported 2 wt. % palladium fixed bed catalyst. The formation of undesirable products in edible oil hardening (e. g. trans fatty acids) is significantly decreased with a DELOXAN® supported 1 wt. % platinum fixed bed catalyst in sc CO₂.

1. INTRODUCTION

Supercritical fluids (scf) are highly compressed liquids or gases. The latter already have an established role in "clean" extraction (substitution of chlorinated/organic solvents) on an industrial scale (e. g. decaffeination of coffee and tea, extraction of hops, spices, etc.). The specific physical and chemical properties of scf make them particularly suitable for a variety of other applications, e. g. reactions, powder technology and impregnation.

The (i) continuously tunable density of scf, (ii) their high solubilities for solids, liquids and especially for gases (e. g. hydrogen, oxygen), (iii) good heat and mass transfer properties combined with (iv) the chemical inertness of CO₂ and (v) the ease of separation of product and solvent creates new possibilities to perform chemical reactions in such media. The low viscosity, good thermal and mass transport properties of scf make them ideal to be used in flow systems (e. g. homogeneous and heterogeneous catalytic reactions) [1, 2, 3].

The hydrogenation of fats and oils is a very old technology. It was invented in

1901 by Normann. In order to increase the melting point and the oxidation stability of fats and oils, these are selectively hydrogenated. Since the melting point increases during the hydrogenation, the reaction is also expressed as hardening.

Selective hydrogenation of edible oils means for instance, that the carbon-carbon double bonds in position 12 and 15 in *cis*-9, *cis*-12, *cis*-15 octadecatrienoic acid are saturated with hydrogen, whereas the position 9 remains unsaturated.

The melting behavior of the hydrogenated product is determined by the reaction conditions (temperature, hydrogen pressure, agitation, hydrogen up-take). For applications in food industry edible oils are hydrogenated selectively, whereas free fatty acids are completely hydrogenated for oleochemical applications (e. g. detergents).

The reaction mechanism in the selective hydrogenation of edible oils is quite complex. There are several parallel, consecutive and side reactions. Oleic acid (*cis* 18:1) is the desired product when the reaction starts with linolenic (all-*cis* 18:3) or linoleic acid (*cis*, *cis* 18:2). In a *cis*/*trans* isomerization reaction elaidic acid (*trans* 18:1) is formed. From the dietetic point of view elaidic acid is an undesired product. On the other hand, its presence increases in a desirable way the melting point of the product. Stearic acid (18:0) is formed in a consecutive reaction.

The current process has some disadvantages: discontinuous operation, strong hydrogen mass transfer control and low space-time-yields. The nickel on kieselguhr catalyst causes also some problems: undesirable by-products, formation of nickel soaps in free fatty acid hydrogenation and disposal of nickel residues.

To overcome the existing problems with the state-of-the-art technology in edible oil and free fatty acid hardening, we decided to have a look on hydrogenation reactions in *sc* CO₂ using precious metal fixed bed catalysts on acid resistant supports.

2. EXPERIMENTAL

Catalytic tests in *sc* CO₂ were run continuously in an oil heated flow reactor (200°C, 20 MPa) with supported precious metal fixed bed catalysts on activated carbon and polysiloxane (DELOXAN®). We also investigated immobilized metal complex fixed bed catalysts supported on DELOXAN®. DELOXAN® is used because of its unique chemical and physical properties (e. g. high pore volume and specific surface area in combination with a meso- and macro-pore-size distribution, which is especially attractive for catalytic reactions). The effects of reaction conditions (temperature, pressure, H₂ flow, CO₂ flow, LHSV) and catalyst design on reaction rates and selectivities were determined. Comparative studies were performed either continuously with precious metal fixed bed catalysts in a trickle bed reactor, or discontinuously in stirred tank reactors with powdered nickel on kieselguhr or precious metal on activated carbon catalysts. Reaction products were analyzed off-line with capillary gas chromatography.

3. RESULTS AND DISCUSSION

For the complete hardening of free fatty acids in sc CO₂ the optimized reaction conditions were 140°C and 14.0 MPa (H₂ + CO₂). With a DELOXAN® supported 1 wt. % palladium fixed bed catalyst we observed a decrease in the iodine value (IV) for oleic acid from 88.1 g I₂/100 g product to 0.3 g I₂/100 g product at a space velocity (LHSV) of 6.2 h⁻¹. In the trickle bed hardening (170°C, 2.0 MPa H₂) with the same catalyst we observed a decrease in the IV to 42.1 g I₂/100 g product at a LHSV of 5.0 h⁻¹. The hydrogen partial pressures in the trickle bed and scf hardening were comparable.

In the hardening of free tallow fatty acids in sc CO₂ we measured iodine values (IV) below 1 g I₂/100 g product at a space velocity of 15 h⁻¹. In comparison to trickle bed hardening reactions with activated carbon and titania supported 2 wt. % palladium fixed bed catalysts, between 6 to 15 times higher space time yields were determined when the hardening was carried out in sc CO₂. The hydrogen partial pressures in both processes were comparable (2.0 MPa H₂).

Since the hardening is carried out at a lower temperature compared to the conventional processes, the acid value of the fatty acids (as a measure for the selectivity of the reaction) remains at a very high level. In catalyst life time tests we observed a 3 times higher catalyst productivity when using a DELOXAN® supported 1 wt. % palladium fixed bed catalyst compared to the same catalyst in a trickle bed hardening process.

Edible oils and fatty acid esters were selectively hardened in sc CO₂ at temperatures between 60°C and 90°C and at a total pressure of 10.0 MPa. In order to get different degrees of hardening, we investigated activated carbon and different DELOXAN® supported precious metal fixed bed catalysts at space velocities (LHSV) between 5 and 60 h⁻¹.

In Table 1, results for the selective hydrogenation of edible oils in sc CO₂ are shown in comparison to hydrogenation reactions in a discontinuous stirred tank reactor and in a continuous trickle bed reactor. Space-time-yields in discontinuous hydrogenation reactions with powdered nickel on kieselguhr and activated carbon supported precious metal catalysts are smaller than 1 m³ oil/(h x m³ reactor vol.). A large amount of undesired trans fatty acids is formed in the triglyceride molecule as a consequence of strong hydrogen mass transfer control. The continuous hydrogenation with a DELOXAN® AP II supported 1 wt. % palladium fixed bed catalyst in the trickle phase results in a higher space-time-yield. However, the linoleate selectivity as a measure of the non-formation of unsaturated fatty acids is very low. Since especially large amounts of saturated fatty acids are formed, the overall trans fatty acid content remains at a lower level. The increase of the hydrogen partial pressure results in a further increase in space-time-yield. This result indicates, that the reaction is strongly hydrogen mass transfer controlled.

In sc CO₂ the hydrogenation activity is increased even further. Supercritical CO₂ lowers the viscosity of the reaction medium and increases mass transfer and

Table 1 Selective hardening of edible oils in discontinuous stirred tank reactors (STR), continuous trickle bed reactors and in continuous flow reactors operating with supercritical CO₂

20

Catalyst	Process	T [°C]	H ₂ - pressure [bar]	Space-time-yield [m ³ oil/h x m ³ reactor vol.]	Hydrogenation activity [mol H ₂ /h x g active metal]	Linoleate- selectivity [-]	max. trans-fatty acid content [GC area-%]
25 % Ni- kieselgur (powder)	discont. STR/ mass transfer controlled	120	3	< 1	4,1	10,8	40
5 % Pd/C (powder)	"	120	3	< 1	65,4	72,5	60
5 % Pt/C (powder)	"	120	3	< 1	43,1	6,2	37
1 % Pd/Deloxan® AP II	continuous trickle bed	60	5	5	6,3	1,9	20,9
1 % Pd/Deloxan® AP II	continuous trickle bed	60	20	30	28,5	2,1	20,6
0.5 % Pd/C	new continuous fixed bed process	60	100 (H ₂ + CO ₂)	30	9,8	2,9	16
1 % Pd/Deloxan® AP II	"	60	100 (H ₂ + CO ₂)	60	52,3	3	19
1 % Pd/Deloxan® HK I	"	60	100 (H ₂ + CO ₂)	30	13,3	13,1	15,5
2 % Pt/Deloxan® AP II	"	60	100 (H ₂ + CO ₂)	30	3,1	7,8	7,5

diffusivity. This results in a higher hydrogenation activity. In addition the linoleate selectivity is increased.

With an activated carbon supported 0.5 wt. % palladium fixed bed catalyst in sc CO₂ we determined a more than 5 times lower hydrogenation activity compared to the DELOXAN® AP II supported 1 wt. % palladium fixed bed catalyst.

Even though sc CO₂ was used in order to increase mass transfer and diffusivity, the activated carbon supported 0.5 wt. % palladium fixed bed catalyst shows a lower hydrogenation activity compared to the 1 wt. % palladium on DELOXAN® AP II catalyst tested in the conventional trickle bed hardening process. This result indicates the outstanding advantage of DELOXAN® supported precious metal fixed bed catalysts, which can be ascribed to their unique chemical and physical properties.

With a DELOXAN® supported palladium complex catalyst, DELOXAN® HK I, the linoleate selectivity is further increased. In comparison to the commercial batch hydrogenation with a nickel on kieselguhr catalyst, the DELOXAN® supported palladium complex catalyst in combination with sc CO₂ as a solvent gives higher space-time-yields, a higher linoleate selectivity and a significantly decreased cis/trans isomerization rate.

DELOXAN® AP II supported platinum catalysts in sc CO₂ are less active than DELOXAN® AP II supported palladium catalysts, but they show an improved linoleate selectivity and a significantly lower cis-trans isomerization rate. The overall yield of undesirable trans fatty acids is 7.5 GC area-% in the edible oil hardening with a DELOXAN® AP II supported 2 wt. % platinum catalyst. In a batch hydrogenation using the commercial powdered nickel on kieselguhr catalysts the undesirable trans fatty acid content was determined to 40 percent.

4. CONCLUSIONS

The combination of DELOXAN® supported precious metal fixed bed catalysts together with supercritical CO₂ creates new possibilities for continuous fixed bed hydrogenations with significantly improved space time yields and catalyst life times. Short residence times and a well-balanced diffusion and desorption of products and reactants results in a decrease of undesirable by-products and thus higher selectivities.

REFERENCES

- 1 E. Kiran and J. M. H. Levelt Sengers (Editors), Supercritical Fluids, Kluwer Academic Publishers, Dordrecht, The Netherlands, 1994
- 2 Proceedings of the 3rd International Symposium on Supercritical Fluids, Tome 3, Strasbourg, 17 - 19 October 1994
- 3 P. E. Savage et. al., Reactions at Supercritical Conditions: Applications and Fundamentals, AIChE Journal, July 1995, Vol. 41, No. 7., 1723 - 1778

This page intentionally left blank

The Importance of Surfactants for Polymerizations in Carbon Dioxide

D. E. Betts, J. B. McClain, J. M. DeSimone

Department of Chemistry, CB#3290, Venable and Kenan Laboratories - The University of North Carolina at Chapel Hill, Chapel Hill, NC 27599-3290
phone: (919) 962-2166; fax: (919) 962-5467; email: desimone@email.unc.edu

1. INTRODUCTION

Over the past decade, carbon dioxide has become an attractive alternate solvent for a variety of polymer synthesis and processing applications due to its environmentally benign nature and chemical inertness¹⁻³. Properties of CO₂, such as dielectric constant and density are sensitive to the temperature and pressure of the system. The fluid density and dielectric constant, can be fine tuned using temperature and pressure profiling. In addition, CO₂ offers an environmentally sound medium with the potential to eliminate organic and aqueous waste streams in manufacturing facilities.

Although CO₂ dissolves many small molecules readily, it is a very poor solvent for most high molecular weight polymers. Currently, only amorphous or low melting fluoropolymers and silicone polymers are known to be very soluble in CO₂ (T < 100 °C, P < 400 bar), or CO₂-philic, while many industrially important polymers are relatively insoluble. In 1992, we reported the successful homogenous free radical polymerization of a CO₂-philic fluorinated acrylate, 1,1-dihydroperfluorooctyl acrylate (FOA)². Homogenous polymer synthesis in CO₂ is fundamentally limited however, by the extremely low solubility of most polymers at readily accessible conditions.

In order for CO₂ to be an effective continuous phase for polymerizations, heterogeneous reaction systems must necessarily be developed analogous to classical emulsion, inverse emulsion, dispersion, suspension and precipitation polymerization processes. With some highly reactive monomers such as acrylic acid⁴ and tetrafluoroethylene⁵, free-radical precipitation polymerization can afford polymers with high yields and molecular weight. However, many industrial monomers require the utilization of surfactant stabilized reaction conditions². We have reported the utilization of nonionic — homopolymer, block copolymer and reactive macromonomer — surfactants consisting of covalently bound CO₂-philic and CO₂-phobic segments in the dispersion polymerization of various CO₂-insoluble polymers^{2, 6-11}. These reactions produce a stabilized polymer colloid in CO₂ solution and dry, free flowing powders after isolation.

In a study by Consani and Smith, over 140 commercial and commonly available surfactants have been screened for application in CO₂ resulting in only a handful with, at best, minute CO₂-solubility¹². Recent research in various laboratories, including our own, has developed more soluble surfactants active in CO₂ based on the incorporation of CO₂-philic fluorinated and silicone materials^{3,7,13-15}. Herein we describe the effects of various surfactant and stabilizer systems as they apply to polymerizations in CO₂.

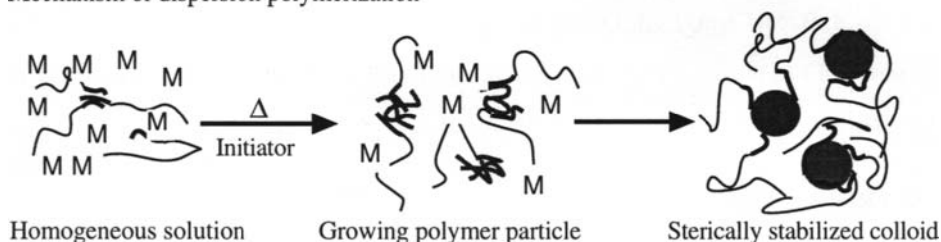
1.1 Mechanism of colloid stabilization: The role of surfactant

The dispersion polymerization of lipophilic monomers in CO₂ is initiated homogeneously with chain collapse into a discrete polymer particle at a critical molecular

weight as shown in Figure 1. The surfactant then stabilizes the polymer particle as a colloid and prevents flocculation through steric stabilization.

Figure 1.

Mechanism of dispersion polymerization



The effectiveness of a given surfactant in the above scheme is governed by two factors; first there must be sufficiently strong anchoring to the polymer particle, second the soluble segment must be chain extended into the continuous phase facilitating a negative steric interaction between particles (e.g. of sufficient solvation and chain length). These factors are controlled in CO_2 polymerizations by synthetic variation of both the composition and architecture of the surfactants in response to different polymer particles and conditions and by control of the density of CO_2 .

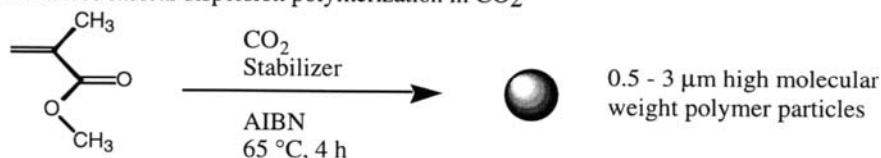
2. DESIGN AND APPLICATION OF SURFACTANTS FOR POLYMERIZATIONS IN CO_2

2.1 Methyl methacrylate polymerization

For the stabilization of various insoluble hydrocarbon polymers in carbon dioxide, it has been found that no one surfactant works well for all systems. Therefore it has become necessary to tailor the surfactants to the specific polymerization reaction. Through variation of not only the composition of the surfactants, but also their architectures, surfactants have been molecularly-engineered to be surface active—partitioning at the interface between the growing polymer particle and the CO_2 continuous phase. The surfactants utilized to date include poly(FOA) homopolymer, poly(dimethylsiloxane) homopolymer with a polymerizable endgroup, poly(styrene-*b*-FOA), and poly(styrene-*b*-dimethylsiloxane). Through the utilization of these surfactants, the successful dispersion polymerization of methyl methacrylate (MMA), styrene, and 2,6-dimethylphenol in CO_2 has been demonstrated.

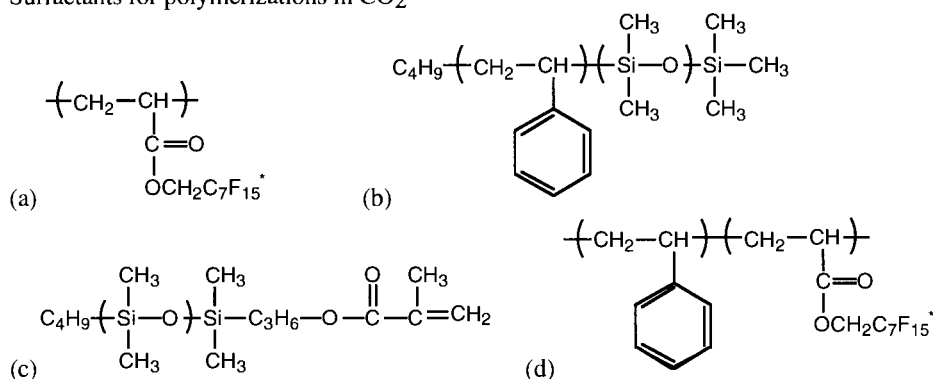
The polymerization of MMA was the first example of a successful dispersion polymerization conducted in CO_2 . The polymerization of MMA in CO_2 was stabilized by the use of poly(FOA) homopolymer and the product was isolated in high yields as a free flowing powder². Scanning electron microscopy (SEM) of the product revealed the product morphology to consist of spherical particles. In contrast, the same reaction conducted in the absence of poly(FOA) stabilizer gives a nondescript morphology in low yields. In the polymerization of MMA, two different molecular weight samples of poly(FOA) were used—a low molecular sample with $M_n \approx 1.0 \times 10^5$ g/mol and a high molecular sample with $M_n \approx 1.4 \times 10^6$ g/mol. In both cases the successful dispersion polymerization of MMA was obtained. The low molecular weight poly(FOA) stabilizer consistently gave smaller sized PMMA particles than the high molecular weight poly(FOA) (Table 1).

Scheme 1.
General free radical dispersion polymerization in CO₂



Methyl methacrylate

Figure 2.
Surfactants for polymerizations in CO₂



(a) Poly(FOA) homopolymer — * the fluorinated alkyl side chain contains ca. 25% CF₃ branches per chain (b) Polystyrene-*b*-PDMS diblock copolymer (c) PDMS macromonomer (d) Polystyrene-*b*-Poly(FOA) diblock copolymer

Table 1.

Results of MMA polymerizations with AIBN as the initiator in CO₂ at 204 bar and 65 °C; stabilizer is either LMW or HMW poly(FOA).

Stabilizer (w/v %)	Yield (%)	$\langle M_n \rangle$ (kg/mol)	PDI ^a	Particle size (μm)
0%	39	149	2.8	—
4% LMW	92	220	2.6	1.3 (± 0.4)
4% HMW	95	321	2.2	2.5 (± 0.2)

^a Polydispersity index of the molecular weight distribution, M_w/M_n .

In addition to studying the effect of the stabilizer molecular weight on the MMA dispersion polymerization, the effect of the stabilizer concentration was also analyzed⁸. The concentration of poly(FOA) stabilizer was systematically varied while the amount of MMA was held constant at 21 w/v % in CO₂ (Table 2). It was found that as little as 0.24 wt. % (based on monomer) is needed to stabilize the polymerization and give spherical particles. Additionally, excess surfactant could be washed from the finished particle surface with CO₂, resulting in

residual surfactant levels of less than 0.5 wt. %. The very low amount of polymeric stabilizer needed for a successful dispersion polymerization attests to the high amphiphilicity and strong anchoring effect of poly(FOA) in the PMMA-CO₂ system.

Table 2.
Effect of the concentration of poly(FOA) (21 w/v % MMA, 4 h)

poly(FOA) (wt %)	Yield (%)	M _n (kg/mol)	PDI ^a	Particle size (μm)	Particle size distribution
0	47	85	3.72	—	—
0.24	86	255	2.40	2.86	1.17
1.2	89	252	2.56	2.08	1.01
4.5	92	316	2.09	2.44	1.02
16	90	293	2.33	1.55, 0.93 ^b	1.08

^a Polydispersity index of the molecular weight, M_w/M_n. ^b PMMA particles exhibit bimodal particle size distribution. Both primary and secondary particle diameters are reported.

Furthermore, it has been found that a commercially available poly(dimethylsiloxane) macromonomer terminated with a polymerizable endgroup can also be used for the successful dispersion polymerization of MMA in CO₂ (Figure 2)⁸. The macromonomer had a number average molecular weight of 1.13×10^4 and a polydispersity index (PDI) of 1.1. Although using a very small amount of PDMS macromonomer in the reaction gave a considerable increase in yield and molecular weight over the reaction done without stabilizer, powdery products comprised of relatively monodisperse particles were only obtained when greater than 3.5 wt. % of PDMS macromonomer was used. In addition, a bimodal particle size distribution was obtained for reactions conducted with less than 3.5 wt. % PDMS macromonomer (Table 3). Again, excess surfactant could be washed from the particle surface with CO₂ and the residual surface coating was less than 0.3 wt. %. In comparison, unfunctionalized PDMS homopolymer (lacking the polymerizable endgroup) was explored as a stabilizer and found to be ineffective. Using 6.8 wt. % PDMS homopolymer with a M_n of 1.33×10^4 and a PDI of 1.1, gave results similar to those obtained when only 0.05 wt. % PDMS macromonomer was used.

Table 3.
Dispersion polymerization of MMA in CO₂^a

Stabilizer	Wt. %	Yield (%)	<M _n > (kg/mol)	PDI ^b	Particle size (μm)
none	0	24	65	3.7	—
PDMS	6.8	51	210	2.5	—
PDMS macromonomer	0.05	56	271	2.4	—
PDMS macromonomer	0.26	67	280	2.1	2.8
PDMS macromonomer	1.7	70	200	2.6	2.8
PDMS macromonomer	3.5	80	383	2.1	2.8

^a Reactions were conducted at 65 °C and 340 bar for 4 h with 2.1 g of MMA and 0.0070 g AIBN. ^b Polydispersity index of the molecular weight distribution, M_w/M_n.

2.2 Styrene polymerization

Although it has been shown that poly(FOA) is an effective stabilizer for the polymerization of MMA in CO₂, it was not an effective stabilizer for the polymerization of styrene in CO₂. This is believed to be due to ineffective anchoring of the stabilizer on the growing polymer particle. To increase the anchoring ability of the surfactants, amphiphilic block copolymers were designed which contained a polystyrene segment to serve as the anchoring moiety and a poly(FOA) or PDMS segment to serve as the steric stabilizing moiety (Figure 2)^{10,11}. The solution behavior of these amphiphilic block copolymers was examined in CO₂ (Table 4). It was found that while many of the polystyrene-*b*-poly(FOA) block copolymers were soluble in CO₂, giving a clear solution, the polystyrene-*b*-PDMS block copolymers were insoluble, giving cloudy dispersions in solution. This is due to the much higher solubility of poly(FOA) in CO₂ than PDMS and hence the ability of poly(FOA) to solubilize larger polystyrene segments. But at the start of a typical dispersion polymerization, with 20 % styrene monomer present, the initial solution is clear and homogeneous since the monomer can act as a cosolvent to help solvate the stabilizer.

Table 4.
Polystyrene block copolymers and solubility in CO₂ as a function of composition

Diblock copolymer <M _n > (kg/mol)	mol % Styrene	Solubility (4% wt/vol)	
		40 °C 340 bar	65 °C 340 bar
PS3.7k -b- PFOA14k	54.0	insoluble	insoluble
PS3.7k -b- PFOA17k	49.4	cloudy	cloudy
PS3.7k -b- PFOA28k	37.0	translucent	cloudy
PS3.7k -b- PFOA40k	28.9	clear	clear
PS3.7k -b- PFOA61k	20.9	clear	clear
PS4.5k -b- PFOA25k	44.5	translucent	cloudy
PS6.6k -b- PFOA35k	45.1	cloudy	cloudy
PS4.3k -b- PDMS25k	10.9	insoluble	insoluble
PS4.3k -b- PDMS65k	4.5	insoluble	insoluble
PS9.6k -b- PDMS24k	22.2	insoluble	insoluble
PS9.6k -b- PDMS64k	9.7	insoluble	insoluble

In this system using a polystyrene containing block copolymer, the polystyrene segment should readily partition into the lipophilic polystyrene particle core while the poly(FOA) or PDMS block is solubilized in the CO₂ continuous phase to provide steric stabilization and prevent coagulation. In comparison of the polystyrene-*b*-poly(FOA) diblock copolymers to the polystyrene-*b*-PDMS diblock copolymers, it was found that the use of a polystyrene-*b*-PDMS stabilizer gives much more monodisperse particles. This most likely arises from the synthetic technique employed in the surfactant synthesis. The blocks in the polystyrene-*b*-PDMS block copolymers have a much narrower polydispersity than the blocks in the polystyrene-*b*-poly(FOA) block copolymers. It was noted that the particles obtained in

this system are much smaller ($< 1 \mu\text{m}$) than the particles obtained in the PMMA-CO₂ system employing poly(FOA) homopolymer as stabilizer ($> 1 \mu\text{m}$) (Table 5).

Table 5.
Results of styrene polymerizations in CO₂

Stabilizer	Stabilizer concn. (w/v %)	yield (%)	M_n (kg/mol)	PDI ^c	Particle size (μm)
^a none	0	22.1	3.8	2.3	—
^a poly(FOA)	4	43.5	12.8	2.8	—
^a PS3.7k -b- PFOA17k	4	72.1	19.2	3.6	0.40
^a PS4.5k -b- PFOA25k	4	97.7	22.5	3.1	0.24
^a PS6.6k -b- PFOA35k	4	93.6	23.4	3.0	0.24
^b PS4.3k -b- PDMS25k	2	90.6	65	3.6	0.22
^b PS9.6k -b- PDMS24k	2	91.7	56	4.3	0.46
^b PS4.3k -b- PDMS65k	2	52.2	21	9.2	coagulated
^b PS9.6k -b- PDMS64k	2	90.9	39	8.1	coagulated

^a Polymerization in CO₂ at 204 bar and 65 °C with 2.0 g styrene and 2.4×10^{-2} M AIBN.

^b Polymerization in CO₂ at 204 bar and 65 °C with 2.0 g styrene and 1.2×10^{-2} M AIBN

^c Polydispersity index of the molecular weight distribution, M_w/M_n .

It was also found that the polystyrene-b-PDMS block copolymers were not only effective at stabilizing styrene polymerizations in CO₂, but also in stabilizing MMA polymerizations. When using a polystyrene-b-PDMS block copolymer as the stabilizer the resulting PMMA was recovered in 94.1% yield with a $M_n = 1.8 \times 10^5$ g/mol and a PDI = 2.8. The particles obtained are much smaller and more polydisperse than the particles obtained when using poly(FOA) homopolymer as the stabilizer (particle size = 1.55 - 2.86 μm vs. 0.23 μm and particle size distribution = 1.05 vs. 1.46).

2.3 Polymerization of 2,6-dimethylphenol

In addition to being a good stabilizer for the polymerization of styrene in CO₂, polystyrene-b-poly(FOA) block copolymers were also found to be successful stabilizers of poly(2,6-dimethylphenylene oxide), (PPO), in CO₂¹². Polystyrene and PPO are miscible with each other and so the polystyrene block is anchored to the polymer particle by blending with the PPO while the poly(FOA) block is solvated and provides steric stabilization. It can be seen in comparison to other stabilizers, that the use of polystyrene-b-poly(FOA) leads to a higher yield and a higher molecular weight. Although polystyrene-co-poly(FOA) random copolymer gave higher yields, the product obtained is of a very low molecular weight. Conversely, the molecular weight increased while the yield decreased upon the use of poly(FOA) homopolymer as the stabilizer. The polystyrene-b-poly(FOA) diblock copolymer was the most effective stabilizer for the synthesis of poly(phenylene oxide) in CO₂ as it gave both high yields and high molecular weights (Table 6).

Scheme 2.
Polymerization of PPO in CO₂

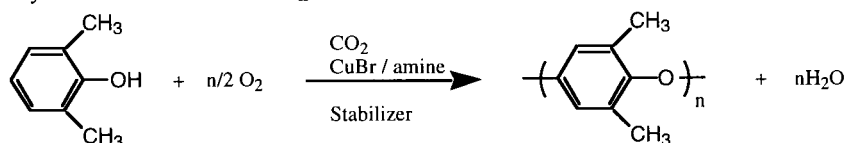


Table 6.
Results of phenylene oxide polymerizations in CO₂^a

Stabilizer	Stabilizer concn. (w/v %)	Yield (%)	M _n (kg/mol)	PDI
none	0	67	6.1	1.6
PFOA	2.8	50	8.7	1.6
PS4.5k -b-PFOA25k	2.8	74	17.2	5.8
PS-co-PFOA ^b	2.8	83	3.0	2.8

^a Polymerization conditions: 345 bar, 40 °C, 20 h, using a copper:amine:monomer ratio of 1:22:75 with pyridine as the amine. ^b 46.3% styrene : 53.7% FOA

3. CHARACTERIZATION OF SURFACTANTS IN CO₂

Small angle neutron scattering (SANS) has been employed in the characterization of both CO₂-philic homopolymers and self assembled polystyrene-*b*-poly(FOA) surfactant molecules in CO₂.^{14, 15} Experiments were preformed at the W. C. Koehler 30 m SANS spectrometer at the Oak Ridge National Laboratory.¹⁶ Utilizing SANS we are able to determine the weight average molecular weight (M_w), the radius of gyration (R_g), and the second virial coefficient (A_2) of solvated macromolecules. We also determined the degree of aggregation and characteristic dimensions of surfactant molecules in a micelle.

Dilute concentration series of two different molecular weight samples of PFOA were analyzed over a range of temperatures and pressures (40 °C < T < 65 °C and 340 bar < P < 395 bar). A_2 values were found to be positive, indicating that supercritical CO₂ is a thermodynamically good solvent for PFOA over these conditions. The radius of gyration was found to be 110 Å for the high molecular weight sample ($M_w \approx 1.4 \times 10^6$ g/mol) and 35 Å for the low molecular weight sample ($M_w \approx 1.1 \times 10^5$ g/mol). Analysis was preformed on 1.3×10^4 g/mol PDMS and 1.6×10^4 g/mol poly(hexafluoro propylene oxide), Krytox[®], at similar conditions finding that CO₂ is a poor solvent for PDMS and approximately a Theta (Θ) solvent for Krytox[®].

A series of block copolymers were studied by SANS in which the CO₂-philic PFOA block length was varied (16,600 < M_n (g/mol) < 61,100) and the CO₂-phobic polystyrene block was held constant ($M_n = 3,700$ g/mol). Fitting of the scattering curves to a core shell model predicts spherical structures with an average degree of association of 7 surfactant molecules per micelle. This value was constant for the series of materials as would be expected

for surfactants with the same insoluble or 'core' segment. The total radius, however, increases smoothly (80 to 100 Å) with the increasing soluble or 'shell' segment length.

4. CONCLUSIONS

Polymerization of industrially important monomers can be realized in CO₂ with the application of logically designed surfactant technology. The binding segment of the surfactants has been tailored to specific growing polymer particles. Both chemical binding and physical absorption have been displayed as mechanisms for stabilization of polymer colloids during synthesis. The synthesis of commodity and engineering plastics in environmentally benign CO₂ could facilitate the removal of tremendous amounts of aqueous and organic waste in the chemical process industry.

REFERENCES

- (1) McHugh, M. A.; Krukonis, V. J. *Supercritical Fluid Extraction-Principles and Practice*; 2nd ed.; Butterworths-Heinemann: Stoneham, Boston, 1993.
- (2) DeSimone, J. M.; Maury, E. E.; Menciloglu, Y. Z.; McClain, J. B.; Romack, T. J.; Combes, J. R. *Science* **1994**, *265*, 356.
- (3) Johnston, K. P.; Harrison, K. L.; Clarke, M. J.; Howdle, S. M.; Heitz, M. P.; Bright, F. V.; Carlier, C.; Randolph, T. W. *Science* **1996**, *271*, 624.
- (4) Romack, T. J.; Maury, E. E.; DeSimone, J. M. *Macromolecules* **1995**, *28*, 912.
- (5) Romack, T. J.; Treat, T. A.; DeSimone, J. M. *Macromolecules* **1995**, *28*, 8429.
- (6) DeSimone, J. M.; Maury, E. E.; Combes, Y. Z.; Menciloglu, Y. Z. *Polym. Prepr. (Am. Chem. Soc. Div. Polym. Mat. Sci. Eng.)* **1993**, *68*, 41.
- (7) Guan, Z.; DeSimone, J. M. *Macromolecules* **1994**, *27*, 5527.
- (8) Hsiao, Y.; Maury, E. E.; Johnston, K. P.; Mawson, S.; DeSimone, J. M. *Macromolecules* **1995**, *28*, 8159.
- (9) Shaffer, K. A.; Jones, T. A.; Canelas, D. A.; Wilkinson, S. P.; DeSimone, J. M. *Macromolecules* **1996**, *29*, 2704.
- (10) Canelas, D. A.; Betts, D. E.; DeSimone, J. M. *Macromolecules* **1996**, *29*, 2818.
- (11) Canelas, D. A.; Betts, D. E.; DeSimone, J. M. *Polym. Prepr. (Am. Chem. Soc. Div. Polym. Mat. Sci. Eng.)* **1996**, *74*, 400.
- (12) Kapellen, K. K.; Mistele, C. D.; DeSimone, J. M. *Macromolecules* **1996**, *29*, 495.
- (13) Consani, K. A.; Smith, R. D. *J. Supercrit. Fluids* **1990**, *5*, 51.
- (14) Fulton, J. L.; Pfund, D. M.; McClain, J. B.; Romack, T. J.; Maury, E. E.; Combes, J. R.; Samulski, E. T.; DeSimone, J. M. *Langmuir*, **1995**, *11*, 4241.
- (15) McClain, J. B.; Londono, J. D.; Combes, J. R.; Romack, T. J.; Canelas, D. A.; Betts, D. E.; Wignall, G. D.; Samulski, E. T.; DeSimone, J. M. *J. Am. Chem. Soc.* **1996**, *118*, 917.
- (16) Koehler, W. C. *Physica (Utrecht)* **1986**, *138B*, 320.
- (17) Barrett, K.E. J.; *Dispersion Polymerization in Organic Media*, Wiley: London, 1975.
- (18) Napper, D. H.; *Polymer Stabilization of Colloidal Dispersions*, Academic Press: London, 1983.

Integration of Indirect Electrochemistry and Separation by Supercritical Fluids

U. Leffrang, U. Galla and H. Schmieder

Forschungszentrum Karlsruhe, Institut für Technische Chemie, Bereich Chemisch-Physikalische Verfahren, P.O. Box 3640, D - 76021 Karlsruhe, Germany

1. INTRODUCTION

Many industrial wastewaters and landfill leachates are contaminated with organic pollutants, which are biologically persistent. Due to the low concentration levels, the removal of such effluents by incineration is not favourable. Therefore, an integrated method is under development at our institute to extract organic pollutants in a first step with supercritical fluids (especially CO₂) and to further destroy them in a second step by an indirect electrooxidation process.

The same combination of supercritical fluid extraction (SFE) and mediated electrooxidation (MEO) has an application potential for synthesis of organic compounds. In an industrial scale one limiting factor for the efficiency of the production of organic compounds is the amount of by-products. With the novel integrated method the selectivity of the desired reaction can be influenced and so the space-time-yield enhanced.

2. EXPERIMENTAL METHODS

2.1. Mediated Electrooxidation (MEO)

A principle advantage of electrochemistry can be found in the ecological benefit by using a non-polluting redox species, the electrical current, so that possible emissions of additional chemicals can be avoided.

It is known from former publications that by the use of some transition metals in the highest oxidation state organic substances can be oxidized to a useful reaction product (synthesis) (1, 2) or oxidized totally to CO₂ (waste destruction) (3-5). In a procedure using indirect electrooxidation, the organic substance (pollutant or reactant) is brought in contact with an aqueous phase, where the oxidizing agent is continuously produced by anodic oxidation. The oxidant finally reacts with the organic substance to the desired products. During reaction the redoxmediator is reduced, stays in the electrolyte and can be anodically oxidized again so that a closed cycle is formed (see Figure 1).

Mediated Electrooxidation has a wide range of applications caused by the use of different mediators. Mediators with higher standard potential (Ag²⁺ / Ag⁺: E₀ = 1.98 V, Co³⁺/Co²⁺: E₀ = 1.81 V) are mainly used for the total oxidation in waste management (3 - 5). For our

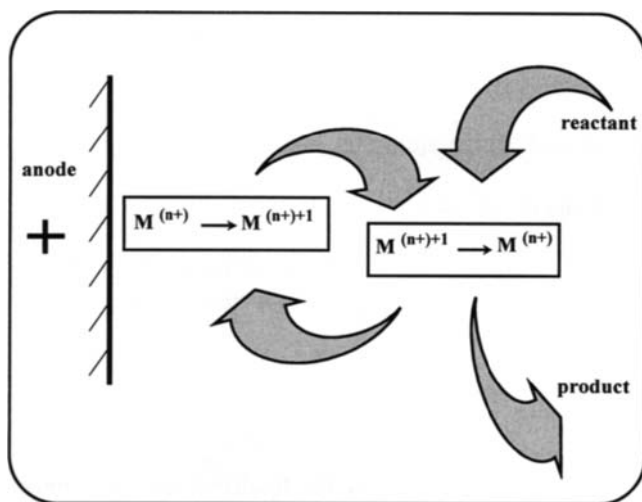


Figure 1. Principle of Mediated Electrooxidation

experiments in waste destruction we chose Co^{3+} as oxidation agent because of the high redox potential of the $\text{Co}^{3+}/\text{Co}^{2+}$ redox couple and its property to be produced with great current efficiencies in electrolytic cells, which do not need a cell diaphragm (6). The behaviour of a cell diaphragm under high pressure conditions is not yet investigated. No insoluble cobalt chlorine compounds are known so that no precipitations must be handled like in the case of silver as mediator.

Mediators with lower standard potential (Ce, Mn, sometimes Co) are mainly used in selective organic synthesis (1, 2). We chose Ce^{4+} ($E_0 = 1.61 \text{ V}$) as oxidation agent to avoid total combustion to CO_2 and because of the large solubility of its salts in aqueous solutions.

2.2. Supercritical Fluid Extraction (SFE)

Separation by supercritical fluids is characterized as well by a large ecological benefit. In our case we use the property of various gases to change their solvent power for different organic substances in dependence of temperature and pressure. The solubility for organic substances in CO_2 under ambient conditions is very low and increases with density. At the critical point (for CO_2 : $P_c = 73 \text{ bar}$; $T_c = 31 \text{ }^\circ\text{C}$; $\rho_c = 0.466 \text{ g/cm}^3$) and above the solvent power achieves values of „classical“ solvents and is tuneable by variation of pressure and temperature. Therefore supercritical CO_2 can be used as a substitute for „classical“ solvents like chlorinated hydrocarbons or hexane. The transport properties like viscosity or diffusivity are favourable (7). CO_2 is non flammable, non toxic, environmentally compatible and can be easily separated (expansion step). Supercritical CO_2 has applications for the extraction of organic pollutants from organic contaminated solids or liquids (8, 9) and as a solvent for organic synthesis (10).

3. DESCRIPTION OF THE METHOD AND APPARATUS

3.1. Integration of SFE and MEO for Synthesis

In our institute a novel method is under development to integrate mediated electrooxidation and supercritical fluid extraction for synthesis of organic compounds. Figure 2 shows the principle of this combination

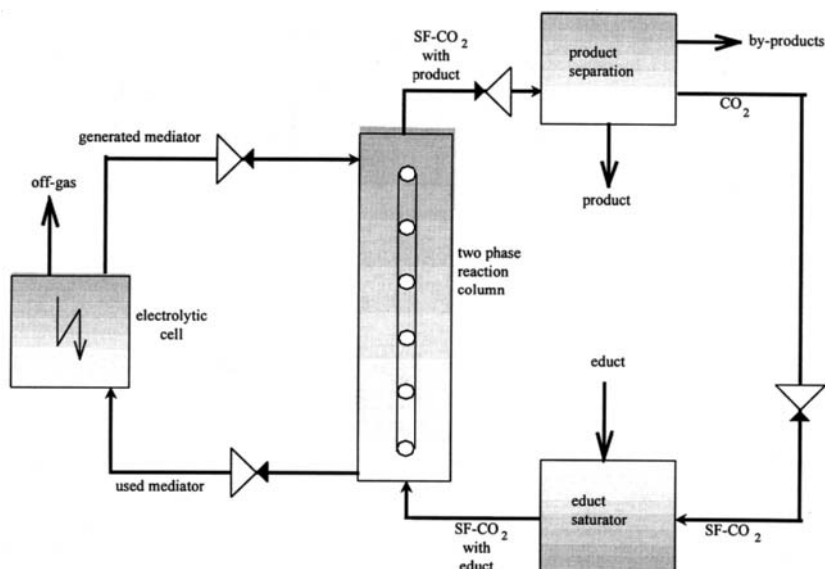


Figure 2. Principle of integration of SFE and MEO for synthesis

With regard to an economically beneficial synthesis an organic reactant is dissolved in supercritical CO₂ and brought in contact with the aqueous electrolyte in a two-phase reaction column. The mediator, dissolved in the electrolyte, oxidizes (or reduces) the reactant to the desired product. In an ideal case the formed product stays in the SF-CO₂ phase, leaves the column with the CO₂ and can be isolated in an expansion step. The electrolyte is recycled outside the pressure apparatus in a conventional electrolytic cell. Electrolysis gases and CO₂ dissolved in the electrolyte leave the apparatus from the electrolytic cell.

The flexibility of this apparatus is rather large. The electrolyte composition as well as the supercritical fluid itself can be varied. Different types of reactions can be investigated: oxidations and reductions with either the supercritical fluid or the aqueous electrolyte being the continuous phase. Residence time is variable in a wide range by varying the density of the supercritical fluid and the height of the column. The apparatus is designed for a single drop method, so that experiments regarding mass transfer can be performed.

Selectivity can be enhanced by changing the mediator (redox couple and electrolyte composition) and by varying the residence time. The apparatus can be used up to a pressure of

350 bar and a temperature up to 90°C. The mediator concentration amounts 0.1 - 0.5 M in 0.5 - 3 M sulfuric acid. Due to the high corrosivity of the electrolyte, especially under high pressure conditions, all parts of the apparatus, which are in contact with the electrolyte, are made of titanium. Figure 3 shows a piping and instrumentation diagram of the apparatus.

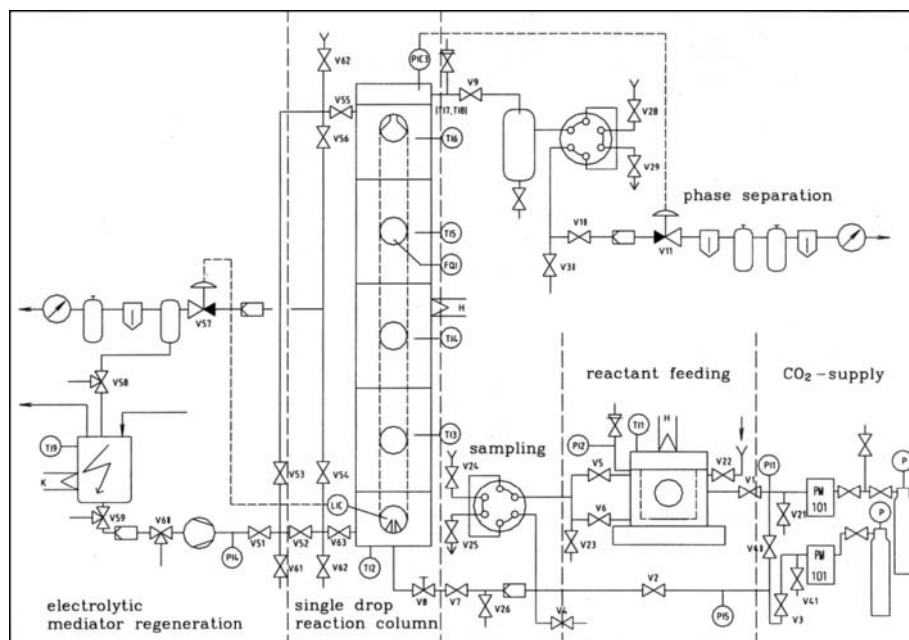


Figure 3. Piping and instrumentation diagram of combination for synthesis

First experiments show for the sidechain oxidation of toluene to benzaldehyde and the oxidation of naphthalene to naphthoquinone by cerium the principal applicability of this method.

3.2. Combination of SFE and MEO for Waste Destruction

With regard to waste destruction organic contaminated liquids or solids can be extracted with supercritical CO₂. The organic pollutant is dissolved in the CO₂ and can be decomposed by indirect electrooxidation under the same conditions. Figure 4 shows the principle of this method.

As a benefit the product of the electrooxidation process is CO₂ and can be used, after separation of excess CO₂ and other gaseous reaction products, for the extraction procedure. A pressure cell has been constructed, where the CO₂ loaded with the organics is contacted with the electrolyte containing the oxidation agent, so that the pollutants can be destroyed by oxidation. Figure 5 shows the piping and instrumentation diagram of this apparatus.

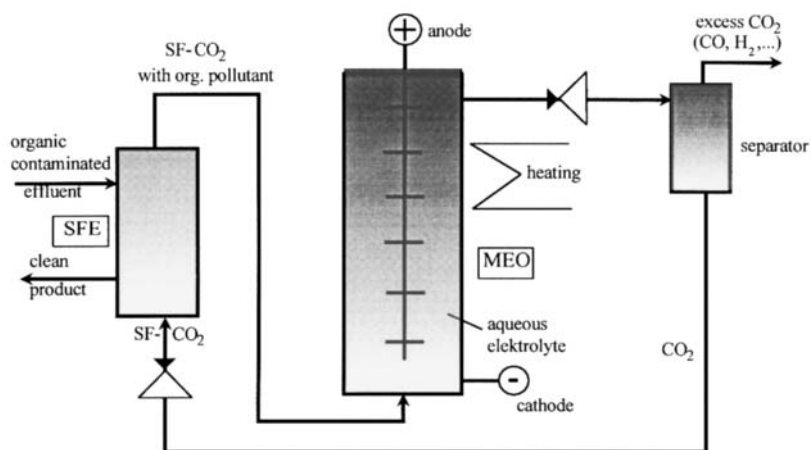


Figure 4. Principle of integration of SFE and MEO for waste destruction

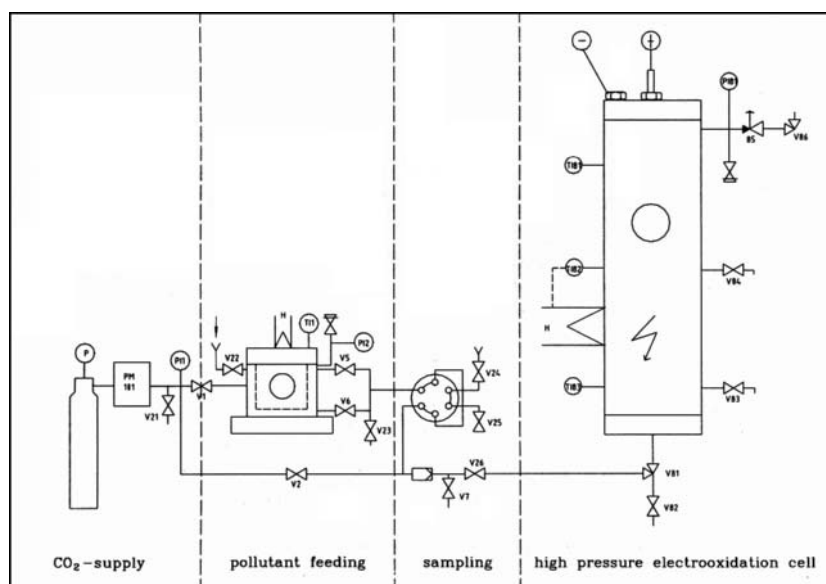


Figure 5. Piping and instrumentation diagram of combination for waste destruction

The apparatus is designed for a pressure up to 350 bar and a temperature up to 90 °C. The electrolyte composition is 0.5 M cobaltsulphate in 3 M sulfuric acid. Due to the high corrosivity of the electrolyte the apparatus is made of titanium as well.

The regeneration of the electrolyte is carried out within the high pressure cell. The casing is used as cathode, a platinated central bar with additional sieve plates as anode. The function of these installations is to form an effective dispersion between the supercritical CO₂ phase and the aqueous electrolyte phase. Current density ranges up to 100 mA/cm², the cell voltage amounts 3 - 5 V.

Up to now SFE is simulated by a saturating unit, where organic model substances can be dissolved in supercritical CO₂ and decomposed in the high pressure electrolytic cell by the mediator. CO₂ recycling has not been established yet.

4. SUMMARY

A novel combination of two non-polluting engineering steps has been demonstrated: mediated electrooxidation (MEO) and supercritical fluid extraction (SFE). The combination has an application potential for waste destruction and organic synthesis. A small apparatus has been constructed for each application.

In case of organic synthesis the electrolyte recycling is performed outside of the pressure apparatus, in case of waste destruction inside of the apparatus.

REFERENCES

1. P. Vaudano, E. Plattner and C. Comninellis, *Chimia* 49 (1995) 12.
2. N. Ibl, K. Kramer, L. Ponto and P. Robertson, *AIChE Symp. Ser.* 75 (185) (1979) 45.
3. J. C. Farmer, F. T. Wang, P. R. Lewis and L. J. Summers, *TransIChemE Symp. Ser.* 70B (1992) 158.
4. D. F. Steele, J. P. Wilks and W. Batey, 1992 Incineration Conference, Thermal Treatment of Radioactive, Hazardous Chemical, Mixed and Medical Wastes (1992) 167.
5. J. Bringmann, K. Ebert, U. Galla and H. Schmieder, *J. Appl. Electrochem.* 25 (1995) 846.
6. U. Leffrang, K. Ebert, K. Flory, U. Galla and H. Schmieder, *Separation Science and Technology* 30(7-9) (1995) 1883.
7. M. A. McHugh and V. J. Krukonsis, *Supercritical Fluid Extraction*, Butterworths, London 1986.
8. G. Brunner, *Chemie Ingenieur Technik* 59(1) (1987) 12.
9. N. Dahmen, J. Schön, H. Schmieder, *Chemie Ingenieur Technik* 67 (1995) 1501.
10. G. Kaupp, *Angew. Chem.* 106(14) (1994) 1519.

CSTR-System for Kinetic Investigation for Hydrogenation Reactions

Andreas G. Zwahlen^a and Alberto Bertucco^b

^a F. Hoffmann - La Roche AG, High Pressure Centre, CH-4070 Basel, Switzerland

^b Istituto Impianti Chimici, Università di Padova, via Marzolo 9, I-35131 Padova PD Italy

ABSTRACT

For design, scale-up, optimisation and control of a commercial reactor it is essential to have accurate kinetic data at hand. In the past, hydrogen reactions in the fine chemicals and pharmaceutical production were carried out with powder catalysts and in a batch mode. Due to more economic and environmental constraints, the application of continuous fixed bed reactors will become more important in the future. It is therefore necessary to have a system for finding the optimal catalyst as well as to study the kinetics of the reaction free of mass transfer and other disturbing effects. The reactor system can be used for hydrogenations with and without solvents, or with supercritical CO₂ as a solvent. Emphasis will be in particular on the reactor design as such, the control strategies, and the necessary peripherals will be described in detail. The suitability of this system has been extensively tested with the model hydrogenation reaction of methyl-cinnamate in methanol and with an intermediate for the production of vitamins with CO₂ as solvent.

1 INTRODUCTION

Hydrogen reactions play an important role in the production of fine chemicals, vitamins and pharmaceutical products. In recent years continuous reactors rather than the traditional batch reactors are becoming more interesting.

For the economic analysis, the design and scale up of commercial reactor systems it becomes more important to use modern mathematical modelling tools and therefore it is necessary to get more insight into the macro kinetic aspect as well as the understanding of the behaviour of the phase equilibrium. As well for investigating the aspects of choosing the optimal catalyst it is necessary to have a suitable technology available.

In the past, laboratory batch reactors (which are still our workhorses) with powder catalysts were applied and somehow showed their limitations with pellet catalysts.

Differential internal recycle reactors have become important tools in recent years for the investigation of catalytic processes and a number of such reactors have been reported in literature with the main emphasis on the actual reactor design [1,2]. In this work a similar reactor, which has been developed by the main investigator for gas-phase reactions under low pressure and high temperature, where it proved its suitability, is described. [3]

Recycle reactors working at high internal recycle ratios approximate differential conditions on the catalyst bed quite well and therefore can be treated as a CSTR, where the production rate of each organic reactant j can be calculated from a mass balance by:

$$r_j = \frac{F}{W_{cat}} (w_j - w_{jF}) / MW_j \quad (1)$$

Where : r_j = production rate of component j in $[\text{mol}/(\text{h g}_{cat})]$, F = feed mass flow rate; W_{cat} = mass of catalyst; w_j, w_{jF} = weight fraction of component j in the outlet and feed stream, respectively, MW_j = molecular weight of component j .

2 EXPERIMENTAL SYSTEM

In order to apply this reactor principle to a multi-phase system such as hydrogenation reactions and under high pressure, further development of the reactor and relevant peripheral components had to be tested with special emphasis of the control strategy.

The system was developed to perform two types of operating modes for commonly encountered hydrogenation reactions in the production of fine chemicals and pharmaceuticals.

- Hydrogenation with pure substrate and/or diluted with conventional solvents, the so-called classic method
- Hydrogenation using supercritical CO_2 as a solvent

The relevant components and control loops are shown in Figure 1.

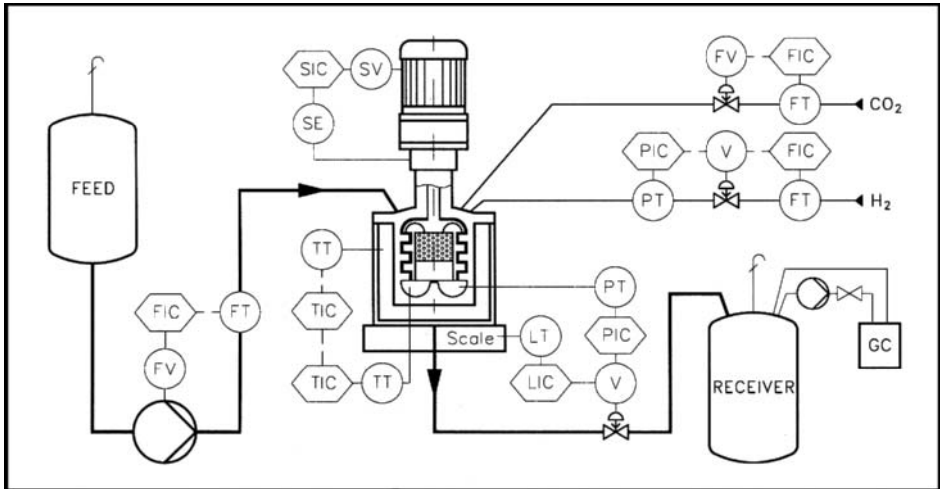


Figure 1: P & I Diagram of the Experimental System for both Types of Operating Modes

All relevant measurements such as temperature, pressure and flow rates were continuously controlled and data acquired with a Eurotherm Control System TCS 100/1000. The liquid feed was supplied from the feed tank using a (Lewa) membrane pump (max. 25 l/h at 300 bar). The hydrogen flow was controlled by a (High-tech Bronkhorst) flow controller - all the other flows were measured by Rheonik flowmeters. The reactor temperature was heated by means of an electrical heater (2 kW) using a thyristor and cooled using a separate cooling coil with water/glycol as a cooling medium. The temperature was kept constant by a cascaded control arrangement between 0 and 300 °C. The revolution of the turbine was controlled between 100 and 4500 RPM. Samples were taken at the outlet of the reactor and periodically analysed with an on-line GC (Siemens).

2.1 Preliminary Tests

In order to check the suitability of such a system under reaction conditions a number of preliminary tests were carried out using the hydrogenation of methyl-cinnamate as model substance.

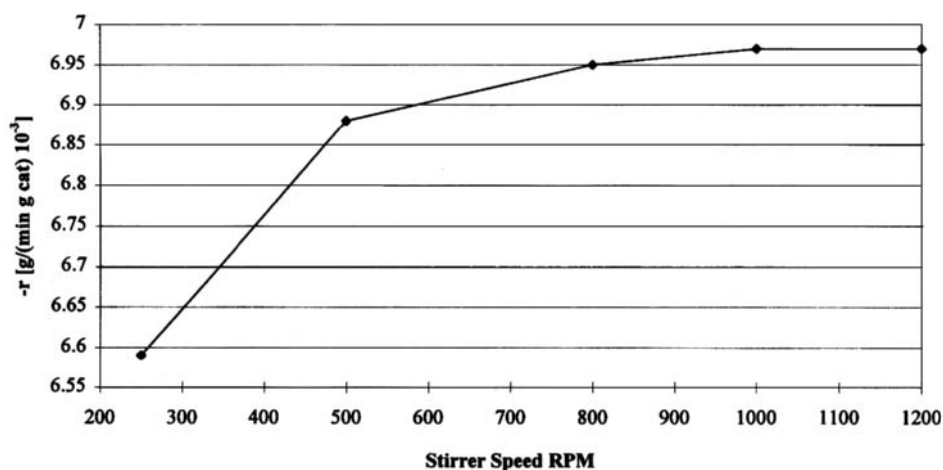


Diagram 1: Reaction Rate as a Function of Stirrer Speed

Diagram 1 shows the influence of the stirrer speed on the reaction rate. This was done in order to ensure the absence of external mass transfer limitations. Stirrer speed above 1000 RPM showed no influence on the reaction rate anymore. Investigations below that speed show mass transfer limitations and will be of interest for further studies.

Diagram 2 shows the influence of the degree of filling, that means the ratio of substrate to active catalyst sites. With this test it was ensured that all the active sites on the catalyst were wetted and in use. Investigation below 180 g would only utilise part of the catalyst and therefore would be meaningless.

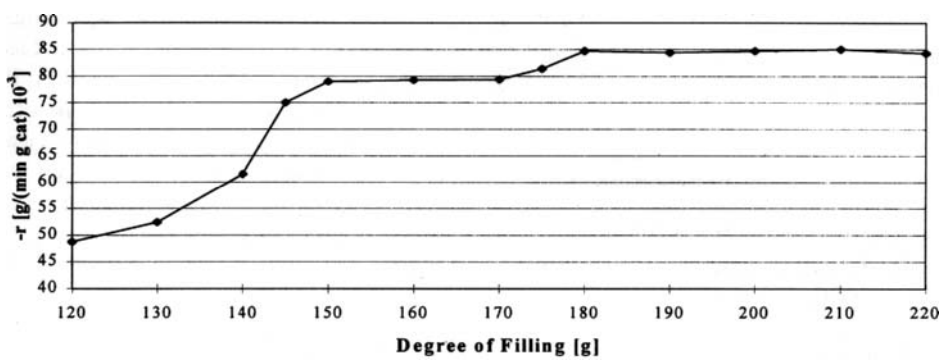


Diagram 2: Reaction Rate as a Function of the Degree of Filling

2.2 Hydrogenation using the classic method

In this mode the amount of the substrate was controlled by massflow controllers and the pressure by the inlet of the hydrogen. The amount of substrate in the reactor at any time was measured by an overall weight balance.

In order to keep the amount of substrate (or virtual level) constant in a three phase system, the whole reactor was placed with flexible tubing on a Mettler scale with a special resolution of 0.1 g. This signal was used as the input to the weight (level) controller. The substrate feed was kept at a constant value by controlling the feed pump.

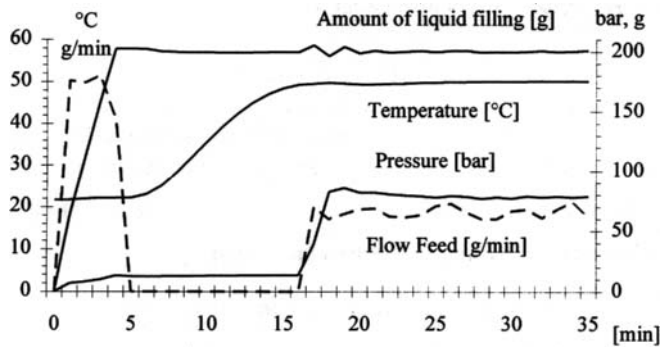


Diagram 3: Results of the Relevant Control Loops of the Classic Hydrogenation

Diagram 3 shows the reactor system under non-reactive conditions using ethanol as a test substance with a feed rate of 20 g/min, pressure 80 bar, temperature 50 °C. In the first 6 minutes the reactor was filled by the feed pump to the desired degree of filling. After that the heating control was switched on, reaching the desired temperature after another 12 min, then the feed flow and pressure control were activated. Under these conditions the reactor reached a steady state after a total time of 20 min.

2.3 Hydrogenation using CO₂ as a solvent

In a second stage the suitability of the reactor system was tested for hydrogenations using supercritical CO₂ as a solvent. This operating mode required another control strategy, where all the mass flows to the reactor were controlled separately. The pressure was maintained by valve in the exit line. Experiments were carried out using an intermediate from the production of vitamin at F. Hoffmann-La Roche AG.

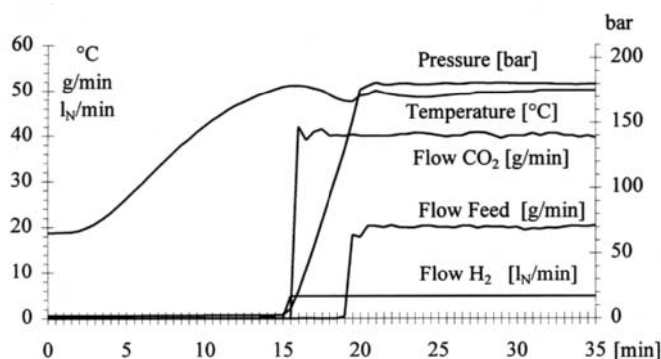


Diagram 4: Results of the Relevant Control Loops for the Hydrogenation with CO₂

3 RESULTS OF KINETIC EXPERIMENTS

The operating methods were tested with two relevant model reaction. The kinetic data obtained were fitted to simple power-law models as well as more complicated ones and parameters estimated by the least-square method, activation energies and volumes could be determined and an adequately accuracy in the reproduction of experimental results was always achieved.

3.1 Kinetics of the classical Method

Experiments were carried out hydrogenating a 5 % (weight) methyl-cinnamate in methanol solution as a model substance on a commercial catalyst. The temperature range was between 50 - 150 °C, the pressure between 20 - 100 bar, the feed flow rate 10 - 150 g/min, the catalyst mass 5 - 67 g and the amount of filling was kept at 200 g. The following power-law model (2) for the rate of disappearance of methyl-cinnamate represented the data well; the influence of pressure in this region was small and therefore neglected:

$$-r = k_0 \exp\left(-\frac{E_A}{RT}\right) \omega_E^{m_E} \quad (2)$$

were $\omega_E^{m_E}$ represents the amount of methyl-cinnamate (g/g) of the reaction mixture, with a frequency factor $k_0 = 385.1 \text{ g}^{(1-0.587)}/(\text{min g cat})$, activation energy $E_A = 16.6 \text{ kJ/mol}$, and an apparent reaction order of $m_E = 0.59$, the correlation coefficient of the parameter estimation was 0.9747

3.2 Kinetics with CO₂ as a Solvent

Experiments were carried out hydrogenating two double-bonds of an unsaturated ketone, an intermediate in the production of vitamins, with a commercial catalyst. The temperature range was between 150 - 220 °C, the pressure between 120 - 175 bar, the feed flow rate of the unsaturated ketone at 30 g/min, the feed flow rate of CO₂ of 15 - 100 g/min, the feed flow rate of hydrogen 2.2 - 6. l_N/min and a catalyst mass of 10 - 30 g. Results incorporating more sophisticated models with emphasis on the calculation of the phase equilibrium have been employed and are reported separately in [4].

4 CONCLUSION

The experimental system developed has proven its applicability for kinetic studies as well as for testing the catalyst in the development of commercial high pressure processes and is extremely useful for the fundamental understanding of these types of reactions. The results reported showed that kinetic data at high pressure can be measured with a high reproducibility accurately and can be regressed accurately by means of kinetic models with different degree of complexity. Even though the system was developed for hydrogenation reactions, it can be used as well for a variety of other multi-phase reactions.

5 ACKNOWLEDGEMENTS

The authors are very grateful to J. Harwalik, Fachhochschule Furtwangen for the contribution of process automation, and to T Kircher, Fachhochschule Aalen and L. Devetta, Universita di Padova for their contribution in applying this system for kinetic studies. As well, many thanks to all the members of VFH at F. Hoffmann La-Roche AG for their invaluable help, namely R. Bernauer, B. Kern, H. Kleisner, Dr. F. Roessler, P. Rindisbacher and R. Zimmer.

6 REFERENCES

1. Berty J.M. 20 Years of Recycle Reactors in Reaction Engineering; Plant/Oper. Prog., 1984, 3, 163-168.
2. Tiltscher H., Schelchshorn J., Wolf H., Dialer K., Differential Recycle Reactors for Investigation of Heterogeneous Systems at High Pressures and Temperature; Ger. Chem. Eng. 313-320.
3. Zwahlen A. G., Agnew J. Modification of an Internal Recycle Reactor of the Berty Type for Low-Pressure High Temperature Catalytic Gas-Phase Reaction; CHEMECA 1987, I, 50.1-50.7, Melbourne, Australia.
4. Bertuccio A, Canu P., Devetta L., Zwahlen A.G.; Catalytic Hydrogenation in Supercritical CO₂: Kinetic Measurement in a Gradientless Recycle Reactor, Submitted for publication in Industrial and Engineering Chemistry Research, April 1996

Hydrogenation of Fats and Oils at Supercritical Conditions

Magnus Härröd^a and Poul Møller^b

^a Chalmers University of Technology, Department of Food Science,
c/o SIK, PO Box 5401, S-402 29 Göteborg, Sweden

^b Marselis Boulevard 38¹⁴, DK-8000 Aarhus C, Denmark

1. INTRODUCTION

1.1 The traditional process

Ever since W. Normann in the beginning of the century invented his process for hydrogenation of fats and oils, it has mainly been performed in the original way, i.e. in a batch reactor where the oil, hydrogen and the catalyst as a slurry are mixed intensively. Alternatively, the loop reactor by Buss AG and some continuous systems have been in operation.

The purpose of the hydrogenation is to create the desired melting profile and texture of the oils, before they can be used for production of margarine or shortening. Due to the hydrogenation, the oils become less sensitive to oxidation and their stability increases [1]. The annual production of hydrogenated oils is about 25 million tons [2, 3].

In nature almost all double bonds in fatty acids are *cis*-bonds. During hydrogenation another kind of double bond is formed, the *trans*-bond. From a medical point of view the *trans*-fatty acids are seriously questioned [4].

The half hydrogenation theory [5, 6] predicts that, the higher the hydrogen concentration at the catalyst, the lower the formation of *trans*-fatty acids. The theory has been verified by many experiments [e.g. 7, 8].

The low solubility of hydrogen in oils [9] and the transport-resistances in the gas/oil/catalyst interface restrict the reaction rates and cause the high content of *trans*-fatty acids [10]. Much research has been focused on development of new catalysts and new reactor designs. However, the success has been limited [1].

1.2 The new process

For the first time ever, we have succeeded in radically overcoming the solubility problem and the transport-resistances for the hydrogen. We can control the concentration of hydrogen at the catalyst surface almost unlimitedly.

We use a solvent miscible with both oil and hydrogen, thus forming a substantially homogeneous phase to pass the catalyst surface. The solvent is near-critical or supercritical propane. The oil does not prevent the hydrogen from entering the pores of the catalyst anymore.

By adding propane to the reaction mixture, we have attained extremely high reaction rates, up to 1000 times higher than with the traditional technique. These results occur when the whole mixture of propane, oil and hydrogen is in a supercritical or near-critical state.

These reaction rates are very important to the process economy for both full and partial hydrogenation of triglycerides.

At partial hydrogenation of triglycerides, the traditional process gives high amounts of *trans*-fatty acids. Oils with *trans*-fatty acid concentrations acceptable from medical point of view can be produced using our new process [11].

2. METHODS

2.1. Products

We have hydrogenated triglycerides (TG) and fatty acid methyl esters (FAME).

2.2. Equipment

A flow sheet for the continuous reactor used is shown in Figure 1. Below we will several times refer to the abbreviations in this figure.

The amounts of hydrogen and oil were controlled according to known principles [12]. Propane, hydrogen and oil were mixed at room temperature (see M). The mixture was heated to the desired reaction temperature and brought into an HPLC tube filled with a catalyst powder (see Temp and reactor). After the reactor samples were collected from the high pressure section using an HPLC valve (see A and [13]). The pressure was reduced to atmospheric pressure (see P), and the oil and the gases were separated (see Sep). Finally, the gas flow was measured (see F). This flow, mainly propane, was controlled by a pressure-reduction valve (see P).

2.3. Analytical methods

The product quality was analysed using silver-ion-HPLC and gradient elution [14]. This method was developed from an isocratic method [15]. The kind (*cis* / *trans*) and the amount of the FAME was determined. From these data the iodine value (IV) was calculated.

The densities of hydrogen and propane are required to control the mixing and to estimate the reaction times. The densities were calculated from the Peng-Robinson equation of state [16].

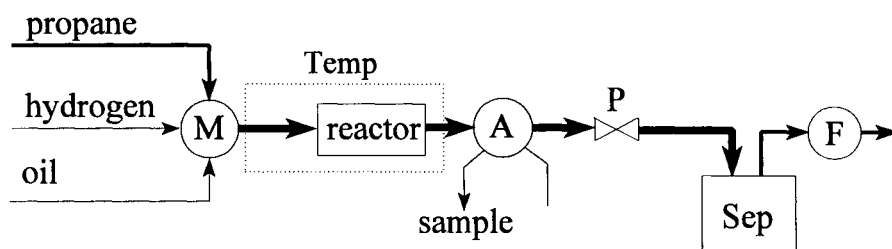


Figure 1. Flow sheet for the reactor used.

M. Mixer

A. Sampling-valve for analyses

Sep. Separation gas / oil

Temp. Temperature control

P. Pressure reduction valve

F. gas flow-meter

3. RESULTS AND DISCUSSION

3.1. Optimized conventional hydrogenation process

The concentration of *trans*-fatty acids has recently been minimized for the conventional hydrogenation process. When they used the same catalyst as we did, 5%Pd on carbon, their productivity of partly hydrogenated triglycerides became 700 kg / m³ h and the concentration of *trans*-fatty acids became 34% at 60 °C and 7 bar. The IV was 67.5 [8].

3.2. Hydrogenation at supercritical conditions

The results from our initial study are illustrated in Table 1 and in Figure 2.

We have attained a tremendous productivity of completely hydrogenated FAME, 700 000 kg / m³ h (see, e.g. Table 1 exp. 2). With this productivity, a reactor volume of 3 m³ is enough to cover the worldwide production of hydrogenated oils!

The tremendous reaction rates we have attained are primarily due to the substantially homogeneous phase surrounding the catalyst. The kind of catalyst is a secondary question.

We have attained a very high productivity for full hydrogenation of FAME both using a commercial palladium catalyst (see Table 1, exp.2) and a commercial nickel catalyst (see Table 1, exp.3). We have also attained a high productivity for full hydrogenation of triglycerides (see Table 1 exp.4).

For partial hydrogenation, we have managed to reduce the *trans*-fatty acid concentration to 15%, and still maintain a very high productivity, 80 000 kg of FAME / m³ h, (see Table 1 exp.1).

However, the degree of hydrogenation decreased with time. The decrease was mainly related to the amount of processed oil. This phenomenon is illustrated in Figure 2. During an experiment, samples were taken and analysed by HPLC. The compositions of the samples are shown on the y-axis. The x-axis represents the amount of oil that had passed the catalyst.

In the experiment illustrated in Figure 2, the composition of the FAME at the reactor inlet was as follows: 8.7% saturated; 66.2% *cis*; 14.6% *cis+cis*; and 10.5% *cis+cis+cis*. This composition gives an iodine value (IV) of 109.

When the catalyst was fresh, the IV at the reactor outlet was about 50. At the end of this experiment the IV had increased to 85. The increase was due to a decrease in the saturated FAME and an increase in the *cis* FAME. The *trans* and poly *cis* FAME concentrations were roughly constant at 15% and 5%, respectively. (see Figure 2)

In our experiments the life time of the palladium-catalyst was similar to the life time attained in traditional industrial reactors (about 50 kg oil / g Pd).

3.3. Development

At present, intensive research is done to find optimal reaction conditions (concentration, temperature, pressure, flow rate, lifetime of catalyst, etc....) for different catalysts.

Table 1.
Hydrogenation of oils (TG or FAME) at near-critical or super-critical conditions.

Exp. no	Reaction Mixture				Reaction Conditions						Product Quality	
	Propane w%	Oil w%	Hydrogen w%	IV ^a	Catalyst	Volume μl	Time ms	Temp. °C	Pressure bar	Productivity kg _{product} / m ³ _{reactor} h	IV ^a	trans %
1	99.7	0.26 ^b	0.002	110	Pd ^d	7	40	50	120	80 000	70	15
2	95.7	4.16 ^b	0.140	110	Pd ^d	7	80	90	70	700 000	< 1	< 0.1
3	99.13	0.85 ^b	0.017	110	Ni ^e	9	65	190	155	90 000	< 1	< 0.1
4	93.6	6.30 ^c	0.043	140	Pd ^d	2500	12 000	50	100	5 000	0.1	< 0.1

a Iodine value

b Fatty methylesters from rapeseed oil

c A commercial vegetable oil, i.e. triglycerides

d 5% Pd on activated carbon (E 101 O/D 5% Degussa AG)

e Nickel (Ni-5256 P, Engelhard)

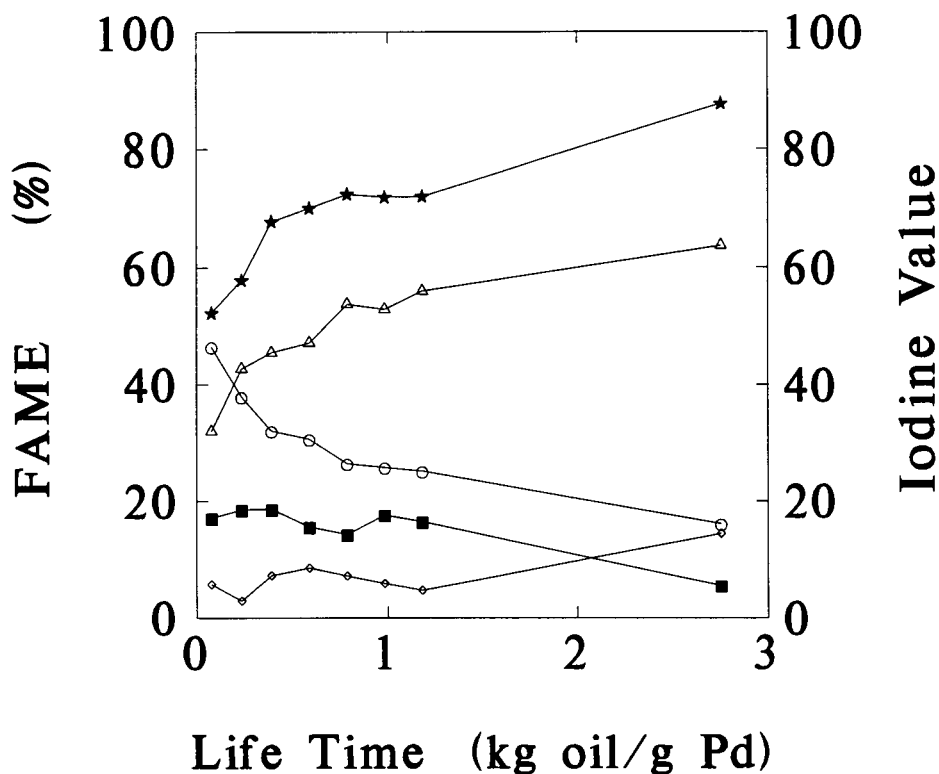


Figure 2. Product composition at the reactor outlet as a function of the amount of FAME processed and the amount of Pd in the reactor.

The reaction conditions were the same as those presented in exp.1 in Table 1.

★ Iodine value; ■ *trans*; ◇ *poly cis*; △ *mono cis*; ○ saturated

4. CONCLUSIONS

With the new supercritical hydrogenation technique:

- the productivity was very much higher (roughly a factor 1 000 higher) than ever attained using the traditional hydrogenation technique.
- the concentration of *trans* fatty acids was considerably reduced compared to conventional processes using the same catalyst and the same degree of hydrogenation.
- the consumption of catalyst was similar to the consumption using traditional techniques.

REFERENCES

1. Hui Y. H., 1996, *Bailey's industrial oil and fat products*, Vol.4, 5th ed., Wileys, New York
2. Mielke S., 1992, *INFORM*, 3(6), 695-696
3. Fitch Haumann B., 1994, *INFORM*, 5(6) 668-678
4. Wahle K.W.J., W.P.T James 1993, *European J. Clinical Nutrition*, 47, 828-839
5. Allen R.R., A.A. Kiess 1955, *J.Am.Oil Chem.Soc.*, 32(July), 400-405
6. Allen R.R., 1986, *J.Am.Oil Chem.Soc.*, 63(10), 1328-1332
7. Hsu N., L.L. Diosady, L.J. Rubin 1989, *J.Am.Oil Chem.Soc.*, 66(2), 232-236
8. Berben P.H., P.J.W. Blom and J.C. Sollie 1995, In *Proceedings of AOCS meeting, May 1995*
9. Wisniak J., L.F. Albright 1961, *Ind. Eng. Chem.*, 53(5), 375-380
10. Grau R.J., A.E. Cassano, M.A. Baltanás 1988, *Catal. Rev. -Sci. Eng.*, 30(1), 1-48
11. Härröd M., P. Möller 1995, *PCT patent application*, PCT / SE95 / 00824
12. Pickel K.H. 1991, In *Proceedings of 2nd international symposium on supercritical fluids.* (ed McHugh M.) Johns Hopkins University, Baltimore, MD, p.457.
13. Härröd M., I. Elfman 1995, *J.Am.Oil Chem.Soc.*, 72(6), 641-646.
14. Elfman I., S. van den Hark, M. Härröd 1996, *J.Am.Oil Chem.Soc.*, Accepted
15. Adlof R.O. 1994, *J.Chromatogr. A*, 659, 95-99.
16. Dohrn R. 1994, *Berechnungen von Phasengleichgewichten*, Vieweg, Braunschweig /Wiesbaden, Germany

Application of RESS to Several Low Molecular Weight Compounds

P. Subra^a and P. Debenedetti^b

^aLaboratoire d'Ingénierie des Matériaux et des Hautes Pressions, Institut Galilée, Université Paris XIII, Avenue Jean-Baptiste Clément, 93430 Villetaneuse, France

^bDepartment of Chemical Engineering, Princeton University, Princeton, New Jersey 08544, United States

1. INTRODUCTION

The rapid expansion of supercritical solutions (RESS) has been explored recently as a novel route for the production of small and monodispersed particles (1-2). Particle formation involves nucleation, growth and agglomeration. In RESS, nucleation is induced by a rapid decompression; growth and agglomeration occur within the expanding solution. The thermodynamics of the supercritical mixture influences the relative importance of these mechanisms, and thus play a key role in sizes or size distribution of final particles.

This experimental work explores selected RESS conditions - preexpansion pressure, concentration and postexpansion temperature- upon the particle size of the products. Four compounds were processed in order to assess the general trends of the experimental conditions upon the particle size.

Some properties of the solutes investigated are given in Table 1. The morphologies are the ones obtained by crystallization from solution (3). Characteristic peaks of the X-Rays (2θ) are also reported.

Table 1
 Properties of solutes

compound	formulae	MW	morphology	X-Rays angle	T _m
caffeine	C ₈ H ₁₀ N ₄ O ₂	194.2	nd, hex. pr	12;26;27	238
salicylic acid	2-OHC ₆ H ₄ COOH	138.1	nd, mcl. pr	10;16;24;27;28	159
anthracene	C ₁₄ H ₁₀	178.2	ta, mcl. pr	9;18;20;24;25	215
theophylline	C ₇ H ₈ N ₄ O ₂	180.2	nd, pl	6;11;13;22-29	274

T_m=melting temperature (°C); nd=needle; hex.pr=hexagonal prism; mcl.pr=monoclinic prism; ta=tablet; pl=plate

2. APPARATUS

The apparatus has been previously described (4). The dissolution column consists of a stainless steel tube (2.54cm O.D x 30 cm length), packed with 1g of solute mixed with glass beads ($d = 3\text{mm}$). The column operates in parallel with a by-pass line; two regulating valves at the outlets adjust the flow rates coming from the two lines (column and by-pass) allowing to dilute the solute concentration up to a dilution ratio of 8. The supercritical solution then enters into a high pressure chamber (Ruska Cell 2329-800; 100cm^3) through a thermostated stainless tube at the end of which a silica capillary is held in place. A feedback-controlled cable heater is wrapped around the section, allowing a control over the preexpansion temperature (T_p) and preventing the solvent condensation and freezing during the expansion. When the solution flows through the expansion capillary, it experiences a rapid decompression which results in precipitation of the solute. The solute is then deposited in a glass beaker inside the expansion chamber, whose pressure (P_e) and temperature (T_e) are respectively controlled with a micrometric valve, and by immersion in a cooled ethylene glycol bath. Particles are observed by optical or scanning electron microscopes (ZEISS microscope and JEOL JSM-840; samples coated with gold-palladium) and cristallinity is monitored through the use of a powder X-Rays diffraction (Scintag Inc., PAD-5).

3. SOLUBILITY AND RELATION WITH THE PROCESS

In RESS, nucleation is induced by the reduction of pressure that occurs when the mixture is expanding through the nozzle. However, depressurization may not be the only driving force of nucleation. Since the supercritical mixture is overheated to counterbalance expansion cooling, the temperature may also induce nucleation. These two driving forces occur when experimental conditions correspond to a decrease in solubility upon heating, therefore in the retrograde region of solubility. The relation between trends in particle size observed experimentally and the evolving of the solubility -i.e. the solute concentration- vs pressure and temperature has been unequivocally shown through the modeling of the aerosol formation by Kwauk and Debenedetti (5).

Except for theophyllin, the solubilities are similar: at a dissolution temperature (T_d) and a dissolution pressure (P_d) of 65°C and 250bar, respectively, the mole fractions are of $2.5\text{e-}4$ for anthracene, $5\text{e-}4$ for caffeine and $6.5\text{e-}4$ for salicylic acid. Theophyllin is an order of magnitude lower, with a value of $0.2\text{e-}4$. The mole fractions allow one to estimate the maximum production rate for the experimental set up. Assuming a recovery of produced particles of 100%, and no dilution required for processing, the production rates are 1.0 , 1.2 , 0.5 and 0.04 g/h for caffeine, salicylic acid, anthracene and theophyllin, respectively (conditions: $P_d = 220\text{bar}$, $T_d = 65^\circ\text{C}$, capillary $= 1.5\text{cm} \times 75\mu\text{m}$; flow rate of liquid $\text{CO}_2 = 11.2\text{ml/min}$)

From solubility curves, it is shown that caffeine exhibits the distinguishing feature of a wide retrograde behavior (cross over pressure of 240bar), while the retrograde region of the other compounds is narrower (170bar). Since the experimental set up imposes the pressure limit, operating above the cross over pressure was not always possible. Indeed, many processing difficulties (plug of the capillary originating unsteadiness of flow and of the expansion chamber temperature) occurred frequently with caffeine and salicylic acid, and especially when the diameter of the capillary was of 50micron. To limit these drawbacks, it was necessary to dilute the mixture or to use a higher capillary diameter (75micron, or 150micron for a convergent nozzle in the apparatus at LIMHP). The dilution ratio can be varied depending the pressure, in order to investigate separately the role of the pressure or the mole fraction on the produced particles.

4. RESULTS AND DISCUSSION

4.1. Particle size

Experimental conditions and size of produced particles are given in Tables 2 and 3. Other parameters were fixed as follows: capillary length= 1.5cm; Preexpansion temperature=92°C; Pressure of expansion chamber= 15bar. Y is the mole fraction of the solute ($\times 10^{-4}$), C.D. the capillary diameter (micron) and particle sizes are expressed in micron.

Modelling of the aerosol formation predicts that the particles produced in partial expansions are small, in the submicron range (5-6). However, experimental size are usually larger, indicating that growth or agglomeration occur within the free jet. Indeed, the temperature of the expansion chamber was found to be a sensitive parameters: runs #105/140, #104/137 for anthracene, #147/149/148 for caffeine, #130/131 for salicylic acid show that the lower the temperature, the smaller are the particles.

The effect of pressure is illustrated through runs #137/138, or #104/105, or #106/108 for anthracene, #76/78/80 or #85/147/159 for caffeine, #122/123 or 134/135 for salicylic acid. An increasing pressure leads to a decreasing size of particle, whether the solute concentration in the fluid is kept constant or varies with the pressure. In order to investigate the respective role of the pressure or the mole fraction on the particle size, further experiments and computational works are currently performed.

Regarding anthracene particles formed in the range of 140bar (run#104), one can see agglomerated structures and particle of 2 μ m thickness. When the pressure is increased, agglomeration still exists (#105), unless the temperature of the expansion chamber is lowered (#138,139). With the of 50 μ m capillary, the morphology of caffeine changes from needle to a curved filament by increasing the pressure (#76/78/80); none of the runs performed with the 75 μ m capillary had led to similar morphology. A filament morphology was obtained for

salicylic acid (#123). Experimental conditions were in the same range as for caffeine, except for the higher concentration and the capillary of 75 μ m.

Table 2.

Conditions and results of Anthracene and Caffeine experiments.

run	Td	Pd	Te	Y	Morphology distribution		d/L	C.D
Anthracene								
104	42	142±2	68±2	0.4	tablets^	large	<30/ 4-50	75
105	42	216±2	78±1	0.7	thin tablets^	large	<10/ 1-15	75
140	43	220±3	46±1	0.7	tablets	medium	<7/ 1-7	75
μparticles								
138	62	215±5	26±4	0.4	μparticles	narrow	<3 / 3	75
137	63	148±4	36±2	0.4	tablets^	large	<12/ 1-20	75
139	62	215±5	31±2	1.0	tablets	narrow	<10/ 1-10	75
μparticles								
106	42	216±3	63±3	0.4	tablets*	large	<14/ 2-20	50
108	42	272±8	58±5	0.4	tablets	narrow	<2/ 2-10	50
μparticles								
Caffeine								
85	42	105±5	47±5	0.1	needles	large	<1.2/ 3-62	75
147	42	150±5	52±2	0.8	needles	UN	<0.6/ 2-12	75
159	42	217±6	52±2	0.7	needles	narrow	<0.8/ 1-6	75
76	46	151±7	55±9	0.4	needles^	large	<0.8/ 2-13	50
78	43	182±6	55±5	0.4	filament	UN	<0.4/ UN	50
80	43	223±6	45±5	0.4	filament	UN	<0.3/ UN	50
149	42	153±8	67±3	0.8	needles	UN	<0.6/ 2-12	75
148	43	148±8	82±6	0.8	needles	large	<1.2/ 5-24	75
96	42	144±2	73±7	0.4	needles	medium	<0.2/ 2-57	75

* from optical microscope- ^agglomeration- UN=undefined

large distribution= many particles of larger size - narrow= only few particles of larger size

In the pressure range of 150bar, and crystallization temperature of 50°C (#121,122), salicylic acid needles exhibit a secondary structure of small appendix.. From optical microscope observations, some needles also branch out and form long structures of 320 μ m and diameter of 4 μ m. Appendices or branches seem to be related to a high temperature in the crystallization unit in conjunction with low pressure, since they disappear when other conditions are set. On the other hand, they are specific to this compound since none of the solutes exhibits such structures in similar experimental conditions.

Theophyllin shows a singular behavior with pressure: from 150 to 215bar

(#111/112) the morphology changes from needles to very thin bands, despite an increase in concentration. Similar trend is observed from 220 to 300bar (#115/118), where branch structures of similar dimensions than the skeleton are seen.

Table 3.

Conditions and results of Salicylic acid and Theophyllin experiments.

run	Td	Pd	Te	Y	Morphology	distribution	d/L	C.D
Salicylic acid								
121	44	155±9	48±3	0.7	needles	large	<5/10-80	75
					appendix			
122	45	143±3	51±1	2.3	needles	large	<8/10-60	75
					appendix		1/5	
123	45	214±3	49±4	2.3	filament	UN	<3.5/ UN	75
134	63	150±9	28±4	2.2	needles*	UN	<1/30	75
135	63	218±4	28±6	2.2	needles*	UN		75
128	43	223±2	36±2	2.3	needles*	large	<4/ 2-55	50
130	45	287±8	36±2	2.5	needles*	medium	<4/ 2-65	50
131	76	282±2	4±1	>8	needles*	narrow	<2/ 2-20	50
Theophyllin								
111	45	150±9	65±2	<0.07	needles	medium	<0.9/ 4-12	75
112	42	215±5	66±2	0.07	band	UN	<4/ <20	75
113	61	210±9	57±2	0.12	needles	UN	<0.9/ <10	75
115	65	225±9	47±2	0.12	needles	UN	0.4/ <10	50
116	85	300±10	18±5	0.19	band^	UN	<1.2/ UN	50
					branch			
118	65	300±10	39±5	0.13	band^	UN	<0.9/ UN	50
					branch			
119	77	205±5	28±5	0.14	needles	UN	1-2/<8	75

4.2. Crystallinity

Crystallinity was checked by comparing X-Rays diffraction patterns of the products and feed. Measurements were performed directly on the material collected on the slide held in the crystallization unit. For caffeine, the filament structure gives only a weak major peak and a broad band between the 2θ values of 18 and 32, indicating some disorder compared to the crude sample. Needles morphology does not provide necessarily the complete x-rays pattern. No correlation was found between experimental conditions and the lack of minor peaks. Furthermore, when the slide was overloaded with material collected from the beaker sides, most of the peaks were detected. So the lack of minor peaks may be most likely due to insufficient quantity of material but can also represent a partial loss of crystallinity for a specific material. Similar trends were

observed for salicylic acid. Anthracene always exhibited the complete x-rays pattern. Since very little material was usually collected for theophyllin despite a run time of 2 to 3 hours, crystallinity was checked once (#112). Surprisingly, the pattern exhibited different peaks compared to the feed product; this may be related to the unusual band morphology obtained. Further investigations are required to draw precise conclusions.

5. CONCLUSION

The RESS process leads easily to 1-10 micron-sized particles; larger particles (80micron) can also be produced, but size distributions are quite larger. Except for theophyllin for which insufficient information was obtained, caffeine, salicylic acid and anthracene behave similarly. For ease of processing, a 75 micron capillary is preferable to a 50 micron one because it allows a higher solute concentration without plugging, and hence increases the production rate. Small particles obtained at a dissolution pressure of 280bar with a 50 μ m capillary can be advantageously produced at lower pressures (220bar range with the 75 micron capillary) provided a low expansion temperature (30°C range) is maintained. Theoretical and computational work aimed at interpreting the above results is in progress.

REFERENCES

1. P. Debenedetti, J. Tom, X. Kwauk and S.-D. Yeo. *Fluid Phase Equilibria*, 82, (1993) 311
2. P. Subra. *Ann. Chim. Fr.*, 20, (1995) 305
3. N. Lange. *Handbook of Chemistry*, 9th Edition, Handbook Publishers Inc., Sandusky, Ohio USA (1956)
4. J. Tom, P. Debenedetti and R. Jerome. *J. Supercritical Fluids*, 7, (1994) 9
5. X. Kwauk and P. Debenedetti. *J. Aerosol Sci.*, 24 (1993) 445
6. H. Ksibi. Thesis of University Paris 13, Paris (1995)

Wet Oxidation of Organics under near Critical Conditions

E. Pongratz^a; S. Peter^a; G. Härtel^b; C. Freese^b

^aFriedrich-Alexander-University of Erlangen-Nürnberg, Department of Technical Chemistry II, Egerlandstr. 3, 91058 Erlangen, Germany

^bFreiberg University of Mining and Technology, Department of Environmental Process Engineering, Leipziger Str. 28, 09596 Freiberg, Germany

1. INTRODUCTION

The formation of residual waste-water is unavoidable in many manufacturing processes. When the dissolved organic substances are toxic or hard to decompose biologically, a decomposition of these substances by oxidation is of interest. The decomposition of organic residual matter by hydrothermal oxidation was first proposed and investigated by Modell [1,2]. Due to the high critical pressure of water and the high temperatures necessary to suitable reaction rates, the operation pressure exceeds 25.0 MPa. These hard conditions cause severe corrosion problems, especially when the substances to be decomposed contain halogens. Therefore, there is some interest in looking for methods of corrosion prevention under the conditions of hydrothermal oxidation. In this connection, the objective of the investigations should also deal with the question for a suitable catalyst, which allows for reduction of temperature and pressure.

2. EXPERIMENTAL PROCEDURE

2.1. Wet-Oxidation

The set up used in this study was a laboratory-scale, continuous-flow reactor system. Solution and oxidizing agent were pumped by metering pumps to a mixing cross beneath the tube reactor. The flow rates of both were digitally displayed by a mass flow meter assembly. A pre-heater assembly was used only for heating the pressurized feed solution. Hydrogen peroxide as oxidizing agent was pumped in at ambient temperature to minimize the self-disintegration before being mixed with the waste-water stream. In order to maintain a constant pressure signal, two pulsation absorbers were installed directly behind the pumps. After reaction the effluent was cooled in a first heat exchanger below 470 K before passing the back-pressure valve and a second heat exchanger. The gas flow was vented after a sample was collected. The liquid phase was split into the streams of effluent and partial reflux. All parameters such as temperatures or flow rates were indicated in the control station and registered by a personal computer.

After circulating the prepared feed solution to stabilize flow rates and temperatures, the oxidizing agent was added. The temperature after mixing, which was equivalent to the reaction temperature at the reactor inlet was measured by a thermocouple placed within the mixing

cross. Temperatures in the middle and at the end of the reactor were also registered within the reaction solution. At these same positions samples were taken. The maximum flow rate was about 18 l/h corresponding to a residence time of 1 minute. The reactor-tube had an inner diameter of 14.5 mm and a length of 180 mm corresponding to a global reactor volume of 300 ml.

Three samples were collected for each measuring point. The integral standards as COD (Chemical Oxygen Demand) and TOC (Total Organic Carbon) were determined. The oxidized product was analyzed using gaschromatographic techniques. The pH-value of the liquid reactant and samples was registered by a pH-meter at the end of pipe. Hydrogen peroxide in a concentration of 35 wt.% and a nitrogen/oxygen-mixture (60:40 vol.%) were used as an oxidizing agents. Phenol, 4-chlorphenol, pyridine and aniline were used for the experiments.

2.2. Corrosion Experiments

In addition to the organic compounds, waste water contains dissolved salts. This causes severe corrosion problems under conditions of operation in the near-critical region of water. The corrodibility of different materials in contact with waste water and oxidizing agents was investigated at temperatures up to 573 K and pressures up to 15 MPa. Furthermore, the applicability of appropriate inhibitors for corrosion protection was studied under mentioned conditions of wet oxidation.

For these investigations the metallic samples were fixed in cylindrical autoclaves and installed in an insulated block which was thermostated by electric heating. The autoclaves were kept in a continuous motion throughout the experiment. Thereby a steady contact of the material samples with the gas as well as the liquid phase of the reaction fluid could be maintained. After an operation time of two or three weeks at constant temperature the autoclaves were opened, the samples were weighed, visually examined and a part of them analyzed. The residual samples were put back in the autoclaves for further treatment.

For better judgement of corrosion and, respectively, the corrosion inhibition, REM photographs of the sample surface were taken. An energy-disperse analysis gives information about the chemical composition of the surface layer. The material samples were made out of building-steel St 1203 and V2A-high-grade steel 1.4541.

3. RESULTS AND DISCUSSION

The basic idea was to carry out the oxidation in an alkaline regime to minimize the corrosion potential of the reaction solution. This offers the possibility to use common materials e.g. as high-grade steel or carbon steel. Furthermore to use hydrogen peroxide as oxidizing agent due to its easier handling in comparison with oxygen, its great oxidation potential and its ability to form peroxo-radicals. The nitrogen/oxygen mixture as oxidizing agent was used to compare the activity with hydrogen peroxide.

3.1. Wet Oxidation

3.1.1. Model substances

Aqueous solutions of phenol, 4-chlorphenol, pyridine and aniline were used as examples for studying the performance of the set up. In addition to that, a general view of the hydrothermo-

lytical oxidation process should be obtained. The influence of pH-value and temperature on the course of reaction was investigated. As the enhancement of the pH of the reacting system may possibly reduce the corrosion rate, its influence on reaction rate is of great interest. Figure 1 shows as example 4-chlorophenol and COD decomposition at pH 3 and pH 9 as a function of residence time at 300°C and 10.0 Mpa.

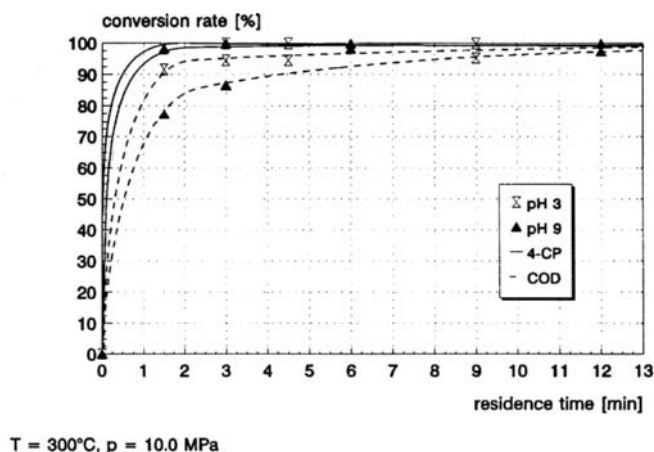


Figure 1. Decomposition of 4-chlorophenol by oxidation at pH 3 and pH 9

The influence of the pH-value on the decomposition of 4-chlorophenol is not very significant, whereas the COD reduction is better at pH 3 than at pH 9. Pyridine and aniline are very stable compounds, so even residence times of more than 10 minutes at 340°C and a pH of 7 are leading to conversion rates of about 65 %. As shown in figure 2, it is obvious that an alkaline regime has a negative influence on the decomposition due to its lower oxidation potential. Stable fragments can not be degraded even after a longer residence time.

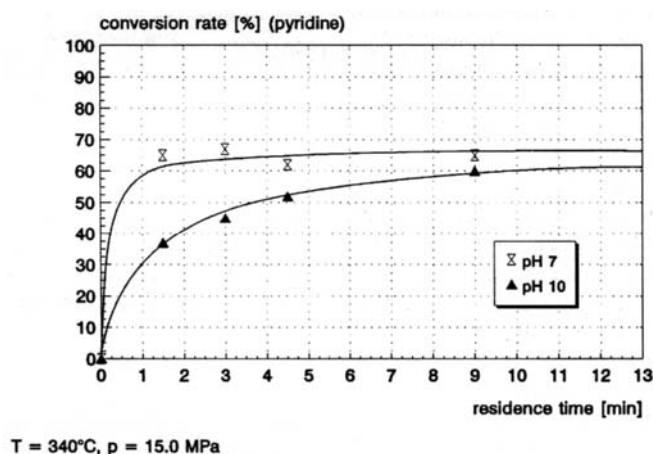


Figure 2. Decomposition of pyridine by oxidation at pH 7 and pH 10

3.1.2. Enriched air (40 vol.% O₂) as oxidizing agent

In comparison with H₂O₂, enriched air has a lower oxidation potential but is much cheaper with regards to the operating costs. For phenol, the reduction with H₂O₂ is higher than with N₂/O₂ as oxidizing agent in a noncatalytic reaction. By increasing the reaction pressure it is possible to improve the conversion rate with N₂/O₂ as a result of a higher content of dissolved oxygen.

3.1.3. Catalysis

The reduction of operation temperature and pressure is possible by using a suitable catalyst. Especially in combination with N₂/O₂ as oxidizing agent an effective catalysis is of great interest. As metal-catalysts platinum, palladium and iron oxide (poroton) were investigated.

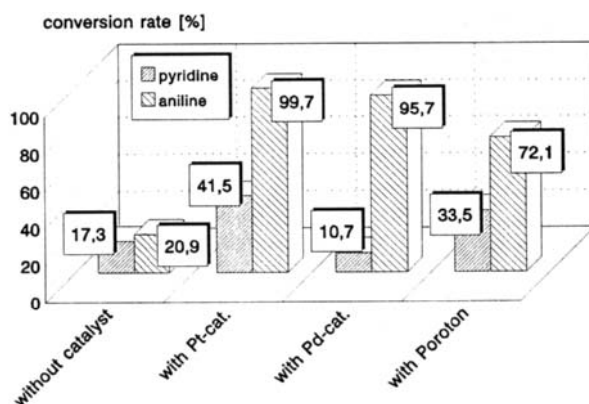


Figure 3. Effectivity of catalysts

The decomposition of pyridine and N₂/O₂ as oxidizing agent at 300°C was improved by a factor of 2.5. Increasing the pressure up to 14.0 MPa leads to a greater content of dissolved oxygen and a conversion rate of more than 85%. By increasing the temperature to 330°C a pyridine decomposition of more than 90% is possible. Without a catalyst the reduction is only a third in comparison to the catalyst platinum.

3.1.4 Treatment of real waste water

The results of the wet oxidation of the model substances were transferred to waste water from the pharmaceutical industry. The non-degradable compounds were converted into harmless substances which can be decomposed biologically. This results were confirmed by a Zahn-Wellens-test. The combination of wet-oxidation and following biological treatment allows a TOC reduction of more than 90%.

3.2. Corrosion experiments

The investigations on corrosion and corrosion inhibition were carried out under the conditions of the oxidation experiments and also at elevated temperatures up to 523 K. The metallic samples were not pre-treated. On the surface of carbon steel St 1203 as well as high-grade steel 1.4541 without addition of an inhibitor corrosion and pitting can clearly be seen after the

short period of time of about 1 week at 200°C and a concentration of chloride-ions of about 50 g/l. (fig. 4 and fig. 5)

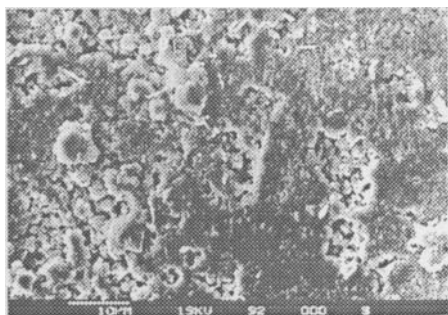


Figure 4. St 1203 after treatment at pH 7 (c_{Cl^-} = 50 g/l, T = 200°C, 1 week)

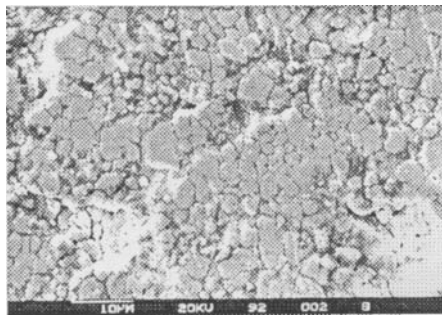


Figure 5. 1.4541 after treatment at pH 7 (c_{Cl^-} = 50 g/l, T = 200°C, 1 week)

By a shift of pH-value from pH 7 to pH 11 and in presence of 100 g/l KBO_2 as corrosion inhibitor the sample's surface shows a more homogeneous structure (fig. 6 and fig. 7). A weight loss could not be observed even after 2 weeks of treatment.

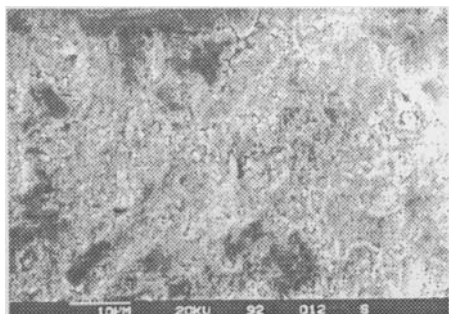


Figure 6. St 1203 after treatment at pH 11 (c_{Cl^-} = 50 g/l, c_{KBO_2} = 100 g/l, T = 200°C, 2 weeks)

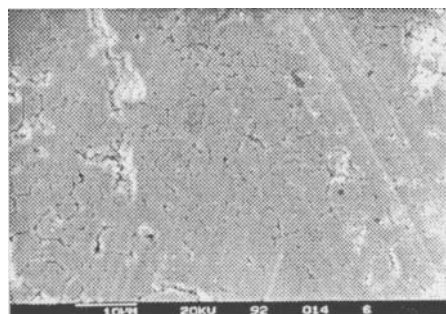


Figure 7. 1.4541 after treatment at pH 11 (c_{Cl^-} = 50 g/l, c_{KBO_2} = 100 g/l, T = 200°C, 2 weeks)

An extra improvement was achieved by addition of CaO in ration 1:1 to KBO_2 . As consequence of $Ca(BO_2)_2$ forming a very stable and dense layer was built up. These results were confirmed by tests with 4-chlorphenol under real conditions at 300°C and with H_2O_2 as oxidizing agent. A concentration of 7.5 g/l KBO_2 and 5 g/l CaO was proved to be as an acceptable compromise between salt formation and necessary corrosion inhibition.

3.3. Economics

By application of enriched air as oxidizing agent the usage of noble metals as catalyst like platinum is required so that the operating costs are increasing. By using hydrogenperoxide as oxidizing agent a catalyst can be cancelled due to its high oxidation potential. Generally the capital costs for waste water treatment of non-degradable compounds can be decreased about 10% by using common materials in contrast to hastelloy or inconel. However, to run the process autothermally a minimum content of organics (COD about 20g/l) has to be guaranteed.

4. CONCLUSIONS

Since corrosion is a severe problem of hydrothermolytical oxidation, corrosion control deserves close attention in the course of further development. The presented process offers the possibility to use common reactor materials e.g. high-grade steel 1.4541 or in selected applications even carbon steel St 1203. If calciumborate as corrosion inhibitor is used special alloys like hastelloy or inconel are not absolutely necessary for wet oxidation in presence of chloride-ions.

Increasing of the pH-value of the reaction mixture results in a corrosion decrease, but the rate of oxidation decreases simultaneously. The decrease of the reaction rate could be compensated by increasing the reaction temperature or by adding suitable catalysts. Increasing the pH-value from 4 to 9 causes also a decrease of reaction rate. The increase of temperature from 473 K to 573 K redoubles the reaction rate. The global reaction order ranges also in this case between 0.5 and 1, as reported in earlier studies [3,4,5]. As shown by the treatment of real waste water the combination of wet oxidation and biological treatment afterwards leads to satisfactory results [6,7].

5. ACKNOWLEDGEMENT

The authors would like to express their thanks to Deutsche Forschungsgemeinschaft for financial support (DFG / SFB 222 / proj. C11).

REFERENCES

1. Modell, M.: Processing Methods for the Oxidation of Organics in Supercritical Water, U.S. Patent No 4.338.199, 1982
2. Modell, M.: Processing Methods for the Oxidation of Organics in Supercritical Water, U.S. Patent No 4.543.190, 1985
3. Thornton, T.D. and P. E. Savage: Phenol Oxidation in Supercritical Water, J. of Super crit. Fluids, Vol. 3, No. 4, 1990, p. 240
4. Pruden, B.B. and H. Le: Wet Air Oxidation of Soluble Components in Waste Water, Can. J. Chem. Eng., Vol. 54, 1976, p. 319
5. Jaulin, L. and E. Chornet: High Shear Jet-Mixers as Two-Phase Reactors: An Application to the Oxidation of Phenol in Aqueous Media, Can. J. Chem. Eng., Vol. 65, 1987, p. 64
6. Pongratz, E.: Korrosionsinhibition und Katalyse bei der Naßoxidation organischer Abwasserinhaltsstoffe, Dissertation, Universität Erlangen, 1996
7. Pongratz, E., G. Härtel and S. Peter: Verfahren zur Naßoxidation von Abwasser, DE 196 12 635.5

OXIDATION OF ORGANIC MATERIAL IN SUPERCRITICAL WATER AND CARBON DIOXIDE

H. Goldacker, J. Abeln, M. Kluth, A. Kruse, H. Schmieder and G. Wiegand

Forschungszentrum Karlsruhe GmbH, Institut für Technische Chemie, Bereich Chemisch Physikalische Verfahren, Postfach 3640, D-76021 Karlsruhe

Keywords: Supercritical Water, Supercritical Carbondioxide, Hazardous Organics, Oxidation, Separation

1. INTRODUCTION

The industrial application of the SCWO process strongly depends on the solution of two major technical problems: corrosion of the reactor material when halogenated compounds are processed and precipitation of inorganic product salts plugging the reactor. Consequently, research programmes were established to investigate appropriate construction materials and modify reactor configurations. The principles of the most outstanding constructions are shown in figure 1:

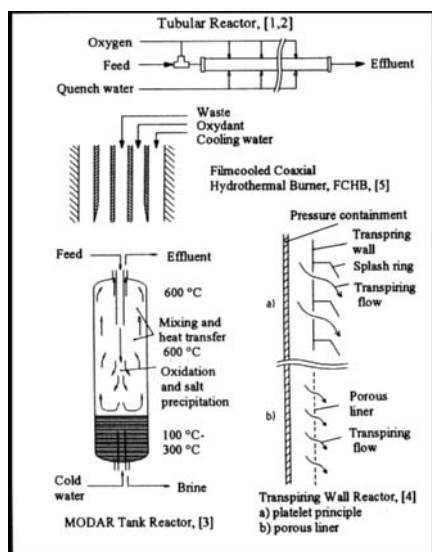


Fig. 1: Principles of the most outstanding SCWO reactor configurations: a) tubular reactor developed at the university of Austin, Texas /1/, commercialized by EWT, operated in Huntsville, Texas /2/, capacity 5 gpm; b) vessel reactor, MODAR Inc., Massachusetts /3/; c) transpiring wall reactor, Summit Research Corp., Santa Fe, New Mexico /4/; filmcooled coaxial hydrothermal burner developed at the ETH Zürich, Switzerland /5/

Whereas the tank type and the transpiring wall type are experimentally operated in bench scale rigs, the tubular reactor with multiple feedpoints for oxygen and quenching water is already commercialized for the treatment of solutions, such as long-chain alcohols and amines, without the risks arising from salt formation and corrosive compounds.

The fourth type, the filmcooled coaxial hydrothermal burner /5/ is under development at the ETH Zürich and, to our knowledge, it is operated experimentally with model substances at pilot scale level.

In 1991 a programme was started at the Research Center of Karlsruhe (FZK/ITC-CPV), comprising the oxidation of hazardous organic material in supercritical water /6/. For this purpose two continuously operated test facilities of different scale were constructed. Simultaneously a separation process of lubricating cooling oils from metal machining residues by means of supercritical CO₂ extraction (SC-CO₂-Extraction) was developed and presently has good chances to be commercialized /7/. In parallel, a liquid/fluid countercurrent extraction column is connected to the CO₂ test rig and basic investigations concerning drop formation and mass transfer have been started.

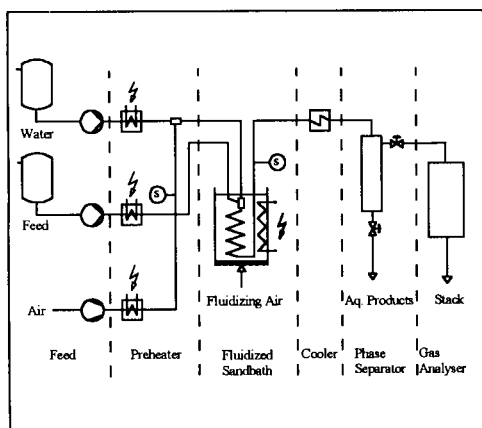


Fig. 2: Principles of the SCWO plants (1 kg/h and 10 kg/h water) operated in the FZK/ITC-CPV

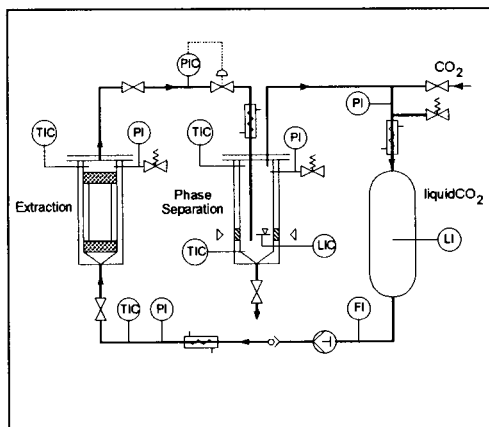


Fig. 3: Principles of the SF-CO₂ test rig, capacity 30 kg/h CO₂ /7/

The methods of supercritical extraction and of supercritical oxidation in carbondioxide can favourably be integrated in one process if the extracted solute has to be disposed.

The VISCO code, developed at FZK/ITC-CPV in former times is now used both for process monitoring and for process modelling. First results will be presented at this conference /8/.

2. EXPERIMENTS IN THE SCWO LABSCALE PLANT /9/

Design data are: 1kg water per hour, $P < 300$ bar and $T < 600$ °C kept constant by a fluidized sandbath in which a 6 m tubular reactor coil with an inner diameter of 2 mm is submerged. 33 thermocouples measure the reaction temperature profiles. Water, organic material and the pressurized air can be preheated.

Oxidation experiments started with ethanol and were continued with further model substances like n-hexane, cyclohexane, benzene, toluene and nitrobenzene, etc. Investigated parameters include fluidized sandbath temperature levels of 350 °C to 550 °C, the water throughput of 300 g/h to 1200 g/h and oxygen stoichiometry varying between 1.2 and 2.0. Organic waste concentration ranged between 2.5 and about 10 w%. In-line instrumentation in the product gas provides continuous data for the concentrations of CO, CO₂ and O₂, whereas samples from the aqueous phase provide information about the residual TOC and soluble organic products de-

tected by GC-MS and IC. The resulting TOC values of 12 % in maximum show a clear dependency on bath temperature and contact time. The influence of the stoichiometry varied by a factor of nearly 2 is not clearly visible. Fig. 4 gives an example for the benzene and nitrobenzene oxidation at 240 bar and 550 °C. The dominating influence under these conditions of water throughput and residence time respectively is shown by the figure 4.

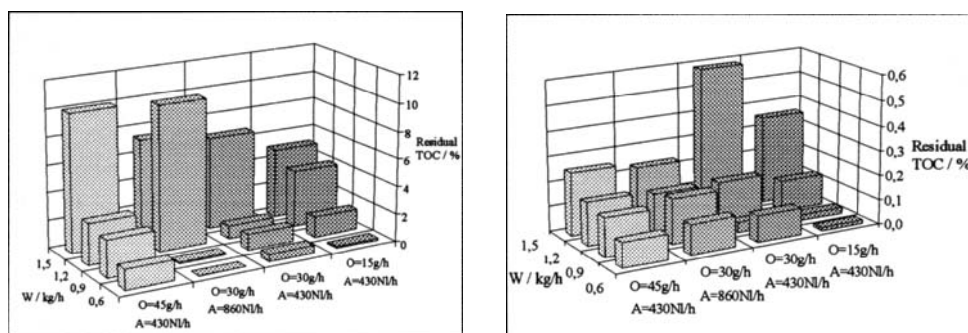


Fig. 4: Residual TOC data for the oxidation of benzene (left) and nitrobenzene (right) in the labscale plant. Temperature 550 °C, pressure 240 bar. Parameters are throughput of water (W), air (A) and organic material (O)

In preparation for an integrated separation and oxidation of organic wastes, preliminary oxidation tests with ethanol and toluene in supercritical CO₂, substituting the water, were recently performed successfully /10/, figure 5.

At a constant pressure of 240 bars, about 350 g/h CO₂ loaded with 10 w% ethanol and a 1.5 fold stoichiometric excess of oxygen in air were fed to the system. The tests showed that TOC values of 0.01 % can be obtained similar to the SCWO process. It is remarkable that the reaction seems to continue for more than 2.5 hours at temperatures of the reaction tube substantially below 300 °C. This is in contrast to the ethanol oxidation in water only starting above 360 °C. In the near future these tests, investigating optimized reaction temperatures and the influence of water will be continued in the lab system.

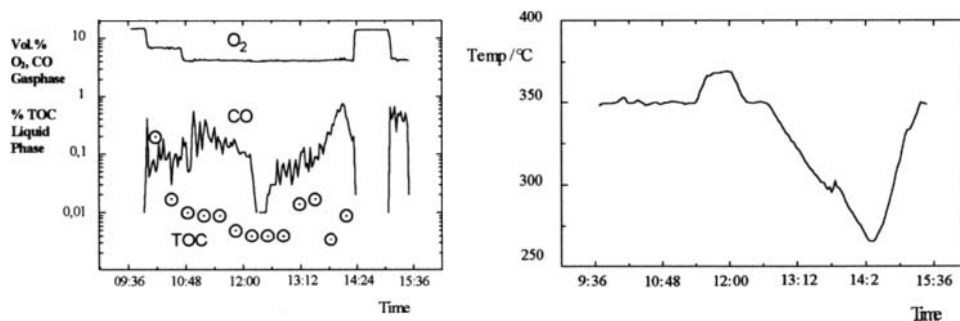


Fig5.: Oxidation of ethanol in supercritical CO₂, 350 g/h CO₂, 240 bar, 35 g/h ethanol, 1.5 fold stoichiometric excess of oxygen

3. EXPERIMENTS IN THE BENCHSCALE PLANT /11/

The benchscale plant principally follows the design scheme of the labscale plant, but is equipped with a tubular reactor coil made of Inconel 625, 15 metres in length, the 8 mm inner diameter of which is good for a throughput of 10 kg/h of water. Tests with model substances like ethanol and toluene showed results comparable to those of the labscale plant.

In order to prepare experiments with real wastes, a 0.8 w% sodiumsulfate solution under various flow conditions was used to test the reactor performance in the presence of precipitations. It could be demonstrated that the system can be operated for a limited time with moderate salt concentrations in the effluent. Salt cakes accumulating to about 150 grammes in total and plugging the 8 mm tube were redissolved by flushing with water at temperatures below 100 °C.

The results of first tests with industrial effluents are shown in Tab. 1. They comprise solutions such as pharmaceutical waste originating from the synthesis of penicillin and carrying low solid but high soluble salt concentrations, de-inking effluents from a paper mill and municipal sludge, both charged with mainly solid organics. As it could be expected, the system was operable only for a limited time after starting the feed at controlled bath temperatures. Several samples taken within one run proved steady state conditions.

Especially the first two examples demonstrate that the carbon conversion depends on the temperature. The stoichiometric oxygen excess for the three runs was kept high at values of 8 and higher. The volumetric throughput varied between 6 and 10 kg/h. The mass flows resulted in residence times in the range of 25 to 50 seconds related to the bath temperatures and the whole reactor volume. The said operating conditions show that the carbon conversions are not optimized with respect to temperatures and residence times. However, the comparison of gaschromatographical data showed that no more feed compounds could be found in the product solutions.

TAB. 1: Results with industrial wastes in the bench scale plant

Waste type	Feed-TOC ppm	Conversion %	Temperature °C	Salt-concentration %	Operating time h
Pharmaceutical waste water	7.000	83	410	1	2 (RP)
	20.000	97	550	3	0.5
Paper mill sludge	2.000	98	450	0.1	2 (FE)
	2.000	99	500	0.1	2
Sewage sludge	1.000	85	500	< 0.1	3 (PP)

RP: Reactor plugging, FE: Feed finished, PP: Pump valve plugging

4. CORROSION TEST PROGRAMME /12/

In two test rigs materials like Inconel 625, Haynes 214, Hastelloy C-276, Nicrofer 5923 and 6025 were tested in aqueous solutions containing 0.5 mol/kg oxygen and 0.05 to 0.5 mol/kg HCl. One of the rigs offers the possibility to test five tubes in parallel at pressures between 240 to 400 bars and at temperatures up to 600 °C. Practically all types of material showed heavy local corrosion after some tens of hours. More encouraging results were obtained for oxide ceramics, small samples of which are presently under test.

Fig. 6 gives an impression of the local corrosion depending on temperature.

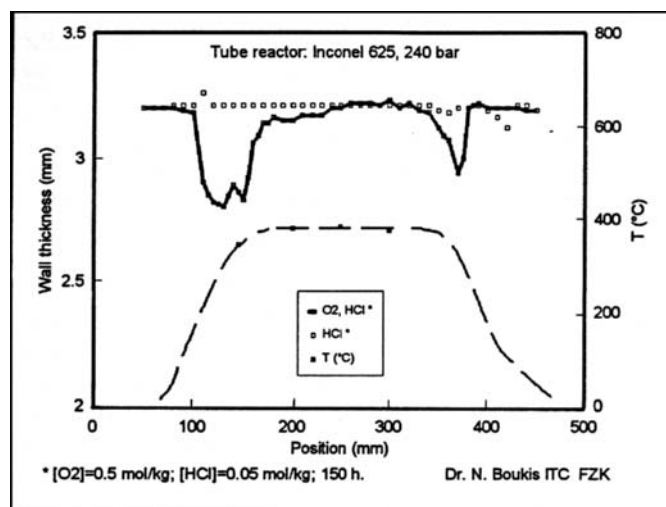


Fig. 6: Corrosion in an Inconel 625 tube at 240 bar and 400 °C operating temperature. Results after 150 hours in 0.5 mol O_2 and 0.05 mol HCl per kg of water, flowrate 60 ml/h, /12/

The attack at a pressure of 240 bar is very severe at temperatures between 300 and 390 °C where the local gradient is steep. In the steady state section at 400 °C, the bite is comparatively moderate. Further corrosion tests indicate that at higher pressures the bite speeds up and that a higher steady state operating temperature has a minor influence on the corrosion rate.

5. FUTURE WORKING PROGRAMME

Salt precipitation and corrosion are the technical key problems of the economical solution which will make the SCWO process an important tool for the treatment of hazardous organic wastes.

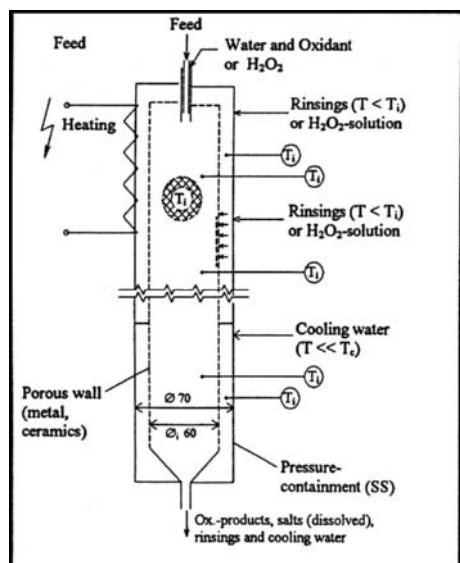


Fig. 7: Principles of the transpiring wall reactor configuration

The development of a corrosion resistant material e. g. may take a time too long for industrial implementation in a competitive market situation. Transpiring wall or filmcooled coaxial burner techniques have a high potential to solve said problems by design supported by a material test programme.

If not, the SCWO process will be technically and economically restricted to special applications in a small waste section. In parallel to the described activities, a transpiring wall reactor configuration has been designed and is presently under construction, comp. Fig. 7. A concentric porous tube separates the supercritical reaction volume from the pressure bearing containment. This porous tube can be made of sintered metal, what is presently intended, or of porous oxide ceramics. At the beginning the choice of materials will be limited to hardware on stock which can be changed for experimental reasons at comparatively low costs. First experiments will concentrate on the prevention of salt accumulation at the wall. Subcritical water is thought to remove precipitations under falling film conditions. Improved corrosion resistance is the second reason to follow this concept. Parameters for optimization are: Flow ratio of film water and feed, qualification of the sintered material, heat transfer between film and reacting bulk solution, energy input to start the SCWO reaction, output of gas charged salt brine. The system is planned to go into operation at the end of 1996.

6. REFERENCES

- /1/ E. F. Gloyna, L. Li, and R. N. Brayer, *Wat. Sci. Tech.*, Vol. 9 (1994) 1-10
- /2/ ECO WASTE TECHNOLOGIES, Information Package 1995, 2305 Donley Dr., Suite 108, Austin, Texas 78758
- /3/ H. E. Barner, C. Y. Huang, T. Johnson, G. Jacobs, M. A. Martch and W. R. Killilea, *J. Hazardous Mat.*, 31 (1992) 1-17
- /4/ Th. G. McGuinness, 1. Int. Workshop on SCWO, Jacksonville, Florida, Febr. 6-9, 1995
- /5/ H. L. La Roche, M. Weber, Ch. Trepp, 1. Int. Workshop on SCWO, Jacksonville, Florida, Febr. 6-9, 1995
- /6/ H. Schmieder, H. Goldacker, G. Petrich, *Interdiscipl. Science Reviews* 18 (1993), 207 -215
- /7/ J. Schön, N. Dahmen, H. Schmieder in *chemie-anlagen + verfahren* 12 (1994), 10-11
- /8/ G. Petrich, J. Abeln, H. Schmieder, this symposium
- /9/ G. Wiegand, H.J. Bleyl, H. Goldacker, G. Petrich, H. Schmieder, 1 Int. Workshop on SCWO, Jacksonville, Florida, Febr. 6-9, 1995
- /10/ H.-J. Bleyl, J. Abeln, N. Boukis, H. Goldacker, M. Kluth, A. Kruse, G. Petrich, H. Schmieder, G. Wiegand, *Colloquium Produktionsintegrierter Umweltschutz*, Bremen 11.- 13. Sept. 1995
- /11/ J. Abeln, N. Boukis, H. Goldacker, M. Kluth, G. Petrich, H. Schmieder, GVC-Conference, Erlangen, 1996
- /12/ N. Boukis, R. Landvatter, W. Habicht, G. Franz, S. Leistikow, R. Kraft, O. Jacobi, 1. Int. Workshop on SCWO, Jacksonville, Florida, Febr. 6-9, 1995

Clean Chemistry in Supercritical Fluids

Martyn Poliakoff, Steven M. Howdle and Michael W. George

Dept of Chemistry, University of Nottingham, Nottingham, England NG7 2RD.

E-mail:- *Martyn.Poliakoff@nottingham.ac.uk*

Supercritical fluids, particularly supercritical CO₂, scCO₂, are attractive solvents for cleaner chemical synthesis. However, optimisation of chemical reactions in supercritical fluids is more complicated than in conventional solvents because the high compressibility of the fluids means that solvent density is an additional degree of freedom in the optimisation process. Our overall aim is to combine spectroscopy with chemistry so that processes as varied as analytical separations and chemical reactions can be monitored and optimised in real time. The approach is illustrated by a brief discussion of three examples (i) polymerisation in scCO₂ (ii) hydrogen and hydrogenation and (iii) miniature flow reactors for synthetic chemistry.

1. INTRODUCTION

Supercritical fluids are making an increasingly large impression on chemical science [1]. In recent years, much of this interest has focussed on the replacement of conventional solvents in chemical reactions, either to improve the efficiency of a process or to render it environmentally more acceptable, so-called "Clean Technology". The supercritical research group at the University of Nottingham has concentrated largely on inorganic and analytical chemistry [2]. The emphasis of most of this work has been to combine spectroscopy with chemistry so that processes can be monitored *in situ*. There is a broad range of on-going research projects including:-

- (i) Chemical Reactions, particularly those involving organometallic compounds. The objective has been to generate compounds which would be difficult or even impossible to isolate from conventional solvents. Much of the work has exploited the complete miscibility of H₂ and N₂ with supercritical fluids to generate new dinitrogen and dihydrogen compounds [3]. Recently, a miniature photochemical flow reactor has been used [4, 5] to isolate the labile organometallic complexes *without* the use of any additional solvents, e.g Cr(CO)₅(C₂H₄), from the reaction of Cr(CO)₆ and supercritical C₂H₄.

- (ii) Spectroscopic monitoring of the impregnation and extraction of organometallics into polymers [6] and porous solids as potential precursors for catalysts or formation of thin films [7].
- (iii) Nanosecond time-resolved IR spectroscopy for monitoring the kinetics of reactions in supercritical fluid solution [8, 9].

We have recently reviewed the use of vibrational spectroscopy in supercritical fluids [2] and the theme common to most of our projects is the use of spectroscopy for *real-time optimisation* of processes in supercritical solution. Such optimisation is considerably more important in supercritical fluids than in conventional solvents because the tunability of the fluids results in a greater number of parameters which can affect the outcome of a reaction. Thus, the chances of hitting the optimal conditions purely by “trial and error” are much less in supercritical solution than in conventional reactions. Below, we give three examples of our approach, synthesis of polymers, transition metal hydrogen compounds, and the use of flow-reactors.

2. EXPERIMENTAL

The miniature high pressure equipment used in these experiments has been described previously [5, 10]. Briefly, our strategy is always to work on the smallest scale possible with highly modular equipment which can be quickly modified or rearranged as the science demands. High pressure fluids are generated using a commercial pneumatically operated pump (NWA GmbH, Lörrach, module PM-101) with a maximum pressure of ca. 500 bar. In most experiments, the key components, valves, cells, etc are attached to small industrial magnets, which are used to fix the components onto a steel bench-top. These magnetic mounts provide good rigidity while still allowing rapid rearrangement of the layout. Spectroscopic cells were fitted with CaF_2 windows (IR and UV transparent). CO_2 and C_2H_4 (BOC) were used without further purification. All spectra were recorded at 2 cm^{-1} resolution on Nicolet FTIR interferometers (Models 205 or 730). Time-resolved IR spectra were recorded with the Nottingham spectrometer, based on tunable semiconductor diode lasers (Mütek GmbH) [8].

3. SYNTHESIS OF POLYMERS

Polymerisation is one area where the introduction of supercritical fluids is especially appealing. Not only have many polymers traditionally been synthesised using solvents which are now considered environmentally unacceptable for long term use, but also the increased demand for so-called “specialty” polymers has led to the need for ever greater control of the polymerisation process itself. Supercritical fluids offer both environmental acceptability and the potential of extra control of the process. This potential arises from the gas-like nature of the fluids which allows pressure (and hence, fluid density) to be used as an additional parameter in the tuning of

chemical reactions. This is a rapidly expanding field; for example, J.M. DeSimone and coworkers have shown that scCO_2 really can play a useful role as a *solvent* in a wide range of polymerisation processes [11], including the replacement of CFCs in the synthesis of fluoropolymers, which are virtually insoluble in non-halogenated solvents.

Here, we describe the use of vibrational spectroscopy to monitor the progress of polymerisation reactions *in situ*. Figure 1 shows the results of monitoring the polymerisation of a fluorinated acrylate ester similar to that used by DeSimone [11a]. The reaction was carried out in scCO_2 (200 bar) with AIBN, a common radical initiator. Under these conditions both the monomer and the final polymer are soluble in scCO_2 so the mixture remains as a single phase throughout the reaction.

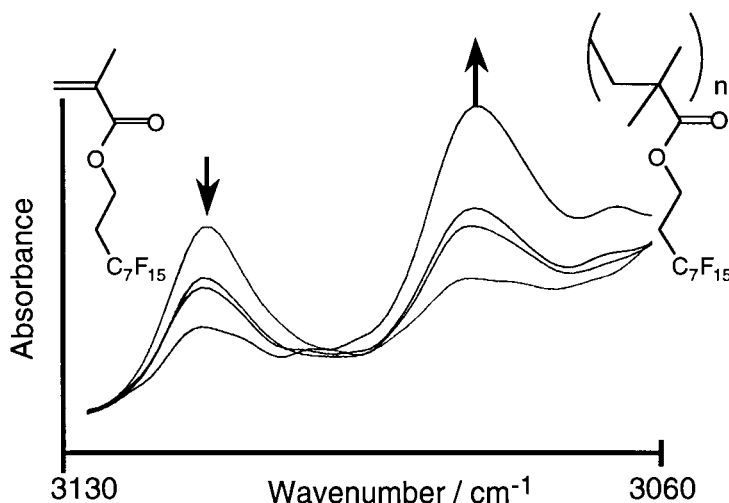
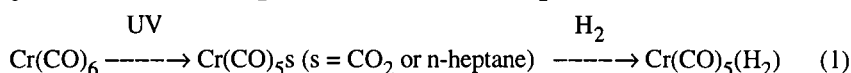


Figure 1 FTIR spectra recorded over a period of 24 hr, showing the polymerisation of a fluorinated acrylate in scCO_2 . ↓ indicates the decay of a characteristic band of the monomer and ↑ marks the growth of a band of the polymer.

A large proportion of polymerisation processes are heterogeneous and recently, DeSimone has reported the use of fluorinated and polysiloxane based stabilisers for such polymerisation in scCO_2 [12]. These stabilisers provide a method for controlling the size of the polymer particles. In collaboration with US groups, we have used FTIR spectroscopy to show for the first time, that reverse micelles of *water solutions* can be stabilised in scCO_2 by fluorinated surfactants [13]. Quite a range of inorganic salts can be dissolved in scCO_2 including KMnO_4 , which generates “purple CO_2 ” [14] reminiscent of the classic “purple benzene”, an early triumph of crown ether complexing agents [15]. Such systems should allow us to develop other heterogeneous polymerisations in supercritical fluids, eg reverse emulsion polymerisation.

4. HYDROGEN AND HYDROGENATION REACTIONS

Recent work by Noyori and coworkers [16] has highlighted the accelerating effects of supercritical solvents on the catalytic hydrogenation of CO_2 . Part of this acceleration is believed to be due to the miscibility of H_2 with scCO_2 which leads to a much higher effective concentration of H_2 than in a conventional solvent under similar conditions [see 3]. Time-resolved infra-red spectroscopy (TRIR), a combination of UV flash photolysis and very fast IR spectroscopy, now permits reactions to be monitored on a nanosecond time-scale [8, 9]. Figure 2 shows TRIR traces, monitoring the formation of $\text{Cr}(\text{CO})_5(\text{H}_2)$, formed by photolysis of $\text{Cr}(\text{CO})_6$ in n-heptane and scCO_2 under high pressures of H_2 , eqn 1.



Allowing for the difference in pressure of H_2 , the reaction in scCO_2 is $\text{ca} \times 16$ faster than in the n-heptane, a consequence of the enhanced solubility of H_2 in scCO_2 and the weaker interaction of CO_2 with the reaction intermediate, $\text{Cr}(\text{CO})_5$.

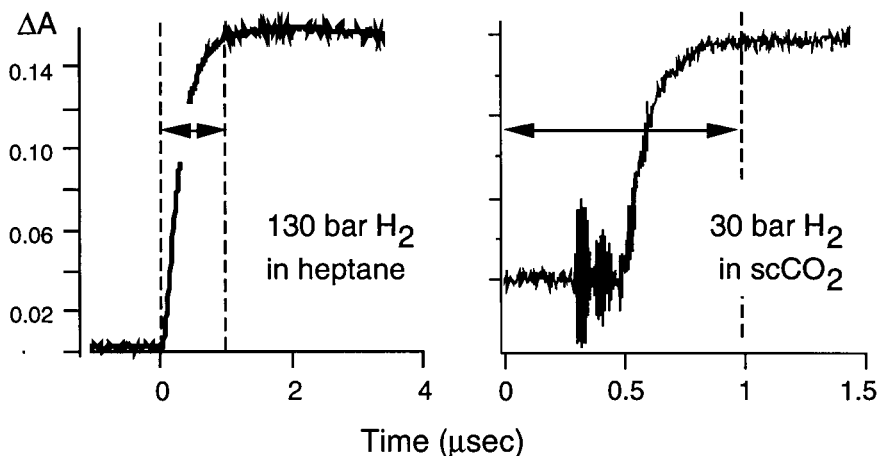


Figure 2: TRIR traces recorded at $\text{ca. } 1970 \text{ cm}^{-1}$ comparing the rate of formation of $\text{Cr}(\text{CO})_5(\text{H}_2)$ in n-heptane and scCO_2 (total pressure 150 bar at 40°C).

5. MINIATURE FLOW-REACTORS

Flow reactors offer considerable advantages over sealed autoclaves for supercritical reactions. Not only do flow-reactors require a much lower volume than a batch reactor for a given throughput of material (with obvious safety advantages) but also it is much easier to optimise reaction conditions in a flow reactor. We have already reported [4,5] the use of a miniature flow-reactor for the *photochemical* preparation of unstable metal complexes. We are now extending these techniques to the study of *thermal* and catalytic reactions. As an initial stage we

have studied reactions of metal carbonyl complexes with scC_2H_4 where C_2H_4 is both the solvent and one of the reactants. Many carbonyl compounds undergo rather slow thermal reactions. Thus our strategy has been to synthesise compounds with rather labile ligands, by conventional Schlenk line techniques, and then to use these compounds for the supercritical reaction, Scheme 1.

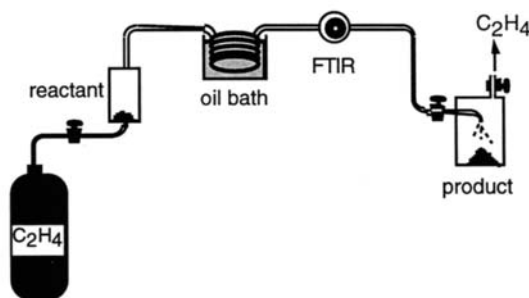
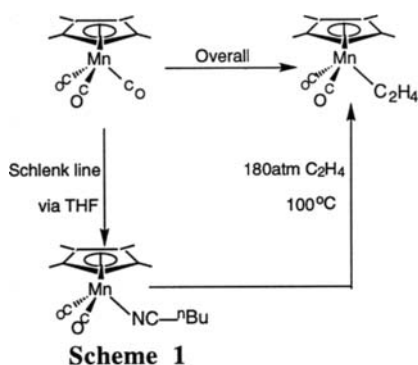


Figure 3 shows a schematic view of a flow reactor. It is similar to the photochemical reactor previously described in [5] but the UV photolysis cell has been replaced by a 1 m. stainless steel coil in a heated oil bath. As before, FTIR is used to monitor the conversion and optimise the conversion of reactant to product. Using such a system $(\text{C}_5\text{Me}_5)\text{Mn}(\text{CO})_2(\text{C}_2\text{H}_4)$ can be obtained in a high yield as in Scheme 1. We are now scaling up this miniature reactor to a technical scale, ultimately with the aim of carrying out “solvent-free” reactions on a kilogramme scale.

6. ACKNOWLEDGEMENTS

This paper includes work by our coworkers D. J. Gilbert, X-Z. Sun, E. F. Walsh, P. D. Lee and S. Seebald. We are grateful for the support of EPSRC Clean Technology Unit, the Royal Society, The EU Human Capital and Mobility Programme, ICI, Zeneca and the Royal Academy of Engineering. We thank Mr M. Guyler and Mr K. Stanley for their assistance.

REFERENCES

1. see for example Poliakoff, M.; Howdle, S.M. *Chem in Britain*, **1995**, 31, 118.
2. Poliakoff, M.; Howdle, S. M.; Kazarian, S. G. *Angew. Chem. Intl. Ed.* **1995**, 34, 1275.
3. Howdle, S. M.; Poliakoff, M. *J. Chem. Soc. Chem. Commun.* 1989, 1099; Howdle, S. M.; Healy, M. A.; Poliakoff, M. *J. Am. Chem. Soc.* **1990**, 112, 4804.
4. Banister, J. A.; Howdle, S. M.; Poliakoff, M. *J. Chem. Soc. Chem. Commun.* **1993**, 1814.
5. Banister, J.A.; Lee, P.D.; Poliakoff, M. *Organometallics* **1995**.

6. Cooper, A. I.; Howdle, S. M.; Hughes, C.; Jobling, M.; Poliakkoff, M.; Johnston, K. P. *Analyst* **1993**, *118*, 1111; Howdle, S. M.; Ramsay, J. M.; Cooper, A. I. *J. Polymer Science: Part B: Polymer Physics* **1994**, *32*, 541.
7. Howdle, S.M.; Antonov, E.N.; Bagratashvili, V. N.; et al. *Proceedings 3rd International Symposium on Supercritical Fluids*; Strasbourg, **1994**, *3*, 369.
8. George, M. W.; Poliakkoff, M.; Turner, J. J. *Analyst* **1994**, *119*, 551.
9. George, M. W.; Sun, X.-Z.; Poliakkoff, M. *J. Am. Chem. Soc.* submitted.
10. Howdle, S. M.; Poliakkoff, M. in *Supercritical Fluids - Fundamentals for Applications* (Kiran, E.; Levelt Sengers, J. M. H., eds) *NATO ASI Series e*, **1994**, 273, 527, Kluwer Academic Publications, Dordrecht.
11. (a) DeSimone, J. M.; Guan, Z.; Elsbernd, C. S. *Science* **1992**, *257*, 945.;
(b) Combes, J. R.; Guan, Z.; DeSimone, J. M. *Macromolecules* **1994**, *27*, 865.
12. K.A. Shaffer, K. .A.; Jones, T. A.; Canelas, D. A.; DeSimone, J. M. *Macromolecules* **1996**, *29*, 2704; Canelas, D. A.; Betts, D. E.; DeSimone, J. M. *Macromolecules* **1996**, *29*, 2818.
13. Johnston, K. P. ; Harrison, K. L.; Clarke, M. J.; Howdle, S. M.; Heitz, M. P.; Bright, F. V.; Carlier, C.; Randolph, T. W. *Science* **1996**, *271*, 624.
14. Clarke, M. J.; Howdle, S. M. to be published.
15. Sam, D. J.; Simmons, H. F. *J. Am. Chem. Soc.* **1972**, *94*, 4024.
16. (a) Jessop, P. G.; Ikariya, T.; Noyori, R. *Nature* **1994**, *368*, 231; (b) Jessop, P. G.; Hsiao, Y; Ikariya, T.; Noyori, R. *J. Am. Chem. Soc.*, **1994**, *116*, 8851; (c) Jessop, P. G.; Hsiao, Y; Ikariya, T.; Noyori, R. *J. Chem. Soc. Chem. Commun.* **1995**, 707; (d) Jessop, P. G.; Ikariya, T.; Noyori, R. *Chem. Rev.*, **1995**, *95*, 273.

Use of Metallocene Catalysts in the Polymerization under High Pressure

G. Luft

Department of Chemical Engineering, University of Darmstadt, Petersenstraße 20, D-64287 Darmstadt, Germany

1. INTRODUCTION

Metallocene catalysts are increasingly used in the polymerization of olefins under low pressure. By means of single-site metallocene catalysts homopolymers having a narrow molecular weight distribution and copolymers with a high chemical uniformity can be produced. These resins are superior to the products from processes with conventional multi-site Ziegler-Natta catalysts. At present, Ziegler-Natta catalysts are used in different polymerization processes, one of them is the polymerization of ethylene and its copolymerization with 1-olefins under high pressure [1-3]. Small amounts of metallocene based polymers are manufactured by high pressure processes recently developed. Only few papers consider the application of metallocene catalysts in the polymerization under high pressure [4-6]. The aim of this work was therefore to investigate the performance of such catalysts in the high pressure process and to evaluate the properties of the resulting polymers.

2. EXPERIMENTAL

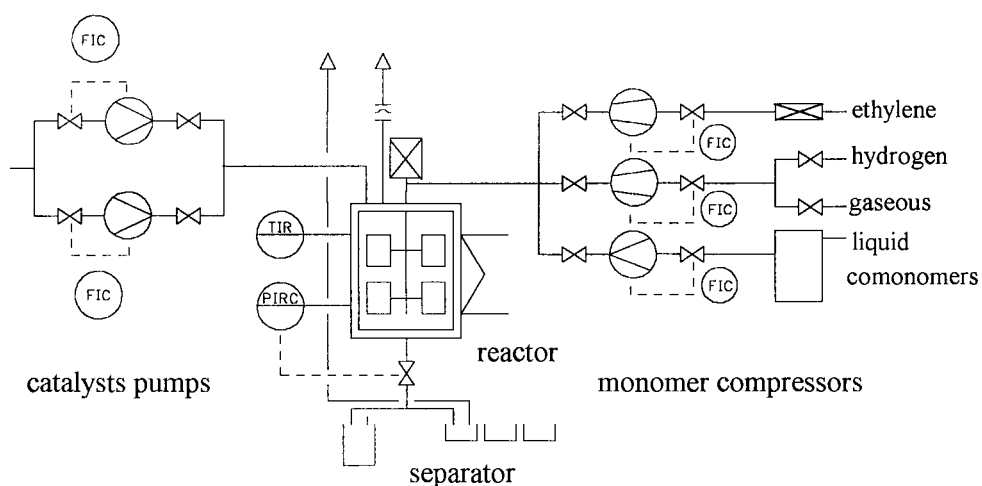


Figure 1 Polymerization unit

Because of their acceptable thermal stability ansa-metallocenes are suitable catalysts for high pressure polymerization at temperatures fairly above 100°C. In this investigation a modified silyl-bridged bis(tetrahydroindenyl)zirconocene in toluene as the solvent was used. The cocatalyst was methylaluminoxane (MAO) which was available in a 10 wt% solution also in toluene. The polymerization experiments were performed in a continuously operated laboratory unit equipped with a stirred autoclave (Figure 1). It is described in detail in [6].

3. RESULTS

The rate of polymerization was determined from the amount of polymer obtained per unit of time. The productivity of the metallocene catalyst was calculated from the quantity of polymer and the catalyst metal fed into the reactor. The resulting polymers were investigated by gel permeation chromatography (GPC) to determine the molecular weight distribution together with the average molecular weights. The density was measured on pressed films by means of the suspension method in a mixture of water and isopropanol. ^{13}C -NMR-spectroscopy was applied to analyze the composition of copolymers and to evaluate their structure.

First the influence of the ratio of cocatalyst to catalyst was investigated at a constant pressure of 1500 bar, a temperature of 180°C and 240 s residence time. Using a catalyst concentration of 0.01 mole ppm in the reactor feed, the ratio of the two components was varied between 3600 and 29000 mole Al/mole Zr. An excess of cocatalyst shifts the reaction between catalyst and cocatalyst toward the catalytically active species formed in this reaction. Though catalyst productivity and the rate of polymerization increases with increasing ratio of cocatalyst to catalyst. This is shown in Figure 2 in which the productivity determined from the amount of polymer and the amount of catalyst metal is plotted versus the ratio of aluminium to zirconium. At ratios below 10000 mole Al/mole Zr only low productivities result. At higher

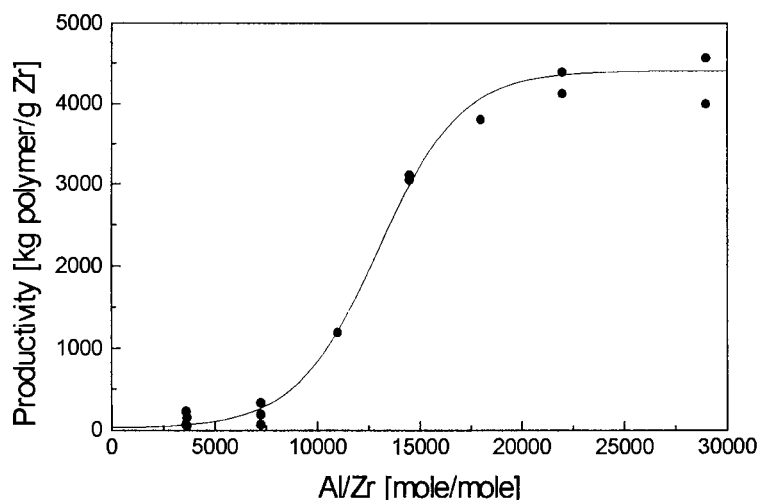


Figure 2 Influence of the Al/Zr ratio on the productivity

Al/Zr ratios the productivity increases steeply to a constant value of around 4400 kg polymer/g Zr. In the following experiments a high ratio of 22000 mole Al/mole Zr was applied to exclude the influence of cocatalyst concentration.

In order to investigate the influence of the pressure experiments were performed at different pressure of 500 to 1500 bar. All other parameters were kept constant: temperature 180°C, residence time 240 s, catalyst concentration 0.01 mole ppm in the feed and 22000 mole Al/mole Zr.

As to be seen from Figure 3 productivity (curve a) and rate of polymerization (curve b) increased both with increasing pressure. At the highest pressure of 1500 bar a very high productivity of 4400 kg polymer/g Zr resulted. Also the rate of polymerization at this pressure was high and was in the range of 0.4 kg polymer/s/m³.

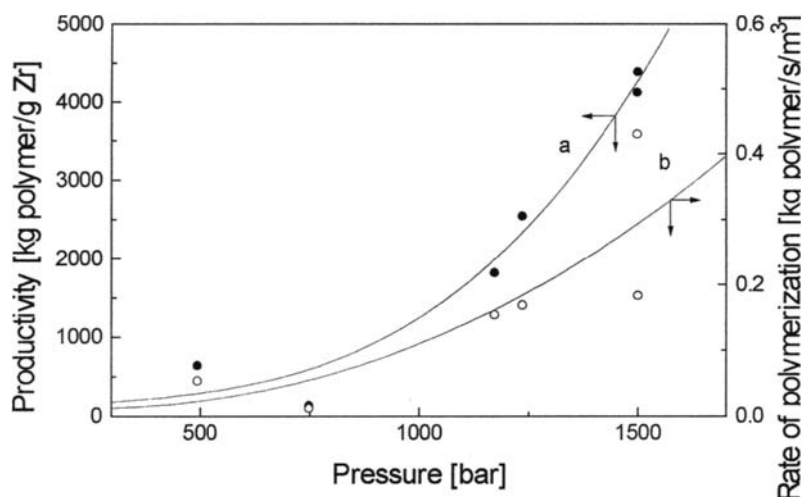


Figure 3 Influence of the pressure on productivity and rate of polymerization
Curve a: productivity; curve b: rate of polymerization

The influence of the temperature was investigated at 1500 bar in the broad range of 80 to 260°C. The change of the productivity with the temperature is shown in Figure 4. The productivity of 4400 kg polymer/g Zr was obtained at 180°C. When the temperature was decreased below 180°C the productivity increased steeply. At the lowest polymerization temperature of 80°C an extremely high productivity was observed. The change of the productivity with the temperature was only small above 180°C.

In the high pressure polymerization narrow molecular weight distribution curves result which are typical for single site catalysts. Both the number average and the weight average molecular weight decrease with increasing polymerization temperature.

Besides the performance of metallocene catalysts in the homopolymerization of ethylene also their ability for copolymerization under high pressure was proofed. As comonomers a number of 1-olefins and dienes were used. In Figure 5 the change of the productivity with the concentration of the comonomer in the feed is shown for the copolymerization of ethylene with

propene, 1-hexene and 1,5-hexadiene. The polymerization tests were performed at 180°C and 1500 bar. The concentration of the comonomer could be varied up to 100 mole%.

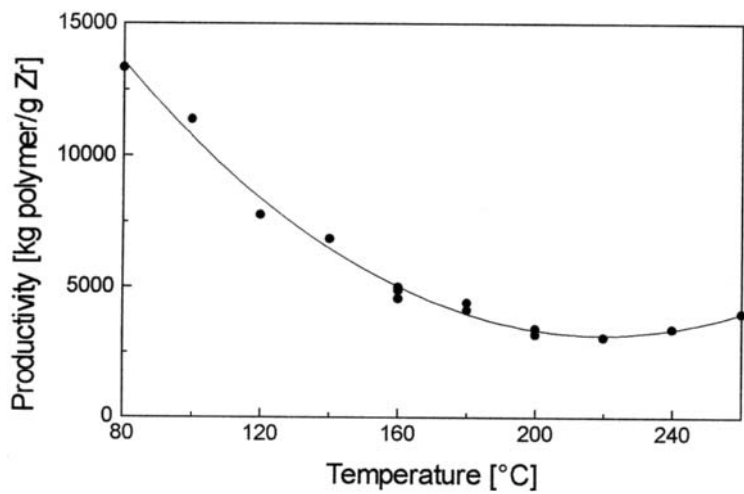


Figure 4 Dependency of the productivity on the temperature

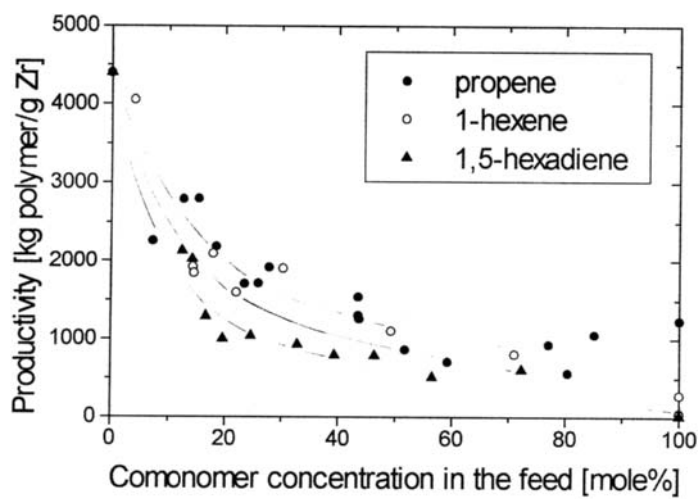


Figure 5 Productivity in the copolymerization of ethylene with 1-propene, 1-hexene or 1,5-hexadiene

The highest productivity of 4400 kg polymer/g Zr resulted in the homopolymerization of ethylene. It was found lower in the copolymerization with propene, 1-hexene and 1,5-hexadiene. With increasing concentration of the comonomer in the feed the productivity decreased and was only 50 to 600 kg polymer/g Zr in the homopolymerization of the pure comonomers. The lowest productivity was observed with 1,5-hexadiene.

4. DISCUSSION

From the rate of polymerization r_{pol} measured at different pressures (Figure 3) an activation volume for the polymerization of ethylene catalyzed by metallocenes can be determined. For this purpose first an overall rate constant k_{pol} was evaluated from the relation

$$r_{pol} = k_{pol} \cdot c^*[E] \quad (1)$$

in which $[E]$ denotes the concentration of ethylene and c^* stands for the concentration of the active sites of the catalyst. The activation volume Δv^\ddagger was then obtained from the well known

$$\text{expression} \quad \left. \frac{d \ln k_{pol}}{dp} \right|_T = \frac{-\Delta v^\ddagger}{RT} \quad (2)$$

A value of $\Delta v^\ddagger = -20$ ml/mole was obtained which is in the same range as the activation volume of the radical initiated high pressure polymerization [7]. From the negative activation volume it can be concluded that the volume of the activated complex formed in the transition state is smaller than that of the initial reactands. This is in agreement with ab initio calculations of Koga et al [8] for the insertion of ethylene into the Zr-C bond which show a shortening of Zr-C distance in the four-centered, nearly coplanar transition structure. According to Equation 2 the overall rate constant k_{pol} increases with increasing pressure when the activation volume is negative.

The molecular weight of the polymer prepared in this work ranged from 100000 to 560000 g/mole, the density was between 0.91 and 0.97 g/cm³ (Figure 6). High polymerization temperatures resulted in a low average molecular weight and low density, whereas at low temperature polyethylenes having a high molecular weight and a high density could be prepared.

The polymerization tests with ethylene and 1-olefines as well as with dienes showed a good ability of the metallocene catalyst for copolymerization. Interesting results from practical and theoretical point of view could be gained in the copolymerization of ethylene and 1,5-hexadiene. During polymerization first a complexation of one of the double bonds of 1,5-hexadiene takes place at the vacant coordination side of the transition metal. After insertion into the polymer chain the complexation of the second double bond occurs followed by intramolecular cyclisation of the 5-membered ring. Analysis of the ¹³C-NMR spectra reveals an incorporation of 4.2 mole% 1,5-hexadiene and a predominance of trans rings caused by the diastereoselectivity of the cyclisation step.

The advantages of high pressure known from the radical polymerization process for low density polyethylene are listed in Table 1. They can also be observed in the polymerization with metallocene catalysts.

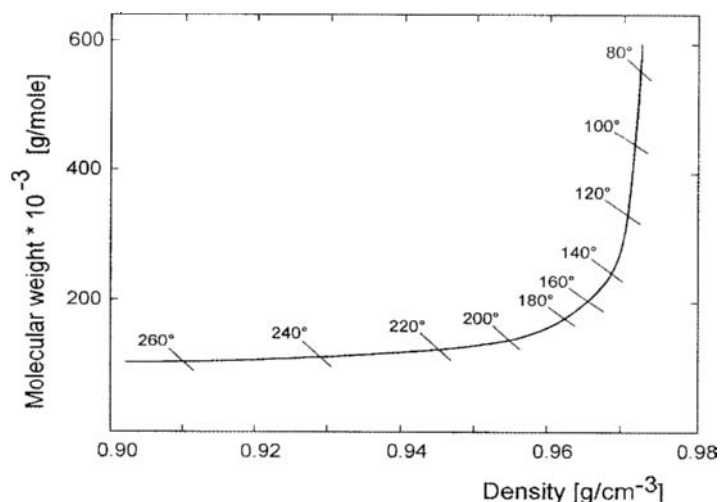


Figure 6 Range of molecular weight and density

Table 1

Advantages of the high pressure processes

Radical polymerization	Polymerization with metallocenes
Only small quantity of solvent	Improved product properties
High rate of polymerization	Wide range of molecular weight and density
Short residence time	Easy metering of soluble metallocenes
Small reactor volume	Process modifications
Variety of comonomers	Swing from metallocene to low density polyethylenes
Established technology	
Stirred autoclave or tubular reactor	

REFERENCES

1. EP 16 707 (1980), Société Chimique des Charbonnages, Invs.: J.P. Machon, F. Raviola, A. Sauzea.
2. EP 30 171 (1981), ATO Chimie, Inv.: R. Gouarderes.
3. DE 31 50 270 (1983), Erdölchemie, Invs.: A. Kolwecz, J. Herwig.
4. G. Luft, B. Batarseh and R. Cropp, *Angew. Makromol. Chem.*, 212 (1993) 1547.
5. X. Olonde, A. Mortreux, F. Petit and K. Bujadoux, *J. Mol. Catal.*, 82 (1993) 75.
6. C. Bergemann, R. Cropp and G. Luft, *J. Mol. Catal., A Chemical*, 102 (1995) 1.
7. G. Luft in J. Jurczak, B. Baranowski (eds.): *High pressure chemical synthesis*, Elsevier Publ. Amsterdam 1989, p. 374.
8. N. Koga, T. Yoshida and K. Morokuma in G. Fink, R. Mühlhaupt, H.H. Brintzinger (eds.): *Ziegler Catalysts*, Springer Verlag, Berlin 1995, p. 275.

Integration of Lipase Catalysis and Product Separation in Supercritical Carbon Dioxide

Helga Gunnlaugsdottir and Björn Sivik

Department of Food Technology, University of Lund, Box 124, 221 00 Lund, Sweden

SUMMARY

In this work the effect of different flow rates on the selective extraction of the ethyl esters synthesised in a lipase catalysed alcoholysis reaction of cod liver oil was studied. Further, we investigated the phase behaviour of the reaction medium. The results showed that a fast flow rate both results in a higher extraction rate of ethyl esters and shifts the equilibrium of the reaction towards further synthesis. In addition, this work has established that the reaction medium comprises of two phases.

1. INTRODUCTION

In recent years lipase catalysis in water-poor non-aqueous media (NAM), such as organic solvents, have received increased attention [1]. Supercritical fluids (SCF) are a unique class of NAM, that have been considered as an attractive alternative to organic solvents. These fluids offer the same advantages for lipase catalysis, such as solubilisation of the hydrophobic lipid substrates, simple recovery of enzyme, as well as the possibility for the reversal of hydrolysis reactions in favour of synthesis, as organic solvents. Biocatalysis in SCF have recently been reviewed [2, 3]. One of the most unique properties of SCF is that they offer the possibility of a combined process of enzyme synthesis and product recovery. In addition, by selectively extracting either the desired product or the by-product from the reaction mixture one can shift the equilibrium of the enzyme reaction in the direction of further synthesis. The effect of shifting the thermodynamic equilibrium in this way was first investigated by Doddema et al. [4]. In that study, the ethanol produced in a continuous lipase-catalysed alcoholysis of ethyl acetate and nonanol, was removed. Adschiri et al. [5] improved the equilibrium in a batch interesterification reaction between tricaprylin and methyl oleate, by a selectively removing the by-product, methyl caprylate, from the reaction mixture with supercritical carbon dioxide (SCCO₂). Further, Shishikura et al. [6] reported on a improved lipase-catalysed incorporation of long-chain fatty acids into medium-chain triglycerides, in a batch reaction, by extraction of the by-product with SCCO₂.

Fish oils are a potential source of long chain n-3 polyunsaturated fatty acids such as eicosapentaenoic acid (EPA) and docosahexaenoic acid (DHA). Clinical

studies suggest that these n-3 fatty acids may have beneficial health effects. Consequently, there is a demand for enriched concentrates of these fatty acids.

In this paper we describe lipase catalysed ethanol-lysis of cod liver oil (CLO) in SCCO₂, this is an especially attractive process solvent for enzymatic catalysis as it is non-hazardous and inexpensive. CLO is a fair source of EPA and DHA containing approximately 10% of each fatty acid. The enzyme reaction under investigation results in a complex mixture of lipid components consisting of triglycerides (TG), diglycerides (DG), monoglycerides (MG) and ethyl esters (EE). We set out to preferentially extract the EE synthesised during the course of the experiment from the multicomponent reaction mixture. The EE produced during the enzyme reaction are of interest because of the ethyl eicosapentaenoate and ethyl docosahexaenoate, which could be concentrated in a later step of the process. An integrated process of the kind described here opens new possibilities for the application of biocatalysis in industrial process.

In our previous work [7] we have showed that the synthesised EE can be preferentially extracted at low pressures from the unconverted CLO and its side-products. The objectives of this work were to study; i) the phase behaviour of the reaction medium ii) the effect of flow rate on the extraction rate and recovery of EE. iii) whether the equilibrium of the enzyme reaction could be effected by increasing the flow rate of the extraction fluid.

2. MATERIALS

Immobilised lipase (Novozym 435) from *Candida antarctica* supported on a macroporous acrylic resin was purchased from Novo Nordisk A/S (Bagsvaerd, Denmark). The cod liver oil used was of commercial quality and obtained from Lysi h.f. Iceland. Dimodan LS is a commercial MG product made by Grindsted, Denmark, this product contains mainly monooleoyl- and monolinoleoyl glycerol.

3. METHODS

3.1. Enzyme reactions in SCCO₂

Figure 1 presents the experimental equipment used to conduct all lipase reactions in supercritical carbon dioxide. Cod liver oil (4.0 g), ethanol (2.4 g ; 99.5%) and enzyme (0.8 g) were placed in a 30 cm³ reactor. The reactor was then connected to the equipment (Fig. 1) and pressurised by pumping CO₂ into the reactor. The substrates were continuously mixed using a magnetic stirrer. The sampling line for the gas phase was located on the top of the reactor. The outgoing CO₂ was depressurized to atmospheric pressure by opening a heated micrometering valve (12). This was first opened 60 min after the desired working pressure had been reached; thereafter the reactor was semi-batch. Both the flow rate and the amount of outgoing CO₂ were monitored on a mass flow meter (17). The sampling line for the liquid phase was located on the bottom of the reactor. The reaction was carried out for 330 min at 90 bar and 40 °C. Two flow rates of CO₂ were tested; 15 mL CO₂ (at atm)/min and 150 mL CO₂/min. Three samples of both the gas and liquid phase were taken during the experiment. Ethanol (0.35 mL, 99.5 %) was added three times during the experiment to the reactor via a sample loop (8).

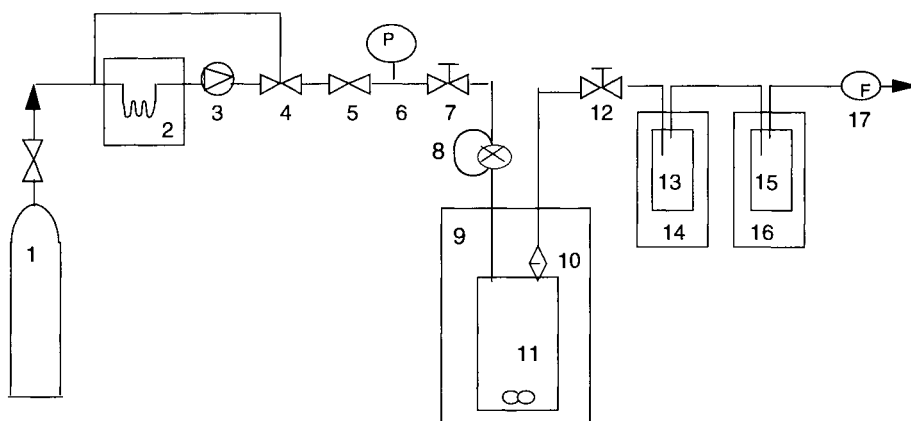


Figure 1. Schematic diagram of the experimental apparatus. 1. Gas tube, 2. Cool bath (-10°C), 3. Pump, 4. Relief valve, 5. Check valve, 6. Pressure meter, 7. Shut-off valve, 8. Loop, 9. Water bath (40°C), 10. Filter; 3.2 mm OD x 0.8 mm thick, $0.25\mu\text{m}$ 11. Reactor, 12. Micrometering valve, 13. and 15. Cold traps, 14. Cooler (at 0°C), 16. Cooler (at -60°C), 17. Flow meter

After the reaction had been carried out for 330 min the reactor was depressurized to atmospheric pressure, the residue dissolved in 40 mL 2-propanol and filtered through a Munktell No 3 filter paper into a previously weighed round bottom flask. A rotary evaporator was used to remove the solvent and the amount of residue was determined gravimetrically. The residue obtained was used in the phase behaviour experiments. All the data presented here represent the mean of two determinations.

3.2. Phase behaviour experiments

The apparatus used to study the phase behaviour of the lipids in SCCO_2 has been described in details by Hammam and Sivik [8]. All experiments were carried out at 90 bar and 40°C . In this work the sapphire cell used was charged with 0.25 g lipid sample and 0.16 g ethanol (99.5 %) and the phase behaviour of this mixture observed visually. The amount of ethanol and lipid sample was chosen so that they would represent the proportions of ethanol, lipids and SCCO_2 present in the actual enzyme reaction experiment.

3.3. Analysis

The overall content of tri-, di- and monoglycerides and fatty acid ethyl esters, was determined by a method previously described [7].

4. RESULTS AND DISCUSSION

4.1. Phase behaviour

At the beginning of the experiment the oil is present in the form of TG. During the reaction, the lipase splits the individual fatty acids from the glycerol backbone to form EE (a non-polar lipid component) as well as DG and MG (more polar lipid

components). Polar lipids, such as DG and MG, are amphiphilic i.e. they have a hydrophilic part (a polar head group) and a hydrophobic part (a non-polar lipid tail). Amphiphilic components are usually surface active and thus good emulsifiers. It was thus considered possible that the presence of these lipid classes might effect the phase behaviour of the mixture of ethanol/lipid sample in SCCO₂. In order to study this, the phase behaviour of mixtures of ethanol and lipid samples with different lipid class composition were studied visually using a high pressure view cell, the results from these investigations are compiled in Table 1.

Table 1.

Phase behaviour of mixtures of ethanol and different lipid samples in SCCO₂ at 90 bar and 40 °C

Lipid sample	Lipid class composition	Phases observed without mixing	Phases observed with mixing
Unreacted CLO ¹⁾	TG 98%	Clear gas phase & yellow liquid phase	Hazy gas phase & yellow liquid phase
Residue A ²⁾	TG 24%, EE 39% DG 12%, MG 7%	Clear gas phase & yellow liquid phase	Hazy gas phase & yellow liquid phase
Residue B ²⁾	TG 13%, EE 42% DG 10%, MG 8%	Clear gas phase & yellow liquid phase	Hazy gas phase & yellow liquid phase
Residue A/ Dimodan ²⁾ (50/50 w:w)	TG 12%, EE 20% DG 6%, MG 53%	Clear gas phase & yellow liquid phase	Hazy gas phase & yellow liquid phase

¹⁾ Emulsion at atm, that becomes transparent when the cell is charged with SCCO₂

²⁾ Transparent yellow mixture at atm

Residue A: remaining lipid residue when the flow rate of 15 mL/min was used

Residue B: remaining lipid residue when the flow rate of 150 mL/min was used

The main difference between the lipid samples under investigation is their lipid class composition (Table 1). The unreacted CLO contains nearly only TG while the main difference between Residue A and B was the amount of TG present in the sample. As there was no large difference in the amount of amphiphilic components, i.e. DG and MG, present in the two residues studied, additional MG (Dimodan) was added to one of the residues to investigate the effect of this. The results showed that two phases, a gas phase and a yellow liquid phase, were observed in all sample mixtures studied (Table 1). To study whether intensive mixing of the two phases present would effect their phase behaviour, the sapphire cell was turned up and down a couple of times. This resulted in a hazy gas phase, while the yellow liquid phase remained transparent. However, when the cell was merely swirled around once or twice, exclusively the gas phase in immediate vicinity to the phase boarder became hazy. These results suggest that

in the actual enzyme reaction experiments the continuous mixing of the substrates in the liquid phase probably results in a hazy gas phase close to the phase boarder. The reason why the gas phase becomes cloudy is unknown to us, probably some kind of structural rearrangement of the components present in the gas phase due to critical phenomena occurs upon mixing. Most importantly this study has established that the reaction medium comprises of two phases. Thus the risk for poor extraction selectivity due to a one phase system does not exist.

4.2. Flow rate effects

The effect of different flow rates on the extraction rate of EE from the reaction mixture is illustrated Figure 2. The results show that the higher flow rate results in a faster extraction and a higher recovery of the EE. This is probably largely due to the fact that the reaction mixture is exposed to more extraction fluid during a set time period. However, this may also be partly due to a faster reaction rate in this experiment. The reaction rate of the enzyme reaction under investigation has not been determined. Nevertheless, the total conversion of the TG substrate to EE was found to be higher when the higher flow rate was used, or 57% at the flow rate of 150 mL/min as compared to 38% when the flow rate of 15 mL/min was applied, this suggests that the reaction rate was faster in the former case. The total conversion is here defined as; sum of the amount of TG converted to EE in the residue and of that converted and present in the extract. The fact that the conversion to EE was higher when the faster flow rate was used indicates that the selective extraction of EE from the reaction mixture shifts the equilibrium of the reaction in the direction of further synthesis. These results are in agreement with the results presented by Adschiri et al. [5] and Shishikura et al. [6].

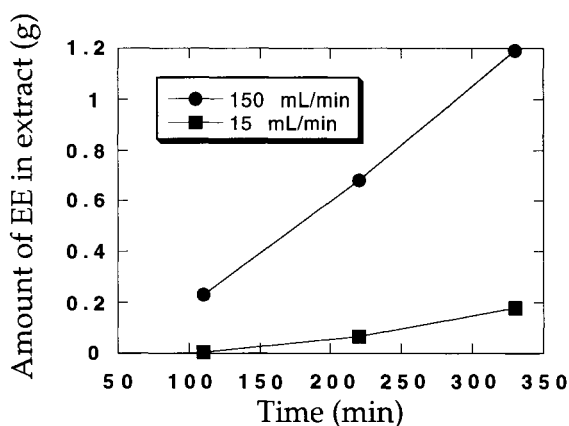


Figure 2. The effect of different flow rates on the extraction rate of EE from the reaction mixture.

As can be seen from Table 1, residues A and B both contained unextracted EE. At least some of these unextracted EE are probably located within the porous surface of the immobilisation support for the lipase enzyme. The extraction of these EE is

limited by the diffusion of the EE through the pores of the immobilisation support to the surface. It was observed, that no bulk liquid oil phase was present at the end of the 330 min long experiment when the faster flow rate was applied. This further supports the theory that the remaining EE are actually located within the immobilisation support.

The solubility of the EE in CO₂ at the two different flow rates is shown in Figure 3. At the higher flow rate the concentration of the EE was found to be approximately the same in all samples of the extract or about 30 mg EE/L CO₂. This suggest that equilibrium flow rate was obtained in this experiment.

However, when the flow rate of 15 mL/min was applied the concentration was found to increase with time. This observation can be explained by experimental start-up effects, i.e. the flow rate is so slow that the extracted lipid components precipitate and build up in the tube section between the reactor (11) and the first cold trap (13), rather than being collected in the cold trap. Secondly, there was less conversion to EE when the slow flow rate was used. Hence, the proportional amount of EE available for solubilisation in CO₂ was inferior when this slow flow rate was applied.

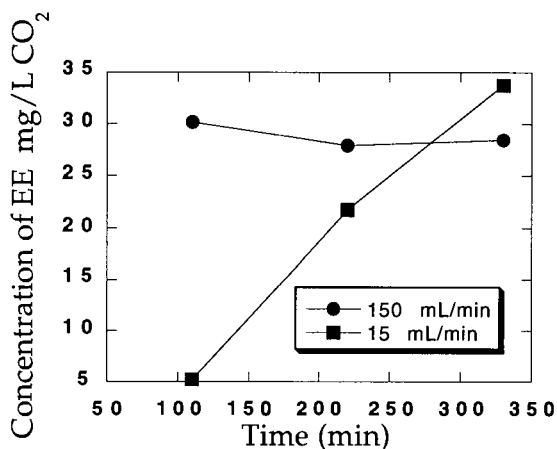


Figure 3. The concentration of the EE in CO₂

REFERENCES

1. S. Bloomer, Lipase-catalyzed lipid modifications in non-aqueous media, Thesis, Lund University, Sweden, 1992.
2. O. Aaltonen, and M. Rantakylä, *Chemtech*, 21 (1991) 240.
3. S.V. Kamat, E.J. Beckman, and A.J. Russell, *Critical reviews in biotechnology*, 15 (1995) 41.
4. H.J. Doddema, *et al.* Enzymatic reactions in supercritical carbon dioxide and integrated product-recovery. 5th European Congress on Biotechnology, Christiansen *et al.* (eds.), Copenhagen, 1990.
5. T. Adschiri, *et al.*, *J. Chem. Eng. Japan*, 25 (1992) 104.
6. A. Shishikura, *et al.*, *J. Am. Oil Chem. Soc.*, 71 (1994) 961.
7. H. Gunnlaugsdottir, and B. Sivik, *J. Am. Oil Chem. Soc.*, 72 (1995) 399.
8. H. Hammam, and B. Sivik, *J. Supercrit. Fluids*, 6 (1993) 223.

Supercritical Carbon Dioxide as a Medium for Enzymatically Catalyzed Reaction

M. Habulin, V. Krmelj and Ž. Knez

Faculty of Chemistry and Chemical Engineering, University of Maribor,
Smetanova 17, 2000 Maribor, Slovenia

The present work reports results and observations on the enzymatic synthesis of oleyl oleate (which is a synthetic analogue of jojoba oil) in supercritical carbon dioxide. Special stress was laid on the comparison between batch and continuous systems for the above mentioned synthesis. Influence of different reaction parameters on the reaction yield and initial reaction rates was studied.

1. INTRODUCTION

After initial findings that some enzymes were active and stable in SCF's [1,2], several other studies on enzyme catalysis in SCF's have been carried out. The majority of systems explored to date have used model reactions [3,4] of which only a few show a possibility for practical and commercial purposes [5].

The enzymatic esterification of oleic acid and oleyl alcohol to obtain oleyl oleate, which is a synthetic analogue of jojoba oil, was studied. The reaction was catalyzed by a commercially available immobilized lipase from *Rhizomucor miehei*. As solvents, carbon dioxide and liquid n-butane were used. Reactions were performed in a batch and in continuously operating high pressure reactors.

Investigations were oriented towards the comparison between a batch and continuous system at supercritical conditions. Reaction yields in both systems as well as initial reaction rates in the batch system were observed. Reactions were carried out at different reaction conditions and the influence of reaction parameters on the yield and initial reaction rates was studied.

2. MATERIALS AND METHODS

2.1. Reagents

Enzyme preparation. The enzyme preparation Lipozyme IM, which is a *Rhizomucor miehei* lipase, immobilized on a macroporous anion exchange resin, was kindly donated from NOVO Nordisk AS (Copenhagen, Denmark).

Lipase activity. Lipase activity was measured by NOVO Nordisk AS. The activity of Lipozyme used for syntheses was:

- 45 BIU/g in the high pressure batch reactor and
- 49 BIU/g in the high pressure continuous reactor.

Chemicals. Oleyl alcohol (85%) was supplied by Aldrich Chemical Co. (Milwaukee, WI) and oleic acid (extra pure) was purchased from Merck (Darmstadt, Germany). All other chemicals were from Kemika (Zagreb, Croatia). Carbon dioxide was 99.97% volume pure and was supplied by Linde Plin (Linde, Celje, Slovenia).

2.2.Procedure

Analytical method. For quantitative determination of the oleic acid amount in the reaction mixture a volumetric method was used and qualitative analysis of the product was done with IR spectroscopy.

Reaction performance. Supercritical carbon dioxide was used as a reaction media for the enzymatic synthesis of oleyl oleate directly from oleic acid and oleyl alcohol. Reaction was catalyzed by immobilized lipase from *Rhizomucor miehei*-Lipozyme IM. Reactions were carried out in the high pressure batch and continuous reactor.

High pressure batch stirred tank reactor. Substrates (equimolar solution of oleic acid and oleyl alcohol) were filled into thermostated autoclave and mixed. Enzyme preparation was added and finally CO₂ was pumped with a high pressure pump up to desired pressure. Reactor volume was 0.5 L ($P_{\max} = 450$ bar, $T_{\max} = 200^{\circ}\text{C}$) (Figure 1).

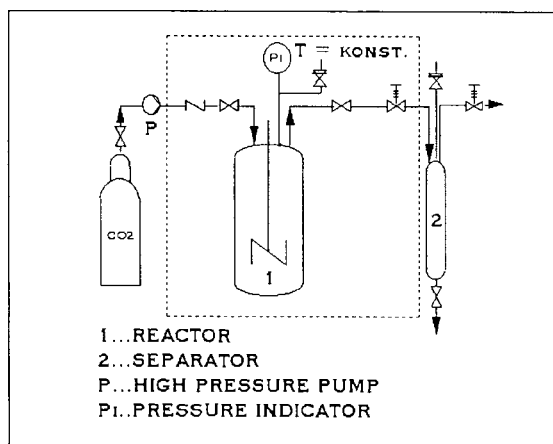


Figure 1. Design of experimental batch apparatus for synthesis of oleyl oleate under supercritical conditions.

High pressure continuously operated reactor. The design of the continuously operated apparatus is shown in Figure 2. An air operated high pressure pump delivered CO₂ in the system. The gaseous fluid was dried when passing through columns packed with molecular sieves. The flow rate of CO₂ was 1.0 L per min. Equimolar solution of substrates (oleic acid and oleyl alcohol) was pumped into the system with an HPLC pump. Carbon dioxide and substrates were equilibrated in the saturation column. The reaction was performed in a

continuously operated fixed-bed reactor packed with Lipozyme. Supercritical CO_2 was depressurized through the expansion valves to the separators. The gaseous CO_2 phase left the system after flow rate measurement through a rotameter or could be recycled on a large scale unit.

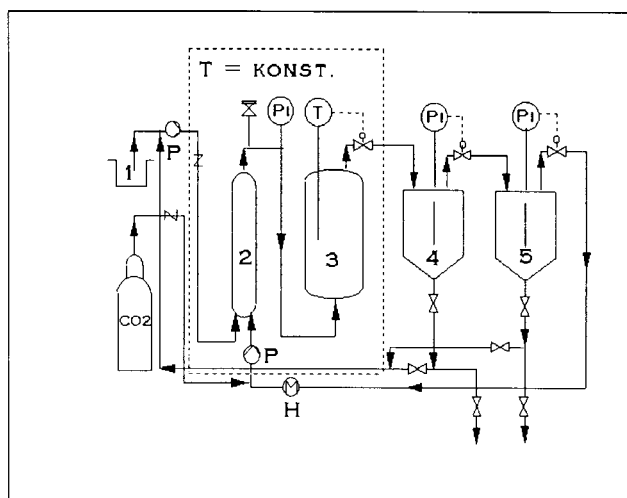


Figure 2. Design of continuously operating experimental apparatus for the synthesis of oleyl oleate under supercritical conditions: 1-substrates, 2-saturation column, 3-enzymatic reactor, 4, 5-separators, P-high pressure pump, P_i -pressure indicator, T-temperature indicator, H-heat exchanger.

3. PRESSURE AND TEMPERATURE INFLUENCE

3.1. High pressure operated batch stirred tank reactor

Equilibrium conversion is not affected much by pressure. The highest values in the temperature range between 40°C and 80°C are at the pressure of 80 bar (Table 1). With higher pressure conversion slightly decreases.

Table 1

Equilibrium conversion (in %) in the high pressure batch operated reactor as a function of temperature and pressure.

	80 bar	150 bar	200 bar	300 bar	450 bar
40°C	84	83	83	80	80
50°C	90	86	84	83	81
60°C	87	88	84	83	82
70°C	86	84	76	77	77
80°C	86	76	76	75	71

Initial reaction rates at temperatures from 40°C to 60°C increase when the pressure is increased from 80 bar to 300 bar, and decrease with higher pressure (Figure 3). Probably, at lower pressure the adsorption of the ester to the enzyme takes place, causing inhibition of the enzyme. Solubility of the ester increases with higher pressure, so SC CO₂ flushes away the ester from the enzyme and activity of the enzyme increases. The same explanation was found in lit. [6]. On the other hand, at high pressure too much water may be extracted from the biocatalyst resulting in lower reaction yields [7].

At higher temperatures (70°C and 80°C) maximal initial rates are at 200 bar and with higher pressure they decrease.

Temperature influence at pressures from 80 bar to 300 bar was the same as at atmospheric pressure. Optimal temperature for esterification was 50°C. The enzyme is less active below and above this temperature.

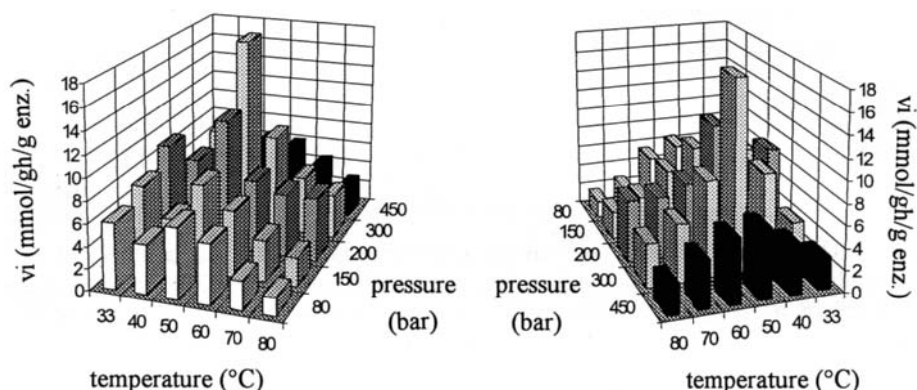


Figure 3. Initial reaction rates in a BSTR as a function of pressure and temperature. (Rotational speed was 600 rpm, enzyme/substrate ratio was 0.04 g/g.)

3.2. High pressure continuously operated reactor

Experiments at different temperature and pressure combinations showed that the greatest activity of Lipozyme is at pressures near the critical value and decreases with higher pressure (Figure 4). The highest conversion was at 60°C and 80 bar. At temperatures above the critical point of CO₂, there is a strong pressure influence on the conversion, e.g. at 50°C conversion decreases from 45% at 80 bar to 15% at 150 bar. There is no strong influence of the pressure on the conversion at temperatures below T_C of CO₂. At 20°C and 30°C, decrease in conversion between 80 bar and 150 bar is only some percent. At subcritical pressure of CO₂, reaction yields are lower probably due to lower diffusivity and higher viscosity of substrates - liquid CO₂ mixture. With the increase of temperature from 35°C to 60°C the enzyme activity rises in the same way as in the same system at atmospheric pressure [8].

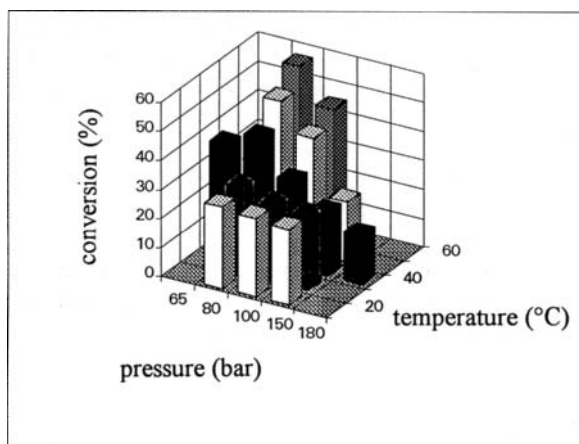


Figure 4. Conversion as a function of temperature and pressure in a high pressure continuous reactor (flow rate of CO_2 was 1 L/min).

4. REACTION PERFORMANCE IN n-BUTANE

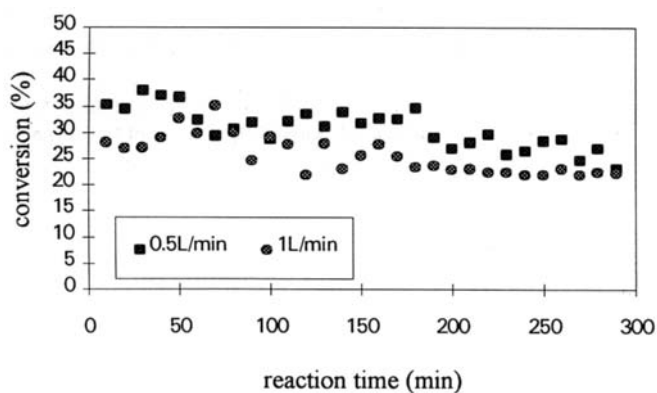


Figure 5. Percent conversion vs. reaction time for continuous synthesis of oleyl oleate in n-butane

Solubility of fatty acid compounds in n-butane are higher than in SC CO₂. Therefore test reactions at 150 bar and 40°C were performed in n-butane. The flow of the gas was 0.5 and 1 L per min. The results showed that Lipozyme loses its activity in this media. The conversion continuously decreases from 50% at the beginning to 22% after 300 min of the reaction operation (Figure 5).

5. CONCLUSION

There is considerable difference in the system behavior at high pressure batch and continuous performance. In the continuous system the decrease in conversion between 80 bar and 150 bar is about 30% at 50°C and not only some percent as in the batch system. The difference may be that in the continuous system at high pressure the water is removed from the enzyme and in the batch system, although it is solubilized in SC CO₂, it remains in the system and the activity of the lipase only slightly decreases.

- In the batch system pressure influence on initial reaction rates is different at lower and at higher temperatures.
- In the continuous system the extraction of water from enzyme beads is an overriding process at higher pressures.
- Because of enzyme deactivation in n-butane, SC CO₂ is a properer reaction media than n-butane.

To confirm our findings about the system behavior at the batch and continuous performance further investigations will be conducted.

REFERENCES

1. T.W. Randolph, H.W. Blanch, J.M. Prausnitz and C.R. Wilke, *Biotechnol. Lett.*, 7 (1985) 325.
2. K. Nakamura, Y.M. Chi, Y. Yamada and D. Misiti, *Chem. Eng. Commun.*, 45 (1986) 45.
3. E. Cernia, C. Palocci, F. Gasparini and D. Misiti, *Chem. Biochem. Eng. Q.*, 8(1) (1994) 1.
4. M. Perrut, *Chem. Biochem. Eng. Q.*, 8(1) (1994) 25.
5. H. Gunnlaugsdottir and B. Sivik, *JAOCs*, 72(4) (1995) 399.
6. D.C. Sleytler, P.S. Moulson and Reynolds, *J. Enzyme Microb. Technol.*, 13 (1991) 221.
7. Ž. Knez, V. Rižner, M. Habulin and D. Bauman, *JAOCs*, 72(11) (1995) 1345.
8. M. Habulin and Ž. Knez, *Fat Sci. Technol.*, 95(7) (1993) 249.

Synthesis of *N,N*-Dimethylformamide by Heterogeneous Catalytic Hydrogenation of Supercritical Carbon Dioxide

O. Kröcher, R.A. Köppel and A. Baiker

Department of Chemical Engineering and Industrial Chemistry, Swiss Federal Institute of Technology, ETH-Zentrum, CH-8092 Zürich, Switzerland.

Sol-gel derived hybrid materials are used as heterogeneous catalysts for the synthesis of *N,N*-dimethylformamide (dmf) using scCO_2 as both solvent and reactant. Results are compared to conventional homogeneous and heterogeneous catalysts. The turnover numbers exceed those reported so far for dmf synthesis by heterogeneous catalytic routes by more than three orders of magnitude.

1. INTRODUCTION

In recent years, researchers have become increasingly interested in the use of carbon dioxide as a source of carbon because of its ideal properties as a C_1 -unit in future chemistry[1-3]. The three most important advantages are its abundancy, low cost and non-toxicity. Supercritical carbon dioxide (scCO_2) has also been considered as an ideal apolar solvent for chemical reactions due to its increased diffusion rates and reactant solubilities, and to its easy product separation compared to conventional solvents [4-7].

As potential and valuable chemicals, alcohols, hydrocarbons and amines have been

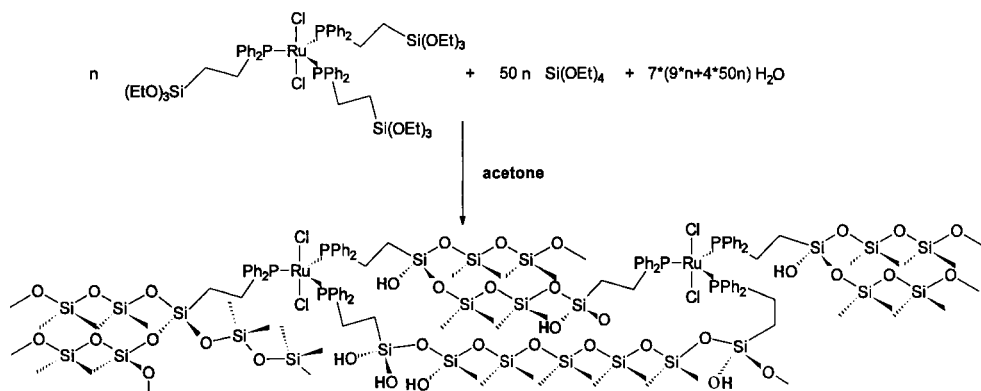


Figure 1. Incorporation of $\text{RuCl}_2\{\text{PPh}_2(\text{CH}_2)_2\text{Si}(\text{OEt})_3\}_3$ into a silica matrix.

investigated [8]. The homogeneous catalytic formation of *N,N*-dimethylformamide from carbon dioxide in liquid solvents has also been reported, but yields remained unsatisfactory. Recently it has been shown that the use of supercritical carbon dioxide as both reaction medium and reactant offers an efficient way for the homogeneous catalytic synthesis of dmf from CO₂ [1, 9]. The main technical disadvantage of this method is the use of homogeneous catalysts, which prevents easy separation of the desired product.

In this study we report a heterogeneous catalytic route for the synthesis of dmf from CO₂, H₂ and dimethylamine (dma) under supercritical conditions, employing sol-gel derived hybrid materials as catalysts. Highly active and stable catalysts can be produced by incorporation of specially tailored silylether complexes within a porous silica network, thus providing access to the catalytically active centres [10]. The highest turnover numbers achieved with these catalysts are more than three orders of magnitude higher than that reported so far for heterogeneous catalyzed dmf synthesis [11, 12]. The fixed complexes are usually more stable against oxygen and water than their free analogues. Figure 1 illustrates the gelation process for silica modified with RuCl₂{PPh₂(CH₂)₂Si(OEt)₃}₃.

2. EXPERIMENTAL SECTION

The complexes *cis*-/*trans*-PdCl₂{PPh₂(CH₂)₂Si(OEt)₃}₂, *cis*-PtCl₂{PPh₂(CH₂)₂Si(OEt)₃}₂, RhCl{PPh₂(CH₂)₂Si(OEt)₃}₃, and IrCl{PPh₂(CH₂)₂Si(OEt)₃}₃, used as homogeneous catalysts, were obtained from PdCl₂(COD), PtCl₂(COD), [RhCl(COD)]₂, and [IrCl(COD)]₂, by ligand exchange reaction with PPh₂(CH₂)₂Si(OEt)₃. Since this route failed in case of ruthenium, these complexes were prepared from RuCl₃·xH₂O and PPh₂(CH₂)₂Si(OEt)₃, using NaBH₄ as reductant.

Silica matrix stabilized transition metal complexes were prepared following a method of Schubert *et al.* [13]. The silylether complex and the calculated amount of tetraethoxysilane were dissolved in acetone under argon. A sevenfold excess of 2.8 n orthophosphoric or acetic acid was added, after which the solution was moderately stirred for 24 h. Then a continuous argon flow was passed through the flask for 3 d, evaporating the acetone. The resulting glassy coloured lumps were kept for further 4 d in an open beaker. The lumps were crushed, washed thoroughly with water and acetone, and finally dried for 6 h at 0.1 Torr. Undestructured incorporation of the complexes into the matrix was confirmed by ³¹P NMR spectroscopy of both liquid precursors and solid catalysts.

3. RESULTS AND DISCUSSION

3.1. Catalyst screening

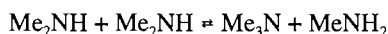
Several group(VIII) metal complexes were screened as potential homogeneous catalysts for the synthesis of dmf from scCO₂. Table 1 summarizes the results of the catalytic tests carried out with these complexes. Note that reaction parameters were varied sometimes, to find suitable reaction conditions. Under the conditions used carbon dioxide and hydrogen are expected to be in the supercritical region, whereas dma, dmf and water are in liquid state. Jessop *et al.* [14] found swelling of the liquid dimethylamine phase by dissolved CO₂ thus providing high local concentrations of educts.

Table 1. Screening of potential catalysts for the production of *N,N*-dimethylformamide from dimethylamine, hydrogen and carbon dioxide

Catalyst	dmf		Yield (%)		
	TON ^a	TOF/h ⁻¹ ^b	dmf	tma ^c	mf ^d
RuCl ₃ NO(PEt) ₃	4633	265	62	0.1	-
<i>cis</i> -RuCl ₂ (CO) ₂ {PPh ₂ (CH ₂) ₂ Si(OEt) ₃ } ₂	452	30	3	0.1	-
<i>cis</i> -RuCl ₂ (CO) ₂ (PPh ₃) ₂	298	24	2	2	-
RuCl ₂ (PPh ₃) ₃	5186	343	84	-	-
RuCl ₂ {PPh ₂ (CH ₂) ₂ Si(OEt) ₃ } ₃	5088	356	96	-	-
<i>trans</i> -PdCl ₂ (PEt ₃) ₂ [*]	496	38	9	-	-
Pd(PPh ₃) ₄	132	9	2	-	-
RhCl(PPh ₃) ₃	143	10	2	4	-
Rh(CO)Cl(PPh ₃) ₂ [*]	519	39	7	-	-
Ir(CO)Cl(PPh ₃) ₂ [*]	11	1	2	-	-
Co ₃ (CO) ₁₂ [*]	21	1	0.3	2	-
Re(NO)(CO)Cl ₂ {PPh ₂ (CH ₂) ₂ Si(OEt) ₃ } ₂ [15]	79	6	2	0.4	-
RuCl ₃ ·xH ₂ O ^{*e}	1208	72	94	-	-
ZnCl ₂ ^{*e}	15	1	1	-	-
PdCl ₂ ^{*e}	34	3	2	-	-
PtCl ₂ ^{*e}	65	4	4	0.1	-
Pd/Al ₂ O ₃ ^{ef}	681	45	59	7	2
CuO/Al ₂ O ₃ ^{ef}	37	3	84	3	1
RhCl{PPh ₂ (CH ₂) ₂ Si(OEt) ₃ } ₃ ^{*g}	530	35	4	-	-
IrCl{PPh ₂ (CH ₂) ₂ Si(OEt) ₃ } ₃ ^{*g}	2900	190	23	-	-
PdCl ₂ {PPh ₂ (CH ₂) ₂ Si(OEt) ₃ } ₂ ^g	1410	90	11	-	-
PtCl ₂ {PPh ₂ (CH ₂) ₂ Si(OEt) ₃ } ₂ ^g	1490	100	10	0.2	-
RuCl ₂ {PPh ₂ (CH ₂) ₂ Si(OEt) ₃ } ₃ ^g	3234	216	25	-	-
RuCl ₂ {PMe ₂ (CH ₂) ₂ Si(OEt) ₃ } ₃ ^g	13 670	900	94	-	-
_h	110850	1860	82	-	-

Reactions were carried out in a 500 cm³ stainless steel autoclave agitated by a magnetically coupled suspension stirrer. The products were analysed by gas chromatography. Reaction conditions: *n*[catalyst] = 5·10⁻⁵ mol (expressed as amount of group(VIII) metal), *n*[Me₂NH] = 0.28 mol, *p*[H₂] = 8.5 MPa, *p*[CO₂] = 13.0 MPa, *T* = 386 K, *t* = 15 h, stirring rate = 1000 min⁻¹. ^a TON = mol dmf (mol catalyst)⁻¹. ^b TOF = TON/h. ^c tma = trimethylamine. ^d mf = *N*-methylformamide. ^e *n*[catalyst] = 2·10⁻⁴ mol. ^f *T* = 463 K. ^g *n*[Me₂NH] = 0.7 mol, *p*[H₂] = 8.5 MPa, *p*[CO₂] = 13.0 MPa, *T* = 373 K, *t* = 15 h, stirring rate = 300 min⁻¹, *n*[catalyst] = 5·10⁻⁵ mol. ^h *n*[Me₂NH] = 6.4 mol, *T* = 406 K, *t* = 60 h, stirring rate = 500 min⁻¹, *n*[catalyst] = 1.8·10⁻⁵ mol. * = decomposition under reaction conditions.

The main product observed was generally dmf (Table 1). Some complexes exhibited also activity in trimethylamine production, which is a thermodynamically favoured disproportion product of dimethylamine at higher temperatures.



For low catalytic conversions a white precipitate was obtained, melting at room temperature. It could be identified as dimethylammonium *N,N*-dimethylcarbamate [14], formed reversibly in a temperature and pressure dependent side reaction of dimethylamine and carbon dioxide. Under GC conditions this carbamate decomposes to amine and carbon dioxide.



The ruthenium complexes with different patterns of chlorine and phosphine ligands proved to be most active. The complex $\text{RuCl}_2\{\text{PPh}_2(\text{CH}_2)_2\text{Si}(\text{OEt})_3\}_3$ with silylether phosphine ligands exhibited the same activity as the corresponding triphenylphosphine complex. In comparison, activity dropped significantly for $\text{RuCl}_2(\text{CO})_2(\text{PPh}_3)_2$ and $\text{RuCl}_2(\text{CO})_2\{\text{PPh}_2(\text{CH}_2)_2\text{Si}(\text{OEt})_3\}_2$ with stabilizing CO ligands. However, these complexes were the only ruthenium complexes, stable enough to be stored in air for a long time. So stability and reactivity showed an antagonistic behaviour. $\text{RuCl}_3\text{NO}(\text{PET})_3$ has special properties in this series of ruthenium complexes. On the one hand it is stabilized by a NO ligand, that limits its activity, on the other hand its high solubility in *n*-hexane, known to be similar to scCO_2 , is expected to increase the catalytic activity. The poisoning effect of CO in this reaction is supported by the poor results obtained with the iridium, rhodium, cobalt, and rhenium carbonyl complexes. Since many of the compounds decomposed during the reaction, leading to metal depositions on the reactor wall, it was not possible to judge unequivocally if low conversions were due to the intrinsic properties of the complexes or to fast decomposition.

In addition to the homogeneous metal complexes, some group(VIII) metal chlorides and alumina supported group(VIII) metals were tested for dmf synthesis. Among the metal salts investigated, $\text{RuCl}_3 \cdot x\text{H}_2\text{O}$ proved to be most promising, showing high activity and only little metal deposition on the reactor wall. In contrast, palladium, platinum and zinc chloride exhibited low activity, possibly due to severe decomposition.

Another interesting result is the high yield reached with palladium on alumina. Beside the desired product dmf, trimethylamine, *N*-methylformamide and traces of *N,N*-dimethylurea were identified by GC-MS. The utilization of such a stable and disposable catalyst could be interesting for developing the solvent-free hydrogenation of carbon dioxide on an industrial scale.

3.2. Test of sol-gel catalysts

All sol-gel derived catalysts were stable under reaction conditions, except the rhodium and iridium catalysts, whose colour changed significantly during reaction. The catalysts could easily be separated from the reaction mixture by simple filtration. The filtrated liquid product, that flew out colourless, exhibited no further catalytic activity. GC analysis of the liquid phase indicated the production of dmf with 100% selectivity in all cases, except for the platinum containing catalyst (Table 1).

The catalytic activity, expressed as turnover frequency (TOF), increases in the order $\text{Rh} < \text{Pd}, \text{Pt} < \text{Ir} < \text{Ru}$. The ruthenium catalyst with methylphosphine instead of phenylphosphine

ligands exhibited the highest activity; a turnover number (TON) of 110 850 with a selectivity to dmf of 100% was reached. This behaviour can probably be attributed to the structural and electronical similarity of its ligand sphere to $\text{RuCl}_2(\text{PMe}_3)_4$, the highest active homogeneous catalyst for this reaction reported so far [9].

3.3. Parametric sensitivity

For optimization of the reaction conditions several reaction parameters were varied, using a catalyst made of $\text{RuCl}_2\{\text{PPh}_2(\text{CH}_2)_2\text{Si}(\text{OEt})_3\}_3$ and tetraethoxysilane in a ratio of 1:50. The temperature dependence described by the Arrhenius-equation indicated an activation energy of 70 kJ mol^{-1} . The suitable temperature range of the reaction is between 370 and 400 K. The upper temperature limit is given by the thermal stability of the catalyst. No significant dependence of the reaction rate on the stirring frequency was observed in the frequency range $100 - 500 \text{ min}^{-1}$. Furthermore, the rate increased linearly with increasing amount of catalyst, indicating that the observed rate was not disguised by mass transfer phenomena. Carbon dioxide pressure had only a marginal effect on rate in the partial pressure range 3 - 18 MPa, indicating a zeroth order dependence.

4. CONCLUSION

Among a series of group(VIII) metal complexes, ruthenium compounds proved to be most active for the homogeneous catalytic synthesis of dmf from CO_2 , H_2 and dimethylamine. Most of the other complexes tested suffered from low catalytic activities and decomposition under reaction conditions. In contrast, a heterogeneous palladium on alumina catalyst was stable but exhibited markedly lower activity. Optimum results could be obtained with new sol-gel derived hybrid materials, which combine the high activity of the homogeneous complex with the stability of heterogeneous catalysts. Among these catalysts, ruthenium containing silica gels exhibited the highest activities for the production of dmf with TON's up to 110 850.

REFERENCES

1. P.G. Jessop, T. Ikariya and R. Noyori, *Chem. Rev.*, 95 (1995) 259-272.
2. W. Leitner, *Angew. Chem., Int. Ed. Engl.*, 34 (1995) 2207-2221.
3. A. Behr, *Angew. Chem. Int. Ed. Engl.*, 27 (1988) 661-678.
4. M. Poliakoff and S.M. Howdle, *Proc. 3rd Int. Symp. on Supercritical Fluids*, Strasbourg, October 17-19, 1994, pp. 81-92.
5. G. Kaupp, *Angew. Chem. Int. Ed. Engl.*, 33 (1994) 1452-1455.
6. K.P. Johnston, *Nature*, 368 (1994) 187.
7. H. Tiltscher and H. Hofmann, *Chem. Eng. Sci.*, 42 (1987) 959-977.
8. A. Baiker and R.A. Köppel, *Proc. Int. Conf. on Carbon Dioxide Utilization*, Bari, September 26-30, 1993, pp. 295-302; A. Baiker and R.A. Köppel, *3rd Int. Conf. on Carbon Dioxide Utilization*, Norman, Oklahoma, 1995.
9. P. G. Jessop, T. Ikariya and R. Noyori, *J. Am. Chem. Soc.*, 116 (1994) 8851-8852.
10. U. Schubert, *New J. Chem.*, 18 (1994) 1049-1058.
11. O. Kröcher, R.A. Köppel and A. Baiker, *J. Chem. Soc., Chem. Commun.*, (1996), in press.

12. K. Kudo, H. Phala, N. Sugita and Y. Takezaki, *Chem. Lett.*, (1977) 1495-1496.
13. U. Schubert, K. Rose and H. Schmidt, *J. Non-Cryst. Solids*, 105 (1988) 165-170.
14. P.G. Jessop, Y. Hsiao, T. Ikariya and R. Noyori, *J. Am. Chem. Soc.*, 118 (1996) 344-355.
15. Prepared by D. Rattat, Institute of Inorganic Chemistry, University of Zuerich.
Crystallographic data is available on request.

Photooxidation Reactions in Supercritical CO₂

Seiichiro Koda, Yoshito Oshima, Junichiro Otomo and Tokuro Ebukuro

Department of Chemical System Engineering, School of Engineering,
The University of Tokyo, Hongo, Bunkyo-ku, Tokyo 113, Japan

KrF excimer laser-induced reactions in the mixture of hydrocarbon/O₂/CO₂ under sub- and super-critical conditions were investigated. In the ethylene mixtures, the main products were ethylene oxide and acetaldehyde. The total quantum yield decreased with the increase of mixture density, but the branching ratio between the two products were almost independent on the density. The branching ratio was found to be what is expected if the reactive species is O(³P). The reaction for other hydrocarbons including ethane and cyclohexane is also discussed.

1. INTRODUCTION

In our previous research [1], it was found that relatively large amounts of oxidized products were obtained when a mixture of ethane (C₂H₆)/O₂ was photolysed with KrF excimer laser light at 30-40 °C at pressures close to the supercritical one, in spite of the fact that both C₂H₆ and O₂ do not absorb the KrF excimer laser light under ordinary pressures. At that time, the mechanism of the 248 nm light absorption was not clarified. Later we studied the effect of pressurized foreign gases on the photoabsorption of O₂ in the 230-280 nm wavelength range [2]. The photoabsorption by O₂ in the mixtures with C₂H₆, CO₂ and various other gases was found to increase considerably with cross sections proportional to the number density of the foreign gases. It was concluded that the mechanism of the absorption augmentation is the collision-induced relaxation of the selection rule for the dipole-forbidden Herzberg III system (A³Δ_u - X³Σ_g⁺). In the neighborhood of supercritical point, light scattering also contributes to decrease the transmitted light intensity. This scattering, in some cases, might be useful in order to lengthen the effective absorption path length which is important for complete absorption of photon.

On the other hand, it is interesting to use the supercritical CO₂ as an alternative solvent for various photochemical reactions, particularly for photo-initiated oxidation reactions, due to the non-ignitability of CO₂. Thus we are studying photo-induced oxidation reactions of ternary mixtures of hydrocarbon/O₂/CO₂. Partially oxidized products have been found to be produced in the case of C₂H₆, ethylene (C₂H₄) and cyclohexane (C₆H₁₂) which have been studied so far. The present paper mainly reports the case of C₂H₄ in order to understand the behavior of typical olefinic hydrocarbons which are expected to trap some active species during the reaction.

2. EXPERIMENTAL

The experimental apparatus is shown in Fig. 1. The reaction cell consists of a stainless-steel cylinder (length, 31 mm; inner diameter, 16 mm) with quartz windows at both ends for light introduction. After evacuating the cell, C_2H_4 and O_2 were introduced into the reactor to an individual fixed pressure (typically, C_2H_4 , 20 atm; O_2 , 6 atm), followed by the addition of CO_2 up to the reaction pressure. The contents were mixed with a magnetic stirrer inside of the cell for 5 min., and then a KrF (at 248 nm) excimer laser (Lambda Physik Lextra 100) was used to irradiate the mixture at 10 Hz for a desired period (5 - 60 min.), with keeping the stirring of the contents all through the irradiation. The reaction cell was placed in a constant temperature bath (typically, 308 K). After the irradiation of a desired period, the contents were expanded into a container at 1 atm for quantitative analysis by gas chromatography.

Photoabsorption measurements were also performed using a deuterium lamp (Hamamatsu Photonics L544) as a light source. The transmitted light was resolved by a monochromator (Nikon P-250) and detected by a photomultiplier (Hamamatsu Photonics R928).

The PVT relation of the mixture was estimated using the modified BWR equation with appropriate parameters. The estimated critical parameters for the $C_2H_4(20 \text{ atm})/O_2(6 \text{ atm})/CO_2$ is: $T_c = 296.0 \text{ K}$, $P_c = 71.0 \text{ bar}$, and $\rho_c = 10.4 \text{ mol/l}$ (0.44 g/cm^3).

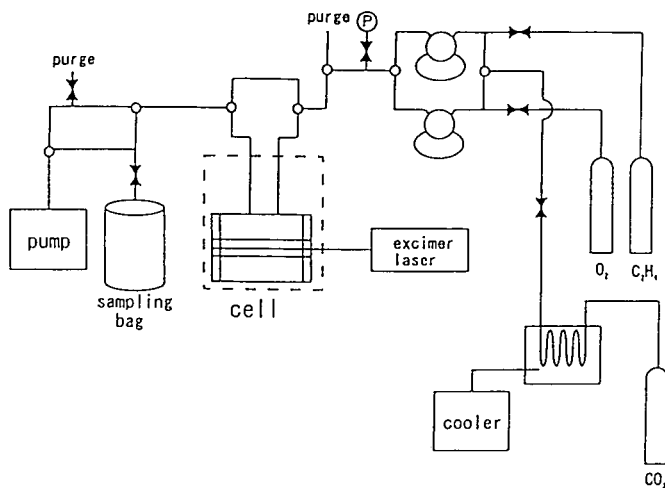


Figure 1. Experimental apparatus

3. RESULTS AND DISCUSSION

3.1. Products

Ethylene oxide (C_2H_4O) and acetaldehyde (CH_3CHO) were found as main products. CO was also detected. Figure 2 shows the time dependence of these three products. The yield of C_2H_4O increases linearly with time, which indicates that C_2H_4O does not react to any appreciable extent through secondary reactions or subsequent photolysis. The yield of

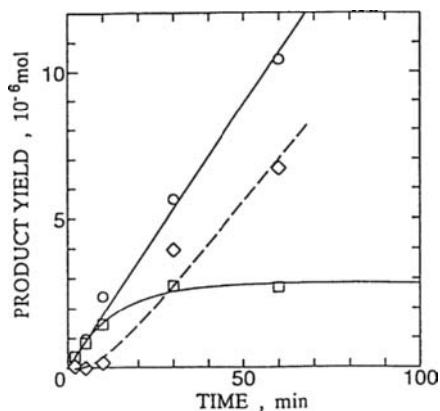
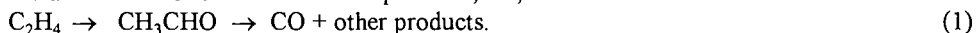


Figure 2. Yield of C_2H_4O (○), CH_3CHO (□) and CO (◇) vs. irradiation time at 40 mJ under 65 atm.

CH_3CHO , however, shows a tendency to become flat upon the continuation of the irradiation, and CO has a certain initial time delay. The concerted behavior of these products strongly suggests that the primarily produced CH_3CHO is photolysed further upon the continuation of irradiation and CO is one of the main products, i.e.,



The other products may contain CH_4 , whose quantitative analysis, however, was not performed. The same secondary photolysis was found to proceed in the irradiation of the C_2H_6/O_2 mixtures as reported before [1].

By extrapolating the obtained fraction of CH_3CHO against the sum of C_2H_4O and CH_3CHO as a function of the irradiation time, the fraction at the beginning of the irradiation was determined. Eventually, it was 0.56 ± 0.06 in the case shown in Fig. 2. The dependence of the fraction against the pressure or density will be shown later.

3.2. Product yield against the density

The total yield of C_2H_4O and CH_3CHO obtained at the 5 min. irradiation time is plotted against the mixture density in Fig. 3. The absorbance of the mixture was also measured and plotted in the same figure. The photoabsorption is considered to be mainly due to the partially allowed Herzberg III absorption due to O_2 itself, C_2H_4 and CO_2 according to the previous research [2]. However, the observed absorbance in the higher density region was larger by 2 to 3 times than what is estimated according to the following equation

$$\sigma_{\text{total}} = \sigma_0 + \sigma_1 O_2 + \sigma_1 CO_2 + \sigma_1 C_2H_4, \quad (2)$$

using the σ coefficients obtained in the previous research [2]. This may be mainly ascribed to the increased scattering of the mixture, which gives us some difficulty to precisely estimate the number of absorbed photons in the reaction cell. However, for simplicity, we estimated the quantum yield of the sum of C_2H_4O and CH_3CHO , assuming that the observed absorbance precisely corresponds to the real absorption. The quantum yield estimated as above is also shown in Fig. 3 by a dashed line.

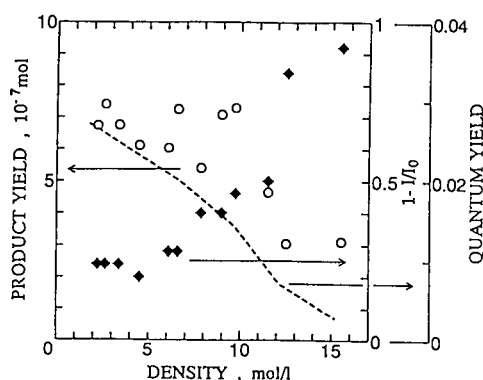


Figure 3. The total yield (O), absorbance (◆) and quantum yield(---) vs. mixture density.

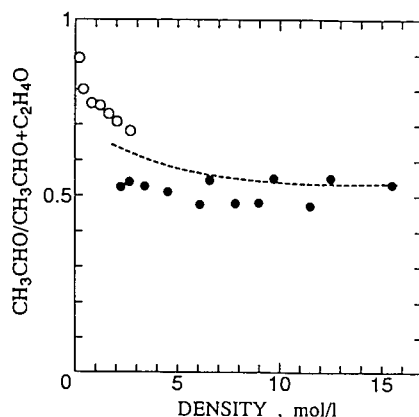


Figure 4. Fraction of CH_3CHO (●) vs. mixture density. The fraction extrapolated to time = 0 is also shown (---). The fraction for $\text{O}(^3\text{P})$ reaction (O) is also shown [7].

The quantum yield has a tendency to decrease with the increase of the density, which shows that some relevant intermediate species are quenched and/or diffusion-limited under higher densities.

3.3. Fraction of CH_3CHO against the density

The fraction of CH_3CHO against the sum of CH_3CHO and $\text{C}_2\text{H}_4\text{O}$ obtained at the 5 min. irradiation time is plotted against the mixture density in Fig. 4. The above fraction is slightly smaller than the value at the beginning of the irradiation. The initial fraction estimated as explained in 3.1. is also drawn by a dashed line in the figure.

3.4. Reaction mechanism

We have already suggested that the initial excited species under the KrF excimer laser irradiation is O_2 in its A' state due to the absorption augmentation. The reactivity of $\text{O}_2^*(\text{A}', ^3\Delta_u)$ is, however, not known. Some possible subsequent processes in the present mixtures are:



The reaction (3) is considered to proceed, consulting the recent observation of the O_3 production at 248 nm irradiation [3-5] and subsequent discussions for the mechanism. It is stated that vibrationally excited O_2 can react with O_2 to yield $\text{O} + \text{O}_3$ and that $\text{O}_2(\text{A}', ^3\Delta_u)$ may easily convert to vibrationally excited O_2 and *vice versa*. At the same time, if O_2 molecules keep some energy even after the quenching (4) until at the next laser pulse, they may be photo-dissociated to yield $\text{O}(^3\text{P})$.

The product of the $O(^3P)$ reaction with C_2H_4 at relatively high pressure and/or in liquid phase is C_2H_4O and CH_3CHO [6,7]. The similarity of the products between the $O(^3P)$ reaction and the present reaction is worthy to note. The fraction of CH_3CHO from the $O(^3P)$ reaction with C_2H_4 measured under the pressurized N_2 [7] is compared with that of the present experiment in Fig. 4. The fraction from the two reaction systems is quite similar. We suspect that $O(^3P)$ is produced in the present system, and that it subsequently reacts with C_2H_4 . Some part of the O_3 produced from the reaction (3) may be photolysed with subsequent laser pulses to yield $O(^1D)$, which should be quenched instantaneously to $O(^3P)$. Some part of O_3 can also react directly with C_2H_4 [8], whose products are not known in the present mixtures. We do also not know what kind of products are expected from the reaction of $O_2(A' ^3\Delta_u)$ with C_2H_4 , if it proceeds.

According to the above discussion, $O(^3P)$ is one of the most plausible oxidants in the present mixture. The decrease of the quantum yield with the increase of the mixture density can be ascribed to the increase of the contribution of quenching processes.

3.5. Other hydrocabons

Experiment was also conducted for C_2H_6 and C_6H_{12} in place of C_2H_4 . In the case of C_2H_6 , main products were CH_3CHO and ethanol, which were the same in the previous oxidation reaction in the C_2H_6/O_2 mixtures [1]. In the case of C_6H_{12} , the main products were cyclohexanone and cyclohexanol. These products are considered to be produced via certain radical reactions which are derived by the excited oxygen molecules and/or oxygen atoms.

4. CONCLUSION

The main products from the mixture of $C_2H_4/O_2/CO_2$ irradiated by a KrF excimer laser are C_2H_4O and CH_3CHO under pressurized conditions. The primary absorption of the laser light produces $O_2(A' ^3\Delta_u)$, while the ratio of the reaction products suggests the principal contribution of $O(^3P)$ as the real oxidant.

REFERENCES

1. K. Iguchi, Y. Oshima and S. Koda, J. Photochem. Photobiol. A: Chem., 80 (1994) 439.
2. Y. Oshima, Y. Okamoto and S. Koda, J. Phys. Chem., 99 (1995) 11830.
3. J. Shi and J. R. Barker, J. Geophys. Res., 97 (1992) 13039.
4. H. Park and T. G. Slanger, J. Chem. Phys., 100 (1994) 287.
5. R. A. Copeland, J. Chem. Phys., 100 (1994) 744.
6. S. Hirokama and R. J. Cvetanovic, Can. J. Chem., 51 (1973) 373.
7. U. Bley, P. Dransfeld, B. Himme, M. Koch, T. Temps and H. Gg. Wagner, Twenty-second Symp. (Int.) on Combust. (1988) 997.
8. C. S. Kan, J. G. Calvert and J. H. Shaw, J. Phys. Chem., 85 (1981) 2359.

This page intentionally left blank

Enzymatic Reaction in Supercritical Carbon Dioxide Internal Mass Transfer Limitation

P. Bernard and D. Barth

Laboratoire de Thermodynamique Chimique et Appliquée-E.N.S.I.C.
1, rue Grandville - BP 451 - 54001 NANCY Cédex, France

1. INTRODUCTION

Enzymatic reactions in non-aqueous solvents are subjected to a wide interest. A particular class of these solvents is the supercritical fluid (1) such as carbon dioxide that has many advantages over classical organic solvents or water : no toxicity, no flammability, critical pressure 7.38 Mpa and temperature 31°C, and allowing high mass transfer and diffusion rates.

Several authors have shown the stability and the catalytic activity of enzymes in supercritical carbon dioxide (SC CO₂) [2 to 25]. Some authors [14,17,18] have shown the difference of activity of enzyme in SC CO₂ and in organic solvent.

The intrinsic catalytic properties of enzymes are modified either during immobilization or after they were immobilized [25-27]. In heterogeneous catalysis such as is carried out by immobilized enzymes, the rate of reaction is determined not simply by pH, temperature and substrate solution, but by the rates of proton, heat and substrate transport, through the support matrix to the immobilized enzyme. In order to estimate this last phenomenon, we have studied the internal mass transfer limitation both in hexane and in SC CO₂, with different enzymatic support sizes.

2. MATERIAL AND METHODS

Myristic acid was purchased from Sigma (St Louis, MO) and ethanol (99.85 %) from Prolabo (France). Ultra pure carbon dioxide (99.995 %) was purchased from Airgaz (France). The lipase (E.C. 3.1.1.3.) was a commercial enzyme from *Mucor miehei* kindly supplied by Novo Nordisk (Denmark). This lipase (Lipozyme TM) is immobilized on Duolite A568 (Rohm and Hass). The resin particles have a size comprised between 300 to 600 µm. In order to see if a phenomenon of internal mass transfer occurs during the enzymatic esterification, we sieved the support into different size series. The average granulometry was determined by Coulzer Sizer method (Table I).

Table I

Nitrogen content of the enzymatic support

Support series (µm)	0-200	200-250	250-300	300-400	400-500
Average size (µm)	181	212	239	310	396
% (N/CHN)	11.93	11.96	12.05	11.93	11

2.1. Supercritical fluid reactor (Figure 1)

Before each experiment, the jacketed stainless steel (Top Industrie, Dommarie-Les-Lys, France) reactor is opened. A precise amount of substrates and water (Table 2) are introduced within the reactor. After sealing, pressurization is achieved by pumping liquid carbon dioxide (Minipump, Dosapro-Milton Roy, Pont-St-Pierre, France) to the desired final pressure (12.5 MPa). The reactor is then isolated from the CO₂ circuit. Then 20 mg of lipozyme TM of various diameter distributions (Table 1) is introduced in the reactor with an original system, giving the zero time of the reaction and the stirring is switched on. A 6-way HPLC valve (Rheodyne 7125) permits to withdrawn 50 µl samples for analysis without depressurization.

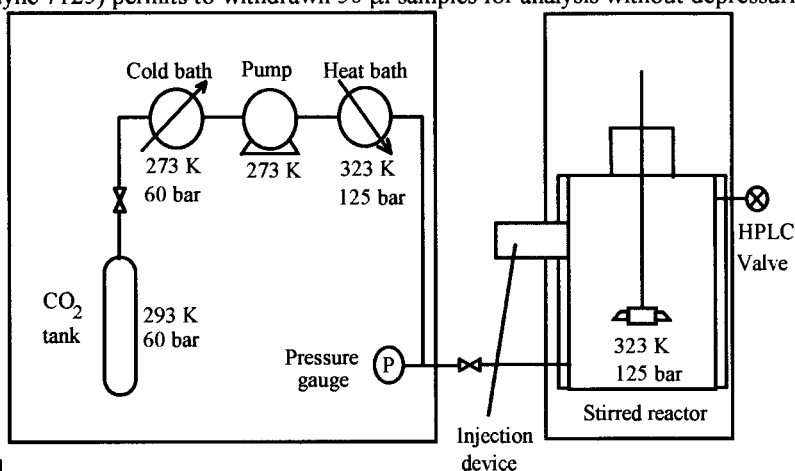


Figure 1

Laboratory reactor flow-sheet

2.2. Two liquid-phase reactor

The reaction was carried out in a glass with a round bottom, in order to prevent the enzyme support attrition, filled with 100 ml n-hexane, in which substrates, water and enzyme were added. The reaction mixture is incubated and agitated with magnetic stirring.

2.3. Experimental reaction conditions

Hexane and SC CO₂ experiments were performed in a batch mode reactor (100 cm³). In both cases, added enzyme and substrate quantities, reaction volume and temperature were similar as shown in table 2.

Table 2

Experimental conditions in hexane and SC CO₂ cases

	Hexane	SC CO ₂	
		(a)	(b)
[Myristic acid] (mM)	4	4	10
[Ethanol] (mM)	8	8	100
[Water] (mM)	1.1	44	44
Lipozyme TM (mg)	20	20	20
Temperature (K)	323	323	323
Pressure (Mpa)	0.1	12.5	12.5
Stirring (rpm)	1000	300	300

Only the quantities of water introduced in both solvents are not similar, because the water is necessary for the active enzyme conformation and not for the reaction. The water effect was studied elsewhere [13,14].

From these measurements, the conversion rate was determined from the ratio between ethyl myristate production and myristic acid feed. Then the initial velocity was graphically measured.

2.5. Analytical method

The samples were analysed by capillary gas chromatography GC 6000 (Carlo Erba) with FFAP-CB phase (Chrompack) that is special for free fatty acid analysis. The FID temperature was 235°C, the injector was an on-column system and the oven gradient was 40°C during 2 min, then increasing to 210°C at 45°C/min. The injected quantity was 2µl with no dilution.

2.6. Enzyme content

We have formulated the hypothesis that the enzyme content of the different particle series is the same. In order to verify this hypothesis, the elemental analysis was realised for the different support sizes. As shown in table 1, the enzyme content measured as nitrogen is identical ; this equality was verified mathematically by the Student's law.

2.7. Effect of stirring on the reaction rate

By varying the speed of the stirrer from 200 to 500 rpm no effect on the reaction velocities is observed in SC CO₂ or in n-hexane. However, without stirring, the reaction velocities decrease 6 % and 13 % respectively. All further SC CO₂ studies are performed at 300 rpm. So, no external diffusion limitation can be assumed ; however, internal diffusion limitations may happen, as discussed in the following section.

3. THE GENERALIZED THIELE MODULUS

Froment [29] et al have shown that the mass balance on a pellet should be written as :

$$\eta = \frac{\sqrt{2}}{Lr(S_e)} \left[\int_{S_e}^{S'} D(S') r(S') dS' \right]^2 \quad (1)$$

The generalized Thiele modulus is defined by : $\eta = \frac{1}{\phi_G}$ (2)

This concept should be applied to a Michaelis-Menten kinetic [30] :

$$\phi_G^2 = \frac{L^2}{2} \frac{V_{\max}^2 S_e^2}{(K_M + S_e)^2} \frac{1}{D} \frac{1}{V_{\max} \left(S_e + K_M \cdot \ln \frac{S_e + K_M}{K_M} \right)} \quad (3)$$

$$\text{or} \quad \phi_G^2 = \frac{1}{2} \phi^2 \frac{\beta_e^2}{(1 + \beta_e)^2} \frac{1}{\beta_e - \ln(1 + \beta_e)} \quad (4) \quad \text{with } \beta = \frac{S}{K_M}$$

According to the result presented by J.M. Engasser [29], we have plotted $\eta(\phi_G)$ versus ϕ for several values of β_e .

Dumont demonstrated [14] that the esterification of myristic acid by ethanol has shown to follow Ping Pong Bi Bi kinetics with competitive substrate inhibition by ethanol :

$$r = \frac{V_m AB}{AB + K_{mB} A + K_{mA} B(1 + B / K_i)} \quad (5)$$

In this case, it can be demonstrated, if one molecule has a higher diffusion coefficient, that modelisation should be realized as a single molecular reaction with a Michaelis-Menten mechanism : ethanol diffusion coefficient is higher than that of myristic acid in solution.

$$\bar{r}(S_e) = \eta r(S_e) \quad (6) \quad r(S_e) = k S_e \quad (7)$$

$$\text{with } \eta = \frac{3\phi_G \cot g(3\phi_G) - 1}{3\phi_G} \quad (8) \quad \phi_G^2 = \frac{kL^2}{D'} \quad (9) \quad L = \frac{dp}{6} \quad (10)$$

$$\text{and } D' = f(\beta_e) \cdot D \quad (11) \quad \text{with } f(\beta_e) = 2 \frac{1 + \beta_e}{\beta_e} (\beta_e - \ln(1 + \beta_e)) \quad (12)$$

The apparent diffusion coefficient D' is determined by minimizing the difference between the experimental and the calculated apparent velocity versus $dp/6$. Then we have to determine two parameters : K_m and V_{max} . V_{max} does not depend on the particle size so these two parameters are determined by studying the influence of myristic acid concentration on apparent velocity .

$$\bar{r}(S_e) = \eta r(S_e) = \eta \frac{V_{max} S_e}{K_M + S_e} \quad (13) \quad \phi_G^2 = \frac{1}{2} \phi^2 \frac{\beta_e^2}{(1 + \beta_e)^2} \frac{1}{\beta_e - \ln(1 + \beta_e)} \quad (14)$$

4. RESULTS AND DISCUSSION

The experimental results are summarized in table 3 and 4 for the two reaction media. In the case of SC CO₂ we can study the concentration effect of ethanol on the diffusion coefficient : it is twice smaller in (a) than in (b). It has been shown that ethanol added to SC CO₂ should contribute to increase a binary diffusion coefficient [30].

Table 3

Kinetic parameters and diffusion coefficients : comparison between hexane and CO₂ SC

	[Myristic acid] = 4mM [Ethanol] = 8mM	[Myristic acid] = 10mM [Ethanol] = 100mM	
	Hexane	SC CO ₂ C(a)	SC CO ₂ (b)
$D' \text{ (m}^2 \cdot \text{s}^{-1}\text{)}$	$2.37 \cdot 10^{-9}$	$4.34 \cdot 10^{-9}$	$10.6 \cdot 10^{-9}$
$V_{max}^* \text{ (mmol.(s.kg)}^{-1}\text{)}$	13.6	3.1	10.3
K_M^*	5.9	1.28	4.92
Diffusion coefficient (m ² .s ⁻¹)	$1.43 \cdot 10^{-9}$	$3.01 \cdot 10^{-9}$	$7.85 \cdot 10^{-9}$

(a), (b) : see table 2 * $d_p=450\mu\text{m}$.

We can observe (Table 4) that the concentration effect on Thiele modulus is very poor. Due to the Thiele modulus values, we can say that in SC CO₂ an intermediate rate between the reactional and diffusional rates was apparent. The kinetic parameters, V_{max} and K_M , in both reaction media are very different : V_{max} is higher in n-hexane ($13.6 \text{ mmol.(s.kg)}^{-1}$) than in SC CO₂ ($3.1 \text{ mmol.(s.kg)}^{-1}$) so n-hexane should be a better solvent than SC CO₂. But the myristic acid diffusion coefficient is lower in n-hexane than in SC CO₂ and we can observe the

unfavorable effect on the efficiency. The internal diffusion seems to be higher in n-hexane than in SC CO₂ essentially if the particle size is greater than 310 μm .

Table 4

Thiele modulus versus duolite particle size : comparison between hexane and CO₂ SC.

Particle size (μm)	Thiele Modulus		
	Hexane	SCCO ₂ (a)	SCCO ₂ (b)
181	0.50	0.20	0.22
212	0.68	0.27	0.30
239	0.87	0.35	0.38
310	1.46	0.59	0.63
396	2.38	0.96	1.03
464	3.27	1.31	1.42

(a), (b) : see table 2.

5. CONCLUSION

We have demonstrated for the first time that we could apply the theory of generalized Thiele modulus to an enzymatic reaction both in n-hexane and SC CO₂. The comparison between the two reaction media is not so clear : in n-hexane the « real » reaction velocity is higher than that obtained in SC CO₂. Nevertheless, the Thiele modulus values indicates a limitation due to the internal mass transfer rate $\phi_G^2 \gg 1$. Thus we observed, in the hexane case, a diffusional control, while in SC CO₂ an intermediate rate between the reactional and diffusional rates was apparent. It therefore, seems that SC CO₂ should be the solvent of choice in reactions catalyzed by immobilized enzymes, since it reduces problems with internal mass transfer. An other advantage is that the value of the inhibition constant is 43 mM in n-hexane and 120 mM in SC CO₂ [14], so SC CO₂ should be more convenient if we have to work with higher ethanol concentration. The economic feasibility of an industrial scale lipase catalyzed reaction on CO₂ may depend upon possible costs for high-pressure equipment.

REFERENCES

1. N. Kakamura, INPL (eds), 3nd Int. Symp.Supercritical Fluids, Strasbourg,17-19/9/1994, ISBN 2-905267-23-8, 3 121.
2. A.J. Russel, A. Chaudhary and E.J. Beckman, INPL (eds), 3nd Int. Symp.Supercritical Fluids, Strasbourg,17-19/9/1994 ISBN 2-905267-23-8, 3 209.
3. E. Castillo, A. Marty, D. Combes and J.S. Condoret,INPL(eds),3nd Int. Symp.Supercritical Fluids, Strasbourg,17-19/9/1994, ISBN 2-905267-23-8,3 207.
4. N. Saito, O. Sato, Y. Ikushima, K. Mataluda, and S. Ito, INPL (eds), 3nd Int. Symp.Supercritical Fluids, Strasbourg,17-19/9/1994, ISBN 2-905267-23-8,3 179.
5. B.J. Hrnjez, M. Chen and M. Landwehr, INPL (eds), 3nd Int. Symp.Supercritical Fluids, Strasbourg,17-19/9/1994, ISBN 2-905267-23-8,3 167
6. E. Cermia, C. Palocci, S. Soro, N. Fagnano, F. Gasparini and D. Misiti, INPL (eds), 3nd Int. Symp.Supercritical Fluids, Strasbourg,17-19/9/1994 ISBN 2-905267-23-8,3 161
7. I.B.de Carvalho, T.C. de Sampaio and S. Barreiros INPL (eds), 3nd Int. Symp.Supercritical Fluids, Strasbourg,17-19/9/1994 ISBN 2-905267-23-8, 3 155.

8. 8. M. Harröd, M. Lilja-Mallber and I. Elfman, INPL (eds), 3rd Int. Symp.Supercritical Fluids, Strasbourg,17-19/9/1994 ISBN 2-905267-23-8, 3 149.
9. 9. Z. Knez, V. Rizner and M. Sherget, INPL (eds), 3rd Int. Symp.Supercritical Fluids, Strasbourg,17-19/9/1994 ISBN 2-905267-23-8, 3 143.
10. 10. Y. Ikushima, N. Saito, O. Sato, K. Hataluda and S. Ito, INPL (eds), 3rd Int. Symp.Supercritical Fluids, Strasbourg,17-19/9/1994 ISBN 2-905267-23-8, 3 131.
11. T. Adshiri, H. Akiya, I.C. Chin, K. Arai and K. Fujimoto, J. Chem. Japan, 25 (1992) 104.
12. Y.M. Chi, K. Nakamura, T. Yano, Agric. Biol. Chem, 52 (1988) 1541.
13. T. Dumont, D. Barth and M. Perrut, Proceeding of the Second International Symposium on Supercritical Fluids, Boston, US, (1991) 150.
14. T. Dumont, D. Barth, C. Corbier, G. Branlant and M. Perrut, Biotechnol. & Bioeng., 39 (1992) 329.
15. J.C. Erikson, P. Schyns, C.I. Cooney, AIChE J., 36 (1990) 299.
16. D.A. Hammond, M. Karel, A.M. Klinanov and V.J. Krukonis, Appl. Biochem. Biotechnol.. 11 (1985) 393.
17. J.F. Martins, T.C. Sampaia, I.B. Carvalho, M. Nunes Da Ponte and S. Barreiros, High Pressure and Biotechnology Colloque INSERM/John Libbey Eurotext Ltd. 224 (1992) 411.
18. A. Marty, N. Chulalaksananukul, J.S. Condoret, R.M. Willemot and G. Durand, Biotechnol. Lett., 12 (1990) 11.
19. A. Marty, N. Chulalaksananukul, J.S. Condoret and S. Combes, High Pressure and Biotechnology. Colloque INSERM/John Libbey Eurotext Ltd, 224 (1992) 461.
20. D.A. Miller, H.W. Blanch, J.M. Prausnitz, Ind. Eng. Chem. Res., 30 (1991) 939.
21. K. Nakamura, Y.M. Chi, Y. Yamada and T. Yano, Chem. Eng. Commun., 45 (1985) 207.
22. T.W. Randolph, H.W. Blanch, J.M. Wilke, Biotechnol. Lett., 7 (1989) 325.
23. M. Taniguchi, M. Kamihia and T. Kobayashi, Agric. Biol. Chem., 51 (1987) 593.
24. A.M.N. Van Eijs, J.P.I. Dejong, H.H. Doddema, D.R. Lindebom, Proceeding of the first International Symposium on Supercritical Fluids, Nice, France, (1988) 933.
25. W. Hartmeier, Immobilized Biocatalyst. An introduction. Ed. Springer Verlag, Paris, (1988).
26. G. Durand, P. Monsan, Les Enzymes : Production et utilisations industrielles, Ed. Gauthier-Villars, France, 1982.
27. Handbook of Enzyme Biotechnology, Second edition, Ed. A. Wiseman, Ellis Horwwod limited, Chichester, 1987.
28. G.F. Froment, K.B. Bischoff, Chemical reactor : Analysis and design, Ed. John Wiley, & Sons Inc. New-York, 1979.
29. J.M. Engasser and C. Horwarth, J. Theo. Biol., 42 (1973) 137.
C. Horwarth and J.M. Engasser, Biotechnol. Bioeng., 16 (1974) 909.
30. S.A. Smith, V. Shenai and M.A. Matthews, J. Supercritical Fluids, 3 (1990) 4 175.

Supercritical Carbon Dioxide Aided Catalyst Design, its Characterisation and Behaviour in Reacting Environment

Sermin G. Sunol^a, Zeynep Tosyali^a, Aydin K. Sunol*

*University of South Florida, Chemical Engineering Department,
Tampa FL 33620 USA

^aBogazici University, Chemical Engineering Department,
80815 Bebek, Istanbul TURKEY

ABSTRACT

Gels of metal oxide catalysts (NiO/Al₂O₃ gels), prepared by the sol-gel method, are dried using supercritical drying to obtain aerogel catalysts as porous powder. The supercritical drying is carried out at two temperatures and pressures of carbon dioxide. Also, volume of the autoclave is varied. A factorial design is applied to the experiments and effects of the variables are studied using Yate's Algorithm. Gels are also dried in air and under vacuum in order to compare densities of xerogels with those of aerogels.

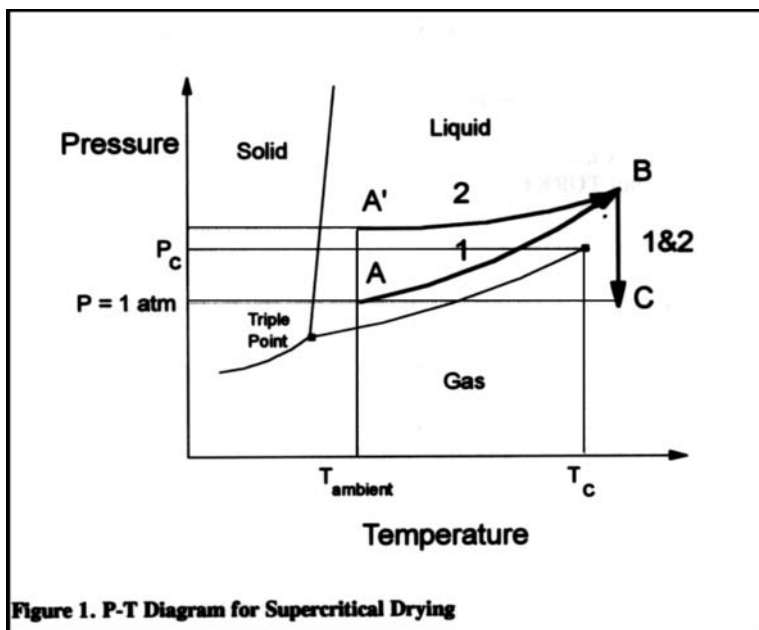
INTRODUCTION

Aerogels show great promise in catalytic applications, especially due to their unique morphological properties (high porosity and high surface area) as well as excellent chemical properties (high chemical activity) which can not be easily achieved with other types of catalysts (1). Therefore, it is worthwhile to investigate aerogel catalyst preparation (2).

In sol-gel process, metal alkoxide is dissolved in alcohol which can be readily removed from the gel matrix upon the formation. The gelation process involves hydrolysis and condensation reactions of metal alkoxides. Due to its unfavorable drying conditions, water is not used as a solvent, however, it is utilized during the hydrolysis reaction. If the solvent is evaporated slowly from the gel, a xerogel is obtained. During evaporation, large capillary forces are exerted as the liquid - vapor interface moves through the gel. These forces cause shrinkage of the pores within the gel. Removal of the solvent (alcohol) from the gel under supercritical conditions results in the formation of aerogels. Since this drying method eliminates liquid-vapor interfaces, aerogels are formed in the absence of capillary forces. Aerogels retain the morphology of the original alcogel.

There are several methods developed for removing the solvent from the gel under supercritical conditions. The first one is the one suggested in the pioneering work by Kistler (3), in which the solvent is brought to supercritical conditions in an autoclave and evacuated under these conditions. In order to pressurize the autoclave to a pressure above

the critical value for the alcohol, more alcohol is added to the autoclave (4). Supercritical conditions of the solvent are reached by supplying heat to the autoclave. After the system pressure reaches a preselected value which is above the critical, the temperature is raised at constant volume. Once the temperature is above its critical value, the supercritical fluid is vented out of the autoclave at constant temperature (5). The P-T behavior for this procedure is shown as route A-B (1) in Figure 1.



This method was later improved by van Lierop and co-workers (6). In this improved version of the method, vaporization of the solvent is completely suppressed by pressurizing the autoclave with an inert gas prior to heating while the subsequent heating is carried out batch at constant volume. Thus, the entire procedure is carried above the vapor-liquid interface of a Pressure-Temperature (P-T) diagram, shown as route A'-B (2) in Figure 1.

Different researchers have utilized solvent exchange prior to supercritical drying. In this method, the solvent (alcohol) was substituted with liquid Carbon Dioxide. This method was applied to the production of silica aerogel by Tewari et al. and Rangarajan et al. (7, 8).

In another method, developed by Jacobucci and co-workers (9), alcohol is removed by supercritical CO_2 extraction in a semi-continuous system.

In this present work, the objective is to develop a supercritical drying method which prepares aerogel catalysts with tunable physical and chemical properties. For this purpose, catalysts are prepared using supercritical drying and bulk densities of the catalysts are measured and compared with the ones of the xerogels.

EXPERIMENTAL

Gel Preparation: $\text{NiO}/\text{Al}_2\text{O}_3$ gels are prepared using the method suggested by Teichner and co-workers (4). Aluminum sec-Butylate is dissolved in sec-Butanol while Nickel Acetate is dissolved in Methanol separately. Water is added to the second mixture in near stoichiometric amounts necessary for the hydrolysis reactions. The two solutions are mixed and a precipitate of alumina is immediately formed. Gels are dried immediately after preparation, in order to eliminate the effect of aging (2).

Drying of Gel:

Supercritical Drying of the Alcohol: In this method, the system is first pressurized with CO_2 and CO_2 -Alcohol mixture is brought to a supercritical condition and the supercritical fluid is removed slowly from the gel. The experimental set-up for this system is shown in Figure 2.

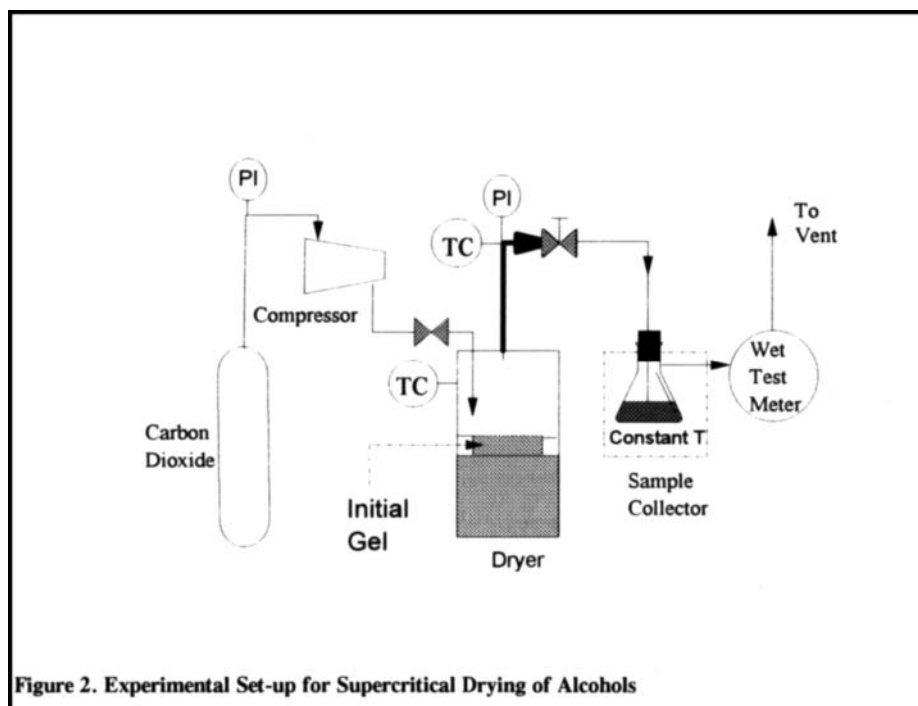


Figure 2. Experimental Set-up for Supercritical Drying of Alcohols

Prior to experiments, the reactor containing the gel is pressurized with CO₂. CO₂ feed is compressed before it is fed to the drying vessel that contains the wet gel. The drying vessel is an autoclave with 400cm³ volume. In some experiments autoclave volume is decreased to 110cm³ by inserting a metal block into the autoclave. After a predetermined pressure is reached, the autoclave is heated with the heating mantle surrounding it to a temperature above the critical value of the CO₂-Alcohol mixture. The system is kept under these conditions for a specified time. The supercritical fluid is then vented out of the system keeping the temperature of the reactor constant. At the end of the experiment, the gel is swept with fresh CO₂ or H₂ to remove remaining trace amounts of alcohol and water and to either calcine or reduce the catalyst. The system is subsequently cooled and the aerogel catalyst is removed.

Air and Vacuum Drying of the Alcohols. Xerogels are prepared by air and vacuum drying. Air drying is performed at 110°C for 15 hours and vacuum drying is performed at 60°C for 35 hours.

RESULTS AND DISCUSSION

Aerogel catalysts are obtained at different conditions of temperature, pressure and autoclave volume. Densities of aerogels are given in Table 1. Most important parameters which are expected to affect physical properties of the aerogels are temperature, pressure, volume of autoclave (amount of CO₂ used for pressurization of the autoclave). It is important to be able to produce aerogels with high surface area and porosity at low temperatures and pressures. In order to have an idea about the porosity of the aerogels, their bulk densities are measured. Bulk densities of aerogels which are produced under different drying conditions are similar (Table 1). All of the aerogels produced have densities an order of magnitude lower than that of xerogels. Xerogel densities obtained by air and vacuum drying have densities of 0.8320 and 1.2613 g/cm³ respectively. Pore size distribution of the catalysts should be investigated to show the effect of drying conditions on the characteristics of the aerogels.

A full 2³ factorial design was used to study the effect of drying conditions (temperature, pressure, autoclave volume) on the density of dry aerogel prepared by flushing the aerogel with hydrogen in order to reduce the catalyst.

The effects were calculated using Yates algorithm. Table 2 summarizes the effect analysis for density of dried aerogel. The level of experimental design at low temperature, pressure and autoclave volume was denoted “-” while more severe conditions were “+”.

The average density for aerogels was 0.0874 g/cm³. If the analysis is converted into an empirical model and all the possible terms for the experimental design are included, density (Y) can be given at the vertices of design by

$$Y = 0.0874 - (0.0118/2) PT - (0.0116/2) P - (0.0109/2) PV - (0.0106/2) PTV \\ - (0.0053/2) T - (0.0046/2) TV + (0.0091/2) V$$

Table 1. Densities of Aerogels

Temperature (°C)	Pressure (bars)	Volume (cm ³)	Flash Gas	Density (g/cm ³)
100	48.26	400	CO ₂	0.0872
200	62.05	400	CO ₂	0.0868
200	96.53	400	CO ₂	0.0953
100	62.05	400	CO ₂	0.0917
100	96.53	400	CO ₂	0.0891
200	62.05	110	CO ₂	0.0899
200	96.53	110	CO ₂	0.0967
100	62.05	110	CO ₂	0.1024
200	62.05	400	H ₂	0.0942
200	96.53	400	H ₂	0.0797
100	62.05	400	H ₂	0.1120
100	96.53	400	H ₂	0.0817
200	62.05	110	H ₂	0.0834
200	96.53	110	H ₂	0.0815
100	62.05	110	H ₂	0.0829
100	96.53	110	H ₂	0.0834

When the effect values are plotted against probability using a normal plot, P, V, PT, and TV effects could not be attributed to experimental error. Here, we are assuming the errors to be normally distributed.

The pressure and PT effects are due to enhanced solubility of the alcohols in the carbon dioxide. The TV and V effects is possibly due to increase in reflux at higher temperatures and larger volumes.

Furthermore, one can use the highest order interaction PVT to estimate the experimental standard deviation to be 0.0106

Table 2. Effect Analysis for Dried Aerogel Density

LEGEND		
VARIABLE	-	+
TEMPERATURE(°C)	100	200
PRESSURE (bars)	62.05	96.53
AUTOCCLAVE VOLUME(cm ³)	110	400

ANALYSIS					
P	T	V	Density (g/cm ³)	Effect	Estimate
-	-	-	0.0829	MEAN	0.0874
+	-	-	0.0834	P	-0.0116
-	+	-	0.0834	T	-0.0053
+	+	-	0.0815	PT	-0.0118
-	-	+	0.1120	V	0.0091
+	-	+	0.0817	PV	-0.0109
-	+	+	0.0942	TV	-0.0046
+	+	+	0.0797	PTV	0.0106

CONCLUSIONS

A new method was introduced for drying the alcogels, where for the first time in literature, CO₂ is used in order to pressurize the reactor prior to the experiments. The use of CO₂ instead of an inert gas for this purpose is found to be extremely useful for carrying out the drying at lower temperatures. With the new method, aerogels are dried at temperatures which are 180°C or more lower than the critical temperature of the alcohols.

ACKNOWLEDGMENTS

SGS would like to thank NATO for a Research Fellowship; the authors acknowledge the Research and Creative Scholarship funds provided by the University of South Florida.

REFERENCES

1. Schneider, M. Titania Based Aerogel Catalysts, PhD Dissertation, ETH, Zurich, 1994.
2. Sunol, S.G., Sunol, A.K., Keskin, O., Guney, O., "Supercritical fluid aided preparation of aerogels and their characterization", in "Innovations in Supercritical Fluids Science and Technology" Chapter 17, pp 258-268, edited by K. W. Hutchenson and N. R. Foster, ACS Symposium Series 608 (1995).
3. Kistler, S.S. J. Phys. Chem. **1932**, 36, 52.
4. Gardes, G.E.E.; Pajonk, G.M. and Teichner, S.J. J. Catalysis **1974**, 33, 145.
5. Schmitt, W.J.; Grieger-Block, R.A. and Chapman, T.W. In Chemical Engineering at Supercritical Conditions; Paulaitis, M.E. et al. eds.; 1983, p 445-460.
6. Van Lierop, J.G.; Huizing, A.; Meerman, W.C.P.M. and Mulder, C.A.M. J. of Non-Crystalline Solids **1986**, 82, 265.
7. Tewari, P.H.; Hunt, A.J. and Lofftus, K.D., Mater. Lett., **1985**, 3, 363.
8. Rangarajan, B.; Lira, C.T. J. of Supercritical Fluids, **1991**, 4, 1.
9. Ayen, R.J.; Jacobucci, P.A. Rev. Chem. Eng. **1988**, 89, 157.

Enzymatic Catalysis in Supercritical Carbon Dioxide: Effect of Water Activity

H. Michor, R. Marr and T. Gamse

Institut für thermische Verfahrenstechnik und Umwelttechnik, Technische Universität Graz, Inffeldgasse 25, A-8010 Graz, Austria

1. INTRODUCTION

Many enzymatic processes can be of practical value, if they are carried out in anhydrous media instead of water. While biocatalysis in organic solvents is well established, the use of supercritical fluids, in particular supercritical carbon dioxide (SC-CO₂), is still restricted to research on laboratory scale.

SC-CO₂ offers some advantages over organic solvents. It is not flammable, non toxic and relatively cheap and what's more it offers the possibility of an integrated separation process.

To take advantage of the stereoselectivity of enzymatic catalysis we chose the transesterification of (±)-menthol as our model system. Esterase EP10 from *Pseudomonas marginata* proved to be a suitable catalyst for the production of enantiomerically pure (-)-menthyl acetate. With isopropenyl acetate as the acylating reagent the enantioselectivity was as high as 180 (Michor et al., 1996). Soon we realized that the water content of the reaction medium is an important factor governing the reaction rate of the transesterification. Various groups have investigated the role of water content on reaction velocity. Miller et al. (1991) conducted the interesterification of trilaurin and myristic acid, catalyzed by a lipase from *Rhizopus arrhizus*, in a continuous-flow packed-bed reactor. They did not find an effect of the water content of the SC-CO₂ on the pseudo-first-order rate constant. Marty et al. (1992) on the other hand obtained a maximum of the initial reaction velocity at a water content of 10% (w/w) of the immobilized lipase Lipozyme TM from *Mucor mihei*. Dumont et al. (1991) finally demonstrated, that, when they switched from saturated to dry SC-CO₂ flowing through their fixed bed reactor, the conversion rate decreased reversibly. Like Marty et al. they were using Lipozyme TM.

* This work was performed within the SFB Biocatalysis at the TU-Graz. It was funded by the FWF (project no. F0110)

In this work we used an aluminium oxide humidity sensor to measure inline the water vapour pressure. We investigated the partitioning of water between SC-CO₂ and the enzyme preparation and we determined the influence of water activity on the initial reaction velocity.

2. MATERIALS AND METHODS

2.1. Materials

Esterase EP10 from *Pseudomonas marginata* was supplied by Prof. Schwab from the Department of Biotechnology at the Graz University of Technology (Stubenrauch et al., 1995). Carbon dioxide (99.95 % (v/v), 35 ppmv water) was purchased from Linde. The aluminium oxide sensor is a product of PANAMETRICS.

2.2 Methods

Reactions, the determination of adsorption isotherms and the calibration of the humidity sensor were performed in a batch reaction system of a total volume of 168 ml or 178 ml depending on the size of the enzyme reactor (Figure 1).

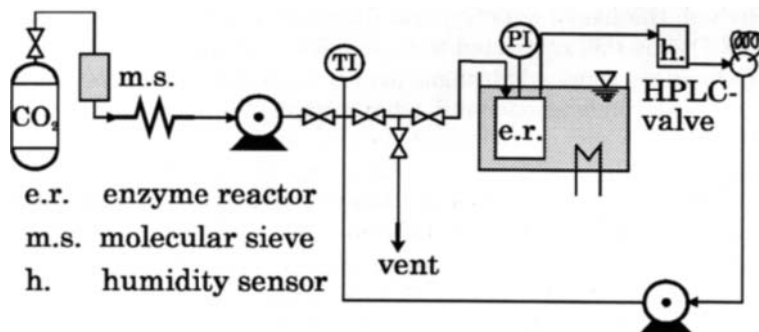


Figure 1: Batch reaction system

For the *calibration* of the humidity sensor a 140 ml reaction vessel was used. Portions of water of 20 or 100 μ l were added via a HPLC valve and readings were taken after approximately one hour. The water vapour pressure proved to be a linear function of the water content. However the solubility of water in SC-CO₂, as calculated using the Chrastil correlation together with the parameters determined by Chrastil (1982), was found to be too high to apply a Henry's Law type analysis. We therefore employed the Peng-Robinson equation of state (EOS) to calculate the fugacity of water. Using the conventional mixing rules with one adjustable interaction parameter k_{ij} the progress of the water vapour pressure as a function of the water content could be described reasonably

well (Figures 2 and 3). Serious deviations occurred at 154 bar when the water content of SC-CO₂ exceeded 250 mg/l.

Mixing rules used with the Peng-Robinson EOS:

$$a_m = \sum_i \sum_j x_i x_j (a_i a_j)^{1/2} (1 - k_{ij})$$

$$b_m = \sum_i x_i b_i$$

For temperatures around 50°C k_{ij} was set 0. At 32°C it had to be adjusted to 0.090. A temperature dependent interaction parameter has also been postulated by Sako et al. (1991). At 50°C they proposed a value of -0.0100.

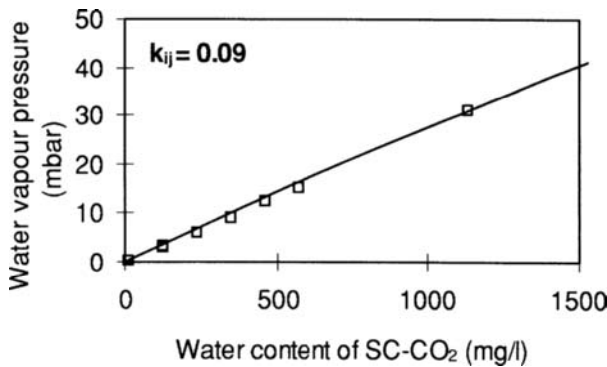


Figure 2: Calibration curve of the humidity sensor at 32°C and 95 bar. The curve was calculated by the Peng-Robinson EOS.

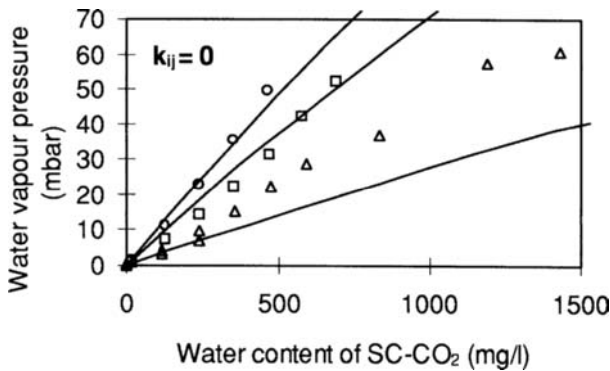


Figure 3: Calibration curves of the humidity sensor. O: 51.8°C, 105 bar, □: 48.6°C, 104 bar, Δ: 48.9°C, 154 bar. Curves were calculated by the Peng-Robinson EOS.

Adsorption isotherms were determined using a 150 ml reaction vessel equipped with a sight glass. 1 g of the enzyme preparation was placed in the reactor, the whole system was flushed with CO₂ and finally pressure and temperature were adjusted to the desired values. Once again portions of 20 or 100 μ l of water were added. From the corresponding water vapour pressure the amount of dissolved water was calculated. The amount of water bound to the enzyme preparation was calculated as the difference between the amount of water added and the amount of water found in the SC-CO₂.

Reactions were carried out in the 140 ml reaction vessel. (\pm)-menthol and 200 mg of the enzyme preparation were placed in the reactor and the reactor connected to the system. The whole system was flushed with CO₂ after which pressure and temperature were adjusted to 100 bar and 50°C. Water activity was set to the desired value by adding portions of water via the HPLC valve. The reaction was started by the addition of 1 ml of isopropenyl acetate once again via the HPLC valve. Final substrate concentrations were 20 mM menthol and 54 mM isopropenyl acetate. Stirring of the enzyme reactor was accomplished by a magnetic stirrer. In addition the reaction medium was pumped in a circle using a gear pump. The enzyme was retained in the enzyme reactor by a nylon membrane. Samples were taken via the HPLC-valve with a 500 μ l sample loop, the content of which was expanded into hexane, and analyzed on a HP 5890 Series II gas chromatograph.

3. RESULTS AND DISCUSSION

3.1. Adsorption isotherms

An adsorption isotherm at 104 bar and 50°C is shown in figure 4. At a water activity of approximately 0.1 the previously powdery enzyme preparation started to aggregate. This process of aggregation continued until the last portion of water was added.

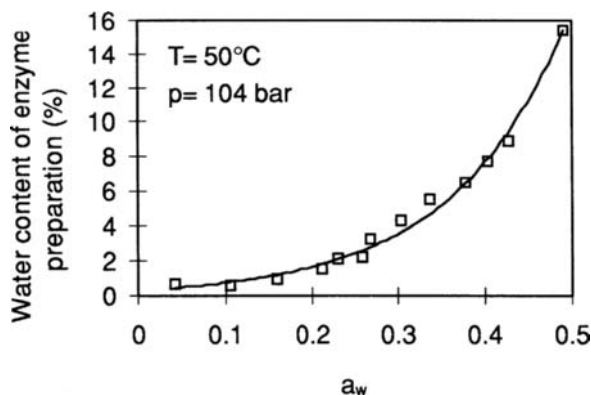


Figure 4: Water content of the enzyme preparation as a function of the water activity a_w .

3.2. Effect of water activity on initial reaction velocity

The effect of different water activities on the initial reaction velocity v_i is summarized in figure 5. Experiments were carried out at 100 bar and 50°C. Unlike Marty *et al.* (1992) we did not experience a maximum in the reaction velocity but a steady decrease as the water activity increased. At an a_w of 0.27, corresponding to a water content of the enzyme preparation of 3% (w/w), the residual activity was as low as $9 \mu\text{mol h}^{-1}\text{g}^{-1}$ enzyme (i.e. 4.5% of the activity at $a_w = 0.03$). Since there is no decrease in activity at low water activity, we conclude, that, in the case of esterase EP10, SC-CO₂ does not strip essential water from the enzyme. This makes esterase EP10 a very easy to use catalyst, since the water content of the SC-CO₂ has merely to be kept very low to ensure maximum activity.

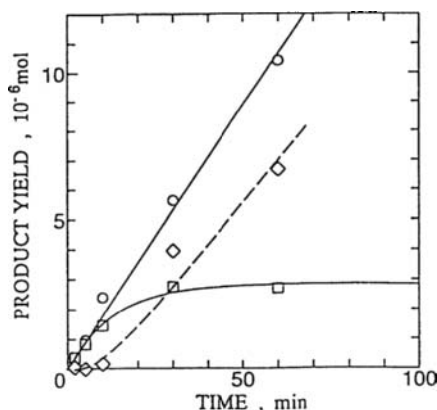


Figure 5: Initial reaction velocity v_i of the enzymatically catalyzed transesterification of (\pm)-menthol and isopropenyl acetate in SC-CO₂ as a function of water activity a_w

The inline measurement of the water vapour pressure makes it possible to monitor its progress in the course of the reaction. The water vapour pressure does not stay constant but slowly decreases until a very low value is reached. In the absence of the enzyme however no such decrease was detected (Figure 6). We believe that the enzymatically catalyzed hydrolysis of isopropenyl acetate is responsible for this decrease in water content. The hydrolysis occurs as a parallel reaction to the transesterification of isopropenyl acetate to menthyl acetate. It is not yet clear how significant the contribution of this parallel reaction to the overall decrease in (transesterification) reactivity is. If we assume that the rate constants for the hydrolytic reaction are of the same order of magnitude as those for the transesterification such a parallel reaction would lead to a significant decrease in the rate of transesterification as the water activity rises. At low water activities the hydrolytic reaction might be responsible for the observed decrease in reactivity. Very likely however the accumulation of water around the enzyme

particles and their aggregation is the main reason why esterase EP10 is nearly completely inactive at a water activity of 0.27.

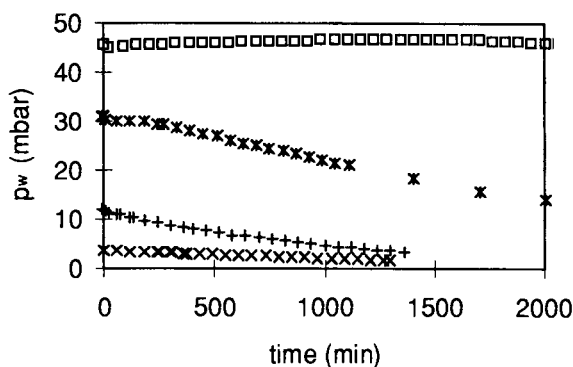


Figure 6: Progress of water vapour pressure p_w in the course of the enzymatically catalyzed transesterification of (\pm)-menthol and isopropenyl acetate in SC-CO₂ at different starting values of p_w . □: no enzyme was added, $p_w = 45.6$ mbar, *: $p_w = 30.9$ mbar, +: $p_w = 12.1$ mbar, x: $p_w = 3.8$ mbar

REFERENCES

- Chrastil, J. (1982), *J. Phys. Chem.*, 86, 3016-3012
- Dumont, T., Barth, D. and Perrut, M. (1991), *Proceedings of the 2nd International Symposium on Supercritical Fluids*, McHugh, M.A., ed., Boston, 150-153
- Marty, A., Chulalakasanukul, W., Willemot, R.M. and Condoret, J.S. (1992), *Biotechnol. Bioeng.*, 39, 273-280
- Michor, H., Marr, R., Gamse, T., Schilling, T., Klingsbichel, E. and Schwab, H. (1996), *Biotechnol. Lett.*, 18(1), 79-84
- Miller, D.A., Blanch, H.W. and Prausnitz, J.M. (1991), *Ind. Eng. Chem. Res.*, 30, 939-946
- Sako, T., Sugeta, T., Nakazawa, N., Okubo, T. and Sato M. (1991), *J. Chem. Eng. Japan*, 24(4), 449-455
- Stubenrauch, G., Griengl, H., Klempier, N., Faber, K. and Schwab, H. (1995), Patent no. AT-399.886

Behaviour of a Cooled Wall Reactor for Supercritical Water Oxidation

M. J. Cocero, J. L. Soria, O. Ganado, R. González, F. Fdez-Polanco

Chemical Engineering Department .- Facultad de Ciencias
Universidad de Valladolid.- 47011 Valladolid .- SPAIN

ABSTRACT

Supercritical Water Oxidation (SCWO) has been proved to be a suitable process for treatment of several toxic and hazardous organic wastes due to its high removal efficiency. SCWO requires of hard reaction conditions (22.1 MPa and over 374°C). Special reactors are needed to support these conditions. An original reactor design is presented here wich has been tested in the treatment of alcohols+ammonia solutions in water. Performance results are presented here for ammonia and alcohols. Destruction efficiency greater than 99.9% are reached for both compounds, probing the correct performance of the reactor.

INTRODUCTION

Supercritical Water Oxidation (SCWO) is a technology for the total destruction of wastes, specially hazardous and very toxic ones^{1,2}. The process is based on the reaction of organics and oxygen in a SCW medium, that is, in water at temperture greater than 374 °C and pressure greater than 22.1 MPa. At supercritical conditions organics, oxygen and water are mixed in a single homogeneous phase and react almost completely with very low residence time. In this process organics are mainly oxidized to CO₂ and H₂O.

In previous designs of SCWO reactors, special materials such as Hastelloy, Inconel or Gold¹ were needed to withstand such drastic operation condition of temperature and pressure to reduce corrosion effects imposed by the oxidizing atmosphere

In this work is presented a new reactor model in wich pressure and temperature effects are isolated. This is achieved using a cooled wall vessel wich is maintained near to 400 °C, and a reaction chamber, where reactants are mixed and reaction takes place. This reaction chamber works over 625°C and is made of a special material wich supports the oxidazing atmosphere.

EQUIPMENT

For our studies, a SCWO pilot plant was designed and built. The process diagram is presented in figure 1.

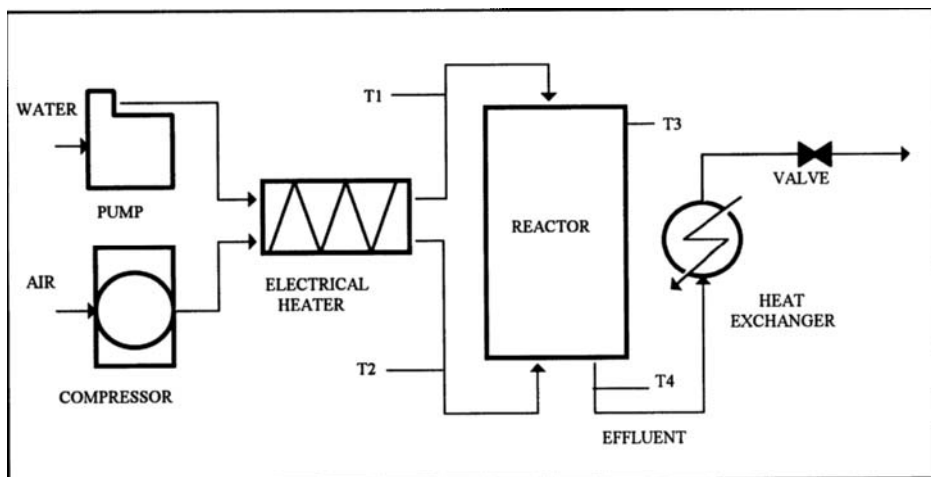


Figure 1 .- Process diagram of the SCWO pilot plant.

The pilot plant is able to treat 25 L/h of wastewater with an organics content between 10% and 15% w/w. Wastewater is pressurized with a plunger pump to 27.5 MPa. Air is used as oxidant previously pressurized in a four stages compressor to 28.0 MPa.

Both streams pass through an electrical heater, which is turned up during the starting-up. Once the oxidation reaction begins, the heat released is used for the thermal conditioning of the wastewater. At this point, the electrical heater is then switched-off.

Air and wastewater are mixed in the reactor chamber where oxidation of organics takes place. This reactor is an original design and has granted the patent P9500388.

It consists of two parts: the reaction chamber and the main vessel. The reaction chamber is made of Inconel and supports inside the oxidant atmosphere of the reactants at a maximum temperature of 650°C and a pressure of 27.5 MPa. It is enclosed in the main vessel which is pressurized with the feedstream. As the reaction chamber supports inside and outside the same pressure, wall thickness is reduced. The main vessel is cooled with the feedstream before entering the reaction chamber, so that it works about 400°C and does not suffer the oxidant atmosphere. It has been made of stainless steel with a relatively low thickness.

A diagram of the reactor is shown in figure 2.

Although the reactor can operate as a mixed reactor, it was filled with alumina spheres and worked as fixed bed reactor. Residence times in the reaction chamber are about 1 minute.

Reaction temperature depends on the flowrates and concentrations but they are consistently between 580°C and 650°C.

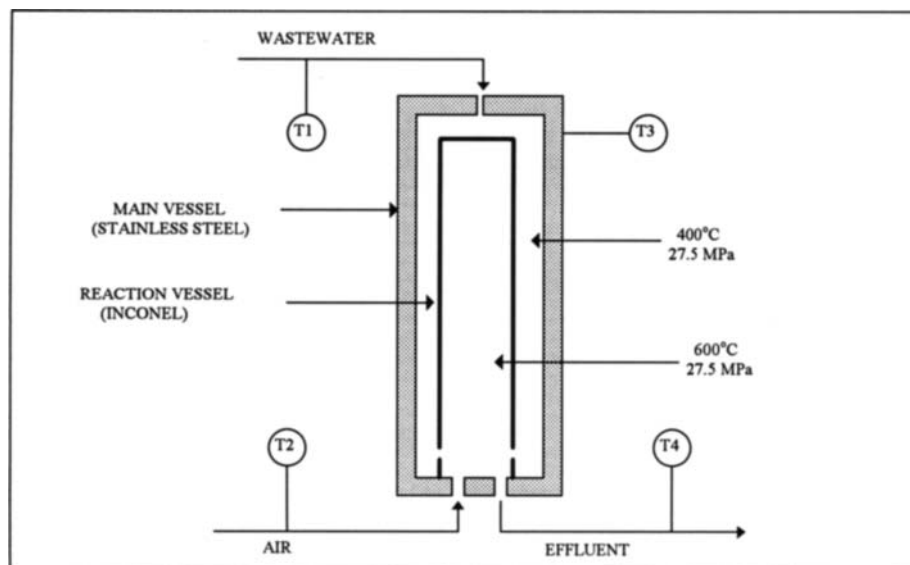


Figure 2 .- Reactor scheme.

Reaction products leave the reactor and are cooled in two countercurrent heat exchangers with water. Effluent is then depressurized to atmospheric pressure. Samples are collected for the analysis.

Wastewater flowrates tested varied from 12.1 L/h to 18 L/h and oxygen excess (O.E.) between 10 and 70%. Temperature and pressure were measured in different parts of the system and their values were stored in a PC computer for their later study.

EXPERIMENTS

The reactor was tested with the treatment of alcohol solutions in water (ethanol and isopropanol). These products have been chosen due to their thermal stability. With these solutions, a safe starting-up strategy was established. A typical experience is described below.

Feed consisted of a solution of 12.5% w/w of isopropanol in water, which represents an enthalpy content of $4.5 \cdot 10^3$ kJ/kg. This solution was fed to the reactor at a maximum flowrate of 16.1 L/h. Oxygen excesses of 10%, 30%, 50% and 70% were selected and tested.

Figure 3 shows the evolution of the temperatures in this experience. During the starting-up period, which last over 100 minutes, air and water were heated in an electrical heater. Initial flowrates were low and they were increased as the reaction temperature began to raise. When the reaction temperature was high enough, the electrical heater was switched off and water flowrate was fixed at 16.1 L/h. Then, the system evolved to its steady state. Air was finally fed at 120 °C due to the temperature increase produced in the compression stage.

Although reaction temperature was greater than 600°C in the steady state, the feedstream (which comes in the reactor near 40°C) cools the outer reactor wall to 400°C. This fact confirms the proper design and operation of the reactor. Removal efficiency were greater than 99.9%.

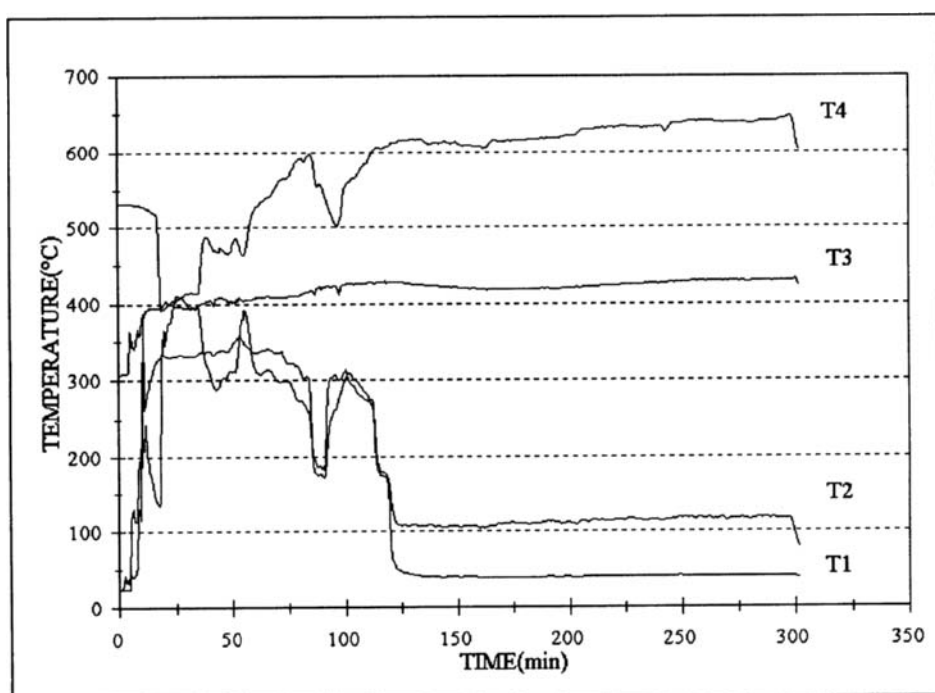


Figure 3 .- Temperature evolution during a typical experience.

Once the correct performance of the reactor was established for alcohols, ammonia-isopropanol solutions were also treated. Ammonia was chosen for its chemical and thermal stability^{3,4}. Solutions consisted of 12.5% isopropanol + 0.5% ammonia. Figure 4 shows the chemical analysis obtained from a typical experience. It was carried out with a feed flowrate of 16.1 L/h and variable oxygen excesses of 10%, 30%, 50% and to 70 %. TOC, isopropanol, NH₃ and nitrates were analyzed in the liquid effluent. TOC was analyzed with a TOC analyzer, isopropanol was analyzed by GC and NH₃ and NO₃⁻ were analyzed with selective electrodes⁵. In the gaseous effluent, NO_x were measured with a Dräger kit.

For 10% oxygen excess (OE), around 1000 mg/L of TOC were found in the liquid effluent and characterized by GC as isopropanol and acetone. At 30% OE there was a sharp decrease to around 100 mg/L of TOC with a small decrease for further OE increases (figure 4).

Ammonia concentration in the effluent showed a similar trend; starting at 1000 mg/L for 10% OE, sharp decrease for 30% OE but regular decrease for higher OE.

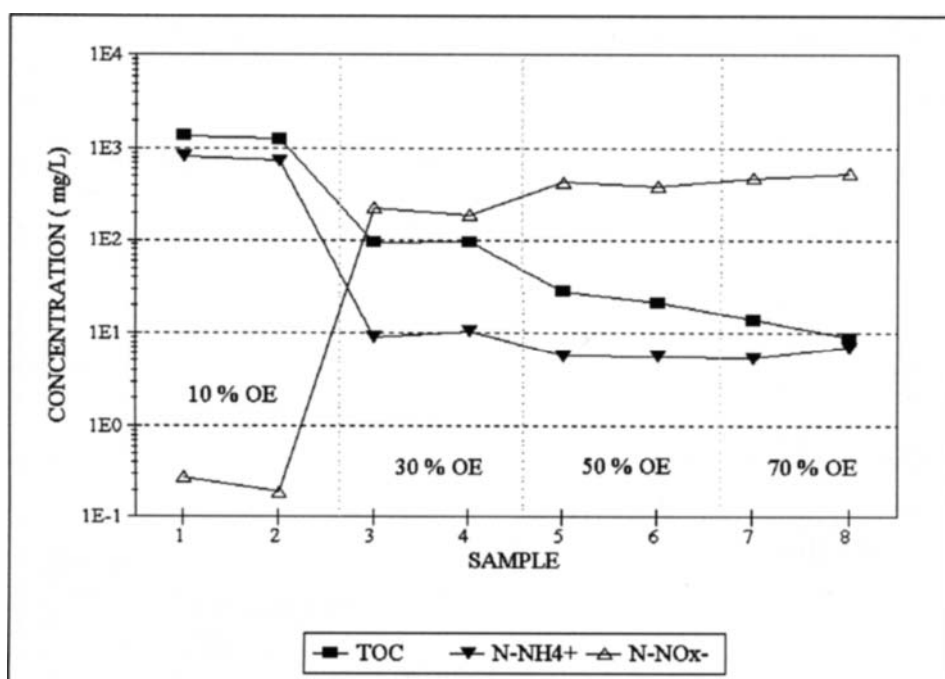


Figure 4 .- Influence of the oxygen excess (OE) on the reaction products

As expected, NO_x⁻ in the effluent showed the opposite trend; started at below 1 mg/L for 10% OE, increased to around 200 mg/L for 30% OE and reached 500 mg/L for 70% OE. Maximum amount of NO_x in the gas effluent was found to be 48 mg/m³ for 70% OE.

In terms of removal efficiency a 99.99% was found for isopropanol and 99.9% for ammonia at 70% OE.

CONCLUSIONS

- Reactor performance in terms of temperature stability and removal efficiency is suitable for the purposes it was designed and built.

- Isopropanol and ammonia mixtures in water can be destroyed with efficiency greater than 99.99% and 99.9% respectively, with residence times about 1 minute.
- End products of reaction include small amounts of isopropanol, acetone and NO_x , their concentrations being dependent upon oxygen excess.

REFERENCES

- 1.- J. W. Tester et al., *Supercritical Water Oxidation Technology*, ACS Symposium Series, 518 (1993) 35-76
- 2.- D. M. Harradine et al, *Oxidation Chemistry of energetic materials in Supercritical Water* Hazardous Waste and Hazardous Materials, vol. 10-2 (1993) 233-246
- 3.- W. R. Killilea et al., *The fate of nitrogen in Supercritical-Water Oxidation*, The Journal of Supercritical Fluids, 5 (1993) 72-78
- 4.- P. A. Webley et al, *Oxidation kinetics of ammonia and ammonia methanol mixtures in Supercritical Water in the range temperature range 530-700°C at 246 bar*, Ind. Eng. Chem. Res. 30 (1991) 1745-1754
- 5.- APHA, AWWA, WPCF, *Standard Methods for the Examination of Water and Wastewater*

ACKNOWLEDGMENTS

The authors wish to thank EMGRISA for providing technical and financial support.

Enzyme Catalysed Reactions, Enantioselectivity And Stability Under High Hydrostatic Pressure

O. Guthmann^a, R. Schwerdtfeger^b, A. Rieks^b, G. Antranikian^b, V. Kasche^b, G. Brunner^a,

^aDept. of Chemical Engineering, TU Hamburg-Harburg, Germany

^bDept. of Biotechnology, TU Hamburg-Harburg, Germany

Keywords: enzyme, hydrostatic pressure, stereoselectivity, stability, enantioselectivity

SUMMARY

Pressure activation and inactivation is investigated for several enzymes like penicillin amidase (*E.coli*), glutamate dehydrogenase (*P. woesei*) and lipase (*Rhizopus arrhizus*) in the pressure range between 1 bar and 4000 bar. In dependence of pressure and temperature the enzymes are activated or inactivated and hence their enantioselectivity can be directed. The activation of the enzymes corresponds to a decrease in the K_M value which results in a higher substrate affinity.

INTRODUCTION

The properties of enzymes under high hydrostatic pressure as denaturing or activating "agent" have been investigated for several enzymes. The activity was measured in a high pressure cell equipped with a magnetic stirrer and a heater. The kinetic measurements were carried out by a photometer coupled to the high pressure cell by a fiber optic adapter. It was possible to perform kinetic measurements up to 4000 bar and 150 °C in situ under pressure. Enzymes undergo large conformational changes during the catalytic reaction and hence should significantly change their activity under pressure. A pressure dependence of the enzyme activity indicates that some of the conformational changes are stabilized or destabilized under pressure. According to the EYRING-THEORY of the activated complex the pressure dependence of the enzyme catalysed reaction is described as in equation (1) and (2).

$$\left(\frac{\partial \ln k}{\partial p} \right)_T = - \frac{\Delta V}{RT} \quad (1)$$

$$\Delta V = V^* - V^E \quad (2)$$

V^* : volume of the activated complex

R : gas constant

V^E : volume of the free educts

T : temperature

k : reaction rate constant

ΔV means the volume difference of the activated complex and of the educts which are the substrates and the free enzyme. A difference in the volumes of the activated complex and of the educts leads to an increase or decrease of the reaction rate depending upon a positive or negative volume change. According to Chen the enantioselectivity is defined as

$$\frac{\ln\left(\frac{[A]}{[A_0]}\right)}{\ln\left(\frac{[B]}{[B_0]}\right)} = E = \frac{\left(\frac{k_{cat}}{K_M}\right)_D}{\left(\frac{k_{cat}}{K_M}\right)_L} \quad (3)$$

Considering that the enantioselectivity (E) is dependent on high hydrostatic pressure the K_M and v_{max} value should also be dependent on pressure. In view of the enzyme catalysed reactions volume changes due to conformational changes of the enzymes should expect larger sensitivity of the reaction rates compared to the uncatalysed ones.

Changes in the K_M value under pressure show a relationship of the substrate affinity under pressure and hence helps to explain a mechanism of the catalytic steps. A decrease in the K_M value indicates an increase in the substrate affinity and vice versa. A determination of the K_M value in conjunction with a change of the activity under pressure could help to explain whether the activation is caused by a decrease of the activation energy or by an increase of the substrate affinity.

PENICILLIN AMIDASE (PA) (*Escherichia coli*)

Penicillin amidase (EC 3.5.1.11) from *E. coli* is a common enzyme used in industry for preparing semisynthetic antibiotics. This work presents a strong dependence in the stereoselectivity for penicilline amidase with D-/L-Phenylglycylacetamidobenzoic acid (D-/L-PGNAB) and D-/L-Phenylglycinamid (D-/L-Phenglycamid). These chromogenic substrates are model substrates for semisynthetic antibiotics. The activity and the change of the K_M values of penicillin amidase were different under high hydrostatic pressure for each substrate. Hence penicillin amidase also shows a pressure dependent enantioselectivity. The pressure dependence of the enantioselectivity is substrate specific. Figure 1 presents the results of the change of enantioselectivity of D-/L-Phenylglycinamid (PGA) and D-/L-Phenylglycinacetamidobenzoic acid (PGNAB). The enantioselectivity for D-/L-PGNAB is about 5 to 10 times higher than for D-/L-PGA under pressure. For both substrates the enantioselectivity decreases with increasing pressure and therefore the pressure induced conformational changes lead to a decrease of the enantioselectivity for these substrates. The „larger“ substrate molecule D-/L-PGNAB has more functional groups to interact with amino acids in the active site of PA and hence the enantioselectivity is larger. The change of the enantioselectivity of D-/L-PGA is much larger than for D-/L-PGNAB probably due to larger conformational changes of the active site under pressure. Determination of the k_{cat} and K_M values for D-/L-PGNAB showed that the k_{cat} and K_M values for L-PGNAB are nearly independent on high hydrostatic pressure. Therefore it becomes evident that the decrease in the enantioselectivity is a result of changes of the k_{cat}/K_M values for D-PGNAB. The increase of the K_M value corresponds to a loss of the enzyme substrate binding affinity and therefore reduces the reaction rate for D-PGNAB (see table 1).

Table 1 k_{cat} and K_M values and enantioselectivity of penicillin amidase under pressure for D-/L-PGNAB.

Pressure	k_{cat}		K_M		k_{cat} / K_M		Enantiosel.
	D-form	L-form	D-form	L-form	D-form	L-form	
1	4,00	0,05	1,50	2,50	2,67	0,02	0,01
1000	45,65	2,65	2,50	1,40	18,26	1,89	0,10
2000	78,26	2,74	7,50	1,60	10,43	1,71	0,16
3000	84,78	1,55	9,70	1,00	8,74	1,55	0,18
4000	1,74	2,65	3,90	0,52	0,45	5,10	11,43

GLUTAMATE DEHYDROGENASE (*PYROCOCCLUS WOESII*)

Extremophilic organisms are generally exhibited to extreme conditions which means high pressure, high / low temperatures and high temperatures. Thermophilic ones in particular the archaea are well adapted to high temperatures. The activity of the thermophilic glutamatdehydrogenase (GDH) (EC 1.4.1.4) from *P. woesei* is investigated under high hydrostatic pressure at different temperatures. GDH is a hexameric enzyme of 270 kDa isolated from shallow water, Vulcano Island in Italy. It requires NAD⁺/NADP⁺ as cofactors. The aim was to find out a correlation between activity, stability, pressure and temperature. GDH has a strong dependance on pressure and temperature. The activity in dependence of the temperature at different high hydrostatic pressures is shown in figure 2. It's maximum activity at ambient pressure lies slightly above 80 °C. The highest activity has been found at 85 °C and 500 bar. GDH is activated under pressure and the maximum activity is shifted towards higher pressure with increasing temperature from 80 °C to 90 °C. The activity increases with pressure up to 85 °C and decreases at higher temperatures due to an increase in thermal inactivation. An explanation for this phenomenon could be a stabilizing effect of pressure of the weak interactions that dominates the tertiary protein structure. Thermal energy causes enzyme inactivation due to partially unfolding the protein while hydrostatic pressure could prevent an increase in enzyme flexibility.

LIPASE (*RHIZOPUS ARRHIZUS*)

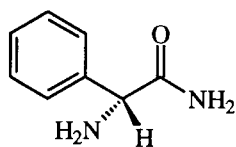
Lipases are the most common enzymes used in non conventional media like organic solvents and supercritical carbon dioxide. Lipases usually hydrolyse fats into fatty acids and glycerol. The special property of lipases is their ability to act at the interface between water and oil. In these experiments lipase (EC 3.1.1.34) from *Rhizopus arrhizus* (Boehringer Mannheim) was used to investigate the effects of lipase under hydrostatic pressure. The analysed reaction was the hydrolysis of p-Nitrophenyllaureate at different concentrations at 35 °C. The dependance of the kinetic constants between 1 bar and 3000 bar is presented in table 2. Like the thermophilic GDH at 1000 bar lipase is activated under pressure as well. The initial reaction rate increases by a factor of 1.5 at 1000 bar compared to the initial reaction rate at ambient

Table 2

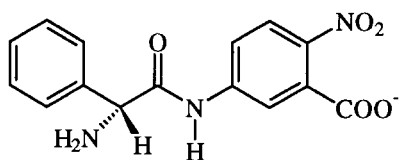
 V_{max} and K_M values of lipase under pressure

Pressure [bar]	v_{max}	K_M [μ M]
1	0,12	10,9
1000	0,17	6,3
3000	0,08	11,90

pressure. While v_{max} increases the K_M value decreases as a result of the higher substrate affinity. It seems that pressure up to 1000 bar stabilizes the enzyme substrate complex and probably decrease the activation energy of the activated complex.



D-/L-Phenglycamid



D-/L-PGNAB

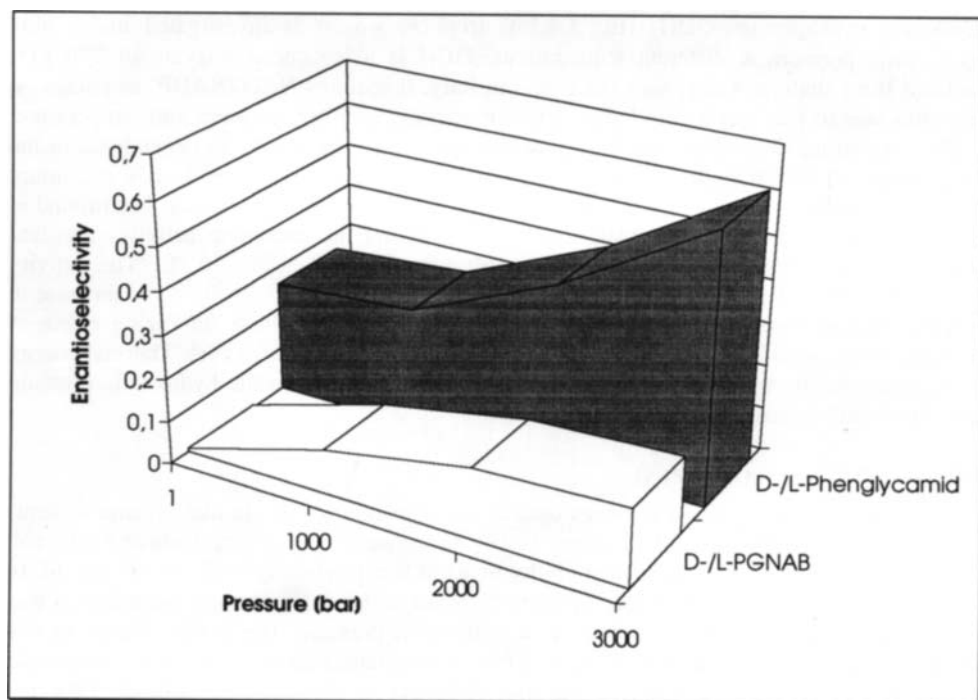


Figure 1. Pressure dependent enantioselectivity of penicillin amidase

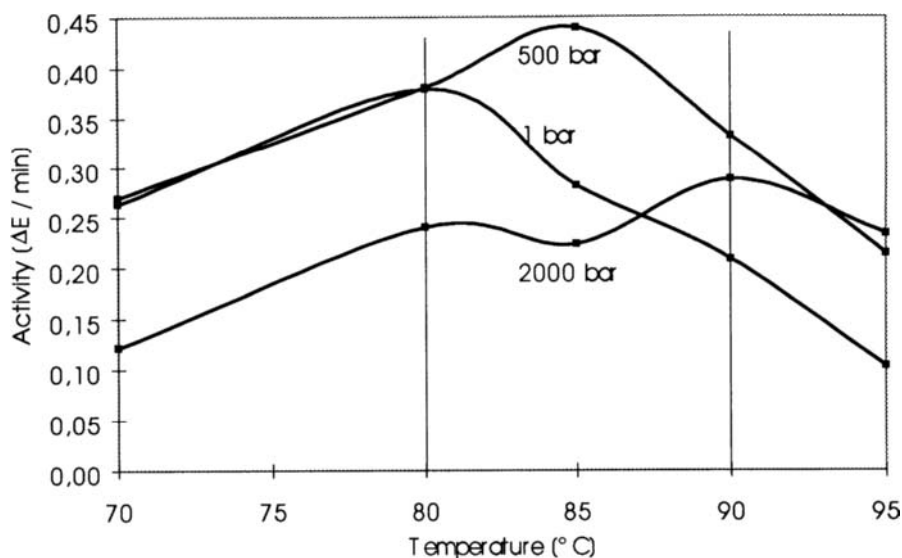


Figure 2. Activation of glutamate dehydrogenase under high hydrostatic pressure.

CONCLUSIONS

Generally it is possible to activate enzymes under pressure, but at high hydrostatic pressure a decrease in activity occurs due to pressure induced inactivation. The impact of pressure on the reaction rates is quite complex because of the different susceptibilities of the catalytic steps. It should be useful to perform enzyme catalysed reactions under hydrostatic pressure because pressure and temperature can have contrary effects.

REFERENCES

1. Isaacs, N. S. 1981. Liquid Phase High Pressure Chemistry. John Wiley & Sons
2. Duggleby, H. J., Tolley, S. P., Hill, C. P., Dodson, E. J. Dodson, G., Moody, C. 1995. 3. Penicillin acylase has a single-amino-acid catalytic centre. *Nature* **373**: 264-268.
3. Gross, M., Jaenicke, R. Proteins under Pressure. 1994 **221**: 617-630.
4. Weber, G., Drickamer, H. G., 1983 The effect of high pressure upon proteins and other biomolecules. *Quart. Rev. Biophys.* **16**: 89-112
5. Kasche, V., Hauffler, U., Markowsky, D., Melnyk, S., Zeich, A. 1978. Penicillin amidase from *E. coli* - enzyme heterogeneity and stability. *Ann N. Y. Acad. Sci.* **501**: 97-102
6. Taniguchi, Y., Suzuki, K. 1983. Pressure inactivation of α -Chymotrypsin. *J. Phys. Chem.* **87**: 5185-5193
7. Mozhaev, V., Heremans, K. Frank, J., Masson, P., Balny, C., 1994, Exploiting the effects of high hydrostatic pressure in biotechnological applications, *Tibtech.* **12**: 493-501
8. Chen, C.-S., Sih, C. J. Enantioselective biocatalysis in organic solvents with lipases. *Angew. Ch.* **101**: 711-724

This page intentionally left blank

Kinetic Study of Titanium Tetraisopropoxide Decomposition in Supercritical Isopropanol

V. Gourinchas-Courtecuisse, K. Chhor, J.F. Bocquet, C. Pommier

Laboratoire d'Ingénierie des Matériaux et des Hautes Pressions, C.N.R.S.,
Université Paris XIII, Avenue Jean-Baptiste Clément, 93430 - Villetaneuse, France

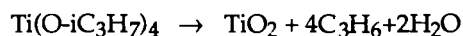
Decomposition of $\text{Ti}(\text{O-iC}_3\text{H}_7)_4$ dissolved in supercritical isopropanol leads to the formation of titanium oxide. The reaction is studied in the temperature range 531 to 568 K under 10 MPa and a mechanism is proposed. The obtained kinetic results are further used to optimize a continuous reactor producing submicronic TiO_2 powder at a laboratory pilot scale.

1. INTRODUCTION

We recently used titanium isopropoxide, $\text{Ti}(\text{O-iC}_3\text{H}_7)_4$ (referred to hereafter as TTIP) as a precursor for TiO_2 submicronic powder synthesis or thin film deposition [1,2]. Reactions were performed in supercritical isopropanol or alcohol- CO_2 mixtures. Advantages of such processes were the recover of partially crystallized powders without further washing and drying steps removing solvent and by-products simply by decompressing the system at temperature above the alcohol critical point. Furthermore, homogeneous TiO_2 films, of about 5 μm thickness, can be formed on an alumina substrate in less than 10 minutes, i.e. much more rapidly than by conventional CVD methods.

In order to model and optimize the behaviour of a continuous system for TiO_2 powder production on a laboratory pilot scale, we need kinetic data for the involved reaction. The aim of this study is then to get such informations on TTIP decomposition in supercritical isopropanol.

The TTIP thermal decomposition has been studied by various authors. Although the usually accepted overall reaction can be written as



conflicting results about kinetic rate laws and mechanisms have been reported.. These discrepancies appear to originate in the different experimental conditions in which the various studies were performed.

TTIP decomposition becomes detectable above about 623 K in a clean glass reactor; while it has a significant rate at temperatures as low as 523 K when the

reactor walls are covered with previously formed TiO_2 [3]. The presence of alumina, which is known to catalyse alcohol dehydration at temperature higher than 473 K, has been shown to greatly influence the alkoxide transformation [4,5]. Various overall reaction orders have been reported from kinetic studies. The order 0.5 was proposed in TiO_2 powder synthesis [6] while values between 0 and 2 were found from CVD experiments in which TTIP partial pressure and temperature are measured [4, 7-10]. A reaction mechanism was first proposed by Siefering et al. [7] in order to explain their experimental results. The three elementary steps were successively : (i) activation of a TTIP molecule by collisional excitation with another one in the gas phase, (ii) adsorption of the activated species, (iii) surface decomposition. Depending on the conditions, the limiting step, as well as the overall reaction order, can change.

Few authors reported measurements on activation energy. From these studies, two sets of values can be distinguished : around 100 to 150 kJ.mole^{-1} [8,9] or around 20 or 27 kJ.mole^{-1} [11,12]. In the latter case, a rather high oxygen content in the gas phase of the CVD system has been shown to favor the film formation. The addition of water in CVD experiments also increases the film growth rate [12,13].

2. EXPERIMENTAL

The reactor used is a closed 240 cm^3 stainless steel vessel fitted with temperature and pressure measurement sensors and with a device allowing the withdrawal of small samples at regular time intervals. The temperature was regulated within ± 2 K and the pressure was fixed at around 10 MPa. A TTIP solution in isopropanol, with concentration between 0.1 and 0.6 mole.l^{-1} was first introduced into the system and heated up to the study temperature (531 to 568 K) at 5 K.min^{-1} . At this temperature, the reaction was followed analysing successive withdrawn samples. The concentration of alkoxy groups bonded to a titanium atom and remaining in solution was determined by IR spectrometry by measuring the intensity of the absorption band at 1025 cm^{-1} attributed to C-O stretching vibration. The overall error in concentration is estimated to be around ± 10 %.

Isopropanol (critical point $T_c = 508$ K, $P_c = 4.7$ MPa) has a purity higher than 99 %. TTIP was distilled under reduced pressure at 368 K before being used.

In preliminary experiments, it was shown that the internal surface state of the reactor has an important influence on the reaction rate. Therefore, special care was taken to keep it as reproducible as possible from one experiment to the other by leaving a small film of strongly held TiO_2 particles on the internal walls.

3. RESULTS

As mentioned above, reaction advancement was followed from IR spectrometric measurements. In so far as the total withdrawn sample volume can be neglected compared with the initial one, the volumic molar concentrations of OR alkyl groups

in the liquid at room temperature and in the supercritical reaction medium at temperature T (noted $[A]$ and $[A]'$ respectively) can be related by

$$[A]' = [A] \frac{\rho_{SCF}}{\rho_L} = [A] \frac{V_L}{V_R}$$

where ρ_{SCF} and ρ_L are densities of the supercritical fluid and liquid respectively, V_R is the reactor volume, V_L is the introduced liquid solution.

In the initial TTIP alcoholic solution of concentration C_i , the alkoxy group concentration is $[A]_i = 4C_i$. If no reaction occurs during heating up to the study temperature T_R , and before data collection is started (at time $t=0$), the above equations lead to $[A]_0' = 4C_i \cdot \frac{V_L}{V_R}$. This is really not the case and the measured values are 20 to 35 % lower.

Experimental $[A]_t'$ values can be fitted as various functions of time in order to determine an overall kinetic reaction order. For the five investigated reaction temperatures in the range 531 to 568 K, the best linear fit is obtained plotting $\ln[A]_t' = f(t)$, in accordance with a first order reaction. The kinetic constants derived from curves in figures 1 and 2 are reported in table 1. Figure 3 shows an Arrhenius plot allowing calculation of the activation energy. Taking into account the previously estimated errors in T_R and $[A]$, the value $E_a = 113 \pm 16 \text{ kJ.mole}^{-1}$ can be proposed. Such a value is close to that reported when a thermal decomposition reaction is the limiting step [7,8].

4. DISCUSSION

As pointed out above, many studies on TTIP "decomposition" emphasize the influence of water formed in a dehydration reaction of alcohol present either as solvent or as traces. Such a chain mechanism involving a first alcohol molecule producing one water molecule which, by the hydrolysis reaction, gives two additional alcohol molecules has been shown by Bradley and al. studying zirconium alkoxides [11]. Curiously, such a "hydrolytic" decomposition of titanium derivatives has not been taken into account in the most recently reported studies on CVD experiments from TTIP [8-10].

We have previously shown that solid particle formation from TTIP in supercritical alcohol occurs at lower temperature than for pure vapor decomposition [1]. This allows us to assume that the first step in TiO_2 formation from titanium alkoxide under our experimental conditions is alcohol dehydration followed by hydrolysis reactions.

In support of this hypothesis, we studied Raman spectra recorded on samples withdrawn at various moments from the reaction medium. We shown that the intensities associated with Ti-OR, Ti-OH and Ti-O-Ti vibrational stretching bands decrease with time, but that the intensity ratios of two $\nu(Ti-O)$ lines remain nearly

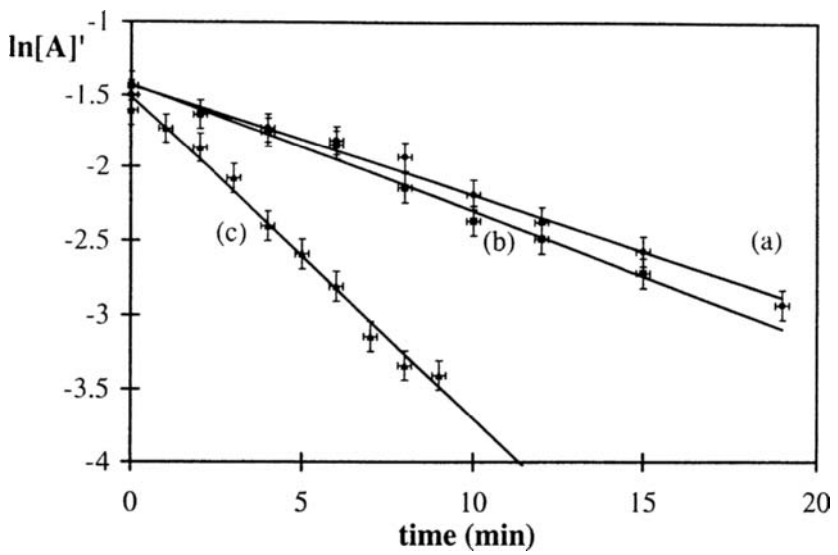


Figure 1 : First order kinetics plots at temperature 531 K (a), 536 K (b), 546 K (c).

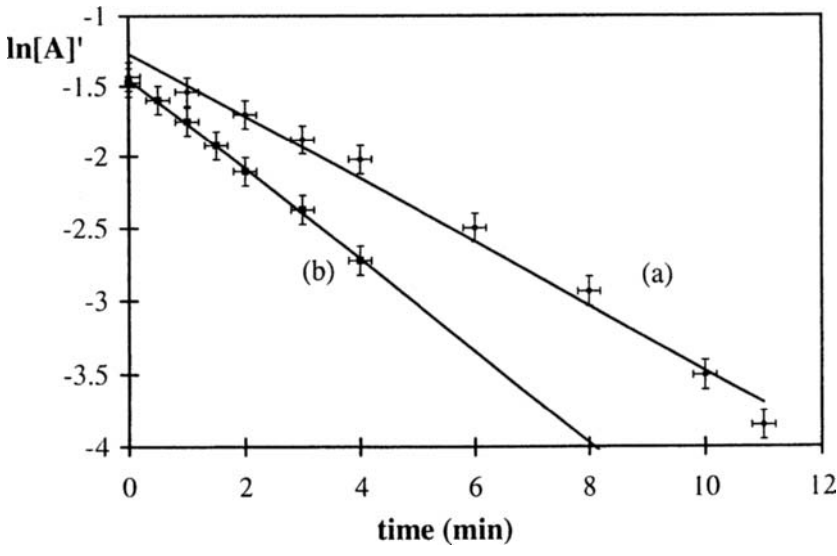


Figure 2 : First order kinetics plots at temperature 556 K (a), 568 K (b).

Table 1
Rate constants and
activation energy

T(K)	k(min ⁻¹)
531 ± 2	0.076 ± 0.008
536 ± 2	0.088 ± 0.009
546 ± 2	0.219 ± 0.022
556 ± 2	0.220 ± 0.022
568 ± 2	0.405 ± 0.041
Ea = 113 ± 16 kJ. mole ⁻¹	

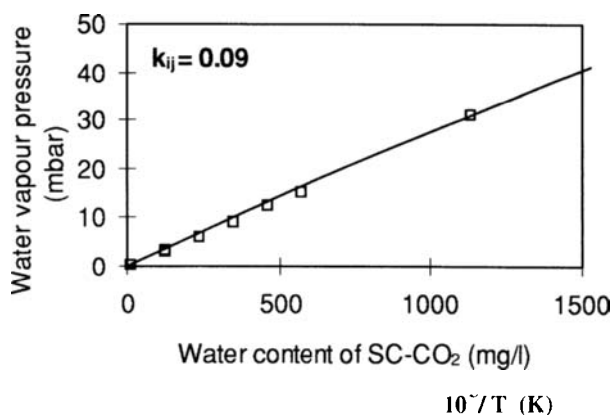
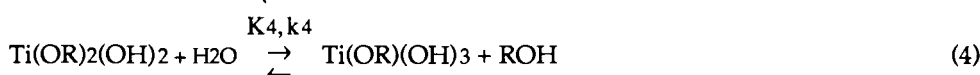
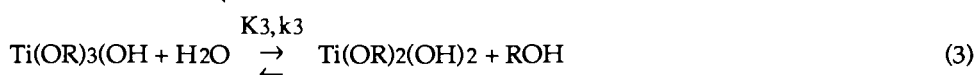


Figure 3 : Arrhenius plot for the kinetic constants k.

constant. These results indicate that hydrolysis equilibria are established in the system at a given temperature.

The following mechanism can then be proposed for transformation of TTIP into TiO₂ under our experimental conditions (R is the isopropyl group, R' is C₃H₆):



where k_i (or k'_i) and K_i are rate constants and equilibrium constants respectively.

It has been previously shown [5] that around 613 K, reaction (1) catalysed by Al₂O₃ is about 10 times faster than the alkoxide thermolysis. It is also well known [12] that the rate of successive hydrolyses decreases when the number of already reacted radicals increases. Therefore, we only mention the first 3 steps in the above sequence. Furthermore hydrolysis reactions are known to be faster than dehydration and dealcoholation of intermediate Ti(OR)_{4-x}(OH)_x species [13]. In the proposed mechanism, reactions (3') and (4') can then be considered as the limiting steps and the disappearance rate of OR groups bonded to Ti atom in the supercritical solution can be expressed as :

$$\frac{d[A]'}{dt} = -2k'_3[\text{Ti(OR)}_2(\text{OH})_2] - k'_4[\text{Ti(OR)(OH)}_3]$$

Using classical expressions of the equilibrium constants K_2 , K_3 , K_4 , it follows :

$$\frac{d[A]'}{dt} = - \left[\frac{2k_3'}{K_4[H_2O]} + k_4' \right] \frac{[A']}{Z}$$

where Z depends on K_2 , K_3 , K_4 and is a function of $[H_2O]$ and $[ROH]$.

A steady state between relative concentrations of various species containing titanium can be assumed as shown from the Raman study, so that water and isopropanol concentrations can be considered as constants. The kinetic law of the overall reaction can then be written $\frac{d[A]'}{dt} = -k[A']$. The reaction is then found to be first order as observed from experimental data.

CONCLUSION

The present study on TiO_2 powder formation from $Ti(O-iC_3H_7)_4$ in supercritical isopropanol has allowed the determination of reaction kinetic constants and activation energy in a temperature range from 531 to 568 K at 10 MPa. The proposed mechanism is based on a hydrolytic decomposition of the alkoxide initiated by water formed in alcohol dehydration catalysed by reactor walls. The derived reaction kinetic order is unity in accordance with experimental results. Such a mechanism also explains that special cares must be taken about the internal surface state of the reactor in order to obtain reproducible results.

REFERENCES

1. K. Chhor, J.F. Bocquet and C. Pommier, *Mater. Chem. Phys.* 32 (1992) 249.
2. J.F. Bocquet, K. Chhor and C. Pommier, *Surface and Coatings Technol.* 70 (1994) 73.
3. Y. Shimogaki and H. Komiyama, *Chem. Letters* (1986) 267.
4. Y. Takahaschi, H. Suzuki and N. Nasu, *J. Chem. Soc., Farad. Trans. I*, 81 (1985) 3117.
5. S.A. Kurtz and R.G. Gordon, *Thin Solid Films* 147 (1987) 167.
6. T. Kanai, H. Komiyama and H. Inoue, *Kagaku Kogaku Ronbunshu* 11 (1985) 317.
7. K.L. Siefering and G.L. Griffin, *J. Electrochem. Soc.* 137 (1990) 814.
8. W.G. Lai and G.L. Griffin, P. Vincenzini (eds), *Performance Ceramic Films and Coatings*, 151, Elsevier, 1991.
9. Z. Chen and A. Derking, *J. Mater. Chem.* 3 (1993) 1137.
10. H.Y. Lee and H.G. Kim, *Thin Solid Films* 229 (1993) 187.
11. D.C. Bradley and M.M. Faktor, *Trans. Farad. Soc.* (1959) 2117.
12. E.A. Barringer and H.K. Bowen, *Langmuir* 1 (1985) 414.
13. T. Ishino and S. Minami, *Tech. Rep. Osaka Univ.* 3 (1953) 357.

Enantioselective hydrogenation in supercritical fluids. Limitations of the use of supercritical CO₂

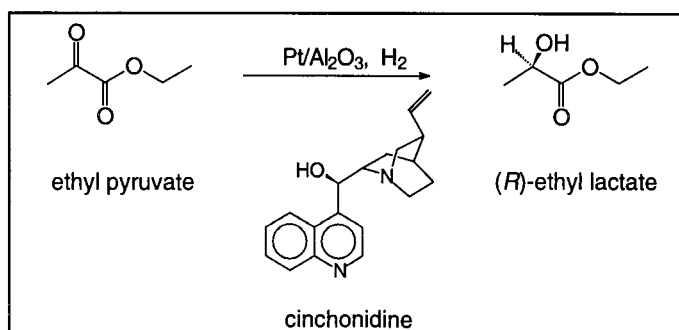
B. Minder, T. Mallat and A. Baiker

Department of Chemical Engineering and Industrial Chemistry, ETH Zentrum, CH-8092, Zürich, Switzerland

The Pt-catalyzed enantioselective hydrogenation of ethyl pyruvate to (*R*)-ethyl lactate was considerably faster (by a factor of 3-3.5) in supercritical ethane than in the conventional apolar solvent toluene, whereas the enantioselectivity was unaffected. Complete catalyst deactivation was observed in CO₂, which was shown by FTIR to be due to the reduction of CO₂ to CO via reverse water gas shift reaction. The catalyst could be regenerated by exposing it to ambient air, while hydrogen treatment was less efficient. This is the first evidence to the limitation of catalytic hydrogenations over Pt metals in supercritical CO₂.

1. INTRODUCTION

There is a rapidly growing interest in performing chemical reactions in supercritical solvents. Intrigued by the unique properties and technological advantages of supercritical fluids, a broad range of chemical transformations have been studied in this medium [1-3]. Interestingly, there are hardly any data available on catalytic hydrogenations [4, 5]. Here we report a rather demanding reaction, the enantioselective hydrogenation of an α -ketoester to the corresponding α -hydroxyester (scheme 1) in some supercritical solvents. The catalyst is Pt/alumina, chirally modified by a preadsorbed alkaloid, cinchonidine [6-8].



Scheme 1

2. EXPERIMENTAL

2.1 Hydrogenation reaction

A 5 wt-% Pt/alumina catalyst (Engelhard, 4759, Pt-dispersion of 0.22 by CO chemisorption) was prereduced at 400 °C for 2 h in 30 ml min⁻¹ flowing hydrogen, and then transferred to the reactor under argon. Ethyl pyruvate was freshly distilled before each reaction. The critical pressures and temperatures of CO₂, ethane and propane are 73 bar/304 K, 48 bar/305 K and 43 bar/370 K, respectively [9].

The hydrogenation reaction was carried out in a thermostated 500 ml MEDIMEX SS stirred autoclave. Under standard conditions, 20 ml ethyl pyruvate, 0.45 g catalyst, 88 mg cinchonidine and 121 g solvent were used. Ethane, propane and CO₂ were measured with a Rheonik flow controller. The reactant/solvent ratio was always 1.5 mmol/g. Under the conditions applied, the ethane/H₂ and CO₂/H₂ mixtures are in the supercritical region [10, 11].

Enantiomeric excess (ee) and conversion were determined gas-chromatographically (WCOT, CP-Cyclodextrin-β-2,3,6-M-19). Standard deviation of determining ee (absolute value of $\{[R]-[S]\}/([R]+[S]) \times 100$, in %) was ± 1 %.

2.2 FTIR measurements

The *in situ* diffuse reflectance FTIR studies were carried out on a Perkin Elmer (model 2000) instrument, including a diffuse reflection unit and a reaction chamber. The gas flow of 30 ml min⁻¹ was passed through the reaction chamber, containing the catalyst on an alumina sample holder. The spectra were measured in the reflection mode, with 25 scans and 8 cm⁻¹.

Before the measurement shown in Fig. 1, the catalyst was first pretreated at 673 K for 1.5 h in H₂ (99.999 %). The background spectrum (100 scans, 8 cm⁻¹) was measured after cooling the catalyst to 313 K in N₂ (99.995 %). The cell was flushed with H₂ at 1 bar for 2 min, then the pressure was increased to 10 bar. Hydrogen was substituted by a mixture of CO₂ (99.99 %) and H₂ in a 1 : 4 ratio, and the pressure was increased to 15 bar. The experimental procedure for Fig. 3 is schematically illustrated in Fig. 2. The KBr background spectrum was measured at 493 K in nitrogen (500 scans, 8 cm⁻¹).

3. RESULTS AND DISCUSSIONS

3.1 Enantioselective hydrogenation of ethyl pyruvate in supercritical solvents

Conversions and enantiomeric excesses (ee), obtained in ethane under supercritical conditions, are shown in Table 1. Favorable conditions for achieving good ee are high hydrogen pressure (≥ 70 bar) and low temperature [8]. The latter parameter is limited by the critical temperature of the ethane/hydrogen mixture [10]. Selectivities are about the same as those obtained in the best conventional apolar solvent, toluene. Initial reaction rates of the fast reaction could not be determined accurately. The reaction times, required for complete conversion of ethyl pyruvate, were 3 - 3.5 times lower in ethane than in toluene under otherwise identical conditions, likely due to the absence of mass transfer limitations in ethane.

In the hydrogenation of α -ketoesters, high ee can be achieved only at ambient temperature or below [8]. The number of supercritical solvents, available for this temperature range, is very limited. The ee in propane is moderate (Table 1), due to the necessary high reaction temperature. Supercritical CO₂ seemed to be an ideal choice as solvent due to its low

polarity and critical temperature. Astonishingly, a complete catalyst deactivation was observed in CO₂ in a broad range of pressures and temperature, and no conversion higher than 3 % could be obtained even after several hours reaction time (Table 1). The attempted hydrogenation of another α -ketoester, ethyl benzoylformate, also failed in this solvent.

Table 1

Enantioselective hydrogenation of ethyl pyruvate in supercritical and conventional solvents

N°	Solvent	P _{solvent}	P _{hydrogen}	Temp.	Conv.	Ee.
		bar	bar	K	%	%
1	Ethane	60	70	293	98	74
2	Ethane	60	70	323	96	74
3	Ethane	60	70	343	98	71
4	Ethane	60	70	373	68	33
5	Ethane	60	10	323	81	64
6	Ethane	60	30	323	99	69
7	Ethane	60	100	323	96	74
8	Ethane	60	140	323	92	74
9	Propane	50	70	373	40	34
10	Carbon dioxide	80	20	313	2	29
11	Carbon dioxide	80	70	313	3	28
12	Carbon dioxide	180	70	373	2	7
13	Toluene	-	70	323	100	75
14	Toluene	-	70	373	99	41

3.2 In situ FTIR study of catalyst poisoning in CO₂

FTIR model experiments were performed to reveal the nature of catalyst deactivation in CO₂. The spectrum taken at 15 bar in a CO₂/H₂ mixture is shown in Fig. 1. The bands at 2060 and 1870 cm⁻¹ indicate considerable coverage of Pt by linearly and bridge-bonded CO [12], formed by the reduction of CO₂ on Pt (reverse water gas shift reaction). The three characteristic bands at 1660, 1440 and 1235 cm⁻¹ are attributed to CO₂ adsorption on Al₂O₃, likely as carbonate species [13, 14]. It is well known [15] that CO is a strong poison for the hydrogenation of carbonyl compounds on Pt, but can improve the selectivity of the acetylene \rightarrow olefin type transformations. Based on the above FTIR experiments it cannot be excluded that there are other strongly adsorbed species on Pt formed in small amounts. It is possible that the reduction of CO₂ provides also -COOH and triply bonded COH, as proposed earlier [16].

The possibilities of regenerating Pt/alumina after CO poisoning is illustrated in Fig. 3. If the catalyst (stored in air) is exposed to H₂, the CO peaks at 2030 and 1860 cm⁻¹ appear immediately (curve b). The minor shift compared to Fig. 1 may be due to the different

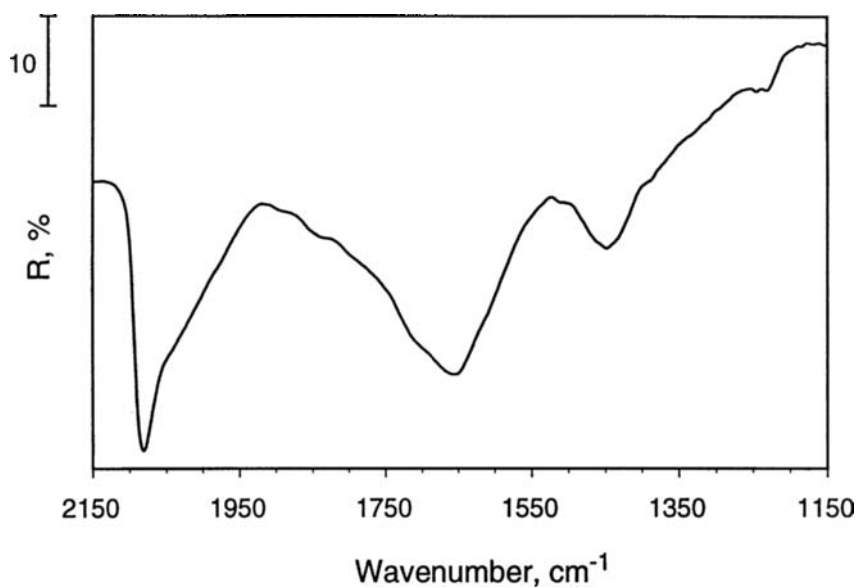


Figure 1. FTIR spectrum of the 5 wt-% Pt/Al₂O₃ catalyst measured after prereduction at 673 K (catalyst cleaning) and cooling to 313 K; atmosphere: 3 bar CO₂ + 12 bar H₂.

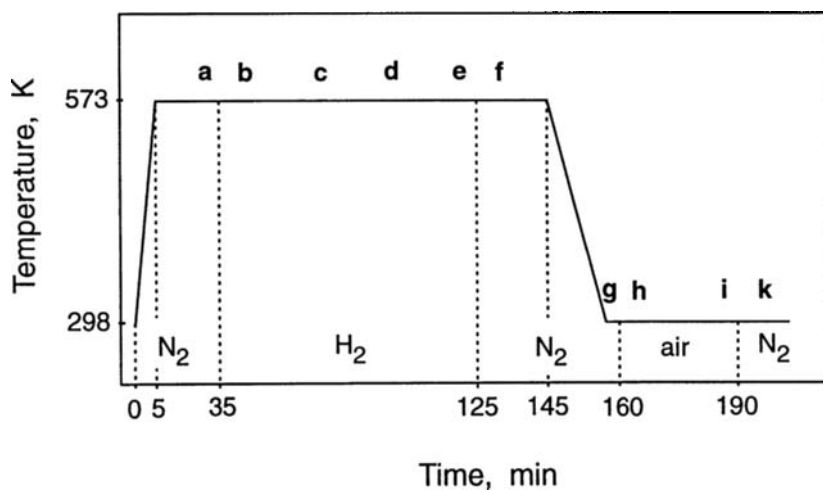


Figure 2. Sample pretreatment before and during FTIR analysis shown in Fig. 3

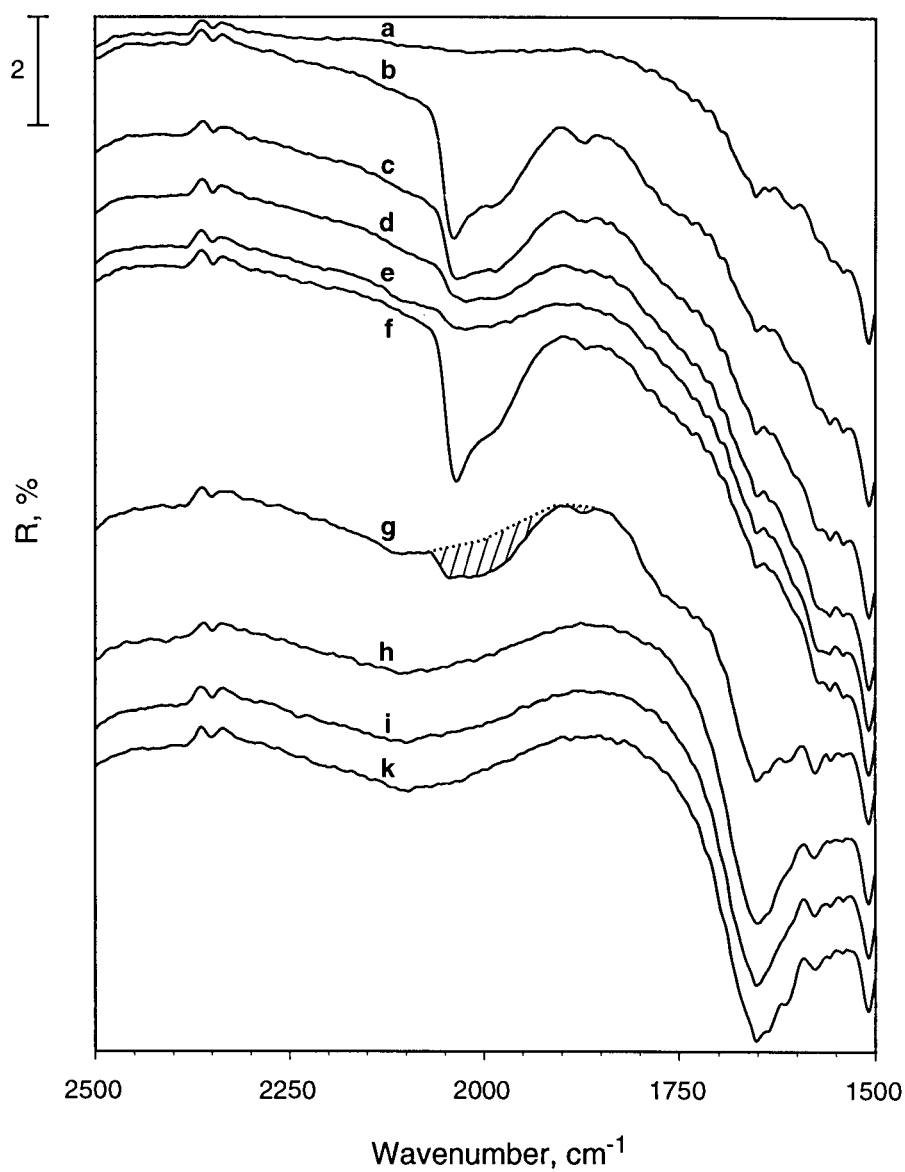


Figure 3. FTIR spectra of the 5 wt% Pt/Al₂O₃ catalyst during its treatment in nitrogen, hydrogen and air; for denotation of a - k see the scheme in Fig. 2.

conditions and the small amount of CO. Removal of CO by competitive adsorption of H_2 is slow and incomplete even at 573 K (slow diffusion of CO from Pt to Al_2O_3 , curves c-e), and CO appears again when substituting H_2 to N_2 (curve f). Note that CO adsorption on the Lewis centers of Al_2O_3 (at 2190 cm^{-1}) is only detectable at high CO pressures.

In contrast, oxidation of CO on Pt is rapid and complete. During cooling to room temperature, CO is partly oxidized to CO_2 by the low O_2 content of the N_2 flow (<50 ppm). The remaining CO is immediately oxidized in air, and the CO peaks do not appear again in N_2 (curves g-k). The adsorption of the product CO_2 on alumina is indicated by the carbonate and bicarbonate species at $1600\text{-}1750\text{ cm}^{-1}$.

4. CONCLUSIONS

Our results suggest that due care should be taken when applying supercritical CO_2 as solvent in hydrogenation reactions. Platinum metals catalyze the reduction of CO_2 to CO (reverse water gas shift reaction) even at ambient temperature, and CO can poison the catalyst (e.g. in carbonyl reductions) and contaminate the recycled CO_2 .

ACKNOWLEDGEMENTS

Financial support of this work by Hoffmann - La Roche AG (Switzerland) and the Swiss National Science Foundation (Program CHiral 2) is gratefully acknowledged.

REFERENCES

1. T. G. Squires, C. G. Venier and T. Aida, *Fluid Phase Equil.*, 10 (1983) 261.
2. K. M. Dooley and F. C. Knopf, *Ind. Eng. Chem. Res.*, 26 (1987) 1910.
3. B. C. Wu, S. C. Paspek, M. T. Klein and C. LaMarca, in T. J. Bruno and J. F. Ely (Eds.), *Supercritical Fluid Technology*, CRC, Boca Raton, 1991, p.511.
4. P. G. Jessop, T. Ikariya and R. Noyori, *Nature*, 368 (1994) 231.
5. M. J. Burk, S. Feng, M. F. Gross and W. Tumas, *J. Am. Chem. Soc.*, 117 (1995) 8277.
6. Y. Orito, S. Imai and S. Niwa, *J. Chem. Soc. Japan*, (1980) 670.
7. J. T. Wehrli, A. Baiker, D. M. Monti, H. U. Blaser and H. P. Jalett, *J. Mol. Catal.* 57 (1989) 245.
8. H. U. Blaser, *Chem. Rev.*, 92 (1992) 935.
9. T. E. Daubert and R. P. Danner (Eds.), *Physical and Thermodynamic Properties of Pure Chemicals; Data Compilation*, Taylor and Francis, Washington, 1993.
10. A. Heintz and W. B. Streett, *J. Chem. Eng. Data*, 27 (1982) 465.
11. C. Y. Tsang and W. B. Streett, *Chem. Eng. Sci.*, 36 (1981) 993.
12. T. Inoue and T. Iizuka, *J. Chem. Soc., Faraday Trans.*, 82 (1986) 1681.
13. N. D. Parkyns, *J. Chem. Soc. (A)*, (1967) 1910.
14. Z. M. Liu, Y. Zhou, F. Solymosi and J. M. White, *Surf. Sci.*, 245 (1991) 289.
15. M. Freifelder, *Practical Catalytic Hydrogenation*, Wiley-Intersci., New York, 1971.
16. S. Taguchi and A. Aramata, *Electrochim. Acta*, 39 (1994) 2533.

Investigation of Various Zeolite Catalysts under Supercritical Conditions

Fenghui Niu and Hanns Hofmann

Institute of Technical Chemistry I, University of Erlangen-Nürnberg, Egerlandstrasse 3, 91058 Erlangen (Germany), Tel. (+ 49-9131) 857420, Fax. (+ 49-9131) 857421

Three different zeolites (USY-zeolite, H-ZSM-5 and H-mordenite) were investigated in a computer controlled experimental equipment under supercritical conditions using the disproportionation of ethylbenzene as test reaction and butane or pentane as an inert gas. Experiments were carried out at a pressure of 50 bar, a flow rate of 450 ml/min (at standard temperature and pressure), a range of temperatures (573 - 673 K) and 0.8 as molar fraction of ethylbenzene (EB) in the feed. The results showed that an extraction of coke deposited on the catalysts strongly depends on the physico-chemical properties of the catalysts. Coke deposited on Lewis centres can be more easily dissolved by supercritical fluid than that on Brønsted centres.

1. INTRODUCTION

Many heterogenous catalytic processes are often accompanied by side reactions, which lead to deposition of higher-molecular-weight polynuclear compounds on the catalyst surface. This "coke" deposits give rise to the reduction of the number of accessible active centres and thus to deactivation of catalysts. In situ regeneration of the coked catalysts by supercritical fluids has more advantages than the traditional burn-off in air [1]. It is based on the well-known high ability of supercritical fluids for dissolving solids of large molar masses already demonstrated experimentally [2] and theoretically [3].

Y-zeolite, ZSM-5 and mordenite are three important industrial zeolites because of their pore structure and surface acidity. The coke extraction from the strongly coked HYZ catalyst has already been investigated under supercritical conditions [4,5]. However, investigations on ZSM-5 and mordenite under supercritical conditions can not be found in literatures.

In this paper three zeolite catalysts from Süd-Chemie AG (USY-zeolite Si/Al 2.3-2.5, H-ZSM-5 Si/Al 15 and H-mordenite Si/Al 10) have been investigated in a gradientless reactor under supercritical conditions using the disproportionation of ethylbenzene (EBD) as test reaction and butane or pentane as inert. A previous publication reported investigations on those three catalysts at normal pressure and the details about the geometry of the three zeolites [6].

2. EXPERIMENTAL

The computer controlled experimental equipment consists of a feeding system, a gradientless reactor, a gas chromatograph for the analysis of the reaction mixture as well as data processing and control unit consisting of two PCs. A detailed description of the experimental setup can be found in reference [1].

The coke content of the coked catalyst samples was determined by a microbalance [7]. The

nature and the number of acid centres of catalysts have been determined by means of the IR-spectroscopy [1]. The catalyst sample (particle size 0.63 - 0.8 mm) was calcined for 6 hours at 673 K under nitrogen.

3. RESULTS AND DISCUSSION

3.1. USYZ

The experiments on the USY-zeolite (USYZ) at normal pressure showed that the USYZ had a low activity and deactivated slowly, but its coke contents were not small [6]. This means that the USYZ has a strong coking tendency. Therefore experiments on USYZ under supercritical conditions are interesting. Figure 1 shows the conversion against time on stream at different temperatures each at 1 bar and 60 bar. It can be seen clearly that the conversion levels under supercritical conditions are higher than those at normal pressure in spite of the much larger flow rate at 60 bar.

This means that the coking tendency can be prevented or decelerated under supercritical conditions. On the other hand, there is also an optimum temperature, at which the conversion can remain constant during time on stream because of an equilibrium between coking and coke extracting. Compared with the results on other catalysts one can find that this regularity is generally valid only for the Y-zeolite. The reason may be that Y-zeolite has three-dimensional channels and the larger pore diameter. For two-dimensional ZSM-5 and the one-dimensional H-modernite it is difficult for the dissolved coke precursor to diffuse out of the pore of the catalyst. Comparing coke contents on the USYZ catalyst at 1 and at 60 bar (Figure 2), one can find that the coke extraction of supercritical fluids also plays an important role on the catalyst which has lower activity and deactivates slowly.

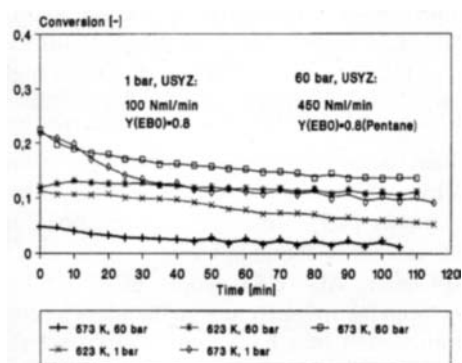


Figure 1 Conversion against time on stream at different temperatures each at 60 bar and 1 bar (Nml/min represents flow rate ml/min at standard temperature and pressure.)

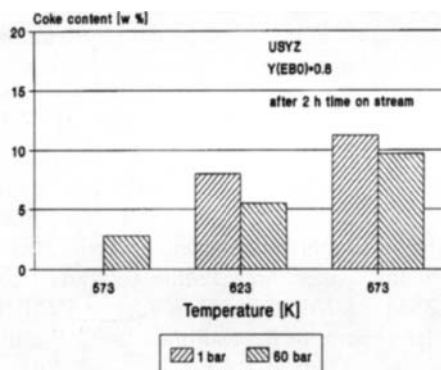


Figure 2 Coke contents at different temperatures on USYZ

Figure 3 shows the relative areas of the different acid centres of USYZ in dependences of temperature and pressure. It can be seen that acid centres were less reduced by coking at 623 K under supercritical conditions than under normal pressure. This confirms a high capacity of the

coke extraction of supercritical fluids. At 673 K there are different behaviors for the three absorption bands. Thus the supercritical conditions bring about an increase of coke deposit on Brønsted centres, while Lewis centres show on the contrary a lower coking tendency at this temperature than at normal pressure.

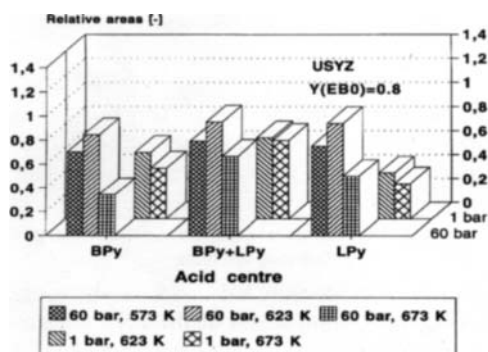


Figure 3 Relative areas of different acid centres on USYZ in dependences on temperature and pressure (*Lpy*, *Bpy* and *Bpy+Lpy* represent respectively Lewis centre, Brønsted centre and Lewis centre and Brønsted centre in common.)

3.2. ZSM-5

A higher activity and a lower coking tendency of ZSM-5 were shown at normal pressure [6]. The highest benzene concentration was also observed at high temperature under normal pressure indicating an ability for dealkylation. Because of the low coking tendency of ZSM-5, investigations were performed under supercritical conditions only at two higher temperatures (623, 673 K). Figure 4 shows the conversion level vs. time on stream under supercritical conditions and at normal pressure. It can be seen that the degree of conversion at normal pressure is much higher than that at high pressure and the same temperature. The reason is the larger flow rate (450 Nml/min) at high pressure than at normal pressure (100 Nml/min). In order to keep the conversion level at higher flow rate, more acid centres of catalyst are required. This means that for a definite amount of catalyst the EB-conversion decreases with increasing flow rate. Owing to the weak coking tendency of ZSM-5 the supercritical fluid plays only a small role for the activity of ZSM-5.

From Figure 4 it can be found that the activity of the catalyst and the coking tendency increase quickly with increasing temperature. By comparison of the coke contents formed on ZSM-5 at normal pressure with those under supercritical conditions (Figure 5), it can be deduced that at lower temperature (623 K) the ability of coke extraction is larger than the coking tendency under supercritical conditions. Inversely more coke occurred at higher temperature and at 60 bar. This implies that the coking tendency increases more quickly with increasing temperature under supercritical conditions than the ability of coke extraction.

Figure 6 shows the concentrations of products vs. time on stream on ZSM-5 each at normal pressure and under supercritical conditions. It can be seen that at normal pressure the amount of benzene is much larger than that of DEB, particularly at high temperature. Under supercritical conditions the amount of benzene is yet slightly larger than the DEB amount only at high temperature (673 K). Both get closer slowly with time on stream. This illustrates that the supercritical conditions can improve the product distribution of EBD on ZSM-5. The side reactions of DEB to benzene and light alkane are strongly reduced at high pressure. This is because of the principle of Le Chatelier, on which the equilibrium of the dealkylation reactions

is shifted to the side of reactant by increased pressure.

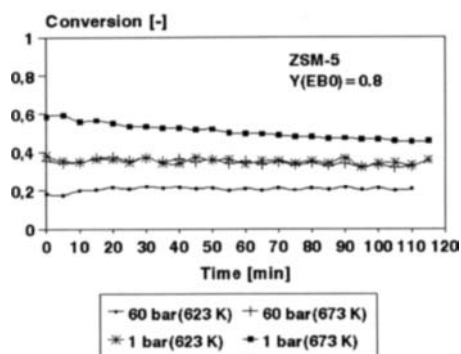


Figure 4 Conversion level vs. time on stream under supercritical conditions and at normal pressure

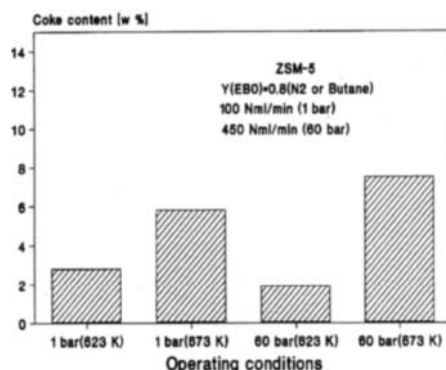


Figure 5 Comparison of the coke contents on ZSM-5 at normal pressure and in supercritical state

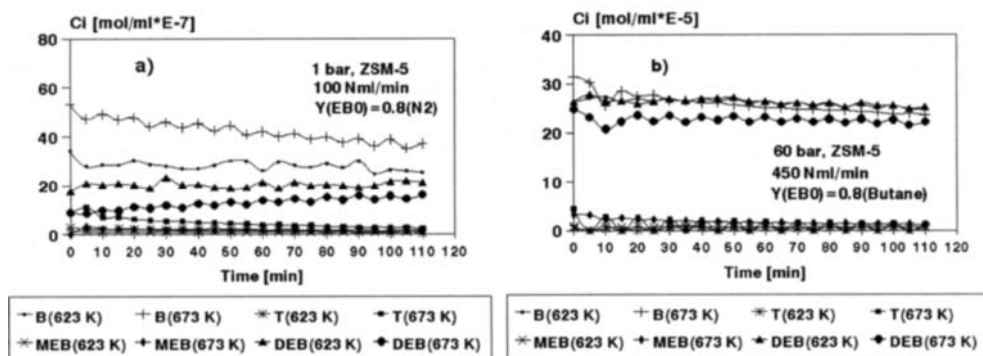


Figure 6 Comparing product concentrations on ZSM-5, a): at normal pressure; b): under supercritical conditions (*B*, *T*, *MEB* and *DEB* represent respectively benzene, toluene, methylethylbenzene and diethylbenzene.)

Figure 7 shows the relative areas of different acid centres on ZSM-5 in dependences on temperature and pressure. It can be found that the acid centres were less reduced at 623 K under supercritical conditions than those at normal pressure. Especially on Lewis centres the coking tendency is weak. This implies that the coke deposited on Lewis centres may be loosely built and can be easily removed by supercritical fluid. At 673 K the acid centres of ZSM-5 disappeared almost totally. This indicates that coking tendency increases more quickly with increasing temperature than the ability of coke extraction.

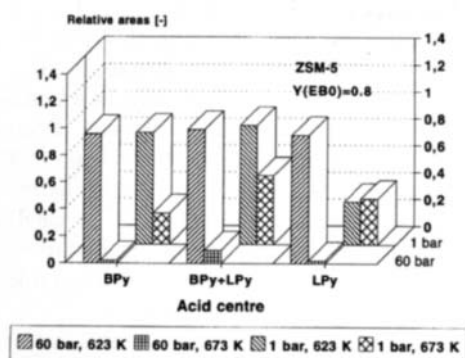


Figure 7 Relative areas of different acid centres on ZSM-5 in dependences on temperature and pressure

3.3. H-mordenite

At normal pressure H-mordenite deactivated quickly only at 673 K and small molar feed fraction ($Y_{EB0}=0.2$) [6]. Thus, at high pressure and large molar feed fraction ($Y_{EB0}=0.8$) investigation on H-mordenite was performed only at high temperature. The experiment at 623 K and 60 bar shows a low conversion. Therefore an experiment was carried out at 623 K in the initial period and after about 60 minutes the temperature was raised to 673 K. The conversion vs. time on stream is shown in Figure 8 a). It can be found that on H-mordenite the EB-conversion is strongly dependent on temperature under supercritical conditions in a range of 623 - 673 K. The conversion at 673 K is much higher than that at 623 K and decreases slowly with time on stream. The large temperature dependency of the activity on H-mordenite can be attributed to its one-dimensional pore structure. This channel system prevents the diffusion of the reactant to the catalytically active inner-surface of the catalyst. This suggests that the internal mass transport plays an important role for the EBD on H-mordenite. The higher the temperature, the more reactants can achieve the catalytically active inner-surface of the catalyst.

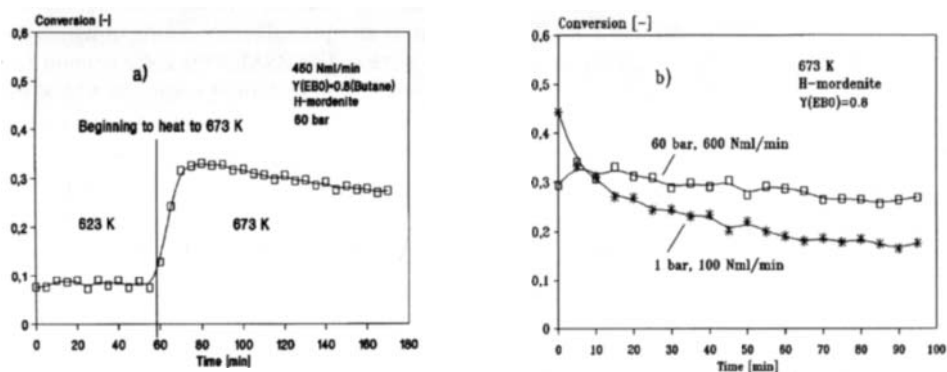


Figure 8 Conversion level vs. time on stream on H-mordenite, a): at lower temperature with temperature change; b): at higher temperature and different pressures

As shown in Figure 8 b), the H-mordenite deactivated more quickly at normal pressure than under supercritical conditions. This means that the coke extraction from the coked H-mordenite

is also clearly larger under supercritical conditions. However the coking tendency is as well stronger at higher temperature (673 K). The slow deactivation of H-mordenite illustrates that at high temperature the coking tendency is a little greater than the ability of coke extraction.

From Figure 9 one can see that there is no overall tendency for both acid centres as a function of pressure change. So Brønsted centres are reduced by coking at higher pressure, whereas Lewis centres are increased by coke extraction (compared with those at normal pressure). The coke content is practically identical for both experimental conditions. Therefore a displacement of reaction conditions into the supercritical range does not bring a coke decrement on catalyst, but only a different coke distribution on the special centres. From the comparison of conversion vs. time on stream (see Figure 8 b)) it is deduced that the Lewis-centres play the greatest role in the EBD.

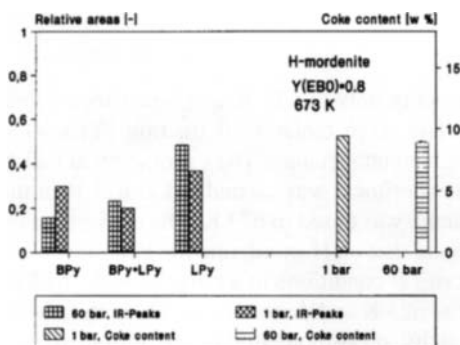


Figure 9 Relative areas of different acid centres and coke contents on H-mordenite in dependences of pressure and of flow rate at 673 K

4. CONCLUSION

The coke extraction by supercritical fluids is strongly dependent on the type of catalyst. The three-dimensional USYZ is easier accessible for the "solvent" than the two-dimensional ZSM-5 and the one-dimensional H-modernite. For USYZ there is an optimal temperature, at which the supercritical fluid has the highest ability for coke extraction. For ZSM-5 the coke content and the rest of the acid centres of catalyst are strongly dependent on the temperature. At 623 K the acid centres decreased only about 5%, but at 673 K they were almost totally decimated. Due to the faint coking tendency of ZSM-5 the supercritical fluid plays only a small role for the regeneration of the catalyst. But the supercritical fluid can ameliorate the product distribution of the EBD on ZSM-5. For H-mordenite the conversion of EB is strongly dependent on the temperature in the range of 623 - 673 K because of its one-dimensional channel system.

REFERENCES

1. F. Niu, Dissertation, Universität Erlangen-Nürnberg 1996
2. H. Tiltcher, H. Wolf and J. Schelchshorn, *Angew. Chem.* 93 (1981) 907
3. G. Manos and H. Hofmann, *Chem. Eng. Technol.*, 14 (1991) 73
4. F. Niu and H. Hofmann, *International Meeting on Chem. Eng. and Biotechn.*, 15-20 May, 1995, Beijing, China
5. F. Niu and H. Hofmann, *The Canadian J. of Chemical Engineering*, to be published
6. F. Niu and H. Hofmann, *Applied Catalysis*, 128 (1995) 107
7. G. Kolb, Dissertation, Universität Erlangen-Nürnberg 1993

Coking Mechanism of Zeolite for Supercritical Fluid Alkylation of Benzene

Yong Gao, Yi-Feng Shi, Zhong-Nan Zhu and Wei-Kang Yuan*

UNILAB Research Center of Chemical Reaction Engineering,
East China University of Science and Technology,
Shanghai 200237, P. R. China

Abstract Alkylation of benzene with ethylene over Y-type zeolite has been carried out under supercritical conditions. Two aspects of the reaction have been paid attention to: slowing down the deactivation rate and decreasing the by product selectivity. Experiments have revealed the existence of some coke precursors that are partly removed from the catalyst surface. By product xylenes are decreased and are explained due to high diffusivity in the supercritical fluid.

Keywords: zeolite, coke precursor, supercritical fluid, deactivation.

1. INTRODUCTION

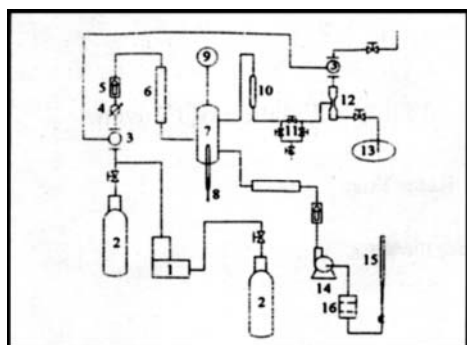
Catalyst deactivation due to coke formation is relatively speedy for a reactions such as alkylation of benzene to ethylbenzene over zeolite, particularly when the benzene to ethylene ratio is low. Another problem of this reaction is the formation of xylenes, the major by-products. Though their total amount produced in the process is very limited, they are harmful to the process because of the difficulty to remove them from the desired product ethylbenzene. Therefore, investigating the mechanism of catalyst coking is of practical significance for finding the potential ways for prolonging the reactor runtime and decreasing the xylenes selectivity.

2. EXPERIMENTAL

In order to study the catalyst deactivation phenomenon under supercritical conditions and the difference between the liquid phase (LP) and supercritical fluid phase (SCFP) reactions, experiments were carried out in an isothermal tubular reactor ($D=12$ mm, $L=600$ mm) packed with grounded Y-type zeolite pellets of 60 mesh. The experimental equipment for the LP and SCF reaction processes is illustrated in Figure 1.

To take the catalysis properties and the fluids critical properties of the reactant mixtures into consideration, both LP and SCFP alkylation reactions were run under the conditions shown in Table 1.

* To whom the correspondence should be addressed.



- | | |
|-----------------------|-------------------------|
| 1 compressor | 2 ethylene vessel |
| 3 pressure controller | 4 flowmeter |
| 5 one way valve | 6 heater |
| 7 reactor | 8 thermocouple |
| 9 pressure gage | 10 condenser |
| 11 sampling device | 12 gas-liquid separator |
| 13 product tank | 14 pump |
| 15 feeder | 16 strainer |

Figure 1. Schematic of experimental equipment

With the experimental data^[1], the reacting temperature and pressure of the SCFP alkylation is above its critical point when the Benzene/Ethylene molar ratio is 4.5.

Table 1. Reaction conditions for LP and SCFP

Phase	Temp., K	Pres., MPa	B/E (molar)	Catalyst, g	Space velocity, hr ⁻¹	Remark
LP	523.15	6.5	4.5	4.0	1.3	$T < T_c, P > P_c$
SCFP	548.15	6.5	4.5	4.0	1.3	$T > T_c, P > P_c$

3. COKE PRECURSOR DETERMINATION

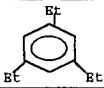
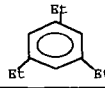
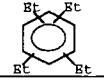
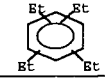


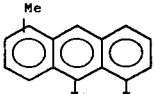
According to the coke formation process on the zeolite catalysts, side reactions exist inevitably to a certain extent in the alkylation of benzene. Some of the by-products may deposit on the catalyst surface as coke precursors, and finally turn to coke. SCFP reaction operation is therefore considered for alkylation of benzene to remove the deposited coke precursors partially and slow down the coking process due to its high molecular diffusivity^[2] (100 times higher than that of liquid phase) and high solubility^[3] (1000 times higher than that of gas phase).

GC-MS (Hitachi M-80, Japan) was applied to determine the existing components in both alkylation products. Besides the main products ethylbenzene (EB) and diethylbenzene (DEB), triethylbenzene (TrEB) and tetraethylbenzene (TeEB) were found in the LP alkylation products. However, in the SCFP alkylation products, in addition to the LP alkylation products, 2-ethylbiphenyl (EBP), 2,2-biethylbiphenyl (BiEBP) and 1,5,6-trimethylanthracene (TMA) were found, as shown in Table 2. Benzene as a solvent was used to dissolve the deposited component on partially deactivated catalyst. Trace amounts of EBP, BiEBP and TMA were also found in the solution to evidence the presence of the precursors. The authors suppose that EBP, BiEBP and TMA may be the coke precursors of the reaction which can be leached out from the catalyst surface under the SCF conditions, while in the LP alkylation the deposited precursors mainly stay on the catalyst surface and thus can not be found in the products.

The authors also suppose that EBP, BiEBP and TMA may be the coke precursors of the reaction that are leached out from the catalyst surface under the SCF alkylation condition, but

not under the LP alkylation condition. The latter allows these aromatics to stay on the catalyst surface where they gradually turn to coke. Similar results are obtained from analysis of the solutions in which components deposited on the partially deactivated catalyst surface are dissolved. More aromatics of the mentioned above were found to exist on the LP used catalyst surface than on the SCFP used catalyst surface. Due to the much higher diffusivity (compared with liquid phase) and solubility (compared with gas phase) of the SCF, the catalyst deactivation can obviously be slowed down.

Table 2. Names, structure and molecular weight for coke precursors

LARGE MOLECULAR FOR LP			LARGE MOLECULAR FOR SCF		
Name	Structure	Molecular Weight	Name	Structure	Molecular Weight
triethylbenzene		162	triethylbenzene		162
tetraethylbenzene		190	tetraethylbenzene		190
			ethylbiphenyl		182
			biethylbiphenyl		210
			trimethylanthracene		218

4. CATALYST TESTS

To obtain the coking mechanism of zeolite catalyst for SCFP alkylation of benzene, two kinds of the zeolite used in LP and SCFP alkylation processes were analyzed by using the conventional catalyst analysis methods. Fresh zeolite is also analyzed for comparison.

4.1. BET test

The total specific surface and pore volume shown in Table 3 are determined (MICROMETERITICS ASAP-2400, USA).

Table 3. The results of BET analysis for fresh and used catalysts

Zeolite	Fresh	SCF used (60 hr)	LP used (14 hr)
Color	White	Gray	Black
Total specific surface(m ² /g)	606.95	328.28	108.22
Volume (ml/g)	0.3597	0.2539	0.1413

Compared with the fresh catalyst, it was found that for the same reaction time, the SCF used catalyst has a less coverage than that of the LP used catalyst.

4.2. X-ray diffraction

X-ray diffraction (RIGAKU D MAX/RB, Japan) is used to test the fresh and two used catalysts. Compared with the fresh catalyst, no obvious crystal structure change of the used catalysts is found.

4.3. Scanning electron microscope observation

The outer surface of the zeolite is observed by using a scanning electron microscope (CAMBRIDGE STEREOSCAN 250 MK3, England). Compared with the fresh catalyst, some foreign matter is found to be covered on zeolite surface in the LP alkylation, but slight coverage is observed in the SCFP alkylation.

4.4. Transmission electron microscope observation

Internal surface of the zeolite is also observed with a transmission electron microscope (JEM-1200, Japan). Similar phenomena to the results of scanning electron microscope are observed: coverage on the LP used catalyst and slight coverage on the SCFP used catalyst.

4.5. Infrared spectrum analysis

In order to observe the difference of functional groups between the LP used and SCFP used catalyst surface, infrared spectrum (FTIR 55XC, USA) is applied. Results show that no obvious change appears.

4.6. Element analysis

Concentrations of carbon and hydrogen on the catalysts (fresh, LP used and SCFP used) surface are measured by using element analysis (Italy). It is found that SCF used catalyst has a lower carbon content than that of the LP used, shown in Table 4.

Table 4. The results of element analysis

Carbon Wt %	Hydrogen Wt %	Remark
0.000	0.000	Fresh catalyst
1.290	0.107	T=532K, P=6.5 MPa only fed benzene for 8 hours.
14.400	0.584	T=532K, P=6.5 MPa only fed ethylene for 10 min.
15.900	0.578	reaction in gas phase for 5 hours. T=735 K, P=1.8 Mpa.
10.370	0.393	reaction in LP for 14 hours.
6.810	0.282	reaction in SCF P for 60 hours.

For a fresh catalyst, no carbon and hydrogen exist on its surface. With benzene as the reactant, hydrogen/carbon (molar) is close to unity. Under the same temperature and pressure, coke formation for the ethylene feeding is serious. With the Y-type zeolite, when the temperature increases in the gas phase alkylation, the coke is easily formed, with its concentration on the catalyst surface also high. The same result also appear for the LP alkylation after 14 hours, while the coke concentration in the SCFP alkylation is low even after 55 hours.

5. CATALYST ACTIVITY TESTS

5.1. Reaction phase

Both LP and SCFP reactions are realized under conditions shown in Table 1. In the LP alkylation, ethylbenzene concentration in the product starts decreasing obviously after 12 hours. However, in the SCFP alkylation, the ethylbenzene concentration remained almost the same for about 55 hours. The activity changes of Y-type zeolite are shown in Figure 2.

This fact shows that coke precursors are removed in the SCFP reaction. So the SCFP operation possess some potential advantage to decrease coke formation and prolong the reactor runtime.

5.2. Reaction temperature

Several operating temperatures above the critical point of the reactant mixture are tested for the SCFP alkylation, shown in Figure 3. Experimental results show that higher temperature speeds up the deactivation. So the reaction temperature should be kept slightly higher than the critical temperature of the reactants mixture.

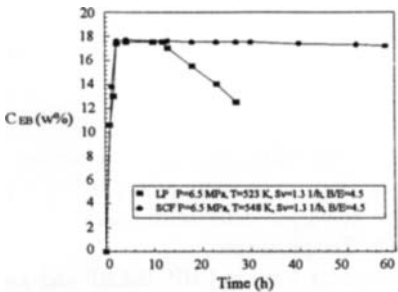


Figure 2. Relation between time and concentration of ethylbenzene

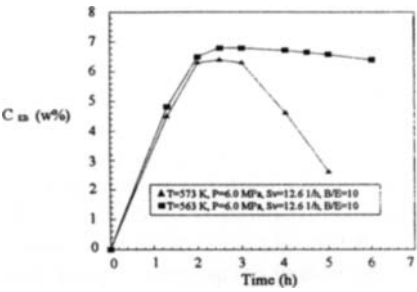


Figure 3. The influence of reaction temperature on catalyst activity

5. 3. Reaction pressure

When the operating pressure is higher than the critical pressure of the reactant mixture, no obvious effect of the reaction pressure on deactivation is observed as shown in Figure 4, though a higher pressure is seemingly harmful, probably because the diffusivity under a high pressure is lower.

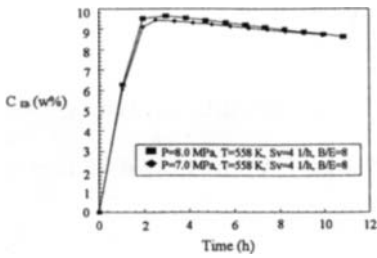


Figure 4. The influence of pressure on catalyst activity

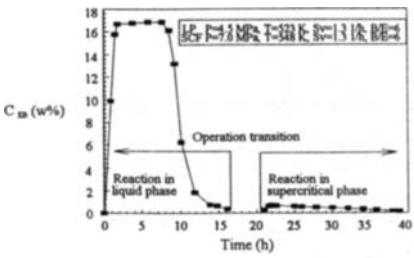


Figure 5. Experimental results of catalyst activity recovery

5. 4. Activity recovery

To explore the activity recovery possibility of deactivated catalyst, or the ability to remove the deposited species, special experiments are carried out, their results are shown in Figure 5, which express that almost no activity recovery can be expected.

6. REACTION SELECTIVITY

As another aspect in the alkylation of benzene with ethylene, side reaction selectivity is also a key problem. In this present case, xylenes are the major by-products of the reaction. The main products ethylbenzene and the by-products xylene are isomers with very close boiling points, which cause great difficulty in separation xylenes from ethylbenzene.

Xylenes might be produced through isomerization of ethylbenzene as follows:



Since the side reaction is a consecutive one, higher diffusivity certainly benefits selectivity of the main product. With the same zeolite also used in LP alkylations, when operated under SCFP reaction conditions, no xylenes are found.

7. CONCLUSION

Based on the above experimental results and analysis, the main conclusions concerning the SCFP alkylation of benzene with ethylene over Y-type zeolite can be summarized as follows:

- (1) SCFP reaction is an efficient method to slow down the catalyst deactivation speed during alkylation of benzene with ethylene over Y-type zeolite;
- (2) Multi-ring components (regarded as coke precursors), such as EBP, BiEBP and TMA, lead to deactivation of the catalyst and finally provoke coke formation;
- (3) SCFP reaction has no activity recovery effect on deactivated catalyst;
- (4) SCFP reaction can decrease the selectivity of the series reaction caused by the by-products xylenes.

ACKNOWLEDGMENT: This work is done under the support of the National Natural Science Foundation of China and the China Petrochemical Corporation (SINOPEC).

REFERENCES

- [1] Wu Zhi-long, Wu Zhi-hua and Huang Li-jun, Ethylene and Industrial Derivatives, Chemical Industry Press, 1980, Part one: 227-230.
- [2] Yong Gao, Yi-feng Shi, Zhong-nan Zhu and Wei-kang Yuan, Journal of East China University of Science and Technology, 1994, 20(4)417.
- [3] Yong Gao, Xiao-meng Zhu, Zhong-nan Zhu and Wei-kang Yuan, Journal of Catalysis (China), 1995, 16(1)44.

Model and Simulation of Supercritical Water Oxidation

G. Petrich, J. Abeln, H. Schmieder

Institut für Technische Chemie, CPV
 Forschungszentrum Karlsruhe, Postfach 3640, D-76021 Karlsruhe, Germany

1. INTRODUCTION

Oxidation in supercritical water (SCWO) to destroy potentially hazardous organic compounds is an emerging technology for which a broad technological knowledge base is not yet available. This gap should be filled as fast as possible if SCWO, in spite of its evident advantages, is to compete successfully against other technologies. Basic research projects in SCWO are time consuming and costly and should therefore be largely supported by the deduction of process parameters from early screening or prototype experiments with the help of computer techniques, such as extensive data logging and numerical simulation and possibly a combination of both.

Experiments in our tubular SCWO reactors are described in [1]. A model for SCWO in a Modular vessel reactor was published recently [2]. This paper will describe our present work on a model for tubular flow SCWO reactors. Some numerical simulation results will demonstrate the use of the model to understand time dependent temperature instabilities. The paper also presents first results to derive process parameters from operational process data.

2. FLOW AND REACTION MODEL

As described in [1] the aqueous feed and the air feed are preheated separately and are mixed in the mixing chamber with the organic feed. The total mixed mass flow $M_{\text{feed}}(t)$ is assumed to constitute one single homogeneous phase even below the critical temperature. Density ρ and specific heat c_p of feed and fluid within the reactor are calculated from tabulated values of the pure phases by smooth cubic interpolation [3]. Non-ideal mixing effects on density and specific heat are neglected.

The temperature profile $T(z,t)$ of the fluid at time t along the location z of the tube is approximated by neglecting radial effects

$$\frac{\partial T}{\partial t} = - \frac{\partial (u \cdot T)}{\partial z} + \frac{\partial^2 (D_T \cdot T)}{\partial z^2} + \frac{H_C \Phi(z,t) + 2k_w (T_w - T) / r}{\rho(z,t) \cdot c_p(z,T)} \quad (1)$$

with the axial velocity $u(z,t) = M_{\text{feed}}(t) / (\pi r^2 \rho(z,t))$. D_T is the eddy thermal conductivity, H_C the heat of combustion, k_w the heat transfer coefficient and r the radius of the tube. T_w is either the temperature of the sand bath or of the wall, if a simultaneous equation for the temperature profile of the reactor tube is included. For the rate $\Phi(z,t)$ of organic oxidation

$$\Phi(z,t) = k_0 \exp(-E_a/(RT))c(z,t)O(z,t) \quad (2)$$

a first order lumped reaction is presently assumed with activation energy E_a and organic concentration $c(z,t)$. To allow for a simple way to simulate low oxidant concentrations $O(z,t)$ in cases where a zero order oxidant reaction is quoted in the literature [4], the factor

$$O(z,t) = O_{\text{feed}} - (\text{stoichiometric oxidant demand}) (c_{\text{feed}} - c(z,t)) \quad (3)$$

is included. It is close to 1 for a large oxidant excess but reduces Φ in the case of oxidant depletion.

The organic concentration $c(z,t)$ is calculated simultaneously from

$$\frac{\partial c}{\partial t} = -\frac{\partial(u \cdot c)}{\partial z} + \frac{\partial^2(D_c \cdot c)}{\partial z^2} - \Phi(c,T) \quad (4)$$

with D_c the eddy diffusivity.

3. INTEGRATION PROCEDURE

The partial differential equations of the previous section are numerically solved. In order to minimize the number of spatial pivots required for a given accuracy, a central differences scheme was chosen. For certain flow problems the results may become unstable and the algorithm then allows for a smooth transition to one-sided differences with the penalty of an increased local error which has to be compensated by a larger number of pivots.

To further increase accuracy without an increase of computer time the mesh density of spatial pivots may vary non-uniformly. This allows a higher mesh density at locations where the spatial gradients are larger. When a parameter estimation procedure is superposed, the mesh points can be chosen at exactly those positions where experimental data (e.g. wall temperatures) are taken.

The boundary conditions of the parabolic differential equations at the feed point $z=0$ and at the exit $z=L$ are of the type

$$[d(D_T T)/dz]_{z=0} = [uT]_{z=0} - [uT]_{\text{feed}} \quad \text{and} \quad [d(D_T T)/dz]_{z=L} = 0 \quad \text{respectively.} \quad (5)$$

Integration of the resulting system of ordinary differential equations is called once for the desired time interval from the interpreter module of our interactive data acquisition and modeling software VISCO [5].

4. PARAMETER ESTIMATION FROM OPERATIONAL DATA

The standard method of least-square fitting the model parameters from experimental data is only applicable if the deviation of estimated parameter-based model results from measured data can be explicitly calculated. To obtain the matrix of model error changes with the individual changes of each parameter for series of time dependent data points as measured in a

dynamic process requires the repeated solution of the model equations given above for each iteration of the estimation procedure. The main problem is to control the error propagation induced by the numerical procedure when approximating the model results for a series of measured data sets at different time intervals. The spatial mesh with pivots at least at the locations of the temperature sensors and a time step control of the integrator to match exactly the times when data are taken avoid additional interpolation errors. A Marquard algorithm is called once for each iteration from the interpreter of VISCO. Any changes in the model, in the selection and weighing of data or the sequence of estimation control are performed interactively by the interpreter.

5. RESULTS AND DISCUSSION

Figure 1 shows an example of the time development of the spatial profiles of Ethanol concentration, temperature and fluid velocity for a 10m reactor tube with $E_a=340$ kJ/mol and $k_0=6.46E21/\text{sec}$ [6]. Heat transfer is kept constant at $4\text{kJ/s/m}^2/\text{K}$. Steady state is reached at about 100sec. The bath temperature of 500°C is too low for complete oxidation under these conditions. Pivot spacing increases with reactor length and the axial mixing coefficients D are $0.5\text{m}^2/\text{sec}$. The fluid velocity is constant beyond $z=2\text{m}$.

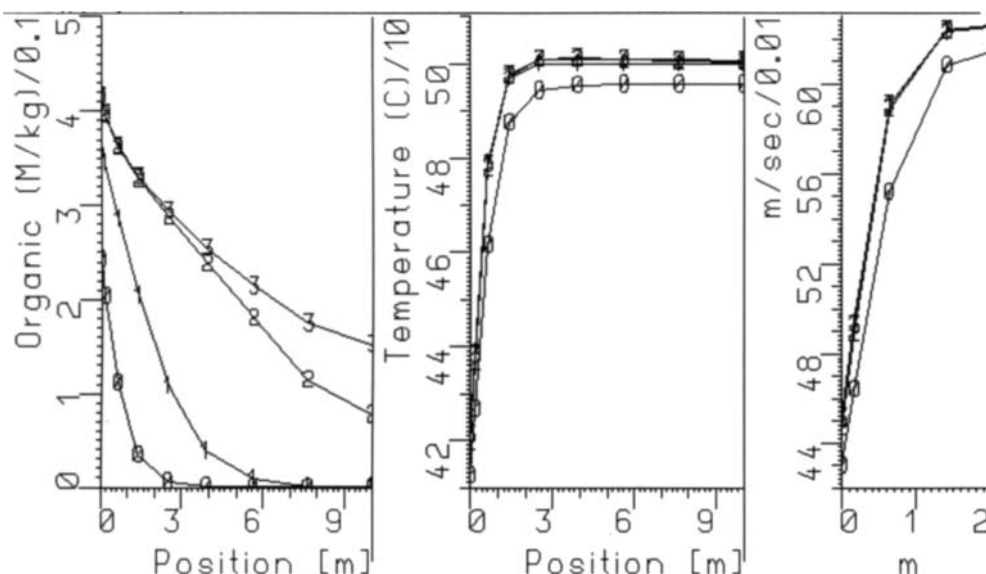


Figure 1. Ethanol concentration (left), temperature (mid) and fluid velocity (right) as functions of reactor position. 0.25 kg/h Ethanol, 10 kg/h water and 10.4 kg/h air enter at 0 m with 300°C , bath temperature $T_w=500^\circ\text{C}$, $r=0.004$ m. Symbols 0 after 1 sec, 1 after 3 sec, 2 after 12sec, 3 after 1000 sec.

The effects of axial mixing and of overall heat transfer are shown in figure 2, where the curves 1 and 2 show the steady state profiles at zero axial mixing, while curves 0 and 3 are calculated with $D=0.5\text{m}^2/\text{s}$. Curves 2 and 3 are calculated from the temperature dependent overall heat transfer coefficients of [4] which are higher than the value of $4\text{kJ/s/m}^2/\text{K}$ used for

curves 0 and 1. It is interesting to note that the higher temperatures of curves 2 and 3 which are calculated with the larger heat transfer coefficients result in a poorer oxidation of Ethanol than curves 0 and 1. This is due to the large increase of fluid velocities with temperature beyond the critical temperature which leads to shorter residence times close to the feed point. Beyond $z=2\text{m}$ temperatures and velocities are almost constant.

The values of axial mixing coefficients D and overall heat transfer coefficients k_w are typical values derived from applying the parameter estimation procedure on operational data of the reactor transient temperatures during start-up and shut-down. Mass flow, composition and temperature of the feed are linearly interpolated in the time intervals between data samples used for estimation. Transient temperatures are measured at 5 locations along the reactor. Convergence of the estimation procedure is fast for the model with one common temperature profile for fluid and tube wall. Preliminary results for D vary in the range of about 0.1 to 2 m^2/s and correspond to Péclet numbers of the order 0.04 to 0.002; Reynolds numbers are between 15000 and 30000. k_w is found in the range 0.5 to about 10 $\text{kJ/s/m}^2/\text{K}$. No systematic evaluation was conducted up to now. In particular, the parameters given above were obtained under the assumption to be constant over temperature ranges of up to 100°C. If the general temperature dependence of $k_w(T)$ is taken from [4], for our particular reactor tube this results in a slightly better least-square deviation with a scale factor of 0.3 and 0.5 compared to the original.

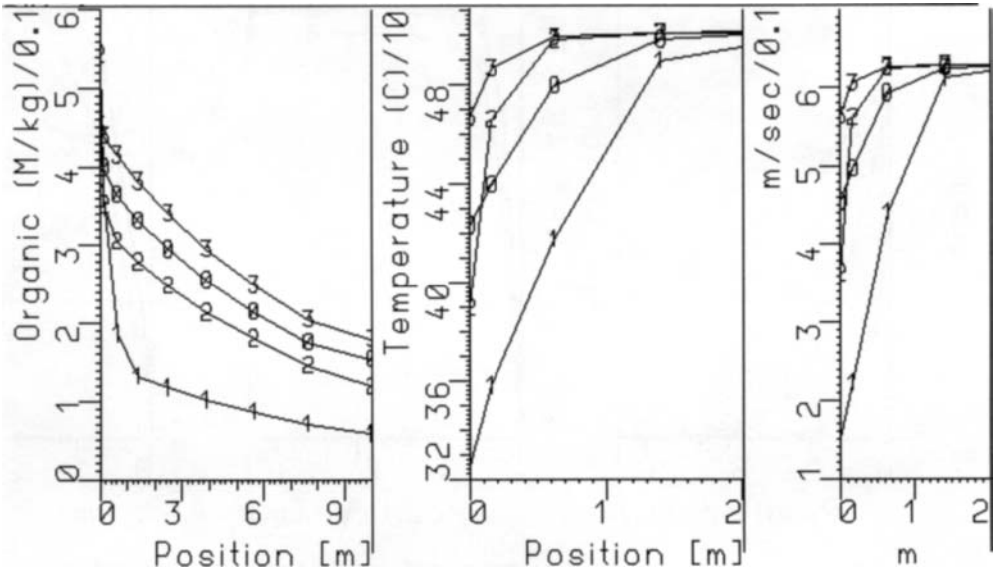


Figure 2. Effect of axial mixing D : symbols 1 and 2 denote $D=0$, symbols 0 and 3 are calculated with $D=0.5\text{m}^2/\text{sec}$. Symbols 0 and 1 at constant $k_w=4\text{kJ/s/m}^2/\text{K}$, symbols 2 and 3 with the temperature dependent heat transfer coefficient of [4]. $T_w=500^\circ\text{C}$.

One objective of this work is to calculate fluid temperatures inaccessible to direct measurement from the model equations by synchronizing the model with the real time process via the measured wall temperatures. For this purpose the individual heat transfer coefficients between fluid and wall k_w and between wall and sand bath k_s have to be determined. First

estimation tests seem to indicate k_w to be about one order of magnitude larger than k_s . At present error control still requires time steps for integration which are too small for practical purposes.

The effect of variations in fluid velocity is one possibility to explain local fluctuations of temperature observed occasionally in our experiments. Figure 3 shows the limiting non steady state profiles of a stationary oscillation with a period of 1.6 sec at $z \approx 6$ m. The oscillation becomes possible when a positive temperature gradient in flow direction meets unreacted organic and if dissipation of reaction heat is insufficient. Then the reaction rate increases and within fractions of a second the local temperature rises which again leads to a higher reaction rate until the organic depletes locally or the local fluid velocity becomes high enough to dissipate the heat. Local temperature then drops again. Without countermeasures the flow will supply fuel again until its concentration is large enough to restart the cycle. If the oscillation occurs close enough to the exit of the reactor large changes of product quality may result.

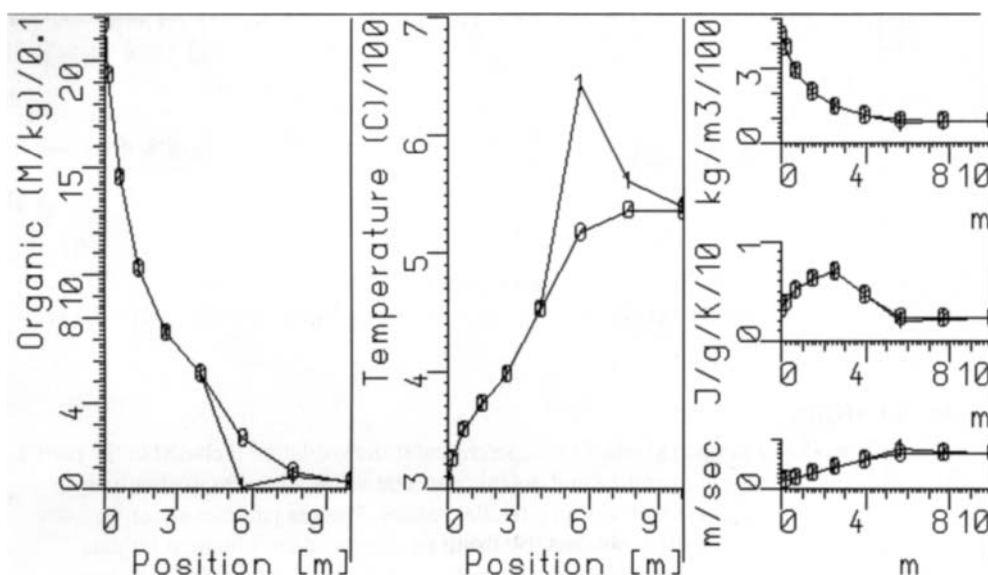


Figure 3. Local temperature oscillations at $T_w=528^\circ\text{C}$ and $k_w=0.75\text{kJ/s/m}^2/\text{K}$. Symbols 0 are the initial profiles and symbols 1 the profiles at the maximum temperature 1.6 sec later.

The range of conditions where local oscillations occur may be rather narrow. While in figure 3 the temperature of the sand bath T_w was kept at 528°C , T_w was set to 534°C in figure 4. The reaction rate is locally increased leading to a higher temperature and finally to a depletion of organics. More heat is generated than can be dissipated with the downstream flow and by transfer to the thermostat and a hot zone starts to travel upstream. Within the frame of this model peak temperature increases while the peak is moving since organic concentrations are higher close to the feed point. In the order of seconds the reaction front moves toward the feed point. Now either the reactor is destroyed or the reaction is quenched by the lower temperature feed flow. This may be a stable situation and the product is fine. Or unreacted fuel is transported downstream again and reaction rates increase when the temperature rises

downstream. Instances of oscillations with a traveling hot spot were observed in the course of the simulations and possibly also in some of our experiments.

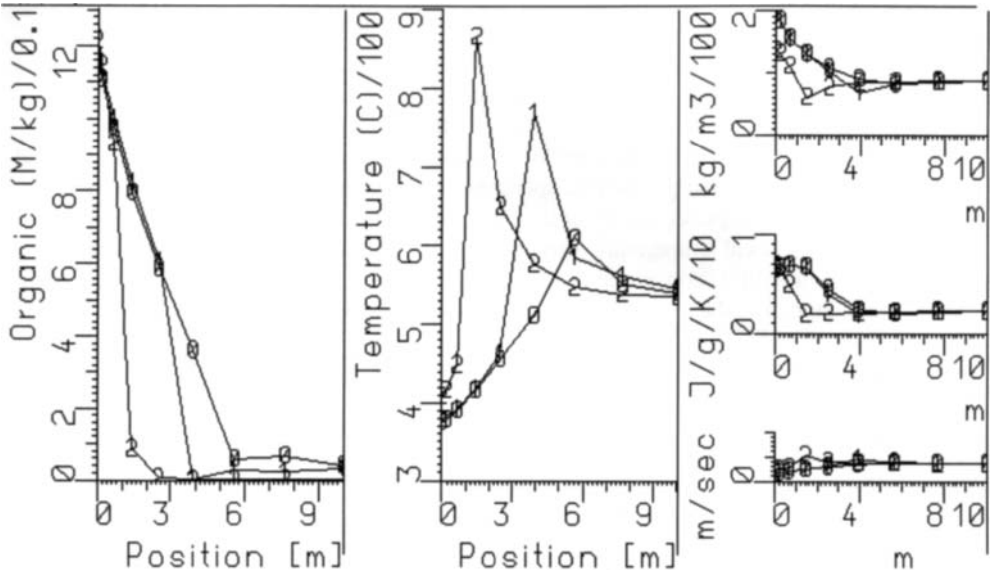


Figure 4. Dynamic profiles of a reaction zone moving upstream at $T_w=534^\circ\text{C}$, $k_w=0.75\text{kJ/s/m}^2/\text{K}$. Symbols 0 are 6.7 sec after start of maloperation, symbols 1 after 7.2 sec and symbols 2 after 14 sec.

CONCLUSIONS

A simple model of lumped kinetics for supercritical water oxidation included in the partial differential equations for temperature and organic concentrations allows to qualitatively simulate the dynamic process behavior in a tubular reactor. Process parameters can be estimated from measured operational data. By using an integrated environment for data acquisition, simulation and parameter estimation it seems possible to perform an online update of the process parameters needed for prediction of process behavior.

REFERENCES

- (1) H. Goldacker et al., this conference
- (2) C.H.Oh, R.J.Kochan, in 'Supercritical Water Oxidation Workshop', Amelia Island 1995
- (3) H.Akima, Journal ACM 17,589 (1970)
- (4) E.F.Gloyne, L. Li, Waste Management 13, 379-394 (1993)
- (5) H.J. Bleyl, in 'Supercritical Water Oxidation Workshop', Amelia Island 1995
- (6) R.K.Helling, J.W.Tester, Envir.Sci.Technol., 22, 1319-1324 (1988)

Degradation Processes In Sub- And Supercritical Water

Th. Hirth, R. Schweppe, S. Jähnke, G. Bunte, N. Eisenreich, H. Krause

Fraunhofer-Institut für Chemische Technologie
Joseph-von-Fraunhoferstr. 7
D-76318 Pfinztal 1 (Berghausen), F.R.G

Keywords: Supercritical Water Oxidation (SCWO), waste disposal, halogenated compounds, flame retardants, printed circuit boards

The synthesis as well as the recycling and disposal of halogenated compounds such as Polyvinylchloride (PVC), flame retardants (for example Tetrabromobisphenol A), γ -Hexachlorocyclohexane (γ -HCH), Hexachlorobenzene (HCB) leads to the formation of byproducts and residues. Polymers, for example, as well as printed circuit boards or shredder residues include problematic substances which, for ecological reasons, cannot be passed on to the environment but have to be supplied to a specific and proper recycling or disposal process. Prior to this background so called "Supercritical Fluids" are of special interest. Supercritical fluids can be used for the synthesis of polymers in an environmentally friendly way as well as for recycling and disposal processes.

1. PRINCIPLE OF SCWO

This paper deals with the degradation of substances like PVC, Tetrabromobisphenol A, γ -HCH and HCB in supercritical water. This process is called "Supercritical Water Oxidation", a process which gained a lot of interest in the past. The difference between subcritical and supercritical processes is easy to recognize in the phase diagram of water. The vapor pressure curve of water terminating at the critical point, i.e. at 374 °C and 221 bar. The relevant critical density is 0.32 g/cm³. This corresponds to approx. 1/3 of the density of normal liquid water. Above the critical point, a compression of water without condensation, i.e. without phase transition is possible. It is within this range that supercritical hydrolysis and oxidation are carried out. The vapor pressure curve is of special importance in subcritical hydrolysis as well as in wet oxidation.

The operating pressure is obtained from the vapor pressure and the partial pressure of the gaseous educts and products. In this process, the temperatures applied are between 150 and 500 °C. In recent times, supercritical fluids have attracted a great deal of attention as potential extraction agents and reaction media in chemical reactions. This has resulted from an unusual combination of thermodynamic properties and transport properties. As a rule supercritical reactions like hydrolysis or oxidation are carried out in water. Above the critical point of water, its properties are very different to those of normal liquid water or atmospheric steam.

The following properties of supercritical water are of special interest:

- Complete miscibility with organic compounds
- Complete miscibility with air or oxygen
- Complete miscibility with gaseous reaction products
- Low solubility of inorganic compounds

A sudden increase in hydrocarbon solubility can be reckoned within the critical temperature and pressure range. Aromatic hydrocarbons dissolve at lower temperatures than aliphatic hydrocarbons.

The solubility of inorganic compounds, such as e.g. salts, decreases in the same way as the solubility of organic compounds in the supercritical state increases. This decrease is combined with the decrease of the dielectric constant of water. The supercritical water oxidation process is described in the following figure.

SUPERCRITICAL WATER OXIDATION

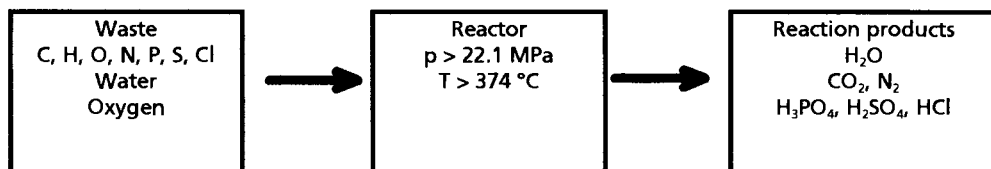


Figure 1: SCWO - Process

Waste characterized by the following elements i.e. carbon, hydrogen, oxygen, nitrogen, phosphorus, sulfur and chlorine would be oxidized in the presence of oxygen and water at temperatures above 374 °C and pressures above 221 bar in a batch-reactor to the following reaction products: water, carbon dioxide, nitrogen, phosphorus acid, sulphuric acid and chlorine acid.

2. EXPERIMENTAL ASSEMBLY

Figure 2 shows the construction of the apparatus for examining hydrolysis and oxidation reactions in sub- and supercritical water. The reaction vessel is made of a high-strength and corrosion-resistant Cr-Ni-Mo-steel. The available interior volume reaches from 0.2 to 2 liters. This autoclave can be used for temperatures up to 600 °C and pressures up to 1000 bar. At the top the reaction vessel is sealed with a conical tightening piston. A rotary permanent magnet unit is supported on axial and radial bearings in a pressure tight housing screwed onto the autoclave lid. An outer unit of the same magnetic material is driven mechanically. The inner magnet unit is connected with the stirrer. The piston is perforated and communicates with the manometer or pressure transducer, the safety valve and the expansion valve. Via the expansion valve the autoclave is connected with the sample removal apparatus. Through another opening thermocouples can be introduced.

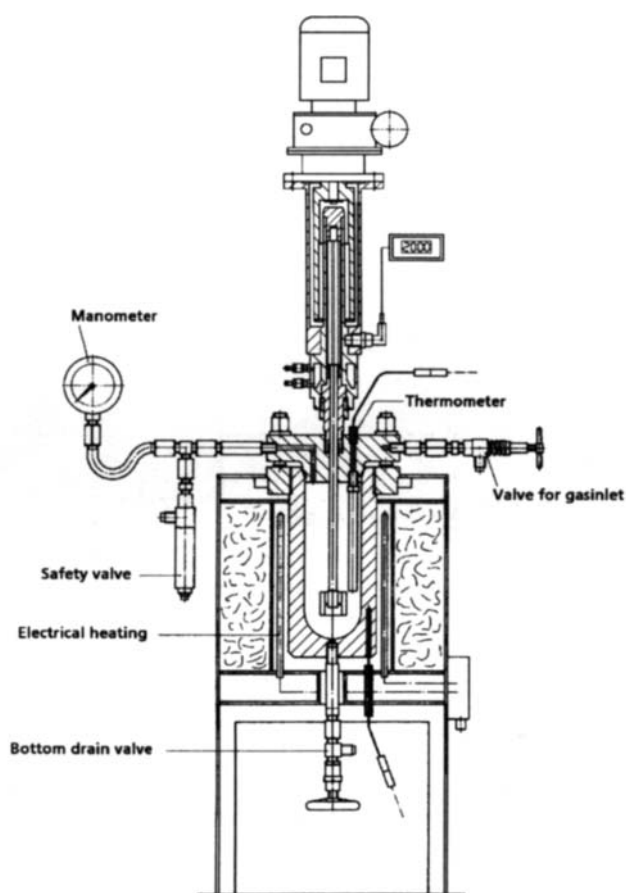


Figure 2: SCWO-Autoclave

3. CHARACTERISATION OF REACTION PRODUCTS

The knowledge of the various reaction products is important for the judgement of the destruction efficiency of the hydrolysis process. Therefore all phases involving the gas phase, the aqueous solution and the solid residue were thoroughly analysed. The following species and values were determined.

Gas phase:

- * H_2 , O_2 , N_2 , CH_4 and CO , CO_2 , C_2H_2/C_2H_4 , C_2H_6 and C_3H_8 : with GC-TCD
- * Br_2 , Cl_2 , HBr and HCl with Draeger® adsorption tubes.

Aqueous solution:

- * Br^- , Cl^- and HCO_3^- anion exchange chromatography with electrical conductivity detector
- * Liquid-liquid-extraction with toluene, GC-MSD-Screening of halogenated components

Solid residue:

- * CH-analysis (Leybold Heraeus)
- * Determination of Br^- and Cl^- -content
- * IR-spectra of KBr-pellets (FT-IR NICOLET 60SX)

4. RESULTS

PVC:

Investigations on the break-down of PVC at 150 °C have shown that less than 1 % of the organically bonded chlorine can be split off the polymer chain. The basic polymer chain is not destroyed in doing this. When alkaline hydrolysis is carried out in the supercritical range, e.g. at 500 °C, we find over 93 % of the organic bonded chlorine in the aqueous phase after the reaction. In this process the principal polymer chain is also decomposed. The main products are hydrogen and carbon dioxide, with methane and C_2 -hydrocarbons occurring as secondary products. By the addition of an oxidizing agent, a complete breakdown to CO_2 and H_2O is possible. Under supercritical water oxidation conditions we found more than 99 % of the organic bonded chlorine in the aqueous phase. A formation of chlorine, hydrogen chloride and dioxines as in thermal decomposition was not observed.

Tetrabromobisphenol A:

First results have shown that flame retardants like Tetrabromobisphenol A break down in supercritical water to form carbon dioxide, hydrogen and inorganic bromide.

At temperatures above 500 °C more than 90 % of the organic bonded bromine was converted into bromide. By adding oxygen complete breakdown to carbon dioxide, bromide and water is possible. Under supercritical water oxidation conditions more than 99 % of the organic bonded bromine was found in the aqueous phase. A formation of bromine, hydrogen bromide and dioxines as in thermal decomposition was not observed.

After treatment of shredded printed circuit boards we received the following results: The brominated epoxy resin has been oxidized to carbon dioxide, water and bromide. Glas fibers and residual metals are not changed through this process. The weight reduction was approx. 50 %.

With these results we are able to adapt the SCWO-process together with industrial partners to printed circuit boards and shredder residues. Our strategy consists in the oxidation of organic components to recover process energy, the recovery of inert components e.g. metals and glass fibers and the recovery of bromine.

γ -HCH, HCB:

The most influential parameter on the reaction products is the reaction temperature. Under subcritical conditions only a hydrolytic separation of 80 % (γ -HCH) respectively 60 % (HCB) of the chlorine atoms was detected. In supercritical water the decomposition of the organic attached chlorine in γ -HCH and HCB into inorganic chloride amounts more than 99 % Cl^- at 500 °C. In parallel there is a considerable decomposition of the hydrocarbon framework mainly to water soluble hydrocarbons and to gaseous products like carbon dioxide. SCWO conditions leads to a completely decomposition of these compounds into environmental friendly reaction products without the formation of Cl_2 , HCl and dioxines.

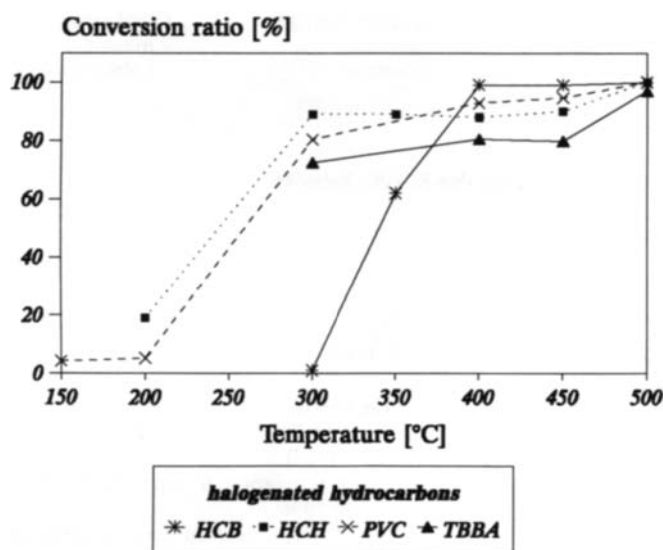


Figure 3: Supercritical Water Oxidation of Halogenated Hydrocarbons

5. CONCLUSIONS

The SCWO-Process in particular demonstrate a number of highly notable advantages. These can be summarized as follows: They are suitable for organic waste materials containing little water and waste waters containing few organic substances.

The reactions take place in a closed system. The organics are oxidized in a controlled but rapid reaction. A single-phase reaction system is involved. Air, oxygen or hydrogen peroxide can be used as oxidizing agents. The reaction times are shorter than those involved in wet oxidation by a magnitude of one. The reaction temperature is lower than that found in incineration. The basic hydrocarbon structure is oxidized to carbon dioxide and water. The carbon dioxide could be used in a different step as a solvent for extraction. Halogens, sulfur and phosphorus are converted to the corresponding mineral acids. Nitrogen is for the most part converted to molecular nitrogen.

The next figure shows some possible application fields for the SCWO-process

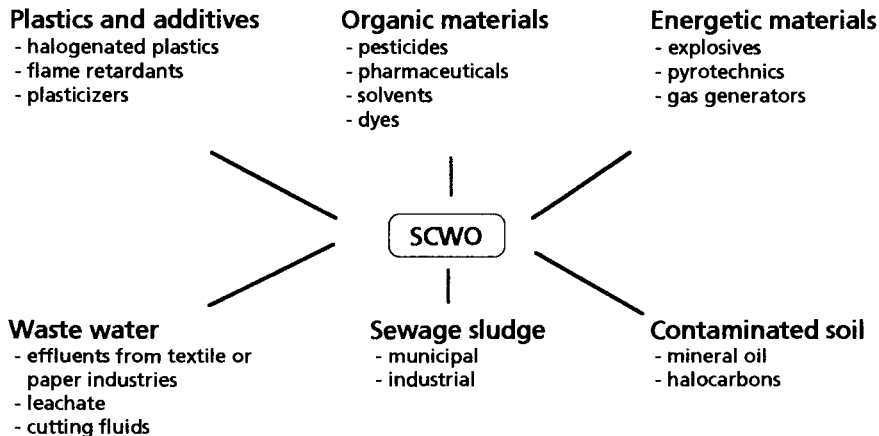


Figure 4: Application Fields for the SCWO-Process

Literature

1. R. W. Shaw, T. B. Brill, A. A. Clifford, C. A. Eckert, E. U. Franck, Chem. Eng. News, Dec. 23 (1991)
2. Th. Hirth, G. Bunte, N. Eisenreich, H. Krause, Elektroschrott, DVM-Tagung, Berlin 1993
3. Th. Hirth, G. Bunte, N. Eisenreich, H. Krause, Abfallwirtschaftssymposium, Berlin 1993
4. Th. Hirth, E. U. Franck, Chem. Ing. Techn. 10, (1994)
5. Th. Hirth, G. Bunte, N. Eisenreich, H. Krause, R. Schweppe, B. Michelfelder, S. Jähnke, DECHEMA-Jahrestagung, Wiesbaden 1995 und 1996
6. Th. Hirth, Hydrolyse und Oxidation von Kunststoffen und Additiven in unter- und überkritischem Wasser ,
in: Hans Sutter: Erfassung und Verwertung von Kunststoff, EF-Verlag,
7. Th. Hirth, Anwendungsperspektiven von Überkritischen Medien, Positionspapier der DECHEMA und des VDI-Technologiezentrum, Frankfurt, 1995

Determination of the Volumetric Gas-Liquid Mass Transfer Coefficients at Pressures up to 5 MPa

M. Bichari, C. Roizard, A. Laurent, N. Midoux

Laboratoire des Sciences du Génie Chimique, CNRS-ENSIC-INPL, 1 rue Grandville, B.P. 451, 54001 NANCY Cedex, France

1. INTRODUCTION

Many processes of gas absorption with chemical reaction are set up at high pressures, result of technical and/or economical requirements. That is, for example, processes of hydrocracking and hydrotreating of heavy oils and processes of oxydation of liquid effluents. However, if many chemical systems are found to determine the mass transfer parameters in an industrial reactor at atmospheric pressure by using the chemical method, they become scarce at elevated pressures. Several physical and chemical methods have been proposed; chemical methods present some severe drawbacks, since one has to replace the gas-liquid system of interest by another one, presenting different physical properties (specially a different coalescence behaviour).

The principle of the physical absorption technique we used, is based on the continuous observation of the absorption kinetics of a solute gas by following the total pressure in the gas phase of a stirred reactor closed to both phases (manometric method). This physical technique was first described by Teramoto et al. [1]; these authors used it to determine the liquid side mass transfer coefficient k_{La} . This technique was then employed with success at high pressures and temperatures by different authors [1-6]. For this reason we have selected this method to determine the liquid side as well as the gas side mass transfer coefficient k_{Ga} .

2. EXPERIMENTAL SET-UP

The experimental set-up [7] is shown in figure 1. The main parts are the reactor and the gas mixing chamber, where temperatures are kept constant at 30°C using two thermostatic bathes. Owing to the selected manometric method, we only need measurements of total pressure versus time and in case of diluted CO₂, of the gas phase composition (gas chromatography). Pressures, gas compositions and temperatures are automatically recorded versus time.

The physical absorption of CO₂ (pure or dilute in N₂) into pure water is experimented; the operating parameters are the total pressure which was varied within the range of 0.5 to 6 MPa, the CO₂ partial pressure from 0.1 to 2.5 MPa and finally the stirring speed from 50 to 150 rpm.

A schematic diagram of the reactor is presented in figure 2. The stirred reactor is closed to both the gas and the liquid phases with a plane interface. The stirring system consists of an impeller in the gas phase, three impellers in the liquid and a special interfacial impeller which increases the liquid side mass transfer coefficient $k_L a$ [7].

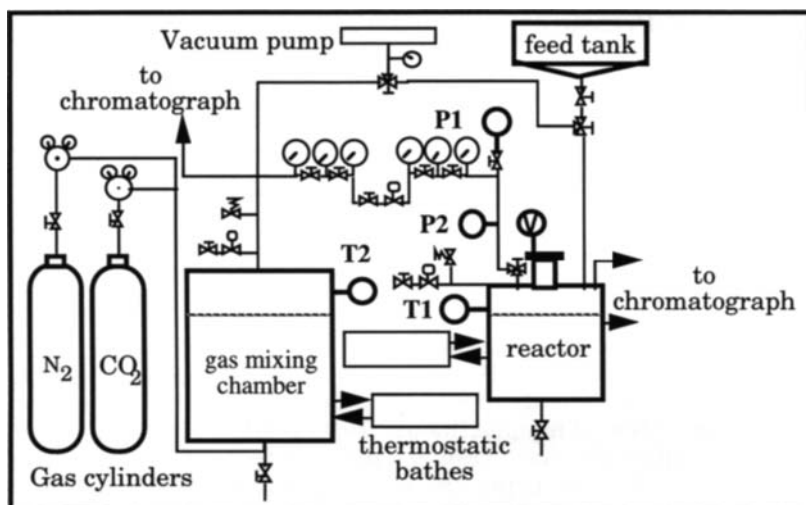


Figure 1. Schematic diagram of the experimental set-up.

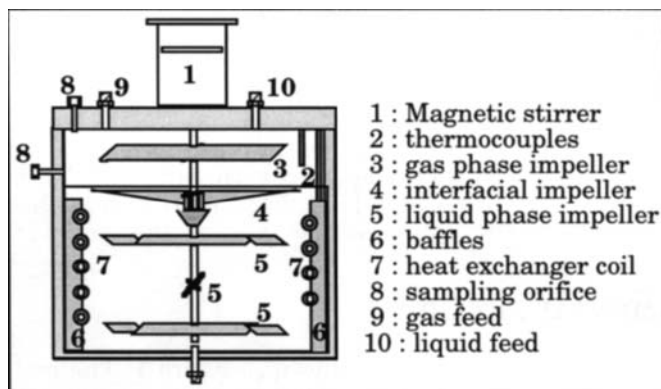


Figure 2. Scheme of the reactor

For purpose of calculations, physical properties of the liquid phase are considered independent of pressure (specific mass, viscosities and diffusivities). Concerning the gas phase, it is clear that these properties are functions of the pressure: compressibility factors and fugacity coefficients are calculated by the

Redlich-Kwong equation of state [8]. Solubilities of carbon dioxide into different liquids were determined experimentally [7], and can be well-represented by the equation of Krishevsky-Ilinskaya [9].

3. LIQUID SIDE MASS TRANSFER COEFFICIENT

3.1 Experimental determination of $k_L a$

Mass transfer coefficients $k_L a$ have been measured by experiments of pure CO_2 absorption into water. The mass balance and the classical expression of the absorption flux lead to the following expression [7]:

$$k_L a = \frac{\Phi}{(C_i - C)} = \left(\frac{1}{(C_i - C)} \right) \left(- \frac{V_G}{RTV_L} \frac{d(P/Z)}{dt} \right)$$

where C is calculated from the mass balance equation (closed reactor) and C_i from the equilibrium relationship.

From the experimental pressure versus time curve, the derivative $\frac{d(P/Z)}{dt}$ is calculated at every time; a plot of the absorption flux Φ versus the concentration difference ($C_i - C$) leads to a straight line whose slope gives directly $k_L a$.

3.2 Influence of the total pressure

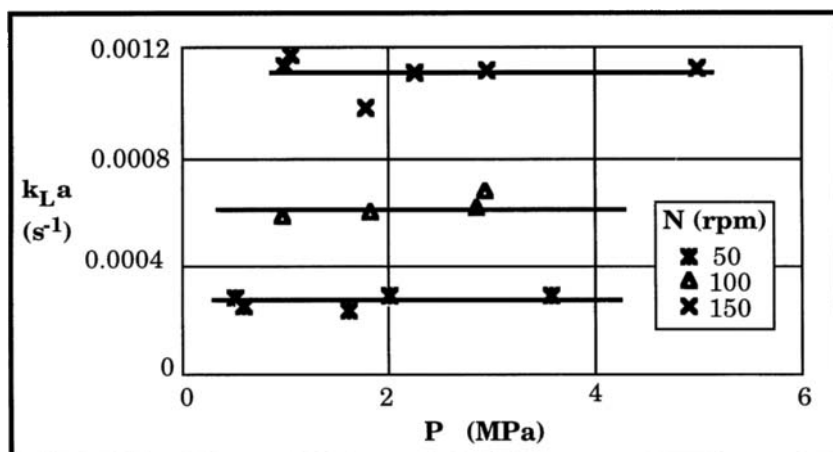


Figure 3. Influence of total pressure on the liquid side mass transfer coefficient.

Experimental values of $k_L a$ are plotted versus the total pressure for three values of the stirring speed (figure 3). It is clear that $k_L a$ is independent of pressure and only depends on the system's hydrodynamics, as it could be expected since pressure has no influence on the liquid properties.

3.3 Influence of the stirring speed

$k_L a$ increases with the stirring speed (figure 4) . It is possible to correlate these results by using a modified Sherwood number Sh_L^* and a liquid Reynolds number Re_L such as:

$$Sh_L^* = \frac{k_L a D^2}{D_L} \text{ and } Re_L = \frac{\rho_L N D^2}{\mu_L}$$

A plot of Sh_L^* versus Re_L in logarithmic coordinates (figure 5) leads to the following correlation:

$$Sh_L^* = 3.84 \cdot 10^{-3} Re_L^{1.33}$$

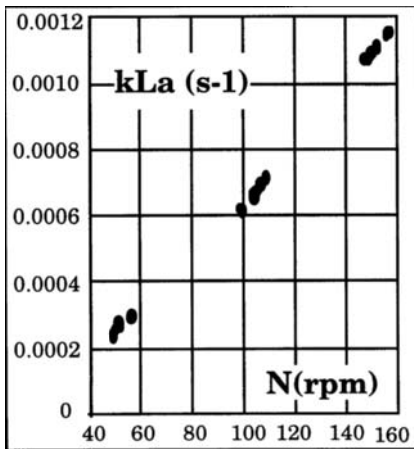


Figure 4. Influence of N

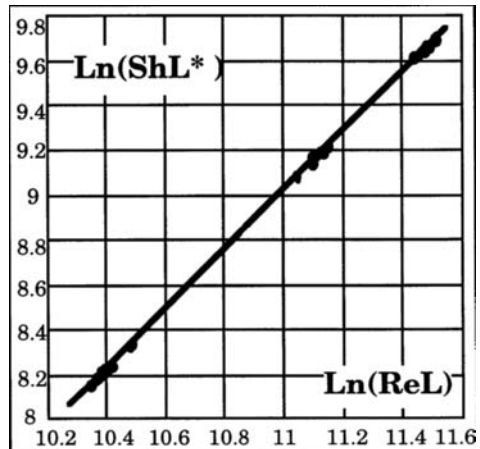


Figure 5. Correlation Sh_L^* vs Re_L

4. GAS SIDE MASS TRANSFER COEFFICIENT

4.1 Experimental determination of $k_G a$

Experiments of physical absorption of CO_2 diluted with N_2 into pure water allow to measure gas side mass transfer coefficients. In this case, we measure the total mass transfer resistance (liquid+gas), using the method for the $k_L a$ determination (& 3.1). Knowing the liquid resistance, we can then calculate the gas side one. The pressure of interest in this case is the partial pressure of CO_2 , which is obtained by simultaneous measurements of total pressure and molar fraction of CO_2 versus time.

4.2 Experimental results and discussion

Experimental values of $k_G a$ are plotted versus the total pressure in figure 6 for three values of N. It appears clearly that $k_G a$ increases with the stirring speed and decreases with the total pressure.

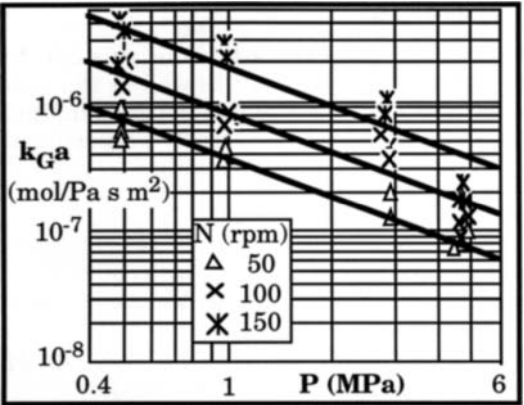


Figure 6. k_{Ga} vs P

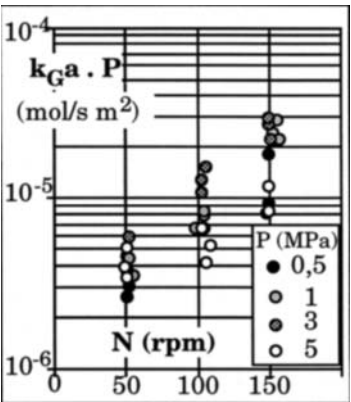


Figure 7. $k_{Ga} \cdot P$ vs N

In figure 6, slopes of the straight lines obtained for the different values of the stirring speed are nearly equal to unity ; in figure 7, the product $k_{Ga} P$ is plotted vs the stirring speed, where scattering of the data is mainly due to the experimental precision. It can be then concluded that k_{Ga} is *inversely proportional to the total pressure*, this is also obtained if we look at the variation of instantaneous k_{Ga} versus pressure during one experiment. This behavior leads to the fact that k_G is directly proportional to the diffusivity coefficient of CO_2 (a being constant, which corresponds to a plane interface), this result is in accordance with the double film theory of Whitman. Versteeg et al. [10] obtained results corresponding to the penetration theory, that is, k_{Ga} proportional to $D_G^{0.5}$. Their experimental system was quite different from ours with a range of pressure within 0,13 to 1 MPa.

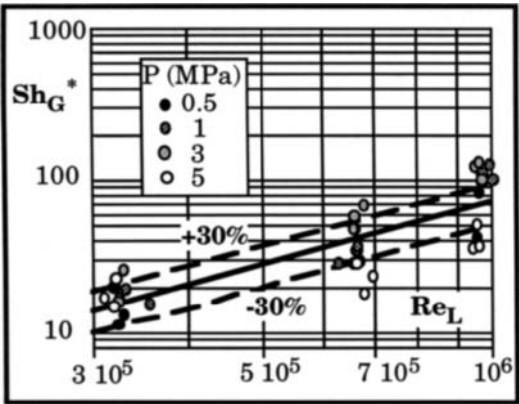


Figure 8. Sh_G^* vs Re_L

From an hydrodynamical point of view, k_{Ga} is related to the liquid motion at the interface; hence, results have been correlated using the liquid Reynolds number Re_L leading to the following correlation with a mean standard deviation of 30% (figure 8):

$$Sh_G^* = 1.43 \cdot 10^{-5} \cdot Re_L^{1.33}$$

$$\text{with } Sh_G^* = \frac{k_{Ga} D^2 R T}{D_G}$$

5. CONCLUSION

The physical absorption technique (manometric method) is suitable to determine the liquid side volumetric mass transfer coefficient as well as the gas-side one. Results show that k_{La} is independent of pressure and depends mainly on the system's hydrodynamics and secondly, that k_{Ga} is inversely proportional to the total pressure and can be related to the liquid Reynolds number.

REFERENCES

1. Teramoto M., Tai S., Nishii, Teranishi H., Chem. Eng. J., 8 (1974) 223
2. Ledakowicz S., Nettelhoff H., Deckwer W. D., Ind.Eng.Chem. Fundam., 23 (1984) 510
3. Albal R. S., Shah Y. T., Schumpe A., Carr N. L., Chem. Eng. J., 27 (1983) 61
4. Karantir B. M., Ph. D. thesis, Univ. of Pittsburg, PA, U.S.A. (1986)
5. Miller S. A., Ekstrom A., Foster N. R., J. Chem. Eng. Data, 35 (1990) 125
6. Richard G., Rice and Eugene L., Benoit L., Chem. Eng. Sci., 41 (1986) 2629
7. Bichari, M., thesis, Institut National Polytechnique de Lorraine, Nancy, France (1995)
8. Reid, R.C. Prausnitz, J.M. Poling, B.E., The properties of gases and liquids, Mac Graw-Hill, New-York (1987)
9. Krichevsky, I.R. Ilinskaya, Acta Physicochimica URSS, 20 (1945) 327
10. Versteeg, G.F. Blauwhoff, P.M.M. Van Swaaij, W.P.M., Chem. Eng. Sci., 42 (1987) 1103

NOMENCLATURE

C	liquid phase concentration of CO ₂ (mol m ⁻³)
D	diameter of the interfacial impeller (m)
<i>D</i>	diffusivity (m ² s ⁻¹)
k_{Ga}	gas side volumetric mass transfer coefficient (mol Pa ⁻¹ m ⁻³ s ⁻¹)
k_{La}	liquid side volumetric mass transfer coefficient (s ⁻¹)
N	stirring speed (s ⁻¹)
P	total pressure (Pa)
R	gas constant (Pa m ³ mol ⁻¹ K ⁻¹)
t	time (s)
T	temperature (K)
V	volume (m ³)
Z	compressibility factor (-)
Φ	absorption flux (mol s ⁻¹ m ⁻³)
ρ	density (kg m ⁻³)
μ	dynamic viscosity (Pa s)

subscripts

G	relative to gas
i	value at the gas-liquid interface
L	relative to liquid

Cloud-Point Curves in Ethylene-Acrylate-Poly(ethylene-co-acrylate) Systems

M. Buback, M. Busch, H. Dietzsch, T. Dröge, K. Lovis

Lehrstuhl für Technische und Makromolekulare Chemie,
Institut für Physikalische Chemie der Georg-August-Universität,
Tammannstraße 6, D-37077 Göttingen

Understanding of phase behavior in ethylene - polar comonomer - copolymer systems within extended ranges of pressure, temperature, copolymer composition, monomer and polymer concentrations, and of polymer size and architecture are of key importance toward modeling and optimizing high-pressure ethylene copolymerizations. Reactions of ethylene with polar monomers, such as acrylic esters, are carried out at conditions similar to those of the ethylene homopolymerization up to about 300 °C and 3000 bar. The phase equilibrium thermodynamics and the copolymerization kinetics need to be simultaneously known for a detailed understanding of these processes within an extended fluid range as monomer conversion, copolymer properties and phase behavior are intimately linked together. Moreover, information about phase behavior is required to design the separation process.

Investigations into the cloud-point behavior of high-pressure ethylene homo- and copolymer systems under conditions close to the ones in technical processes have primarily been performed by the groups of Luft [1,2], McHugh [3,4,5,6], Rätzsch [7,8,9,10] and Radosz [11,12,13]. Within these studies cloud-points are measured in systems prepared from well characterized copolymer material which is dissolved in ethylene (and also in a few other fluids). With the exception of the study by Luft and Subramanian [1] the solvent did not contain the comonomer which makes the situation clearly different from the one in the technical process. Another restriction in the existing phase behavior studies relates to the appreciable time required for dissolving the polymeric material and for heating the system to the experimental pressure and temperature conditions. During this time interval polymerization may occur giving rise to changes in copolymer composition and concentration. If inhibitor is added to prevent polymerization, this component may influence the phase behavior, in particular at higher temperatures where significant amounts of inhibitor are required. To eliminate these problems, a novel experiment has been devised where copolymer is produced in a continuously stirred tank reactor (CSTR1) and the reaction mixture is directly fed into a second autoclave, CSTR2, equipped with a sapphire window for visual observation of the internal volume. Under stationary copolymerization conditions in CSTR1, p and T of the mixture in CSTR2 are varied and the cloud-point p - T -curve is mapped out for a particular reaction mixture produced at constant polymerization conditions (constant p , T , monomer feed and monomer conversion) in CSTR1. The overall assembly is highly flexible as copolymer concentration, polymer size and structure may be systematically changed by varying the reaction conditions in CSTR1. Figure 1 presents a scheme of the experimental setup.

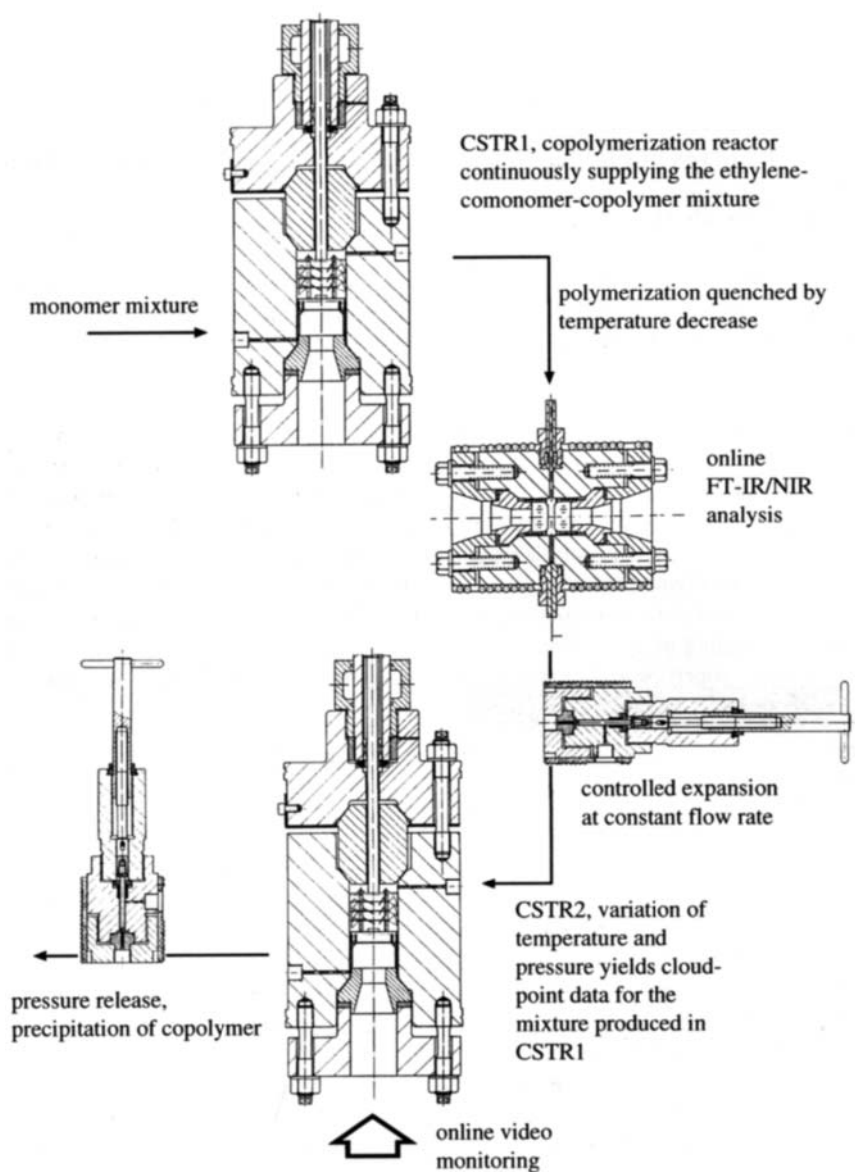


Fig. 1: Schematic view of the experimental setup

The two autoclaves, CSTR1 and CSTR2, each of about 50 cm^3 internal volume are virtually identical. The design of these reactors which may be operated up to 300°C and 3000 bar is presented in more detail elsewhere [14]. Copolymerization within CSTR1 has been carried

out under conditions of „thermal initiation“ that is without using any chemical or photochemical initiator. The advantage of this type of initiation consists in the ease by which polymerization behind CSTR1 may be stopped by reducing the temperature. Via Fourier-Transform infrared/near infrared analysis in a simple transmission type optical high-pressure cell [15] both monomer concentrations and ethylene and acrylate units within the copolymer may be determined under high pressure high temperature conditions. The spectroscopic analysis is used to monitor stationary reaction conditions in CSTR1. Via the special pressure release valves which were constructed and built in the mechanical workshop of the Göttingen institute, pressure may be varied in CSTR1 and CSTR2. Cloud-point data are determined by changing the CSTR2 pressure at constant temperature. To map out one cloud-point curve, this procedure is repeated at several CSTR2 temperatures. During the measurement of one such cloud-point p - T -curve, the copolymerization reactor CSTR1 provides an identical ethylene-comonomer-copolymer mixture.

Figure 2 shows a series of cloud-point curves determined for the system ethylene-2-ethylhexyl acrylate-poly(ethylene-co-2-ethylhexyl acrylate). Each cloud-point curve corresponds to one stationary copolymerization condition in CSTR1. The compositions and concentrations referring to the five monomer-polymer mixtures, including one ethylene homopolymerization reaction (Experiment 1), are listed in Tab. 1. F_A is the concentration of the acrylate units within the copolymer (in mole-%), f_P and f_A denote the concentrations of polymer and of acrylate monomer in the monomer-polymer mixture, respectively. As can be seen from Fig. 1 and from Tab. 1, increasing acrylate content in the copolymer lowers the cloud-point pressure.

N°	F_A / mole-%	f_P / wt%	f_A / wt%
1	0.0	1.0	0.0
2	9.2	1.6	3.3
3	9.2	0.8	3.7
4	17.0	2.6	6.6
5	19.8	4.9	10.0

Tab. 1: Composition and concentration data of the monomer-polymer mixtures of the individual cloud-point curve experiments

Similar observations have been made by Byun et al. [16] on ethylene-poly(ethylene-co-butyl acrylate) systems. It should be noted from Tab. 1 that, in addition to F_A , also f_A changes in a systematic way within the series of cloud-point curves in Fig. 2. In order to allow for an investigation of the individual effects of copolymer composition F_A and of residual monomer content f_A , the experimental set-up in Fig. 1 has been extended to enable the introduction of additional comonomer directly into CSTR2. By this modification, f_A may be independently varied under conditions of F_A being kept constant and being given by the stationary polymerization conditions in CSTR1. Based on the idea of a separation of the (stationary) production of the monomer-comonomer-copolymer mixture from the cloud-point determination in a second autoclave, promising aspects for a study of the individual influences of concentrations and compositions of monomer and copolymer on the cloud-point behavior in ethylene-acrylate systems are foreseen. Measuring and modeling of these individual contributions is underway in our laboratory.

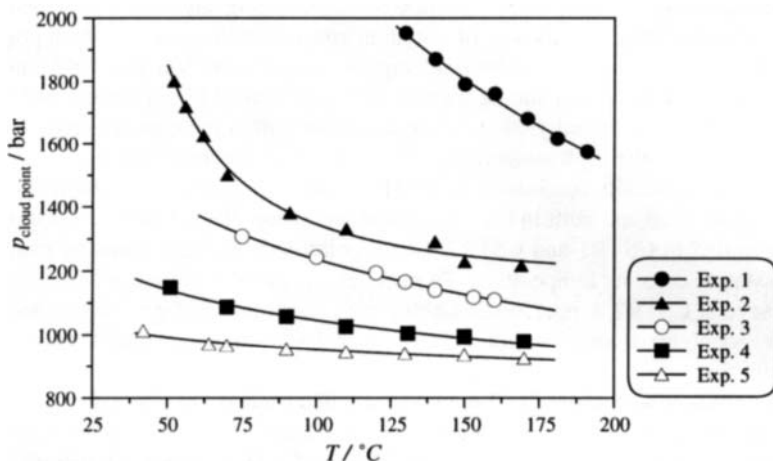


Fig. 2: Cloud-point curves for the system ethylene-2-ethyl-hexyl acrylate-poly(ethylene-co-2-ethylhexyl acrylate). The compositions and concentrations of the individual experiments are listed in Tab. 1.

The authors are grateful to the *Deutsche Forschungsgemeinschaft* for generous support of this study within the Schwerpunkt „Stoffeigenschaften komplexer fluider Gemische“. Valuable discussions with Professor M. McHugh (Baltimore) are gratefully acknowledged.

1. G. Luft, N. S. Subramanian, *Ind. Eng. Chem. Res.* 26 (1987) 750
2. G. Luft, R. W. Wind, *Chem.-Ing.-Tech.* 64 (1992) 1114
3. S.-H. Lee, M. A. LoStracco, B. M. Hasch, M. A. McHugh, *J. Phys. Chem.* 98 (1994) 4055
4. M. A. Meilchen, B. M. Hasch, S.-H. Lee, M. A. McHugh, *Polymer* 33 (1992) 1922
5. M. A. Meilchen, B. M. Hasch, M. A. McHugh, *Macromolecules* 24 (1991) 4874
6. S. H. Lee, M. A. LoStracco, M. A. McHugh, *Macromolecules* 29 (1996) 1349
7. M. T. Rätzsch, P. Wagner, D. Wohlfarth, D. Heise, *Acta Polym.* 33 (1982) 463
8. C. Wohlfarth, P. Wagner, M. T. Rätzsch, S. Westmeier, *Acta Polym.* 33 (1982) 468
9. M. T. Rätzsch, P. Wagner, D. Wohlfarth, D. Heise, *Acta Polym.* 34 (1983) 340
10. Ch. Wohlfarth, P. Wagner, M. Glindemann, M. Völkner, M. T. Rätzsch, *Acta Polym.* 35 (1984) 498
11. C. J. Gregg, F. P. Stein, C. K. Morgan, M. Radosz, *J. Chem. Eng. Data* 39 (1994) 219
12. S. J. Chen, M. Banaszak, M. Radosz, *Macromolecules* 28 (1995) 1812
13. B. Folie, M. Radosz, *Ind. Eng. Chem. Res.* 34 (1995) 1501
14. M. Buback, M. Busch, K. Lovis, F.-O. Mähling, *Chem.-Ing.-Tech.* 67 (1995) 1652
15. M. Buback, H. Lendle, *Z. Naturforsch.*, 34a (1979) 1482
16. H. S. Byun, B. M. Hasch, M. A. McHugh, F. O. Mähling, M. Busch, M. Buback, *Macromolecules* 29 (1996) 1625

Continuous Extraction of Contaminated Soil with Supercritical Water

A. Firus, G. Brunner^a

^a TU Hamburg-Harburg, Thermische Verfahrenstechnik, Eißendorfer Str. 38, 21073 Hamburg, Germany

1. SUMMARY

A new apparatus was built for continuous extraction of contaminated soil with supercritical water ($T_c = 647$ K, $p_c = 22.1$ MPa). Extraction times could be reduced to 28 s at operating conditions of 663 K and 24 MPa (0.5 wt% soil in water).

2. INTRODUCTION

During the last 2 decades supercritical water oxidation has become an established technology and was investigated by several research groups [e.g. 1, 2], but literature data is scarce when solid matter is involved [3].

Supercritical fluids are unique solvents and reaction media due to liquid like density and gas like viscosity. Diffusion is not limited by any interface. Under ambient conditions hydrocarbons and water are nearly immiscible. Phase equilibrium changes significantly in the supercritical region of water ($T_c = 647$ K, $p_c = 22.1$ MPa). Hydrocarbons and supercritical water become miscible at any ratio, whereas supercritical carbon dioxide and hydrocarbons still have a broad miscibility gap [4].

The application of supercritical fluids for decontamination of soil material was often investigated with carbon dioxide ($T_c = 304$ K, $p_c = 7.3$ MPa) as solvent [5]. *Weber* [6] found out, that CO_2 is a weak solvent compared to water if soil material is used, which is weathered for many years. The suitability of supercritical water for decontamination of soil material could be proofed by several semibatch extraction experiments [7]. At operating conditions of 653 K and 25 MPa extraction results of hydrocarbons from soil material are excellent, even if it is weathered for more than 20 years, the content of contamination is high (19 %) and the amount of fine particles (< 63 μm) is large (99 %). Just this kind of soil material, often the uncleaned effluent of a soil washing process, can not be further decontaminated by biological treatment due to the high content of silt and hydrocarbon contamination. It must be incinerated or deposited. With semibatch extraction after 6 h all of the initial contamination could be removed from the soil material. Extraction results are excellent, but extraction times are long. In order to shorten clean-up times the extraction process has to be operated continuously.

3. APPARATUS

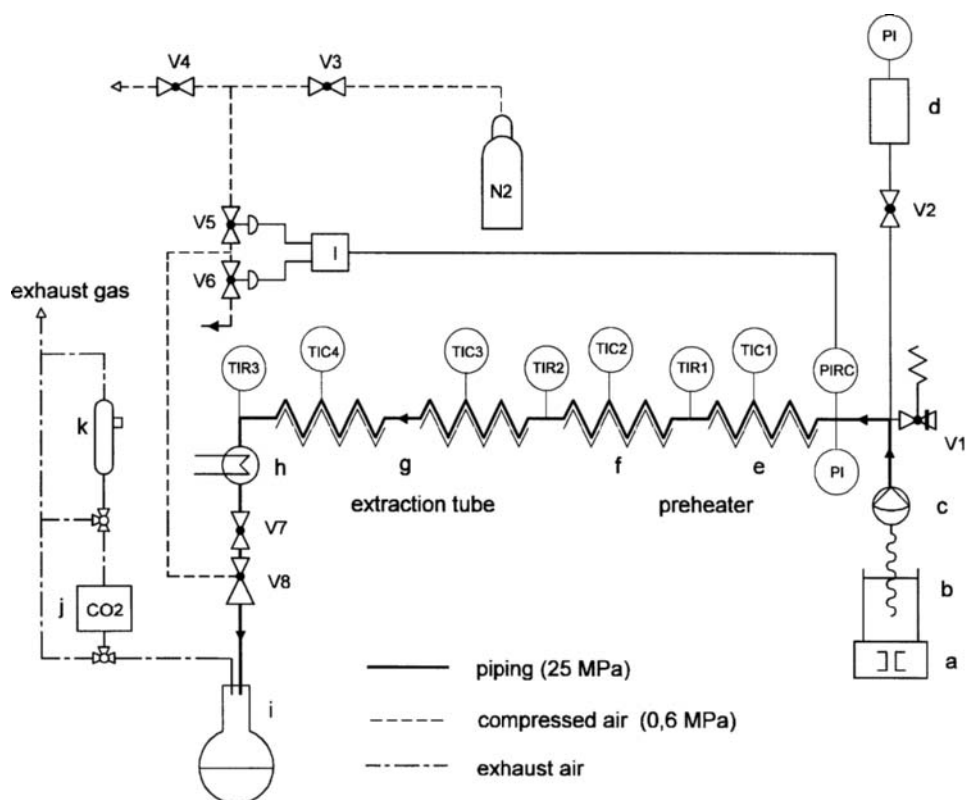


Figure 1: Flow scheme of continuous extraction apparatus: *a* magnetic stirrer, *b* feed vessel, *c* membrane pump, *d* buffer vessel, *e, f* preheater (28 ml), *g* extraction pipe (38 ml), *h* cooler, *i* flask, *j* CO₂-meter, *k* evacuated glass vessel

A new apparatus was built for continuous extraction experiments with contaminated soil material and supercritical water. Figure 1 shows a flow scheme of the apparatus. For homogeneous charge an electromagnetic stirrer (*a*) is placed in the feed vessel (*b*). A static mixer in the vessel prevents the suspension from performing a tornado. Soil in water suspensions (< 10 wt%) are brought into the piping by a conventional membrane pump (*c*). Suction and discharge valve of the pump are operated with two balls each. By means of valve V1 the whole apparatus is protected against excessive pressure (> 35 MPa). For buffering system pressure, a relief holder (*d*) filled with nitrogen, can be attached to the extraction piping by valve V2. After having passed two preheaters (*e, f*) the suspension enters the extraction pipe (*g*, o.d. 0.25 inch, i.d. 0.125 inch, 38 ml) at operating conditions. The extraction tube is heated by 4 heating muffs, which can be regulated separately (TIC1-4). Temperatures at the end of each preheater (TIR1, TIR 2) are recorded as well as the temperature at the beginning (TIR3) and at the end (TIR4) of the extraction course. System pressure can be visually checked by PI1 and is also recorded by a pressure transducer (PIRC). After the extraction

process the suspension is cooled down (*h*). Through a pneumatically operated check valve (V8), which is regulated by a pressure control system (*l*), the suspension is expanded to ambient pressure. For proper operation the ceramic spindle of the check valve requires a pressure of 0.6 MPa (compressed nitrogen). An abrupt opening of the valve prevents the seat from sedimentation. Valves V3 and V4 are used only for starting and stopping operation of check valve V8. Valve V7 serves for slow pressure release at the end of an experiment. Extracted soil material and loaded solvent are separated in a flask (*i*) from the gaseous phase. Subsequently the gaseous phase passes a CO₂-meter (*j*) and an evacuated glass vessel (*k*).

For analysis soil material and the oil-in-water emulsion were separated in a separating funnel by sedimentation. The soil material was analysed for hydrocarbons by supersonic extraction with cyclohexane/acetone (vol 1:1) as solvent. The overall oil content of the loaded water was determined by infrared spectroscopy and single hydrocarbons components in the gaseous phase by gaschromatography. The volumetric content of CO₂ in the gaseous phase was measured on-line by a CO₂-meter.

The soil material used for the experiments was taken from the field of a former paint factory, a clayey loam with an equivalent particle diameter of 10 μm . It was weathered for more than 20 years and contained 19 wt% hydrocarbons (37 % long alkanes, 34 % monoaromatic, 16 % diaromatic, 12 % polyaromatic hydrocarbons). Only the agglomerate fraction (hydrocarbons and sand) smaller than 355 μm was employed. As supercritical solvent demineralized water was used.

With the apparatus described, concentrations of soil material in water up to 10 wt% were investigated for operating conditions of 523-637 K at 24 MPa.

4. RESULTS

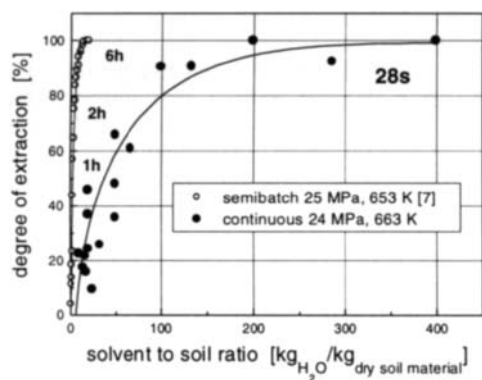


Figure 2: Semibatch and continuous extraction results versus solvent to soil ratio

Figure 2 shows semibatch and continuous extraction results in dependence of solvent to soil ratio. Compared to semibatch extraction, residence times could be reduced remarkably by continuous operation. Extraction results up to 100 % are yielded within a residence time of only 28 s, but high solvent to soil ratios are needed for an acceptable degree of extraction. Only below 0.75 wt% soil in water (above 133 kg_{water}/kg_{soil material}) more than 90 % of contamination could be removed from the soil material (s. Table 1). Due to extraction under parallel flow, solvent to soil ratios must be high for sufficient dilution of contamination in the fluid phase respectively a high concentration gradient.

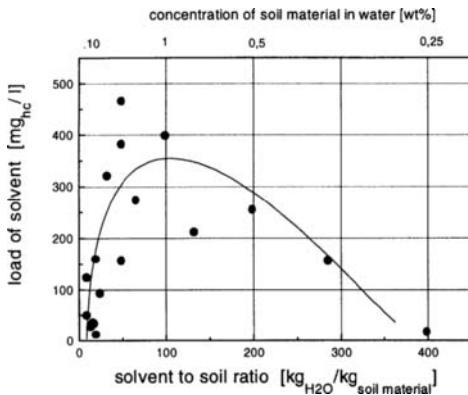


Figure 3: Load of liquid phase versus concentration of soil material in water at 663 K and 24 MPa

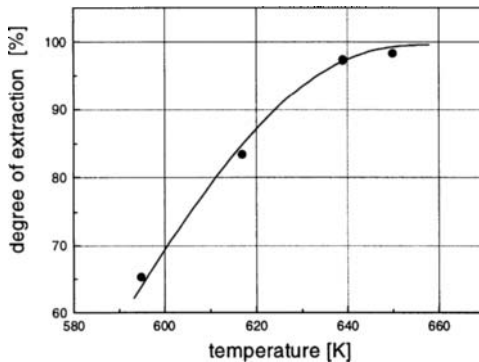


Figure 4: Extraction results versus temperature at 24 MPa, residence time: 45 s (1 wt% soil in water)

At a constant concentration of 1 wt% of soil in water the extraction result could be improved about 8 % by extending the residence time from 28 s to 45 s (s. Table 1, 2).

At low solvent to soil ratios ($< 50 \text{ kg}_{\text{water}}/\text{kg}_{\text{soil material}}$) the degree of extraction is lower than 50 %. Then the soil material must be charged again. Longer residence times (up to 60 s) without regeneration of solvent do not lead to better extraction results. Experiments with a suspension of 2 wt% of soil material showed, that after 3 runs of extraction the clean-up result could be improved up to 94 %. The time of extraction was not longer than 80 s.

Figure 3 shows the load of hydrocarbons in the liquid solvent phase as a function of solvent to soil ratio. From the data one can conclude that there is a maximum of the hydrocarbon load in water versus solvent to soil ratio. The left rising branch of the curve can be explained by the low extraction results shown in Figure 2. At low solvent to soil ratios only a small amount of hydrocarbons are extracted from the soil material. This amount rises with increasing solvent to soil ratio, so does the load in the liquid phase. When extraction results reach a considerable degree ($> 100 \text{ kg}_{\text{water}}/\text{kg}_{\text{soil material}}$), the amount of soil material in water decreases and so does the amount of extractable contamination.

Experiments with different temperatures between 595 K to 660 K (24 MPa) have been carried out at a constant concentration of soil in water of 1 wt % and a residence time of 45 s (s. Table 2). Figure 4 describes an increase in the degree of extraction with increasing temperature. Though the hydrocarbon contamination is already miscible with water at 623 K (25 MPa) [7] best extraction results were obtained at 650 K (24 MPa).

Due to thermal decomposition and hydrolytic reactions carbon dioxide and methane could be determined in the gas phase, particularly above 660 K (24 MPa). The measured amount of CO_2 in the gaseous phase rises linear with increasing solids in suspension.

Table 1

Extraction results of weathered contaminated soil material in water at 663 K at 24 MPa

Solvent to soil ratio	concentration of soil in water	flow rate	T	residence time	degree of extraction	load of liquid phase
$\left[\frac{\text{kg}_{\text{water}}}{\text{kg}_{\text{soil material}}} \right]$	[wt %]	$\left[\frac{\text{l}_{\text{suspension}}}{\text{h}} \right]$	[K]	[s]	$\frac{(c^0 - c)}{c^0} \cdot 100 \%$	$\left[\frac{\text{mg}_{\text{hydrocarbon}}}{\text{l}_{\text{water}}} \right]$
399	0.25	0.98	655	34	100	17
284.7	0.35	0.97	657	30	92.46	157
199	0.5	1.02	658	28	100	254
199	0.5	0.8	669	27	53.7	137
132.3	0.75	0.88	655	38	90.7	211
99	1.0	0.8	660	32	90.5	397
65.7	1.5	0.8	666	28	61.1	273
49	2.0	0.84	663	28	35.8	156
49	2.0	1.0	666	23	65.8	382
49	2.0	0.8	665	28	48.3	465
32	3.0	0.86	661	27	32.3	320
24	4.0	0.86	664	26	18.0	93
19	5.0	0.8	664	31	36.9	-
19	5.0	1.02	662	28	45.9	159
17.2	5.5	0.83	660	31	15.9	33
15.7	6.0	0.86	662	28	21.8	36
15.7	6.0	0.86	658	28	24.3	12
(13.3	7.0	1.13	652	46	17.6	-)
(9	10.0	0.95	648	53	22.6	124)

Table 2

Extraction results of weathered contaminated soil material in water for different temperatures at 24 MPa

T	Solvent to soil ratio	concentration of soil in water	flow rate	residence time	degree of extraction
[K]	$\left[\frac{\text{kg}_{\text{water}}}{\text{kg}_{\text{soil material}}} \right]$	[wt %]	$\left[\frac{\text{l}_{\text{suspension}}}{\text{h}} \right]$	[s]	$\frac{(c^0 - c)}{c^0} \cdot 100 \%$
595	99	1	2.0	47	79.7
617	99	1	1.8	48	83.4
639	99	1	1.6	46	97.3
650	99	1	1.4	43	98.3

* c^0 : initial load of hydrocarbons on soil material, c : current load

5. CONCLUSION

A new apparatus was developed for continuous extraction of contaminated soil material for high pressure (25 MPa) and high temperature (663 K) operating conditions. The extraction of hydrocarbon contaminants from long weathered and highly contaminated soil material could be realised with supercritical water under parallel flow. Within a residence time of only 28 s suspensions of less than 0.75 wt% soil in water could be cleaned ($\geq 90\%$). For a concentration of 1 wt% soil in water 43 s were needed to achieve a clean-up result of 98.3 %. The continuous extraction process can be carried out multistage. Then higher concentrated suspensions (2-4 wt%) can be also cleaned by supercritical water extraction.

ACKNOWLEDGEMENT

This work is gratefully acknowledged by the Deutsche Forschungsgemeinschaft, Sonderforschungsbereich 188.

REFERENCES

1. H.E. Barner, C.Y. Huang, T. Johnson, G. Jacobs, M.A. Martch, W.R. Killilea;
Journal of Hazardous Materials 31 (1992) 1-17
2. D. Kodra, V. Balakotaiah;
Ind. Eng. Chem. Res. 33 (1994) 575-580
3. M. Modell;
Tappi Journal 75 (1992) 195-202
4. A. Kordikowski, G.M. Schneider;
Fluid Phase Equilibria 90 (1993) 142-162
5. S. Michel;
Thesis University of Dortmund (1992)
6. W. Weber;
Diplomwork Technical University of Hamburg-Harburg (1995)
7. K. Nowak;
Thesis TU Hamburg-Harburg (1995)

Supercritical Fluid Extraction of a High-Ash Brazilian Mineral Coal

S.R.P. Rocha^a, J.V. Oliveira^a and S. G. d'Ávila^b

^aDepartment of Chemical Engineering, Federal University of Santa Catarina, 88010-970, Brazil

^bDepartment of Chemical Engineering, UNICAMP, 13081-970, Brazil

ABSTRACT

The effects of extraction temperature, solvent density and addition of cosolvents on the conversion, liquid yield and also on the characteristics of the extracts and residues from SCFE with toluene of a high-ash Brazilian mineral coal were experimentally investigated (Rocha [1]). The experiments were performed in a semi-batch laboratory-scale unit in the coal pyrolysis region - 593 to 673 K and with pressures up to 11.5 MPa. It was observed a reduction in the total sulfur content up to 44%, whereas providing residues with maximum losses of 16% of the original heat-content. The extracts were characterized by a reliable, non-destructive Preparative Liquid Chromatography method - PLC-8 (Karam et al. [2]), providing eight discrete fractions with well defined chemical functionality. With the addition of 5 mol% tetralin 21.7% conversion was obtained, that means an increase of 15% when compared to pure toluene, while with n-methyl-2-pyrrolidone (NMP) and ethanol the conversion decreased.

1. INTRODUCTION

The mineral coal reserves are one of the most important non-renewable energy sources in the world [3]. The same is true when it refers to the Brazilian energy context where they represent 60% of our non-renewable energy sources. The largest reserves are located in South Brazil and, as in other countries with large coal reserves, SCFE is here proposed as an upgrading process for Brazilian mineral coal.

The aim of the present work is to study the effects of extraction temperature, solvent density and addition of cosolvents on the conversion and liquid yield and also on the characteristics of the extracts and residues obtained from SCFE of a high-ash (29.1%) Brazilian mineral coal. For this purpose a Butiá coal, sub-bituminous coal, was employed under different experimental conditions in a semi-batch laboratory-scale unit using toluene as primary solvent, over the range of 593-673 K in temperature and 4.7-11.5 MPa in pressure.

2. EXPERIMENTAL

2.1 Apparatus and Procedure

The experimental apparatus is shown in Figure 1. It consists of a 140 ml extraction vessel with an electrical heater provided with a proportional temperature controller (Coel, GMP) with

a precision of ± 1 K. The pressure is monitored by an absolute pressure transducer (Smar, LD 301) which is equipped with a remote seal for measurements at high temperatures (Smar, SR 201T-211). The pressure data acquisition is made by a portable programmer (Smar, HT 201) and the precision is ± 0.012 MPa.

After the desired extraction temperature is reached about 80 g of sample, with particle size of 16-20 mesh-size, is charged into the extraction vessel, supported by two 260 mesh wire disks. The system is immediately closed and the solvent is continuously fed into the vessel by a high pressure pump (TSP, constaMetric 3200 P/F). The pressure is controlled by a micrometering valve from where the solvent and the extract are withdrawn into a glass collector. The experiments were accomplished in 195 min. (unless otherwise stated), isothermally, at constant pressure and using a solvent flow of approximately $3 \text{ cm}^3/\text{min}$ in all runs.

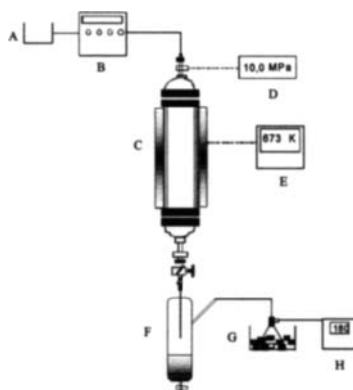


Figure 1. Schematic diagram of the SCFE apparatus

A - solvent reservoir; B - high pressure pump; C - extraction vessel; D - absolute pressure transducer; E - electrical heating with temperature control system; F - glass collector; G - trap; H - flow meter.

The overall conversion of coal to liquid and gaseous products and the liquid yield are defined by:

$$\text{Conversion \%} = 100 \times \left(\frac{\text{wt daf coal} - \text{wt daf residue}}{\text{wt daf coal}} \right), \quad (1)$$

$$\text{Liquid yield \%} = 100 \times \left(\frac{\text{wt extract}}{\text{wt daf coal}} \right), \quad (2)$$

where daf \equiv dry, ash-free.

2.2 Coal characterization

A high-ash sub-bituminous coal, Butiá-Brazil, was used in the experiments, being its proximate and ultimate analysis given in Table 1.

Table 1

Proximate and ultimate analysis of Butiá coal

Proximate analysis (wt %)		
Moisture	4.1	
Ash	29.1 ^{db}	
Volatile matter	29.9 ^{db}	42.2 ^{daf}
Fixed carbon	41.0 ^{db}	57.8 ^{daf}
Ultimate analysis (wt %)		
C ^{daf}	71.0	
H ^{daf}	5.2	
N ^{daf}	1.2	
(S+O) ^{daf,a}	22.6	

^{db} - dry-basis; ^a - calculated by difference

2.3 Extract analysis

The extracts were fractionated by a Preparative Liquid Chromatography method - PLC-8 [2], in eight distinct chemical classes: F1-saturated hydrocarbons (HC), F2-monoaromatics, F3-diaromatics, F4-triaromatics, F5-polynuclear aromatics, F6-resins, F7-asphaltenes and F8-asphaltols. This method, proposed by Karam et al. as an extension of SARA method [4], was especially developed for coal-derived liquids. It combines solubility and chromatographic fractionation, affording discrete, well-defined classes of compounds which are readable for direct chromatographic and spectroscopic analysis.

3. RESULTS AND DISCUSSION

The effects of extraction temperature, solvent density and addition of cosolvents were studied in relation to the conversion and liquid yield and also with regard to the characteristics of the extracts and residues obtained from SCFE of a high-ash Brazilian mineral coal (the proximate and ultimate analyses of the residues and also the ultimate analyses of the extracts are available upon request).

3.1 The effect of temperature

To study the effect of temperature, three temperature levels, ranging in both the coal pyrolysis region and in the vicinity of the critical point of toluene, were chosen: 593 K, 623 K and 673 K. The experiments were run at constant density of 4 mol.l⁻¹ (estimated by the generalized Peng-Robinson equation of state [5]).

It can be observed from Table 2 that very low liquid yields were obtained compared to the results presented in the literature at similar experimental conditions such as in the study of Sakaki et al. [6]. As pointed out by Cahill et al. [7], these low liquid yields might be related to both the high-ash and high oxygen content present in the coal matrix - see Table 1.

In Table 3 is presented the distribution of the PLC-8 fractions from where it can be observed that at 673K the level of thermolysis is superior to the other two temperatures, and hence, the amount of lighter compounds (F1-F5) obtained is about twice higher. The amount of intermediate molecular weight compounds (F6) is almost invariant with temperature while the amount of the heavier fractions (F7-F8) decreases with increasing temperature.

Table 2

Effect of extraction temperature on the liquid yield and on the characteristics of the residues from SCFE of Butiá coal with toluene at 4 mol.l⁻¹

	Coal	Residue		
T (K)	-	593	623	673 ¹
P(MPa)	-	4.7	7.3	11.5
η^2 %	-	3.9	5.5	3.0
HV ³ (KJ.Kg ⁻¹)	24,012	21,874	20,054	21,573
HV maintenance %	-	91	84	90

¹ - 17 min. extraction; ² - liquid yield; ³ - heating value

Table 3

Effect of temperature on the distribution of the fractions of the extracts from SCFE of Butiá coal with toluene at 4 mol.l⁻¹: PLC-8 fractionation

T (K)	593	623	673
P (MPa)	4.7	7.3	11.5
F1 - Saturated HC	1.3	0.8	4.3
F2 - Monoaromatics	1.0	1.0	1.3
F3 - Diaromatics	1.0	0.9	1.8
F4 - Triaromatics	2.6	1.7	5.6
F5 - Polynuclear aromatics	5.9	5.6	10.7
F6 - Resins	64.0	66.6	63.2
F7 - Asphaltenes	11.3	12.0	5.8
F8 - Asphaltols	12.9	11.4	7.3
	11.8	10.0	23.7
	24.2	23.4	13.1

3.2 The effect of density

Table 4 summarizes the results of the liquid yield and conversion from SCFE of Butiá coal with pure toluene at 623 K and at 3, 4 and 5 mol.l⁻¹ solvent density. The liquid yield and conversion figures are again lower than those reported in the literature for different coals. The conversion reached a maximum at 4 mol.l⁻¹; this effect has been shown in the literature [8], though at higher pressures. More investigation is being carried out to clarify this effect. Since the experiments were accomplished at constant temperature - assuring the same depolymerization/thermolysis of the coal structure, the increase in the liquid yield and conversion could be attributed to an enhancement in solvent density (solvent power).

Table 4

Effect of solvent density on the liquid yield, conversion and on the characteristics of the residues from SCFE of Butiá coal with toluene at 623 K

	Coal	Residue		
P(MPa)	-	5.1	7.3	10.9
ρ (mol.l ⁻¹)	-	3	4	5
η %	-	5.1	5.5	6.0
Conversion %	-	14.9	18.8	11.1
HV (KJ.Kg ⁻¹)	24.012	21.179	20.054	22.267
HV maintenance %	-	88	84	93

It can be noticed from Table 5 that the heavy compounds content (F7-F8) increases with increasing density and at 5 mol.l⁻¹ the amount of F7-F8 sharply increases, reaching almost 50% while the F6 (resins) is, for the first time, lower than 60%.

Table 5

Effect of solvent density on the distribution of the fractions of the extracts from SCFE of Butiá coal with toluene at 623 K: PLC-8 fractionation

ρ (mol.l ⁻¹)	3	4	5
P (MPa)	5.8	7.3	10.9
F1 - Saturated HC	1.7	0.8	1.3
F2 - Monoaromatics	1.9	1.0	0.6
F3 - Diaromatics	1.5	0.9	0.5
F4 - Triaromatics	3.7	1.7	1.3
F5 - Polynuclear aromatics	9.8	5.6	6.6
F6 - Resins	65.9	66.6	39.9
F7 - Asphaltenes	4.4	12.0	38.1
F8 - Asphaltols	11.1	11.4	11.7
	18.6	10.0	10.3
	15.5	23.4	49.8

3.3 The effect of cosolvent

One can observe from Table 6 that there was a great reduction in the total sulfur content - up to 44 %, especially with pure toluene and with 5 mol% tetralin. There was also a reduction with addition of NMP and ethanol but in less extent, although it is still high when compared to other coals [9].

In addition to the great sulfur reduction in the coal, as already remarked in previous reports [10], the addition of 5 mol% tetralin caused an increase in conversion - 15% in this work, as can be seen in Table 6, while the presence of ethanol and NMP caused a negative effect in conversion.

Table 6

Effect of addition of 5 mol% cosolvent on the liquid yield, conversion and on the characteristics of the residues from SCFE of Butiá coal at 623 K and 4 mol.l⁻¹, with toluene

Cosolvent	η %	Conversion %	S reduction%	HV maintenance%
-	5.5	18.8	44	84
Ethanol	4.1	9.9	29	94
NMP	-	10.3	41	84
Tetralin	-	21.7	35	95

In Table 7 is presented the effect of addition of 5 mol% ethanol to toluene on the characteristics of the extracts. It can be seen a great increase in the grouped fraction F1-F5 - around 60%, while the resin content was not significantly changed and the asphaltenes-asphaltols distribution decreased dramatically. Since ethanol is a small-chain polar solvent,

these results were expected due to its capacity to solubilize compounds of lower molecular weight and, in a certain extent, fractions with higher polarity.

Table 7

Effect of addition of 5 mol% ethanol on the distribution of the fractions of the extract from SCFE Butiá coal at 623 K and 4 mol.l⁻¹: PLC-8 fractionation

Fraction	Toluene	Toluene with 5 mol% ethanol
F1 - Saturated HC	0.8	1.4
F2 - Monoaromatics	1.0	0.7
F3 - Diaromatics	0.9	0.6
F4 - Triaromatics	1.7	5.5
F5 - Polynuclear aromatics	5.6	8.0
F6 - Resins	66.6	69.6
F7 - Asphaltenes	12.0	10.9
F8 - Asphaltols	11.4	3.3
	23.4	14.2

4. CONCLUSIONS

The maximum conversion obtained was 21.7% with 5 mol% tetralin, and 6.0% liquid yield with pure toluene at 10.9 MPa and 623 K. These figures are rather small when compared to literature data, being necessary to investigate different levels of thermal depolymerization and different solvents to optimize the conversion of the high-ash sub-bituminous Butiá-coal. High levels of sulfur reduction were observed - up to 44%, and it has been also shown that the desulfurization of the coal under study is selective with regard to the solvent mixture.

The PLC-8 fractionation method is shown to be an appropriate procedure for analyzing the effects of temperature, solvent density and addition of cosolvents on the characteristics of the extracts, allowing the maximization of specific chemical fractions.

REFERENCES

1. S.R.P. Rocha, M.Sc. Thesis, Federal University of Santa Catarina, Brazil, (1995) 161p.
2. H.S. Karam; H.M. McNair and F.M. Lanças, LC-GC, 5 (1987) 41.
3. N. Gangoli and G. Thodos, Ind. Eng. Chem. Prod. Res. Dev., 16 (1977) 208.
4. F.M. Lanças; J.H.Y. Vilegas; S. Martins and E.A.F. Gobato, J. of High Resolution Chromatography, 17 (1994) 237.
5. D.Y. Peng and D.B. Robinson, Ind. Eng. Chem. Fundam., 15 (1976) 59.
6. T. Sakaki; M. Shibata; Y. Adachi and H. Hirose, Fuel, 73 (1994) 515.
7. P. Cahill; G. Harrison and G.J. Lawson, Fuel, 68 (1989) 1152.
8. J.R. Kershaw and J. Jezko, Separation Science and Technology, 17 (1982) 151.
9. N.P. Vasilakos; J.M. Dobbs and A.S. Parisi, Ind. Eng. Chem. Process Des. Dev., 64 (1985) 883.
10. M. Canel; K. Hedden and A. Wilhelm, Fuel, 69 (1990) 471.

Interaction of Density, Viscosity and Interfacial Tension in Countercurrent Extraction with Near-Critical Fluids

S. Peter, Institut für Technische Chemie
 Universität Erlangen-Nürnberg, Egerlandstraße 3, D-91058 Erlangen, Germany

The influence of viscosity, interfacial tension and difference of the density between the coexisting phases on hydrodynamics and mass transfer are discussed. When the activity of the near-critical extractant exceeds a certain limit a flowing liquid film becomes unstable. Thereby the alternative exists to carry out a separation process in the film regime or

INTRODUCTION

Systems containing a near-critical or supercritical fluid are characterized by the following behavior: density difference between coexisting phases, viscosity of the liquid and gas phases and interfacial tension change markedly with pressure. The viscosity of the liquid phase is reduced with increasing activity of the near-critical fluid, where that of the gas phase is enhanced. As an example the viscosity of the coexisting liquid phase of the binary system oleic acid/ethane is shown in Figure 1. At greater activities of the dense fluid the interfacial tension decreases dramatically to values less than 2 mN/m. This is shown in Fig.2 by means of the binary system linoleic acid/carbon dioxide.

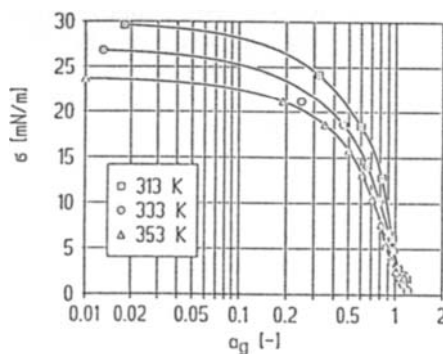
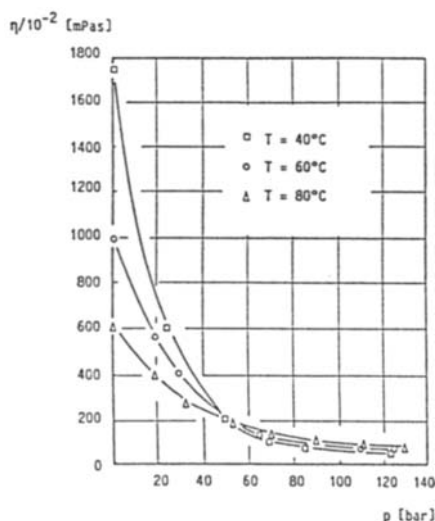


Fig.1: Dynamic viscosity of the liquid phase of the System oleic acid/ethane [1]. Fig.2: Interfacial tension for the system linoleic acid/carbon dioxide [2].

Whereas the density of the gas phase generally increases with increasing pressure the change of the density of the liquid phase with increasing pressure is more differentiated. This is shown in Figure 3 in which the density of the coexisting liquid phase for the systems oleic

acid/carbon dioxide and oleic acid/ethane is plotted as a function of pressure. For comparison the density of pure oleic acid is also figured as function of pressure.

The density of the liquid phase of the system oleic acid/carbon dioxide increases with increasing pressure, whereas the density of the liquid phase of the system oleic acid/ethane decreases with increasing pressure. Therefore the hydrodynamics in a countercurrent column and mass transfer may dramatically depend on the activity of the near-critical fluid.

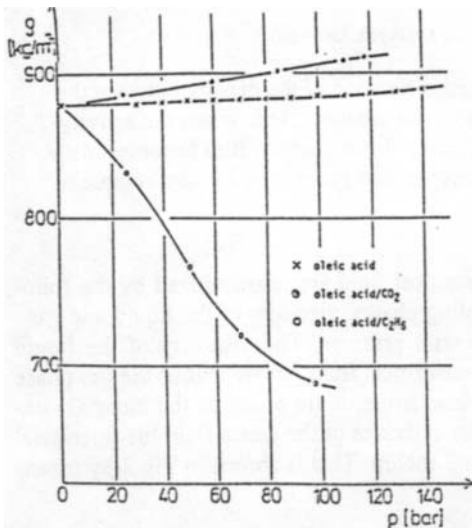


Fig.3: Density of the coexisting liquid phase of the system oleic acid/carbon dioxide, oleic acid/ethane and pure oleic acid as function of pressure [3].

Hydrodynamics of a flowing film

A flowing film was established by means of a plate of 400 mm length and 70 mm breadth which was installed inside of a revolving autoclave. The film thickness at liquid inlet could be varied by means of an adjustable weir. Depending on the inclination angle α of the plate the mean film thickness δ yields

$$\delta = \{(3 \cdot v_l^2) / (g \cdot \sin \alpha)\}^{1/3} \cdot Re_l^{1/3}$$

with $Re_l = V_l / (v_l \cdot U)$; U =film breadth; v_l =liquid kinematic viscosity; V_l =volume flow of liquid

The hydrodynamic behavior of liquid films can be characterized by the dimensionless Weber number $We = (\delta^2 \cdot \rho \cdot g \cdot \sin \alpha) / \sigma$. In Figure 4 the Weber number of a falling film ($\sin \alpha = 1$) is plotted against the activity of ethane for the system oleic acid/ethane. At low temperatures the temperature dependence of the Weber number is small. The Weber number changes little at low activities. For activities greater than 0.8 the Weber number increases sharply. The transition region from the first appearance of instability to disintegration into droplets or trickles corresponds with the sharp increase of the Weber number.

As an example, the first appearance of instability and the disintegration of a falling film of oleic acid as function of pressure and temperature in equilibrium with carbon dioxide and ethane is shown in Figure 5. In the presence of ethane instability and disintegration occur at lower pressure than in the presence of carbon dioxide.

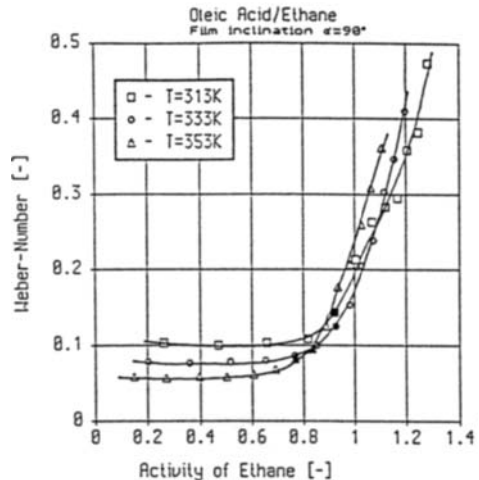


Fig.4: Weber number of a falling film for the system oleic acid/ethane as a function of ethane activity [4].

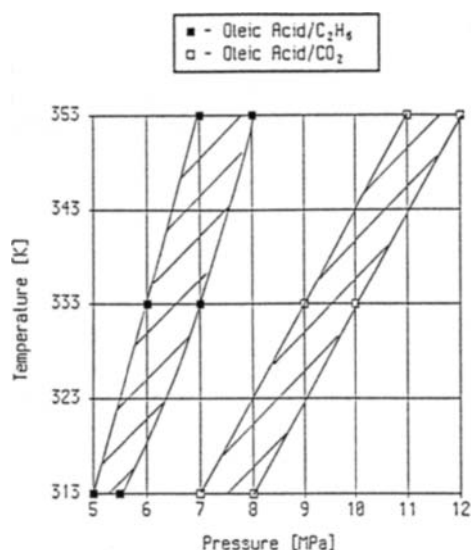


Fig.5: First appearance of instability and disintegration of a falling film for the systems oleic acid/carbon dioxide and oleic acid/ethane [5].

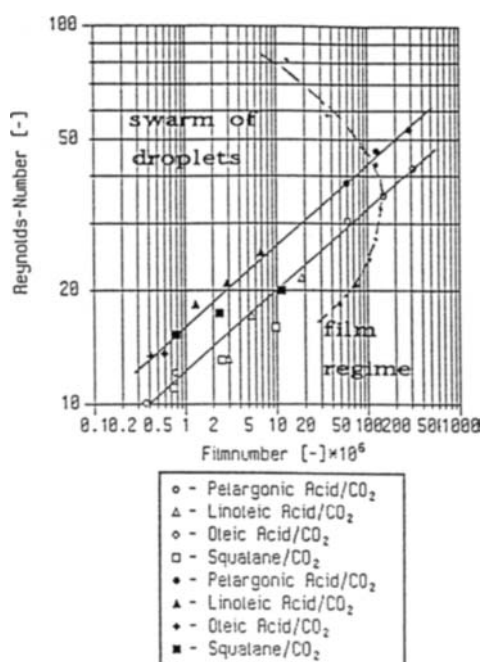


Fig.6: Logarithm of Reynolds number versus logarithm of Film number at first appearance of instability (light points) and film disintegration (full points) of several binary systems.

A linear function between the logarithm of the Reynolds number and the logarithm of the film number (reciprocal Kapitza number) at the first appearance of instability of a flowing film was found by Graef [6]. Thereby the film number is defined by the following equation

$$K_f = (\rho \cdot \sigma^3) / (g \cdot \eta^4)$$

with K_f = Film number; ρ_f = liquid density; σ = interfacial tension; g = earth acceleration; η = dynamic liquid viscosity

A double logarithmic plot of the Reynolds number against the Film number at the beginning of instability and at the disintegration into droplets of several systems with carbon dioxide as near-critical component is shown in Figure 6. Within experimental error the measured values of the investigated systems fall on a straight line. The obtained straight lines for first appearance of instability and for disintegration into droplets extent parallel to each other. Since film instability and film disintegration are visually observed the accuracy of the data is limited.

When pressure is enhanced at constant mass flow and constant temperature, the viscosity of the liquid phase and the interfacial tension decrease. Therefore Reynolds number and Film number increase until first appearance of film instability. This is shown in Figure 6 by means of the system pelargonic acid/carbon dioxide at 333 K. With further increase of pressure at constant mass flow the Film number decreases, whereas the Reynolds number increases. At constant temperature and constant mass flow the Film number and also the Reynolds number depend on pressure and vary in a large range. This is a unique feature of near-critical extraction.

When temperature and pressure are given, the Reynolds number can be enhanced by increasing the flux of the liquid phase at constant Film number. In this way the droplet regime can be adjusted by increasing the flux provided that the flooding point is above the line of film disintegration. In the droplet regime the volumetric mass transfer coefficient $A\beta$ (A =volumetric area for mass transfer; β =mass transfer coefficient) may be greater than in the film regime. In this case, near-critical countercurrent extraction in the droplet regime is recommendable. In the droplet regime the volumetric mass transfer coefficient $A\beta$ (A = volumetric area for mass transfer; β = mass transfer coefficient) may be greater than in the film regime. In this case, near-critical countercurrent extraction in the droplet regime is recommendable.

Axial dispersion and column efficiency

In order to obtain a commercial loading of the near-critical extractant, the extraction is sometimes carried out at enhanced pressures in the droplet regime. In such cases the liquid phase does not flow downwards as a film adhering to the packings of a column as is usually assumed, rather it falls down as a swarm of droplets. On the basis of the separation of a mixture of partial glycerides the behavior of packed columns in the droplet regime (unstable flowing films) the efficiency of different column installations are compared. A mixture of 55 wt.% propane and 45 wt.% carbon dioxide is used as an extractant.

The phase equilibria of the quasi-ternary system carbon dioxide/propane/glycerides mixture at 12 MPa and 313 K is shown in Figure 7 for several monoglyceride contents of the glycerides mixture. With increasing monoglyceride content the two phase region of the system is enlarged.

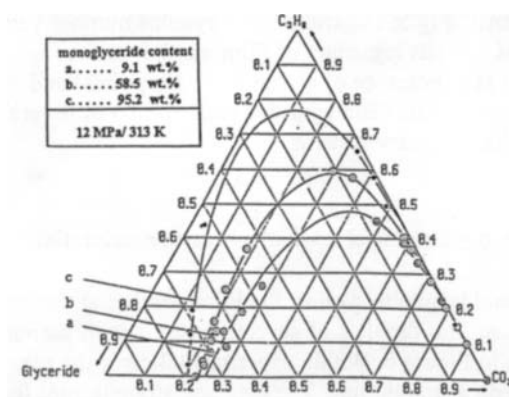


Fig.7: Phase equilibria of the quasi-ternary system carbon dioxide/propane/glycerides mixture at 12 MPa and 313 K

A schematic flow sheet of the pilot plant used for the investigations is shown in Figure 8. The device comprises a counter-current extraction column and a column for the regeneration of the extractant.

The internal diameter of the columns is 69 mm. The extraction column is made of two parts of 1000 mm length. It is designed for a pressure of 15 MPa at 453 K.

The efficiency of the following packings are investigated and compared with each other: Sulzer CY, Sulzer CY + distributors, Sulzer SMV + distributors, collector-distributors,

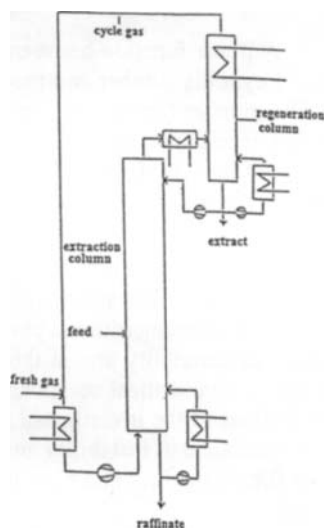


Fig.8: Schematic flow sheet of the pilot plant [8].

and spray column. The height of the packings totaled to ca. 1.9 - 2.0 m in each case. The packings type Sulzer CY and Sulzer SMV are arranged so that successive elements are twisted by 90° in order to ensure a consistently good distribution of the liquid phase over the cross section of the column. The installation of collector-distributor elements serve for reducing the wall effect of flow.

The primary products are fed at the top of the extraction column. The composition of feed, extract, raffinate, and extractant is analysed in dependence on superficial velocity of the gaseous (continuous) phase. In two series of experiments either the phase ratio or the spraying density are kept constant. The stage construction is made by means of a computer program.

The monoglycerides of the raffinate (the bottom product) is shown in Figure 9 as a function of the superficial velocity of the gas phase at a phase ratio of 19. At an superficial velocity of 10 mm/s the raffinate obtained with different packings is nearly the same except for the Sulzer Packing SMV. At lower superficial velocities the wire mesh packings (Sulzer CY) provide the best yields. The experiments are made at conditions where a falling film disintegrates into drops. Therefore, it seems understandable that the efficiency of the spray column and that of the collector-distributor installations do not much differ.

The monoglyceride content of the raffinate is shown in Figure 10 as a function of the superficial gas velocity at a constant spraying density of $450 \text{ kg m}^{-2}\text{h}^{-1}$.

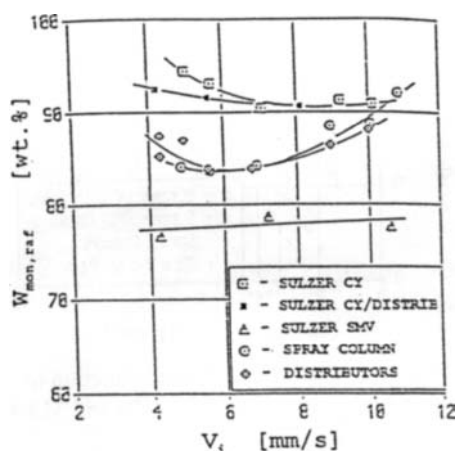


Fig.9: Monoglyceride content of the raffinate as a function of superficial gas velocity at a constant phase ratio of 19 at 12 MPa and 313 K [8].

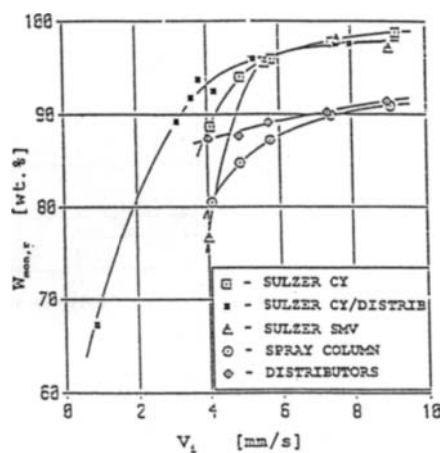


Fig.10: Monoglyceride content of the raffinate as a function of superficial gas velocity at 12 MPa and 313 K for constant spray density of $450 \text{ kg m}^{-2}\text{h}^{-1}$ [8].

For further information of the hydrodynamic conditions in a countercurrent column working in the droplet regime, the axial dispersion was investigated. By means of oleic acid monoglyceride in form of a single phase mixture with propane as a tracer the behavior of residence time is investigated at 12 MPa and 313 K and with pure propane as circulating extracting agent. The tracer is injected at different height of the column. The detection of the tracer is carried out by an UV-detector LC-95 of Perkin Elmer.

In several tests series the point of tracer feeding and the column installations are changed and the axial dispersion coefficient is measured as a function of superficial gas velocity. The radial rate profiles are neglected. In a first approximation propane is taken incompressible as the pressure loss is neglectable compared to the operating pressure of 12 MPa.

In Figure 11 the Bodenstein-number is plotted versus superficial gas velocity at different distances between tracer input and detection. The effects of efflux at the top of the column cause the sharp bend at about 5 mm/s of superficial gas velocity. The Reynolds number at this point amounts to about 2000. The Bodenstein number is defined as:

$$Bo = (U \cdot L) / D_{ax}$$

with U = superficial gas velocity; L = height of packings; D_{ax} = axial dispersion coefficient. At low values of the superficial gas velocity the Bodenstein number increases linearly and develops into a plateau at high values.

The axial dispersion of the different column installations investigated are compared in Figure 12. The wire mesh packing Type Sulzer CY with distributors has the highest Bodenstein number (i.e. the lowest axial dispersion) within the interfacial gas velocities investigated. The axial dispersion increases in the sequence: wire mesh packing Sulzer type CY, collector-distributor, mixing packing Sulzer type SMV, spray column.

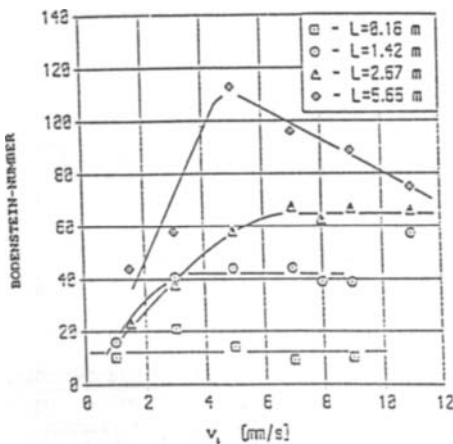


Fig.11: Bodenstein number (semi open system) as a function of superficial gas velocity at different distances between tracer input and detection [8].

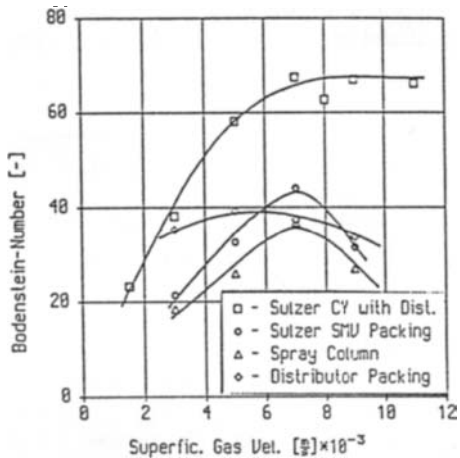


Fig.12: Bodenstein number as a function of superficial gas velocity at 12 MPa and 313 K.

The number of theoretical stages per meter of height of packings is plotted versus the Bodenstein number in Figure 13 for the different installations investigated. at a phase ratio $\phi = 19$. There, the theoretical stages match the separation of oleic acid monoglycerides from the mixture with di-, triglycerides, and free fatty acids at 12 MPa and 313 K. Within the accuracy of measurement the data all fall on the same curve. It was observed that the liquid phase flowing downwards in the column was disintegrated into drops under the process conditions. The differences in the efficiency of the packings are mainly caused by axial dispersion due to microturbulences of the continuous phase.

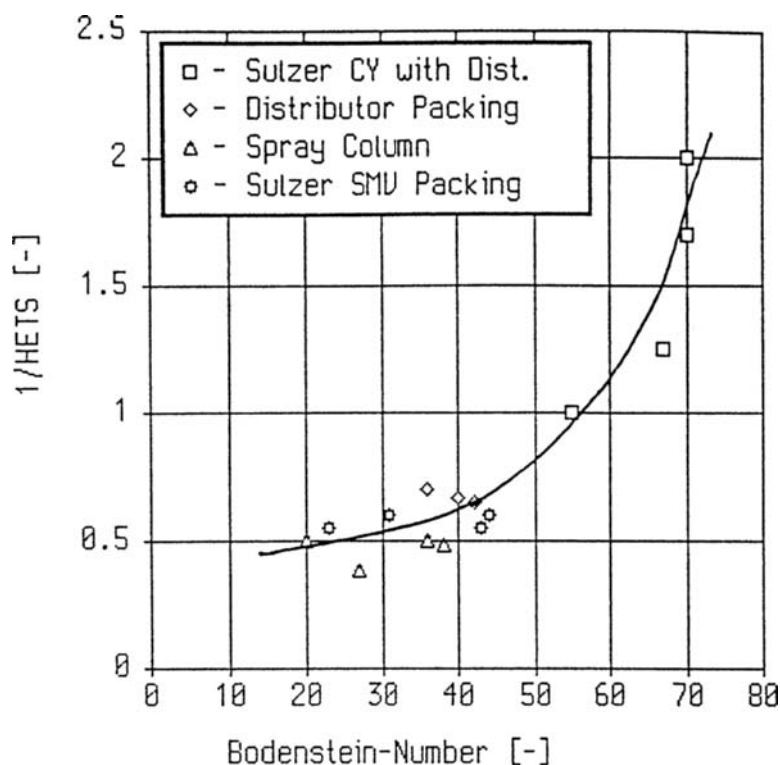


Fig.13: Theoretical stages per meter packings as a function of the Bodenstein number for near-critical extraction of monoglycerides from a mixture of mono-, di-, and triglycerides at 12 MPa and 313 K in the droplet regime.

Conclusion

As the interfacial tension and the viscosity are markedly decreased in systems containing a dense near-critical substance the stability of liquid films may be reduced in case of near-critical fluid extraction. Therefore, axial dispersion should be an essential argument in making the choice of suitable packings. On the whole a suitable packing for a countercurrent process should fulfill the following requirements: greatest possible surface, low pressure loss, and low axial dispersion. The latter should not be neglected as is often done.

References

- [1] Peter, S., Jakob, H., J. Supercritical Fluids **4**, 116-172 (1991).
- [2] Hiller, N., Schiemann, H., Weidner, E., Peter, S., Chem.Eng.Techn. **16**, 206-212, (1993); Schiemann, H., Weidner, E., Peter, S., J.Supercritical Fluids, **6**, 181-189, (1993).
- [3] Jakob, H., Ph.D. Thesis Erlangen, 1990.
- [4] Blaha-Schnabel, A., Ph.D. Thesis, Erlangen 1992.
- [5] Beyer, A., Ph.D. Thesis, Erlangen 1990.
- [6] Blaha-Schnabel, A., Beyer, A., Czech, B., Schiemann, H., Weidner, E., Peter, S., Chem.Eng.Comm. 1996 in Press.
- [7] Czech, B., Peter, S., Preprint AIChE Annual Meeting, Miami Beach 11.-18- Nov. 1995.
- [8] Czech, B., Ph.D. Thesis, Erlangen 1991.

This page intentionally left blank

The Heat Transfer to Supercritical Carbon Dioxide in Tubes with Mixed Convection

T. Walisch, M. Müller*, W. Dörfler and Ch. Trepp

Institute of Process Engineering and Cryogenics, Swiss Federal Institute of Technology,
ETH Zentrum, CH-8092 Zurich, Switzerland

1. SUMMARY

The heat transfer to supercritical carbon dioxide was measured in horizontal, vertical and inclined tubes at constant wall temperature for turbulent flow at Re-numbers between 2300 and 1×10^5 . The influence of the variation of physical properties due to the vicinity of the critical point was examined, as well as the influence of the direction of flow. Therefore most of the measurements were conducted at pseudocritical points. At those supercritical points the behaviour of the physical properties is similar to the behaviour at the critical point, but to a lesser degree. At such points the heat capacity shows a maximum; density, viscosity and heat conductivity are changing very fast. [1]

Due to the variations in physical properties, especially under the influence of buoyancy, the heat transfer can be significantly altered compared to the well-known conditions at buoyancy-free turbulent flow. [2]

At the pseudocritical points that are nearest the critical point, this behaviour is most accentuated.

2. EXPERIMENTAL

2.1. Apparatus

A schematic representation of the experimental apparatus is shown in Figure 1.

The carbon dioxide is circulated in a closed system which has been designed for pressures from 1 to 500 bar and temperatures from 30 to 180°C. The test section is heated with a thermosyphon. Temperatures of the carbon dioxide are measured only at the inlet and outlet of the test section. The wall temperatures of the carbon dioxide leading tube within the heatpipe are measured for controlling purposes.

* Ciba Geigy AG, Ingenieur-und Verfahrenstechnik, CH-4133 Pratteln 1, Switzerland

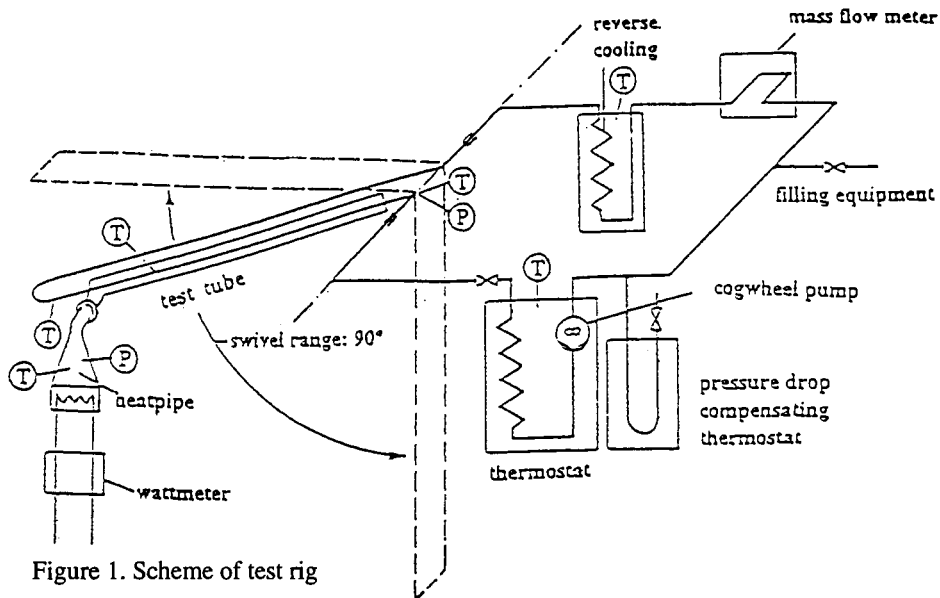


Figure 1. Scheme of test rig

Flow in horizontal tubes as well as inclined tubes can be studied at Pr-numbers from 0.8 to 22, Re-numbers up to 1.5×10^5 and Gr-number up to 8×10^8 .

In order to measure the carbon dioxide inlet and outlet temperatures, those thermocouples have been preceded by static mixing elements. To be certain to have a fully developed hydrodynamic profile at the entrance of the heating section, an entering section of 200 mm ($=20x_{d_i}$) has been placed between the inlet and outlet thermocouples and the heating section. [3]

The carbon dioxide leading tube was configured in such a way, that the thickness of the condensate film at the outside of this tube does not influence the heat transfer measurements, regardless of the angle of inclination. For that purpose the tube has been finned on the outside. The geometry of those fins as well as the distances between them have been chosen in such a way, that the temperature differences on the outer wall along the tube never exceed 0.5°C , regardless of the inclination of the tube.

The carbon dioxide used in this study was purchased by PanGas, Schlieren, with a reported purity of 99.99% and recondensed from the gas phase.

2.2. Method

Because of the strong variations of the heat capacity and therefore of the local heat transfer coefficient at a pseudocritical point, the LMTD (logarithmic mean temperature difference) cannot be used for the evaluation of all of our measurements.

The following method of evaluation doesn't require any of the simplifications that have been assumed for the use of the LMTD. The only assumption that has to be made, is that of a constant wall temperature.

It is allowed that: $c_p = c_p(t)$; $\alpha = \alpha(t)$

The heat transfer over the entire heating section has to be described in such a way that:

$$\dot{Q} = \bar{\alpha} A \Delta \bar{T}$$

Global medium heat transfer coefficient:

$$\bar{\alpha} = \frac{1}{A} \int_A \alpha \, dA = \frac{\dot{M}}{A} \int_{t_{in}}^{t_{out}} c_p(t) \frac{dt}{(T_{wi} - t)} \quad (1)$$

Global medium temperature difference:

$$\Delta \bar{T} = \frac{\int_{t_{in}}^{t_{out}} c_p(t) \, dt}{\int_{t_{in}}^{t_{out}} c_p(t) \frac{dt}{(T_{wi} - t)}} \quad (2)$$

The global medium temperature difference as well as the corresponding temperature profile are fixed by the knowledge of $c_p(t)$, t_{in} and t_{out} .

Global medium physical properties:

In order to take the rapid variation of the physical properties into full consideration, one has to use the medium value of the integration between the inlet and outlet temperatures:

$$\bar{c}_p = \frac{1}{t_{out} - t_{in}} \int_{t_{in}}^{t_{out}} c_p(t) \, dt \quad (3)$$

The same definition is valuable for $\bar{\rho}$, \bar{v} and $\bar{\lambda}$.

Those physical properties are used in the determination of the dimensionless Nu-, Re-, Gr-, and Pr-numbers. The values of the enthalpie at the inlet and at the outlet and the mass flow of the carbon dioxide are used to calculate the *input of energy*:

$$\dot{Q} = \dot{M} (h_{out} - h_{in}) \quad (4)$$

3. RESULTS AND DISCUSSION

Only the results at the two extreme conditions of carbon dioxide will be discussed here.

- The supercritical condition at 80 bar and at a mean temperature of 363 K.

- The pseudocritical point in the vicinity of the critical point, at 120 bar and at a mean temperature of 323 K.

General observations

- The heat transfer at 80 bar, except for vertically upstreaming carbon dioxide, can still be described by the usual heat transfer formulas for buoyancy-free turbulent flow [2], with an uncertainty of 20%. These results are in accordance with the results of Jurgensen and Montillon [4].

- Due to the buoyancy effects at pseudocritical points the heat transfer is significantly enhanced at Re-numbers between 2300 and 10 000. This enhancement is completely independent of the flow geometry. At Re-numbers above 70 000 forced convection is dominating, regardless of the flow direction, and the heat transfer is back to normal again. At Re-numbers between 10 000 and 70 000 the heat transfer is dependent of the flow geometry. For downstreaming or horizontally streaming carbon dioxide the buoyancy induced enhancement of heat transfer slowly disappears. For upstreaming carbon dioxide the heat transfer can be decreased below the normal values at pseudocritical as well as not pseudocritical points.

- The vicinity of the critical point not only enhances the different heat transfer phenomena that have been observed between the Re-numbers 2300 and 70 000, in general the heat transfer is enhanced.

Results

• 80 bar

Except for the vertically upflowing carbon dioxide the deviation from the formula of Gnielinski [2] is below 20%.

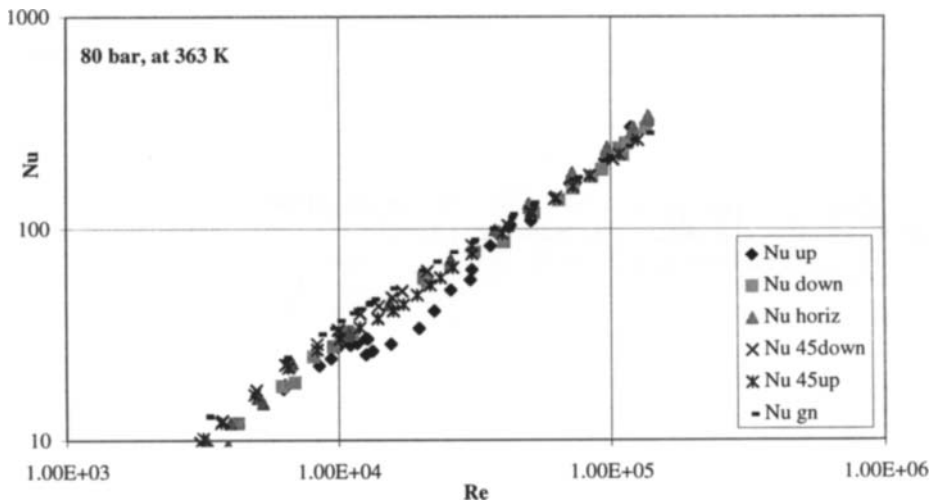


Figure 2. Heat transfer at a not pseudocritical point at 80 bar.

• 120 bar

Only at high Re-numbers the deviation from the formula of Gnielinski [2] is below 20%.

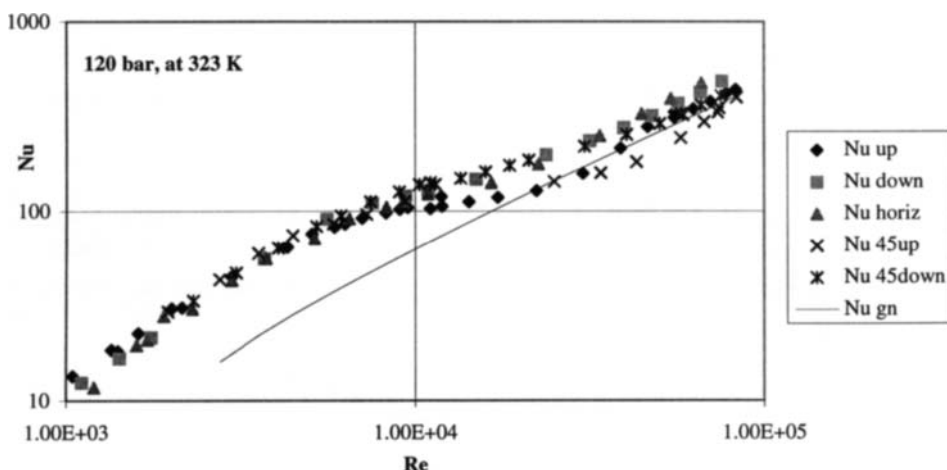


Figure 3. Heat transfer at a pseudocritical point at 120 bar at a small distance from the critical point.

4. CONCLUSIONS

The great heat capacity and the strong variations in density are mainly responsible for these observed heat transfer phenomena.

The great heat capacity enhances the heat transfer regardless of the Re-numbers and the flow geometry. The effect of the density variations is dependent of the Re-numbers. At Re-numbers below 1×10^4 buoyancy enhances the transfer of heat. At Re-numbers between 1×10^4 and 7×10^4 the direction of flow becomes important: at downflow and at horizontal flow buoyancy increases turbulence, which is mainly responsible for the transfer of heat; at upflow buoyancy reduces turbulence and therefore the transfer of heat. At Re-numbers above 7×10^4 forced convection produces such a strong turbulence, that buoyancy has no effect on the heat transfer any more [5], [6].

ACKNOWLEDGEMENTS

This research is supported by the Swiss Federal Institute of Technology (ETH) Zurich.

REFERENCES

1. R.J. Neumann, E.W.P. Hahne, Int. J. Heat Mass Transfer, 23 (1980) 1643.
2. V. Gnielinski, Engineering Research, 41 (1975) 1.
3. F. Herning, Stoffströme in Rohrleitungen, VDI-Verlag, 1961.
4. D.F. Jurgensen, G.H. Montillon, Univ. Minnesota, Minneapolis, 1935.

5. W.B. Hall, J.D. Jackson, Am. Soc. Mech. Engrs., Paper Nr. 69-HT-55, 1969.
6. B. Métais, Ph. D. Thesis, TH. Karlsruhe, 1960.

SYMBOLS

$LMTD = \frac{\Delta T_h - \Delta T_c}{\ln \frac{\Delta T_h}{\Delta T_c}}$	K	logarithmic mean temperature difference:
T	K	Temperature
t	K	temperature of carbon dioxide
$\Delta T_h = \bar{T}_{wi} - t_{out}$	K	temperature difference at the hot side
$\Delta T_c = \bar{T}_{wi} - t_{in}$	K	temperature difference at the cold side
α	W / (m ² K)	heat transfer coefficient
λ	W/(m K)	heat conductivity
ν	m ² / s	viscosity
ρ	kg / m ³	density

Indices

down	downstreaming
i	at the inner side
in	streaming into the heat exchanger
o	at the outer side
out	streaming out of the heat exchanger
up	upstreaming
w	at the wall
45	inclination of 45°

POROCRITICAL FLUID EXTRACTION: A NEW TECHNIQUE FOR CONTINUOUS EXTRACTION OF LIQUIDS WITH NEAR-CRITICAL FLUIDS. Marc Sims, James R. Robinson and Anthony J. Dennis, (Marc Sims SFE, Setec Inc., Tastemaker), 1012 Grayson St., Suite A, Berkeley, CA 94710

A new supercritical fluid process has been developed for the continuous extraction of liquids. The most useful solvent employed in the recently patented process is supercritical or near-critical carbon dioxide(1). At the heart of the process are porous membranes. Their porosity combined with a near-critical fluid's high diffusivity create a dynamic non-dispersive contact between solvent and feed liquid. The technique is dubbed porocritical fluid extraction and will be commercialized as the Porocrit™ Process.

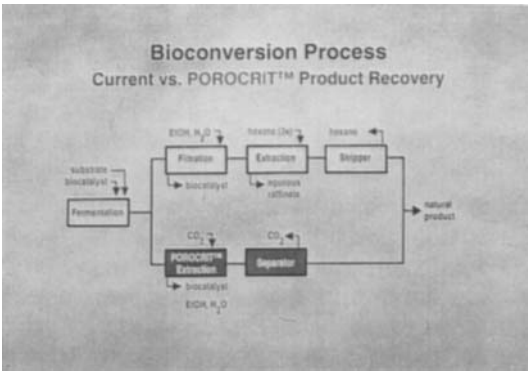
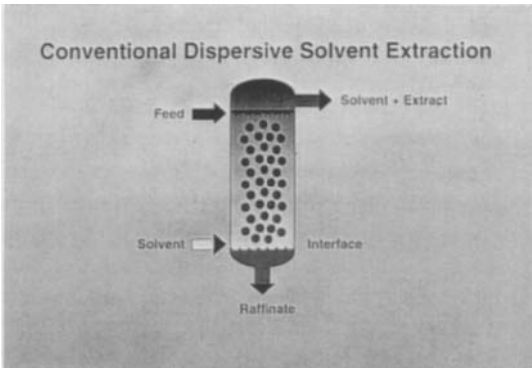
Extracting liquids continuously with near-critical fluids (NCF) such as CO₂ is usually done with contacting columns which disperse one phase in the other. In the new nondispersive technique of porocritical fluid extraction, a feed liquid continuously flows through a porous membrane module. Near-critical fluid flows counter-current on the other side of the membrane. Typical membranes are polypropylene with 0.2 micron pores and configured as hollow fiber bundles or spiral wound sheets. Transport of solutes from feed to NCF is very efficient. It is driven by the concentration gradient as expressed by the distribution coefficients. The high diffusivity of the NCF's minimizes the intramembrane resistance and shell-side bypassing which limit mass transfer when using conventional liquid solvents.

The feed can be many pumpable fluids, including suspensions, so the range of applications is wide. Organics can be stripped from aqueous streams such as fruit juices, fermentation broths, enzyme reaction mixes and waste water. Carbon dioxide soluble components can also be stripped from oils. Applications are seen to be especially appropriate in the flavors, pharmaceuticals, environmental, analytical and fine chemicals sectors.

Porocritical fluid extraction is a more efficient alternative to conventional contacting columns which disperse one fluid phase in another. Advantages include high throughput capacity without column flooding or emulsion formation, independence of density difference between solvent and feed, and modularity of design. There are no large expensive vessels in a typical Porocrit™ application. The reduced process complexity and expense can enable a broader industrial use of carbon dioxide's attributes as a non-toxic, environmentally benign extraction solvent.

Typical Applications for CO₂ Porocrit™ Processing

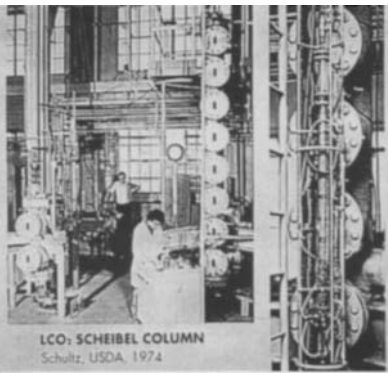
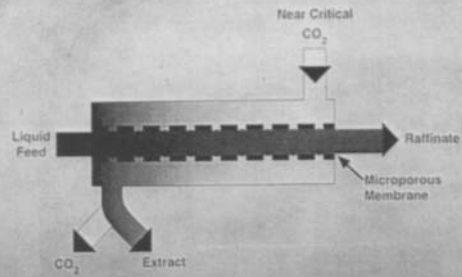
Aqueous	Oils	Suspensions
fruit juice flavors wine aromas waste water organics	edible aromas marine, deodorizing nut flavors	fermentation broth enzyme conversion vegetable purees dairy products

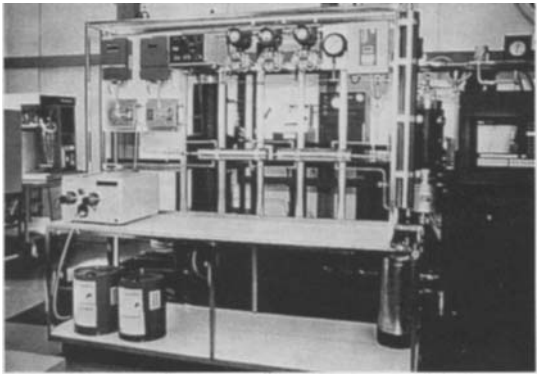
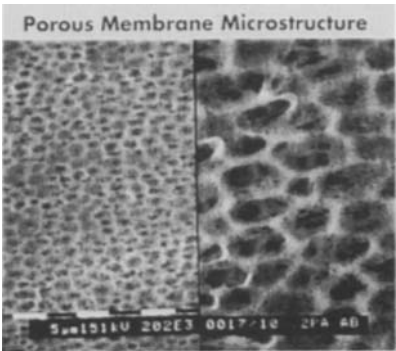
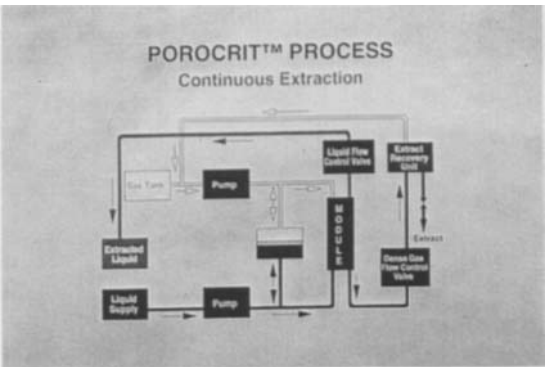


Comparison of Contactors in Solvent Extraction

	Conventional	Membrane
can form emulsion	yes	no
requires fluid density differences	yes	no
contact area per volume (-efficiency)	1	10-100
modular design	no	yes
limited throughput and velocity	yes	no
maintain sterility	no	yes
cleans without dismantling	no	yes
handles suspensions	no	yes
breaks emulsions	no	yes

Supercritical Fluid Extraction





CO₂ EXTRACTION IN AQUEOUS FRUIT AROMA

	Ppm in feed	Conc. factor in extract	Porocrt™ % depletion	Scheibel Column % depletion
methanol	4,220	3	-	
ethanol	105,000	7	20	
1-propanol	270	82	69	
amyl alcohol	17	115	81	26
hexanol	3	109	95+	83
octanol	5	110	95+	
z-3-hexenol	10	127	95+	
A-terpineol	10	98	95+	
terpinen-4-ol	4	106	95+	75
ethyl-acetate	29	106	85	40
Et-butyrate	23	106	88	56
acetal	37	147	39	
E-2-hexenal	19	132	88	
hexanal	10	100	84	
octanal	5	156	95+	74
citronellal	3	62	95+	62

Conditions: 100 bar, 24°C, 2:1, CO₂ : feed
Scheibel Column: W. Schutz, USDA, 1974

References

1. Robinson, J.R. and M. Sims; Method and System for Extracting a Solute from a Fluid Using Dense Gas and a Porous Membrane; U.S. Patent 5,490,884; February 13, 1996.
2. Siebert, A.F., Py, X., Mshewa, M., and J.R. Fair; Hydraulics and Mass Transfer Efficiency of a Commercial-Scale Membrane Extractor; *Separation Science and Technology*, Vol:28(1-3), pp. 343-359, 1993.
3. Pratt, K.F. and J. Pawliszyn; Gas Extraction Kinetics of Volatile Organic Species from Water with a Hollow Fiber Membrane; *Analytical Chemistry*, Vol:64(18), pp. 2101-2106, 1992.
4. Yang, M.J. and J. Pawliszyn; Extraction of Semivolatile Organic compounds from Aqueous Samples Using High-Density Carbon Dioxide and Hollow Fiber Membrane Module; *Analytical Chemistry*, Vol:65(18), pp. 2538-2541, 1993.
5. Prasad, R. and K.K. Sirkar; Dispersion-Free Solvent Extraction with Microporous Hollow-Fiber Modules; *AIChE Journal*, Vol:34(2), pp. 177-188, 1988.
6. Prasad, R. And K.K. Sirkar; Hollow Fiber Solvent Extraction: Performances and Design; *Journal of Membrane Science*, Vol:50, pp. 153-175, 1990.

This page intentionally left blank

Crystallization under Gas Pressure

H.Freund and R.Steiner*

*Institut für Technische Chemie, Friedrich-Alexander-Universität Erlangen-Nürnberg,
Egerlandstr. 3, D-91058 Erlangen

The economy of melt crystallization processes depends on the product purity, which is normally increased by an additional cleaning step. The application of gases under pressure is investigated to show possibilities of product quality improvement. Experimental devices for the determination of the freezing curve under gas pressure and for a solid layer crystallization process are shown. The influence of gas and pressure in respect to the freezing curve are explained on the basis of two binary mixtures (trioxane/water and para-/meta-dichlorobenzene) under CO₂- and N₂- pressure are presented. Furthermore the results of solid layer crystallization experiments with naphthalene/biphenyl and para-/meta-dichlorobenzene mixtures are shown.

1. INTRODUCTION

Although melt-crystallization as a purification process has become more common in the recent years it is still a barely realized separation technique. There are different designs used for crystallization units, whereby the dynamic-layer melt-crystallization, i.e. in a falling film crystallizer, is a modification which became more important during the last years. Crystallization is normally used for the purification of organic substances where other unit operations are not applicable. Reasons for the failure of other processes might be the formation of azeotrope mixtures, problems with the stability of substances at their boiling temperature and so on. An essential part of the purification by melt-crystallization is usually an additional step to remove the enclosed impurities of the crystal layers. This is normally realized with the so called „sweating“-step. Due to partial remelting of the solid layers by rising the temperature near to the melting point of the pure substance the enclosed liquid impurities are able to reach the surface and finally drop down („sweat“).

The main idea of the presented work is to improve this sweating-step by the application of gases under high pressure.

Applying pressurized gases for melt crystallization is advantageous due to their enhanced solubility in liquids. Correspondingly the freezing curve (liquidus curve) depends on pressure, sort of gas and melt. In this the effects of inert gases (i.e. N₂) are small and similar to static pressure, but those of more soluble gases (i.e. CO₂) are much more distinct.

In course of crystallization the liquid impurities including solved gas are trapped in the solid layer. During expansion the volume of the enclosed gas is increasing and breaks up the solid, so that impurities are transported to the surface without remelting parts of the crystals.

2. FREEZING CURVE UNDER GAS PRESSURE

2.1 Apparatus

Figure 1 gives a schematic drawing of the equipment for determination of freezing points. The heart is the sightcell (Figure 2). It is designed for a maximum pressure of 200 bar and temperatures between 25°C and 150°C. The inner volume is 20 cm³. The cell is supplied with sapphire glasses which allow the observation of crystal growth under pressure. A cooling pipe is attached horizontal through the sightcell, which is used to initiate crystallization in the middle of the cell.

The pipe is cooled down rapidly by expansion of carbon dioxide (see Figure 1). This procedure allows short cooling periods to start nucleation, so that the rest of the melt is hardly cooled down.

Pressure is regulated by the used gas (in this case N₂ or CO₂). Temperature of the melt respectively of the crystals is measured with a Ni-CrNi thermocouple directly at the throttle position (Figure 2).

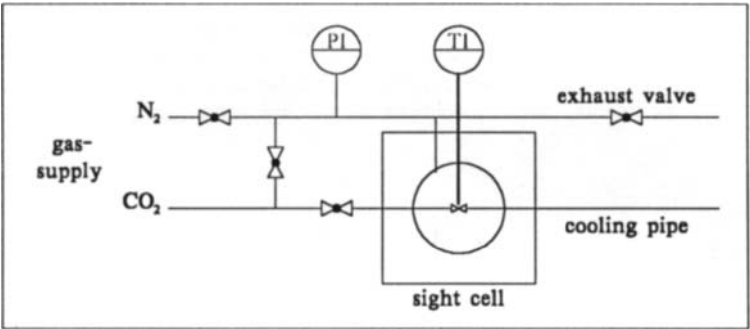


Figure 1 : Schema of experimental apparatus

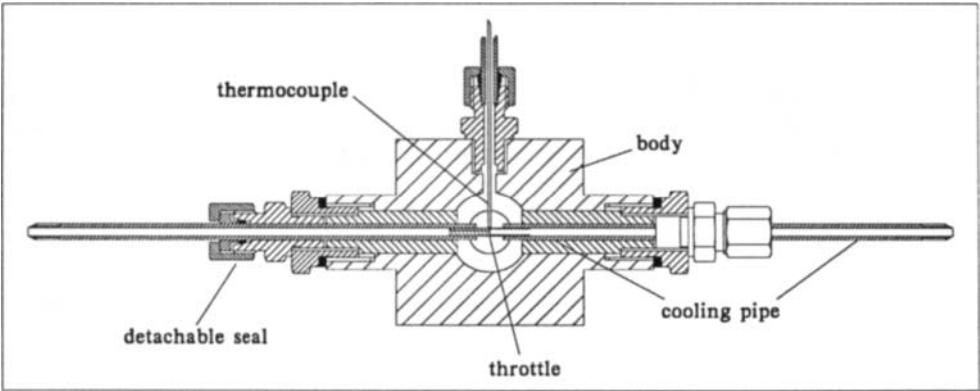


Figure 2 : Sight cell cross-section

2.2 Measuring

To determinate the freezing point under gas pressure the cell is filled with melt of known composition. Then the wanted pressure is adjusted with the used gas. The measuring procedure is started when the phase equilibrium between melt and gas phase at a temperature tight upon expected freezing point is reached.

At the beginning of the determination the CO₂ valve to the cooling pipe is opened for a brief moment to start nucleation at the surface of the cooling pipe, so that the temperature at the throttle decreases between 3 and 8 K (see Figure 3, point 1 to 2). Because of heat exchange between the remaining melt and the cooled area, the temperature of the cell will finally reach a level which is about 0.5 K below starting value (Point 2 to 3). If the temperature is still above the melting point, the crystals will melt again.

The cooling procedure is repeated until the melt reaches a temperature, which is low enough to allow the nucleuses to remain or to grow slowly. Now the system temperature is at or slightly below the freezing point, which itself lies between the end-temperatures of the last but one (point 4) and the last cycle (point 5).

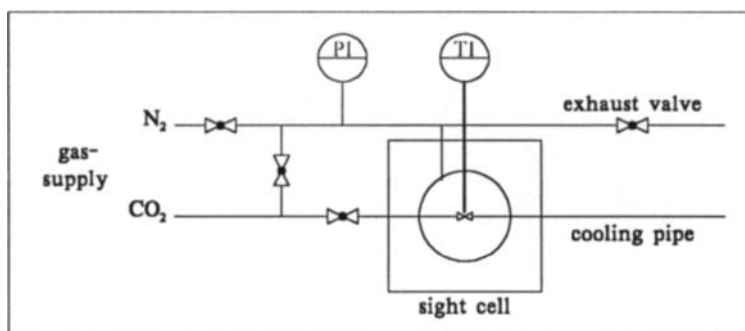


Figure 3 : Determination of the freezing point in the temperature vs. time plot

2.3 Results

The freezing points for the systems para-/meta-dichlorobenzene (p-/m-DCB) (Figure 4) and trioxane/water (Figure 5) under 200 bar static pressure, 200 bar N₂ atmosphere, 15 bar CO₂ atmosphere and normal pressure are compared.

The experimental results show the influence of different gases on binary mixtures, which is mainly based on different solubilities in the examined samples.

At 200 bar static pressure the freezing temperature is usually between 4°C and 5°C higher than at normal pressure. Under 200 bar N₂ atmosphere the increase is about 40 % lower. Physical solubility of N₂ results in a relatively small decrease of the freezing point, so that the effect of static pressure is still dominant.

Using CO₂ leads to a complete different behavior. Based on the good solubility of CO₂ in the molten mixtures, only 15 bar pressure are sufficient to lower the freezing temperature between 6°C (p-/m-DCB) and 8°C (trioxane/water).

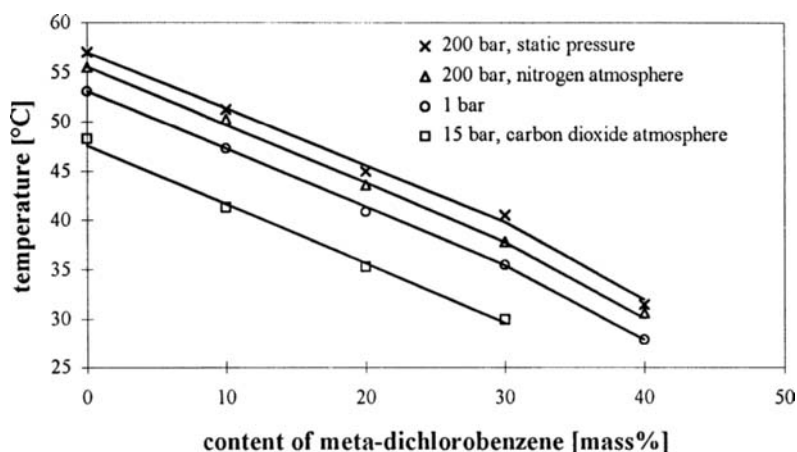


Figure 4 : Freezing curve of para-/meta-dichlorobenzene

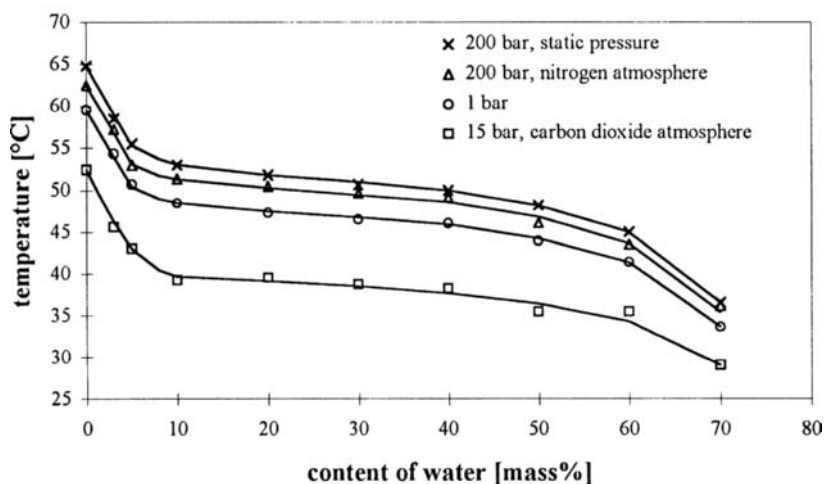


Figure 5 : Freezing curve of trioxane/water

The shape of the DCB curves show within the measuring area the expected eutectic behavior (Figure 4). Because of the similar structure of para and meta DCB the charts under different atmospheres are parallel.

Trioxane/water has a peritectical point at about 7% water (Figure 5). Additional experiments resulted in an eutectic composition of about 90% water under normal pressure.

3. CRYSTALLIZATION UNDER GAS PRESSURE

3.1 Apparatus

The process is designed as a dynamic layer crystallization. The heart of the experimental equipment is an autoclave which is mounted in a way that its incline can be adjusted between 0 and 90 degrees (see Figure 6). An important feature are four 35 mm diameter windows, which allow to observe the beginning and the end of the trickling film on the crystallization device (see Figure 7). It was necessary to divide the crystallization surface into six parallel channels,

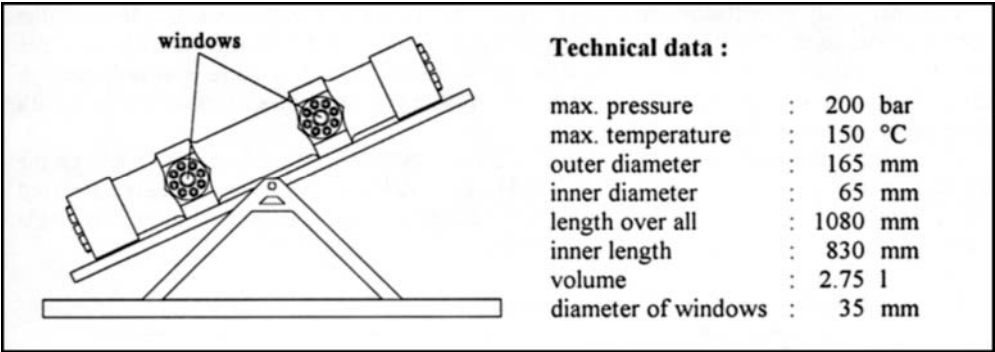


Figure 6 : High pressure crystallizer

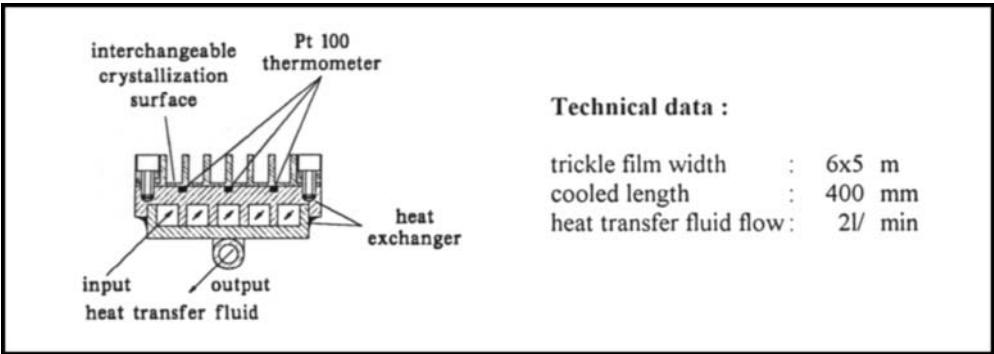


Figure 7 : Crystallization device cross section

to get an equal distribution of the melt on the entire crystallization surface during the complete experiment. Without channels the trickling film is destroyed by crystallized substance and therefore melt flows down in narrow streams so that only a small part of the cooled surface is moistened and used for crystallization.

3.2 Results

Crystallization without any cleaning step and with thermal sweating is compared with crystallization and following pressure sweating in respect to purity and yield of the product (see Table 1). The effects of N₂ and CO₂ under different pressures on the crystallization of a p-/m-DCB mixture with 8% m-DCB and a naphthalene/biphenyl mixture with 33% biphenyl are investigated.

In both cases the product purity is significant increased by the pressure sweating step. The highest purities, however, are reached with the thermal sweating. The yield is generally decreasing with increasing purity because the improvement of the product is based on the separation of sweating oil from the crystal layer.

The final purity after the pressure sweating step is limited by the melt which adheres at the porous crystal layer. Therefore there is no significant difference between the experiments under 15 bar CO₂, 50 bar N₂ and 175 bar N₂ atmosphere which means that there is already enough gas solved at 15 bar CO₂ respectively 50 bar N₂ in the liquid impurities to transport them with the escaping gas to the crystal layer surface.

By the thermal sweating the crystal layer is washed by remolten product. This leads on the one hand to high purities and on the other hand to poor yields. If thermal sweating is compared with pressure sweating with the same final purity the yield achieved by the pressure sweating is higher because reducing pressure to dissolve the gas leads not to a melting of the crystals.

Table 1 : Results of the crystallization experiments

System	conditions	yield	purity
para-/meta-Dichloro-benzene (92/8)	no cleaning step	100 %	96,3 %
	thermal sweating I	57 %	98,7 %
	thermal sweating II	87 %	97,0 %
	pressure sweating, 50 bar N ₂	90 %	97,0 %
	pressure sweating, 175 bar N ₂	90 %	97,0 %
	pressure sweating, 15 bar CO ₂	91 %	96,8 %
Naphthalene/Biphenyl (67/33)	no cleaning step	100 %	73 %
	thermal sweating I	32 %	90 %
	thermal sweating II	64 %	80 %
	pressure sweating, 50 bar N ₂	81 %	80 %
	pressure sweating, 175 bar N ₂	81 %	80 %
	pressure sweating, 15 bar CO ₂	76 %	81 %

4. CONCLUSIONS

The freezing point apparatus allowed an easy, reliable and reproducible determination of freezing points under gas pressure. The experiments resulted in remarkable effects of different gases to the melting points of the examined mixtures due to solubility of the gases in the melts.

The tests showed possibilities and limits of the application of pressurized gases on crystallization. An additional economic aspect to yield and purity is that the pressure step requires less time than the thermal sweating. Therefore the pressure sweating might be a technical alternative if it can be done at relative low pressure (i.e. with CO₂) and product quality is high enough. Also a combination of pressure and thermal sweating might be useful to get a higher yield at high product purities.

Formation of Biocompatible Polymer Microspheres for Controlled Drug Delivery by a Supercritical Antisolvent Technique

Alberto Bertucco^a, Paolo Pallado^a and Luca Benedetti^b

^aIstituto di Impianti Chimici, Universita' di Padova, v. Marzolo, 9 - I 35131 Padova, Italy

^bFidia Advanced Biopolymers, v. Ponte della Fabbrica, 3 - I 35031 Abano Terme, Italy

1. INTRODUCTION

The importance of biocompatible and biodegradable polymers is continuously increasing in medical applications. These materials are extensively used in sutures, medical implants to treat bone fractures, skin implants and regeneration, and controlled drug delivery devices [1]. For this last applications the biocompatible substance has to be loaded with a drug. The drug is then released either by erosion of the polymeric host [2] or by diffusion through the polymer. In this case, the dimension and shape of the polymer matrix assume a relevant role especially when the polymer is gradually degraded in vivo to non-toxic products: in fact, from these two factors depends the way of application to the patient and the rate of drug release.

In the present work, the hyaluronic acid benzylic ester (HYAFF-11) is considered. The HYAFF polymers have raised particular interest in various applications [3]. Depending on the alcoholic group, the polymer degrades to compatible products helping skin regeneration, or remains in the organism acting as a substrate for cellular replication. At present, this biodegradable material is produced in different shapes: thin films, perforated membranes, thread, and microspheres.

The production of polymeric HYAFF microspheres loaded with the pharmaceutical is currently performed by solvent emulsion precipitation [4]. This process requires the preparation of an emulsion of two immiscible liquids. The polymer and the co-precipitated pharmaceutical can be inactivated or degraded due to the temperature that is required for solvents removing. Moreover, a complete separation of the residual solvents cannot be achieved and a relevant percentage of liquid is retained within the final product. Finally, liquid solvent and antisolvent cannot be recovered.

An alternate method which takes advantage of the favourable properties of solvents at a or supercritical state was explored. Nowadays, SCFs are becoming extremely attractive as extraction and reaction media also in the pharmaceutical industry [5,6]. An application of promising interest is the micronization of pharmaceuticals, which can be achieved by different techniques: the rapid expansion of supercritical solutions (RESS) [7] and the supercritical anti-solvent process (SAS) [8]. This work is concerned with the production of HYAFF particles through a batch SAS technique. Its applicability is assessed and the influence of operating variables to dimension, shape and morphology of the product is considered. The coprecipitation of drugs within the HYAFF polymer is also investigated.

The possibility to obtain a full solvent-free product, controlling in the same time the dimension of particles, is probably the most important feature when pharmaceutical substances are used. In the SAS process the SCF is used as the antisolvent. An organic solvent has to be involved in addition to the SCF and the solid solute. Basically, the process is performed by first dissolving the solid of interest in the organic liquid; then, the SCF, which has low solvent capacity with respect to the solid but is completely miscible with the liquid, is added to the solution to get the precipitation of the solid. This method has been proposed by Gallagher and coworkers [8] to crystallize difficult-to-handle high explosives. Recently, other applications have been set forth to produce crystals of pharmaceuticals [9,10].

The volumetric expansion of the liquid when it is contacted with the SCF plays the key role in the process. The behaviour reported by Yeo et al. [10] and by Kordikowski et al. [11] for the dimethylsulfoxide (DMSO)-CO₂ system at two temperatures shows that CO₂ produces a remarkable volumetric expansion of DMSO near the mixture critical point. The increase of antisolvent amount in the mixed solvent and the evaporation of the organic liquid into the SCF eventually cause the precipitation of the solute. A cleaning step, carried out with pure antisolvent, is necessary after the precipitation, in order to remove completely the liquid solvent from the solid particles: the antisolvent pushes the liquid out of the vessel, then it has to extract the residual solvent from the solid and the dry solid particles can be collected.

2. EXPERIMENTAL SECTION

A jacketed precipitator (internal volume: 0.4 Nl) is the main unit of the SAS arrangement, as shown in Figure 1. The loading of CO₂ into the cell was operated from the bottom, with a metallic filter (frit) acting as a distributor; after the desired pressure (normally 100 bar) was reached, the washing step was started with the solution leaving the precipitator from the top. Solid particles were trapped by the frit located at the top. During each run, the chamber temperature was kept constant with values which ranged from 35°C to 50°C, depending on the specific run. The pressure was regulated with a millimetric valve which was located downstream the precipitator. In the post expansion vessel, operating at atmospheric conditions, liquid DMSO was collected and the CO₂ was vented to the metering section (dry test meter; rotameter UCAR, mod. Matheson, type 7640T; measuring tube mod. 603).

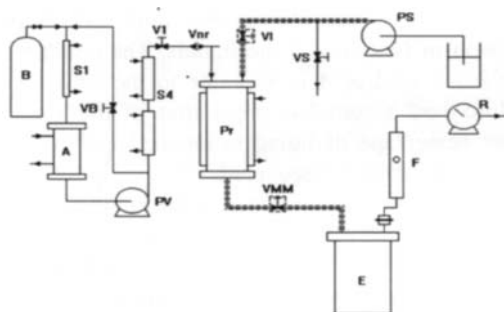


Figure 1: Schematic of the experimental apparatus. Legend: CO₂ reservoir (A); CO₂ bomb (B); expansion vessel (E); flow indicator (F); precipitation vessel (PR); HPLC pump (PS); CO₂ pump (PV); flow meter (R); heat exchanger (S#); valve (V#); regulating valve (VMM).

The process required four steps: the loading of the cell, with the CO₂ entering from the bottom of the precipitator and bubbling through the liquid solution; the washing out of the solvent; the purification of the product; the depressurization of the vessel.

Pressure gradients from 5 to 20 bar/min were used during the loading step, up to 100 bar. To dry the particles, CO₂ flow rate was kept at 8 to 12 NI/min for 90 to 150 min depending on the temperature and the amount of starting solution. Three polymer concentrations were used: 0.5, 1.0 and 1.5 % by weight (HYAFF in DMSO). In the co-precipitation runs, the drug was dissolved in the organic liquid solution. The solid particles collected from the vessel were examined by scanning electron microscopy (SEM).

2.1. Materials

The HYAFF-11 polymer used in all the experimental runs was supplied by F.A.B. (Fidia Advanced Biopolymers, Abano Terme, Italy). The HYAFF-11 (US patent 4,851,521) is a hyaluronic acid ethyl ester in which all the acid carboxylic groups are esterificated with benzylic alcohol. The hyaluronic acid is a polysaccharide widely distributed in animal organisms; it is composed by D-glucuronic acid and N-acetyl D-glucosamine monomers in repeated sequence. The acid molecular weight vary between 2×10^4 and 7×10^6 Da, while for the HYAFF polymer the range is between 180,000 and 200,000 Da. The HYAFF-11 monomer form is a dimer with a molecular weight of 469.34. Co-precipitation runs were performed on two steroids (herein called *Ex* and *Nx*) and a protein (herein called *Cx*), all of them supplied by F.A.B. The DMSO (Rudi Pont, reagent grade) was used as an organic solvent. It shows high solvent power with respect to HYAFF (250÷270 mg/ml at 25°C) and high expansivity when contacted with carbon dioxide. Pure liquid CO₂ (99.9%) was purchased from Rivoira, Italy. The CO₂ was cooled and stored in an insulated vessel provided with an internal cooler. Sub-cooled CO₂ was pumped by means of a high pressure piston pump (Off. Mecc. Gallaratesi, mod. 2M-10×70, MI, Italy).

3. RESULTS AND DISCUSSION

In the batch SAS process the low pressure gradient value, coupled with a uniform distribution of the antisolvent into the liquid, leads to a uniform expansion of the solution. Due to the relatively low expansion time, macro particles should be obtained; however, at the pressure where the solvent power dramatically decreases, the CO₂ mole fraction in the liquid phase is expected to be around 0.9, so that the supersaturated solid molecules are highly dispersed in an expanded media and a high number of critical nuclei is produced. Combining these features one could obtain, in principle, small spherical particles with a narrow size distribution. Furthermore, the amorphous nature of the polymer, coupled with its high molecular weight and high purity and absence of localized electric charges, influences the growth process so that a spherical geometry for the nucleating particles is attained.

Experimental conditions of temperature and pressure were chosen in order to avoid liquid phase segregation. The temperature has a negligible effect on the morphology and dimension of the powders obtained; therefore, its value was selected to avoid the polymer degradation and to shorten the drying time.

We noted that polymer concentration in the liquid solution affects the nucleation process. From dilute solutions an aggregate structure of particles fused together is produced.

By suspending the sample on water and sonicating the solution, it was not possible to separate the single particles. When higher concentrations were used, micronic spheres with a narrow size distribution were formed, as reported in Figure 2. A light dependence of particle dimensions on concentration was observed: moving to higher concentrations smaller microspheres were obtained. To control particle size, pressure gradient in the loading step and solution stirring can be used.

A typical particle size distribution of sample as in Figure 2 is shown in Figure 3. Every run produced particles smaller than 1 μm , average diameter is around 0.4 μm . Compared to the liquid antisolvent process, the improvement achieved in term of particle size is remarkable; in addition, the number of organic solvents used is now reduced to one and both solvent and antisolvent can be recovered.



Figure 2: SEM photo of microsphere formed at $T=40^{\circ}\text{C}$, $P=100$ bar, $G_{\text{CO}_2}=8.0$ gr/min; $\text{Conc.}_{\text{HYAFF}}=1.0$ %w/w in DMSO (bar= $1\mu\text{m}$, $\times 10000$).

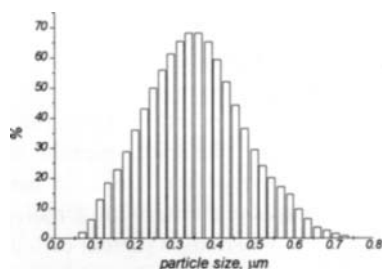


Figure 3: Particle size distribution for the SAS batch run as in Figure 2.

The co-precipitation of pharmaceuticals with the polymer was performed to assess the possibility of producing a controlled drug delivery system. Different drugs were initially solubilized with the biopolymer in the same liquid solvent. The process was carried out at similar operating conditions and the results and product obtained were again satisfactory, as depicted in Figure 4. Average particle sizes, analyzed with a Coulter Nanosizer, are reported on Table I for drug Cx.

Table I

Mean particle size, as a function of SAS operating conditions, for the co-precipitation of drug Cx. Precipitator pressure is set equal to 100 bar for all the experimental runs, HYAFF concentration is set equal to 1% w/w. $\Delta P/t$ is the pressure gradient in the loading step.

run	T, $^{\circ}\text{C}$	$\Delta P/t$, bar/min	mean size, nm
Cx1	40	15	360
Cx2	40	15	400
Cx3	35	20	340
Cx4	35	20	320

The yield of drug precipitation in the collected particles is acceptable for drug Cx, as it can be seen in Table II. However, a problem arised when the drug used has a non-negligible solubility in the supercritical antisolvent: in this case, the step for removing DMSO turned to be an extractive step for the drug already co-precipitated in the microspheres, as reported on Table II for *Ex* and *Nx* drugs.

Table II

Initial and final drug loading in HYAFF-11 microspheres for different pharmaceuticals. HYAFF concentration is set equal to 1% w/w. Drug content is referred to HYAFF.

run	drug	T, °C	drug content	
			initial	final
<i>Ex</i> 1	<i>Ex</i>	40	30 mg/gr	5.5 mg/gr
<i>Ex</i> 2	<i>Ex</i>	40	300 mg/gr	61.0 mg/gr
<i>Nx</i> 1	<i>Nx</i>	40	250 mg/gr	n.d.
<i>Nx</i> 2	<i>Nx</i>	40	500 mg/gr	n.d.
<i>Cx</i> 1	<i>Cx</i>	40	1.5 IU	1.0 IU
<i>Cx</i> 2	<i>Cx</i>	40	10 IU	9.2 IU
<i>Cx</i> 3	<i>Cx</i>	40	5 IU	4.3 IU
<i>Cx</i> 4	<i>Cx</i>	35	10 IU	8.6 IU

In all cases, the SAS process ensured the total recovery of the polymer initially charged in the precipitator. The residual DMSO content was usually lower than 1.5%, and this value can be further decreased by increasing the length of the purification step.

Finally, Figure 5 shows preliminary results of in-vivo experiment: the blood levels in rats for drug *Ex* are reported as a function of time after the injection into the animal. The microspheres were formulated into pessaries, each pessary containing 25 µg of drug, as well as control pessaries were prepared containing the same amount of *Ex*. The pessaries were administrated to 4 groups of 5 rats, each rat weighing approximately 300 g.

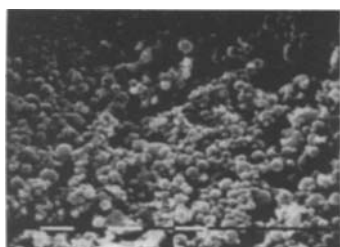


Figure 4: SEM photo of microsphere formed at the same conditions of Figure 2 but with drug Cx co-precipitated (bar=1µm, ×10000).

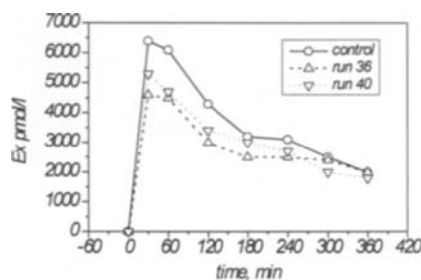


Figure 5: In vivo release of drug *Ex* from HYAFF-11 microspheres (Δ, ∇) compared to control release (○).

Comparison between the release profiles obtained with the two formulations is displayed. Since drug *Ex* has an appreciable solubility in SC CO₂, it remains preferably on the surface of the HYAFF particle so the drug release for the two formulation presents no substantial difference.

4. CONCLUSIONS

A supercritical CO₂-based technique was applied to produce a biocompatible polymer in form of microspheres. With the SAS process carried out in a batch mode, micronic particles of polymer were obtained with a narrow particle size distribution. Co-precipitation of pharmaceuticals for the production of controlled drug delivery systems has been proposed as a preliminary result, since further analyses are under development. The experimental apparatus is easy-to-use and the purification of the precipitated solid from the solvent can be achieved by suitably increasing the time for solvent removing.

ACKNOWLEDGEMENT

We thank Mr. Claudio Bedin for the professional help during the plant design and construction. The authors acknowledge the M.U.R.S.T. 40 % (Ministero dell'Universita' e della Ricerca Scientifica e Tecnologica) for financial support.

REFERENCES

1. Larson, K.A. and King, M.L., *Biotech. Prog.* 2 (1986) 73-82.
2. Heller, J., R.S. Langer, D.L. Wise (eds.), CRC Press, Boca Raton, FL, 1984.
3. European Patent 0535200, 1993.
4. US Patent 4,851,521.
5. Krukoniš, V.J., M. Perrut (ed.), *Proc. of Int. Symp. on Supercritical Fluids*, INPL, Nice (1988) 541-560.
6. Savage, P.E., Gopalan, S., Mizan, T.I., Martino, C.J. and Brock, E.E., *AIChE J.* 41 (1995) 1723-1778.
7. Matson, D.W., Fulton, J.L., Petersen, R.C. and Smith, R.D., *Thin Films, and Fibers. Ind. Eng. Chem. Res.*, 26 (1984) 2298-2306.
8. Gallagher, P.M., Coffey, M.P., Krukoniš, V.J. and Klasutis, N., K.P. Johnston and J.M.L. Penninger (eds.), *Supercritical Fluid Science and Technology*, ACS Symp. Ser., No. 406, Chap. 23 (1989) 334-354.
9. Chang, C.J. and Randolph, A.D., *AIChE J.* 35 (1989) 1876-1882.
10. Yeo, S.D., Lim, G.B., Debenedetti, P.G. and Bernstein, H., *Biotech. and Bioeng.* 41 (1993) 341-346.
11. Kordikowsky, A., Schenk, A.P., van Nielen, R.M. and Peters, C.J., *J. Super. Fluids*, 9, (1995) 205-216.

Powder Generation from Polyethyleneglycols with Compressible Fluids

E. Weidner^a, R. Steiner^a, Z. Knez^b

^a University of Erlangen-Nürnberg, Institut für Technische Chemie, Egerlandstr.3, D-91058 Erlangen, Germany

^b University of Maribor, Faculty of Chemistry and Chemical Engineering, Smetanova 17, SLO-2000 Maribor, Slovenija

A new developed process PGSS (Particles from Gas Saturated Solutions) was applied for generation of powder from polyethyleneglycols. Principle of PGSS process is described and phase equilibrium data for the binary systems PEG-CO₂ for the vapour-liquid and the solid-liquid range are presented in a "master diagram". The influence of the process parameters on particle size, particle size distribution, shape, bulk density and crystallinity is discussed.

1. INTRODUCTION

Several new processes for formation of solid particles with defined particle size and particle size distribution using supercritical fluids were developed in the past years. Examples are crystallisation from supercritical fluids, rapid expansion of supercritical solutions (RESS), gas antisolvent recrystallisation (GASR), and PGSS (Particles from Gas Saturated Solutions)-process [1,2].

Polyethyleneglycols (PEGs) are water soluble polymers, which are due to their physiological acceptance used in large quantities in pharmaceutical, cosmetic and food industry. The general formula of PEG's is $H(OCH_2CH_2)_nOH$, where n is the number of ethylene oxide groups. PEG is, like other polymers, a mixture of homologues where n varies between certain numbers. PEG's up to molar mass of 600 g/mol are liquid while those with higher molar masses are solid. PEG is usually manufactured as flakes but in some applications it is used as a powder which is obtained by milling of flakes. Milling is possible for PEG's with molar masses between about 2000 g/mol and 10000 g/mol. PEG's of lower molar mass are too greasy and higher PEG's are too hard. Not only with respect to flexibility for different feedstocks, the new developed process - PGSS - is favourable for the generation of fine particles.

2. PGSS - PROCESS

The solubility of compressed gasses in liquids is usually quite high.. Dependent on pressure and temperature concentrations of highly compressible media between 5 - 50 % by weight can be dissolved in the solute (liquid). Due to the solubilized gas the properties of the liquid are changed.

Gas saturated solutions possess lower viscosity (e.g. in the region of viscosity of water). The surface tension between gas and liquid phase is also lowered. By the expansion of such gas saturated solution over a nozzle or other expansion device the compressed medium is set free, due to its high vapour pressure. Therefore the solution is cooled. At the same time high

supersaturation occurs and fine particles are formed. The crystallinity, particle size and particle size distribution can be influenced by the process parameters.

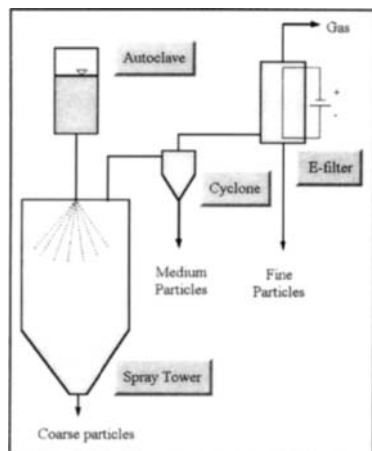


Figure 1: Basic scheme of a process for production of particles from gas saturated solution

On Figure 1 a schematic diagram of a process for production of particles from gas saturated solution is presented.

The equipment consists of a high pressure part where the highly compressible medium/gas is dissolved in the substance which has to be micronised. The second part of the equipment is the expansion device, where the gas saturated solution is rapidly depressurized through a nozzle into a spray tower where the particles with a diameter $>10\ \mu\text{m}$ are separated.

The depressurized gas, which contains smaller particles ($1\text{-}10\ \mu\text{m}$), is led into a cyclone where they are collected at the bottom. The finest particles $<1\ \mu\text{m}$ can be separated from the gas stream in an electrofilter.

3. PHASE EQUILIBRIUM IN THE BINARY SYSTEM PEG-CO₂

For the design of a process for formation of solid particles using supercritical fluids, data on solid - liquid and vapour - liquid phase equilibrium are essential. PGSS process is only possible for systems where enough gas is solubilized in the liquid.

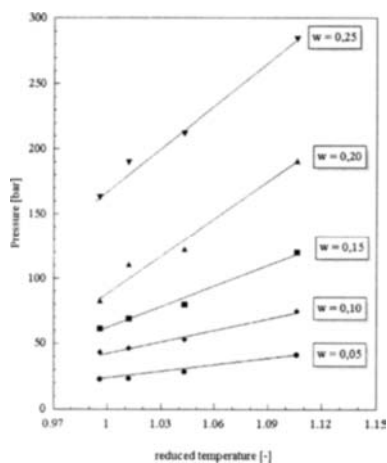


Fig 2: Lines of constant composition (isoplethes) for PEG 1500 - CO₂ (vapour-liquid)

Several authors [3-9] studied the solubility of polymers in supercritical fluids due to research on fractionation of polymers. For solubility of SCF in polymers only limited number of experimental data are available till now [e.g. 4,5,10-12]. Few data (for PEG's with molar mass up to 1000 g/mol) are available on the vapour-liquid phase equilibrium PEG -CO₂ [13]. No data can be found on phase equilibrium solid-liquid for the binary PEG's -CO₂. Experimental equipment and procedure for determination of phase equilibrium (vapour -liquid and solid -liquid) in the binary system PEG's -CO₂ are presented in [14]. It was found that the solubility of CO₂ in PEG is practically independent from the molecular mass of PEG and is influenced only by pressure and temperature of the system.

The values of measured phase equilibrium data were plotted in P-T diagrams (fig.2) as lines of constant composition (shown for PEG 1500). On the abszisse a

reduced temperature is indicated, which is the ratio between the actual temperature and the melting temperature of the PEG under consideration.

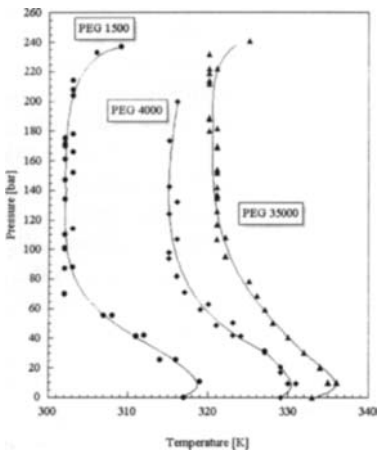


Figure 3. *P-T* diagram for solid-liquid transition of PEG in presence of CO_2 .

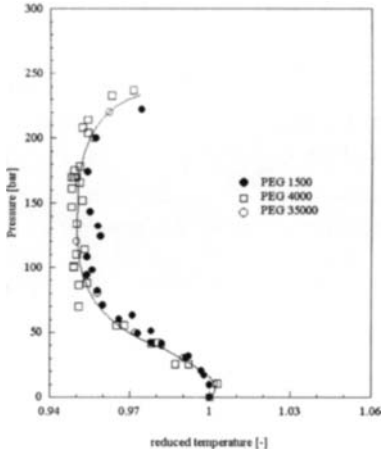


Figure 4. *P-T_{red}* diagram for systems polyethyleneglycol- CO_2 .

The isoplethes are approximately a linear function of pressure and T_{red} . The slope of constant composition lines depend on vapour pressure of a component in solution. With increased solubility of gas in PEG the incline of the isoplethes and vapour pressure increases. In the measurements of *P-T* diagram for a system PEG- CO_2 a liquid solution of CO_2 in PEG is established even below the melting point of PEG at ambient pressure. This phenomenon is caused by a reduction of the liquefaction temperature of PEG in presence of pressurized CO_2 .

Measured data for the solid-liquid transition of PEG-1500, PEG-4000, and PEG-35000 g/mol are presented in Figure 3.

On Figure 4 the liquefaction of PEG in presence of CO_2 is shown in a *p-T_{red}* plot. At low pressures the liquefaction temperature slightly increases compared to the melting point of the pure PEG. Then a sharp decrease is observed. The liquefaction temperature passes a minimum and increases again. The curvature can be interpreted as follows:

Gas saturated solutions of CO_2 in PEG liquify at temperatures which may be considerably lower than the melting point of PEG. This effect is influenced by

- pressure dependency of pure PEG's melting point,
- gas solubility and
- pressure dependency of gas solubility.

At low pressures the solubility of CO_2 in PEG is low. The increase of the melting point of PEG with (static) pressure outweighs the diminishing effect of CO_2 . In a medium pressure range the reducing effect of CO_2 dominates. At a further pressure increase, the amount of dissolved CO_2 in the liquid increases. At the same time pressure dependency of the gas solubility decreases (see fig. 2, slope of 0,05 line and 0,25 line).

Thus at higher gas concentrations (= higher pressures) again the liquefaction temperature increases with pressure.

Extrapolation of constant composition lines (from Fig. 2) to the S-L line (reduced melting point line) gave the pressure and temperature at which a certain composition of PEG- CO_2 solution can be obtained (or is reached). Because melting point line in *P-T_{red}* diagram is valid

for the whole range from 1500 to 35000 g/mol we can suppose that the diagram on Figure 5 is valid for all PEG-CO₂ solutions up to PEG 35000 g/mol.

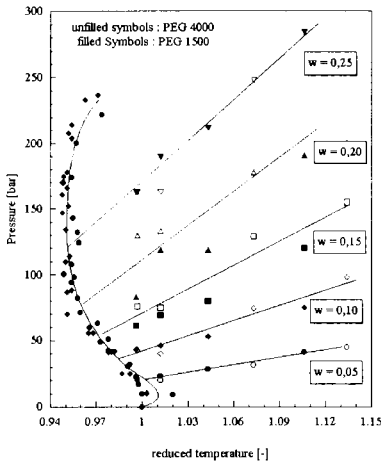


Figure 5. P - T_{red} diagram with melting point line and constant composition lines.

In such a diagram the expansion according to the PGSS-process is represented by the isoplethes (the composition does not change during the expansion). The gas saturated solution is established at pressures and temperatures which are on the right hand side of the liquefaction curve (s-l-v line). On the left hand side of the liquefaction curve solid PEG coexists with gaseous CO₂. The starting conditions have to be chosen in that way, that the end conditions after expansion are in the s-v-region of the binary system. An initial estimation can be performed by an energy balance [15] which takes into account:

- enthalpies of CO₂ before and after expansion (e.g. from an T,S-diagram)
- enthalpies of PEG before and after expansion (e.g. from heat capacity of liquid and solid PEG)
- enthalpy of solution of CO₂ and PEG (e.g. derived from phase equilibrium data)
- heat of crystallisation of PEG (from literature data or DSC)
- mechanical energy for the formation of new interface (is in most cases two to three orders lower than the thermal energies and can therefore be neglected).

For the production of fine dispersed PEG by expanding CO₂-saturated solutions the initial guess indicates that the starting conditions should be near the liquefaction curve in order to allow to reach the solid-gas region after the expansion. This is further illustrated by the spraying experiments.

4. PGSS of PEG

The experiments were performed in a lab-scale plant with sample sizes of about 200 - 400 g powder and in a small pilot plant with sample sizes of 1 - 3 kg powder. Depending on the nozzles (orifices 0,4 / 0,5 / 1,0 mm, spraying angles 30° and 90°), the kind of PEG (MW 1500/4000/8000/35000) and on pressure (100-250 bar) and temperature (45 - 70 °C) the spraying times reached from about 45 s to 180 s. The obtained particles were characterised by Scanning Electron Microscopy, Differential Scanning Calorimetry and by granulometric analysis. The results can be summarised as follows:

- Three classes of particles were obtained based on process parameters: fibers, spheres and

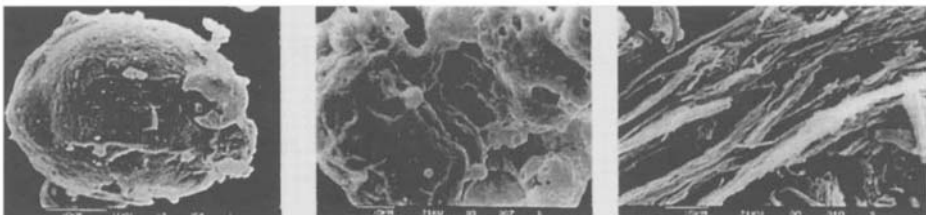


Figure 6: Shape of the particles of PEG obtained by PGSS process

sponges as presented in Figure 6. Spheres are obtained when the initial temperature is so high (approx. 30 K above the melting point), that the product is not completely powderous. Fibres are preferably obtained, when the molar mass of the PEG increases. The „normal“ configuration are the sponges.

- From DSC measurements of fresh powders (some minutes old) it was derived, that the crystallinity is between 85 to 90%. Elder powders (1 - 6 weeks) have a crystallinity which correspond to the conventional PEG's.

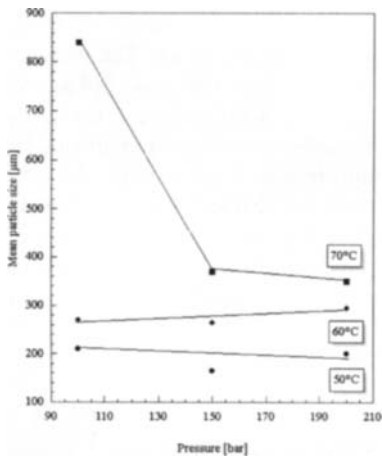


Fig. 7: Particle Size of PEG 4000 as function of pressure and temperature

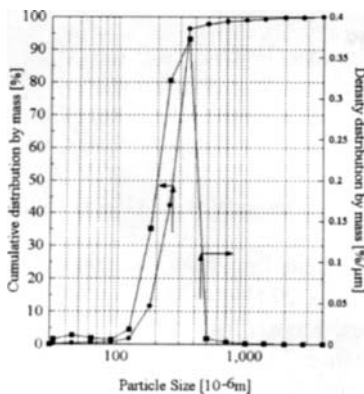


Fig. 8: Cumulative distribution and density distribution by mass of PEG 1500

- In the investigated pressure range the saturation pressure has almost no influence on the mean particle size (fig. 7). With increasing temperature the obtained particles become bigger.

The increase in particle size at high saturation temperature (70 °C) and low pressure (100 bar) indicates, that at these conditions the substance is not completely powderous.

- Pressure and temperature have almost no influence on the bulk densities. Freshly produced powders ($T_{\text{sat}} = 50$ and 60 °C) of PEG 4000 have bulk densities between 105 and 130 kg/m³.
- The diameter of the nozzle influences the mean particle size. Spraying of PEG 4000 in the pilot plant with a 0,4 mm nozzle result in mean particles sizes of 170 - 370µm (depending on saturation temperature, fig.7). A 1 mm nozzle gave particles between 350 - 500µm.

An increase in nozzle dimensions gave also an increase in bulk densities. The bulk densities of the powders obtained with 1 mm nozzle are about 50% higher than those of the 0.4 mm nozzle.

- The particle size distributions (PSD) are quite narrow. As an example the PSD of PEG 1500 which has been saturated at 45 °C and 120 bar with CO₂ is shown in Fig. 8.
- An easy-to-measure indication that the starting conditions does not allow to obtain a completely powderous product is the temperature in the spray tower, which is than in the range of the melting point of PEG. In this case a further cooling can be achieved by adding additional CO₂ before the expansion of the gas saturated solution. By this method the temperature after expansion may be brought to low values, e.g.

20- 40 K below the melting point. The overall CO₂ consumption rises from 0,17 - 0,3 kg / 1 kg of PEG to 0,4 - 0,7 kg / 1 kg of powdered PEG. At the same time the mean particle size is decreased by a factor of up to three compared to the experiments without CO₂-addition.

5.SUMMARY

The PGSS-Process is a versatile and simple method to produce fine dispersed powder of Polyetheneglycols. Compared to milling processes it allows to treat not only PEG with lower molar mass (which are too greasy), but also polymers with higher molar mass (up to 35.000 g/mol), which are too hard for grinding in conventional machines. The particles are relatively small (150 to 400 µm), with bulk densities between 100 and 180 kg/m³. By adjusting suitable process parameters (temperature, nozzle, CO₂-addition) the particles, particle size distribution and the morphology can be adapted to specific requirements. Due to the good solubility of CO₂ in PEG the gas consumption is low. Typical ratios are between 0,17 to 0,8 kg of gas per 1 kg of PEG powder. These values are also low compared to classical processes like spray drying, solvent crystallisation or freeze grinding. Typical values of gas consumption (e.g. drying or cooling gas) for such processes are from 2 to 20 kg gas/kg solid. The PGSS-produced PEG powders are solvent free, which is an important boundary condition e.g. for pharmaceutical applications.

REFERENCES

1. E. Weidner, Z. Knez, and Z. Novak, Proceedings of the 3rd International Symposium on Supercritical Fluids, Strasbourg, France, T3 (1994) 229.
2. E. Weidner, Z. Knez, and Z. Novak, "Process for Preparing Particles or Powders, -PCT patent application 1995, WO 95/21688.
3. S. Ali, Zeitschrift für Physikalische Chemie Neue Folge, 137 (1983) 13.
4. M. Daneshvar, and E. Gulari, ACS Symp. Ser. (Supercrit. Fluid Sci. Technol.), 406 (1989) 72.
5. M. Daneshvar, S. Kim, and E. Gulari, J. Phys. Chem., 94 (1990) 2124.
6. E. Kiran, V. P. Saraf, and Y. L. Sen, Int. J. Thermophys., 10(2) (1989) 437.
7. S. K. Kumar, U. W. Suter, and R. C. Reid, Fluid Phase Equilibria, 29 (1986) 373.
8. M. A. McHugh and V. J. Krukoni, Encycl. Polym. Sci. Eng., Wiley Publisher, New York, N.Y., 16 (1989).
9. W. H. Tuminello, G. T. Dee, and M. A. McHugh, Macromolecules, 28 (1995) 1506.
10. D. C. Bonner, Polym. Eng. Sci., 17(2) (1977) 65.
11. R. A. Davis, R. E. Menéndez, and O. C. Sandall, J. Chem. Eng. Data, 38 (1993) 119.
12. A. Garg, E. Gulari, and C. W. Manke, Macromolecules, 27 (1994) 5643.
13. L. J. Gerhardt, A. Garg, C. Manke, and E. Gulari, Proceedings of the 3rd International Symposium on Supercritical Fluids, Strasbourg, France, T3 (1994) 265.
14. E. Weidner, V. Wiesmet, Z. Knez, and M. Skerget, submitted to J. Supercrit. Fluids, (1996).
15. E. Weidner, Habilitationsschrift, Erlangen 1996, submitted

Regeneration of Loaded Supercritical Carbon Dioxide with Activated Carbon

I. Reiß, A. Schleußinger, S. Schulz

University of Dortmund, Institute for Thermodynamics, Emil-Figge-Str. 70, D - 44227 Dortmund, Germany

Supercritical fluid extraction (SFE) is a suitable process for many separation problems. The regeneration of the supercritical fluid is as important as the extraction step itself. Therefore this paper presents a method to do this in a more isobaric way than the customary pressure reduction regeneration. For the example of soil remediation we have investigated the activated carbon regeneration of supercritical carbon dioxide loaded with the low-volatile polycyclic aromatic hydrocarbon (PAH) pyrene. Characteristics of supercritical fluid extraction for soil remediation are elevated temperatures and pressures up to 370 K and 300 bar. For this reason adsorption isotherms of pyrene on activated carbon up to these conditions are measured first. Subsequently this method is used to regenerate carbon dioxide in a closed solvent cycle plant with a 4 l extractor. An economic analysis using these results indicate that the soil remediation costs will decrease for about 20 - 30 % by means of an activated carbon adsorber.

1. INTRODUCTION

In recent years, supercritical fluid extraction has received widespread attention for the removal of non- or low-volatile organic components from liquid and solid matrices. This process has many potential applications like analytical extractions, applications in the food and drug industry, activated carbon regeneration or soil remediation.

In the field of soil remediation, a great number of bench scale experimental and theoretical studies have been published showing the applicability of the SFE process for the cleanup of hydrocarbon contaminated soils for instance [1-4]. For further process development from laboratory plant scale to technical plant scale the expense of the cleanup are the main criterion if the efficiency of the SFE has been proved successfully. Whereas the extraction step of the SFE is well examined in the literature, possibilities for regenerating the loaded supercritical fluid are only investigated by few authors [5,6]. For a process in larger scale the regeneration and recycle of the supercritical fluid is a must to lower the costs of the SFE.

A great advantage of supercritical fluids is the possibility to separate the extracted solute from the solvent by simple pressure reduction to subcritical pressures. The solubility of most solutes in supercritical fluids virtually vanishes and therefore the solutes precipitate at these conditions. For example, pyrene solubil-

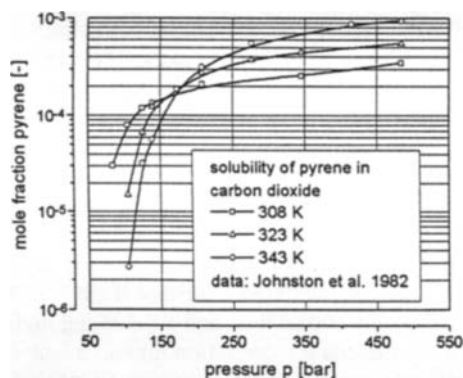


Figure 1. pyrene solubility in carbon dioxide [7]

ity isotherms are shown in figure 1. It can be realised that the solubility of pyrene decreases several orders of magnitude in the vicinity of the critical pressure of carbon dioxide (73.8 bar). But the disadvantage of this separation process is the high specific energy consumption for recompressing the solvent. Therefore, alternative separation processes with a smaller pressure reduction or isobaric methods like absorption, adsorption or the use of membranes are interesting. Up to now results for a supercritical fluid separation by membranes are disappointing due to blocked and compacted membranes and very small permeating solvent streams [6]. On the other hand the absorptive regeneration of supercritical fluids is already used in technical scale for example for the regeneration of caffeine loaded carbon dioxide by water [8]. This is feasible due to the very low solubility of the absorbent water in carbon dioxide and the hydrophilic nature of the solute caffeine. But most of the organic liquid absorbents are miscible with carbon dioxide at high pressures so it is very difficult to find an absorbents for hydrophobic solutes like PAH with very low solubility in carbon dioxide. For that the most favourable technique is the adsorption at activated carbon because activated carbon has a high adsorption capacity and very low output concentrations can be achieved. This kind of separation is also used for the regeneration of carbon dioxide loaded with caffeine up to pressures of 30 MPa and temperatures up to 318 K [9]. In our research work we transfer this separation for the regeneration of carbon dioxide in a closed solvent-cycle-plant for the remediation of soil which is contaminated with low-volatile PAH pyrene.

2. ADSORPTION ISOTHERMS

Adsorption isotherms of pyrene on activated carbon were obtained by measuring breakthrough curves. The adsorption experiments involved passing a stream of carbon dioxide containing a known concentration of pyrene through a bed of activated carbon and monitoring the UV absorbance of the column effluent until breakthrough occurred. Mathematical analysis of these curves allows the construction of adsorption isotherms. A schematic diagram of the experimental apparatus is presented in figure 2.

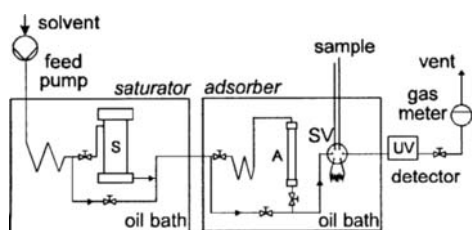


Figure 2. setup of the adsorption apparatus

Liquid carbon dioxide is charged into a high-pressure liquid pump and compressed to the desired pressure. The stream is passed through a preheater in the first oil bath, where it is brought to bath temperature, and through a column (saturator), filled with a mixture of 1 mm diameter glass beads and the organic solid solute of interest in excess. Disks of sintered metal at the ends of the column prevent entrainment of the solute. After exiting the first column, the saturated carbon dioxide flows into a second oil bath, where it is heated to the adsorption temperature. In this second oil bath, the carbon dioxide passes through another column (adsorber), filled with activated carbon. Both columns could be bypassed, the adsorption column could be completely isolated if necessary. Then the effluent flows through a 6-port sample valve with a 100 μ l loop and a following high-pressure UV detector. The UV detector provides a continuous concentration measurement of the effluent. The 6-port valve is used, to take samples of the carbon dioxide stream for analysis and calibration of the UV detector. For this the loop volume is injected into a pressurised stream of a suitable HPLC solvent. This mixture is carefully discharged into a tared vial, and

the sample is then analysed by HPLC. The UV detector provides a continuous concentration measurement of the effluent. The 6-port valve is used, to take samples of the carbon dioxide stream for analysis and calibration of the UV detector. For this the loop volume is injected into a pressurised stream of a suitable HPLC solvent. This mixture is carefully discharged into a tared vial, and

the sample loop and tubing is flashed with additional solvent. This mixture is analysed by HPLC. Finally, the flowrate and the total amount of carbon dioxide is monitored by a gas meter, placed after the metering valve. The temperatures of the two oil baths are controlled within 0.1 K and the pressure is measured and controlled with an accuracy of ± 0.03 MPa. The carbon dioxide flowrates used during the experiments ranged from 0.3 to 0.5 l/min at STP.

The technique with two different oil baths enables one to achieve different solute concentrations

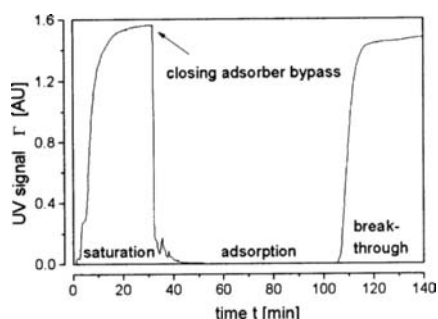


Figure 3. typical breakthrough curve

in the carbon dioxide by adjusting the temperature of the first oil bath. But it is important to note that this setup has some limitations due to the order of the solubilities in the two oil baths. To prevent supersaturation and precipitation of the solid solute in the adsorber oil bath, the temperatures of the oil baths has to be adjusted according to the pressure. For a pressure below the crossover pressure (see figure 1) the adsorber temperature must be lower than the saturator temperature, and vice versa above the crossover pressure. A typical breakthrough curve is shown in figure 3. There is nearly no pyrene in the carbon dioxide stream during the adsorption

time and the breakthrough curve is very steep.

Results of these experiments are shown in figure 4 and figure 5. The particle size of the used activated carbon (supplied by Merck) was 0.3 mm with a N_2 -BET surface of approximately $600 \text{ m}^2/\text{g}$. Figure 4 shows the adsorption isotherms as a function of the pyrene concentration in the inlet stream at different temperatures and a pressure of 250 bar. Figure 5 presents the dependence on temperature and pressure at saturation conditions due to figure 1 in the inlet. Lines in figure 4 are results of a regression between the measured adsorption data and the Freundlich model for adsorption. The Freundlich isotherm provides a good fit and describes the general shape of the experimental data.

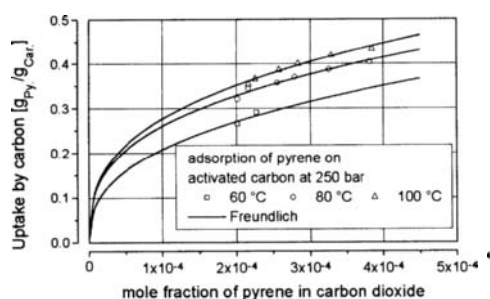


Figure 4. adsorption isotherms for pyrene

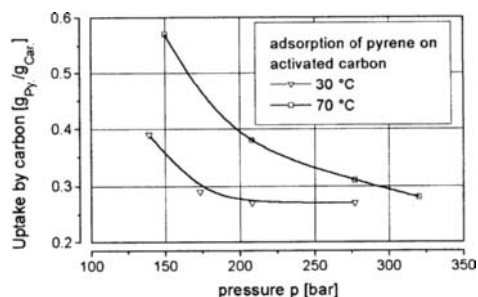


Figure 5. pressure influence on the adsorption

The adsorption capacity of activated carbon for pyrene is very high (up to 0.6 g/g). The uptake decreases with increasing pressure but increases with temperature. This is in correspondence with results from literature found for the adsorption of DDT [10] or phenanthrene [11] on activated carbon. One important information is the shape of the adsorption isotherms. This kind of isotherm shape is generally favourable for adsorption. For that it is possible to regen-

erate loaded carbon dioxide with activated carbon moreover even at 300 bar and 70 °C the uptake is roughly 0.3 g/g. But on the other hand it would be nearly impossible to regenerate PAH loaded activated carbon by supercritical carbon dioxide.

3. CARBON DIOXIDE REGENERATION

The setup of the technical scale extraction plant with a capacity up to 6 kg soil and a possible carbon dioxide mass flow of 40 kg/hr in a closed-solvent-cycle is shown in figure 6. The carbon dioxide from the storage tank reaches extraction conditions by passing a pump and a heat exchanger. The carbon dioxide flows through the extractor and gets loaded with the contaminants. After pressure reduction the solvent is led into the separation vessel where the solid contaminants either precipitate due to pressure reduction or deposit on activated carbon. A more detailed drawing of the separator with the basket filled with activated carbon is shown in figure 7. The regenerated solvent flows back into the storage tank and can be used again for extraction.

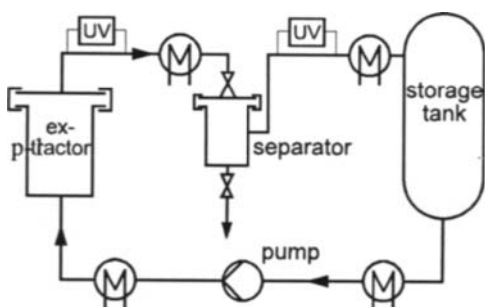


Figure 6. extraction plant

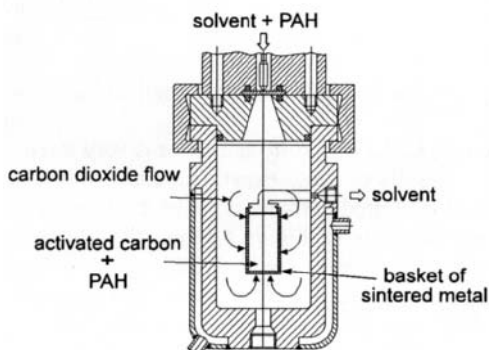


Figure 7. design drawing of the separator

The extraction plant is equipped with two UV detectors, one after the extractor and the other after separator to provide a continuous concentration measurement of the effluents. Moreover it is possible to take samples of the carbon dioxide at the same places for analysis and calibration of the UV detectors (not shown in figure 6) the same way as described for adsorption isotherms measurement.

Figure 8 shows the course of pyrene concentration in the carbon dioxide stream leaving the extractor and the separator for an extraction of pyrene contaminated sand at 180 bar and 80 °C and a pressure reduction regeneration at 90 bar and 60 °C (supercritical conditions, too). It is obvious that the pyrene concentration in the extractor effluent reaches high values up to 430 mg/kg. The saturation concentration at these conditions is about 1100 mg/kg (see figure 1). Due to the volume of the piping between extractor and separator and the volume of the separator itself the concentration in the separator effluent raises only weakly and has a slight maximum with about 40 mg/kg long time after the highest concentration in the extractor effluent was reached.

Figure 9 presents the effluent concentrations of the separator. Due to the pressure resistance of the separator only adsorption pressures up to 120 bar can be realised. So an isobaric regeneration of the carbon dioxide was not possible. Results for 110 bar and 70 °C

(supercritical conditions) are shown in figure 9. There is a significant difference between the pressure- and the pressure-adsorption-separation (note the axis break). Due to the construction of the sintered metal basket filled with activated carbon there was first still a certain pyrene concentration in the carbon dioxide because of a possible short circuit flow (see figure 7). This was changed by another construction of the basket blocking the upper section of the sintered metal basket. The results with this basket are significantly better. Now there was almost no pyrene in the effluent detectable. Although an isobaric regeneration was not possible, these results show the possibility to raise the separator pressure without getting a worsen separation. Figure 9 shows also the influence of water on the separation (dotted line). Water is a natural part of soil, so in practice the carbon dioxide gets loaded with water during the extraction step. For that experiments were made with moistened (10 weight percent water) soil, but only a small influence on the regeneration could be investigated, which has to be regarded in detail elsewhere.

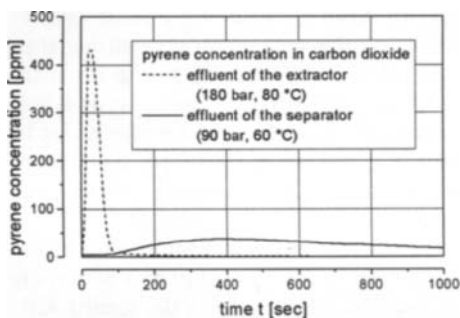


Figure 8: course of concentration in the extractor and separator

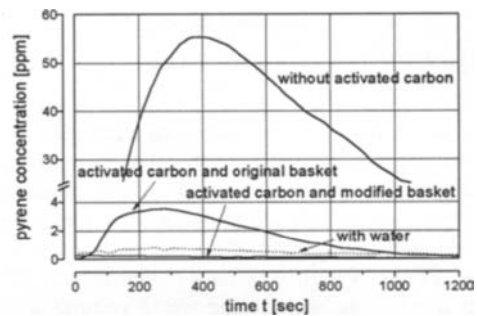


Figure 9: influence of activated carbon on the separator concentration at 110 bar, 70 °C

4. ECONOMIC ANALYSIS

Calculations of treatment costs for supercritical soil remediation were made with a computer model that evaluates the capital and operating costs depending on plant capacity, carbon dioxide conditions for extraction and separation, operating conditions, soil transport and pre-treatment and other boundary conditions like maintenance, depreciation or insurance. Some additional important parameters for the plant design are given in table 1.

Table 1
Parameters for a proposed SFE technical plant

Material	pyrene contaminated soil 400 mg/kg
Extraction Conditions and Time	300 bar, 140 °C, 1.0 hr
Solvent	23.000 kg/hr carbon dioxide
Operation	2 shifts, 5 days/week, 40 weeks/yr.
Extractor	2 with 2.3 m ³ volume
Capacity	10.000 t/yr. (bulk density 1.300 kg/m ³)
Time for Depreciation	4 years
Activated Carbon Capacity	0.3 g/g
Activated Carbon Replacement and Incineration	7 \$/kg

Results of these calculations are shown in figure 10 depicting the costs for personnel, investment, energy and accessory agents like make up carbon dioxide or activated carbon as a function of the separation pressure. The separation temperature is fixed by the isenthalpic expansion from extraction conditions to separation pressure. Costs for activated carbon include replacement and waste disposal by incineration. This figure indicates that the costs will decrease for about 20 - 30 % by the use of an activated carbon adsorber for the carbon dioxide regeneration. The reasons are the smaller energy consumption and lower investment cost due to a smaller pump and heat exchangers. The costs for the accessory agents raises because of the activated carbon. But this cost increase is smaller than the other costs decrease so the summary costs for the SFE will decrease. It is important to note that the presented treatment costs of about 200 \$ per ton soil are only a clue to show the influence of the activated carbon regeneration. Costs down to 100 \$ per ton soil are reachable for SFE plants with greater capacities and other boundary conditions. These costs compare favourably with other soil treatment techniques.

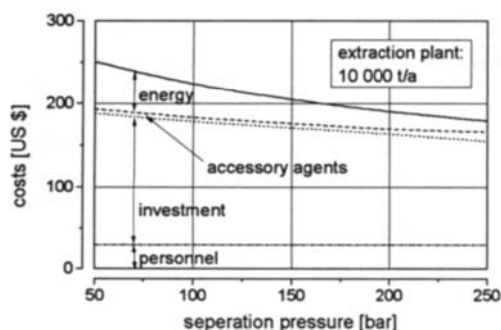


Figure 10. Influence of separation pressure on the costs for soil remediation

However, one limit of the regeneration by activated carbon is the contamination level of the soil. For soils with very high contamination levels (some thousands of mg/kg) this process is not practicable because the waste volume reduction from the treated soil to the loaded activated carbon would not be significant. For example 16.7 kg activated carbon with a capacity of 0.3 g/g are necessary to deposit the pyrene of 1 ton soil with a contamination level of 5.000 mg/kg on it. So the cost increase by activated carbon replacement and disposal would be greater than the cost reduction due to energy and investment.

REFERENCES

1. Andrews, A. T.; Ahlert, R. C.; Kosson, D.S.; *Environmental Progress* 1990, 9(4), 204.
2. Dooley, K. M.; Ghonasgi, D.; Knopf, F. C.; Gambrall, R. P.; *Environmental Progress* 1990, 9 (4), 197.
3. Hess, R. K.; Erkey, C.; Akgerman, A.; *J. Supercritical Fluids* 1991, 4, 47.
4. Brady, B. O.; Kao, C.-P. C.; Dooley, K. M.; Knopf, F. K.; Gambrell, R. P.; *Ind. Eng. Chem. Res.* 1987, 26, 261.
5. Madras, G.; Erkey, C.; Akgerman, A.; *Environmental Progress* 1994, 13(1), 45.
6. Birtigh, A.; Brunner, G.; *Chem.-Ing.-Tech.* 1995, 7, 829.
7. Johnston, K.P.; Ziger, D.H.; Ekert, C.A.; *Ind. Eng. Chem. Fundam.* 1992, 21, 191.
8. Zosel, K.; *Chemie für Labor und Betriebe*, 1977, 28, 262.
9. McHugh, M.; Krukonis, V.; *Supercritical Fluid Extraction*; Butterworth-Heinemann, 1994
10. Macnaughton, S.J.; Foster, N.R.; *Ind. Eng. Chem. Res.* 1995, 34, 275.
11. Madras, G.; Erkey, C.; Akgerman, A.; *Ind. Eng. Chem. Res.* 1993, 32, 1163.

A New Mixing Rule for Accurate Prediction of High Pressure Vapor-Liquid Equilibria of Gas/Large n-Alkane Systems

Chongli Zhong and Hirokatsu Masuoka*

Department of Chemical Engineering, Faculty of Engineering
Hiroshima University, Higashi-Hiroshima 739, JAPAN

ABSTRACT

By introducing a correction factor to the G^E from the UNIFAC in the MHV1 model, a new mixing rule was proposed, which could accurately predict high pressure VLE of gas/n-alkane systems. The correction parameters have been generalized as a simple function of carbon number for CO_2 /n-alkanes, CH_4 /n-alkanes and C_2H_6 /n-alkanes, respectively. The results showed that the new mixing rule could give satisfactory VLE predictions for both binary and ternary systems, which is particularly useful for engineering purposes.

Key words: Vapor-liquid equilibria, Gas/large n-alkanes, High pressure, Mixing rule, Equation of state, UNIFAC.

1. INTRODUCTION

Combination of excess Gibbs free energy(G^E) model with equation of state(EOS) was first proposed by Vidal(1978). The method has been receiving much attention since then, and a lot of attempts have been made to improve it to allow simple EOSs to describe complex systems(Huron and Vidal, 1979; Michelsen, 1990a,b). Though any G^E models can be used, the predictive ones such as UNIFAC are of rather usefulness, as only these allow the EOSs to become strictly predictive tools. As a result, the Michelsen mixing rules(Michelsen, 1990b; Dahl and Michelsen, 1990) coupled with UNIFAC(both original UNIFAC and modified UNIFAC) have been widely tested and used to predict VLE of complex systems of similar sizes successfully(Dahl and Michelsen, 1990; Dahl et al., 1991; Holderbaum and Gmehling, 1991). Unfortunately, when they are applied to highly asymmetric systems, for example gas/large n-alkane systems, the predictive accuracy is poor,

* Author to whom correspondence should be addressed.

which becomes worse with increasing carbon number. As a result, more accurate predictive models are necessary, which is the motive of this work, and an attempt has been made to improve the predictive accuracy of one of the existing models, MHV1, for gas/large n-alkane systems in this work.

2. THERMODYNAMIC MODEL

2.1. The Equation of State

Although any two-parameter cubic EOS can be used, the SRK EOS(Soave, 1972) was adopted in this work. Since it is a famous EOS, it is no necessary to give detailed introduction here.

2.2. The Excess Gibbs Free Energy Model

The original UNIFAC model(Fredenslund et al., 1975) was used in this work, as it is a widely applicable model with the most available parameters which are updated and extended regularly. For gas/n-alkane systems, temperature dependent interaction parameters were used, and the UNIFAC expression:

$$\psi_{nm} = \exp\left(-\frac{a_{nm}}{T}\right) \quad (1)$$

was replaced by(Holderbaum and Gmehling,1991):

$$\psi_{nm} = \exp\left(-\frac{a_{nm} + b_{nm}T + c_{nm}T^2}{T}\right) \quad (2)$$

The volume and area parameters for CO₂, CH₄ and C₂H₆, and the interaction parameters for gas/CH₂ pairs were obtained by Holderbaum and Gmehling(1991).

2.3. Mixing Rules

2.3.1. MHV1(Michelsen,1990b)

By equating the G^E from an EOS at zero pressure to that from a G^E model, a mixing rule was proposed by Michelsen(1990b) as follows:

$$\alpha = \sum_i z_i \alpha_i + \frac{1}{q_1} \left[\frac{G^E}{RT} + \sum_i z_i \ln\left(\frac{b_m}{b_i}\right) \right] \quad (3)$$

and

$$b_m = \sum_i z_i b_i \quad (4)$$

where z_i is mole fraction of component i , $\alpha = a_m/(b_m RT)$. q_1 is EOS-dependent, which is set to -0.64663 for SRK EOS(Holderbaum and Gmehling, 1991).

2.3.2. LCVM model(Boukouvalas et al., 1994)

Recently, Boukouvalas et al.(1994) proposed a new mixing rule, which is a linear combination of Vidal(1978) and Michelsen(1990b) mixing rules:

$$\alpha = \lambda \alpha_v + (1 - \lambda) \alpha_M \quad (5)$$

where α_v and α_M are given by expressions from Vidal and Michelsen mixing rules, respectively. Their relative contributions to α are determined by a weight factor λ .

2.3.3. New mixing rule(MR1)

The G^E/RT from the original UNIFAC, the SRK EOS with MHV1, and the experimental data from Shen et al.(1990) for the system n-C₆H₁₄/n-C₁₆H₃₄ at 298.15 K and 0.1 bar are shown in Fig. 1.

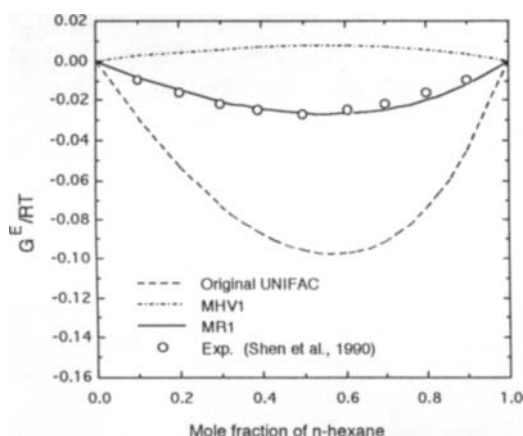


Fig. 1 G^E/RT versus mole fraction of n-hexane for n-hexane + n-hexadecane at 298.15 K and 0.1 bar.

From the figure, two points can be drawn. (1) SRK EOS with MHV1 can not reproduce the G^E of the G^E model used in the mixing rule for asymmetric systems even at low pressure. (2) The original UNIFAC is not accurate for asymmetric systems with large n-alkanes. The first point reflects the defect of MHV1 for asymmetric systems, while the second point is caused by the bad predictability of UNIFAC for systems containing large n-alkanes. However, it was interested to find that when a

correction factor was added to the G^E from the original UNIFAC in MHV1, that is using $G_{EOS}^E = 1.36 G_{UNIFAC}^E$ instead of $G_{EOS}^E = G_{UNIFAC}^E$, the SRK EOS with MHV1 could reproduce the experimental G^E data very good(Fig. 1). The fact led us to propose a modified mixing rule as follows:

$$\alpha = \sum_i z_i \alpha_i + \frac{1}{q_1} \left[\frac{G^E}{RT} (1 + f) + \sum_i z_i \ln \left(\frac{b_m}{b_i} \right) \right] \quad (6)$$

where b_m is calculated with eq.(4). f is a parameter which can correct the defects of both the original UNIFAC and MHV1 for highly asymmetric systems. For symmetric systems, no correction is necessary, and f is set to be zero. In this case, MR1 reduces to MHV1.

3. Results and Discussion

3.1. Binary Systems

3.1.1. CO₂/n-alkane systems

CO₂ is an important industrial gas, consequently, the study of phase behavior of CO₂/n-alkane systems is necessary. Though they are nonpolar systems, the predictive accuracies of MHV2(Dahl and Michelsen, 1990) and PSRK(Holderbaum and Gmehling, 1991, using MHV1) are dramatically bad for large n-alkanes (Boukouvalas et al., 1994). So, it is necessary to do some modification to improve the predictive accuracy for them, which is the motive of this work.

The average absolute deviation(AAD) of vapor pressure versus carbon number for CO₂/n-alkanes for SRK EOS with MHV1

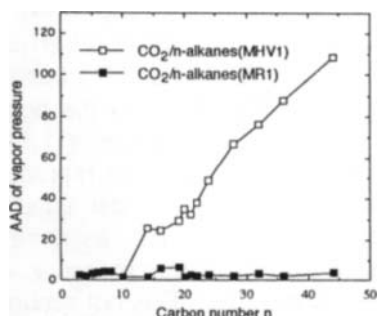


Fig. 2 AAD of vapor pressure versus carbon number for CO₂/n-alkane systems

carbon number is proposed:

$$f = 0.215 + 0.00375n \quad (n > 10) \quad (7)$$

and

$$f = 0 \quad (n \leq 10) \quad (8)$$

where n is carbon number.

The AADs of vapor pressure for MR1 with eq.(7) were shown in Fig.2, and the grand AAD was listed in **Table 1**, where the results for LCVM and MHV1 were also listed. Obviously, MR1 showed much better accuracy than MHV1, which is also better than LCVM, especially for relatively large n-alkanes.

It should be pointed out that for MHV1 and MR1, the UNIFAC group interaction parameter were obtained with VLE data for CO₂/n-alkanes up to n-C₁₀H₂₂ (Holderbaum and Gmehling, 1991), while for LCVM, VLE data up to n-C₂₈H₅₈ were used(Boukouvalas et al., 1994).

is shown in **Fig.2**(The definition of AAD is shown in the footnotes of Table 1). It is evident that when the carbon number is larger than about 10, the errors rapidly become large. So, it is necessary to improve the accuracy for systems of carbon number larger than 10.

Based on the analysis of the optimum parameters for MR1 for large n-alkanes from n-C₁₄H₃₀ to n-C₄₄H₉₀, a linear function of

3.1.2. C₂H₆/n-alkane and CH₄/n-alkane systems

The AADs of vapor pressure for C₂H₆/n-alkanes and CH₄/n-alkanes were shown

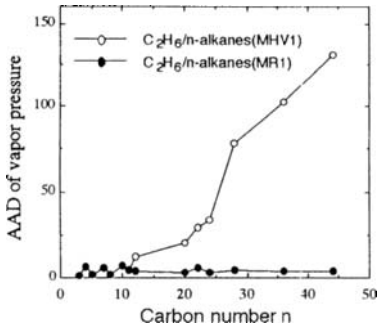


Fig. 3 AAD of vapor pressure versus carbon number for C₂H₆/n-alkane systems

Using similar methods, two simply generalized expressions were obtained.

For C₂H₆/n-alkanes:

$$f = 0.315 + 0.00375n \quad (n > 10) \quad (9)$$

For CH₄/n-alkanes:

$$f = -0.317 + 0.441 \log n \quad (n > 10) \quad (10)$$

The results for MR1 with eqs.(9) and (10) were shown in Figs. 3 and 4, respectively, and the grand AADs were listed in Table 1. Obviously, MR1 gave much better accuracy than MHV1, and also better than LCVM.

Table 1. Comparisons of different mixing rules

system**	AAD*		
	MHV1	LCVM	MR1
CO ₂ /n-alkanes ^a	52.2	5.4	3.0
C ₂ H ₆ /n-alkanes ^b	58.5	5.3	4.0
CH ₄ /n-alkanes ^c	63.5	6.6	5.3
CO ₂ /n-C ₁₅ /n-C ₁₆	11.1	10.0	2.0
CH ₄ /C ₂ H ₆ /n-C ₂₂	51.6	0.5	2.4

* $AAD = (1/N) \sum |p^{exp.} - p^{cal.}| / p^{exp.} \times 100$

** For data sources see Zhong and Masuoka, 1996

^a n-C₁₄, n-C₁₆, n-C₁₉₋₂₂, n-C₂₄, n-C₂₈, n-C₃₂, n-C₃₆, n-C₄₄

^b n-C₁₂, n-C₂₀, n-C₂₂, n-C₂₄, n-C₂₈, n-C₃₆, n-C₄₄

^c n-C₁₂, n-C₁₆, n-C₂₀, n-C₂₈, n-C₃₆

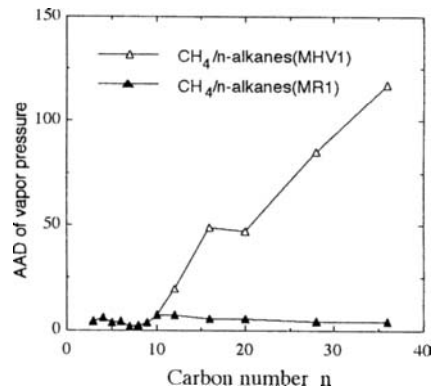


Fig. 4 AAD of vapor pressure versus carbon number for CH₄/n-alkane systems

3.2. Multicomponent Systems

The following expression was proposed for mixture parameter f of multicomponent systems:

$$f = \sum_i \sum_j \left(\frac{z_i + z_j}{2} \right) f_{ij} \quad (11)$$

where f_{ij} is the parameter f for binary components i and j , and $f_{ij}=f_{ji}$, $f_{ii}=0$. Obviously, for a binary system, $f=f_{12}$, eq.(11) results in the same f as used before.

Two ternary systems have been used to test the three models. The results were listed in Table 1, which showed that MR1 also worked well for ternary systems.

4. CONCLUSIONS

A new mixing rule has been proposed and tested coupled with SRK EOS and UNIFAC in this work. The new mixing rule, which is obtained by introducing a correction parameter to the G^E from the original UNIFAC in MHV1, is accurate for both binary and ternary gas/large n -alkane systems. The correction parameters have been correlated as a simple function of carbon number for a certain kind of gas/ n -alkane system, which is convenient for engineering purposes.

Finally, we would like to point out that in this work SRK EOS is used to test the new mixing rule, but we believe it is applicable to other cubic EOSs, though the correction factor to G^E from UNIFAC may be different.

REFERENCES

- Boukouvalas, C., N. Spiliotis, P. Coutisikos, N. Tzouvaras and D. Tassios, *Fluid Phase Equilibria*, **92**(1994)75-106.
- Dahl, S., Aa. Fredenslund and P. Rasmussen, *Ind. Eng. Chem. Res.*, **30**(1991)1936-1945.
- Dahl, S. and M.L. Michelsen, *AIChE J.*, **36**(1990)1829-1836.
- Fredenslund, Aa., R.L. Jones and J.M. Prausnitz, *AIChE J.*, **21**(1975)1086-1099.
- Holderbaum, T. and J. Gmehling, *Fluid Phase Equilibria*, **70**(1991)251-265.
- Huron, M.J. and J. Vidal, *Fluid Phase Equilibria*, **3**(1979)255-271.
- Michelsen, M.L., *Fluid Phase Equilibria*, **60**(1990a)47-58.
- Michelsen, M.L., *Fluid Phase Equilibria*, **60**(1990b)213-219.
- Shen, W., X.Q. An, P.J. McElory and A.G. Williamson, *J. Chem. Thermodyn.*, **22**(1990)905-914.
- Soave, G., *Chem. Eng. Sci.*, **27**(1972)1197-1203.
- Vidal, J., *Chem. Eng. Sci.*, **33**(1978)787-791.
- Zhong, C. and H. Masuoka, *J. Chem. Eng. Japan*, **29**(1996)315-322.

High Pressure Multiphase Equilibria in the Ternary System Carbon Dioxide-Water-1-Propanol

T. Adrian and G. Maurer

Lehrstuhl für Technische Thermodynamik, Universität Kaiserslautern, D-67653 Kaiserslautern, Germany

1. INTRODUCTION

Ternary high-pressure equilibria in systems gas-water-polar solvent are encountered for example in supercritical extraction of products from aqueous solutions with carbon dioxide and a polar entrainer or in supercritical fluid chromatography. At elevated pressures the phase behaviour of such ternary systems can be very complex. It has been recognized since the 1950s [1], that homogeneous liquid mixtures of water and a polar solvent split into two, in some cases even into three liquid phases when pressurized with gases like e.g. carbon dioxide. The liquid phase can coexist with a gaseous phase. As that phase is not very dense it contains only small amounts of water and polar solvent. It has been proposed to make use of such high-pressure multiphase equilibria e.g. for the recovering of alcohols and organic acids from aqueous solutions, but there are also other applications like the extractions of fermentation products from diluted brothes.

The present paper gives an overview of results on high-pressure phase equilibria in the ternary system carbon dioxide-water-1-propanol, which has been investigated at temperatures between 288 and 333 K and pressures up to 16 MPa. Furthermore, pressure-temperature data on critical lines, which bound the region where multiphase equilibria are observed were taken. This study continues the series of previous investigations on ternary systems with the polar solvents acetone [2], isopropanol [3] and propionic acid [4]. A classification of the different types of phase behaviour and thermodynamic methods to model the complex phase behaviour with cubic equations of state are discussed.

2. EXPERIMENTAL

Phase equilibria and pressure-temperature coordinates of critical points in ternary systems were taken with a high-pressure apparatus based on a thermostated view cell equipped with two liquid flow loops which has been described in detail elsewhere [3]. The loops feed a sample valve which takes small amounts of probes for gas-chromatographic analysis. In addition to temperature, pressure and composition data, the densities of the coexisting liquid phases are measured with a vibrating tube densimeter. Critical points were determined by visual observation of the critical opalescence.

3. PHASE BEHAVIOUR OF THE CARBON DIOXIDE-WATER-1-PROPANOL SYSTEM

The qualitative phase behaviour of the carbon dioxide-water-1-propanol system is discussed for the temperatures 303 and 333 K in Figure 1, where isothermal Gibbs phase diagrams are arranged in prisms to show the influence of pressure on phase equilibrium.

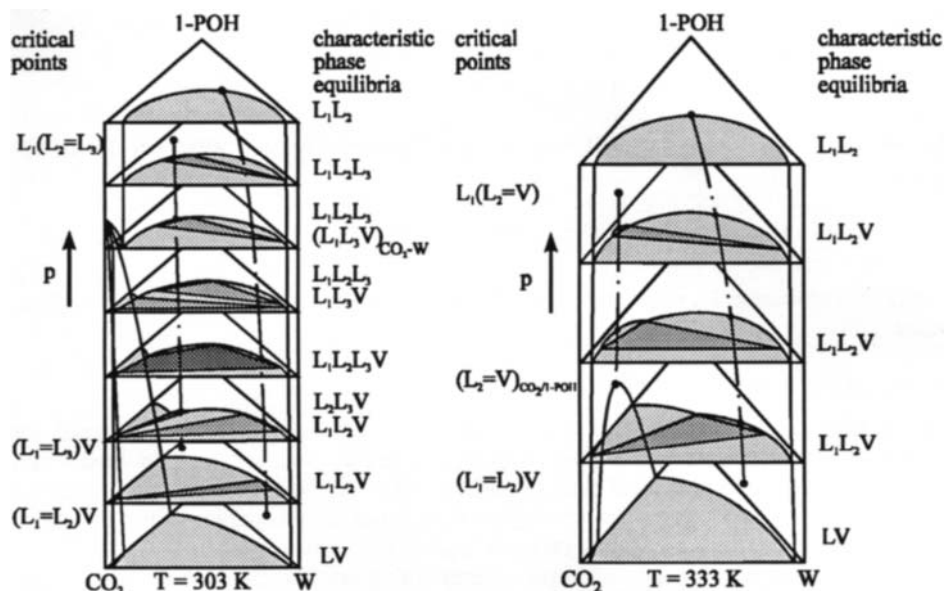





Figure 1. Qualitative diagram of the phase-behaviour of carbon dioxide-water-1-propanol at 303 (left) and 333 K (right);  two-phase region,  three-phase region,  four-phase region

The right prism in Figure 1 shows qualitatively the phase behaviour of the carbon dioxide-water-1-propanol system at 333 K. It is typical for many other systems containing carbon dioxide, water and a polar solvent. At low pressures, a vapor-liquid two-phase region LV stretches out from the carbon dioxide-water to the carbon dioxide-1-propanol binary system. When pressure is increased the liquid splits into two phases resulting in a liquid-liquid-vapor three-phase region L_1L_2V . It first appears at a lower critical point $(L_1=L_2)V$, where the two liquid phases are critical and coexist with the vapor phase. A dash-dotted line indicates the location of the critical points $(L_1=L_2)$. A second dash-dotted line is shown in that prism. It starts at the critical pressure of the vapor-liquid equilibrium in the binary carbon dioxide-1-propanol, and ends at an upper critical point $L_1(L_2=V)$, where the propanol-rich liquid phase L_2 and the vapor phase V are critical and coexist with the water-rich liquid phase L_1 . At higher pressures, only two-phase equilibria L_1L_2 are observed.

At lower temperatures, e.g. at 303 K, the phase behaviour is more complicated (Figure 1, left side). At low pressures the phase behaviour is very similar to that at 333 K. However at elevated pressure a second three-phase region L_2L_3V appears. With increasing pressure both three-phase regions approach, touch - forming a four-phase equilibrium $L_1L_2L_3V$ - and split again into two three-phase equilibria designated by L_1L_3V and $L_1L_2L_3$. According to the Gibbs phase rule an isothermal four-phase equilibrium can only exist at a single pressure. With further increasing pressure the L_1L_3V three-phase region does not disappear in a ternary critical point but degenerates to the binary three-phase equilibrium of carbon dioxide-water. The $L_1L_2L_3$ -region disappears at a much higher pressure at an upper critical point $L_1(L_2=L_3)$ similar to the behaviour of the three-phase equilibrium designated L_1L_2V at 333 K. At higher pressures only a two-phase equilibrium region designated by L_1L_2 remains.

Figure 2 shows a quantitative pressure-temperature diagram for the ternary system carbon dioxide-water-1-propanol. The location of four phase equilibria is represented by a line. Three-phase equilibria are found in areas, and three-phase equilibria, where two phases are critical are again represented as lines. Furthermore, the diagram shows the vapor-pressure curve of carbon dioxide and the binary three-phase line of the subsystem carbon dioxide-water. Increasing the pressures at 333 K, three-phase equilibria L_1L_2V are observed after passing the critical line $(L_1=L_2)V$. With further increasing pressure a second critical line $L_1(L_2=V)$ is reached, where the difference between the less dense liquid phase L_2 and the vapor phase V vanish in the three-phase equilibrium L_1L_2V .

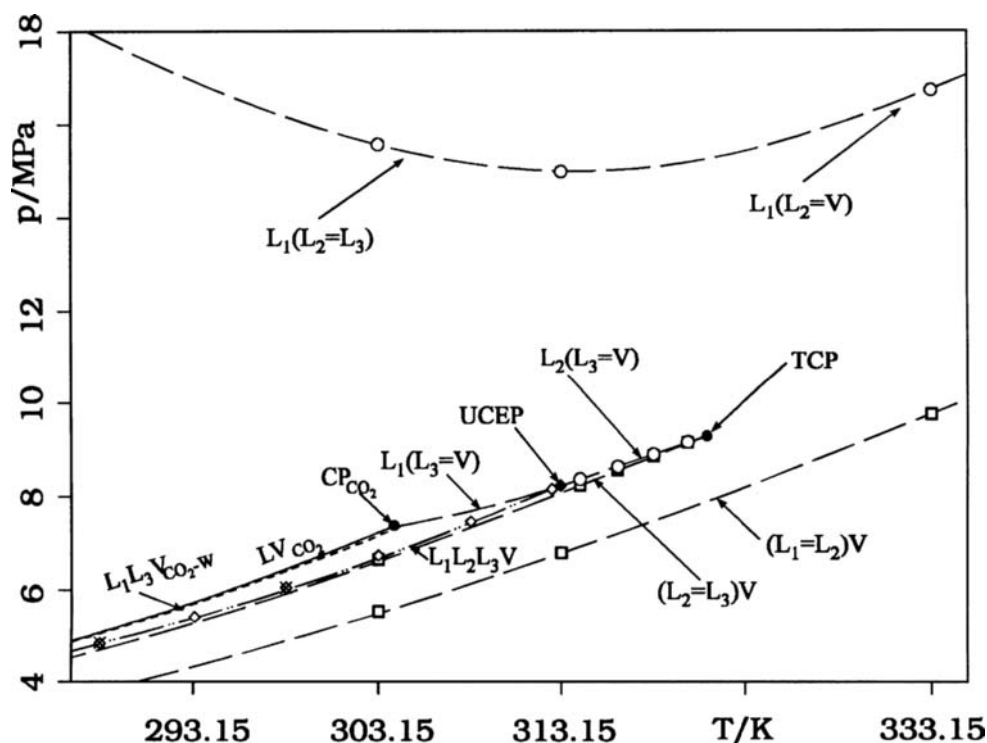


Figure 2. Quantitative pressure-temperature diagram for carbon dioxide-water-1-propanol; O, \square exp. ternary critical points, this work; \diamond four-phase equilibria, this work; \times four-phase equilibria, Fleck et al. [5]

At 303 K, with increasing pressure first the $(L_1=L_2)V$ -line and later the $(L_2=L_3)V$ line are crossed. In the small pressure range between both lines only three-phase equilibria L_1L_2V exist. In crossing the line $(L_2=L_3)V$, a second three-phase region L_2L_3V appears. At a somewhat higher pressure, the four-phase line is located, marking the condition where both three-phase equilibria touch. Above the four-phase line two three-phase regions, L_1L_3V and $L_1L_2L_3$, are found. The L_1L_3V region disappears at the three-phase pressure of the binary system carbon dioxide-water, the $L_1L_2L_3$ -region vanishes at the ternary critical line $L_1(L_2=L_3)$ at much higher pressures.

The four-phase line shows an upper critical endpoint (UCEP) at 313.10 K and 8.232 MPa. At higher temperatures an interesting phenomenon can be observed. With increasing temperature the two critical lines $(L_2=L_3)V$ and $L_2(L_3=V)$, which bound the three-phase region L_2L_3V , approach and finally meet at a common endpoint, a tricritical point where phases L_2 , L_3 , and V become critical simultaneously. The procedure to determine the tricritical point has been described previously [4]. The tricritical point TCP was determined to 320.75 K and 9.26 MPa.

4. CLASSIFICATION OF PHASE BEHAVIOUR

Pressure-temperature diagrams offer a useful way to depict the phase behaviour of multicomponent systems in a very condensed form. Here, they will be used to classify the phase behaviour of systems carbon dioxide-water-polar solvent, when the solvent is completely miscible with water. Unfortunately, pressure-temperature data on ternary critical points of these systems are scarcely published. Efremova and Shvarts [6,7] reported on results for such systems with methanol and ethanol as polar solvent, Wendland et al. [2,3] investigated such systems with acetone and isopropanol and Adrian et al. [4] measured critical points and phase equilibria of carbon dioxide-water-propionic acid. In addition, this work reports on the system with 1-propanol. The results can be classified into two groups. In systems behaving as described by pattern I, no four-phase equilibria are observed, whereas systems showing four-phase equilibria are designated by pattern II (cf. Figure 3).

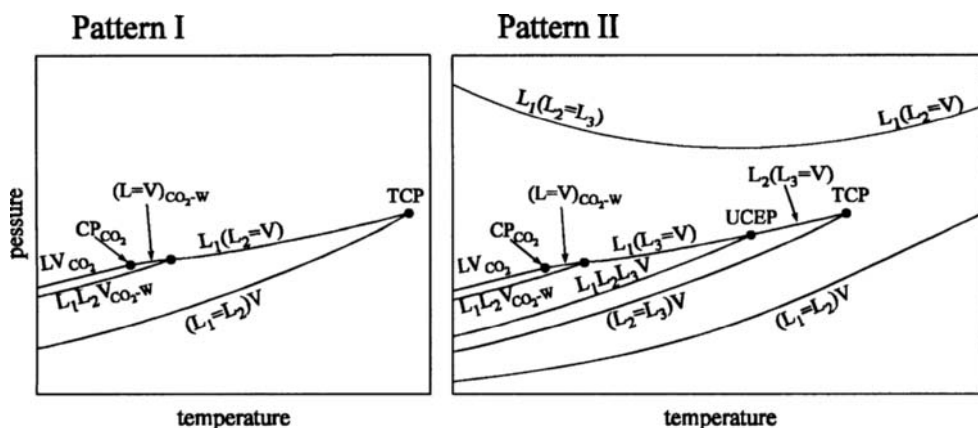


Figure 3. Classification of phase-behaviour for systems carbon dioxide-water-alcohol

The phase behaviour of systems with low molecular alcohols methanol and ethanol as well as of systems with acetone and propionic acid is relatively simple (pattern I). At lower pressures the single three-phase region is bound by a critical line $(L_1=L_2)V$, at higher pressure the three-phase region is limited by either an upper critical line $L_1(L_2=V)$ or the binary three-phase line of the system carbon dioxide-water depending on temperature.

The phase behaviour of systems with 1-propanol and isopropanol is designated by pattern II. It is more complicated. The most striking additional feature is the formation of a second three phase equilibrium region which leads to four-phase equilibria.

5. MODELING THE PHASE BEHAVIOUR OF THE CARBON DIOXIDE-WATER-1-PROPANOL SYSTEM WITH CUBIC EQUATIONS OF STATE

Due to restriction for space the results on modeling the high-pressure phase behaviour of the system carbon dioxide-water-1-propanol are presented only briefly. The model used in this work was the Peng-Robinson EOS [8] with an temperature dependent attractive term due to Melhelm et al. [9]. Although several mixing rules have been tested, the discussion will be restricted to the two-parameter mixing rule of Panagiotopoulos and Reid [10].

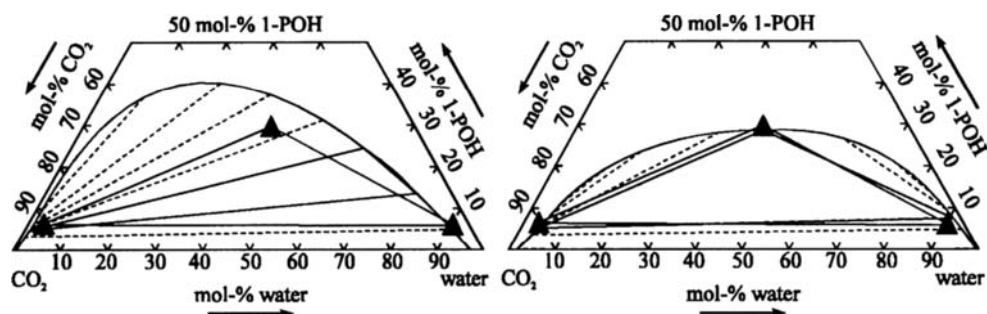


Figure 4. Three-phase equilibrium L_1L_2V in the system carbon dioxide-water-1-propanol at 333 K and 13.1 MPa; \blacktriangle exp., this work; --- Calculated with Peng-Robinson EOS using Panagiotopoulos and Reid mixing rule, left side: prediction from pure component and binary data alone, right side: interaction parameters fitted to ternary three-phase equilibria at temperatures between 303 and 333 K

Figure 4 shows a comparison between experimentally determined and calculated phase equilibria. When all parameters are determined from pure component and binary data alone, only a qualitative description of the ternary phase behaviour is possible in that system. Although the equation of state predicts all critical lines found in the experiment, the quantitative representation is poor regardless of the mixing rule. For example, the pressure predicted for the upper critical line $L_1(L_2=L_3)$ is too large by a factor of about 7 (about 100 MPa in comparison to experimental pressures of around 15 MPa, depending on temperature). In addition the predicted area of liquid-liquid phase-equilibria is also too large. The presentation of the ternary phase behaviour can be considerably improved by fitting binary interaction parameters to data of ternary three-phase equilibria. Figure 5 shows the resulting pressure temperature diagram calculated by the equation of state using interaction parameters fitted to ternary data. Although interaction parameters were fitted to three-phase equilibria, the correlation is not able to represent the experimental data within the experimental uncertainty. Thus more work is required for the presentation of high pressure multiphase equilibria in aqueous systems.

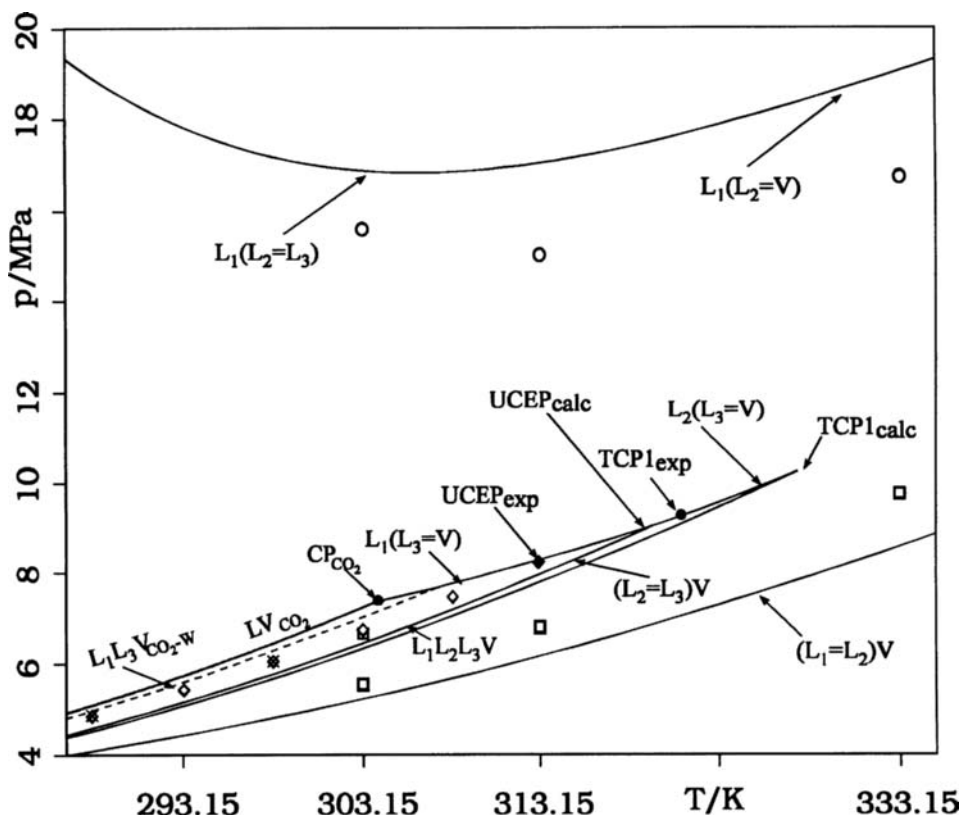


Figure 5. Pressure-temperature diagram for carbon dioxide-water-1-propanol; — critical lines calculated with Peng-Robinson EOS using the mixing rule of Panagiotopoulos-Reid, parameters fitted to ternary three-phase equilibria at temperatures between 303 and 333 K

REFERENCES

1. J.C. Elgin and J.J. Weinstock, *J. Chem. Eng. Data*, 4 (1959) 3-12.
2. M. Wendland, H. Hasse and G. Maurer, *J. Supercrit. Fluids*, 7 (1994) 245-250.
3. M. Wendland, H. Hasse and G. Maurer, *J. Supercrit. Fluids*, 6 (1993) 211-222.
4. T. Adrian, H. Hasse and G. Maurer, *J. Supercrit. Fluids*, (1996) in press.
5. R.N. Fleck, Ph.D.-Dissertation, University of California, Berkeley (1967).
6. G.D. Efremova and A.V. Shvarts, *Russ. J. Phys. Chem.*, 43 (1969) 968-971.
7. A.V. Shvarts and G.D. Efremova, *Russ. J. Phys. Chem.*, 44 (1970) 614-615.
8. D.Y. Peng and D.B. Robinson, *Ind. Eng. Chem. Fund.*, 15 (1976) 59-64.
9. G. A. Melhelm, R. Saini and B.M. Goodwin, *Fluid Phase Equil.*, 47 (1989) 189-237.
10. A.Z. Panagiotopoulos, R.C. Reid, in *Supercritical Fluids: Chemical Engineering Principles and Applications*, T.G. Squires and M.E. Paulaitis (eds), ACS Symposium Series 329, American Chemical Society, New York 1987, 115-129.

Extraction of Spray-Particles with Supercritical Fluids

R.Eggers^a, H. Wagner^b and P. Jaeger^a

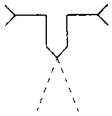
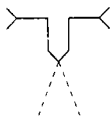
^a Technische Universität Hamburg - Harburg, Verfahrenstechnik II, D-21071 Hamburg

^b Unilever Research Laboratory, Vlaardingingen, The Netherlands

1. SPRAY PROCESSES - APPLICATIONS - OBJECTIVES

In recent years several processes applying supercritical fluids in a spraying device have been proposed and investigated. The general aim of using this technique is to improve mass transfer by generating fine drops with a high surface area. One example is the so-called RESS-process where a designated component is dissolved in a supercritical fluid which is expanded adiabatically within a capillary nozzle [1]. This results in a supersaturation causing the component to precipitate as the finest possible particles. Besides the expansion of a single compressed fluid phase within a nozzle, processes in which the supercritical medium is sprayed together with a liquid have gained importance. In this case, the aim is to reach a material transport between these two phases. If the gas phase is absorbed by the dispersed liquid phase a component is obtained which was dissolved in a dense gas phase previously presuming favourable distribution coefficients. Conversely, a material dissolved in the liquid phase can be isolated if the dispersed liquid is dissolved in the gas phase. In both cases mass transfer occurs between the dispersed drops and the surrounding gas phase. In order to describe the mass transfer, the drop size distribution as well as the fluid dynamics of the dispersed liquid must be known. According to table 1, it can be distinguished whether the supercritical or the liquid phase is loaded with the component designated for separation before the atomization. Usually the component is dissolved before the spraying; however, it can also be available in a dispersed form.

Table 1 Various SCF Spray Processes

SCF Spray Flow Principle	Dispersed Phase, d	Continuous Phase, c	Direction of Mass Transfer	Process	Product	Example
	liquid droplets	gas	$c \rightarrow d$	Absorption of extract E Spray Tower	SCF	Absorption of caffeine from CO ₂ (CO ₂ - Regeneration)
	gas bubbles	liquid	$d \rightarrow c$	Supersaturation of E by pressure reduction or temperature alteration	E	Generation of micro - particles of E in liquid phase and protecting colloids (LAS Process)
	liquid droplets	gas	$d \rightarrow c$	Extraction of l	E	Deoiling of lecithin [2,3]
					E	Generation of micro particles (GAS Process [4])
					E volatiles of l+E	coating of E Enrichment or Refinement

2. RELEVANT PARAMETERS AND METHODS OF CALCULATION

The drops which are to be extracted can be formed by disintegration of the liquid jet from a pressure nozzle if it enters the gaseous atmosphere at high speed. For those processes described in table 1, drop formation is achieved by high kinetic energy of the fluid gas flow tearing the liquid jet into fine droplets within a fluid assist spraying device. Formation of fine droplets is enhanced by an increasing dynamic pressure of the fluid gas flow and a decreasing internal pressure of the drop being formed. In order to characterise the drop formation, the Weber number is derived from the ratio of the dynamic pressure of the fluid and the internal pressure of the liquid drops.

$$We = \frac{P_p}{P_\sigma} = \frac{w_g^2 \rho_g d_p}{\sigma} \quad (1)$$

In addition, the Ohnesorge number describes the influence of the viscosity of the liquid.

$$Oh = \frac{\eta_l}{\sqrt{\rho_l d_p \sigma}} \quad (2)$$

A high velocity of the flow, w_g , an elevated density of the fluid as well as a low viscosity of the liquid phase and a low interfacial tension between liquid and fluid represent favourable conditions for high pressure spraying. Pressurised gases evidently possess characteristics similar to those of liquids with respect to the atomisation so that the relationships which are valid for liquid/liquid spraying may lead to realistic results. In the case presented here, a modified Nukiyama-Tanasawa distribution [5] has been used to specify the maximum drop diameter in the spraying process:

$$d_{p,\max} = 22,3D(We Re)^{-0,29} \quad (3)$$

with D representing the capillary diameter for the liquid and with the Reynolds number:

$$Re = \frac{w_g D \rho_l}{\eta_l} \quad (4)$$

Thus the volume fraction in drop size distribution is yielded by integrating of the following empirical function:

$$\frac{dQ_3}{d(d_p)} = 10^6 (We Re)^{-0,24} \frac{d_p^5}{d_{p,\max}^6} \exp(-22,3[We Re]^{-0,04} \frac{d_p}{d_{p,\max}}) \quad (5)$$

3. THE SPRAY DEVICE AND PRESENTATION OF A THEORETICAL MODEL

An apparatus according to Figure 1 is used. The liquid feed is compressed by a reciprocating pump and fed into a mixing zone. Here it is mixed with and dispersed by high turbulent CO_2 . So, a part of the kinetic energy of the CO_2 is used for increasing surface area by obtaining very small drops. The resulting two-phase flow runs through an extraction zone in which a uniform extraction at very short diffusion paths occurs and the fluid phase is loaded with those components subjected to separation. The raffinate is collected in a

vessel while the loaded CO₂ is expanded through a pneumatically controlled throttle valve into the separation stage. Changing pressure and temperature causes a reduction of the solubility in the CO₂ and so the extract falls out.

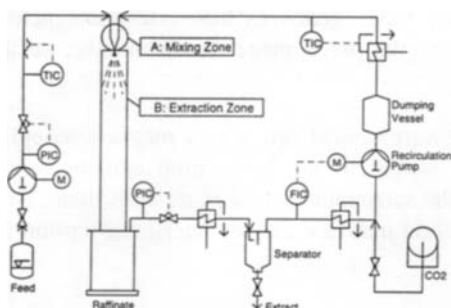


Figure 1. SCF spray device

two different distances from the spray formation. Together with the inlet conditions and the final concentration of the raffinate, a profile of the fluid loading can be stated over the entire length of the extraction zone. The drop size distribution formed in the spraying device can be described by dimensionless characteristic numbers (equation 5). The viscosity of the mixture and the surface tension had to be obtained experimentally. The mass transfer is described by two different particle models. Liquid drops are extracted as shrinking particles by convective mass transfer [6].

$$Sh = 2 + 0,6Sc^{1/3} Re_p^{1/2} \quad (6)$$

The solution of liquid extract out of solid particles is described according to a shrinking particle model by convective mass transfer and diffusion in the particle structure.

The binary diffusion coefficient of liquid extract in supercritical CO₂ is calculated with correlations based on the rough-hard-sphere-theory [7]. Within the particle structure diffusion is determined by various effects. First, the diffusion can occur only in the void fraction of the particle. Secondly, the diffusion path is given by the contorsion of the pores.

4. DETERMINATION OF MATERIAL DATA

In those liquid-fluid systems under consideration, interfacial tension is reduced at elevated pressures which favors creation of new interfacial area by droplet breakage. In addition, the rapid dissolution of the supercritical fluid in the liquid drops leads to a reduction in viscosity and thus to a generally positive mass transfer behaviour in the high-pressure spray extraction.

The pendant drop method was applied in order to determine interfacial tension and was carried out by photographing the drop in a high pressure optical cell evaluating the contour

A mathematical model of the drop formation and the extractive mass transfer is necessary for the optimisation of the mixing and the extraction zone, which are considered separately for different liquids depending on extraction conditions. Only these two sections are relevant for the extraction of liquid drops. The modelling results are verified by the measurement of the fluid loading. Therefore, gas sampling devices are set into the extraction tube in

with a microscope [8]. Measurements were carried out up to pressures of about 90 MPa and temperatures of 423 K.

The present apparatus allows sizing of the pendant drop by a computerised image analysing system equipped with a video camera which generates high resolution pictures with squared pixels. A frame grabber digitalises the pixel image synchronously, so that there are no distortions in the drop image.

Beyond this, the combination of a high pressure optical cell with a magnetic coupling balance provides a possibility to measure the weight of the liquid drop and the related density difference between the drop phase and the surrounding fluid phase with time. Thus, a relation between the mass transfer across the fluid interface and the interfacial tension can be detected.

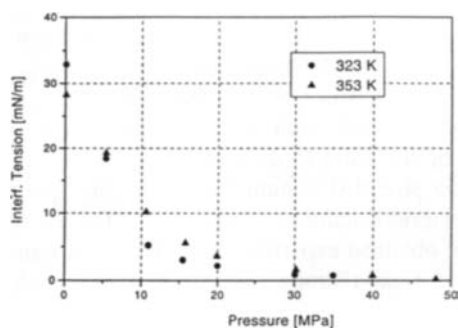


Figure 2. Interfacial Tension of coffee oil - CO₂

In Figure 2, the interfacial tension of coffee oil with a high content of volatile flavours against CO₂ is depicted. Mixtures like this are of particular interest for high pressure spray extraction. At increasing density of the fluid CO₂ - phase, interfacial tension is decreased by dissolution of CO₂ at the interface. In this case, presence of surface active material in the liquid phase, e.g. proteins, rather seem to be of subordinate

importance. With respect to foam formation these surfactants neither show their known stabilising effect as long as no polar phase such as water is added.

Viscosities of liquids mixed with CO₂ have been measured in a high-pressure rotational viscometer, which works according to a Searle-system. The pressure influence on the viscosity of the pure liquid can be described with known correlations [9].

A light increase of viscosity at higher pressures is disadvantageous for the break-up of drops, but inside the spraying device a mixture of liquid and CO₂ is formed. The diminished viscosity of this mixture dominates and as a consequence the diffusive mass transfer inside the droplet will be enhanced.

5. APPLIED MATERIALS AND RESULTS

Until now, oil-phospholipid mixtures, raw seed oils, aromatic vegetable oils, essential oils aqueous solutions and aqueous dispersions have been sprayed and extracted with supercritical CO₂ in the high pressure spraying apparatus (Figure 1). For instance aqueous roasted coffee extract was sprayed with CO₂ in order to rise concentration for posterior production of instant powder. Due to low process pressures (under 20 MPa) and increased

process temperatures (120°), a part of the water and of the unwanted off-flavours are dissolved in CO₂, so that an increase in concentration from 30 w.-% of the dry matter to 40 w.-% is reached. An energetically favourable spray drying and an improved taste were achieved. If the process pressure is increased to e.g. 40 MPa, caffeine is additionally removed from the aqueous coffee solution. This process is limited by the phase distribution equilibrium of the caffeine between the liquid and the fluid phase. For the extraction of sprayed coffee oil drops (see Figure 2), approximately 20% of the feed flow can be obtained as a flavour-enriched extract fraction.

The limitation of the high pressure spray extraction is given by the rapid movement of the droplets, i.e. the residence time for mass transfer to occur between the drop surface and the fluid. In Figure 3, the extraction of soy oil from raw lecithin is shown for two different process pressures - 48 MPa and 70 MPa. The rest oil content in the raffinate (powdery pure lecithin) is given as a function mass flow ratio $\mu = \dot{M}_{CO_2} / \dot{M}_{Feed}$. At first mass transfer is significantly enhanced at increasing CO₂ mass flow. The values for the Weber number (equation 1) and the Reynolds number (equation 4) increase. This results in smaller drops (equations 3 and 5) and in a generally larger mass transfer (equation 6). However, this effect ends at $\mu = 80$ kg CO₂/kg feed. With a further increase of the mass- flow ratio, an increase in the extraction of spray particles can no longer be reached. The residence time of the drops in the spray zone is too short for a further increase of the mass transfer, which is determined mainly by diffusion within the drops.

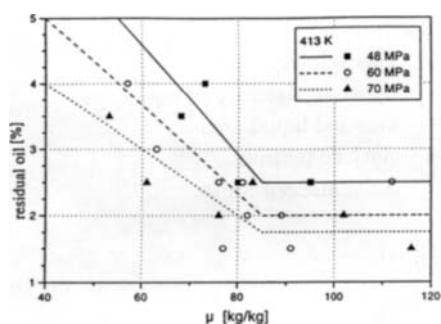


Figure 3. SCF Spray extraction depending on solvent/feed ratio

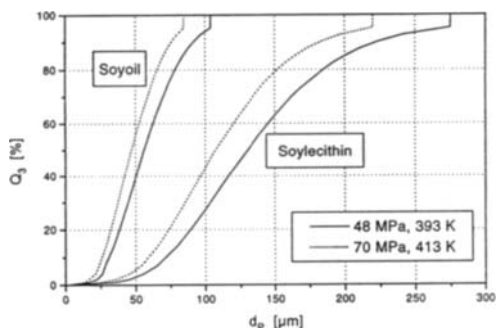


Figure 4. Drop size distribution for spraying of liquids with SC-CO₂

Figure 4 shows the results of determined droplet diameters according to equations (3) and (5) for the high pressure atomisation of raw lecithin (app. 2/3 insoluble phospholipids and 1/3 soluble lecithin oil) and for crude soy oil (app. 1 w.-% insoluble phospholipids) by the two extraction pressures of 48 MPa and 70 MPa.

The two graphs for each medium represent the bounds of drop sizes in the range of applied extraction conditions. A maximum drop diameter in the distribution is considered (equation 5).

6. SUMMARY AND FUTURE WORK

Processes for the extraction of spray particles involving pressure nozzles and fluid assist spraying devices as well as different directions of mass transfer have been introduced. In a special high pressure apparatus, liquid solvents and dispersions with CO_2 can be extracted under high pressure. Relevant properties for the formation of drops are the viscosity of the liquid phase as well as the interfacial tension between the drop phase and the fluid phase. Results for oily and aqueous systems show a drop size distribution that is very suitable for the mass transfer.

In order for further development of high pressure extraction processes, the existing plant will be equipped with varied geometrically shaped extraction zones. The aim is to reach longer residence times. Just as well, the present co-current spraying will be tested in a countercurrent flow with a pressure nozzle only for the liquid phase.

Furthermore, investigations on mass transfer across the interface will be continued in order to determine the mass transfer coefficient for drops exposed to the hydrodynamic flow and to be able to state the influence of surfactants on the interfacial tension under high pressure. For those systems implying solid particles their geometrical structure will need to be characterized with the aim of describing diffusion mechanisms.

NOTATION

d_p :	particle (droplet) diameter	w_g :	Gas velocity
D :	nozzle diameter	η_l :	dynamic viscosity of liquid
\dot{M} :	Mass Flow	ρ_g, ρ_l :	Gas and liquid Density
p_p :	dynamic pressure	σ :	Surface tension
p_σ :	inner pressure	μ :	Solvent/Feed Ratio
Q_3 :	Volume fraction in drop size distribution		

REFERENCES

1. P.G. Debenedetti, J.W. Tom, X. Kwank, S.D. Yeo, Fluid Phase Equilibria 82 (1993), 311.
2. R. Eggers, H. Wagner, J. of Supercritical Fluids 6 (1993) 31.
3. H. Wagner, Doct. Thesis, T.U. Hamburg-Harburg 1995.
4. D.J. Dixon, K.P. Johnston, AIChE J. 37 (1991) 10, 1441.
5. R.D. Ingebo, H. Foster, NACA Technical Note, Oct. 1957.
6. W. Ranz, W.R. Marshall, Chem. Eng. Prog., 48 (1952) 141.
7. C. Erkey, H. Gadalla, A. Akgerman, J. of Supercritical Fluids 3 (1990) 180.
8. R. Eggers, Ph.T. Jaeger, Wärme- und Stoffübertragung 29 (1994) 373.
9. R.C. Reid, J.U. Prausnitz, B.E. Poling, The Properties of Gases and Liquids, Mc Graw Hill 1987.

Application of Supercritical Fluid Extraction for Spices and Herbs with Pressures up to 800 bar

E. Lack, H. Seidlitz

NATEX Prozeßtechnologie GesmbH, Hauptstraße 2, A-2630 Ternitz, Austria

1. INTRODUCTION

When Gore 1861 [1] found, that various substances are soluble in liquid CO₂, the idea of using liquified gases as solvent was borne. The first industrial development was in the mid - 1930s, when compressed propane for de-asphalting of petroleum at near critical conditions was developed. In the 1960s Zosel developed extraction processes specifically based on the solvent power of supercritical gases. The industrial application in the food industry was in the early 1980s for decaffeination of coffee and extraction of hops by means of supercritical CO₂ at pressures up to 300 bar. In these days several investigations at pressures up to 1000 bar especially for the extraction of oils and waxes were executed and corresponding patents granted. The years between the 70s till about mid 80s was the most innovative period regarding high pressure extraction and beside others proper attention was paid on process development for the extraction of aromas, essential oil, spices and herbs applying pressures ranging from 80 up to 400 bar [2]. Although several publications [2] demonstrated higher solubilities at higher pressures - i.e. piperin, no commercial application was executed in these days.

In the mid of the 80s a lot of investigations were done to find out the solubility isotherms of higher molecular polar constituents of spices. For example at 600 bar and 80°C the solubility of piperin in CO₂ is about 6 g per kg compared to 0,8 g per kg at 300 bar and 40°C [2]. The extraction of food colours like anatto bixin, β -carotene, curcumin, paprika etc. using Supercritical Carbon Dioxide was investigated up to 1380 bar and 93°C [3].

It was obvious that some spice constituents can be extracted economically at higher pressures and several companies [4] offered plants up to 700 bar or even 1000 bar for smaller scales.

2. EXPERIMENTAL APPARATUS AND PROCEDURES

The experimental investigations were done in one of the laboratory plants of NATEX Prozeßtechnologie GesmbH. The plant consists of one extractor, one separator, one CO₂ working vessel, a membrane pump and several heat exchangers. The extractor has been designed for an extraction pressure of 1000 bar and 150°C. The net volume of the basket is 5 litres. The separation vessel is designed for 160 bar and 120°C. The plant was later equipped with a second separator to enable a two stage separation process. The CO₂ working vessel has a volume of 22 litres and is designed for 100 bar and 100°C.

The CO₂ cycle of the plant is as follows: Liquid CO₂ from the working tank passes a coil cooler to precool the CO₂ before entering the membrane pump. By means of the pump CO₂ is compressed to extraction conditions and passes a heat exchanger to reach extraction temperature before entering the extractor. During flowing through the raw material, which is kept in a basket, from the bottom to the top, CO₂ extracts the soluble substances. The loaded CO₂ is depressurized in the first separation step (about 90 - 130 bar) through a pneumatically driven regulation valve. After this it is depressurized again down to the second separation pressure. After the separation vessel the gaseous CO₂ is liquified in a condenser and sent back to the working tank for recirculation.

3. EXPERIMENTAL INVESTIGATIONS AND RESULTS

3.1. Defatting of food ingredients

The target of these investigations was to produce food ingredients with low content of oil, animal fat or cholesterol. These food ingredients are desired for low fat/low calorie and low cholesterol food.

Extraction of egg yolk powder:

Egg yolk powder contains normally 56% total lipids (consisting of triglycerides, lecithine and cholesterol), 30% protein, ash and some other substances. From these substances only triglycerides and cholesterol are soluble in CO₂ and can be separated from protein and lecithin. For all tests with egg yolk powder the same raw material was used. The maximum extractable yield was 40% with a twenty hour test at 500 bar.

The feed quantity was 1500 g, CO₂ throughput 28 kg/h and the extraction temperature 40°C. Egg yolk powder is very temperature sensitive and extraction temperatures should not exceed 50°C.

After 100 kg CO₂ throughput or 3 hours the following extraction yields were obtained:

Table 1

Extraction of egg yolk powder

Extraction pressure [bar]	290	450	460	700	850	max.
Extraction yield [wt%]	28	32	35	38	39	40

The initial cholesterol content of the powder was 3%wt. After extraction at 290 bar the cholesterol content was reduced to 1,3%wt. For extraction pressures between 450 and 850 the cholesterol content was reduced to 0,56%wt. respectively 0,33%wt. Above 500 bar the mass transfer is better but not as high as expected, the same is valid for the reduction of cholesterol which is similar between 600 and 850 bar.

Defatting of almonds:

It was tried to defat whole almonds to use it as low-fat ingredient for low calorie snack food. Between 300 and 700 bar only 20% of the CO₂ solubles (52%) could be extracted in 3 hours. The mass transfer is mainly controlled by diffusion, therefore higher extraction pressures have no advantages. Ground almonds with a particle size below 1 mm can be extracted at 850 bar within half of the extraction time or half of the CO₂ throughput compared to 500 bar. During the extraction the cell structure of the almonds gets lost and a defatted tasteless powder

remains in the extractor. A compromise was to crush the almonds to a particle size of 2-3 mm and to remove only 30%wt. of the oil, but further work has to be done.

Defatting of cocoa powder:

For the processing of cocoa powder the finely ground roasted cocoa nuts are defatted in hydraulic presses. After pressing 11-12%wt. cocoa butter still is in the powder. For some purposes it is necessary to reduce the butter content below 1%wt. The defatting of cocoa powder is one of the few defatting processes by means of CO₂ which is already done on industrial scale.

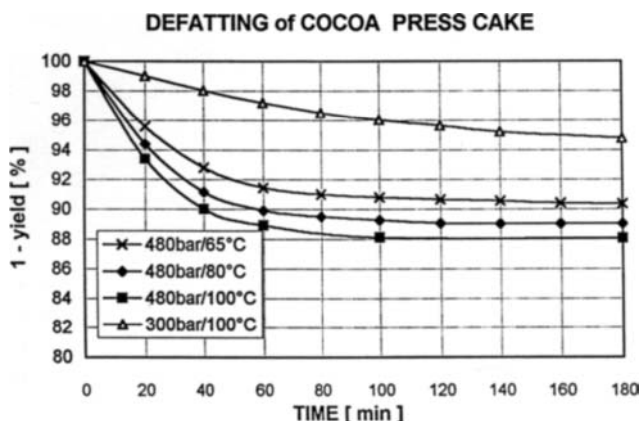


Figure 1. Extraction of cocoa butter from cocoa press cake

The best conditions were found at 480 bar and 100°C. A residual butter content below one per cent can be reached in 1,5 hours. The extraction temperature is limited at about 100°C. At higher temperature the content of free fatty acids increases, because it seems that a part of the triglycerides is splitted to fatty acids. The aroma losses are low and the defatted cocoa powder is of high quality.

In general higher pressures for defatting processes give an advantage only in the case when extraction temperatures are in a range between 80°C to 100°C, the aroma remains, due to unsolubility, in the defatted product and the extraction is not controlled by diffusion.

3.2. Extraction of antioxidants

Some of the spices and spice extracts have a strong antioxidative effect. In 1952 in the research work of Chipault [5] it was found, that rosemary and sage have the best antioxidant activity, followed by oregano, thyme, clove, allspice and black pepper. A lot of companies produce rosemary and sage extracts with conventional solvent extraction. Solvent extracts have the disadvantage to content the green colour like chlorophyll and the strong flavour of rosemary which can only be removed by expensive further purification steps. With the CO₂ extraction the carnosolic acid, the most effective substance in this respect, can be enriched to high concentrations without chlorophyll, which is not soluble in CO₂. Below 300 bar carnosolic acid is nearly unsoluble in CO₂ and mainly essential oil, fatty and waxy substances are extracted in a quantity of about 3,5%. Above 500 bar there is a strong solubility increase of carnosolic acid in CO₂ till 700 bar. The best results were found at 700 bar and 80°C. The

extract (about 8%wt. extraction yield) was separated in two fractions in a carnosolic acid fraction of 5% and an aroma fraction of 3%. The content of carnosolic acid in the first fraction reaches 30%wt. and the ratio between carnosolic acid and carnosol remains 6 : 1. This means that carnosolic acid is not oxidized to carnosol which is usual obtained with solvent extraction. With the antioxidant fraction stability tests on lard were investigated.

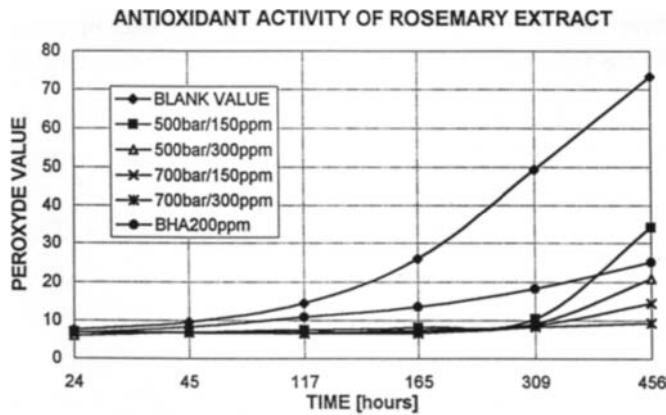


Figure 2. Shows the antioxidant activity of different rosemary extracts in comparison with Butylated Hydroxy Anisole (BHA). Although only 150 ppm of rosemary extract was used to stabilize lard, the antioxidant activity was higher compared to BHA.

3.3. Extraction of natural dyes, chilli, paprika and turmeric

Paprika:

With the two step separation it is possible to enrich the colour fraction in the first and the aroma fraction in the second step.

The colour value of the extract is mainly dependent on raw material. Between 400 and 700 bar we got the same colour value for the same raw material, but the extraction time or the CO2 throughput can be reduced up to 50% with increased extraction pressure.

Table 2
Extraction of paprika

Species	Colour values Raw material	colour values Oleoresins	Remark
Sweet paprika Hungary (whole pods)	50 ASTA	350 - 500 ASTA	with seeds and stems
Paprika sweet Hungary „Kolocsaï“	140 ASTA	1500 - 1650 ASTA	without seeds
Chilli sweet India	150 ASTA	1800 - 2000 ASTA	without seeds
Paprika sweet Spain	200 ASTA	2200 - 2500 ASTA	without seeds
Paprika sweet South Africa	240 ASTA	>2500 ASTA	without seeds

Table 2. shows extract colour values obtained from different raw materials

All raw materials were extracted between 500 bar and 700 bar, with an extraction temperature of 60°C for all paprika tests. After an extraction time of two hours a colour value of 20 - 25 ASTA remains in the residual, whereat this value was nearly independent from extraction pressures.

Turmeric:

The colour pigment of turmeric is curcumin. Curcumin is relatively polar and almost insoluble in CO₂ at extraction pressures below 400 bar. At pressures higher than 500 bar a yellow mixture of oil and cristalline curcumin can be obtained. The extraction yield varies between 5 and 12% depending on raw material.

3.4. Extraction of spices with long chain fatty acids

Coriander:

For the tests Austrian coriander containing about 10% fat and 1% essential oil was used.

The triglycerides of the fat consist mainly of long chain saturated fatty acids. The CO₂ extract is a yellow oleoresin which is semisolid at room temperatures.

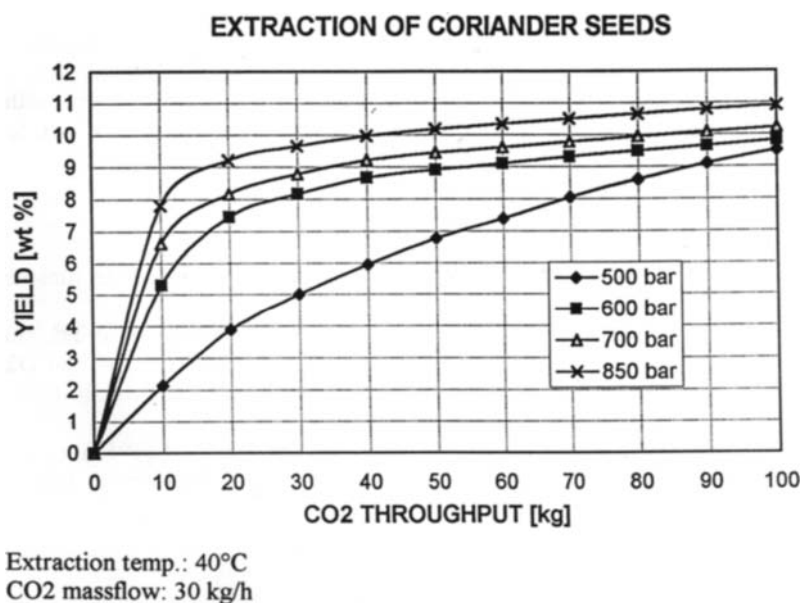


Figure 3. Extraction of coriander seeds

It can be seen on figure 3, that extraction pressures between 600 and 850 bar give the best results. After an extraction time of one hour, which is a minimum for production plants, an extraction yield of 90% at 700 bar and 80% at 600 bar was obtained. To reach 90% at 500 bar 3 hours are necessary, which is too long for an economical production of a cheap product like coriander extract. The extraction behaviours of nutmeg and mace are similar but the viscosity of extract is higher for nutmeg and lower for mace compared to coriander extract.

3.5. Extraction of food ingredients with a high content of essential oils, like cloves, camomille, marigold, cinnamon

For all extracts for which the content of essential oils is important, extraction pressures above 300 bar are not suitable. If raw materials like cloves, cinnamon, camomille flowers are extracted at 500 bar the extraction yields are higher compared to 300 bar, but there are so many additional undesired substances in the extracts like dyes, waxes etc. that these extracts are not acceptable by the market.

4. SUMMARY

From the said above it is obvious, that extraction processes at pressures above 500 bar can have remarkable advantages for selected raw materials. Out of our tested materials a feasibility study pays preference to coriander, rosemary and sage as well as for natural dyes like paprika, chilli and turmeric [6].

For the defatting processes higher pressures can give some advantages, but the extraction by means of propan seems to be ahead of the CO₂ process, as much lower necessary pressures require less investment costs.

The application of higher pressures for herbs and spices like camomille flowers, cinnamon bork, clove and others gives no advantage at all, because the yield regarding essential oils is equal and additional extracted substances are not desired.

REFERENCES

- [1] G. Gore; (1861) Proc. Roy. Soc. (London) 11, 85
- [2] E. Stahl, H.W. Quirin, D. Gerard; Dense Gases for Extraction and Refining, Saarbrücken, Germany, 1986
- [3] A.J. Jay, T.W. Smith, P. Richmond; Int. Symposium on Supercritical Fluids, Nice, France, (1988) p. 821-827
- [4] Extraktionstechnik - Marktübersicht, Lebensmitteltechnik Nr. 1-2; Jänner/Februar 1990, 22, p. 16-22
- [5] JR Chipault, GR Mizuno, JM Hawkins, WO Lundberg; Food Res 46; 46-55 (1952)
- [6] E. Lack, H. Seidlitz; 3rd Int. Symposium on Supercritical Fluids, Strasbourg, France (1994), p. 235-239

High-Pressure Investigations on the Solubility of Synthetic and Natural Dye-stuffs in Supercritical Gases by VIS-Spectroscopy up to 180 MPa

Gerhard M. Schneider, Cornelia B. Kautz, and Dirk Tuma

Lehrstuhl für Physikalische Chemie II, Ruhr-Universität Bochum, D-44780 Bochum, Germany

1. SUMMARY

In this paper solubility measurements of synthetic and natural dyestuffs are presented using VIS-spectroscopy. The investigations concentrate on two different methods. I. β -carotene was measured as a function of temperature and pressure in near- and supercritical CO_2 (289 to 309 K, 10 to 160 MPa) and CClF_3 (297 to 326 K, 12 to 180 MPa), respectively, using a static method. II. Additionally, the solubilities of 1,4-bis-(n-alkylamino)-9,10-anthraquinones (with n-alkyl = butyl, octyl) were determined with a dynamic method in temperature and pressure ranges from 310 to 340 K and 8 to 20 MPa, respectively; this method permits a continuous purification from better soluble impurities as well as the measurement of solubilities at the same time. For both anthraquinone dyestuffs intersection points of the solubility isotherms were found in the plot of concentration versus pressure. This behavior can be explained by a density effect.

2. INTRODUCTION

Recently supercritical carbon dioxide has been used as a solvent in dyeing textiles and fibers. In comparison with conventional techniques, this method has the advantage of complete separation of the remaining dyestuff from the solvent. Furthermore, there is no need in purification of waste water or in drying textiles [1-5].

Solubility data of the dyestuffs are of interest for the optimization of this particular dyeing technique. Therefore an apparatus was developed for the determination of the solubilities in supercritical solvents at temperatures from 250 to 500 K and pressures up to 250 MPa according to the *static* analytical method [6, 7]. In particular, investigations on the solubility of some selected anthraquinone dyes in supercritical CO_2 and N_2O and more recently of β -carotene in supercritical CO_2 and CClF_3 were performed as a function of temperature and pressure (see section 4.). For the 1,4-bis-(n-alkylamino)-9,10-anthraquinones the alkyl chains were systematically varied in the homologous series in order to study the effects of molecular size and polarity on the solubility phenomena [6-10].

Recently additional measurements on some of these anthraquinone dyes were carried out with a *dynamic* method using a supercritical fluid chromatography (SFC) technique. This method permits the measurement of solubilities as well as the continuous purification from better soluble impurities which might cause serious errors in the solubility data (see section 3.).

3. SOLUBILITY MEASUREMENTS OF ANTHRAQUINONE DYESTUFFS WITH A DYNAMIC METHOD (SFC)

3.1. Experimental

The apparatus has already been described elsewhere [11, 12]. It mainly consists of a commercial HPLC equipment which has been modified for solubility measurements.

Carbon dioxide is condensed into a syringe pump under its own vapor pressure. To heat the mobile phase up to a supercritical temperature the gas is pumped through a heat exchanger which is integrated inside an air thermostat. Two 6-port valves are placed in the same thermostat. One of the valves is used for on-line extraction of the dyestuff from the surface of a kieselguhr in an extraction column. The temperature of the column is controlled by means of a platinum resistance thermometer. For the detection of the substances a diode array spectrophotometer is used. The flow-through cell of the diode array is also placed inside the air thermostat and coupled to the detector with fiber optics. After passing the detector cell the supercritical fluid is pumped through a column filled with charcoal. At the outlet of the chromatographic system the mobile phase is expanded through a two-stage reducing valve. The flow-rate which is adjusted by means of the second stage of the reducing valve and a needle valve is measured with a soap bubble flow meter. All experimental data are sampled and handled by personal computers.

CO₂ (99.995 %) was purchased from Messer Griesheim GmbH. 1,4-Bis-(n-alkylamino)-9,10-anthraquinones were synthesized in our laboratories [7]. Chromosorb G-AW was purchased from WGA GmbH and silanized kieselguhr from Merck KGaA.

Concentrations are determined from the integral absorbance, i.e. the area below the spectrum. The spectra are recorded in the wave-length range from 400 to 750 nm. Calibration of the integral absorbance has been performed in the flow-through cell of the chromatograph by using different solvents. By this, all systematic errors that arise from the construction of the cell, the fiber optics, and the unknown optical path-length could be eliminated. The wave-length of maximum absorbance depends on the solvent; the area below the absorption peak, however, is independent of it within experimental accuracy and only depends on concentration and the optical path-length of the cell. A modified Lambert-Beer's law describes the dependence on these parameters [9, 10].

For the equilibrium measurements the dyestuffs were precipitated on the surface of selected kieselguhrs as stationary phases and filled into a chromatographic column. Then temperature and pressure were adjusted. Before each measurement series a reference spectrum was recorded. Firstly, purification from better soluble impurities of the dyestuffs was performed in a continuous flow. In the following, the dependence of the saturation concentration on the flow-rate and the time which is necessary for equilibration was determined. Within the experimental accuracy no dependence on these parameters was found. Nevertheless, for equilibration the substance was treated more than 10 min under isothermal-isobaric conditions.

3.2. Results and Discussion

For a successful purification it is useful to remove the dyestuff from the flow and to repeat the process after some time. Because of the use of the diode array spectrophotometer and the continuous flow the irradiation time is very short. Besides the advantage of continuous purification the light induced degradation is consequently minimized.

For most systems under test there exists an equilibrium between a solid dye and a fluid phase. In supercritical solutions it is common that melting point depression occurs. Because of the melting point depression a fluid/fluid equilibrium for isotherms near the melting points might appear (for a discussion of this effect in the case of 1,4-bis-(octylamino)-9,10-anthraquinone see [7, 10, 11]).

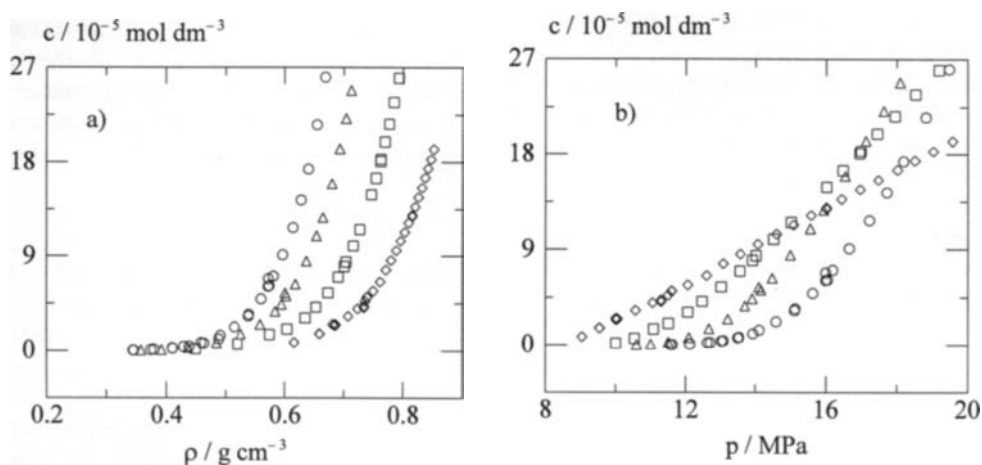


Figure 1. Solubilities of 1,4-bis-(octylamino)-9,10-anthraquinone on silanized kieselguhr in CO₂ as a function of a) density ρ and b) pressure p [11]
(\diamond $T = 310.1 \text{ K}$, \square $T = 320.0 \text{ K}$, Δ $T = 329.9 \text{ K}$, \circ $T = 340.1 \text{ K}$)

For both dyestuffs the plot of concentration versus density shows (Figure 1a) that the solubility increases with rising density of the supercritical fluid. The density was calculated from the EOS given by Span and Wagner [13]. At a constant density the solubility of the dyestuffs increases with rising temperature. For high temperatures the solubilities increase more rapidly with increasing density. In the concentration versus pressure plot (Figure 1b), however, the isotherms have two intersection points. Between the first and the second intersection point the decrease of density and solvent power dominates with increasing temperature. This effect of temperature on solubility might be useful for the dyeing process of fibers and textiles [1]. Above the second intersection point the normal temperature dependence of solubility is found. This region could not be reached for 1,4-bis-(butylamino)-9,10-anthraquinone.

Preceding measurements by Swidersky on the same dyes were carried out with the static method [7, 8, 9, 14]. The differences between the measurements result from an incomplete purification of the same sample during preceding investigations. Recent experiments on purer dyes using the same static method agree very well with the measurements according to the dynamic method [15]. An adsorption effect of the stationary phase that has been used to precipitate the dyestuff on its surface is not found within the experimental accuracy.

4. SOLUBILITY MEASUREMENTS OF β -CAROTENE WITH A STATIC METHOD

Carotenoids (especially β -carotene) find widespread applications in food industry. These pigments not only give an attractive color to a wide variety of food products but it is also known that β -carotene and various other members of this substance family play an important role in cancer prevention.

Plant materials often contain large amounts of β -carotene. Although most β -carotene used commercially is synthetic, the extraction from natural sources with supercritical gases becomes more and more important, especially because of the ecological advantages towards the “classical” extraction techniques with organic solvents. Therefore, solubility measurements are needed to understand and to design such extraction processes. Solubility data of β -carotene in supercritical fluid solvents, specifically phase equilibrium measurements, are given in the references [16-19].

4.1. Experimental

In our present work we performed the experiments with a static method similar to Jay et al. [17, 18]. The main part of our apparatus is a high-pressure autoclave with two sapphire windows and magnetic stirring [6-10, 14]. A detailed description has already been published [9].

CO_2 (99.5 %) and CClF_3 (99.0 %) were purchased from Messer Griesheim GmbH. β -Carotene (97 % (UV)) was supplied by Fluka GmbH, respectively.

A calibration was performed in the same way as described in section 3.1., but in place of the detector cell cuvettes were used. The calibration curve was determined with *stable* solutions of known concentrations in several organic solvents.

For the solubility measurements themselves an amount of β -carotene was introduced into the cell to ensure saturation at all conditions. There exists an equilibrium between a solid β -carotene precipitate and a fluid phase (CO_2 as well as CClF_3 saturated with β -carotene). Before the autoclave was adjusted to the temperature and pressure conditions under test, impurities produced thermally and by light induced degradation [20], which could be seen in the VIS-region, were blown off by sudden releases of the gaseous phase from the cell [7, 10, 14].

Solute and solvent were equilibrated when absorbance at a fixed wave-length remained constant. This was achieved within a period ranging from ca. 30 min up to several hours, the latter especially at pressures above 100 MPa.

4.2. Results and Discussion

In this work the solubility of β -carotene was investigated as a function of temperature and pressure in near- and supercritical CO_2 and CClF_3 .

In Figure 2 the experimental solubilities are represented as concentration (pressure) and concentration (density) isotherms for CO_2 at four different temperatures. The dependence of solubility versus temperature or density is quite usual, as it increases when one of these parameters is raising. CO_2 is a better solvent for the apolar β -carotene than CClF_3 . The lower solvent power of CClF_3 can be explained from its dipole moment ($1.7 \cdot 10^{-30}$ C m) [21]. The non-polar CO_2 enables interactions between the solvent molecule and the solute whereas in the case of CClF_3 these effects are restrained. The thermodynamic background to this particular behavior can e.g. be derived from considerations by Prausnitz et al. [22].

For CO₂ maximum concentrations were found on all isotherms at a pressure of about 100 MPa corresponding to densities of about 1.00 to 1.15 g cm⁻³. This particular effect is no artifact but it is consistent with thermodynamic behavior. When the partial molar volume of β -carotene in the fluid phase reaches the value of the molar volume of the pure solid β -carotene a maximum mole fraction is found.

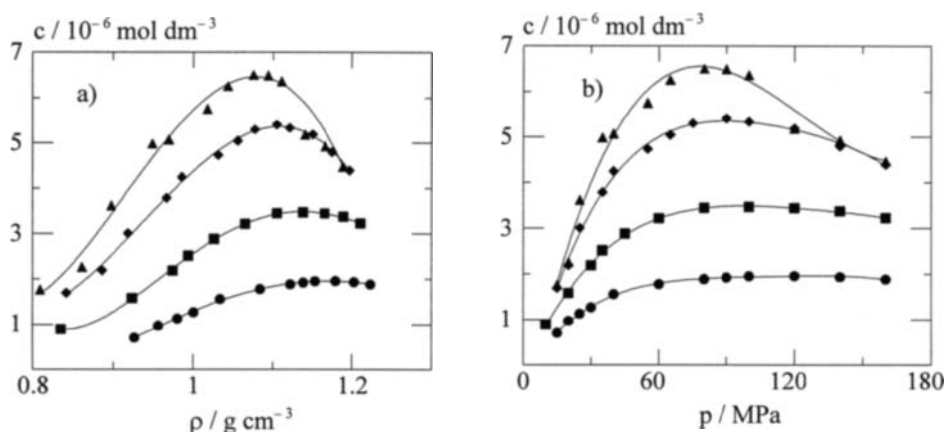


Figure 2. Solubilities of β -carotene in CO₂ as a function of a) density ρ and b) pressure p (\bullet $T = 288.7$ K, \blacksquare $T = 296$ K, \blacklozenge $T = 304$ K, \blacktriangle $T = 309$ K)

The reason why this behavior is rarely mentioned in the literature lies in the fact that reaching those high pressures is technically difficult. Nevertheless, similar phenomena were found for other systems [6, 7, 9, 10, 14, 23]. The experimental data reported by Sakaki [19] agree quite well with the presented data. Sakaki also performed his measurements by using a fluid-chromatograph. Jay et al. [17, 18] found in their measurements a deviation towards higher values at higher temperatures. The authors [17, 18] used a sample from the same supplier (Fluka GmbH) and with the same specifications (i.e. β -carotene, 97 % (UV)) as in the present investigations. For this disagreement the reason might be that they used the β -carotene without further purification. In our experiments we found out that products of light and heat induced degradation showed significant absorption in the VIS-region. In order to remove the impurities sudden releases of the gaseous phase were effective.

5. CONCLUSIONS

The dynamic method permits the purification from better soluble impurities as well as continuous solubility measurements at the same time. An adsorption effect of the stationary phase which is used to precipitate the dyestuff on its surface is not found within the experimental accuracy. The measurements of 1,4-bis-(*n*-alkylamino)-9,10-anthraquinone (with *n*-alkyl = butyl, octyl) show two intersection points in the plot of pressure versus concentration.

CO₂ is a better solvent for the apolar β -carotene than CClF₃. The lower solvent power of

CClF₃ can be explained from its dipole moment. The non-polar CO₂ facilitates interactions between the solvent molecule and the solute whereas in the case of CClF₃ these effects are restrained. For CO₂ maximum concentrations were found on all isotherms at a pressure of about 100 MPa corresponding to densities of about 1.00 to 1.15 g cm⁻³.

ACKNOWLEDGEMENTS

Financial support of the Deutsche Forschungsgemeinschaft and the Fonds der Chemischen Industrie is gratefully acknowledged.

REFERENCES

1. K. Poulakis, M. Spee, G. M. Schneider, H.-J. Buschmann, and E. Schollmeyer, *Chemiefasern/Textilindustrie* 10 (1991) 142.
2. G. M. Schneider, in *Supercritical Fluids: Fundamentals for Application*, E. Kiran and J. M. H. Levelt Sengers (eds.), Kluwer Academic Publishers, Dordrecht, 1994, p. 91 ff.
3. D. Knittel, W. Saus, and E. Schollmeyer, *J. Text. Inst.* 84 (1993) 534.
4. D. Knittel and E. Schollmeyer, *Melliand International* 3 (1995) 201.
5. German patent, Offenlegungsschrift DE 3906724A1 (1990); and other patents.
6. U. Haarhaus, Doctoral Dissertation, Ruhr-Universität Bochum, 1992.
7. P. Swidersky, Doctoral Dissertation, Ruhr-Universität Bochum, 1994.
8. P. Swidersky, U. Haarhaus, D. Tuma, and G. M. Schneider, *Proceed. of the 3rd Internat. Symp. on Supercritical Fluids*, Oct. 17 - 19, 1994, Strasbourg (France), tome 1, p. 191 ff.
9. U. Haarhaus, P. Swidersky, and G. M. Schneider, *J. Supercrit. Fluids* 8 (1995) 100.
10. P. Swidersky, D. Tuma, and G. M. Schneider, *J. Supercrit. Fluids* 9 (1996), in press.
11. C. B. Kautz, Doctoral Dissertation, Ruhr-Universität Bochum, 1996.
12. G. M. Schneider, U. Dahlmann, C. B. Kautz, U. Klask, K. Maag, and G. Neumann, *Proceed. of the 3rd Internat. Symp. on Supercritical Fluids*, Oct. 17 - 19, 1994, Strasbourg (France), tome 3, p. 405 ff.
13. R. Span and W. Wagner, *J. Phys. Chem. Ref. Data* (1996), in press.
14. D. Tuma, Diploma Thesis, Ruhr-Universität Bochum, 1994.
15. D. Tuma, Doctoral Dissertation, Ruhr-Universität Bochum, in preparation.
16. M. L. Cygnarowicz, R. J. Maxwell, and W. D. Seider, *Fluid Phase Equilibria* 59 (1990) 57.
17. A. J. Jay, D. C. Steytler, and M. Knights, *J. Supercrit. Fluids* 4 (1991) 131.
18. A. J. Jay and D. C. Steytler, *J. Supercrit. Fluids* 5 (1992) 274.
19. K. Sakaki, *J. Chem. Eng. Data* 37 (1992) 249.
20. R. C. Mordi, J. C. Walton, G. W. Buton, L. Hughes, K. U. Ingold, D. A. Lindsay, and D. J. Mofatt, *Tetrahedron* 49 (1993) 911.
21. *CRC Handbook of Chemistry and Physics*, 74th ed., D. R. Lide (ed.), CRC Press, Boca Raton, FL, 1993.
22. J. M. Prausnitz, R. N. Lichtenthaler, and E. G. Azevedo, *Molecular Thermodynamics of Fluid-Phase Equilibria*, 2nd ed., Prentice-Hall, Englewood Cliffs, NJ, 1986.
23. U. K. Deiters and I. Swaid, *Ber. Bunsenges. Phys. Chem.* 88 (1984) 791.

Modeling Solubility of Biological Compounds in Supercritical Fluids

E. Neau^a, S. Garnier^a, P. Alessi^b, A. Cortesi^b, I. Kikic^b

^aLaboratoire de Chimie Physique, Université de Luminy, Aix-Marseille II, France

^bDept. of Chemical Engineering, Environmental and Raw Materials, DICAMP, Univ. of Trieste, P.le Europa, 1, 34127 Trieste, Italy

1. ABSTRACT

Solubility data of biological compounds taken from literature are considered in this work. Different thermodynamic models based on cubic equations of state and UNIFAC are used in the correlation of experimental data. Interaction parameters are obtained by group contribution approach in order to establish correlations suitable for the prediction of the solid solubility.

2. INTRODUCTION

Since to measure solid solubility data is time consuming and the cost of the operation is quite high the existing data should be considered in the framework of optimizing the experimental effort and reducing the overall expenses by applying a suitable thermodynamic model.

In this work solubility data of biological compounds taken from literature were considered.

Different thermodynamic models based on cubic equations of state (EOS) are used in the correlation of experimental data. The interaction parameters are described on the basis of group contribution (G.C.) approach in order to establish correlations suitable for the prediction of the solubility of compounds of similar molecular structure.

3. SOLUBILITY OF SOLIDS IN SUPERCRITICAL FLUID

The solubility of a solid solute (component 2), in a supercritical fluid is calculated, if the solid phase is a pure component, by:

$$Y_2 = \frac{P^{\text{sub}}}{P\phi_2^{\text{scf}}} \exp \left[\frac{v_2^{\text{s}}}{RT} (P - P^{\text{sub}}) \right] \quad (1)$$

where at temperature T , P^{sub} is the sublimation pressure, v_2^{s} is the solid molar volume and ϕ_2^{s} is the fugacity coefficient in the supercritical phase at pressure P .

The fugacity coefficient ϕ_2^{s} is calculated by using a thermodynamic model. In this work the SRK (Soave) and Peng Robinson (PR) Equations of State were considered.

The EOS energy parameters were determined by using classical mixing rules or UNIFAC method.

In any cases, the critical parameters T_c and P_c , and acentric factor ω are unknown and should be estimated by G.C. methods. Different approaches are available in literature and have been applied for the calculation of the solubility.

4. INFLUENCE OF CRITICAL PROPERTIES

Four G.C. approaches for the evaluation of T_c , P_c and ω have been used for characterizing steroids and non steroidal drugs. In particular, the Ambrose approach [1] was used by calculating the normal boiling point T_b with Constantinou and Gani approach (method 1) and with the Lydersen method modified by Joback [1] (method 2); the method 3 is the Lydersen approach modified by Joback; the method 4 is the Constantinou and Gani approach [2, 3]. The results obtained with the different methods using the PR EOS [4] and fitting the parameter k_{12} of the classical Van der Waals mixing rules are reported in Table 1. For these calculations the sublimation pressure P^{sub} and solid volume v'_2 were taken from the literature.

By comparing the different deviations $dY\%$ on the solubility of the solid in the supercritical phase, some remarks can be made: steroidal compound solubilities are generally better correlated by method 1, while method 4 seems more suitable for the other compounds. This can be explained by considering the values of the critical pressures for steroidal compounds. The Constantinou and Gani approach (method 4) is underestimating P_c (for example, for cholesterol: $P_c/\text{bar} = 11.9$ with method 4, and 17.7 with method 1) with close values of T_c . This behaviour can be due to the particular structure of steroids which mainly contain naphthenic carbons for which few experimental data of P_c are available in the literature. On the contrary, for the other molecules having many different functional groups (esters, aromatics, heterocycles ...) the more detailed Constantinou and Gani method leads to more realistic critical pressures (for example, for nitrendipine, with similar T_c , method 4 gives 12.2 bars while method 1 gives 45.1 bars). Methods 2 and 3 give intermediate results. Also the Somayajulu method [12] was applied and led to deviations comparable to method 2 and 3.

In further calculations we focused on steroidal compounds and only method 1 was used for the estimation of the pure solid properties.

5. THERMODYNAMIC MODEL

5.1. Influence of the equation of state

The original Peng Robinson EOS (Table 1) is compared in Table 2 with:

- the PR EOS with the volume correction of Peneloux (PR_{cor}) [13];
- the Soave-Redlich-Kwong EOS (SRK) [14];
- and the PR EOS with a modification of the volume function in the attractive part (PR_{mod}) where the assumption of the one fluid model is not more valid [15].

For all the calculations the parameter k_{12} of the classical van der Waals mixing rules was fitted. It can be seen from Table 2 that the volume correction does not give a significant improvement; slightly worst results are obtained with SRK EOS while the PR_{mod} shows a clear improvement at lower temperatures (as in the case of Cholesterol, Progesterone..).

Table 1

Choice of critical properties for the calculation of solubility (y) of solids in CO_2 using the PR equation (1 - Ambrose with T_b Constantinou Gani; 2 - Ambrose with T_b Lydersen modified by Joback; 3 - Lydersen modified by Joback; 4 - Constantinou and Gani).

Compounds	T/K	1	2	3	4	Authors
		Dy%	Dy%	Dy%	Dy%	
Cholesterol	308.15	32.48	70.17	86.10	86.10	Wong and Johnston (1986), [5]
	318.15	66.18	69.11	69.21	69.21	
	328.15	66.54	59.47	63.37	63.27	
Cholesterol	328.15	18.40	38.19	83.56	59.43	Kosal and al. (1992), [6]
	333.15	33.00	41.81	82.81	58.81	
Cholesterol	313.15	20.38	73.49	96.87	85.59	Yun and al. (1991), [7]
	323.15	18.08	73.98	90.08	87.37	
	333.15	23.28	66.70	86.27	73.73	
Progesterone	308.15	17.75	58.82	84.58	53.80	Kosal and al. (1992), [6]
	313.15	18.67	52.56	73.96	51.04	
	318.15	17.03	44.63	71.64	43.90	
	328.15	35.01	66.72	80.46	67.09	
Progesterone	313.15	27.46	12.06	41.40	11.93	Valli (1995), [8]
	333.15	19.43	13.79	44.13	13.44	
Testosterone	308.15	14.26	43.79	68.36	56.92	Kosal and al. (1992), [6]
	313.15	21.78	49.45	66.88	61.22	
	318.15	32.11	57.49	77.61	70.51	
	328.15	21.72	32.33	45.10	40.34	
Stigmasterol	308.15	45.07	85.07	87.74	87.23	Wong and Johnston (1986), [5]
	323.15	50.84	80.42	84.95	80.38	
	333.15	70.31	81.25	83.80	85.81	
Ketoprofene	312.50	17.18	21.33	20.90	15.13	Mosca (1995), [9]
	331.50	26.58	33.63	28.02	20.92	
Piroxicam	312.50	29.33	13.74	25.34	15.57	Mosca (1995), [9]
	331.50	25.15	12.04	20.17	14.90	
Nimesulide	313.15	28.11	20.84	10.27	9.52	Schuchardt (1995), [10]
	333.15	48.24	39.03	16.73	24.61	
Nitrendipine	333.15	53.42	44.07	29.73	12.08	Knez and al. (1995), [11]
	350.15	57.37	46.10	40.60	23.24	
	373.15	65.85	51.75	21.18	21.23	
Nifedipine	333.15	55.01	47.39	24.73	16.24	Knez and al. (1995), [11]
	353.15	52.04	44.48	19.60	19.75	
	373.15	61.87	47.20	24.21	20.40	

Table 2

Fitting of k_{12} using different EOS (PR with volume correction (PR_{corr}), SRK, PR with modified volume function (PR_{mod})) and pure prediction using UNIFAC model with scaling factor

Compounds	T/K	PR _{corr}	RKS	PR _{mod}	UNIFAC	Authors
Cholesterol	308.15	27.02	38.93	22.45	64.26	Wong and Johnston (1986), [5]
	318.15	64.42	68.70	71.36	59.72	
	328.15	64.21	69.92	75.76	65.35	
	global	51.88	59.18	56.52	63.11	
Cholesterol	328.15	17.66	20.63	25.36	53.83	Kosal and al. (1992), [6]
	333.15	31.33	35.62	35.06	66.49	
	global	21.76	25.12	28.13	57.64	
Cholesterol	313.15	20.52	21.34	4.28	17.03	Yun and al. (1991), [7]
	323.15	16.12	19.44	4.43	18.77	
	333.15	22.26	24.57	11.06	22.97	
	global	19.48	21.62	6.33	19.39	
Progesterone	308.15	18.01	18.61	9.32	28.93	Kosal and al. (1992), [6]
	313.15	16.18	21.48	7.17	23.53	
	318.15	16.13	18.28	16.29	26.86	
	328.15	34.66	36.84	27.76	35.19	
	global	21.24	23.80	15.14	28.63	
Progesterone	313.15	28.69	25.91	35.38	93.33	Valli (1995), [8]
	333.15	19.28	22.82	40.45	88.69	
	global	24.41	24.51	37.68	91.22	
Testosterone	308.15	15.22	13.75	14.80	72.54	Kosal and al. (1992), [6]
	313.15	20.27	23.64	17.46	64.71	
	318.15	30.92	34.25	23.52	64.93	
	328.15	19.89	24.85	38.95	66.66	
	global	21.61	24.13	23.84	67.27	
Stigmasterol	308.15	40.28	49.46	36.12	>100	Wong and Johnston (1986), [5]
	323.15	48.59	54.65	46.17	>100	
	333.15	66.43	74.97	75.63	>100	
	global	51.16	59.16	51.77	>100	

5.2. Influence of mixing rules

The UNIFAC model was introduced in the attractive parameters of the EOS using a scaling factor L_{12} according to Garduza [16] and Garnier [17]; this approach is similar to the method proposed by Wong and Sandler [18]. The calculations performed with the original UNIFAC parameters [19, 20, 21] do not give satisfactory results. This probably is due to the use of the reported interaction parameters a_{nm} between CO_2 and the functional groups present in paraffins instead of those characteristic of cyclic paraffins which are present in the steroidal structure. Fitting the solubility data new parameters a_{nm} and a_{nm} , setting b_{nm} and c_{nm} equal to zero, were obtained; these parameters with a single scaling factor L_{12} were used for the pure prediction of

solubility data presented in Table 2. The deviations are sometimes in the same order as with classical mixing rules fitting one k_{12} parameter and, as it was expected, in other cases the prediction is very poor.

5.3. Influence of sublimation pressure

As it was pointed out by Chen et al. [22] the calculation of solubility data requires a proper estimation of sublimation pressures. The data were correlated using the PR EOS with classical mixing rules and the UNIFAC model with previously determined a_{mn} parameters.

Table 3

Influence of sublimation pressure (P^{sub}) on the calculation of the solubility (for PR and UNIFAC models, k_{12} and L_{12} were fitted respectively together with the parameters of the sublimation pressure).

Compounds	T/K	PR		UNIFAC		Authors
		P^{sub}	dY%	P^{sub}	dY%	
Cholesterol	308.15	$1.10 \cdot 10^{-10}$	16.47	$1.18 \cdot 10^{-10}$	16.86	Wong and Johnston (1986), [5]
	318.15	$9.27 \cdot 10^{-10}$	46.35	$1.09 \cdot 10^{-09}$	46.34	
	328.15	$6.81 \cdot 10^{-09}$	33.49	$8.75 \cdot 10^{-09}$	32.77	
	global		32.10		31.99	
Cholesterol	328.15	$7.37 \cdot 10^{-08}$	13.09	$4.33 \cdot 10^{-08}$	13.23	Kosal and al. (1992), [6]
	333.15	$1.44 \cdot 10^{-07}$	33.42	$1.56 \cdot 10^{-07}$	33.36	
	global		19.19		19.27	
Cholesterol	313.15	$6.01 \cdot 10^{-10}$	5.38	$5.31 \cdot 10^{-10}$	5.25	Yun and al. (1991), [7]
	323.15	$2.12 \cdot 10^{-09}$	7.33	$2.09 \cdot 10^{-09}$	7.50	
	333.15	$6.98 \cdot 10^{-09}$	5.93	$7.56 \cdot 10^{-09}$	7.05	
	global		6.23		6.57	
Progesterone	308.15	$6.71 \cdot 10^{-11}$	7.91	$7.45 \cdot 10^{-11}$	7.81	Kosal and al. (1992), [6]
	313.15	$1.35 \cdot 10^{-10}$	6.22	$1.51 \cdot 10^{-10}$	6.01	
	318.15	$2.67 \cdot 10^{-10}$	14.73	$2.98 \cdot 10^{-10}$	14.59	
	328.15	$1.02 \cdot 10^{-09}$	20.84	$1.10 \cdot 10^{-09}$	22.00	
	global		12.43		12.60	
Progesterone	313.15	$6.70 \cdot 10^{-09}$	10.45	$6.66 \cdot 10^{-09}$	10.36	Valli (1995), [8]
	333.15	$5.36 \cdot 10^{-08}$	13.79	$5.32 \cdot 10^{-08}$	14.31	
	global		11.97		12.16	
Testosterone	308.15	$1.60 \cdot 10^{-10}$	14.02	$1.97 \cdot 10^{-10}$	13.95	Kosal and al. (1992), [6]
	313.15	$3.41 \cdot 10^{-10}$	15.53	$4.19 \cdot 10^{-10}$	15.87	
	318.15	$7.12 \cdot 10^{-10}$	24.02	$8.68 \cdot 10^{-10}$	25.07	
	328.15	$2.89 \cdot 10^{-10}$	22.04	$3.49 \cdot 10^{-09}$	21.49	
	global		18.99		19.18	
Stigmasterol	308.15	$2.18 \cdot 10^{-12}$	15.71	$1.94 \cdot 10^{-12}$	15.62	Wong and Johnston (1986), [5]
	323.15	$2.90 \cdot 10^{-11}$	13.43	$3.00 \cdot 10^{-11}$	13.76	
	333.15	$1.43 \cdot 10^{-10}$	21.15	$1.63 \cdot 10^{-10}$	20.46	
	global		16.71		16.56	

In each case two parameters for correlating the sublimation pressure were fitted together with the k_{12} (classical mixing rules) or L_{12} (UNIFAC scaling factor) parameter. Results of the calculations are reported in Table 3.

In both cases there is a clear improvement of the estimation of the solubility when using a proper evaluation of the sublimation pressure. Similar conclusions were drawn by Chen et al [22], but using a higher number of parameters.

Furthermore, the order of magnitude of the P^{sub} obtained in both cases is realistic. It must be underlined that the values of the solubility y_2 and the sublimation pressure are close even if the two approaches are different.

6. CONCLUSIONS

The importance of a suitable G.C. method for evaluating the pure solid properties was evidenced. The limitations of the different G.C. methods are due to the limited experimental data available in the literature for heavy multifunctional compounds. The PR EOS with classical mixing rules gives the same results than the most complex UNIFAC approach. The importance of the sublimation pressure for correlating solubility data was underlined.

ACKNOWLEDGEMENT

The authors acknowledge financial support from MURST and CNR.

REFERENCES

1. R.C. Reid, J.M. Prausnitz and B.E. Poling, New-York, 1987.
2. L. Constantinou and R. Gani, *AIChE*, 40(10) (1994) 1697.
3. L. Constantinou, R. Gani and J.P. O'Connell, *Fl. Ph. Eq.*, 103 (1995) 11.
4. D.Y. Peng and D.B. Robinson, *Ind. Chem. Fundam.*, 15 (1976) 59.
5. J.M. Wong and K.P. Johnston, *Biotech Progress*, 2 (1986), 29.
6. E. Kosal and C.H. Lee, G.D. Holder, *J. of Supercritical Fluids*, 5 (1992) 169.
7. S.L. Yun, K. Liong, G.S. Gurdial and N.R. Foster, *Ind. Eng. Chem. Res.*, 30 (1991) 2476.
8. M. Valli, Thesis. (DICAMP, University of Trieste, Italy) 1994.
9. T. Mosca, Thesis. (DICAMP, University of Trieste, Italy), 1995.
10. A. Schuchardt, Thesis. (DICAMP, University of Trieste, Italy) 1995, in press.
11. Z. Knez, M. Skerget, P. Sencar-Bozic and A. Rizner, *J. Chem. Eng. Data*, 40 (1995).
12. G.R. Somayajulu, *J. Chem. Eng. Data*, 34 (1989) 106.
13. A. Péneloux, E. Rauzy and R. Fréze, *Fl. Ph. Eq.*, 8 (1982) 7.
14. G. Soave, *Chem. Eng. Sci.*, 27 (1972) 1197.
15. L. Trassy and E. Neau, Personal Communication, Pau, France, 1995.
16. O. Hernandez Garduza, Thesis. Aix-Marseille III, France, 1993.
17. S. Garnier, Master of science report, Aix-Marseille III, France, 1995.
18. D. S. H. Wong and S.I. Sandler, *AIChE*, 38(5) (1992) 671.
19. T. Holderbaum and J. Gmehling, *Fl. Ph. Eq.*, 70 (1991) 251.
20. J. Gmehling, L. Jiding and M. Schiller, *Ind. Eng. Chem. Res.*, 32 (1993) 178.
21. K. Fischer and J. Gmehling, *Fl. Ph. Eq.*, 112 (1995) 1.
22. P.C. Chen, Y.P. Chen and D.S.H. Wong, *Fl. Ph. Eq.*, 83 (1993) 175.

HIGH PRESSURE TREATMENT OF VEGETABLES

R. Stute¹, M.N. Eshtiagi², S. Boguslawski², D. Knorr²

¹CPC Europe Consumer Foods Ltd., Institute for Research and Development,
Knorrstrasse 1, 74074 Heilbronn, Germany

²Berlin University of Technology, Dept. Food Technology, Königin-Luise-Strasse 22,
14195 Berlin, Germany

1. INTRODUCTION

The application of high pressure (HP) for improving the shelf life of foods goes back to 1899 [1], but was not seen as an attractive technology in the food area until the early eighties of this century, when research on HP was reinitiated at the University of Delaware [2] and especially since after, according to an initiative of Hayashi [3], the Ministry of Agriculture, Forestry & Fishery established in 1989 the "Association for the Study on Ultra High Pressure Applied Technology in the Food Industry" [3]. Based on these activities various HP-treated products (juices, jams, yoghurt) have been introduced into the market in Japan since 1990. Concerted European activities have been taking place since 1992 (4).

Obviously within the worldwide discussions on proper technologies for the production of "minimal processed foods", the application of high pressure was seen as a suitable technology which was based on the following facts:

- a) High pressure (HP) effects only secondary and tertiary (non-covalent) bonds. This means only large molecules, cell membranes, enzymes etc. are denatured and, therefore, microorganisms and enzymes as the dominating sources for food spoilage can be inactivated without heat application (even at sub zero temperatures).
- b) Primary or covalent bonds are not affected. This means low molecular weight quality determining components like vitamins, pigments, flavor substances as well as their precursors which are highly affected by the traditional thermal processing, remain intact.

Thus in contrast to heat preserved foods HP-preserved foods retain their "uncooked" ("fresh") status.

It has recently been shown [5] that just looking on primary, secondary and tertiary bonds is a too simple viewpoint for the description of HP-effects. Covalent bonds are not directly affected by HP. However, since a food is a complex, multicomponent system reactions between the different components can be accelerated by HP.

- c) In contrast to thermal processing (where depending on the heat transfer, the temperature gradient in the product etc. an overcooking or flavor and vitamin losses cannot be avoided), HP acts immediately and is independent from size and shape of the product. Furthermore, the HP-treatment can be applied in hermetically sealed (flexible) containers used for the final delivery and distribution.

Thus, the application of HP could not only be seen as an attractive method for the production of minimal processed foods, but specifically also for the inpackage preservation resp. shelf life extension of freshly cut vegetables or vegetable mixes. It was the goal of the following investigations to evaluate the HP-potential for this application. Three vegetables were investigated: potatoes (as an example for a food rich in starch), carrots (as example for a non starch containing vegetable) and green beans (as a product containing a highly heat resistant peroxidase).

2. Reduction of the "natural" microbial contamination

In vegetables the dominating microorganisms are enterobacteriaceae (besides *E. coli*). The average total counts (CFU) of freshly harvested products are in the range of 10^6 - 10^8 . The microorganisms are mostly located at the surface and cannot be removed by washing. Table 1 shows the reduction of the total counts for potato cubes after a HP-application (in this case since $10 \times 10 \times 10$ mm cubes from the inside of the tuber were used, microorganisms which were washed off from the surface were added to reach an initial count of 10^6 CFU/ml).

Tab. 1

Effect of a high pressure application on the reduction of total counts (CFU/ml) in comparison to water blanching

°C	High-pressure 400 MPa/15 min	Water blanching at 100°C	
	CFU/ml	sec	CFU/ml
5	$< 10^2$	60	10^3
20	$< 10^2$	90	$< 10^3$
35	$< 10^2$	120	$< 10^3$
50	$< 10^2$	150	$< 10^3$

HP reduces the total counts similar to a mild blanching (which at 150 sec. is sufficient for a complete inactivation of the polyphenoloxidase an enzyme involved in the enzymatic browning of the products). Obviously and in line with the present "state of the art", spores cannot be inactivated sufficiently at temperatures up to 50°C by a HP-treatment; but temperatures above 65°C [6] are needed. However, this leads to heat-induced changes in the texture, flavor etc. A product treated under these conditions,

therefore, can no longer be called a "minimal processed" food. Within the present study, the incomplete inactivation was not a problem, since the HP-treated products were shelf stable (which means no microbial spoilage) for at least 5 months of cold storage (4°C).

3. Inactivation of enzymes

In contrast to vegetative microorganisms most food related enzymes are pressure tolerant. Fig. 1 and 2 demonstrate that only the polyphenoloxidase (PPO) and only in carrots and potatoes can be inactivated at 900 MPa, whereas an inactivation of the peroxidase (POD) is not possible even at this very high pressure. Fig. 1 and 2, furthermore, demonstrate that the inactivation is strongly depending on the corresponding vegetable and is more easily achieved in carrots in comparison to potatoes and most difficult in green beans (which show a similar resistance against heat).

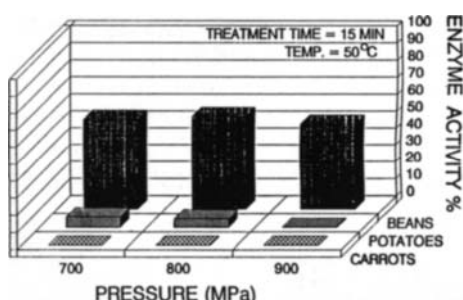


Fig. 1 Influence on the PPO-activity

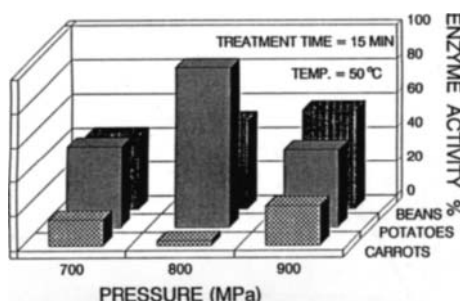


Fig. 2 Influence of UHP on the POD-activity

At 400 MPa which is the pressure most commonly used for food applications, the inactivation of the enzymes is even more incomplete (e.g. PPO about 70 % residual activity at room temperature and 40 % at 50°C). This leads to a denaturation of the cell membranes and the destruction of cell compartments, but limited inactivation of the enzymes. Therefore, in contrast to the intact cells, membrane bound enzymes and the corresponding substrates get into contact. In case of the PPO (in the presence of oxygen) this means a rapid and severe browning as shown in fig. 3 for potato cubes after opening an oxygen-tight pouch. In oxygen permeable pouches like polyethylene this severe browning occurs already in the pouch. Therefore, a non-oxygen permeable packaging is the precondition for a proper shelf life of HP-treated vegetables.

4. Texture and cooking behaviour

The texture of HP-treated vegetables has to be seen under 2 aspects:

- The texture during storage after the HP-treatment until consumption. In this case the texture should be almost identical to the fresh vegetable.
- The texture after cooking which is the usual way of preparation prior to consumption.

Due to the destruction of the cell membranes and the (at least partial) liberation of the cell liquor, a HP-treatment causes a certain but acceptable softening of the uncooked tissue. Due to this fact apple cubes in the apple jams being on the market in Japan show a crispy raw texture very similar to fresh apples. But since (in contrast to apples) vegetables normally are cooked prior to consumption, the texture after cooking is more important. Fig. 4 shows that HP-treated carrots no longer soften during cooking as non-treated vegetables do. This is the case also for potatoes, green beans, broccoli, celeriac, lentils, apples, bell pepper, and also for leafy vegetables as leek or Brussels sprouts.

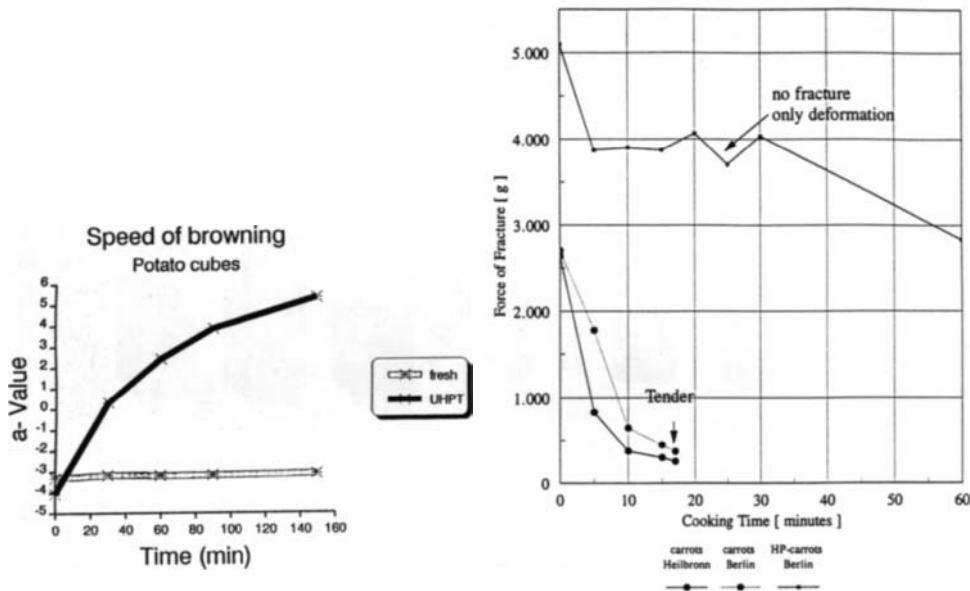


Fig. 3 Speed of enzymatic browning after a UHP-treatment Fig. 4 Texture of carrots (HP-treated 600 Mpa/15 min./ 20°C vs. non treated)

The softening upon cooking is known to be the result of a pectin degradation (preferably of a β -elimination which means a splitting of the highly methylated pectin chain besides a methoxyl group) leading to a swelling of the middle lamella of the plant cell wall and the corresponding softening of the tissue. Thus, alterations of pectin could be suggested and indeed a loss of the water and alkaline solubles resp. an overall loss of the extractable pectin has been detected after a HP-treatment.

Since the determination of the water, oxalate and alkaline soluble pectin is just an extraction followed by a precipitation, this loss could be either the result of a poorer extractability or of a degradation into lower molecular weight pectin fractions which no longer can be precipitated by ethanol. Obviously the degradation is negligible, because the viscosity of pectin solutions which should be a sensitive indicator for the breakage of already few bonds is not altered by the application of HP.

Finally, the alteration of the pectin extractability and the corresponding tissue hardening is the result of the liberation and insufficient inactivation of enzymes especially of the Pectinmethylesterase (PME) during a HP-application, which could be shown by our investigations and was also confirmed by Japanese researches [7].

5. Pectinmethylesterase activity and its effect on tissue hardening

PME activity is almost not affected in the usual pressure range up to 600 MPa [7]. In the intact cell, PME is bound to the cell wall, upon HP-application PME is liberated and gets into contact with its substrate the highly methylated pectin. This causes a de-esterification not only during the HP-application, but a continuous further deesterification can be observed after release of the pressure [8]. Therefore, the tissue hardening and poor cooking behaviour is even more pronounced after a storage of 3 - 4 days (fig. 5, 6).

Hardness of 12 min. cooked carrots

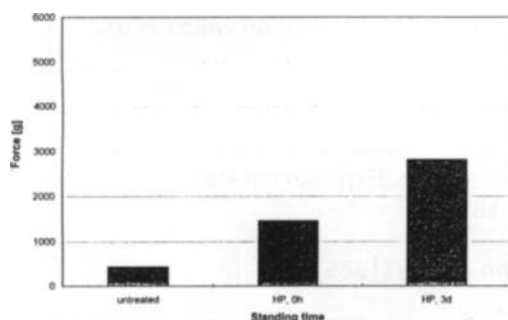


Fig. 5 After UHP-treatment 570 MPa, 15 min. at 20°C

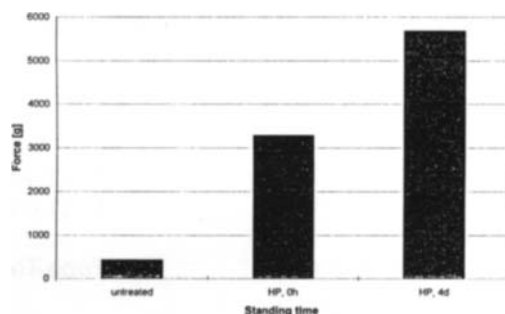


Fig. 6 After UHP-treatment 570 MPa, 15 min. at 50°C

Furthermore, the hardening effect is strongly depending on the temperature during HP-treatment (fig. 6). This is also clearly related to PME which shows a temperature optimum of the range of 50 - 60° C.

This activation of the PME at 50 - 60° C is well-known and used e.g. in the LTLT-blanching process (Long-Time-Low-Temperature) applied in the canning industry or in the precooking processes of the potato puree production processes. The mechanism of this tissue firming effect (which in canning reduces resp. avoids the tissue disintegration during the sterilization) has been described first by Bartolomé et al. [9].

Since heat (as well as HP) causes a denaturation of the cell membranes and also liberates the PME, the divalent cations (Ca, Mg) from the cell liquor come into contact with the deesterified pectin and form Ca-bridges. Within canning, this tissue firming effect is further promoted via the addition of Ca-salts.

Thus, it can be concluded that the HP-effect is very similar to what is known from canning. However, since tissue firming by HP is much more pronounced than described in canning pretreatments, it is suggested that the stronger hardening upon a HP-treatment is the result of a higher degree of deesterification, because the tissue softening during cooking is caused by a β -elimination.

6. Discussion and Conclusions

In spite of the fact that spores cannot be inactivated in the usual pressure range and at temperatures low enough to be in a range which can be called "minimally processed", microbial inactivation is not the barrier problem in the HP-treatment of vegetables and fruits. The main problem is that the enzymes are liberated from their location in the intact cells at much lower pressure (below 400 MPa) and even at much higher pressure same are not properly inactivated. Whereas certain effects can be overcome, e.g. the PPO-related severe browning by using packaging materials not permeable for oxygen, the effects of other enzymes, especially the tissue hardening effects of the PME, can currently not be properly avoided. Further investigations are needed to identify, if conditions can be selected where these effects can be utilized in a positive way, e.g. similar to the firming effect caused by the PME-activation which is used in canning.

REFERENCES

1. B. HITE
West Virginia Agric. Exp. Station Bulletin
58 (1989) 15
2. D. HOOVER et el.
Food Techn. 43 (3) (1989) 99
3. R. HAYASHI
Use of High Pressure in Food
Shokohin to Kaihatsu 22 (7) (1987) 55
4. EC PROJECT
"AIR" CT 92-0296
5. B. TAUSCHER
Annual Reports 1992, 1993, 1994, 1995
Bundesforschungsanstalt für Ernährung, Karlsruhe
6. T. OKAZAKI et el.
High Pressure Bio Science & Food Science
San-Ei Suppan Co, Kyoto (1994) 242
7. A. YAMAMOTO et el.
Nippon Shokulin Koggo Gakkaishi
39 (7) (1992/571)
8. S. CRELIER et el.
9th World Congress of Food Science & Techn.
Budapest, 31.07. - 04.08.1995; Poster P211
9. L.G. BARTOLOME et el.
J. Agric, Food Chem.
20 (2) (1972) 266

Partitioning of Carbohydrates in the Three-Phase Region of Systems Containing Carbon Dioxide, Water and a Modifier at High Pressure

O. Pfohl^a, R. Dohrn^b and G. Brunner^a

^aTU Hamburg-Harburg, AB Thermische Verfahrenstechnik, 21071 Hamburg, Germany

^bBayer AG, Zentrale Forschung und Entwicklung, ZF-T5, 51368 Leverkusen, Germany

Partitioning of carbohydrates in the vapor-liquid-liquid regions of the acetone+water+carbon dioxide system and the 2-propanol+water+carbon dioxide system has been investigated experimentally between 313 and 343 K and between 4 and 13 MPa. Both series yielded the same qualitative results. Partitioning of the carbohydrates between the two liquid phases of the vapor-liquid-liquid equilibria (VLLE) shows the dependencies of the carbohydrate K-factors on pressure and temperature. The Soave-Redlich-Kwong equation of state is suitable to reproduce carbohydrate partitioning in the glucose+acetone+water+carbon dioxide system.

1. INTRODUCTION

Experimental investigation of VLLE in acetone (or 2-propanol) + water + carbon dioxide systems has been of interest for many research groups^{1,2,3,4,5,6}. On the other hand there has been interest in partitioning of carbohydrates in high pressure vapor-liquid equilibria (VLE) of systems containing carbon dioxide, water and modifiers^{7,8,9,10}. Carbohydrates like glucose and fructose were taken as model compounds for more expensive carbohydrates which are separated by pharmaceutical and health industry. Usage of modifiers yielded mole fractions of carbohydrates in the vapor phase a thousand times higher than without modifier, but still too low to raise industrial interest in a separation of carbohydrates based on carbon dioxide.

In order to further increase the solubility of carbohydrates in the second phase necessary for separation and keeping the system pressure low, we investigated partitioning of carbohydrates between the liquid phases in the VLLE region of modifier + water + carbon dioxide systems.

2. EXPERIMENTAL

The experimental setup, procedure and analysis are described in detail by Pfohl et al.^{11,12}. For the systems containing acetone and 2-propanol, two different apparatuses have been used. Each apparatus (~1000 cm³, static-analytical method) is placed in a thermostated bath and equipped with sampling capillaries, thermocouples and high-precision pressure transducers.

The condensable part of a sample is separated from carbon dioxide by an expansion through cold traps. The condensate in the cold traps is weighed and analyzed with Karl-Fischer titration (water) and HPLC (carbohydrates). The modifier mass is calculated by weight difference. The weight-fraction ratio carbohydrates/water was 15/85 in the beginning of all experiments. In the systems containing 2-propanol, experiments have been carried out filling the autoclaves

once and changing temperature or pressure the succeeding days, while in the systems containing acetone the apparatus has been filled with fresh feed every day.

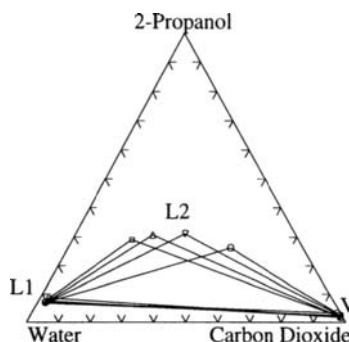
3. RESULTS

The results of the measurements in the quaternary systems glucose+2-propanol+water+carbon dioxide and glucose+acetone+water+carbon dioxide are listed in Table 1 and 2. Glucose was never detected in the gas phase, therefore the glucose mole fractions in the gas phase have been estimated according to a procedure described below. The data are well-behaved, showing the dependencies of all component mole fractions on pressure and temperature. Like in the glucose-free ternary subsystems¹⁻⁶ increasing temperature (at constant pressure, Figure 1) and decreasing pressure (at constant temperature) lead to a L2-phase composition more similar to the L1-phase composition until both phases become identical. Opposite changes of temperature and pressure lead to a L2-phase composition more similar to the gas-phase composition until the L2 phase and the gas phase become identical.

Figure 1.

Glucose-free projections of VLLE three-phase regions in the glucose + 2-propanol + water + carbon dioxide system at 9.6 MPa and different temperatures:

- = 325.65 K
- △ = 328.15 K
- ▽ = 333.15 K
- = 338.15 K



Partitioning of glucose shows an expected behaviour: when the middle phase becomes more similar to the (nearly glucose-free) carbon dioxide-rich upper phase the carbohydrate solubility in the middle phase decreases. Partitioning of glucose between the two liquid phases as a function of temperature and pressure is shown in Figure 2 and 3 for the 2-propanol and acetone systems. Using the Soave-Redlich-Kwong EOS¹³ with a modified α -function after the proposal by Schwartzentruber et al.¹⁴ and the mixing rule proposed by Mathias, Klotz and Prausnitz¹⁵ it is possible to predict the extent of the three-phase region in the glucose + acetone + water + carbon dioxide system and reproduce glucose partitioning between the two liquid phases. The binary interaction parameters for all binaries without glucose have been optimized to minimize deviations of experimentally determined phase compositions from calculated ones in the binary subsystems. The binary interaction parameters for glucose were regressed from the glucose K-factors determined in the quaternary system. The parameters and the literature sources for the binary data are listed in Ref. 11. The calculation results for the glucose K-factors (x^{L2}/x^{L1}) are plotted in Figure 3 together with the experimentally determined values. Agreement is good, it is within 20% covering a range from 0.00005 to 0.01.

Table 1
Mole Fractions from VLLE of the
Glucose+2-Propanol+Water+CO₂ System

P/MPa	Glucose	2-Prp.	Water	CO ₂
T/K				
9.14 V	$\sim 2 E-07$	0.015	0.006	0.979
333.15L2	5.10E-03	0.303	0.484	0.208
L1	3.16E-02	0.066	0.874	0.028
9.67 V	$\sim 2 E-07$	0.020	0.006	0.974
333.15L2	3.87E-03	0.302	0.439	0.255
L1	2.98E-02	0.054	0.888	0.028
10.17 V	$\sim 3 E-07$	0.027	0.008	0.965
333.15L2	2.32E-03	0.293	0.400	0.305
L1	2.26E-02	0.065	0.883	0.029
10.69 V	$\sim 5 E-07$	0.042	0.012	0.946
333.15L2	1.05E-03	0.290	0.372	0.337
L1	1.59E-02	0.065	0.889	0.030
11.19 V	$\sim 5 E-06$	0.088	0.034	0.878
333.15L2	6.63E-04	0.270	0.289	0.440
L1	1.38E-02	0.062	0.894	0.030
11.40 V	$\sim 1 E-05$	0.108	0.052	0.840
333.15L2	4.36E-04	0.263	0.261	0.475
L1	9.18E-03	0.059	0.906	0.026
11.60 V	$\sim 1 E-05$	0.127	0.069	0.804
333.15L2	3.41E-04	0.253	0.243	0.504
L1	6.27E-03	0.045	0.927	0.022
9.63 V	$\sim 4 E-07$	0.018	0.008	0.974
343.15L2	7.13E-03	0.268	0.571	0.154
L1	2.87E-02	0.059 ^a	0.887 ^a	0.026
9.67 V	$\sim 2 E-07$	0.017	0.007	0.976
338.15L2	4.35E-03	0.288	0.520	0.188
L1	2.30E-02	0.084	0.864	0.028
9.63 V	$\sim 2 E-07$	0.018	0.007	0.975
333.15L2	2.83E-03	0.305	0.447	0.245
L1	2.37E-02	0.074	0.875	0.027
9.62 V	$\sim 2 E-07$	0.023	0.007	0.970
328.15L2	1.35E-03	0.310	0.345	0.343
L1	2.31E-02	0.067	0.887	0.023
9.66 V	$\sim 6 E-07$	0.032	0.011	0.957
325.65L2	5.19E-04	0.262	0.227	0.511
L1	2.12E-02	0.068	0.887	0.024
9.45 ^b V	$\sim 3 E-07$	0.019	0.007	0.974
328.15L2	1.96E-03	0.307	0.342	0.349
L1	3.70E-02	0.045	0.893	0.025

Table 2
Mole Fractions from VLLE of the
Glucose+Acetone+Water+CO₂ System

P/MPa	Glucose	Actn.	Water	CO ₂
T/K				
4.02 V	$\sim 3 E-10$	0.014	0.003	0.983
313.0 L2	1.90E-05	0.383	0.107	0.510
L1	2.09E-02	0.066	0.885	0.028
6.11 V	$\sim 2 E-10$	0.014	0.003	0.983
313.0 L2	1.00E-06	0.183	0.031	0.786
L1	1.82E-02	0.019	0.934	0.029
4.10 V	$\sim 7 E-09$	0.022	0.008	0.970
323.0 L2	9.20E-05	0.442	0.187	0.371
L1	2.15E-02	0.083	0.870	0.025
6.10 V	$\sim 1 E-09$	0.020	0.005	0.975
323.0 L2	5.20E-06	0.311	0.051	0.638
L1	1.93E-02	0.032	0.924	0.025
4.16 V	$\sim 7 E-09$	0.030	0.008	0.962
333.0 L2	3.00E-04	0.450	0.253	0.297
L1	2.09E-02	0.094	0.856	0.029
6.07 V	$\sim 2 E-09$	0.030	0.006	0.964
333.0 L2	2.30E-05	0.350	0.113	0.537
L1	2.04E-02	0.059	0.894	0.027
8.23 V	$\sim 2 E-09$	0.031	0.006	0.963
333.0 L2	1.00E-06	0.171	0.041	0.788
L1	1.96E-02	0.011	0.944	0.025

^aOutlier, ^bIt is obvious, that within one series of experiments (either at constant temperature or at constant pressure) the ratio glucose/water decreases in all phases with increasing residence time of the carbohydrate in the autoclave (i.e. with rising pressure at constant temperature or at decreasing temperature at constant pressure, see above). We believe that the degradation of the carbohydrate has no influence on the phase equilibrium (especially glucose partitioning) within measuring accuracy. An additional experiment carried out with a new autoclave filling (9.45MPa, 328.15K) yielded the same results within measuring accuracy as an experiment with an autoclave filling as old as two weeks (9.62MPa, 328.15K) with lower carbohydrate content in all phases due to degradation.

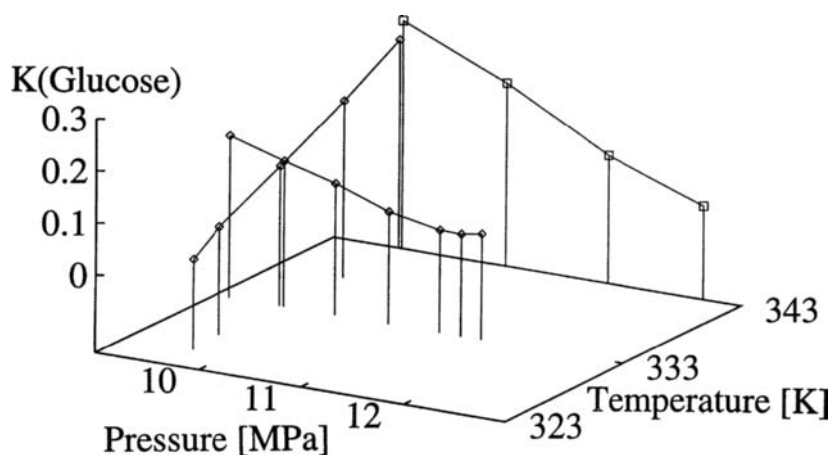


Figure 2. Glucose K-factors (x^{L2}/x^{L1}) from VLLE measurements in carbohydrate+2-propanol+water+carbon dioxide systems against system temperature and pressure. (\diamond = data from the glucose+2-propanol+water+carbon dioxide system, \square = data from the glucose+fructose+xylose+maltose+saccharose+2-propanol+water+carbon dioxide system from Ref. 12)

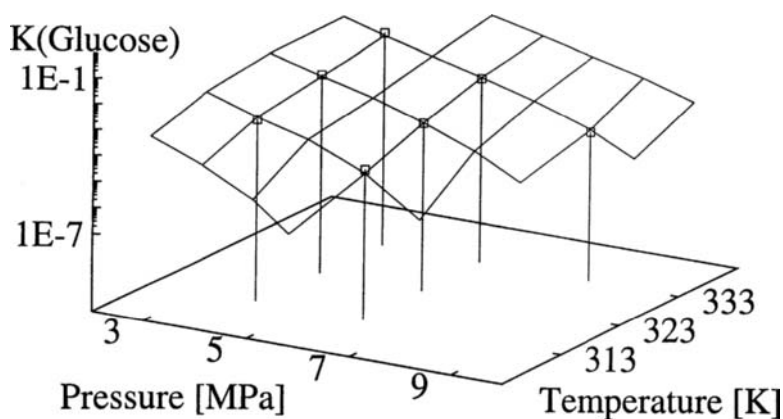


Figure 3. Glucose K-factors (x^{L2}/x^{L1}) from VLLE measurements in the glucose+acetone+water+carbon dioxide system against system temperature and pressure. (\square = experimental data, grid = calculation results with Soave-Redlich-Kwong EOS, see text)

4. COMPARISON WITH VLE DATA FROM LITERATURE

Bünz¹⁰ measured vapor-liquid equilibria in glucose + 2-propanol + water + carbon dioxide systems at temperatures between 313.15 and 343.15 K and pressures between 13.8 and 30 MPa. The overall weight ratio carbohydrates/water was the same as intended in this study: 15/85. Glucose K-factors in the systems with modifier increased when approaching the plait point of the glucose-free projection on the 2-propanol + water + carbon dioxide surface. This behavior is the equivalent to the results obtained here: K-factors (x^{L2}/x^{L1}) for glucose between the two liquid phases approach unity when the two liquid phases merge. Figure 4 shows a plot of all glucose K-factors from Bünz and this study against the water K-factor in glucose + 2-propanol + water + carbon dioxide systems. The points lie on one straight line through the critical points where the phases of interest merge ($K_{\text{glucose}}=K_{\text{water}}=1$). From this empirical relationship $K_{\text{glucose}} = K_{\text{water}}^{2.4}$ for the glucose+2-propanol+water+carbon dioxide system, the glucose mole fractions in the vapor phase of our experiments can be estimated based on the water K-factor y/x^{L1} and the glucose fraction in L1. y/x^{L2} -K-factor pairs glucose-water then automatically come to lie near the same line. In addition to the experimentally determined K-factors (x^{L2}/x^{L1} , solid symbols: ●, ■) these extrapolated K-factors (y/x^{L1} and y/x^{L2}) of glucose are plotted in Figure 4 against the experimentally determined K-factors of water for the 2-propanol (○) and acetone (□) containing systems. Glucose K-factors in the acetone systems lie systematically lower than in the 2-propanol systems indicating 2-propanol is a better modifier for glucose + water + carbon dioxide systems. This is not unexpected because of chemical similarity of 2-propanol and glucose due to the hydroxy groups and because pure acetone is a poor solvent for glucose.

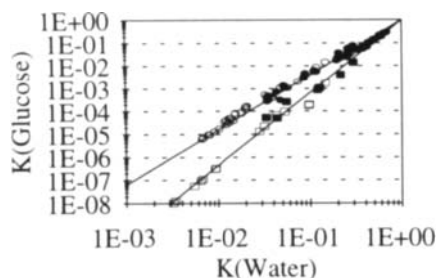


Figure 4. ● = Experimentally determined x^{L2}/x^{L1} of VLLE in glucose + 2-propanol + water + carbon dioxide systems here and y/x of VLE¹⁰, ■ = exp. determined x^{L2}/x^{L1} of VLLE in glucose + acetone + water + carbon dioxide systems, ○, □ = extrapolated y/x^{L1} and y/x^{L2} of VLLE in systems with 2-propanol and acetone

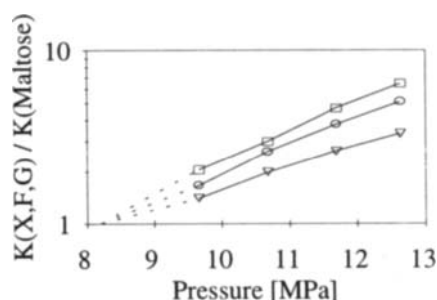


Figure 5. Separation factors between different carbohydrates (□ = xylose, ○ = fructose, ▽ = glucose) and maltose in the xylose + fructose + glucose + maltose + saccharose + 2-propanol + water + carbon dioxide system at 343.15 K and different pressures¹².

The well-known disadvantage of performing separations in the vicinity of the critical point where the phases of interest become identical, is, that the separation factors ($\alpha_{a,b}=K_a/K_b$)

between compounds to separate approach unity in the vicinity of the critical point. Our data¹² for carbohydrate separation between L1 and L2 in the glucose+fructose+xylose+saccharose+maltose+2-propanol+water+carbon dioxide system also show this (Figure 5), enforcing a higher number of theoretical plates for the separation and minimizing the benefit of high carbohydrate solubility in the upper liquid phase

5. CONCLUSIONS

Phase compositions of VLLE in the systems glucose + acetone + water + carbon dioxide and carbohydrates + 2-propanol + water + carbon dioxide have been determined experimentally. Like for VLE of related systems from literature, the carbohydrate solubility in a phase rises when the phase becomes more similar to the water-rich lower liquid phase. At the same time separation of different carbohydrates becomes more difficult because selectivity decreases. Theoretically based models can help to find an optimum of capacity and selectivity and to minimize the number of necessary experiments. A simple model based on the Soave-Redlich-Kwong EOS which can reproduce glucose partitioning between the two liquid phases in VLLE in the glucose + acetone + water + carbon dioxide system is presented. 2-Propanol is shown to be a better modifier for these systems than acetone, but denaturation of carbohydrates in the carbohydrate + 2-propanol + water + carbon dioxide system limits industrial applications.

ACKNOWLEDGMENTS

This work was supported by the Deutsche Forschungsgemeinschaft with the 'Gerhard-Hess-Förderpreis'.

REFERENCES

- (1) J.R. DiAndreth and M.E. Paulaitis, *Fluid Phase Equilibria* 32 (1987) 261
- (2) M. Radosz, *Ber. Bunsenges. Phys. Chem.* 88 (1984) 859
- (3) M. Wendland, H. Hasse and G. Maurer, *The Journal of Supercritical Fluids* 6 (1993) 211
- (4) A.Z. Panagiotopoulos and R.C. Reid, in: *ACS Symposium Series* 329 (1987) 115
- (5) P. Traub and K. Stephan, *Chem. Eng. Sci.* 45 (1990) 751
- (6) M. Wendland, H. Hasse and G. Maurer, *The Journal of Supercritical Fluids* 7 (1994) 245
- (7) E. Stahl and W. Schilz, *Chem.-Ing.-Tech.* 50(7) (1978) 535
- (8) R. D'Souza and A.S. Teja, *Fluid Phase Equilibria* 39 (1988) 211
- (9) J.S. Yau and F.N. Tsai, *The Journal of Supercritical Fluids* 7 (1994) 129
- (10) A.P. Büinz, PhD thesis, TU Hamburg-Harburg, AB 6-03 (1995)
- (11) O. Pfohl, J. Timm, R. Dohrn and G. Brunner, accepted by *Fluid Phase Equilibria* 12/95
- (12) O. Pfohl, J. Petersen, R. Dohrn and G. Brunner, submitted to *The Journal of Supercritical Fluids* 3/96
- (13) G. Soave, *Chem. Eng. Sci.* 27 (1972) 1197
- (14) J. Schwartzentruber, H. Renon and S. Watanasiri, *Fluid Phase Equilibria* 52 (1989) 127
- (15) P.M. Mathias, H.C. Klotz and J.M. Prausnitz, *Fluid Phase Equilibria* 67 (1991) 31

THE FRACTIONATION OF HIGH MOLECULAR WEIGHT ALKANE MIXTURES WITH SUPERCRITICAL FLUIDS

I. Nieuwoudt

Department of Chemical Engineering, University of Stellenbosch, Stellenbosch, 7599, South Africa

SUMMARY

In this study it was shown that propane or mixtures of propane and butane may be used as supercritical solvents to fractionate mixtures of high molecular weight alkanes. By using an optimum reflux ratio, selectivities better than that of molecular distillation can be obtained. It was also found that for the system in this study, the operating costs of a supercritical extraction unit may be marginally lower than that of a molecular distillation unit.

1. INTRODUCTION

Alkane mixtures of high polydispersity can be used in many applications, but markets also exist for alkane fractions with low polydispersity. These include markets such as ink, varnish and hot melt adhesive applications and thermostat wax. In the past alkane fractions were produced by means of liquid-liquid extraction and solvent crystallization. The lack of sharpness of the fractions as well as the residual solvents in the products counted against these processes. More recently molecular distillation was used to fractionate alkane mixtures, but high operating temperatures limit the molecular weight of distillate that can be produced. The aim of this study was to develop a process to produce alkane fractions with lower polydispersity than that of competing technologies. The low operating temperatures used in supercritical extraction makes it particularly attractive for the fractionation of heat labile substances of low volatility.

2. PHASE EQUILIBRIUM MEASUREMENTS AND MODELLING

Although CO₂ is the most common solvent for supercritical extraction processes because of its abundance, non-toxicity and non-flammability, other compounds may prove to be better solvents in certain instances. In choosing a solvent, a balance between solubility and selectivity has to be struck. In the case of solutes with a melting point well below the decomposition temperature, it is usually desirable to perform a liquid-supercritical fluid extraction to circumvent the problems associated with handling solids at high pressures. In

this case it makes sense to choose a solvent with a critical temperature close to the cloud point of the solute to prevent congealing problems. The difference between the solvent's critical temperature and the solutes' cloud point will be dictated by the balance between solubility and selectivity. In this study the solutes were Tetrapentacontane($n\text{-C}_{54}\text{H}_{110}$, melting point $\approx 95^\circ\text{C}$) and Hexacontane($n\text{-C}_{60}\text{H}_{122}$, melting point $\approx 98^\circ\text{C}$). Propane with a critical temperature of 96.8°C or LPG (inexpensive mixtures of propane, iso-butane and n-butane) were considered to be the most appropriate solvents. With only one data set of relevance to this study available in the literature [1], a variable volume equilibrium cell was used to measure vapour-liquid equilibrium and density data for model binary systems. A schematic diagram of the cell is shown in figure 1.

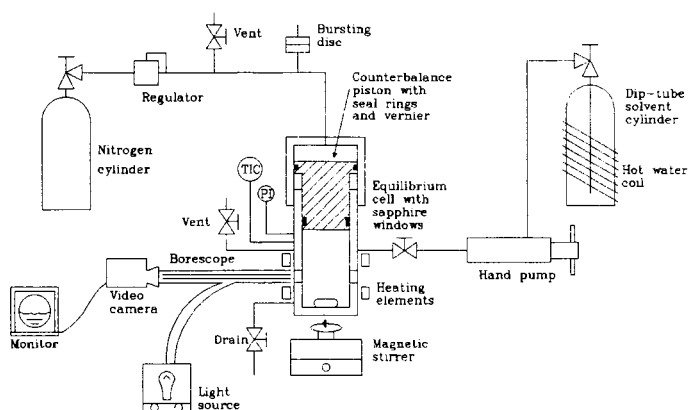


Figure 1. Variable volume equilibrium cell

The experimental procedure was described in a previous publication[2]. Data sets were measured for the following systems: n-Butane + Tetrapentacontane, n-Butane + Hexacontane, LPG(n-Butane rich) + Hexacontane and LPG(Propane rich) + Tetrapentacontane. The first three data sets were reported previously[2,3]. The vapour-liquid equilibria and density data for the system LPG + Tetrapentacontane is shown in figures 2 and 3 respectively. The composition of the propane rich LPG used in the LPG + Tetrapentacontane measurements, as determined with capillary GC with an FID detector, is shown in table 1.

Table 1
Composition of Propane rich LPG

Component	Mass %
Propane	93.1
iso-Butane	3.9
n-Butane	2.1
Butene isomers	0.9

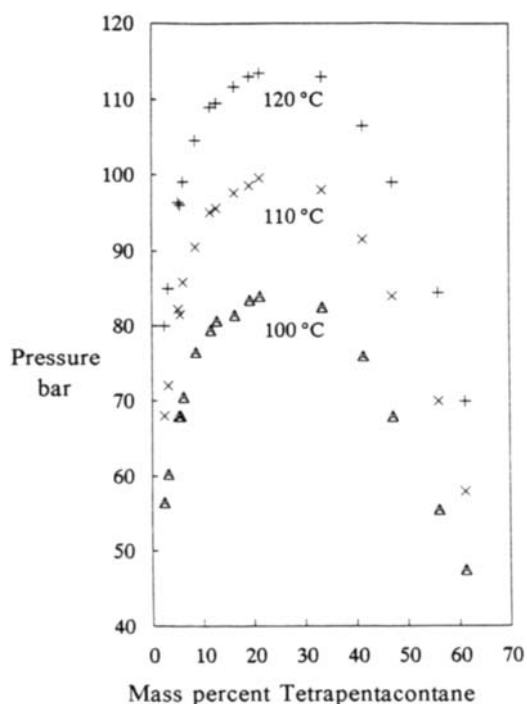


Figure 2. Vapour-liquid equilibria for the system LPG + Tetrapentacontane

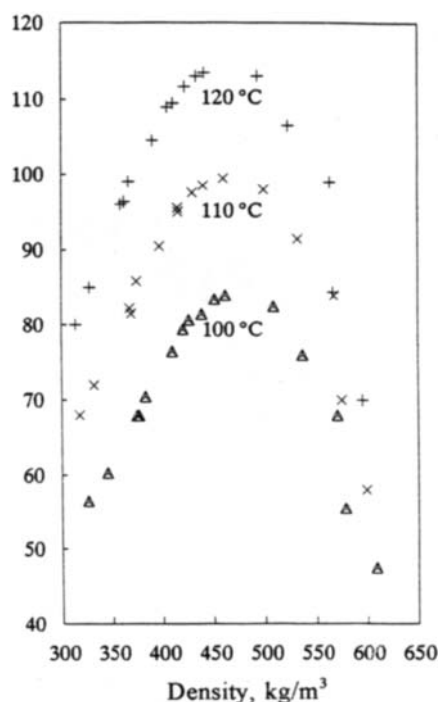


Figure 3. Density data for equilibrium mixtures of LPG + Tetrapentacontane

From figure 2 and 3 it can be seen that the vapour phase contains a significant amount of the solute and that the density difference between the liquid and vapour is adequate.

Although equations of state based on statistical mechanics, like the Perturbed Hard Chain and Chain of Rotators equations of state are good at predicting phase equilibria at conditions far from the critical point of mixtures, a critical evaluation of six of these type of equations of state showed that they are rather inaccurate in the mixture critical region[3]. Satisfactory correlation of the data is obtained with a Peng Robinson equation of state using two interaction parameters per binary as proposed by Shibata and Sandler[4]. The correlations of Huang[5] were used for the pure component parameters.

$$P = \frac{RT}{v - b} - \frac{a(T)}{v(v + b) + b(v - b)} \quad (1)$$

$$\alpha = \left[1 + m(\omega) \left(1 - T_R^{0.5} \right) \right]^2 \quad (2)$$

$$m(\omega) = 0.379642 + 1.48503 \omega - 0.164423 \omega^2 + 0.016666 \omega^3 \quad (3)$$

$$a = \sum_i^N \sum_j^N x_i x_j a_{ij} \quad (4)$$

$$b = \sum_i^N \sum_j^N x_i x_j b_{ij} \quad (5)$$

$$a_{ij} = (1 - k_{ij}) \sqrt{a_i a_j} \quad (6)$$

$$b_{ij} = (1 - l_{ij}) \frac{(b_i + b_j)}{2} \quad (7)$$

Following Twu et al [6] and Johnston et al [7] and simulation packages such as PRO II, the interaction parameter will be allowed to vary with temperature to account for some of the inaccuracies in the equation of state:

$$k_{ij} = k_{ij}^0 + k_{ij}^1 T(^{\circ}\text{C}) \quad (8)$$

It is also assumed that, in the case of n-alkane mixtures, the k_{ij} -values are independent of the chain length of component j . Dimitrelis and Prausnitz[8] showed that there is a systematic deviation from the Carnahan and Starling[9] repulsive term as the difference in molecular size between two molecules increase. It is thus expected that the value of the interaction parameter l_{ij} will be related to the difference in size between the two molecules. It is assumed that the value of l_{ij} will approach a constant value when this difference becomes large. The interaction parameters for propane and n-butane were found by fitting this equation of state to the data mentioned above. The parameters are shown in table 2:

Table 2

Binary Interaction parameters for the supercritical solvents with Tetrapentacontane and Hexacontane

Component	k_{ij}^0	k_{ij}^1	l_{ij}
Propane	0.0119	4.0×10^{-5}	0.102
i-Butane	0.0446	2.3×10^{-4}	0.126
n-Butane	0.0615	3.3×10^{-4}	0.139

Since the concentration of i-Butane in commercially available LPG is generally low, it was assumed that the binary interaction parameters between i-butane and the high molecular weight n-alkanes can be estimated by interpolation between that of propane and n-butane. *This model and interaction parameters must not be misconstrued as being an attempt at proposing a fundamental model. It must merely be seen as an empirical fit to the data that enables us to do multi-stage calculations for these systems.* The fit of this model to the Propane + Hexacontane data of Peters et al[1] and the n-Butane + Tetrapentacontane data of the author[2] are shown in figures 4 and 5. Reasonable agreement between the

agreement between the experimental data and the equation of state was obtained. This model was incorporated in a countercurrent extraction simulation.

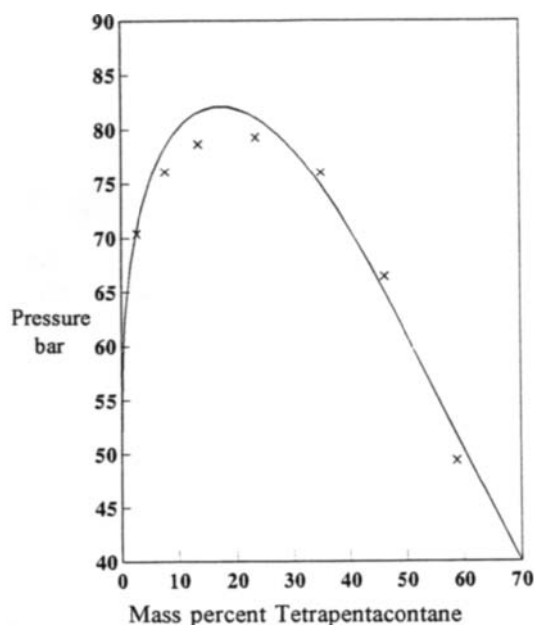


Figure 4. Vapour-liquid equilibria for the system n-Butane + Tetrapentacontane at 180 °C [2]

Solid line: Peng Robinson EOS

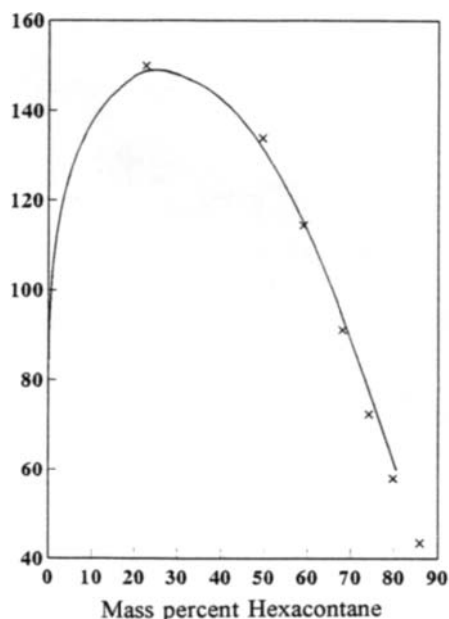


Figure 5. Vapour-liquid equilibria for the system Propane + Hexacontane at 146.9 °C [1]

Solid line: Peng Robinson EOS

3. COUNTERCURRENT FRACTIONATION OF ALKANE MIXTURES

As was pointed out earlier, molecular distillation is normally used to fractionate mixtures of components of very low volatility. It is proposed that a supercritical fractionation process, as schematically shown in figure 6, can be used to produce fractions superior to that of molecular distillation. In order to test this, a molecular distillation model must be used. As a first approximation, the molecular distillation of high molecular weight alkanes is viewed as a simple flash. The vapour pressure data of Kudchadker et al[10] was used in the flash calculations.

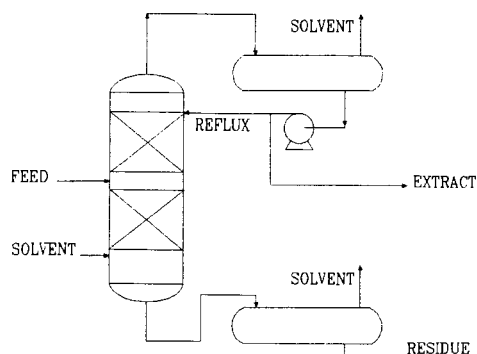


Figure 6. Countercurrent supercritical fractionation with reflux

As an example, 50 mass % of a feed, consisting of 50 mole% Tetrapentacontane and 50 mol% Hexacontane, was flashed off. The operating conditions were 20 Pa and 300°C. A selectivity for this separation is defined as follows:

$$S_{i,j} = \frac{x_{i,dist} / x_{i,bot}}{x_{j,dist} / x_{j,bot}} \quad (9)$$

In the case of a flash this is simply the K-value. In this example, a K-value of 1.98 was obtained. The selectivities of the proposed supercritical extraction process will be compared with this value.

In order to make a comparison, a countercurrent supercritical extraction column with 12 theoretical stages and a solvent to feed ratio of 15:1 was used in the simulations. An extraction temperature of 115°C was used in all the simulations. Countercurrent extraction without reflux yielded a selectivity of 1.8. This means that countercurrent extraction without reflux will not be able to match the selectivity of molecular distillation. In the cases with reflux, 6 stages above and 6 stages below the alkane feed point was used. In using reflux, there are two opposing forces: In general a higher reflux ratio will give better separation, but in order to keep the extract at 50 mass% of the feed at these higher reflux ratios, the pressure has to increase to increase the solubility. At higher pressures the selectivity is adversely affected as was also found by de Haan[11]. This means that an optimum reflux ratio exists. This is illustrated in figure 7. In this example, the optimum reflux ratio is 2.15, giving a selectivity of 2.45. *If the number of theoretical stages is increased from 12 to 20 at a reflux ratio of 2.15, a selectivity of 2.80 is predicted.*

Calculations have also shown that the operating costs of a this supercritical fractionation unit may be marginally lower than that of a molecular distillation unit.

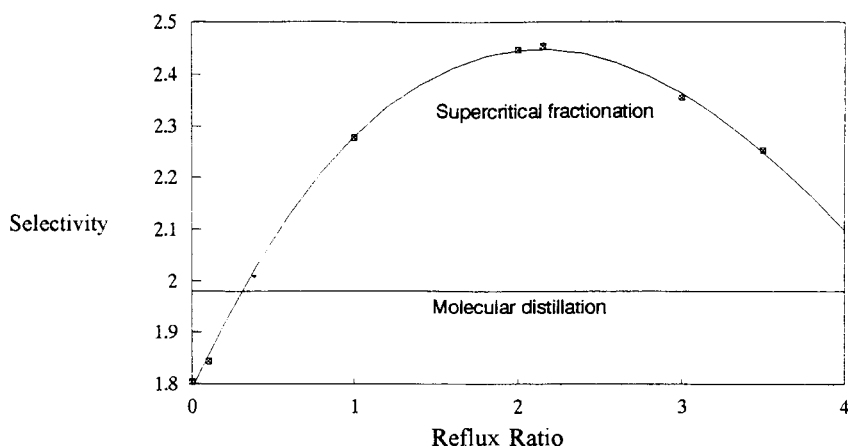


Figure 7. Selectivity as a function of reflux ratio for a supercritical propane extraction unit. Feed is an equimolar mixture of Tetrapentacontane and Hexacontane. Residue is 50 mass% of the feed. Solvent to feed ratio = 15:1 Number of theoretical stages = 12
Temperature = 115°C

4. CONCLUSIONS

Supercritical fractionation of high molecular weight alkane mixtures with propane or LPG may be used to produce products with lower polydispersity than that of molecular distillation. Operating temperatures just above the cloud point of the mixtures can be used compared to the high temperatures needed in molecular distillation. It was also shown that an optimum reflux ratio exists for every set of operating conditions. For this system it was also found that the operating costs of a supercritical fraction unit is marginally less than that of a molecular distillation unit.

LIST OF SYMBOLS

α	Defined in equation 2	
a	Energy parameter in Peng Robinson equation of state	(Nm ⁴ /mol ²)
b	Co-volume parameter in Peng Robinson equation of state	(m ³ /mol)
k	Binary interaction coefficient for energy parameter in Peng Robinson equation of state	
l	Binary interaction coefficient for co-volume parameter in Peng Robinson equation of state	
m	Defined in equation 3	
P	Pressure	(Pa)
R	Universal gas constant	(J/mol/K)
S	Selectivity defined in equation 9	
T	Temperature	(K)
v	Molar volume	(m ³ /mol)
x	Mole fraction	

SUBSCRIPTS

i	Component i
j	Component j
R	Reduced conditions
dist	Distillate
bot	Bottom product

REFERENCES

1. Peters, C.J., de Roo, J.L. and de Swaan Arons J. Phase equilibria in binary mixtures of propane and hexacontane, Fluid Phase Equilibria, Vol. 85, 1993, pp. 301 - 312.
2. Nieuwoudt, I. Ph.D. Thesis, University of Stellenbosch, South Africa, 1994.
3. Nieuwoudt, I. Vapour-liquid equilibrium and density data for the system n-butane + hexacontane, Journal of Chemical and Engineering Data, Accepted for publication.
4. Shibata, S.K. and Sandler, S.I. Critical Evaluation of Equation of State Mixing Rules for the Prediction of High-Pressure Phase Equilibria, Ind. Eng. Chem. Res., Vol. 28, 1989, pp. 1893-1898.
5. Huang, S H.-W. Synthesis Gas Solubility in Fischer-Tropsch Slurry, Ph.D. Purdue University, 1987, U.M.I, Ann Arbor, MI, USA.
6. Twu, C.H., Bluck, D., Cunningham, J.R. and Coon, J.E. A Cubic Equation of State with a New Alpha Function and a New Mixing Rule, Fluid Phase Equilibria, Vol. 69, 1991, pp. 33-50.
7. Johnston, K.P., Peck, D.G. and Kim, S. Modelling supercritical mixtures: How predictive is it? , Ind. Eng. Chem. Res., Vol. 28, 1989, pp. 1115 - 1125.
8. Dimitrelis, D and Prausnitz, J.M. Comparison of two Hard-Sphere Reference Systems for Perturbation Theories for Mixtures, Fluid Phase Equilibria, Vol. 31, 1986, pp. 1-21.
9. Carnahan, N.F. and Starling, K.E. Intermolecular Repulsions and the Equation of State for Fluids, AIChE Journal, Vol. 18, No. 6, November 1972, pp. 1184-1189.
10. Kudchadker, A.P. and Zwolinski, B.J. Vapor Pressures and Boiling Points of Normal Alkanes, C_{21} to C_{100} , Journal of Chemical and Engineering Data, Vol. 11, No. 2, April 1966, pp.253-255.
11. de Haan, A.B. Supercritical Fluid Extraction of Liquid Hydrocarbon Mixtures, Ph.D., Delft University of Technology, CIP-Gegevens Koninklijke Bibliotheek, Den Haag, 1991.

Separation of Multicomponent Mixtures of Fatty Acid Ethyl Esters from Fishoil by Countercurrent SFE

C. Tiegs ^a, V. Riha ^b, G. Brunner ^b and K. Steiner ^a

^aF. Hoffmann-La Roche Ltd., Vitamins & Fine Chemicals Division, High Pressure Center, CH-4070 Basel, Switzerland

^bTechnische Universität Hamburg-Harburg, Eissendorfer Strasse 38, D-21071 Hamburg

A trend to an enrichment of active substances on a high concentration level out of natural products can be noticed in the recent years. Attention is paid to the added value as well as to the stability of the product. A disadvantageous treatment of thermolabile compounds may cause a cracking or oxidation of the product. In many cases extraction with compressed gases (e.g. with CO₂) will match the requirements, set by the above mentioned trend.

This paper demonstrates the purification of fatty acid ethyl esters, FAEE, due to their chain length.

1. INTRODUCTION

Since the publication of Bang and Dyerberg (1971) on coronary heart disease of Eskimos more attention was paid to the influence of polyunsaturated fatty acids (PUFA) on health. Meanwhile a lot of publications dealing with the benefits of PUFA application are available. Along with this knowledge an increasing interest for suitable commercial processes to recover PUFAs in concentrated forms can be monitored. To overcome some disadvantages of conventional methods such as n-hexane extraction or vacuum distillation, an extraction with supercritical carbon dioxide (SC-CO₂) in a counter current multistage high pressure column was tested. The method is suitable for separation due to chain length. The high-value substances EPA and DHA are enriched in their chain length fraction, Nilsson (1988). SC-CO₂ as a non toxic and inflammable extraction solvent offers the advantage for fractionation and recovery at moderate temperatures, Staby (1993).

For the production of EPA- resp. DHA-rich fractions three runs at different extraction conditions which split between C18 / C20, C20 / C22 and C22 / >C24 are necessary.

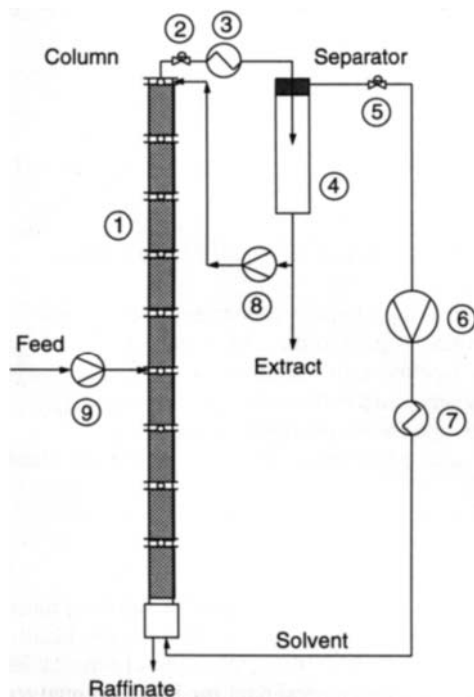
In this paper the first separation step between the C18- and the C20 chain length will be described.

The separation analysis by established methods of McCabe -Thiele or Ponchon Savarit are compared with a flow sheeting program ASPEN+. It will be demonstrated, that a reliable scale-up is possible combining all these methods.

The fishoil ethyl esters, used in all experiments are derived from sardine oil. Analysis was carried out with a Hewlett Packard 5890 Series II gas chromatograph with 30 m x 0,32 m ID Stabilwax column (Restek Corp., Bellefonte, PA), Riha et al. (1996).

2. EXPERIMENTAL SETUP

The separation experiments were carried out in a pilot-plant column with an inner diameter of 68 mm and an effective height of 12 m. Following the principle flow scheme in figure 1, feed (9) entering e.g. the middle of the separation column (1) is separated into top and bottom product. Top product is expanded (2) and passed through heat exchanger (3). Temperature and pressure in the separator (4) are adjusted to conditions, which gives liquid product and



completely regenerated CO_2 . The CO_2 -circle is closed by a compressor (6) and heat exchanger (7). Reflux is added to the top of column (1) with pump (8). System pressure in the extraction and separation part are controlled via back pressure valves (2) resp. (5). A second CO_2 circle is installed, which allows to recover nearly all dissolved CO_2 in the liquid products (not shown in figure 1). Column (1) and the upper part of the separator (4) are filled with wire mesh Sulzer packing, type CY. Each flange of the column is equipped with a special device for gas- resp. liquid sampling in order to monitor concentration profiles along the column. The experiments were carried out under isothermal and isobaric conditions. Typical experimental operation conditions are summarized in table 1.

Table 1: Typical experimental operation conditions

Temperature	[K]	333
Pressure	[MPa]	14 - 16
m (feed)	[kg/h]	2 - 2.5
m (solvent)	[kg/h]	250 - 300

Figure 1: Principle flowscheme of pilot plant

3. PHASE EQUILIBRIUM

Phase equilibrium measurements with supercritical SC-CO_2 as solvent were performed with a variable volume static cell, Riha 1996. Isotherms and partition coefficients were determined for 13 oils. Each oil represents a separation product.

The experimental data are correlated with equation of state models. The calculation of binary phase equilibrium data for FAEE is commonly based on the Peng-Robinson-equation-of-state, Yu et al. (1994). Up to now only the solubility of the oil components in the solvent has been subject of various studies. No attention was paid to a correlation of ternary data. The computation of ternary or multicomponent phase equilibrium is the basis to analyse and optimise the separation experiments.

Table 2: Equations for the phase equilibrium correlation

Peng- Robinson	$P = \frac{RT}{v_m - b} - \frac{a(T)}{v_m^2 + 2bv_m - b^2}$
Attraction Parameter	$a(T) = \sum_{i=1}^m \sum_{j=1}^m x_i x_j a_{ij}$
Melhem mixing rule	$a = \sum_{i=1}^N \sum_{j=1}^N x_i x_j \sqrt{a_i a_j} \left(1 - k_{ij} + (k_{ij} - k_{ji}) \frac{x_i}{x_i + x_j} \right)$
Interaction parameters	$k_{ij} = k_{ij}^a + k_{ij}^b \cdot T$
Objective Function	$\sum_i \left\{ \left[\frac{(x_i^{calc} - x_i^{mess})}{x_i^{mess}} \right]^2 + \left[\frac{(y_i^{calc} - y_i^{mess})}{y_i^{mess}} \right]^2 + \left[\frac{(K_i^{calc} - K_i^{mess})}{K_i^{mess}} \right]^2 \right\}$

Table 3: Physical data of the pseudo components

Pseudo component	M [g/mol]	T _B [K]	T _C [K]	p _C [MPa]	ω [-]
CO ₂	44.01	194.7	304.2	7.38	0.239
LVC	309	637.7	787.3	1.18	0.945
HVC	331	656.9	802.1	1.09	1.044

Table 4: Results for the binary interaction parameters and the corresponding AAD-values

ij	k^a	k^b		
12	-1.59E-3	2.70E-1	AAD-x	8.10E-3
13	-2.13E-4	-5.89E-1	AAD-y	1.24E-3
21	-1.83E-4	9.21E-2	AAD-Ki-LVC	2.29E-2
23	-1.57E-4	-1.35E-2	AAD-Ki-HVC	2.08E-2
31	3.44E-4	-1.03E-1		
32	-1.24E-4	-1.42E-2		

Table 3 lists the critical data used for the computation. The physical data for HVC is equal to C18 and for LVC to C20.

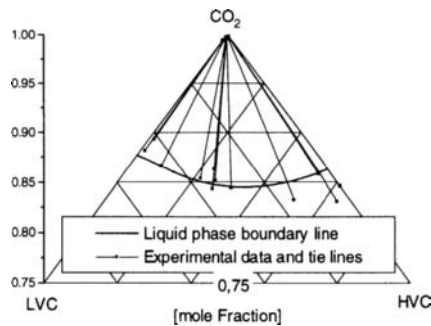


Figure 2: Measured and calculated phase equilibrium at T = 333 K and p = 14 MPa

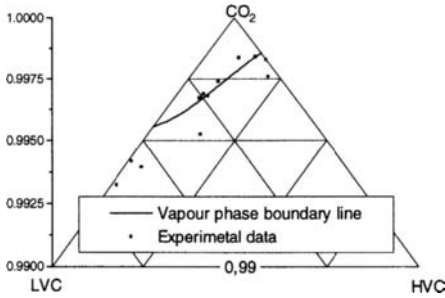


Figure 3: Selective enlargement of the vapour phase

Basically the distribution of a component between the two phases is a function of the chain length. Therefore components with an identical chain length and a variation between their degree of saturation are lumped together into one pseudo component. This procedure gives an opportunity to monitor and describe the phase equilibrium behaviour.

In a first step the ternary phase equilibrium is calculated using the Peng-Robinson-equation-of-state, Table 2. All components with a volatility higher or equal C18 are lumped into one pseudo component, HVC, while all components that tend to enrich in the liquid phase form the Low-Volatile pseudo Component, LVC. The emphasis of the computation lies on a correct interpretation of the phase composition. Therefore attention has to be paid to the solubility as well as to the partition coefficient, K_j , between the oil components HVC and LVC.

The good agreement between experimental and calculated values is pointed out by the average absolute deviation, AAD. The results demonstrate the possibility to compute the solubility as well as the partition coefficients with the Peng-Robinson-equation of state and a mixing rule with two interaction parameters.

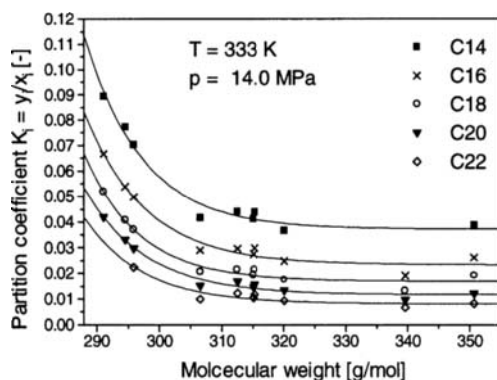


Figure 4: Correlation between the partition coefficient for the pseudo components versus the molecular weight of the mixture

partition coefficient as a function of the composition. The partition coefficient K_i of a pseudo component has been found to be a function of the molecular weight, Riha 1996.

4. SEPARATION

The parameters for the separation were varied in the range given in table 1. The results of one experiment are presented in table 5. The solvent mass flow in this case was 300 kg/h with a

Table 5

Experimental results

	Extract	Feed	Raffinate
\dot{m} [kg/h]	1.60	2.40	0.80
C14 [wt.-%]	12.6	8.4	0
C16 [wt.-%]	50.5	33.7	0
C18 [wt.-%]	32.9	22.3	1.0
C20 [wt.-%]	4.0	21.2	55.8
C22 [wt.-%]	0	14.4	43.2

mass flow is considerably high. A yield of 93 % at a purity of 99 % related to the C20 and C22 fraction in the raffinate indicates a promising start point for a scale-up.

4.1 Modelling the separation

Established methods like McCabe-Thiele or Ponchon-Savarit may be used to compute the number of theoretical stages for a given separation. Both methods are limited to a binary

Table 4 shows the results for a regression to 209 data points. Figure 2 and 3 are plots of the phase equilibrium calculations at $T = 333$ K and $p = 14$ MPa. The tie lines in Figure 2 represent the measured values. The implementation of an additional term into the objective function improves drastically the results for the K_i -values.

Hence it is possible to compute the ternary phase equilibrium data with a equation of state. The effort to transfer these results to a multi-component system is tedious. Therefore a simple empirical model is used to correlate the partition coefficient K_i of a pseudo component has been found to be a function of the molecular weight, Riha 1996.

It also points out the high standard of this technique. Compared to literature data the

Table 6: Number and height of theoretical stages

	NTU	HETP [m]
McCabe-Thiele	40	0.30
Ponchon-Savarit	38	0.32
Aspen+	≈ 45	0.27

system in respect to the involved oil components. This case is identical to the ternary phase equilibrium computation mentioned above. The separation of a real fishoil system is connected to the separation of directly adjacent pseudo components. In our case this is the separation between the C18 and the C20 component. The separation factor α as the ratio between the K_i -

values for these components assumes a minimum value. A dependence of the separation factor on the molecular weight could be observed. An average value of $\alpha = 1.33$ can be taken to model the separation. The phase boundary- and tie-lines for the Ponchon-Savarit-method are calculated with the results from the ternary phase equilibrium study. Table 6 lists the calculated number of theoretical stages, NTU, and the resulting height for one theoretical plate, HETP. An efficiency equal to one was assumed for each theoretical plate.

The simulation of a multi-component system was done with the flow sheeting program Aspen+. An external routine replaced the internal K_i -calculation with a fit function through the experimental K_i -values as given in figure 4. The multistage column was split into a cascade of flash modules. Each module is connected to two other modules following the theory of a theoretical separation unit. The separator at the top of the column

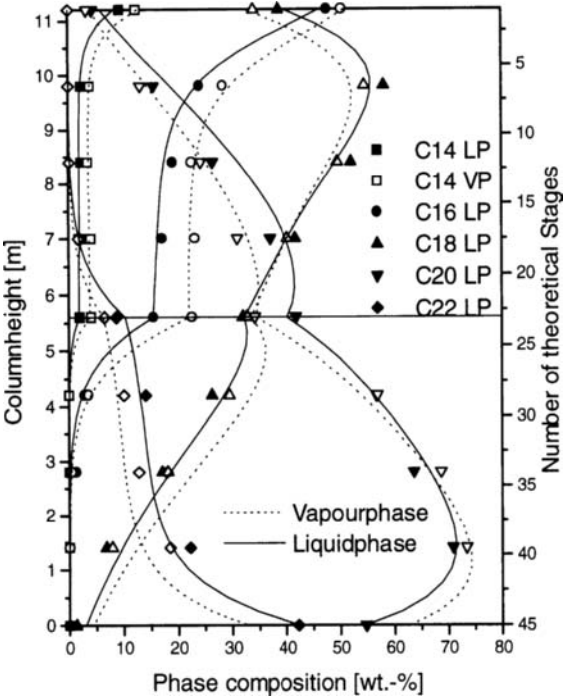


Figure 5: Measured and with Aspen+ calculated column profile for five pseudo components

is represented by a split module. Aspen+ iterates until all mass balances and phase equilibrium conditions are fulfilled. Energy balances are neglected. The obtained results have to be compared with the experiments. Solving the problem with Aspen+ takes the number of theoretical stages as a input value. Therefore the determined value is the result of an iterative procedure and no exact value compared to both other methods, table 6. A comparison between the measured and calculated multicomponent column profile fixed the NTU-value close to 45 stages. Figure 5 sketches the result for the Aspen+ method.

All three methods lead to similar results. An average value of 40 plates with a height of 0.3 m can be assumed to describe the separation correct. These results are the basis to optimise the experiments and for some straight forward scale-up ideas.

5. Optimisation and Scale-Up

The optimisation is based on the Aspen+ model. In this case the NTU-value is fixed at 45 theoretical plates. Since the throughput is limited by the hydrodynamic, Riha et al. 1996, a

variation in the reflux ratio directly affects the feed mass flow. Table 7 gives the results for three calculations at optimum conditions in respect to the extract and raffinate mass flow.

Table 7: Optimisation of reflux ratio and scale-up

Variation		Reflux ratio			NTU		
NTU	[-]	45	45	45	30	45	60
Extract	[kg/h]	1.3	1.5	1.9	1.6	1.6	1.6
Feed	[kg/h]	2.0	2.4	3.0	2.4	2.4	2.4
Raffinate	[kg/h]	0.7	0.9	1.1	0.8	0.8	0.8
Reflux ratio	[-]	9.4	7.9	6.1	7.2	7.2	7.2
HVC-Extract	[%]	98.0	97.4	96.0	93.0	94.4	95.0
HVC-Raffinate	[%]	2.9	4.1	6.8	5.1	2.1	0.8

A second optimisation procedure fixes the mass balance to the experimental results and investigates the influence of the NTU-value on the product quality. Figure 6 shows both results graphically.

It is evident that an increase in the reflux ratio improves

the product quality and simultaneously reduces the overall FAEE throughput. On the other hand the number of theoretical transfer units dominates the influence of the reflux ratio. A theoretical column heightening of 1/3 leads to a product purity of over 99.2 % with a yield of 93 %.

An improvement with respect to the yield requires an optimum mass distribution between both product streams as shown in the variation of the reflux ratio.

Products with a purity of 99 % and a probable yield of more than 95 % should be possible with an optimised continuous counter current separation and

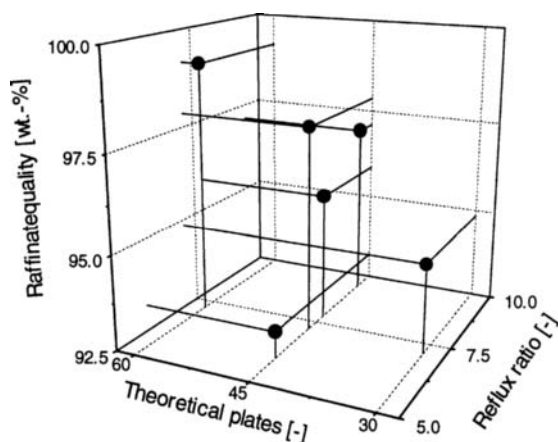


Figure 6: Influence of the reflux ratio and NTU-value on the product quality

SC-CO₂ as solvent. Therefore attention has to be paid to the column height and the reflux ratio as well as to an optimum mass balance.

REFERENCES

- H.O. Bang, J. Dyerberg and A.B. Nielsen, *Lancet* (1971) 1143
W.B. Nilsson, E.J. Gauglitz, J.K. Hudson, V.F. Stout and J. Spinelli, *J. Amer. Chem. Oil Soc.* 65(1988)1, 109 - 117
V. Riha, dissertation, in preparation, 1996
V. Riha, J.-T. Meyer, A. Birtigh and G. Brunner in: D.C. Shallcross, R. Paimin and L.M. Prvcic (eds.), *Value Adding Through Solvent Extraction*, Vol. 2, The University of Melbourne, 1996, pp. 979 - 985
Z.-R. Yu, B. Singh, S.S.H. Rizvi and J.A. Zollweg, *The Journal of Supercritical Fluids*, 7(1994)1, 51 - 59
A. Staby, *Application of Supercritical Fluid Techniques on Fish Oil and Alcohols*, Dissertation, Lyngby, Denmark 1993

Cocoa Butter Fractionation with Supercritical Carbon Dioxide

A. R. Bhaskar^a, S. S. H. Rizvi^a and C. Bertoli^b

^aInstitute of Food Science, Cornell University, Ithaca, NY 14853, USA.

^bNestec S. A., Nestlé Research Center, 1000 Lausanne 26, Switzerland.

1. INTRODUCTION

Cocoa butter (CB) is unique among vegetable fats because of its composition and crystallization behavior. It is present in chocolate at levels up to 40%, and in exceptional cases even higher. The hardness of CB has a major effect on chocolate characteristics. CB hardness and crystallization behavior depend on a number of factors, such as processing, origin, seasonal and climatic conditions. Generally, CB made up from a mixture of cocoas of different origin is used in chocolate processing to minimize this variability. It is, therefore, possible to achieve the desired consistency by blending hard and soft CBs, but this means that one always has to have a stock of different CBs on hand. This can be a big problem, specially for the North American market, due to the preponderance of soft South American CBs and hot summer conditions leading to shorter product life [1]. Fractionation of CB offers a feasible approach to this problem, e.g. stearins of soft Brazilian CB would have the same properties as a hard Malaysian CB. Common fractionation techniques include melt crystallization with or without solvents. Weyland [1] fractionated different CBs into a stearin and an olein fraction, but did not indicate processing conditions or yields of the fractions obtained except that they showed differences in composition and solid fat contents (SFC). Traitler et al. [2] fractionated CB into two fractions using hexane as a solvent. The stearin fraction had a composition very similar to CB but the olein fraction was significantly different.

Based on its ability to enhance solvating power by increasing fluid density, supercritical fluid extraction offers an attractive alternative for fractionation of fats and oils. It works by the phenomena of selective distillation and simultaneous extraction, as has been shown by many researchers [3-5]. While the use of supercritical fluids in the extraction of numerous biomaterials has been reported, its commercialization has been limited to the decaffeination of coffee and tea and to the extraction of flavors from hops and spices. The chemical complexity of most food ingredients and their tendency to react and degrade at elevated temperatures, emphasize the difficulties of supercritical solvent selection. Carbon dioxide is the preferred supercritical solvent (its properties have previously been cited [6]).

The possibility of CB fractionation with supercritical carbon dioxide (SC-CO₂) has not yet been fully explored. Coenen & Kriegel [7] claimed that fats can be fractionated using SC-CO₂ without giving examples. Rossi et al. [8] only observed minor changes in the triacylglycerol compositions of fats extracted from cocoa nibs and shells as a function of time, temperature and pressure. A real fractionation of the fat, however, was not achieved.

This study is a preliminary investigation for evaluating the possibility of fractionating CB with SC-CO₂.

2. FRACTIONATION METHODS

2.1. Supercritical carbon dioxide fractionation

A pure prime pressed CB was supplied by De Zaan B.V., Koog aan de Zaan, NL. Two different SC-CO₂ systems were used. A static recirculation system allowed the equilibrium solubility of CB in SC-CO₂ to be measured following the procedure of Yu et al. [9]. Equilibrium measurements were performed at two different pressures and constant temperature, with and without ethanol as an entrainer. Fractionation of CB was carried out on a continuous pilot-scale SC-CO₂ system as shown in Figure 1. The system consists of a packed column (6) and four separation vessels (S1-S4). The column was packed with SS 304 Goodloe knitted mesh packing (Glitsch Inc., Dallas TX, USA) and was 1.8 m long and 4.9 cm in internal diameter with six inlet/outlet ports. The column was operated in countercurrent mode with CB being fed to the center of the column and CO₂ to the bottom. The packed column and the separators were equipped with sampling valves and heating jackets. A positive displacement reciprocating pump (maximum flow rate: 113 l/h) was used to compress the gas to the desired operating pressure. Pressure in the system was maintained with the help of back pressure regulators. The CB and CO₂ flow rates were monitored by rotameters.

The SC-CO₂ with the dissolved fat passes into the first separation vessel, S2, through a pressure reduction valve. Those triacylglycerols becoming insoluble at the reduced pressure precipitate in the separation vessel. The mother liquor passes to the next vessel S3. By again reducing the pressure the remaining triacylglycerols are precipitated. The volumetric flow rate of CO₂ was measured by a dry test meter before venting it to the atmosphere. The raffinate, which is removed at S1, represented those triacylglycerols insoluble in SC-CO₂ at the pressure, temperature, and solvent-to-feed ratio in the extraction column.

Data were collected periodically for feed and solvent flow rates and amount of fractions from each separator and raffinate. A material balance check was performed at the end of each run. If the material balance was more than 90%, the samples were analyzed. The packed column was considered to be in steady state when the amount of fractions and flow rates (solvent and feed) obtained were constant for three successive time intervals. A typical run required one hour to reach steady state.

2.2. Melt Crystallization

Melt crystallization (MC) fractions, which were prepared according to Traitler et al. [2], were obtained from Sofinol S. A., Manno, CH. Using hexane as solvent two fractions were obtained. Fractionation was performed at -20 °C and the ratio of CB to hexane was 1:5 w/v.

3. ANALYSES

Triacylglycerol composition was analyzed by GLC (GLC 8000, Carlo Erba Instruments, Rodano/MI, I). The fats were dissolved in hexane and directly injected onto a 10 m x 0.32 mm Permabond OV-1-DF-0.10 column (Macherey-Nagel, Düren, D). Oven program: 80 °C 2 min iso, 5 °C/min to 200 °C, 1 min iso, 5 °C/min to 310 °C and 17 min iso. Carrier gas: hydrogen. *Fatty acid* composition was determined by GLC analyses of the fatty acid methyl esters using a 30 m x 0.25 mm DB-WAX column, film thickness: 0.25 µm (J&W Scientific, Folsom CA, USA). GC: HR5160 Mega Series, Carlo Erba Instruments, Rodano/MI, I. Oven program: 40 °C 2 min iso, 15 °C/min to 145 °C, 1 min iso, 3 °C/min to 195 °C, 5 °C/min to 220 °C, 20 min.

Carrier gas: hydrogen. *Solid fat content* of the samples, which were tempered according to IUPAC method 2.150 procedure 6.3.2 [10], was measured by low resolution pulsed NMR (minispec pc20, Bruker Physik AG, Karlsruhe-Forchheim, D). Measurements were done using the direct method (RD 2 and ENH 1). Thermal profiles of the fats were measured by *Differential Scanning Calorimetry* (DSC) using a DSC-7 (Perkin Elmer, Rotkreuz, CH). Measuring program: melting at 60 °C, 5 min iso, cooling to -50 °C at 5 °C/min, 5 min iso, reheating to 60 °C at 5 °C/min.

4. RESULTS AND DISCUSSION

4.1 Solubility and operating conditions

Initial experiments were done on the static system to find the equilibrium solubility of CB in SC-CO₂ at different pressures. At 19.3 MPa/40 °C the solubility of CB was 0.46 wt% which increased with pressure to 0.59 wt% at 24.1 MPa/40 °C. It has been shown that the solubility of fats and oils in SC-CO₂ is strongly correlated to CO₂ density, which increases with pressure at constant temperature [9]. CB is a simple fat as compared to other fats and oils in terms of its composition. It mainly contains three triacylglycerols (carbon number ranging from C50-C54) which make up to 98% of the total triacylglycerols and hence has a low solubility compared to other fats and oils, e. g. milk fat. To improve CB solubility at 24.1 MPa/40 °C, ethanol at different concentrations was used as an entrainer. Solubility increased more than two-fold with increasing ethanol concentration, but there was no improvement in selectivity as seen in Table 1, i.e. the vapor phase did not show any significant changes in composition.

Table 1
Equilibrium solubility and composition of CB in SC-CO₂ at 40 °C

Pressure (MPa)		23.2		24.7		24.9	
Ethanol (wt%)		None		5		12	
Solubility (wt%)		0.59		1.18		1.54	
Triacylglycerols:	CB	Vapor	Liquid	Vapor	Liquid	Vapor	Liquid
C50	20.5	25.7	19.9	26.4	20.2	25.2	19.9
C52	47.0	47.6	46.8	47.5	46.6	47.2	47.3
C54	30.9	25.6	31.8	24.7	30.5	26.2	31.2
Others	1.6	1.1	1.5	1.4	2.6	1.3	1.7

CB could be fractionated into 3 fractions on the continuous pilot-scale system without ethanol. Table 2 shows experimental conditions and yields of the fractions obtained. Trials were run at 24.1 MPa and 40 °C and the solvent-to-feed ratio (S/F) was 116-120. The S/F ratio was chosen based on our work with milk fat. The optimum S/F for fractionation of milk fat at the same temperature and pressure was 55-60 [4]. Composition of CB is significantly different from that of milk fat. Twice the S/F ratio as that for milk fat was used. The solubility of CB in SC-CO₂ under the given extraction conditions was 0.58 wt%. As mentioned earlier, CB solubility is low in SC-CO₂ compared to other fats and oils, e.g. milk fat has an equilibrium solubility of 2.1 wt% at 24.1 MPa/40 °C.

4.2. Chemical and physical properties

Table 3 shows the fatty acid composition of the CB fractions from SC-CO₂ and MC techniques. The extract from SC-CO₂ was split into two fractions, olein1 and olein2, whereas only one olein was obtained from MC. The main difference between the two techniques is seen in the distribution of saturated fatty acids. The MC olein had a low concentration of palmitic and stearic acids while the SC-CO₂ stearin had a high concentration of the same. MC fractionation is based on melting points of the triacylglycerols whereas SC-CO₂ fractionation is based on molecular weight, degree of unsaturation and polarity. The MC olein had a high concentration of unsaturated fatty acids, but the SC-CO₂ fractions did not show any change in the unsaturated fatty acid concentration.

Table 2
Operating conditions for CB fractionation with SC-CO₂

Parameters	CB	Stearin (Raffinate)	Olein 1 (Separator 1)	Olein 2 (Separator 2)
Pressure (MPa)	24.1	24.1	17.2	6.9
Temperature (°C)	40	40	50	60
Yield (wt%)	100	30	31	39

Table 3
Fatty acid distribution for CB fractions by GLC

Fatty acids	CB	Stearin	Olein 1	Olein 2
Melt Crystallization:				
C16:0	25.2	24.4	21.0	N/A *)
C18:0	35.3	34.9	19.9	N/A
C18:1	33.5	34.2	43.0	N/A
C18:2	3.0	2.5	11.4	N/A
SC-CO ₂ :				
C16:0	25.2	20.0	27.9	28.0
C18:0	35.3	41.0	33.1	31.9
C18:1	33.5	33.5	33.8	33.5
C18:2	3.0	2.5	3.0	3.0

*) : only one olein was obtained from melt crystallization

Table 4 shows the triacylglycerol distribution for the CB fractions from the two techniques. Triacylglycerols of carbon numbers C50 and C52 decrease in the MC olein whereas the opposite is true for SC-CO₂ where the stearin has a higher concentration of these triacylglycerols. The SC-CO₂ stearin was significantly different, the two oleins, however, had almost similar compositions when compared to the feed. The opposite was found for MC fractions.

Figure 2 shows the SFC profiles for CB fractions from the two techniques. The SFC profiles for the SC-CO₂ oleins are not shown here. The SC-CO₂ olein1 had a similar, however, olein2 had lower SFC values when compared to CB. The SC-CO₂ stearin had significantly higher SFC values when compared to CB. The MC stearin showed SFC values very similar to these of CB, but the olein fraction had significantly lower SFC values. The higher saturated fat content of the SC-CO₂ stearin was also reflected in the SFC data.

Figure 3 shows the DSC curves for CB, the SC-CO₂ stearin and olein1. The fractions showed a single peak similar to that of CB but the stearin peak showed a slight shift to the right indicating a higher melting point. DSC measurements were not done on the MC fractions.

Table 4

Triacylglycerol distribution for CB fractions by GLC

Triacylglycerol	CB	Stearin	Olein 1	Olein 2
Melt Crystallization:				
C48	0.3	0.2	0.2	N/A *)
C50	18.1	16.9	14.6	N/A
C52	46.5	45.7	40.5	N/A
C54	33.8	35.3	42.3	N/A
C56	1.4	2.0	2.4	N/A
SC-CO ₂ :				
C48	0.3	-	0.4	0.5
C50	18.1	11.2	21.4	21.8
C52	46.5	43.0	48.2	47.7
C54	33.8	43.2	29.0	29.1
C56	1.4	2.6	0.9	0.8

*) : only one olein was obtained from melt crystallization

CONCLUSIONS

This study shows that it is possible to fractionate CB with SC-CO₂. The SC-CO₂ stearin shows differences in both physical and chemical properties, i. e. increased hardness, whereas the SC-CO₂ olein is very similar to CB. Composition of the fractions obtained is dependent on process parameters. Further work is in progress to study the effect of different operating conditions and S/F ratios on yields and composition of the fractions, especially the olein fraction.

REFERENCES

1. M. Weyland, *The Manufacturing Confectioner*, 5 (1992) 53.
2. H. Traitler, A. Dieffenbacher and P. Ducret, Swiss Patent no. 666 160 (1988).
3. J. Arul, A. Bourdeau, J. Makhoul, R. Tardif and M.R. Sahasrabudhe, *J. Food Sci.*, 52 (1987) 1231.
4. A.R. Bhaskar, S.S.H. Rizvi and J.W. Sherbon, *J. Food. Sci.*, 58 (1993) 748.
5. C.K. Ooi, A.R. Bhaskar, M.E. Yener, D.Q. Tuan, J. Hsu and S.S.H. Rizvi, *J. Am. Oil Chem. Soc.*, 73 (1996) 233.
6. S.S.H. Rizvi, A.L. Benado, J.A. Zollweg and J.A. Daniels, *Food Technol.*, 40 (1986) 55.
7. H. Coenen and E. Kriegel, *Offenlegungsschrift DE 28 43 920* (1980).
8. M. Rossi, C. Arnoldi, G. Salvioni and A. Schiraldi, *Ital. J. Food Sci.*, 3 (1989) 41.
9. Z.R. Yu, S.S.H. Rizvi and J.A. Zollweg, *J. Supercritical Fluids*, 5 (1992) 123.
10. *Standard Methods for the Analysis of Oils, Fats and Derivatives of IUPAC*, 7th revised and enlarged ed., prepared by C. Paquot and A. Hautfenne, Blackwell Scientific Publications, Oxford, 1987.

Fractionation of Citrus Oil by Cyclic Adsorption Process in Supercritical CO₂

M. Sato, M. Goto, A. Kodama, N. Tanoue and T. Hirose

Department of Applied Chemistry, Kumamoto University,
2-39-1 Kurokami, Kumamoto 860, Japan

A cyclic adsorption process for citrus oil processing in supercritical carbon dioxide (SC-CO₂) was studied with silica gel adsorbent. Based on the adsorption equilibrium properties, where adsorbed amounts decreased with the increase in the solvent density and oxygenated compounds were selectively adsorbed on silica gel, a continuous cyclic operation between the adsorption step at 8.8 MPa and 313 K, and the desorption step at 19.4 MPa and 313 K was demonstrated. Highly concentrated fraction of oxygenated compounds was continuously obtained for the desorption and blowdown step. The proposed system showed the feasibility of the continuous operation for citrus oil processing.

1. INTRODUCTION

The fractionation of citrus oil is an important subject in perfume industry. Citrus oil consists of terpenes (over 95 %), oxygenated compounds (less than 5 %), waxes, and pigments. Terpenes must be removed to stabilize the products and to dissolve it in aqueous solution. Terpenes are conventionally removed by distillation or solvent extraction, which involves higher temperature process resulting in thermal degradation of essential oil. Furthermore, nonvolatils such as waxes and pigments must be eliminated because of turbidity in the oil and phototoxic activity [1-2].

Supercritical fluid extraction has been focused for the deterpenation of citrus oil as a lower temperature process [1-6]. Coppella and Barton [4], Stahl and Gerard [5], and Temelli et al. [6] studied the extraction process for the removal of terpenes in citrus oil. However, the simple extraction process does not give sufficient selectivity and yield. A continuous countercurrent extraction process is one of the method to achieve higher selectivity between terpenes and oxygenated compounds. Perre et al. [7] and Sato et al. [8] succesfully developed the continuous extraction process.

Introducing adsorbents into a supercritical fluid extraction system is an alternative attractive method to improve the selectivity for the citrus oil processing. Several applications using silica gel as adsorbent have been reported in the last decade [1-3]. Yamauchi and Saito [3] fractionated lemon peel oil into 3 fractions with gradual increase in pressure by supercritical fluid chromatography, where terpene rich fraction, ester rich, and alcohol and aldehyde rich fraction were obtained at 10 MPa, 20 MPa, and 20 MPa with ethanol as a cosolvent,

respectively. Barth et al. [1] and Chouchi et al. [2] also studied the fractionation of citrus peel oil by SC-CO₂ desorption at increasing pressure. They obtained high quality essential oil containing less terpenes and less nonvolatiles. These adsorption processes indicate oxygenated compounds could be selectively adsorbed on silica gel in SC-CO₂ and relatively higher pressure is required to desorb them.

Our objective is to develop the continuous adsorption process for citrus oil processing. In this work, the adsorption breakthrough curves and desorption curves were analyzed to understand the adsorption-desorption behavior of citrus oil on a silica gel adsorbent in SC-CO₂. A cyclic adsorption-desorption process was developed and demonstrated for the removal of terpenes from orange oil.

2. MATERIAL

Silica gel for HPLC (Wakogel LC-50H, Wako Pure Chem.) of particle diameter of 50 μ m was used as adsorbent and CO₂ was used as solvent. Cold-pressed orange oil from Brazil was used as raw material. The raw orange oil contained 93.1 % of limonene, 0.68 % of linalool and over 200 other components, involving waxes and pigments. Limonene and linalool are principal constituents of terpene and oxygenated compounds in orange oil, respectively. Most of nonvolatiles such as waxes and pigments in raw orange oil were removed by decantation at 263 K and mixing step with CO₂ before introducing into adsorption column.

3. ADSORPTION AND DESORPTION BEHAVIOR

Adsorption equilibria is important fundamental property to design and develop the adsorption process. We have measured the adsorption equilibrium constant of limonene and linalool in SC-CO₂ by an impulse response technique [9]. Figure 1 shows the adsorption equilibrium constant at a temperature of 313 K - 333 K and a pressure of 11.8 MPa - 23.5 MPa. Linalool was adsorbed more selectively than limonene. Adsorption equilibrium constants were correlated linearly in log-log plot as a function of the density of SC-CO₂ independent of pressure and temperature. Adsorbed amounts decreased with the increase in the solvent density for both limonene and linalool. These results suggest the possibility of a process where oxygenated compounds are selectively adsorbed on the adsorbent at a lower pressure and then desorbed at a higher pressure.

Adsorption and desorption behavior of cold-pressed orange oil were measured at 313 K by using the column with 10 mm i.d. x 500 mm in length. The feed dissolved in SC-CO₂ was continuously passed through the column packed with silica gel at 8.8 MPa for adsorption step, and then, after the equilibrium, pure SC-CO₂ was passed through

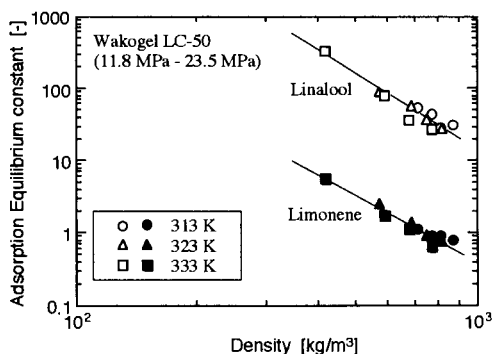


Figure 1 Relation between adsorption equilibrium constant and solvent density.

the column at 19.4 MPa for desorption step. Employed flow rate of CO_2 and feed was 0.052 g/s and 0.002 g/s, respectively for the adsorption step and CO_2 flow rate of 0.013 g/s was used for the desorption step. Figure 2 shows the breakthrough curves for major components in orange oil at 8.8 MPa. The solid and open symbols are terpenes and oxygenated compounds, respectively. Terpenes were slightly adsorbed on the adsorbent and immediately breakthroughed the column. A behavior of the competitive multicomponent adsorption was observed among the oxygenated compounds, that is, weakly adsorbed components eluted with the concentration higher than the feed.

Figure 3 shows the desorbed amounts and the variation in concentration factor of each components in effluent at 19.4 MPa. Concentration factor is defined by the concentration of solutes desorbed divided by that in feed. Terpenes in the void space of the column were effused in the beginning of the desorption step, then oxygenated compounds gradually desorbed. Linalool in the raw orange oil was concentrated 50 times at the end of the desorption step. These results indicated that the rinse (or purge) step for the effluent of the terpene presented in the void region of the column is required to obtain the highly concentrated oxygenated compounds in the desorption step.

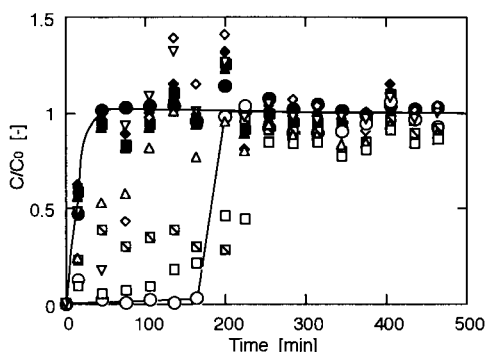


Figure 2 Breakthrough curve of raw orange oil at 313K and 8.8MPa.

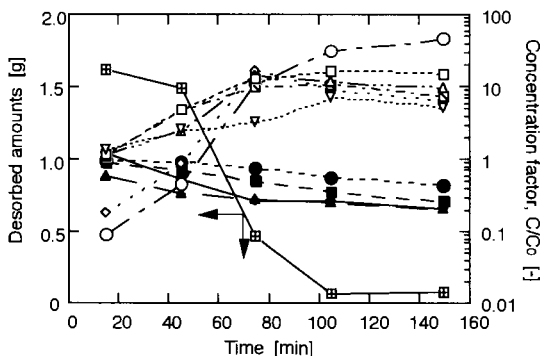
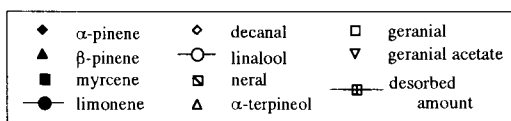


Figure 3 Variation of desorbed amount and concentration factor for desorption step at 313K and 19.4MPa.

4. CYCLIC ADSORPTION PROCESS

4.1. Experimental

The experimental apparatus developed for citrus oil processing is shown in Figure 4. The empty column was equipped before the adsorption column in order to dissolve the raw oil completely in SC-CO_2 and to avoid the adsorption of waxes and pigments, where they were removed easily due to the small solubility in SC-CO_2 . A pair of 0.5 m long and 9 mm i.d. columns packed with silica gel were used for adsorber.

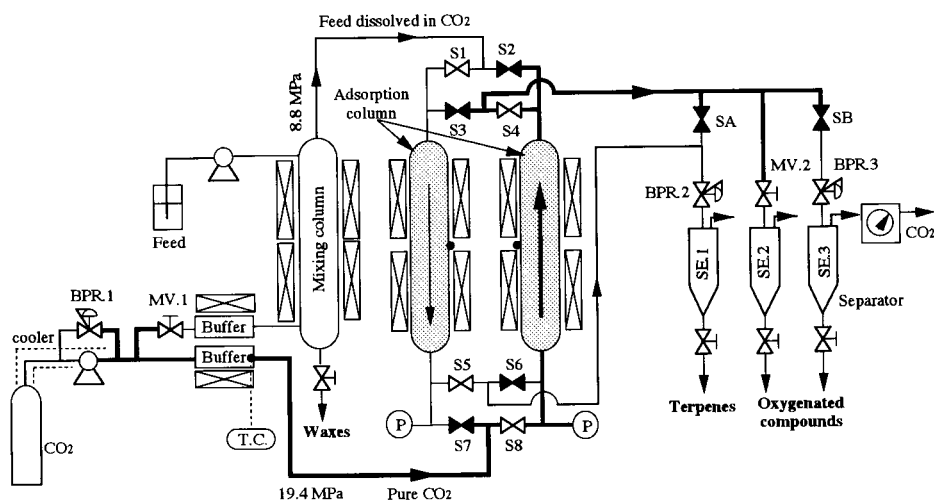


Figure 4 Experimental set-up for citrus oil processing.

A set of 10 solenoid valves (Atkomatic Inc.) were used for switching the adsorption-desorption cycle. The solenoid valves were controlled by a programmable controller (SYSMAC-mini, OMRON). The operation of solenoid valves and the pressure change of the system are schematically shown in Figure 5. When the solenoid valves S1-S4-S5-S8 were opened while the others represented by S2-S3-S6-S7 remained close, left column was in the adsorption step and right column was in the desorption step, and vice versa. The pressure was controlled by 3 back-pressure regulators. BPR.1 was set at 19.4 MPa, and BPR.2 and 3 were set at 8.8 MPa. For the rinse step to remove solute in the void region, SA valve remained open, where the pressure of whole system kept at 8.8 MPa, and the effluent from both column was collected in SE.1. For the blowdown step, the pressure of one column kept at 19.4 MPa for the desorption step was quickly reduced to 8.8 MPa for next adsorption step by opening SB valve.

The CO_2 flow rate used was 0.047 g/s for the adsorption step at 8.8 MPa and 0.010 g/s for the desorption step at 19.4 MPa. Temperature of the system was kept at 313 K. CO_2 was passed through a cooled line and compressed to operating highest pressure of 19.4 MPa by a high pressure pump. The compressed CO_2 was

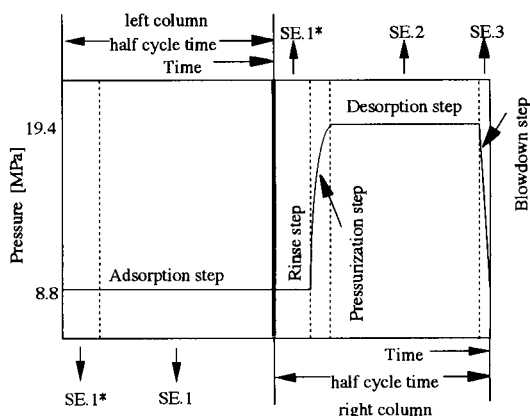


Figure 5 Configuration of a cyclic operation with two beds for the citrus oil processing in supercritical carbon dioxide.

passed through a heated buffer tank to reach the desired temperature. A part of CO_2 was reduced to a pressure of 8.8 MPa through the micrometering valve MV1. Feed and CO_2 at 8.8 MPa were countercurrently contact in the mixing column. Nonvolatiles in feed remained undissolved at the wall and bottom of the column. The fluid exiting the mixing column was homogeneous phase with feed and CO_2 , and flowed from the top to the bottom of the adsorber for the adsorption step. On the other hands, pure CO_2 at 19.4 MPa flowed from the bottom to the top of the adsorber for the desorption step. The CO_2 flow rate was measured with dry test meter equipped after the separator.

The effluents collected in SE1, SE2, and SE3, were weighed and analyzed by a capillary gas chromatograph equipped with FID detector. The GC analysis was performed with a Shimadzu GC-14A equipped with a J&W DB-WAX (30 m x 0.25 mm i.d., 0.25 μm film) fused silica capillary column and FID. Temperature of GC oven was programmed linearly from 343 K to 473 K at a rate of 3 K/min. Helium with split ratio of 1/100 was used as carrier gas.

4.2. Result and Discussion

A continuous cyclic operation between the adsorption step, where a cold-pressed orange oil in SC-CO_2 was continuously passed through the column at 8.8 MPa and 313 K, and the desorption step, where pure SC-CO_2 was passed through the column at 19.4 MPa, including the rinse step was demonstrated. Figure 6 shows the average concentration factors of oxygenated compounds for each steps as a function of concentration of feed operated at a half cycle time (t_c) of 60 min. As discussed above, oxygenated compounds were concentrated for the desorption step. However, for the blowdown step where the pressure in the column was immediately reduced from 19.4 MPa to 8.8 MPa, higher concentrated fraction of oxygenated compounds were obtained than that for the desorption step, since the adsorbed solutes on the adsorbent were eluted with the convective flow in the pores of the particle induced by the quick expansion of the fluid. The concentration factor decreased with the increase in the concentration of feed. Because the desorption time is not sufficient to compensate the increase in the adsorbed amounts due to the increase in the concentration.

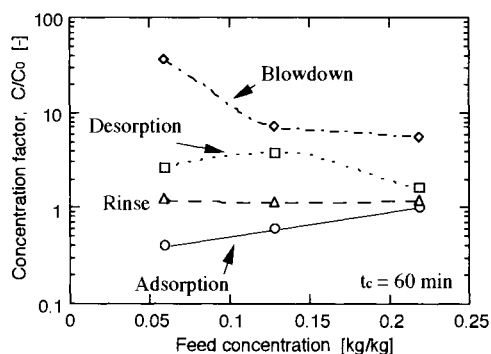


Figure 6 Effect of feed concentration on the concentration factor of oxygenated compounds for each steps.

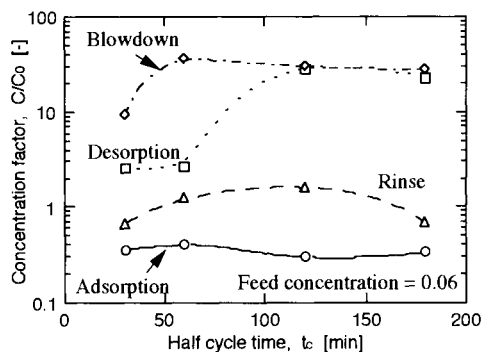


Figure 7 Effect of half cycle time on the concentration factor of oxygenated compounds for each steps.

Figure 7 shows the effect of half cycle time on the concentration factor of oxygenated compounds for each steps. An increase in the half cycle time caused higher concentration factor for both the desorption step and blowdown step. Higher concentration factors up to 25 were obtained at a half cycle time of 120 min. These concentration factors satisfy the commercially required value of 5 - 10.

5. CONCLUSION

A continuous cyclic operation between the adsorption at a lower pressure and the desorption at a higher pressure, involving the rinse step to remove the solutes in the void region of the adsorber, was demonstrated for citrus oil processing with silica gel adsorbent in SC-CO₂. Terpeneless citrus oil was successfully obtained in the desorption step and blowdown step. The proposed system showed the feasibility of the continuous operation of the cyclic adsorption process.

Acknowledgment

This work was supported by a Grant-in-aid for Scientific Research (No. 04238106) from the Ministry of Education, Science, Sports and Culture, Japan. We thank for receiving the JSPS Research Fellowships for Young Scientists (No. 2362) to carry out this work. We also thank Givaudan-Roure Flav. Ltd. for supplying citrus oil.

REFERENCES

1. D. Barth, D. Chouchi, G. D. Porta, E. Reverchon, and M. J. Perrut, *J. Supercrit. Fluids*, 7 (1994) 177.
2. D. Chouchi, D. Barth, E. Reverchon, and G. Della Porta, *Ind. Eng. Chem. Res.*, 34 (1995) 4508.
3. Y. Yamauchi and M. Saito, *J. Chromatography*, 505 (1990) 237.
4. S. J. Coppella and P. Barton, *ACS Symp. Ser.*, 366 (1987) 201.
5. E. Stahl and D. Gerard, *Perfumer and Flavorist*, 10 (1985) 29.
6. F. Temelli, C. S. Chen, and R. J. Braddock, *Food Tech.*, 42 (1988) 145.
7. C. Perre, G. Delestre, L. Schrive, M. Carles, *Prec. 3rd Int. Sym. Supercritical Fluids*, 2 (1994) 465.
8. M. Sato, M. Goto, T. Hirose, *Ind. Eng. Chem. Res.*, 34 (1995) 3941.
9. M. Sato, M. Goto, T. Hirose, *Proc. Fifth Int. Conf. Fundam. Adsorption*, (1995) Su-7.

Gas Anti-Solvent Fractionation of Natural Products

O. J. Catchpole *, S. Hochmann and S. R. J. Anderson

Industrial Research Ltd., P.O. Box 31-310, Lower Hutt, New Zealand

Gas anti-solvent fractionation was carried out using CO₂ on mixtures of lecithin/Soya oil/hexane; coriander seed triglycerides/essential oil/hexane; and pure components of the mixtures. Separation of the mixtures into individual components was demonstrated at a laboratory scale. The degree of separation possible was a function of the volume expansion of the liquid solvent phase. The pressure/volume expansion at which a pure component precipitated was qualitatively related to its solubility in supercritical CO₂. The volume expansion was a function of temperature and pressure. The pressure required to reach a certain volume expansion increased as both the temperature and triglyceride content increased.

1. INTRODUCTION

Organic solvent extraction of natural products is a widespread industrial scale operation to recover edible oils, flavour and fragrance extracts, and extracts for pharmaceutical products. Most of these processes require many refining steps after solvent extraction to obtain the final product, including removal of solvent residues, and components that are not desirable in terms of colour, oxidative stability, and effect on flavour. As an example, the refining of edible oils requires steps to remove phospholipids which cause gumming, chlorophyll which gives rise to an undesirable colour, free fatty acids which give a rancid taste, peroxides which cause oxidative instability, and solvent residues which must be removed to meet food grade specifications [1]. Each step requires either heat, other chemicals, or adsorbents and results in yield loss of oil at each stage. Gas anti-solvent fractionation (GAS) is being evaluated in this work as a process to replace all of the refining steps after solvent extraction. GAS is a relatively new separation technique that utilises the anti-solvent power of a near-critical gas when dissolved in organic solvents. The solubility of the gas in the solvent increases with pressure, and the solvent power decreases. Closely associated with the decrease in solvent power is an expansion of the liquid phase volume [2]. CO₂ is the most suitable gas anti-solvent, due to its convenient critical temperature and high solubility in most commonly used organic solvents such as hexane, acetone and ethanol. GAS has already been applied to the recovery of a wide range of solids from solution including explosives [2]; polyaromatic hydrocarbons [3,4]; citric acid [5]; and b-carotene and acetaminophen [6]. So far, there have been no published reports on the GAS fractionation of mixtures containing a liquid solute. In this work, we investigate the effects of temperature, pressure and composition of the solvent phase on the separation of lecithin from Soya oil; and coriander triglycerides from essential oil at a lab scale.

2. EXPERIMENTAL

Gas anti-solvent fractionation was performed with the apparatus shown schematically in figure 1. Carbon dioxide was compressed to 200 bar by an air driven diaphragm compressor C1, and

then heated to 313K as it passed through buffer vessels BV1 and BV2, housed inside a waterbath. The CO₂ then passed through a forward regulator set to the desired pressure (± 0.5 bar), and into a view cell VC1 (Jergusson gauge) contained within a second waterbath ($\pm 0.1^\circ\text{C}$). The carbon dioxide entered through bottom valve V1 during expansion of the liquid phase, with the top valve V2 closed. At the desired pressure, CO₂ flowed through the view cell, and then through a depressurization valve V4 and into collection vessel CV1, to recover dissolved/entrained solvent. The degree of expansion of the solvent phase was determined by comparing the liquid height with a height/volume calibration curve for the view cell. The solvent phase was added to the apparatus either by pipette at atmospheric pressure, or a metering pump at the experimental pressure.

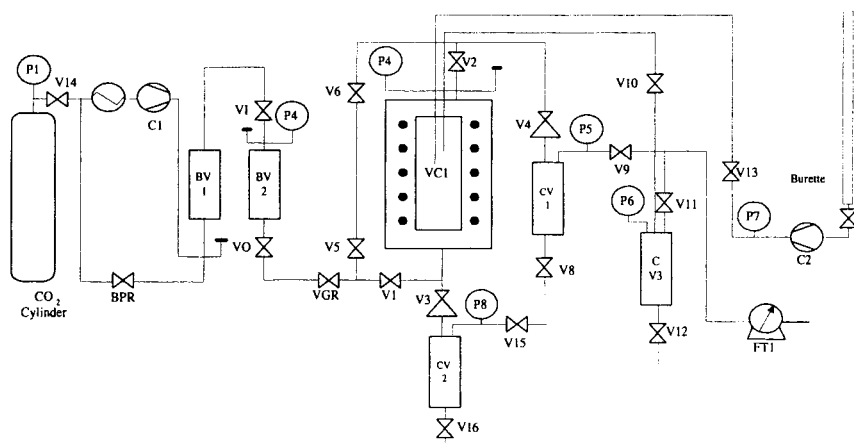


Figure 1 Schematic of Experimental Apparatus

Samples were taken from the precipitated bottom phase, the solvent phase, and the CO₂ vapour phase. The sampling procedure for the bottom phase depended on whether the precipitate was a liquid (triglyceride oil), solid (lecithin) or a mixture of both components. Samples of liquid bottom phase were withdrawn from valves V3 and V16 positioned at the base of the view cell, with valve V1 shut. Valves V5, V6 and V2 were opened to ensure constant pressure inside the view cell during sampling. Samples of solid lecithin were recovered by first removing the solvent phase under pressure as above, followed by depressurization, and then solvent washing of the apparatus. Lecithin was retained on a filter placed above valve V3. For mixtures of lecithin and Soya oil, the two sampling procedures were combined. The Soya oil was first removed under pressure, followed by the solvent phase. The apparatus was then depressurized and solvent washed. Samples of the solvent phase at pressure were also taken via valve V4 and collection vessel CV3, to measure the CO₂ content, and the concentration of solute still in solution.

The experiments carried out are summarised below. The temperature and pressure range was 298-313K, and 40-75 bar respectively. Expansion experiments were carried out on both single solute solutions in hexane; and mixtures of lecithin (L) and Soya oil (S); and coriander essential (CE) and fixed oil (CT) in hexane. The single solute concentrations were: 5 and 10 % by weight L; 5, 10 and 20 % by weight CE; and 10, 20, 30 and 40 % by weight of S or CT. The mixture concentrations in hexane were 40 % S, and 10 % L by weight; 20 % S and 1, 2.5, and 5 % L by weight; and 10, 20, 30 % CT with a constant CE ratio of 1:5 essential oil to fixed oil.

3. RESULTS AND DISCUSSION

3.1. Single solute solutions

Precipitation trials over a range of temperatures and pressures revealed that up to 100 percent of lecithin, 95 percent of triglycerides and no essential oil could be recovered from solution. At a fixed temperature, lecithin precipitated at lower pressures than triglycerides, suggesting that separation should be possible. The precipitation behaviour can be qualitatively related to solubility in supercritical CO₂. Lecithin, which is completely insoluble, precipitates at low pressures, whilst essential oil, which is very soluble, cannot be precipitated. The coriander essential oil acted like a second solvent: mixtures of hexane and coriander essential oil expanded to a larger degree than pure hexane. The degree of expansion of the liquid phase, $\nabla V/V_i$, and the pressure range over which precipitation of lecithin occurred did not depend on the initial concentration of lecithin in solution over the concentration range investigated. The expansion behaviour of triglyceride/hexane solutions was dependent on the concentration. The concentration of lecithin and triglyceride

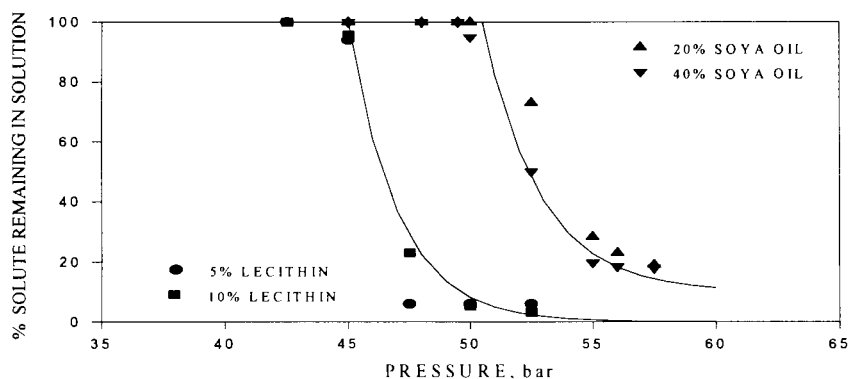


Figure 2 Solute remaining as a function of pressure at 298 K

remaining in solution is shown in figure 2 at 298 K for lecithin concentrations of 5 and 10% by weight; and triglyceride contents of 20 % and 40 % by weight respectively. The pressure gap between the precipitation of lecithin and that of triglycerides is clearly evident. The concentration remaining in solution could be correlated against the degree of expansion of the solvent phase as shown in figure 3 or the concentration of CO₂ in the solvent phase, resulting in a single lecithin curve for all temperatures investigated. This finding is consistent with the observation that the expansion of pure solvents at all temperatures could be correlated against the CO₂ content of the solvent [7]. The curves for 20 % and 40 % by weight triglycerides show different behaviour. The volume expansion required to cause precipitation decreased as the concentration increased. The expansion level at which the 40 % solution begins to precipitate is close to the lecithin curve, suggesting that separation would not be possible under these concentration conditions.

3.2. Two solute solutions

The degree of separation of lecithin from triglycerides, and coriander essential oil from triglycerides depended on the concentration of triglyceride in solution. As the concentration of

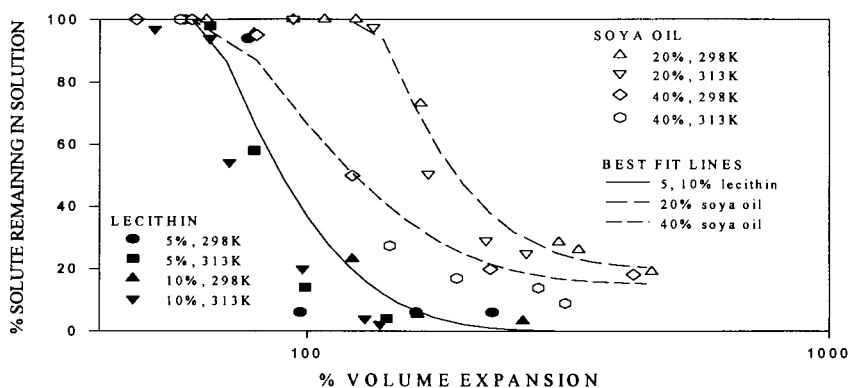


Figure 3 Solute remaining as a function of volume expansion at 298 and 313 K

triglyceride increased, the pressure range over which lecithin precipitated was translated upwards. No separation was possible at a triglyceride content of 40% by weight. The triglyceride that precipitated redissolved the lecithin which had co-precipitated. At lower triglyceride concentrations separation was possible. The percentage of solute (lecithin or triglyceride) remaining in solution as a function of pressure at 313 K is shown in figure 4 for three lecithin concentrations and a Soya oil concentration of 20 % by weight. The desired outcome is a low % lecithin, and high % Soya oil remaining in solution. Also included for comparison is the pure solute precipitation curves.

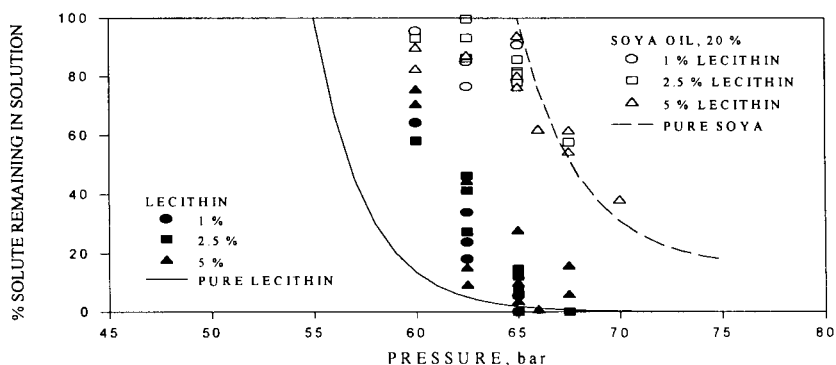


Figure 4 Solute remaining as a function of pressure for lecithin/Soya oil mixtures

The shift upwards in pressure for lecithin is pronounced, whilst the Soya oil precipitation behaviour is unaffected by the initial lecithin concentration. The pressure range over which triglycerides precipitated was very similar to the single solute experiments and independent of the lecithin content over the concentration range used. The mixture results for lecithin and triglycerides could again be correlated against the degree of expansion of the liquid phase. The percentage solute (lecithin or triglyceride) remaining is shown in figure 5 as a function of the degree of expansion of the liquid phase at temperatures of 298 and 313 K for three lecithin concentrations and 20 % by weight Soya oil. Again, the pure component expansion curves are

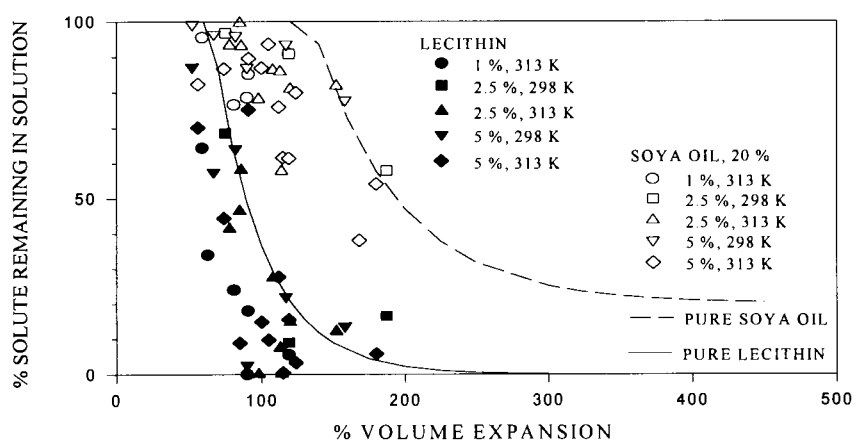


Figure 5 Solute remaining as a function of volume expansion for lecithin/Soya oil mixtures

shown for comparison. The lecithin precipitation data points are very similar to the pure component curve, whilst the Soya oil data points are lower. The presence of Soya oil reduces the degree of expansion as a function of pressure. The degree of expansion is the key parameter in determining the separation efficiency. The results also suggest that it may be possible to precipitate lecithin and Soya oil in an isobaric two stage process. Lecithin is precipitated in the first stage at a high temperature and low volume expansion. The temperature is then reduced in the second stage, resulting in a high volume expansion, and precipitation of soya oil.

The separation of coriander triglycerides from coriander essential oil required higher pressures than those used for Soya oil/lecithin mixtures, as the aim was to try and precipitate all the triglycerides. Essential oil could not be precipitated from hexane in pure component trials, but was not completely recovered from precipitated triglycerides. The limitations of the experimental apparatus resulted in lower than expected purity and recovery of essential oil. The passage of carbon dioxide upwards through the view cell caused entrainment of triglycerides, lowering the top phase purity. Contacting between the carbon dioxide and solvent phase was also not optimised, as large bubbles were observed passing upwards through the centre of the column only. Contacting could be improved with the use of a suitable packing. Experiments carried out under

continuous addition of carbon dioxide and liquid mixtures to the view cell resulted in the best separation of triglycerides from the remaining essential oil and hexane solvent. The top and bottom phase (solvent and triglyceride phase) concentrations of essential oil are shown in figure 6 for selected P, T combinations under continuous operating conditions. Under the optimum conditions, a 90% by weight coriander essential oil fraction was recovered.

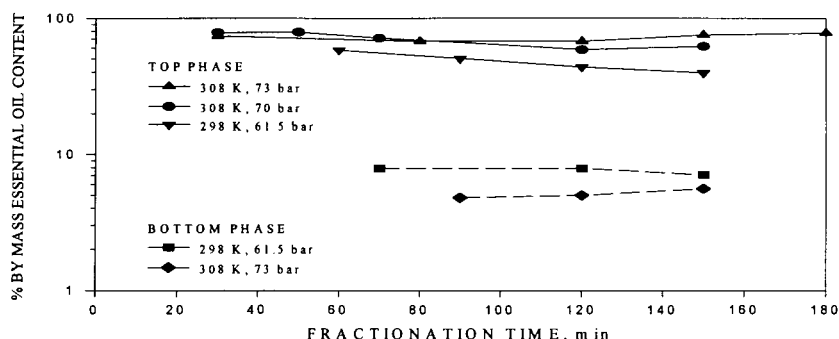


Figure 6 Essential oil concentrations in top and bottom phases using a continuous feed.

4. CONCLUSIONS

The separation of lecithin from Soya oil and coriander essential oil from coriander triglycerides using GAS fractionation was achieved at a laboratory scale. The degree of separation was correlated against volume expansion of the liquid phase. The precipitation of lecithin as a function of volume expansion was similar for the pure component and in mixtures with Soya oil. The pressure required to achieve separation from the mixture increased relative to the pure component for lecithin, but was unchanged for Soya oil. High expansion levels were required to achieve separation of triglycerides from essential oil. Under the optimum conditions used, a 90% by weight essential oil fraction was recovered.

REFERENCES

1. V. Young, Chem. Ind. (1978) 693
2. P. M. Gallagher, M. P. Coffey, V. J. Krukons, and N. Klasutis. Supercritical Fluid Science and Technology, K. P. Johnston and J. M. L. Penninger, (eds.), ACS Symp. Ser. 406, Washington, DC, 1989, 334
3. C. J. Chang, Y. Liou, and W-J Lan. Can. J. Chem. Eng. 72, (1994), 56
4. C. J. Chang and Y. Liou. J. Chem. Eng. Jpn. 26, (1993), 517
5. A. Shishikura, K. Kanamori, H. Takahashi, and H. Kinbara. J. Agric. Food Chem. 42, (1994), 1993
6. C. J. Chang and A. D. Randolph. AIChE. J. 36, (1990), 939
7. A. Kordikowski, A. P. Schenk, R. M. Van Nielen, and C. J. Peters. J Supercritical Fluids, 8, (1995), 205

Separation of Metals from Simulated Mixed Waste Streams through Hydrothermal Crystallization in Supercritical Water

R. L. Smith, Jr., P. Atmaji, Y. Hakuta, T. Adschiri and K. Arai

Tohoku University, Department of Chemical Engineering,
Aoba Aza Aramaki, Sendai 980-77, Japan

ABSTRACT

Recovery techniques are needed to separate metals from high level radioactive liquid waste streams. We examined hydrothermal crystallization in supercritical water (SCW) and separation factors for removing metals from simulated radioactive liquid waste streams. Aqueous metal nitrates can react to form metal oxides or hydroxides at these conditions. The 21 element simulated waste stream consisted of nitrates of Cs (6030 ppm), Sr (1220 ppm), Pd (50 ppm), Na (26200 ppm), Ba (3610 ppm), Ag (150 ppm), Cd (250 ppm), Y (1090 ppm), La (2780 ppm), La (2780 ppm), Ce (8530 ppm), Pr (3890 ppm), Nd (9610 ppm), Sm (2000 ppm), Eu (340 ppm), Gd (17840 ppm), Zr (7330 ppm), Cr (1850 ppm), Mo (720 ppm), Mn (880 ppm), Fe (10240 ppm) and Ni (1830 ppm) aqueous solutions. The experimental apparatus consisted of a batch apparatus heated in a salt bath with conditions from 373-723 K, 20-40 MPa and reaction time from 2 - 30 minutes. After completion of the each experiment, the reactor contents were filtered and analyzed with ICP, X-ray diffraction and SEM, as appropriate. Results are summarized for the 21 element stream at 30 MPa and 30 minutes reaction time. For Mo, Zr, and Fe, a sharp decrease in the liquid phase concentration was observed from the previous stated concentrations to approximately 2, 20, and 40 ppm, respectively as the system entered supercritical conditions. The temperature ranges, where the metals could be recovered, varied. For Mo, a sharp increase in recovery occurred at about 423 K and reached 98%; for Fe, the increase in recovery began at about 473 K and reached 99%. For Zr, the recovery occurred over a wider range and began from about 373 K and reached 98% at 673 K. For Cr, 75% recovery was approached. More than 99% of Pd could be recovered. Sr, Cs, and Na showed relatively little or no changes in liquid phase concentration. A series of experiments were performed to determine the density effects on metal reactivity. Other metals could be recovered from 4% to 98%. Only Cr, Ce, Pr, Mn, and Ni had recoveries that were affected by density. For these elements, recoveries showed a downward trend with increasing density. An empirical model with a function form for Type V adsorption was found to provide an excellent fit of the data. From the results presented it is possible to selectively separate mixed metals streams with hydrothermal crystallization in supercritical water. For the simulated stream studied, approximately 42 wt% of the metals can be removed by elevating the stream to supercritical conditions. Further experiments using a flow apparatus and modeling of the reactive solubility are in progress.

INTRODUCTION

Greater than 30% (10 million MW-days/year) of electrical energy used in Japan is derived from nuclear sources (JIE, 1994). One problem in using nuclear energy is the high level liquid waste (HLLW) that is generated at a rate of approximately 378 L waste per ton of fuel processed (Burns and Irish, 1976). HLLW can be stabilized by a solidification process (vitrification) in which the waste is mixed with molten glass particles and then allowed to solidify. Prior to permanent disposal however, solid waste must undergo extensive treatment to reduce content of heat and reactivity that is dominated by ^{90}Sr and ^{137}Cs . If these elements could be separated from the other elements, only 3% of the waste would require processing. Additionally, volatilization of fusion product ruthenium poses potential problems in nuclear fuel processing and waste consolidation operations (Cains et al., 1992). Separation of Ru and certain valuable metals such as Pd and Rh are of high industrial interest. In 1988, Japan's Atomic Energy Commission recommended that R&D for treatment of HLLW to be divided into four groups: (i) transuranic elements (TRU), (ii) strontium-cesium (iii) technetium-platinum group, and (iv) other metals (Kubota, 1993). Because many processing streams consist of substantial amounts of water, however, there exists a considerable opportunity for separation and recovery of the metals through the addition of thermal energy to increase the metal ion activities selectively. Recently, metal ions have been shown to have high reactivity in hydrothermal and supercritical water (SCW) systems (Adschiri et al., 1992). The objective of this research is to examine recovery of metal ion systems of HLLW through manipulation of the properties of sub- and supercritical water.

MATERIALS AND METHODS

Water used in the experiments was doubly distilled and passed through an ion exchange unit. The conductivity was approximately 1×10^{-6} S/m. Simulated HLLW consisted of 21 metal nitrates in an aqueous 1.6 M nitric acid solution as shown in Table 1 and was supplied by EBARA Co. (Tokyo, Japan). Concentrations were verified by AA for Na and Cs with 1000:1 dilution and by ICP for the other elements with 100:1 dilution. Total metal ion concentration was 98,393 ppm. The experimental apparatus consisted of nominal 9.2 cm³ batch reactors (O.D. 12.7 mm, I.D. 8.5 mm) constructed of 316 stainless steel with an internal K-type thermocouple for temperature measurement. Heating of each reactor was accomplished with a 50%NaNO₂ + 50% KNO₂ salt bath that was stirred to insure uniform temperature. Temperature in the bath did not vary more than ± 1 K. The reactors were loaded with the simulated HLLW waste at atmospheric conditions according to an approximate calculated pressure. Each reactor was then immersed in the salt bath for 2 min - 24 hours. After a predetermined time, the reactor was removed from the bath and quenched in a 293 K water bath. The reactor was opened and the contents were passed through a 0.1 μm nitro-cellulose filter while diluting with water. Analysis of the liquid was performed with methods in Table 1. Analysis of filtered solids were carried out with X-ray diffraction with a CuK α beam and Ni filter. Reaction time was defined as the time that the sample spent at the desired temperature. Typical cumulative heat-up and cool-down time was on the order of one minute. Results of this work are reported in terms of recoveries as defined by:

$$\text{Recovery (\%)} = \frac{C_0 - C}{C_0} \times 100\% \quad (1)$$

where C_0 is the initial aqueous metal ion concentration (ppm) and C is the final aqueous metal ion concentration (ppm). Since it is apparent that metals can be leached from the reactor vessels, experiments were also performed by heating nitric acid solutions without simulated HLLW to determine baseline levels of chromium, nickel, manganese and iron.

RESULTS AND DISCUSSION

Initially, reaction times were varied from 2 minutes to 24 hours at 573 K and 673 K. These experiments revealed that 30 minutes reaction time was sufficient for the mixtures to achieve chemical reaction equilibrium. Therefore, further experiments were all performed with 30 minutes reaction time. Figures 1 and 2 provide a summary of smoothed results as discussed later. Approximate densities (g/cm^3) were 0.97, 0.93, 0.89, 0.83, 0.75, 0.64, 0.36, and 0.15 for temperatures (K), 373, 423, 473, 523, 573, 623, 673, 723, respectively. All metals were found to be soluble in the aqueous 1.6 M HNO_3 solution at room temperature. Considering eqn. (1), the metal must react to a form that is insoluble in the liquid phase for the recovery to increase. Moreover, according to the experimental procedure, the reacted metal must be insoluble in the liquid phase at room temperature as the batch reactor is cooled before analysis. For this complex system, there are a number of reactions that take place. For metal nitrate salts, the following general reactions have been found to occur in supercritical water (Adschiri et al., 1992):

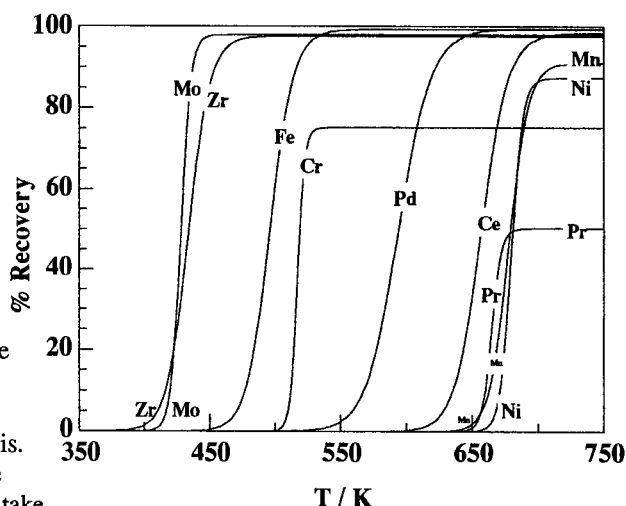
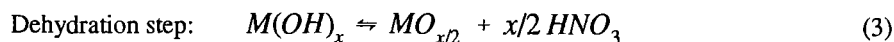
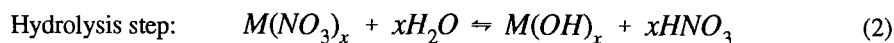


Figure 1. Recovery versus temperature for metals in the 50-100% recovery range. See Table 2 for model parameters.



Metal hydroxides formed according to eqn. 2 are dehydrated according to eqn. 3 to form metal oxides which are generally insoluble in water. As shown in Figure 1, at 423 K, Zr and Mo exhibited a sharp decrease in solubility, which lead to a sharp increase in the recovery. Beginning at 0% recovery at temperatures below 400 K, as temperature was increased to

423 K, recovery for Zr and Mo attained a value around 20-23 %. At 473 K, approximately 98% of Zr and Mo could be recovered. As the temperature was increased to 548 K, the solubility of Fe decreased, which lead to a recovery of 99%. At these conditions, Cr also started to precipitate. However, only approximately 75% of Cr could be recovered regardless of the temperatures examined. To some extent, this might due to the leaching of the chromium from the reactor walls, although this cannot completely explain the plateau in Cr recovery since we checked the baseline levels as discussed in the previous section. At 653 K, Pd could be recovered close to 100%. Silver seemed to reach its maximum value of about 10% at a temperature just above

420 K as shown in Figure 2.

As the temperature increased further to 673 K, Ce, Mn, and Ni could be recovered at 98%, 91%, and 87%, respectively. Above 673 K, Pr, Y, Eu, Sm, and Cd began to show reactivity and could be recovered at about 50%, 10%, 9%, 9%, and 10% respectively. At the highest temperatures studied, Gd, La, Nd, Ba showed recoveries of less than 7%. The elements Cs, Sr, and Na did not precipitate at any of the conditions studied.

Analysis of the solids collected provided additional information. At 423 K, all solid product collected was amorphous. At 473 K, the only solid product that could be identified with XRD was Fe_2O_3 (hematite). Hematite was present in all samples for

temperatures of 423 K or higher. At 573 K and 623 K, CrO_2 could be identified. At 673 K and 723 K, CeO_2 and PrO_2 could also be identified in addition to hematite and CrO_2 . Only limited analysis is possible since many oxides are soluble to some extent in acidic solutions. In addition to eqns. 2-3, a number of reduction-oxidation reactions must occur since Cr, Ce, and Pr change oxidation states from +3 to +4. At present, the redox couples are unknown.

We also examined the pressure (density) effects at 673 K. For metals that were highly reactive (Zr, Mo, Fe, Pd), or relatively unreactive (Y, Eu, Gd, La, Nd, Sm, Ag, Cd, Ba, Sr, Cs, Na), no density effect was observed. For other metals (Cr, Ce, Pr, Mn, Ni) however, we could observe moderate effects of the pressure (density) on the recovery. As density increased, recoveries decreased. This implies that the solubilities increased or that the reactions shifted to more soluble products with increasing density. At 723 K, the recoveries were found to be independent of density in the range of 0.08 - 0.15 g/cm³.

To correlate the data, in view of the numerous complex factors discussed above, we noticed that the form of the data resembles that of Type V adsorption isotherm behavior that

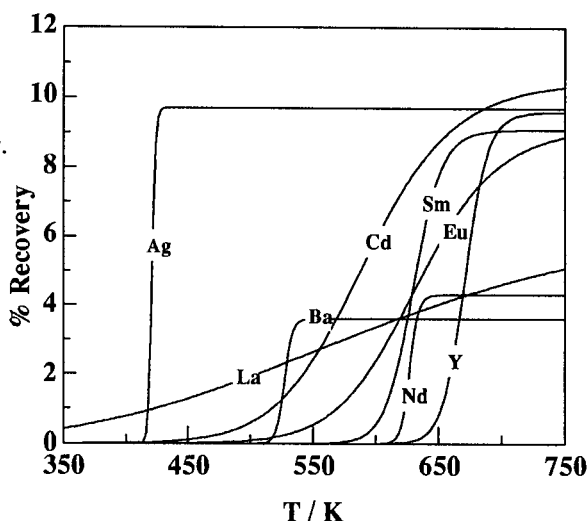


Figure 2. Recovery versus temperature for metals in the 0-12% recovery range. Gd (not shown) had a 4.5% recovery at 723 K. Sr, Cs, and Na always remained in the liquid phase at the conditions studied. See Table 2 for model parameters.

is used for ion exchange and mass action analysis. In terms of the independent variable, temperature, this becomes:

$$\text{Recovery} = \frac{R_{\max}}{(T_{1/2}/T)^S + 1} \quad (4)$$

where, R_{\max} is the maximum recovery possible, $T_{1/2}$ is the temperature at which half of the maximum recovery is obtained and S is an exponent that describes the sharpness of the recovery as is termed as a separation index. Using eqn. (4), experimental data were fit with a least squares technique with good results as shown in Table 2 by the R^2 values. Figures 1 and 2 show the smoothed results of eqn. 4. Parameters determined are also given in Table 2 and the order of the elements, in terms of $T_{1/2}$ show that metals can be selectively separated. Values of S higher than 50 or so indicate very sharp recoveries. Metals that had high recoveries, such as those in Figure 1, tended to have sharp (high) separation indices, whereas those with low recoveries, such as those in Figure 2, tended to have low separation indices. One can compare, La, Cd, and Pd, which are in increasing order of S .

CONCLUSIONS

The results show that separation of metals from simulated high level liquid wastes is possible and that approximately 42 wt% of the metals can be recovered. From the experiments performed, there is some interaction between the metals and redox couples must exist as determined by the change in oxidation states of Cr, Ce, and Pr from +3 to +4. Periodic table Group I metals were found to remain in solution. It is not known at this point whether the metals in solution are unreacted nitrates or whether they have reacted to some species that are soluble in 1.6 M HNO_3 . A simple model based on an adsorption model was found to adequately describe the data. Because of the experimental technique, it is not possible to know the precise metals and percentages that can be recovered from the solutions studied at supercritical conditions. More detailed experiments with a flow experiment and further research will answer many of these questions. This research on these points is in progress.

REFERENCES

- Adschiri, T.; Kanazawa, K.; Arai, K. *J. Am. Ceram. Soc.* **75**, 1019 (1992).
- Burns, R. E.; Irish, E. R. *AIChE Symposium Series* **72**(154), 17 (1976).
- Cains, P.W.; Yewer, K. C.; Waring, S. *Radiochimica Acta* **56**, 99 (1992).
- Kubota, M. *Radiochimica Acta* **63**, 91 (1993).
- , *Journal of the Japan Institute of Energy* **73**, 807 (1994).

Table 1

Elements and Concentration of Simulated High Level Liquid Waste (HLLW)

Element	Form of Starting Material	Conc (ppm)	Method
Cesium, Cs	CsNO ₃	6,000	AA
Strontium, Sr	Sr(NO ₃) ₂	1,223	ICP
Palladium, Pd(II)	Pd(NO ₃) ₂	595	ICP
Sodium, Na	NaNO ₃	17,650	AA
Barium, Ba	Ba(NO ₃) ₂	3,612	ICP
Silver, Ag	AgNO ₃	155	ICP
Cadmium, Cd	Cd(NO ₃) ₂ • 4H ₂ O	252	ICP
Yttrium, Y	Y(NO ₃) ₃ • 6H ₂ O	1,088	ICP
Lanthanum, La	La(NO ₃) ₃ • 6H ₂ O	2,776	ICP
Cerium, Ce(III)	Ce(NO ₃) ₃ • 6H ₂ O	8,529	ICP
Praeseodymium, Pr(III)	Pr(NO ₃) ₃ • 6H ₂ O	3,885	ICP
Neodymium, Nd	Nd(NO ₃) ₃ • 6H ₂ O	9,606	ICP
Samarium, Sm	Sm(NO ₃) ₃ • 6H ₂ O	2,001	ICP
Europium, Eu	Eu(NO ₃) ₃ • 6H ₂ O	344	ICP
Gadolinium, Gd	Gd(NO ₃) ₃ • 6H ₂ O	17,836	ICP
Zirconium, Zr	ZrO(NO ₃) ₂ • 2H ₂ O	7,333	ICP
Chromium, Cr(III)	Cr(NO ₃) ₃ • 9H ₂ O	1,849	ICP
Molybdenum, Mo (VI)	Na ₂ MoO ₄ • 2H ₂ O	716	ICP
Manganese, Mn(III)	Mn(NO ₃) ₂ • 6H ₂ O	878	ICP
Iron, Fe(III)	Fe(NO ₃) ₃ • 9H ₂ O	10,239	ICP
Nickel, Ni(II)	Ni(NO ₃) ₂ • 6H ₂ O	1,826	ICP

Table 2

Model parameters for recovery as a function of temperature. T_{1/2} is the temperature at which one-half of the maximum recovery, R_{MAX} is obtained.

Element	T _{1/2} , K	R _{MAX} , %	S	Unweighted R ²
Silver, Ag	421	9.7	301.7	0.94731
Molybdenum, Mo (VI)	428	97.9	112.3	0.99996
Zirconium, Zr	434	97.6	52.7	0.99920
Iron, Fe(III)	496	99.2	56.3	0.99991
Chromium, Cr(III)	517	75.2	188.7	0.99601
Barium, Ba	527	3.6	165.6	0.88598
Cadmium, Cd	592	10.5	16.8	0.73407
Palladium, Pd(II)	594	99.4	48.2	0.99923
Lanthanum, La	604	6.8	4.9	0.81774
Neodymium, Nd	627	4.3	183.4	0.84116
Samarium, Sm	630	9.1	56.3	0.91726
Europium, Eu	633	9.2	19.7	0.96889
Cerium, Ce(III)	657	98.4	65.3	0.99963
Praeseodymium, Pr(III)	665	50.2	181.4	0.99433
Yttrium, Y	671	9.6	74.8	0.99998
Manganese, Mn(III)	678	91.1	92.4	0.99225
Nickel, Ni(II)	680	87.4	158.4	0.99785
Gadolinium, Gd	723	4.6	—	—

Thermal Swing Adsorption in Supercritical Fluids

B. D. Mierau and A. K. Sunol

Department of Chemical Engineering, University of South Florida, 4202 East Fowler Avenue, Tampa, Florida, U.S.A.

ABSTRACT

The success of thermal swing adsorption in the separation of multiple solute mixtures, depends on the ability to control thermal wave velocity relative to each solute velocity as they pass through the column. For a ternary system operating conditions must be cycled such that the velocity of the thermal wave in one instance exceeds the velocities of both solutes, in another the velocity of one component is exceeded, and finally that the velocities of both solutes exceed that of the thermal wave. The sensitivity of supercritical solvents to thermally induced changes in heat conductivity provides a unique means of controlling the velocity of the thermal wave, in order to affect such separations. A dynamic model is presented which allows prediction of the wave velocities for use in determining the appropriate operating conditions for a given mixture. A pilot scale separation unit under investigation for recycled thermal swing separations is also described.

THERMAL SWING PROCESSES IN SUPERCRITICAL FLUIDS

The general properties of supercritical fluids make them an attractive alternative to liquid solvents in column operations where transport effects come into play. If supercritical CO₂ is employed as the solvent, this advantage is further supplemented by the non-flammable, non-toxic nature of the fluid, and the relative ease of solvent recovery. Supercritical solvents also offer the potential to greatly enhance thermally driven separations through dramatic changes in component solubility, adsorptive characteristics, and thermal conductivity near the critical region.

For the separation of components in a ternary mixture, the column must be operated in such a manner that the relative velocities of the binary solutes through the bed can be controlled. By employing three operational conditions in succession such that in one instance both solutes move at a rate slower than the thermal front, one solute moves faster and one slower than the front, and where both solutes move faster than the thermal front; a concentration shock wave can be induced to form for each species to be separated¹. The dramatic changes in heat transfer characteristics of the fluid phase near the critical point allows for greater flexibility in selecting these operating conditions. Successful design of processes which operate in this region will depend on the ability to model adsorption, desorption, and possibly retrograde phenomena accurately enough to enable scaling to production sizes.

MODEL DEVELOPMENT

In this report, a kinetic model based on the solid film linear driving force assumption is used. Unlike the equilibrium-dispersive model, which lumps all transfer and kinetic effects into an effective dispersion term, the kinetic model is effective when the column efficiency is low and the effects of column kinetics are significant.

The dynamic behavior of an adiabatic adsorption column has been previously solved by a number of investigators, the majority of these solutions involving incompressible fluids or having been restricted to systems where dilute solution approximations apply. Raghavan and Ruthven² presented a model for an incompressible system represented well by a reversible isotherm, axial dispersion, and external film as well as pore diffusional resistances to mass transfer. The model presented below is essentially the same as the one developed by these authors, except adjustments have been made to allow for changes in model parameters as the simulation progresses. In order to avoid intractable computational problems, fluid velocity is taken to be a discontinuous property estimated at discrete points along the length of the column. The velocity is assumed to remain constant over each column segment, and is determined through mass balances involving equation of state or empirically based correlations for the viscosity and density of the fluid phase. The model parameters effected by changes in velocity can be adjusted at these discrete points. Mathematically, the interactions of solute with the adsorbent can be described as a linked set of Partial Differential Equations (PDEs), Ordinary Differential Equations (ODEs) and algebraic equations. This system is transformed into a set of ODEs, with the PDEs discretized by orthogonal collocation and the algebraic expressions either written into the ODEs or treated as adjustable parameters. The resulting set of equations was solved using SPEEDUP™.

RESULTS

In order to demonstrate the feasibility of thermal swing separations for a ternary supercritical mixture, a pair of Langmuir adsorption isotherms was generated using the data of Tan and Liou³. Non-competing isotherms for two hypothetical components have been constructed, whose slope varies slightly from that reported for toluene. We have not adjusted the isotherm constants to account for density changes, as the resulting alterations in isotherm slope will not significantly effect the outcome of this demonstration. The feed concentration was assumed to be 1.0 mmol/L as reported by Tan and Liou.

The pore diffusivity used in this analysis was determined by the Renkin equation⁴, the axial dispersion coefficient calculated by assuming a constant Peclet number of 0.2, and the mass transfer coefficient from the bulk to the particle surface calculated by the correlation of Wakao and Kagui²⁰. The product of the heat capacity and density of the solid phase was taken to be the same as that used by Raghavan and Ruthven¹⁷. The density of the fluid phase was assumed to be that of pure CO₂ and was calculated from data provided by the Dionix Corporation in their AI-450 SFC software. Constant pressure heat capacities for the mobile phase were also assumed to be that of pure CO₂ and were taken from Brunner⁵.

The model parameters listed in Table 1 were used in each simulation and are in an appropriate range for supercritical CO₂ systems. Table 2 shows the model parameters

which were varied in the three phases of a thermal swing cycle. This in effect accounts only for the large changes in thermal conductivity with temperature.

The parameters described result from writing the model equations in dimensionless form, and are defined as

$$Q_0 = \frac{q_0}{c_0}, \quad \delta = \frac{-\Delta H}{R_g T_0}, \quad Pe_m = \frac{uL}{D_L}, \quad Pe_h = \frac{\rho_f C_p u L}{K_L}, \quad \gamma = \frac{(-\Delta H)c_0}{\rho_f C_p T_0}$$
$$\Psi = \frac{T}{T_0}, \quad \beta = \frac{k_f R_p}{D_p}, \quad \alpha = \frac{R_p^2 u}{D_p L}, \quad \lambda_0 = \frac{b_0 c_0}{1 + b_0 c_0}, \quad \phi = \frac{\rho_f C_p}{\rho_s C_p}$$

Table 1
Constant Dimensionless Model Parameters

Q_0 component 1	1.46	δ component 1	27.2	λ_0	4.38×10^{-8}
Q_0 component 2	2.98	δ component 2	13.33	β	145.013
Pe_m	700.93	Pe_h	700.93	α	1.672

Table 2
Temperature Dependent Dimensionless Model Parameters

Feed Temperature K	ψ_0	$\psi_{initial}$	ϕ	γ
313.15	1.0	1.192	3.19	4.845×10^{-5}
333.15	1.064	1.0	0.8248	1.762×10^{-4}
373.15	1.192	1.064	0.2887	4.494×10^{-4}

Figures 1-3 show the concentration and temperature breakthrough profiles for the three phases of a thermal swing cycle.

Figure 1

Figure 2

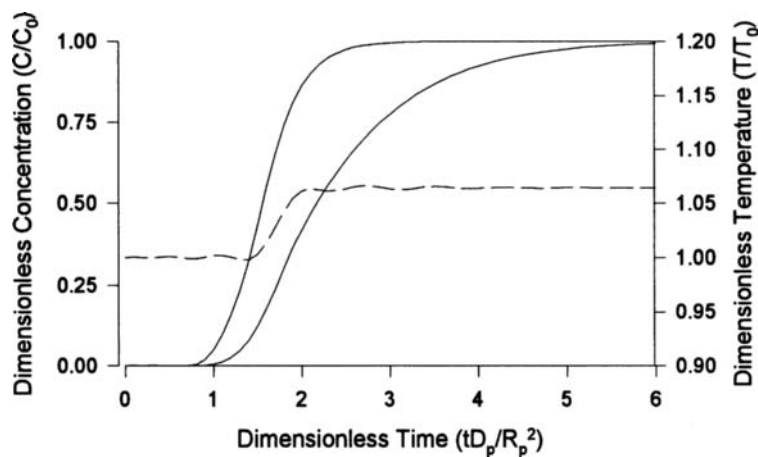
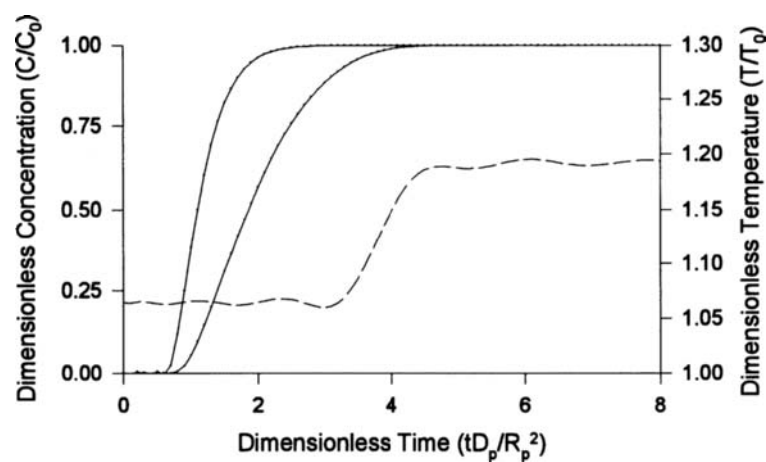


Figure 3



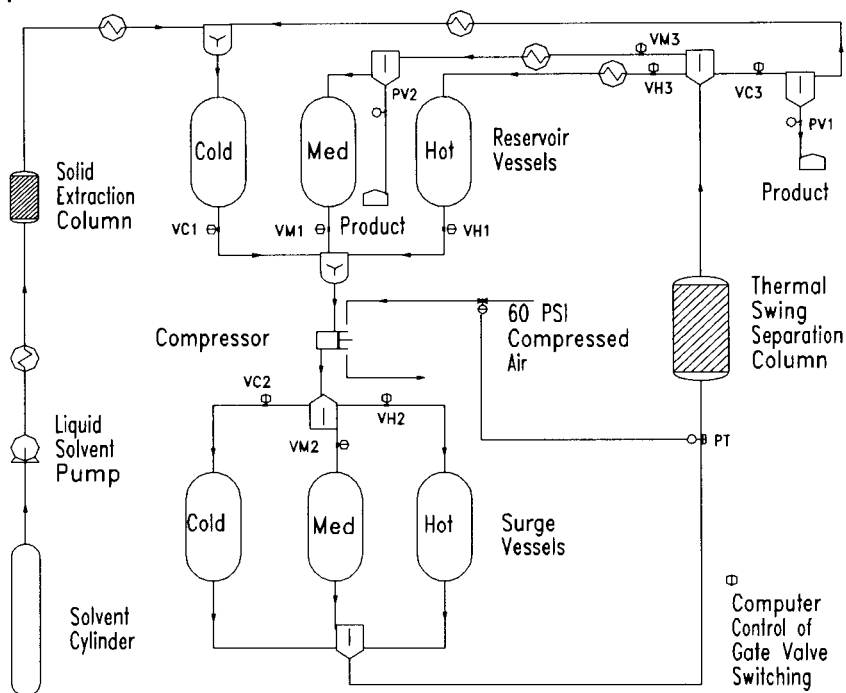
In Figure 1, a cold feed is the influent for a hot column and the thermal wave (dashed line) is seen to have a higher velocity than either solute. Figure 2 describes the breakthrough profiles for an initially cold column with an intermediate feed temperature, where the thermal wave velocity is faster than only one solute velocity. In Figure 3, the thermal wave is shown to exit the column more slowly than either solute, for a column initially at an intermediate temperature with a hot influent.

Thus in a sufficiently long column, the faster moving solute will be concentrated at the region between the cold and intermediate temperatures and the solute with a slower velocity between the intermediate and hot temperatures.

EXPERIMENTAL SETUP

A processing scheme for recycled thermal swing separation of a ternary mixture has been synthesized, and the existing pilot facilities are in the process of being retrofitted. Figure 4 shows a simplified P&ID for a system comprised of three thermal reservoirs which supply a reciprocating diaphragm compressor. A surge vessel is used to suppress pump pulses and facilitate pressure control, and is provided for each temperature to minimize mixing of the thermal fronts.

Figure 4



DISCUSSION

Thermal swing operations appear to have potential in systems employing supercritical solvents. The dramatic alterations in thermal conductivity of these fluids in response to density changes at constant pressure allows temperature to be the thermodynamic variable cycled in driving the separation. Thermal swing separations appear to have potentially less utility in other media since for gaseous systems pressure can be cycled much more rapidly and in liquid systems concentration generally has a greater effect on the distribution between solid and liquid phases⁶. Temperature cycling is

considered here because it allows for ease in application of the driving force for separation and imparts no contaminants to the system.

Operation of thermal swing systems for separation in the traveling wave mode (thermal wave propagation through the adsorbent bed) seems to be restricted to gas/dense gas regimes, because of the inability to adjust the velocity of the thermal wave in liquid systems. Liquid systems generally require the use of fixed temperature zones.

The model is currently being refined to better allow for concentration related changes in the velocity of the shock waves, as well as improvements in modeling the density dependent parameters of the simulation. Work continues on the determination of adsorption and desorption isotherms for several ternary systems, as well as the thermal and mass transfer characteristics for the column and media being employed. Accurate determination of the model parameters will be required for optimization of the of the operational regime.

Glossary

b_0	= adsorption equilibrium constant at feed conditions, cm^3/mole	L	= axial length, cm
c_0	= feed concentration, mole/cm^3	q_0	= solid phase concentration in equilibrium with feed, mole/cm^3
Cp_f	= fluid-phase heat capacity, $\text{cal}/\text{g}\cdot^\circ\text{C}$	R_g	= ideal gas constant, $\text{cal}/\text{mole}\cdot\text{K}$
Cp_s	= solid-phase heat capacity, $\text{cal}/\text{g}\cdot^\circ\text{C}$	R_p	= particle radius, cm
D_L	= axial mass dispersion coefficient, cm^2/sec	ρ_f	= fluid density, g/cm^3
D_p	= pore mass molecular diffusivity, cm^2/sec	ρ_s	= density of solid, g/cm^3
ΔH	= heat of adsorption, cal/mole	T	= fluid temperature, K
k_f	= mass transfer coefficient, cm/s	T_0	= fluid feed temperature, K
K_L	= axial heat dispersion coefficient, $\text{cal}/\text{cm}\cdot\text{sec}\cdot^\circ\text{C}$	t	= time, sec
		u	= interstitial velocity, cm/sec

¹ Wankat, P. C.; Dore, J. C., Multicomponent Cycling Zone Adsorption, *Chemical Engineering Science*, **1976**, 31, 921-927.

² Raghavan, N. S.; Ruthven, D. M. Dynamic Behaviour of an Adiabatic Adsorption Column, *Chemical Engineering Science*, **1984**, 39(7-8), 1201-1212.

³ Tan, C. S.; Liou, D. C., Adsorptive Equilibrium of Toluene from Supercritical Carbon Dioxide on Activated Carbon. *Ind. Eng. Chem. Res.*, **1990**, 29(7), 1412-1415.

⁴ Lee, C. H.; Holder, G. D., Use of Supercritical Fluid Chromatography for Obtaining Mass Transfer Coefficients in Fluid-Solid Systems at Supercritical Conditions, *Ind. Eng. Chem. Res.*, **1995**, 34, 906-914

⁵ Brunner, G. Gas Extraction. Steinkopff Darmstadt Springer, New York, 1994.

⁶ Kirkland, J. J. (ed.), Modern Practice of Liquid Chromatography. Wiley (Interscience), New York, 1970.

Monte Carlo Simulation for Distribution Equilibrium between Supercritical Fluid and Slit Pores

Takeshiro Shigeta and Tomoshige Nitta

Department of Chemical Engineering, Faculty of Engineering Science,
Osaka University, Toyonaka, Osaka, 560 JAPAN

Abstract

Monte Carlo simulation techniques are used for calculating the distribution coefficients of benzene between supercritical CO₂ and slitpores at infinite dilution. The Lennard-Jones potential model is used for representing the pair interactions between CO₂, benzene, and graphite carbon. The effects of temperature, slitwidth, and benzene-surface interaction potential on the distribution coefficients are explored at constant density and constant pressure.

1. INTRODUCTION

The supercritical fluid chromatography (SFC) is now widely used for the analytical separation for its rapidity, flexibility, and the ability to allow the analysis of substances which cannot be analyzed by the conventional gas chromatography [1-3]. Though the phase equilibrium of supercritical fluid is complicated, the understanding of the distribution behavior of solutes between the stationary and the mobile phases at the supercritical condition is needed for designing SFC. The distribution coefficient of a solute at a supercritical region, K_2 , which is the key thermodynamic property for the chromatography, shows different characteristics from gas or liquid chromatography. Recently, experimental data of K_2 in the supercritical region have been analyzed by use of an equation of state combined with the Langmuir equation [4] or the solution theory [5]; however, molecular approach is needed for better understanding of the distribution behavior.

Followed by the rapid development of computer power, Monte Carlo (MC) and molecular dynamics (MD) simulation methods have been applied to many fields so as to connect the microscopic interaction model with the macroscopic properties, such as pVT relation, phase equilibria and so on [6]. They have also been used to analyze the adsorption characteristics of supercritical fluid [7-9]; however, the simulation studies for adsorption phenomena in supercritical fluid mixtures are still limited.

In the present work, we performed MC simulations at different operation conditions, constant fluid density and constant pressure, for calculating K_2 to investigate the distribution behavior in the supercritical region. We selected CO₂, benzene, and graphitic slitpore as a model system by adopting the Lennard - Jones (LJ) potential function for intermolecular interactions.

2. SIMULATION MODEL AND PARAMETERS

The LJ pair potential between gas molecules i and j , $\phi_{ij}(r)$, separated by distance r is given in Eq. (1).

$$\phi_{ij}(r) = 4\epsilon_{ij} \left[\left(\frac{\sigma_{ij}}{r} \right)^{12} - \left(\frac{\sigma_{ij}}{r} \right)^6 \right] \quad (1)$$

The potential function of molecule i interacting with a solid surface, $\phi_{is}(Z)$, is described by the so called '10-4-3' potential [10],

$$\phi_{is}(Z) = 4\pi A_{is} \left[\frac{2}{5} \left(\frac{\sigma_{is}}{Z} \right)^{10} - \left(\frac{\sigma_{is}}{Z} \right)^4 - \frac{\sigma_{is}^4}{3\Delta(Z + 0.61\Delta)^3} \right] \quad (2)$$

where Z is the normal distance between a molecule and a surface passing through the atomic centers of a basal plane, $A_{is} (= \epsilon_{is}\sigma_{is}^2 / a_s)$ is a constant, a_s the surface area of a graphite basal unit, and Δ the spacing between adjacent graphite basal planes. The potential energy $\Phi_i(Z)$ for molecule i located at distance Z is calculated as

$$\Phi_i(Z) = \sum_j \phi_{ij}(r_{ij}) + \phi_{is}(Z) + \phi_s(H - Z) \quad (3)$$

where H is the slitwidth of the pore defined as the distance between the carbon centers of the surface planes. The suffix j runs over different molecules in the pore. The pair potential is cut off at a distance of $\min[3.5\sigma_{22}, L/2]$, where L is the length of a simulation box and σ_{22} is the LJ size parameter of benzene. The long range correction is applied to the fluid phase but not to the pore region where the cut-off radius is essentially $3.5\sigma_{22}$.

The LJ parameters, ϵ/k and σ , have been determined from the critical constants, T_c and p_c , by adopting the recommendation of Nicolas et al. [11]: $kT_c/\epsilon = 1.35$ and $p_c\sigma^3/\epsilon = 0.142$. However, different values for the potential depth of benzene, ϵ_{22} , have been determined so as to fit the vapor pressure at temperatures from 307.2 K to 553.2 K. The LJ

Table 1 LJ parameters and binary parameters for simulation

	ϵ/k [K]	σ [nm]
CO ₂ (1)	225.3	0.3910
C ₆ H ₆ (2)	[307.2 K] 470.5	0.5506
	[553.2 K] 425.0	
Carbon (s)	28.0	0.340

$$k_{12} = 0.1232, k_{1s} = 0.170, k_{2s} = -0.15, 0.0, 0.15$$

parameters used in this work are summarized in Table 1, where the parameters for graphitic carbon atom are taken from those suggested by Steele [10]. We used the modified Lorentz - Berthelot rule for the cross parameters, that is, the arithmetic mean for σ and the geometric mean for ϵ by introducing the binary parameter k_{ij} defined as Eq. (4).

$$\epsilon_{ij} = \sqrt{\epsilon_i \epsilon_j} (1 - k_{ij}) \quad (4)$$

The values of k_{ij} listed in Table 1 are the same as those used in the previous work [9]. The value of k_{2s} is varied as -0.15, 0.0, and 0.15 in the present work for studying the effect of adsorption energy of an adsorbate.

3. SIMULATION METHODS

3.1 Distribution coefficient and residual chemical potential

The distribution coefficient of benzene, K_2 , between the pore and the fluid phases is defined as the ratio of the molar concentration of benzene in the pore phase, $\rho_{2,p}$, to that in the fluid phase, $\rho_{2,f}$, at infinite dilution in both phases.

$$K_2 \equiv (\rho_{2,p} / \rho_{2,f})^\infty = \exp\left\{(\mu_{2,f}^{\text{res}} - \mu_{2,p}^{\text{res}})^\infty / kT\right\} \quad (5)$$

The residual chemical potentials of benzene, $\mu_{2,f}^{\text{res}}$ and $\mu_{2,p}^{\text{res}}$, and that of CO_2 in the fluid phase, $\mu_{1,f}^{\text{res}}$ are calculated by Widom's test particle insertion method, Eq. (6) [6], which has been embedded in all the simulation programs.

$$\mu_i^{\text{res}} = -kT \ln \langle \exp(-\Phi_i/kT) \rangle \quad (6)$$

where $\langle \cdots \rangle$ denotes the ensemble average and Φ_i is the potential that a test particle inserted feels from other molecules (and walls in case of a pore phase).

3.2 Calculation procedure

The NVT (constant ρ_f) and the NpT (constant p) ensembles are used for simulating the fluid phase while the μVT ensemble is used for the pore phase. The strategy of calculating K_2 at infinite dilution both in the pore and in the supercritical CO_2 is as follows:

- (i) to carry out the NVT or the NpT ensemble MC simulation for pure CO_2 fluid. During the simulation, test molecules of CO_2 and benzene are inserted for calculating $\mu_{1,f}^{\text{res}}$ and $\mu_{2,f}^{\text{res}}$.
- (ii) to calculate the chemical potential of CO_2 , μ_1 , by specifying the mole fraction of CO_2 to be unity.

$$\mu_1 = kT \ln \rho_f^* + \mu_{1,f}^{\text{res}} \quad (7)$$

where ρ_f^* ($=\sigma_{11}^{-3}\rho_f$) is the dimensionless fluid density.

- (iii) to carry out the μVT ensemble MC simulation for pure CO_2 in a pore of different slitwidths, $H = 1.2, 1.5$, and 2.0 nm, by specifying the set of variables, μ_1 , V_p and T . Test molecules of benzene are inserted to calculate $\mu_{2,p}^{\text{res}}$ during the simulation.
- (iv) to calculate K_2 through Eq. (5) from $\mu_{2,f}^{\text{res}}$ and $\mu_{2,p}^{\text{res}}$.

For calculations at constant fluid density, ρ_f^* is set at 0.2 (5.53 mol/l) and 0.3 (8.29 mol/l). For calculations at constant pressure, the reduced pressure, p^* ($=p\sigma_{11}^3/\epsilon_{11}$), is set at 0.2 (10.39 MPa) and 0.3 (15.59 MPa). The temperature is varied from 307.2 K to 553.2 K. We used 256 particles in both the NVT and the NpT ensembles and 200~400 particles in the μVT ensemble for the single component (CO_2) system. In the μVT simulation, one cycle consists of 700 displacements and the number of trials for particle transfer (creation or destruction) per displacement step is chosen within 5 and 10. The first 1000 cycles were discarded and the last 3000 cycles were used for ensemble averages.

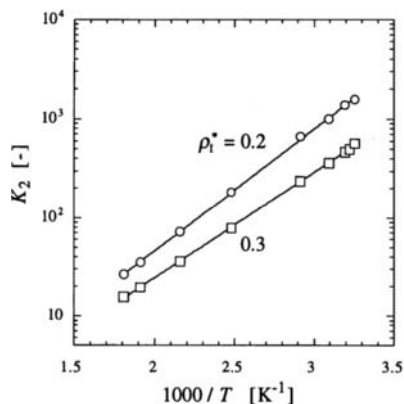


Fig. 1 Distribution coefficient of benzene against reciprocal temperature at constant fluid density: $\rho_f^* = 0.2$ and 0.3 ; slitwidth $H = 2.0$ nm.

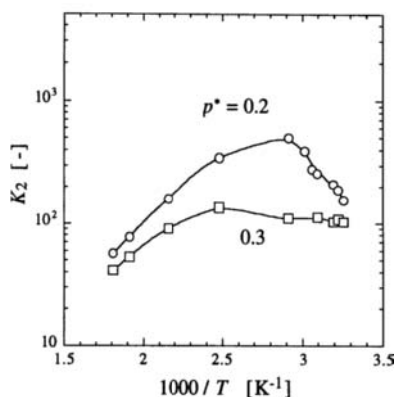


Fig. 2 Distribution coefficient of benzene against reciprocal temperature at constant pressure: $p^* = 0.2$ and 0.3 ; slitwidth $H = 2.0$ nm

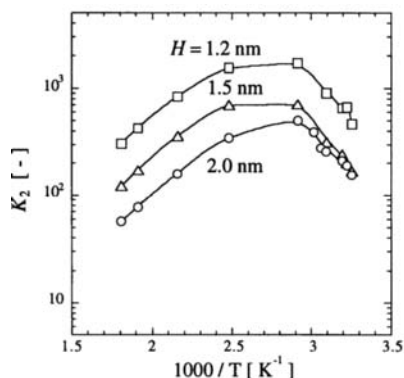


Fig. 3 Distribution coefficient of benzene against reciprocal temperature at constant pressure: $p^* = 0.2$; slitwidth $H = 1.2, 1.5$, and 2.0 nm

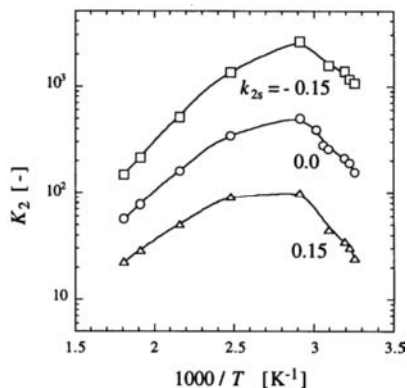


Fig. 4 Distribution coefficient of benzene against reciprocal temperature at constant pressure: $p^* = 0.2$; $k_{2s} = -0.15, 0.0$, and 0.15

4. RESULTS AND DISCUSSION

4.1 Results for distribution coefficients

Figure 1 shows $\log K_2$ at constant fluid density, $\rho_f^* = 0.2$ and 0.3 , against the reciprocal temperature, $1000/T$. Both curves increase linearly with increasing reciprocal temperature (decreasing temperature), and the curve at $\rho_f^* = 0.2$ is higher than that at $\rho_f^* = 0.3$.

Figure 2 shows $\log K_2$ at constant pressure, $p^* = 0.2$ and 0.3 . Both curves at the constant pressures show a maximum and then decrease with decreasing temperature; the curve at higher pressure, $p^* = 0.3$, has a maximum at 403.2 K while the curve at lower pressure, $p^* = 0.2$, shows a maximum at 343.2 K and then it rapidly decreases with decreasing temperature.

Figure 3 shows the effect of the slitwidth on K_2 at constant pressure, $p^* = 0.2$, against

$1000/T$. In Fig. 3, $\log K_2$ increases with a decrease in slitwidth since the benzene-surface interaction potential becomes deeper with a decrease in slitwidth.

Figure 4 shows the effect of benzene-surface interactions parameter, k_{2s} , on K_2 at $p^*=0.2$ for the slitwidth $H = 2.0$ nm. Negative value of k_{2s} means that the solute molecule has larger adsorption energy. In Fig. 4, the curve of K_2 increases with decreasing k_{2s} as expected.

4.2 Density effect on residual chemical potential

In addition to the simulation data for K_2 , which were presented in the above sections, the simulation outputs provide more information to look insight into the factors influencing K_2 . According to Eq. (5), K_2 is evaluated from the exponential of the difference between $\mu_{2,f}^{\text{res}}/kT$ and $\mu_{2,p}^{\text{res}}/kT$. Therefore, it is important to know how the residual chemical potentials of benzene in two phases change with the temperature and densities.

Figure 5 shows the pore density of pure CO_2 , ρ_p^* , and the residual chemical potentials of benzene, $\mu_{2,f}^{\text{res}}/kT$ and $\mu_{2,p}^{\text{res}}/kT$, against the reciprocal temperature at constant fluid density, $\rho_f^* = 0.2$ and 0.3 ; the slitwidth of a pore is 2.0 nm. The solid lines represent the calculated results at $\rho_f^* = 0.2$ and the broken lines those at $\rho_f^* = 0.3$. The open and gray keys stand for the fluid and the pore phases, respectively.

In Fig. 5(a) two lines for ρ_p^* increase almost linearly with an increase in $1/T$ and the solid line is lower than the broken line. It is noteworthy here that the difference between two lines for ρ_p^* decreases with decreasing temperature though the difference for ρ_f^* is constant. This indicates that the pore has been filled so as to resist further loadings in the low temperature region.

In Fig. 5(b), one important feature is that the two lines for the fluid phase are negative, which indicates that the benzene molecule is controlled by the attractive interactions with surrounding CO_2 . In addition, the lines for the pore phase are much more negative than those for the fluid phase, which means that the benzene molecule is stabilized more through the interactions with wall surfaces. Another important feature of Fig. 5(b) is the reverse relation between the solid and the broken lines for the two phases; that is, the solid line for $\mu_{2,f}^{\text{res}}/kT$ is higher than the broken line while the solid line for $\mu_{2,p}^{\text{res}}/kT$ is lower than the broken line.

According to Widom's test particle method for calculating μ_2^{res}/kT , the test molecules (benzene) inserted in each simulation do not influence the molecular movements of pure CO_2 in any sense. Therefore, the stabilization of a test molecule in the fluid phase occurs through two conditions: (i) the increase in the number of

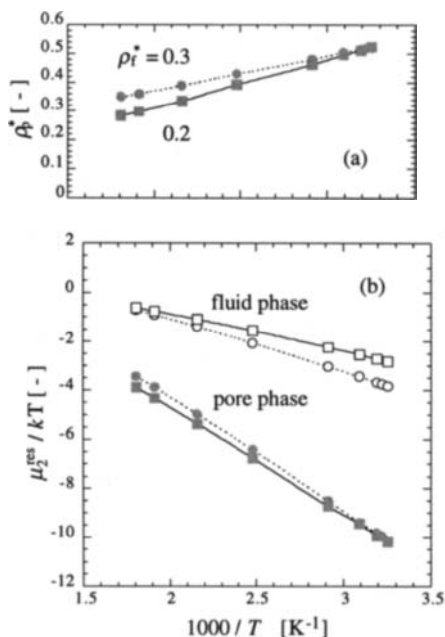


Fig. 5 (a) Pore density of CO_2 and (b) residual chemical potentials of benzene in fluid and pore phases at constant fluid density (\circ, \square : $\rho_f^* = 0.3$, \bullet, \blacksquare : $\rho_f^* = 0.2$); slitwidth = 2.0 nm

CO₂ molecules interacting with a test molecule and (ii) the existence of holes accommodating the test molecule. One plausible configuration for supercritical CO₂ to fulfill both conditions is the assembly of clusters of CO₂ molecules having dense and sparse regions. If the fluid density increases much more, the number of holes will decrease in the fluid; therefore, the residual chemical potential of a solute will go up, which we may call the repulsive-interaction-controlling state in the high density region.

In the case of slitwidth $H = 2.0$ nm, the pore consists of four CO₂ layers; two layers near the walls are the monolayers and others are in the middle region. When the monolayers are almost saturated with CO₂ molecules, the number of holes available for a test benzene molecule in the monolayers decrease dramatically. The decrease in the number of holes in the monolayers makes the pore phase to be repulsive-interaction-controlling, which results in the higher value of $\mu_{2,p}^{\text{res}}/kT$ as the pore density of CO₂ increases.

5. CONCLUDING REMARKS

The distribution coefficients of benzene, K_2 , between slitpores and supercritical CO₂ phases at infinite dilution have been calculated by use of the MC simulation techniques and the effects of the temperature, operation conditions, slitwidth and k_{2s} have been investigated. The curves of $\log K_2$ show almost linear dependence with the reciprocal temperature at the condition of constant fluid density, while they show a maximum at constant pressure. The decrease in k_{2s} and slitwidth result in the increase of K_2 . The effects of density on the residual chemical potentials, from which K_2 is evaluated, are remarkably different between the pore and the fluid phases; that is, $\mu_{2,f}^{\text{res}}$ gets stabilized with increasing fluid density since the number of CO₂ molecules interacting with a benzene molecule increase with the fluid density, while $\mu_{2,p}^{\text{res}}$ becomes unstable with increasing pore density mainly because the number of holes for benzene molecules decrease in monolayers where the benzene molecule is most stabilized through interactions with wall surfaces.

REFERENCES

1. Smith, R. M. (ed.), *Supercritical Fluid Chromatography*, The Royal Society of Chemistry (1988).
2. de Castro, M.D.L., M. Valcarcel and M.T. Tena, *Analytical Supercritical Fluid Extraction*, Springer-Verlag, Berlin (1994).
3. Saito, M., Yamauchi, Y. and Okuyama, T. (eds.), *Fractionation by Packed-Column SFC and SFE: Principles and Applications*, VCH, New York (1994).
4. Kelly, F. D. and E. H. Chimowitz, *AIChEJ.*, **36**, 1163-1175 (1990).
5. Shim, J.-J. and K.P. Johnston, *J. Phys. Chem.*, **95**, 353-360 (1991).
6. Allen, M.P. and D.J. Tildesley, *Computer Simulation of Liquids*, Clarendon Press, Oxford (1987).
7. van Megen, W. and I. K. Snook, *Mol. Phys.*, **54**, 741-755 (1985).
8. Nitta, T. and J. Yoneya, *J. Chem. Eng. Japan*, **28**, 31-37 (1995).
9. Shigeta, T., J. Yoneya, and T. Nitta, *Mol. Sim.*, **16**, 291-305 (1996).
10. Steele, W.A.: *Surface Sci.*, **36**, 317-352 (1973); *The Interaction of Gases with Solid Surfaces*, Pergamon Press, Oxford (1974).
11. Nicolas, J.J., K.E. Gubbins, W.B. Streett, and D.J. Tildesley, *Mol. Phys.*, **37**, 1429-1454 (1979).

Removal of Xanthines from Cacao

Josef Sebal, Josef Schulmeyr and Manfred Gehrig
Hopfen-Extraktion HVG Barth, Raiser & Co., Auenstrasse 18-20, D-85283 Wolnzach

1 INTRODUCTION

Removal of stimulants like caffeine from (green) coffee beans and black tealeafs is practised since the beginning of the century because of potential health hazards to consumers. Since about 15 years supercritical Carbon dioxide is used as solvent.

In 1982 a method has been presented to remove xanthines like theobromine, theophylline and caffeine from cacao products [1] working very similar to the procedures applied to the decaffeination of coffee and tea. The authors intend to reduce the quantity of xanthines, but like to keep the content of valuable cacao butter unchanged. For this purpose they suggest to swell the cacao material (nibs) with water to about 40 % w/w and extract the undesired components with Carbon dioxide. They claim that the concentration of theobromine is reduced, caffeine is removed completely without affecting the cacao butter.

Li et al [2] are trying to improve the extraction process adding a co-solvent, ethanol, to Carbon dioxide to enhance the concentration of caffeine and especially of theobromine in the solvent by orders of magnitude thus reducing time and quantity of solvent to be cycled. In the same way the concentration of cacao butter in the solvent is increased. Consequently the xanthines and fats are extracted simultaneously. Moreover they monitored solubilities of the important ingredients theobromine, caffeine and cacao butter.

Brunner et al. [3] used shells from the production of cacaomass having a composition of 1 % theobromine, 0,1 % caffeine, 5 % fat and 8 % water. They are stating that theobromine can be extracted from the shells to some extend without adding water but for the extraction of caffeine one needs to increase the moisture content to about 50 %. In all cases large quantities of solvent are needed. Being a waste product and used as source for the xanthines only the content of butter has no importance.

The results presented in the literature can be summarised shortly:

- Theobromine and caffeine can be extracted from cacao nibs with carbon dioxide after swelling of the nibs with water without affecting the concentration of cacao butter.
- Theobromine and caffeine can be extracted out of cacao nibs with carbon dioxide adding ethanol as cosolvent in much shorter times. Simultaneously cacao butter is extracted.
- Theobromine and caffeine can be extracted out of cacao shells with carbon dioxide after swelling the shells with water. Large quantities of solvent are to be cycled.

With some screening tests we tried to verify the findings summarised above. It turned out that none of the procedures described in the cited literature is feasible for the demand: removal of the xanthines without a reduction of cacao butter (being a valuable component of the cacao mass). According to our investigations it is possible to remove caffeine from swollen nibs but it is not possible to reduce theobromine by simply using Carbon dioxide. The procedure of Li et al. [2] is not suitable because of the coextraction of cacao butter. Only with a combination of the approaches cited above the scope claimed already in the patent specification EP 61 017 [1] can be achieved:

2 EXPERIMENTAL EQUIPMENT

Tests have been performed in a lab scale plant with extraction vessels with a volume up to 1 l. For scaling up procedure a pilot plant with extraction vessels with volumes of 200 l has been used.

3 TEST PROGRAM

For the tests roasted cacao nibs have been used with the following composition

Theobromine	Caffeine	Theophylline	cacao butter
% w/w	% w/w	% w/w	% w/w
1,17	0,12	traces	52

The effects of parameters influencing the solubility of the components in the solvent like

- extraction pressure
- extraction temperature
- addition of entrainers
- composition of the entrainer

and the diffusion in the cells to the surface like

- swelling with water
- grinding

have been investigated in screening tests.

In the tables monitoring the effects of changing the single parameters all results represent the average of at least two tests. In the tables the concentrations of the ingredients of the starting material are given in % w/w. The variations of the concentrations as a result of the test runs are monitored as relative figures: Reduction of the components (e. g. 100 % minus concentration of theobromine after the treatment to concentration of theobromine in the starting material).

3.1 Screening tests

3.1.1 Influence of the extraction pressure

From our experience in the decaffeination of coffee and tea and the extraction of oils and other valuable ingredients from natural materials it has been deducted that pressures between 250 and 400 bars will be suitable for the extraction of the nibs. Because of the limiting design pressure of larger production plants for all tests the extraction pressure was fixed to 300 bars.

3.1.2 Influence of the extraction time

extraction temperature, °C	60
relative solvent flow, kg/kg	Variation
entrainer	water and ethanol
composition of the entrainer	1 : 1
pre-treatment of the raw material	swelling of the nibs with water to a content of 20 % w/w, no grinding

The extraction time is presented as quantity of solvent flowing through the material, because not the time but the solvent performs the extraction. Circulated solvent and extraction time are proportional via the flow rate of the solvent. To allow comparison of tests with different quantities of starting material the relative quantity of solvent is used as parameter (relative quantity of solvent=quantity of solvent/quantity of starting material).

relative quantity of solvent	<i>Theobromine</i> % w/w or reduction	<i>Caffeine</i> % w/w or reduction	<i>Theophylline</i> % w/w or reduction	<i>cacao butter</i> % w/w or reduction
starting material	1,17	0,12	traces	52
75 kg/kg	20 %	90 %	not detectable	15 %
150 kg/kg	50 %	95 %	not detectable	15 %
300 kg/kg	65 %	not detectable	not detectable	15 %

Result: Caffeine can be reduced nearly complete with a comparatively small quantity of solvent. Theobromine can be reduced to 1/3 of its original concentration only with large quantities of solvent under the applied conditions. Cacao butter is lost to a considerable and not tolerable extent.

3.1.3 Influence of the extraction temperature

extraction temperature, °C	Variation. 60 and 90 °C
relative solvent flow, kg/kg	150
entrainer	water and ethanol
composition of the entrainer	1 : 1
pre-treatment of the raw material	swelling of the nibs with water to a content of 20 % w/w, no grinding

extraction temperature	<i>Theobromine</i> % w/w or reduction	<i>Caffeine</i> % w/w or reduction	<i>Theophylline</i> % w/w or reduction	<i>cacao butter</i> % w/w or reduction
starting material	1,17	0,12	traces	52
60 °C	50 %	95 %	not detectable	15 %
90 °C	60 %	98 %	not detectable	20 %

Results: Higher extraction temperatures favour the reduction of the xanthines, unfortunately also the loss of cacao butter.

3.1.4 Influence of the entrainers and their composition

extraction temperature, °C	60
relative solvent flow, kg/kg	150
entrainers	Variation: no entrainer, water and ethanol
composition of the entrainer	Variation: 1:1 and 1:2
pre-treatment of the raw material	swelling of the nibs with water to a content of 20 % w/w (see table), no grinding

<i>entrainers and pre-treatment</i>	<i>Theobromine % w/w or reduction</i>	<i>Caffeine % w/w or reduction</i>	<i>Theophylline % w/w or reduction</i>	<i>cacao butter % w/w or reduction</i>
starting material	1,17	0,12	traces	52
dry CO ₂ , no swelling	(-53 %)	(-50 %)	traces	65 %
water, no swelling	2 %	90 %	traces	15 %
water, swelling	5 %	90 %	traces	15 %
water+ethanol 1:1, swelling	50 %	95 %	not detectable	15 %
water+ethanol 1:2, swelling	38 %	95 %	not detectable	15 %

Result: Extraction of dry nibs with pure CO₂ seems to increase the concentration of the ingredients apparently. In reality the quantity is kept unaltered but gets higher because of the loss of cacao butter (this is contrary to the results of Li and Hartland). Independently to the pre-treatment and to the composition of the co-solvent the reduction of caffeine reaches about 90 %. Theobromine is reduced remarkably only with ethanol as co-solvent. Only with the knowledge of later tests the worse reduction of theobromine at a composition of the co-solvent of 1:2 water:ethanol can be understood: The concentration of ethanol in CO₂ becomes too small.

3.1.5 Influence of a pre-treatment of the starting material: Swelling with water

extraction temperature, °C	60
relative solvent flow, kg/kg	150
entrainer	water and ethanol
composition of the entrainer	1 : 1
pre-treatment of the raw material	Variation: swelling of the nibs with water to a content of 20 % w/w, no grinding

<i>pre-treatment</i>	<i>Theobromine % w/w or reduction</i>	<i>Caffeine % w/w or reduction</i>	<i>Theophylline % w/w or reduction</i>	<i>cacao butter % w/w or reduction</i>
starting material	1,17	0,12	traces	52
no swelling	50 %	95 %	not detectable	15 %
swelling	45 %	95 %	not detectable	15 %

Results: Pre-treatment of the nibs with water slightly impairs the reduction of theobromine. Caffeine removal is not affected.

3.1.6 Influence of a pre-treatment of the starting material: Grinding

extraction temperature, °C	60
relative solvent flow, kg/kg	150
entrainer	water and ethanol
composition of the entrainer	1 : 1
pre-treatment of the raw material	swelling of the nibs with water to a content of 20 % w/w
	Variation: no grinding/grinding with a coffee mill

<i>pre-treatment</i>	<i>Theobromine % w/w or reduction</i>	<i>Caffeine % w/w or reduction</i>	<i>Theophylline % w/w or reduction</i>	<i>cacao butter % w/w or reduction</i>
starting material	1,17	0,12	traces	52
no grinding	50 %	95 %	not detectable	15 %
grinding	42 %	95 %	not detectable	18 %

Results: These results may be unexpected on a first glance. One can speculate that grinding smears over the cacao butter thus preventing to some extent the diffusion of the xanthines concentrated in the solid parts of the nibs.

3.1.7 Conclusions from the screening tests

- Xanthines like theobromine and caffeine can be extracted out of (roasted) cacao nibs using carbon dioxide and a mixture of water and ethanol as entrainer. With dry CO₂ the xanthines cannot be removed.
- Caffeine can be reduced to about 10 % of its original level with solvent flow of less than 70 kg/kg starting material. The addition of ethanol as cosolvent wouldn't be necessary but accelerates the process.
- Reduction of theobromine needs water and ethanol as cosolvents and a solvent flow of at least 150 kg/kg.
- Water acts as inhibitor for the extraction of cacao butter, but some losses cannot be avoided. Without water as cosolvent, butter and xanthines are extracted simultaneously. Therefore it is preferred to inject a mixture of water and ethanol to CO₂ before it enters the extraction vessel.
- Higher extraction temperatures favour the extraction velocity thus the flow of solvent can be diminished for a fixed level. A maximal temperature of 90 °C seems to be suitable without causing deteriorations of the nibs.
- Swelling of the starting material does not improve the extraction.
- Grinding also does not improve the extraction.

3.2 Optimisation tests

The results of the screening tests are elucidating that caffeine can be removed sufficiently but the reduction of theobromine needs too much solvent (long extraction times and thus high costs). Also the losses of cacao butter are not yet satisfying.

As potential candidate for improvements the increasing of the concentration of the cosolvents in CO₂ seem to be attractive in the screening tests the concentration of ethanol was not larger than 2 % w/w with respect to CO₂). The solubility of water in CO₂ is limited but there is no miscibility gap between ethanol and CO₂ at extraction conditions. Increasing the concentration of ethanol in CO₂ thus changes drastically the ratio of water to CO₂ in the solvent. The composition of the feed must be adjusted to the solubility in CO₂ in order to prevent that remaining, not dissolved water is precipitated and wets the nibs. Additionally a vessel has been installed before the extraction vessel to trap exceeding water.

3.2.1 Influence of higher concentrations of ethanol in CO₂

extraction temperature, °C	90
relative solvent flow, kg/kg	150
entrainer	water and ethanol
composition of the entrainer and concentration in CO ₂	Variation: CO ₂ saturated with water, ethanol concentration changing
pre-treatment of the raw material	no swelling, no grinding

	<i>Theobromine</i> % w/w or reduction	<i>Caffeine</i> % w/w or reduction	<i>Theophylline</i> % w/w or reduction	<i>cacao butter</i> % w w or reduction
starting material	1,17	0,12	traces	52
concentration of ethanol in CO ₂				
5,26 %	70 %	not detectable	not detectable	17 %
6,84 %	89 %	not detectable	not detectable	19 %
9,52 %	97 %	not detectable	not detectable	25 %

Results: Increased concentrations of ethanol in CO₂ accelerate the reductions of the xanthines considerably. Caffeine is removed completely. Unfortunately the loss of cacao butter is large. Additional tests have shown that the reductions received in the test with a concentration of 6,84 % ethanol can be balanced with smaller concentrations of 5,26 % ethanol only in twice the time (or twofold the flow of solvent). Higher temperatures would even reduce the extraction time but the limit will be close to 90 °C because of possible damage of the nibs.

REFERENCES

1. EP 61 017/GB 2,095,091 (1982):Margolis,G., Pagliaro, F. A. and Chiovini, J., Societe des Produits Nestle S. A.
2. Li, S. and Hartland, S.: Influences of co-solvents on solubility and selectivity in extraction of xanthine stimulants and cacao butter from cacao beans with supercritical CO₂, 2nd International Symposium on Supercritical Fluids, Boston 1991
3. Brunner, G., Zwiefelhofer, U. and Simon, A.: Extraction of xanthines from plant material with Carbon dioxide, 2nd International symposium of High Pressure Chemical Engineering, Erlangen 1990

Solubilities and Phase Equilibria for the System Furfural - CH₃COOH - H₂O and Supercritical CO₂

T. Gamse^a; R. Marra^a; F. Fröschl^b; M. Siebenhofer^b

^a Institut für Thermische Verfahrenstechnik und Umwelttechnik, Technische Universität Graz, Inffeldgasse 25, A-8010 Graz, Austria

^b VTU - Engineering, Grottenhofstraße 3, A-8053 Graz, Austria

1. INTRODUCTION

Furfural is produced by hydrolysing pentoses of several natural products. As a by-product, furfural is also formed during decomposition of wood in paper mills. It must be separated from the aqueous effluent rapidly or secondary reactions will cause an increasing furfural loss by polymerisation or polycondensation. Distillative separation methods lead to a diminished recovery of furfural of only 35%.

Recovery of furfural and acetic acid from aqueous effluents of a paper mill has successfully been achieved on an industrial scale by a process based on the extraction of furfural and acetic acid with the solvent trioctylphosphinoxide (TOPO). Both products must be upgraded by distillation.

The recovery and purification of furfural from aqueous effluents by high-pressure extraction is of technical interest. Alternative extraction tests with supercritical carbon dioxide were carried out [1,2]. Further research [3-5] led to the conclusion that carbon dioxide is a good alternative to organic solvents with comparable and even better extraction results. For all these experiments the system furfural - water without acetic acid was used.

In the present research program the high-pressure extraction of furfural from aqueous effluents, considering the multi component system furfural - acetic acid and water, has been studied. Solubilities of furfural in supercritical CO₂ were measured at different temperatures and pressures. Further on phase equi-

librium data with consideration of the effect of acetic acid on the extractability of furfural have been investigated.

2. MATERIALS AND METHODS

2.1. Materials and Chemicals Used for Investigation

Furfural ($C_5H_4O_2$): Furfural was bought from Merck Company (Merck no. 804012). It is not stabilised and before application it must therefore be purified by distillation.

Acetic acid ($C_2H_4O_2$): 100% acetic acid from Merck Company (Merck no. 63) was used.

Potassium hydroxide solution (KOH): Acetic acid concentrations were analysed by titration with 0.1 M Titrisol[®] solution of potassium hydroxide (Merck no. 9921.0001).

Carbon dioxide (CO_2): The experiments have been performed with carbon dioxide of technical grade from Linde Company.

Water (H_2O): Deionized water, produced by a neutralising plant, has been used.

Recording Spectrophotometer: The furfural concentration has been determined with the Shimadzu recording spectrophotometer UV 160A.

Titration: Acetic acid has been analysed by titration with 0.1 M KOH with the titration processor Titralab[™] from Radiometer Copenhagen.

2.2. Experimental Evaluation of Solubility Measurement

For the solubility measurements of furfural in compressed CO_2 a high-pressure equilibrium cell with a total volume of 300 ml was used. This cell can be operated up to 400 bar at 373 K. To achieve good phase contact on one hand a magnetic stirrer is placed on the bottom of the cell and on the other hand the CO_2 -phase is withdrawn from the top of the cell and recycled at the bottom (see figure 1). In this cycling loop a 6-port HPLC valve including a 200 μ l sample loop and a pneumatic piston pump are installed. For taking samples under equilibrium conditions the volume of the sample loop is expanded into a cooling trap and dissolved in a solvent, in this case methanol. This methanol-furfural mixture was analysed by spectrophotometry and the solubilities were calculated by

the concentration of the cooling trap and the CO₂ volume of the sample loop. CO₂ data were calculated using the equation of Bender [6,7].

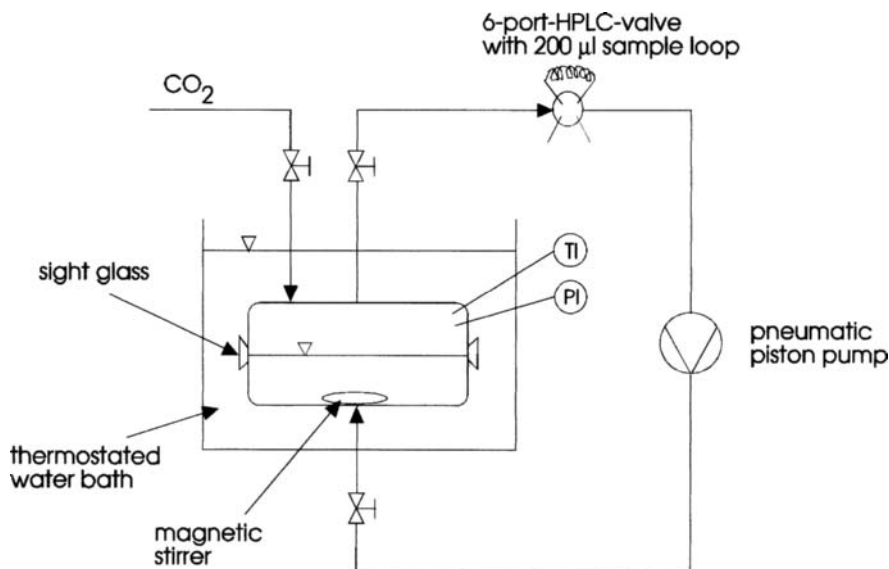


Figure 1. Scheme of high-pressure cell for solubility measurements

2.3. Experimental Evaluation of Equilibrium Data

For the determination of equilibrium data a high-pressure reactor with a total volume of 530 ml was used. This reactor can be operated at a maximum pressure of 325 bar at 473 K and is equipped with a reciprocating stirrer for better phase contact. Samples can be taken as well from the liquid phase at the bottom as from the CO₂ phase at the top of the reactor. In this work a defined volume of the liquid phase was withdrawn for analytical purpose and the amount of substances dissolved in the CO₂ phase was calculated via mass balance.

3. RESULTS AND DISCUSSION

3.1. Solubility of Furfural in Supercritical CO₂

The solubilities of furfural in supercritical CO₂ were determined in the equilibrium cell at temperatures of 298, 313 and 333 K within a pressure range of 80

to 340 bar. With the experimental results the parameters for the equation of Chrastil [8] (see equation 1) were calculated. Figure 2 shows the measured solubilities of furfural in CO₂ as well as the calculated data by the equation of Chrastil.

$$c = \rho^k \exp(a/T + b) \quad (1)$$

with concentration c [g/l], CO₂ density ρ (g/l), temperature T (K) and the calculated parameters k , a and b for furfural are:

$$k = 7.485; \quad a = 2116.29; \quad b = -52.41$$

As demonstrated by Figure 2, the solubility of furfural in CO₂ increases with increasing pressure but decreases with increasing temperature.

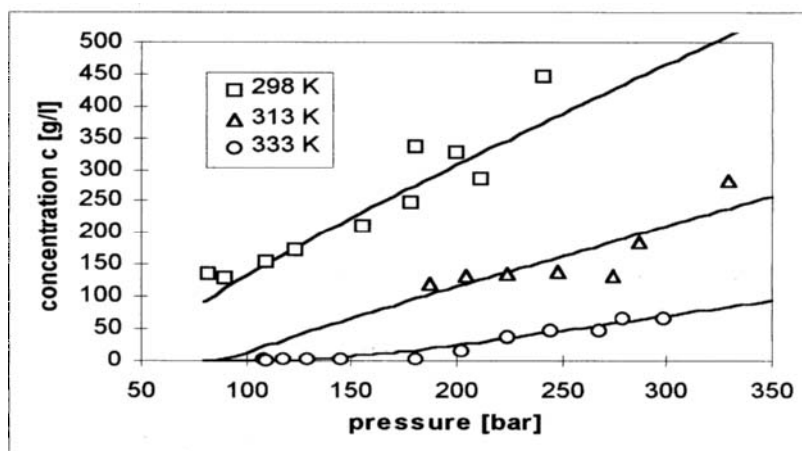


Figure 2. Experimental solubilities of furfural in supercritical CO₂ and with equation of Chrastil calculated data

3.2. Phase Equilibrium of the Quaternary System Furfural-Acetic Acid-Water-CO₂

The ternary system furfural-water-CO₂ has been studied before in different research works [1,2,9]. In this project the influence of acetic acid on the distribution of furfural was determined. According to the results of the solubility measurements temperatures were adjusted at 298 and 313 K and the equilibria were investigated at pressure levels of 90, 130 and 160 bar. Furtheron the con-

centrations of furfural (1, 2 and 4 wt%) and of acetic acid (0, 3, 5, 7 and 10 wt%) were varied.

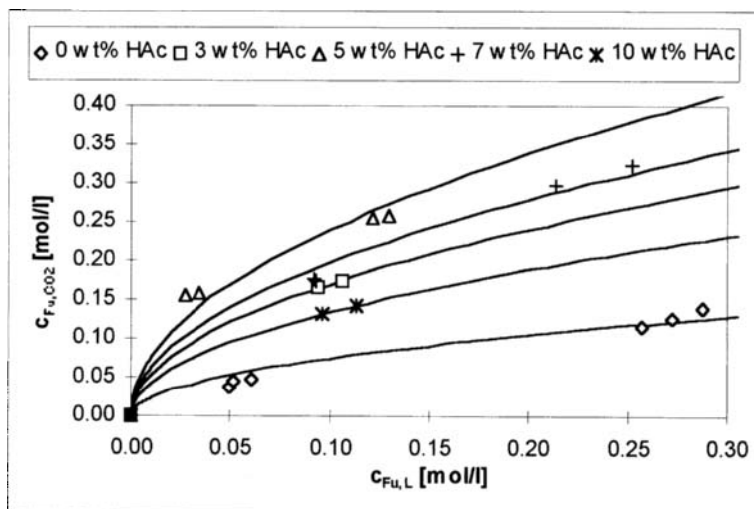


Figure 3. Influence of acetic acid on the furfural distribution at 160 bar and 298 K

The effect of acetic acid on the distribution of furfural is significant as shown in figure 3. Acetic acid has modifier properties up to a concentration of 5 wt% and enhances furfural extraction. Further increase of acetic acid concentration results in a loss of these modifier properties. This effect is present at all studied temperature and pressure levels. The distribution of furfural was calculated with equation 2.

$$c_{\text{Fu},\text{CO}_2} = n(K c_{\text{Fu},\text{L}})^n \quad (2)$$

The coefficient K in equation 2 is the distribution coefficient based on Law of Mass Action and a plot of K versus acetic acid concentration at 298 K and different pressures is given in figure 4. It is obvious that increasing pressure results in higher solubility of furfural in CO_2 and that the optimum acetic acid concentration of 5 wt% is independent from pressure.

The influence of furfural on the distribution of acetic acid is the other way round, because increasing concentrations of furfural result in decreasing solubility of acetic acid in CO_2 . Further on increasing temperature reduces as well

furfural as acetic acid solubility but acetic acid has again maximal modifier properties for furfural at 5 wt%.

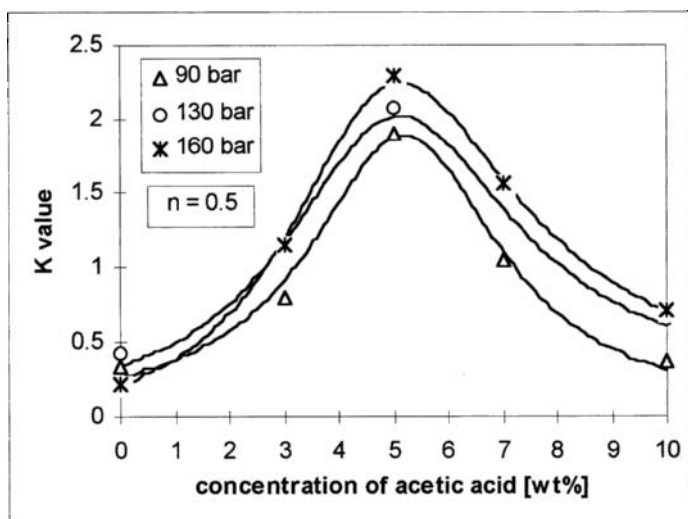


Figure 4. Modifier properties of acetic acid for furfural by K value at 298 K

REFERENCES

1. G.Bunzenberger, R.Marr, in Proc. Int. Symp. on Supercritical Fluids, Vol. 2, Nice, (1988), 613.
2. G.Bunzenberger, Zur Stofftrennung mit Kohlendioxid unter Druck in flüssig-flüssig und flüssig-fest-Systemen, Dissertation, TU Graz, (1988).
3. T. Sako, T. Sugeta, N. Nakazawa, T. Okubo, and M. Sato, J. Chem. Eng. Japan, 25 (4), (1992), 372.
4. T. Sako, T. Sugeta, N. Nakazawa, T. Okubo, and M. Sato, J. Chem. Eng. Japan, 24 (4), (1991), 449.
5. T. Sako, T. Sugeta, N. Nakazawa, T. Okubo, and M. Sato, in Proc. 3rd Int. Symp. on Supercritical Fluids, Vol. 2, Strasbourg, (1994), 25.
6. E.Bender, in Proc. 5th Symp. Thermophys. Prop., Am. Soc. Mech. Eng., New York, (1970), 227.
7. U. Sievers, Die thermodynamischen Eigenschaften von Kohlendioxid, Fortschr.-Ber.VDI-Z., Reihe 6, Nr. 155 (1984).
8. J.Chrastil, J. Phys. Chem., 86, (1982), 3016.
9. A. W. Francis, J. Phys. Chem., 58, (1954), 1099.

Supercritical Fluid Extraction of Polar Nitrogen Containing-Substances

M. Niehaus*, U. Teipel, G. Bunte, H. Krause, W. Weisweiler

Fraunhofer Institut für Chemische Technologie (ICT),
Joseph von Fraunhofer Str. 7, D-76327 Pfinztal, Germany

ABSTRACT

The solvent supercritical carbon dioxide offers unique possibilities, like non-toxicity and therefore reduction of environmental pollution or access to low-temperature processing resulting in additional process safety. Therefore knowledge to the influence of modifiers of the solubility of the polar substances is important for evaluating novel manufacturing techniques like the RESS or GAS-process. Dynamic supercritical fluid extraction of pentaerythrite-tetranitrate (PETN), nitroguanidine (NIGU) and cyclo-trimethylene-trinitramine (RDX) with pure and modified carbon dioxide indicated that all explosives except nitroguanidine were extracted though for cyclo-trimethylene-trinitramine and 3-nitro-1,2,4-triazole use of modifiers proved to be necessary. The results show the high capacity of modified supercritical carbon dioxide as a solvent in RESS and GAS processes.

1 INTRODUCTION

Supercritical carbon dioxide is a good solvent for a variety of substances. Due to low temperatures and pressures being necessary to achieve supercritical conditions, production techniques work under relatively mild conditions /1/. Another important feature of supercritical carbon dioxide is the gaslike viscosity causing favourable transport properties, so that for example supercritical fluid extractions (SFE) are achieved faster than with traditional methods. Carbon dioxide is intoxic and so incurs less costs for disposal than conventional organic solvents /2/.

Hence the use of supercritical carbon dioxide as a solvent for propellants and drugs is discussed both in analytical chemistry /3, 4/ and processing technology /5, 6/.

In contrast to conventional disposal techniques like burning, recycling of propellants prevents pollution and does not waste the high energetic content of the material /3/. Despite high investment costs, recycling of propellants might be a more economical alternative.

Production of fine, solvent free powders is of great importance in the pharmaceutical industry /5/. Conventional techniques produce particles with broad particle size distributions. Moreover, particles may be irregular or contain solvents. Hence the development of procedures such as Rapid Expansion of Supercritical Solutions (RESS) or the Gas Antisolvent Recrystallisation (GAS) is in progress /5, 6/

2 FUNDAMENTALS

Considering the phase equilibrium between liquid and gas phase, the allotment of the liquid phase rises with increasing pressure. An increase in temperature therefore displaces the allotment of the liquid phase in favour of the gas phase.

As pressure and temperature increase, the properties of the gas and liquid phase, for example density or dielectricity, get to be more and more identical. The critical point is defined as the temperature (T_c : critical temperature) and pressure (p_c : critical pressure) at which the properties of the phases become identical and so merge into a single, supercritical phase. The critical point is a specific parameter for a substance and for carbon dioxide it is at $T_c = 31.3\text{ }^\circ\text{C}$ and $p_c = 73.8\text{ bar}$ /1/.

The solvent capacity of supercritical carbon dioxide changes with the variation of density and so it can be easily modulated by the variation of pressure. Adding small amounts of co-solvents (modifiers) changes the chemical and physical properties, like the solvent capacity or the critical point. To ensure supercritical conditions it is thence crucial to know the critical parameters as a function of the modifier concentration. Table 1 lists the critical pressure and temperature as a function of the co-solvent concentration in carbon dioxide/2/.

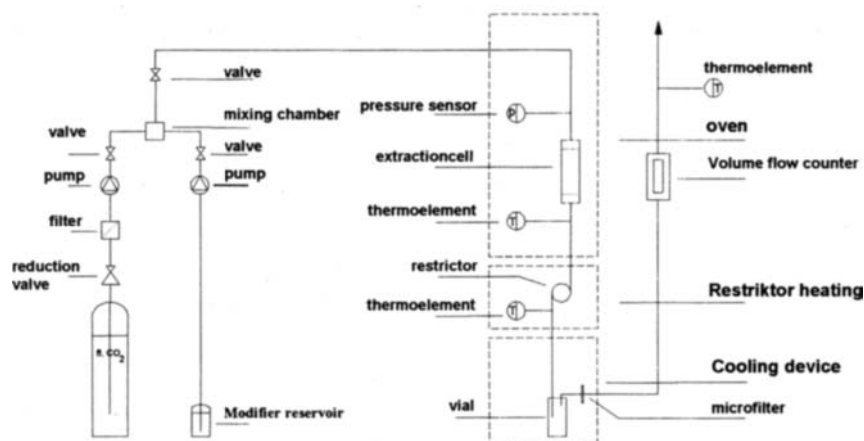
Table 1: Critical parameters of modified carbon dioxide /7/

Mol% Modifier	Aceton		Methanol		Ethanol		n-Propanol		i-Propanol		n-Butanol	
	$T_{c,in}$ $^\circ\text{C}$	$p_{c,in}$ bar	$T_{c,in}$ $^\circ\text{C}$	$p_{c,in}$ bar	$T_{c,in}$ $^\circ\text{C}$	$p_{c,in}$ bar	$T_{c,in}$ $^\circ\text{C}$	$p_{c,in}$ bar	$T_{c,in}$ $^\circ\text{C}$	$p_{c,in}$ bar	$T_{c,in}$ $^\circ\text{C}$	$p_{c,in}$ bar
1	34.7	77.9	32.7	76.5	32.7	76.6	35.5	76.8	34.5	76.2	36.5	80.3
2	36.8	79.7	34.7	78.2	35.7	78.3	39.1	80.5	37.4	79.3	42.5	87.5
4	43.7	85.7	37.7	81.7	40.5	84.3	47.2*	90.0*	43.5	85.1	56.1*	108*

*: 3.77 Mol% n-propanol. **: 3.34 Mol% n-butanol

3 EXPERIMENTAL

Picture 1 shows the device for extracting samples using supercritical carbon dioxide/modifier mixtures. Extractions were made at 300 bar, 50 °C in 30 minutes and with modifier concentrations not exceeding 4 mol%, thus ensuring supercritical conditions (tab. 1).



Picture 1: Apparatus for extracting samples using supercritical carbon dioxide/modifier mixtures.

The supercritical fluid flushes the extraction cells with a volume of 10 ml and is then expanded in the restrictors. In order to prevent the drive out of solid particles, there are frits with 5 μm pore size at the ends of the extraction cell. With fluid expansion, extracted particles precipitate and are kept in the vials which contain an organic solvent for sampling. Measured average carbon dioxide currents at the end of the extractor were 12 liters at a temperature of 28 °C and 1 bar pressure, resulting in a current of 0.81 ml/min carbon dioxide at the above-mentioned extraction conditions.

Extracts were cured with ultrasound for several minutes in order to separate remaining carbon dioxide from the washing solution and then they were quantitatively analysed with an HPLC apparatus made by Hewlett Packard, type 1048 B.

Recovery R is defined as shown in equation 1:

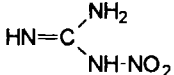
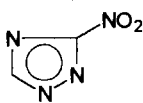

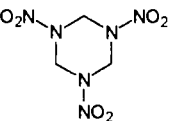
$$R = \frac{m_{\text{Extrakt, Solut}}}{m_{\text{Total, Solut}}} \cdot 100 \quad (1)$$

Table 2 lists mutual solubilities of the samples with different modifiers for comparison with the extraction results. Table 3 lists the standard melting points and standard dipol-moments of the samples.

Table 2: Properties of modifiers and mutual solubilitys with samples at 1 bar

Solvent	Dipolemoment (gasphase) in D /8/	Melting point in °C /8/	Solubility of Cyclo-trimethylene-trinitramine in g/100 g ^(23°C)	Solubility of Pentaerythrit-tetranitrate in g/100g ^(23 °C)	Solubility of 3-Nitro-1,2,4-triazole in g/100g ^(23 °C)
Acetone	2.88	56	4.021	14.922	1.331
Acetonitrile	3.92	81.6	6.811	18.664	0.403
2-Propanol	1.66	82	0.054	0.040	0.007
Methanol	1.70	65	0.48	0.500	0.387

Table 3: Properties of the samples

Sample	Nitroguanidine	3-Nitro-1,2,4-triazole	Pentaerythrit-tetranitrate	Cyclo-trimethylene-trinitramine
Structure				
Melting point in °C	246 /8/	183-186 /9/	141.3 /8/	204 /8/
Dipolemoment (Dioxan) in D	6.95 /8/	6.74 /9/	2.48 /8/	5.79 /8/

4 RESULTS

Diagram 1 shows the recovery of cyclo-trimethylene-trinitramine as a function of the modifier concentration. Without co-solvents, the recovery of cyclo-trimethylene-trinitramine is about 0.8 percent, thus indicating complete insolubility in supercritical carbon dioxide. Small amounts of cyclo-trimethylene-trinitramine recovered may be due to material driven out with a particle diameter smaller than the diameter of the frits at the end of the extraction cell.

Except for ethanol, all modifiers enhance the solvent capacity of the extraction fluid at 2 mol% and 4 mol%. Still, large enhancements only occur with carbon dioxide modified with cyclohexanon and especially with acetonitrile.

The influence of different modifiers on extraction efficiency with a concentration of 4 mol% is pointed out in diagram 2. With pure supercritical carbon dioxide, only pentaerythrit-tetranitrate is recovered. Recovery of the other samples is below 1 %, indicating no mutual solubilities with supercritical carbon dioxide. Using modifiers, recoveries of nitro-triazole and cyclo-trimethylene-trinitramine can be greatly enhanced.

For example, a mixture of 4 mol% 2-propanol with carbon dioxide extracts up to 35 percent of nitro-triazole and a mixture of 4 mol% acetonitrile extracts up to 95 percent of cyclo-trimethylene-trinitramine.

Different modifiers lead to different effects for the samples, thus indicating the specific interactions between modifier and solute.

The comparison of the results with the mutual solubilities of solute and modifier at standard conditions (table 2) and with the standard dipole moments (table 2, 3) proves, that there is no correlation and therefore suitable modifiers must be found empirically. Chemical interactions dominate strongly, so that there is no possibility to correlate the influence of dipole moments with solubility.

Results indicate the good potential for pentaerythrit-tetranitrate in establishing the RESS process for the production of fine particles. The GAS process could be more suited for particle formation of nitroguanidine, cyclo-trimethylene-trinitramine and nitro-triazole. If additional small amounts of modifiers are acceptable, then the flexible handling of both RESS - and GAS-process can be proposed for cyclo-trimethylene-trinitramine and nitro-triazole.

5 LITERATURE

- 1 McHugh M, Krukonis V., *Supercritical Fluid Extraction*, Butterworth-Heinemann, Boston, 2nd Edition, 1994
- 2 De Castro L., Valcárel M., Tena M.T., *Analytical Supercritical Fluid Extraction*, Springer Verlag, Berlin, 1st. Edition, 1994
- 3 Morris J., McNesby K., Pesce-Rodriguez R., *Extraction of Nitramine Propellants using Supercritical Fluids*, 24th Int. Annu. Conf. ICT of Energetic Materials: Insensitivity and Environmental Awareness, pp. 37-1/37-12, 1993
- 4 Jenkins T., Davidson G., Poliakoff M., *Comparison of Xe and CO₂ as Mobile Phase in On-Line SFC-FTIR: Chromatographic Considerations*, Journal of High Resolution Chromatography, Vol. 15, pp. 819-826, 1992
- 5 Tom J., Lim G., Debenedetti P., Prud'homme R., *Applications of Supercritical Fluids in the Controlled Release of Drugs*, Supercritical Fluid Engineering Science: Fundamentals and Applikations, pp. 238-257, 1993
- 6 Gallagher P., Coffey M., Krukonis V., *Gas Anti-Solvent Recrystallization of RDX: Formation of Ultra-fine Particles of a Difficult to Comminute Explosive*, The Journal of Supercritical Fluids, No.5, pp. 130-142, 1992
- 7 Gurdial G., Foster N., Tilly K., *Supercritical Fluid Engineering Science, Fundamentals and Applications*, ACS Symposium Series, No. 514, pp. 45-53, 1993
- 8 Weast R., *Handbook of Chemistry and Physics*, 49th Edition, CRC-Press, Cleveland (Ohio), 1968
- 9 Pevzner M., Fedorova E., *Heterocyclic Nitro Compounds, 4. Dipole Moments of 3(5)-Nitro-1,2,4-Triazoles*, Chem. Het. Compd. (Engl. Transl.), Vol. 7, pp. 252-254, 1971

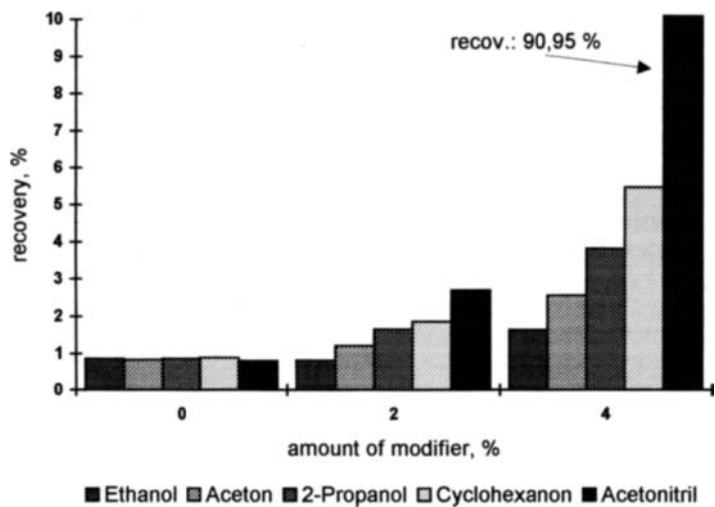


Diagram 1: Influence of modifier-concentration on recovery of cyclo-trimethylene-trinitramine

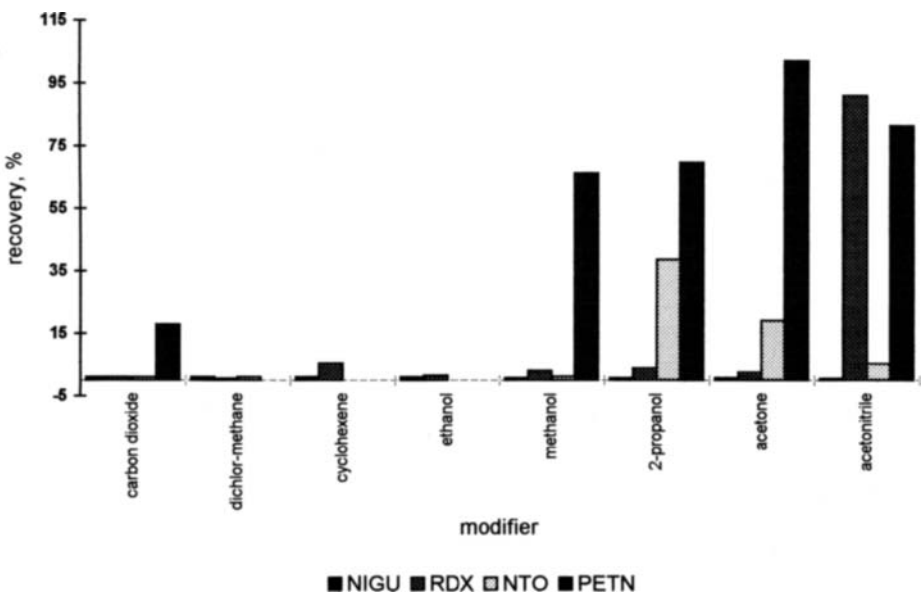


Diagram 2: Recovery of samples as a function of modifier

Solubility of solids in supercritical fluids using equations of state - excess Gibbs free energy models.

C. Verotti Filho^a and G.M.N. Costa^b

^a Petrobrás S. A., Av. Antonio Carlos Magalhães, 1029, Pituba, Salvador, Bahia, Brazil, CEP 41850-900

^b Department of Chemical Eng., Universidade Federal da Bahia, R. Aristides Novis, 2, Federação, Salvador, Bahia, Brazil, CEP 40210-630

ABSTRACT

Solubilities of several organic solids in four supercritical fluids are calculated with Soave and Peng-Robinson equations of state, incorporating excess Gibbs free energy into the mixing rules, with Heidemann-Kokal, Wong-Sandler and MHV2 procedures. Three excess Gibbs free energy models are used in the mixing rules: NRTL, UNIQUAC and UNIFAC. Furthermore, a comparison between these mixing rules and conventional two-binary-parameter form and modification of the excluded volume parameter in the MHV2 procedure is also presented. The best result were obtained with NRTL model and the Wong-Sandler mixing rule.

keywords: equation of state, supercritical fluids, mixing rules.

1. INTRODUCTION

The design and development of supercritical extraction processes depend on the ability to model and predict the solubilities of solid solutes in supercritical solvents. The prediction is usually difficult due to the large differences in sizes and molecular interactions between the solvent and solute molecules.

Cubic equations of state (EOS), which have been extensively applied in vapor-liquid equilibrium calculations, have been also used in computing the solubilities of solids in supercritical fluids by Johnston et al. (1), Haselow et al. (2). They suggested that there is a need to develop new mixing rules. The prediction for phase equilibria using the EOS- G^E models, combining excess free energy (G^E) models and EOS at zero pressure standard state has been actively studied. These mixing rules have been extensively discussed for vapor-liquid equilibria calculations. There have been only scattered attempts to apply these mixing rules to supercritical calculations (Sheng et al. (3)).

The aim of this paper is to explore the feasibility of the three mixing rules: Wong-Sandler (4), Heidemann-Kokal (5) and MHV2 (Dahl-Michelsen (6)) to the solid-fluid equilibria occurring in the binary systems composed of a organic solid and four supercritical fluids, with the calculations of solubility and density of the mixture.

2. MIXING RULES

The SRK (Soave (7)) and PR (Peng-Robinson (8)) equations of state, have been used for all mixing rules investigated. The three different mixing rules are extensively described in the references. The results are compared to those using the traditional Van der Waals mixing rules suggested by Soave (9). A modification for the mixing rules of the excluded volume parameter in the MHV2 mixing rule, have been presented. In this case a deviation of the linear combination is considered, with two additional parameters.

The different mixing rules and nomenclature used are described in table 1. The simplex algorithm modified by Nelder-Mead (10) is used to fit the model parameter to experimental solubility.

Table 1
Models used to compare mixing rules

method	mixing rule	G ^E model	EOS
M1	Wong-Sandler	NRTL	SRK
M2	Wong-Sandler	NRTL	PR
M3	MHV2	NRTL	SRK
M4	MHV2	NRTL	PR
M5	MHV2	UNIFAC	SRK
M6	MHV2	UNIFAC	PR
M7	MHV2	UNIQUAC	SRK
M8	MHV2	UNIQUAC	PR
M9	Heidemann-Kokal	NRTL	SRK
M10	Heidemann-Kokal	NRTL	PR
M11	Heidemann-Kokal	UNIFAC	SRK
M12	Heidemann-Kokal	UNIFAC	PR
M13	Heidemann-Kokal	UNIQUAC	SRK
M14	Heidemann-Kokal	UNIQUAC	PR
M15	Empirical Rules	-	SRK
M16	Empirical Rules	-	PR
M17	MHV2 [*]	NRTL	SRK
M18	MHV2 [*]	NRTL	PR

* quadratic mixing rules for the covolume-parameter

3. RESULTS

In the present study, we tested the validity of the EOS-G^E models by applying different treatments for 21 binary solid/supercritical fluid systems listed in table 2. In those systems, the supercritical component is one of the following fluids: carbon dioxide, ethane, fluoroform and chlorotrifluoromethane; and the solid component is either a nonpolar compound

(naphthalene, biphenyl or phenanthrene) or a polar compound (acridine, benzoic acid or 1,4-naphthoquinone).

Table 2
Summary of binary systems studied ^a

mixture (1) / (2)	data points	T (K)	mixture (1) / (2)	data points	T (K)
CO ₂ / Phenanthrene	5	318	C ₂ H ₆ / Acridine	6	308
CO ₂ / Benzoic acid	9	308		10	318
	12	318		9	328
	12	328	CClF ₃ / Phenanthrene	4	318
	7	343		4	328
CO ₂ / 1,4-Naphthoquinone	6	318	CClF ₃ / Naphthalene	7	308
	6	328		7	318
	6	343		7	328
CO ₂ / Acridine	6	308	CClF ₃ / Benzoic acid	6	318
	8	318		7	328
	7	328	CClF ₃ / 1,4-Naphthoquinone	6	318
	7	343		6	328
C ₂ H ₆ / Phenanthrene	6	318	CClF ₃ / acridine	5	318
	6	328		5	328
C ₂ H ₆ / Naphthalene	15	308	CHF ₃ / Phenanthrene	4	318
	12	318		4	328
	14	328	CHF ₃ / Naphthalene	6	308
C ₂ H ₆ / Biphenyl	5	308		6	318
	5	318		6	328
C ₂ H ₆ / Benzoic acid	8	308	CHF ₃ / Benzoic acid	5	318
	8	318		5	328
	7	328	CHF ₃ / 1,4-Naphthoquinone	6	318
	7	343		6	328
C ₂ H ₆ / 1,4-Naphthoquinone	7	308	CHF ₃ / Acridine	6	318
	7	318		6	328
	7	328	CHF ₃ / Anthracene	3	328
	7	343		3	343

^a Data source: Schmitt-Reid (11)

The pressure range of about 60-360 bar and temperature range from 35-70 °C are involved. Table 3 reports the results of the solubility calculations with 18 selected models. An important point must be emphasized: the Wong-Sandler mixing rule coupled with the UNIQUAC model generated a serious instability such that it was impossible to converge. Table 4 illustrates the variation of solid solubility and mixture density for a typical binary mixture.

Table 3

Average absolute deviation (percent) of solute solubility (y) and mixture density (ρ)

Model	% y	% ρ	Model	% y	% ρ
M1	7.25	11.31	M10	23.42	5.78
M2	6.74	5.50	M11	22.09	10.56
M3	26.79	10.78	M12	21.38	8.57
M4	29.55	6.28	M13	20.52	10.88
M5	26.61	11.54	M14	23.60	4.60
M6	29.07	10.59	M15	24.10	10.37
M7	16.64	11.51	M16	26.65	5.59
M8	17.28	6.55	M17	19.36	8.96
M9	21.95	10.42	M18	12.94	3.11

Table 4

CO₂/ACRIDINE - performance for solute solubility (y) and mixture density (ρ)

Model	% y	% ρ	Model	% y	% ρ
M1	4.45	14.61	M10	13.68	3.86
M2	4.26	5.10	M11	13.63	18.81
M3	11.56	14.42	M12	14.05	3.86
M4	17.62	5.07	M13	13.06	8.87
M5	13.62	10.80	M14	20.76	3.32
M6	17.78	5.07	M15	13.74	14.30
M7	10.83	8.86	M16	14.38	5.17
M8	16.15	4.06	M17	8.96	10.81
M9	13.51	14.41	M18	7.41	3.84

4. CONCLUSIONS

The following comments summarize our observations on the performance of these mixing rules:

1. The most successful method is M2, with a 6.4% mean deviation in solid solubility;
2. Regarding the solid solubility, the EOS influence is inconclusive (for some mixing rules Peng-Robinson was the best, while for others ones, Soave);
3. Soave equation gives rather deviations in mixture density with all mixing rules;
4. Wong-Sandler mixing rule is extremely sensitive to the initial parameters estimation, such that with the UNIQUAC method it was not capable to converge in most of the mixtures;
5. In order to use the UNIQUAC pure parameters in all the mixing rules, it was necessary to regress them, because its value obtained from group contribution did not perform well;

6. Attempts to use the G^E interaction parameters available in literature did not work, neither as initial estimation;
7. We use the quadratic mixing rule for the covolume parameter in the MHV2 method, instead of the original linear development. This modification largely increases the performance, as can be noticed on table 4, when we compared the prediction of M3 and M17 methods, as well as M4 and M18 methods;
8. Comparing two adjustable parameters only, the classical mixing rules (M15, M16 methods) give the same performance as more complicated rules (M9, M10, M3 and M4 methods);
9. It should be noted that as temperature increases, it does not mean a corresponding increase in the average absolute deviation solubility;
10. The results given in table 3 clearly indicate the lack of relationship between mixture density and solid solubility quality calculations;
11. To attempt phase equilibria predictions in regions where experimental results are not available, methods with no adjustable parameters for each binary system can be analyzed (M5, M6, M11 and M12). The M12 method provides better predictions.

ACKNOWLEDGMENT

The authors wish to thank Helen Ferraz and Gabriela Carvalho for their assistance in several calculations.

REFERENCES

1. K. P. Johnston; D. G. Peck; S. Kim, *Ind. Eng. Chem. Res.*, 28 (1989) 1115.
2. J. S. Haselow; S. J. Han; K. C. Chao, *ACS Symp. Ser.*, 300 (1986) 156.
3. Y. Sheng; P. Chen; Y. Chen; D. S. H. Wong, *Ind. Eng. Chem. Res.*, 31 (1992) 967.
4. D. S. H. Wong and S. I. Sandler, *AIChE Journal*, 38 (1992) 671.
5. R. A. Heidemann and S. L. Kokal, *Fluid Phase Equilibria*, 56 (1990) 17.
6. S. Dahl and M. L. Michelsen, *AIChE Journal*, 36 (1990) 1829.
7. G. Soave, *Chem. Eng. Sci.*, 27 (1972) 1197.
8. D. Y. Peng and D. B. Robinson, *Ind. Eng. Chem. Fundam.*, 15 (1976) 59.
9. G. Soave, *Chem. Eng. Sci.*, 39 (1984) 357.
10. J. A. Nelder and R. Mead, *Comp. Journal*, 7 (1965) 308.
11. W. J. Schmitt and R. C. Reid, *J. Chem. Eng. Data*, 31 (1986) 204.

This page intentionally left blank

Supercritical Fluid Extraction of Medicinal Plants

B. Simandi^a, A. Kery^c, E. Lemberkovics^c, M. Oszagyan^a, E. Ronyai^a, I. Mathe^d, J. Fekete^b,
E. Hethelyi^c

^a Department of Chemical Engineering, Technical University of Budapest, H-1521 Budapest, Hungary

^b Department of General and Analytical Chemistry, Technical University of Budapest, Hungary

^c Institute of Pharmacognosy, Semmelweis University of Medicine, Budapest, Hungary

^d Department of Pharmacognosy, Albert Szent- Györgyi Medical University, Szeged, Hungary

^e Caola Ltd., Budapest, Hungary

Different plants including spearmint (*Mentha spicata* L.), rosemary (*Rosmarinus officinalis* L.), dill (*Anethum graveolens* L.), clary sage (*Salvia sclarea* L.) and chamomile (*Matricaria chamomilla* L.) were extracted with CO₂ in a high pressure apparatus with 5 L extractor vessel volume. Fractionation of extracts was carried out by releasing the separation pressure at two stages. The extracts were separated into essential oil rich 'oil' and fatty/waxy products. The extracts were collected as separate samples successively in time. The extraction with carbon dioxide was compared to conventional steam distillation (essential oils) and to Soxhlet extraction with hexane (fatty oils).

1. INTRODUCTION

Plants and plant extracts have been used as medicine, culinary spice, dye and general cosmetic since ancient times. Plant extracts are seen as a way of meeting the demanding requirements of the modern industry. In the past two decades, much attention has been directed to the use of near critical and supercritical carbon dioxide solvent, particularly in the food pharmaceutical and perfume industries. CO₂ is an ideal solvent because it is non-toxic, non-explosive, readily available and easily removed from the extracted products. At present the major industrial-scale applications of supercritical fluid extraction (SFE) are hop extraction, decaffeination of coffee and tea, and isolation of flavours, fragrances and other components from spices, herbs and medicinal plants [1-4].

* This work was supported by OTKA (Hungarian National Science Foundation) under grant numbers T007693 and T016880.

2. EXPERIMENTAL

2.1. Materials

Commercial dried medicinal plants, leaves of spearmint and rosemary, fruits of dill, leaves and flowering tops of clary sage and flowers of chamomile were used. The CO₂ used in this work was 95-96% (w/w) pure and supplied by Messer Griesheim Hungaria.

2.2. Apparatus and extraction

The air-dried plants were ground and extracted with carbon dioxide in a high pressure apparatus equipped with 5 L volume extractor vessel. Fractionation of extracts was carried out by releasing the separation pressure at two stages. A more detailed description of the apparatus and extraction is given extensively elsewhere [5]. 1000 g of the plant material was weighed accurately and supplied into the extraction vessel. The desired temperature and pressure were adjusted and CO₂ feed was started. The accumulated product samples were removed and weighed at certain time intervals. Two or three parallel experiments were made at each extraction and separation circumstances.

2.3. Analysis

Standard methods were used for the determination of moisture, essential oil (hydro-distillation) and oleoresin (hexane Soxhlet extraction) content of the raw and residual plant materials. The moisture content and yields obtained by different extraction methods are given in Table1. Volatile oil contents of the fractionated extracts were also determined by steam distillation. The analysis of particle size distribution was performed by passing the ground plant material through sieves of various mesh size and weighing the fraction taken from each tray.

Table1

The percentage amounts of the moisture and different extracts (w/w% on the basis of dry weight) of plant materials

Plant	Moisture	Hydro-distillation	Hexane extraction	SFE products	
				1st sep.	2nd sep.
Spearmint	11.2	0.6	-	2.5	0.8
Rosemary	11.6	1.3	-	2.8	1.3
Dill	15.2	2.5	12.8	8.5	4.4
Clary sage	9.5	0.2	5.49	2.8	1.8
Chamomile	3.5	0.2	-	3.3	2.4

SFE parameters (pressure (P), temperature (T)) : extractor P =300 bar, T =40 °C; 1st separator P =76-78 bar, T =32-34 °C; 2nd separator P= 20-22 bar, T= 20-25 °C.

Thin layer chromatography (TLC) was used for quick comparison of the various samples (Silicagel-GF₂₅₄, toluene-ethylacetate (93:7), hexane-ethylacetate (95:5), dichloromethane-ethylacetate-acetone (95:3:2), chloroform-methanol (90:10), UV (365 nm) and normal light detection after derivatization).

The volatile compound identification was carried out by injecting 2 µl of diluted extract (200 µl oil + 1500 µl hexane) into a Hewlett - Packard Gas Chromatograph- Mass Spectrometer (GC-MS) equipped with a HP-1 capillary column. Injector temperature was maintained at 250 °C. Column temperature was kept at 100 °C for 4 min and programmed from 100 °C to 250 °C at 7 °C/min. N₂ at the flow rate of 0.543 ml/min was used as a carrier

gas. For the qualitative and quantitative analysis of essential oil rich products, we used gas chromatography (Jeol JGC 1100, FID-detector, packed column coated by 3 % OV-17 on Gas chrom Q of 100-120 mesh) and Shimadzu 14 GC 30m*0.25 mm capillary column, stationary phase OV 54, $d_f=0.26\mu\text{m}$.

3. RESULTS AND DISCUSSION

Major components and compositions of CO_2 extracted and distilled spearmint oils are shown in Table 2. A comparison of composition of the produced spearmint oils with the composition of other mint oils (published in the literature [6]) shows that a very special population was investigated. In particular, carvone and its related compounds and pulegone have been found as main components. Gas chromatographic analysis showed significant differences in composition of the SFE products and the distilled oil. The distilled essential oil contained more dihydrocarvone and less pulegone than the CO_2 extracted counterpart.

Table 2

Comparative chemical composition of *Mentha spicata* oil obtained by SFE and steam distillation (% of peak area)

Compound	SFE samples				Hydro-distillation
	1	2	3	average	
α -Pinene + β -Pinene	2.6	tr	tr	1.4	0.9
Limonene	6.5	2.2	tr	4.1	4.7
Dihydrocarvone	3.4	2.9	1.9	3.0	9.5
Carvone	31.5	33.5	28.6	31.7	33.9
Pulegone	34.9	43.8	50.3	40.1	31.9

tr = trace < 0.2 %

The compositions of distilled and SFE extracted rosemary oils are compared in Table 3.

Table 3

Comparative chemical percentage composition (w/w%) of rosemary (*Rosmarinus officinalis* L.) oil produced by SFE and Hydrodistillation (Run5)

Compound	Hydrodistillation	SFE
α -Pinene	15.8	13.4
Camphene	3.7	2.7
p-Cimene	1.3	1.3
Limonene	4.3	5.0
Cineol	16.8	17.3
Linalool	1.9	1.5
Champhor	11.4	14.5
Borneol	7.7	8.2
Terpine-4-ol	0.9	1.0
α -Terpineol	2.2	2.2
Verbenon	11.0	15.0
Fencol	1.7	1.0
Caryophyllene	1.8	2.6

Examinations of the volatile constituents of the rosemary oils resulted in the conclusion that distilled and SFE product contain the same components. Although the concentrations are different in the products somewhat higher levels of more volatile components (pinene, camphene) were found in the distilled oil. While the concentrations of camphor and verbenon were higher in SFE product.

The rosemary extracts were collected as separate samples successively in time. Each of them was analysed separately and the results are listed in Table 4. The concentrations of α -pinene, champhene, p-cimene and limonene decreased with extraction time, while that of the oxygenated derivatives (cineol, linalool, camphor, borneol and verbenon) increased significantly.

Table 4

Major components and percentage composition (w/w%) of rosemary oil subsequent samples (Run 6)

Compound	SFE				
	6/1	6/2	6/3	6/4	6/5
α -Pinene	15.1	14.9	15.1	4.5	1.3
Champhene	3.1	2.9	2.7	0.9	0.3
p-Cimene	1.5	1.5	1.3	0.7	0.1
Limonene	5.9	5.3	4.9	2.3	0.5
Cineol	17.4	16.7	18.4	16.3	16.9
Linalool	1.7	1.1	1.6	1.7	2.1
Champhor	14.3	13.4	14.1	16.8	19.7
Borneol	7.5	8.2	7.6	10.0	10.9
Terpinene-4-ol	1.0	1.3	1.2	-	-
α -Terpineol	2.0	2.3	2.3	2.8	2.6
Verbenon	13.8	13.5	15.26	20.0	23.9
Fencol	1.2	0.9	0.7	0.9	0.8
Caryophyllene	2.7	2.7	2.7	2.4	1.4

Table 5 gives the percentage of the major components of dill 'oil' obtained as subsequent samples by SFE and composition of the distilled oil.

Table 5

Comparative chemical composition of dill oil (% of peak area, Run3)

Compound	SFE					Hydrodistillation
	3/1	3/2	3/3	3/4	average	
α -Pinene	tr	tr	tr	tr	tr	3.4
α -Phellandrene	tr	tr	tr	tr	tr	0.2
Limonene	56.6	24.6	12.1	9.1	42.6	55.7
trans-Dihydrocarvone	0.6	2.5	2.1	8.2	1.9	1.2
cis-Dihydrocarvone	2.8	6.0	4.1	10.3	4.2	3.5
D-Carvone	39.3	66.9	79.6	69.2	50.2	36.5

tr = trace < 0.2 %

Examinations of the volatile constituents of the different 'oils' (See Tables 2, 4 and 5) resulted in the conclusion that the concentrations of the terpene hydrocarbons (pinene, limonene) decreased with extraction time, while that of the oxygenated derivatives (champhor, verbenon, carvone) increased significantly. Thus the extraction was initially rapid for the less polar terpene hydrocarbons.

Table 6

Comparative chemical composition of the volatile oils of different plants obtained by hydrodistillation and SFE

Plant	Compound	Hydrodistillation %	SFE products %
Lavandin [7] (<i>Lavandula intermedia</i> Em.)	Linalool	46.0	31.0
	α -Terpineol	3.6	-
	Linalyl acetate	20.4	37.5
	Geranyl acetate	4.3	7.2
Clary sage (<i>Salvia sclarea</i> L.)	Linalyl acetate	15.9	23.6
	Linalool	25.0	3.9
	α -Pinene	0.8	5.19
Thyme [8] (<i>Thymus vulgaris</i> L.)	p-Cimene	7.2	14.3
	γ -Terpinene	5.2	24.9
	Thymol	62.5	13.3
	Carvacrol	16.3	33.3
Chamomile (<i>Matricaria chamomilla</i> L.)	Farnesene	20.1	7.8
	α -Bisabolol	25.5	6.4
	En-in-dicycloethers	11.7	30.3
	Herniarin	1.7	10.0
	Chamazulene	6.6	-
	Matricin	-	*
Coriander [5] (<i>Coriandrum sativum</i> L.)	Pinene	15.3	7.7
	Linalool	68.5	75.5
Celery [5] (<i>Apium graveolens</i> L.)	Limonene	50.5	33.4
	3-Butylphthalide	23.6	40.6
Parsley [5] (<i>Petroselinum crispum</i> Mill.)	α -Pinene	24.0	1.5
	β -Pinene	21.9	3.0
	Myristicin	7.4	4.0
	Apiole	38.5	84.9

* matricin was identified by TLC

Alteration of essential oil components during distillation can be recognised by comparing the oils obtained by steam distillation and SFE (See Table 6). The hydrolysis of esters (e.g. linalyl acetate) to the corresponding alcohols was observed in lavandin and clary sage oils. The hydrolysis of thymol bound in glycosides resulted different thymol concentrations in thyme oils, which was proved by appropriate treatments (acidic and enzymatic) of the previously CO₂ extracted plant material. In the distillation of the oil of chamomile flowers the blue chamazulene, an artefact was produced from the colourless matricin, while chamazulene was missing in the SFE extract. Numerous changes in the composition of distilled oils, like formation of α -terpineol, terpinen-4-ol in the lavandin oil and dihydrocarvone in the spearmint oil have no certain explanation and need further research.

The fatty/waxy products contained the lipophilic substances, including fatty oils, waxes, resins and colorants. Valuable pharmacological effects were proved for some minor constituents of these products (e.g. triterpenes, diterpenes, sterols and carotenoids). Thin layer chromatography and on-line UV-VIS spectroscopy were used for the quick identification and quantity determination of these compounds using authentic samples as standards. The SFE method proved favorable in terms of both extraction yield and speed of carotenoids. The CO₂ extracts of the lavandin, clary sage and thyme have been enriched in triterpenic compounds (α - β -amyrin, oleanic acid, ursolic acid, etc.) and phytosterols. Both free and esterified triterpenoids were present in the extracts of the different samples. Furthermore carnosol and other diterpenes were detected in the SFE extract of Lamiaceae plants. The fatty acid composition was only slightly different for extracts obtained by SFE and conventional hexane extraction.

REFERENCES

1. M. A. McHugh and V. J. Krukonis, *Supercritical Fluid Extraction Principles and Practice*, Butterworths, Boston, 1986.
2. E. Stahl, K.-W. Quirin and D. Gerard, *Verdichtete Gase Zur Extraktion und Raffination*, Akademie-Verlag, Berlin, 1987.
3. M. Perrut, 2^{ème} Colloque sur les Fluides Supercritiques, INPL, Paris, p. 11, 1991.
4. G. Brunner, *Gas Extraction: an Introduction to Fundamentals of Supercritical Fluids and the Application to Separation Processes*, Steinkopff, Darmstadt, 1994.
5. B. Simandi, J. Sawinsky, A. Deak, S. Kemeny, J. Fekete, A. Kery, M. Then and E. Lemberkovics, in D. H. Logsdail and M. J. Slater (eds.), *Solvent Extraction in the Process Industries*, SCI-Elsevier, London, p. 676, 1993.
6. M. Wichtl (ed.), *Teedrogen*, Wissenschaftliche Verlagsgesellschaft mbH, Stuttgart, p. 283., 1989.
7. B. Simandi, A. Kery, E. Lemberkovics, M. Oszagyan and E. Hethelyi, *Planta Med.*, 59 (1993) Supplements A626.
8. M. Oszagyan, B. Simandi, J. Sawinsky, A. Kery, E. Lemberkovics and J. Fekete, *Flavour Fragr. J.* 11 (1996) (accepted)

Kinetics of Extraction of Macroporous Solid Bodies with a Dense Gas

F. Stüber, M.A. Larrayoz and F. Recasens

Departament d'Enginyeria Quimica, ETSEIB, Universitat Politècnica de Catalunya. Diagonal, 647, E-08028 Barcelona

ABSTRACT

The extraction of toluene and 1,2 dichlorobenzene from shallow packed beds of porous particles was studied both experimentally and theoretically at various operating conditions. Mathematical extraction models, based on the shrinking core concept, were developed for three different particle geometries. These models contain three adjustable parameters: an effective diffusivity, a volumetric fluid-to-particle mass transfer coefficient, and an equilibrium solubility or partition coefficient. K as well as K_G were first determined from initial extraction rates. Then, by fitting experimental extraction data, values of the effective diffusivity were obtained. Model predictions compare well with experimental data and the respective value of the tortuosity factor around 2.5 is in excellent agreement with related literature data.

1. INTRODUCTION

Modelling the extraction of porous solids is of increasing interest for scale-up calculations in various applications of supercritical fluid technology. Among them are the extraction of spices, the degreasing of metallic parts, the cleanup of contaminated soils, etc. So far seeds have been mostly considered as porous bodies when mathematical modelling has been attempted [1-2]. According to the studies of various authors[3-6], the shrinking core concept is very useful for predicting extraction time of a packed bed of seeds.

In this work extraction models are developed for three different particle geometries using the shrinking core concept. Model calculations will be compared and fitted to extraction data of toluene and 1,2 dichlorobenzene (DCB) from shallow packed beds in order to obtain values of the effective diffusivity (D_e) and the tortuosity factor.

2. EXPERIMENTAL SECTION

Sintered metallic particles (pellets) were first impregnated with toluene and DCB and then extracted from shallow (differential) fixed bed using SC CO₂. Complete curves of weight fractions extracted vs time were determined as a function of the following operating variables: pressure, temperature, fluid flow rate, flow direction of fluid and particle size. The experimental setup and procedures are described in detail elsewhere [7] and will not be discussed here. The specifications of the fixed beds and particles used as well as the range of operating variables studied were: temperature ranged from 310-360 K, pressures from 8 to 20 MPa, and fluid velocities from 0.6 to $6.7 \cdot 10^{-4}$ m/s (at column conditions). Solutes used were either toluene or DCB impregnated on small or large cylinders, porous in nature. The equivalent sphere diameters were 1 and 2 cm, respectively. During flow of fluid across the pellet packing the values of dimensionless numbers were $Re = 8-90$, $Gr = 0.35-20 \cdot 10^8$ and $Sc = 1.5-10$. Further details on the experiments are given in [7].

3. EXTRACTION MODELS

The present models describe the extraction of porous particles completely filled with a liquid solute. The dissolution of liquid is followed by intraparticle diffusion up to the particle surface and then by external diffusion through a solvent boundary layer into the flowing solvent bulk. Three different particle geometries were modeled: spheres, cylinders with ends mechanically sealed and cylinders with open ends available for extraction.

Frequently, the concept of the shrinking core is applied to quantify the dynamic dissolution rate of the liquid core in the particles [3-6]. When the solute concentration is much higher than the solubility of the solute in the solvent as in our case, a sharp liquid-solvent boundary is likely to exist and the liquid core shrinks regularly with the progress of the extraction.

In order to derive fundamental equations of the extraction process, the following assumptions have been made:

- P , T , V_{SCF} and ϵ_B are constant (K , D_e and K_G are isotropic)
- The external interfacial area is taken to be that of the pore mouths, as we assume that external mass transfer only takes place through the liquid-solvent surface of the pore mouths.
- The change of fluid concentration in the pores with time is taken to be negligible with respect to the change with radial position (pore diffusion is considered to be pseudo stationary $\frac{\partial C_i}{\partial t} \approx 0$).
- For cylinders with open ends, superposition of the two extreme cases of extraction either through the ends (as in a flat plate) or in radial direction was postulated to be valid.

The resulting fundamental expressions are given for the case of cylindrical geometry with sealed ends for an integral packed bed without axial dispersion:

1) Mass balance in the bulk fluid phase

$$\frac{\partial C_G}{\partial t} + \frac{u \partial C_G}{\partial z} = \frac{2}{R} \epsilon_p \left(\frac{1 - \epsilon_B}{\epsilon_B} \right) (C_R - C_G) \quad (1)$$

2) External mass transfer

$$\left(-\frac{\partial N}{\partial t} \right) = 2\pi \epsilon_p R L K_G (C_R - C_G) \quad (2)$$

3) Pore Diffusion

$$\frac{D_e}{r} \frac{\partial}{\partial r} \left(r \frac{\partial C_i}{\partial r} \right) = 0 \quad (3)$$

4) Mass transfer rate in the pores

$$\left(-\frac{\partial N}{\partial t} \right) = 2\pi r_C L D_e \left(-\frac{\partial C_i}{\partial r} \right)_{r_C} \quad (4)$$

5) Dissolution of liquid core

$$\left(-\frac{\partial N}{\partial t}\right) = 2\pi\rho_L \varepsilon_p r_C L \left(-\frac{\partial r_C}{\partial t}\right)_{r_C} \quad (5)$$

6) Extracted mass fraction

$$X = 1 - \frac{N}{N_0} = 1 - \left(\frac{r_C}{R}\right)^2 \quad (6)$$

7) Initial and boundary conditions

$$r = R \quad C_i = C_R \quad (7)$$

$$r = r_C \quad C_i = C_G^* \quad (8)$$

$$t = 0 \quad C_G = 0 \quad (9)$$

$$r = R$$

Using equations (4) through (9), the unknown concentration C_R can be eliminated and a system of linked differential equations for the fluid concentration C_G and the core radius r_C is obtained.

8) Resulting equation system for cylinders with open ends

Concentration in the fluid phase

$$\frac{\partial C_G}{\partial t} = \frac{2}{R} \varepsilon_p \frac{1 - \varepsilon_B}{\varepsilon_B} \frac{K_G D_e}{\varepsilon_p \ln\left(\frac{r_C}{R}\right) R K_G - D_e} (C_G^* - C_G) - \frac{u \partial C_G}{\partial z} \quad (10)$$

Radius of liquid core

$$\frac{\partial r_C}{\partial t} = \frac{K}{C_G^*} \frac{1}{r_C} \frac{R K_G D_e}{\varepsilon_p \ln\left(\frac{r_C}{R}\right) R K_G - D_e} (C_G^* - C_G) \quad (11)$$

Numerical solution of equations was performed for a differential bed model using the IMSL integration subroutine DIVPAG (method of Gear).

4. EVALUATION OF MODEL PARAMETERS

The system of differential equations describing the extraction of porous particles with SC CO₂ contain 3 adjustable parameters: external mass transfer coefficient (K_G), a solute solubility (K) and an effective diffusivity of solute in the pores. In order to avoid simultaneous fitting of these parameters that may result in non significant values, the following strategy was adopted to reduce the number of adjustable parameters.

4.1 Solubilities in SC CO₂

Solubility of toluene in SC CO₂ can be found in the literature [8]. In a previous study in our laboratory, the solubility of DCB in SC CO₂ was measured by [9] and was thus available. Figure 1 gives the solubilities (mol fraction) of DCB in SC CO₂ vs pressure calculated for 3 temperatures using the Peng-Robinson EOS with an interaction parameter $k_{12} = 0.1175$

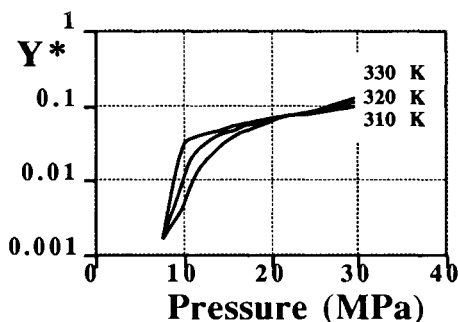


Figure 1 Estimated solubilities of DCB in SC CO₂

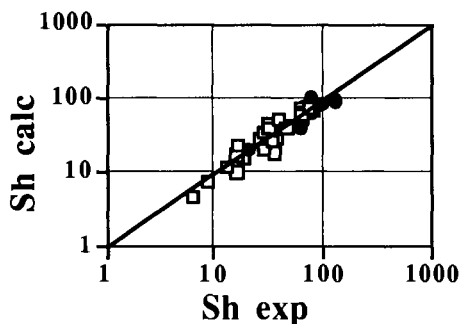


Figure 2 Comparison of predicted vs experimental mass transfer data using the correlation.

4.2 External mass transfer coefficient

Solution of the shrinking core model at zero time ($t=0$) depends only on two parameters: the solubility of solute in SC CO₂ and the external particle to fluid mass transfer coefficient K_G . Hence, knowing the solubility, measurements of the initial extraction rates allow to determine the values of K_G . Detailed discussion on the evaluated mass transfer coefficients are given in [7]. These authors found that the overall mass transfer from particles to fluid depends upon both free and forced convection mechanism. Figure 2 illustrates a parity plot of the experimental values of Sh number (evaluated by zero-time solution of the shrinking core model) and the calculated Sh number (using an appropriate mass transfer correlation).

4.3 Intraparticle diffusivity

With the available values of solubility and external mass transfer coefficient, we proceeded to evaluate intraparticle diffusivities by fitting experimental extraction data.

Table 1

Predicted time for 50% extraction of DCB at $T = 313$ K, $P = 20$ MPa (small pellets with extractor operated in downflow mode)

Parameters	Bi = 2.5	Bi = 25	Bi = 250
De	160 s (10^{-8} m ² /s)	610 s (10^{-9} m ² /s)	3600 (10^{-10} m ² /s)
K_G	600 s ($5.5 \cdot 10^{-4}$ m/s)	670 s ($5.5 \cdot 10^{-5}$ m/s)	1300 s ($5.5 \cdot 10^{-6}$ m/s)
K		180 s (1.0)	
		600 s (0.3)	
		1600 s (0.1)	

It can be anticipated that prediction of diffusivities should be best with larger particles since the diffusion path is physically longer. A few simulation runs with different values of diffusivity, solubility and external mass transfer coefficient, show that the most sensitive parameter (or resistance) are intraparticle diffusivity and solubility while the effect of external mass transfer coefficient is small.

Table 1 gives a summary of calculated times for 50% extraction of solute ($t_{50\%}$). Simulations conditions are $P = 20$ MPa, $T = 313$ K and $Re = 40$ for the system DCB/small cylinders and downflow operation. From Table 1, it is seen that for a constant value of K_G , a decrease of De and K lead to a significant increase of $t_{50\%}$ irrespective of the Biot number. On the other hand, the influence of K_G is found to be significant only in the higher range of Biot number ($Bi = 250$) where the external mass transfer gradient may become limiting (K_G is very small).

5. RESULTS AND DISCUSSION

Applying the above mentioned strategy, intraparticle diffusivities were evaluated as a function of pressure, temperature and fluid flow rate for two different sizes of particle.

Within the limits of experimental error, the effective diffusivity increases with temperature and decreases with pressure as it is observed for molecular diffusivity. In general, the tortuosity factor was found to be constant at different flow rates and for different particle sizes. Figure 3 illustrates a comparison of predicted and experimental extraction curves for both small particles ($d_p = 1$ cm, $\epsilon_p = 0.20$) and large particles ($d_p = 2$ cm, $\epsilon_p = 0.25$) at $T = 313$ K, $P = 20$ MPa, $Re = 40$ using DCB as solute and the extractor in downflow operation.

The effective diffusivities of DCB in SC CO₂ for these runs are optimized to $De = 4 \cdot 10^{-9}$ m²/s. The corresponding tortuosity factors amount to $D_M/De = 2.3$ and 2.5 when estimating the molecular diffusivity by means of the correlation of [10]. These values are in reasonable agreement with respect to those found in the literature. For example in a related study of diffusion of naphthalene in a porous sintered rod of bronze ($d_p = 1$ cm, $L = 15$ cm, $\epsilon_p = 0.30$), [11] obtained very similar tortuosity factors in the range of 1.35 (at 328 K) to 1.74 (at 308 K) for average pore sizes between 8 and 20 μ m.

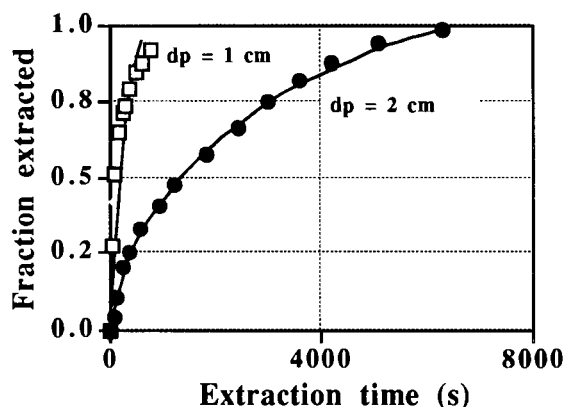


Figure 3 Comparison of predicted and experimental extraction curves for both small and large particles using DCB as a solute and downflow operation : $P = 20$ MPa, $T = 313$ K, $Re = 40$

6. NOMENCLATURE

Bi	Biot number for mass, $Bi = \frac{K_G R}{D_e}$
C_G	Solute concentration in the fluid phase, kmol/m ³
C_G^*	Saturation concentration of solute at equilibrium, kmol/m ³
C_i	Solute concentration in the particle pores, kmol/m ³
C_R	Solute concentration at the particle surface, kmol/m ³
D_e	Effective diffusivity, m ² /s
K	Molar partition coefficient, $K = \frac{C_G^*}{C_L} = \frac{\rho_G^*}{\rho_L}$
K_G	Volumetric fluid-to-solid mass transfer coefficient, m/s
L	Length of cylinders, m
N	Number of mols of solute, kmol
N_0	Initial number of mols of solute, kmol
P	Pressure, MPa
r_c	Core radius, m
r	Radius, m
R	Radius of cylinder, m
T	Temperature, K
t	Time, s
V_{SCF}	Fluid velocity at supercritical conditions, m/s
X	Extracted weight fraction
ϵ_B	Bed void fraction
ϵ_p	Particle porosity
ρ_G^*	Density of solute/CO ₂ mixture at saturation, kmol/m ³
ρ_L	Density of solute kmol/m ³

7. REFERENCES

1. G. Brunner, Phys. Chem., 88 (1984) 88.
2. M. Goto, B. C. Roy, Y. Nomura, T. Hirose, Proceed. 3rd. Int. Symp.Supercrit. Fluids, 2 (1994) 16.
3. MC. Jones, CRC Press, Boca Ratón, Fl, USA, (1991).
4. M.B. King, T.R. Bott, M.J. Barr, R.I. Mahmud and N. Sanders, Sep. Sci. Tech., 22 (1987) 1103.
5. O. J. Catchpole, E.W. Andrews, G. N. Toikka and G.T. Wilkinson. Proceed. 3rd. Int. Symp.Supercrit. Fluids, 2 (1994) 47.
6. B.C. Roy, M. Goto, T. Hirose, Ind. Eng. Chem. Res., 35 (1996) 607.
7. F. Stüber, A. Vázquez, M.A. Larrayoz, F. Recasens, Ind. Eng. Chem. Res. (submitted 1996).
8. S. D. Fink, H. S. Herskey, Ind. Eng.Chem. Res., 29 (1990) 295.
9. J. Puiggené, M.A. Larrayoz, F. Recasens, Chem. Eng. Sci. (submitted 1995).
10. O. J. Catchpole, M.B. King, Ind. Eng. Chem. Res., 33, (1994) 1828
11. G. Knaff, E.U. Schlünder, Chem. Eng. Process., 21 (1987) 193.

AKNOWLEDGMENTS

Financial support from the Spanish CICYT (Plan Nacional I+D, Project number AMB95-0042-CO2-02) and CIRIT (SGR95 grant), is thankfully acknowledged.

Solids Formation by Rapid Expansion of Supercritical Solutions

P. Gerber, U. Teipel, H. Krause

Fraunhofer - Institut für Chemische Technologie (ICT), P.O. Box 1240,
76318 Pfinztal, Germany

A pilot plant is presented, which has been built to prepare fine particles ($< 4 \mu\text{m}$) by the Rapid Expansion of Supercritical Solutions (RESS - process). In this study carbon dioxide loaded with anthracene was used. By varying process parameters, the particle size distribution can be influenced. Changes of the post-expansion pressure have no provable influence on the particle size distribution.

1. INTRODUCTION

When a solution is rapidly depressurized, the dissolved solid becomes insoluble in the low pressure gas. The rapid expansion of supercritical solution (RESS) exploits this phenomena. During the process, a loaded supercritical fluid is expanded through a nozzle creating high supersaturation in the jet. Fast nucleation and growth of the crystalline particle occurs. If carbon dioxide is used as a supercritical fluid the RESS process offers advantages over conventional size reduction methods. Heat sensitive and solvent free products can be achieved with this process. This technology may find application in the production of certain drugs and energetic materials.

The rapid expansion of supercritical solutions (RESS) was explored by several authors as a novel route to the formation of microparticles. Ohgaki [1] produces fine stigmaterin particles by the rapid expansion of a supercritical CO_2 solution. Amorphous fine particle and whisker-like crystals ($0,05 - 3 \mu\text{m}$) were obtained with different pre-expansion pressures. Johnston [2] obtained submicron particles from different polymers. Loth [3] described the micronisation of phenacetin with supercritical fluids.

The influence of the parameters concentration, pre- and post-expansion pressure and pre- and post-expansion temperature and geometry of the nozzle on the particle size distribution wasn't studied at all. Merely Mohamed [4] examined the influence of concentration, pre- and post-expansion pressure and temperature of the system carbon dioxide - naphthalene. No particle size distribution was measured, only the size of the smallest and biggest particles were measured. For these investigations, anthracene was used as a model substance, while the solubility of anthracene in carbon dioxide [5] is approximately more then 100 times smaler than for naphthalene.

2. EXPERIMENTAL

With the pilot plant which was built in cooperation with SITEC AG (Switzerland) it is possible to carry out extractions up to 80°C and 300 bar. The maximum massflow of carbon dioxide is limited to 20 kg CO₂/h. Figure 1 shows the diagrammatic view of the pilot plant.

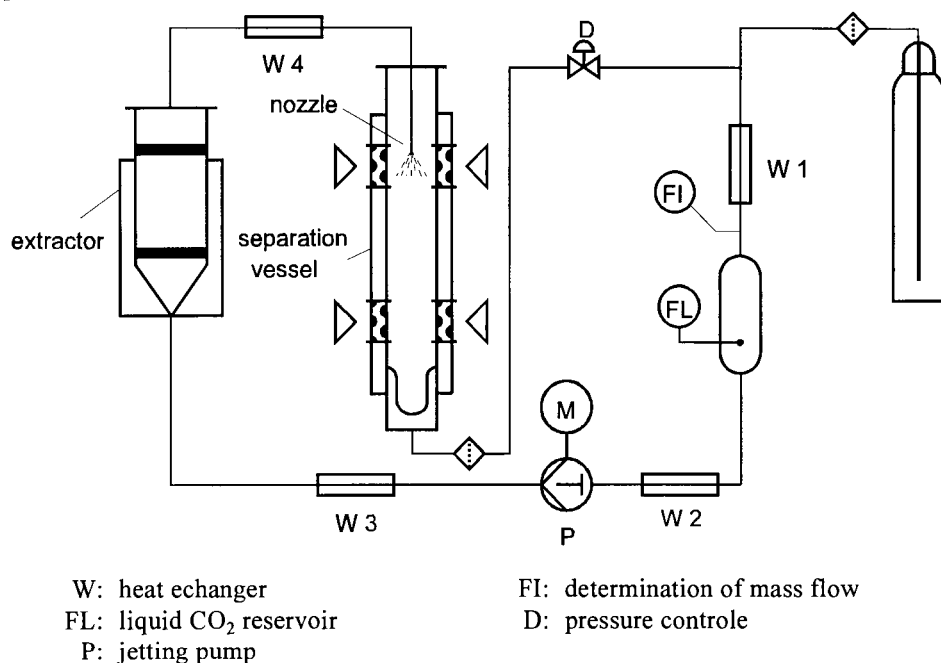


Figure 1. diagrammatic view of the experimental apparatus

Liquid carbon dioxide (purity 99,95 Vol %) was undercooled (W2) to avoid cavitation in the membran pump (P). After the compression to pre-expansion pressure, the fluid is heated to the extraction temperature (W3). The supercritical fluid loaded with anthracene leaves the extractor ($V = 0,6$ l). With a additional heat exchanger (W4), the solution is heated to pre-expansion temperature. In the separation vessel, the supercritical solution is expanded through a nozzle. The expanded gas will be condensed (W1) and recompressed or let off. After the experiment, the separation vessel is opened and the particles were collected. The particle size is measured by laser diffraction spectroscopy (Malvern Master Sizer X).

3. RESULTS AND DISCUSSION

A typical particle size distribution for anthracene, which is recived by the RESS - process, is shown in figure 2. The particle size distribution varied from $x_{10,3} = 0,6$ μm til $x_{90,3} = 3,5$ μm , the mean particle size was measured to 1,5 μm .

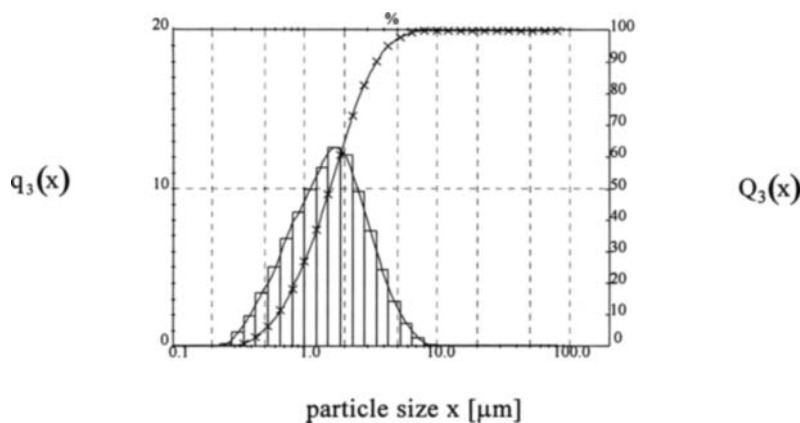


Figure 2. volume sum distribution $Q_3(x)$ and volume density distribution $q_3(x)$

To determine the influence of the internal nozzle diameter on the particle size distribution in dependence on the post-expansions pressure at constant pre-expansion temperature $T = 110^\circ\text{C}$ and pre-expansion pressure $p = 220\text{ bar}$, two nozzles with different internal nozzle diameter ($d = 100\text{ }\mu\text{m}$, $d = 150\text{ }\mu\text{m}$) were under investigation. As it is shown in figure 3, the particle size is smaller for the nozzle diameter $d = 150\text{ }\mu\text{m}$ and these differences were smaller as the consistency of the measuring results.

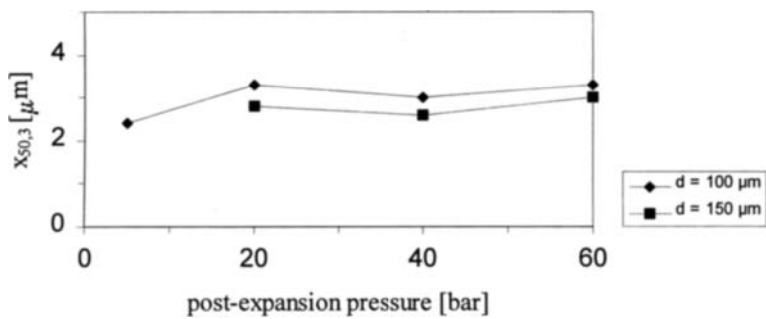


Figure 3. particle size in dependence on post-expansions pressure for two different internal nozzle diameter

At constant pre-expansion pressure, the post-expansion pressure was varied from 5 bar til 60 bar. As it is shown in figure 4 at constant pre-expansion temperature $T = 110\text{ }^\circ\text{C}$, there is no provable influence of the post-expansion pressure on the particle size distribution for these three pre-expansion pressures. It is not necessary to expand the supercritical solution til atmospherical pressure, the gas could be expanded to 60 bar and re-compressed.

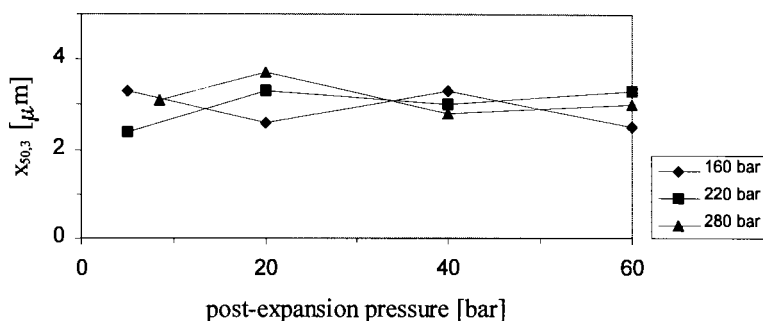


Figure 4. particle size in dependence on post-expansions pressure for three different pre-expansion pressures

4. SUMMARY

A pilot plant was built to study the influence of different process parameters on the particle size produced by RESS-process (Rapid Expansion of Supercritical Solutions). Particles smaller than 4 μm were obtained for the system carbon dioxide-anthracene.

The influence of the internal nozzle diameter ($d = 100 \mu\text{m}$, $d = 150 \mu\text{m}$) on the particle size distribution in dependence upon the post-expansions pressure was determined. The particle size is smaller for the nozzle diameter $d = 150 \mu\text{m}$, and these differences were smaller as the consistency of the measuring results. At constant pre-expansion pressure, the post-expansion pressure was varied from 5 bar til 60 bar. No provable influence of the post-expansion pressure on the particle size was studied.

REFERENCES

1. K Ohgaki, H. Kobayashi, T. Katayama, N. Hirokawa, Whisker formation from jet of supercritical fluid solution, *J. of Supercritical Fluids*, 3 (1990), 103-107
2. S. Matson, K. P. Johnston, J. R. Combes, J. M. DeSimone, Formation of Poly (1,1,2,2 -tetrahydroperfluorodecyl acrylate) submicron fibers from particles from supercritical carbon dioxide solutions, *ACS, Macromolecules* 1995, 28, 3182 - 3191
3. H. Loth, E. Hemgesberg, Properties and dissolution of drugs micronized by crystallization from supercritical gases, *International Journal of Pharmaceutics* 32, 1986, 2-3
4. R. S. Mohamed, D. S. Halverson, P. G. Debenedetti, R. K. Prud'homme, Solids formation after the expansion of supercritical mixtures, *SCS Symp. Series 406, Am. Chem. Soc.* (1989 b) 355 - 378
5. L. Rößling, Löslichkeit und Solventshift von Anthracen in zehn Flüssigkeiten und Gasen bis 300 bar und 280°C, Dissertation, Universität Karlsruhe, 1981

Solubility, extraction and modification of polymers and polymer additives in supercritical carbon dioxide

L. Merz and O. Muth

Fraunhofer-Institut Chemische Technologie, Postfach 12 40, D-76318 Pfinztal

Abstract

In this paper first results of the solubility and extraction of low molecular weight polymers and plasticizers with supercritical carbon dioxide are presented and compared to the results of phase equilibria measurements. Additionally the formation of sub-micrometer particles during polymerization of acrylic acid and derivatives thereof in scCO_2 are examined and compared with recent works [2]. Finally there are some aspects to modification of polymers by absorption of scCO_2 and reactive components solved therein.

1. EXTRACTION AND PHASE EQUILIBRIA

1.1. Extraction of low molecular weight polymers

The debinding of powder injection molding workpieces, which consist of about 60 vol.% of a solid matrix (metal or ceramic powders) and thermoplastic polymer binders, was examined by extraction with scCO_2 [1]. By this technique the debinding time could be reduced from 1-2 days for pyrolysis to 1-2 hours for SFE.

The self-designed extraction facility consists of a high pressure liquid pump, two heat exchangers, two parallel extraction tubes and a separator with a window and a throttle valve. A mass flow meter gives information about flow rate (kg/h), density, temperature and total mass of the solvent.

Extraction rates in dependance of temperature and pressure are very different and are shown in figure 1. At 50°C the extraction efficiency is very low. Between 60°C and 70°C extraction is more effective and depends little on the carbon dioxide flow rate. For a given temperature the variation of pressure has only a small influence on the extraction rate, whereas the variation of temperature at a fixed pressure leads to great differences in extraction efficiency. The parts treated at 50°C often show cracks or bubbles. At 75°C they soften and deform. The optimal temperature range for this binder system is 60-70°C. Here it is possible to extract up to 70 vol.% of the binder without damaging the workpieces. As a result of the reached porosity it is possible to reduce the time of the furthermore necessary pyrolysis of the remaining binder components drastically (heating rate 10°C/min from r.t. up to 1000°C). The dimensions of the examined parts were 4 x 5 x 60 mm.

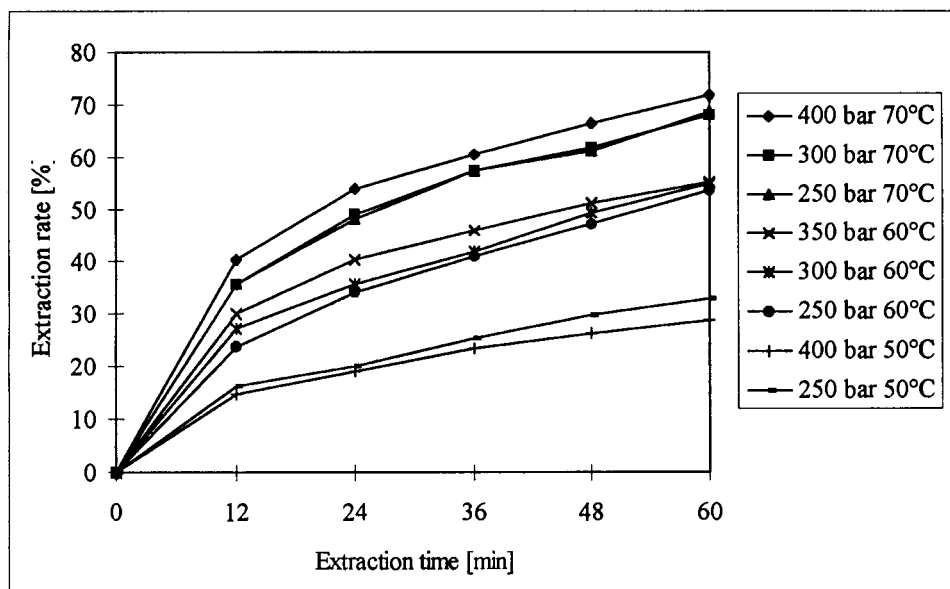


Figure 1. Extraction rate of polymer binders in dependence of pressure and temperature

1.2. Phase equilibria

The measurements were done in a phase equilibria cell by the synthetic method. The cell has an inner diameter of 25mm, an outer diameter of 80 mm, a sapphire window and a movable piston. The volume can be varied from 20 cm³ to 50 cm³. The maximum pressure is 500 bar. First the solid component is filled in and then the cell is evacuated. The liquid carbon dioxide is added from a high pressure cylinder, which can be weighed with an accuracy of 0.1 grams. Figure 2 shows the p-T-dependance of the solubility of paraffin in carbon dioxide for different weight fractions of paraffin.

Calculations of the solubility with a modified Peng-Robinson-EOS lead to remarkably lower equilibrium pressures for the given temperature ranges. The reason for this effect is, that the calculations are done for two-component systems. The paraffin used for the measurements and the production of the workpieces, however, is a mixture of homologue n-alkanes, so the calculation should be done for a multicomponent system. Up to now it was not possible to find a set of thermodynamic data, which represent this n-alkane mixture and lead to two-component-calculation results according to the measurements.

Extraction and phase equilibria measurements have shown, that in the temperature range with good extraction rates the solubility is rather poor. Nevertheless it was possible to extract 70 vol.% of the binder within one hour without damaging the parts. This is a good improvement compared to usual pyrolysis or extraction processes with organic solvents or water, which last 1-2 days for parts of the described geometry.

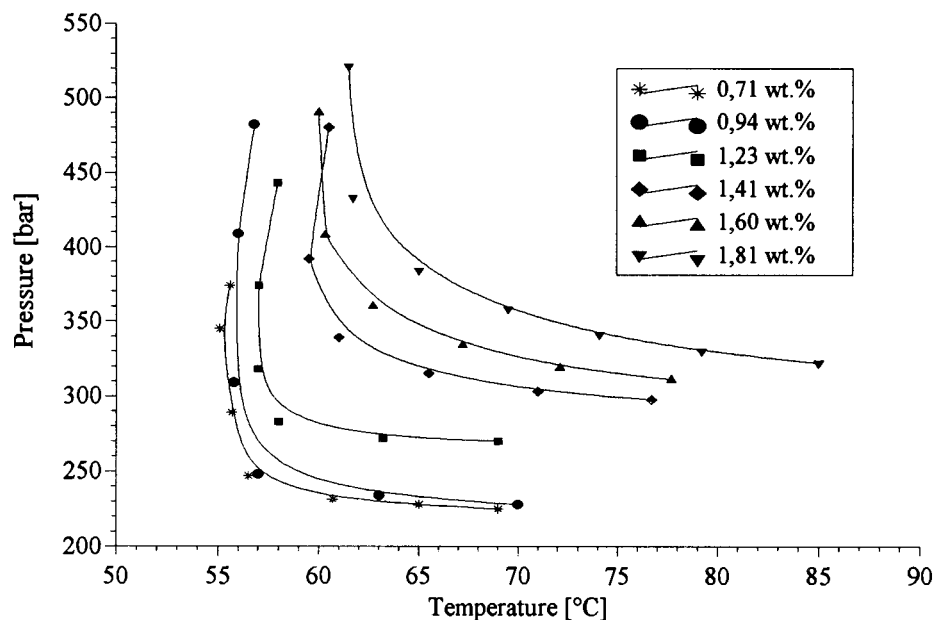


Figure 2. p-T-dependence of the solubility of paraffin in carbon dioxide for different weight fractions of paraffin

2. POLYMERIZATION AND POLYMER MODIFICATION

2.1. Polymerization of acrylic acid in supercritical carbon dioxide

As a comparison and reproduction to recent works done by DeSimone and coworkers [2], attempts were made in the free radical polymerization of acrylic acid (AA) in supercritical carbon dioxide (scCO₂) with Azobisisobutyronitrile (AIBN) as initiator.

The experiments were run in a 200 ml vessel with electrical heating and stirring by a magnetic bar. The pressure was followed by a Digibar. AA and AIBN (both from Merck) were used as received, CO₂-SFE-grade was used from Messer Griesheim. For visual experiments a stainless-steel optical cell with movable piston could be used. The reaction conditions were 65°C and 200 bar and the reaction time was about 6h.

Only a few experiments concerning this matter were run. During the course of reaction the poly-acrylic-acid (PAA) precipitated out of the homogeneous solution. After cooling and venting of the reactor a fluffy, electrostatic charged white powder could be obtained. Figure 3 shows a scanning electron microscopy-(SEM)-photograph of the supercritical fluid product in comparison to a commercially available PAA. It can be seen that at high resolution of the used SEM the commercial PAA has a shape like planets seen through a telescope while the

supercritical fluid PAA still looks cloudy, which is according to published work [2]. Aqueous GPC with polyethyleneglycol (PEG) standards lead to M_N (M_w)-values of 1107 kg/mole and 2219 kg/mole resp., which means a distribution of 2.0 (in relation to PEG-standards). DSC-analysis gave no further information.

Additional attempts in the polymerization of methyl-methacrylate (MMA) and styrene (S) with AIBN lead to a thin film on the walls of the reactor, which was caused by a low conversion rate. Copolymerization attempts of AA with MMA resp. S led to undefined waxkind products.

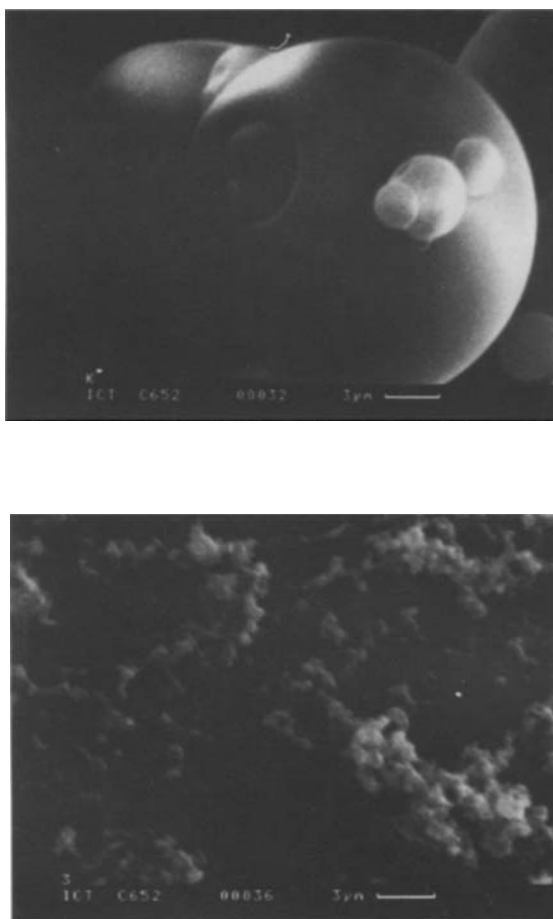


Figure 3. SEM Photographs of PAA; top: commercial product, bottom: SCF-product

2.2. Modification of polymers with supercritical carbon dioxide (scCO₂): Absorption of scCO₂ into polyvinylchloride (PVC) sheets at elevated temperatures.

Recent works show, that there is a great field of application in modification of polymers with supercritical fluids [3, 4]. However, there are only few data available which concern the interaction of scCO₂ with polymers at higher pressures and higher temperatures. The better interaction between and polymers is achieved, the more modification of the polymers can be expected. For this reason the incorporation of CO₂ into PVC-sheets was determined similar to the method described by Berens [5].

Commercially available PVC-sheets (thickness 0.5 mm, no additives) were cut into squares (2 x 2 cm), cleaned with propanol, weighed and put into a porous gasket within stainless steel vessel (volume: 30 ml). Then the cell was purged and filled with different amounts of CO₂ and heated to the desired temperature with a heating tape. After a certain „soaking time“ the cell was depressurized quickly and the sample put on a balance (resolution 0.01 mg) and the weight recorded for a period of 30 min. The weight loss was plotted against the square-root of time. Because of Fickian diffusion this plot should be linear and so its possible to extrapolate the mass of absorbed CO₂ to the time of venting the vessel.

Figure 4 shows a plot of the absorption kinetics at 60°C and 200 bar. A saturation of the PVC-sheets is reached between 2 and 3 hours.

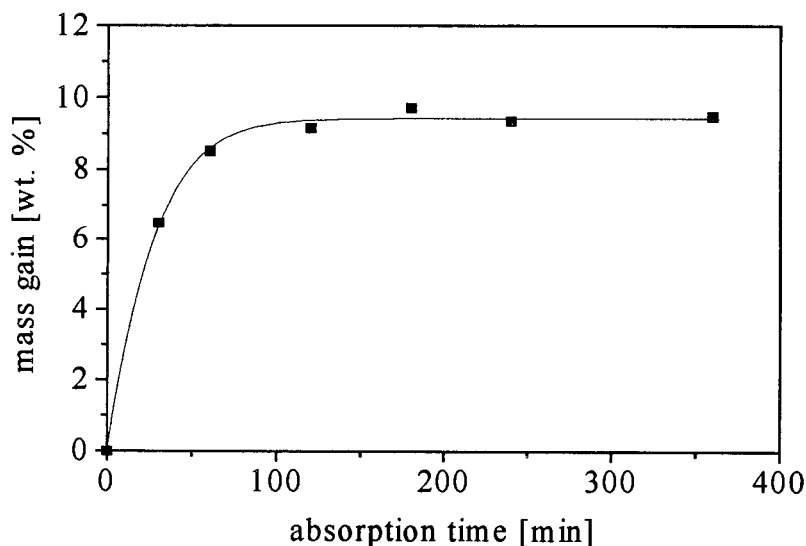


Figure 4. Absorption kinetics of PVC-sheets at 60 °C and 200 bar

Figure 5 shows the absorption isotherms of the PVC-sheets from 80 to 400 bar. The absorption time was 4 hours. With increasing temperature the mass gain decreases. For each isotherm there is an increase in mass gain with increasing pressure. Before „soaking“ the samples were transparent, after absorption the samples appeared white. The reason for this could be the disorientation of the polymer chains, which was fixed because of the rapid venting. If these white samples were heated above the glass temperature of the sheets (70°C), they became transparent again after a few hours.

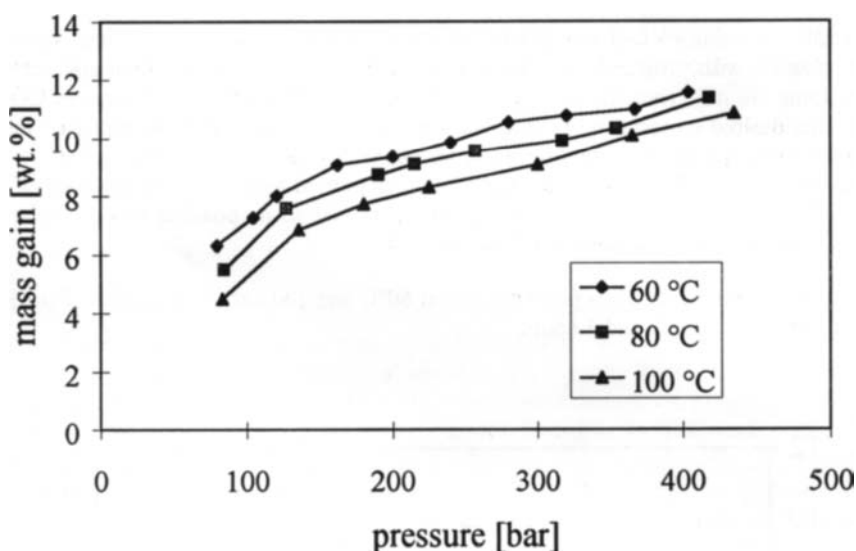


Figure 5. Absorption isotherms of PVC in CO₂, absorption time: 4 h

For the future there are the following tasks: Chemical modification of the PVC-sheet and absorption/modification experiments with other polymers in scCO₂.

References

- [1] L. Merz, Th. Hirth, B. Michelfelder, Proc. of the 3rd International Symposium on Supercritical Fluids, Strasbourg, France, October 17-19, 1994
- [2] T.J. Romack; E.E. Maury and J.M. DeSimone, *Macromolecules* 28 (1995), 912- 915
- [3] A.R. Berens, G.S. Huvard, R.W. Korsmeyer, U.S. Patent 4,820,752; (1986)
- [4] J.J. Watkins, Th.J. McCarthy, *Macromolecules* 27 (1995), 4845-4847
- [5] A.R. Berens; G.S. Huvard; in *Supercritical Fluid Science and Technology*, ACS Symposium Series 406; Washington D.C., (1989), Chapter 14

Design of Experiments for Thermodynamic Model Discrimination Applied to Phase Equilibria at High Pressures

C. Dariva^a, E. Cassel^b and J.V. Oliveira^a

^aDepartment of Chemical Engineering, Federal University of Santa Catarina, 88010-970, Brazil

^bChemical Engineering Program, Federal University of Rio de Janeiro, 68592-970, Brazil

ABSTRACT

Traditionally, the screening of thermodynamic models in phase equilibria is carried out based on the full data set and, therefore, after having obtained all the experimental points. The aim of this work is to show that sequential model discrimination may be used as a guide for obtaining experimental data for systems at high pressures. We have compared two discrimination procedures in order to select the next experimental point, one of them considering only the predicted responses (Hunter and Reiner [1]) and the other taking also into account the error limit inherent to each model (Ferraris and Forzatti [2]). In order to test these methodologies, literature data were used along with current thermodynamic models. It is shown that the sequential discrimination leads to the same conclusions as obtained when using the full data set, but with much less effort.

1. INTRODUCTION

The design of experiments associated with model discrimination is a technique aimed to optimize experimental data collection and thus causing a cost reduction. The necessity of model discrimination arises as we observe the large number of existing equations of state (EOS) and also due to the possibility of optimizing data collection process. It has been shown by Cassel and Oliveira [3] that this rationalization is effective in vapor-liquid equilibrium at high pressures, making the sequential model discrimination an important tool for the screening of EOS. However, in such a investigation, these authors have not considered the error limit to each model and, hence, the discrimination procedure has been accomplished based only on the predicted responses. In this work we use the least square method to estimate the parameters and the Hunter-Reiner[1] and Ferraris-Forzatti[2] discrimination strategies along with the Fisher F-Distribution Function to proceed the model discrimination. The Peng Robinson[4] EOS (PR-EOS) with five different mixing rules was employed to evaluate the potential of the discrimination methodologies presented here.

2. THEORY

The vapor-liquid equilibrium can be described by:

$$\hat{\phi}_i^L x_i = \hat{\phi}_i^V y_i \quad (1)$$

where $\hat{\phi}_i^V$ and $\hat{\phi}_i^L$ are the fugacity coefficients for the component "i" in the vapor and liquid phases, respectively; which are calculated in this work by the generalized PR-EOS. The calculation of a and b parameters of this equation was performed using five mixing rules in order to verify which of them best describes the phase equilibria at high pressures. We used the following mixing rules[5]: van der Waals 1, Schwartzentruber-Renon, van der Waals 2, Panagiotopoulos-Reid and Strijck-Vera, as shown in Table 1. The sequential discrimination procedure is divided in two steps: the first one is the parameter estimation and the second step is accomplished by determining the place in the experimental space where the next experiment should be run. These steps are presented below.

Table 1
PR-EOS mixing rules

Mixing Rule	Functional Form	Parameters
Model 1 van der Waals 1	$a = \sum_i \sum_j z_i z_j (a_i a_j)^{1/2} (1 - k_{ij})$ $b = \sum_i z_i b_i$	k_{ji}
Model 2 Schwartzentruber-Renon	$a = \sum_i \sum_j z_i z_j (a_i a_j)^{1/2} \left[1 - k_{ij} - l_{ji} \frac{m_{ij} z_i - m_{ji} z_j}{m_{ij} z_i + m_{ji} z_j} (z_i + z_j) \right]$ $b = \sum_i z_i b_i$	k_{ij} l_{ji} m_{ij}
Model 3 van der Waals 2	$a = \sum_i \sum_j z_i z_j (a_i a_j)^{1/2} (1 - k_{ij})$ $b = \sum_i \sum_j z_i z_j \frac{(b_i + b_j)}{2} (1 - k_{ji})$	k_{ij} k_{ji}
Model 4 Panagiotopoulos- Reid	$a = \sum_i \sum_j z_i z_j (a_i a_j)^{1/2} (1 - k_{ij} + (k_{ij} - k_{ji}) z_i)$ $b = \sum_i z_i b_i$	k_{ij} k_{ji}
Model 5 Strijck-Vera	$a = \sum_i \sum_j z_i z_j (a_i a_j)^{1/2} (1 - z_i k_{ij} - z_j k_{ji})$ $b = \sum_i z_i b_i$	k_{ij} k_{ji}

2.1 Parameter Estimation

The parameters of the mixing rules are estimated using the least square method. In the calculations "Y" (P) is the output variable and the errors of the experimental measurements are considered to be normally distributed. Next, the fit is performed by minimizing the following objective function with respect to the vector of parameters:

$$S = \sum_{i=1}^{N_{\text{exp}}} \frac{(y_i^{\text{exp}} - y_i^{\text{cal}})^2}{(\sigma_y^2)_i} \quad (2)$$

The variance of the estimation procedure is defined as:

$$s^2 = \frac{1}{(N_{\text{exp}} - N_{\text{par}})} \sum_{i=1}^{N_{\text{exp}}} (y_i^{\text{exp}} - y_i^{\text{cal}})^2 \quad (3)$$

where N_{exp} is the number of experimental points, N_{par} the number of parameters and exp and cal refer to experimental and calculated values.

The absolute average deviation is defined as:

$$AAD = \frac{100}{N_{exp}} \sum_{i=1}^{N_{exp}} \left| \frac{P_i^{exp} - P_i^{cal}}{P_i^{exp}} \right| \quad (4)$$

2.2 Sequential Model Discrimination

There are many alternatives for modeling high pressure phase equilibria. Therefore, it is required a discrimination procedure capable to screen these models satisfactorily. In this work we have compared two discrimination methods in order to select the next experimental point. The first one is the Hunter-Reiner methodology that considers only the predicted response of each model according to the following equations:

$$d_{ij}(x) = [y_i(x) - y_j(x)]^2 \quad (5)$$

and,

$$D(x) = \sum_i^{N_{mod}} \sum_{j=i+1}^{N_{mod}} d_{ij}(x) \quad (6)$$

where $d_{ij}(x)$ is the squared difference between the responses of models “i” and “j” and $D(x)$ is the difference among the responses of all models.

The next experimental point should maximize $D(x)$ to one value greater than the experimental error, otherwise the divergence between the models can be explained in terms of experimental error variance.

The Ferraris-Forzatti methodology takes also into account the error limit inherent to each model, as presented by Equations (7) to (13) of reference [2]. According to Ferraris- Forzatti, an adequate indicator of the divergence among the model responses relative to the error limit is:

$$T(x) = \frac{\sum_{i=1}^{N_{mod}} \sum_{j=i+1}^{N_{mod}} (y_i - y_j)^2}{(N_{mod} - 1)(N_{mod} \sigma^2 + \sum_{i=1}^{N_{mod}} \hat{\sigma}_i^2(x))} \quad (7)$$

being the estimated variances of the responses given by:

$$\hat{\sigma}_i^2(x) = g_i^T(x)(G_i^T G_i)^{-1} g_i(x) \sigma^2 \quad (8)$$

where N_{mod} is the number of models, $T(x)$ is the difference among all models, σ^2 is the experimental variance, $\hat{\sigma}_i^2(x)$ the estimated variance of the responses, g_i is a vector containing the model derivatives with respect to the parameters, g_i^T its transposition and G_i is a matrix (N_{exp} rows and N_{par} columns) containing the g_i vector calculated at experiment i .

The next experimental point should maximize $T(x)$ to one value greater than 1, otherwise the divergence among the models can be explained in terms of experimental error variance plus

the variance of the expected responses. In both cases, after we have the input variables that maximize $D(x)$ and $T(x)$, the experiment is run and the parameters are estimated. These two steps - estimation and discrimination - are repeated sequentially until the mixing rule that best fits the experimental data is chosen or until $D(x) < \sigma^2$ (Hunter-Reiner) or until $T(x) < 1$ (Ferraris-Forzatti). The first parameters are fitted with four experimental data, and it is found the liquid phase mole fraction where the maximum deviation occurs (D or T , depends on the methodology). Then, the parameters are estimated again with this new experiment. It is important to mention that we have not performed a spline with the data in order to obtain the response (P) related to the selected liquid phase mole fraction of CO_2 ; actually, we have chosen the closest reported experimental data. Moreover, when the discrimination procedure gives an experimental condition previously used, we have avoided repetition making use of the next deviation and its required experimental point.

After the parameter estimation, the discarding of the mixing rules begins using the F-Test, that points out with 99% confidence whether or not the tested model is equivalent to the experimental variance. If there is an equivalence the discrimination goes to the next step; on the other hand the model is discarded and the discrimination procedure continues for the remaining models. If no models is discarded three consecutive times the confidence is decreased down to 95% until one or more models are eliminated.

3. RESULTS AND DISCUSSION

To verify, among the employed mixing rules, the one or ones that best represent the equilibrium data, the $CO_2(1)$ -Diphenyl(2) at 343.2 K and $CO_2(1)$ -n-Propylbenzene(2) at 353.2 K systems were used. The data and their conditions are presented in the works of Zang et al. [6] and Maurer et al. [7], respectively. The pure properties of the components are given in Reid et al.[8]. The standard deviation of the measured output variable is: $\sigma_p=0.05MPa$ and $\sigma_p=0.07MPa$, respectively.

The sequential planning for the systems CO_2 -Diphenyl and CO_2 -n-Propylbenzene is shown in Tables 2 and 3, respectively. In Figure 1 is depicted the Hunter-Reiner and Ferraris-Forzatti deviations for the CO_2 -n-Propylbenzene system. It can be noted that the selected points for both methodologies are (essentially) the same. This can be explained due to the very small estimated variances of the responses and, hence the Ferraris-Forzatti methodology reduces to the Hunter-Reiner, as can be verified by Equations (5) to (7). This occurred because of, for the systems studied here, the parameters were estimated with small uncertainties. So, the additional effort of the Ferraris-Forzatti methodology is not justified for these systems (the same result was obtained for the CO_2 -Diphenyl). However, the same can not be true when considering multiple responses.

Table 2
Experimental planning for the CO_2 -Diphenyl system

Next Point	CO_2 mole fraction	$D(MPa^2)$	$T(MPa^2)$	Models Discarded
5	0.795	345.25	38.75	-
6	0.656	214.73	24.56	-
7	0.619	2.65E-4	4.59E-5	1 and 5

Table 3
Experimental planning for the CO_2 -n-Propylbenzene system

Next Point	CO ₂ mole fraction	D(MPa ²)	T(MPa ²)	Models Discarded
5	0.365	197.65	27.32	-
6	0.360	204.67	37.52	-
7	0.404	16.85	3.68	1
8	0.362	14.79	3.81	1
9	0.720	2.12E-5	1.19E-6	1 and 5

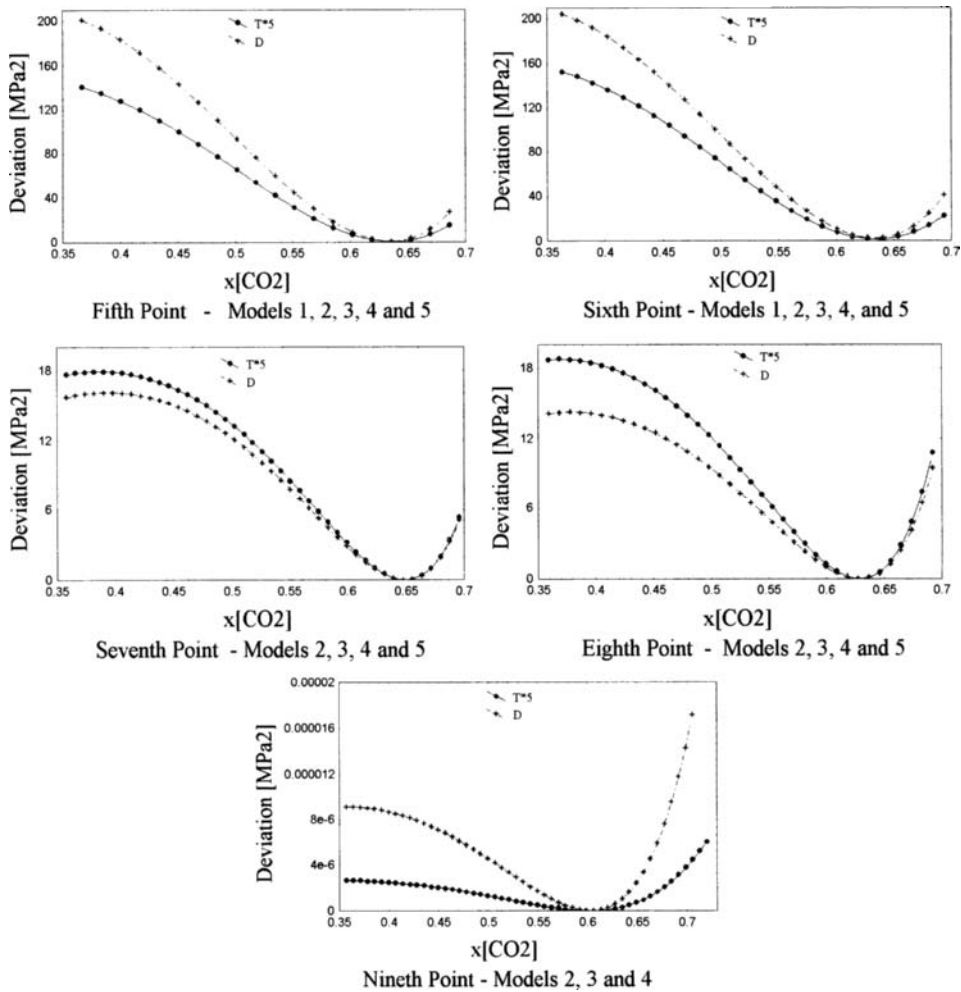


Figure 1. Deviations of the discrimination strategies as a function of the CO₂ mole fraction.

To check the reliability of the results it was also performed the parameter estimation using the full data set. It can be noticed from Table 4 that there is no loss of fitting quality for the system CO₂-Diphenyl and the parameters are approximately the same when we compare the conventional and the discrimination procedures.

Furthermore, an aspect much more relevant to be noticed is that the use of the sequential discrimination led to the same conclusions as obtained when using the full data set, but with much less effort. This statement can be verified by comparing the confidence for each model at the end of the discrimination procedure with the ones resulting from full data set (the same result was obtained for the CO₂-n-Propylbenzene).

Table 4

Estimated parameters and confidence level at the end of the discrimination procedure and using the full data set for the CO₂-Diphenyl system.

Number of points	van der Waals 1	Schartzentruber-enon	van der Waals 2	Panagiotopoulos-Reid	Strijck-Vera
6	k_{12} 7.993E-2	k_{12} 8.265E-2 l_{12} 5.234E-2 m_{12} -7.89E-3	k_{12} 9.902E-2 k_{21} 8.348E-2	k_{12} 9.902E-2 k_{21} 8.348E-2	k_{12} 1.056E-1 k_{21} -7.89E-2
	AAD 9.617 s^2 1045.61	AAD .558 s^2 1.298	AAD .559 s^2 1.365	AAD .559 s^2 1.365	AAD 12.486 s^2 987.45
	Conf. % 99.36	87.98	88.28	88.28	99.25
	Full Data Set	k_{12} 8.501E-2 l_{12} 4.985E-3 m_{12} -7.23E-3	k_{12} 9.915E-2 k_{21} 8.345E-2	k_{12} 9.915E-2 k_{21} 8.345E-2	k_{12} 9.871E-2 k_{21} -6.987E-2
22	AAD 18.231 s^2 1556.7	AAD 1.424 s^2 2.640	AAD 1.465 s^2 2.680	AAD 1.465 s^2 2.680	AAD 18.445 s^2 1235.465
Conf. %	99.998	90.123	90.265	90.265	99.997

4. CONCLUSIONS

We have presented a comparison between two model discrimination procedures using literature data for phase equilibria at high pressures. Though the application of these methodologies furnished essentially the same results for the systems investigated here, they seem to be useful for experimental design in the field of phase equilibria. A more rigorous treatment should consider the case of multiple responses and also the experimental error in the independent variables; these topics are now under investigation.

REFERENCES

1. W.G. Hunter and A.M. Reiner, *Technometrics*, 7 (1967) 307.
2. G.B. Ferraris and P. Forzatti, *Chem. Eng. Sci.*, 38 (1983) 225.
3. E. Cassel and J.V. Oliveira, *The Journal of Supercritical Fluids*, In press.
4. D.Y. Peng and D.B. Robinson, *Ind. Eng. Chem. Fundam.*, 15 (1976) 59.
5. A. Anderko, *Fluid Phase Equilibria*, 61 (1990) 145.
6. D.L. Zhang; W. Wang; W. Sheng and B.C.Y. Lu, *Can. J. Chem. Eng.*, 69 (1991) 1352.
7. A. Bamberger and G. Maurer, *The Journal of Supercritical Fluids*, 7 (1994) 115.
8. R.C. Reid; J. M. Prausnitz and B.E. Poling, *The Properties of Gases and Liquids*, Mc Graw-Hill Book Company, 4th edition (1987).

Predictive Quasilattice Equation of State for Unified High Pressure Phase Equilibria of Pure Fluids and Mixtures

Sung Jae Yoo^a, Hun Yong Shin^a, Ki-Pung Yoo^a, Chul Soo Lee^b and W. Arlt^c

^aDepartment of Chemical Engineering, Sogang University, Seoul 121-742, Korea*

^bDepartment of Chemical Engineering, Korea University, Seoul 136-701, Korea

^cInst. für Verfahrenstechnik, TU Berlin, D-10623, Berlin, Germany

Based on a rigorous solution derived from the lattice statistical-mechanical theory, a unified group contribution equation of state[GC-EOS] was formulated. The GC-EOS was found to be applicable for the simultaneous prediction of thermodynamic properties of pure fluids and mixtures in general over a wide range of pressure. The GC-EOS uses a single set of group segment size and interaction energy parameter for both pure fluids and mixtures. Quantitative applicability was demonstrated for vapor pressures of pure fluids and vapor-liquid equilibrium properties of mixtures with emphasis on the high-pressure region including the supercritical fluid systems.

1. INTRODUCTION

After the seminal work of Guggenheim on the quasichemical approximation of the lattice statistical-mechanical theory[1], various practical thermodynamic models such as excess Gibbs energies[2-3] and equations of state[4-5] were proposed. However, the quasichemical approximation of the Guggenheim combinatory yields exact solution only for pure fluid systems. Therefore one has to resort to numerical procedures to find the solution that is analytically applicable to real mixtures. Thus, in this study we present a new unified group contribution equation of state[GC-EOS] which is applicable for both pure or mixed state fluids with emphasis on the high pressure systems[6,7].

2. EQUATION OF STATE AND GROUP CONTRIBUTION

The GC-EOS based on a series expansion of the nonrandom lattice-hole theory is written by[1,6],

* This work was supported by the Korea Science and Engineering Foundation and The Korea Ministry of Trade, Industries, Energy.

$$P = \frac{1}{\beta V_H} \left\{ \left(\frac{z}{2} \right) \ln \left[1 + \left(\frac{q_M}{r_M} - 1 \right) \rho \right] \right\} - \left(\frac{z}{2} \right) \theta^2 \left(\frac{\varepsilon_M}{V_H} \right) \quad (1)$$

$$\varepsilon_M = \frac{1}{\theta^2} \left[\sum \sum \theta_i \theta_j \varepsilon_{ij} + \left(\frac{\beta}{2} \right) \sum \sum \sum \sum \theta_i \theta_j \theta_k \theta_l \varepsilon_{ijkl} (\varepsilon_{ij} + 3\varepsilon_{kl} - 2\varepsilon_{ik} - 2\varepsilon_{jl}) \right] \quad (2)$$

The GC-EOS requires the calculation of the molecular segment number r_i and the interaction energy parameter ε_{ij} from functional group characteristics, r_i^G and ε_{ij}^G [7]. They are written by the sum of temperature-dependent group parameters as

$$r_i = \sum_{j=1}^s \nu_{ij} r_j^G \quad (3)$$

$$r_i^G = w_j^G + h_j^G (T - T_0) + c_j^G [T \ln(T_0 / T) + T - T_0] \quad (4)$$

$$\varepsilon_{ij} = \sum_{k=1}^s \sum_{l=1}^s \theta_{ik}^G \theta_{jl}^G \varepsilon_{kl}^G = \sum_{k=1}^s \sum_{j=1}^s \nu_{ik} \nu_{jl} q_k^G q_l^G \varepsilon_{kl}^G / \sum_{k=1}^s \sum_{j=1}^s \nu_{ik} \nu_{jl} q_k^G q_l^G \quad (5)$$

$$\varepsilon_j^G / k = a_j^G + b_j^G (T - T_0) + d_j^G [T \ln(T_0 / T) + T - T_0] \quad (6)$$

where $\beta = 1/kT$, q_M and r_M are given as mole fraction averages of relevant properties. ν_{ij} is the number of group j in species i and θ_{ik}^G is the surface area fraction of group k in species i . T_0 is an arbitrarily chosen reference temperature (298.15K). Also, we set $z=10$ and $N_A V_H = 9.75 \text{ cm}^3 \text{ mol}^{-1}$. Preliminary studies for the possible applicability have been made [7,8].

Table 1
Coefficients in the segment number correlation defined by eq (4)

Group	w_j^G	h_j^G	c_j^G	Temperature Range(K)
-CH ₃	2.654657	0.000203	0.001786	270 - 450
-CH ₂	1.539918	-0.000201	0.001218	270 - 450
-ACCH ₃ *1	2.975477	0.000146	0.001625	270 - 450
-ACH	1.400666	0.000188	0.001062	270 - 450
-CO	1.377142	0.001917	0.001526	270 - 450
-CO ₂	3.782112	0.004755	0.004512	270 - 450

*1AC denotes aromatic carbons.

3. PREDICTION OF PHASE-EQUILIBRIA

The numerical parameters in eqns (4) and (6) are shown in Table 1 and 2 for some groups. As an illustration, the predicted vapor pressure of pure alkanes and distillation phenomena of alkane mixtures are shown in Figure 1. It is obvious that the description of configurational properties of real fluids is reduced to functional group characteristics which are the group segment number and the group-group interaction energy parameter. As molecular simulation studies do,

the present group contribution method can be utilized to calculate binodals, critical properties, and mixture phase equilibria for which no experimental data are available[8].

Table 2

Coefficients in the group-group interaction parameter defined by eq (6)

Group-Group	a_{ij}^G	b_{ij}^G	d_{ij}^G	Temperature Range(K)
CH ₃ -CH ₃	78.174322	0.050459	0.388018	270 - 450
CH ₃ -CH ₂	96.049727	0.011347	-0.273514	270 - 450
CH ₂ -CH ₂	112.776346	0.049733	0.070320	270 - 450
ACH-ACH	119.958040	-0.011889	-0.104178	270 - 450
CO ₂ -ACH	93.858901	-0.060056	-0.232417	270 - 450
CO ₂ -ACCH ₃	84.697966	-0.023877	-0.109467	270 - 450
CO ₂ -CO ₂	84.919753	-0.099498	-0.345484	270 - 450
ACH-ACCH ₃	117.763895	0.012471	-0.077352	270 - 450
ACCH ₃ -ACCH ₃	113.004523	0.039160	-0.00130	270 - 450
CH ₃ -CO	142.569937	-0.223408	-0.406103	270 - 450
CH ₂ -CO	178.078211	-0.143040	0.130141	270 - 450
CO-CO	612.056821	-0.784793	-2.063104	270 - 450

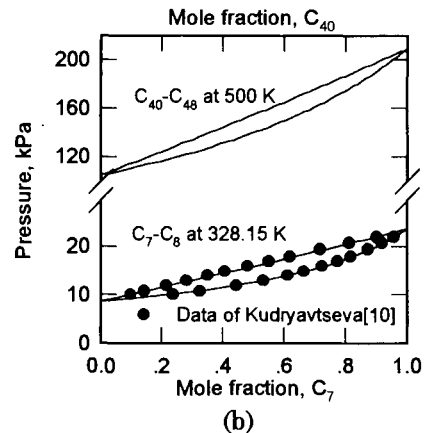
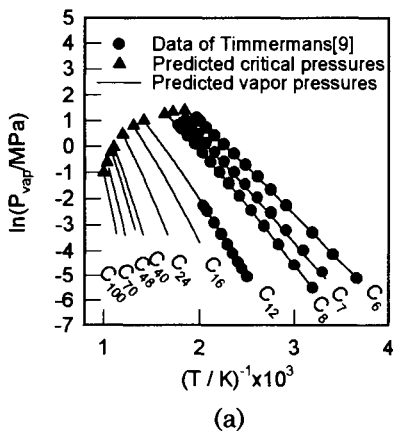


Figure 1. Predicted vapor pressures of pure alkanes (a) and vapor-liquid equilibria for C₇-C₈ at 328.15 K and C₄₀-C₄₈ at 500 K by the unique set of parameters given in Table 1 and 2(b).

In Figure 3, the predicted P-x-y equilibria for CO₂-toluene system up to 16Mpa is shown uniquely by the group parameters in Table 1 and 2. Also, in Figure 4, the predicted P-x-y equilibria for ethane-acetone system at 298.15K and up to 5Mpa is illustrated. The predictions are included the pseudocritical point of the mixtures. Although we omit here further demonstrations, the GC-EOS is found to be comprehensively applicable to various phase equilibria of

complex mixtures including the macromolecular systems.

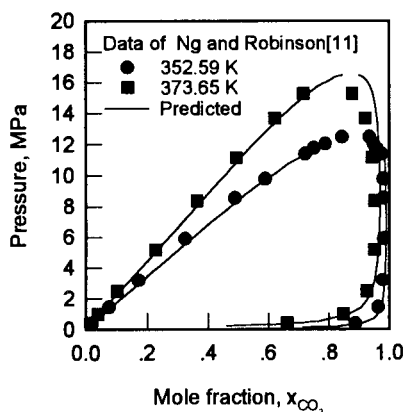


Figure 3. Predicted P-x-y equilibria for CO₂-toluene system

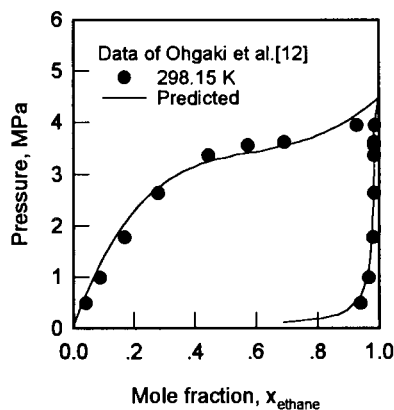


Figure 4. Predicted P-x-y equilibria for ethane-acetone system

In summary, based on a rigorous approximation to the quasichemical solution derived by the present authors, a generalized GC-EOS was proposed for the estimation and the prediction of properties of real pure fluids and mixtures. Its applicability was demonstrated for high pressure vapor-liquid equilibria of pure or mixed fluids. Although not shown here, we have further results with other functional groups which indicate the extended applicability of the present method.

REFERENCES

1. E. A. Guggenheim, *Mixture*, Oxford Clarendon Press, London, 1952.
2. D. S. Abrams and J. M. Prausnitz, *AIChE J.*, 21 (1975) 16.
3. A. Fredunslund, A. Jones and J. M. Prausnitz, *AIChE J.*, 21 (1975) 1086.
4. I. C. Sanchez and R. H. Lacombe, *Nature*, 252 (1974) 381.
5. C. Panayiotou and J. H. Vera, *Polymer J.*, 14 (1982) 681.
6. S. S. You, K.-P. Yoo and C. S. Lee, *Fluid Phase Equil.*, 93(1994), 193, 215.
7. K.-P. Yoo and C. S. Lee, *Fluid Phase Equil*, in Press, March (1996)
8. K.-P. Yoo, S. J. Yoo and C. S. Lee, *J. Am. Chem. Soc.*, submitted, Feb.(1996).
9. J. Timmermans, *Physicochemical Constants of Pure Organic Compounds*, Vol. 1. Elsevier Amsterdam, 1950.
10. L. S. Kudryavtseva, K. Viit and O. G. Eizen, *Eesti NSV Tead. Akad. Toim, Keem. Geol*, 20 (1971) 292.
11. H.-J. Ng and D. B. Robinson, *J. Chem. Eng. Data*, 23(1978) 325.
12. K. Ohgaki, F. Sand and T. Katayama, *J. Chem. Eng. Data*, 21(1976) 55.

Static and Dynamic Light Scattering Test of Polymer Particles Formation Process in Supercritical Fluid

D.Yu.Ivanov, R.Tufeu, and A.V.Soloviev

Université Paris XIII, Laboratoire d'Ingénierie des Matériaux et des Hautes Pressions, CNRS. Avenue Jean-Baptist Clément 93430, Villetaneuse, France.

1. Introduction

In the last years supercritical fluid (SCF) technology has occupied a significant place in the high pressure chemical engineering. Due to their specific properties as liquid-like densities, gas-like viscosities and diffusivities intermediate between gas and liquid values, SCF have large potential in extraction and separation processes, polymer science and technology and in elaboration of new materials [1-4]. In these last cases, to control the size of particles, we have to deal with the kinetics of their formation.

This communication which is a continuation and a development of our previous study [5] is devoted to closer examination of the polystyrene particles formation process in supercritical n-butane induced by small pressure variation. This study was carried out using both DLS (dynamic light scattering) and SLS (static light scattering), which permitted us to investigate the fast (10-30 sec) process of appearance and the aggregation of the particles, to determine their mean radius (R) and concentration (N).

2. Experimental Setup

The DLS-measurements were made in the homodyne technique of photon-correlation spectroscopy by using a 16-bit, 255 canal PC board plugged digital correlator (Unicor, OGRI RAS), with different time scale mode and with the sample time range from 100 ns to 1 sec. A 20-mW He-Ne laser (Spectra-Physics Co, $\lambda=632.8$ nm) was used as the light source. The cylindrical high-pressure optical cell was placed into the specially designed thermostat with a temperature control of ± 0.1 K. Two photodiodes were used to measure the optical thickness (γ) of the system under study:

$\gamma = -\ln(I_t / I_0)$, where I_t, I_0 - the intensities of transmitted and laser light, respectively.

The experimental setup allows the simultaneous measurements of the autocorrelation function and intensities of 90° scattered (I_s), transmitted (I_t) and laser (I_0) light. The values of the light intensities (I_s, I_t, I_0), of the pressure (P), of the temperature (T) and also the correlation functions were automatically registered every 5 sec.

As a correlation function is recorded, the correlator offers the decay time (τ), particles diffusion coefficient (D), and particles mean radius (R). The two latter are related with by Stokes-Einstein equation [6].

$$R = \frac{k_B T}{6 \pi \eta D}$$
, where k_B is the Boltzmann constant and η - the shear viscosity of the fluid.

Knowing R , the extinction efficiency factor (Q) can be found, by Mie scattering theory for the sphere [7]. Then the particles concentration is: $N = \gamma / (Q\pi R^2 L t^2)$, where L is the distance between windows, t is the transparency of the window.

The experimental setup and this method have been tested on aqueous suspensions of monodisperse latex spheres with 94 and 302 nm diameters (SIGMA Chemical Co) and different concentrations from $5 \cdot 10^{-5}$ to $2 \cdot 10^{-3}$ gram/m³. The radii being calculated by analysis of the correlation functions were verified within a few percents. The concentrations has been calculated from the optical thickness and turned to be within 2-5% in accordance with those found by evaporating and weighting the latexes.

3. Results and discussion

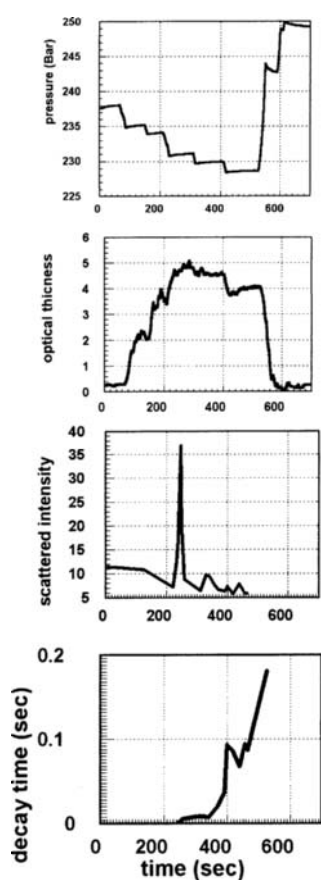


Fig.1 a,b, c, d

We have studied the demixion of a monodisperse polystyrene ($M = 3700$) solution in n-butane ($T_c = 425.16K$ $P_c = 3.796$ MPa). The previously weighted polystyrene sample was placed in the cell which was then evacuated and heated up to the temperature of experiment, i.e. 433K. The solvent was introduced through the lower part of the cell at the pressure 30MPa. The cell temperature and the pressure were kept constant for 48 hours.

The time dependences of pressure, optical thickness, intensity of scattered light and decay time are presented in Fig.1. The pressure was slowly decreased, the optical thickness being constant indicating that the solution was not initially saturated. At a pressure 23.5MPa (Fig. 1a) the optical thickness (Fig.1b) began to increase due to the demixion of the solution and formation of particles. After that measurable correlation functions were observed (Fig.1d) with increasing decay time. The latter indicated the growth of the polystyrene rich particles mean radius because of the particles coalescence (Fig.2).

The time independence of optical thickness in the following stage of the process shows in our opinion that the polystyrene deposition on the windows took place. This made difficult the further observations of the particles formation in the volume. That is the reason why the light correlation technique allowed us to observe, unfortunately, only the initial stage of this process. At the end of this stage the light scattering is no more single one and requires an application of the multiple scattering theory. As shown in [8,9], it would lead to underestimate the particles radius. The further increase in the decay time (Fig.1d) was not related to the particles growth in the cell volume, but

was probably due to by the droplets coalescing on the windows. This deposition of the polystyrene rich phase formed the speckles patterns (on the screen placed behind the photodiode registering the transmitted light), changing with time. Finally, when all the motions were vanished, we could assume from these patterns [10], that the film deposited on the windows became homogeneous.

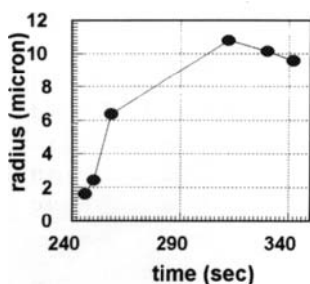


Fig.2

The sharp picks of the scattered light intensity (Fig.1c) indicated the formation and the falling of the great droplets. The width of these picks allowed us to estimate the maximal size of these droplets to be equal to 5-10 micron. Quantitative theory of these phenomena is in the course of development.

4. Conclusions

Study of the particles formation and their growth from the demixion of the polystyrene-n-butane system by small pressure variations have demonstrated high efficiency of combined DLS and SLS measurements and allowed:

- to estimate the size of forming particles and to observe the dynamics of their growth.
- to make the preliminary calculation of maximal size of particles and to find the speed of the precipitation process.

More detailed calculations will be published later.

Acknowledgement

D.I. and A.S. are very grateful for the opportunity to work and for kind hospitality at the L.I.M.H.P. and the Institut Galilée.

References

1. M.A. Mchugh and V.J. Kruconis, Supercritical Fluid Extraction: Principles and Practice, Butterworth-Heinemann, Boston, 1994.
2. Supercritical Fluid Science and Technology, ed. Johnston K.P. and Penninger J.M.L., ACS Symp. Ser. 406, 1989.
3. M. Poliakoff and S.M. Howdl "Proceedings of the 3-rd International Symposium on Supercritical Fluids", Strasbourg, 17-19 October. 1994, tome 3, p.81
4. P.G. Debenedetti "Proceedings of the 3-rd International Symposium on Supercritical Fluids", Strasbourg, 17-19 October. 1994, tome 3, p.213
5. D.Y. Ivanov and R.Tufeu "Proceedings of the 3-rd International Symposium on Supercritical Fluids", Strasbourg, 17-19 October. 1994, tome 3, p.327.
6. E.R. Pike and H.Z. Cummins (eds), Photon Correlation and Light Beating spectroscopy. Plenum, New York, 1974
7. G. Mie, Ann Physik 30 (1909) 57-136
8. D. Yu. Ivanov, A.F. Kostko, and V.A. Pavlov, Phys. Lett., A138 (1989) 339.
9. P.C. Colby, L.M. Narducci, V. Bluemel, and J. Baer. Phys. Rev., A12 (1975) 1530.
10. J.-Z. Xue, D.J. Pine, S.T. Milner, X.-I. Wu, and P.M. Chaikin, Phys. Rev., A45 (1992) 6550

This page intentionally left blank

Resolution of Ibuprofen and *cis*-Chrysanthemic Acid by Supercritical Fluid Extraction

S. Keszei^a, B. Simandi^a, E. Fogassy^b, J. Sawinsky^a, Cs. Niklós^a, R. Lovas^a

^a Department of Chemical Engineering, Technical University of Budapest, H-1521 Budapest, Hungary

^b Department of Organic Chemical Technology, Technical University of Budapest, Hungary

Experimental work on resolution of ibuprofen and *cis*-chrysanthemic acid by supercritical fluid extraction using carbon dioxide was carried out. The effects of extraction temperature and pressure were investigated on the yield and enantiomeric excess of extracts and raffinates. An efficient extraction procedure was developed for production of (-)-*cis*-chrysanthemic acid and (+)-*cis*-chrysanthemic acid resulting in 90 % enantiomeric excess.

1. INTRODUCTION

The majority of syntheses of organic compounds is performed under macroscopic symmetrical conditions, thus optical activity is not resulted. The product is the racemate containing two mirror image isomers that can be separated by molecular chiral recognition.

The oldest example of molecular chiral recognition described by Pasteur [1] is the separation of enantiomers based on diastereoisomeric salt formation and subsequent fractionated crystallisation. The principle of the enantiomeric differentiation is that one of the salts formed with a chiral reagent is less soluble than the other, and thus precipitates from the solution. This enrichment of one of the enantiomers leads to the optical resolution.

Even nowadays, particularly in industrial processes, the separation of enantiomers of racemic acids and bases is based on this molecular chiral recognition. The less soluble, i.e. the more stable of these diastereomer salts crystallizes even if the chiral agent in the better soluble salt is replaced by an achiral reagent of similar chemical character, or eventually eliminated, or substituted by a solvent. In this case, a mixture enriched with the more stable diastereomer can be isolated by filtration from the solution of the achiral salt of the enantiomeric mixture or the free enantiomers [2,3].

For preparative and industrial scale separations of enantiomers the supercritical fluid extraction (SFE) seems very promising. The process of SFE with carbon dioxide allows variations in extraction parameters (pressure, temperature and extraction time) to find an optimal range both for maximum quantity and maximum optical purity of the product[4].

* This work was supported by OTKA (Hungarian National Science Foundation) under grant numbers F016880 and T0148887.

In addition SFE has the advantage of being carried out at low temperature, and thus it does not cause racemization or thermal decomposition of the enantiomers. In our previous work we have observed the molecular chiral recognition in supercritical carbon dioxide for several compounds [5]. The present study was designed to explore the applicability of supercritical carbon dioxide for extraction of ibuprofen and *cis*-chrysanthemic acid.

2. EXPERIMENTAL

2.1. Materials

Both the racemic mixtures of various acids and the resolution agents (Table 1) were prepared in our laboratory. All the reagents were checked by analytical methods before use and no significant impurities were found.

Other reagents and solvents were obtained from commercial sources. The samples were prepared by mixing various chiral bases with racemic acids in 0.5:1 molar ratio. A porous supporting material (Perfilt), impregnated with these mixtures, was put into the extractor vessel and extracted with supercritical carbon dioxide.

Optical rotation of extracts and raffinates was measured on a PERKIN-ELMER 241 polarimeter.

2.2. Apparatus and extraction

Figure 1 shows the simplified flow diagram of the laboratory equipment. First the extractor is filled with the prepared raw material and pressurised. Once the system has attained the required temperature and pressure, the carbon dioxide is expanded into the separator through a micrometering valve, and the extract is precipitated in the separator. The carbon dioxide is evaporated and its volume is measured by a gas meter.

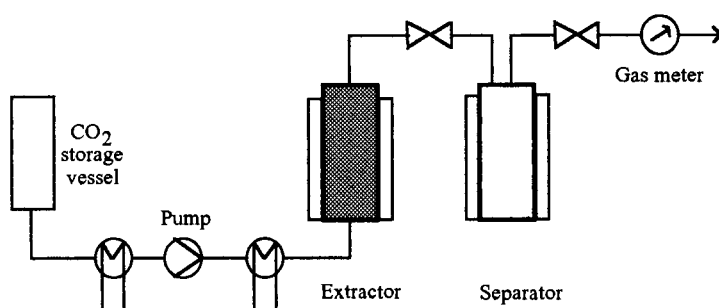


Figure 1. Flow diagram of the laboratory equipment

3. RESULTS AND DISCUSSION

The extraction of raw materials was carried out separately. Figure 2 shows the cumulative extraction yield (mass of extract /mass of raw material) as a function of the specific carbon dioxide consumption. Straight lines were obtained, from the slope the approximate solubility of the compounds was evaluated. The solubility data obtained this way are summarized in Table 1.

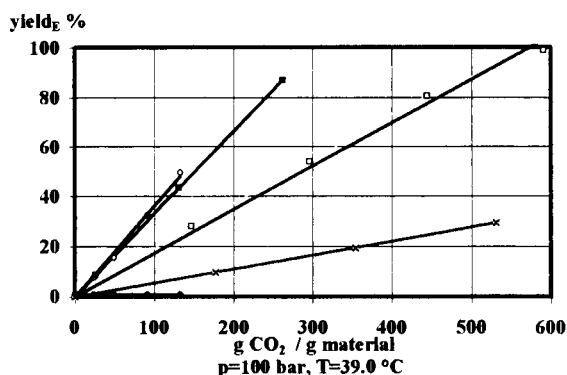


Figure 2. Solubility conditions of the raw material (○ (±)-*cis*-chrysanthemic acid ■ (±)-ibuprofen □ *S*-(+)-2-benzylamino-1-butanol x *R*-(+)-1-phenylethylamine ● Perfilt)

Table 1. Determined solubility data

compound	solubility wt %
(±)-ibuprofen	0.36
<i>R</i> -(+)-α-phenylethylamine	0.17
(±)- <i>cis</i> -chrysanthemic acid	0.25
<i>S</i> -(+)-2-benzylamino-butanol	0.05
Perfilt (supporting material)	0

The mixtures of racemic acids and chiral bases were extracted with supercritical carbon dioxide. The extracts were collected as separate samples successively in time. Each of them was examined separately. The results of ibuprofen extraction are presented in Figure 3a. The extracts contained the (+)-enantiomer in 20-40 % optical purity while the raffinate was rich in (-)-enantiomer (enantiomeric excess= 44.7 %). Further purification of the extracts can be carried out by multiple extraction (Figure 3b). We have succeed to separate the *cis*-chrysanthemic acid mixture in a single extraction step with excellent enantiomeric excess for the (-)-enantiomer (greater than 95 %). The enantiomeric excess of the (+)-enantiomer was 90 % after three subsequent extraction. The resolution of ibuprofen was less efficient. The

maximum enantiomeric excess of the (-)-enantiomer in the first extract was 44.4 %. Multiple extraction (two extraction steps) resulted (+)-enantiomer in 52 % enantiomeric excess.

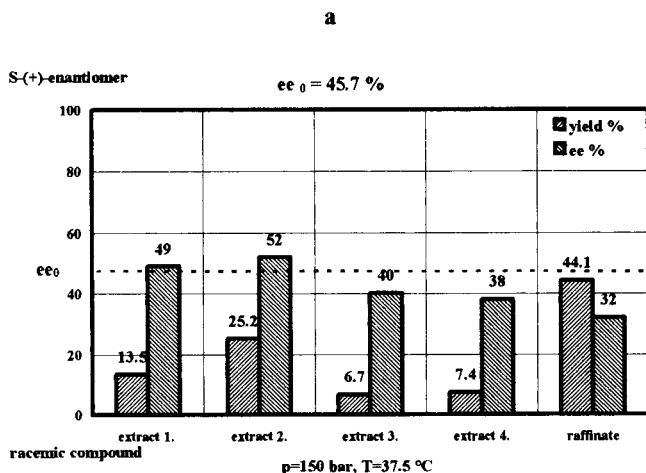
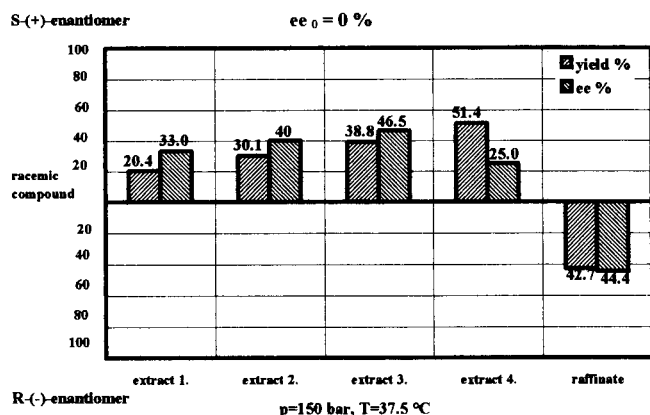


Figure 3. Resolution of racemic ibuprofen by SFE using *R*-(+)-1-phenylethylamine
a: simple extraction **b:** multiple extraction

The pressure of the carbon dioxide (in the range of 90-150 bar) was found to have direct effect on the yield. Figure 4a shows the effect of the pressure on the extraction curves of ibuprofen. All four runs were performed at 38.5°C . When the pressure was increased from 90 bar to 150 bar the carbon dioxide consumption was reduced to about 1/5 times. The enantiomeric excess of the extracts obtained from single extraction increased by 1.4 times for both acids (Figure 4b).

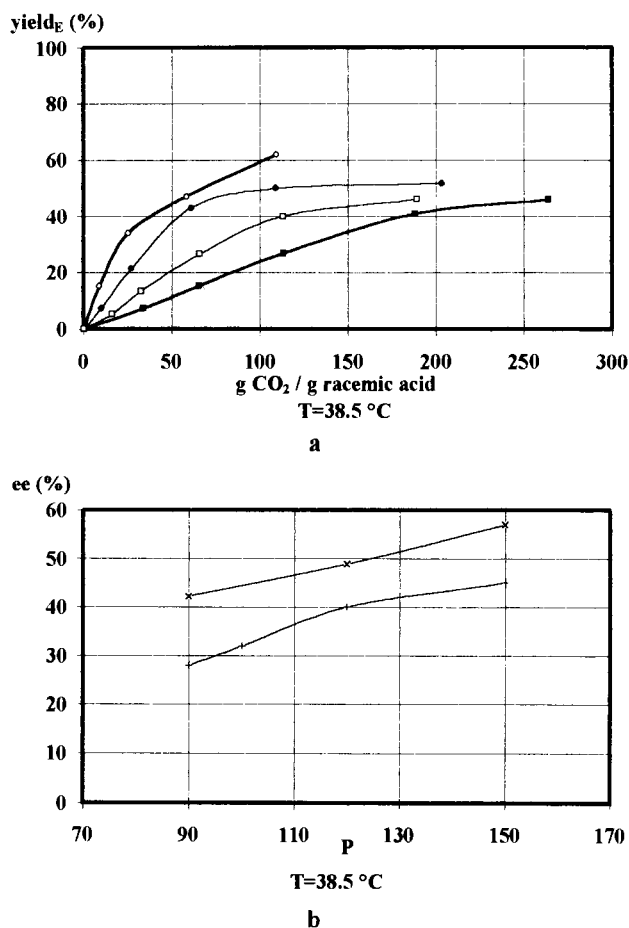


Figure 4. Effect of the pressure on the extraction curve (pressure: ○ 150 bar ● 120 bar □ 100 bar ■ 90 bar) and b) on the enantiomeric excess ((x *cis*-chrysanthemic acid + ibuprofen)

The effect of the temperature was investigated only in the supercritical range (32.5-50 °C). A rise in temperature at constant pressure led to an increase in extraction yield (Figure 5a). Similar temperature effects was observed for *cis*-chrysanthemic acid. The temperature dependency of enantiomeric excess of the extracts obtained from single extraction was different for the different acids. The enantiomeric excess of the *cis*-chrysanthemic acid extracts were 38 % and 75 % at temperatures 47 °C and 32 °C respectively. The enantiomeric excess of the ibuprofen was independent of the temperature (Figure 5b).

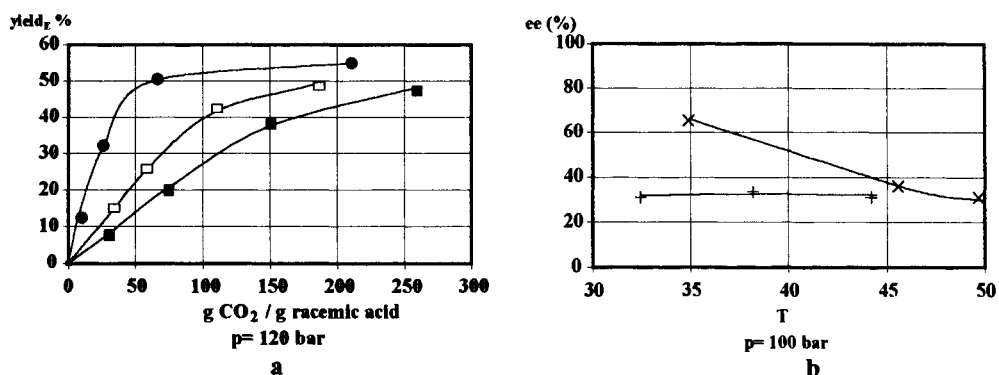


Figure 5. Effect of the temperature a) on the extraction curve (temperature: ● 32.5 °C □ 38.5 °C ■ 44 °C) and b) on the enantiomeric excess ((x *cis*-chrysanthemic acid + ibuprofen)

The racemic acids were mixed with the resolution agents in different molar ratios (from 0.25 to 0.75 base/acid ratios). A rise in molar ratio resulted in a decrease in the yield (Figure 6a) and an increase in enantiomeric excess. (Figure 6b)

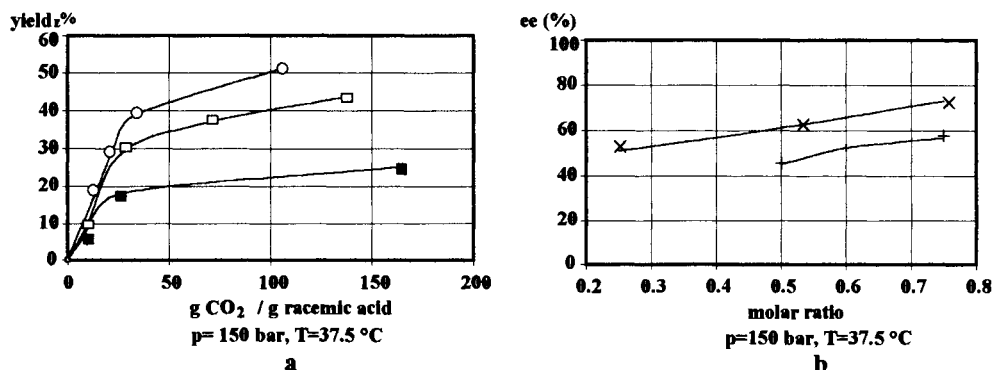


Figure 6. Effect of the molar ratio a) on the extraction curve (molar ratio: ○ 0.5 □ 0.6 ■ 0.75) and b) on the enantiomeric excess ((x *cis*-chrysanthemic acid + ibuprofen)

REFERENCES

1. Pasteur, L. *Ann. chim, et phys.*, **1848**, 24, 442.
2. Sheldon R. A. *Chirotechnology: Industrial Synthesis of Optically Active Compounds*, Marcel Dekker Inc., New York, **1993**.
3. Jacques, J.; Collet, A.; Wilen, S.H. *Enantiomers, Racemate and Resolutions*, Wiley and Sons, Inc., New York, **1981**.
4. Simándi, B.; Sawinsky, J.; Kemény, S.; Fogassy, E.; Ács, M.; Szili, T. *Proceedings of the International Symposium on Supercritical Fluids*, Strasbourg, **1994**, 2, 153.
5. Fogassy, E.; Ács, M.; Szili, T.; Simándi, B.; Sawinsky, J. *Tetrahedron Lett.* **1994**, 35, 257.

Extraction of Useful Components from Herbs using Supercritical CO₂: Experimental Findings and Data Modelling

Regina Santos^a, Tiejun Lu^a, Lars Schlieper^a, Michael B. King^a and João Bastos^b

^a School of Chemical Engineering, University of Birmingham, B15 2TT, UK

^b Faculdade de Engenharia da Universidade do Porto, Departamento de Engenharia Quimica, 4099 Porto Codex, Portugal

ABSTRACT

Extraction of Thyme and Rosemary with CO₂ at 25 and 40°C and pressures up to 250 bar is described and the results modelled, Single Sphere Models being best. Good data fits were obtained for both herbs when effective diffusivities D_e were fitted at each temperature and pressure but variations of D_e with temperature and pressure were physically more convincing for Thyme.

1. INTRODUCTION

This work is part of an EC funded study (1) of the best techniques for extracting saleable components from *Thymus zygis*, a herb which will survive in arid conditions where other plants are difficult to grow. This is a collaborative study involving participants from Portugal and France as well as England (2).

Several extraction techniques are being studied, but the work described in the present paper is limited to extraction of *Thymus zygis* (Thyme) and *Rosmarinus officinalis* (Rosemary) with compressed CO₂ and the modelling of the data obtained. The latter aspect is important if the data are to be 'scaled up' with a view to the design and costing of potential processes.

The herbs came from Portugal and had been sun dried but sufficient water remained in the dried stems and leaves to produce a volume of aqueous extracts which often exceeded that of the essential oils. Initial water contents for Rosemary and Thyme were 8.14% and 8.59% respectively. The residual water content after extraction were 1.85% for Rosemary and 3.53% for Thyme.

Both an aqueous phase and an oily phase (including waxes and essential oils) were extracted from the herbs. These were collected separately as described in the next section. The essential oils in the oily extract were camphor, verbenone, β -myrcene, 1,8 cineole and limonene for Rosemary and thymol, geraniol and geranyl acetate, carvacrol and borneol for Thyme.

Three models were used to simulate the observed extraction rates for the oily components. Each employed the effective diffusivity D_e as an adjustable parameter. They were the Characteristic Time Model (3) two other published models here designated Single Sphere Models I (4,5) and II (6). In these models it is assumed that the solute is extracted from a particulate bed composed of porous

inert spheres which are all at the same stage of extraction and that the solute dissolves readily in the CO₂ within the porous structure. The last-named assumption is not unrealistic when applied to the early stages of the extraction of essential oils from herbs (for the most part these oils are quite highly soluble in CO₂). In the later stages however, the proportion of heavier (and less soluble) components in the extracts increases and the physical basis for the models, is then less clear. The rate of extraction of material from a given sphere is taken to be limited only by the rate of pore diffusion into the bulk gas phase (in the case of model I) or by pore diffusion and the resistance to mass transfer offered by a surface film (in the case of model II).

Single Sphere Model I: The problem of diffusion of matter from a sphere initially at a uniform concentration when the surface concentration is maintained constant has been solved by Crank (7) and his equation (6.20) is (on substituting D_e for D) the same as the expression for the mass extracted as a function of time given by single sphere model I.

$$\frac{m}{m_0} = \left[1 - \frac{6}{\pi^2} \sum_{n=1}^{\infty} \left(\frac{1}{n^2} \right) e^{-\frac{D_e n^2 \pi^2 t}{R^2}} \right] \quad (1)$$

D_e here is the effective diffusivity of the solute in the pores, t is the extraction time and R is the radius of the spheres, m is the mass of material extracted up to time t and m_0 is mass of extractable material initially present (In Crank's notation $m_0 = M_{\infty}$, the mass that would be extracted over an infinite extraction period). Since all particles are assumed to be at the same stage of extraction, Eq (1) can be applied equally to extractions from a single sphere and from an assembly of particles in a bed, provided the boundary conditions are satisfied. According to Eq (1) m/m_0 should be universal function of t/τ where:

$$\tau = \frac{R^2}{D_e \pi^2} \quad (2)$$

When using Eq (1) for data fitting the summation to infinity was carried through until the difference between one term and the next fell below 0.0001. Physically D_e in Eq (1) would be expected to be proportional to the average of the diffusion coefficient of the extracted components in the extractant gas, the constant of proportionality being dependent on pore characteristics and porosity. It should therefore be an increasing function of temperature and either a decreasing function of pressure or independant of pressure, depending on whether pore diffusion is predominately molecular or Knudsen in type. In order to compare this model with experimental results values are required for m_0 and τ for the given herb and conditions. These may either both be fitted to the data directly or alternatively an estimate for m_0 may be obtained from tests with other solvents in which case only τ need be fitted to the data. Having determined τ in this way D_e may be estimated from it using Eq (2) with experimental values of R .

Single Sphere Model II (Equations 4, 5, 8, 9 and 10 in reference 6): In this model allowance is made for the resistance to mass transfer offered by the surface film surrounding the herb particles. The mass transfer coefficient k_f was obtained from correlations proposed by Catchpole et al (8, 9) for mass transfer and diffusion into near-critical fluids. An average of the binary diffusivities of the major essential oil components present was used in calculating k_f (these diffusivities were all rather similar because of their similar structures).

Characteristic Time Model: This model was developed by Reverchon and Osséo in 1994. As in model I it is assumed that the extraction is uniform along the bed (and in the form used) that the external film resistance can be neglected (see Equations 8 and 9 in reference 3).

2. MATERIALS AND METHODS

The extraction equipment used is shown in Figure 1. The CO₂ stream leaving the extractor vessel (V) contains dissolved material from the bed in solution and is decompressed in two stages (to 8 barg and to ambient pressure) at valves X and Y, throwing dissolved material out of solution. Extract collectors (at M and R) following the two pressure reductions are maintained at about ambient temperature and -85°C respectively. The extraction proceeds in stages. At the end of each stage, volatile material deposited in the medium pressure collector M and linking piping is transferred to R using a warm air stream. Likewise less volatile material not collected initially at M is washed from the first expansion valve and the tubing between this and M using hot acetone solvent.

In the (usually brief) intervals between extraction stages the beds were allowed to stagnate at the appropriate temperature and pressure. Tests on the beds of Thyme and similar materials in which we have varied the stagnation and flow periods over wide ranges have shown that, for these systems, it is the flow time of the CO₂ which determines the extent of extraction, *ie* that extraction during the periods of stagnation is negligible for our equipment within the accuracy of our experiments.

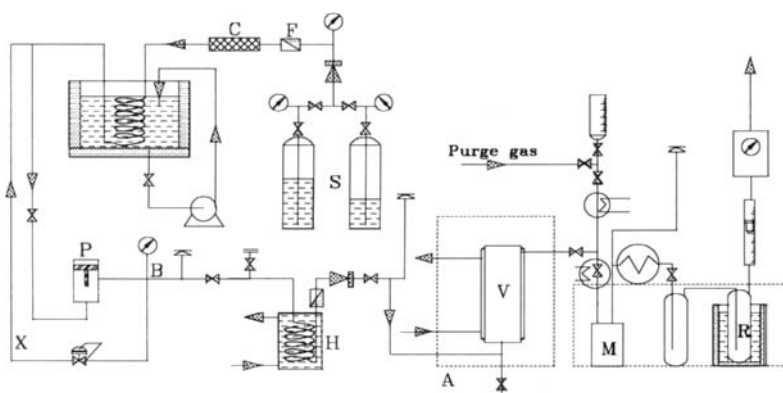
Two grades of CO₂ were used, an industrial grade (99.8% purity BOC grade LQ) and a higher grade (99.995% purity BOC Grade N4.5(CP)). Most of the impurity in the industrial grade is water. Only data for CP CO₂ are reported here. Industrial grade gave significantly (about 20%) higher yields for both Thyme and Rosemary at 200 and 250 bar and 40°C. This was probably due to the higher water content of this grade but this is still to be confirmed.

A leaf/flower mixture (mostly leaf) was used for the extraction tests on Rosemary. A leaf/stalklet mixture (54% by weight leaf and 46% thin stalklets) in which the stalklets had been cut into 0.5 cm lengths was used for most tests on Thyme. However two tests were carried out in which leaves only were extracted.

Apart from Thyme extraction (25°C) and Rosemary extraction (40°C) at 100 bar (with flow rates 450 g hr⁻¹ and 350 g hr⁻¹ respectively) the CO₂ flow rates used were 505 ± 15 g hr⁻¹ in the Rosemary extractions and 360 ± 11 g hr⁻¹ in the Thyme extractions. The bed diameter was 30.5 mm.

Representative samples of the pre-treated material were analysed for water content for each herb using a Dean and Stark equipment and also for content of "oily" material (essential oils + natural oils + waxes) using the method of Bligh and Dyer (10). Samples were also subjected to a sieving procedure and examined microscopically to determine the range of sizes and shapes present. Samples of the residue material were analysed for water content.

Figure 1: Flow Diagram of the Extraction Equipment



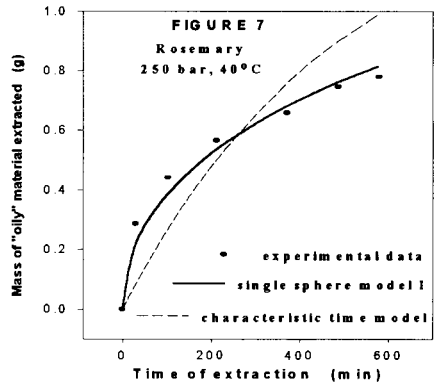
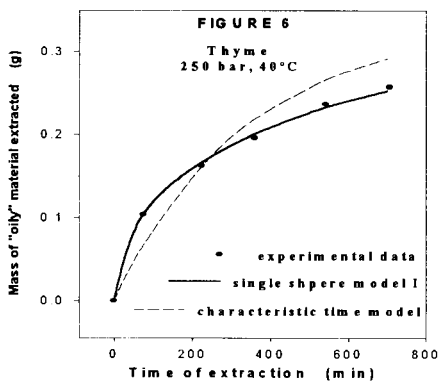
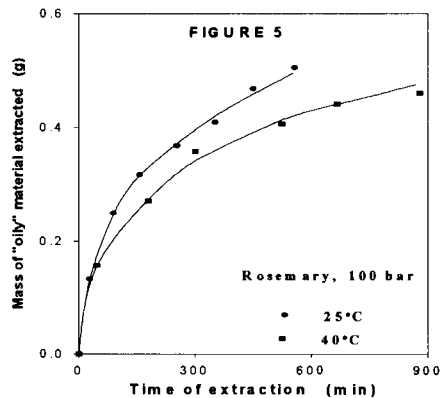
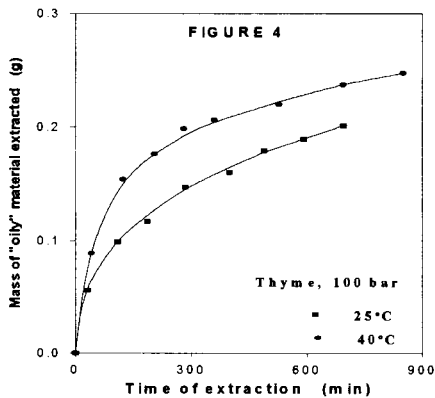
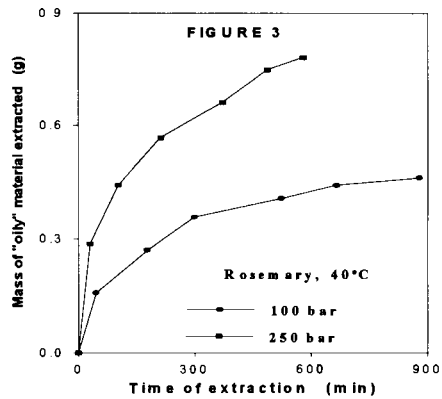
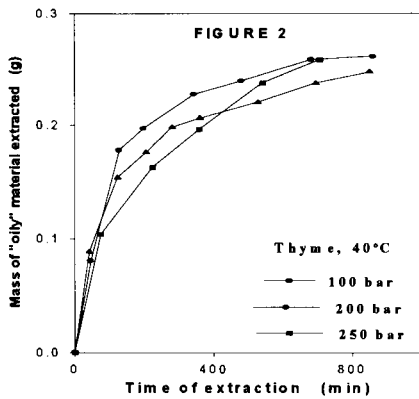
3. RESULTS AND DISCUSSION

3.1. Effects of pressure and temperature on extraction of "oily" material from 20g herb samples (CP grade CO₂ unless otherwise stated)

The effect of pressure in range 100 to 250 bar for a temperature of 40°C is shown in Figures 2 and 3 for Thyme and Rosemary respectively. It is seen that whereas an increase in pressure beyond 100 bar produced only small changes in the mass of Thyme collected, a substantial increase occurred with Rosemary. (A similarly large increase was also observed between 200 and 250 bar in less detailed tests with *Origanum virens* (2)).

Typical extraction curves for Thyme and Rosemary at 25 and 40°C for an extraction pressure of 100 bar are shown in Figures 4 and 5 respectively where an increase in yield with temperature is shown for Thyme only. As pointed out in section 3.2., the behaviour of Thyme is more in accord with the premises of Single Sphere theory than is that of Rosemary.

In the leaf-only tests for Thyme (not reported in detail) the yield was about 30% higher than for the leaf-stalklets mixtures, implying a stalklet yield about half of that for the leaf.



3.2. Data modelling (Nomenclature as in Eqs (1) and (2)).

For Thyme and Rosemary the values adopted for m_0 for 20g samples were 0.333 and 1.44g respectively at all temperatures and pressures considered. The particle radii were 1.40 and 1.62 mm. Based on these radii "best fit" values for D_e in the three models listed in the introduction were deduced from the experimental data and "best fit" curves were generated as in Figures 6 and 7.

The Characteristic Time Model was always found to give the worst fit and the Single Sphere Model II (which is not shown and which allows for film resistance) was not found to be appreciably better than the computationally simpler Model I for these systems. The values of D_e obtained were about two orders of magnitude lower than the estimated binary diffusivities.

In the case of the leaf/stalklet mixture of Thyme at 40°C, for example D_e from the first model was about $5 \times 10^{-12} \text{ m}^2\text{s}^{-1}$ at each of the pressures 100, 200 and 250 bar. At 25°C and 100 bar the value was about $2.4 \times 10^{-12} \text{ m}^2\text{s}^{-1}$. The values of D_{12} for a typical essential oil in CO₂ at 40°C and the above three pressures were estimated (9) to be 240, 140 and $130 \times 10^{-10} \text{ m}^2\text{s}^{-1}$ and, at 25°C and 100 bar, $140 \times 10^{-10} \text{ m}^2\text{s}^{-1}$.

In the case of Rosemary leaves, the values of D_e required varied more widely with temperature and pressure (values range from about $2.3 \times 10^{-13} \text{ m}^2\text{s}^{-1}$ at 50°C and 100 bar, $7 \times 10^{-13} \text{ m}^2\text{s}^{-1}$ at 40°C and 100 bar to $3 \times 10^{-12} \text{ m}^2\text{s}^{-1}$ at 40°C and 250 bar). We believe that the physically unreasonable rise in D_e with pressure at 40°C may be due to incomplete miscibility of some of the extracted components with supercritical CO₂ at 100 bar with consequent break down in model I for this herb at this pressure. However when D_e was fitted at each pressure and temperature considered a good representation of the data was obtained.

In the case of Thyme, Model I is probably adequate for interpolation and extrapolation purposes.

References

1. Report for the Commission of the European Communities Directorate General for Agriculture VI; AIR3-CT 93-0818; Vegextract "Extraction of Useful Food and Cosmetic Ingredients of Vegetable Origin".
2. Esquivel, M, Sousa, C, Rodrigues, M, Bernardo-Gil, MG, Empis, JA, Moldão-Martins, M, Beirão da Costa, ML, Lu, T, Schlieper, L, Santos, R, King, MB, Bastos, J, Rouzet, M. (1996) *3eme Colloque sur les Fluides Supercritiques*, Grasse, France, p 155.
3. Reverchon, E and Osséo, E (1994) *3rd Int. Symp. Supercrit. Fluids*, p 189
4. Spiro, M and Kandiah, M (1990) *Int. J. of Food Sci. and Tech.* **25**, 328.
5. Bartle, KD, Clifford AA, Hawthorne, SB, Langenfeld JJ, Miller, DJ and Robinson, RJ (1995) *J. Supercrit. Fluids* **3**, 143.
6. Reverchon, E, Donsi, G and Osséo, LS (1993) *Ind. Eng. Chem. Res.* **32**, 2721.
7. Crank, J (1975) *The Mathematics of Diffusion* Claverdon, Oxford, p 91.
8. Catchpole, O, Simões, P, King, MB and Bott, TR (1990) *2nd Int. Symp. on High Pressure Chemical Engineering*, Erlangen, Germany, p 153.
9. Catchpole, OJ and King, MB (1994) *Ind. and Eng. Chem. Research*, **33**, 1828
10. Bligh, EG and Dyer, WJ (1959) *Can. J. of Biochemistry and Physiology* **37**, 911.

Application of a Generalized van der Waals Equation of State to Several Non-polar Mixtures at High Pressures

Nguyen Van Nhu^a and U. K. Deiters^b

^aInstitute of Technical Chemistry, Technical University Munich, Lichtenbergstr. 4,
D-85747 Garching, F. R. Germany

^bInstitute of Physical Chemistry, University at Cologne, Luxemburger Str. 116,
D-50939 Köln, F. R. Germany

A recently developed equation of state on the basis of the generalized van der Waals model (GvdW-EOS) has been applied to the calculation of thermodynamic properties of mixtures. Only one adjustable mixing parameter for the critical temperature of the equivalent substance is required. Good agreement with experimental data for vapor-liquid and liquid-liquid equilibria has been obtained over a large temperature range for 29 binary mixtures. The agreement of mixture volumes is also satisfactory. Comparison with the Trebble-Bishnoi-Salim (TBS) equation showed that predictions of volumetric and the liquid-liquid phase equilibrium data are significantly better with the new equation of state, especially at very high pressures.

1. INTRODUCTION

Equations of state play a central rôle in chemical engineering design, especially for the calculation of phase equilibrium and thermodynamic properties at elevated temperatures and pressures. A generalized van der Waals equation of state (GvdW-EOS) for non-polar substances has been proposed recently [1] and applied successfully to the mixture methane + ethane [2]. This work presents in short the application to several binary non-polar mixtures with improved mixing rules. The details will be presented in forthcoming publication [3]. This work also describes the application of the GvdW-EOS to the prediction of the pVT -behavior at very high pressures.

2. FORMULATION OF THE EQUATION OF STATE

The GvdW equation of state contains a hard repulsive term, a van der Waals attractive term linear in density, and a correction term for medium and low densities. The compressibility factor Z is written as

$$Z = Z_h - \frac{a}{v^*} \cdot \frac{y}{RT} + Z_{\text{corr}} \quad (1)$$

Z_h is an expression for hard convex bodies[4]:

$$Z_h = \frac{1 + (3\alpha - 2)y + (3\alpha^2 - 3\alpha + 1)y^2 - \alpha(6\alpha - 5)y^3}{(1 - y)^3} \quad (2)$$

where $y = v^*/v$ is a reduced density and α is a measure of molecular anisotropy. It is calculated from v^* with the help of a modelled geometric core of the molecule given by chemical intuition (rod, disc, polyhedron, prism, etc.) [5, 6]. A universal correlation for the temperature dependence of the hard convex body volume is used, hence v_0^* , the hard convex body volume at zero temperature, is the only adjustable parameter in Z_h . The attractive parameter a/v^* contains mainly the critical temperature, α_c , and the parameter β for an "energetic anisotropy":

$$\frac{a}{v^*} = RT_c \left[12.8 + 9.6(\alpha_c - 1) + 12.03\beta f(\tilde{T}) \right] \quad (3)$$

where α_c denotes α at T_c ; $f(\tilde{T})$ is an universal function of the reduced temperature $\tilde{T} = T/T_c$. β is the only adjustable parameter in the attractive term.

The expression Z_{corr} is the correction for medium and low densities:

$$Z_{\text{corr}} = y \left[(b + cy) \exp \left(- \left(\frac{y}{0.119} \right)^2 \right) + w \exp \left(- \left(\frac{y - y_{\text{rd}}}{0.142} \right)^2 \right) \right] \quad (4)$$

Z_{corr}/y is the sum of two Gaussians, the first centered at $y = 0$ to ensure the correct behavior in the limit of zero density, and the second centered at the rectilinear diameter y_{rd} to provide the correct value of residual Helmholtz energy at high density. The temperature dependence of y_{rd} is given universal [2]. The parameters b and c , which determine the second and third virial coefficients, are given universally for non-polar substances [3]. The pre-exponential factor w has a dominating influence on the vapor pressure. Its temperature dependence requires two substance-specific correction parameters w_1 and w_2 .

To summarize, the GvdW-EOS contains 4 adjustable parameters: v_0^* , β , w_1 , and w_2 . The adjustable parameters for the 11 substances investigated are listed elsewhere [3].

3. MIXING RULES

The mixing rules for the hard convex body part of the GvdW-EOS are given by theory [7].

The most significant parameter for the attractive part of the GvdW-EOS is the critical temperature. For the mixture, this is calculated for an "equivalent substance" as in the previous paper [2]:

$$T_{c,\text{es}} = \sum_i \sum_k x_i x_k T_{c,ik} \quad (5)$$

$$T_{c,ik} = \frac{1}{2} (T_{c,ii} + T_{c,kk}) \cdot \xi \quad (6)$$

Here ξ , the only adjustable mixture parameter, is treated as independent of temperature and composition. The mixing rules for “energetic anisotropy” is

$$\left[\beta f \left(\frac{T}{T_{c,es}} \right) \right]_{\text{mix}} = \sum_i \sum_k x_i x_k \beta_{ik} f \left(\frac{T}{T_{c,ik}} \right) \quad (7)$$

$$\text{with } \beta_{ik} = \frac{1}{2}(\beta_{ii} + \beta_{kk})$$

Finally, the mixing rules for the parameters of the medium and low density correction are

$$w_{1,\text{mix}} = \sum_i x_i w_{1,i} \quad (8)$$

$$w_{2,\text{mix}} = \sum_i x_i w_{2,i} - 2 \sum_i \sum_{k < i} x_i x_k K_{w,ik}^4 \quad (9)$$

where $K_{w,ik}$ is a universal function:

$$K_{w,ik} = \frac{T_{c,ii} v_{c,ii}^* - T_{c,kk} v_{c,kk}^*}{T_{c,ii} v_{c,ii}^* + T_{c,kk} v_{c,kk}^*} \quad (10)$$

4. RESULTS

The binary mixture parameter ξ has been fitted to VLE data for 29 systems; its values are in Table 1. It should be noted that ξ is independent of temperature and always very close to unity. The calculation of phase equilibria was performed by means of the algorithm of Deiters [8, 9]. The reproduction of VLE data and the predictions of LLE data, of excess volumes, of virial coefficients are very good for all 29 binary mixtures investigated [3].

Table 1

Adjustable mixture parameter for the systems investigated. The values were obtained from VLE data by minimizing r.m.s. deviations in mole fractions of coexisting phases.

mixture	ξ	mixture	ξ	mixture	ξ
N ₂ + Ar	0.980	Ar + CH ₄	1.008	C ₂ H ₆ + C ₃ H ₈	0.997
N ₂ + O ₂	0.990	CH ₄ + C ₂ H ₄	0.982	C ₂ H ₆ + C ₄ H ₁₀	1.005
N ₂ + CH ₄	0.950	CH ₄ + C ₂ H ₆	1.021	C ₂ H ₆ + C ₅ H ₁₂	1.012
N ₂ + C ₂ H ₄	0.949	CH ₄ + C ₃ H ₈	1.042	C ₂ H ₆ + C ₆ H ₆	1.010
N ₂ + C ₂ H ₆	0.989	CH ₄ + C ₄ H ₁₀	1.060	C ₃ H ₆ + C ₃ H ₈	1.003
N ₂ + C ₃ H ₆	1.010	CH ₄ + C ₅ H ₁₂	1.072	C ₃ H ₈ + C ₄ H ₁₀	1.005
N ₂ + C ₃ H ₈	1.003	CH ₄ + C ₆ H ₆	1.045	C ₃ H ₈ + C ₅ H ₁₂	1.008
N ₂ + C ₄ H ₁₀	1.025	C ₂ H ₄ + C ₂ H ₆	0.995	C ₃ H ₈ + C ₆ H ₆	1.002
N ₂ + C ₅ H ₁₂	1.064	C ₂ H ₄ + C ₄ H ₁₀	0.970	C ₅ H ₁₂ + C ₆ H ₆	0.980
N ₂ + C ₆ H ₆	1.020	C ₂ H ₄ + C ₆ H ₆	1.025		

Table 2

Comparison of molar volumes of liquid nitrogen(1) + methane(2) predicted with the GvdW and the TBS equations of state with experimental data [10].

x_1	T/K	p/MPa	$V_m/\text{cm}^3\text{mol}^{-1}$		
			exp.	GvdW	TBS
0.000	110.09	1.45	37.639	37.565	37.059
		17.50	36.494	36.504	36.217
		48.00	35.033	35.088	35.220
		76.90	34.009	34.124	34.617
		130.00		32.840	33.901
		200.00		31.655	33.326
	120.00	1.00	39.019	38.987	38.301
		9.00	38.241	38.246	37.645
		42.10	36.094	36.176	36.024
		91.60	34.173	34.335	34.815
		128.10	33.162	33.395	34.274
		200.00		32.051	33.587
1.000	110.09	1.90	44.656	44.679	45.056
		10.70	40.645	40.613	39.608
		56.40	34.500	34.516	33.560
		93.20	32.442	32.479	32.033
		114.50	31.590	31.643	31.473
		137.30	30.852	30.909	31.014
		200.00	29.520 ^a	29.412	30.168
	120.00	2.80	52.139	51.733	55.581
		13.80	42.561	42.487	41.632
		48.60	36.347	36.316	35.145
		99.30	32.962	32.949	32.461
		117.30	32.208	32.187	31.936
		137.40	31.497	31.473	31.471
		200.00	29.940 ^a	29.829	30.500
0.503	110.09	1.45	39.715	39.619	38.566
		10.20	38.385	38.255	37.202
		27.90	36.523	36.452	35.594
		78.10	33.690	33.666	33.513
		108.10	32.586	32.635	32.861
		137.80	31.692	31.836	32.397
		200.00		30.581	31.740
	120.00	3.30	41.731	41.620	40.640
		20.70	38.661	38.561	37.472
		76.30	34.553	34.523	34.172
		107.50	33.283	33.290	33.351
		137.70	32.342	32.380	32.796
		200.00		30.995	32.037

^a data from IUPAC table [11]

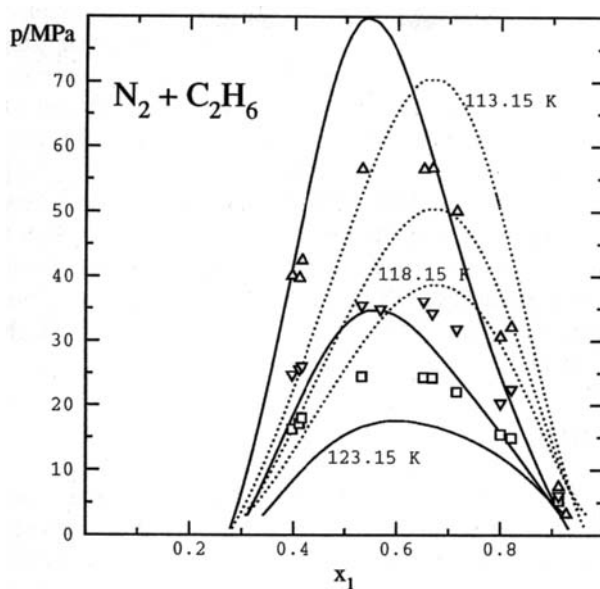


Figure 1. Liquid-liquid equilibria (LLE) for nitrogen + ethane. —, new EOS; ···, TBS equation; symbols, exp. data [12, 13].

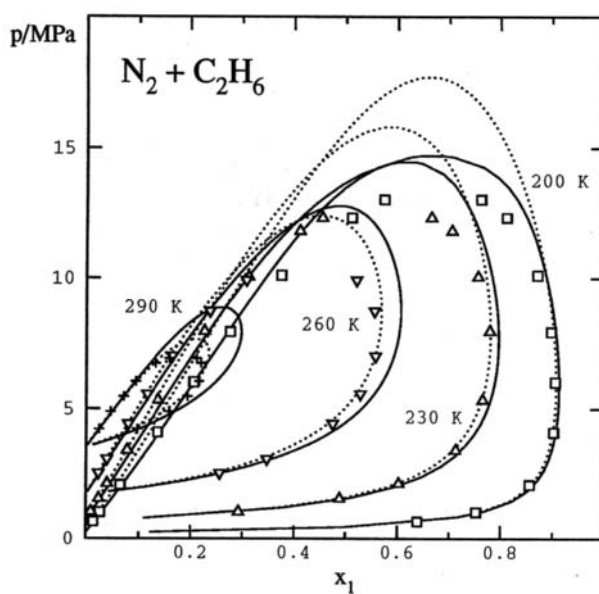


Figure 2. VLE isotherms for nitrogen + ethane. —: new EOS; ···, TBS equation; symbols, exp. data [14].

For comparison, we have also performed calculations with the Trebble–Bishnoi–Salim (TBS) equation, which contains also 4 adjustable parameters, and which is regarded as one of the best cubic equations of state [15]. Here a single binary interaction parameter was fitted to VLE data, too. We obtained a value of 0.035 for nitrogen + methane, and 0.038 for nitrogen + ethane. In the case of the nitrogen + ethane mixture, while the VLE calculations of both equations of state turn out to be of similar quality (the binary interaction parameters were fitted to VLE data), the prediction of the liquid–liquid phase equilibria reveals differences: The TBS calculations give a too high nitrogen content in the nitrogen-rich liquid as well as for the consolute critical points (Figs. 1–2). The predictions of mixture volumes for nitrogen + methane are presented in Table 2. While the GvdW-EOS shows very good agreement at all temperatures and pressures, the TBS-EOS gives too large results at high pressures; also the slopes of isotherms are too high.

5. ACKNOWLEDGMENTS

We express our gratitude to the A. v. Humboldt Foundation for partial support of this work, and to the Deutsche Forschungsgemeinschaft for financial support in the final part. We especially wish to thank Prof. Dr. Friedrich Kohler for many helpful discussions.

REFERENCES

1. Nguyen Van Nhu, G. A. Iglesias-Silva, and F. Kohler, *Fluid Phase Equil.* 91 (1993) 215–237.
2. Nguyen Van Nhu and F. Kohler, *Fluid Phase Equil.* 105 (1995) 153–171.
3. Nguyen Van Nhu and U. K. Deiters, *Fluid Phase Equilibria* . in print.
4. T. Boublík, *Mol. Phys.* 42 (1981) 209–216.
5. T. Kihara, *Rev. Mod. Phys.* 25 (1953) 831–843.
6. P. Svejda and F. Kohler, *Ber. Bunsenges. Phys. Chem.* 87 (1983) 672–680.
7. T. Boublík, *Ber. Bunsenges. Phys. Chem.* 85 (1981) 1038–1041.
8. U. K. Deiters, *Fluid Phase Equil.* 19 (1985) 287–293.
9. U. K. Deiters, G. Hintzen, and M. Bluma, *Thermo-Paket: Anwendungen und Programmstruktur*. Ruhr-Universität Bochum, 1993.
10. S. W. B. Nunes da Ponte, M. and L. A. K. Staveley, *J. Chem. Thermodynamics* 10 (1978) 151–168.
11. S. Angus, K. M. de Reuck, and B. Armstrong, *Nitrogen*, volume 6 of *IUPAC International Tables of the Fluid State*. Pergamon, Oxford, 1979.
12. K. D. Wisotzki, *Fluid-Phasengleichgewichte und kritische Erscheinungen in den binären Systemen N_2 + Ethan, N_2 + Pentan und CF_4 + 2-Methylpropan zwischen 88 K und 313 K und bei Drücken bis 200 MPa*, Doctoral dissertation, Ruhr-Universität Bochum, 1984.
13. K. D. Wisotzki and G. M. Schneider, *Ber. Bunsenges. Phys. Chem.* 89 (1985) 21–25.
14. L. Grausø, A. Fredenslund, and J. Møllerup, *Fluid Phase Equil.* 1 (1977) 13–26.
15. P. H. Salim and M. A. Trebble, *Fluid Phase Equil.* 65 (1991) 59–71.

High-Pressure Phase Equilibria Data of Systems Containing Limonene, Linalool and Supercritical Carbon Dioxide

S.A.B. Vieira de Melo*, P. Pallado, A. Bertucco and G.B. Guarise

Università di Padova, Istituto di Impianti Chimici, Via Marzolo, 9 - 35131, Padova - Italy

A high-pressure circulation-type apparatus was designed and constructed to investigate the vapor-liquid equilibria (VLE) of systems containing limonene, linalool and supercritical carbon dioxide. VLE data of binary and ternary systems of these compounds can be determined in the ranges of pressure and temperature of interest for the deterpenation of cold-pressed orange oil. The preliminary results obtained for the binaries CO₂-linalool and CO₂-limonene were compared to data already published with acceptable accuracy and well correlated by a modified Soave-Redlich-Kwong (SRK) equation of state.

1. INTRODUCTION

Citrus essential oils are widely used as a raw material of flavour in food and perfumery industries. They are also called "cold-pressed oils" and contain more than 200 compounds which can be grouped in three fractions: the hydrocarbon terpenes (unsaturated compounds) that constitute the major amount (from 60 to 98% by weight) but have undesirable off-flavours characteristics; the oxygenated compounds (flavour fraction) that are directly responsible for the characteristic citrus flavour; and the non-volatile residues.

Usually, the terpenes are removed from the cold-pressed oils (deterpenation) to concentrate the flavour fraction, thus resulting in a more stable product with improved solubility in the alcoholic solvents used in food and perfume processing. Supercritical carbon dioxide extraction appears as a promising and alternative technique to refine cold-pressed citrus oils [1, 2, 3]. Potentially, it has the advantages that it can be carried out at mild temperatures, provides better yields and leaves no solvent residues.

A common practice to study each citrus oil is to consider it as a binary synthetic mixture of its two more important components [4, 5, 6, 7]. For instance, the cold-pressed orange oil is usually treated as a mixture of limonene and linalool, representing the terpene and the oxygenated fractions, respectively.

Several works have been done to study the application of the supercritical extraction technique but, from a thermodynamic point of view, there is still a major problem. It is concerned with the opposite tendencies of selectivity and yield; that is, high yields of terpenes

* S.A.B.V.M. gratefully acknowledges his financial support provided by the CNPq (Brazilian Council of Research and Technology). The financial support of the Italian MURST is also acknowledged.

extracted by supercritical CO₂ are obtained with low selectivities between these terpenes and the oxygenated compounds [8, 9, 10] and this fact has to be addressed properly yet.

Some binary phase equilibrium and solubility data of limonene and linalool with supercritical CO₂ can be found in the current literature [11, 12, 13, 14, 15]. However, the different ranges of pressure and/or temperature of these data cause difficulties and inaccuracies to calculate or predict the related compound selectivities.

In this work, the basis for a proper answer to the selectivity problem between the two cited compounds is set. For this purpose, a high-pressure vapor-liquid equilibria circulation-type apparatus was designed and constructed. Some vapor-liquid equilibria (VLE) data of the binary systems CO₂-limonene and CO₂-linalool were determined and compared with data available in the literature. The results obtained were accurately correlated by a modified SRK equation of state that avoids the use of critical constants [16].

The study of the ternary system CO₂-limonene-linalool is in progress and will be the matter of future work.

2. EXPERIMENTAL SECTION

2.1. Equipment and Procedure

The schematic diagram of the high-pressure vapor-liquid equilibrium circulation-type apparatus is shown in Fig.1. The main piece of the equipment is a high-pressure phase equilibrium cell of approximately 100 cm³. The apparatus includes a compressed-air actuated piston-pump that allows to circulate one or both phases to bring the vapor and liquid in close contact with each other. This pump, the cell and all the related valves were placed in a constant-temperature water bath to have and to keep uniformly the desired temperature.

The bath was turned on the day before the experiments. The equilibrium cell and all the lines were first evacuated. Then, the liquid heavy component was loaded from a scaled glass tank above valve V7. Carbon dioxide was finally pumped into the cell from a cooled storage unit through valves V1 and V3 until the desired level of pressure was attained. The pressure was measured by a Data Instruments pressure transducer model AB (range 5000 psi) with an accuracy of 0.1 bar. The temperature inside the cell was measured by a thermoresistance sensor (PT100Ω) within ± 0.1 °C.

The circulation of the vapor phase was initiated by starting up the air-compressed pump and about one hour was required to achieve the equilibrium condition. During this time, the temperature and pressure were recorded. Then, a small sample of the vapor phase was withdrawn through the third way of valve V5 to the sampling loop of the six-way valve V9. A similar procedure was done for the liquid phase through valve V6 to the sampling loop of the six-way valve V13. The volumes of 1 cm³ and 0.5 cm³ for the vapor and liquid loops, respectively, were small enough to insure a negligible pressure drop in the cell during the sampling. Subsequently, valves V9 and V13 were switched in order to decompress the loops through the expansion valves V11 and V15, which were heated properly. Glass traps were placed quite close to the expansion valves, cooled at -20 °C by a salt-ice mixture and filled with a calibrated amount of appropriated organic solvent (n-octane) to recover completely the heavy component. The organic solvent had been previously saturated with CO₂ to avoid its dissolution in the sample. The volume of CO₂ contained in the sample loops was measured by means of a burette connected to a liquid reservoir at atmospheric pressure. An inert liquid was chosen to prevent the absorption of CO₂ and the temperature of the gas inside the burette was

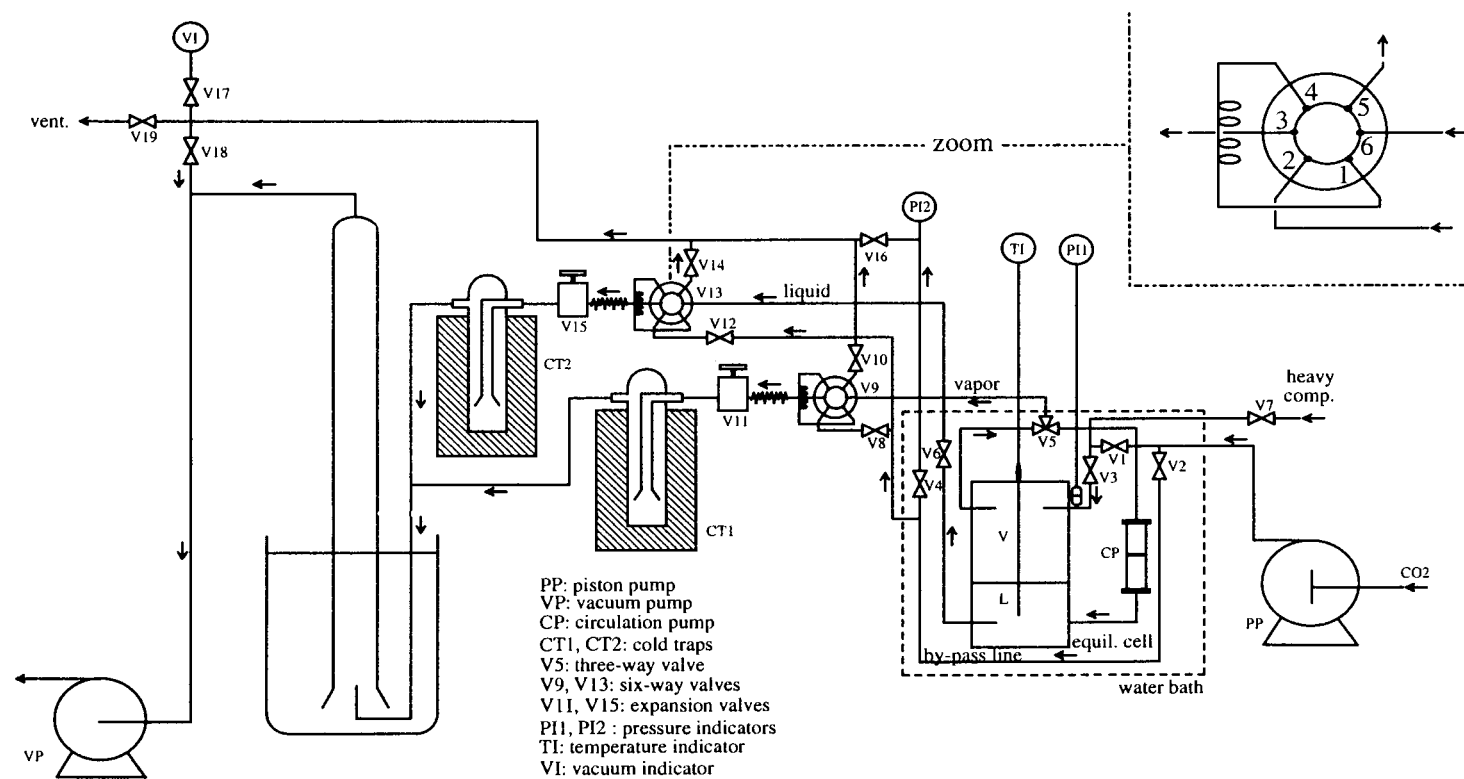


Figure 1. High-pressure vapor-liquid equilibria circulation-type apparatus.

measured. After recording the gas volume, supercritical CO₂ was flowed from the by-pass line through the sampling loops and the expansion valves. This was done to remove and recover completely the heavy component from the sample loops. The amount of heavy component trapped in the organic solvent was determined by gas chromatography in a GC mod. Shimadzu 14-A with a Flame Ionization Detector and a Column Chromosorb W-17W SA-476., with a dimethyl siliconic fluid as a stationary phase.

2.2. Materials

In these preliminary runs, Limonene (97%), Linalool (97%) and n-Octane (99%) purchased from Aldrich Co. were used without further purification. Carbon dioxide with a purity of 99,9% (supplied by Revoira srl) was used as received.

3. RESULTS AND DISCUSSION

3.1. Equilibrium data

As recalled above, for the system CO₂-linalool accurate data were recently published by Iwai et al. [14]. In order to test the presently proposed apparatus and procedure, this same system was first considered and measured. Some results are presented in table 1 and figure 2. It can be seen that the composition in the liquid phase is very close to the values of Iwai et al. [14].

Table 1
Vapor-Liquid Equilibria for CO₂ (1) + Linalool (2).

CO ₂ (1) + Linalool (2)			
Present data at 51 °C		Data of Iwai et al. at 50 °C	
P (bar)	X ₁	P (bar)	X ₁
66.6	0.5398	40.0	0.3449
69.1	0.5508	60.0	0.5167
94.9	0.7887	79.9	0.6906
		90.0	0.8062
		97.8	0.9420

For the system CO₂-limonene, the available data for the liquid phase refer to a pressure range different from that of CO₂-linalool. In particular, we have considered measurements by Matos et al. [11], which were taken at 45 and 50 °C, respectively. In order to investigate a larger pressure range, a temperature of 60 °C was studied. Some results of the liquid phase composition are summarized in table 2. The same results are presented also in figure 3, where it can be seen that an increase of temperature has a strong effect on the amount of CO₂ that solubilizes into the liquid phase. Particularly, this effect is more pronounced from 50 to 60 °C than from 45 to 50 °C.

Table 2
Vapor-Liquid Equilibria for CO₂ (1) + Limonene (2) at 60 °C.

CO ₂ (1) + Limonene(2)	
P (bar)	X ₁
75.4	0.5253
81.8	0.5782
89.0	0.6099
100.7	0.6626

3.2. Correlation

In order to correlate the results obtained, a modified SRK equation of state with Huron-Vidal mixing rules was used. Details about the model are reported in the paper by Soave et al. [16]. This approach is particularly adequate when experimental values of the critical temperature and pressure are not available as it was the case for limonene and linalool. Note that the flexibility of the thermodynamic model to reproduce high-pressure vapor-liquid equilibrium data is ensured by the use of the Huron-Vidal mixing rules and a NRTL activity coefficient model at infinite pressures. Calculation results are reported as continuous curves in figure 2 for the CO₂-linalool system and in figure 3 for CO₂-limonene. Note that the same parameters values were used to correlated the data of CO₂-limonene at 45, 50 e 60 °C.

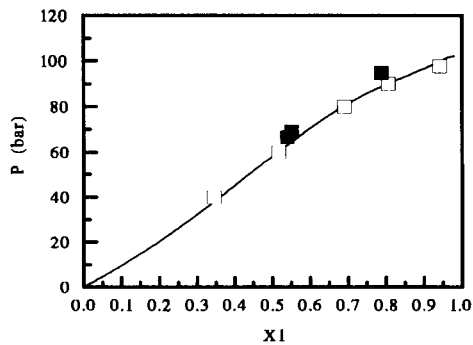


Figure 2. Vapor-liquid equilibria for CO₂ (1) + Linalool (2): ■ present data at 51 °C; □ data of Iwai et al. at 50 °C.

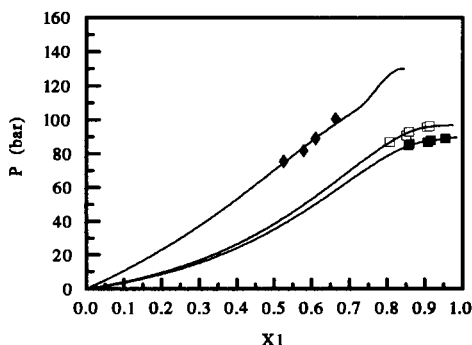


Figure 3. Vapor-liquid equilibria for CO₂ (1) + Limonene (2): ◆ present data at 60 °C; ■ data of Matos et al. at 45 °C; □ data of Matos et al. at 50 °C.

REFERENCES

1. Coppella, S.J. and Barton, P. (1987). In "Supercritical Fluids: Chemical and Engineering Principles and Applications. Ed. Squires, T.G. and Paulaitis, M.E., ACS Symp. Series 329, 202-212, Washington DC.
2. Temelli, F., Chen, C.S. and Braddock, R.J. (1988). Food Technology, June, 145-150.
3. Perre, C., Delestre, G., Schrive, L. and Carles, M. (1994). Proc. 3rd. Int. Symp. on Supercritical Fluids, vol.2, 465-474, Strasbourg.
4. Kalra, H., Chung, S.Y.-K. and Chen, C.-J. (1987). Fluid Phase Equil., 36, 263-278.
5. Sato, M., Goto, M. and Hirose, T. (1994). Proc. 3rd. Int. Symp. on Supercritical Fluids, vol.2, 83-88, Strasbourg.
6. Gironi, F. and Lamberti, L. (1994). Proc. 3rd. Int. Symp. on Supercritical Fluids, vol.2, 459-464, Strasbourg.
7. Vega-Bancel, A. and Subra, P. (1995). Proc. 3rd. Italian Conference on I Fluidi Supercritici e loro Applicazioni, 149-156, Trieste.
8. Temelli, F., O'Connell, J.P., Chen, C.S. and Braddock, R.J. (1990). Ind. Eng. Chem. Res., 29, 618-624.
9. Sato, Goto, Hirose (1995). Ind. Eng. Chem. Res., 34, 3941-3946.
10. Budich, M., Brunner, G., Hoffman, S. and Jung, S. (1996). Proc. 3^{ème} Colloque sur les Fluides Supercritiques, Grasse.
11. Matos, H.A., Azevedo, E.G., Simões, P.C., Carrondo, M.T. and Nunes da Ponte, M. (1989). Fluid Phase Equil., 52, 357-364.
12. Di Giacomo, G., Brandani, V., Del Re, G. and Mucciante, V. (1989). Fluid Phase Equil., 52, 405.
13. Gironi, F. and Lamberti, L. (1995). Proc. 3rd. Italian Conference on I Fluidi Supercritici e loro Applicazioni, 165-172, Trieste.
14. Iwai, Y., Hosotami, N., Morotomi, T., Koga, Y. and Arai, Y. (1994). J. Chem. Eng. Data, 39, 900-902.
15. Stahl, E., Gerard, D. (1985). Perfumer & Flavorist, 10, 29-37.
16. Soave, G.S., Bertucco, A., Sponchiado, M. (1995). AIChE Journal, 41(8), 1964-1971.

High - Pressure Extraction of Cork with CO₂ and 1,4 -Dioxane

Ana M. Miranda ^{a,b}, Ana S. Reis Machado^a, Helena Pereira^b and Manuel Nunes da Ponte^a

a - Instituto de Tecnologia Química e Biológica, Universidade Nova de Lisboa
Rua da Quinta Grande 6, Apartado 127, P-2780 Oeiras-Portugal

b - Departamento de Engenharia Florestal, Instituto Superior de Agronomia, Universidade
Técnica de Lisboa, P -1399 Lisboa Codex, - Portugal

ABSTRACT

The extraction of cork from cork-oak (*Quercus suber* L.) by high-pressure dioxane and supercritical CO₂ mixtures was studied at 170 bar and in the temperature range of 160°C - 180 °C. Suberin is preferably extracted, but extraction percentages were lower than 46%. Lignin extraction percentages are lower than 11%. Extraction selectivity did not change significantly with extracting fluid composition. The results so far obtained support the idea of the existence of an extensive polymeric system across the cell wall and the concept of a close interaction of suberin and lignin, which hinders lignin depolymerization and solubilization in the high-pressure fluid. Fourier transform infrared spectra of cork, extraction residues and extracts are also presented.

Key Words: Cork, high-pressure extraction, supercritical CO₂, 1,4-Dioxane, suberin

1. INTRODUCTION

Extraction of lignocellulosic materials with dioxane has been used for quite some time as a method for lignin isolation at atmospheric pressure (1) or, as recently reported, at high pressure and with supercritical CO₂ mixtures (2-5). In this case, it was possible to extract from wood lignin oligomers with a low degree of chemical modification; hemicelluloses were also depolymerized and extracted, but cellulose remained without significant mass losses.

Cork from the cork-oak (*Quercus suber* L.) differs chemically from wood, mostly by the presence of suberin as a major structural component (ca. 60% of extractive free cork) in addition to lignin and polysaccharides (6). The structure of suberin is not fully elucidated yet. It is a cross-linked polymer with a polyester linked aliphatic domain containing fatty acids, alcohols, hydroxyacids and diacids and a phenolic, probably lignin-like domain.

Recent work using the atmospheric dioxane extraction of cork has proved extremely difficult, yielding only small amounts of a lignin- enriched material (7). This was explained by the presence of suberin, a complex structure of phenolic and aliphatic domains and the interaction with lignin. Further work using a saponified cork stressed these arguments (8).

We report here the first results obtained in high-pressure extractions of cork with dioxane, CO₂ and dioxane - CO₂ mixtures seeking to obtain more information on the structure and interaction of cork cell wall components.

The effect of parameters, such as temperature and fluid composition on extraction yield and selectivity are reported. Fourier transform infrared spectra of cork, extraction residues and extracts are also presented.

2. EXPERIMENTAL

2.1. Apparatus

The apparatus consists of a flow through extraction system that can be operated at pressures up to 400 bar and temperatures up to 200°C. This apparatus was described elsewhere (2). Its main piece is a 19 cm³ reactor, where 4-5 g of 40-60 mesh milled cork were placed between two G3 fritted glass discs. The reaction mixture is expanded into a series of three 35 cm³ precipitation traps. A dual-head high pressure liquid pump was used to compress the solvent. One pump head was cooled with ice to pump liquid CO₂ while the other pump head was used for 1,4-dioxane.

1,4-dioxane proanalysis from Merck (99.5% min. purity) was used throughout the experiments. The water content of dioxane was less than 1%. Pure (99.995%) CO₂ used in this experiment was obtained commercially (Air Liquide, Lisbon).

To start a run, the heat was turned on and CO₂ was pumped at the desired flow rate. When both extraction temperature and pressure were reached, dioxane was pumped into the apparatus. Temperature stabilization was reached within two hours. The temperature gradient from the entrance to the end of the reactor was less than 5°C and the pressure was kept constant within 5 bar. The composition of the extracting fluid was kept constant during extraction within 2 % by adjusting the CO₂ flow rate.

Vapour-Liquid equilibrium measurements were performed for CO₂ +1,4- dioxane mixtures (9) . According to these data, all extractions were performed at conditions of pressure and temperature where the extracting mixture is monophasic.

2.2. Sample preparation and cork analysis

Cork from cork-oak (*Quercus suber* L.) was collected in a mill as residue obtained from the production of stoppers and a 40-60 mesh fraction was separated. This fraction was exhaustively extracted with dichloromethane, ethanol and water in a Soxhlet apparatus. High-pressure extractions were performed upon extractive -free anhydrous cork samples.

The methods used for the determination of chemical compositions of cork and high-pressure extraction residues are adapted from the standard methods used for wood(6). Suberin was determined in extractive-free material by methanolysis (6), 1.5 g sample was refluxed with 250 ml of 3% NaOCH₃ in CH₃OH for 3 h, filtered and the residue refluxed again with 100 ml CH₃OH for 15 min. After filtration the combined filtrates were acidified to pH 6 with 2 M H₂SO₄ and evaporated to dryness in a rotating evaporator. This residue was suspended in 100 ml H₂O and extracted three times with 200ml of CHCl₃. The combined extracts were dried over Na₂SO₄, filtered, evaporated and determined gravimetrically as suberin. The Klason lignin content was determined by a procedure adapted from the Tappi method T222-os-74 that uses smaller sample sizes (10) employing previously desuberinised material. The acid soluble lignin content was determined by ultraviolet absorption in the 200 -

208 nm region. Carbohydrate content was determined from hydrolysis liquors resulting from Klason lignin determinations by gas-liquid chromatography (GC) of the monosaccharides after derivatization to alditol acetates.

2.3. Fourier transform infrared spectroscopy (FTIR)

A Bio-Rad FTS 165 equipped with a DTGS detector was employed for recording the spectra using the KBr pellet technique. The resolution of the spectrometer is 4 cm^{-1} and the spectra were taken with 32 scans and a KBr pellet as background. SPECAC KBr spectroscopic grade was used. Both KBr and the samples were milled previously for 10 minutes in a Retsch ball-mill and placed in a oven at 105°C for 24 hours. KBr pellets were prepared with a sample concentration of 0.5%. Spectra of the following samples were taken : extractive-free cork, cork after being submitted to high-pressure extractions (extraction residues) and extracts obtained from high-pressure dioxane extractions. These extracts were isolated by the following procedure: extraction liquors were distilled under vacuum until dryness at 50°C to remove dioxane. The material was placed in a oven at 105°C for 24 hours.

3. RESULTS AND DISCUSSION

3.1. Effect of extraction temperature and extracting fluid composition

In Table 1 the chemical composition of the cork used in this work is presented. It shows that the material used contains lignocellulosic tissues, probably from the phloemic remains of the cork bark in the planks used for the production of stoppers. The extraction percentages of the cork constituents were calculated based on the amount of constituents initially present in the extractive - free cork

Table 1
Cork chemical composition.

	Cork
Extractives (%)	13.8
Suberin (%)	29.9
Klason Lignin (%)	25.3
Acid soluble lignin (%)	1.3
Polysaccharides (%)	29.0
Ashes (%)	1.4

Extractions with high-pressure dioxane at 170 bar and 0.41 g min^{-1} mass flow rate were carried out at three different temperatures, 160°C , 170°C and 180°C . Extraction mass losses for these extraction conditions were approximately constant and about 19%. In Figure 1 are depicted the extraction mass losses and extraction percentages of the several cork constituents as a function of temperature. Lignin contents represent the total lignin content (Klason lignin + acid soluble lignin). No significant variations of extraction percentages with temperature were observed. In these conditions suberin is preferably extracted. Polysaccharide and lignin extraction percentages are low. These results differ significantly from the ones obtained for wood (2), in which at 180°C total hemicellulose removal occurred

and cellulose extraction percentages higher than 60% were obtained while at temperatures lower than 180°C no significant cellulose mass losses occurred.

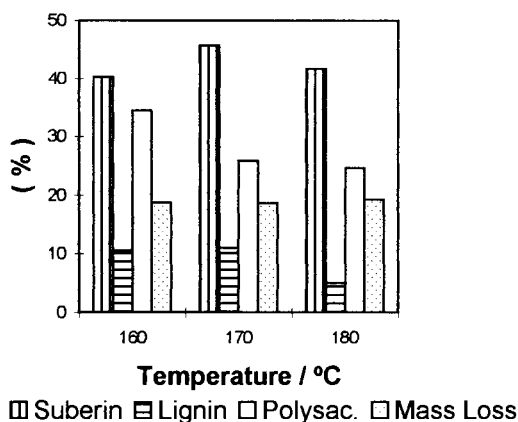


Figure 1. Extraction mass losses and extraction percentages of suberin, lignin and polysaccharides as a function of temperature for extractions carried out with dioxane at 170 bar and 0.41 g min⁻¹ mass flow rate.

Similar results were obtained for extractions carried out at 170°C, 170 bar using CO₂ (5.3 g min⁻¹) or dioxane - CO₂ mixtures (dioxane mass flow rate was kept constant and equal to 1.38 g min⁻¹) as extracting fluid. Extraction mass losses were in the range 5% - 15%. Lignin extraction percentages were lower than 6%. Suberin extraction percentages were in the range 30% - 39%. No significant change of selectivity with the composition of extraction fluid was noticed. Once again, a completely different trend was observed when wood was submitted to the same extraction conditions. In this latter case, selectivity towards lignin increased with increased dioxane content in the extracting mixture (2).

3.2. Characterization by Fourier transform infrared spectroscopy (FTIR)

In figure 2 the following FTIR spectra are presented: a - extractive-free cork, b - cork after being submitted to high-pressure extractions (extraction residues) and c - extracts obtained from high-pressure dioxane extractions.

The spectrum of cork is characterized by a dominant C - H band with two peaks at 2927 cm⁻¹ and 2854 cm⁻¹ from aliphatic and olefinic C-H bonds in suberin and an intense C=O band at 1740 cm⁻¹ to 1738 cm⁻¹ from aliphatic acids and their esters in suberin (7). Bands that are used as a diagnostic for the presence of lignin in a sample are : 1600 cm⁻¹, 1510 cm⁻¹, 1465 cm⁻¹ and 1425 cm⁻¹ (11). All these bands with exception of the band at about 1600 cm⁻¹ are visible in the spectrum of cork. The intense broad band centered at about 1046 cm⁻¹ due to the presence of carbohydrates is also present.

All the bands observed in the spectrum of cork are also visible in the spectra of high-pressure extraction residues (spectrum b). Only small changes in bands intensities can be observed.

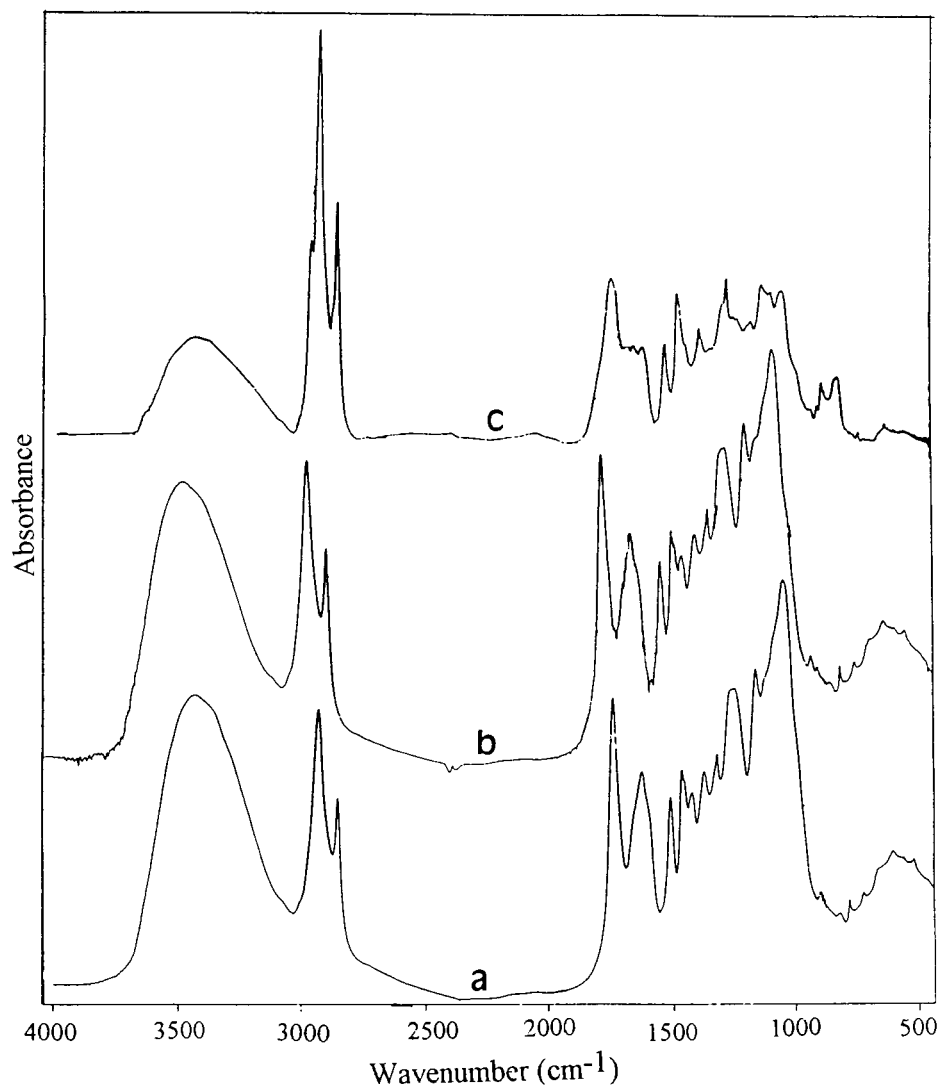


Figure 2. FTIR spectra of : a - extractive-free cork, b - residue of extraction carried out at 170 bar, 170°C with dioxane with a mass flow rate of 1.38 g min⁻¹ and c - extracts obtained from high-pressure dioxane extractions.

The spectrum of the extract obtained in a extraction with high-pressure dioxane (spectrum c) differs significantly from the spectra of cork and extraction residues. The bands due to aliphatic and olefinic C-H bonds are more intense, the C=O stretching band at about 1730 cm^{-1} decreases in intensity; the intense broad band at about 1046 cm^{-1} due to polysaccharides significantly decreases, but it is still visible. These differences are in accordance with the results obtained from chemical composition of residues. This extracted material should be mainly composed of suberin, lower amounts of lignin or lignin degradation products and polysaccharide derived material. Thus, the three bands at about 2957 cm^{-1} , 2925 cm^{-1} , 2854 cm^{-1} characteristic of suberin appear in this spectrum with increased intensity and a better resolution. The characteristic bands of lignin are also visible.

4. CONCLUSIONS

In the conditions studied suberin is preferably extracted. Lignin extraction percentages are low. No significant variations of extraction percentages with temperature were observed. Extraction selectivity did not change significantly with extracting fluid composition. The reason why significant changes of extraction yield and selectivity were not observed for the different conditions studied, is probably due to the close interaction of suberin and lignin, which hinders lignin depolymerization and solubilization in the extracting fluid. FTIR results are in accordance with the chemical composition of the samples showing also a selectivity towards suberin extraction.

REFERENCES

1. A. Björkman, *Svensk Papperstid*, 59 (1956) 477.
2. A. S. Reis Machado, E. Gomes de Azevedo, R.M. Sardinha, M. Nunes da Ponte, J. *Supercritical Fluids*, 7 (1994) 87.
3. A. S. Reis Machado, E. Gomes de Azevedo, R.M. Sardinha, M. Nunes da Ponte, *Proceedings of the "Third Symposium on Supercritical Fluids"*, G. Brunner, and M. Perrut. (eds.), 17 -19 October, Strasbourg, Institut National Polytechnique de Lorraine, Nancy, pp.349 ,1994.
4. A. S. Reis Machado, E. Gomes de Azevedo, R.M. Sardinha, M. Nunes da Ponte, *Holzforschung*, (1996), in press.
5. A. S. Reis Machado, E. Gomes de Azevedo, R.M. Sardinha, M. Nunes da Ponte, *Holzforschung*, (1996), in press.
6. H. Pereira, *Sci. Technol.* 22 (1988) 211.
7. A. V. Marques, H. Pereira D. Meier, O. Faix, *Holzforschung*, 48 (1994) 43.
8. A. V. Marques, H. Pereira, D. Meier, O. Faix, *Holzforschung*, submitted.
9. J. Stoldt and G. Brunner, Technical University of Hamburg - Harburg, unpublished results.
10. M. J. Effland, *Tappi*, 60 (1977) 143.
11. H. L. Hergert, *Lignins. Occurrence, Formation, Structure and Reactions*. K.V. Sarkanen and C. H. Ludwig (eds.), Wiley- Interscience, New York, 1971.

Supercritical Carbon Dioxide Desorption of Organics from Activated Carbon and Zeolithe

G. Vallée, D. Barth

Laboratoire de Thermodynamique Chimique et Appliquée-E.N.S.I.C.

1, rue Grandville BP 451 -F- 54001 NANCY Cédex

1. INTRODUCTION

Much current interest derives from the potential of SC CO₂ as an environmentally acceptable replacement for more conventional solvents. An other potential application of SC CO₂ is to use it to resolve some environmental problems. To recover organic pollutants such as volatil organic compounds (VOC) and/or to reduce their concentration in effluent streams from environmental concern, activated carbon or other adsorbents are customarily employed. Supercritical carbon dioxide has proved to be an effective solvent in regenerating solid matrices due to its original characteristics. Regeneration of spent activated carbon alternative to conventional thermal regeneration, the latter being energy-intensive and accompanied by carbon loss.

It has liquid like densities, gas-like viscosities and diffusivities at least an order of magnitude higher than of liquids which may result in superior mass transfer coefficients. There are some publications in the literature since 1980 [2-12] concerning the experiments and some investigators [13-15] have proposed models.

The first step of this study is to optimize the desorption experiments particularly the mass balance of the desorption process : expecially the separation between the solutes and CO₂. The first step of the process is the adsorption at atmospheric conditions of VOC (butyl acetate and/or xylenes). Two adsorbants were chosen to realize a comparison : activated carbon and zeolithe. We studied the desorption characteristics as a function of pressure, temperature and CO₂ flow rate.

2.MATERIAL AND METHODS

2.1. The apparatus (Figure 1)

The solide matrices are saturated by the organics at atmospheric conditions and 30 g of saturated adsorbants (activated carbon : Acticarbone AC 40 5 mm from CECA S.A. La Défense 5, 92062 PARIS LA DEFENSE or zeolithe Wessalith Day from Degussa AG GB AC P.O. Box 110533 - D 6000 FRANKFURT 11) are introduced in the autoclave, with a stainless steel frit in the inlet and at the outlet column to retain the matrix being extracted.

Butyl acetate (99%) is purchased by SIGMA and the mixture of xylene isomers (\approx 65 %) diluted in ethylbenzene (\approx 35 %) (with a purity of 98 % by SDS (BP 4 - VALDONNE - 13124 PEYPIN). CO₂ (P = 5 MPa, T = 20°C) is cooled, pumped (P_{max} = 25 MPa) then heated to be a supercritical fluid (P_c = 7,23 MB, T_c = 31,1°C). It flows through a thermostated desorption column (L = 290 mm, ϕ = 19 mm). At the outlet column, the mixture CO₂-solute is expanded

trough three valves and are separated in cyclonic separators[16]. At last CO_2 is vented through a rotameter and a gas meter. An originality of the process is to withdraw the solutes at atmospheric conditions everytime we need. The solutes are weighted or analyzed by capillary gas chromatography if they are mixtures. We have also the possibility to use on-line supercritical fluid chromatography. The temperature of the first and second separator is different from the top to the bottom. The third separator temperature is the same as the bottom of the second separator.

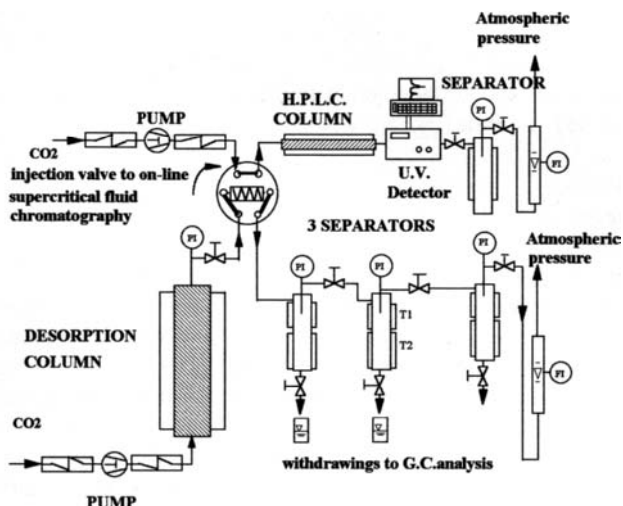


Figure1. Flowsheet apparatus.

2.2. Analytical method

Samples were analysed by gas chromatography on a Fractovap 2900 (Carlo Erba) equipped with a capillary column SE-54 (25 m x 0.32 mm ID). The FID temperature was 100°C, the injector a split-splitless at 120°C, the oven temperature was 100°C. We used an internal standard n-decane for calibration, the samples were diluted in ethanol.

3. RESULTS FROM EXPERIMENT

3.1 Extraction for the separation between CO_2 and VOC.

In order to improve this separation and to obtain a good mass balance, we decided to study the both extraction of butylacetate or xylenes. Cyclonic separators has been built in our laboratory, they are supposed to have a good efficiency but at this moment there are no data in the litterature to calculate such separators. The dimensions and the geometry are determined so the operating parameters were temperature and pressure : if we suppose we have no transfer problems, we have also enough equilibrium thermodynamic data. The results are summarized on table 1.

The solutes are lost by two ways :

- we can suppose that two phases are coexisting inside the separator : a xylenes liquid phase and a CO_2 gaseous phase. When we withdraw the samples by the aim of a valve at the separator bottom, the pressure decrease is high (for example from 4 MPa to the atmospheric pressure), and samples are very volatils components. So a first step to obtain a better recovery

was to keep the bottles in ice, it is the change between experiment one and two. An other idea is to fill up the bottles with glass marbles so it is possible for the solutes to condensate at the surface of the cold glass marbles : such improvement is demonstrated between experiment 5 and 6 : the yield recovery is increasing by 6 %.

-the separation between solutes and CO₂ is assumed by three high performance separators which are cyclones. The efficiency of the separation is depending on the cyclone geometry, temperature, pressure. In fact the efficiency is increasing if the inlet velocity and dispersed phase density are increasing. But it decreases as the mixture viscosity is decreasing. The geometry of the separators is choosen, the decrease of the pressure from the supercritical conditions to the atmospheric conditions is depending on the valves. So the only parameter is temperature of the separators. The comparison between experiment 2 and 5 demonstrates this effect. These separation conditions were kept for all the other experiments with approximatively the same yield recovery.

Table 1

Extraction experiments : mass balance (yield recovery)

Extraction pressure and temperature : 95 MPa, 45°C

The solutes are the mixture of xylenes except for experiment 6

Experiment		1	2	3	4	5	6
Separator top temperature	(°C)	40	30	30	25	25	29
CO ₂ flow rate	(g/s)	0.639	0.508	0.508	0.598	0.346	0.390
Separator bottom temperature	(°C)	10	10	20	15	15	15
First separator pressure	(MPa)	5	5	5.5	5.0	5.5	5.5
Second separator pressure	(MPa)	2.7	2.7	3.5	2.7	2.5	2.5
Third separator pressure	(MPa)	1.2	1.2	1.2	1.2	1.2	1.2
Feed	(g)	6.116	5.838	6.350	6.265	6.573	4.997
Mass recovered	(g)	3.929	4.282	5.070	5.200	5.55	4.538
Yield recovery	(%)	64.2	73.3	79.8	83.0	84.5	90.8

3.2. Extraction experiments

As during extraction, the phenomena are more easy to understand, we realized some experiments with xylenes mixture, butyl acetate and a mixture of two (30 %-50 %). It should be a way to obtain some cofirmation about thermodynamic data. The operating conditions are summarized on table 2.

We can observe (figure 2) that the first step of the extraction is very quick : when butylacetate is extracted by liquid CO₂ (P = 8.5 MPa, T = 25°C), fifty per cent of the feed is extracted within five minutes. The mass fraction of xylenes in SC CO₂ has a value near 7 %. The mass fraction of butylacetate is higher in liquid CO₂ (5,2 %-6 %) than in SC CO₂ (2,3 %-3,75 %). Generally speaking thesolubility of various solutes is higher in liquid CO₂ than in SC CO₂. The mass fraction for the mixture xylenes (butyl acetate is near 10 %)

Table 2
Extraction Experiments

Solute	Feed (g)	CO ₂ flow rate (g/s)	Pressure* (MPa)	Temperature* (°C)	Yield recovery (%)
Butyl acetate	6.034	0.49	8.5	25	88.2
Butyl acetate	6.181	0.42	9.0	40	83.8
Xylenes	4.997	0.39	9.0	40	90.8
Xylenes	6.118	0.30	9.0	40	88.3
AB+XY	7.205	0.37	9.0	40	86.8
AB+XY	7.247	0.27	9.0	40	87.9

*pressure and temperature of the extraction column.
AB + XY : mixture composed with butyl acetate and xylenes isomers (50 %-30 %)

Cumulated butyl acetate extracted mass divided by the feed (%)

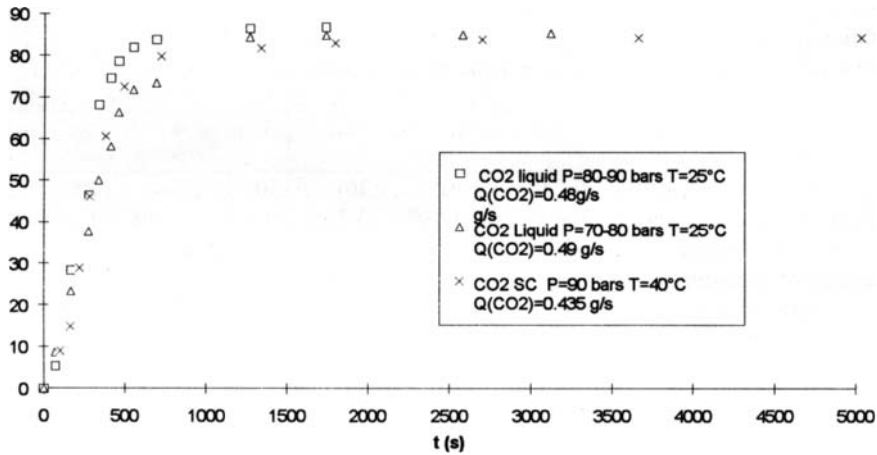


Figure 2.
CO₂ flowrates effect..

3.3. Zeolithe regeneration (Figure 3)

The comparison between the extract mass during the extraction (10 %) and the desorption (1.25 %) shows us that other effects than solubility are more crucial in the desorption process. The butylacetate regeneration is better than xylene regeneration : zeolithe is saturated by a mixture composed with butyl acetate (50 %) and xylenes isomeres (30 %), the extracts composition is butyl acetate (60-65 %) and xylenes isomers (35-40 %). The equilibrium thermodynamic and adsorption data could help us to explain these results. To increase the CO₂ flow rate (Figure 3) contribute to decrease the desorption time but the lowest flow rate does not permit to desorbe completely zeolithe : this is suggestive of a film transfer resistance at lower flow rates.

Cumulated extract mass divided by saturated zeolithe mass (g/g)

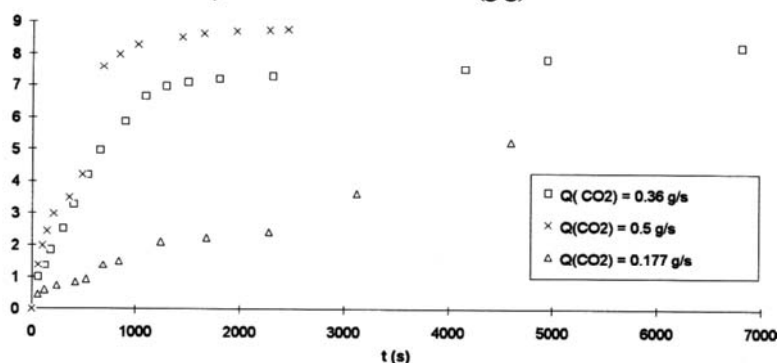


Figure 3

SC CO₂ flow rate effect P=80 bars ; T=40°C

The temperature effects (Figure 4) are in accordance with the results of Tan [7] and Srinivasan [10] who have studied the regeneration of ethylacetate from activated carbon. At a lower operating pressure (8MPa) the density effect seems to dominate, therefore the optimal regeneration condition is in the liquid phase. But at a higher operating pressure (10 MPa), it seems that both density and viscosity effects are important hence an optimal temperature lies somewhere in the supercritical region. At the present time a general rule for obtaining the optimal temperature, however, has not been found yet.

Cumulated extract mass divided by saturated zeolithe mass (g/g)

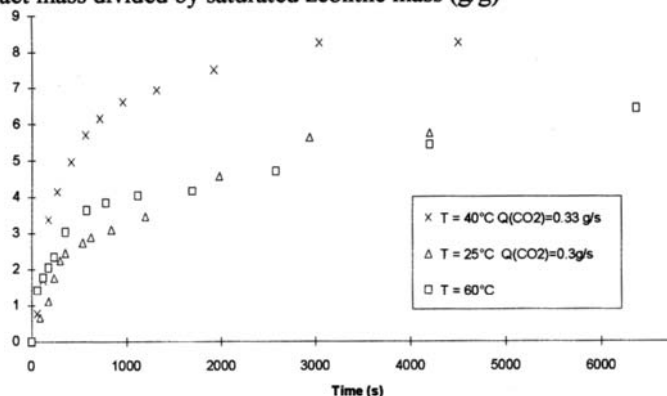


Figure 4

SC CO₂ Temperature effect .P=105 bars

3.4. Activated carbon regeneration

Two experiments were realized at the same pressure (8 MPa) and CO₂ flow-rate (0.38 g/s) but the temperature was changing : 25°C (liquid CO₂) and 40°C (supercritical CO₂). The activated carbon was saturated with the mixture butyl acetate and xylenes isomers (50 %-30 %). The results are in accordance with the literature and our results concerning zeolithe ; the

regeneration with liquid CO₂ has a higher efficiency than supercritical CO₂. The desorption is better with activated carbon than zeolithe : 14 g of VOC (100 g activated carbon) compared to 9 g of VOC (100 g zeolithe).

4.CONCLUSION

The effects of temepature, pressure and flow rate of carbon dioxide on regeneration efficiency are examined. Our results are in accordance with those of the litterature. The originality of these study concerns

-the withdrawn of the VOC at atmospheric conditions so they can be used or destroyed.

- a good mass balance obtained working with VOC.

- the better conditions for the regeneration seem to be obtain with liquid CO₂ (P = 8 MPa, T = 20°C), this is a good new for developping an industrial process to purify air polluted by VOC.

-the better conditions we have found were applied on a pilot plant by Separex Company. The activated carbon mass introduced in the autoclave was 25 kg and the results obtained were in agreement with laboratory experiments.

Now we are collecting the thermodynamic data to developp the process modelling

Acknowledgment

This project was realized in collaboration with two french companies : Renault and Séparex.

REFERENCES

- 1.M. Modell, R.J. Robey, V.J. Krukonis, R.P. de Filippi and D. Oestreich, 87th AICh. E. Meeting, Boston, MA, (August 1979).
- 2.R.P. de Filippi, V.J. Krukonis, R.J. Robey and M. Modell, Report 1980, EPA Washington, DC.
- 3.M. Mc Hugh and V. Krukonis, Supercritical fluid extraction, principles and practice. Butterworth, Stoneham, MA 118 1986.
- 4.R.G. Kander and ME Paulaitis, Chemical Engineering at Supercritical Fluid Conditions, M.E. Paulaitis, J. Penninger, R. Gray, P. Davidson (Eds), Ann. Arbor Science : Ann. Arbor, MI, 1983 136.
- 5.R.D. Picht, T.R. Dillman, D.J. Burke and R.P. de Filippi, 219 (1982), AIChE Symp. Series, 78 136.
- 6.J.W. King, Chapt. 13, Am. Chem. Soc., 1987.
- 7.C.S. Tan and D.C. Liou, Ind. Eng. Chem. Res., 27 (1988) 988.
- 8.C.S. Tan and D.C. Liou, Ind. Eng. Chem. Res., 28 (1989) 1222.
- 9.C.S. Tan and DC Liou, Ind. Eng. Chem. Res., 29 (1990) 1412.
- 10.M.P. Srinivasan, J.M. Smith and B.J. Mc Coy, Chem. Eng. Sci. 45 (1990), 7 1885.
- 11.L.L. Lee and M.D. Cachan, Chapt 15, Am. Chem. Soc., (1993).
- 12.S.J. Macnaughton, N.R. Foster and I. Kikic, 3rd International Symposium on Supercritical Fluids, 17-19 Oct. 1994, Strasbourg, INPL (Ed), 2 1.
- 13.B. Turgay and V. Aleman, 3rd International Symposium on Supercritical Fluids, 17-19 Oct. 1994, Strasbourg, INPL (Ed), 2 177.
- 14.V. Aleman and A.K. Lunol, A.I.Ch.E.J., 37 (1991) 2 215.
- 15.G. Madras, C. Thibaud, C. Erhey and A. Akgerman, 40 (1994) A.I.Ch.E.J., 5 777.
16. M.Perrut, French Patent 85 104 68(1985)

A New Efficient Fractionation Process: The Simulated Moving Bed with Supercritical Eluent

J.Y. CLAVIER, R.M. NICOUD, M. PERRUT.

SEPAREx, BP9, 54250 Champigneulle, France.

1. INTRODUCTION

The development of preparative chromatographic processes in fine chemistry and in pharmaceutical industries is a very important field of research. This new process called SF-SMB (Supercritical Fluid Simulated Moving Bed) is an attempt to optimize preparative chromatography by three ways: the choice of a supercritical CO₂ as eluent, the implementation of the simulated moving bed, and the use of an elution strength modulation in the process, performing a pressure gradient.

If elution and frontal chromatography are still the main implementations used in preparative processes because of the simplicity of their development, processes like true moving bed (TMB) or simulated moving bed (SMB) have been used for about 40 years in large scale separations in petroleum or sugar industries [1,2]. In these processes, a countercurrent between solid and fluid phase is realized (or simulated) in order to improve process productivities and to decrease the eluent consumption. These implementations are now developed for laboratory and small productions and find a lot of applications in pharmaceutical and fine chemistry industries [3,4].

In a lot of industrial adsorption processes like PSA (Pressure Swing Adsorption) or TSA (Temperature Swing Adsorption), a variation of a physical parameter is used to increase the recovery yield of the purified product or to increase the productivity of the process [5]. If such kind of variation is difficult to realize with liquid eluent SMB, the use of supercritical eluent is particularly appropriate to realize an elution strength gradient. In fact, the elution strength of supercritical eluents is varying with pressure and temperature and a lot of simple models describe the retention coefficient variations versus temperature and specific gravity of the eluent [6-8]. If a temperature control is always difficult to handle because of the thermal inertia, this property can be used in SMB performing a pressure gradient between the different zone of the bed [9,10].

After explaining the process concept, this paper presents the two steps of the process development. First a simulation software allows to set the different process parameters and gives an idea of the SF-SMB performances. Then, the pilot plant is described and experimental results confirm the numerical simulation expectations and prove the great interest of this process.

2. PRINCIPLE OF THE PROCESS

The basic principle of a true moving bed is to use a countercurrent contact between solid and fluid phases. The feed to be processed (A + B) is injected in the middle of the column.

The products with lower retention (A) follow the eluent direction enabling recovery at the top of the column. Products with higher retention (B) follow the solid direction where they can be recovered at the bottom of the column.

The main drawback of true moving bed is the lack of control of the solid flow. This is why the simulated moving bed implementation is most often used. The system consists of at least 4 columns connected in series. The solid is therefore fixed as a stationary phase in the different columns. The solid flow is only simulated by shifting the injection and collection points. That is, moving fronts of A and B appear in the system owing to elution, and these fronts are followed by shifting the injection and collection points. Consequently, the profiles are continuously moving within the system, but the effluent concentrations appear almost constant because of shifting of the collection points.

It can be shown that the performances of simulated moving beds are equivalent to those of true moving beds [11]. Also, SMB process has a lot of advantages compared to classical elution chromatography. With a continuous process, purified products are recovered at 100% with a low dilution and a low eluent consumption. Moreover, SMB process are not very sensitive to column efficiency and we can obtain very good product purities with even low column efficiencies [11].

The parameter setting of liquid eluent SMB consist in a right and accurate setting of the inlet and outlet flowrates of the system [12]. SF-SMB is more complex and 4 pressure and 4 flowrates have to be set. The idea of SF-SMB concept to perform a pressure gradient in the different zones of the bed is illustrated in figure 1.

The purpose of zone 1 is to stabilize the concentration front of component B in order to prevent B to be sent in zone 4 in the solid phase direction. The use of a high pressure in this zone allow increase the elution strength of the eluent and to decrease the flowrate in zone 1 leading to reduce eluent consumption and to increase the concentration of the extract flowrate.

Compared to an isocratic process where flowrates in zone 2 and 3 are determined by the objective to stabilize A concentration front in zone 2, and B concentration front in zone 3, in order to recover both components pure at the extract and the raffinate, the realisation of a pressure gradient between these two zones allow to decrease Q_{II} and to increase Q_{III} and therefore to increase the feed flowrate Q_f (as $Q_f = Q_{III} - Q_{II}$) and finally the productivity of the system.

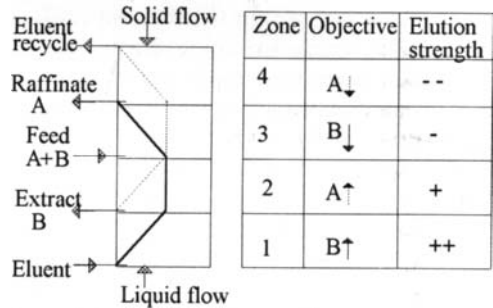


Figure 1 : Explanation of the interest to perform a pressure gradient in a moving bed

3. NUMERICAL PROCESS SIMULATION

Before each separation, process parameters have to be determined through a numerical simulation software. Knowing the size of the system and the adsorption isotherm of the components, the software is able to compute the optimal set of flowrates allowing to perform the separation.

The first step is devoted to the determination of adsorption isotherms. Several adsorption isotherm determination methods have been described [13], and we developed a laboratory apparatus allowing to determine very precise adsorption isotherms in supercritical fluids.

In a second step, we use the thermodynamical data previously obtained, and we compute the SF-SMB separation performances.

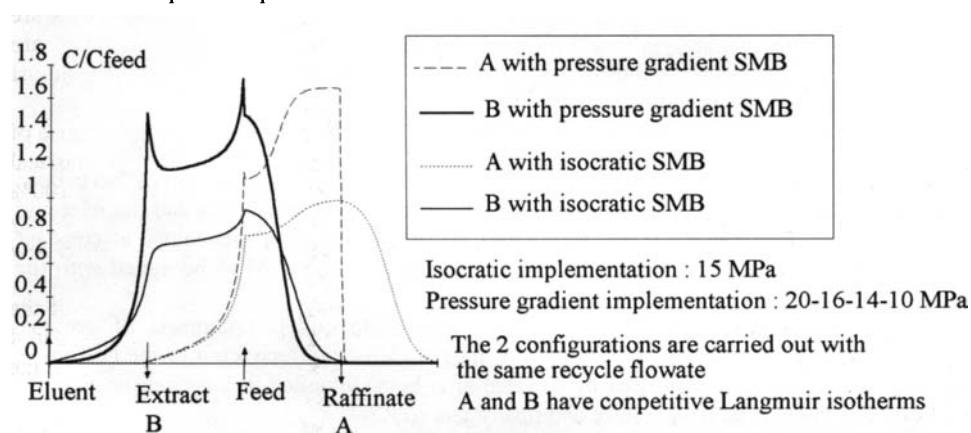


Figure 2 : simulated concentration profile in a TMB with or without a pressure gradient [14]

A first model is used to compute the flowrates allowing to perform the separation with the greatest productivity. Then, the "mixed cell in series" model takes into account thermodynamic, hydrodynamic and kinetic properties of the system and compute the concentration profile inside the columns [14]. In this model, we make the assumptions that the pressure drop inside the column is negligible compared to the pressure drop realized and controlled with the analogical valves, and we model the true moving bed assuming that the performance of SMB and TMB are equivalent. A mass balance equation is written for each stage and a classical Newton Raphson numerical method is used to solve the permanent state of the process [14].

Figure 2 presents a typical exemple of computed concentration profiles obtained with the software using or not a pressure gradient [14].

The production of the pressure gradient implementation is found to be about twice the production that can be achieved by a isocratic implementation (using the same recycling flowrate). This improvement of process separation potential is due to the use of a pressure gradient between the different zones of the bed. If we observe the concentration profile, we see that the mean concentration of the components in the pressure gradient system is higher than the one of isocratic system. The component concentration can even be greater in the column than in the feed. This effect is in fact one of the main limits of pressure gradient because we are obviously limited by the solubility of the solutes in the fluid.

4. PILOT PLANT DESCRIPTION

The pilot plant is composed of 8 columns of 33 mm of internal diameter connected in series. Six automated valves are placed after each column in order to connect the columns to the different inlets and outlets of the process (See figure 3). Analogical valves are located after each column (Un) and are used to control the pressures in the different zones of the process. Five analogical valves control inlets and outlets flowrates.

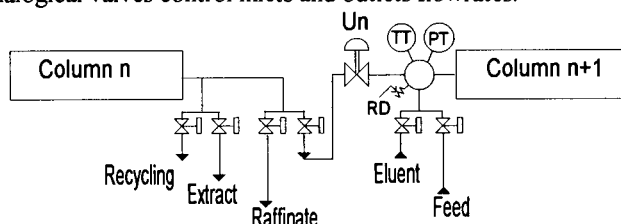


Figure 3: Valve configuration between the columns

Efficient control algorithms based on a representation of analogical valves have been developed in order to control simultaneously the pressure in the four zones and the inlet and outlet flowrates. The eluent pump is filling a high pressure reservoir maintained at constant pressure. The fresh eluent is sent to the eluent inlet and to a mixer M to be mixed with the feed.

The purified products are withdrawn in three separate outlets composed of cyclonic separators connected in series. Pure products, free of eluent are recovered in the bottom of reservoir as the gaseous eluent is easily recycled after being liquefied in a condenser, pumped and heated to the desired temperature and finally sent to R2.

5. EXPERIMENTAL SEPARATION RESULTS

The separation of two fatty ethyl esters (GLA: γ -linolenic ethyl ester and DHA: docosahexaenoic ethyl ester) has been carried out on the pilot plant.

The stationary phase is a C18 bounded silica, granulometry 15 μ m LiChrospher E.Merck.

Two experiments will be compared. The first experiment has been carried out in almost isocratic conditions without the system allowing to perform the pressure gradient. The pressure drop in the column is low (15 bar on the 8 columns). In the third experiment, we add a pressure drop between the columns, using analogical valves, in order to obtain a global pressure drop of 90 bar.

a) Isocratic implementation

The pilot plant is carried out about 24 h with the following parameter setting determined with the numerical simulation software:

zone 1	zone 2	zone 3	zone 4
15.8	15.4	15.0	14.6

Pressure setting in the different zones (MPa)
Step time: 694 sec

Feed	Extract	Raffinate	Recycle
0.69	1.49	0.67	3.18

Inlet and outlet flowrate setting ($\text{kg}\cdot\text{h}^{-1}$)

A system allows to determine the concentration of the components after each column. Figure 4 presents the concentration profile obtained with this configuration.

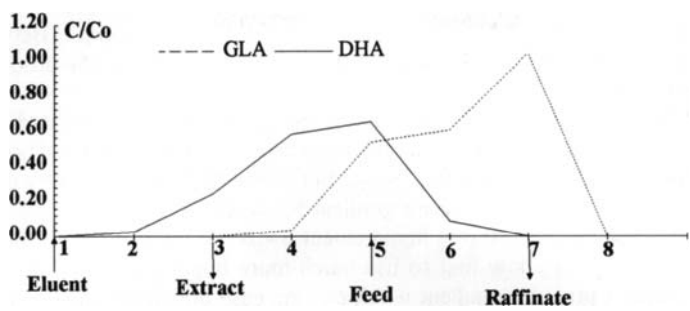


Figure 4: Experimental concentration profile in the simulated moving bed (isocratic implementation)

The purities of the recovered fractions are:

- Extract purity (DHA): 97.8 %
- Raffinate purity (GLA): 97.7 %

The total production of purified oil on the system is 33.1 g/day.

b) Pressure gradient implementation controlled by analogical valves

The new parameter setting determined by the numerical simulation software is :

zone 1	zone 2	zone 3	zone 4
19.5	17.5	12.5	11.5

Feed	Extract	Raffinate	Recycle
2.2	1.3	0.79	7.15

Pressure setting in the different zones (MPa)

Inlet and outlet flowrate setting (kg.h⁻¹)

Step time : 276 sec

The purities of the extract and raffinate recovered fractions are :

- Extract purity (DHA): 99.9 %
- Raffinate purity (GLA): 100.0 %
- The total production of purified oil on the system is 122 g/day.

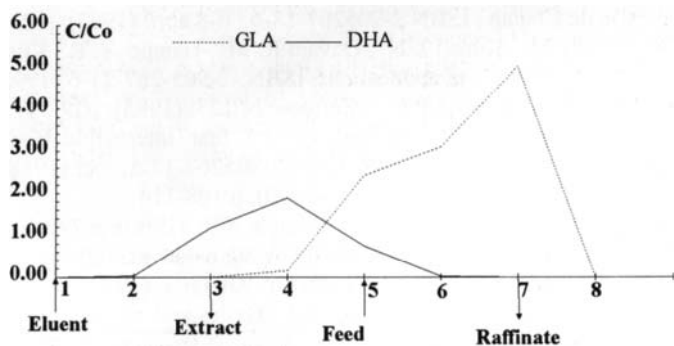


Figure 5: Experimental concentration profile in the simulated moving bed (pressure gradient with automated control through analogical valves)

As it was predicted by the simulation software, the use of a pressure gradient allow to increase process productivity. In this last configuration, the production of the pilot plant is increased about 4 times compared to the first "isocratic" separation. The effect of the pressure gradient on the productivity can be estimated, dividing the experimental production by the

sum of the inlet flowrates in the pilot plant. We compare this way the production for a given amount of stationary phase and a given capacity of the eluent pump. Between the first "isocratic" and the last "pressure gradient" experiments, we increase the productivity of the system more than 2 times.

We also observe that the concentration of the components in the simulated moving bed is higher than it was in the feed. In our case, the main limiting factor of process productivity was the adsorption capacity of the stationary phase, but, when this is the solubility of the solute in the eluent which is limiting, the pressure gradient has to be set in order to take into account this constraint. In fact, compared to a liquid eluent SMB, SF-SMB improve the process by 2 ways: supercritical eluents allow first to use much more important flowrates, and then, it is possible to perform a pressure gradient which can increase drastically the productivity of the system.

6. CONCLUSION

A new preparative chromatographic process has been developed. This process combines the advantages of supercritical eluent in chromatography and those of simulated moving bed implementation. This complex process is developed in 2 steps. In a first step, an adsorption isotherm determination and a simulation software allow to give an estimation of process performances. Then, the separation is carried out on a pilot plant with the setting determined on the simulation software. The numerical and experimental results prove that the concept of this new process that is to perform a pressure gradient along the bed, improves drastically the process productivity. Some economical comparisons will certainly confirm the interest of SF-SMB compared to liquid eluent SMB, PSFC or HPLC technologies.

REFERENCES

- [1] : Broughton D. B., US Patent 2985589 (1961)
- [2] : Johnson J.A. , Kabza R.G. , preparative and production scale chromatography, Eds G. Ganestos P.E. Barker, ISBN 0-8247-8738-2, N°61, (1992), p.257-271
- [3] : Hotier G., Proceeding of the 9th int. symp on prep. and ind. chromatog., Nancy, France, Eds. Société Française de Chimie ; ISBN 2-905267-18-6, 6-8 april (1992), p.235-240
- [4] : Nicoud R. M. , Bailly M. , Kinkel J. N. , Devant R. M. , Hampe T. R., Küsters E. , in Simulated moving bed : basics and applications; ISBN -2-905-267-21-6 (1993), p.665-88
- [5] : Tondeur D., Migault G., Wankat P.C. : Entropie N°123, (1985), p39-54
- [6] : Perrut M., Dellacherie J., Proceedings of the first international symposium on supercritical fluids, Nice, Eds M.Perrut, INPL, ISBN 2-905267-13-5, oct (1988), p.397-413
- [7] : Roth M. , Journal of supercritical fluids, 3, (1990), p.108-114
- [8] : Luffer D., Ecknig W. , Novotny M. , J. Chromatog. 505, (1990), p.79-97
- [9] : Nicoud R.M. , Perrut M, Fr. Patent n° 9205304, n° 9209444, (1992)
- [10] : Hotier G., Nicoud R.M. , Perrut M, Fr. Patent n° 9304703, (1993)
- [11] : Tondeur D., Bailly M., Simulated moving bed : Basics and applications, ISBN 2-905-267-21-6, (1993), p.97-117
- [12] : Nicoud R.M., Basics and applications, ISBN 2-905-267-21-6, (1993), p.54-64
- [13] : Seidel-Morgenstein A. , Nicoud R.M. , Simulated moving bed : Basics and applications, ISBN 2-905-267-21-6, (1993), p.4-34
- [14] : Clavier J.Y., Thesis INPL sept. 1995.

Experimental Measurement of Clathrate Phase Equilibria Containing Carbon Dioxide, Methane, Phenol and p-Cresol

Huen Lee, Ji-Ho Yoon and Seong-Pil Kang

Department of Chemical Engineering, Korea Advanced Institute of Science and Technology, 373-1 Kusung-dong, Yuseong-gu, Taejeon, 305-701, South Korea

Clathrate compounds are crystalline molecules formed by a physical reaction between host molecules and low molecular-weight gases. The gas molecules occupy cavities in a network of host molecules composed of unit crystal structures. Experimental apparatus equipped with sapphire windows for visual observation was uniquely designed and built to measure clathrate phase equilibria. Phenolic compounds such as phenol and p-cresol were used as host molecules and carbon dioxide and methane as guest molecules. The dissociation pressures and temperatures were measured for several binary systems in order to investigate clathrate three-phase (vapor-clathrate-organic liquid) equilibria. In addition, the four-phase dissociation pressure measurements for the ternary carbon dioxide(guest)-water(host1)-phenol(host2) system were carried out in temperature and pressure ranges of 279-307K and 15.1-77.2 bar, respectively. A quintuple point at which the five phases coexist was also carefully measured. This study provides new experimental clathrate equilibrium data for the binary and ternary mixtures containing phenolic compounds.

1. INTRODUCTION

Clathrates are crystalline inclusion compounds formed by the physical reaction between host molecules and low molecular weight gases as guests. In the clathrate structure there are two different types of cages which can entrap guest molecules into the network of host molecules. The three-dimensional clathrate structures can be determined by X-ray diffraction method.

Clathrate compounds are largely divided into two categories, aqueous and nonaqueous, depending on the host molecule. For aqueous systems, the compounds are called clathrate hydrates or gas hydrates. The host molecules for non-aqueous clathrates can be phenol-like compounds such as phenol, hydroquinone, dianin, and substituted phenols. For phenol clathrates it has been reported that two crystallographically distinct types of cages are formed and both cages are capable of including suitably sized guest molecules at limiting compositions (Atwood et al.[1]). Mandelcorn [2] summarized the maximum composition formulas of phenol clathrates and the detailed structure appeared in a paper by von Stackelberg, et al. [3]

The interest in clathrate hydrate research arose from the plugging phenomenon in pipelines used for natural gas transportation, resulting from clathrate formation in the line between contained water and gases, methane, ethane, propane, isobutane, carbon dioxide, and hydrogen sulfide. Nonaqueous clathrate compounds have been not studied to the extent of gas hydrate. Allison and Barrer [4] measured the dissociation pressures of the phenol clathrate with several guest gases such as Kr, Xe, CH₄, and CO₂ over a limited temperature range. Their experimental work was mainly focused on the solid phenol-clathrate-vapor phase boundary lines. Barrer and Shanson [5] found that facile clathration can be effected by merely agitating the host crystals with small ball bearings at temperatures even as low as 77.1 K. Trofimov and Kazankin [6] reported that p-cresol forms the clathrate compounds with the gas species of molecular size smaller than 5.1 Å. They also measured the dissociation pressures of p-cresol clathrates produced by the suitably sized guest molecules such as HCl, HBr, HI, H₂S, Kr, and Xe.

This paper present new clathrate equilibrium dissociation pressure data for the binary phenol-carbon dioxide, p-cresol-methane and ternary water-phenol-carbon dioxide over a range of temperatures above the normal melting temperature of phenol and p-cresol.

2. EXPERIMENTAL

2.1 Materials

The methane used for the present study was supplied by Scientific Gas Products Co. and had a stated purity of 99.99 mol %. The carbon dioxide with a minimum purity of 99.9 mol % was supplied by World Gas Co. The phenol and p-cresol was from Sigma-Aldrich Chemical Co. with a purity of 99.1 and 99.0 mol %, respectively. The distilled water of HPLC grade also supplied by Sigma-Aldrich Chemical Co. was used. All chemicals were used without further purification.

2.2 Apparatus

A schematic diagram of the experimental apparatus is shown in Figure 1. The main part of the apparatus consists of an equilibrium view cell made of 316 stainless steel and equipped with two sapphire windows at the front and back. The sapphire windows allowed visual observation of phase transitions between organic-rich liquid and clathrate phases at pressures up to 350 bar. The internal volume of the cell was about 50 cm³. The cell contents were agitated by a magnetic spin bar with an external magnet immersed in a water bath. The cell temperature was controlled by externally circulating water through refrigerator/heater. The temperature in the cell was measured by a K-type thermocouple with a digital thermometer (Cole-Parmer, 8535-26) of which the resolution is ± 0.1 K. A factory-calibrated Heise gauge (CMM 104957, 0 bar to 600 bar range) having the maximum error of ± 0.1 bar was used to measure the equilibrium dissociation pressure. The thermometer was calibrated with ASTM

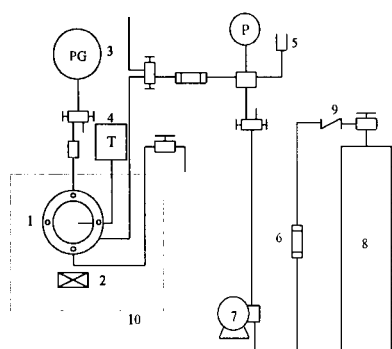


Figure 1. Schematic diagram of experimental apparatus used in this work: 1. equilibrium cell; 2. magnet; 3. pressure gauge; 4. thermometer; 5. rupture disc; 6. check valve; 7. high pressure pump; 8. CO₂ gas; 9. line filter; 10. water bath.

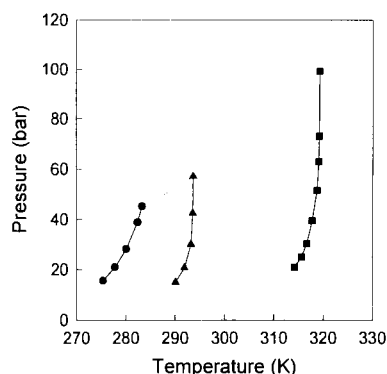


Figure 2. Four phase equilibrium lines for phenol clathrate of carbon dioxide: ●, pure water; ■, pure phenol; ▲, phenol clathrate-carbon dioxide-rich liquid-water-rich liquid-vapor line; , phenol clathrate-phenol-rich liquid-water-rich liquid-vapor line.

D900 mercury thermometer. The high-pressure pump (miniPump®, LDC Analytical, Inc.) was used to pressurize carbon dioxide, while a high pressure generator (High Pressure Equipment Co., 62-6-10) was used for methane.

2.3 Procedure

The experiment began by charging the equilibrium cell with about 30 cm³ of either phenol/p-cresol or phenol-water solution mixture. The cell was then pressurized with either methane or carbon dioxide until the phenol clathrate formed under sufficient pressure. The systems were cooled to about 5 K below the anticipated clathrate-forming temperature. Clathrate nucleation was then induced by agitating the magnetic spin bar. After the clathrates formed, the cell temperature was slowly increased until the clathrate phase coexisted with the liquid and vapor phases. The nucleation and dissociation steps were repeated at least twice in order to diminish hysteresis phenomenon. The clathrates, however, exhibited minimal hysteresis and the excellent reproducibility of dissociation pressures was attained for all the temperatures and found to be within 0.1 K and 1.0 bar at each time. When a minute amount of phenol or p-cresol clathrate crystals remains and the system temperature was kept constant for at least 8 hours after attaining pressure stabilization, the pressure was considered as an equilibrium dissociation pressure at that specified temperature.

Table 1

Equilibrium hydrate and phenol clathrate conditions for water-carbon dioxide, phenol-carbon dioxide and water-phenol-carbon dioxide systems

System	Line type	Temperature (K)	Pressure (bar)
water-carbon dioxide	L_w-H-V	275.4	15.6
		277.8	21.0
		280.1	28.2
		282.4	38.9
phenol-carbon dioxide	L_p-C-V	314.2	21.0
		315.6	25.1
		316.7	30.3
		317.8	39.5
		318.8	51.6
		319.1	63.1
		319.2	73.1
water-phenol-carbon dioxide	L_w-L_p-C-V	290.1	15.0
		291.9	20.8
		293.2	30.0
		293.6	42.5
	$L_w-L_p-L_c-C-V$	293.7	57.2

3. RESULTS AND DISCUSSION

The hydrate and phenol clathrate equilibrium data of the water-carbon dioxide, phenol-carbon dioxide, and water-phenol-carbon dioxide systems are presented in Table 1 and depicted in Figure 2. In order to establish the validity of the experimental apparatus and procedure the hydrate dissociation pressures of carbon dioxide measured in this work were compared with the data available in the literature (Deaton and Frost [7], Adisasmito et al. [8]) and found that both were in good agreement. For the phenol-carbon dioxide clathrate equilibrium results, as seen in Figure 2, the dramatic increase of the dissociation pressures in the vicinity of 319.0 K was observed. It was also found in the previous study (Kang et al. [9]) that the experimental phenol-rich liquid-phenol clathrate-vapor (L_p-C-V) equilibrium line of the binary phenol-carbon dioxide system could be well extended to the phenol clathrate-solid phenol-vapor ($C-S_p-V$) equilibrium line (Nikitin and Kovalskaya [10]). It is thus interesting to note that a quadruple point at which four individual phases of phenol-rich liquid, phenol clathrate, solid

phenol, and vapor coexist in equilibrium appeared at 313.2 K and 19.0 bar. The phenol-rich liquid–solid phenol–vapor (L_p – S_p – V) line starts at the melting temperature of 314.0 K at 1 bar, linearly decreases and finally terminates at the melting temperature of 313.2 K at 19.0 bar.

For the ternary water–phenol–carbon dioxide system, several interesting phenomena were observed. As shown in Figure 2, the four-phase, water-rich liquid–phenol-rich liquid–phenol clathrate–vapor (L_w – L_p – C – V), dissociation pressures were measured at several temperatures near 293.0 K. Like above the phenol–carbon dioxide clathrate equilibrium results, the dramatic increase of the four-phase dissociation pressures was observed in a vicinity of 293.0 K. One of the most interesting results observed in this work is that a quintuple point at which the five phases of water-rich liquid, phenol-rich liquid, carbon dioxide-rich liquid, phenol clathrate, and vapor coexist in equilibrium was carefully measured and found to be 293.7 K and 57.2 bar.

Figure 3 shows the clathrate equilibrium measurements for p-cresol–methane and the results are presented in Table 2. Contrary to phenol–carbon dioxide, the clathrate equilibrium dissociation pressure line for p-cresol–methane monotonously increases with temperature. This dependence is similar to that observed with gas hydrates and clathrates.

4. CONCLUSION

A new experimental apparatus was built to measure the clathrate dissociation pressures and equilibrium compositions of liquid phases which coexist with the clathrate phase. The pressure–temperature behavior of the binary phenol–carbon

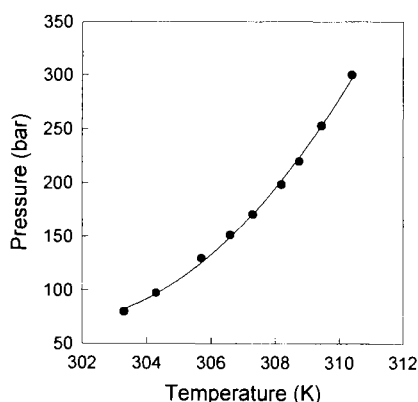


Figure 3. Experimental clathrate dissociation pressures of the p-cresol–methane system

Table 2
Equilibrium dissociation pressures for p-cresol–methane system (p-cresol-rich liquid–clathrate–vapor)

Temperature (K)	Pressure (bar)
310.4	79.7
309.4	97.4
308.7	129.6
308.2	151.2
307.3	170.6
306.6	198.6
305.7	219.8
304.3	252.9
303.3	300.0

dioxide, p-cresol-methane and the ternary water-phenol-carbon dioxide systems was measured over the wide temperature and pressure ranges. For the binary phenol-carbon dioxide system, the dramatic increase of the dissociation pressures was observed in the vicinity of 319.0 K. Three four-phase equilibrium lines of the ternary water-phenol-carbon dioxide system were also measured. In particular, a quintuple point at which five individual phases can coexist in equilibrium condition was carefully measured and found to be 293.7 K and 57.2 bar. A possible application of the clathration process to the separation of phenol from aqueous solution was demonstrated by measuring the isobaric three- and four-phase equilibrium compositions of the ternary system at 30.0 bar and six temperatures ranging from 278.2 to 303.2 K.

REFERENCES

1. Atwood, J. L., J.E.D.Davies and D.D. MacNicol, Inclusion Compounds. Vol. 2. Structural Aspects of Inclusion Compounds formed by Organic Host Lattices, Academic Press, London (1984).
2. Mandelcorn, L., Chem. Rev. 59 (1959) 827.
3. von Stackelberg, M., A.Hoverath and Ch.Scheringer, Z. Elektrochem., 62 (1958) 123.
4. Allison, S.A. and R.M.Barrer, Trans. Faraday Soc., 64 (1968) 549.
5. Barrer, R.M. and V.H.Shanson, J. Chem. Soc., Faraday Trans. I., 72 (1976) 2348.
6. Trofimov, A.M. and Yu.N.Kazankin, Radiokhimiya, , 10, 4 (1968) 445.
7. Deaton, W.M. and E.M.Frost Jr., U.S. Bureau of Mines Monograph 8 (1946).
8. Adisasmitho, S., R.J. Frank and E.D. Sloan Jr, J. Chem. Eng. Data, 36 (1991) 68.
9. Kang, S.-P., J.-H. Yoon, and H. Lee, J. Chem. Eng. Data, submitted (1996).
10. Nikitin, B. A. and M. P. Kovalskaya, Izvest. Akad. Nauk U. S. S. R., Otdel Khim. Nauk, 24 (1952).

Three Phase Flash Calculation under High Pressure Using Continuous Thermodynamics Method[†]

Zhang Cheng_hai and Li Chenglie^{††}

(Petroleum Processing Research Center, East China University of Science and Technology, Shanghai, 200237, China)

Fang Xiangcheng

(Fushun Research Institute of Petroleum Processing, Fushun, 113001, China)

Keywords: three phase flash, continuous thermodynamics, high pressure, petroleum fraction

1. INTRODUCTION

In the past decade many works have been done in the fields of continuous thermodynamics. A long fundamental lines were studied with a particularly important contribution by Gualtier, Kinenid and Morrison[1]. They have stressed on mathematical relationships, representing the viewpoint of theories with little attention to engineering problems. Papers by Cotterman et al [2][3], Ratzch and Kehlen [4][5][6] made great contributions toward potential application. Cotterman et al. compared continuous distribution results with discrete component results on polymer and petroleum systems. Kehlen provided a mathematical analysis for continuous thermodynamics. A comparison of distribution functions for phase equilibrium calculations of continuous mixtures was made by Wang[7]. Application to adiabatic flash and distillation was demonstrated by Chou and Prausnitz[8] and Kehlen and Ratzsch [6]. Ying[9] presented a new method based on spline fit. This new method can be used for any arbitrary distribution of mixtures. Continuous thermodynamics method has great advantages in the aspects of accuracy, efficiency and reliability. So far, the three phase flash calculation using continuous thermodynamics method has not been described in the previous literature, In this paper, the high pressure separator in hydrocracking system is discussed with continuous thermodynamics method. Good results have been obtained.

2. RELATED EQUATIONS:

To fix the problem, temperature, pressure and feed composition are generally specified, so that the composition and relative amounts in outlet are to be calculated. For implicitly, a complex fluid mixture with k discrete components and only one family of continuous fraction are concerned. So the system must satisfy the following equations:

2.1. Material balance:

$$z_i = y_i + \beta(1 - \alpha)x_i^h + (1 - \alpha)(1 - \beta)x_i^l \quad (1)$$

[†] This project is supported by NSFC.

^{††} To whom coorespondence should be address.

$$\eta^F F^F(I) = \alpha \eta^V F^V(I) + (1-\alpha)\beta \eta^L F^L(I) + (1-\alpha)(1-\beta)\eta^{L^h} F^{L^h}(I) \quad (2)$$

2.2 Phase equilibrium:

$$\mu_i^V = \mu_i^L = \mu_i^{L^h} \quad (3)$$

$$x_i^L \phi_i^L = x_i^{L^h} \phi_i^{L^h} = y_i \phi_i^V \quad (3)$$

$$\mu^V(I) = \mu^L(I) = \mu^{L^h}(I) \quad (4)$$

$$\eta^V F^V(I) \phi^V(I) = \eta^L F^L(I) \phi^L(I) = \eta^{L^h} F^{L^h}(I) \phi^{L^h}(I) \quad (5)$$

2.3. Normalization equations:

$$\sum z_i + \eta^F \int_I F^F(I) dI = 1 \quad (6)$$

$$\sum y_i + \eta^V \int_I F^V(I) dI = \sum x_i^L + \eta^L \int_I F^L(I) dI = \sum x_i^{L^h} + \eta^{L^h} \int_I F^{L^h}(I) dI = 1 \quad (7)$$

here:

$F(I)$ --- distribution function I --- distributed variable (e. g. temperature)

η --- mole fraction α --- fraction vaporized

β --- liquid phase splitting factor μ --- chemical potential

subscript:

F --- feed V --- vapor

L^L --- light liquid L^h --- heavy liquid

. Combining these equations, for continuous fraction, it is obvious that:

$$\eta^V F^V(I) = \frac{\eta^F F^F(I)}{\left[\alpha + \frac{(1-\alpha)}{K^L(I)} + \frac{(1-\alpha)(1-\beta)}{K^h(I)} \right]} \quad (8)$$

$$\eta^L F^L(I) = \frac{\eta^F F^F(I)}{\left[(1-\alpha)(1-\beta) + \alpha K^L(I) + \frac{\beta(1-\alpha)K^L(I)}{K^h(I)} \right]} \quad (9)$$

$$\eta^{L^h} F^{L^h}(I) = \frac{\eta^F F^F(I)}{\left[\beta(1-\alpha) + \alpha K^h(I) + \frac{(1-\alpha)(1-\beta)K^h(I)}{K^L(I)} \right]} \quad (10)$$

here define:

$$K^L(I) = \frac{\eta^V F^V(I)}{\eta^L F^L(I)} \quad K^h(I) = \frac{\eta^V F^V(I)}{\eta^{L^h} F^{L^h}(I)} \quad (11)$$

By solving these equations using the method proposed by Mauri[10], α and β can be easily calculated, then the discrete components compositions and continuous fraction distribution in the outlet can be obtained. In the calculation, the distribution function was calculated by a cubic spline fit method by Ying [9].

3. EQUATION OF STATE(EOS) AND DISTRIBUTION FUNCTION:

The P_R EOS for mixtures is taken to calculate the fugacity coefficient. The continuous P_R EOS can be found elsewhere. In our method, normal boiling temperature is taken as the

distributed variable and the distribution function is the experimental TBP distillation. It has great advantages to select distribution function given above.

4. RESULTS AND DISCUSSION:

The flash of 27-multicomponent mixtures in the high pressure hydrocracking separator were calculated in this paper. To those polar components, special treatment were used. The properties M , T_c , P_c of petroleum fractions were calculated by Riazi and Daubert [11](1980) correlations, and ω was calculated by Lee and Kesler's correlation. A group of typical results

Table1 Three Phase Flash-Calculation Results for a Semicontinuous Mixture at 49 C and 164.8bar

component	mol%						
	feed	liquid		water		vapor	
	specified	calcd	exptl	calcd	exptl	calcd	exptl
H2O	0.0349	0.0002	0.0002	0.9311	0.9300	0.0006	0.0007
NH3	0.0013	0.0000	0.0000	0.0330	0.0350	0.0000	0.0000
H2S	0.0036	0.0063	0.0059	0.0359	0.0350	0.0028	0.0019
H2	0.7330	0.0821	0.0999	0.0000	0.0000	0.8521	0.8525
CH4	0.1190	0.0679	0.0721	0.0000	0.0000	0.1309	0.1306
C2-C5	0.0293	0.1631	0.1542	0.0000	0.0000	0.0125	0.0131
Heavies	0.0791	0.6804	0.6677	0.0000	0.0000	0.0018	0.0011

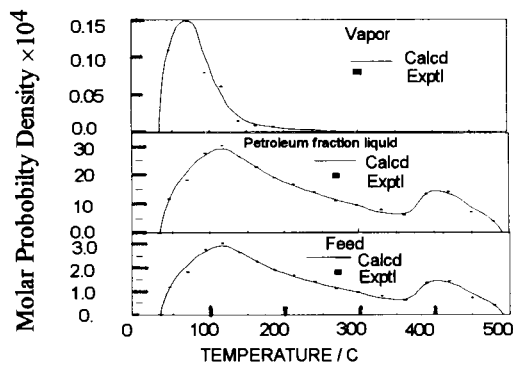


Figure 1 Calculated and experimental distribution of heavies for a semicontinuous mixtures

were shown in Figure 1 and Table 1. The results are reasonable and are in line with the experimental data from a home-made bench-scale equipment in FRIPP, China. Continuous thermodynamics method is also a time saving method. From Figure 1 and Table 1, it is found that the distribution of liquid phase petroleum fraction is very rather similar to that of feed,

because there were little amounts of petroleum fraction which were dissolved in water phase even though the system pressure is very high. Other examples were calculated using this method, similar results were also obtained. It illustrates that continuous thermodynamic method is a good approach for three phase flash calculation of continuous or semicontinuous mixtures.

REFERENCES:

1. Gualtier, J. A.; J. A. Kincaid & G. Morrison; Phase equilibria in polydisperse fluids, *J. Chem. Phys.*, 77, 521-536(1982).
2. Cotterman, R.L.; R. Bender; & J. M. Prausnitz; Phase Equilibria for Mixtures Containing Very Many Components. Development and Application of Continuous Thermodynamics for Chemical Process Design ; *Ind. Eng. Chem. Process Des. Dev.*; 24,194-203(1985).
3. Cotterman, R.L.; & J. M. Prausnitz; Flash Calculations for continuous or Semicontinuous Mixtures Using an Equation of State; *Ind. Eng. Chem. Process Des. Dev.*; 24,434-443, (1986).
4. Ratzsch, M. T.; and H. Kehlen; Application of continuous thermodynamics to the vapor-liquid equilibrium. *Z. Chem. (Leipzig)* 23, 389-394(1983)
5. Kelen, H.; M. T. Ratzsch; & J. Bergmann; Continuous Thermodynamics of Multicomponent System., *AIChE J.*, 31(7), 1136-48 (1985).
6. Ratzsch, M.T., H. Kehlen, & J. Schumann; Flash calculation for a crude oil by continuous thermodynamics, *Chem. Engng. Commun.*, 71, 113-125(1988).
7. Wang, S.H., & W. B. Whiting; A Comparison of Distribution Functions for Calculation of Phase Equilibria of Continuous Mixtures ; *Chem. Engng. Comm.*; 71,127-143(1988).
8. Chou, G. F., and J. M. Prausnitz; "Adiabatic flash calculations for continuous or semicontinuous mixtures using an equation of state." *Fluid Phase Equilibria*, 30, 75-82(1986).
9. Ying, Xugeng; Ye Ruqiang; & Hu ying; Phase Equilibria for Complex Mixtures. Continuous-thermodynamics Method Based on Spline Fit . *Fluid Phase Equilibria*, 53, 407-414(1989).
10. Mauri, C.; Unified procedure for solving multiphase-multicomponent vapor-liquid equilibrium calculation, *Ind. Eng. Chem. Process. Des. Dev.*, 19, 482-489(1980).
11. Sim, W. J. & T. E. Daubert; Prediction of Vapor-Liquid Equilibria of Undefined Mixtures. *Ind. Eng. Chem. Process Des. Dev.* ; 19,386-393 (1980) .

Representation of the Ternary System CO₂ - H₂O - CH₃OH

E. Rauzy, F. Sablayrolles, C. Rébufa and C. Berro

Laboratoire de Chimie-Physique, Faculté des Sciences de Luminy
 13288 Marseille cedex 9, France.

1. INTRODUCTION

Supercritical fluids such as carbon dioxide can be used as solvents to extract organic compounds from aqueous solutions. In order to achieve recoveries of these products often in low concentration, cosolvents as methanol or other alcohols have been added to improve the solubility and the selectivity of the primary fluid. To optimize the extract recovery, the knowledge of phase equilibria of the ternary system carbon dioxide-methanol-water is required at different temperatures and pressures.

The aim of the study is to represent the phase equilibria of three binary systems, carbon dioxide-methanol, carbon dioxide-water and water-methanol and to predict from binary interaction parameters these of ternary system.

The model used combines two equations of state and an excess function. It has been already developed to represent the thermodynamic properties of carbon dioxide-hydrocarbons mixtures [1].

2. DESCRIPTION OF THE MODEL

Briefly, we recall the method described previously [1]. The model « excess function- equation of state » explained elsewhere [2], allows us to write the molar Helmholtz energy at the mixture as follows :

$$A(T, \eta, x_i) - A^*(T, \eta, x_i) = \sum_{i=1}^P x_i [A_i(T, \eta) - A_i^*(T, \eta)] + A_{res}^E(T, \eta, x_i) \quad (1)$$

where A^* and A_i^* are the ideal-gas molar Helmholtz energy and A_{res}^E the excess residual energy defined at constant packing fraction denoted by η .

Thermodynamic properties of pure compounds are calculated by equations of state. For carbon dioxide, an accurate equation of state, the IUPAC equation [3] is used.

For water and methanol, we have chosen the Peng-Robinson type equation of state.

$$P = \frac{RT}{\tilde{v} - \tilde{b}} - \frac{a(T)}{\tilde{v}(\tilde{v} + \tilde{b})} \quad \text{with } \gamma = 2(\sqrt{2} + 1) \quad (2)$$

where \tilde{b} is the pseudo-covolume estimated from critical specificities and $a(T)$ the attractive term calculated according to the Carrier and al. [4] procedure.

It depends on two parameters m_1 and m_2 . The values of the normal boiling temperature T_b , the critical temperature and pressure T_c , P_c and parameters m_1 , m_2 are given in Table 1, for each component.

Table 1 : Thermodynamic properties of the pure compounds and parameters used in the model

Compon	T_b /	T_c /	P_c / b	m_1	m_2
CO ₂	194.7	304.2	-	-	-
H ₂ O	373.1	647.3	221.2	1.358	0.165
CH ₃ O	337.7	512.5	80.9	1.080	-0.170

As shown previously [2], the residual excess Helmholtz energy can be written :

$$A_{res}^E = \frac{1}{2} \sum_{i=1}^P \sum_{j=1}^P \frac{q_i q_j x_i x_j E_{ij}(T)}{\sum_{i=1}^P x_i q_i} \times \frac{Ln(1 + \gamma' \eta)}{\gamma'} \quad \text{with } \gamma' = 20 \quad (3)$$

where E_{ij} is the binary energy parameter and q_i , a surface fraction such as $q_i = \delta_i b_i$, with δ_i an adjusted parameter, in the case of the binaries with the carbon dioxide. The values of δ_i depend on temperature and are respectively $\delta_1 = 4.9704 - 0.00719.T$ for the methanol, and $\delta_2 = 6.349 - 0.00915.T$ for the water.

For the methanol-water system, the surface parameter q_i is substituted by the volume parameter b_i .

The interaction energy parameter owns two forms according the binary studied :

- first form :

$$E_{ij}(T) = E_{ij}^0 \times \left(\frac{T_0}{T} \right)^r \quad \text{with } T_0 = 298.15 \text{ K} \quad (4)$$

Table 2 : Parameters value of binary energy parameter

Systems	E_{ij}^0 / J.c	r
methanol - water	856.31	-1.762
methanol - carbon dioxide	673.15	-1.319

- second form : (used to represent water-carbon dioxide system)

$$E_{ij}(T) = \alpha + \beta.T.Ln(T) + \lambda.T \quad \text{in J.cm}^{-3} \quad (5)$$

with $\alpha = -5018.172$, $\beta = 13.645$, $\lambda = 102.580$.

3. RESULTS AND DISCUSSION

For the three binary systems, the high and low pressure vapor-liquid equilibria results are summarized in Tables 3, 4, 5 and 6.

In the followed tables, the average relative deviations are such as :

$$\left| \Delta P / P (\%) = \frac{100}{N_p} \sum_{i=1}^p (P_{\text{exp}} - P_{\text{calc}}) / P_{\text{exp}} \right. \quad (6)$$

$$\left| \Delta X / X (\%) = \frac{100}{N_p} \sum_{i=1}^p (X_{\text{exp}} - X_{\text{calc}}) / X_{\text{exp}} \right. \quad (7)$$

The root square deviation is defined as follows :

$$\left| d (\%) = 100. \left[(X_{\text{exp}} - X_{\text{calc}}) / X_{\text{exp}} \right]^2 \right. \quad (8)$$

Table 3 : Isothermal Vapor-Liquid Equilibrium results for Methanol-Water

Temperature / K	Pressure / bar	Number of data points	Source of experimental data	$\Delta P / P$ (%)
243 - 474	0.0005 - 39.50	414	[5] to [18]	1.87

Table 4 : Isobaric Vapor-Liquid Equilibrium results for Methanol-Water

Pressure / bar	Temperature / K	Number of data points	Source of experimental data	$\Delta P / P$ (%)
0.26 - 5.07	307 - 421	605	[10],[19] to [44]	2.35

Table 5 : Isothermal Vapor-Liquid Equilibrium results for Methanol-Carbon dioxide

Temperature / K	Pressure / bar	Number of data points	Source of experimental data	$\Delta P / P$ (%)
230 - 478	1.90 - 165.00	306	[45] to [54]	2.52

Table 6 : Isothermal Vapor-Liquid Equilibrium results for Carbon dioxide - Water

Temperature / K	Pressure / bar	Number of data points	Source of experimental data	$\Delta P / P$ (%)
288 - 573	1 - 500	290	[55] to [61]	4.76

Table 7 : Isothermal Vapor-Liquid Equilibrium results for CO₂(1) - H₂O(2) - CH₃OH(3)

T = 313.15 K Experimental data of Yoon [51].										
P / bar	X _{1,exp}	X _{1,calc}	X _{2,exp}	X _{2,calc}	d	Y _{1,exp}	Y _{1,calc}	Y _{2,exp}	Y _{2,calc}	
70.000	0.0390	0.0505	0.2200	0.2175	0.0118	0.9940	0.9935	0.0050	0.0050	
70.000	0.0690	0.0849	0.3540	0.3476	0.0172	0.9930	0.9919	0.0060	0.0069	
70.000	0.1430	0.1484	0.4850	0.4806	0.0069	0.9910	0.9901	0.0070	0.0089	
70.000	0.2330	0.2227	0.5480	0.5537	0.0118	0.9900	0.9888	0.0080	0.0104	
70.000	0.2980	0.2928	0.5740	0.5776	0.0064	0.9890	0.9879	0.0100	0.0116	
70.000	0.3250	0.3161	0.5720	0.5788	0.0112	0.9890	0.9876	0.0100	0.0119	
Average relative deviation : on X ₁ = 10.88% on X ₂ = 1.12%										
T = 298.15 K Experimental data of Chang [47].										
P / bar	X _{1,exp}	X _{1,calc}	X _{2,exp}	X _{2,calc}	X _{3,exp}	X _{3,calc}	d	Y _{1,calc}	Y _{2,calc}	Y _{3,calc}
5.207	0.0279	0.0265	0.8051	0.8034	0.1670	0.1701	0.0022	0.9705	0.0281	0.0014
8.307	0.0469	0.0435	0.7949	0.7963	0.1582	0.1602	0.0037	0.9811	0.0181	0.0008
12.733	0.0670	0.0684	0.7846	0.7828	0.1484	0.1487	0.0023	0.9871	0.0123	0.0005
16.411	0.0830	0.0888	0.7700	0.7649	0.1470	0.1463	0.0077	0.9897	0.0099	0.0004
20.756	0.1070	0.1131	0.7487	0.7435	0.1443	0.1434	0.0080	0.9915	0.0082	0.0003
26.034	0.1427	0.1442	0.7205	0.7194	0.1368	0.1365	0.0019	0.9927	0.0070	0.0003
31.190	0.1775	0.1736	0.6879	0.6913	0.1346	0.1351	0.0052	0.9935	0.0062	0.0002

Table 7 (continued)

35.566	0.2073	0.2019	0.6659	0.6706	0.1268	0.1274	0.0072	0.9939	0.0059	0.0002
40.743	0.2432	0.2349	0.6351	0.6424	0.1217	0.1228	0.0110	0.9941	0.0056	0.0002
45.595	0.2914	0.2381	0.5591	0.6012	0.1095	0.1607	0.0679	0.9944	0.0053	0.0003
Average relative deviation : on $X_1 = 5.46\%$ on $X_2 = 1.20\%$ on $X_3 = 1.39\%$										
T = 273.15 K Experimental data of Chang [47].										
P / bar	$X_{1,exp}$	$X_{1,calc}$	$X_{2,exp}$	$X_{2,calc}$	$X_{3,exp}$	$X_{3,calc}$	d	$Y_{1,calc}$	$Y_{2,calc}$	$Y_{3,calc}$
2.472	0.0193	0.0219	0.8218	0.8187	0.1589	0.1593	0.0041	0.9855	0.0140	0.0005
5.804	0.0474	0.0526	0.7971	0.7930	0.1555	0.1545	0.0066	0.9937	0.0061	0.0002
9.107	0.0766	0.0841	0.7742	0.7684	0.1492	0.1475	0.0095	0.9959	0.0040	0.0001
13.756	0.1197	0.1302	0.7376	0.7295	0.1427	0.1404	0.0133	0.9971	0.0028	0.0001
19.034	0.1802	0.1868	0.6869	0.6821	0.1329	0.1311	0.0081	0.9978	0.0021	0.0001
25.193	0.2504	0.2655	0.6318	0.6199	0.1178	0.1147	0.0192	0.9982	0.0018	0.0001
30.367	0.3522	0.3460	0.5444	0.5504	0.1034	0.1036	0.0086	0.9983	0.0016	0.0001
Average relative deviation : on $X_1 = 7.78\%$ on $X_2 = 0.92\%$ on $X_3 = 1.12\%$										
T = 243.15 K Experimental data of Chang [47].										
P / bar	$X_{1,exp}$	$X_{1,calc}$	$X_{2,exp}$	$X_{2,calc}$	$X_{3,exp}$	$X_{3,calc}$	d	$Y_{1,calc}$	$Y_{2,calc}$	$Y_{3,calc}$
1.631	0.0323	0.0335	0.8062	0.8058	0.1615	0.1606	0.0013	0.9975	0.0024	0.0001
3.353	0.0686	0.0709	0.7777	0.7766	0.1537	0.1525	0.0025	0.9988	0.0012	0.0000
5.602	0.1160	0.1211	0.7306	0.7273	0.1534	0.1516	0.0060	0.9993	0.0007	0.0000
7.111	0.1548	0.1623	0.7092	0.7038	0.1360	0.1339	0.0093	0.9994	0.0006	0.0000
9.431	0.2198	0.2246	0.6469	0.6439	0.1333	0.1315	0.0056	0.9996	0.0004	0.0000
12.331	0.3308	0.3384	0.5604	0.5550	0.1088	0.1066	0.0094	0.9997	0.0003	0.0000
Average relative deviation : on $X_1 = 3.46\%$ on $X_2 = 0.47\%$ on $X_3 = 1.23\%$										

The model used is in good agreement with experimental data in the wide range of temperatures for the methanol-water system which exhibits no difficulty.

The binary methanol-carbon dioxide has been well studied. As can be seen in Table 5, agreement with experiment is satisfactory although several sets of data are in disagreement.

For the system carbon dioxide-water, the measurements at high pressures have not been retained because the IUPAC equation for carbon dioxide is available up to pressures equal to 600 bar. We remark in Table 6 a higher deviation in bubble pressure than for other binaries.

The experimental and predicted results for the ternary system carbon dioxide-methanol-water are listed in Table 7. Chang and Rousseau [47] have measured the solubilities of carbon dioxide in methanol-water mixtures at different pressures and at temperatures below the critical temperature of carbon dioxide while Yoon [51] have measured the liquid and vapor phase equilibrium composition but overestimates slightly these of carbon dioxide in the liquid phase.

4. CONCLUSION

The proposed method allows us to obtain a good agreement with experiment for three binary systems but also to predict the two-phase equilibria of the ternary system. However it seems that the equations of state used for methanol and water are not enough accurate and that the knowledge of vapor-liquid equilibria of binaries including carbon dioxide should be improved.

LIST OF SYMBOLS

a	: attractive term	*	: ideal
A	: free energy	b	: boiling
b	: volume parameter	exp	: experimental
E	: binary energy parameter	E	: excess
m	: adjusted parameter	c	: critical
P	: pressure	calc	: calculated
q	: surface parameter	res	: residual
R	: ideal gas constant		
r	: adjusted parameter		
T	: temperature		
v	: volume		
x	: liquid molar fraction		
y	: vapor molar fraction		
α	: adjusted parameter		
β	: adjusted parameter		
λ	: adjusted parameter		
η	: constant packing fraction		

REFERENCES

1. Rauzy E. & al., *Fluid Phase Equilibria*, 114 (1996) 63.
2. Péneloux A., *Fluid Phase Equilibria*, 47 (1989) 115.
3. Angus S. & al., *IUPAC*, 3 (1973) 36.
4. Carrier B. & al., *Ind.Eng.Chem.Res.*, 27 (1988) 1714.
5. Mokbel I., *Thesis, University of Claude Bernard-Lyon, France*, 1993.
6. Dulitskaya K.A., *Zh.Obshch.Kim.*, 15 (1945) 9.
7. Butler A.V. & al., *J.Chem.Soc. London* (1933) 674.
8. Hall D.J. & al., *NPL Report Chem.*, (1979) 95.
9. McGlashan M.L. & al., *J.Chem.Eng.Data*, 21, 2 (1976) 196.
10. Bredig G. & al., *Z.Phys.Chem.*, 130 (1927) 1.
11. Fergusson J.B. & al., *J.Phys.Chem.*, 33 (1929) 1.
12. Ratcliff G.A. & al., *Can.J.Chem.Eng.*, 47 (1969) 148.
13. Ewert M., *Bull.Soc.Chim.Belg.*, 45 (1936) 493.
14. Kurihara K. & al., *J.Chem.Eng.Data*, 40 (1995) 679.
15. Broul M. & al., *Coll.Czech.Chem.Comm.*, 34 (1969) 3428.
16. Schuberth H., *Z.Phys.Chem. Leipzig*, 255, 1 (1974) 165.
17. Griswold J. & al., *Chem.Eng.Prog.Symp.Ser.*, 48 (1952) 18.
18. Reamer H.H. & al., *Ind.Eng.Chem.*, 47 (1952) 148.
19. Othmer D.F. & al., *Ind.Eng.Chem.*, 37 (1945) 299.
20. Olevesky V.M. & al., *Tr.Giap.VYP*, 6 (1956) 45.
21. Dalager P., *J.Chem.Eng.Data*, 14, 3 (1969) 298.
22. Dunlop M.S., *Thesis Brooklyn Polytechn.Inst.*, 1948.

23. Green S.I. & al., *Ind.Eng.Chem.*, 47 (1955) 103.
24. Griswold J. & al., *Ind.Eng.Chem.*, 41 (1949) 2347.
25. Hughes H.E. & al., *Chem.Eng.Prog.*, 48 (1952) 192.
26. Kato M. & al., (1970)
27. Kato M. & al., *J.Chem.Eng.Data*, 14 (1971) 435.
28. Kohovtova J. & al., *Col.Czech.Chem.Com.*, 35 (1970) 3210.
29. Kurihara K. & al., *J.Chem.Eng.Data*, 38 (1993) 446.
30. Maripuri V.O. & al., *J.Chem.Eng.Data*, 17 (1972) 336.
31. Ochi K. & al., *Kagaku Kogaku*, 35 (1971) 583.
32. Ocon J. & al., *An.Real.Soc.Esp.de Fis.y Quim.*, 548 (1958) 525.
33. Ocon J. & al., *An.Real.Soc.Esp.de Fis.y Quim.*, 558 (1959) 255.
34. Pascal P. & al., *Bull.Soc.Chim.France*, 29 (1921) 9.
35. Ramalho R.S. & al., *Ing.Eng.Chem.*, 53 (1961) 895.
36. Uchida S. & al., *Kagaku Kikai Chem.Eng.*, 17 (1953) 191.
37. Van Zandijcke F. & al., *J.Appl.Chem.Biotechn.*, 24 (1974) 709.
38. Verhoeve L. & al., *J.Appl.Chem.Biotechn.*, 23 (1973) 607.
39. Kojima K. & al., *Kagaku Kogaku*, 32 (1968) 149.
40. Novella E.G. & al., *An.Real.Soc.Espan.de Fis.y Quim.*, 48 (1952) 397.
41. Swami D.R. & al., *Trans.Indian Inst.Chem.Engrs.*, 9 (1956) 32.
42. Uchida S. & al., *J.Soc.Chem.Ind.Jap.*, 37 (1934) Suppl.525.
43. Hirata M. & al., *Computer aided Data of VLE*, Elsevier, 1975.
44. Hirata M. & al., *Kagaku Kogaku*, 31 (1967) 759.
45. Hong J.H. & al., *Fluid Phase equilibria*, 41 (1988) 269.
46. Weber W. & al., *Fluid Phase Equilibria*, 18 (1984) 253.
47. Chang T. & al., *Fluid Phase Equilibria*, 23 (1985) 243.
48. Brunner E. & al., *J.Chem.Thermodyn.*, 19 (1987) 273.
49. Ohgaki K. & al., *J.Chem.Eng.Data*, 21 (1976) 53.
50. Katayama T. & al., *J.Chem.Eng.Jpn.*, 8 (1975) 89.
51. Yoon J.H. & al., *J.Chem.Eng.Data*, 38 (1993) 53.
52. Suzuki K. & al., *J.Chem.Eng.Data*, 35 (1990) 63.
53. Semenova A.I. & al., *Zh.Fiz.Khim.*, 53 (1979) 2502.
54. Leu A.D. & al., *J.Chem.Thermodyn.*, 23 (1991) 979.
55. Gillespie P.C. & al., *Gas Process. Assoc. Research Report*, (1982) RR-48.
56. Houghton G. & al., *Chem.Eng.Sci.*, 6 (1957) 132.
57. Zawisza A. & al., *J.Chem.Eng.Data*, 26 (1981) 388.
58. Nighswander J.A. & al., *J.Chem.Eng.Data*, 34 (1989) 355.
59. Takenouchi S. & al., *Am.J.Sci.*, 262 (1964) 1055.
60. Toedheide K. & al., *Z.Phys.Chem. (Frankfurt)*, 37 (1963) 387.
61. Johari G.P. & al., *J.Chem.Phys.*, 64 (1976) 4484.

Calculation of High-Pressure Phase Equilibria Involving Light Gases

J. Kohlbruch and U. K. Deiters

Institute of Physical Chemistry, University at Cologne, Luxemburger Str. 116,
D-50939 Köln, F. R. Germany

A new correction function for quantum effects in fluids is proposed, which can be coupled to any van der Waals type equation of state. With the new quantum correction, calculations of thermodynamic properties of hydrogen and hydrogen-containing mixtures are significantly improved.

1. INTRODUCTION

The thermodynamic properties of fluids consisting of light molecules sometimes departs markedly from those of heavier molecules. These departures, the so-called quantum effects, result from two different phenomena, the exchange effect and the diffraction effect.

The exchange effect is due to symmetry properties of the ensemble wave function (symmetric or antisymmetric with respect to the exchange of two particles), which govern the occupation of energy levels. Particles with integer spin obey Bose-Einstein statistics, otherwise Fermi-Dirac statistics. The exchange effect is a low-temperature phenomenon and is mainly responsible for the anomalous behavior of helium below 5 K; it is negligible for heavier molecules or higher temperatures.

The diffraction effect has two causes: In a collision, two molecules form short-lived dimers, which have discrete vibrational and rotational energy levels. This vibration effect should be observable for light gases (helium, hydrogen) at low densities. However, de Boer and Michels showed even in 1939 that the influence of the vibration effect on the second virial coefficient is rather small [1], and can be accounted for by using effective pair potentials [2].

The other cause, the density effect, is especially important at high densities, where molecules are more or less confined to cells formed by their neighbors. In analogy to the well-known quantum mechanical problem of a particle in a box, the translational energies of such molecules are quantized, and this has an effect on the thermodynamic properties. In 1960 Levelt Sengers and Hurst [3] tried to describe the density quantum effect in term of the Lennard-Jones-Devonshire cell model, and in 1980 Hooper and Nordholm proposed a generalized van der Waals theory [4]. The disadvantage of both approaches is that, in the classical limit, they reduce to rather unsatisfactory equations of state.

In contrast to this, the method proposed by Deiters [5, 6] can be applied to any van der Waals type equation of state, which consists of an attraction and a repulsion part:

$$p = p_{\text{rep}} + p_{\text{att}} \quad (1)$$

However, this model makes the somewhat unrealistic assumption of cubic cells. Furthermore, it predicts too high corrections at low densities.

2. QUANTUM CORRECTION

2.1. Basic Cell Model

In this work it is assumed that the cells formed by neighbor molecules are roughly spherical in shape:

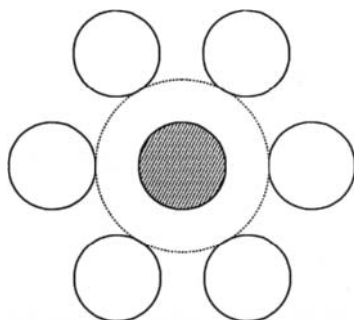


Figure 1. A molecule confined to a spherical cell by its neighbors.

The energy eigenvalues of a particle in a spherical cell of diameter R can be obtained from Schrödinger's equation. It is convenient to write the wave function as a product of an angle-dependent and a distance-dependent function, the latter of which is given by:

$$\frac{d^2\chi}{dr^2} + \frac{1}{r} \frac{d\chi}{dr} + \left[k^2 - \frac{(l + \frac{1}{2})^2}{r^2} \right] \chi = 0 \quad (2)$$

Its solutions [7] are Bessel's cylinder functions of the argument kr . The angle-dependent part of the wave function consists of spherical harmonics. The resulting energy eigenvalues are

$$E_{nl} = \frac{\hbar^2 (kR)_{nl}^2}{2mR^2} \quad (3)$$

where $(kR)_{nl}$ represents the n th solution of the l th cylinder function.

The free volume, defined by

$$\ln \frac{V_f}{V} = \int_{\infty}^V \left(\frac{p_{\text{rep}}}{Nk_B T} - \frac{1}{V} \right) dV \quad (4)$$

is connected with the cell radius:

$$R^3 = p_{\text{geo}} \frac{V_f}{N} \quad (5)$$

The factor p_{geo} accounts for the fact that each cell belongs to several particles.

The partition function of the quantum gas can then be constructed from the single-particle repulsion partition function, q_{rep} and the contribution of attraction, Q^* :

$$Q_{\text{quant}} = \frac{1}{N!} \left(\frac{N q_{\text{rep}}}{p_{\text{geo}}} \right)^N Q^* = Q_{\text{class}} \left[y F_{\text{geo}} \sum_j g_j \exp \left(-\frac{\epsilon_j}{k_B T} \right) \right]^N$$

(6)

with $y = \frac{\Lambda}{R}$

and $\Lambda = \sqrt{\frac{h^2}{2\pi k_B m T}}$ thermal de Broglie wavelength

The g_j are degeneration factors, F_{geo} a geometrical correction factor. The partition function of a classical gas is $Q_{\text{class}} = 1/N! (V/\Lambda)^N Q^*$.

Inserting the eigenvalue spectrum (3) leads to an expression for the partition function, which can be numerically evaluated and expressed a power series:

$$Q_{\text{quant}} = Q_{\text{class}} \left[y F_{\text{geo}} \sum_{n,l} g_{nl} \exp \left(-\frac{\pi}{4} y^2 \left(\frac{(kR)_{nl}}{\pi} \right)^2 \right) \right]^N = \exp \left(\sum_{i=1}^{10} r_i y^i \right) \quad (7)$$

For heavy particles or high temperatures, the quantum correction (square brackets) converge against 1, and the classical partition function is recovered.

The expansion coefficients r_i were obtained by orthogonal expansion; their values are shown in Table 1.

Table 1

Expansion coefficients of new quantum correction, Eq. (7).

i	r_i	i	r_i
1	-0.7598010969	6	2.827697793
2	0.1933832800	7	-2.633022839
3	-0.3166755254	8	1.496117566
4	1.005109730	9	-0.5686938848
5	-2.082501836	10	0.0920579842

From (7) the Helmholtz energy of a quantum gas is obtained relative to that of a classical gas:

$$A_{\text{quant}} = -N k_B T \ln Q_{\text{quant}} = A_{\text{class}} - N k_B T \sum_{i=1}^{10} r_i y^i \quad (8)$$

2.2. The Onion Skin Model

At low densities, the cell model described above is no longer adequate. The spherical cell walls formed by the neighbors of a molecule are no longer totally reflective, but have gaps, so that the central molecule can escape, until it is reflected at another spherical wall further outside.

It is assumed that the central molecule is surrounded by spherical walls in an onion-like fashion, with radii $R_n = nR$, where R is given by Eq. (5). Hence the surface of the n th wall is

$$F_n = n^2 F_1 = 4\pi n^2 \left(\frac{3}{4\pi} x_{\text{geo}} \frac{V_f}{N} \right)^{2/3} \quad (9)$$

with x_{geo} denoting a geometrical constant.

If the molecules are spheres of volume (per mole) v^* , their collision cross section is

$$F_{\text{cross}} = \pi \left(\frac{3}{4\pi} \frac{v^*}{N_A} \right)^{2/3} \quad (10)$$

and the area of the reflecting sphere covered by them is

$$F_{\text{refl},n} = 4\pi x_{\text{refl}} n^2 \left(\frac{3}{4\pi} \frac{v^*}{N_A} \right)^{2/3} \quad (11)$$

This has to be compared to the total surface of the n th spherical wall; the resulting reflection probability is

$$w = x \left(\frac{v^*}{V_f} \right)^{2/3} \quad (12)$$

with x a numerical constant. w denotes the probability that a molecule is reflected at the n th wall. Summation over all walls leads to an averaged sphere radius $\bar{R} = R/w$, which can then be used with Eqs. (6-7) to calculate the improved quantum correction.

3. APPLICATION

In order to demonstrate the effect of the new quantum correction, it is applied to a noncubic equation of state which is known to give reasonably good results for classical gases [8-10]:

$$p = \frac{RT}{V_m} \left(1 + cc_0 \frac{4\xi - 2\xi^2}{(1 - \xi)^3} \right) - \frac{RT^* v^*}{V_m^2} \tilde{T}_{\text{eff}} \left[\exp \left(\frac{1}{\tilde{T}_{\text{eff}}} \right) - 1 \right] I_1 \quad (13)$$

with $\tilde{T}_{\text{eff}} = \frac{1}{Y} \left(\frac{ck_B T}{\epsilon} + \lambda \xi \right), \quad \xi = \frac{Nv^*}{V}$

I_1 and Y are universal functions of density and shape parameter c , which have been explained elsewhere. Eq. (13) has three adjustable parameters, the potential depth ϵ , the molecular volume v^* and the shape parameter c ; the latter is 1 for the substances discussed in this work.

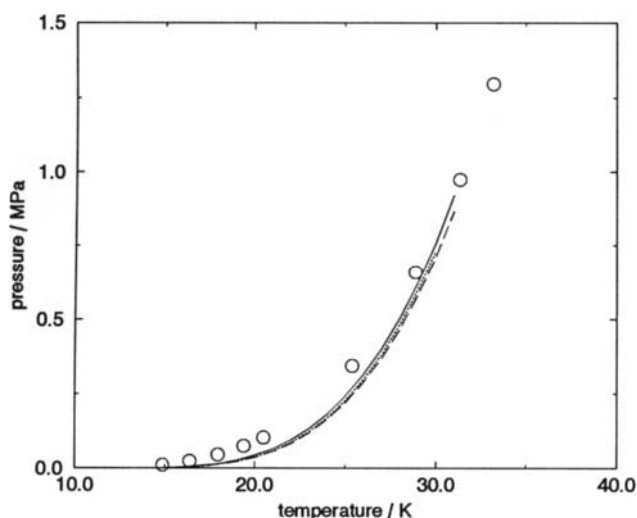


Figure 2. Vapor pressure of hydrogen. - - -: calculated with equation of state (13) without quantum correction; · · · : with old quantum correction; —: with new quantum correction; symbols: exp. data [11].

The parameters ϵ and v^* were obtained from critical data and then used to predict the vapor pressure curves of several light gases. The results for hydrogen are shown in Fig. 2. It appears that there is a significant improvement over the old quantum correction [5]. It must be mentioned that, in contrast to the old quantum correction, the new quantum correction preserves the correct low-density behavior of the underlying equation of state.

We have also applied the new quantum correction to mixtures at high pressures, using the following mixing rules (1-fluid theory):

$$\begin{aligned}
 m^{-0.5} &= \sum x_i m_i^{-0.5} \\
 v^* &= \sum \sum x_i x_k v_{ik}^* \\
 c &= \sum x_i c_i \\
 \epsilon v^* &= \sum \sum x_i x_k \epsilon_{ik} v_{ik}^*
 \end{aligned} \tag{14}$$

After fitting ϵ_{ik} and v_{ik}^* to experimental data of the system ($\text{H}_2 + \text{CO}$), an almost perfect agreement of the calculated isotherms with the experimental phase equilibrium data could be obtained for pressures up to 60 MPa.

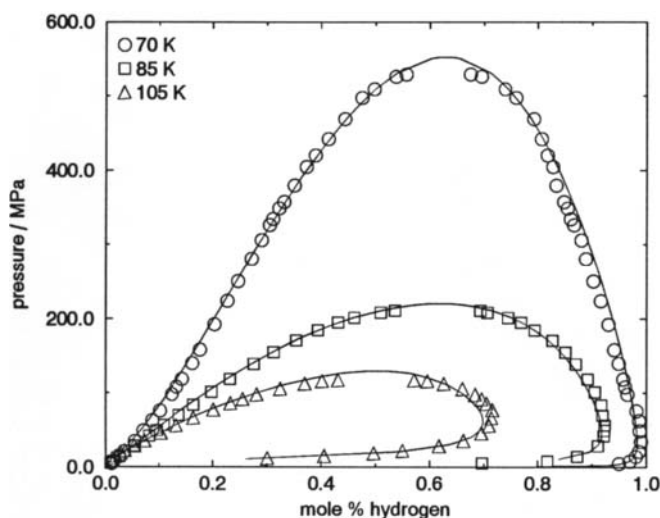


Figure 3. High-pressure phase equilibria of the ($\text{H}_2 + \text{CO}$) system.

—: calculated with equation of state (13) and new quantum correction (7);
 symbols: exp. data [12].

REFERENCES

1. J. de Boer and A. Michels, *Physica* 6 (1939) 409.
2. L. Verlet, *Phys. Rev.* 159 (1967) 98–103.
3. J. M. H. Levelt Sengers and R. P. Hurst, *J. Chem. Phys.* 32 (1960) 96.
4. M. A. Hooper and S. Nordholm, *Aust. J. Chem.* 33 (1980) 2029–2035.
5. U. K. Deiters, *Fluid Phase Equil.* 10 (1983) 173–182.
6. U. K. Deiters, *Fluid Phase Equil.* 13 (1983) 109–120.
7. S. Flügge, *Rechenmethoden der Quantentheorie*. Springer-Verlag Berlin, 1976.
8. U. K. Deiters, *Chem. Eng. Sci.* 36 (1981) 1139–1146.
9. U. K. Deiters, *Chem. Eng. Sci.* 36 (1981) 1146–1151.
10. U. K. Deiters, *Chem. Eng. Sci.* 37 (1982) 855–861.
11. R. D. McCarty, *Hydrogen: Technological Survey — Thermophysical Properties*. NASA Report SP-3089. National Bureau of Standards, Boulder, Colorado, USA, 1975.
12. C. Y. Tsang and W. B. Streett, *Fluid Phase Equil.* 6 (1981) 261–273.

The Study of HP-HT Interaction between Co-Base Melts and Diamond Powders

A.A.Bochechka, V.G.Gargin, A.A.Shulzhenko

V.N.Bakul Institute for Superhard Materials of the National Academy of Sciences of Ukraine, Kiev 254074, Ukraine

The effect of Co on the process of diamond powder compaction has been studied at the pressure of 8 GPa and temperatures between 1400-2000 °C. It is shown that the interaction between liquid Co and diamond particles speeds up the process if not changes the limiting value of shrinkage as compared with solid phase sintering. The dependences of the rate of diamond powder infiltration with cobalt and Co-WC, Co-Mo and Co-Ti melts on the temperature have been studied experimentally under high pressure. It is shown that the infiltration by pure cobalt occurs quicker as compared with that by cobalt-base alloys. Based on the Einstein equation for the viscosity of mixtures, an equation for the infiltration coefficient is derived which is in good agreement with the experimental data for Co-Ti and Co-WC alloys.

1. INTRODUCTION

At present polycrystalline diamond materials produced by high pressure sintering of a diamond powder on a substrate of group WC/Co alloys are widely used in industry. In sintering, a liquid binder, which is a melted cobalt with some quantity of tungsten carbide dissolved in it, migrates from a substrate into the diamond powder, thus improving the strength and hardness of a sintered diamond layer [1].

In this paper we present some results concerning the kinetics of high pressure migration of liquid cobalt and Co-base alloys into a diamond powder vs temperature as well as the migration effect on diamond powder compaction.

2. EXPERIMENTAL

ACM diamond powders 28-40 microns in size produced by the Institute for Superhard Materials (ISM) have been the subject of investigations. High pressure experiments were performed in a toroid-type high pressure apparatus (HPA). Heating current strength and voltage supplied to a heater were recorded by a self-recording measuring device [2].

Diamond powder was placed into the high pressure cell [2], then the pressure of 8.0 GPa was created, the powder was heated up to the necessary temperature, held for a given time and cooled down to the room temperature.

Then the pressure was removed. As-sintered samples were cleaned from graphite and their densities were determined by the hydrostatic weighing.

Then a mixture of diamond and cobalt powders was placed into the cell and subjected to pressure and temperature. Liquid cobalt that wets diamond is pulled out of the compact if the volume occupied by cobalt somewhat exceeds the total volume of pores which remained after shrinkage of diamond powder. When liquid metal is in contact with a graphite heater, the current flow at first increases due to a total drop of the system electric resistance and then decreases because of diamond formation in the heater. In this case, the shrinkage value corresponds to the volume of cobalt in the powder.

To study the kinetics of infiltration, a bar of the alloy under study was placed in the centre of the cell, and a diamond powder being studied was placed between the bar and the tube heater [2]. The upper disc is made of a conducting while the bottom one of nonconducting material.

The heating started after the pressure of the order of 8 GPa was created. In 0.5 s after the heating starts, current force and heating power in the system become constant. In this case, a formation and migration of the liquid from the centre to the heater take place. As soon as the liquid metal reaches the heater inner surface, the current in the system increases abruptly as an electric circuit with a lower electrical resistance is connected parallel to the heater. The distance covered by the liquid for this period is assessed from the thickness of an infiltrated diamond cocompact recovered of the HPA.

The kinetics of diamond powder infiltration with cobalt of VK15 sintered carbide and Co-Mo and Co-Ti melts was studied experimentally at 8 GPa (Fig. 1). Confidence intervals for T and κ values, the reliability being $\alpha = 0,95$, do not exceed 8 %. According to [3], the limit of WC solubility in Co attains 10 mass % or 3.2 at. %. The additive contents of Co-Mo and Co-Ti alloys was 10 mass % (accordingly, the atomic portions were 0.12 Ti and 0.064 % Mo). Samples of alloys were sintered from mixtures of cobalt-molibdenum and cobalt-titanium hydride powders in a vacuum furnace at 1000 °C.

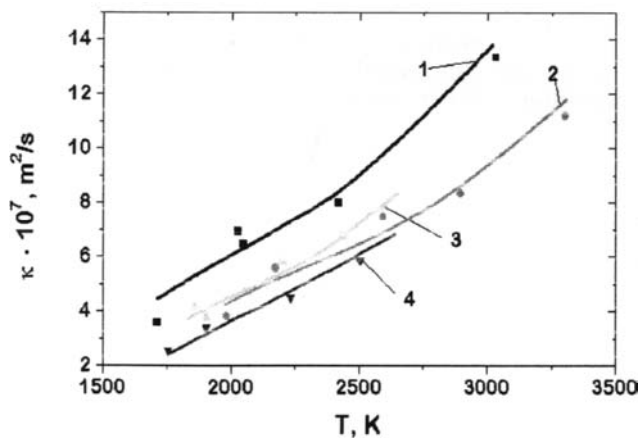


Fig.1. Coefficients of diamond powder infiltration with cobalt-based alloys vs temperature: 1 - Co, 2 - Co-WC, 3 - Co-Ti, 4 - Co-Mo.

3. RESULTS AND DISCUSSION

Under the actions of the pressure of about 8 GPa and the temperature between 1660 - 1700 °C on diamond powders, the density and shrinkage of the samples being sintered attains the maximum for 7 s and the further temperature

increase does not result in an essentially higher compaction [2, 4]. Similar relationship was obtained for the powder under study (Fig. 2).

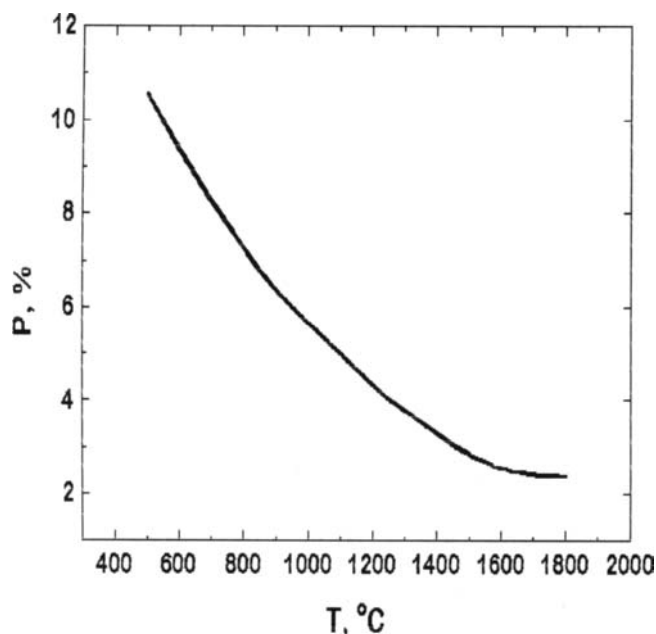


Fig.2. The porosity P of samples sintered from 28-40 μm grain-sized diamond powders for 1.5 minute vs sintering temperature.

In introducing Co-powder into the diamond powder and in sintering, liquid cobalt is pulled out of the compacts if its content is 3 % and higher virtually at the same temperature (Fig. 3). It occurs for 0.5 - 0.7 s after the heating is switched. At the same time if the cobalt content is lower than 3 %, in a slow increase of temperature up to the maximum, cobalt does not contact with the heater. The fact suggests that the volume occupied in the compact by diamond has not exceed the limiting value attained in sintering diamond powder with no additives (see Fig. 2).

Thus, sintering diamond powders with the liquid cobalt present considerably speeds up the compaction process, not changing though the limiting value of shrinkage as compared with the solid phase sintering.

According to the Darcy law in laminar flow of homogeneous liquids via a porous medium with the penetration factor K_p , the process of a liquid

penetration for the depth l depending on the pressure drop Δp , the liquid dynamic viscosity η and time t is described by the equation [5]:

$$(dl/dt) = K_p \Delta p / (\eta l) \quad (1)$$

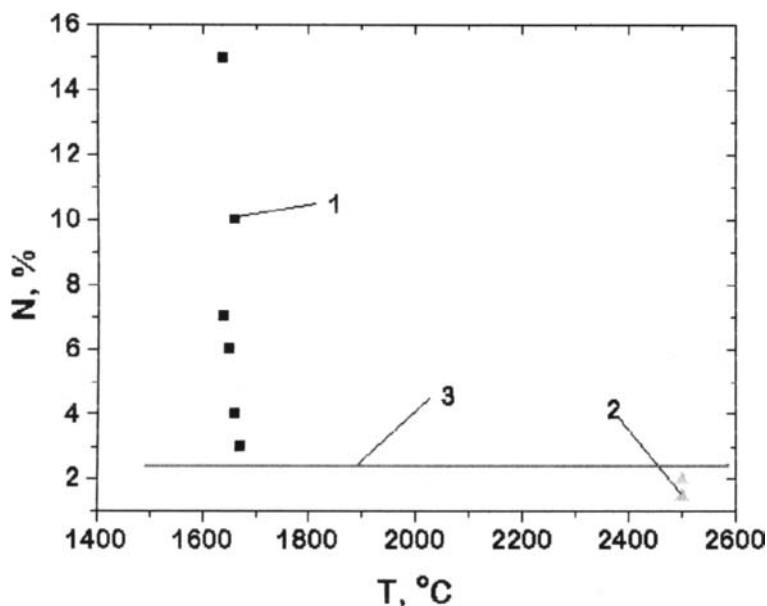


Fig.3. Conditions of the contact of Co and graphite sheath, encasing the mixture of diamond and Co powders:

1 - contact, 2 - no contact, 3 - the value of limiting porosity of solid-phase sintered diamond polycrystals.

In general case, the penetration factor K_p changes with time as along with the liquid flow in the uninfiltated part of a diamond compact, the sintering of diamond particles takes place.

We have established the $K_p(t)$ dependence for diamond powder of 14-20 μm in size at the temperature of 2400 K and the pressure of 7.7 GPa in solid phase sintering. In this case, the $K_p(t)$ becomes constant in 7 s [6]. However, if this powder is cobalt-infiltrated, the $K_p(t)$ becomes constant in 0.5 s. under the same thermobaric conditions. Considering that in our experiments the liquid migration time ranges from 2 to 20 s, let us assume that $K_p(t)$ is constant. Having integrated equation (1) we obtain

$$l^2 = 2(K_p \Delta p / \eta) t = \kappa t. \quad (2)$$

The $\kappa = 2K_p \Delta p / \eta$ value acting as a proportionality factor in Eq. (2) is called a infiltration factor [7]. This factor was found from experimental values of l and t using the following formula:

$$\kappa = l^2/t.$$

Infiltration with Co-WC, Co-Mo and Co-Ti melts occurs more slowly as compared to the infiltration with pure cobalt. The Co-WC migration starts at a higher temperature. Thus, at 1440 °C pure cobalt infiltrates diamond powder to the depth of 2.3 mm for 14.8 s, while cobalt migration from Co-WC alloy was not observed at 1460 °C.

In both the cases, the activation energy of the infiltration process (Fig. 1) is practically the same (≈ 40 kJ/mol) and close to that of the cobalt viscous flow (37.3 kJ/mol) [8], i.e. the observed variations in kinetics of the infiltration are caused by the difference between viscosities of cobalt and its alloys. According to [8] $\gamma = A_0 \exp(E_a/RT)$, where γ is the kinematic viscosity, A_0 is the constant, E_a is the activation energy of viscous flow, R is the universal gas constant, T is the absolute temperature. Correlating this formula with Eq. (2) and considering that $\eta = \rho\gamma$, where ρ is the density of the liquid, we have for κ :

$$\kappa = (K_p \Delta p / 2 \rho A_0) \exp(-E_a/RT),$$

that describes its temperature dependence in diamond powder infiltration with pure cobalt.

To describe the viscosity of binary alloys, let us use Einstein formula for nondissociated low concentration solutions [9]:

$$\eta/\eta_0 = 1 + 2,5 \varphi, \quad (3)$$

where η is the viscosity of mixtures, η_0 is the viscosity of a solvent, φ is the volume portion of additives.

The φ value we present as $(4/3)\pi r_a^3 N/V$, where r_a is the atomic radius of an additive, N is the atomic concentration of the melt, V is the atomic volume of the melt. Substituting V as $(1/k)(4/3)\pi[r^3 n + r_a^3 n_a]$, where r is the solvent atomic radius, n and n_a are numbers of atoms of the solvent and additive, respectively, k is the space factor ($k = (4/3)\pi r^3 N_A \rho / \mu$; μ - molar weight, ρ - solvent density, N_A - Avogadro number) into formula (3), we obtain:

$$\eta/\eta_0 = 1 + 2,5(r^3 + r_a^3)N/[(1-N)r^3 + N(r^3 + r_a^3)] = \kappa_0/\kappa, \quad (4)$$

where κ is the alloy infiltration coefficient, κ_0 is the basic component infiltration coefficient.

Atomic radii of metals in a liquid state are close to those in a solid state as the short-range order in the atom arrangement is retained in a liquid [10]. According to [11], they are: Co - 1.24 Å; Ti - 1.45 Å; Mo - 1.40 Å (when

brought to the coordination number 12, $r_a = 1.43 \text{ \AA}$), and in the WC compound W - 0.39 \AA , C - 2.52 \AA .

Calculated Eq.(4) and experimental values of the κ/κ_0 are given in the Table. It is seen that kinetics of a diamond powder infiltration with the Co-WC and Co-Ti alloys is described by Eq.(4), while for the Co-Mo alloy, κ/κ_0 experimental and theoretical values do not agree and though the κ value decrease as compared with that of pure cobalt, but not to the extent that would be expected from Eq.(4).

Table

Calculated $(\kappa/\kappa_0)_c$ and experimental $(\kappa/\kappa_0)_{ex}$ values of the κ/κ_0 ratio.

Alloy	$(\kappa/\kappa_0)_c$	$(\kappa/\kappa_0)_{ex}$
Co-WC	0,732	$0,76 \pm 0,08$
Co-Ti	0,781	$0,70 \pm 0,08$
Co-Mo	0,870	$0,55 \pm 0,08$

REFERENCES

1. R.H.Wentorf, Jr., R.C.DeVries and F.P.Bundy. Sintered superhard materials, Science, 208(1980), 873-890.
2. A.A.Shulzhenko, V.G.Gargin, V.A.Shishkin, and A.A.Bochechka. Diamond-Base Polycrystalline Materials [in Russian]. Naukova Dumka, Kiev, 1989.
3. V.I.Tretyakov. Fundamentals of Metal Science and Technologies of Sintered Carbide Production [in Russian]. Metallurgiya, Moscow, 1976.
4. V.K.Gerasimenko, O.N.Andreyev, and O.P.Bezpalko. Study of sintered diamond polycrystals by mercury pyrometry//Soviet Journal of Superhard Materials, vol.8, no. 2, pp.12-14.
5. A.E.Sheidegger. Physics of Liquid Flow via Porous Media. Gostoptekhizdat, Moscow, 1960.
6. A.A.Bochechka, V.G.Gargin. The effect of liquid phase on compacting diamond powders under thermobaric conditions//in: Physico-Chemical Processes at the phase boundary in diamond synthesis and formation of diamond-containing composites [in Russian]. ISM AN Ukrainy, 1993.
7. A.F.Lisovsky, Migration of Metal Melts in Sintered Composite Materials [in Russian], Naukova Dumka, Kiev, 1984.
8. G.S.Ershov, Yu.B.Bychkov. Physico-Chemical Principles of Efficient Alloying Steels and Alloys [in Russian]. Metallurgiya. Moscow, 1982.
9. A.Einstein, Annalen der Physik, 19 (1906) 289.
10. D.R.Wilson. Structures of Liquid Metals and Alloys. Metallurgiya. Moscow, 1972.
11. G.V.Samsonov (Ed.). Properties of Elements. Handbook. Part 1 [in Russian]. Metallurgiya, Moscow, 1976.

Extraction of Ethanol from Fermentation Broth Using Supercritical CO₂

A. Güvenç, Ü. Mehmetoğlu and A. Çalimli

Department of Chemical Engineering, University of Ankara, 06100 Tandoğan, Ankara, Turkey

Extraction of ethanol was studied from both the synthetic ethanol solution and fermentation broth using supercritical CO₂ in an extraction apparatus in the ranges of 313 to 333 K and 80 to 160 atmospheres, for varying extraction times. The experimental system consists of mainly four parts: the CO₂ storage system, the high pressure liquid pump, the extractor and the product collection unit. Samples were analyzed by a gas chromatograph. Effects of temperature, pressure, extraction time, initial ethanol concentration and consecutive solvent feeding on extraction yield were investigated. It was found that increasing the initial ethanol concentration and extraction pressure and decreasing the extraction temperature increased the extraction yield. In addition, it was observed that consecutive solvent feeding affected the extraction yield positively. Using the Box-Wilson optimization method, optimum extraction conditions in a batch system for 15 % (v/v) ethanol solution were found to be 313 K, 133 atmosphere and 30 minutes. Extraction yields were found to be 3 g/l for one step and 10 g/l for three step extraction of fermentation broth.

1. INTRODUCTION

In biotechnology, most production processes take place in aqueous media and generally yield dilute solutions of the valuable products. This poses a challenge in achieving higher efficiencies at minimum cost of energy without degrading the quality of the product.

As it is well known, fermentation processes generally produce aqueous solutions of ethanol, the separation of which necessitates a series of distillation processes. Distillation, however, is a very expensive operation and in addition, ethanol-water mixture forms an azeotrope which further increases the cost of purification. Therefore, novel separation methods must be investigated to make the process more feasible and economical.

Supercritical Fluid Extraction (SFE), proposed in recent years, appears to be a promising technique since it requires low energy for separation. Willson [1] showed that although the initial capital cost for a SFE process is about 40% higher than that for distillation, the cost of compression for the supercritical (SC) fluid is one seventh of the cost of the cooling water and the steam required for distillation processes.

There are several studies in literature about the phase equilibria of the ternary system of ethanol-water-CO₂ [2-12] and only one study exists for the quaternary system of ethanol-water-CO₂-entrainer [13]. In general, these studies showed that the extract concentration was positively influenced with increasing the extraction pressure and initial ethanol concentration and with decreasing the extraction temperature.

Thibault et al [14] investigated experimentally the production of ethanol by fermentation under CO_2 pressure, but they were not successful due to the negative effect of pressure on the microorganisms used. L'Italien et al [15] attempted to improve the ethanol fermentation under hyperbaric conditions with limited success. The separation of ethanol from fermentation broth, however, was not investigated thoroughly.

In all of the previous studies, ethanol extraction utilizing CO_2 was investigated using synthetic ethanol solutions, the concentrations of which were higher than those in the fermentation broth. The extraction conditions were not also optimized.

In this study, ethanol extraction using SC CO_2 was achieved from 15 to 75 % (v/v) synthetic ethanol solutions and also from fermentation broth. Effects of temperature, pressure, extraction time and initial ethanol concentration on extraction yield were investigated in the ranges of 313 to 333 K and 80 to 160 atmospheres. Optimum conditions for the batch extraction of 15% (v/v) ethanol solution were found using the Box-Wilson optimization method in a linear form. In addition, the effect of consecutive solvent feeding on extraction yield were investigated both with 15 % (v/v) ethanol solution and with fermentation broth.

2. EXPERIMENTAL

The experimental apparatus is schematically shown in Figure 1. It consists of mainly four parts: the CO_2 storage system (1), the HPLC pump (4) and its cooling unit (5), the extractor (100 ml stainless steel cell)(6) and the extract collection unit (7).

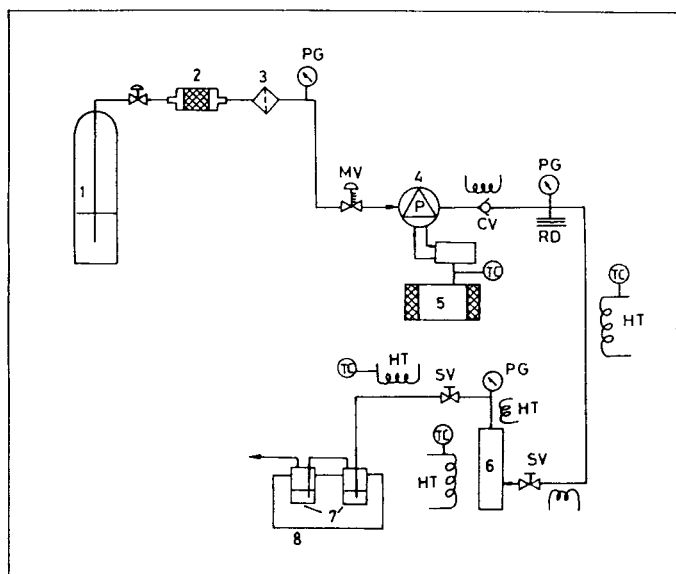


Figure 1. Schematic diagram of the experimental apparatus (PG, pressure gauge; TC, temperature controller; HT, heating tape; MV, metering valve; SV, stop valve; CV, check valve; RD, rupture disc; P, HPLC pump)

The CO₂ was passed through a drier (2) and a filter (3) . It was compressed to the operating pressure by the HPLC pump. Then CO₂ was heated up and sent into the high pressure cell containing the ethanol solution. Ethanol extracted by CO₂ was captured by water in a flask immersed into a water-ice bath (8).

The high pressure cell was heated up to desired extraction temperature by a heating tape attached to a temperature controller. In addition, the valve and the tubes at the exit of the cell were heated to 373 K to vaporize the liquid sample and to avoid condensation .

Extraction experiments were made using 15 to 75 % (v/v) ethanol solutions and also fermentation broth in the pressure range of 80 to 160 atmospheres and at temperatures of 313 to 333 K. Production of ethanol was carried out using *Saccharomyces cerevisiae* (Y-567, obtained from the National Regional Research Center, Peoria, USA) immobilized in Ca-alginate gel. Yeast growth medium and ethanol production media were given in literature [16]. Fermentation broth was centrifuged before using in the extraction experiments.

At the beginning of the experiments, CO₂ was pumped to the extractor to achieve the extraction pressure, and it was waited at this pressure for a predetermined extraction time in the batch experiments. At the end of this extraction time, CO₂ was bled until the system pressure falls to atmospheric pressure. Then CO₂ was pumped to the extractor again without opening the cell and it was waited for the predetermined time again.

Samples were analyzed by GC using packed column with Chromosorb 101 (80/100 mesh) and FID detector. Temperatures of the column, injector and detector are 160, 220 ,250 °C , respectively. Carrier gas was nitrogen and n-propanol was used as the internal standard.

Experimental results given are the averages of three runs.

3. RESULTS AND DISCUSSION

3.1. Effect of initial ethanol concentration on extraction yield

Experiments were made using the solutions which contain 15-75 % (v/v) ethanol in the batch extraction system at 313 K and 120 atmospheres, for 60 minutes. Those experimental conditions were chosen because of the density of SC CO₂ is near to the normal liquid density at these conditions and consequently it has a high solvent power [2]. Experimental results were given at Table 1.

Table 1.
Effect of initial ethanol concentration on extraction yield

C _{E,I} (%v/v)	C _{E,I} (g/l)	C _{E,R} (g/l)	Y _E (g/l)
15	123	115	8
30	269	230	39
60	534	485	49
75	762	698	64

It was found that extraction yield, that is the amount of extracted ethanol from 1 l feed solution increased from 8 g/l to 64 g/l, when the feed solution concentration increased from 15 % to 75 % by volume. The data in the literature also agrees with these results [2,3,9,10,12].

3.2. Effects of temperature and pressure on extraction yield

3.2.1. At high ethanol concentration

Experiments were made using a solution which contains 60 % (v/v) ethanol in the batch extraction system in the pressure range of 80-160 atmospheres and at the temperatures of 313 and 333 K for 60 minutes. Experimental results were given in Table 2. As can be seen, extraction yield raised from 25 g/l to 46 g/l, when temperature decreased from 333 K to 313 K at 80 atmosphere. Similarly, decreasing temperature increased the extraction yield both at 120 and 160 atmospheres. At 313 K, extraction yield raised from 46 g/l to 60 g/l with increasing pressure from 80 to 160 atmosphere. At 333 K, the effect of pressure was not as obvious.

As a result, extraction yield increased with increasing pressure and decreasing temperature. These observations agree with the results of previous researchers who worked at high ethanol concentrations [3,4,5,8,9,11,12].

Table 2.

Effects of temperature and pressure on extraction yield

P (atm.)	T (K)	$C_{E,I}$ (g/l)	$C_{E,R}$ (g/l)	Y_E (g/l)
80	313	534	488	46
	333	534	509	25
120	313	534	485	49
	333	534	519	15
160	313	534	474	60
	333	534	513	21

3.2.2. At low ethanol concentration

The solution containing 15 % (v/v) ethanol was used to simulate the fermentation broth in these experiments. Experiments were made in the batch system at the conditions of 80 and 160 atmospheres, 313 and 333 K and for 30 and 90 minutes.

In literature, inconsistent results were given with respect to the effect of temperature and pressure on extraction yield at low ethanol concentrations [4,7,12]. For this reason, an experimental design was performed utilizing the Box-Wilson method to observe this effect more clearly and for the optimization of the experimental conditions.

3.2.2.1. Experimental design and optimization by the Box-Wilson method

The experimental design was made with three independent variables [17]. Thus the total number of experiments is 8. These independent variables are extraction temperature (U_1), extraction pressure (U_2) and extraction time (U_3); the dependent variable (Y_E) is extraction yield (g/l). Maximum and minimum values for the temperature, pressure and time were selected as 333 and 313 K, 160 and 80 atmospheres, 90 and 30 minutes, respectively.

Experimental design based on these conditions and experimental results obtained are given in Table 3.

Table 3.

Experimental design by Box-Wilson method and the experimental results obtained

Exp.no	1	2	3	4	5	6	7	8
U_1	60	60	60	60	40	40	40	40
U_2	160	160	80	80	160	160	80	80
U_3	90	30	90	30	90	30	90	30
Y_E	5.9	9.4	4.7	8.2	7.0	12.8	10.5	8.2

The equation formed utilizing this method is as follows:

$$Y_{E,P}=8.33-1.28 Z_1+0.43 Z_2-1.31 Z_3+0.16 Z_1Z_2-0.43 Z_1Z_3-1.01 Z_2Z_3 \quad (1)$$

where $Z_i = (U_i - U_{i,ave})/\Delta U_i$; $U_{i,ave} = [(U_i^+) + (U_i^-)]/2$; $\Delta U_i = [(U_i^+) - (U_i^-)]/2$

For the batch extraction with 15 % (v/v) ethanol solution the optimum conditions obtained from this equation are 313 K, 133 atmosphere and 30 minutes.

3.3. Effect of consecutive solvent feeding on extraction yield

15 % (v/v) ethanol solution and fermentation broth (7 % (v/v) ethanol) were used as solutions in the experiments that were made at 313 K and 120 atmosphere. The first batch extraction experiment was carried out for 60 minutes. After bleeding the CO₂ down to the atmospheric pressure, the system pressure was raised again to 120 atmosphere using fresh CO₂. This operation was repeated at the end of 30 minutes. By this way, the ethanol solution was contacted with fresh SC CO₂ at three consecutive steps.

Table 4.

Effect of consecutive solvent feeding on extraction yield

T=313 K Ext.time(min.)	P=120 atm. Number of step	Y_E (g/l) Ethanol solution (15%, v/v)	Y_E (g/l) Fermentation. sol. (7%, v/v)
60	1	8	3
60+30	2	21	-
60+30+30	3	27	10

As can be seen, consecutive solvent feeding increased extraction yield. Extraction yield raised from 8 g/l to 27 g/l at the end of 3 steps for 15 % (v/v) ethanol solution.

ACKNOWLEDGEMENTS

The authors gratefully acknowledge the funding of this work by the Scientific and Technical Research Council of Turkey ,TÜBİTAK (Project No: KT-ÇAG 90).

NOMENCLATURE

$C_{E,I}$	Initial ethanol concentration (g/l)
$C_{E,I}^*$	Initial ethanol concentration (% , v/v)
$C_{E,R}$	Ethanol concentration in the raffinate solution (g/l)
Y_E	Extraction yield (amount of extracted ethanol from 1 l feed solution, g/l)
$Y_{E,P}$	Predicted extraction yield (g/l)

REFERENCES

1. R.C. Wilson, Upstream and Downstream Processing, New York, 1986.
2. R.P. De Filippi and J.M. Moses, Biotech.Bioeng.Symp., No.12 (1982) 205.
3. M.S.Kuk, J.C. Montagna, M.E. Paulaitis, J.M.L. Penninger, R.D.Gray and P. Davidson, (Editors), Chemical Engineering at Supercritical Fluid Conditions, England, (1983) 101.
4. M.L. Gilbert and M.E. Paulaitis, J.Chem.Eng.Data, 31, (1986) 296.
5. Y.S. Feng, X.Y. Du, C.F. Li and Y.J. Hou, Proc.Int.Symp. on Supercritical Fluids, Nice, France (1988) 75.
6. K. Nagahama, J. Suzuki and T. Suzuki, Proc.Int.Symp. on Supercritical Fluids, Nice, France (1988) 90.
7. H.Inomata, K.Arai, S.Saito, S.Ohba and K.Takeuchi, Fluid Phase Equilibria, 53 (1989) 23.
8. S. Furuta, N. Ikawa and R. Fukuzato, 2 nd Int. Symp. on High Pressure Chem. Eng., Erlangen, Germany (1990) 345.
9. G. Di Giacomo, V. Brandani, G. Del Re and O.E.M. Martinez, 2 nd Int. Symp. on High Pressure Chem. Eng., Erlangen, Germany (1990) 231.
10. O. E. M. Martinez, V. Brandani, G. Del Re, G. Di Giacomo and E. Ferri, Fluid Phase Equilibria, 56 (1990) 325.
11. S. Hirohama, T. Takatsuka, S. Miyamoto and T. Muto, J.Chem.Eng. Japan, 26 (1993) 408.
12. J. S. Lim, Y. Y. Lee and H. S. Chun, The Journal of Supercritical Fluids, 7 (1994) 219.
13. H.Inomata, A. Kondo, K. Arai and S. Saito, J. Chem. Eng. Japan, 23 (1990) 199.
14. J. Thibault, A. LeDuy and F. Cote', Biotech. Bioeng.,30 (1987) 74.
15. Y. L'Italien, J. Thibault and A. LeDuy, Biotech. Bioeng.,33 (1989) 471.
16. Ü. Kurnaz (Mehmetoğlu), Ph.D. Thesis, Hacettepe University, Beytepe, Ankara, Turkey, 1984.
17. A. Abilov, Optimisation of Process Models and Control Systems in Petrochemical Technologies, Ankara University Science Faculty Publication (in Turkish), Ankara, 1994.

Solubility calculation of solid compounds in supercritical CO₂ by a group - contribution method

L. BARNA^a, J.-M. BLANCHARD^a, E. RAUZY^b, C. BERRO^b

^aLaboratoire de Chimie Physique Appliquée et Environnement, Institut National des Sciences Appliquées (INSA de LYON), bât. 404, 69621 Villeurbanne, France

^bLaboratoire de Chimie Physique, Faculté des Sciences de Luminy, 13288 Marseille 9, France

INTRODUCTION

Supercritical fluids are found in numerous applications thanks to their properties which vary with temperature and pressure. Supercritical fluids are put in contact with various compounds which also have physico-chemical properties dependant on temperature and pressure. Consequently, mixtures of these compounds with the supercritical solvent must be expected to behave in a complex way. For a binary mixture, for example, several types of phase equilibrium exist : *solid-fluid* for low temperatures, *solid-fluid-liquid* when temperature rises, and *liquid-fluid*.

In our research, we were led to characterise thermodynamically the mixtures composed of an organic compound and supercritical CO₂ in a relatively wide range of temperatures, including several types of phase equilibrium. We looked for a single thermodynamic model which would be predictive (no parameters to adjust to the experimental data), valid for a wide range of temperatures and pressures, and also capable of representing solid-fluid and liquid-fluid equilibria.

1. THE THERMODYNAMIC MODEL

In looking for such a model, certain particularities of the mixtures of the compounds studied must be taken into account. The solutions obtained by dissolution of solid compounds in supercritical solvents are highly asymmetrical, with considerable differences in the size and energy of the molecules. Consequently, the models based on the theory of corresponding states using critical parameters of pure compounds give only qualitative results. Moreover, the model must correctly represent both the pure solute, in the temperature and pressure range of the mixture, and the solvent in the area close to its critical point. Single equation of state models do not satisfy all these requirements. Lastly, the most sophisticated models (for example the models based on the statistical mechanics) are not always the most efficient and are difficult to apply. For these reasons we adopted the "Excess Function-Equation of State" model [1, 2].

The development of a predictive method from a thermodynamic model, for example a group-contribution method, requires a systematic study based on a large number of experimental data. First of all, *hydrocarbon-carbon dioxide* mixtures must be taken into account. The main stages in setting up a group-contribution method are as follows :

1) A study of the representation of liquid-fluid equilibria with the "Excess Function-Equation of State" model and the choice of a group-contribution method. Promising results were obtained here (references [3] and [4]).

2) A study of the representation of solid-fluid equilibria with the "Excess Function-Equation of State" model. The results obtained with [5] and [6] show that this model is as efficient as the HSDW [7], AVDW-DDLC [8], or KBST [9] models.

3) A study of the "continuity" of the model when changing from the solid-fluid to the liquid-fluid field for a fixed mixture; application and "adjustment" of the group-contribution method. It is this third stage and its results that we present below.

1.1. Principle of the thermodynamic model

The "Excess Function-Equation of State" model is based on the relation between the excess Helmholtz energy of the mixture and the equations of state of its components. The excess Helmholtz energy is calculated in Guggenheim's quasi-reticular theory. We chose van der Waals - like equations of state for the constituents of the mixture :

$$z = 1/(1 - \eta) - \Psi'(\eta)/(bRT) \quad (1)$$

with

$$\eta = b/v = b_i/v_i \quad \text{and} \quad b = \sum_{i=1}^p b_i x_i \quad (2)$$

where η is the packing fraction, b is the covolume et $\Psi'(\eta)$ is the attraction term in the equation of state.

The equation of state of a mixture of p compounds is :

$$z = 1/(1 - \eta) - (1/RT) \sum_{i=1}^p \Psi'_i(\eta) x_i / b_i + (1/RT) \Psi'_E(\eta) E(T, x) \quad (3)$$

and the fugacity coefficient of the i compound in the mixture is :

$$\ln \phi_i = (b_i/b)(z - 1) - \ln[z(1 - \eta)] - \Psi'_i(\eta)/(RTb_i) + (1/RT) \Psi'_E(\eta) E'_i(T, x) \quad (4)$$

In relations (3) and (4) $E(T, x)$ is the residual term depending on composition and temperature, $E'_i(T, x)$ and $\Psi'_j(\eta)$ are functions defined by :

$$E'_i = \left(\frac{\partial nE}{\partial n_i} \right)_{T, \eta, n_j} \quad (5)$$

$$\Psi'_j(\eta) = \int_0^\eta \frac{\Psi'_j(\eta)}{\eta} d\eta \quad (6)$$

The use of the precise equations of state for the constituents of the mixture is indispensable for the correct representation of the properties of the mixture. Angus's precise equation of state [10] was used for the carbon dioxide. For the hydrocarbons we chose the corrected cubic

equation with the parameters calculated according to the boiling temperature and not according to the critical parameters ([11], [12]).

The residual term is made up of a function of the packing fraction of the form :

$$\Psi'_E(\eta) = \eta / (1 + 20 \eta) \quad (7)$$

and of the term $E(T, x)$ which we chosen of van Laar -type :

$$E(T, x) = 1/2 \sum_{i=1}^p \sum_{j=1}^p b_i b_j x_i x_j E_{ij} / b \quad (8)$$

The interaction parameter E_{ij} was first adjusted to the experimental data of the liquid-fluid and solid-fluid equilibria. The representation of both types of equilibria was very satisfactory, which proves that the "Excess Function-Equation of State" model with an adjusted parameter is well adapted to both cases ([4-6], [13]).

1.2. Group-contribution method

The transformation of the "Excess Function-Equation of State" model into a group-contribution method is possible through the interaction energy parameter. The interaction parameter E_{ij} between the molecules i and j is expressed by :

$$E_{ij}(\text{gc}) = -\frac{1}{2} \sum_{K=1}^N \sum_{L=1}^N (\alpha_{iK} - \alpha_{jK})(\alpha_{iL} - \alpha_{jL}) A_{KL}(T) \quad (9)$$

in which N is the number of groups and α_{iK} is the surface fraction of groups K in the molecule i . A_{KL} is the interaction parameter between the groups K and L ($A_{KL} = A_{LK}$). The parameter A_{KL} depends on the temperature and is calculated according to a function of the following type:

$$A_{KL} = A_{KL}^0 A_{\text{form}} \left(\frac{T^0}{T} \right)^r \quad (10)$$

wherein A_{form} and r are parameters taking into account the configuration of the molecules and T^0 is the reference temperature ($T^0 = 298,15\text{K}$).

The interaction parameters of the form (10) are appropriate for the liquid-fluid equilibria for a large number of compounds [4]. A study of the "continuity" of the model in the field of solid-fluid equilibria is a pre-requisite for the development of a single all-purpose group - contribution method.

The temperature function appearing in the relation (10) is indeed specific for a couple of given molecules i and j . We analysed the correlation existing between $\ln E_{12}$ and $\ln(T^0/T)$ for hydrocarbon- CO_2 couples with experimentally established liquid-fluid and solid-fluid equilibria (Figure 1). The values of E_{12} are those adjusted to experimental data to be found in the literature.

The interaction parameters adjusted to the experimental data of liquid-fluid and solid-fluid equilibria seem to vary continuously with the temperature. A common definition of the groups

and a single temperature function should satisfy the two fields of the phase diagram of a hydrocarbon-CO₂ mixture. Moreover, a linear variation of the value $\ln E_{12}$ with $\ln(T^0/T)$ is observed for all the compounds, at least in the range of temperatures studied. The parameters of the group-contribution model must be determined by adjustment to the experimental data on equilibria as a whole. For the classes of hydrocarbon studied (normal alkanes, iso-alkanes, cycloalkanes, monocyclic aromatics, polycyclic aromatics), we adopted the following group definition :

- 1 : CH₃ or CH₂ (alkanes and alkyl radicals) 2 : C substituted alkane 3 : CH aromatic
 4 : C alkyl-substituted aromatic 5 : C aromatic condensed or substituted by C aromatic
 6 : CH₂ cycloalkanes 7 : C cycloalkane substituted 8 : C trans-condensed cycles 9 : CO₂

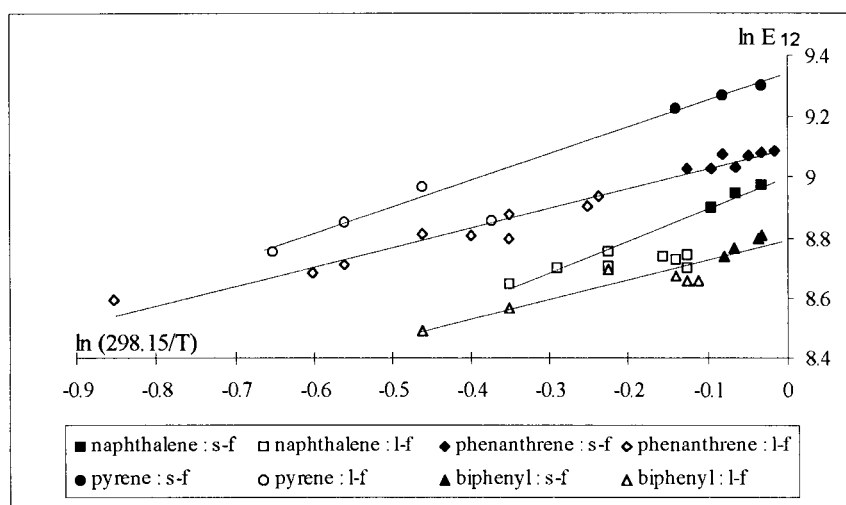


Figure 1. Variation of E_{12} with temperature for binary mixtures comprising solid-fluid and liquid-fluid equilibria.

All possible interactions between the K and L groups were taken into account and $A_{KK} = 0$. The definition contains a minimum number of groups and is satisfactory for most of the binary systems studied. However, it cannot take into account the structural differences which exist between position isomers. This is the case of polycyclic aromatic compounds presenting cycle position isomers or substitute position isomers. Structural differences of this type determine the gaps between the values of certain thermophysical properties of isomers, such as, for example, the fusion temperature or sublimation enthalpy. The further the temperature falls, the more these differences are accentuated. The representation of the solid-fluid (low temperature) equilibria is consequently more difficult and the model must take into account the existing structural differences. We came across this problem in the compounds such as anthracene, phenanthrene, pyrene, methylated naphthalenes, hexamethylbenzene and triphenylmethane. As it was out of the question to increase the number of groups because

experimental data were insufficient, we intervened with increments in the form parameter A_{form} and in the exponent of the function of temperature r :

$$A_{\text{form}} = 1 + \exp\left(\alpha_1 \Delta \ell + \alpha_2 + \alpha_3 C_2 + \alpha_4 C_3 + \alpha_5 C_p - \left(\alpha_6 / C_{\text{as}}\right)^3\right) \quad (11)$$

$$r = \beta_1 \ell^{1.5} + \beta_2 + \beta_3 C_2 + \beta_4 C_3 + \beta_5 C_p \quad (12)$$

In relations (11) and (12), ℓ is a parameter which indicates the length of the chain of normal alkanes; it is equal to the number of carbon atoms in the molecule. α_i and β_i are constants, C_2 , C_3 and C_p are the site fractions occupied in the molecule by the condensed aromatic carbon atoms common to two cycles, three cycles and condensed atoms in angular position. The C_{as} parameter represents the fraction of the sites for the substituted aromatic carbons belonging to condensed cycles, which must be taken into account for the substituted derivatives of naphthalene. Table 1 shows the values of the parameters adjusted to the experimental data of the liquid-fluid and solid-fluid equilibria as a whole.

Table 1. Coefficients α_i and β_i and interaction parameters between groups A_{KL}^0 (J/cm^3)

$\alpha_1 = 0.109$	$\alpha_4 = 16.26$	$\beta_1 = 0.0283$	$\beta_4 = 6.47$
$\alpha_2 = -3.68$	$\alpha_5 = -7.43$	$\beta_2 = 0.50$	$\beta_5 = -4.53$
$\alpha_3 = 8.00$	$\alpha_6 = 0.13$	$\beta_3 = 2.77$	

K/L	1	2	3	4	5	6	7	8	9
1	0								
2	20.00	0							
3	70.97	-	0						
4	724.30	-	250.40	0					
5	777.46	-	912.12	959.53	0				
6	39.00	-	9.15	-	2487.00	0			
7	20.00	-	-	-	-	6055.55	0		
8	-	-	-	-	-	6.36	-	0	
9	442.31	328.30	545.35	733.88	2150.96	620.54	3858.28	733.55	0

The calculation of the liquid-fluid equilibria with the group contribution method has been presented elsewhere [4]. The matrix of the parameters of group interaction (Table 1) contains values readjusted relative to the matrix obtained considering only liquid-fluid equilibria [4]. These parameters are A_{15} , A_{35} , A_{45} and A_{59} . The introduction of supplementary increments for the form of the molecules (α_{3-6} and β_{3-5}) enables good results to be obtained for the calculation of solid-fluid equilibria and does not essentially modify the representation of liquid-fluid equilibria. The average relative deviation $\delta_r(x)$ for the experimental data as a whole is 16.7% for the group contribution method and 13.3% for the model with E_{12} adjusted. The experimental data concern 40 isotherms (P, x) for 11 binary mixtures of solid aromatic hydrocarbon with supercritical CO_2 .

CONCLUSIONS

Predictive models such as group contribution methods have been developed in recent years to represent supercritical liquid-fluid equilibria. However we have not found in the literature models capable of representing accurately several types of phase equilibrium in a wide temperature and pressure range. We made a systematic study of mixtures of the hydrocarbon-supercritical carbon dioxide type in order to develop a single all-purpose model for solid-fluid and liquid-fluid equilibria. We developed an "Excess Function-Equation of State" model with an intermolecular interaction parameter. The interaction parameter was correlated with parameters of interaction between the groups constituting the molecules and the fractions of sites occupied by these groups. The variation of the interaction parameter according to temperature was determined. The group contribution method was developed from experimental data concerning solid-fluid and liquid-fluid equilibria for a large number of hydrocarbons. The representation of solid-fluid and liquid-fluid equilibria is satisfactory. The modelization of solid-fluid equilibria by a predictive method is more difficult because of the structural complexity of compounds of low volatility. The increments introduced for the polycyclic aromatic compounds require validation by extra experimental data.

LIST OF SYMBOLS

A_{KL} = group interaction parameter

b = covolume

E_{ij} = binary energy parameter

n = number of moles in a mixture

N_p = number of data points

p = number of components in a mixture

R = gas constant

T = temperature

v = molar volume

x = mole fraction

z = compressibility factor

$\delta_r(x)$ = relative mean deviation = $\frac{100}{N} \sum |x_{\text{exp}} - x_{\text{cal}}| / x_{\text{exp}}$

η = packing fraction

ϕ = fugacity coefficient

REFERENCES

1. E. Rauzy and A. Péneloux, *International Journal of Thermophysics*, 3 (1986) 635
2. A. Péneloux, W. Abdoul and E. Rauzy, *Fluid Phase Equilibria*, 47 (1989) 115
3. W. Abdoul, Thesis : Université de Droit, d'Economie et des Sciences d'Aix-Marseille, 1987
4. C. Berro, L.R. Barna and E. Rauzy, *Fluid Phase Equilibria*, 114 (1996) 63
5. L. R. Barna, J.M. Blanchard, E. Rauzy and C. Berro, 3rd International Symposium on Supercritical Fluids, Strasbourg, 1994, vol.1, 146
6. L. Barna, E. Rauzy, C. Berro and J.M. Blanchard, *Fluid Phase Equilibria*, 100 (1994) 191
7. J.M. Wong, R.S. Pearlman and K.P. Johnston, *J. Phys. Chem.*, 89 (1985) 2671
8. K.P. Johnston, S. Kim and J.M. Wong, *Fluid Phase Equilibria*, 38 (1987) 39
9. D.M. Pfund, L.L. Lee and H.D. Cochran, *Fluid Phase Equilibria*, 39 (1988) 161
10. I.U.P.A.C. Carbon dioxide. International thermodynamic tables of the fluid state - 3. Pergamon Press, 1973
11. E. Rauzy, Thesis : Université d'Aix-Marseille II, 1982
12. L. Coniglio, E. Rauzy and C. Berro, *Fluid Phase Equilibria*, 87 (1993) 53
13. L.R. Barna, Thesis : INSA de Lyon, 1995

Extraction of Alkaloids from *Lupinus albus* sp. using Compressed Carbon Dioxide

Fernando J. Caetano*, M. Luísa Beirão da Costa**, M. Gabriela Bernardo-Gil¹

*Dep. Engenharia Química - IST, Av. Rovisco Pais, 1096 Lisboa Codex, Portugal

**Dep. Ciên. e Tecn. de Alimentos - ISA, Tapada da Ajuda, 1399 Lisboa Codex, Portugal

ABSTRACT

The extraction of lupanine from lupine (*Lupinus albus* sp.) flour using liquid carbon dioxide (8 MPa, 313 K) and supercritical carbon dioxide (10 MPa, 15 MPa and 20 MPa at 298 K and 313 K) was investigated.

Small quantities of lupanine were obtained at the studied conditions, being the percentages of lupanine related to the total mass of extract between 0.02 % and 1.13 % at 10 MPa and 298 K, and 20 MPa and 313 K, respectively.

INTRODUCTION

For centuries lupine has been used by Andean for several purposes like soil enrichment and as a food crop.

Lupines are known as rich leguminosae in lipids and proteins. This makes them very interesting if they were produced in a large industrial scale. However the presence of bitter and poisonous quinolizidine alkaloids is the main obstacle to overcome for a broader utilisation.

¹ Author to whom correspondence must be addressed.

The traditional way to debitter the grains is leaching with water for several days. Nowadays this process is still used and it takes place in three steps: wetting, boiling and rinsing with water.

Due to its economical interest there has been a large effort in producing free alkaloid lupines. Several techniques have been used to achieve this purpose. Breeders tried to reduce the content of bitter components since the 30's when Von Sengbusch reported the discover of natural occurring lupine seeds with low-alkaloid content (Cantot *et al*, 1983 and Gross *et al*, 1988). Since then there is a considerable number of bred low-alkaloid content of lupine varieties (Neves-Martins, 1993). Other ways of debittering involve the use of enzymes with interesting results (Santana, 1990) and water extraction processes varying cooking media and temperature and time conditions, or simultaneously extracting alkaloids and oil using polar solvents or an aqueous mixture with organic solvents in batch (Beirão da Costa, 1992, 1993).

A new methodology is to use supercritical extraction with carbon dioxide or ethylene oxide. The objective of this work is precisely to use supercritical extraction with CO₂.

EXPERIMENTAL

The extraction of lipids and alkaloids with compressed carbon dioxide was performed at 298 K and 313 K using the pressures 8, 10, 15 and 20 MPa in an apparatus similar to that schematised in Figure 1. The extraction cell is a stainless steel vessel with 220 cm³ of capacity specially built for this purpose.

Carbon dioxide (99.95%, supplied by AR LIQUIDO Portugal) passes through a cold bath at a temperature near 273 K (P1) and is pressed to the desired pressure in a pump (Bodine Electric Co., model Minipump NSI-33R) mounted with a back pressure regulator (PC - Tescon model 26-1T22-042-043). Liquefied CO₂ passes through an heat exchanger (P2) and goes to the extraction cell maintained at the same working temperature. The temperature is thermostated in a water bath with an accuracy of 0.1 K.

Gas expansion to atmospheric pressure is made in two steps controlled with valve V5 and needle valve V6.

Extract is mainly recovered in the collector C1 and is measured by weighing. The quantity of consumed carbon dioxide is measured in a diaphragm gas meter SAMGAS (DGM) with an accuracy of ± 0.005 L.

Figure 2 represents the total yield of lipids and alkaloids as function of consumed CO_2 using liquid and supercritical carbon dioxide at 298 K, and Figure 3 represents the curve of extracted mass per CO_2 mass as function of time at 313 K.

In Figure 4 the extracted mass per CO_2 mass as function of time is presented at 15 MPa, and in Figure 5 the total yield of lipids and alkaloids as function of consumed CO_2 is presented at 20 MPa.

As it was expected, the yield of the extraction increases with the pressure and decreases with the increase of temperature. However at 20 MPa the curves are very similar.

For lower pressures the quantities of carbon dioxide needed to extract the same mass quantity in the same time interval are greater than at higher pressures.

It can be seen that there is a decrease in the extracted mass for the consumed CO_2 with the increase of the temperature.

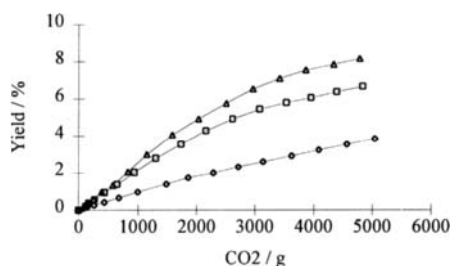


Figure 2 - Mass of extract per mass of lupine flour versus consumed CO_2 at 298 K.
 \diamond 10 MPa; \square 15 MPa; Δ 20 MPa.

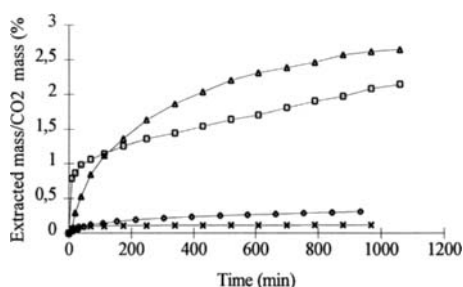


Figure 3 - Mass of extract per consumed CO_2 versus time at 313 K. x 8 MPa;
 \diamond 10 MPa; \square 15 MPa; Δ 20 MPa.

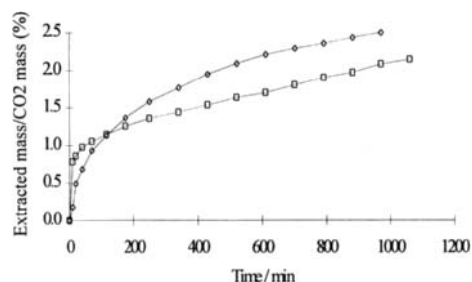


Figure 4 - Mass of extract per consumed CO_2 versus time at 15 MPa. \diamond 298 K; \square 313 K.

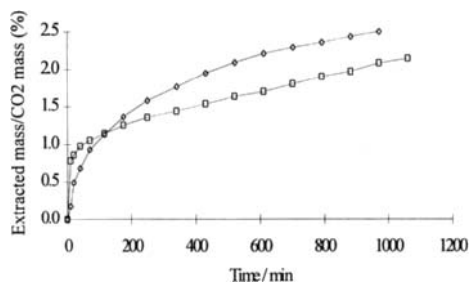


Figure 5 - Mass of extract per mass of lupine flour versus consumed CO_2 at 20 MPa. \diamond 298 K; \square 313 K.

In Figures 6 and 7 the quantities of lupanine extracted using liquid and supercritical carbon dioxide are represented as function of consumed CO_2 , respectively at 298 K and 313 K.

The quantities of lupanine extracted at the studied conditions are small.

From the analysis of the Figures 6 and 7 it can be seen that at 298 K the lupanine solubilities in carbon dioxide are identical for 10 MPa and 15 MPa, being lower at 20 MPa. At 313 K the solubilities of lupanine in CO_2 seems to be similar at the studied pressures. At 313 K the quantities of extracted lupanine in CO_2 increase with pressure, although for shorter extraction times, one inversion between the two curves at 15 MPa and 20 MPa exists.

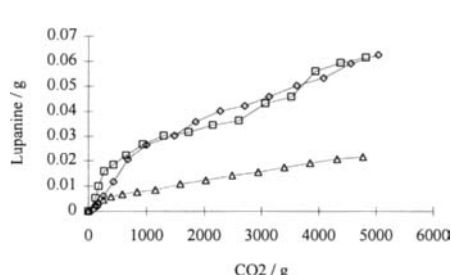


Figure 6 - Extracted lupanine versus consumed CO_2 at 298 K. \diamond 10 MPa; \square 15 MPa; Δ 20 MPa;

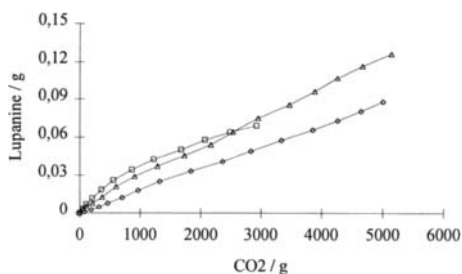


Figure 7 - Extracted lupanine versus consumed CO_2 at 313 K. \diamond 10 MPa; \square 15 MPa; Δ 20 MPa;

For lower consumed CO_2 the quantity of extracted lupanine decreases with temperature but this situation inverts for the lower temperatures with the increase of consumed CO_2 . Thus, a retrograde solubility effect between the curves at 298 K and 313 K seems to exist.

In Table 1 are presented the values of mass percentage of lupanine per mass of extract obtained at the end of extraction.

From the analysis of this table it can be seen that the quantities of extracted lupanine per mass of extract decreases with pressure. However, it was observed that, before the 200 minutes of extraction, the quantity extracted at 15 MPa is greater than the one extracted at 10 MPa.

Table 1. Values of relation of mass of lupanine extraction to total mass of extract (%), at the end of extraction time

Temperature / K	Pressure / MPa		
	10	15	20
298	0.02	0.07	0.17
313	0.15	0.18	1.13

REFERENCES

- Gross, R., von Baer, E., Koch, F., Marquard, R., Trugo, L., Wink, M. Chemical composition of a new variety of the Andean Lupin (*Lupinus mutabilis* cv. Inti) with low-alkaloid content. *Journal of Food Composition and Analysis*, 1, (1988) 353-361.
- Cantot, P., Papineau, J. Discrimination des lupins à basse teneur en alcaloïdes par les adultes de *Sitona lineatus* L. (Col. Curculionidae). *Agronomie*, 3, (9), (1983) 937-940.
- Cho, Y. D., Martin, R. O. Resolution of unambiguous identification of microgram amounts of 22 lupine alkaloids by sequential use of thin-layer and gas-liquid chromatography. *Analytical Biochemistry*, 44, (1971) 19-57.
- Hatzold, T., Elmadfa, I., Gross, R., Wink, M., Hartmann, T., Witte, L. Quinolizidine alkaloids in seeds of *Lupinus mutabilis*. *J. Agric. Food Chem.*, 31, (1983) 934-938.
- Santana, F. C., Beirão da Costa, M. L., Empis, J. M. A. Evaluational enzymatic preparations in the debittering of lupin seeds flowers. *Proc. of the 6th International Lupin Conference, Chile* (1990).
- Beirão da Costa, M. L., Lupins as raw material for alternative products in human nutrition., *Agriculture - Agrimed research Programme - Lupinus mutabilis: its adaptation and production under European pedoclimatic conditions. Proc. of a Workshop held in Cascais*. Portugal, 26-27 April 1991, Commission of the European Communities, 1992.
- Beirão da Costa, M. L. Lupin Technology: A perspective. *Proc. of VII International Lupin Conference, Advances in Lupin Research*, Evora 18-23 April, I.S.A. ed. 1994.
- Neves-Martins, J. M. Characterization in *Lupinus albus* and *Lupinus mutabilis* populations types. *Proc. of VII International Lupin Conference, Advances in Lupin Research*, Évora 18-23 April, I.S.A. ed. 1994.

The Phase Separation of Water + Methyl-di(n-amyl)phosphynoxide at Pressure up to 230 MPa

M. Z. Faizullin and V. P. Skripov

Institute of Thermal Physics, Ural Division of Russian Academy of Sciences, GSP-828,
Ekaterinburg, 620219, Russia*

1. INTRODUCTION

T, p, x surfaces of phase equilibrium of some separating mixtures have a double critical point (DCP). On the critical curve DCP signifies the extremum of temperature or pressure. Here the upper and the lower critical points of the solution separation coincide. The particular role of the DCP is determined by the behaviour of different physical quantities in the vicinity of this point. Kinetic and thermodynamic properties here have clearly defined peculiarities [1, 2]. Investigations of systems with the DCP give answers to a number of questions concerning of second-kind phase transition and are of interest for the subsequent development of the theory of critical phenomena. Aqueous solutions of some phosphinioxides may serve as examples of the systems with DCP. These compounds received wide application as extragents for different non-organic simple and complex salts and acids. The present paper studies the T, p, x surface of liquid-liquid phase equilibrium for $(1-x)\text{water}+(x)\text{methyl-di}(n\text{-amyl})\text{phosphynoxide}$ in the vicinity of the line of lower critical solution temperatures at pressures up to 230 MPa. The behaviour of critical exponents for p, x and T, x phase equilibrium diagrams along the line of critical points and in the vicinity of the DCP was investigated.

2. EXPERIMENT

The pressure dependence of the separation temperature was investigated using a high pressure chamber (Fig.1). The chamber was supplied with windows of leuco-sapphire and made it possible to observe visually the phase separation of liquid mixtures. The pressure transmitting medium (castrol oil) was separated from the liquid under investigation with the help of a bellows. The pressure was created with a piston pressure gauge and measured with an accuracy of 0.5 MPa. For measuring the temperature a copper-constantan thermocouple was used, which was placed inside a steel sheathing made of a thick-walled capillary tube and was introduced directly into the high-pressure chamber. The precision of the temperature measurements was 0.03K in the experiment. The gravimetric method was used to prepare mixtures.

* The work has been carried out with the financial support of the Russian Foundation of Fundamental Investigations, 93-02-16002.

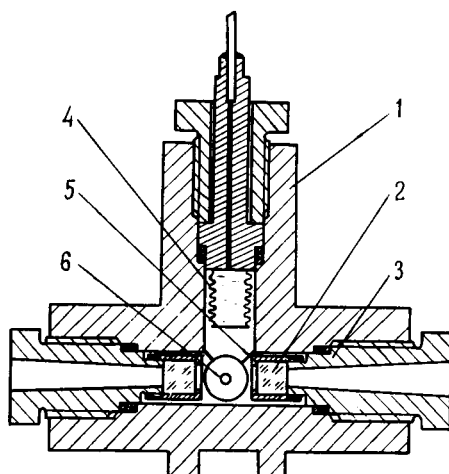


Figure 1. High pressure chamber: 1-body, 2-window, 3-shutter, 4- bellows, 5-cap, 6-thermocouple.

The sample mole fraction was determined with an accuracy of at worst 0.0002. The chamber was filled with the liquid under investigation at a temperature corresponding to the homogeneous state of the sample. Experiments were carried out at a fixed pressure with a gradual temperature increase in the thermostat. At the point of a phase transition, one could observe the turbidity of a sample which preceded the separation.

3.RESULTS AND DISCUSSION

Curves of pressure dependence of the separation temperature of (1-x) water+(x)methyl-di(n-amy)phosphinoxide for six mole fractions have been measured. The results of the measurements are given in Fig 2. Separation lines have been approximated by a third-degree polynomial

$$T=a_0 + a_1p + a_2p^2 + a_3p^3, \quad (1)$$

here the pressure p is taken in GPa.

The values of coefficients in equation (1) and the root-mean-square deviations σ of experimental points from the approximate dependence are given in table 1. This equation has been used to calculate T,x and p,x diagrams of the liquid-liquid phase equilibrium for the mixture under investigation.

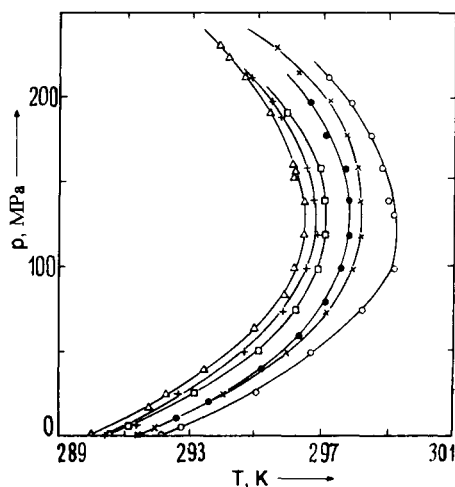


Figure 2. Curves of pressure dependences of the separation temperature for (1-x) water+(x)methyl-di(n-amy)phosphynoxide. \circ , $x=0.006$; \times , $x=0.008$; \square , $x=0.012$; \triangle , $x=0.020$; $+$, $x=0.034$; \bullet , $x=0.041$.

Table 1

Values of the parameters of equation (1) for p,T curves of separation of water+methyl-di(n- amy)phosphynoxide; σ is the root-mean square deviation

x	a_0	a_1	a_2	a_3	σ
0.006	292.18	129.13	-688.7	912.1	0.14
0.008	291.41	117.42	-570.3	610.3	0.09
0.012	290.64	118.55	-630.9	835.7	0.03
0.020	289.88	115.84	-592.1	711.7	0.09
0.034	290.45	110.58	-543.3	557.8	0.18
0.041	291.59	111.97	-577.2	708.1	0.04

The isopleth corresponding to $x=0.020$ is the closest to the line of critical points of the mixture in the region of the DCP. The temperature and the pressure at the temperature maximum point for this curve correspond to the DCP coordinates: $p_D=126.8$ MPa, $T_D=296.5$ K. The line of critical points near the DCP may be described by the power dependence [1]:

$$(p''_c - p'_c)/p_D = 2A(|T_D - T|/T_D)^\lambda, \quad (2)$$

with $\lambda=0.5$. Here, p''_c and p'_c are the upper and lower critical pressure, respectively, at the temperature T . For the isopleth $x=0.020$ the values of the exponent λ and the factor A calculated by the method of least square are 0.508 ± 0.003 and 8.06 ± 0.15 , respectively.

To describe T, x and p, x diagrams of phase equilibrium in the region of a critical transition we used scaling equations:

$$(x''-x')/x_c = 2B_p(|T_c-T/T_c|)^{\beta_p}, \quad (3)$$

$$(x''-x')/x_c = 2B_T(|p_c-p/p_c|)^{\beta_T}. \quad (4)$$

Here, x' and x'' are the mole fractions in the coexisting phases; T_c , p_c and x_c are the temperature, the pressure and the mole fraction at the critical point; β_p and β_T are the critical indices; B_p and B_T are the amplitudes of the equilibrium curves. For the T, x binodal at atmospheric pressure the exponent β_p has a universal value close to $1/3$. An analysis made for several isobars has shown that within the experimental error the quantity β_p retains its value along the line of critical points including the double critical point. The critical exponent β_T for isotherms does not considerably change its value at pressures up to 70-80 MPa, with $\beta_T \cong \beta_p$. In the vicinity of the DCP, one can observe an anomalous increase of β_T . The behaviour of the exponents β_p and β_T along the line of critical points at pressures from atmospheric to 200 MPa is shown in figure 3.

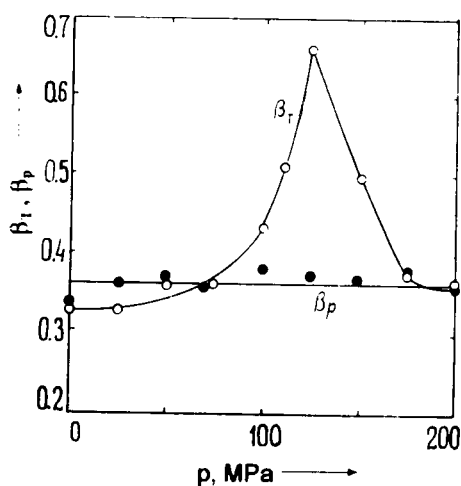


Figure 3. Behaviour of the exponents β_p and β_T along the critical curve for water+methyl-di(n-amyl)phosphynoxide.

The values of the exponent and the amplitude for equations (3) and (4) are calculated by the method of least squares. For T, x diagrams the calculation was carried out in the temperature range $|T_c - T|/T_c < 0.01$. The values of T_c and p_c were determined by making use of the law of rectilinear diameter. The processing of experimental results for p, x diagrams was carried out in the pressure range $p = 30\text{--}50$ MPa or $\Delta p/p_c = 0.5\text{--}1.0$, which corresponds to $\Delta T/T_c = 0.001\text{--}0.01$.

The observed constancy of β_p along the line of critical points and the anomalous behaviour of β_T in the region of the DCP are in agreement with the scaling invariant theory of systems with a DCP [1] according to which critical exponents of the scale relations for solution properties in a plane tangential to the separating surface at the DCP double their values.

REFERENCES

1. M.A. Anisimov, A.V. Voronel and E.E. Gorodetsky, *Z. Exp. Theor. Phys.*, 60 (1971) 1117.
2. A. Deerenberg, J.A. Schouten and N.J. Trappeniers, *Physica*, 103A (1988) 183.

This page intentionally left blank

Scale-up of a Supercritical Extraction Unit for the Deacidification of Olive Oil

P.J.Carmelo^a, P.J.Pereira^a, P.C.Simoes^b and M.Nunes da Ponte^{a,b}

^a Instituto de Biologia Experimental e Tecnológica, Universidade Nova de Lisboa,
Aptd. 12, 2780 Oeiras, Portugal

^b Faculdade de Ciências e Tecnologia, Universidade Nova de Lisboa,
Quinta da Torre, 2825 Monte da Caparica, Portugal

Olive oils with large quantities of free fatty acids must be refined to get a salable product. Supercritical fluid deacidification of these oils has been suggested as a potential “ecological” alternative process as it uses non-toxic solvents and low operating temperatures. Previously measured equilibrium and mass-transfer data were used to scale-up a proposed supercritical extraction unit. A economical evaluation of the unit was also made.

1. INTRODUCTION

Olive oil is a vegetable oil that is obtained by expression processes from the fruit of the olive trees. Due to agricultural and meteorological factors olive oils may have relatively high concentrations of free fatty acids (FFA) making them inappropriate for immediate human consumption. Deacidification is currently done by physical (steam distillation using high temperatures) or chemical (alkaline neutralization) processes which may alter the organoleptic profile of the oil (1).

The use of supercritical carbon dioxide as a solvent for the deacidification of olive oils was suggested (1, 2), according with preliminary results that have shown the selective preference of carbon dioxide towards the FFA fraction and at the same time retaining the nutritional constituents of the oil (1).

An extensive study was carried out to evaluate the best operational conditions for the deacidification of olive oils by supercritical extraction (SCE). The design of an extraction unit was then evaluated.

2. PROCESS DESIGN

First, we measured thermodynamic and mass transfer data of the multicomponent system olive oil/CO₂ (3,4). The phase equilibria was modulated by correlating the partition coefficients ($K_i = y_i/x_i$) of each component present in the mixture as a function of the mole fraction of the FFA fraction in the liquid phase (3). Mass transfer studies were performed in a lab-scale countercurrent packed column. The experimental measured mass transfer coefficients were

modulated with the help of an adequate mass transfer model (4) that was used in the design of the extraction unit. The capacity of the proposed deacidification unit was fixed by market considerations. The steps taken to scale-up and design such a unit are presented below.

2.1 Scale-up of the process

The annual capacity of the extraction unit was fixed in 10 kton of virgin olive oil with an average composition in free fatty acids of 4 wt%. Although this composition may change with the harvesting year it was taken as a mean value for the intake oil. The extraction process is intended to reduce the residual concentration of FFA to a value less than 0.7 wt%.

The operating conditions for the extraction column were selected from the experimental data previously measured by choosing the conditions that yield the more favorable capacity and selectivity of carbon dioxide for the FFA fraction. We selected a pressure of 21 MPa and a temperature of 323K. A flowsheet of the proposed extraction process is shown in Figure 1. The separation of the oil components from the solvent stream exiting the extraction column is made in two steps, named SC_I and SC_{III}, in order to regenerate the most part of the solvent. The raffinate stream, S₂, flows to a third separation column, SC_{II}, to regenerate the carbon dioxide solubilized in that stream.

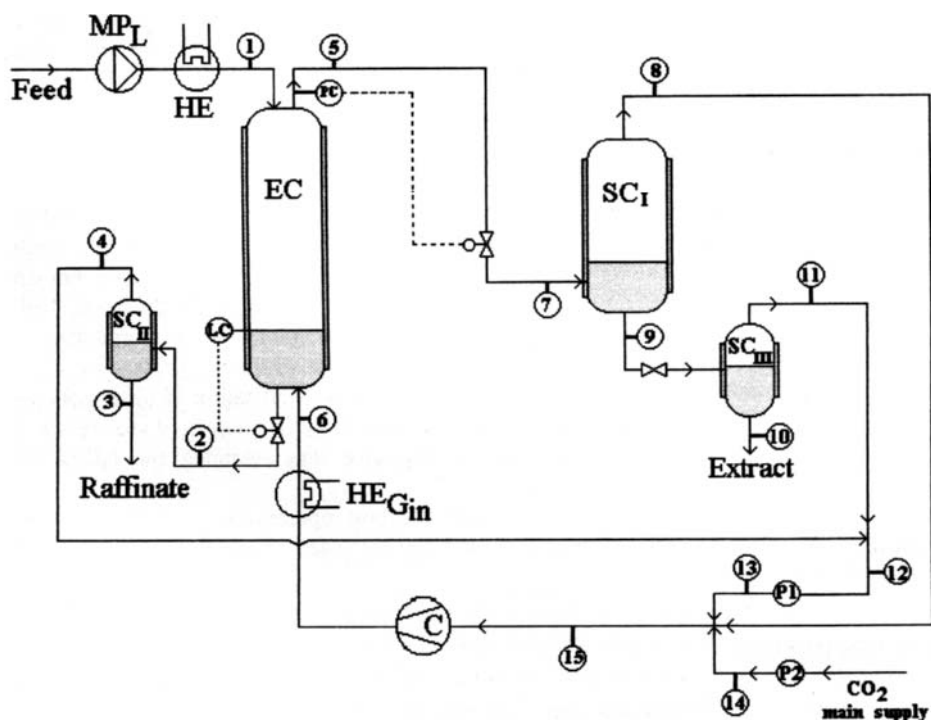


Figure 1. Flowsheet of the deacidification unit of olive oil by supercritical carbon dioxide. Symbols are defined in Table 2; other, PC: pressure control, LC: flow control.

The experimental phase equilibria and mass transfer data were then used to solve the mass balances over the whole unit. The mass flows, pressures, temperatures and compositions of each stream are listed in Table 1. We can see that there is a relatively large amount of carbon dioxide flowing through the extraction column. This is due to the high solvent to feed flow ratio ($S_0/S_1 = 62$) to be used in the column, as a consequence of the small solvent loading on free fatty acids.

Table 1

Conditions of pressure, temperature, compositions and flowrates of each stream.

Stream number	P (MPa)	T (K)	Flow (kg/hr)	Composition		
				CO ₂	fat wt%	FFA
1	21	323	1 389	-	96	4
2	21	323	1 577	25	74.5	0.5
3	1.5	323	1 245	5	94.37	0.63
4	1.5	323	332	100	-	-
5	21	323	85 923	99.76	0.187	0.053
6	21	323	86 111	100	-	-
7	8	323	85 923	99.76	0.187	0.053
8	8	323	85 672	100	-	-
9	8	323	252	18	63.96	18.04
10	1.5	323	217	5	74.1	20.9
11	1.5	323	34	100	-	-
12	1.5	323	366	100	-	-
13	8	323	366	100	-	-
14	8	323	73	100	-	-
15	8	323	86 111	100	-	-

The use of reflux was considered to minimize that high flow of solvent. However, experimental results shown that we would have to use high reflux ratios and higher packing heights in order to fulfill the raffinate specification, which would increase the costs in equipment. We decided not to reflux the extract stream and design carefully the separation columns II and III to regenerate the most part of the solvent circulating in the unit.

2.2 Design of the equipment

The extraction column to be used in the process will have an internal gauze packing - Sulzer BX, that was chosen due to its large interfacial area, high porosity and low pressure drops.

The diameter of the column may be accurately calculated with the knowledge of the maximum capacities attained by the used gauze packing under the current extraction conditions. Although there is no experimental data available for our system, measured flooding data have been lately published in the literature for the system corn seed oil/CO₂ at high

pressures (5) which closely resemble ours. Meyer presented the collected data in a so-called loading diagram in terms of two parameters, a load factor, ϕ , and a flow factor, F :

$$\phi = \frac{L}{G} \sqrt{\frac{\rho_L - \rho_G}{\rho_L}} \quad (1)$$

$$F = u_G \sqrt{\frac{\rho_G}{\rho_L - \rho_G}} \quad (2)$$

The maximum gas velocity flowing through the packing under the operating conditions is a function of the flow factor. The diameter of the column is then calculated by assuming the design velocity of the gas to be 60% of the flooding value. This distant approach to the flooding point is due to the expected high density and viscosity of the extract stream at such high pressure conditions which will limit the range of conditions usable by the system.

The height of the column was calculated with the use of a method proposed by Hufton *et al.* (6) to scale small laboratory structured packing columns to large commercial packed devices. For the same operating conditions, it relates the height of packing for the industrial column, $Z_{ind.}$, to the height for the laboratory column, $Z_{lab.}$, as a function of the ratio of the respective HETS (height of packing equivalent to a theoretical plate) of both columns, as shown:

$$\frac{Z_{ind.}}{Z_{lab.}} = \frac{HETS_{ind.}}{HETS_{lab.}} = \left(\frac{\ln E_{lab}}{\ln E_{ind}} \right) \left(\frac{(E-1)_{ind}}{(E-1)_{lab}} \right) \left(\frac{u_{g,ind}}{u_{g,lab}} \right) \left(\frac{d_{eq,ind}}{d_{eq,lab}} \right)^{0.2} \left(\frac{u_{g,ef,lab} + u_{l,efc,lab}}{u_{g,efc,ind} + u_{l,efc,ind}} \right)^{0.8} \left(\frac{a_{s,lab}}{a_{s,ind}} \right) \quad (3)$$

This ratio is expressed in terms of dimensional groups with the help of a mass transfer model initially proposed by Bravo *et al.* (7) for vacuum distillation columns and lately modified to fit the olive oil/CO₂ system (4) at high pressure conditions. The right term of the last equation comprises the effective velocities of the gas and liquid streams through the packing, a flow ratio, $E=G/L$, and the geometrical characteristics of both packings. The HETS of the laboratory packing column, determined by experimental data, is equal to 0.29 m/stage. The calculated packing height for the industrial column, $Z_{ind.}$, was 2.7 m. Adding 30% to count for possible end effects, the total height of the column is 3.5 m.

The thickness of the column was calculated from the following relation between the yield stress of the steel, σ , the diameter and the design pressure of the column (8):

$$x_w = \frac{P d_{int.}}{\left(\frac{4}{3} \sigma - P \right)} \quad (4)$$

The separation columns were designed by estimating the required gas velocity flowing through the separators for the settling by gravity of the oil components (8). In Table 2 we show the respective design variables. In the same table we present the design parameters for the other main pieces of equipment, namely, heat exchangers and pumps.

Table 2

Operating and design specifications of the equipment used in the proposed process

Extraction Column, EC
d_{int} : 1.3 m; packing: Sulzer BX; height 3.5 m; thickness 0.2 m
Separation column, SC _I
d_{int} : 1.5 m; packing: Sulzer BX; height 2.8 m; thickness 8 cm
Separation column, SC _{II} : d_{int} : 0.7 m; height 1.4 m; no packing
Separation column, SC _{III} : d_{int} : 0.5 m; height 1.1 m; no packing
Metering pump, MP _L : $p = 50$ kW; $L = 1.5$ t/hr
Pumps, P ₁ and P ₂ : $p = 15$ kW
Heat Exchanger for liquid: Area 2.5 m^2 ; $U_o = 600 \text{ J/s m}^2 \text{ K}$
Heat Exchanger for fresh gas: Area 2 m^2 ; $U_o = 200 \text{ J/s m}^2 \text{ K}$
Heat Exchanger for gas in: Area 200 m^2 ; $U_o = 200 \text{ J/s m}^2 \text{ K}$

3. ECONOMICAL EVALUATION

To assess the feasibility of the proposed olive oil deacidification plant we need an economical evaluation of the overall process. An economical study (9) was thus performed by simulating all the debits and credits involved in the industrial plant. The analysis was performed at constant prices instead of real prices, and the units are in Portuguese escudos (PTE).

The total capital investments costs was estimated on the basis of the equipment costs plus a specific installation factor and is shown in Table 3. An additional of 20% of the total installed equipment costs was included for engineering and contingency costs. The main part of these costs are due to the extraction column, EC, (this includes the price of steel to be used to make the column and the packing expenses) and the main gas compressor, C.

Table 3

Estimated Investments Costs (unit price: 10^3 PTE)

Capital costs		Operating costs	
Equipment	Cost	item	Cost
EC	222 624	Raw materials	1 630 000
SC - I	91 311	Utilities	379 000
SC - II and III	3 118	Labour	20 000
HE - L	2 114		
HE - gas input	7 803		
HE - fresh gas	2 120		
C	104 994		
MP - L	52 700		
P ₁ + P ₂	28 570		
Engineering & contingency	103 070		
TOTAL	618 424		2 029 000

The annual operating costs are also shown in Table 3. The raw materials costs were estimated from the average purchase cost of crude olive oil in Portugal in 1994. Supplies were empirically calculated from the scale-up study and include water, electric power, fuel, maintenance, assurances, transports and expedient articles. The labour costs were determined for 4 shifts of 2 persons each, plus supervising personal. With a depreciation time of ten years and an interest rate of 10%, the total annual capital costs was estimated to be 212PTE/kg of oil feed. Several other economical indicators, such as the internal rate of return of the plant, showed a promising economical feasibility for this project.

Market considerations may play an important role in the feasibility of this new extraction process by selling this output as a "green" salable product. Analyses of our raffinates, according to the European Norm for oils, confirmed that the olive oil thus obtained has all the characteristics for human use.

REFERENCES

1. M. Gonçalves, A.M.P. Vasconcelos, E.J.S. Gomes de Azevedo, H.J. Chaves das Neves, M. Nunes da Ponte, *J. Am. Oil Chem. Soc.*, 68:7 (1991) 474.
2. L. Brunetti, A. Daghetta, E. Fedeli, I. Kikic, L. Zanderighi, *J. Am. Oil Chem. Soc.*, 66:2 (1989) 209.
3. P. C. Simões, G. Brunner, *J. Supercritical Fluids*, 1996, in press.
4. P.J. Carmelo, Ph.D. Dissertation, Faculdade de Ciências e Tecnologia, Universidade Nova de Lisboa, 1995.
5. J.T. Meyer, G. Brunner, *Proceedings of the 3rd Int. Symp. on SCF*, Strasbourg, France, Tome 2 (1994), 217.
6. J.R. Hufton, J.L. Bravo, J.R. Fair, *Ind. Eng. Chem. Res.*, 27 (1988), 2096.
7. J.A. Rocha, J.L. Bravo, J.R. Fair, *Ind. Eng. Chem. Res.*, 32 (1993), 641.
8. J.M. Coulson, J.F. Richardson, *Chemical Engineering, Volume VI: Design*, Pergamon Press, Oxford, 1983.
9. M.S. Peters, K.D. Timmerhaus, *Plant Design and Economics for Chemical Engineers*, 3rd ed., McGraw-Hill, New York, 1980.

Gas-Liquid Mass Transfer in High Pressure Trickle-Bed Reactors : Experiments and Modelling

M. Cassanello^a, F. Larachi^b, A. Laurent^c, G. Wild^c and N. Midoux^c

^a PINMATE, Departamento de Industrias, FCEyN, Universidad de Buenos Aires
1428 Ciudad Universitaria, Buenos Aires, Argentina

^b Department of Chemical Engineering
Laval University, Sainte-Foy, Québec, Canada, G1K 7P4

^c Laboratoire des Sciences du Génie Chimique. CNRS, ENSIC, INPL.
1, Rue Grandville, BP 451 - 54001, Nancy cédex France

Abstract—Gas-liquid interfacial areas a and volumetric liquid-side mass-transfer coefficients $k_L a$ are experimentally determined in a high pressure trickle-bed reactor up to 3.2 MPa. Fast and slow absorption of carbon dioxide in aqueous and organic diethanolamine solutions are employed as model reactions for the evaluation of a and $k_L a$ at high pressure, and various liquid viscosities and packing characteristics. A simple model to estimate a and $k_L a$ for the low interaction regime in high pressure trickle-bed reactors is proposed.

1. INTRODUCTION

Trickle-bed reactors —TBRs—, i.e. packed beds fed cocurrently downwards with a two-phase gas-liquid flow, find widespread applications in the chemical, petrochemical and biochemical industries. Key processes of the oil refining, e.g. hydrodesulfurization and catalytic hydrofinishing, as well as many wastewater treatments are performed in TBRs. Even though most of the commercial TBRs operate at high pressure/temperature, information on key parameters (e.g. pressure drop, hold-up, mass transfer coefficients, ..) for TBR design at actual operating conditions has been poorly reported in the literature.

Gas-liquid mass transfer can have a strong effect on TBR overall performance; therefore its accurate evaluation is essential for achieving successful design and scale-up. In spite of the vast information available on gas-liquid mass transfer characteristics of atmospheric TBRs [1,2] only a few researchers have studied how interfacial areas, a , and volumetric liquid-side mass transfer coefficients, $k_L a$, evolve at elevated pressures. For example, it has been reported that both a and $k_L a$ increase as gas density is risen while the gas superficial velocity is kept constant [3-5]. Similar observations regarding gas hold-up and two-phase pressure drop, as well as the delay in the onset of pulsing have also been reported [6].

In this study, a and $k_L a$ are measured in a TBR in the pressure range [0.3-3.2 MPa] using fast and slow chemical absorption of carbon dioxide into diethanolamine (DEA) aqueous and organic solutions. Only the trickling regime and trickling/pulsing transition have been explored. A simple model to explain the increase of interfacial area and mass transfer

coefficient driven by pressure is proposed. It assumes that at high pressure part of the flowing gas is dispersed as tiny bubbles in the liquid films trickling over the packing. Such bubbles would be responsible for the increase in interfacial area. Bubble size is assumed to be determined from a balance between the viscous stress exerted by the liquid, which tends to deform and break the bubble and the counteracting Laplace pressure which tends to keep the bubble spherical.

2. EXPERIMENTAL

Experiments are performed in a 0.395 m high and 23 mm internal diameter stainless steel reactor, packed with various particles (Table 1). a is measured via CO_2 fast absorption into 1.5 kmol/m³ DEA aqueous solutions of varying viscosity through addition of ethylene-glycol (ETG). $k_L a$ is measured via CO_2 slow absorption into 0.05 kmol/m³ DEA in ETG. All the experiments are carried out at 298 K. The gas mixture is obtained by mixing 5% vol. CO_2 in pure N_2 . CO_2 conversion is determined by gas phase chromatography analysis. Physico-chemical properties of the liquids tested are shown in Table 1.

Table 1
Properties of the liquid solutions and particles employed

	d (mm)				
polypropylene extrudates	3.2				
activated carbon cylinders	1.5				
glass beads	0.9-1.2-2-3.1				
alumina spheres	2.0				
A=CO ₂ —B=DEA	ρ_L kg/m ³	μ_L mPa.s	σ_L mN/m	$10^9 \times D_A$ m ² /s	$10^9 \times D_B$ m ² /s
CO ₂ /DEA/H ₂ O	1016	1.2	64	1.7	0.76
CO ₂ /DEA/H ₂ O+20%ETG	1037	2.3	59	1.0	0.43
CO ₂ /DEA/H ₂ O+40%ETG	1061	3.8	57	0.7	0.26
CO ₂ /DEA/ETG	1112	18	48	0.3	0.15

3. GAS-LIQUID INTERFACIAL AREA

3.1. Effect of gas density and superficial velocity

The effect of superficial gas velocity on gas-liquid interfacial areas for different operating pressures is shown in Fig. 1. For very low liquid or gas flow rates, a is almost independent of a change in pressure. However, for higher liquid flow rates, an increase in pressure induces a significant increase in a for gas superficial velocities above a critical gas velocity $u_{gc} \approx 2$ to 3 cm/s. Gas and liquid superficial velocities over which pressure effects are no longer negligible are coincident with the ones for which gas hold-up becomes pressure-sensitive [6]. Thus a relation between the change in interfacial areas and hold-ups due to pressure is expected.

A physical assumption explaining those observations has already been suggested previously [3]. As pressure or gas density increases, gas shear over the trickling liquid film becomes more important for a given superficial gas velocity. The momentum transfer through the gas-liquid interface may then be large enough so as to make gas to be entrained into the

liquid, specially at certain points where the particles leave very small interstitial space. The gas will disperse in the liquid film forming bubbles. Bubble size in the gas-liquid suspension will be determined from a competition between the liquid viscous shear stress which tends to deform and break the bubbles and the force induced by interfacial tension, which tends to stabilise them. The bubbles formed will then be transported within the liquid films, thus increasing gas hold-up and gas-liquid interfacial area.

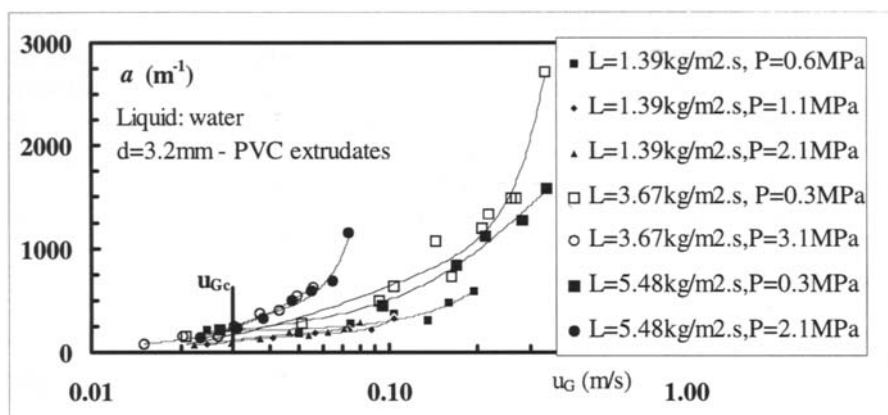


Figure 1. Typical effects of pressure and fluid velocities on gas-liquid interfacial area

3.2. Model to estimate the increase of a due to pressure

To quantify the increase of a due to pressure, a mean bubble diameter has been estimated using Taylor's stability theory [7] on bubble deformation and break-up in sheared emulsions. According to this theory, bubble size in a sheared emulsion results from a balance between viscosity and surface tension forces. The dimensionless number that describes the ratio of these forces is called the capillary number Ω . For large bubble deformations, the maximum stable bubble diameter in a shear flow is expressed as [8] :

$$\Omega = \frac{\tau D_{\text{Max}}}{\sigma_L} = C \lambda^{-1/6} \quad (1)$$

where τ is the viscous shear stress exerted by the gas-liquid emulsion on the bubbles; D_{Max} is the maximum bubble size that can stand the external force without being broken; Ω is a critical capillary number that gives the conditions at bubble burst; λ is the ratio of dispersed (gas) to continuous phase (liquid) viscosities, and C is a numerical constant fitted from experimental data.

For this model to be valid the following assumptions have been considered : i) very small satellite bubbles formed in the break-up do not significantly contribute to gas hold-up and gas-liquid mass-transfer; only relatively large bubbles are considered; ii) bubble Sauter

diameter, D_s , is representative of the bubbles dispersed in the films; it is proportional to the maximum bubble diameter, D_{\max} .

Bubble Sauter diameter is defined as :

$$D_s = \frac{6\beta_b \varepsilon}{a_b} = \frac{6(\beta_{L_0} - \beta_L) \varepsilon}{(a - a^0)} \quad (2)$$

where β_b and a_b are, respectively, the excess gas hold-up and the excess gas-liquid interfacial area induced by the bubbles in the liquid films. Such bubbles do not exist for atmospheric conditions in the trickle flow regime. At elevated pressure they may be evaluated from the difference between the actual values of liquid hold-up β_L and interfacial area a and those corresponding to atmospheric conditions, respectively β_{L_0} and a^0 .

Expressing the effective viscosity of the gas-liquid emulsion with Einstein's equation, and replacing the viscous shear stress τ as the product of effective emulsion viscosity and the maximum liquid velocity gradient, and after combining Eq. (2) into Eq. (1), one arrives at the following relationship between a and a^0 :

$$a = a^0 \left\{ 1 + \lambda^{1/6} \kappa \frac{We_L}{Re_L \varepsilon} \left(1 + 2.5 \left(1 - \frac{\beta_L}{\beta_{L_0}} \right) \right) \left(\frac{1}{\beta_L} - \frac{1}{\beta_{L_0}} \right) \right\} \quad (3)$$

where ε is the bed porosity, $Re_L = \rho_L u_L d / \mu_L$ and $We_L = \rho_L u_L^2 d / \sigma_L$.

Table 2
Data bank of the existing high pressure interfacial areas

Reference	Experimental conditions	Number of data
This work	$P = 0.3\text{-}3.2$ MPa, $d = 0.85\text{-}3.1$ mm, $u_L = 10^{-3}\text{-}8 \cdot 10^{-3}$ m/s, $\mu_L = 1.1\text{-}10$ mPa.s	a : 155 $k_L a$: 34
[5]	$P = 0.3\text{-}5.0$ MPa, $d = 3.1$ mm, $u_L = 2 \cdot 10^{-3}\text{-}1.2 \cdot 10^{-2}$ m/s, $\mu_L = 1.7\text{-}4$ mPa.s	a : 42

Table 3
Statistical analysis of the proposed model

	Data bank	Bias	95% Confid. factor	Std-dev.
a	197	0.99	2.34	48.0%
$k_L a$	34	0.98	2.36	47.6%

Eq. (3) is a one-parameter correlation (κ being the unknown parameter) that permits estimation of gas-liquid interfacial areas under high pressure provided the high pressure liquid hold-up β_L is known; the expression between brackets can be seen as an enhancement factor of the interfacial area due to pressure effect. Values of β_{L_0} and a^0 at atmospheric pressure are also required. Using available interfacial area data of Wammes et al. [5] and the data of this work, the best estimate of κ is $4.9 \cdot 10^4$. Predictions of present results and of those reported by

Wammes et al. [5] by the suggested model are shown in Fig. 2. The experimental conditions and the number of data considered are listed in Table 2. To our knowledge these are all the data available on high pressure trickle-bed reactors and they fall within the 48% error. Statistical tests used to evaluate the goodness of fitting of the correlation are shown in Table 3.

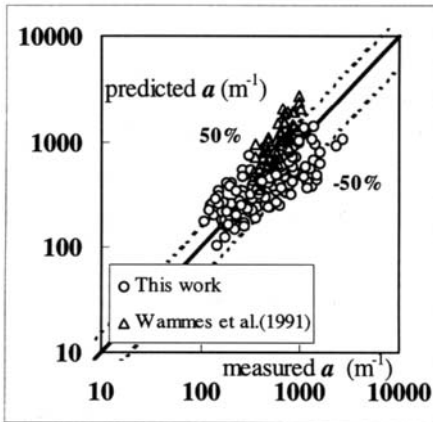


Figure 2. Comparison between a measured vs. calculated with Eq. 3 and experimental data

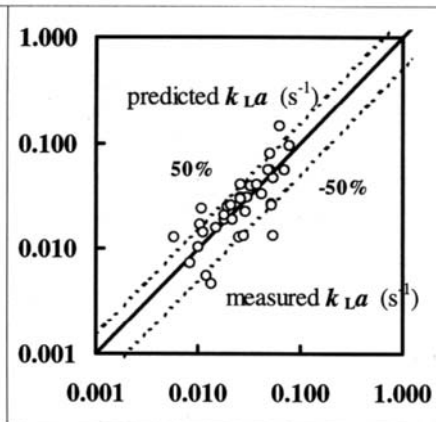


Figure 3. Parity plot of calculated predicted $k_L a$ values

3. VOLUMETRIC LIQUID-SIDE MASS TRANSFER COEFFICIENT

As shown in Fig. 4, the effect of pressure is to increase the corresponding $k_L a$. Similarly to a , $k_L a$ depends on pressure only for gas and liquid velocities above some critical velocities. The effect of pressure can be due either to an increase in k_L or in a , or in both. A literature review on the pressure effect on k_L in different gas-liquid contactors reveals that k_L may be considered as independent of reactor pressure. Hence, $k_L a$ should vary with pressure only via the effect of the interfacial area. Following the assumption of the presence of small bubbles in the liquid films, gas-liquid mass transfer can be split into : a mass transfer from the continuous gas to the liquid film, with a mass transfer coefficient equal to the one at atmospheric conditions and a mass transfer from the bubbles to the surrounding liquid, as if bubbles were suspended in a stagnant medium. Then, contribution brought about by bubbles is calculated as the product of the excess interfacial area a_b and the mass transfer coefficient of a bubble in a stagnant medium ($Sh = 2$):

$$k_L a = (k_L a)^0 + k_L^{(Sh=2)} a_b \quad (4)$$

The parity plot of calculated vs. experimental results of $k_L a$ under high pressure conditions is shown in Fig. 3. Even though measured data are scattered, they constitute to our knowledge the only existing experimental values obtained in a pressurised TBR. Experimental results are reasonably well predicted from the previous analysis as can be judged from the statistical test shown in Table 3.

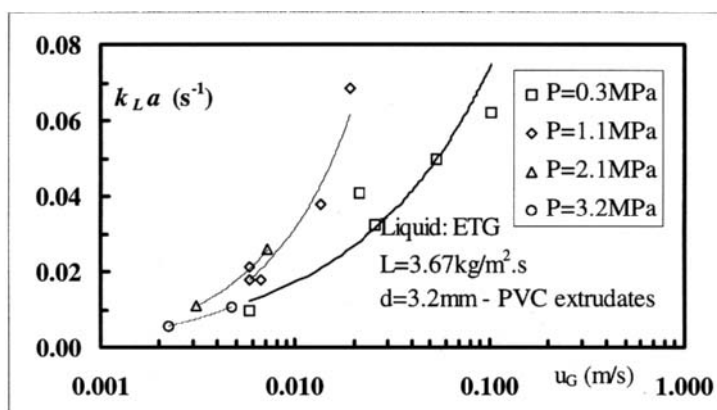


Figure 4. $k_L a$ variation with pressure and gas velocity

CONCLUSION

Gas-liquid interfacial areas, a , and volumetric liquid-side mass transfer coefficients, $k_L a$, are measured in a high pressure trickle-bed reactor. Increase of a and $k_L a$ with pressure is explained by the formation of tiny bubbles in the trickling liquid film. By applying Taylor's theory, a model relating the increase in a with the increase in gas hold-up, is developed. The model accounts satisfactorily for the available experimental data. To estimate $k_L a$, contribution due to bubbles in the liquid film has to be added to the corresponding value measured at atmospheric pressure. The mass transfer coefficient from the bubbles to the liquid is calculated as if the bubbles were in a stagnant medium.

ACKNOWLEDGEMENTS

Financial support from Institut Français du Pétrole, France & Algerian Ministry of Education are acknowledged.

REFERENCES

1. B.I. Morsi, A. Laurent, N. Midoux, G. Barthole-Delauney, A. Storck and J.C. Charpentier, Chem. Eng. Commun., 25 (1984) 267.
2. G. Wild, F. Larachi and J.C. Charpentier, in Heat and Mass Transfer in Porous Media, M. Quintard and M. Todorović (eds), Elsevier, Amsterdam (1992) pp. 616-632.
3. F. Larachi, A. Laurent, G. Wild and N. Midoux, Chem. Eng. Sci., 47 (1992) 2325.
4. A. Lara-Marquez, F. Larachi, G. Wild and A. Laurent, Chem. Eng. Sci., 47 (1992) 3485.
5. W.J.A. Wammes, J. Middelkamp, W.J. Huisman, C.M. deBaas and K.R. Westerterp, AIChE J., 37 (1991) 1849.
6. G. Wild, F. Larachi and A. Laurent, Rev. Inst. Franç. Pétr., 46 (1991) 467.
7. J.O. Hinze, AIChE J., 1 (1955) 289.
8. B.J. Bentley and L.G. Leal, J. Fluid Mech., 167 (1986) 241.

Influence of mechanical stresses on phase transitions of polydimethylsiloxane and diacetate cellulose solutions

E.V. Rusinova and S.A. Vshivkov

Ural State University, Ekaterinburg, Russia

1. SUMMARY

Phase transitions in the system polydimethylsiloxane (PDMS)-methyl ethyl ketone (MEK) showing an upper critical solution temperature and in the gel-forming systems: cellulose acetate (CA)-acetone-water, CA-dioxane-water were studied under shear field and in static conditions. An inversion of the effect that the field has on phase transitions was discovered for the system PDMS-MEK: compatibility of the components in the flow increases under low shear stress and decreases under the high one. The shear stress leads also to the qualitative change of boundary curves, testifying to the change of the mechanism of the phase decompositions of solutions. For the gel-forming systems it was discovered the increase of the compatibility of the components under flow. The mechanism of these phenomena is suggested.

2. INTRODUCTION

It is well known that the polymer systems undergo various mechanical treatments during their exploitation. This leads to the change of component compatibility and to the shift of boundary curves. The theory of this phenomenon has been worked out. The present article is dealing with the study of influence of the shear rates ($\dot{\gamma}$) and stresses (σ) on phase transitions in the systems: PDMS ($\bar{M}_w=2.7 \cdot 10^5$)-MEK and CA-I ($\bar{M}_n=6.1 \cdot 10^4$, degree of substitution (DS) 2.4)-dioxane-water, CA-II ($\bar{M}_w=6.9 \cdot 10^4$, DS=2.5)-acetone-water.

3. EXPERIMENTAL

The solutions of PDMS in MEK and CA in mixed solvents were prepared at 313 K during several days. The phase separation temperatures (T_{ph}) for the solutions under shear field and in static conditions were determined by cloud-point method and viscometric measurements using rotational reometer PVR-2. The spinodal was determined by the light scattering method according to [11].

3.1. Results and discussion

The binodal(1) and spinodal curves for the systems PDMS-MEK are shown on Fig.1. These curves coincide in critical point with parameters UCST=291 K, $C = 5.5$ g/dl.

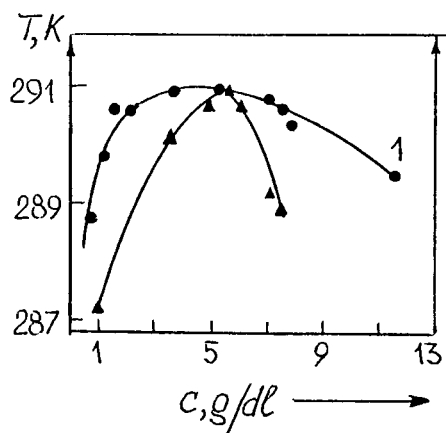


Fig. 1.

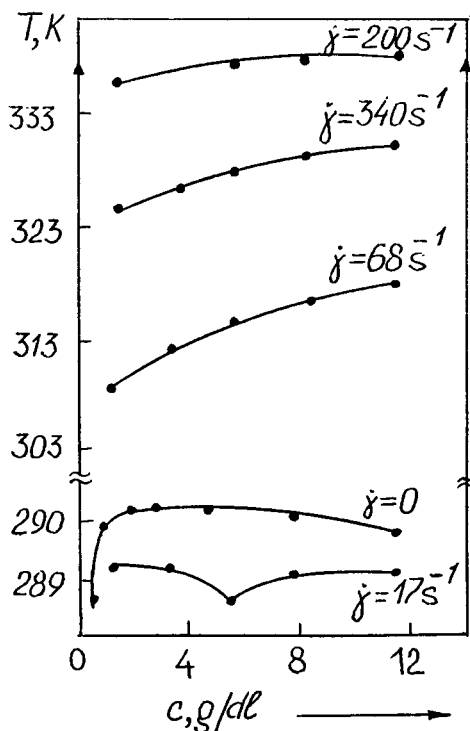


Fig. 2.

Fig.2 shows the boundary curves for PDMS-MEK system under static and dynamic conditions. One can see that shear deformation causes the shift of the boundary curves: at the low shear rate ($\dot{\gamma}$) and stress ($\dot{\sigma}$) ($\dot{\sigma} = \eta \dot{\gamma}$, where η - the viscosity of the system) the component compatibility increases that manifests itself in the decrease of T_{ph} , at the high ($\dot{\gamma}$) or ($\dot{\sigma}$) the shear field causes the increase of T_{ph} testifying to the decrease of the mutual compatibility. So an inversion of the effect that the shear field has on phase transitions was discovered for this system.

The surface energy of PDMS is equal to $\sigma'_2 = 24 \cdot 10 \text{ J/m}^2$, that practically coincides with one for the MEK $\sigma'_1 = 24.6 \cdot 10 \text{ J/m}^2$. Therefore the value of $\sigma'_{12} = \sigma'_1 - \sigma'_2$ is very small and shear field can break-down the new phase nuclei that leads to the increase of the component solubility. As can be seen from Fig.2, the shear-dissolution effect shows to a great extent for the solution of critical composition, because in this case the composition of two coexisting phase are very close and σ'_{12} is very small.

Under high ($\dot{\sigma}$) the binodal is transformed to the curve for the gel-forming system. It can testify about the change of the mechanism of the phase separation of solutions. At the high shear rate the macromolecules can form the adsorption-entanglement layers on the surface of the rotor and stator [2] that can lead to the formation of the gel-like particles and, finally to the phase separation.

The reversible character of phase transitions in the case of low $\dot{\gamma}$ and irreversible one in the case of high $\dot{\gamma}$ testify also about the different phase separation mechanism. Experimentally it shows in the disappearance of the turbidity upon heating in the former case and in the irreversible solution tyrbidity in the second case.

The boundary curves for the systems CA-I-acetone-water and CA-II-dioxane-water are shown in Fig.3.(a,b).

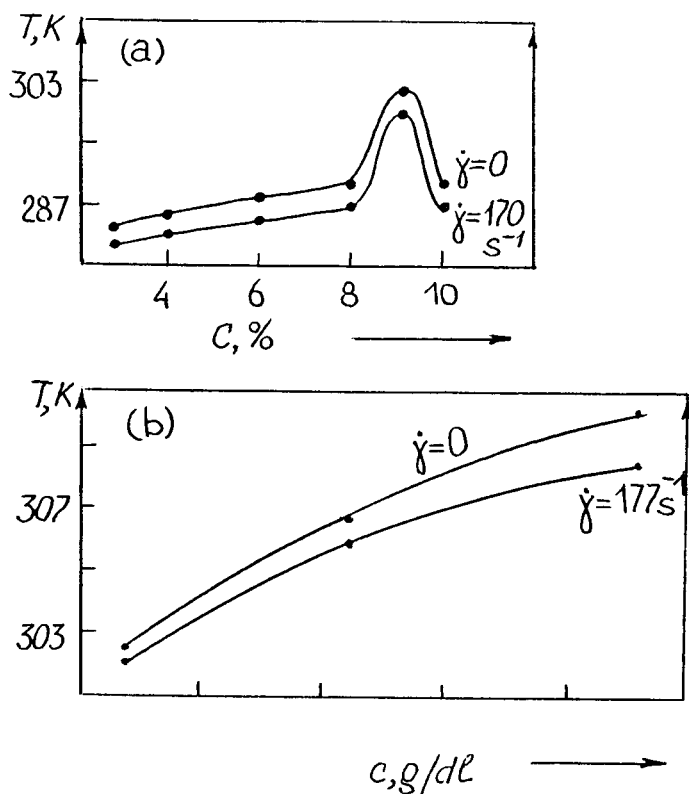


Fig.3.

One can see that for the both systems shear field causes an increase in miscibility of the components, it leads to the a decrease of gel formation temperatures. So the aggregates of macromolecules formed upon cooling are not stable and can be destroyed by the mechanical field.

REFERENCES

1. B.Chu, F.Z.Schoenes, M.E.Fisher, Phys.Rev.Lett.,185 (1969) 219.
2. P.J.Barham, A.Keller, Macromolecules, 23 (1990) 303.

ADSORPTION PROPERTIES OF SYNTHESIZED DIAMOND AS A FUNCTION OF MICRODOPING OF THE SOLUTION- MELT SYSTEMS

G.P. Bogatyreva, A.V. Andreyev, and V.L. Gvyazdovskaya

V.N.Bakul Institute for Superhard Materials, 254074 Kiev (Ukraine)

1. INTRODUCTION

In the different fields of science and engineering during the past few years the interest in diamond powders as the multipurpose materials with a wide set of physico-chemical properties has considerably increased. So, the production of diamond powders with specific properties, particularly with specific chemical and energy properties of a diamond grain surface, is the important research and technology topics.

It is suggested that to grow diamonds possessing different adsorption and energy properties of the surface, one should use metal melts with different diamond-melt interfacial energies. Really, it is well known [1] that the interfacial energy between crystal and its uterine melt defines to a great extent the morphology and surface microstructure of the crystal formed. The free energy of formed surfaces with edges should satisfy the following expression:

$$F = \sum \sigma_i ds_i + T dS \quad (1)$$

The first term of the expression presents a change of the free energy connected with the formation of new surfaces. The second one presents an intensity of the atom exchange between the crystal surface and uterine media.

As follows from eq.(1), the opportunities appear for the changes of the values of crystal surface with the changes of the interfacial energies without a violation of the requirement of free energy minimum. In this sence, a decrease of the interfacial energy increases the values of crystal surface and vice versa. So, to obtain diamond grains with a more developed surface, one should

obviously use metal melts having lower diamond-melt interfacial energies.

In this paper, we report the results of our investigations into the changes of chemical and energy properties of diamond grain surfaces with changes in physico-chemical and capillary properties of diamond crystallization media. We have carried out a set of special studies to establish main regularities of the correlations between properties of the crystallization media and adsorption-structural properties of synthetic diamond crystals.

2. EXPERIMENTAL PROCEDURE

The wettability of diamond with Ni-Mn alloys having Ga, Ge, Sn, Mg, Al and Si additives was determined by means of the sessile drop method at high pressure (5.5 GPa) and temperature (1400° C) following a special procedure [3,4]. The metal pellet melted and attained its equilibrium form owing to surface forces on the diamond plane surrounded by molten NaCl that gives a quasi-hydrostatic environment and suppress oxidation of the metal.

To determine the diamond equilibrium solubility in the metal melts in a range of its thermodynamic stability we also used a special method which was originally developed early. Based on the data obtained we estimated carbon supersaturations in the melts [4,5].

In our investigations, the energy levels of the diamond grain surfaces was determined by the experimental isotherm of nitrogen adsorption on the diamond surface at pressure $P/P_s=0.7$ and temperature of a liquid nitrogen (77 K) [6]. For estimation of energy inhomogeneity of the grain surfaces we calculated a function of the adsorption potential distribution with the aid of a specially developed graphic-analytical procedure [6]. Based on the isotherm, the specific surface area and ultimately saturated pore value were also calculated. The differential and integral pore-size distributions were determined and the Gibbs free energy values at the diamond-vacuum and diamond-nitrogen interfaces were evaluated following the procedure described in [6,7].

3. RESULTS AND DISCUSSION

The isotherms of diamond surface wettability with Ni-Mn-base alloys versus the amount of a third alloy component are shown in Fig.1. The Ga, Ge and Sn additives up to 10 at% in the alloys decrease the wetting angles on the diamond surface. At the same time the Al, Mg and Si additives increase the wetting angles over the concentration range under investigation. Such a behaviour of the wettability curves is defined by both a chemical affinity of a third component to carbon atoms and the intensity of the interaction of the alloy component atoms with each other according to [8]. So, for our further investigations we used the Ni-Mn alloys and 7 at% of the Si-additive and 7 at% the Ga-additive which exhibited the highest and the lowest wetting angles on diamond surface, respectively.

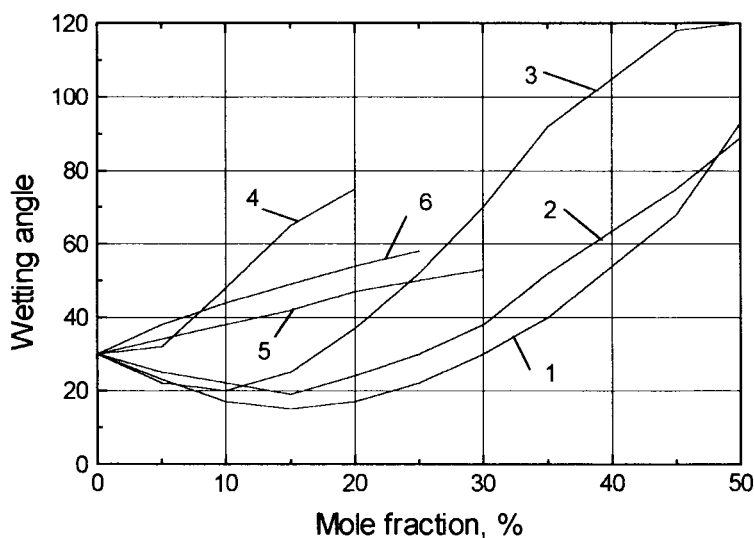


Fig. 1. Wettability of diamond with Ni-Mn-base alloys at high pressure (5.5 GPa) and temperature (1400° C). 1 - NiMn+Ga, 2 - NiMn+Ge, 3 - NiMn+Sn, 4 - NiMn+Si, 5 - NiMn+Al, 6 - NiMn+Mg.

For these alloys we determined the equilibrium carbon solubility and calculated carbon supersaturation with respect to diamond. We also grew diamond using the alloys and established the average yield of the diamond transformation. The data are listed in Table 1.

Table 1.

Relationship between physico-chemical properties of the crystallization medium (Ni-Mn-Ga-C and Ni-Mn-Si-C systems) and physico-mechanical, physico-chemical properties and performance characteristics of synthesized diamond powders.

Characteristic	Measured values	Units	Results	
			Si-doped	Ga-doped
Physico-chemical characteristics of the Ni-Mn doped alloys	Wetting angle	θ°	38	27
	Carbon supersaturation of the metal melts	mas. %	0.14	0.95
Synthesis process characterizations	Diamond raw material yield	ct/cycle	17.6	32.0
	Mass fraction of 63/50 diamond in the raw material	%	14.5	10.0
Energy characteristics of 63/50 diamond grains	Specific surface	m^2/g	0.033	0.190
	The total diamond grain surface produces per synthesis cycle	m^2	0.0160	0.1216
	Exposed porosity	ml/g	$21 \cdot 10^{-5}$	$35 \cdot 10^{-5}$
	σ_w at the diamond-vacuum interface	J/m^2	3.0	2.0
	σ_a at the diamond-nitrogen interface	J/m^2	0.3	0.2
Physico-mechanical and performance characteristics of 63/50 diamond powders	Strength measure	N	14.6	15.1
	Abrasive action of powders pastes	δ/p	9.3	6.3
		δ/p	309	330
	Strength criterion of polycrystals	sec/mm^3	239	352

In Table 1 and in Fig.2 are also shown the data of adsorption-structural properties of the produced diamond powders which were determined and calculated by the experimental low-temperature adsorption isotherms.

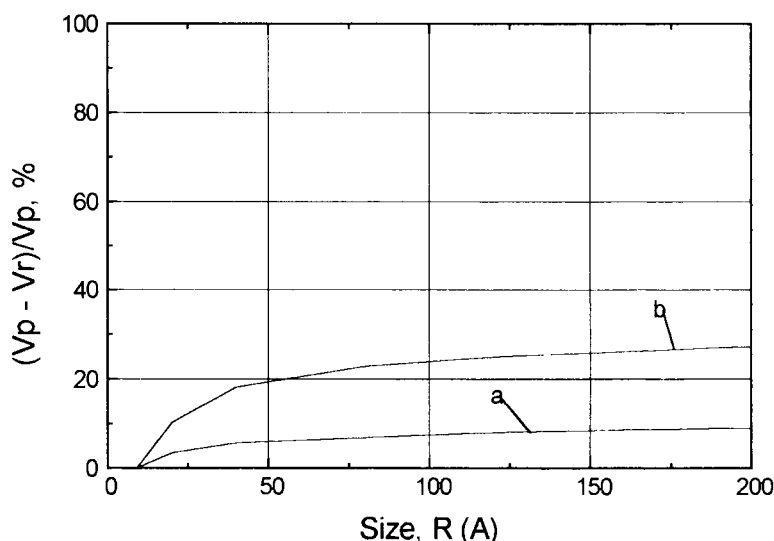


Fig. 2. The total porosity of Ga-doped ($V_p = 26 \cdot 10^{-5}$ ml/g) - (a) and Si-doped ($V_p = 97 \cdot 10^{-6}$ ml/g) - (b) diamond powders.

Diamond powders synthesized from Ni-Mn+7at%Si and Ni-Mn+7at%Ga alloys were found to have significantly different adsorption-structural and energetic characteristics of their surfaces. The Ni-Mn +7at% Ga alloy with the lower interfacial energy (a lower wetting angle) was determined to provide the yield of diamond grains with a more developed specific surface. The powder from these diamonds also have higher adsorption properties, lower diamond-nitrogen and diamond-vacuum interfacial energies and a more developed porosity.

As is seen from Table 1, the diamond powders synthesized in the Ni-Mn-Ga-C system have higher physico-mechanical and performance characteristics than those synthesized in the Ni-Mn-Si-C system. The diamond polycrystals sintered from these diamond powders were tested for wear. Wear of the polycrystals sintered

from the Ga-doped powder was a fraction of wear of the polycrystals from the Si-doped powder (see Table 1).

So, our investigations allow us to establish the correlation between physico-chemical properties of the crystallization media (capillary properties of the diamond-metal melt interface, carbon supersaturation in the melt with respect to diamond) and adsorption-structure and energy properties of the produced diamond powders. Our findings permit us to extend scientific and technological potentialities for production of diamond grinding and micron powders having unique properties.

REFERENCES

1. A. A. Chernov et al., Modern Crystallography (Science, Moscow, 1980).
2. A. V. Andreyev, in Y. Tzeng et al.(Eds.), Application of Diamond Films and Related Materials, Elsev.Sci.Publ. B.V. 1991, p.143.
3. A. V. Andreyev, Diamond and Related Materials, 3(1994)1262.
4. A. V. Andreyev, I. S. Belousov, Diamond and Related Materials, 3(1993)7.
5. S. A. Ivakhnenko, A. V. Andreyev and I. S. Belousov, Sov.J.of Superhard Mater., 14 N4(1992)11.
6. V. G. Aleshin, A. A. Smekhnov, G. B. Bogatyreva, and V.B. Kruk, Chemical of Diamond Surface (Naukova Dumka, Kiev, 1990).
7. I. J. Gregg, K. S. W. Sing, Adsorption, Surface Area and Porosity (Academ.Press, London and New York, 1967).
8. Yu.V.Naidich, V.M.Perevertailo, E.M.Lebovich, Melt Adhesion and Soldering of Materials, 1(1976)28 (in Russian).

Impregnation of Porous Supports with Active Substances by Means of Supercritical Fluids

C. Magnan^a, C. Bazan^a, F. Charbit^a, J. Joachim^b, and G. Charbit^a

^aLaboratoire d'Etudes et d'Applications de Procédés Séparatifs
Université d'Aix-Marseille, Campus de St Jérôme
Avenue Escadrille Normandie-Niemen
13397 Marseille CEDEX 20, France

^bLaboratoire de Pharmacie Galénique Industrielle, Faculté de Pharmacie
58 Boulevard Charles Livon 13007 Marseille, France

1. INTRODUCTION

In the pharmaceutical industry the impregnation of porous and inert solids with drugs is classically achieved by a two-step process. During the first step, a solution of the active molecule in an organic solvent is brought into contact with the solid. The second phase deals with the evaporation of the excess solvent. Some problems arise from this method. The elimination of the solvent can cause a degradation of thermosensitive drugs ; furthermore, residual traces of solvent resulting from an uncomplete elimination may cause a risk of toxicity. To overcome these problems it has been suggested to achieve the impregnation using a micronized dispersion of the drug in water. This method is successful in a number of cases but fails in other because of a possible hydrolysis of the drug. We thought that the use of a supercritical solvent (CO₂) instead of an organic liquid could constitute an interesting alternative with the following advantages :

- Unlike most of the organic solvents carbon dioxide is exempt from toxicity.
- Elimination of CO₂ from the medium is quantitatively done by returning to a low pressure.
- Elimination is instantaneous, which is time saving.

One of the major disadvantages of CO₂ is its low power of solubilization with respect to polar molecules and consequently to most of the molecules offering a therapeutic activity. The presence of a polar co-solvent added in small quantity to CO₂ is a solution to this problem. However, with regard to the particular aim of this study, a number of co-solvents must be avoided because of their toxicity. For the first experiments we chose a molecule offering a rather good solubility in CO₂ without co-solvent, the α Tocophérol acetate (α TA), though this compound does not present an extensive pharmaceutical interest. It appears in the European pharmacopoeia under the form of a dispersion of the molecule in gelatin, or an adsorption on silicic acid. The latter must have a weight concentration of 25% which is thus

the aim to be reached. No reference could be found in literature relatively to the chosen compound except Ferreira and Nunes Da Ponte [1] who reported that tocopherols can be extracted by supercritical CO_2 . This paper describes the first experiments carried out in order to develop the method and to compare the quantitative results to those obtained by classical ways. The two criteria of evaluation are the impregnation ratio R defined by the mass of active substance laid down by mass unit of porous solid, and the time necessary for the impregnation.

2. EXPERIMENTAL

2.1. Equipments

Two experimental apparatuses were developed. The first setup described elsewhere [2], was used under static conditions to measure the solubility of the α TA in the supercritical fluid.

The second equipment described in Figure 1 worked dynamically to carry out the impregnation.

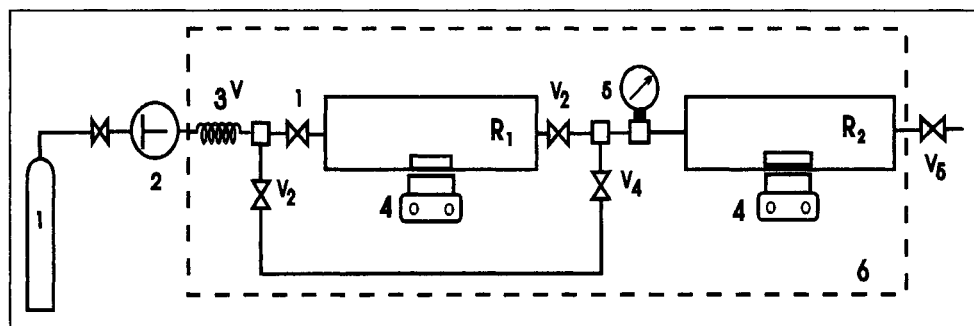


Figure 1. Pilot plant for dynamic impregnation

Two serial reactors R_1 and R_2 with an internal volume of 8.3 ml, are fed with CO_2 by an air driven pump (2) through a preheating coil (3). The content of the reactors is mixed by two stirring devices (4); a pressure gauge (5) and a water bath (6) allow a precise setting of the P and T experimental conditions. By-passing of R_1 can be achieved through an adequate combination of valves V_1 to V_4 . A decompression needle valve V_5 adjusted in combination with the pump, allows to set the levels of both flow rate and pressure within the apparatus.

2.2. Methods

Known amounts of solute and porous support are respectively introduced in R_1 and R_2 . All valves being opened, the apparatus is flushed with pure CO_2 and temperature is set at a fixed value. During the first step of the experiment, all valves are closed except V_1 . Carbon dioxide is fed into R_1 and the mixture CO_2 - α TA is stirred during half an hour to initiate the solubilization of the drug. Valve V_2 is then opened while V_3 and V_4 remain closed, thus locking the by-pass. The high pressure pump is switched on while the needle valve V_5 is adjusted in order to establish a fixed pressure. Periodically the flow rate of CO_2 is measured by bubbling the mixture flowing out, in an aqueous saturated solution of CO_2 . The analysis of the effluent, is done by periodical bubbling in ethanol. Two different procedures were tested to stop the run.

The first one consists in switching the pump and depressurizing the setup slowly. In the second method the reactor R_1 is by-passed by the flow of pure CO_2 which drains R_2 and eliminate the solute present in the supercritical phase before decompression. Each run last at least threefold the residence time τ .

2.3. Analyses

The α tocopherol acetate is analysed by UV absorption at 284nm. Within the range from 0 to 320mg of α TA/g of ethanol, the absorption of the solution varies linearly with concentration. The measurement of the solubility of α TA in supercritical CO_2 is directly done on the ethanolic solution. The determination of the quantity of α TA deposited on Aerosil is performed in the same way after successive extractions of the solute from the solid by ethanol.

3. RESULTS AND DISCUSSION

3.1 Preliminary experiments

As a comparison, in a first series of experiments, we carried out the impregnation of the Aerosil supports by means of ethanolic solutions of α TA according to the classical technique. A known amount of solid is brought into contact with the ethanolic solution for at least two hours. The mixture is then filtered, dried, and weighted. The α TA is then extracted from the Aerosil by ethanol and analysed. Though having the lowest specific area the Aerosil 972 support gives the best results, because of its organophilic properties, while, on the contrary, the Aerosil 200 is rather hydrophilic. Table 1 shows data obtained for Aerosil 972 (mean values of several runs).

Table 1.

Impregnation of Aerosil 972 by an ethanolic solution of α Tocopherol Acetate

Concentration of the ethanolic solution (mg α TA/g ethanol)	Amount of Aerosil (mg)	Amount of α TA deposited (mg)	R (mg α TA/mg solid)
1.53	8.3	0.084	0.01
62.5	500	200	0.4

Within the range of the study, the ratio of impregnation R varies linearly with the concentration of α TA in the ethanolic solution. It is then possible to calculate the equilibrium constant K defined by : $K = R/C$.

The value thus obtained is : $K = 6.4 \cdot 10^{-3}$

The study of the solubility carried out within the range of 150-300 bars for the pressure and 313-328°K for the temperature [2], showed that the solute displays the cross point phenomenon [3], since at low pressure an increase of the temperature can lead to a decrease of the solubility. Taking into account the fact that the highest solubility is obtained at 313 °K and 300 bars, all the experiments of impregnation were performed under these conditions.

3.2. Impregnation

For each experiment of this series, the analysis of the composition of the R_2 effluent vs. time yields a curve similar to Figure 2 which is relative to the particular case of a CO_2 flow rate of 0.184 ml/mn, under the experimental conditions of pressure and temperature.

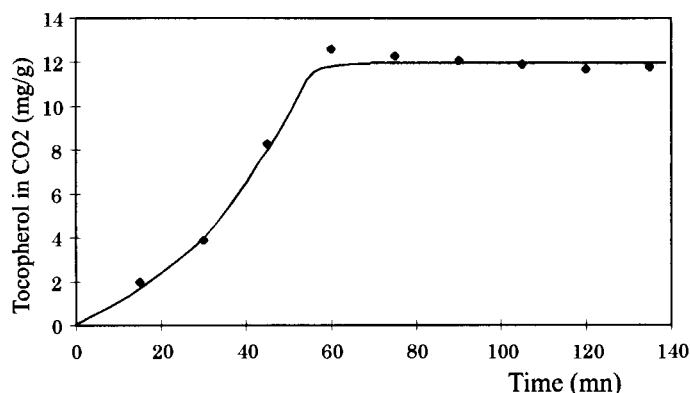


Figure 2. Weight concentration of α Tocopherol acetate in the supercritical phase leaving the setup vs. time

The general aspect of this curve with an inflexion point is typical of the dynamic behaviour of a second-order overdamped system in response to a step perturbation, i.e. Heaviside function [4]. A property of this curve is that the concentration reached at the plateau is equal to the concentration of the fluid entering R_2 . Data of these runs are summarized in table 2 and presented in Figures 3 and 4.

Table 2
Data of the dynamical experiments of impregnation

Run	Flow rate of supercritical CO_2 (ml/mn)	t (mn)	α TA Concentration in the effluent of R_2 (mg/g)	R %	Draining of R_2
1	.36	23.0	2.9	4.7	no
2	.17	49.0	6.9	21.4	no
3	.16	52.0	7.7	20.5	no
4	.18	45.0	11.3	7.5	yes
5	.125	66.0	22.5	12.8	yes
6	.087	95.0	19.8	24.2	yes

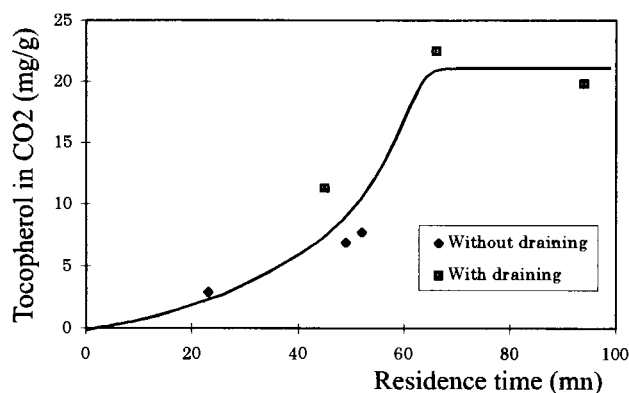


Figure 3. Concentration of solute in the supercritical phase vs. residence time

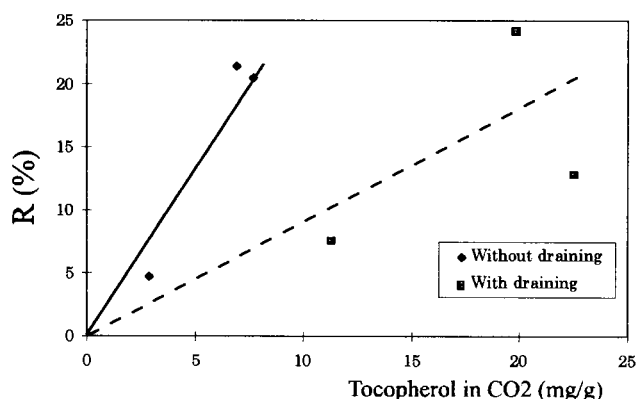


Figure 4. Ratio of impregnation vs. Composition of the supercritical phase

3.3. Discussion

Some dispersion of the data is observed due to :

- the physical properties of the Aerosil. This compound chosen because of its high porosity, is extremely pulverulent, and its density is very low (60kg.m^{-3}). As a consequence only a very low quantity of aerosil (0.5-0.6g) was involved in each run which led to a relative imprecision of the analyses.

- in the case of experiments 4,5 and 6, insufficient as well as excessive draining may result in erroneous data.

- Figure 3 shows that the concentration of the solute in the supercritical fluid increases with the residence time τ ; the kinetics of solubilization of the drug in R_1 is slow. Such a phenomenon is typical of slightly soluble products. A possible improvement could result from a more intensive stirring in R_1 .

- A plateau value (21 mg of α TA/g of CO_2) seems to be reached for a residence time roughly equal to 70 mn. Higher values of τ (i.e. lower flow rate of CO_2) will not improve this concentration which is the saturation concentration of the drug in CO_2 under 300 bars and 313 °K.

- Runs 1,2 and 3 which are carried out without draining the reactor R_2 at the end of the experiment, yield to values of R overestimated. This is due to a partial condensation of the α TA in R_2 during the decompression.

- Figure 4 shows a linear dependence of R with the concentration of the drug in the supercritical phase. Taking into account the only data of runs 4, 5 and 6, an equilibrium constant K can be estimated in spite of a relative imprecision. The value thus obtained is : $K = 8.2 \cdot 10^{-3}$. This equilibrium constant is slightly better than the one obtained for the ethanol ($6.4 \cdot 10^{-3}$). This means that for an equal concentration of α Tocopherol acetate in supercritical CO_2 or ethanol, the impregnation is quantitatively better in the former case.

- A comparison of the duration of the impregnation by the traditional method and by the procedure here proposed is favourable to the latter. This is related to mass transfer easier in a supercritical medium than in liquid phase because of higher diffusivity of the species. The advantage of the supercritical method is all the more marked since further steps of filtration and elimination of the solvent are necessary in the classical technique.

4. CONCLUSION

The first experiments reported here lead us to think that the impregnation of porous supports by drugs can be achieved by means of supercritical fluids. This one-step method yields a final product exempt from any residual trace of toxic solvent. The kinetics of the mass transfer is faster, besides the thermodynamics of the adsorption seems more favourable here. The main problem encountered up to now is the weak solubility of many active molecules in pure CO_2 , which induces a limitation of the percentage of deposited product. However, this difficulty can be overcome by the use of few amount of an entrainer. In particular, ethanol which does not show any toxicity, would greatly extend the range of active substances which could be used.

REFERENCES

1. P.J. Perreira, L. Ferreira and M. Nunes Da Ponte, Proceedings of the 3rd International Symposium on Supercritical Fluids, Strasbourg 1994, vol. 1, p. 89
2. F. Isnardon « Application des fluides supercritiques à l'élaboration des médicaments », D.E.A. Université d'Aix-Marseille, 1995.
3. M. A. Mc Hugh, V. J. Krukons, Supercritical fluid extraction : principes and practices., 2nd Ed., Butterworth Heineman Ed., 1994
4. W. L. Luyben, « Process modeling, simulation and control for chemical engineers », second edition, McGraw-Hill Publishing Company Ed., New York 1990.

ACKNOWLEDGEMENTS

Authors wish to carefully acknowledge LABORATOIRES LAPHAL (Allauch-France) for financial support.

Solubility of Technical Oils in Supercritical CO₂

N. Dahmen, H. Schmieder, J. Schön, H. Wilde

Forschungszentrum Karlsruhe, Institut für Technische Chemie CPV
P.O.B. 3640, D-76021 Karlsruhe, Germany

1. INTRODUCTION

For the design of a technical SFE process for deoiling and degreasing of metal parts and of grinding waste from the glass and metal working industry, different extraction parameters have to be studied [1,2]. One important parameter is the solubility of the metal working oils in the supercritical carbon dioxide acting as the extraction solvent. Roughly the used oils can be divided into mineral, synthetic or native oils, characterized by different composition of their hydrocarbon components and by their additives. The resulting phase behavior of these complex mixtures was measured applying the synthetic method at temperatures from 40 to 80°C and at pressures from 10 MPa up to 46 MPa. In order to measure phase equilibria of technical oils a commercial apparatus was optimized in regard to better reproducibility of the data.

2. EXPERIMENTAL

To perform the experiments a commercial phase equilibrium apparatus (Sitec PH 251-500K) schematically shown in Figure 1 was used. The cell, equipped with sapphire windows, has a variable volume of 12 to 25 cm³ controlled by a nitrogen-driven piston. The position of the piston was monitored by inductive measurement. Temperature in the cell was maintained using an electrical heating jacket. Starting an experiment, a known amount of oil was filled into the cell A. By adding CO₂ using a screw press C a homogeneous mixture at a given temperature was obtained. To speed up the equilibration a magnetic stirrer B was used. The amount of carbon dioxide was calculated from the cell volume, which was accurately known from the inductive measurement of the piston position, and the solvent density at given temperature and pressure. The composition of the mixture was controlled by taking a sample after the experiment. The oil was adsorbed on charcoal filters (Supelco EnviCarb) and was determined gravimetrically. CO₂ was sampled and weighed in a gas-flask. During sampling the pressure was kept constant by means of the piston. By repeating the experiments for different amounts of oil isotherms were obtained.

To determine the phase boundary pressure was lowered, until phase separation occurred, which could be observed visually by a camera system D. At first the pressure lowering was done by means of a hand-valve. To keep the pressure rates more constant the process was then automated using a computer controlled back pressure regulator E (Tescom ER2000). In comparison to pure substances, phase separation of mixtures is a slow process, because the components of different molecular mass or chemical nature separate successively from the mixture. To get an objective measure for the phase separation the clouding of the mixture was

monitored by a device containing a photocell F recording the transmission of the light in the cell. From the resulting clouding curve a distinct point was chosen characterizing the begin of the separation.

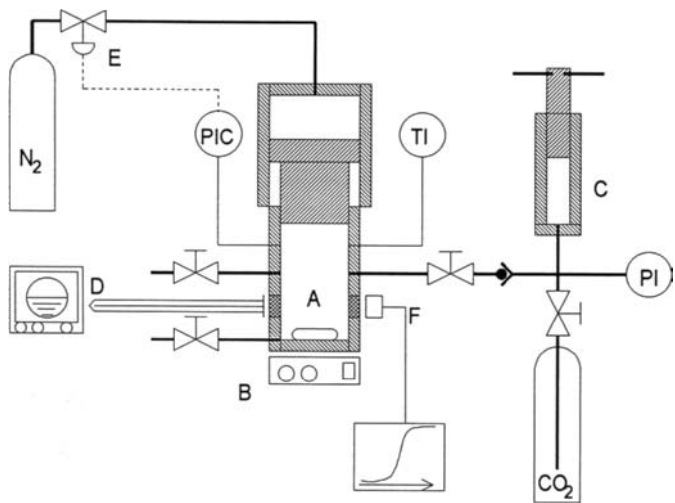


Figure 1. Phase equilibrium apparatus with variable volume cell A, magnetic stirrer B, screw press C, camera system D, pressure relief valve E and photocell F for transmission monitoring

Table 1
Characterization of the oils under test

Oil symbol	Composition	Viscosity ^a	Liquid density ^b
A	native oil with esters, additives	5.0	0.855
B	mineral oil, vegetable fatty oil, additives	15	0.880
C	synthetic esters and hydrocarbons, additives	6.5	0.817
D	mineral oil	—	—
E	hydrated mineral oil, additives	—	—
F	synthetic aliphatic hydrocarbons	3.4	0.775
G	mineral oil, additives	34	0.870

^a mm² s⁻¹ at 40°C; ^b g cm⁻³ at 20°C

3. RESULTS

In Figure 2 the clouding points of different oils are shown in dependence of pressure at 50°C. For simplicity the oils of different producers and applications are termed by the capitals A-F. The main characteristics of the oils are presented in Table 1. In addition to the different composition of their hydrocarbon content the oils contain a variety of additives, e.g. aging inhibitors, anticorrosives, detergents, pourpoint depressants, foam inhibitors and others.

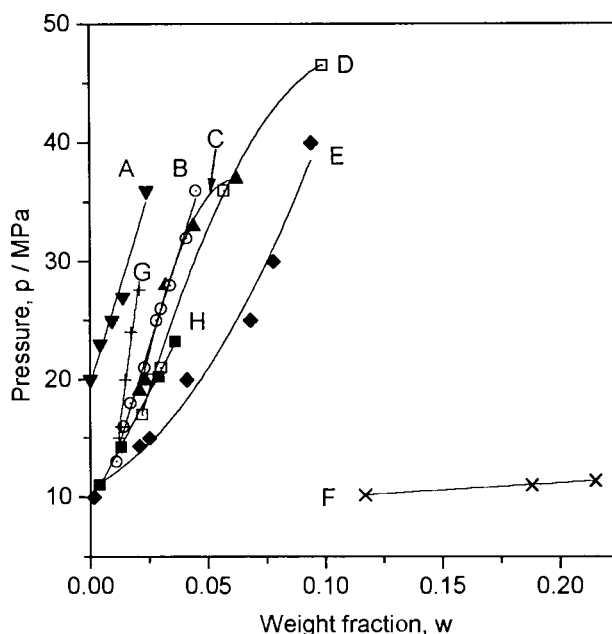


Figure 2. Solubility of metal working oils in supercritical CO₂ at 50°C; A-G: see Table 1; H: Squalane (C₃₀H₆₂) for comparison

Most of the oils (B-E) show a solubility behavior as it is typical for substances of low volatility [4]. But there are two oils showing markedly different solubility data. One of the exceptions is the native ester-based oil A with lower solubility in comparison to the mineral oils. This can be explained by the ester-oil components of larger molecular size in the native oil. How large solubility can differ is shown by the two synthetic oils C and F; C being an oil of synthetic hydrocarbons and esters, containing some additives, F being a colorless synthetic mixture of hydrocarbons comparable to pharmaceutical white oils. For comparison, solubility data of squalane [3] as an oil representative hydrocarbon (C₃₀H₆₂) are plotted in Figure 2 showing a behavior similar to the majority of the oils. An increase of pressure from 15 to 35 MPa leads to an increase of the solubility by a factor 2 to 4.

The influence of temperature on the solubility, e.g. of oil E, is shown in Figure 3. At a constant pressure the lower temperature of 50°C results in a higher solubility due to the larger solvent density of 0.785 g cm⁻³ in comparison to a density of only 0.595 g cm⁻³ at 80°C.

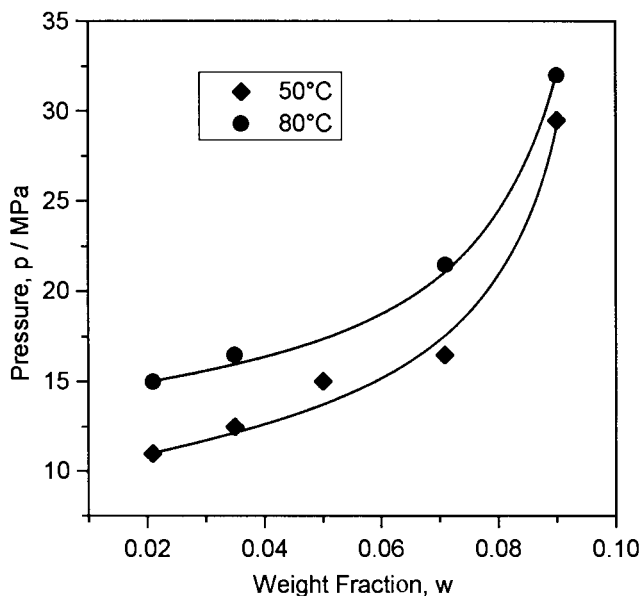


Figure 3. Temperature dependence of oil E at 50°C and 80°C

4. CONCLUSION

Although most of the oils tested in this study show a similar solubility behavior, significant differences can occur, depending on the composition of the oils with respect to their hydrocarbon fraction and the chemical nature and the amount of additives. With the specifications given by the producers like density and viscosity at standard conditions (see Table 1) no correlation could be found to the experimental data. Further information about the composition is hardly available and an exact analysis is not only undesired but also nearly impossible. This lack of information also makes phase equilibrium calculations to be not very useful for the correlation or prediction of these solubility data. In every single case the solubility has to be determined experimentally.

REFERENCES

1. J. Schön, N. Dahmen, H. Schmieder and K. Ebert, proceedings of the 9th Symposium on Separation Science and Technology for Energy Applications, Gatlinburg, October 22-26, 1995, to be published in Sep. Sci. Tech.
2. J. Schön, N. Dahmen, H. Schmieder and K. Ebert, ACS Symposium Series of the 1996 ACS Spring National Meeting, New Orleans, March 24-28, 1996
3. W.J. Schmitt and R.C. Reid, Chem. Eng. Comm., 65 (1988) 155
4. K.D. Bartle, A.A. Clifford, S.A. Jafar and G.F. Shilstone, J. Phys. Chem. Ref. Data, 20 (1991) 713-756

Separation of Non-Volatile Components by Expansion with High-Pressure Gases

B. Bungert^a, R. Tipl^b, G. Sadowski^a, W. Arlt^a

^aInstitut für Verfahrenstechnik, Fachgebiet Thermodynamik,
Technische Universität Berlin, TK 7, D-10623 Berlin, Germany

^bInstitut für thermische Verfahrenstechnik und Umwelttechnik,
Technische Universität Graz, A-8010 Graz

For the design of new, innovative processes to separate low-volatile components such as drugs or polymers with supercritical fluids, experimental data are needed. We designed and built a new apparatus capable of investigating phase equilibria in the occurring complex systems up to 200 bar and 250°C. Phase transitions are determined optically. Samples of the coexisting phases even at high concentration and viscosity are taken. Solid particles can be collected.

1. INTRODUCTION

In the last ten years new, innovative processes utilizing supercritical fluids have received increasing attention. Here, we focus on two examples: the *Gas AntiSolvent* process (GAS) [1], also known as PCA (*Precipitation with a Compressed fluid Antisolvent*) [2], and *Supercritical Antisolvent induced phase Separation* (SAS)[3, 4].

In GAS, a compressed gas acting as antisolvent is dissolved in the solution of a non-volatile component with gas contents in the order of equimolar mixtures. This causes a volumetric „expansion“ and hence a remarkable reduction in solvent power. Consequently, precipitation or crystallisation of the solute occurs, leading to ultrafine particles and fibers in the micrometer range. Furthermore, the precipitates e.g. pharmaceutical products are purified while impurities remain in solution.

In SAS, a compressed gas is added to a polymer solution. The upper critical solution temperature (UCST) and lower critical solution temperature (LCST) of that solution are shifted to higher and lower temperatures respectively until they finally merge to one region of immiscibility over the whole temperature range. This process can be used for solvent recovery in solution polymerisation processes as well as for molecular weight fractionation of polymers.

For the understanding of these processes and for the design and evaluation of new separation processes, it is crucial to get a better insight in the underlying principles and phase equilibria. Especially in the investigation of complex systems such as polydisperse polymers with additives or drugs with impurities, it is necessary to get information on the composition of the coexisting phases. Up to now, there is almost no such information available.

Therefore, we designed and built a new apparatus, capable of investigating liquid-liquid-vapor equilibria (LLVE) and solid-liquid-vapor equilibria (SLVE) of complex systems with non-volatile components such as drugs or polymers.

2. EQUIPMENT AND EXPERIMENTAL PROCEDURE

Main part of the experimental setup is a variable-volume autoclave of 1000ml designed for pressures up to 200 bar and temperatures up to 250°C (Figure 1). It is equipped with a special closing mechanism at the bottom that allows for very fast opening. A filter consisting of glass-fiber filter paper fixed between two steel sheets is mounted to the cylinder-like closure and sealed at the outer diameter with a teflon seal. Windows allow for visual observation of the whole inner diameter. The volume is varied with a metal bellows between 840 ml and 880 ml. Samples can be drawn from the phases via short stainless steel capillary tubes. Mixing is achieved by rocking the autoclave with variable angles from the horizontal position.

Autoclave and sampling lines are electrically heated. The temperature is to an accuracy of $\pm 0.1\text{K}$. Pressure is measured with a pressure transducer) that is connected to the top by means of a diaphragm-type chemical seal to $\pm 0.3\text{bar}$. It is calibrated for different temperatures.

For GAS experiments the autoclave is filled with the non-volatile component and closed. Then, solvent is drawn into the evacuated vessel. With a pneumatically driven compressor a thermostated buffer vessel is filled with gas. From there it enters the high-pressure cell through the filter or the gas inlet at the top. Thus, the amount of gas can be determined by pVT measurement. Very fast pressure built-up rates can be achieved. After precipitation, the autoclave is placed in vertical position. The solution is then filtered and drained through the bottom valve. During that process the pressure is held constant by adding gas from the top. After the filtration step the solids can be washed with additional gas to remove any residual solvent.

For SAS experiments, the autoclave is filled in a similar manner. Steel balls are added to achieve better mixing. When the desired temperature is reached, the pressure is adjusted by either adding some more solvent with a syringe pump or by pumping hydraulic fluid into the bellows with a second syringe pump. Once a homogeneous one-phase solution is established, the autoclave is moved to the vertical position. Samples are taken from the bottom and the top to confirm proper mixing and to confirm the concentration. Then, the pressure is lowered until the solution becomes cloudy. Upon further lowering the pressure, samples are taken from the coexisting phases after allowing sufficient time for phase separation.

In both experiments small amounts of samples are displaced into stainless steel sample bombs while the pressure is kept constant by adding more hydraulic fluid into the metal bellows. The sampling lines have an inner diameter of 1mm and a length of 100mm. Therefore, it is possible to handle highly viscous samples without having too much dead volume. The samples are weighed to $\pm 0.005\text{g}$. After cooling the sample bombs the gas content is determined by PvT measurement. They are then flushed with additional solvent. Solids concentration is determined by HPLC, vibrating-tube density measurement, refractive index measurement or by stripping the solvent in a rotary evaporator under vacuum and weighing the

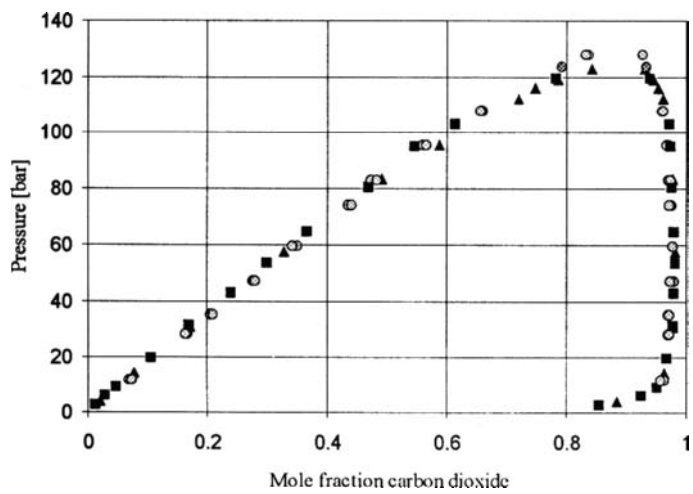


Figure 2: VLE toluene-CO₂ (Triangles: Ng and Robinson, Squares: Morris and Donohue, open circles: this work)

In Figure 3 the equilibrium solubility of naphthalene in toluene „expanded“ with carbon dioxide at 25°C is shown. There is a considerable deviation to the data of Dixon et al [2]. In both works, it was made sure that excess solids were present. Proper filtration of the naphthalene particles in situ prior to sampling is the crucial step of the experiment. Therefore, small amounts of particles leaking through the filter can cause an error in concentration determination. The samples in this work were analysed for naphthalene content by density measurement and additionally by refractive index measurement. The reproducibility was better than 0.8 mole percent.

Figure 3: SLVE naphthalene-toluene-CO₂; literature data vs. data from this work

In a third set of experiments we compared cloud-point data of the polystyrene-cyclohexane-carbon dioxide system (9.6 wt% polystyrene, 9.6 wt% CO₂) to the data of de Loos (9.4 wt% polystyrene, 5.0 wt% and 9.1 wt% polystyrene, 10.0 wt% CO₂) [7]. This author used the identical polymer sample. The isopleths in Figure show an almost linear increase in pressure as the temperature is risen. Interpolation of the cloud-point temperature with carbon dioxide content and polystyrene content yields excellent agreement of the data.

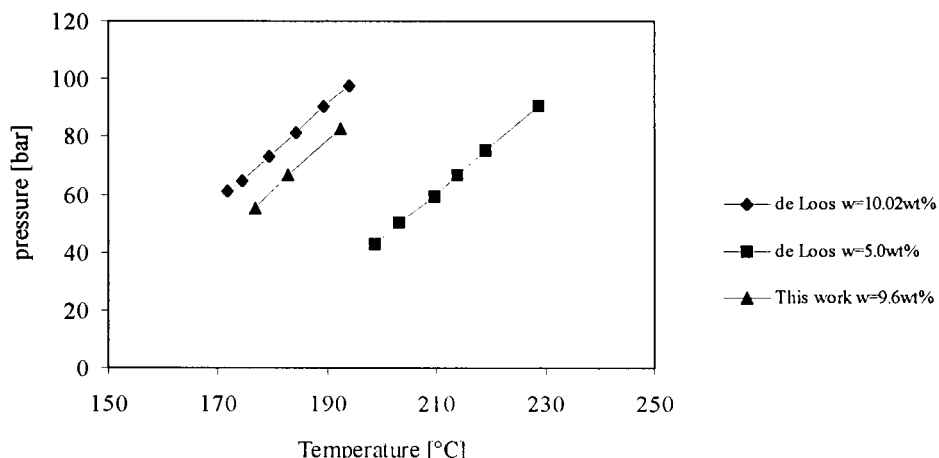


Figure 4: LLE polystyrene-cyclohexane-CO₂, literature data vs. data from this work (CO₂ content as indicated)

5. CONCLUSIONS

A new, versatile apparatus for the determination of reliable SLV and LLE phase-equilibrium data has been designed and tested. In a first project this equipment will be used for the separation of polymers by molecular weight with the SAS process. We will test the concept of using pressure, temperature and gas content to fine-tune the selectivity of that process.

6. ACKNOWLEDGMENTS

This work was supported by the Deutsche Forschungsgemeinschaft under grant Ar 236/2-1. R. Tippl acknowledges funding by the ERASMUS student exchange program. The authors want to thank Lothar Kroll and Klaus Gatzmann for machining the equipment and Oliver Kastner for extensive support. The polystyrene was kindly donated by BASF AG, Ludwigshafen.

REFERENCES

1. Gallagher P.M., Coffey M.P., Krukonis V.J., Klasutis N., Gas Antisolvent Recrystallisation: New Process to Recrystallize Compounds Insoluble in Supercritical Fluids, ACS Symp. Ser. 406, 1989, 335-54
2. Dixon D.J., Johnston K.P., Molecular Thermodynamics of Solubilities in Gas Antisolvent Crystallisation, AIChE J. 1991, 37(19), 1441-49
3. Seckner A.J., McClellan A.K., McHugh M.A., High-Pressure Solution Behavior of the Polystyrene-Toluene-Ethane System AIChE J. 1988, 34(1), 9-16
4. Chen C.-K., Duran M.A., Radosz M., Supercritical Antisolvent Fractionation of Polyethylene Simulated with Multistage Algorithm and SAFT Equation of State: Staging Leads to High Selectivity Enhancements for Light Fractions, Ind. Eng. Chem. Res. 1994, 33(2), 306-10
5. Ng H.-J., Robinson D.B., Equilibrium Phase Properties of the Toluene-Carbon Dioxide System, J. Chem. Eng. Data 23, 1978, 23(4), 325-27
6. Morris W.O., Donohue M.D., Vapor-Liquid Equilibria in Mixtures Containing Carbon Dioxide, Toluene, and 1-Methylnaphthalene, J. Chem. Eng. Data 1985, 30(3), 259-63
7. de Loos T.W., personal communication, Delft 1994

Mathematical Models for Supercritical Extraction of Oregano "*Origanum virens* L."

M. Mercedes Esquivel¹, Cláudia L. de Sousa, M. Albertina Ribeiro, M. Gabriela
Bernardo-Gil

Dep. Engenharia Química, IST, Av. Rovisco Pais, 1096 Lisboa Codex, PORTUGAL.

KEYWORDS:

Origanum virens L., Supercritical Extraction, Fixed Bed, Mass Transfer.

1. ABSTRACT

The extraction of essential oil from oregano-*Origanum virens* L.- using liquid carbon dioxide (7 MPa and 298 K) and supercritical carbon dioxide (10 and 15 MPa and 313 K) was investigated. Experimental results were obtained in a laboratory scale plant equipped with a 100 mL tubular extractor.

During the extraction an unsteady process prevails. The present paper presents an unsteady state mathematical model for a fixed bed extractor (model I). The overall mass transfer coefficients were calculated by matching the calculated and experimental values of oil loading in CO₂. The results are compared with those obtained by the model developed by Catchpole *et al.*, 1994 (model II). Good agreement between both models results and our experimental measurements were obtained, although the model II allows the best fit over the entire extraction curve.

2. INTRODUCTION

Plants represent a very important role in human nutrition, due to the large quantities of proteins, carbon hydrates, lipids, vitamins, antioxidants and mineral salts that its can supply. Sometimes the nutritional aspect can be associated with the flavour and fragrance of the extracts producing a high value products. In recent years one can observe an increase in research for natural sources, in particular from plant matrices, of additives with application in the food, cosmetic and pharmaceutical industries.

¹ Author to whom correspondence must be adressed.

Oregano *Origanum virens* L. is an perennial herb with 40-70 cm high and very aromatic. This plant grows in open and dry countries, at altitudes lower than 500-700 m. The major components of essential oil from *Origanum virens* L. are terpineol, α -pinene, camphor, thymol, carvacrol and cineole. Compounds such as alcohols and dipentene are also present.

Extraction of essential oils from plants using supercritical fluids is a very interesting application of this technology since it offers the possibility to improve the extraction yields and/or to obtain new flavours or aromas by the control of pressure and temperature of extraction.

The solute is disseminated in a solid matrix in the most of the supercritical extractions of natural products. If the interactions between solute and solid matrix are not important, the mass transfer models can be developed from the equations of microscope balances to a volume element of the extractor. If the mass transfer resistance is in its solid phases, the mathematical models must consider the solute transport within the solid particles or the surface phenomena.

Some attempts are being made to model the supercritical extraction of natural products. Most of the models proposed consider: the rate of extraction determined by the rate of mass transfer out of the matrix; the solute is present in small amounts in the matrix, and during extraction the concentration of the solute in the supercritical fluid is well below the solubility limit (Brunner, 1984; Bartle *et al*, 1990; Reverchon *et al*, 1993 and Catchpole *et al*, 1994).

The present paper presents an unsteady state mathematical model for a fixed bed extractor (model I). This model only takes into account the external mass transfer resistance. The overall mass transfer coefficients were calculated by matching the calculated and experimental values of extract loading in CO₂. The results are compared with those obtained by the model developed by Catchpole *et al* (1994) for the extraction of oils from plant matrices (model II). This model contains three parameters and takes into account both internal and external mass transfer resistances.

3. THEORY

If the bed is made of non porous particles and if axial dispersion in the bed is negligible, the mass balance for the oil in solvent phase is given by:

$$\varepsilon \frac{\partial Y}{\partial t} = -U \frac{\partial Y}{\partial l} + Ka(Y_i - Y) \quad (1)$$

and for the solid phase:

$$\frac{dX}{dt} = -Ka(Y_i - Y) \frac{\rho}{\rho_{ap}} \quad (2)$$

with the following boundary conditions:

$$t = 0 \quad 0 \leq l \leq H \quad X = X_0 \quad (3)$$

$$\begin{array}{lll}
 t \geq 0 & l = 0 & Y = 0 \\
 t \geq 0 & l = \infty & Y = Y_i
 \end{array} \quad (4)$$

Model I is based on the assumptions that the fluid flow rate, temperature, pressure, solvent density and bed properties are constant during extraction.

The mass balance equations can only be solved if the relation between Y_i and X are known. We assumed a linear relation for the equilibrium curve. This relation is given by the equation $Y_i = K_e X$, where K_e is a equilibrium constant experimentally determined.

To solve the mass balance equations, we considered the extractor being divided in N layers, being obtained a system discretisation in relation to the bed height. The generic layer n is described by the following two equations:

$$\frac{dY_n}{dt} = -\frac{U}{\varepsilon} \frac{(Y_n - Y_{n-1})}{(H/N)} + \frac{Ka}{\varepsilon} (Y_i - Y_n) \quad (6)$$

$$\frac{dX_n}{dt} = -Ka (Y_i - Y_n) \frac{\rho}{\rho_{ap}} \quad (7)$$

in which Y_n and Y_{n-1} are the oil loading in the solvent at the exit and at the entrance of the layer n , X_n is the oil loading in its layer bed ($n = 1$ to N).

The equations (6) and (7) are integrated in order to time for each layer using the equation $Y_i = K_e X$ as an auxiliary. The first layer corresponds to the fresh entrance of the solvent where $Y_0 = 0$ whatever the value of t and $X = X_0$ for $t = 0$. The layer N corresponds to the extractor exit. In each layer an oil enrichment in the solvent fluid phase occurs.

Rapid convergence in the integration of equations (6) and (7) was obtained using a computer program. We used the LSODA routine for solving the differential equations from ODEPACK Library (Aiken, 1985).

4. EQUIPMENT

The schematic diagram of the supercritical apparatus used in this work is shown in Figure 1. The carbon dioxide from the bottle at nearly 6 MPa passes through a cold bath at near 273 K (E1) and is fed to a Air Driven Liquid Pump (Haskel Inc., USA) that presses it to the desired pressure. Liquefied CO₂ passes through a heat exchanger (E2) being preheated to the temperature of extraction, prior to being fed to a 100 mL tubular extractor in stainless steel which holds the vegetal material. The bed of solids is 8.5×10^{-2} m high and as an internal diameter of 2.13×10^{-2} m. The extractor was thermostated in a water bath and the temperature controlled with a digital controller (Ero Electronic, Italy) with an accuracy of ± 0.2 %. The pressure at the exit of the extractor was measured with a differential manometer (Skalenwert 2, Germain) with an accuracy of 0.2 MPa.

The needle valve V3 controls the exit flow of the solvent. From V1 to V3 the pressure is reduced at several levels up to atmospheric pressure, recovering the essential oil in the first collector (C1) at about 8 MPa and 313 K. Water and some volatile components are

segregated in the second collector (C2) at a temperature of 203 K and at atmospheric pressure. The amount of essential oil deposited in the first collector was measured by weighing. The volume of carbon dioxide delivered was measured by a diaphragm gas meter SAMGAS (DGM) with an accuracy of ± 0.005 L. Pressure and temperature conditions were measured at the end of assembly. After each sampling, the pipes around the extractor were washed with acetone.

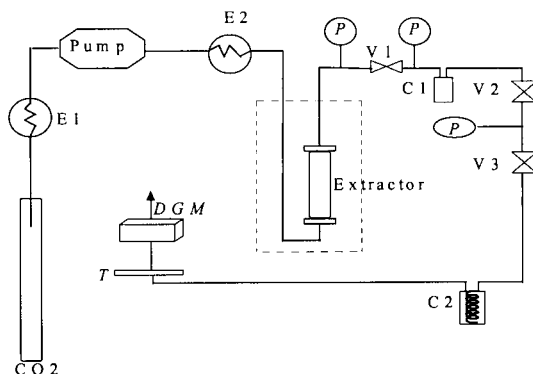


Figure 1. Schematic diagram of the supercritical apparatus.

5. RESULTS AND DISCUSSION

Oregano leaves just after harvest and dried during two months at room temperature were used in tests. Figure 2 shows the yield percentage obtained in extraction tests on *Origanum virens* L. leaves as functions of extraction time. The yield percentage were calculated by dividing the mass of extract collected in the first collector (C1) by the initial bed mass (6 g). The extraction temperature in the tests shown was 313 K for pressures of 10 and 15 MPa and 298 K for 7 MPa and the superficial velocity was 0.06×10^{-2} m/s.

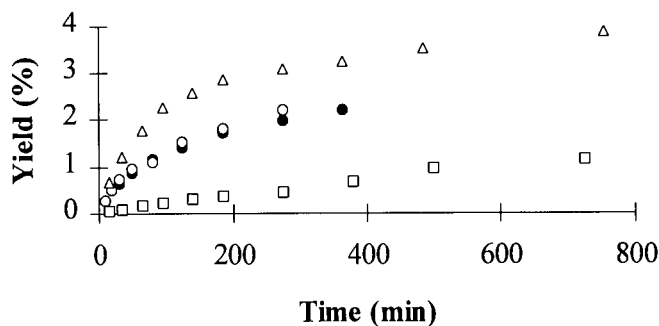


Figure 2: Extraction of *Origanum virens* L. leaves. □ - Dry oregano, P = 7 MPa, T = 298 K; ● - Oregano just collected, P = 10 MPa, T = 313 K; ○ - Dry oregano, P = 10 MPa, T = 313 K; Δ - Dry oregano, P = 15 MPa, T = 313 K.

The extraction yield rises with pressure at 313 K due to the increasing of the supercritical CO₂ density as the pressure increases at constant temperature, increasing the solvent power of carbon dioxide. The yield of extraction with liquid CO₂ was lower than with supercritical CO₂. No differences in extractions results were observed with the two types of oregano used.

Models were applied to the results obtained in the first collector, since the extract obtained in the second collector was made up of water and some volatiles that can not be separated. A Hewlett Packard 5890 Series II fitted with a flame ionisation detector was used to analyse the extract obtained in the first collector. A capillary column HP5 (cross linked phenyl silicone gum phase) was used. The separation was carried out with nitrogen as carrier gas using a detector at 523 K. Terpineol was the major component of the precipitated matter ($\approx 65\%$ w/w).

To obtain the parameters presented in table I we considered that the particle diameter is the weight mean diameter calculated by sieving, the extract was considered as terpineol, the diffusion coefficient was obtained by the equation proposed by Tan *et al* (1988) and the overall transfer coefficient for model II is related to the diffusivity and to the external mass transfer coefficient by the relationship proposed by Catchpole *et al* (1990).

Table 1

Parameters inserted in models and the best fit values obtained from the two models for extractions of oregano

Vegetal Material			Oregano	
Particle diameter $\times 10^3$ (m)			1.1	
$k_f a$ 15 MPa $\times 10^5$ (m ² s ⁻¹)			2.3	
$k_f a$ 10 MPa $\times 10^5$ (m ² s ⁻¹)			4.2	
$k_f a$ 7 MPa $\times 10^5$ (m ² s ⁻¹)			2.8	
Mass flow rate (kg h ⁻¹)			0.5	
Predicted D_{12} at 15 MPa $\times 10^9$ (m ² s ⁻¹)			8.1	
Predicted D_{12} at 10 MPa $\times 10^9$ (m ² s ⁻¹)			12.7	
Predicted D_{12} at 7 MPa $\times 10^9$ (m ² s ⁻¹)			7.2	
P (MPa)/ T (K)	Model I		Model II	
	Best fit $Ka \times 10^5$ (s ⁻¹)	Mean Absolute Error of Fit (%)	Best fit $De \times 10^{12}$ (m ² s ⁻¹)	Mean Absolute Error of Fit (%)
7 / 298	0.2	3.4	0.3	6.3
10 / 313	1.3	13.3	4.0	3.9
15 / 313	4.0	10.2	5.4	9.9

Model results are shown by a continuous line for model I and by a dashed line for model II in figure 3.

The model I is very simple, and it is not very sensitive to the physical properties of the bed, but the values of the overall mass transfer coefficients optimised are strongly dependent from the equilibrium relation assumed and it only is able to describe the initial part of the extraction. Ke was determined by mass balance assuming a uniform distribution in solid bed. Ke values of 0.5, 0.2, and 0.6 were obtained for 7, 10 and 15 MPa. Assuming $a = 3000$ m²m⁻³, the mass transfer coefficients calculated with model I are of some orders of magnitude lower than those for external mass transfer coefficients. This type of models have being applied with success to the extraction of edible oils from seeds where the solute is in a

free form, but seems to fail to describe processes where the intra-particle diffusion is the controlling stage.

A light increase of the effective diffusivity De (model II) with pressure was observed but this variation must be analysed carefully with more experimental data, since this variation is not foreseen. The effective diffusivity must have the same variation as the diffusion coefficient if the particle porosity remain constant during the extraction process. The values obtained at 7 MPa and 313 K are of the same order of magnitude to those obtained for herbaceous matrices [$(1.5 \text{ to } 2.8) \times 10^{-13} \text{ m}^2 \text{ s}^{-1}$] by Reverchon *et al* (1993).

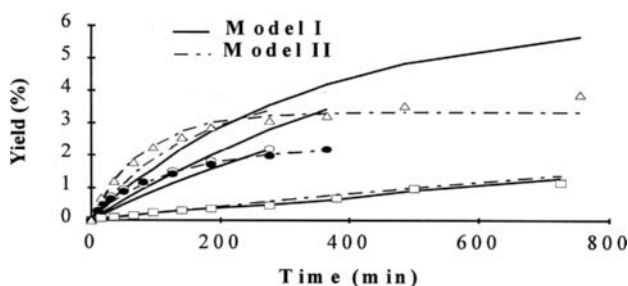


Figure 3: Experimental and predicted results for the extraction of *Origanum virens* L. leaves.

□ - Dry oregano, P = 7 MPa, T = 298 K; ● - Oregano just collected P = 10 MPa, T = 313 K;
○ - Dry oregano, P = 10 MPa, T = 313 K; △ - Dry oregano, P = 15 MPa, T = 313 K.

NOMENCLATURE

a	- Interfacial area	($\text{m}^2 \text{ m}^{-3}$)
H	- Bed height	(m)
K	- Mass transfer coefficient	(m s^{-1})
t	- Time	(s)
	- Superficial velocity	(m s^{-1})
X	- Oil loading in bed	(kg oil/kg solid)
Y	- Oil loading in the solvent	(kg oil/kg solvent)
Y_i	- Oil loading in equilibrium	(kg oil/kg solvent)
ϵ	- Bed voidage	
ρ, ρ_{ap}	- Solvent and apparent bed densities	(kg m^{-3})

REFERENCES

- Aiken, R. C., *Stiff Computation*, (1985) Oxford University Press, 169.
 Bartle, K. D.; Clifford, A. A.; Howthorne, S. B.; Langenfeld, J. J.; Miller, D. J.; Robinson, R., *J. Super. Fluids*, 3 (1990) 143.
 Brunner, G., *Ber. Bunsenges. Phys. Chem.* 88 (1984) 887.
 Catchpole, O. J.; Andrews, E. W.; Toikka, G. N.; Wilkinson, G. T., 3thrd Int. Symp. on Supercritical Fluids, France, (1994) 47.
 Catchpole, O.; Simões, P.; King, M. B.; Bott, T. R., *Proc. 2nd Int. Symp. on High Pressure Chemical Engineering*, Erlangen, Germany, (1990) 153.
 Reverchon, E.; Donsi, G.; Osséo, L. S., *Ind. Eng. chem. Res.*, 32 (1993) 2721.
 Tan, C. S.; Liang, S-K; Liou, D-C, *Ind. Eng. Chem.*, 27 (1988) 988.

Searching Prodrug Substances from Natural Resources by Supercritical Carbon Dioxide Extraction and Bioassay Tests

Y. H. Choi^a, E. J. Park, J. S. Lee, J. Kim^a, M. J. Noh^b, E. S. Choi^b and K. P. Yoo^b

^aCollege of Pharmacy, Seoul National University, Seoul 151-742, Korea*

^bDept. of Chem. Eng., Sogang University, C.P.O. Box 1142, Seoul, Korea*

Supercritical fluid extraction(SFE) combined with five types of bioassay tests is extensively applied to explore some bioactive substances from thirty types of natural resources available in Korean peninsula. To evaluate comparatively the economic viability of the SFE, organic liquid solvent extraction(LSE) with *n*-hexane, chloroform and methanol was also performed. To characterize the extracts, GC and HPLC are employed. Also, the column chromatography is used to isolate some target compounds from the total extracts. For all the samples, the optimum SFE condition for each sample which gives maximum yield and cytotoxicity were discussed.

1. INTRODUCTION

In the Orient, numerous natural products have long been used in folk medicine. Also, in recent years some pharmaceutical industries and universities in Korea are placing their efforts on the quantification of cytotoxic phytochemicals from the natural resources. As a part of those efforts, the present authors are involved on the two-fold critical evaluations of the possible implementation of the supercritical fluid extraction(SFE) to obtain extracts from the natural resources: one is the establishment of the optimum SFE condition for each sample resource which gives maximum extraction yield and cytotoxicity, and the other is the high-purity isolation of some specific compounds from the SFE total extracts.

To figure out comparatively whether the SFE is advantageous or not, the traditional Soxhlet organic liquid solvent extraction(LSE) with *n*-hexane, chloroform and methanol was carried out. Also, simple but reliable *in vitro* bioactivity tests were established and applied to the extracts. The bioassays

* This work was supported by the Korea Science and Engineering Foundation and SKI, Korea

included cytotoxicity, bleb forming, DNA binding, oxygen free radical scavenger and Xanthine oxidase inhibitor tests.

2. SFE BY CO₂ AND LIQUID SOLVENT EXTRACTION

Two types of SFE equipment are used. One is a large scale flow type apparatus(1.5l) which is used to obtain the total extracts. The SFE condition in this equipment was 50 °C and 30 MPa. The other is a microscale extractor(60 ml) which is used to establish the optimal SFE conditions. In the SFE, carbon dioxide is mainly used and the experiment is performed in the ranges of 35-55 °C and 10-30 MPa.

In the LSE, a glass-type equipment is used and the extractions with chloroform, methanol and *n*-hexane are carried out. The LSE is usually takes about 12 hours with 5 g of each sample. Since we discussed elsewhere the experimental procedures of both the SFE and the LSE, we omit here further descriptions[1, 2].

3. BIOACTIVITY TESTS

The bioactivity tests are carried out to all the sample extracts based on the systematized methods described elsewhere[3] and, thus we omit here further description of each analytical procedure. Employed bioassays are included cytotoxicity, bleb forming, DNA binding, Oxygen free radical scavenger and Xanthine oxidase inhibitor tests.

4. CHROMATOGRAPHIC ANALYSIS

For the analysis for extraction yield of each target compound, any one of GC, HPLC or column-chromatography was used. For the case of GC, the oven temperature was 260 °C, injector temperature was 275 °C and detector(FID) temperature was 290 °C. For the case of HPLC the mobile phase was acetonitrile and water (40:60) and the UV wavelength was 254 nm[4].

5. RESULTS AND DISCUSSION

5.1. Bioactivity tests to the total extracts

For thirty natural resources, total extracts are obtained by both the SFE at 45°C and 30 MPa and the LSE by *n*-hexane, chloroform and methanol, respectively. For all the extracts, five types of bioassays were performed and the qualitative results are summarized in Table 1. For the case of the cytotoxicity assay, the extracts of *Angelica gigantis Radix*, *Aralia Cordata*, *Bupleurm falcatum*, *Acanthopanax Cortex* and *Spirodelae Herba* by the SFE showed much higher

cytotoxicity (each ED₅₀ was lower than 30 µg/ml) than those by the LSE as briefly shown in Table 1. Also, for the cases of bleb forming and DNA binding assay, the SFE extracts of *Ginkgo* leave, *Polygalae Radix*, *Ephedra Herba* and *Plantaginis* semen were more active than those by the LSE.

In Xanthine oxidase inhibition assay, the SFE extract show almost no bioactivity as the case of the LSE. In the oxygen free radical scavenger assay, the SFE extracts of *Schizandrae fructus* and *Moutan Cortex Radicis* were more active than the case of the LSE.

Table 1

Bioassay results for the extracts obtained from the natural resources by the SFE†

Sample	<i>Lycium chinense</i> ▲◆	<i>Schizandra chinensis</i> ▲	<i>Citrus unshiu</i> ▲	<i>Angelica gigas</i> ●	<i>Cornus officinalis</i> ◆	<i>Cnidium officinale</i>
Sample	<i>Ginkgo biloba</i> ■●◆	<i>Aralia cordata</i> ●	<i>Evodia officinalis</i>	<i>Crataegus pinnatifida</i>	<i>Paeonia lactiflora</i>	<i>Leonurus sibiricus</i> ■
Sample	<i>Sophora japonica</i> ■	<i>Artemisia capillaris</i> ◆	<i>Plantago asiatica</i> ■	<i>Ephedra sinica</i> ■	<i>Aconitum carmichaeli</i>	<i>Scolopendra subspinipes</i> ■
Sample	<i>Paeonia suffruticosa</i>	<i>Coptis japonica</i> ◆	<i>Pueraria thunbergiana</i>	<i>Polygalae tenuifolia</i> ■◆	<i>Eucommia ulmoides</i> ◆	<i>Astragalus membranaceus</i>
Sample	<i>Bupleurm falcatum</i> ◆	<i>Artium lappa</i>	<i>Acanthopanax sessiliflorum</i> ●	<i>Morus alba</i>	<i>Epimedium koreanum</i> ◆	<i>Spirodela polyrhiza</i> ●◆

†: For the bioassay tests given below, the extract obtained by the SFE shows significant bioactivities, respectively.

● : Cytotoxicity assay(P388), ■ : DNA binding assay, ● : Bleb forming assay,
▲ : Oxygen radical scavenger, ◆ : Xanthine oxidase inhibition assay

5.2. Establishing optimum SFE conditions

Based on the bioassay tests, SFE with the microscale equipment was carried out for all the sample resources in the ranges of 35-55°C and 10-30 MPa. In establishing the optimum condition for each sample, emphasis was given to a condition which guarantees the maximum cytotoxicity. It was found that there exist a unique optimum condition for each sample. In Figure 1, the variations of cytotoxicity of the *Aralia Cordata* extracts with respect to the extraction methods are shown illustratively. The cytotoxicity is increasing with decreasing pressure for the case of SFE. In general SFE extracts show higher cytotoxicity than those by the LSE. The other cases, for example, the optimum SFE conditions which give maximum cytotoxicity of *Angelica gigantis Radix* and *Bupleurm falcatum* were 55 °C, 30 MPa and 45 °C, 10 MPa, respectively.

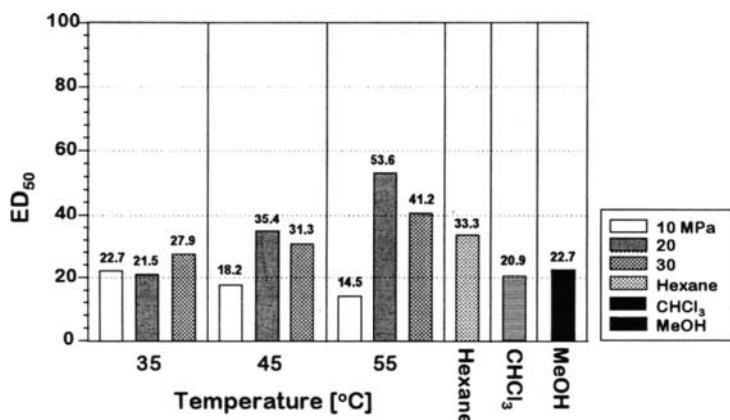


Figure 1. Variations of bioactivities for the extract of *Aralia Cordata* by the SFE and LSE

5.3. Selective Isolation of Target Compounds

To obtain the high-pure compounds from the candidate total extracts, column chromatographic separation is performed for some illustrative total extracts. For example, *squalene* and *podophyllotoxin* with high purity are isolated from the related extracts. Upon comparison with the LSE, we found that *squalene* can be easily obtained from the SFE extract than the case of LSE. Although we are not shown here similar interesting results are obtained for other substances. For example, high-purity *podophyllotoxin* derivatives, which has been known for antitumor activity[4] can be obtained easily from the SFE extract of *Podophyllum peltatum*.

In summary, we examined extensively the SFE for the alternative replacement of the traditional LSE in pharmaceutical industry. We found that for many sample resources, the SFE is found to be advantageous over the LSE. Furthermore, by cooperating column chromatography with several types of bioassay tests, we demonstrated a sufficient economic feasibility of the implementation of the SFE for the selective separation of the total extracts and subsequently the high-purity prodrug substances from the natural medicinal products.

REFERENCES

1. Y. H. Choi, J. Kim, M. J. Noh, E. M. Park and K. P. Yoo, KJChE, in press, April, (1996).
2. M. J. Noh, E. S. Choi, K. P. Yoo, Y. H. Choi, Y. H. Yeo, J. S. Lee, E. J. Park, J. Kim, H. K. Park and K. H. Kim, Chem. Ind. and Tech. in press, April, (1996).
3. K. Hostettmann (ed.), Assays for Bioactivity, Academic Press, New York, 1991.
4. E. Bedows and G. M. Hatfield, J. Nat. Prod., 45 (1982) 725.

Extraction of brominated flame retardents with supercritical CO₂

G.Bunte*, Th. Härdle, H. Krause, E. Marioth

Fraunhofer-Institut für Chemische Technologie (ICT), P.O.Box 12 40, 76318 Pfinztal,
Federal Republic of Germany

Keywords:

supercritical fluid extraction, SC-CO₂, composed plastics, flame retardents

ABSTRACT

In the field of polymer recycling and/or disposal of e.g. polymer composites of mass consumer products new techniques are highly required. For safety reasons polymer housings of mass consumer products e.g. computers, radios, TVs and other electrical household tools contain flame retardents, preferably brominated organic substances in amounts of 10 to 20 %. Commonly used disposal techniques of these halogen containing composites like incineration have the disadvantage that corrosive brominated gases and dioxines are formed and require costly and large-scale flue gas collectors. A direct recycling is not possible due to the fact that the components are difficult to separate.

One promising way to separate halogenated flame retardents out of polymer composites seems to be the extraction by supercritical fluids like CO₂. Main objective of this paper is to find the suitable conditions for high extraction efficiencies. For model mixtures involving the flame retardents TBBA, TBPA and HBCD the extraction efficiency from the inert matrix MgSO₄ was examined in relation to extraction pressure, temperature and time. The data form the basis for realistic tests on ABS composites with different flame retardents.

1. INTRODUCTION

For safety reasons polymer housings of mass consumer products e.g. computers, radios, TVs and other electrical household tools contain flame retardents, preferably brominated organic substances in amounts of 10 to 20 %. Commonly used disposal techniques of these halogen containing composites like incineration have the disadvantage that corrosive brominated gases and dioxines are formed and require costly and large-scale flue gas collectors. A direct recycling is not possible due to the fact that the components are difficult to separate.

Because of the governmental orders like the 'Elektroschrottverordnung' and the related cradle-to-grave ownership as far as the increasing disposal costs new recycling technologies and/or new disposal concepts are highly required. Any kind of reducing disposal costs and/or reusing of the plastics needs the separation of the halogenated components from the polymer matrix.

One promising way to proceed seems to be the extraction of the halogenated components by supercritical fluids. This technique is called supercritical fluid extraction (SFE). Because of their special properties supercritical fluids show solubilities like organic solvents and transport properties like gases. Especially carbon dioxide with its low critical data ($T_c = 31,3\text{ }^{\circ}\text{C}$, $p_c = 7,28\text{ MPa}$) was found to be a good candidate for the extraction of organic substances. There are several applications of the SFE-technique with SC- CO_2 for instance in the field of:

- production of flavour substances
- regeneration of activated charcoal
- extraction of pollutants from contaminated soils
- extraction of pollutants from polluted waste waters.

2. OBJECTIVES OF THE STUDY

Main objective of this paper was to study basic principles to apply the SFE-technique in the field of separation of brominated additives from polymer composites. This means especially to find the suitable conditions for high efficiencies using SC- CO_2 as extraction medium. For model mixtures involving the flame retardents TBBA, TBPA and HBCD the extraction efficiency from the inert matrix MgSO_4 was examined in relation to extraction pressure, temperature and time. Furthermore the transferability of the produced data was verified in realistic tests on ABS composites with different flame retardents.

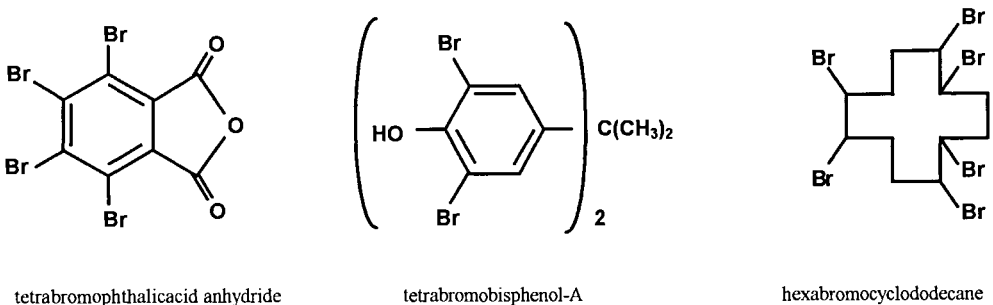


Figure 1: Typical brominated flame retardents examined in this study

3. EXPERIMENTAL

Basic experiments were carried out with an extractor in analytical scale (SFE-703, DIONEX). For a typical experiment the extraction cells (10 ml internal volume) were fully filled with a homogeneous mixture of the flame retardant and the inert MgSO_4 and placed into the oven chamber of the extractor. After reaching the desired extraction conditions (pressures of 250 to 500 bar and temperatures of 60, 80 or 100 °C) the samples were extracted for 45 min. The extracted components were analysed by gravimetric, spectroscopic and/or chromatographic methods (IR, GC-MSD). Further experiments were made with realistic brominated ABS composites (granulated composites) in analytical scale and also with an extraction autoclave in laboratory scale (500 ml internal volume).

4. RESULTS AND DISCUSSION

4.1 Extraction efficiency as a function of extraction pressure

To find the suitable extraction conditions for the separation of brominated substances like tetrabromobisphenol-A (TBBA) from polymer matrices the extraction efficiency was firstly studied e.g. for TBBA / MgSO_4 mixtures under different extraction pressures while the other conditions were held constant ($T = 80\text{ °C}$, $t = 45\text{ min}$).

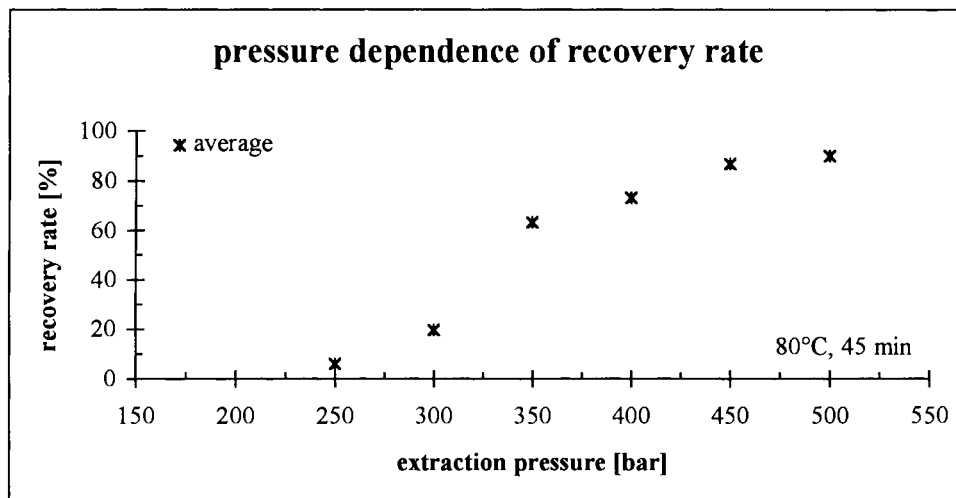


Figure 2: Recovery rate of TBBA as a function of the used SC-CO_2 -pressure

In dependence of the applied SC-CO₂-pressure different amounts of TBBA were detected after the experiments. As figure 2 shows the extraction efficiency is strongly influenced by the extraction pressure and therefore by the density of the supercritical CO₂. For extraction pressures of 250 or 300 bar the extraction rates of TBBA are very low (8 % and 20 %). Between 300 and 400 bar the extraction efficiencies are strongly increased (64 % for 350 bar and 74 % for 400 bar). In this pressure region the detected increase is the highest observed. A further rising of the extraction pressure yielded only to slightly higher extraction rates (87 % recovery at 450 bar and 90% at 500 bar). The experiments show that for higher pressures and therefore densities the solubility of the extraction medium for TBBA is increased.

4.2 Extraction efficiency as a function of temperature

Under constant conditions of 350 bar and an extraction period of 45 minutes the temperature dependence of the extraction efficiency of e.g. TBBA out of the inert MgSO₄ was examined. From the viewpoint of density a temperature increase means that the density of the extraction medium and therefore its solubility is lowered.

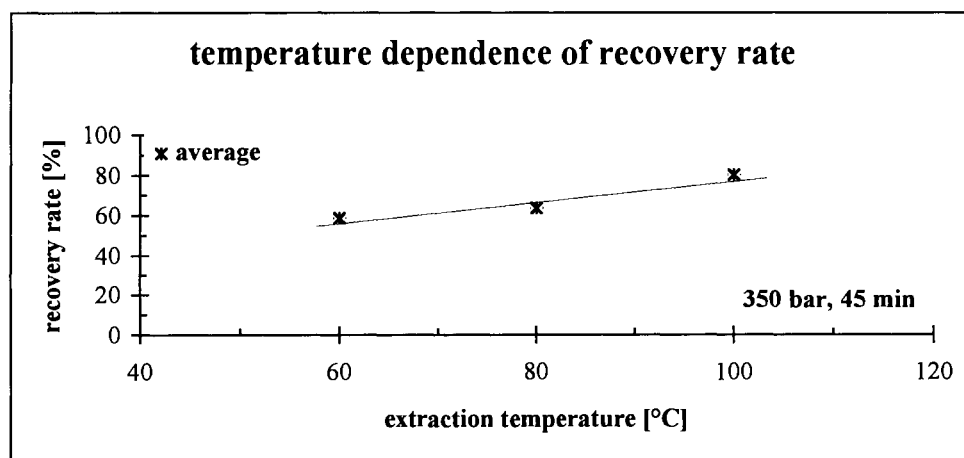


Figure 3: Recovery rate of TBBA as a function of the used SC-CO₂-temperature

As figure 3 shows the detected recovery rates for the halogenated fire retardant are increased for increasing extraction temperatures. This means that the extraction process depends not only on the density but is also diffusion controlled. The positive effect of the better diffusion of the fire retardant exceeds the lowered solubility of SC-CO₂.

4.3 Extraction efficiency as a function of extraction time

The time dependence of the extraction process is showed in figure 4. Under constant extraction conditions of 350 bar and 80 °C an extraction period of 10 minutes yielded to a recovery rate of < 2 %. This means that the extractor needed about 10 min for getting the desired extraction conditions and the extraction process started. After 30 min about 62 % of the used amounts of TBBA were extracted. Increasing the extraction time by a factor of four yielded to a recovery of 80 %. As expected from the theory longer extraction times yielded only to slightly higher extraction efficiencies. To make the extraction process more effective it would be better to rise e.g. the extraction pressure.

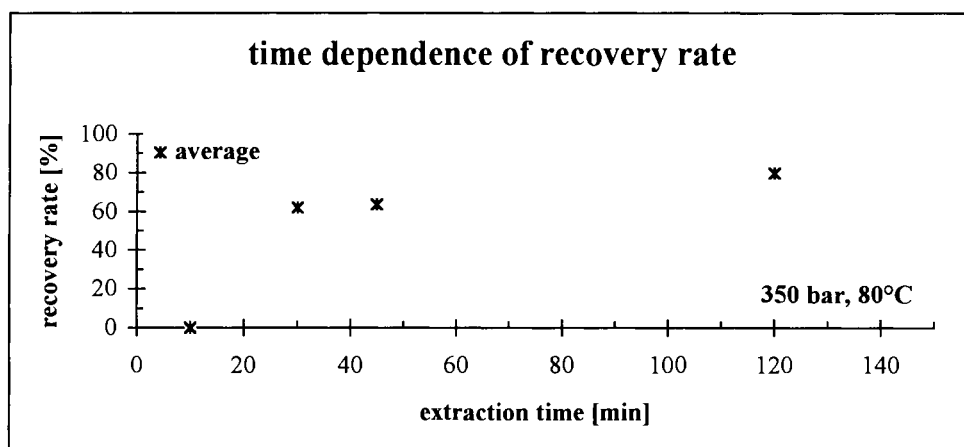


Figure 4: Recovery rate of TBBA as a function of the used extraction time

4.4 Extraction of ABS composites

Extraction experiments with different realistic ABS composites (granulats particles of $1.8 * 2 * 2.2 \text{ mm}^3$) showed that under conditions of 450 bar and 45 min the above mentioned temperature dependent diffusion effect was further increased. Rising the extraction temperature from 60 to 100 °C lead to increased extraction rates (factor of 8 to 10 higher). This means that the extraction of the flame retardant out of the polymer matrix (diffusion controlled process) seems to be better under higher extraction temperatures where the polymer possibly begins to flow. Experiments in laboratory scale showed good results so that a scale-up of the SFE-technique and its use as an effective method for separating halogenated flame retardends from plastics seems to be promising.

This page intentionally left blank

A Method for the Determination of Pressure Dependence of Liquid-Liquid Phase Behavior in High Viscous Systems

H. Lentz, U. Michel, Siegen University, 57068 Siegen, Germany

L. Kleintjens, DSM Research, Postbus 18, 6160 MD Geleen, the Netherlands

1. INTRODUCTION

High viscous homogenous mixtures such as polymer blends of well defined components are often difficult to prepare and even more problematic is a production of the relative big sample quantities necessary for some conventional investigation methods. Hence there are demands for "mini method", especially for a method to determine the phase behavior as a function of temperature and pressure. This task is solved to one part by the recently developed "mini extruders" of DSM (1), which enable a very good premixing of small amounts of polymer samples.

A "mini-optical-cell" necessary for the observation and indication of phase behavior of small amounts of viscous systems has been developed consequently and is described in this contribution in details.

The method described here is of some general interest, because the investigation of the p, T, x phase behavior of mixtures of expensive components is not a seldom problem in physical engineering chemistry.

2. MINIATURE INSTRUMENTATION

2.1. The DSM Mini Extruders

Three types of mini extruders have been developed at DSM Research. The smallest extruder consists of a single shaft rotating in a thermostatted cylinder. Its volume is 2 cc. Polymers can be mixed in the extruder at a certain temperature. By opening the attached valve the mixture can be extruded through a needle. The polymer mixture can be pressed into any small sample holder.

Further developments ultimately resulted in other self-cleaning twin-screw mini-extruders (ref. 2), with a total volume of 5 to 15 cc through which the blend can be circulated if so desired. The extruders are given a conical shape so that it could combine the benefits of large and small screws, i.e. easy feeding of the granulate and additives, rapid compression and high extrusion pressures. This DSM MINI-EXTRUDER moreover has adjustable speed control, two heating zones and a force transducer. The force transducer provides an indication of the viscosity and the degree of degradation or crosslinking.

As the mini-extruder must be suitable for many different kinds of plastics, including abrasive and corrosive grades, it is made of high-quality tool steel that has been subjected to a special heat treatment and then coated to make it abrasion resistant and easy to clean.

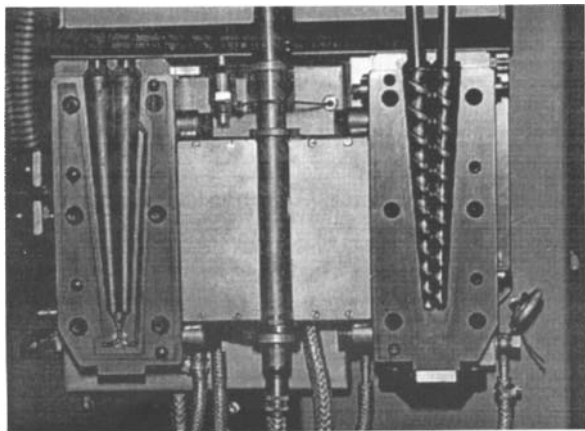


Fig. 1. DSM mini extruder

2.2. Capillary cell

The sample is injected from the mini-extruder in a capillary of 22 mm length and of a inner diameter of 1 mm (outer diameter 1.5 mm) or alternatively inner diameter 6 mm, outer diameter 7 mm. The capillary is sealed with a floating plug of graphit filled teflon. In order to keep the capillary in a vertical position a "mini frame" is used as support. The capillary and the supporting frame are shown in Fig. 2.

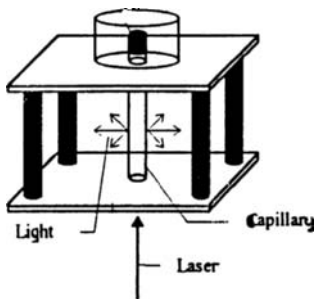


Fig. 2. Capillary sample cell and the supporting frame

2.3. Window autoclave

The capillary cell can be placed in a small autoclave, i.d. 25 mm, o.d. 50 mm, inner volume 11 cm³ (Fig. 3) with 2 bigger windows of safety glass or synthetic sapphire (d 30 mm, h 15 mm) and 1 small window from sapphire (d 10 mm, h 6 mm).

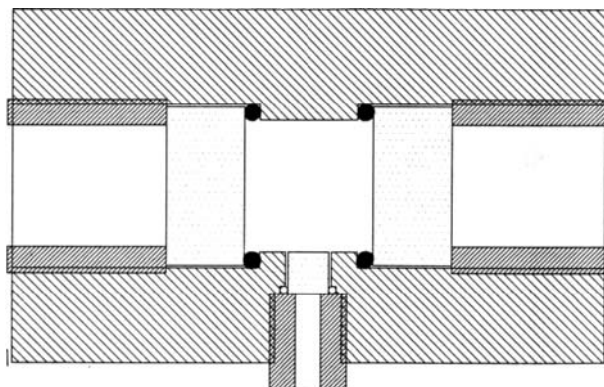


Fig. 3. Window autoclave

The windows are sealed with viton O-rings, the big windows at the front surface and the small windows at the cylinder surface. In the middle of the cylinder are 2 high pressure entrances in order to connect the inner volume of the autoclave with the high pressure periphery and in order to introduce a thermo couple in the inner volume.

Silicon oil was used as the pressure transmitting medium. The pressure periphery is conventional and a description can be omitted. The gauge used is of 0.1 class and hence accuracy of the pressure measurement is around ± 1 bar.

3. INDICATION OF PHASE TRANSITION BY SCATTERED LIGHT

A laser beam is passing the small sapphire window, entering the capillary cell at the lens-shaped bottom end and passing along the cell axis through the viscous liquid. Inhomogenities in the liquid will result in a scatter of the light and hence the scattered light can be used to indicate the phase transitions in the mixture as will be demonstrated later.

The instrumentation for the measurement of variations of the intensity of the scattered light are schematically shown in Fig. 4.

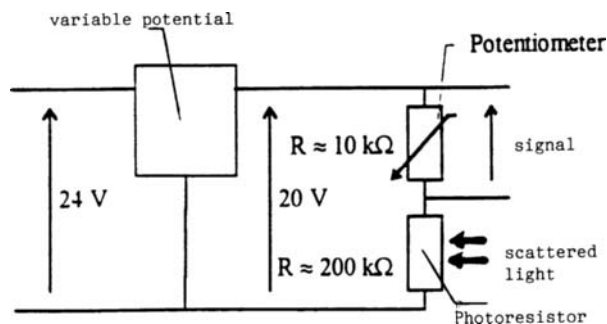


Fig. 4. Electronic device for the measurement of the intensity of scattered light (I_{90})

The change of a photo resistor collecting the light scattered under an angle of 90° (I_{90}) is measured accurately and registered by a computer together with e.g. the (increasing) temperature in a isobaric run.

This is demonstrated for the low viscous system 2-butoxy-ethanol/water in Fig. 5. Short time intervals - e.g. 2 sec. - between the measured points result obviously in a stronger variation of the measured cloud points as with longer intervals (e.g. 10 sec in Fig. 5). The phase transition temperature (around 62.6°C for this mixture) of an isobar can be estimated with an accuracy of $\pm 0.5\text{ K}$.

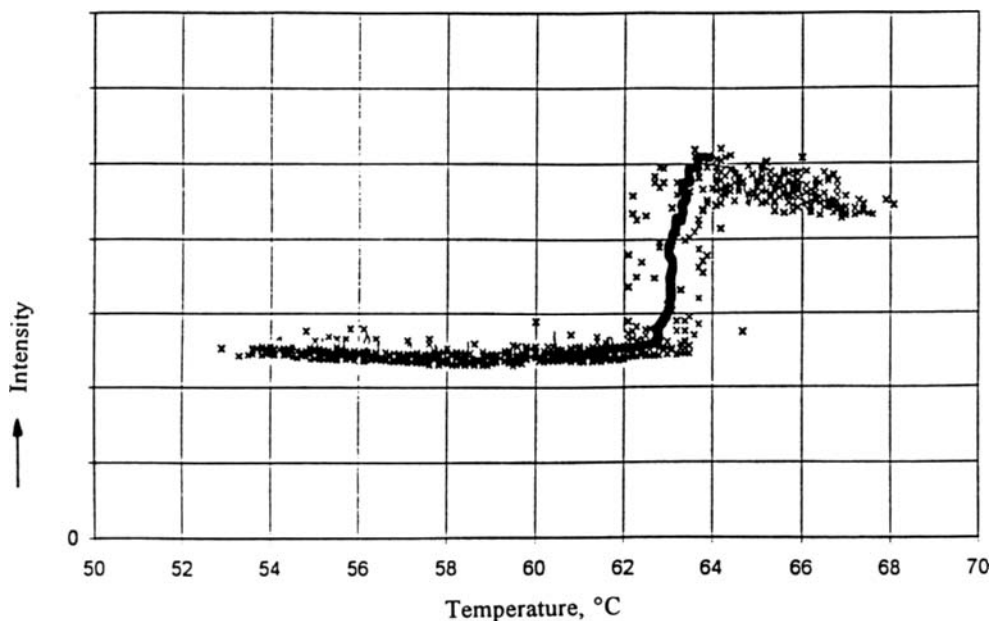


Fig. 5. Intensity of the scattered light (I_{90}) as a function of temperature.
System 2 Butoxyethanol/water at 172 bar, $x(\text{H}_2\text{O}) = 0.975$
Line represents intensity averages every 10 sec.

For high viscous systems the indication of a phase transition is remarkable more difficult as for the low viscous system (3). Fig. 6 shows a typical example of the system 8.5 % PMMA/91.5 % SAN (Polymethylmethacrylate/Styrene acrylonitrile copolymer). The estimated accuracy is in this case (at LCST cloud point transition temperature around 208.9°C) $\pm 1\text{ K}$.

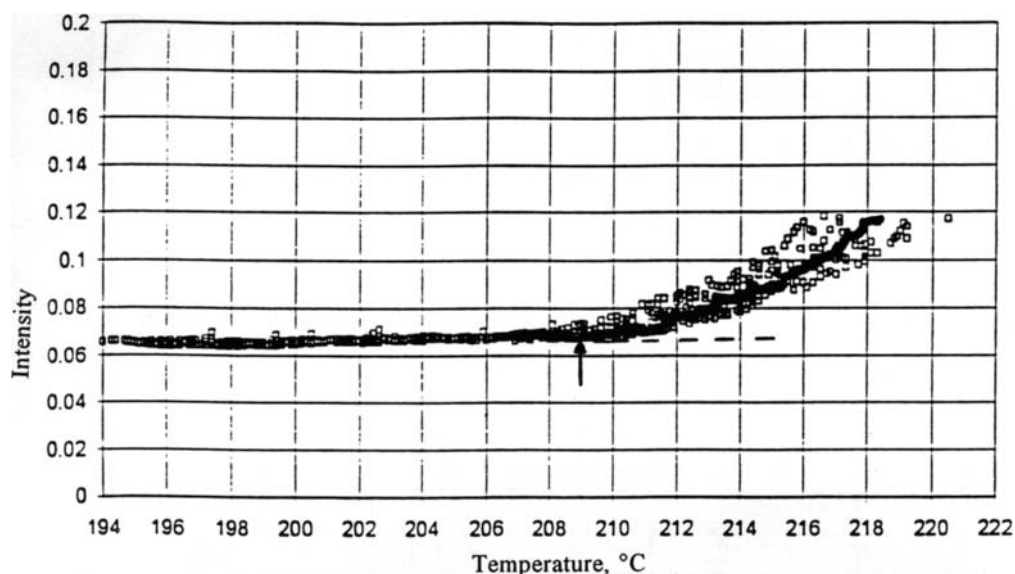


Fig. 6. Cloud point measurement in the system PMMA/SAN (8.5/91.5) at 100 bar. Heating rate 1K/min. Line represents intensity averages every 10 sec.

The influence of different capillary diameters and filling length were studied as were different kinds of optical observation methods. We found a pronounced decrease of the LCST cloud point temperature of this blend of PMMA/SAN with increasing pressure (3). However, further improvement is well possible by using smaller heating rates. Of course an remarkable improvement is achieved when using bigger amounts of a sample. A drastic example is given for the low viscous system (Fig. 7, normal pressure isobar) and Fig. 8 (172 bar) caused solely by the change of the capillary with the inner diameter of 1 mm to one with an inner diameter of 6 mm (requiring however a 36 times bigger sample amount).

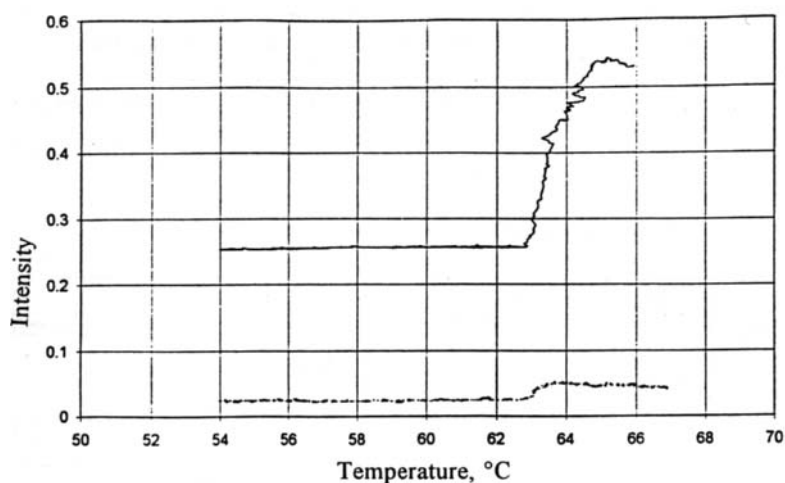


Fig. 7. Comparison of experimental scattering Intensity in two different sample holders (— : 6 mm, 1 mm diameter) at 172 bar.

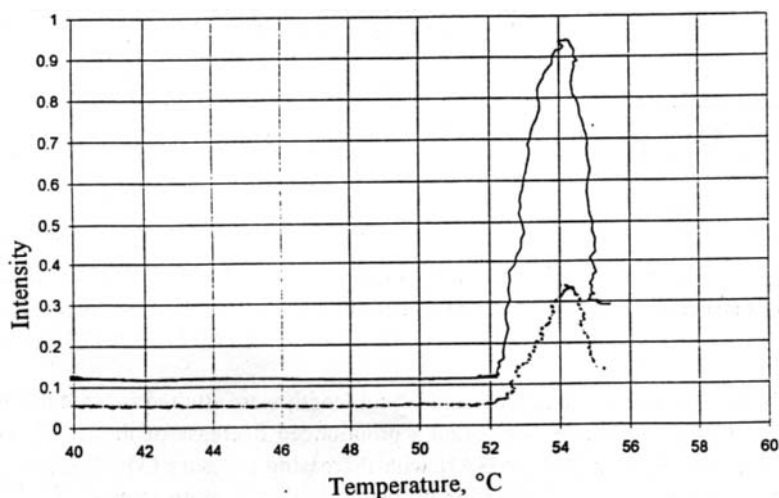


Fig. 8. Comparison of experimental scattering Intensity in two different sample holders (— : 6 mm, 1 mm diameter) at ambient pressure.

REFERENCES

1. M. Bulters and S. Martens, DSM internal communication
2. DSM Research product information
3. V. Zeuner, H. Lentz, L.A. Kleintjens, *Macromol. Symp.* **102**, 337 (1996)

An Experimental Method to Determine the Sorption and Swelling Behavior of Solids at High Pressures

C.A. Lockemann, Th. Riede, and P. Magin

BASF AG
Engineering R&D
D - 67056 Ludwigshafen

Gases interact with solids at high pressures, either by adsorption to crystal surfaces or by dissolution into amorphous materials, leading to volume changes. An experimental method to study the behavior of solids in the presence of dense gases has been developed. Sorption equilibria and solubilities are determined gravimetrically. Diffusion coefficients are derived with the help of suitable mass-transfer models. The swelling behavior of the solids is observed visually.

1. INTRODUCTION

At elevated pressures, gases adsorb to crystalline matrices or dissolve in amorphous solids, which they cause to swell. Such behavior is observed in a large variety of materials:

- In the production of polymer foams, pressurized gas is dissolved in the polymer. As the polymer undergoes rapid depressurization, the gas desorbs, forming bubbles which reach their final size once concentration of gas in the polymer drops below that of the glass point at the given temperature. Optimization of a foaming process requires knowledge of gas solubilities and diffusivities as well as of glass points. Diffusivities are required to estimate how long it takes to initially saturate the polymer with gas and to explain the distribution of gas bubbles in the foam.
- Certain materials are designed to interact with compressed gases, such as polymers used to manufacture pervaporation membranes employed in gas separation processes. The efficiency of the separation is strongly affected by the solubilities and the diffusivities of the gaseous components in the membrane. In other materials, swelling is considered undesirable, such as in fibers or gasket materials exposed to frequent pressure fluctuations, where volume changes caused by desorption of gases affect structural and mechanical properties. The aim is here to decide which maximum pressures and which frequencies of pressurization / depressurization are acceptable to ensure reliable performance of the material.
- Adsorption and desorption at elevated pressures also play an important role in zeolithes employed in catalytic conversion of gases. Chemisorption of a gaseous component to a reactive surface is a suitable method to determine the surface area of a porous solid.
- Polymerization frequently is performed in gas-phase reactors at intermediate pressures. The role of heterogeneous catalysts and the interaction between reaction kinetics and mass transfer can only be understood if sorption effects, solubilities of gases in solids, volume changes, and diffusivities at reactor conditions are known.

The high relevance of these phenomena to industrial manufacturing processes has generated considerable academic interest in swelling and sorption of compressed gases in polymers, resulting in numerous publications on laboratory measurements and theoretical modelling. The work of Wissinger and Paulaitis [1] ranks among the important papers despite the publication of more recent work. Funke [2] launched a detailed investigation into sorption and swelling behavior of gases into isotropic membrane polymers and onto zeolites. By contrast, many of the papers reporting experimental testwork do not distinguish between volume (swelling) and mass (sorption) effects, nor do they discriminate between isotropic and anisotropic materials (which swell unevenly in different directions). Finally, the techniques described in literature have generally not been able to describe volumetric properties of *particles* exposed to pressurized gases.

Because of the wide field of industrial applications, the need exists to develop simple and reliable techniques for the characterization of solids behavior in the presence of dense gases. From our experience we know that information on sorption equilibria or solubilities of gases in solids, on mass-transfer kinetics, and on volume changes are the most relevant in process design. We have therefore developed experimental methods to obtain these properties through laboratory testwork.

The purpose of the paper is to discuss possibilities to improve the experimental method and to identify aspects which require further investigation.

2. EXPERIMENTAL

2.1. Set-up

The experiments are conducted with the help of the sorption balance shown in Figure 1. The sorption balance operates according to the principle developed and described by Lösch et al. [3].

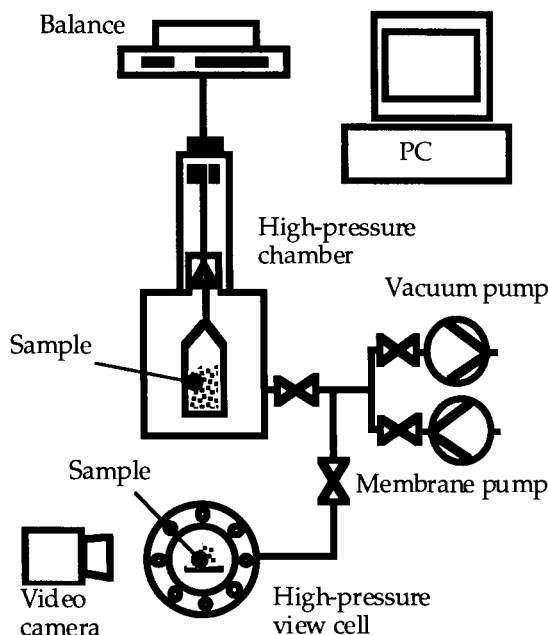


Figure 1. Experimental set-up.

The solid material is placed into a small vial that is introduced into a thermostated high-pressure chamber (volume 79 ml). The vial is attached to a suspension device that is magnetically coupled to the balance during measurement. The device is lowered to a neutral position when no recording of a mass point takes place, thus allowing for the balance to be tared before each measurement. This is of particular importance in slow processes in which thermodynamic equilibrium is attained only in the course of several hours or even days. The chamber may be evacuated with a vacuum pump at the beginning and at the end of each experiment. The dense gas is taken from a cylinder and, if necessary, compressed to system pressure with the help of a membrane piston pump.

Tubing connects the chamber and a high-pressure view cell, which is thermostated to the same temperature as the chamber. In order to observe swelling behavior, some of the solid material is also placed into the view cell. It thus is in contact with the gas at the same pressure and temperature as the material in the suspended vial. The interior of the view cell may be observed through a video camera. The video images are scanned into a PC and analyzed for changes in size.

The entire system is monitored by PC. Pressure and temperature within the chamber and the view cell as well as the weight of the sample are recorded continuously.

Momentary mass of a sample may be derived from momentary weight only if the density of the gas, and thus the buoyancy of the sample, are known. Volumetric data of pure gases are calculated from precise equations of state, as they exist for carbon dioxide and other gases, or taken from tables. Cubic equations of state are used to calculate densities of gas mixtures. We have always employed van-der-Waals mixing rules and fitted the interaction parameter to vapor-liquid equilibria determined by ourselves or taken from literature.

This method is equally suited for toxic or inflammable gases or vapors.

2.2. Procedure

The sample is filled into the vial which then is attached to the suspension device. Then the high-pressure chamber is firmly closed and heated or cooled to system temperature. More of the sample material is placed within the view cell. The apparatus then is evacuated to remove air and to obtain a reliable value for initial mass. The thermostated dense gas is charged into the chamber and the view cell until system pressure is attained. Pressure build-up only takes a few seconds because of the small volume of the chamber. The weight of the sample rises as gas dissolves in or is being adsorbed to the sample and asymptotically nears its equilibrium value. At the same time, the dissolution of the gas in the solid leads to volume changes, a process observed with the sample particles enclosed in the view cell. Their size is recorded with the camera and evaluated with the help of a PC. The apparatus is evacuated again at the end of each experiment to remove the entire gas.

2.3. Limitations of the method

There are several limitations to the method. Determination of sample weight, and thus mass, fails when the densities of the solid and the gas become equal. Near the critical point of the gas, precise measurements are impossible due to density fluctuations of the gas. It is needless to say that no experiments are possible for materials consisting of components that exhibit significant solubility in the compressed gas.

Most limitations, however, concern the investigation of the swelling behavior. Anisotropic materials do not swell evenly in all directions. For such solids, several particles must be placed randomly in the view cell to ensure that, statistically, every possible orientation is recorded by the video system. Even then, the difficulty remains to correctly describe volumetric effects on the basis of two-dimensional video images, a problem that will be discussed more thoroughly in

Chapter 3. The behavior of fine powders is difficult to observe due to the limited resolution of the video optics. Analysis of changes in size becomes more difficult for particles of irregular shape. Finally, the volumetric changes undergone by porous materials are not generally observed, since these changes affect the size of interior pores rather than the outside shape which alone is visible to the camera.

3. THEORETICAL

3.1. Equilibrium concentration of the gas

The amount of gas dissolved in or adsorbed to the solid is determined from the final weight and the final size of the sample. Sample weight is the difference between actual mass and buoyancy. Buoyancy in turn is the mass of the gas displaced by the solid, which is the product of gas density and sample volume. The volume increase of the sample has to be derived from the two-dimensional video image which shows projected areas of the particles in the view cell. Particle technology has been dealing extensively with this problem. Conventional wisdom has it that particle volume is the same as that of a sphere with an equal projected area; however, this is a reasonable assumption only if all of the following three conditions apply:

- The particles are concave.
- The particles are not extremely flat or elongated.
- The number of particles studied is sufficiently large to have particles positioned randomly without any preferred orientation. This is to ensure that, statistically, the material is viewed from all sides.

Then, the volume ratio may be approximated by

$$\frac{V_{VC}(t)}{V_{VC,0}} = \left(\frac{A_{proj,VC}(t)}{A_{proj,VC,0}} \right)^{3/2} \quad (1)$$

Hence, the equilibrium value X^* then becomes

$$X^* = \frac{M_\infty}{M_0} - 1 = \frac{W_\infty}{M_0} + \left(\frac{A_{proj,VC,\infty}}{A_{proj,VC,0}} \right)^{3/2} \cdot \frac{\rho_g}{\rho_{s,0}} - 1, \quad (2)$$

where M_0 and M_∞ are the initial mass and the terminal mass of the sample in the pressure chamber, $A_{proj,VC}$ is the projected area of the particles in the view cell, ρ_g is the density of the gas, and $\rho_{s,0}$ is the initial density of the solid material.

3.2. Mass transfer

Mass-transfer rates are determined from the changes of mass that the sample undergoes as a function of time. Diffusion coefficients are derived from these rates by applying the laws of mass-transfer kinetics.

If the amount of gas absorbed in an experiment is small compared to the overall mass of the solid and the particles are roughly spherical, the diffusion coefficient of the gas in the solid is described by the following equation:

$$\delta = \frac{9}{2\pi^5} \cdot \frac{d^2}{t} \cdot \left[-1 + \sqrt{1 + \left(\frac{\pi^3}{18} \cdot \ln \left(\frac{1 - \left(M_{g,ads}(t=0) / M_{g,ads}^* \right)}{1 - \left(M_{g,ads}(t) / M_{g,ads}^* \right)} \right) \right)^2} \right], \quad (3)$$

In Equation (3), δ is the diffusion coefficient, d is the mean diameter of the particles, and $M_{g,ads}$ is the amount of gas adsorbed into the solid at time t . The asterisk $*$ refers to thermodynamic equilibrium.

4. RESULTS AND DISCUSSION

4.1. Experimental results

The result described in this chapter was obtained for a polymer used to manufacture foams.

Polymer foams are made by first mixing (molten) polymer and compressed gas at high pressures, where the gas dissolves in the polymer. The mixture is then pressed through a die, after which it has ambient pressure and cools rapidly. The solubility of the gas in the polymer drops sharply, causing the gas to desorb and to form cavities. As temperature drops below the glass point of the polymer (which is a function of pressure and thus, gas content), the bubbles are "frozen" into the polymer, thereby creating the foam. Specifications commonly require foams to contain many small bubbles. At the same time, the polymer should retain a smooth surface and its intended shape.

Pressures and temperatures for such a process must be chosen such that bubbles of the correct size and number form. At the same time, conditions must be avoided that cause significant changes in polymer structure, such as a high degree of deformation or brittleness.

The properties of such a foam depend both on the type of polymer and gas used as well as on the conditions at which manufacturing takes place. The size of the bubbles depends on interfacial tension, but also on the solubility of the gas in the polymer and on diffusivity, both which may be determined with the method described in this publication. Diffusivities also play a role during initial saturation of the polymer with the gas.

Fig. 3 shows the solubility of carbon dioxide in a polymer intended to be used in a foaming process.

Gas uptake initially is low. At a pressure of 25 bar, however, the temperature of 40°C at which the experiments were performed corresponds to the glass point of the polymer, which at ambient pressure is at 100°C. The polymer macromolecules possess the ability to move more freely against each other; hence, solubility rises sharply at 25 bar.

Above 50 bar, the video image clearly exhibits a high degree of deformation of the polymer. This structural transformation is reflected by the flattening of the solubility curve: an increase in pressure does not lead to a corresponding rise in CO₂ solubility in the polymer. The deformation of the polymer at elevated pressures is irreversible even after depressurization.

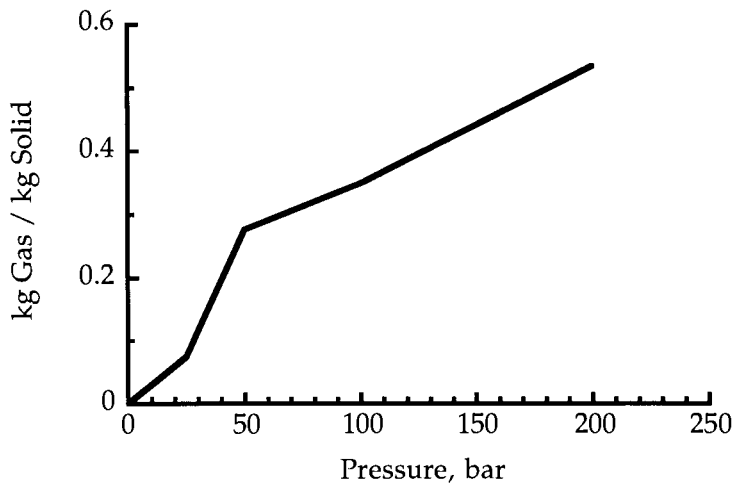


Figure 3. Solubility of carbon dioxide in a polymer at 40°C.

The testwork reveals that at 40°C the polymer is suitable for foaming at pressures between 25 and 50 bar.

Diffusivities of the gas in the polymer at 40°C exhibit a similar behavior. Beyond the pressure of 25 bar, the diffusion coefficient rises from $2 \cdot 10^{-10} \text{ m}^2/\text{s}$ to $7 \cdot 10^{-10} \text{ m}^2/\text{s}$. Analysis of mass-transfer rates is less precise at elevated pressures because of the increasing difficulty to calculate accurate surface areas due to the strong deformation of the polymer.

4.2. Conclusions

We have successfully developed a method which allows us to determine the sorption (mass) and the swelling (volumetric) behavior of materials exposed to pressurized gases. The laboratory technique described in this paper is suitable for a large variety of solids and gases. It meets many of the demands of the chemical industry.

However, there are a few limitations to the method which have been pointed out above. While the method is a successful attempt at determining some of the most important aspects of gas-solid phase behavior, the design of a complex process requires integrated solutions which cannot be found by chemical industry alone. From our point of view, there are two aspects of particular importance which should be solved through academic research: a) work on techniques that overcome the experimental difficulties stated above through precise, albeit technically demanding, measurements; and b) models that are useful in determining volumes from two-dimensional projections with great precision.

REFERENCES

1. R.G. Wissinger and M.E. Paulaitis, J. Polymer Sci. B: Polymer Physics 25 (1987) 2497.
2. H. Funke, Dissertation, University Heidelberg, 1991.
3. H.W. Lösch, R. Kleinrahm, and W. Wagner, Chem.-Ing.-Tech. 65 (1993) 1117.

UV/vis Biochemical Spectroscopy under High Pressure

C. Balny^a, J.-L. Saldana^a, R. Lange^a, M. J. Kornblatt^b and J. A. Kornblatt^b

^aINSERM, Unité 128, BP 5051, 34033 Montpellier, Cedex 1, France

^bConcordia University, 1455 de Maisonneuve Blvd W, PQ H3G 1M8 Canada

Abstract

High hydrostatic pressure induces changes in protein conformation, solvation and enzyme activities via reversible and non-reversible effects on intra- and inter-molecular interactions (noncovalent bonds) [1]. To have access to these structural modifications, spectroscopic investigations are required which necessitate special spectroscopic adaptations. Two improvements are presented : first for enzyme reactions and second for structural determination.

1. INTRODUCTION

A complete study of catalytic reactions involving a succession of very rapid different steps, consists of the exploration of the properties of these steps, including thermodynamic parameters obtained by the action of temperature and pressure. One difficulty in measuring kinetics using spectroscopic detection method is the relatively long dead-time of the high-pressure techniques. Different devices have been proposed to eliminate sources of errors in time and temperature. These techniques include *in situ* initiation of the reaction after the heat of compression has been dissipated. To reduce the dead-time with respect to the reactions studied, we have combined low temperature which decreases reaction velocities according to the Arrhenius expression, with the stopped-flow method which provides the rapid mixing of two compounds.

The second recent spectroscopic improvement is second and fourth derivative spectroscopies in the ultraviolet region of proteins. Derivative spectroscopy is a new tool for analyzing the effects of pressure on proteins. It permits one to enhance selectively spectral changes due to the UV absorbance of phenylalanine, tyrosine and tryptophan. The solvent polarity affects the amplitude, the position and the shape of the second and fourth derivative spectral bands.

2. THE HIGH PRESSURE STOPPED-FLOW APPARATUS

The relatively long dead-time of high-pressure techniques using spectroscopic detection is the first important limitation to exploiting enzyme kinetics. If the system under study can be characterized via optical detection

(absorbancy, fluorescence), the stopped-flow method is easily used. The second limitation deals with the temperature control which must be efficient to compensate the heat of compression. To solve these problems, devices were designed to mix samples under high pressure, at controlled temperatures. The first apparatus was described by Grieger and Eckert and modified by Sasaki *et al.*. Both systems were thermostated and used the breakage of a foil diaphragm for the mixing of two components. After different improvements, the Heremans' group described a stopped-flow apparatus designed for spectroscopic detections of fast reactions at pressures up to 120 MPa by means of immersing a stopped-flow unit in a high-pressure bomb. Since then, other high-pressure stopped-flow devices have been described [2].

To reduce the dead-time with respect to the reactions studied, we have developed an apparatus which permits rapid mixing. The high pressure stopped-flow system functions at low temperature thereby slowing reaction velocities according to the Arrhenius equation. The design of our instrument incorporates certain features of previous stopped-flow systems described for cryoenzymological studies and for investigations under high-pressure. The general design, already published [3,4], consists of a powerful pneumatic system driving the syringe mechanism, two vertical drive syringes containing the samples to be mixed, a mixing chamber, an observation chamber with quartz windows, and a waste syringe. Both temperature and pressure homogeneities are maintained by housing the whole apparatus in a high-pressure thermostated bomb. The stopped-flow apparatus can operate in absorbance or fluorescence mode over temperature and pressure ranges of + 40 to - 35 ° C and of 1 to 300 MPa, respectively. The system is mounted either on an Aminco DW2 spectrophotometer or on a spectrofluorometer specially designed in the laboratory (wavelength limits : 230 - 650 nm). The dead-time, nearly independent of pressure, is less than 5 ms using aqueous solutions at room temperature.

Using this device, different biological systems have been examined allowing the development of cryobaroenzymatic studies [1, 5].

3. DERIVATIVE SPECTROSCOPY METHODS

The main problems for a protein chemist or enzymologist who wishes to study the effects of pressure on a protein are a) to observe and quantitate the effects and b) to interpret them. The majority of proteins do not contain easily studied chromophores but they do contain substantial amounts of the aromatic amino acids, tryptophan and tyrosine. These amino acids are characterized by strong but overlapping absorption bands in the ultraviolet. A protein that contains five to ten of each of the aromatics presents a spectrum that is a composite of the contributions of each. A change in a protein, such as a conformational change, dissociation, or denaturation, may result in a change in the environment of one or more of these residues. However, the UV spectrum of a protein is broad and featureless; the changes of interest are masked by the contributions from all the other aromatics whose environment has not changed.

3.1 Second derivative spectroscopy

Second derivative spectroscopy is a means to extract information from the spectrum. In contrast to the relatively featureless UV spectra, the second derivatives of UV spectra are characterized by 2 sharp peaks and troughs [6,7]. Figure 1 shows the ultraviolet spectra of yeast enolase at 0.28 and 200 MPa and Figure 2 shows the second derivative of those spectra.

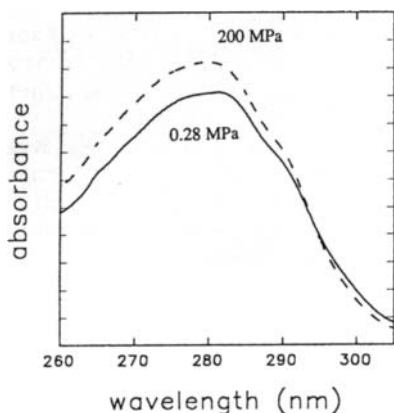


Figure 1. UV spectra of yeast enolase at 0.28 and 200 MPa

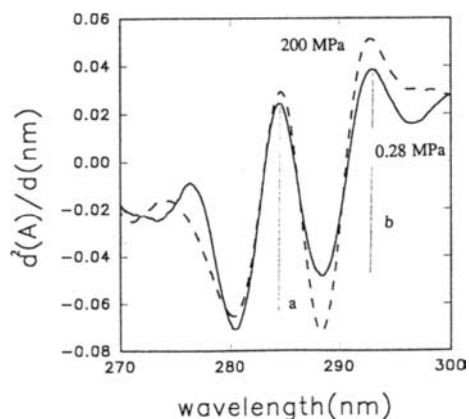


Figure 2. Second derivative of the UV spectra

Ragone [7] has determined the effects of solvent polarity on the second derivative spectra of model compounds. For both tyrosine and tryptophan, as the solvent polarity goes from non-polar (as when the residue is buried inside a protein) to polar (exposed to solvent), the peak and trough positions shift to the blue (shorter wavelengths). There are also changes in amplitude, which are best described by calculating the ratio ($r = a/b$) of the two peak-to-trough values marked in Figure 2 [6,7]. For tyrosine, the value of r decreases as solvent polarity decreases, while the value of r for tryptophan is almost independent of solvent polarity. Thus, in the second derivative spectrum of a protein, the ratio of the peak to trough values and the positions of the peaks and troughs are a function of the relative amounts of the two amino acids and of the average polarity of the environments of the tyrosines as well as that of the tryptophans. For the protein shown in Figure 2, increasing pressure from 0.28 to 200 MPa has decreased the average polarity around the tyrosine residues, while not changing the environment around the tryptophan residues.

Extracting the physical meaning of the changes in second derivative spectra relies on knowing the amino acid composition of the protein and using the constituent spectra to simulate the observed spectra. Simulations were performed by combining the second derivative spectra of tyrosine- and tryptophan-ethylester in solvents of various dielectric constants, in a molar ratio of 9 tyr to 5 trp (that of enolase). Figure 3 shows the observed spectra of native (dimeric) yeast enolase and that of tyr in water and trp in 100 and 50 % ethanol. The simulations produce average values for changes in polarity. When an X-ray structure is also available, it may be possible to assign the changes in polarity to changes in the environment of specific tyrosines or tryptophans.

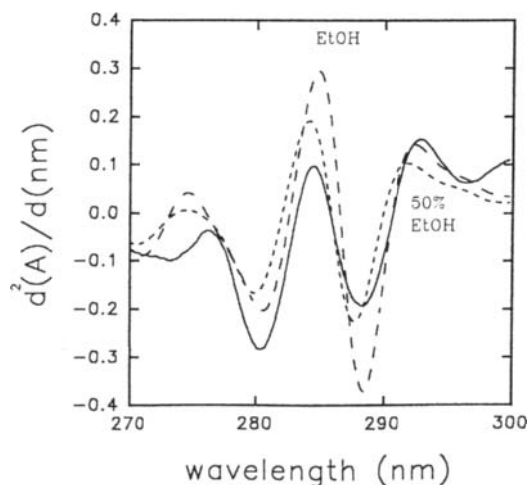


Figure 3. Simulated spectra of enolase. (—) native enolase ; a) tyr in water and trp in 100 % ethanol, b) tyr in water and trp in 50 % ethanol

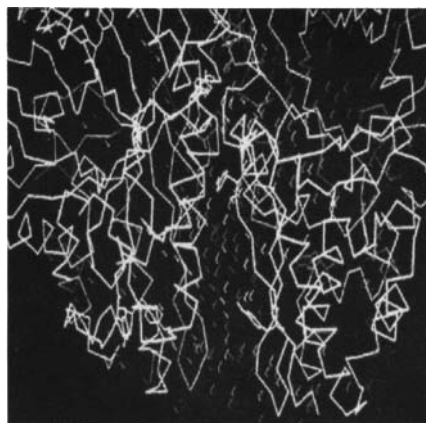


Figure 4. X-ray structure of enolase

Pressure has previously been shown to dissociate the enolase dimer into monomers [8] ; the pressure range in which this occurs is the same as that in which we observe changes in the second derivative spectra. Dissociation is accompanied by a net hydration of the surface buried at the subunit interface.

The second derivative results indicate that the average tyrosine polarity decreases, the opposite of what one would expect if hydration is occurring. Using the X-ray structure (Figure 4) [9], we can resolve this apparent contradiction [10]. In the dimeric form, there is a water-filled cleft between the two monomers. Two tyrosines from each monomer point into this cleft. As dissociation occurs, these tyrosines go from a region in which they are exposed to relatively rigid waters - ergo fixed dipoles - to one in which they are exposed to bulk water. The net change is a decrease in polarity that accompanies a net increase in hydration.

The use of second derivative spectroscopy allows us to observe the effects of pressure on this enzyme, to quantitate the changes occurring (we can use the values of r to calculate K_{eq} as a function of pressure and hence ΔG and ΔV for dissociation) and to interpret those changes in terms of the known structure of the enzyme. Second derivative spectroscopy has both advantages and disadvantages vis-à-vis fourth derivative spectroscopy. With second derivatives, one uses the ratio of the amplitudes, which is independent of the absolute absorbance. Therefore, one does not have to correct the spectra for compression effects and can easily compare samples studied at different times. The changes, however, are dominated by the contributions of tyrosines and provide much less information about the tryptophan residues.

3.2 Fourth derivative spectroscopy

The selective resolution enhancement in derivative spectroscopy is pushed even further in the fourth derivative mode. As in the case of second derivative spectroscopy, the amplitude and the position of the derivative spectral bands of the aromatic amino acids are related to the polarity of the medium. We have undertaken a systematic investigation of these spectral features of the N-acetyl O-ethyl esters of tyrosine and tryptophan in various solvents of different polarity (from cyclohexane to water). Astonishingly, a simple relationship between the spectral parameters of the fourth derivatives and the dielectric constant was found [11]. As shown in Figure 5, for tyrosine it is the position of λ_{\max} , and for tryptophan it is the derivative amplitude which depends linearly on the dielectric constant ϵ_r . Since in addition the fourth derivative spectra of these model compounds do not depend significantly on pressure (at least up to 500 MPa), these spectral features may be used as an intrinsic probe to sense the dielectric constant in the vicinity of tyrosine and tryptophan.

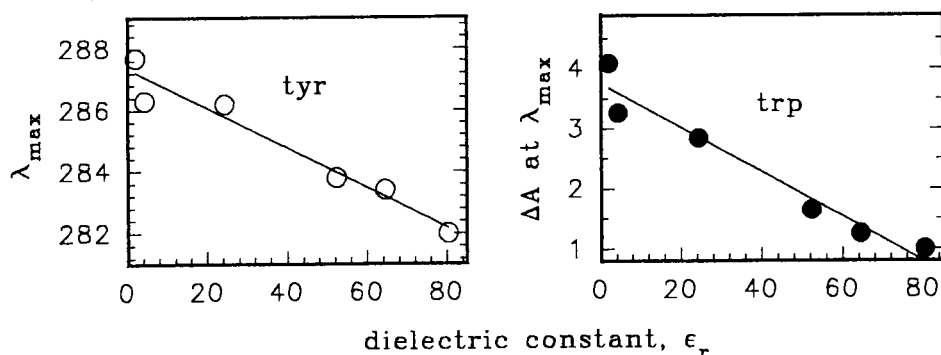


Figure 5. Relation between amplitude and λ_{\max} of the 4th derivative spectra of tyrosine and tryptophan on the dielectric constant ϵ_r .

A good example of application is given by the protein structural changes of bovine ribonuclease A in the course of its denaturation by pressure. The UV spectrum of RNase is dominated by the absorbance of tyrosine - this RNase does not contain tryptophan. As shown in Figure 6, an increase of pressure from 1 to 500 MPa results in a blue-shift of the 4th derivative maximum from 285.7 ± 0.05 to 283.5 ± 0.05 nm. This shift of 2.2 nm corresponds to an increase of the mean dielectric constant from 25 to 59. It is characteristic of the exposure to the aqueous solvent of part of the 6 tyrosines, as it is expected for a partly denaturation. The transition is fully reversible with clear isosbestic points. The pressure effect can therefore be described by a simple two-state model between the native ($\epsilon_r = 25$) and the partially denatured ($\epsilon_r = 59$) state. A simulation on the basis of this model permitted us to determine the thermodynamic parameters of this transition: $\Delta G^\circ = 10.3$ kJ/mol and $\Delta V = -52$ ml/mol. A comparison with results obtained by other methods indicates that the ($\epsilon_r = 59$) state corresponds to an intermediate in the defolding process which has molten globule like characteristics [12]. It thus appears that fourth derivative

spectroscopy under high pressure is a suitable technique to investigate protein structural changes occurring during the folding or defolding processes.

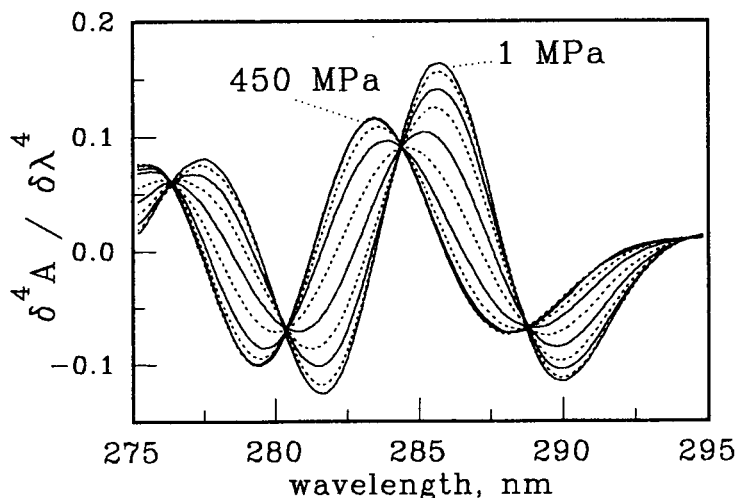


Figure 6. Effect of pressure on the fourth derivative spectra of RNase A at pH2.

4. ACKNOWLEDGMENTS

The authors thank Mrs N. Bec for her technical help and NSERC Canada for financial support.

5. REFERENCES

- 1 V. V. Mozhaev, K. Heremans, J. Frank, P. Masson and C. Balny, *Proteins : Structure, Function, and Genetics*, 24 (1996) 81.
- 2 J.-L. Saldana and C. Balny in *High Pressure and Biotechnology* (C. Balny et al. eds) J. Libbey Eurotext/INSERM, Montrouge, France, vol. 224 (1992) 529.
- 3 C. Balny, J.-L. Saldana, and N. Dahan, *Anal. Biochem.*, 139 (1984) 178.
- 4 C. Balny, J.-L. Saldana, and N. Dahan, *Anal. Biochem.*, 163 (1986) 309.
- 5 C. Balny, P. Masson and F. Travers, *High Pres. Res.*, 2 (1989) 1.
- 6 K. Ruckpaul, H. Rein, D.P. Ballou and M.J. Coon, *Biochem. Biophys.*
- 7 R. Ragone, G. Colonana, C. Balestrieri, L. Servillo and G. Irace,
- 8 A.A. Paladini and G. Weber, *Biochemistry* 20 (1981) 2587.
- 9 B. Stecand L. Lebioda, *J. Mol. Biol* 211 (1990) 235.
- 10 J.A. Kornblatt, M.J. Kornblatt and G. Hui Bon Hoa, *Biochemistry*, 34 (1995) 1218.
- 11 R. Lange, J. Frank, J.-L. Saldana and C. Balny, *Eur. Biophys. J.* (1996) in press.
- 12 R. Lange, N. Bec, V.V. Mozhaev and J. Frank, *Eur. Biophys. J.* (1996) in press.

A High Pressure Combustion Cell Based on Numerical Flow Simulation and Reaction Zone Radiation Modelling

B. Michelfelder^a, B. Noll^b, M. Weindel^a, W. Eckl^a, N. Eisenreich^a, M. M. Herrmann^a

^aFraunhofer-Institut Chemische Technologie
Joseph-von-Fraunhoferstr. 7, 76327 Pfinztal (Berghausen), Germany

^bESG - Emissionsmeßtechnik und Strömungsmechanik Entwicklung und Anwendung GmbH
D-76532 Baden-Baden, Germany

ABSTRACT

A flame in supercritical water was first observed and studied by Franck et al. at the University of Karlsruhe [1, 2]. The aim of the presented work was to investigate flame reactions in stationary conditions and to develop a new high pressure combustion cell (100 MPa) designed by combining a numerical code for reacting flow field simulation and modelling of infrared radiation emitted by a hot reaction zone. The simulation of the reactive flow field, taking into account fluid properties at high pressures, allowed optimised reactor geometry and combustion conditions. The modelling of the emitted radiation from the reaction zone allows prediction of radiative energy transfer and detectable signals. A description of the two used computer codes will be given in the paper to demonstrate their use as a constructive tool in high pressure applications and the complete set-up of the supercritical water plant is presented. For flame studies, the application of non-intrusive optical diagnostics like spectroscopy [3,4] or digital frame analysis is necessary, therefore, the reaction chamber has been equipped with six sapphire windows, allowing simultaneously the detection of different signals.

1. INTRODUCTION

Supercritical water exhibits interesting effects above the critical point at 374 °C and 22.1 MPa. The dielectric constant decreases drastically from 80 to lower than 5 [5]. Water under supercritical conditions behaves like a perfect organic solvent. Organic substances form a homogeneous mixture, inorganic substances precipitate and gases like O₂, N₂, CO₂ and H₂ are completely dissolved. It is possible to degrade organic materials in supercritical water by hydrolysis or oxidation processes [6,7]. A mixture of water, oxidiser and some organic materials should produce pure carbon dioxide and water. Inorganics precipitate.

The objective is to provide a waste disposal technology with the high pressure combustion in supercritical water which does not burden air and water with harmful effluents. The quality of this technology is that the wastes are completely mineralised to CO₂, water and salts. The products like CO, SO₂, NO_x, dioxins, arsenic, mercury, etc., typical for incineration, are avoided only harmless end-products remain.

2. NUMERICAL FLOW SIMULATION

The modelling of super critical water oxidation (SCWO), up to now not been used in large scale industrial applications, is important for design of pilot plants and, later, industrial plants. The applied programme to model the continuous flow in a reactor is called CAST (Computer Aided Simulation of Turbulent Flows [8]) and is based on the method of the finite volume. That means that the balance equations were integrated over the surfaces of each control volume.

CAST, a two-dimensional FEM computer code solves the mass-balance equation, the Navier-Stokes-equations which result from the momentum balance for flows with friction and the energy balance in each control volume of the calculation grid. All equations can be written in a general form [9]:

$$\underbrace{\frac{\partial \phi}{\partial t}}_{\text{local variation with the time}} + \underbrace{\frac{\partial(\rho v_j \phi)}{\partial x_j}}_{\text{convection}} = \underbrace{\frac{\partial}{\partial x_j} \left(\Gamma \frac{\partial \phi}{\partial x_j} \right)}_{\text{diffusion}} + \underbrace{S\phi}_{\text{source term}} \quad (1)$$

CAST allows two dimensional calculation of laminar or turbulent flows with heat transfer at low Mach numbers.

To use the code for modelling a high pressure combustion chamber at supercritical conditions several changes had to be done:

In the transport equation for the x-component of the velocity u the force of the buoyancy is

$$F_A = -(\rho(x, y) - \rho_{ref}) \cdot g \cdot V \quad (2)$$

added to the source term.

Two additional transport equations had to be solved

$$\frac{\partial(\rho Y_i)}{\partial t} + \frac{\partial(\rho u_i Y_i)}{\partial x_j} = \frac{\partial}{\partial x_j} \left[\frac{\mu}{Sc} \frac{\partial Y_i}{\partial x_j} \right] + S_i \quad (3)$$

A combustion model for gaseous fuels based on the ratio of components was implemented assuming that all fluids which are mixed are also combusted [10]. The hypothesis is that mixing of reaction partners by diffusion is much slower than reaction kinetics. To calculate increasing of temperature during oxidation the global reaction



is presumed. The temperature field is calculated by the following steps, which were repeated during the iterative calculation:

- 1.) solving of the transport equation for the ratio of components:

$$\frac{\partial(\rho u_i f)}{\partial x_i} = \frac{\partial}{\partial x_i} \left(\frac{\mu}{Sc} \frac{\partial f}{\partial x_i} \right) \quad (4)$$

- 2.) calculation of the fuel concentration from the distribution of the ratio of components
- 3.) estimation of the reaction rate r_f

$$r_f = \frac{\partial(\rho u_i Y_f)}{\partial x_i} - \frac{\partial}{\partial x_i} \left(\frac{\mu}{Sc} \frac{\partial Y_f}{\partial x_i} \right) \quad (5)$$

- 4.) solving the momentum equation and pressure correction
- 5.) evaluation of the temperature equation:

$$\frac{\partial(\rho u_i T)}{\partial x_i} = \frac{\partial}{\partial x_i} \left(\frac{\mu}{Pr} \frac{\partial T}{\partial x_i} \right) + \frac{r_f H_u}{c_p(T)} \quad (6)$$

with H_u as the heating value of the fuel.

Variable material constants (ρ , Sc , c_p) for water, fuel, oxidiser and reaction products were included. Density, Schmidt-Number and specific heat capacity are calculated at all points of the calculation grid depending on local temperature and pressure inside the reactor. The Schmidt-Number is a value for the diffusive mass transfer from methanol in water.

To improve the convergation ratio of the calculations a modified pressure correction algorithm and changed calculation of velocities on the boundaries were implemented.

The calculated temperature and velocity distribution of a methanol flame in supercritical water at 50 MPa and 500°C is shown in Figure 1.

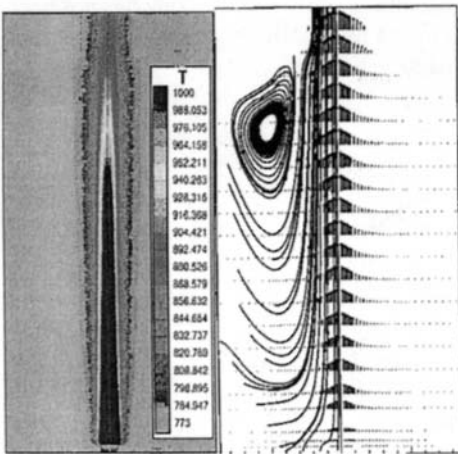


Fig.:1 Calculated temperature and velocity distribution

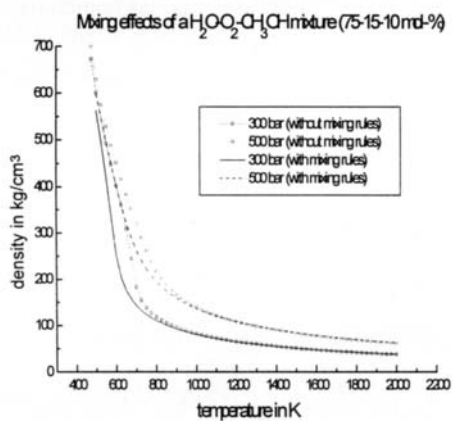


Fig.2: Density with and without mixing rules

3. EXCESS VOLUMES

A PVT-data-code was generated to calculate phase equilibria, critical curves and thermodynamic excess quantities of quaternary systems. The program uses the Christoforakis-Franck-equation of state [11]

$$p = RT \frac{V_m^3 + V_m^2 \beta_x + V_m \beta_x^2 - \beta_x^3}{V_m (V_m - \beta_x)^3} + RT \frac{B_x}{\left(V_m^2 - V_m \frac{C_x}{B_x} \right)} \quad (7)$$

This equation bases on the Carnahan-Starling-One-Fluid Model for the repulsion term and the Square-Well-Pade-approximant for the attraction term.

Methanol as fuel, oxygen and water were chosen to get the needed basic data. Figure 2 shows the density of a mixture of 75% Water, 15% oxygen and 10% methanol at 30 MPa and 50 MPa. There are two possibilities to calculate the density of a mixture. One is to add the volumes of the different substances weighted with their concentrations, the other is to calculate the excess volumina by mixing rules and correct the density. Figure 2 shows, that at temperatures above 900 K there is no difference between the density calculated with and without the mixing rules. So in case of high pressure combustion, calculation can be done without excess volume.

4. MODELLING OF IR-RADIATION

Spectroscopy in supercritical water is limited by high pressure, strong gradients and the strong absorbent medium. Nevertheless there have been efforts to investigate combustion processes of hydrocarbons under these conditions. Transmission and emission spectroscopy of the OH radical in the UV have been used to determine rotational temperatures, but the resulting values are unusually high and questionable [3]. Laserspectroscopic methods have failed because of strong temperature and density gradients. NIR/IR-spectroscopy has not been considered up to now, as water has numerous bands in this region. But hydrocarbons and their combustion product CO_2 have only bands in the infrared.

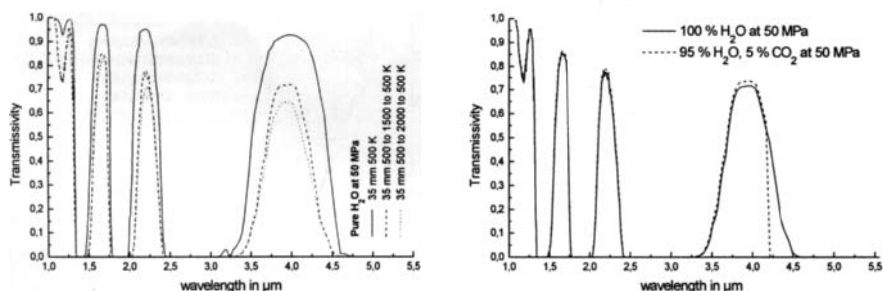
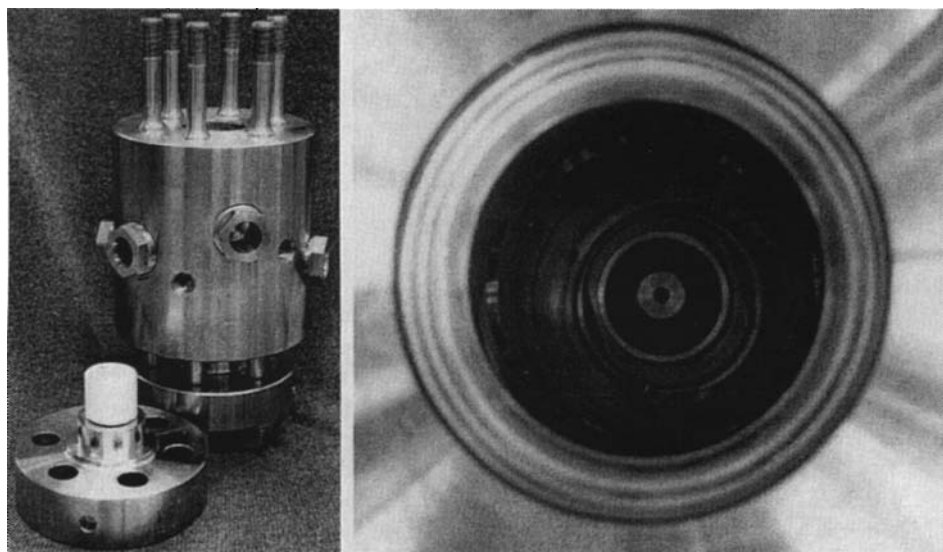


Fig. 3a: Transmissivity of water (50 MPa, 500 K and more, optical pathlength 35 mm);

Fig. 3b: Comparison of two calculated transmission spectra at 50 MPa, 35 mm optical pathlength and a temperature profile of 5 mm at 500 K / 1000 K / 1500 K / 1000 K / 500 K of pure water and water with 5 % carbondioxide



*Fig. 4: left: high pressure combustion cell with sapphire windows and a ceramic inlay at the end of the combustion area;
right: combustion chamber with the fuel and oxidiser nozzle*

The following theoretical calculations have been done in order to estimate possibilities of spectroscopy in the infrared despite the numerous bands of water. Using a band modelling program based on experimental data of the NASA [12], transmissivity of water has been calculated at 50 MPa, > 500 K and an optical pathlength of 35 mm (reactor conditions). As sapphire (Al_2O_3) windows are used in experiment, only their transmissive region up to $5.5\ \mu\text{m}$ have been regarded. Figure 3a shows that there are only some narrow regions remaining ($1 - 1.3\ \mu\text{m}$, $1.6 - 1.7\ \mu\text{m}$, $2.1 - 2.25\ \mu\text{m}$ and $3.7 - 4.3\ \mu\text{m}$), which will transmit infrared light.

Concluding these calculations, NIR/IR-spectroscopy can obtain following results for supercritical water combustion:

- estimation of temperature in reaction zone by fitting experimental transmission or emission spectra to theoretical calculations;
- detection of hydrocarbons on account of a narrowed transmission window at $3.7\ \mu\text{m}$ caused by the CH-stretch vibration band about $3.3\ \mu\text{m}$;
- detection of carbondioxide on account of a narrowed transmission window at $4.3\ \mu\text{m}$ caused by the CO_2 band at $4.3\ \mu\text{m}$ (see Fig. 3b).

5. SET UP OF THE CONTINUOUS SCWO FACILITY

The facility allows to feed two liquid and one gaseous stream separately controlled in a reactor. The fluids are pressurized by two membrane pumps for water and fuel and one compressor for oxygen. The maximum mass-flows are 5 l/h for water and 2 l/h for the fuel. The compressor allows overstoichiometric oxygen concentrations under all conditions. Behind the pumps pulsedampers were installed so that the fluidstreams are free from pulsations. The fluidstreams can be heated electrically so the mass flow and the temperature

of each component can be selected independently. The reaction products are cooled down in a condenser in two steps. The first cooling section is supplied by air, the second by water. So the thermostress in the wall of the high pressure pipe is low enough. For the hot areas of the facility 1/4" high pressure tubes made of inconell 625 were used.

ACKNOWLEDGEMENT

The authors gratefully acknowledge support by European Union (Environment Programme, Projects: EV5V-CT94-0545 and EV5V-CT92-0241).

REFERENCES

1. Schilling, E. U. Franck; "Combustion and Diffusion Flames at High Pressures to 2000 bar"; Ber. Bunsengesellschaft Phys. Chem. 92 (1988), 631
2. U. Franck, Th. Hirth, G. Pohsner, J. Steinle; "Combustion and Flames to 1000 bar"; Poster presented at the 23rd Symposium on Combustion; The Combustion Institute; Orleans, France, July 22-27, 1990
3. U. Franck, Th. Hirth, G. Pohsner, J. Steinle; "High Pressure Combustion Flames in Supercritical Water"; 22nd ICT Conference, Karlsruhe, Germany, July 2-5, 1991
4. Th. Dreier, M. Ridder, G. Schiff, "Collisional Narrowing and Spectral Shift in CARS Spectra of Molecular Nitrogen and Oxygen at Pressures up to 2500 bar and Temperatures of 850 K", Ber. Bunsenges. Phys. Chem. 97, 1726-1728 (1993) No. 12
5. K. Heger, M. Uematsu, E.U. Franck; "The Static Dielectric Constant of Water at High Pressures and Temperatures to 500 MPa and 550°C", Ber. Bunsengesellschaft Phys. Chem. 84 (1980), 758 - 762
6. Th. Hirth, H. Krause, N. Eisenreich, "Degradation and Combustion of Organic Materials in Supercritical Water "; Institut Supérieur Industriel Liégeois (Veranst.): Industrie et Environnement (Liège 1992). Liège: Selbstverl., 1992
7. G. Bunte; N. Eisenreich; T. Hirth, H. Krause; "Entsorgung von Explosivstoffen mit überkritischen Verfahren"; Fraunhofer-Institut für Chemische Technologie (Veranst.): Energetic Materials - Insensitivity and Environmental Awareness (24th Int. Ann. Conf. of ICT Karlsruhe 1993). Pfinztal: Selbstverl., 1993, S. 70/1-70/11
8. M. Peric, G. Scheuerer, "CAST: A Finite Volume Method for Predicting Two-dimensional flow and heat transfer phenomena", Gesellschaft für Reaktorsicherheit, Garching, Germany, GRS-SRR-89-01
9. B. Noll, "Numerische Strömungsmechanik", Springer Verlag, ISBN 3-540-56712-7, 1993
10. B. Noll, "Möglichkeiten und Grenzen der numerischen Beschreibung von Strömungen in hochbelasteten Brennkammern", Habilitationsschrift, Lehrstuhl und Institut für Thermische Strömungsmaschinen, Universität Karlsruhe, 1992
11. M. Heilig, E.U. Franck, "Phase Equilibria of Multicomponent Fluid Systems to High Pressures and Temperatures", Ber. Bunsenges. Phys. Chem. 94, 27-35 (1990)
12. Ludwig, C. B. et al., Handbook of Infrared Radiation from Combustion Gases, NASA SP 3080, 1973

Required Fuel Contents for Sewage Disposal by Means of Supercritical Wet Oxidation (SCWO) in a Pilot Plant Containing a Wall Cooled Hydrothermal Burner (WCHB)

MARKUS WEBER and CHRISTIAN TREPP

Institut für Verfahrens- und Kältetechnik, Eidgenössische Technische Hochschule Zürich
CH - 8092 Zürich Switzerland

SUMMARY

For toxic and hazardous waste water to be disposed, in some cases Supercritical Wet Oxidation (SCWO) appears to be a suitable process. Due to corrosion and possible plugging in the pressurised reaction vessels its industrial application is hardly realised. A reactor containing a Wall Cooled Hydrothermal Burner (WCHB) needn't be entered by preheated feedstreams and hence alleviates the two main problems mentioned above (LA ROCHE *et al.* [1]). The economic viability of an industrial plant with this kind of configuration will strongly depend on the minimum fuel mass fraction that is required to keep the oxidation in the thermal regime of a flame. In this paper an attempt was made to find a theoretical background for both the location in a relation inlet temperature vs. fuel mass fraction and the shape of extinction lines. The aim was to verify one extinction line given from measurements with one specific kind of fuel without varying the geometric parameters of the burner. It was found that the application of a Three-Environment Model (3EM) can lead to reasonable results if the 3EM is extended by taking into account an enthalpy term. As a result, a list of ideas to reduce the fuel consumption, as well as a lower limit, could be found. In addition, the calculated extinction lines will help in comparisons and explanations of future experimental measurements.

1. PROBLEM

The work presented here takes as its starting point the need of disposal processes for organically contaminated waste water containing non-biodegradable substances or requiring a particularly high reaction efficiency.

1.1 Significance and Principles of Supercritical Wet Oxidation (SCWO)

Mixtures of water (main component), organic substances and gases such as O₂ or CO₂ are multiphase systems under normal conditions. Pressures above 221 bar and temperatures higher than 374 °C generally provide single-phase behaviour and facilitate very fast oxidation reactions. These advantages led to the attempt to turn SCWO into a commercially available industrial process for sewage disposal especially in the case of hazardous waste.

Although in laboratory experiments excellent results had been shown concerning reaction velocities, the completeness of the reactions and the harmlessness of the products, two

drawbacks seem to be inevitable. Due to the strong decrease of the ion product of water in the range of 400 °C (at 250 bar) two severe technical problems arise whenever the waste water and hot parts of the containment stand in direct contact. One of these drawbacks is the corrosion of the load-bearing vessel walls the other one being the plugging of the reaction vessel due to precipitant solids, especially salts.

1.2 SCWO bench-scale plant containing a Wall Cooled Hydrothermal Burner (WCHB)

In a bench-scale plant located in our laboratory containing a WCHB, the degradation reactions of the organic components of the waste water take place in the thermal regime of a flame. A flame typically provides heat transfer from the hot products to the cold educts not through fixed walls, but by conduction, radiation and (if radiation and conduction are too weak) turbulent mixing through the flow field. Therefore the flame regime can be established even if the preheating of the feed streams is reduced or absent.

Figure 1 shows the bottom part of the reaction vessel used in this work in a longitudinal section. It can be seen that the waste water (artificial) was fed through the core pipe, high pressure oxygen was supplied in the inner annular flow and the cooling stream entered the vessel through the outer annular flow. The distance between the edges of the core tube and of the coaxial tube was about 40 mm. This section has to be considered as wall cooled and is the stabilisation zone, while above the edge of the coaxial tube the far more efficient film cooling takes place.

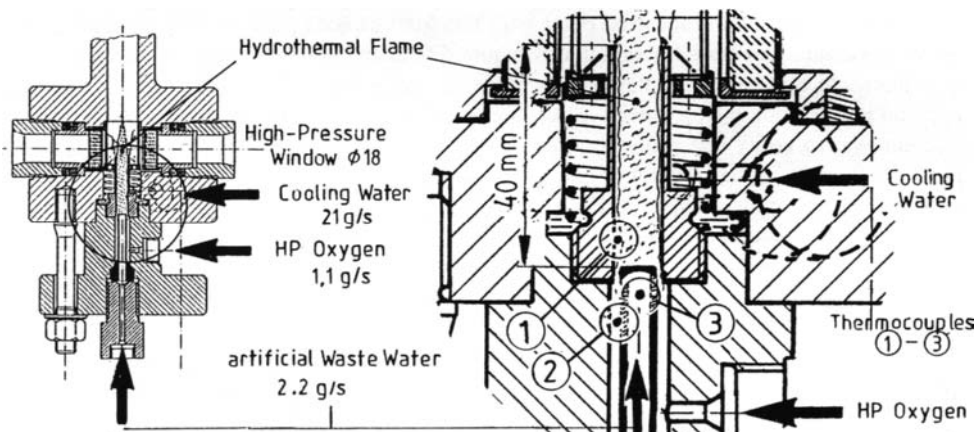


Figure 1 Longitudinal section through the bottom part of the high-pressure vessel used in this work ($p=250$ bar) with indication of all feed streams (representative values) and all locations of thermocouples.

1.3 Selection of only one aspect in the renewed evaluating of the SCWO Process

In comparison to the well known results achieved in plug flow systems, the flame regime causes a number of differences: corrosion and plugging are markedly alleviated and acceptable decomposition efficiencies aren't achieved except in special cases, whereby the process cost increases to a considerable extent. Amongst the several components contributing to the overall process cost, the required fuel mass fraction of the waste water (more exactly: the overall heating value of the mixture of water and fuel) would appear to be the most important one.

2. MEASUREMENTS

A first series of experiments showed that the required fuel content of the waste water depends strongly upon the inlet temperature and the geometry of the burner, while mass flow rate and excess oxygen are of smaller importance.

With regard to the following theoretical analysis that had to be carried out in order to allow a sound interpretation of the results, experiments varying only the inlet temperature and the fuel content seemed to be most suitable and easy to perform. As a consequence, an extinction line was recorded. All experiments were performed in a burner with a configuration according to fig. 1 and with methanol as fuel.

2.1 The draw-up of an extinction line, experimental procedure

After ignition (fuel mass fraction $w_{\text{Fuel},1} = 16.5\%$, temperature at the outlet of the preheater $\vartheta_{0,1} = 580^\circ\text{C}$) the mass fraction of methanol was set to the desired amount by switching a three-way tap. At the same time, the outlet temperature of the preheater was decreased gradually. At the moment the flame was extinguished, the characteristic temperatures of the last operating point before extinction were recorded. This procedure was repeated once or twice for every fuel mass fraction in order to estimate the accuracy of the results. Different extinction temperatures for one fuel mass fraction were mostly in the range of 10°C . A series of extinction points ($w_{\text{Fuel},1}$ ranging from 4% to 25%) resulted in a so-called extinction line.

2.2 Experimental results

The extinction temperatures depend strongly on the fuel quality. Fig. 2 shows that they vary between 550°C (or even higher) related to 4% mass fraction of CH_3OH and values equal to or lower than 100°C when 25% methanol was used. The lines for different locations of the temperature measurements intersect. This intersection is due the heat transfer that takes place in the narrow area around the core tube tip. This fact will be examined further.

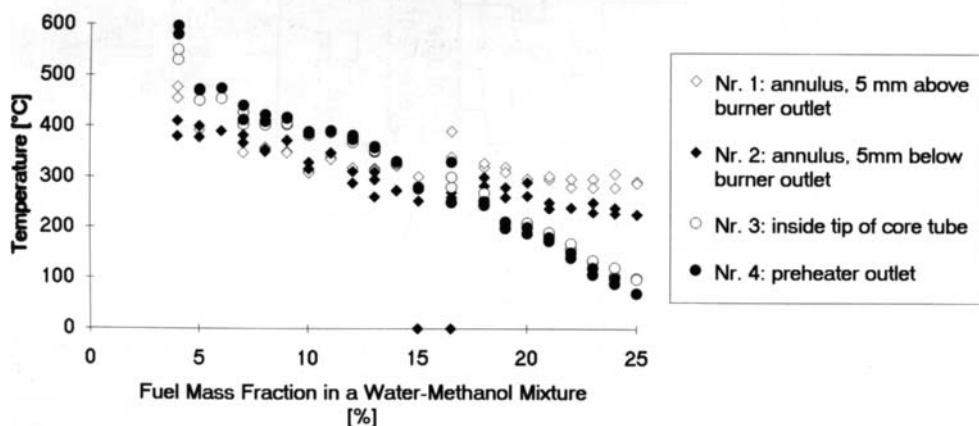


Figure 2 Extinction line: extinction temperature as a function of fuel mass fraction. Results of experimental work with a reaction vessel and a burner configuration shown in fig. 1

3. APPLICATION OF A „THREE-ENVIRONMENT MODEL“ (3EM)

The „Three-Environment Model“ (3EM) presented by RITCHIE and TOBGY [2] is based on the „Two-Environment Model“ from NG and RIPPIN [3] and will be extended in this work by the introduction of an enthalpy term. It belongs to the group of Lagrangian models for the theoretical description of combined turbulent flow, mixing and chemical reaction. Most of the formulas are developed from the viewpoint of a *moving observer* and therefore belong to the age α of a particle fraction, to its residual lifetime λ and to the Residence Time Distribution (RTD) in a vessel. The biggest drawback of the 3EM is its weak or even missing reference to the Eulerian system.

3.1 Standard definitions and enthalpy extension

The model is based on the definitions of “macromixing” and “micromixing” as its counterpart. In a reaction vessel the degree of macromixing is completely described by the RTD $E(t)$. Micromixing is characterised by the introduction of two boundary states: “Complete Segregation” (CS) and its opposite, “Maximum Mixedness” (MM). The inner volume of a reaction vessel with two separate inlet streams and one outlet stream is divided into three parts: two “Entering Environments” (E.E.₁ and E.E.₂) and one “Leaving Environment” (L.E.). A state of micromixing is assigned to every part or subregion.

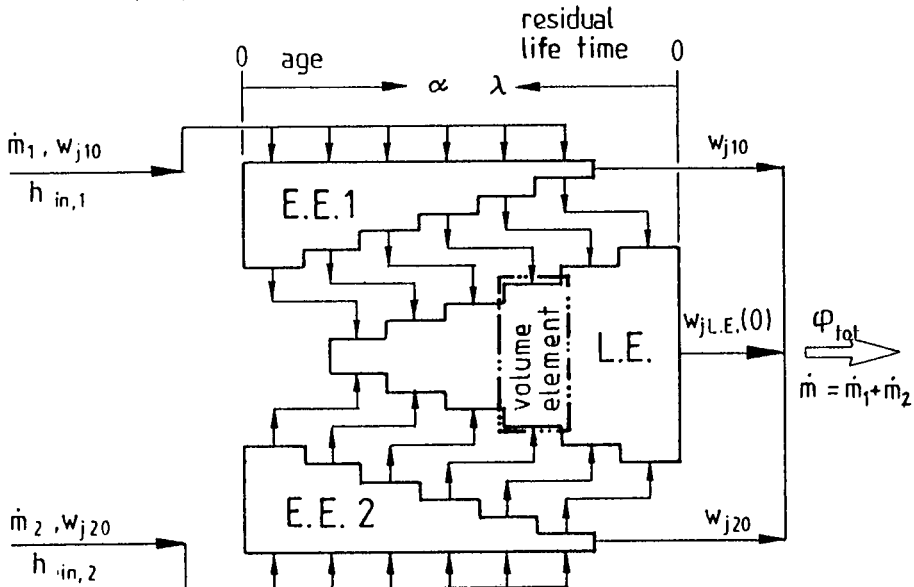


Figure 3 Subdivision of the inner region of a reaction vessel in three regions. Each is characterised by one of the boundary states of micromixing. CS is assigned to the two Entering Environments (E.E.₁ and E.E.₂) where no chemical reaction can take place. MM prevails in the Leaving Environment (L.E.) and makes chemical reactions possible.

According to the state of micromixing in the E.E.'s, which is CS, all particles in each E.E. are classified with respect to their age α . As MM prevails in the L.E., all particles in it are

assigned to classes of the same residual lifetime λ . Due to the fact that the L.E. is the only region where a chemical reaction can take place, all following formulas and considerations are orientated to the parameter λ . As shown in [2], the total mass of the i th feed stream \dot{m}_i in the reactor and its fractions that belong to the i th E.E. or to the L.E. respectively, are expressed by equations (2a-d) based on the substitutions (1a-d). In these equations $E_i(t)$ is the RTD of the i th feedstream.

$$I_i(\lambda) = \int_0^{\infty} E_i(\alpha + \lambda) d\alpha \quad ; \quad II_i(\lambda) = \int_0^{\infty} (1 - G(\alpha)) \cdot E_i(\alpha + \lambda) d\alpha \quad (1a,b)$$

$$III_i(\lambda) = \int_0^{\infty} G(\alpha) \cdot E_i(\alpha + \lambda) d\alpha \quad ; \quad IV_i(\lambda) = \int_0^{\infty} g(\alpha) \cdot E_i(\alpha + \lambda) d\alpha \quad (1c,d)$$

The function $G(\alpha)$ describes the age dependent fraction of the mass in the reactor that remains in the E.E. $g(\alpha)$ is its negative first derivative with respect to α .

$$\text{mass fraction in the E.E.}_i \text{ with life expectation } \lambda \rightarrow \lambda + d\lambda \quad dM_{i,E.E.}(\lambda) = \dot{m}_i \cdot III_i(\lambda) d\lambda \quad (2a)$$

$$\text{mass fraction in the L.E. with life expectation } \lambda \rightarrow \lambda + d\lambda \quad + \left| dM_{i,L.E.}(\lambda) = \dot{m}_i \cdot II_i(\lambda) d\lambda \right| \quad (2b)$$

$$\text{total mass in the reactor with life expectation } \lambda \rightarrow \lambda + d\lambda \quad dM_i(\lambda) = \dot{m}_i \cdot I_i(\lambda) d\lambda \quad (2c)$$

$$\text{mass flow rate from E.E.}_i \text{ to the L.E.} \quad d\dot{m}_{i,E.E. \rightarrow L.E.}(\lambda) = \dot{m}_i \cdot IV_i(\lambda) d\lambda \quad (2d)$$

Applying an irreversible decomposition reaction of a th order in the fuel concentration, of b_j th order in the concentration of the educt j and of Arrhenius type as is given by eq. (3)

$$-Fuel + \sum v_j Ed_j = \sum v_j Pr d_j \quad \Leftrightarrow \quad \frac{\partial c_{Fuel}}{\partial t} = A_p \cdot e^{-\frac{E_A}{RT_{React}}} \cdot c_{Fuel}^a \cdot \prod c_{Ed_j}^{b_j} \quad (3)$$

we obtain a mass balance equation for each species valid for a small volume element of width $d\lambda$. As an example equation (4) represents the balance equation of the fuel.

$$\frac{dw_{Fuel,L.E.}}{d\lambda} = \frac{\partial c_{Fuel}}{\partial t} \cdot \frac{m_{Fuel}}{\rho_{L.E.}(\lambda)} + \frac{\sum \dot{m}_i IV_i(\lambda) \cdot (w_{Fuel,i,0} - w_{Fuel,L.E.})}{\sum \dot{m}_i II_i(\lambda)} \quad (4)$$

Numerical integration of equation (4) commences from a suitably large value of λ with the initial condition $w_{Fuel,L.E.}(\lambda_{\infty})=0$ and finishes at the outlet where $\lambda=0$ to give the total conversion φ_{tot} that is shown in eq. (5).

$$\varphi_{tot} = \frac{\sum \dot{m}_i II_i(0)}{\sum \dot{m}_i} \cdot \frac{(w_{Fuel,0} - w_{Fuel,L.E.}(\lambda=0))}{w_{Fuel,0}} \quad (5)$$

On the right hand side of equation (4) a convective term and a kinetic term compete with each other. As the reaction temperature T_{React} decreases, the total conversion φ_{tot} breaks down from its maximum value to the lowest value possible. This break-down of the conversion is

considered as a theoretical equivalent of the physical event of extinction. While keeping the fuel mass fraction of the feed streams and all other fluid dynamic conditions constant, changing the reactor inlet temperature, *i. e.* lowering it, starting from high values, may cause extinction. Hence, to each fuel mass fraction an inlet temperature is assigned, at which extinction occurs. Computing a number of examples with different fuel mass fractions results in one theoretical extinction line.

The only temperature that influences the kinetic term (excluding density effects) is the reaction temperature. T_{React} is essentially a function of an average inlet temperature and of an average fuel mass fraction. A number of simplifications (WEBER [4]) yield equation (6).

$$T_{\text{React}} = T_{\text{Flame, ad}} = \bar{\vartheta}_{\text{in}} + \frac{\bar{w}_{\text{Fuel}} \cdot \Delta H_R}{\bar{c}_p} \quad (6)$$

Among the assumptions that led to the equation above - T_{React} is equal to the adiabatic flame temperature, conversion is 100% and reference enthalpy is equal to the specific enthalpy of the feed streams - the last one represented by equation (7) seems to be the most questionable one.

$$h_{\text{L.E.}}(\lambda) = h_{\text{in}} \quad (7)$$

If we take into consideration that a cold droplet being in a hot ambient is, for a short time, able to store a relatively large amount of energy while it is being heated and dissolved, we have to revise the right hand side of equation (7) with an expression that contains a Lewis number.

$$h_{\text{L.E.}}(\lambda) = h_{\text{in}} - (\text{Le}_{3\text{EM}}(\lambda) - 1) \cdot \Delta h_0 \quad (8)$$

In equation (8) the specific Lewis number $\text{Le}_{3\text{EM}}$ is the ratio of two integral expressions whose substitutions are explained in equations (1b) and (10) respectively. While $\Pi(\lambda)$ in eq. (1b) contains the undissolved mass fraction $G(\alpha)$ the function $K(\alpha)$ represents the age dependent increase of specific enthalpy in a droplet (9). We assume that the transition from the E.E.s to the L.E. takes place due to the attainment of a transition temperature ϑ_{Trans} , which itself is similar to the vaporisation temperature of subcritical liquids. Hence the enthalpy increase is divided by the greatest possible enthalpy gap Δh_0 .

$$h_{\text{E.E.}}(\alpha) = h_{\text{in}} + K(\alpha) \cdot \Delta h_0, \quad \text{where } 0 \leq K(\alpha) \leq 1 \quad \text{and} \quad \frac{\partial K(\alpha)}{\partial \alpha} \geq 0 \quad (9)$$

$$\Delta h_0 = h(\vartheta_{\text{Trans}}) - h(\vartheta_{\text{in}})$$

$$\tilde{V}(\lambda) = \int_0^{\infty} K(\alpha) \cdot E(\alpha + \lambda) d\alpha \quad (10)$$

$$\Rightarrow \quad \underline{\text{Le}_{3\text{EM}} = 1 + \frac{\tilde{V}(\lambda)}{\Pi(\lambda)}} \quad (11)$$

The functions $G(\alpha)$ and $K(\alpha)$ are dependent and determined by a separate droplet dissolution model. Once calculated they are part of the 3EM where they prescribe the mass fractions in the E.E.s and in the L.E. as well as the enthalpy that is relevant to the calculation of the reaction temperature.

3.2 Results of calculations on the basis of one selected example

As described elsewhere (WEBER [4]) the dissolution model for a cold droplet being heated in a hot ambient at supercritical conditions is based on a number of severe simplifications. Most of the approaches and ideas are given by BEER [5]. The droplet is heated by the energy flux towards its core while it loses the molecules at its surface as soon as they have reached or exceeded ϑ_{Trans} . Therefore, the assumption of a Nusselt law for the heating and the introduction of a transition criterion lead to both the mass and the overall enthalpy of a droplet as a function of its age α . Figure 4 shows how mass, over all energy, average enthalpy and emitted mass flow of a droplet progress with α .

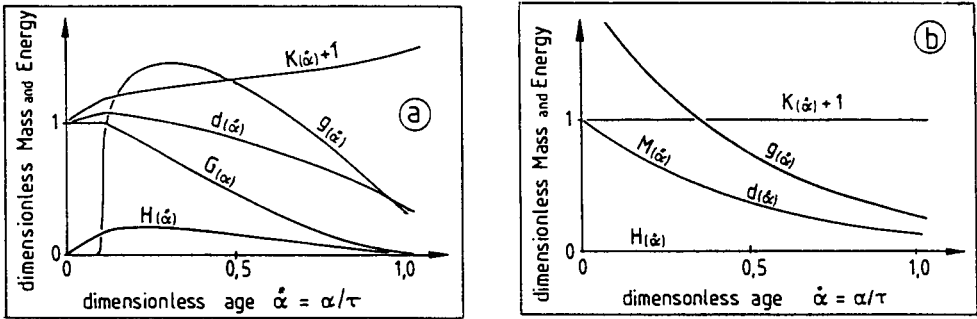


Figure 4 Normalised mass $G(\alpha)$, energy $H(\alpha)$, average enthalpy increase $K(\alpha)$ and transition mass flux $g(\alpha)$ of a droplet for the cases of: (a) enthalpy improved 3EM and (b) for standard 3EM. Ambient temperature $\vartheta_{Flame} = 900^{\circ}\text{C}$, initial temperature $\vartheta_{1,0} = 270^{\circ}\text{C}$, transition temperature $\vartheta_{Trans} = 420^{\circ}\text{C}$, initial droplet diameter $d_{1,0} = 400\mu\text{m}$, Nusselt number ≈ 18 and amplification factor of the heat conduction coefficient due to internal forced convection $k_{eff}/k_{molec} = 2.72$ (BEER [5]), residence time $\tau = 30\text{ ms}$.

Assuming that the RTD is equal to that of 5 ISTR in series and that $\tau_1 = \tau_2 = 30\text{ms}$ and applying equations (1a-d) and (10) the functions $G(\alpha)$, $g(\alpha)$ and $K(\alpha)$ computed above yield the integral expressions I to \tilde{V} so that with equation (9) the Lewis number can be calculated as a function of the residual lifetime.

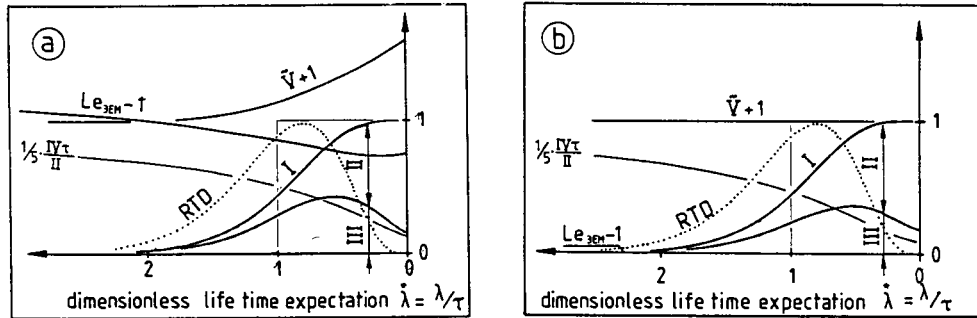


Figure 5 Characteristic functions of the residual lifetime λ . Comparison of the improved 3EM (a) and the standard 3EM (b).

The integration of equation (4) with use of the characteristic values developed in the section above and shown in fig. 5 gives us two examples of a theoretic extinction line. One for the standard 3EM (b) and one for the improved one (a).

The most distinctiv difference between them is their slope for temperatures below ϑ_{Trans} . Above ϑ_{Trans} they are identical.

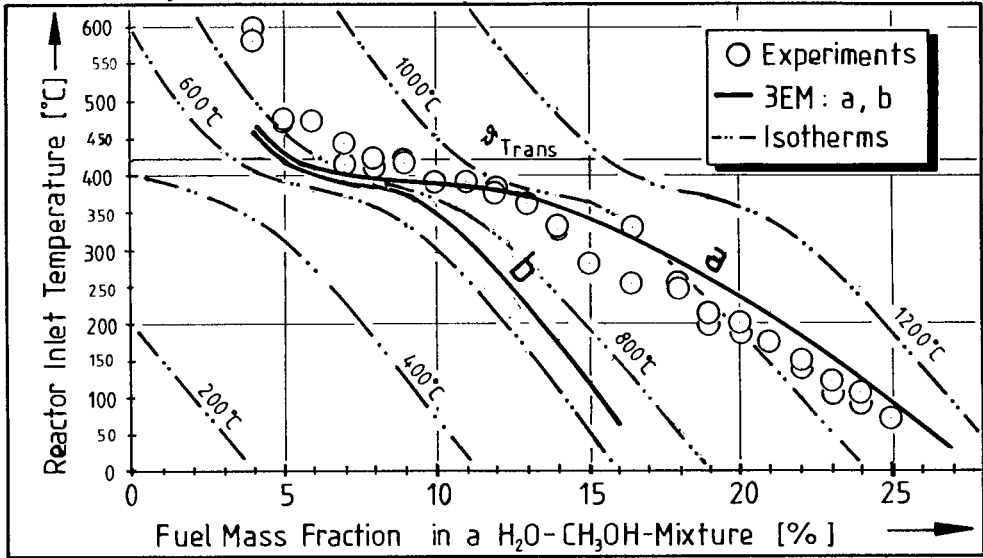


Fig. 6 Comparison of two different theoretical extinction lines with measurements carried out in a reaction vessel shown in fig.1. Kinetic data for eq. 3 are taken from TESTER *et al.* [6]; $A_p = 1.58 \cdot 10^{26}$, $E_A = 408.8$ kJ/mol, $a = 1.0$, $b_{O_2} = 0.0$

Based on the considerations and equations developed in previous sections further simplifications (WEBER [4]) lead to the differential equations (12a) and (12b).

In terms of the adiabatic flame temperature that can be achieved with given inlet temperatures and fuel mass fractions, $T_{fl,ad}$, eq. (12b) represents isotherms, lines of constant flame temperature. A proper interpretation of eq. (12a) may be as follows: Solutions of eq. (12a) are lines of constant flame temperature taking the energy loss from the L.E. to the E.E.'s into account.

From fig. 6 it can be seen that the extinction line of the enhanced 3EM is a solution of the equation (12b) as well as the one according to the standard 3EM, is a solution of equation (12a).

$$\left. \frac{-\partial \vartheta_{in}}{\partial w_{Fuel}} \right|_{\text{extinct}} = \frac{1}{Le_{3EM}} \cdot \frac{\Delta H_R}{\bar{c}_p} \quad ; \vartheta_{in} < \vartheta_{Trans} , \text{ at } \vartheta_{in} > \vartheta_{Trans} : \text{ eq. (12b)} \quad (12a)$$

$$\left. \frac{-\partial \vartheta_{in}}{\partial w_{Fuel}} \right|_{\text{extinct}} = \frac{\Delta H_R}{\bar{c}_p} \quad (12b)$$

4. ANALYSIS OF THE RESULTS AND DISCUSSION

On the one hand the positive correlation between theoretical and experimental results shown in fig. 6 encourages the acceptance of the enthalpy improved 3EM presented in this work as suitable for theoretical analysis and evaluation of future SCWO plants. While, on the other hand, the large number of simplifications might give cause to rigorous investigations and could be the target of severe criticism.

4.1 To what consequences the results may lead

For the reactor inlet temperature to be markedly below 100°C (which avoids the corrosion and plugging problems), fuel mass fractions equivalent to 25% CH₃OH seem to be necessary for the thermal regime of a flame. This value is supported by experiments as well as it is by theory. In a future configuration it can be lowered if the following improvements in comparison to the presented bench-scale reactor are achieved:

- Mass transfer from the cold droplets into the reacting hot ambient (from the E.E.s to the L.E.) must be made as easily possible as heat transfer is. If Le_{3EM} is minimised ($Le_{3EM}=1$) the slope of the extinction line is steepest and hence the fuel content in terms of mass fraction of methanol can be as low as 17%.
- Roughly, an increase of residence time τ by a factor of ten, results in a decrease of fuel content of 1%÷2% provided that all fluid dynamic conditions are kept constant.
- In addition, minimising the heat loss over the whole stabilisation zone results in a displacement of the extinction line in the left direction (towards lower fuel mass fractions). Since cooling causes the heat loss to be minimised, cooling efficiency opposes flame stability.
- The choice of a more suitable kind of fuel might bring an improvement, but because essentially kinetic behaviour is affected, it cannot be predicted quantitatively. Of course, excellent miscibility of water and fuel even at low temperatures (<100 °C) is an advantage and improves flame stability.

4.2 Criticism made to the enthalpy enhanced Three-environment model

The results of the calculations might be in doubt as long as the numerous weaknesses of the model used here aren't removed.

- Different parts of the model have to be connected in a manner that allows for all mutual influences.
- The calculation of all physical properties and of the reaction temperature has to be related to an accurate equation of state in respect to the exact calculations of the reaction equilibrium, so that a connection to the Eulerian system will eventually be made, at least by the interdependence of average density, residence time and the volume of the reactor.
- So far, the dependence of the Lewis number on the inlet temperature wasn't taken into account. Clearly, the functions I to V from the droplet dissolution model depend on the reactor inlet temperature. In future analysis it won't be accurate enough to assume constant functions over a wide range of inlet temperatures as has been done in this work.

Despite these facts it may well be that after all improvements have been accomplished, the results won't be so far from the ones presented in this paper.

5. CONCLUSIONS

With the application of an enthalpy enhanced Three-Environment Model, the progress of the reactor inlet temperature belonging to the event of extinction as a function of the fuel mass fraction of the waste water could be theoretically supported. Correspondence between theoretical and experimental results is satisfactory. The deviation of the extinction line from a flame temperature isotherm appeared to be due to a Lewis number greater than one. If the Lewis number could be lowered, the required fuel mass fraction is supposed to decrease. Experiments with different kinds of fuel as well as modified burner and inlet geometries will either support these theories or give evidence to the contrary.

ACKNOWLEDGEMENTS

The authors owe a great debt of gratitude to the companies *F. Hoffmann - La Roche AG* and *Gebr. SULZER AG* and the KWF ("Kommission zur Förderung der wissenschaftlichen Forschung") for their generous financial support of this work.

LITERATURE

- [1] LA ROCHE, H. LUCAS, M. WEBER and CH. TREPP, „Rationale for the Filmcooled Coaxial Hydrothermal Burner“, *Briefing Book of the 1st International Symposium on Supercritical Water Oxidation*, held on *Amelia Island* Jacksonville, Florida, USA, February 3.-5. 1995, pp. 125-133
- [2] RITCHIE, B. W. and A. H. TOBGY, „A Three-Environment Micromixing Model for Chemical Reactors with Arbitrary Separate Feedstreams“, *The Chemical Engineering Journal*, vol. 17 (1979), pp. 173-182
- [3] NG, D. Y. C. and D. W. T. RIPPIN, „The Effect of Incomplete Mixing on Conversion in Homogeneous Reactions“, *Chemical Reaction Engineering, Proceedings of the 3rd European Symposium*, held at Amsterdam, September 15-17, 1964, pp. 161-166
- [4] WEBER, MARKUS, „Apparate einer SCWO-Anlage und deren Leistungsfähigkeit“, *Ph. D. Thesis ETH Zürich*, to appear 1996
- [5] BEER, STEFAN, „Untersuchung des Wärme- und Stoffaustauschvorgangs zwischen einem unterkühlten Wasserspray und überhitztem Wasserdampf“, *Ph. D. Thesis TU München*, München und Gaisthal, October 1994
- [6] TESTER, JEFFERSON W. *et al.*, „Supercritical Water Oxidation Technology: A Review of Process Development and Fundamental Research“, *ACS Symposium Series*, Paper on *Emerging Technologies for Hazardous Waste Management*, October 1-3, 1991, Atlanta Georgia, MIT EL 91-003, Massachusetts Institute of Technology, Energy Laboratory, Cambridge, Massachusetts

Low Pulsation Design of Piping Systems for High Pressure Reciprocating Pumps

S. Notzon

URACA Pumpenfabrik GmbH + Co. KG
 Sirchinger Str. 15, 72574 Bad Urach, Germany

Since all pressure generators in high pressure process technology cause pressure pulsations in the plant, for a trouble-free operation pulsation reducing measures are necessary.

This paper summarizes different methods of pulsation dampening in high pressure plants, and shows how to control and optimize the effectiveness of damping measures by numerical pulsation analysis.

1. INTRODUCTION

Reciprocating pumps are often used as pressure generators in high pressure process technology. Their main advantages in comparison with other pump types are good control features and energy efficiency.

Like all high pressure pumps, reciprocating pumps provide due to their periodically fluctuating displacement a pulsating flow.

The amount of volume flow fluctuations depends largely on the volumetric efficiency and the number of plungers.

Triplex plunger pumps in which three plungers smooth the discharge flow, are the most widely spread in high pressure applications.

The lower the volumetric efficiency and the higher the number of plungers, the lower the pulsation of the pump.

Figure 1 shows a triplex plunger pump and its flow pulsation at a volumetric efficiency of 95 %. The volumetric efficiency, representing the ratio of the actual volume flow Q to the theoretical flow (equation (1)), depends essentially on the fluid and working chamber elasticity

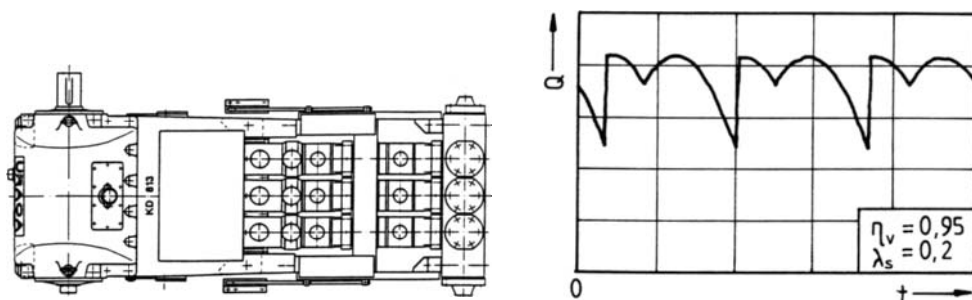


Figure 1. a) triplex plunger pump

b) volume flow pulsation (λ_s = rod ratio)

and the quality of valve action (i - number of plungers, A - cross-sectional plunger area, h - stroke, n - speed).

$$\eta_v = \frac{Q}{i \cdot A \cdot h \cdot n}$$

(1)

The pulsation of volume flow leads to pressure pulsations in the following piping system. Their size depends on the geometry of the piping system and the fluid parameters. The relevant effects on pressure pulsations are summarized in table 1.

Table 1
Influences on pressure pulsations in high pressure plants

Fluid	pump	piping
- density	- volumetric efficiency	- diameter
- velocity of sound	- number of plungers	- length
- viscosity	- speed	- ξ-, λ-values
	- time history of displacement	- branches

Pressure pulsations in high pressure processes are usually undesired and sometimes harmful. The consequences range from vibration excitement of pipes and vessels, over disturbances of measurement and control equipment to fracturing of pipes by low cycle fatigue. Therefore, pressure pulsation need special attention in high pressure piping systems. In many cases pulsation reducing measures, like pulsation dampeners and modifications in the piping system are necessary.

2. PULSATION CONTROL DEVICES

2.1. Pulsation dampeners

Pulsation dampeners work by fluid friction, reflexion of pressure waves and volume elasticity. They represent an effective measure of controlling pulsation.

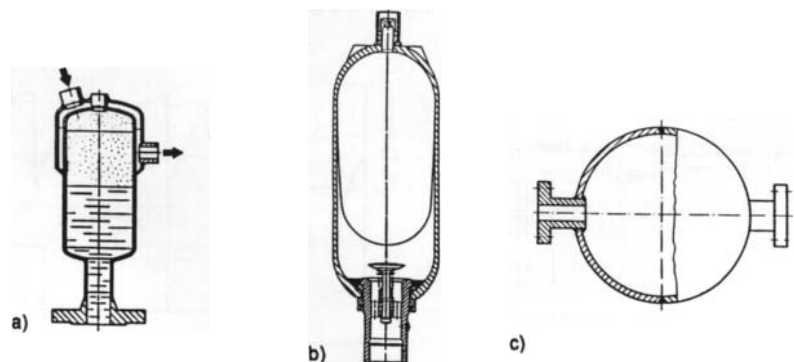


Figure 3. a) gas-filled (head-heated) accumulator b) bladder accumulator c) resonator

Gas-filled accumulators, bladder accumulators and resonators which can be used both on the suction and the discharge side of the pump, are most frequently used. They differ in their quality of dampening, prices and the necessity of maintenance. Bladder type accumulators are limited in use due to the chemical and thermal resistance of the bladder materials inside.

Especially on the discharge side of pumps pulsation dampeners are very expensive. For that reason the attempt to manage pulsation without dampeners is often made. That is sometimes possible, if other kinds of dampening mechanisms can be used.

2.2 Interference of pressure waves

To minimize the pulsation in a plant, two pressure waves can be superimposed with a phase-shift of $\lambda/2$ as shown in Figure 4. If several pumps are in operation (Fig. 4a), it is necessary to synchronize the machines, which can be achieved electrically or mechanically.

Since the synchronisation of pumps is very costly, this procedure has been carried out in only special cases.

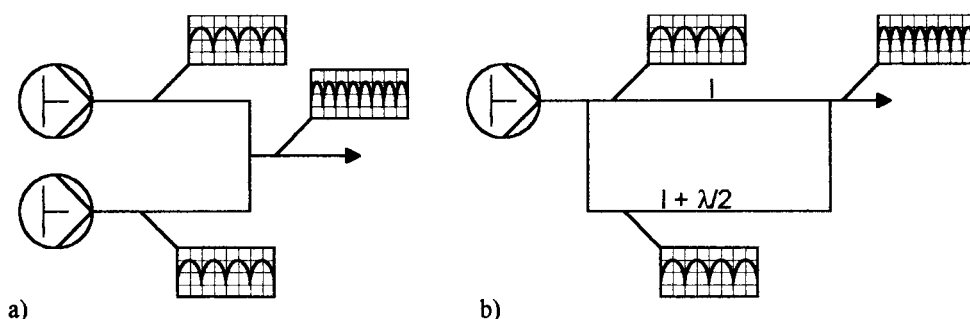


Figure 4. Interference of pressure waves (λ = length of pressure wave)
a) Two pumps operation b) detour-pipe

In the case of Fig. 4b) a detour-pipe splits a wave into two parts and unites it downstream with a phase-shift. The best effectiveness is achieved if the detour-pipe is about half a wavelength ($\lambda/2$) longer than the main pipe.

For slowly running pumps the detour-pipes get very long whereby the applicability of this process is restricted.

A combination of the mentioned methods has often been successful in plants where many reciprocating pumps discharge into the same piping system.

2.3 Orifice plates

Orifice plates are often applied to damp resonant oscillations in existing installations. Their effect is based on frictional losses. Therefore orifice plates shall be placed at pipe positions with a maximum of flow pulsation.

A disadvantage of damping flow pulsations by orifices is the additional pressure loss brought into the system. So the obtainable reduction in pressure pulsation is quite limited.

3. COMPUTER AIDED CONTROL OF PULSATIONS

Modern numerical simulation methods are able to determine pressure pulsations in high pressure plants with high accuracy. Therefore a prediction of pressure pulsations in the planning stage becomes possible and measures for improvements can be taken in time.

Commonly used simulation programs are based on a numerical solution of the one-dimensional classical fluid mechanics equation by the method of characteristics [1-2]. For numerical simulation the piping system is divided in sections with constant cross-sectional areas which are connected by knot-elements.

The pump excitation is modeled by a boundary condition for the flow velocity according to the time history of displacement.

The individual components of the piping system like valves, branches, atomizing nozzles etc. are described by resistance coefficients. Furthermore the modeling of gas-charged dampeners and resonators is possible. The software simulates pressure losses in pipeline as well as radially expansion of pipes due to transition of pressure waves.

In many cases the numerical pulsation study has been proven to be an effective method to minimize pressure pulsation in high pressure plants [3-4].

In the example below a numerical pulsation study was performed to control the effectiveness of the pulsation dampening devices.

4. NUMERICAL PULSATION STUDY OF AN OIL PLANT

4.1 Piping system

Figure 5 gives the flow scheme of a feed oil system. A high pressure plunger pump feeds the reactor with oil at a pressure of about 75 bar. The mass-flow of feed oil is measured by three Coriolis-Flowmeters. The second pump is out of line. The feed oil flow is adjusted by pump speed which is variable in a range of 25 to 110 rpm. Two resonators are used for pulsation damping.

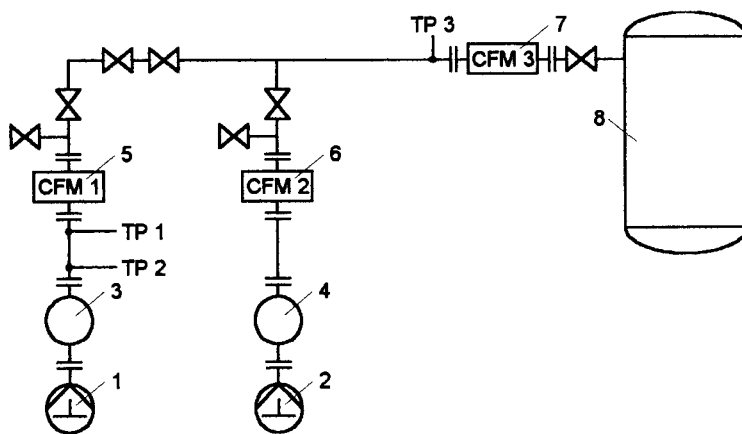


Figure 5. Feed oil system - flow scheme

1, 2 triple plunger pumps
3, 4 resonator

5 - 7 Coriolis-Flowmeter
8 reactor

The allowable pulsation in the plant depends for one thing on possible excitation of the mechanical structure and on the other on the installed Coriolis-Flowmeters (CFMs).

To prevent mechanical pipe vibrations, the pressure pulsation should be less than $\pm 3\%$. Since the CFM is based on the evaluation of mechanical swinging inside the measuring device, it is sensitive to fluid pulsations with high frequencies (> 50 Hz) [5-6]. At frequencies above 50 Hz no appreciable shares of pulsation should be presented.

In relation to the installed CFMs pressure amplitudes have to be lower than 0,2 bar at frequencies above 50 Hz.

4.2 Piping study

To verify the assigned damping measures, a numerical pulsation analysis (piping study) was carried out by "Lehrstuhl für Apparatechnik und Chemiemaschinenbau" of the university Erlangen/Germany. The computer program used (ROLAST) was tested in many verification experiments and returned the existing pressure conditions with high accuracy [5-6]. The piping study was carried out on the following simplifications and assumptions:

- The spherical resonators are represented by a cylinder of the same volume.
- Pressure losses of the resonator are considered by resistance coefficients at the damper outlet.
- Pump 2 is out of service, only pump 1 operates.

The pulsation amplitude for different pump speeds have been computed at three testpoints (TP 1, TP 2, TP 3). The computation indicates, that nearly over the whole speed range the pressure pulsations remain below $\pm 3\%$. At a speed of 45 rpm the pulsation amplitudes pass a maximum which indicates an acoustical resonance (Fig. 6)

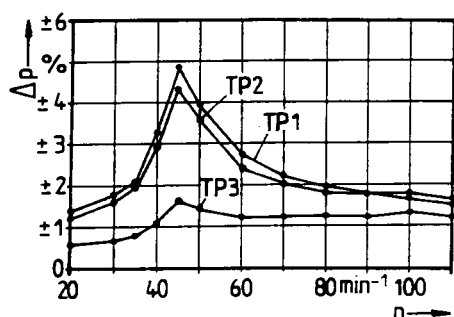


Figure 6. Calculated pressure pulsations in feed oil systems.

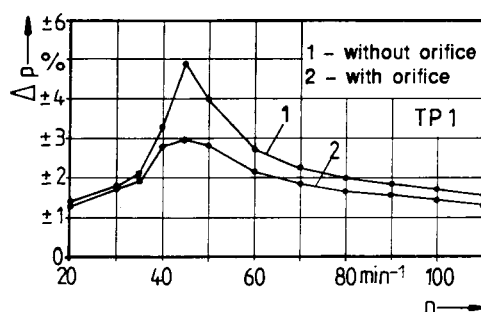


Figure 7. Calculated pressure pulsation with and without orifice plate at TP 1

In case of resonance the maximum pressure pulsations come up to 7 bar or $\pm 4,8\%$ and exceed the specified values. For the nominal speed of 90 rpm a time plot of pressure is shown in Fig. 8a). The spectrum of pressure pulsations at the inlet of CFM 1 shows no appreciable pressure amplitudes at frequencies above 50 Hz (Fig. 8b).

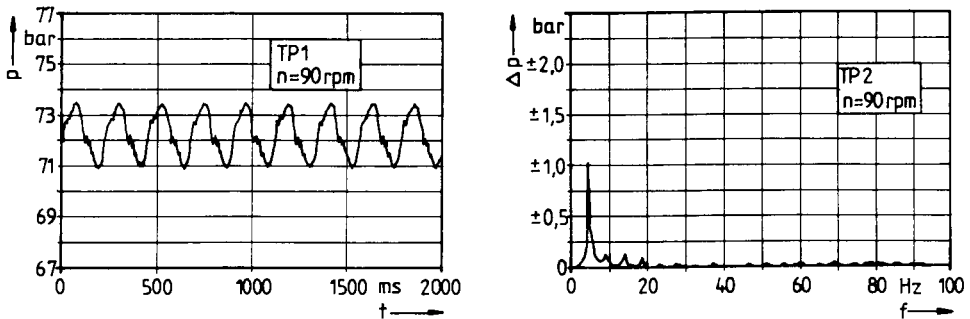


Figure 8. a) Calculated time history of pressure pulsation at TP 1

b) Spectrum at TP 2

Since this fact is valid for all other pump speeds a trouble-free operation of all CFMs will be obtained.

To minimize the pulsation in the plant, a reduction of pressure pulsations by orifice plates was investigated. Therefore an orifice with an inner diameter of 13,5 mm (pipe diameter 80 mm) was placed at the inlet of the reactor. This is the position where maximum flow pulsation arises (open ended pipe).

The result in figure 7 shows, that the orifice plate is able to reduce the pulsation to $\pm 3\%$. At nominal pump speed the orifice leads to additional pressure losses of 2 bar only.

Due to the fact that the pump is rarely used in the range below 60 rpm an additional orifice is not used in this particular case. However, this example shows the ability of numerical pulsation analysis.

REFERENCES

1. Vetter, G., Keller, A.: Druckschwingungen in Rohrleitungen durch oszillierende Verdrängerpumpen. 3R international (1984), 572-581.
2. Vetter, G., Schweinfurter, F.: Computation of Pressure Pulsation in Pumping Systems with Reciprocating Positiv Displacement Pumps. 3rd Joint ASCE/ASME Mechanics Conference, San Diego, 1989, 83 - 89.
3. Vetter, G., Seidl, B.: Pressure Pulsation Dampening Methods for Reciprocating Pumps. Proc. 10th Int Pump Users Symp., Houston TX, USA 1993, 25-39.
4. Seidl, B.: Zur Reduzierung von Druckschwingungen in Rohrleitungssystemen oszillierender Verdrängerpumpen. Dissertation, Universität Erlangen (1992).
5. Vetter, G., Notzon, S.: Effect of pulsating flow on Coriolis mass flowmeters. Flow Measurement and Instrumentation 5 (1994) 4, 263-273.
6. Vetter, G., Notzon, S.: Messungen kleiner pulsierender Flüssigkeitsströme mit Coriolis-Durchflußmessern, ATP 36 (1994) 4, 31-44.

Dyeing of Poly(Ethylene Terephthalate) Fibers in Supercritical Carbon Dioxide

E. Bach, E. Cleve and E. Schollmeyer

Deutsches Textilforschungszentrum Nord-West e.V. (DTNW),
 Frankenring 2, 47798 Krefeld, Germany

1. INTRODUCTION

The supramolecular structure of Poly(ethylene terephthalate) PET can be described as a two phase system with highly ordered crystalline and imperfect amorphous regions which are statistically distributed over the fiber [1-3]. Before dyeing of synthetic fibers the morphology of the fiber is changed by a heat setting process with hot air at temperatures between 160 and 200°C. During this treatment relaxation of the inner tension of the material and crystallization processes in the amorphous regions of the macromolecular structure of the PET occur. Dye-stuff uptake of PET is strongly affected by the crystallinity and orientation of the macromolecules of the fiber. Therefore the diffusion of colour into the fiber is mainly influenced by the amount and accessibility of the free volume of the noncrystalline regions and the intermolecular interactions of the synthetic polymer [4-7].

2. RESULTS AND DISCUSSION

2.1. Experimental

For the examinations three different mono- and multifilament PET-yarns were used. As seen by the effective temperature two of the fibers (220 dtex multifil and 360 monofil) were heat setted in air at 160°C. The experiments in air and supercritical CO₂ were carried out in a 400 ml autoclave, the DSC measurements (Differential Scanning Calorimetry) under pressure in a home-made apparatus with an integrated TA-Instruments calorimeter.

2.2. Melting point and melting enthalpy of PET

Table 1

Comparison of the melting temperature T_m (°C) and -enthalpy H_m (J/g) of PET-fibers under atmospheric pressure at 1 bar in air and in supercritical CO₂ at 280 bar

	air		CO ₂	
	T_m	H_m	T_m	H_m
PET-multifilament 150 dtex	252	54.2	239	33.1
PET-multifilament 220 dtex	258	53.5	244	38.3
PET-monofilament 360 dtex	250	47.7	235	22.0

In contrary to water supercritical carbon dioxide is able to penetrate into the hydrophobic PET-fiber. This was observed by measuring the melting point and the melting enthalpy of PET by Differential Dynamic Heat Flow Calorimetry in air under atmospheric pressure and in supercritical CO_2 at 280 bar. The carbon dioxide acts as a *quasi impurity* by which the melting point of the PET is decreased by 14°C . The results are shown in Table 1.

2.3. Changes in the crystalline structure of PET after treatment in supercritical CO_2

Furthermore the changes in the effective temperature of the three PET-fibers were also investigated by DSC after the treatment of the yarns at different temperatures in air under atmospheric pressure and in supercritical CO_2 during 45 min. The results are presented in Figure 2.

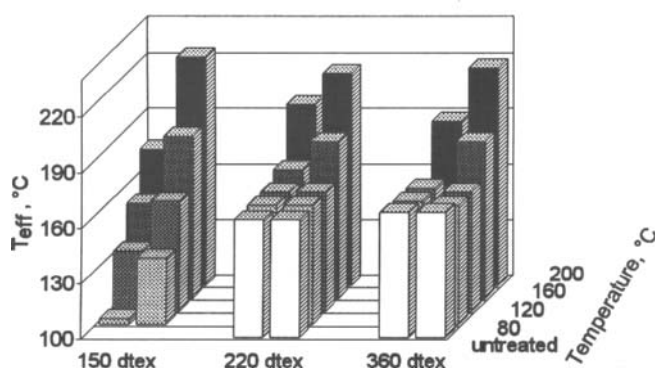


Figure 2. Effect of the process-medium and the treatment-temperature on the effective temperature (T_{eff}) of PET-fibers in air (left hand) and in supercritical CO_2 at 280 bar (right hand).

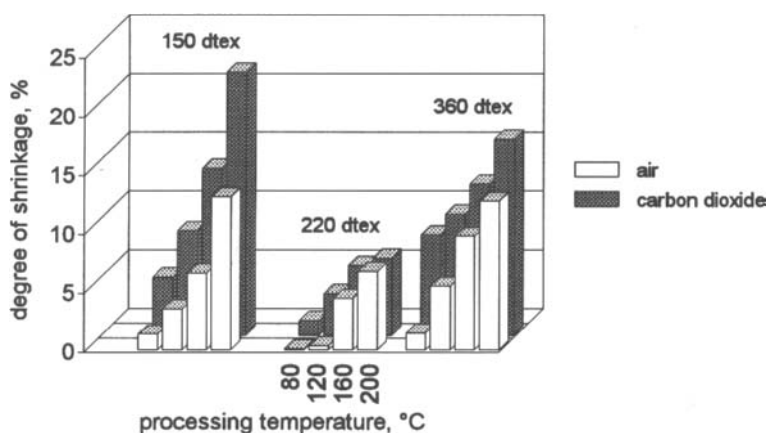


Figure 3. Shrinkage behaviour of PET-fibers treated at different temperatures in air under atmospheric pressure and in supercritical CO_2 at 280 bar.

Structural changes of PET only occur when the material is not heat setted or the processing temperature is near or above the heat setting temperature. The change in the crystal network characterized by the effective temperature is increased by the treatment in CO_2 in comparison to air (Figure 2). This was also found by other authors [8,9].

The shrinkage behaviour of the PET fiber also strongly depends on the process medium as shown in Figure 3. The effect is most distinctive when non-heat setted material was used. The shrinkage of the yarn gives some information about the inner tension of a synthetic fiber and can be explained by a backfolding of the polymer chains instead of a disorientation of the macromolecules [10,11].

As indicated by the decrease of the melting point in Table 1 and the results presented in Figures 1 and 2 the penetration of the carbon dioxide into the PET seems to accelerate changes in the crystalline structure by swelling of the fiber. For PET this effect is also well known with other swelling agents [12,13].

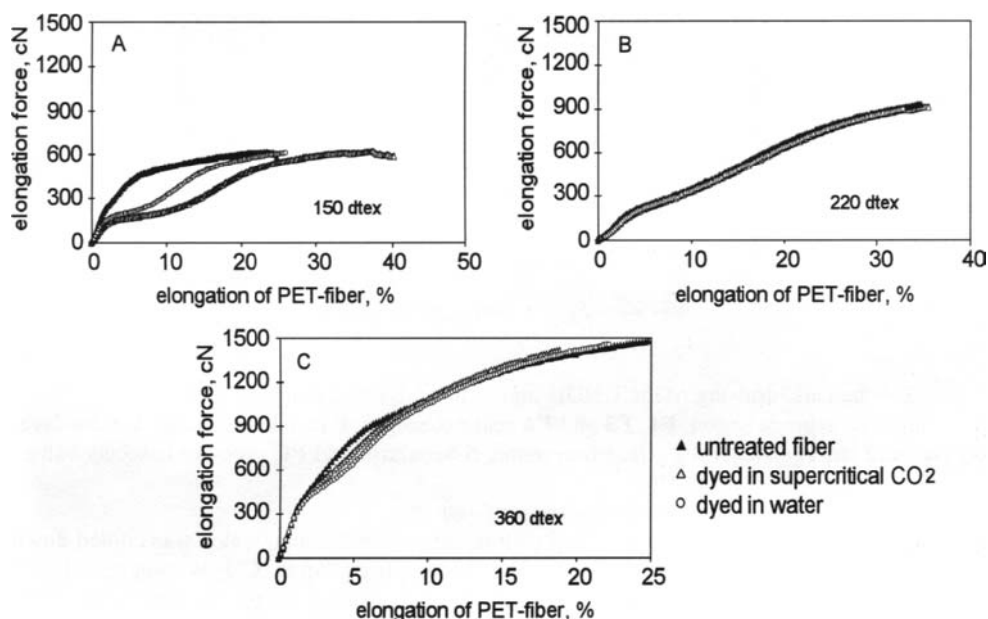


Figure 4. Stress strain-diagrams of PET-fibers dyed in water and supercritical CO_2 at 120°C .

Changes in the structure of PET in the amorphous regions of the fiber are also detectable by viscoelastic measurements [1]. Stress strain-diagrams of non-heat setted PET show a distinctive *shrinkage-saddle* which can be explained by the elongation of tie-molecules in the amorphous regions of the fiber (Figure 4 A). This effect is much stronger in CO_2 than in water at the same dyeing temperature. The width of the saddle directly correlates with the shrinkage of the fiber which was 12.5 % in CO_2 and 9.5 % in water. When heat setted material was used no changes in the stress-strain-behaviour has been observed (see Figure 4 B and C).

2.4. Description of the UHDE supercritical dyeing pilot-plant

Based on the experiences of the DTNW the high pressure engineering works UHDE (Hagen, Germany) constructed a supercritical dyeing pilot-plant with a 30 l autoclave for scaling up of the dyeing process to industrial scale. At the moment the dyeable amount is 3-7 kg PET-yarn per cycle.

A schematic drawing of the machine is shown in Figure 5. Besides the impregnation of textiles with dyestuffs or other soluble components in supercritical CO_2 the UHDE pilot plant can also be used for the extraction of substances from the fibers (e.g. spinning additives, preparation agents, lubricants, coning oils etc.).

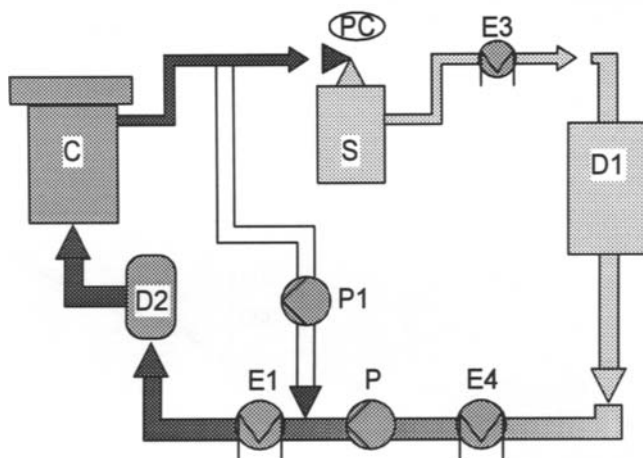


Figure 5. Schematic drawing of the UHDE supercritical dyeing pilot-plant.

D1 liquid CO_2 storage vessel, **E1**, **E3** and **E4** heat exchanger, **P** membrane pump, **C** autoclave, **D2** Dyestuff storage vessel, **P1** circulation pump, **S** Separator and **PC** pressure reducing valve.

The supercritical dyeing pilot-plant is filled with liquid carbon dioxide, which was cooled down in the heat exchanger (**E4**) to make sure that CO_2 is completely liquid. CO_2 is compressed with a membrane pump up to the dyeing pressure of 280 bar. During the pressurizing of the CO_2 the system is heated up (**E1**) to the dyeing temperature. When dyeing conditions are constant, the membrane pump (**P**) is stopped, the dyestuff storage vessel (**D2**) opened and the circulation pump (**P1**) started. The CO_2 -circulation flow was from the inside to the outside of the bobbin without changing the circulating direction. After dyeing the supercritical carbon dioxide is decompressed down to 60 bar (**PC**). In the gaseous CO_2 atmosphere in the vessel (**S**) the dyestuff is insoluble and remains in the vessel. Then CO_2 is cooled (**D3**) down until it is liquid and flows back to the CO_2 -collecting tank (**D1**). The recyclable amount of CO_2 is ca. 90 %.

2.5. First dyeing results obtained with the UHDE supercritical dyeing pilot-plant

The experiments were carried out by using a prewashed PET-multifilament yarn with 32 filaments per bundle and 182.5 dtex. The material has been heat set at 195°C and was dyed with CO2PES MARINE SM1F from Ciba-Geigy (Basle, Switzerland).

The dyestuff uptake and the outside to inside shading of the fiber after the isothermal and isobaric treatment at different temperatures at 280 bar was investigated by measuring the minimum of reflectance at 610 nm of the two bobbins. The higher the dyestuff uptake the lower is the value of reflectance. The bobbin at the bottom of the autoclave in Figure 5 is called bobbin A and the one at the top is named bobbin B.

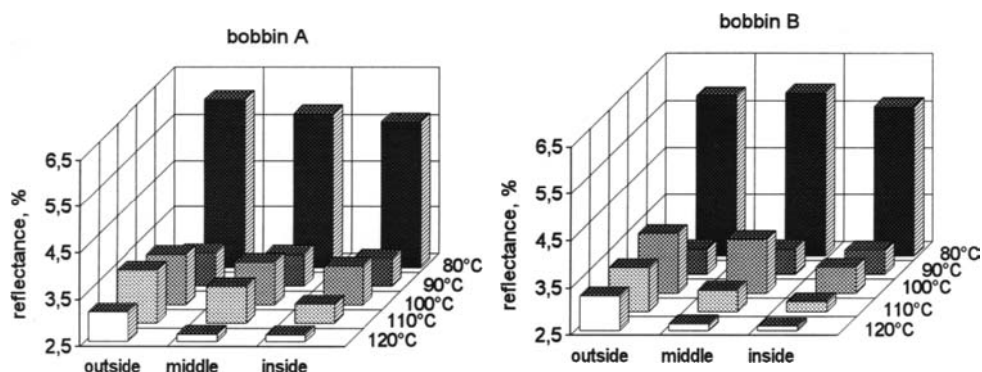


Figure 6. Determination of the outside-to-inside shading of PET-yarn after isothermal dyeing at different temperatures in supercritical CO₂ at 280 bar for 1 h by measuring the reflectance of the fiber at 610 nm.

The best colour levelness is obtained at dyeing temperatures shortly above the glass point of the fiber at 90°C. At higher temperatures the colour strength is much better but with a lack of uniformity. The cause for the outside-to-inside shading of PET-yarn is reasoned in the increasing shrinkage and swelling of the fiber with raising temperatures. The density of the bobbins also increases and acts like a filter for the dyestuff when the circulation direction is from the inside to the outside. The result is a supersaturated fiber in the inside of the bobbin and a shading to the outside.

As seen by fiber cross-sections of PET at low dyeing temperatures up to 100°C ring dyeing effects were observed whereas at 120°C the fiber is completely dyed.

Transferring of these results to an optimum dyeing process starting temperature should be 90°C to obtain an uniform dyestuff uptake and then raising up the temperature to get a completely dyed PET-fiber.

Washing-, rubbing- and light fastness of the dyed PET fibers at different temperatures were also tested. All fastness measurements of the dyed samples with CO2PES MARINE SM1F gave very good results.

2.6. Measurement of cyclic oligomers after dyeing of PET in supercritical carbon dioxide

The solubility of oligomers in supercritical CO₂ which are located at the surface and in the inner of the PET fiber resulting from the spinning process was measured by HPLC with an UV-detector at 240 nm. These oligomers are insoluble in water. In high concentrations they can cause problems during water dyeing because they can precipitate at the surface of the fiber and on the machines [14].

As seen in Table 2 the PET-oligomers - mainly cyclic trimers - are not extracted by supercritical carbon dioxide at dyeing conditions. This was also confirmed by other authors [9]. The surface content of oligomers depends on the dyeing temperature whereas the total amount of cyclic trimers does not change.

Table 2

Content of cyclic oligomers (%) after dyeing of PET in water and supercritical CO₂ as a function of dyeing temperature (°C)

dyeing medium	dyeing temperature	PET-surface oligomers	total content of PET-oligomers
untreated	-	0.02	3.80
water	130	0.01	2.53
CO ₂	80	0.11	3.23
CO ₂	90	0.20	2.96
CO ₂	100	0.38	3.29
CO ₂	110	0.74	3.19
CO ₂	120	0.95	3.14
CO ₂	90-110	0.46	3.18

REFERENCES

1. B. v.Falkai (ed), *Synthesefasern*, Verlag Chemie, Weinheim (1981).
2. S.K. Mukhopadhyaya, *Text. Progress* 18 (1975).
3. H. Batzer (ed), *Polymere Werkstoffe*, Bd. 1, Thieme Verlag Stuttgart (1985).
4. H.-J. Berndt and A. Bossmann, *Polymer* 17 (1976) 241.
5. H.-J. Berndt and G. Heidemann, *Melliand Textilber./Textilber.* 68/105 (1987) 685.
6. G. Heidemann and H.-J. Berndt, *Melliand Textilber.* 57 (1976) 485.
7. G. Heidemann and H.-J. Berndt, *Chemiefasern/Textilind.* 24/76 (1974) 46.
8. D. Knittel, W. Saus, S. Hoger and E. Schollmeyer, *Angew. Makromol. Chem.* 218 (1994) 69.
9. M.J. Drews and C. Jordan, *AATCC Int. Conf Book of Papers* (1994) Res. Frangk Park, NY 261.
10. P.F. Dismore and W.O. Statton, *J. Polym. Sci. (C)* 13 (1966), 133.
11. J.L. Koenig and M.J. Hannon, *J. Macromol. Sci. (Phys. B1)* (1967), 119.
12. H.G. Zachmann and G. Konrad, *Makromol. Chem.* 118 (1968) 189.
13. P. Senner, U. Schwarz, W. Morgenstern and B. Sander, *Melliand Textilber.* 48 (1967) 690, 789.
14. St. Bakardjiewa-Petrowa and R. Naumowa, *Textilveredlung* 17 (1982) 300.

Acknowledgements

We would like to thank Krupp-UHDE GmbH Hagen, Germany for providing the supercritical dyeing pilot-plant, Josef Zimmermann GmbH & Co. KG, Alsdorf-Hoengen, Germany for the special dyeing cones, Ciba-Geigy, Basle, Switzerland for the dyestuff and Hoechst, Bobingen Germany and Neckelmann, Silkeborg Denmark for the polyester yarn.

Also we would like to thank the Minister of Science and Technology of Nordrhein Westfalen for the financial support of our work.

Research with Modular Laboratory and Pilot Equipment in the Field of Supercritical Fluid Processing

R. Sieber and Dr. B. Zehnder

SITEC-Sieber Engineering AG, Aschbach 621, 8124 Maur/Zurich, Switzerland

1. INTRODUCTION

Supercritical Fluids (SF) are known to have unique properties. In several fields of high pressure technology these properties lead to decisive advantages compared to conventional processes.

Apart from fundamental research which mainly is done by universities, R & D groups of different industry branches (flavours and fragrances, pharmaceuticals) have made a great effort in order to find and develop new high pressure applications. This trend is basically forced by the following aspects:

- Replacement of halogenated solvents (e.g. methylenchloride) by physiologically harmless solvents like CO₂ to reduce the economic burden on health services and the environment.
- Development of new products.
- Simplifying of production procedures for instance for the separation of thermolabile, high molecular products.

Since the products and the process steps to which a supercritical fluid process could be successfully applicable are widespread, the demand for high pressure pilot units to check the feasibility arose first of all in the field of Supercritical Fluid Extraction (SFE).

The SFE process has very important economical and ecological advantages whenever low temperature, high selectivity and a simple separation are required. Especially the low process temperature is an important feature for the treatment of natural products.

However, every natural product has its specific characteristics which have to be considered through all process steps, from the harvest to the final conservation and packaging. These characteristics also dictate the process parameters throughout the whole extraction process and consequently also the pattern of the high pressure pilot unit.

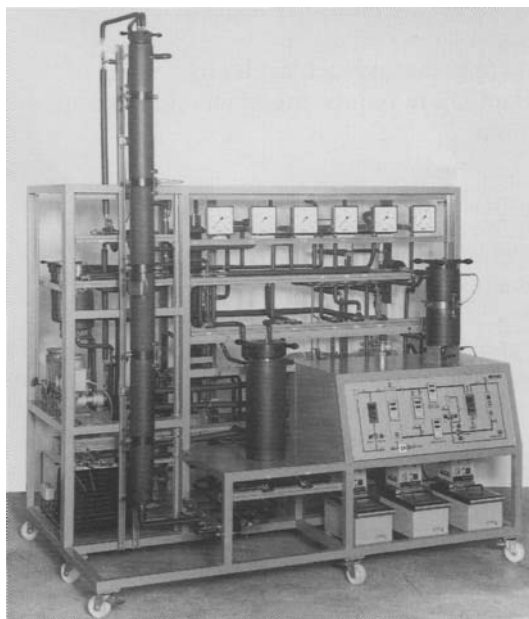
Building supercritical fluid extraction units for an ever growing number of new products it was realized that for laboratory and pilot units only one standard equipment programme was no longer sufficient.

Based on long years of experience with former standard SFE-pilot plants, the SITEC crew started in 1984 to design and develop a modular line of laboratory and pilot plant units. In the meantime, nearly 50 of such units have been built and installed in 14 countries worldwide but all of them have been adapted to the customers' requirements based on these basic moduls.

2. MODULAR LINE OF LABORATORY AND PILOT UNITS

The main aspects which determine the module pattern to be applied are the process parameters, the required process steps including product pre-treatment, extraction and separation, the process enhancements and finally the equipment parameters. The corresponding basic modules and some key components are explained hereafter using current examples of SITEC pilot units built for supercritical fluid extraction purposes.

2.1. Supercritical Fluid Extraction Pilot Units



Picture 1. Multipurpose SFE Pilot Unit (liquids and solids).

The turn-key multipurpose high pressure pilot unit shown in picture 1 can be used for the continuous extraction of liquid products in a column with structured packings and for the batch extraction of solids in a extraction vessel. It is assembled using the following proven basic modules (see also figure 1):

- a. Gas circulation system
(diaphragm metering pump
18 l/h, 30 MPa, 80 °C)
- b. Final separation system
(in liquid gas)
- c. Solid extractor (2 liter)
with quick opening closure
and basket insert
- d. Fluid fluid extraction column
with Sulzer packings
(2 l/h, ID 38 mm, 2m)
- e. Modifier system
(diaphragm metering pump
2 l/h)

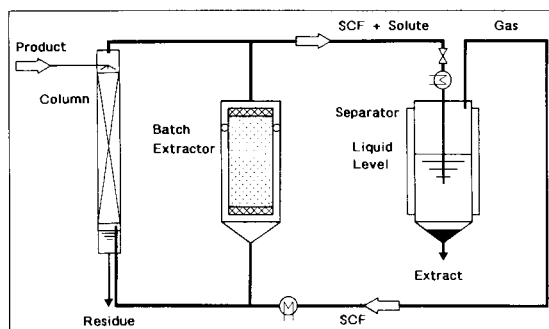


Figure 1. Principle of Multipurpose SFE Unit

The capacities of the extraction vessels, the diameters and lengths of the extraction columns and the pump capacities can easily be varied and adjusted to the product without changing the basic pattern of the extraction unit.

Apart from different capacities of pumps, columns and vessels there are other equipment parameters which have to be chosen in respect to the product or the product group to be treated e.g. the number

and type of separators, the number and arrangement of extractors (parallel, in series or in carousel mode), reflux systems or ex-proof design. A very important tool is the possibility to generate extract fractions using several separators in series. However, depending on the product requirements the separator types have to be chosen carefully because of their different characteristics. The following separators are available as a standard:

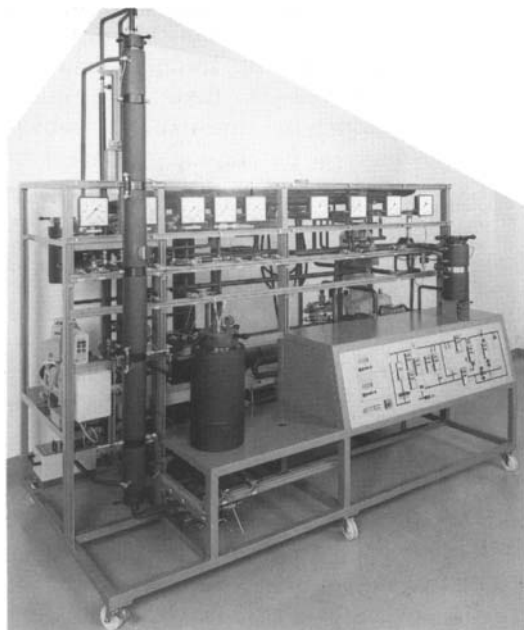
- Vessel with liquid solvent gas: Expansion into the 2-phase region of the solvent gas; used as final separation step; extract can be used as product.
- Adsorption column: Adsorption by activated carbon; used if the dissolved products are wastes (cleaning processes, decaffeination of coffee beans)
- Fluid cyclone: For intermediate separation steps.
- Packed column: For intermediate or final separation in combination with a fluid fluid extraction; the bottom product of the separation column is used as reflux for the extraction column.

Not only the extraction and the separation steps but also the product pre-treatments like grinding, cell-cracking, soaking and steaming etc. influence the extraction process. In addition the yield and the selectivity can be increased using some of the process enhancements listed in the following:

- Modifier or Co-Solvent Systems: Adding a small quantity of a more polar solvent (co-solvent or entrainer fluid) to the solvent fluid in order to modify and adapt the solvent characteristics to the solute.
- Agitators: Magnetic stirrers improve the mass transfer rates, especially with very viscous products where channelling may be encountered.
- Pressure pulsed columns: Increasing of mass transfer rates implying pressure pulses in order to generate microscopic phase changes.

- d. Hydrocarbon Solvent Gases: Propane , butane, ethane and their mixtures with carbon dioxide increase the solvent power for non polar components but require an ex-proof design.

Since the basic moduls as well as these process enhancements are standardized it is easy to prepare a unit for the RETROFIT of additional options like co-solvent systems, additional inbtermediate separators, columns, extractors or a data acquisition system. The flexible design as well as the possibility to prepare the unit for the RETROFIT of options which might be interesting in future are important advantages for everyone who is in charge of R&D.



Picture 2. Multipurpose Pilot Unit prepared for RETROFIT of an additional extractor.

The phase equilibria unit shown in picture 3 is a useful completion for the SFE pilot units. It is built for measurements and detection of phase equilibria and phase transitions by optical and analytical means. The picture from the optical cell is transmitted through the sapphire windows by the directly connected camera system and is displayed on the monitor in the front panel. Whenever samples are drawn out of the cell the directly connected counter-balance piston moves , thus keeping the pressure in the cell constant even during sampling operations.



Picture 3. Phase Equilibria Unit.

Using such a phase equilibria unit, the feasibility of a separation process can roughly be checked and promising process conditions evaluated with only small amounts of educts before running tests with the SFE pilot unit. This will drastically reduce experimental costs.

2.2. Pilot Unit for HP-Micronization and -Spray Drying

In the last few years, an increasing trend towards new high pressure applications could be observed in R & D, all of them in a certain way taking advantage of the remarkable properties of fluids at near critical or supercritical conditions. At the same time the demand for high pressure pilot units for these "new" applications like Supercritical Fluid Reactions, HP-Micronization, HP-Spray Drying and HP-Sterilization increased. In order to also supply customized

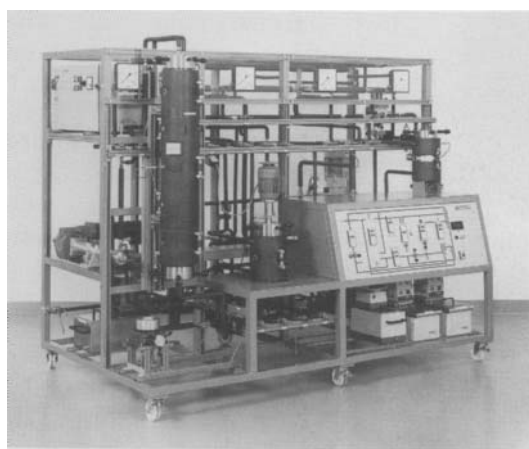
pilot units for applications in these emerging fields, SITEC has adapted basic modules or designed new modules for these applications.

The multipurpose high pressure pilot unit in picture 4 is built for HP-Spray Drying, HP-Micronization and for SFE of solid products. As can be seen on the corresponding flow sheet (figure 2), the CO₂ circulation system and the separation module are exactly the same as in the multipurpose SFE unit. However, the column and the product pump had to be adapted to the requirements of the "new" application.

In order to get a defined spraying condition the pulsation-free feeding of the liquid product is very important. Therefore the unit is equipped with a servo motor driven metering pump which allows to accurately adjust and control the liquid product feed and operates without any pulsations.

Another key component is the spray nozzle which basically has to fulfil the following criteria:

- a. small but well defined spray pattern due to limited inner diameter of HP spray columns



Picture 4. Multipurpose Unit for HP-Micronization and Spray Drying

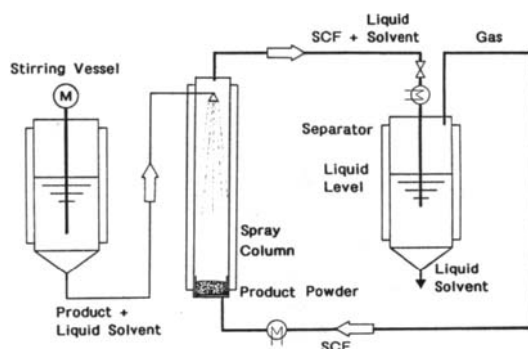
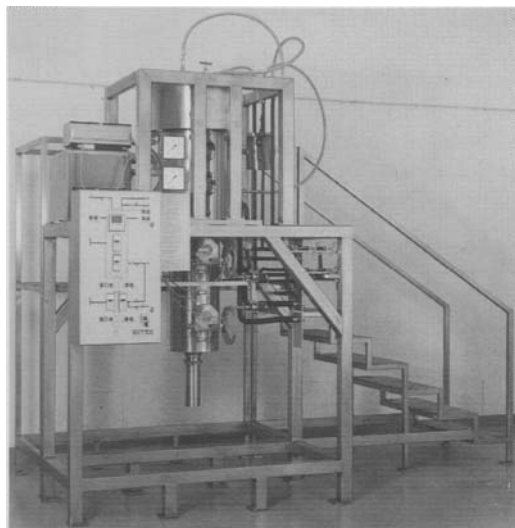


Figure 2. Principle

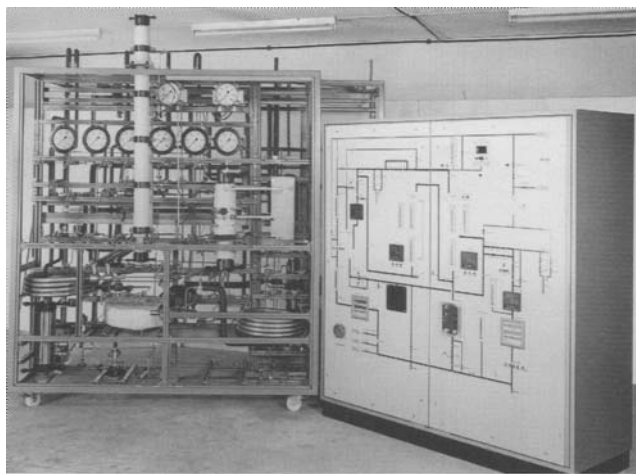


- b. easily exchangeable
- c. small orifice due to the small volumetric flow in the spray drying mode.
- d. high shape stability

The SITEC nozzles consisting of a nozzle holder and exchangeable diamond nozzle pellets excellently fulfil all these requirements and thus allow a fast investigation of the influence of nozzle geometry on the product shape and size.

Picture 5. Pre-Production Spray Column Module for HP Spray Drying with semi-continuous discharging of solid product.

2.3. Pilot Unit for Reactions in or with Supercritical Fluids



Picture 6. Pilot Unit for continuous HP-reactions in or with supercritical fluids using different fixed bed reactors with external recirculation.

3. CONCLUSION

SITEC has successfully developed a modular design for high pressure pilot units which now drastically reduces engineering cost but nevertheless is flexible enough to adapt such units to the researcher's specific requirements.

High Pressure - Process - Diaphragm Pumps Application and Technical Requirements

E. Schlücker and W. Horn^a

^aLEWA, D-71229 Leonberg, Ulmer Str. 10

1. INTRODUCTION

High Pressure Process Diaphragm Pumps (HPDP, Figure 1) are proven as a reliable solution for the pumping of different fluids in all areas of the chemical industry and the process technology. Because of the robustness and diaphragm preserving hydraulic drive, maintenance cycles of a year of continuous operation is the rule, exempting abrasion problems in the valve area. With toxic, aseptic and abrasive fluids the diaphragm pump technology is obligatory in any case. The safety philosophy "sandwich diaphragm" is mandatory for the process technology.

The present essential aspect for the decision in favour of a Diaphragm Pump is its hermetical tightness, which is guaranteed by its stationary and therefore free of wear clamping area. The Diaphragm Pump is the only type of reciprocating pump where the dynamic sealing is not in contact with the fluid.

Because of its larger main dimensions and due to the diaphragm drive and safety device, the Diaphragm Pump is more costly than the traditional Plunger Pump. Saving of maintenance and repair costs are nowadays even more difficult to evaluate because of the hermetic sealing. Therefore often only the existing requirements or problematic fluids motivate the deciding factors in favour of a Diaphragm Pump. But there are a lot more positive aspects.

2. INTEGRATED PRESSURE RELIEF VALVES (PRV)

The mere analysis regarding the price or functional -oriented performance does only make sense, as long as the pump is considered as an isolated unit for a purely functional delivery flow. This aspect however has to be abandoned later on when the pump is regarded as a part of a system.

High-class Hydraulic HDP are generally equipped with a design approved PRV on the hydraulic side. This provides a safety device against overpressure in case the HDP is the only pressure increasing unit in the system.

The PRV assumes the function of a safety valve. When the system pressure exceeds the set pressure then the hydraulic fluid will escape to the hydraulic reservoir via this valve.

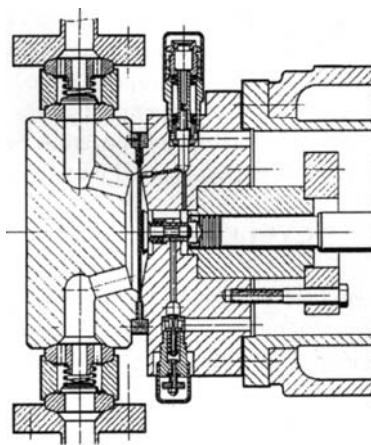


Figure 1: Process Diaphragm Pump Head with PTFE Diaphragm

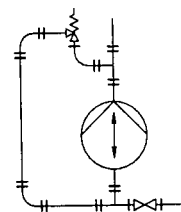


Figure 2: Safety-Valve-Bypass of a Plunger Pump

The minimal alternative to the PRV is an installation on the fluid side as shown in Figure 2. This system has to be designed in compliance with the maximum pressure and will already increase the installation costs noticeably. Perhaps the effort will have to be multiplied in case a return pipe to the suction vessel is necessary. Furthermore, safety valves in contact with the fluid are rather problematic. Since the entire system pressure has to be reduced solely at the sealing of the safety valve, damages and resulting maintenance costs occur often, even after only one opening function. Fluids with solids, melts and adhesive fluids are rather difficult or even impossible to be properly sealed on the fluidside. This leads to expensive solutions such as a combination of a rupture disk and safety valve. The safety valve on the fluidside will be a hazardous spot in case of dangerous returnflows of toxic fluids from a reactor vessel.

The Process Diaphragm Pump therefore integrates already an important part of the system.

3. LIFE CYCLE COST

The bare evaluation including the additional effort for the installation, which shows the Plunger Pump in a better light than the Diaphragm Pump, is only done for price or functional reasons however this is not sufficient. The design of industrial plants requires more and more to consider also the entire expenditures for ecology and lifetime reasons. Not only are the basic initial investment costs decisive for the purchase, but also the total assessment of all life cycle costs inflicted within the lifetime of a pump. The life cycle costs are defined by the actual costs for a definite time of operation f.e. 10 years. These costs include the purchase, installation, energy consumption, maintenance, repair and removal. The above mentioned use of integrated safety valves for the protection of the system is widely done by engineering companies and producers. The system of course also includes the drive and all primary and secondary safety devices, such as protection against dry running, (the PDP is absolutely safe against dry running), and supervision of the flow and temperature. A comparison between an industrial PDP and a Process Plunger Pump relevant to the maintenance costs is shown in table 1.

	PDP	3-Plunger-Pump
Pump type and size	Diaphr. pump ca. 12 m ³ /h, 150 bar	Compareable 3-plunger pump
Investment cost	approx. 350.000,- DM	approx. 180.000,- to 220.000,- DM (50%)
Spare parts per year	no	est: 24.999,- DM (3 parts x 8.000,- DM)*
- plunger	no	est:: 12.000,- DM (3 set x 4.000,- DM)*
- plunger sealing	approx. 1.500,- DM (3 sets x 500,-)	no
- diaphragm	estimation 8.600,- DM (6 set)	estimation 8.600,- DM (6 sets)
- valves		
Maint. costs per activity	proposal: 8 h ≈ 1.600,- DM	proposal: 24 h ≈ 4.800,- DM
Maint. costs per year	approx. 11.700,- DM	approx. 49.400,- DM
After 3 years	approx. 35.100,- DM	approx. 148.200,- DM
Investment costs after 3 years nearly equal.	approx. 350.00,-+ approx. 35.100,- = 385.100,- DM	approx. 220.000,-+ approx. 148.200,- = 368.200,- DM
Additionally: energy costs plunger lubrication syst. leakages	⇒ lower; approx. 2000,- DM/year ⇒ no ⇒ no, hermetical system	⇒ high - due to friction in the plunger sealing ⇒ very often, periodic maintenance. ⇒ leakage !!!!

Table 1: Comparison of investment and maintenance costs of a plunger and a diaphragm pump for methanol:

* optimistic; usual: non-lubrication fluids 2 or 3 sealings per year

Required was a pump for 12 m³ Methanol per hour against 150 bar. Methanol is a non lubri

cant and therefore the sealing and plunger of a Plunger Pump shows wear, in spite of additional lubrication. Based on experience, maintenance cycles of a year may be assumed for the diaphragm (usual) and likewise for the plunger of the Plunger Pump (very optimistic) and the valves, which will be the same for both. The listing of the investment costs and all resulting maintenance costs show the PDP to be more favourable (Break even point: 2-3 years).

This evaluation does not consider the advantage of the hermetical sealing, the system's safeguarding ability of the PDP and the fact that hydraulically actuated Diaphragm Pumps are saving energy due to their better overall energy efficiency.

A similar evaluation relevant to the comparison of efficiency and resulting energy costs with high speed centrifugal pumps, gives a clear indication in favour of the PDP. In a particular case of application, based on an energy price level of 0.12 DM/KWh, the break even point has been reached already after one and a half years.

The PDP under the given conditions represents an economical solution even though when leak tightness is not explicitly required. The use of Diaphragm Pumps is consequently a reasonable step in the direction of the world wide discussed "sustainable development".

4. TREND FOR INCREASED FLOW RATES

An increasing number of plant engineering companies are aware of the importance of life cycle costs and therefore require, together with the pump quotation, an additional cost proposal for a complete pump system. This trend is indicated by an increased demand for Diaphragm Pumps in particular for higher flow rates. Even ten years ago the maximal required flow rate for Triplex Pumps of unit construction has been approximately 50 KW. Today there are units available with nearly ten times the power.

This step of power increase could not be accomplished satisfactorily with a larger number of gear box elements - because of the higher maintenance costs - or simply by a scale up of the individual pump element - due to the very large power dimensions, the couplings, the resulting noise emission and the effect on the entire installation. This was the reason for the development of Triplex PDP. The possible achievement of larger flow rates, high pressures, ultimately calls for a well qualified design according to the high pressure requirements and production which is based on modern calculation and manufacturing processes.

5. MODERN TRIPLEX PROCESS DIAPHRAGM PUMPS

Modern PDP are high grade investment items with a number of ambitious requirements:

- High diaphragm life time
- Sturdy gearboxes and drives
- Costwise favourable highpressure designs
- Reliable valve design for large flow rates
- Low noise emission
- No initiation of vibration - requires calculation of vibration
- Increased requirements relevant to the safety of operation (1 year continuous service without maintenance)
- Consideration of individual properties of fluids.
- Fully compliance with the law to the protection of machines (Transport and operation)
- Components for process automation
- Prevention of costly damages
- Early monitoring of damages
- Large range of flow rate control
- High efficiency of energy consumption
- Explosion proof enclosures
- Thermo safety protection devices

As examples for the requirements the specialities of the valves and diaphragm are described.

5.1 Safe Diaphragm Technology

The diaphragm is the central element which determines the whole pump head design and its size. PTFE diaphragms are predominantly used - for higher pressures metal diaphragms, and for special designs elastomeric diaphragms (Table 2).

Diaphragm material	PTFE	METAL	ELASTOMER
Realized pressure range	up to 350 bar	2000 bar	up to 1000 bar
Realized temperature range	- 20 to 150°C	- 20 to 200°C	5 to 80 °C
Chemical stability	++	++	-
Material-Effect on design	V large, D small	V small, D large	V large, D small
Realized diaphragm shape	plane parallel & corrugated	plane parallel	plane parallel

Table 2: Diaphragm material and range of applications, ++ resistant against almost all fluids, - resistant in a few cases, V - deflection, D - main dimensions of pump.

The best shape of PTFE diaphragms with extreme reliability are being developed at the present time [1, 2]. Apart from the diaphragm shape the diaphragm clamping plays an outstandingly important part. The compression at the clamping area has always to be noticeably above the pressure against which it has to be sealed, and should be static.

For the usual pressure range with *metal diaphragms*, this can be reached by a compression of 70% up to 100% of the yield strength (Figure 3a). However basically the compression has to be within the range covered by the uniaxial stress strain area. The clamping area should be designed in such a way that a transversal contraction and flow of the material is avoided. Consequently, small clamping areas are preferred, since too wide clamping may result in a non-uniform distribution of the compression. Untightness and early fatigue is the result.

PTFE requires a sealing compression which is noticeably above the stress strain diagram (Figure 3b). A reliable sealing is only possible by using special labyrinth geometries matching the PTFE features.

The requirements, relevant to the clamping geometry, are basically increased with the enlargement of the components. Increased diameters result in higher dynamic bending of the cover. This causes an increase of unfavourable micro motions which may result in diaphragm fatigue or leakage. Remedy is only possible by choosing the best design of the clamping area which is closely related to the diaphragm material, and assures that the diaphragm withstands all deformations.

5.2 Reliable Long Life Pump-Check-Valves

With respect to the geometrical scale up there is a linear relationship between the required flow rate and the cross sectional area of the valves. Relevant to the valve diameter, the mass of the valve part is increased nearly by power 3. This results in an increase of the closing energy, as well in the 3rd power, and the danger of a dramatic growth of the noise emission and wear at the valve sealing geometrie. To meet the low noise requirements and low life cycle costs modern valves are designed with a low closing energy. With the help of the Finite Element Method, mass improved valve bodies,

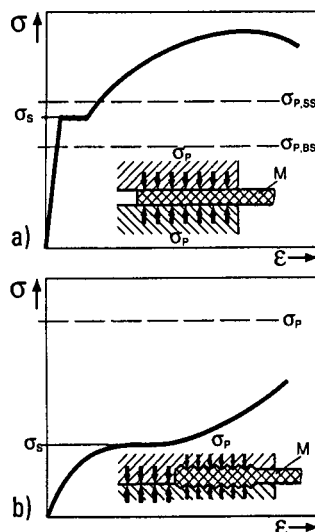


Figure 3: Clamping-Stress σ_p compared with stress-strain-curves: a) metal; b) PTFE; ϵ strain, M diaphragm, BS steel, SS stainless-steel

reliable wear free contours of the sealing area and optimal spring-characteristics (also important for NPSH-values) are essential features of modern valve designs. About 90-95% of all applications are satisfied successfully with conical or crowned sealing geometries and a high variety of rigid, elastic or hardend valve materials. The material has to be choosen with respect to individual operating conditions, to minimize the wear of the valves parts.

Principially the closing action of a check valve may be divided into three stages (Figure 4a): In the *first accelerating phase (I)* the closing body is leaving the upper dead point induced by force of gravity and/or spring induced power. In the *damping phase (II)* the valve body gets decelerated due to fluid layers. In the *impact phase (III)* the closing body is decelerated to zero through elastic deformations by the sealing area. The energy which appears in the sealing area at this time is the kinetic energy at the end of phase II and is following the formula: $E = 1/2 m v_2^2$

The larger the specific energy applied to the sealing area, the larger is the wear of the valve ($\sigma = f(E)$).

An effective damping of the end positions is obviously reducing the wear of valves to a high degree. Possibilities for the damping of the end positions are:

1. Damping by fluid viscosity / jamming soft particles,
2. elastomeric auxiliary sealing,
3. elastic or mass improved valve parts.

The possibility 1 is determined by the fluid and normally not influential but effective. The use of elastomeric sealings often fails because of their limited chemical stability. Therefore elastic and mass improved valve bodies (combined with optimal springs) are the best and universal solution.

A lengthly discussed subject in connection with valves is the material. The first reaction as an answer to increased wear of valves is the use of hardened materials. That 'hardening only' does not necessarily lead to an improvement (Figure 4b). Based on the fact that there is the same compression between the valve closing body (SK) and the valve seat (S) a triangle diagram which consists of the local elastic deformation characteristics is proposed. The kinetic energy at the beginning of the impact phase has to be fully absorbed by the material and therefore corresponds to the hatched area. The size of the deformation results in a typical compression σ . Since more rigid materials (h) have an increased Youngs modulus, the sum of $\epsilon_{SK} + \epsilon_S$ is smaller, but at equal springs and masses the energy input (area of the triangle) remains unchanged. That means that more rigid materials create, most of the time, higher compressions in the sealing area. The correlation is approximately linear: Double Young-Module produces a compression stress that is approximately twice as high. Therefore the use of more rigid materials which are far more expensive, only make sense, if the ratio $\sigma_{admissible}/\sigma$ is increasing. Experiences with Methanol confirm this. Thungsten carbide valve parts have shown wear of the valves (outbreaks) after a short running period. In this case, with valve

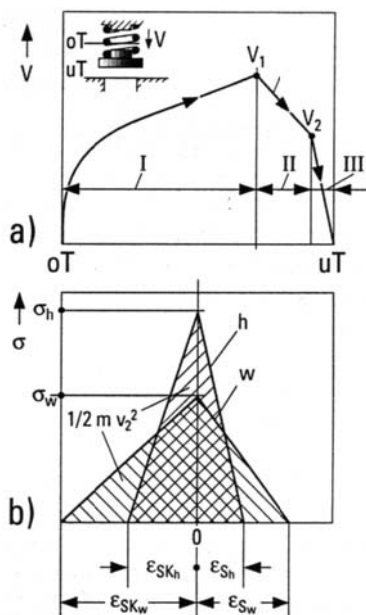


Figure 4: Valves: a) closing velocity of the valve (v); b) sealing-stress (σ) and strain (ϵ) in the closing area, h rigid material, w soft material; v_1 max. velocity, v_2 impact velocity

parts made of high strength steel, however, satisfactory running periods and low life cycle costs were accomplished.

These statements are only valid as long as there are no abrasive particles in the fluid. If abrasive particles are jammed into the sealing area, the only predominant facts are the difference of hardness between the sealing area and the particles. The best economical solution therefore, in this case, is to use expensive hard and most rigid materials. Experience with silicates and Ranney-Nickel etc. confirm this. Finally by installing valve parts of Silicon-Nitride or Tungsten Carbide it was possible to achieve quite acceptable life cycle costs.

6. EXAMPLES OF TRIPLEX PROCESS DIAPHRAGM PUMPS

The following shows a small selection of realized projects where the DPP was the only economical solution and which also assure that this technique is universally usable.

A) Example for Process Diaphragm Pumps with PTFE Diaphragm

Requirements	Design
<ul style="list-style-type: none"> Fluid Al-Alkyl (pyrophoric) Flow rate 9500 - 37720 l/h Discharge pressure approx 90 bar Suction pressure 4 - 8 bar Vapor pressure 1.05 bar Viscosity 2.44 mPa s Velocity of Sedimentation 0.6 m/sec Solids % 13 Drive Steam turbine 	<ul style="list-style-type: none"> PTFE Diaphragm in Sandwich design Drive by steam turbine Valve material SS 316/Ferrotitanium Temperature probe and liquid level switch in the hydraulic fluid Stroke frequency 46 to 184 s/min Shock absorber on discharge Pulsation damper on suction and discharge

B) Example for a Process Diaphragm Pump with Metal Diaphragm

Requirements	Design
<ul style="list-style-type: none"> Fluid : Lecithin Water Mixture with Agent Flow rate: 1.3 m³/h Density: 1 Kg/cm³ Viscosity: approx 1 mPa s Operating temperature: 65 °C Flushing temperature: 25 °C 	<ul style="list-style-type: none"> Sterilization temperature: 125°C Pressure: 1000 bar / 800 bar Suction pressure: 7 bar due to suction piping Drive: Water cooled three phase current motor with frequency converter Required design: Low pulsation without pulsation damper

Design
 CIP - capable pumpheads for sterilizing with hot water or steam. Pumphead design with minimum dead space (high volumetric efficiency) without front back up plate liquid end (easy to clean). Splitting of flow rate with two Triplex Pumps which have been electronically synchronized in a way that the hydraulic pulsation corresponds to a pump with 6 heads This made it possible to comply with the requirement to use no pulsation damper and to still achieve a very low remaining pulsation at the homogenizing nozzle. The synchronizing system consists of two frequency converters for both machines, two absolute reliable speed transmitters with very high resolving power and a micro range adjustment controller that ensures the proper shifting of the cranks which has to be maintained. The short and most frequent cycles of sterilization and the resulting phases for cooling down and heating up between 25 and 125°C are very efficiently accomplished by a heating system very closely located near the liquid end of the pump and controlled by a temperature probe.

REFERENCES

- [1] Schlücker, E.: „Zur Optimierung kreisrunder Plastomermembranen für oszillierende Verdrängerpumpen“, Dissertation, Universität Erlangen-Nürnberg, 1994.
- [2] Vetter, G.; Schlücker, E.: „Diaphragm Development Trends For Safe Leakfree Reciprocating Process Pumps“, Pump User Symposium, Houston USA, 1995.

Hermetic canned motor centrifugal pumps in high-pressure processes

R. Krämer and R. Neumaier
HERMETIC-Pumpen GmbH
D-79191 Gundelfingen / Germany, P.O. box 1220

1. INTRODUCTION

Continuous product flows under high-pressure conditions ($p > 30$ MPa) can only be achieved with hermetic centrifugal pumps. Although the two drive systems that can be used - the permanent magnet coupling and the asynchronous canned motor - have the same mode of operation, they differ in their applications and their safety ranges.

Whilst the canned motor only exhibits a slight loss of efficiency as internal pressure loading increases, the efficiency of the permanent magnet decreases approximately as the square of pressure load. This is why canned motors have won preference over magnetic drive couplings for centrifugal pumps in high-pressure systems and are now used almost exclusively. They can also be used in pumps for transportation of both high-temperature fluids and suspensions.

2. THE MODE OF OPERATION OF THE CANNED-MOTOR CENTRIFUGAL PUMP

The pump and motor are directly combined to form a unit (Figure 1), such that no drive shaft passes through the pressurised casing. A diaphragm known as the 'can', which is integrated into the motor between the stator pack and the rotor, represents a static atmospheric seal and separates the rotor compartment from the stator compartment, such that levels of sealing of $< 10^{-6}$ mbar l/s are achieved. Eighty to ninety-five percent of the motor's heat, depending on the ambient temperature, is carried away by a secondary flow which is taken directly from the flow product on the pressure side, then passing through the rotor/stator gap to the suction side [1].

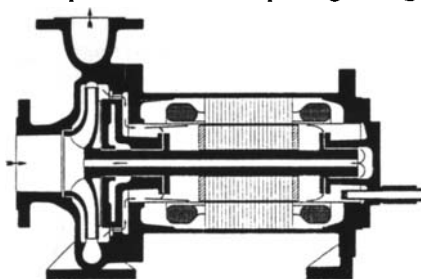


Fig. 1 Operating diagram of a canned motor pump.

3. CANNED-MOTOR CENTRIFUGAL PUMPS IN THE HIGH-PRESSURE RANGE

The versatile drive system of the asynchronous canned motor has set fresh yardsticks for centrifugal pumps operating under high-pressure conditions. The operating limits for pressure, temperature and toxicity of the flow product have been extended by some orders of magnitude. This is the logical result of the response to heightened safety & environment requirements, and means that technical processes can now be implemented for the manufacture of new products.

4. THE CANNED MOTOR UNDER HIGH-PRESSURE CONDITIONS

It is required in the interests of economy that the power requirements of high-pressure pumps should be no worse than those of ordinary canned-motor pumps. In order to minimise electrical and magnetic losses, it is appropriate to utilise cans with the thinnest possible walls. On the other hand, there is the requirement for mechanical strength in the context of high internal pressures and corrosive removal of material. At present, cans are usually made with a wall thickness of 1 mm, using stainless steel or a high-nickel alloy such as to guarantee the required corrosion-resistance over a foreseeable period. This leaves us with the problem of absorbing the high internal pressures.

The stator pack can be modified such that it contributes to transfer of the pressure loads on the can to the stator casing. The necessary steps are as follows:

- I. Modification of the punch section configuration by routing of the grooves for guidance of the copper wires towards the outer periphery such as to accommodate round-section bars for groove wear such that the winding is subjected to no pressure loading (Figure 2).

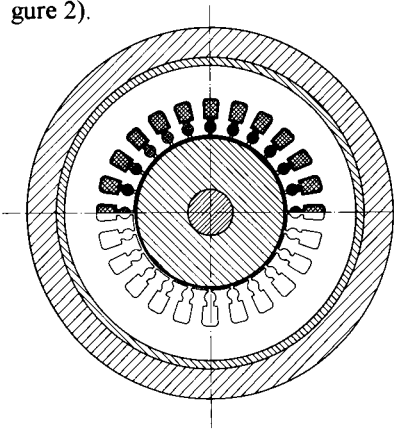


Fig. 2.1 Punch section of a canned motor for system pressures > 90 MPa

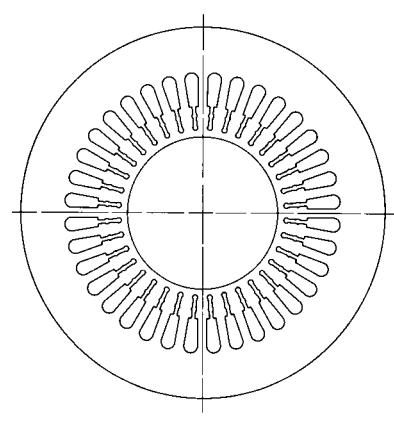


Fig. 2 Punch section of a canned motor in high-pressure specification for system pressures up to 90 MPa

The groove wear bars must be made of a non-magnetic material with a high mechanical load-bearing capacity, so as to cause no additional losses [2]. The remaining groove ends between the can and the round-section bars are given a filling of incompressible, cured potting resin such as to guarantee transfer of pressure loads over the whole range of the circumference. Punch sections of this type are used for internal pressures up to 90 MPa. At a higher pressure loading, the base of the groove undergoes wear as illustrated in Figure 2.1. The routing of the guide grooves for the copper wire produces a reduction in motor output power which can be compensated by increasing the proportion of copper.

- II. Compartmentalisation of the punch sections on the outer and inner supports in order to prevent kinking of the stator plates (Figure 3).
- III. Attachment of reinforcement rings on the outer periphery of the can in the area between the stator pack and the two motor sealing covers (Figure 3). This is where we exploit the extra space gained by the way the groove has been routed. The supporting rings must be made of non-magnetic material and must have a high electrical resistance.

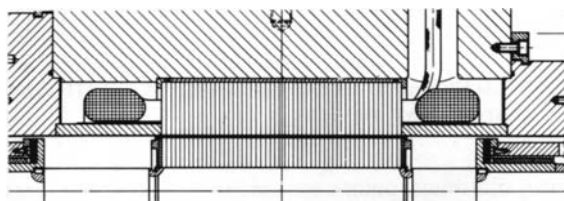


Fig. 3 Compartmentalisation and support of the stator pack

4.1 The stator casing of the canned motor

In order to achieve a favourable load curve, the stator casing is mostly made in the form of a thick-walled hollow cylinder as a semi-finished forging of material C22.8 (as per VdTÜV 350) for temperatures up to 350°C or an austenitic stainless steel. Its cylindrical construction makes it easy to calculate the load curve as described in the AD data sheets (Figure 4). The add-on components, the spacer with the pump casing and the motor sealing cover are bolted to the motor by means of concentrically arranged high-pressure expansion bolts.

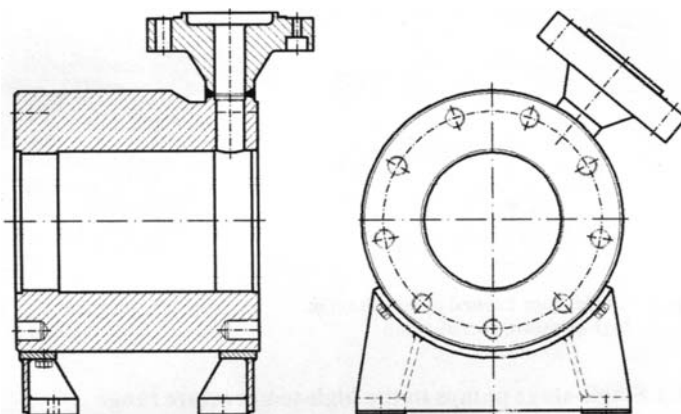


Fig. 4 Stator for high internal pressure loading

The employed seals are ring seals, cleat-section high-pressure seals or even an all-metal seal.

4.2 Cable terminal box

The connection terminals required for power input and the control processes are housed in a high pressure proof terminal box constructed for the corresponding pressure rating (Figure 5). Pressure is at normal atmospheric in the stator compartment, and so there is no particular load on the cable terminal box. However, it is specified on the assumption that it may have to withstand the system pressure and the discharge pressure of the pump and provide sealing in relation to the outside environment. This is a safety precaution to prevent any escape of fluid from the motor in the event of damage to the can, e.g. in the form of corrosion or abrasion. In most applications, high-pressure canned-motor centrifugal pumps are operating in potentially explosive atmospheres, such that the

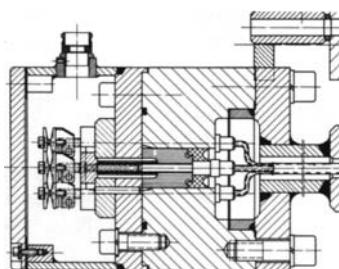


Fig. 5 Terminal box in explosion-proofed and high-pressure specification.

configuration of the terminal box and the stator specification must comply with the provisions of EN 50018 for explosion proofness.

5. TYPICAL APPLICATIONS AND SPECIFICATIONS OF HIGH-PRESSURE CANNED-MOTOR CENTRIFUGAL PUMPS

5.1 Single-stage pumps

In high-pressure circuits, centrifugal pumps are used to overcome the pressures encountered in the pipeline and in the system, such that at lower pressure heads they are usually employed as single-stage pumps (Figures 6 and 6.1). At fluid temperatures of up to 180°C, self-cooling motors of insulation class H are employed.

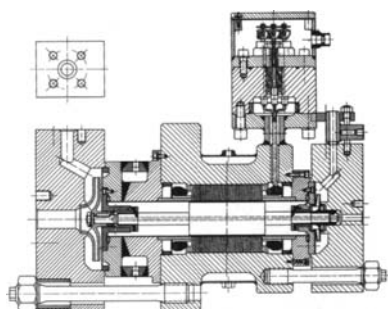


Fig. 6 Single-stage canned motor pump in high-pressure specification



Fig. 6.1 Illustration of canned-motor centrifugal pump as shown in Figure 6

5.1.1 Single-stage pumps in the high-temperature range

Fluid temperatures of more than 180°C necessitate externally cooled motors as per Figure 7. An impeller installed in the canned motor provides flow for a secondary circuit, via an external high-pressure capillary heat exchanger. The primary circuit can operate at temperatures of up to 400°C, whilst the motor circuit temperature will not exceed 60 to 80°C.

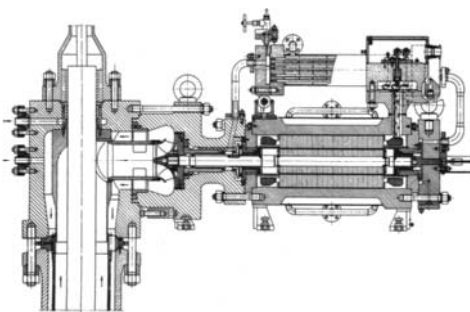


Fig. 7 High-pressure canned-motor centrifugal pump integrated into a nuclear fuel rod ($T_e = 360^\circ\text{C}$; $Q = 600 \text{ m}^3/\text{h}$; $H = 35 \text{ m}$; $P_i = 125 \text{ kW}$; $p_{\text{system}} = 16 \text{ MPa}$)

5.2 Multi-stage pumps

High-pressure specification canned-motor centrifugal pumps can provide the solution for the hardest pumping duties. The pump illustrated in Figures 8 and 8.1 has to pump a corrosive suspension in a continuous flow at a starting temperature of 250°C and an inlet pressure of

70 MPa against 45 metres of resistance from equipment and pipeline.

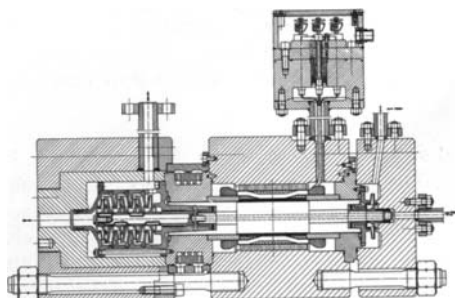


Fig. 8 Sectional view of a multi-stage high-pressure canned-motor centrifugal pump for pumping of an aggressive suspension at 70 MPa inlet pressure and 250°C.

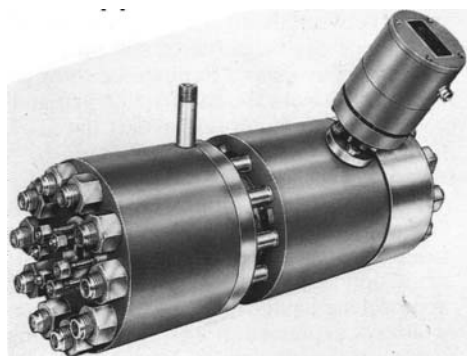


Fig. 8.1 Illustration of high-pressure canned-motor centrifugal pump as per Figure 8

The answer is to house a multi-stage centrifugal pump in a high-pressure casing, where all wetted components consist of an appropriately corrosion-proofed material. A cooling casing is arranged between the pump and the motor in order to prevent any creep transfer of heat between the pump and the motor. An impeller arranged in the motor maintains a cooling circuit via an external heat exchanger (not illustrated here) in order to keep motor temperatures low and to duct away the heat given off.

A reciprocating diaphragm pump (not illustrated here) feeds a sealing fluid into this circuit; a sealing fluid which is compatible with the flow product, and which is fed through a threaded shaft seal into the primary circuit. This prevents solid particles from reaching the rotor compartment.

5.3 Tandem pumps

If high discharge heads also have to be overcome at high system pressures - as in the context of liquid gas, where the flow product has to pass from a low-temperature to a high-temperature section of plant - then multi-stage pumps are required. At a number of stages greater than 6, tandem pumps are used for stress reasons (bending of shaft); see Figures 9 and 9.1.

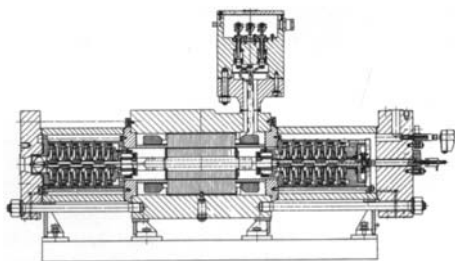


Fig. 9 Twelve-stage canned-motor centrifugal pump in a high-pressure specification barrel construction.

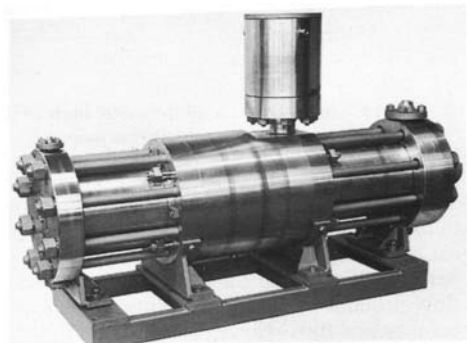


Fig. 9.1 Illustration of tandem high-pressure centrifugal pump as per Figure 9

At a pump speed of 2850 RPM, two centrifugal pumps operating in series (with a canned motor between them) can overcome up to 500 m discharge head, depending on the pump size. This range can be increased still further by frequency conversion [3]. After leaving pump 1, the entire flow passes through the rotor compartment of the motor, dividing into two flows as it passes through the rotor/stator gap and the hollow shaft of the motor. This enables good cooling of the motor and avoids the need for a separate cooling/lubrication flow that would reduce the pump's profitability.

5.4 Semi-hermetic pumps for transportation of supercritical gases

Continuous circuits with internal pressures of 30 to 120 MPa are required as the pre-requisite for liquid transportation in a gaseous, supercritical state of aggregation, as in the case of extraction of vegetable substances. In such operating states, gases reach high density values approaching liquidity, due to their high compression. The *pressure head* of a centrifugal pump is always expressed in metres of the pumped liquid. As density increases, so the *discharge pressure* of such a pump increases. For that reason it is possible - at normal speeds - to reach correspondingly high discharge pressures, although the liquid is in a gaseous state of aggregation. Pumps which are developed for such applications have a similar basic specification to that illustrated in Figures 6 and 6.1, wherein the pump may be single-stage or multi-stage. One difference is that there is a hydrodynamic mechanical seal in a spacer section between the pump and the motor (Figures 10 and 10.1).

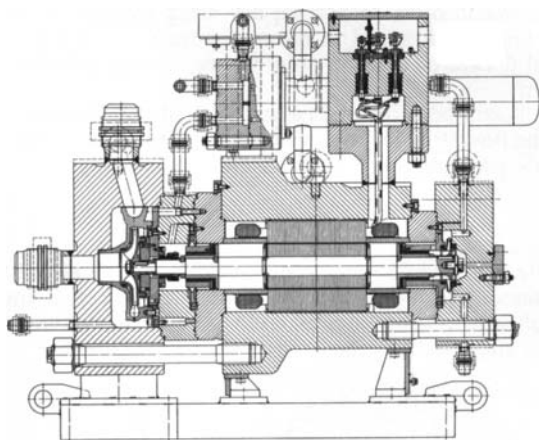


Fig. 10 Single-stage, semi-hermetic high-pressure canned-motor centrifugal pump

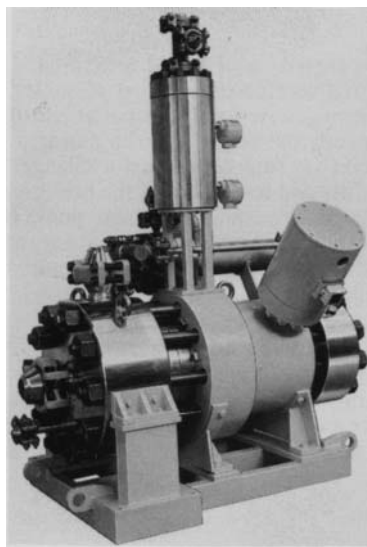


Fig. 10.1 Illustration of a canned-motor centrifugal pump as per Figure 10

The rotor compartment and the cooling system are liquid-filled. An ancillary impeller maintains a secondary motor cooling circuit, thus sustaining the normal conditions for heat disposal, thrust balancing and the hydrodynamic bearing effect. The function of the mechanical seal between the primary and secondary flows is to prevent uncontrolled flow of liquid into the flow product. A gas displacement line from the rotor to the process liquid maintains pressure balance and thus relieves any load on the mechanical seal (Figure 11). A pressure compensation tank is incorporated in this connecting line, and in the tank there is monitoring of the liquid level via a maximum and minimum level contact with opto-electronic sensors. When the minimum level is reached, liquid is automatically supplemented by a metering pump. This provides a simple means for monitoring the leak rate of the mechanical seal, whose pressure loading is

virtually non-existent. This type of pump is called a semi-hermetic centrifugal pump, because it is hermetically sealed in relation to outside, but does require a mechanical seal between its external and internal circuits.

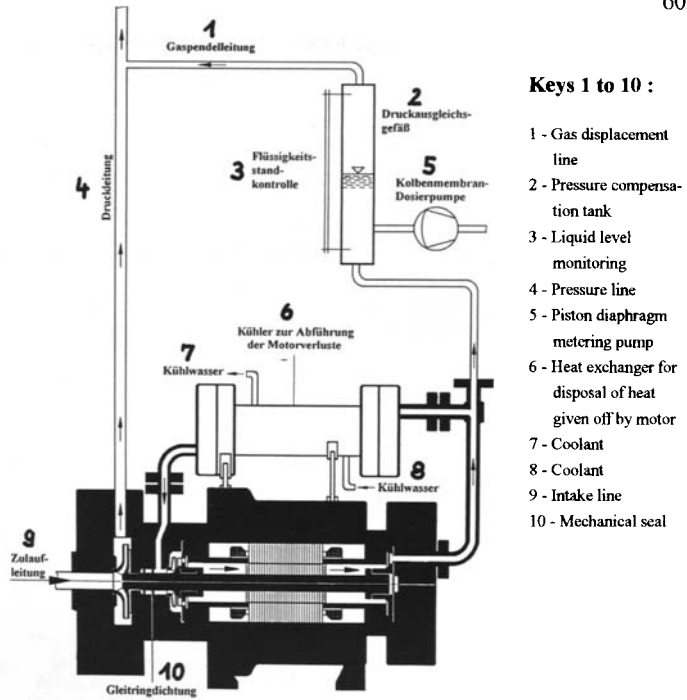


Fig. 11 Differential pressure relief of mechanical seal on a semi-hermetic high-pressure canned-motor centrifugal pump

5.4.1 Semi-hermetic tandem pumps

Semi-hermetic tandem pumps are also used for supercritical gases, in the same way as tandem pumps are used for high system and discharge pressures as described in Section 5.3. In order to separate the liquid-filled rotor compartment from the gas zone, the pump is fitted with two mechanical seals. Accordingly, fluid can no longer be fed from pump 1 to pump 2

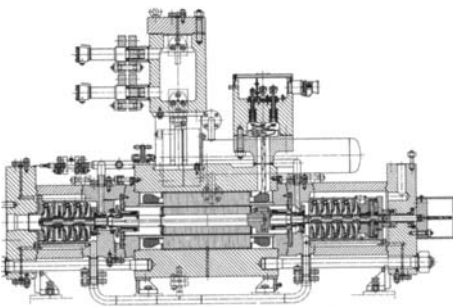


Fig. 12 tandem high-pressure canned-motor centrifugal pump of semi-hermetic specification with a compensation tank

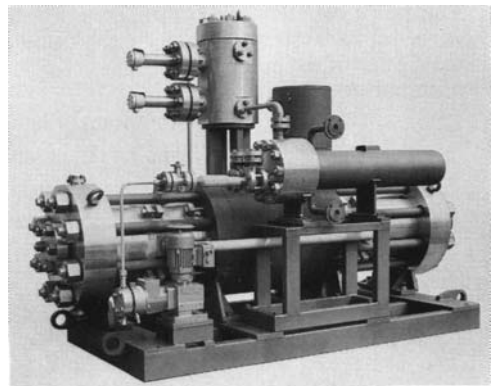


Fig. 12.1 Illustration of tandem canned-motor centrifugal pump as per Figure 12

via the rotor/stator gap and the hollow shaft, but must pass through a separate connecting line (Figures 12 and 12.1) [4].

5.5 Transportation of dual-phase mixes

Where it is necessary to transport liquid gas fractions of differing vapour pressures, there is a risk that where the flow speeds up, e.g. at the pump inlet, the proportion of the fraction of higher vapour pressure could evaporate. Similar occurrences have been observed with fluids in solubility equilibrium. A two-phase mix arises. In addition to the problem of the constriction of the liquid profile due to deposition of vapour bubbles on the suction side of the impeller blades, there is the danger that vapour bubbles may penetrate the rotor compartment. This would impede the cooling/lubrication process of the hydrodynamic shaft seal and would affect axial thrust balancing. In order to prevent such an occurrence, a hydrodynamic shaft seal as shown in Figures 13 & 14 is arranged in the casing section between the pump and the motor. A star-shaped impeller maintains an annular liquid lock of high dynamic density through which it is impossible for vapour bubbles to pass, due to their lower density in relation to the liquid.

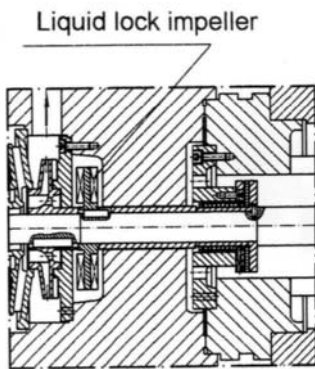


Fig. 13 Principle of a hydrodynamic shaft seal

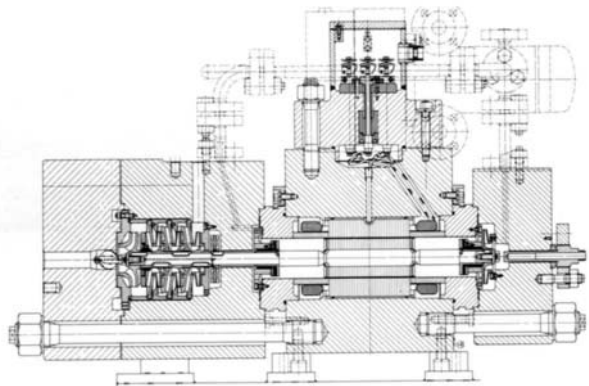


Fig. 14 High-pressure canned-motor centrifugal pump with hydrodynamic shaft seal

6. SAFETY AND MONITORING INSTALLATIONS ON HIGH-PRESSURE CANNED-MOTOR CENTRIFUGAL PUMPS

The extent of safety and control measures to be taken will depend on the hazardousness of the flow media, system availability, explosion prevention provisions and - last but not least - the cost price of the pump.

Features include:

- I Monitoring of liquid level on the intake side
- II Winding temperature monitoring
- III Overcurrent cutout
- IV Cos-phi motor load monitor
- V Rotor position indicator
- VI Vibration meter
- VII Stator pressure monitor instrument

All of these features can be installed as necessitated by the level of hazard, statutory requirements and particular functional parameters. Whilst I, II, III, IV and VII are already familiar forms of monitor, it is worth looking more closely at facilities "V" and "VI".

6.1 Rotor position indicator (V)

In the event of failure of the pump's balance of axial thrust, e.g. because of cavitation or because of exceeding the prescribed operating range, either a visual or an acoustic alarm is activated or the pump is shut down, by means of an "RPM" instrument as per Figures 15 and 15.1. This system provides inductive, contactless monitoring of any change in the axial position of the rotor of the pump motor, and employs a non-ferromagnetic material probe with an integral ferrite core which protrudes in a cap from the motor casing and whose signal is picked off by a measurement value transducer. The system is capable of detecting measurement values from approx $\pm 0,5$ to $\pm 1,5$ mm, which are commonly referred to for monitoring of axial play values in canned-motor centrifugal pumps.

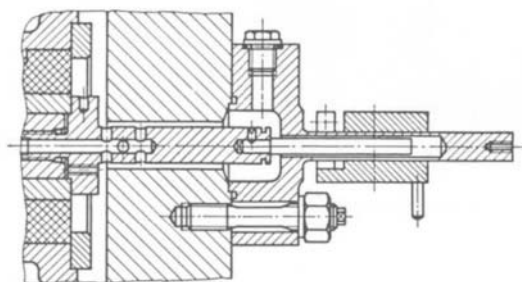


Fig. 15 "RPM" Rotor Position Measurement system

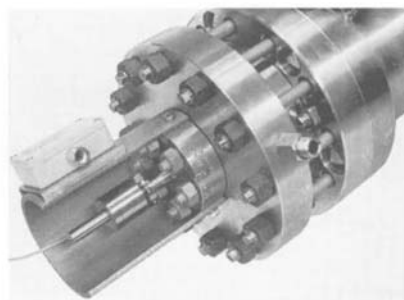


Fig. 15.1 Illustration of an "RPM" measurement installation as per Figure 15

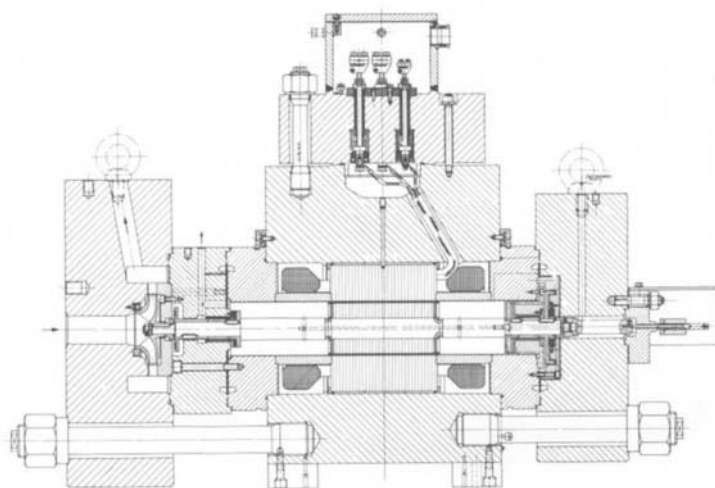


Figure 16 Canned-motor centrifugal pump for 120 MPa input pressure with "RPM" instrument attached

6.2 Vibration meter (VI)

A similar facility for diagnostics and switching to that described in Section 6.1 can be obtained by means of vibration meters which are attached to the motor casing and hence can also be retro-fitted (Figure 17). Cavitation phenomena and bearing wear will result in increased

vibration in the pump, and these phenomena can be picked up by the instrument or instruments and processed as switching commands.

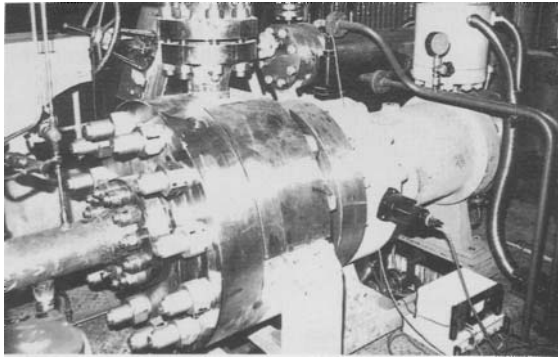


Fig. 17 - Canned motor in a high-pressure specification with a vibration meter attached.

7. SUMMARY

High-pressure specification canned-motor centrifugal pumps solve problems in areas which could not previously be aided by conventional pumps. Simple, space-saving construction, high availability, absence of emissions thanks to prevention of fluid escape and greatly reduced noise output are characteristics that are desired in modern industrial plant not only by operators but also by legislators.

REFERENCES

- [1] Krämer, R. Kreiselpumpen und rotierende Verdrängerpumpen hermetischer Bauart
Neumaier, R. (Hermetic pumps and rotary displacement pumps).
Lederle-Hermetic GmbH company literature, 1989.
- [2] Krämer, R. Entwicklung und Bau einer Hermetic-Umlaufpumpe für hohen System-
Neumaier, R. druck (Development and construction of a hermetic recirculating pump
Schießer, K. for high system pressure).
Verfahrenstechnik (Process technology) 6 (1973).
- [3] Neumaier, R. *Hermetische Pumpen* (Hermetic pumps).
Verlag und Bildarchiv (publishers and image archive) W. H. Faragallah,
1994, ISBN-3 929682-05-2
- [4] Neumaier, R. Hermetisch Fördern mit Spaltrohrmotorpumpen die ökologische Art
des Fluidtransportes - Stand der Technik, Mitteilungen des Pfeiderer-
Instituts für Strömungsmaschinen (Hermetic pumping with canned
motor pumps, the ecological fluid transport method - state of the art,
papers from the Pfeiderer Flow Machines Institute).
Volume 1, September 1994.

Multistage High Pressure Mixer-Settler System

W. Pietzonka and Ch. Trepp

Institute of Process Engineering and Cryogenics,
 Swiss Federal Institute of Technology, Zürich, Switzerland

Summary

An extraction apparatus has been developed for pressures up to 30 MPa and temperatures up to 120 °C, as an alternative to the counter-current column used in supercritical fluid extraction. The apparatus consists of five mixer-settler stages which are arranged in counter-current flow. Regenerative pumps are used as mixers to achieve an intense contact between the two phases and to create a large mass transfer surface area. Cyclones are used as separators to avoid back mixing. Previous work with a single stage module yielded a separation efficiency of about 96%. The achieved mass transfer surface area was 2'000 - 3'000 m²/m³. The multistage apparatus is currently being tested. Results of separation efficiency and behaviour will therefore be presented at the symposium in October 1996.

1 Introduction

The use of supercritical fluids in extraction processes has become well established. Until now, the extraction of liquids, as for example vitamins or vegetable edible oils, has been carried out in countercurrent columns. Dense gases offer several advantages over conventional solvents such as selective dissolving power, reduced thermal stress of the products or its physiological harmlessness. A supercritical fluid also has a density close to those for liquids, the viscosity is nearly 100 times lower and the diffusivity is up to 100 times higher than those of ordinary liquids as can be seen in table 1.

	ρ [kg/m ³]	η [Pa s]	D [m ² /s]
Gases 0.1 MPa, 293 K	0.6 ... 2	(1 ... 3) 10 ⁻⁵	(0.1 ... 0.4) 10 ⁻⁴
Dense gases T_c , p_c	200 ... 500	(1 ... 3) 10 ⁻⁵	0.7 10 ⁻⁷
Dense gases T_c , 4 p_c	400 ... 900	(3 ... 9) 10 ⁻⁵	0.2 10 ⁻⁷
Liquids	600 ... 1600	(0.2 ... 3) 10 ⁻³	(0.2 ... 2) 10 ⁻⁹

Table 1. Typical values of densities ρ , viscosities η and diffusion coefficients D for different fluids [1], where T_{crit} and p_{crit} are the critical temperature and pressure.

Therefore a much higher mass transfer coefficient can be expected for SFE. A comparison of countercurrent extraction columns using supercritical fluids with those using liquid solvents shows, however, that SFE-columns do not reach an efficiency as high as could be expected because of the solvent properties (table 2).

	HTU [m]	HETP [m]
Liquid-Liquid Extraction	0.3 ... 6	0.8 ... 3.5
SFE	0.3 ... 1.5	0.2 ... 1.2

Table 2. HTU and HETP values for SFE and liquid-liquid extraction [2] - [4].

The decrease of the column performance is partially caused by longitudinal mixing and insufficient wetting of the packing due to detachment of the liquid film as shown by Blaha [5]. Another disadvantage of columns is the low gas capacity required to avoid flooding because of the low interfacial tension and the low density differences between the phases.

To reduce the above mentioned problems the mixing and separation zones in an extraction apparatus can be spatially isolated from each other. On the other hand the largest possible surface area should be created actively to increase the mass transfer rates..

From this knowledge, the idea of using a mixer-settler system for the extraction with supercritical fluids was derived. The purpose of this project is to build a multistage high pressure apparatus and to compare the separation efficiency and behaviour of the new system with that for a conventional column.

2 Apparatus

2.1 Single stage mixer-settler system

To meet the supercritical conditions more suitable a mixer-settler unit has been developed by Schaffner [2]. A regenerative pump was used as mixer to achieve an intense contact between the two phases and to create a large mass transfer surface area. This type of pump is capable of conveying gases as well as liquids and creates a high pressure difference which is used to separate the phases in the following fluid cyclone (fig. 1).

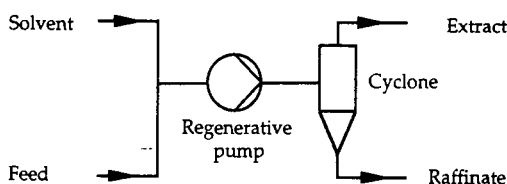


Figure 1. Single stage mixer-settler module [2]

Schaffner coupled the unit with a conventional column in such a way that the system represented a single stage within the extraction column. For testing the module it could also be operated as a single unit.

2.2 Multistage mixer-settler system

Due to the good performance of the single stage unit (see section 3) an extraction plant has been designed and built for pressures up to 30 MPa and temperatures up to 120 °C. The apparatus consists of five mixer-settler modules, as described above, which are composed in counter current flow (fig. 2).

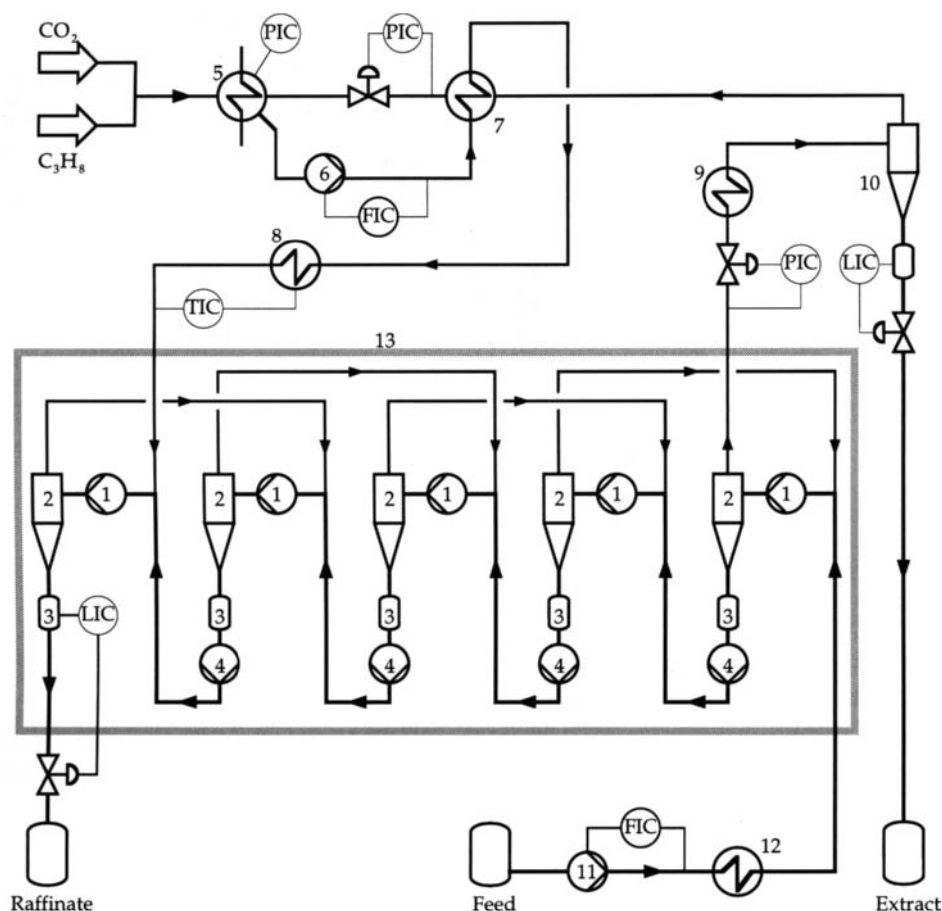


Figure 2. Simplified schematic drawing of the extraction plant (1 regenerative pump, 2 fluid cyclone, 3 storage tank, 4 gear pump, 5 circulation gas condenser, 6 diaphragm pump, 7 heat recovery, 8 preheater, 9 heat exchanger, 10 cyclone separator, 11 feed pump, 12 feed preheater, 13 thermostatic chamber)

The regenerative pumps (1) consist of two double-suction impellers, each with a diameter of 0.036 m in series to increase the total pump head. All pumps are equipped with speed control and differential pressure sensors. The mixed phases enter the fluid cyclone (2) of 0.020 m diameter with a tangential tube entry. The underflow of the cyclones is connected to a small storage tank (3) with level con-

trol and two inspection windows. The heavy phase is pumped from this tank into the next stage by a small high pressure gear pump (4). The light phase leaves the cyclone at the top, passes an inspection glass and flows in counter current to the heavy phase. At the entry of every regenerative pump pressure and temperature is measured. The five stages are built into an air heated thermostatic chamber (13) to maintain isothermal conditions. The solvent (CO_2 or $\text{CO}_2/\text{C}_3\text{H}_8$ mixture) is condensed and subcooled in the condensor (5). The liquefied gas is pumped up to the desired pressure using a diaphragm pump (6), passes through the heat exchanger (7) of the heat recovery and the preheating exchanger (8) to warm up the solvent to the desired temperature and enters the last extraction stage. The extract leaves at the first stage where its mass flow rate is measured. After releasing the pressure the extract passes through another heat exchanger (9) for a further decrease of the solubility. Then the CO_2 is separated from the desired product in a cyclone (10) and flows back into the condensor. The feed is pumped into the first stage using a HPLC-pump (11) while passing through a small heat exchanger (12).

2.3 Substances

To test the system a synthetic feed mixture of α -Tocopherol and α -Tocopherol acetate both of 98 % purity, were used. Vitamin E (α -Tocopherol) is one of the fat-soluble vitamins used as an antioxidant in the food, pharma and cosmetic industries.

The carbon dioxide had a purity 99.99 %.

2.4 Analytic

Samples were taken on-line and pumped through the density meter and injected into the SFC analytic instrument.

The densities of both the light and heavy phase were measured using two density meters DMA 512/DMA 60 from Paar.

For the determination of the concentrations of the light and heavy phases a modified HPLC instrument from Carlo Erba (System 200) was used as an SFC instrument. The columns used were a 10 mm pre column and a 60 mm main column of 2 mm inner diameter packed with Spherisorb (SI 3 μ). Detection was carried out with an UV detector at a wavelength of 284 nm.

3 Results and Outlook

Measurements for the single stage module [2] showed that the regenerative pump is able to create a mass transfer surface area between 2000 and 3500 m^2/m^3 at liquid phase ratios of about 5 %. The drop size distribution was determined and varied between 30 and 200 μm . The measurements were taken at the outlet of the regenerative pump with a photo camera. The calculated surface area was very high compared to conventional packing as shown in table 3.

The specific surface area created by the regenerative pump was 3 - 7 times higher than that in a packed column. In addition to this, it should be noted that the column packing very often is not completely wetted.

Column packing	Size [m]	Area/volume [m ² /m ³]
Montz packing B1 - 300	-	300
Pall ring (random bed)	0.015	368
Raschig ring (random bed)	0.015	378
Rombopak	0.100	350
Sulzer BX	-	500
Sulzer CY	-	720
Mixer-settler system investigated	0.050	2000 - 3500

Table 3. Area per unit volume of different column packing [2], [4], [6]

The maximum separation efficiency of the cyclone was determined to be 98 % by entraining a 2 % gas volume fraction with the liquid phase. In countercurrent flow in the multistage plant these 2 % of gas volume fraction and the not separated liquid in the gas phase will reduce the efficiency of the apparatus because of back mixing.

To determine the module efficiency a feed mixture of 51 - 55 % by weight of Tocopherol acetate was used. For the module as a single unit an average Murphree efficiency of 96 % was calculated [2]. The calculation was based on three concentration measurements for each point.

The multistage apparatus is currently being tested. Results of separation efficiency and behaviour will be presented at the symposium in October 1996.

Some advantages of the new system compared to extraction columns are the higher flow rates at low volumes because no flooding problems occur and a much higher specific surface which leads to a better mass transfer. In addition to this, the start-up of the system is fast, easy and allows a broad operation range. Another point is the low space requirement for the plant. The complete plant which has a flow capacity of 100 kg/h CO₂ and up to 5 kg/h feed, has been built into a 3 x 3 x 3 m room .

As a result the scale-up procedure for the mixer-settler type apparatus will be much more accurate compared to columns and will lead to smaller plants.

4 Acknowledgments

This work is supported by F. Hoffmann-La Roche AG Basel, Switzerland.

5 References

- [1] Brunner, G., Chem. Ing. Tech. 59(1987)1, 12-22
- [2] Schaffner, D.: PhD Thesis Nr. 10358, ETH Zürich 1993
- [3] McCabe, Smith, Harriott: "Unit Operations of Chemical Engineering", McGraw-Hill, New York 5th ed. 1993
- [4] Sattler, K. : "Thermische Trennverfahren", VCH Verlagsgesellschaft mbH, Weinheim 2nd ed. 1995

- [5] Blaha, A: PhD ThesisUniversity of Erlangen 1992
- [6] Billet, R.: "Packed Towers", VCH Verlagsgesellschaft mbH,Weinheim 1995

Energetical optimization of supercritical fluid extraction processes

U. Sievers

Fachhochschule Hamburg, Fachbereich Maschinenbau und Chemieingenieurwesen,
 Berliner Tor 21, D - 20099 Hamburg, Germany

1. INTRODUCTION

Production plants for supercritical fluid extraction of natural substances have now been in operation for several years. Production costs are significantly influenced by the energy requirement. Energy optimization may improve production economy for existing and future extraction plants. Results of optimization calculations were first published by Eggers [1]. These calculations are extended here.

2. BASIS OF OPTIMIZATION

The single-stage supercritical fluid extraction process for solid natural materials is shown schematically in *Figure 1*. The solvent is conveyed from the low pressure to the high pressure by a pump or compressor V. Extraction is at pressure p_{ex} and temperature t_{ex} in extractor E, where the soluble substances are transferred from the natural material to the solvent. Normally, the extractor consists of several autoclaves connected in series in the solvent flow. In throttle valve D the solvent loaded with extract is relaxed to the lower pressure. The extract is separated from the solvent in separator A at separation pressure p_s and temperature t_s . Heat exchangers W1, W2 and W3 are installed to achieve the desired temperatures.

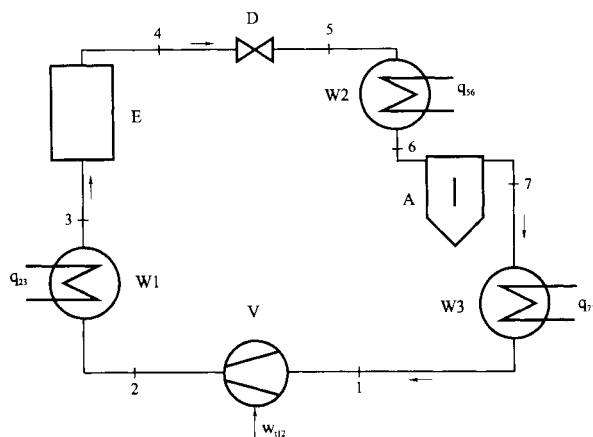


Figure 1. Supercritical fluid extraction process for solid natural materials.

Four different types of processes are investigated here. These can be derived as special cases of the process of *Figure 1*:

- Process 1: Process without heat exchanger W1; extraction temperature t_{ex} equals the solvent exit temperature t_2 of the pump or compressor V;
- Process 2: Process without heat exchanger W3; separation temperature t_{se} equals the solvent entrance temperature t_1 of the pump or compressor V;
- Process 3: Process without heat exchangers W1 and W2; extraction temperature t_{ex} equals the solvent exit temperature t_2 of the pump or compressor V, separation temperature t_{se} equals temperature t_5 behind the adiabatic throttle valve D;
- Process 4: Process with separation at subcritical pressure.

The extraction of hops with solvent CO_2 is taken as an example here. Process calculations are made for the stationary process, i.e. the process without non-stationary pressurization and pressure release required when solids are batch-processed. Calculations are performed for pure fluid CO_2 with thermodynamic properties taken from Sievers [2] under the following assumptions:

- Pressure increase in the pump or compressor V is adiabatic with an isentropic compression efficiency factor $\eta_{isV} = 0.9$.
- Pressure drops in pipelines and equipment are negligible.
- Changes in kinetic and potential energy are negligible.
- Heat is removed from the solvent CO_2 within the extraction plant to the surrounding air. At temperatures of $27.5^\circ C$ and above, heat transfer is direct, using only a cooling tower, whilst at lower temperatures a refrigeration plant with cooling tower is employed. The temperature of cooling water from the refrigeration unit is $5^\circ C$ lower than the lowest CO_2 temperature, and the refrigerant evaporation temperature is $5^\circ C$ below the lowest cooling water temperature, so that the refrigerant evaporation temperature is $10^\circ C$ lower than the lowest CO_2 temperature. The refrigerant used is NH_3 . It is condensed at $27.5^\circ C$ in an air-cooled condenser.

The process calculations yield the mechanical work for the pump or the compressor of the extraction plant and the compressor of the refrigeration unit, in case this unit is necessary, the heat transferred to the CO_2 in the extraction cycle, and the heat transferred via the cooling tower to the surrounding air. The results per kg CO_2 are converted to data per kg hop extract making the assumption that CO_2 saturated with hop extract exits the extractor and the separator. The mass of extract yield per kg cycled CO_2 is given by the difference ΔY in the corresponding solubility data. The solubility of hop extract in CO_2 is taken from Sievers and Eggers [3]. Finally, the overall energy costs per kg hop extract are calculated on the basis of the following energy costs:

Heating by steam or hot water: $19 \cdot 10^6$ DM/kJ

Cooling by cooling tower: $6 \cdot 10^9$ DM/kJ

Mechanical work: $13 \cdot 10^2$ DM/kWh.

Since solubility data for hop extract in CO_2 is available only for pressures up to 300 bar, energy requirements are calculated for extraction pressures p_{ex} of 200, 250 and 300 bar. The investigated extraction temperatures t_{ex} are 40, 60, 80 and $100^\circ C$. Separation pressures p_{se} are 80, 90, 100, 120 and 150 bar for Processes 1 to 3 and 60 bar for Process 4. Separation temperatures t_{se} are 30 and $40^\circ C$ for Processes 1, 2 and 4.

3. RESULTS

The results of the calculations for each process with the mentioned extraction and separation pressures and temperatures are ranked according to their overall energy cost. *Table 1* and *Table 2* show the ten Process 1 and Process 3 variants whose energy costs are lowest.

Table 1.

Energy costs K for supercritical fluid extraction of hops with CO₂ according to Process 1.

p_{ex} bar	p_{sc} bar	t_{ex} °C	t_{sc} °C	t_j °C	ΔY g hop extract/kg CO ₂	100 K DM/kg hop extract
300	120	60	40	36.38	66.4	1.36
300	150	60	40	41.22	57.0	1.42
300	100	60	40	32.77	72.2	1.53
300	80	60	30	28.73	71.2	1.57
300	90	80	40	37.24	75.4	1.63
300	90	60	30	30.81	68.4	1.65
250	120	60	40	39.80	41.2	1.67
250	100	60	40	35.60	47.0	1.70
300	100	80	40	40.63	72.2	1.71
300	150	40	30	26.27	39.6	1.74

Table 2.

Energy costs K for supercritical fluid extraction of hops with CO₂ according to Process 3.

p_{ex} bar	p_{sc} bar	t_{ex} °C	t_{sc} °C	t_j °C	ΔY g hop extract/kg CO ₂	100 K DM/kg hop extract
300	150	60	48.48	41.22	62.3	1.20
300	150	80	61.14	54.04	70.5	1.20
300	120	60	43.57	36.38	68.8	1.31
250	150	60	50.22	45.33	38.1	1.38
300	120	80	52.86	46.57	74.4	1.39
300	100	60	39.13	32.77	71.7	1.41
300	90	60	36.38	30.81	73.4	1.45
250	120	60	44.91	39.80	45.7	1.51
300	150	100	73.44	65.25	64.2	1.52
300	80	60	33.12	28.73	73.3	1.53

Process costs are influenced by various factors which are mutually dependent, so that it is not initially clear which extraction and separation conditions are the most favourable. A large value for ΔY is favourable, since the yield of hop extract per kg CO_2 is then high. A low pressure ratio $p_{\text{ex}}/p_{\text{se}}$ is also favourable, since the mechanical work for compression is then small. Solubility data are however most favourable for extraction when the pressure is high, whilst conditions for separation are most favourable at low pressure. A low initial compressor temperature t_i is favourable, since the mechanical work is then small. Too low a temperature, however, requires a refrigeration unit which increases the mechanical work requirement and is thus unfavourable.

It is found that, for Processes 1 to 3, the most favourable variants generally employ temperatures of 60°C or 80°C . These are the temperatures at which hop extract has its highest solubility at the pressures of 250 and 300 bar. The most favourable variants do not, however, involve the expected separation conditions at the lowest solubility values. At low separation pressure, the solubility is indeed very low, but the pressure ratio $p_{\text{ex}}/p_{\text{se}}$ and therefore the mechanical work of compression is greater, making such a variant more unfavourable than a variant at higher separation pressure. This applies to the Processes 1 to 3. The most favourable variants are thus often those with a separation pressure exceeding 100 bar.

Comparison of the three processes reveals that costs scarcely differ between Processes 1 and 2. The costs K of the first ten variants lie in the range 0.014 - 0.017 DM/kg hop extract, whilst the first ten variants of Process 3 cost approximately 0.002 DM/kg hop extract less. It is thus an advantage that the separation temperature in Process 3 is achieved by pressure release alone, without adding or removing heat. Table 2 includes separation temperatures which often considerably exceed 40°C .

For purposes of comparison, some supercritical fluid extraction processes have been calculated in which the extract is separated at the subcritical pressure $p_{\text{se}} = 60$ bar (Process 4). Such a process corresponds to that in Fig. 1 with the difference that a pump is employed to increase the pressure from state 1 to state 2, since the CO_2 is cooled down to 17°C after separation, i.e. is present in the liquid state before the pressure is increased. Even for the most favourable variant with $K = 0.062$ DM/kg hop extract, the operating costs for this process are significantly higher than for processes employing supercritical separation. They can be reduced significantly by heat recovery with a heat pump as published by Sievers and Eggers [3].

Figure 1 shows the overall costs K for Process 3 as a function of the separation pressure p_{se} for extraction temperatures t_{ex} between 40 and 100°C . As the separation pressure increases, the overall costs K decrease. The saving in mechanical work outweighs the effect of more unfavourable separation conditions at higher separation pressures. The process is more efficient because no heating is necessary, and furthermore, simple pressure release results in a temperature favourable for separation. The same trend is observed when energy costs for mechanical work are about 25 % higher or lower, i. e. 0.10 DM/kWh or 0.16 DM/kWh..

Figure 2 and Figure 3 show the comparison of Processes 1 to 3 when the extraction conditions are 300 bar and 60°C or 80°C . The most favourable variants of these three processes operate at one or other of these temperatures, thus permitting ready comparison of

the processes under these conditions. It is clearly seen that the costs for Processes 1 and 2 are very similar when the process conditions are the same, particularly at higher separation pressures. For a separation temperature of 30 °C, both processes become more costly as the separation pressure is increased. The operating costs for Process 3 are the lowest under all process conditions, and fall steadily as the separation pressure increases.

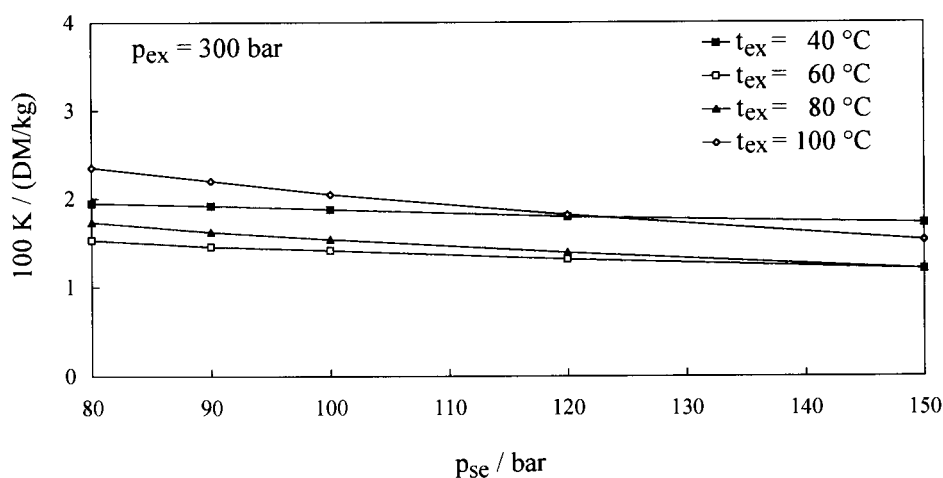


Figure 1. Energy costs K in DM/kg hop extract for supercritical fluid extraction of hops with CO_2 according to Process 3.

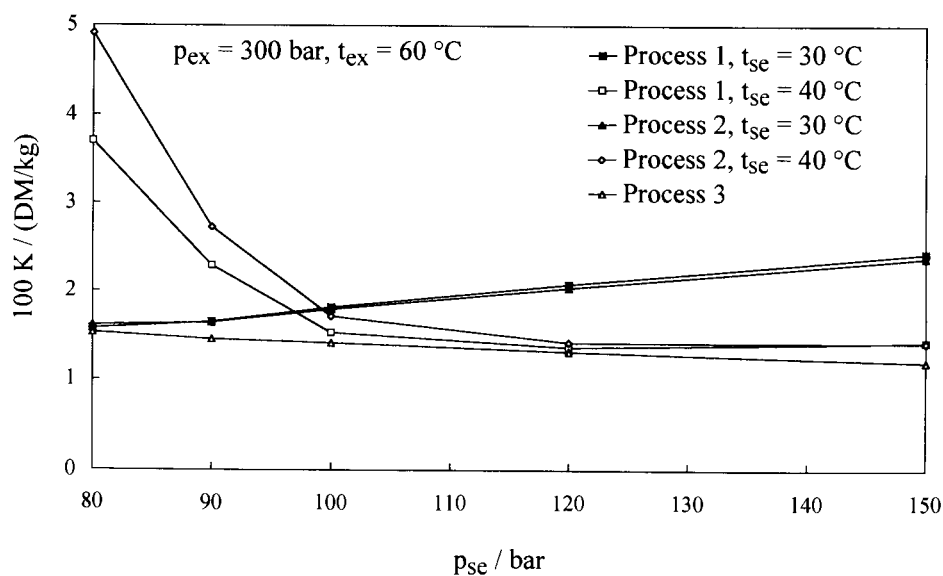


Figure 2. Comparison of energy costs K in DM/kg hop extract for supercritical fluid extraction of hops with CO_2 according to Processes 1 to 3.

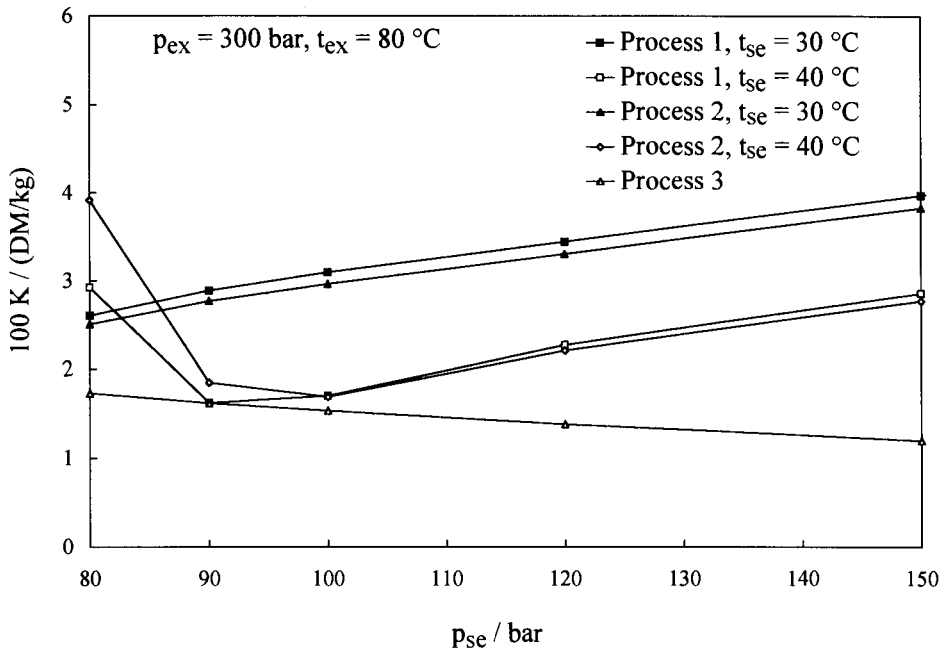


Figure 3. Comparison of energy costs K in DM/kg hop extract for supercritical fluid extraction of hops with CO_2 according to Processes 1 to 3.

REFERENCES

1. R. Eggers, Chem.-Ing.-Tech., 53 (1981) 551-554.
2. U. Sievers, Thermodynamic Properties of Carbon Dioxide, Fortschr.-Ber. VDI-Z., Reihe 6, No. 155, VDI-Verlag, Düsseldorf, 1984.
3. U. Sievers and R. Eggers, Chemical Engineering and Processing 35 (1996), in print.

A New Design of a Multi-Purpose Plant for Extraction of Liquids with Supercritical Fluids

O. Becker, E. Weidner, R. Steiner

Institut für Technische Chemie, Universität Erlangen-Nürnberg, Egerlandstraße 3,
 D-91058 Erlangen

As reported in a lot of reviews, extractions with supercritical solvents have a very promising commercial potential. Until now the commercialization is mainly restricted to batchwise extraction of solids with carbon dioxide (e.g. decaffeination of coffee and tea, extraction of hop). Laboratory experiments and operation of small-scale pilot plants gave favourable economic values for continuous extraction of liquids with CO_2 and other gases. Only a few extractions with CO_2 or C_3H_8 are performed already on a small industrial scale. For research purposes and product development a new high pressure counter-current extraction plant was erected. To get greater amounts of product the explosionproof plant was constructed in pilot scale using a special modular concept and an effective visual control system.

1 BASIC THERMODYNAMICS

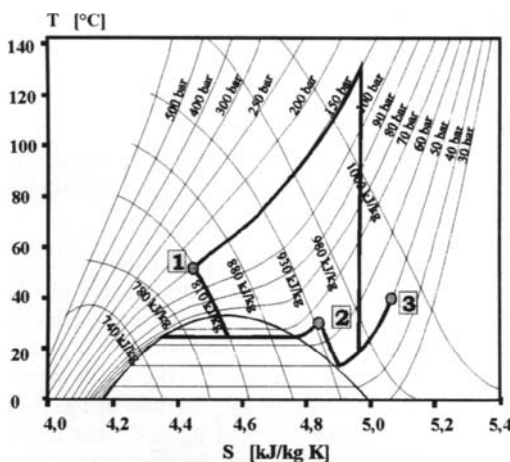


Figure 1: Circular process for extraction with CO_2 in a T-S-scheme

The plant is not only designed for the usage of carbon dioxide, but also for propane and other combustible gases. Carbon dioxide and propane were taken as boundary cases to get the basic design data for the necessary heat exchangers.

The circular process of extraction, regeneration and recompression for the different extraction gases is shown in Figure 1 and Figure 2.

As condition of extraction with CO_2 a pressure of 150 bar and 50°C was assumed. The separation of the dissolved substances takes place in the first regeneration column at a pressure of 65 bar. The first expansion leads into the two-phase region, visible in the T-S-Plot. Therefore it is necessary to supply a sufficient amount of heat to vaporize and overheat the extract phase to an estimated temperature of 30°C. To reach a complete regeneration as well as to have the possibility of a fractionated precipitation (especially with multicomponent systems), a second regeneration column is connected. There the extraction medium is further depressurized to 50 bar and heated to a temperature of 40°C. To recompress the regenerated CO_2 it is of advantage to rise its density through a water-cooled heat exchanger. Because the cooling-water temperature may not be low enough, the two phase region can

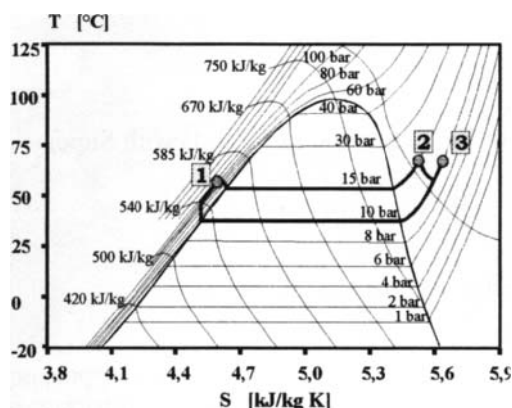


Figure 2: Circular process for extraction with propane in a T-S-scheme

bar, 65°C followed by the second precipitation at 10 bar, 65°C. Afterwards the vapour will be liquified through condensation, recompressed and - in this case - reheated to extraction conditions.

2 CONSTRUCTION

The extraction plant was designed for 160 bar maximum pressure and an upper temperature limit of 180°C. All parts which have to withstand pressure are made of 1.4571 stainless steel. The main extraction column comprises 5 segments with 1,5 meters length each. The packed height of the first regeneration column is 3 meters, the second regeneration column contains 1,5 m packing. The inner diameter of all columns is 67 mm.

2.1 Flowsheet

Figure 3 indicates the complete flowsheet of the multi-purpose high pressure extraction plant. In the following its functional units are described in more detail.

2.1.1 Feedline

The feedline is planned in a way that even high melting, high viscous or oxidation sensitive substances can be fed into the column. The feed vessel has a temperature controlled wall and bottom heating. It is equipped with an inert gas pipe to prevent the feedstock from oxidative reactions. A stirrer ensures a constant heat transfer from the walls to the feed bulk.

The feed tank is mounted on the ceiling using chains and a weighing cell. Continuous weighing of the feed vessel stands for an exact mass balance not influenced by pulsation of the feed pump, volumetric or viscosity effects. To ensure that the connected feed pipes do not block with solidifying liquid they are equipped with an explosionproof electric heating wire which holds an adjustable temperature.

After the feed-pump, a reciprocating plunger pump, a static mixer is installed where the feed liquid can be presaturated with extraction solvent. This is useful for high viscous feedstocks, because their viscosity can be lowered by dissolving gases under pressure. The presaturated feed subsequently flows through a heat exchanger (WT5) where its temperature is adjusted to extraction conditions. Behind that heat exchanger the feed is dosed into the extraction column at the selected height.

probably not be reached. In this case an additional cooler after the recompression unit is necessary to attain extraction conditions.

Particularly extractions of fatty substances are carried out with propane in high pressure liquid/liquid mode. Although this extraction medium may be used in supercritical condition, this limiting case of liquid/liquid extraction was considered for design, because the required vaporization heat is maximized. The extraction is operated at a pressure of merely 80 bar and a temperature of 55°C. The further steps are the first decompression, evaporation and overheating to vapour conditions at 15

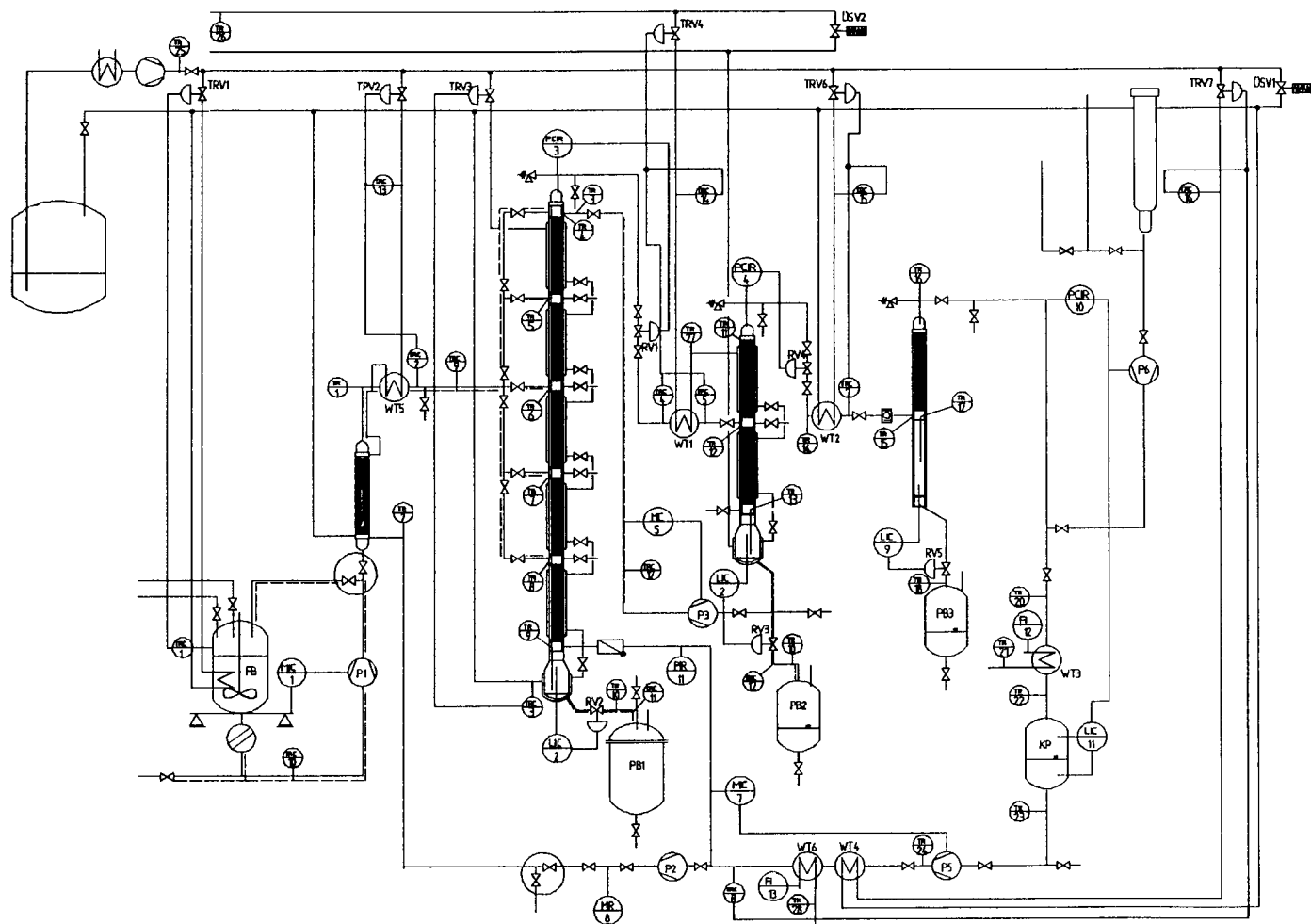


Figure 3: Flowsheet of the extraction plant

2.1.2 Extractant Circuit

The extractant enters the main column above the bottom vessel. After the mass transfer, the loaded gas leaves the extractor at its top. A combination of expansion valve (RV1) and heat exchanger (WT1) is needed to adapt the loaded gas to regeneration conditions.

To investigate the effectivity of the installed wire mesh packing in the first regeneration column, the loaded gas can be fed at the bottom section or in the middle of the column. The partially regenerated gas leaves through the top of the column and is again expanded (RV4) and heated (WT2) to reach a complete regeneration.

Subsequently the pure extraction gas flows through a heat exchanger where it is indirectly cooled with water to rise its density. When possible, it is intended to get a liquid phase which is collected in a connected buffer vessel (KP). The installed membrane compressor is able to pump gas as well as highly compressible liquids, which are withdrawn from the buffer vessel. To achieve a maximum flexibility with respect to extraction medium and operation parameters a cooler (WT6, for gas phase recompression) or a heater (WT4, for liquid phase recompression) can alternatively be used to bring the recompressed solvent back to extraction temperature. Before it is entering the main column a side stream is removed for the feed presaturation.

2.1.3 Product Removal and Reflux

The bottom vessels of all described columns are intentionally of small volume to minimize the column hold-up. This is particularly of advantage when extract reflux is withdrawn from the first regeneration column to the head of the main extraction column, because the time for reaching stationary operation conditions is shortened. The bottom products of all columns are removed continuously through pneumatic controlled valves, which get their signal from capacitive level indicators.

In many cases it is desirable to obtain the raffinate or even the extract in form of a solid powder. Applying the PGSS-method, it is planned to investigate the possibilities of powder generation with different substances of technical significance. Hence a spraying system is installed which can be used to generate fine dispersed particles. The product vessels of extraction and first regeneration column have been designed in a way, that they can be used as spray towers.

2.1.4 Gas Refill System

As products are removed from the extraction and regeneration columns, gas losses are unavoidable. To maintain constant pressure within the extraction system a refill mechanism is installed, which takes the state of gas into account.

The regenerated extraction gas leaves the second regeneration column at its head and is cooled down in (WT3) to a temperature of approximately 20°C. Depending on the type of extraction solvent the buffer vessel (KP) contains liquid phase in equilibrium state with gas or merely gas of high density. In the last case a pressure controlled pneumatic pump feeds fresh solvent into the circular process. If a gas/liquid equilibrium is achieved in the buffer vessel the gas pressure remains constant until a minimal amount of liquid remains there. For this purpose two optical sensors are introduced into the buffer vessel registering the minimum and maximum extraction liquid level. If the level falls below minimum, fresh liquid extraction solvent is refilled.

2.1.5 Heat Exchanger and Heat Supply System

The plant contains four energy requiring heat exchangers and four jacket heatings. Due to safety considerations, energy is delivered by heat transfer oil heated up in two thermostats of 34 kW capacity together. Empirically the heat exchanger after the first expansion step needs the most energy, because vaporization enthalpy has to be brought into the gas (WT1). In the

face of a calculated energy consumption of 10 to 16 kW depending on extractant and operation conditions, this heat exchanger is provided exclusively by one of the thermostats.

To realize a fairly good heat transfer, the heat exchangers WT1, WT2 and the cooler WT4 have been designed as spiral tube heaters having 1 m^2 of exchange area. The spiral is made of 40 m pressure resistant tube. It is inserted in a cylindrical shell with an omitted centre to enlarge the turbulence of the streaming heat transfer oil through minimization of hold up. All other heat exchangers are of tube bundle type.

The temperature of all oil provided heating devices is controlled by pneumatic regulation valves. A good constancy of temperature can be realized, if oil throughput is fairly constant. Therefore at each of the two heating circuits valves are installed to keep the oil pressure on the pressure side of the thermostats constant at an adjustable level.

2.2 Mass Transfer Packings

The extraction column as well as the regeneration columns will be filled with different types of mass transfer packings. It is planned to install commercial packings (e.g. Sulzer Optiflow[®]) as well as a new type of knitted wiremesh packing. It is made of a monofilament wire with rectangular crossection. Different types of these packing elements gave fairly good results in rectification and normal pressure liquid/liquid extraction service.

2.3 Modular Concept

Through its modular design the plant allows to react flexible on different feed substances and experimental requirements. Between the column segments multifunctional sections are inserted. They allow to install all kinds of measurement devices including windows or optical light absorption cells.

To permit the fast change of packing elements as well as to inspect or clean the column internals, all column segments can be removed easily without dismantling the whole column. The principle is shown in Figure 4. A hydraulic lifting system is installed to elevate the upper part of the column. The respective column segment is placed on a small carriage, rolling on two steel girders mounted on the wall. After the screws are removed the segment can easily be pulled out. To allow the elevation of the column fast and without time expensive preparations all connecting pipes are flexible.

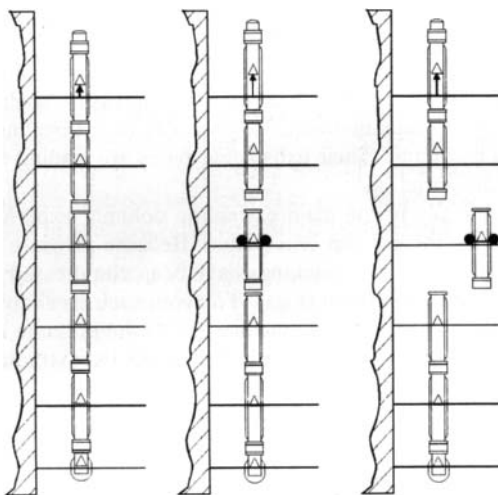


Figure 4: Principle of removing a single column segment without dismantling the whole column

3 INSTRUMENTATION

The plant is equipped with an Eurotherm T100[®] process control system. 21 control circuits, 44 temperature signals, 4 level indications, 4 pressure signals, 4 mass flow indications, 4 pumps and 12 control valves are processed, regulated and indicated with a computer system. Samples can be withdrawn from all important pipes and all column insertion sections.

3.1 Control System

The regulation of heat exchangers and heating jackets is performed by pneumatic regulation valves. It is realized by sequential PID controllers taking into account the oil temperature as well as the gas medium temperature.

If the state of the extractant after the expansion is in the two phase region (v/l), it has to be evaporated. To ensure that only gas phase leaves the heat exchanger, two thermoelements are used to compare inlet and outlet extractant temperature. If the extractant is overheated to a certain adjustable difference a full evaporation can be assumed.

Mass flow measurements are required for several control circuits and for balancing the experiments. For a maximum flexibility, gauges have been installed which measure the mass flow via the Coriolis-forces. The mass of the feed vessel is continuously measured by a weighing cell. The integrated weight loss is used to control the frequency of the feed pump.

The pressure control system is directly connected to the gas refill system. Pressure is measured by pressure gauges at the top of each column. It is kept constant by the subsequently installed pneumatic regulated expansion valves. If the pressure of the second regeneration column becomes too low the gas refill system is activated (see chapter 2.1.4).

For continuous product removal each column is equipped with a capacitive level indicating sensor. Their sensitivity can be adjusted to the concerning extract and raffinate dielectricity constants.

3.2 Safety Precautions

All electrical signals are transferred into 4-20 mA signals. To ensure explosion safety, zener barriers are connected between every sensor or controlling equipment and the process control system. The plant is erected in a high pressure shelter equipped with a heavy gas fan, which avoids the accumulation of combustible or suffocating gases. Safety valves are installed on top of each column. Their exhausting pipes are leading to a flare where combustible components are incinerated.

Especially in the main extraction column, experience has shown, that solidified feedstock can block the column crossection. Because pressure was only measured at the top of the column, the containing packings have been compressed and destroyed by the force of pressure of the circulating extractant gas. To avoid such breakdowns, another pressure gauge was installed at the entrance of the extractant gas. If the pressure difference between top and bottom of the main column exceeds an adjustable value, the extractant gas pump is turned off.

4 CONCLUSION

The new high-pressure counter current extraction plant has various possibilities to investigate supercritical extraction processes. With 7,5 meters packed height of the extraction column and two regeneration columns of 3 meters and 1,5 meters height the plant is designed to solve even difficult extraction problems. The inner diameter of 67 mm permits to produce greater amounts of product which can be removed in liquid state or - if possible - as powder. Its modular concept allows to react flexible on the different requests due to high viscous, high melting or oxidation sensitive substances.

Safety in Supercritical Operations

J.Y. CLAVIER, M. PERRUT

SEPAREx, B.P. 9 - F-54250 CHAMPIGNEULLES

Most supercritical fluid operations do present specific hazards that operators shall take into account : Based on our long-term experience of operating and manufacturing supercritical fluid equipment, we present a list of these various hazards and how to avoid them :

- "Mechanical hazards" : high pressure explosion/rupture, corrosion, frit, plugging , ...
- "Thermodynamical" hazards : dry ice formation, BLEVE phenomenon ;
- "Chemical" hazards : co-solvent, N_2O , corrosion, products,...
- "Biological" hazards : CO_2 , co-solvent, product aerosols, bio-materials contamination,...
- "External" hazards : fire, electricity failure, control failure.

We will also describe some "traps" that must be avoided by an adequate design and wise operation : Pressure control before vessel opening, plugging of tubings, gauges/instruments or frits, leak cure...

1. INTRODUCTION

Equipments handling supercritical fluids and liquefied gases present important hazards that must be taken into account both for equipment design and construction and for operation and maintenance. Safety considerations must influence any technical choice and operation and a detailed analysis of potential hazards must be specifically conducted for any case. In this paper, we would try to list the different classes of hazards and how to cope with them, so that both the process designer and the operator be informed.

2. MECHANICAL HAZARDS

Obviously, any pressure vessel presents a rupture hazard. However, both design standards and official tests that are enforced by state agencies (or equivalent), in combination with strict inspection procedures limit this hazard to a quasi-zero level, especially on large-scale units. But, some mechanical hazards are often underestimated, especially on R&D multipurpose equipments :

- Corrosion : as many products are handled, it might happen that some of them do induce corrosion causing cracks and local weakness of the metal.

- Plugging :

Most solid-fluid extraction equipments use baskets closed by frits ; on large scale units, frit plugging causes frit breakage on decompression but, on lab or pilot-scale equipments, the frit may not break : then, even if the autoclave decompression seems effective, compressed CO₂ may remain in the basket ; on autoclave opening, the basket may be brutally ejected and/or may explode.

So, we strongly recommend to be extremely prudent when the treated material could lead to frit plugging : polymers, "sticking" materials, highly viscous extracts,....

Anyway, in all cases, especially on lab or pilot scale units, it is better to wait around 5 to 10 minutes after autoclave decompression before opening the autoclave, so that CO₂ have time to exit from the basket, even through a plugged frit.

- Tubing connection rupture :

Double-ring connections are commonly used on most small scale equipments, when the service pressure is below 400 bar. These connections are perfectly safe and reliable when the screwing procedures are strictly followed. Otherwise, the rings are not strongly attached to the tubing and a brutal rupture may occur on pressurization.

We recommend to always verify the good setting of the connections rings prior to high pressure use.

- Metal fatigue :

The life duration of high pressure vessels is linked to the number of pressurization/depressurization cycles. Commonly, autoclaves are authorized for 10 000 to 20 000 cycles, depending on their design.

On large scale units that are intensively used, a leaded counter must be installed to verify the cycle number and to stop any operation after the limit number is reached.

- Metal fragilization :

As carbon steel exhibits much better mechanical properties than stainless steel, large scale pressure vessels are commonly built in carbon steel covered by an internal stainless steel cladding. As carbon steel may be subject to phase transition, it becomes brittle when temperature decreases below -20°C ; so it is absolutely necessary to avoid such low temperature "exploration" during depressurization. In fact, adiabatic CO₂ decompression to atmosphere leads to very low temperature and CO₂ ice formation. So hot fluid circulation in the autoclave jacket and a "controlled" decompression could easily eliminate this hazard.

However, it is recommended to set a temperature captor inside the autoclave wall near the autoclave bottom where the lowest temperatures may occur, so that the temperature limit fixed by the autoclave design be not reached ; otherwise, the autoclave must be replaced. Another hazard might also appear on these stainless steel clad autoclave if this cladding is perforated or cracked and CO₂ corrodes the carbon steel (in presence of water) ; so a strict inspection must be made frequently to ensure that no such cladding perforation occurs.

3. THERMODYNAMICAL HAZARDS

- Dry ice :

As said earlier, CO₂ handling often leads to drastic temperature decrease and tubing plugging by water, products or dry ice itself. This plugging might be dangerous when occurring in basket frits, captors tubings, or vent line from safety valves/rupture disks to atmosphere. In order to eliminate this vent line plugging that, in fact, cancels safety devices operation, it is necessary to over-estimated this vent line diameter and design it carefully.

- B.L.E.V.E. :

This means "Boiling Liquid Expanding Vapor Explosion" and characterizes the physical explosion of a liquefied gas/supercritical fluid that is brutally decompressed to atmospheric pressure, in case of pressure vessel rupture or opening. Catastrophic BLEVE occurred when liquefied petroleum gases vessels burst (Mexico, Feyzin,...), followed by the "chemical" explosion due to gas cloud inflammation. In fact, this hazard is directly linked to metal weakening in case of fire around the vessel(s). It is the reason why it is recommended to install fire detectors that could order immediate depressurization of the whole plant in case of fire.

- Safety valves/Rupture disks :

The safety system design is often poor as very few experimental validation with liquefied gases/supercritical fluids have been published until now. We did operate some measurements of flash discharge of liquid/supercritical CO₂ from pressure vessels and proposed a simple model for mass flux evaluation [1] ; these results can be used for safety systems design.

4. CHEMICAL HAZARDS

- N₂O :

As no consensus has been yet driven among the scientific community regarding N₂O comburant behaviour under high pressure, in relation with explosions possibly linked to organic compounds oxidation by supercritical N₂O, we recommend to use N₂O with extreme case when contacted with flammable products.

- Flammable fluids, co-solvents, products :

Explosion proof equipments, buildings and procedures must be enforced when flammable fluids are handled, especially for light hydrocarbons. Explosion atmosphere sensors have to be installed, and connected to high power fans and to fluid reservoirs stop valves.

- Corrosion

As said earlier, this hazard must be evaluated prior to treating any fluid/co-solvent/raw material in the equipment. A considerable corrosion hazard is related to supercritical water oxidation equipments, where special alloys are required.

5. BIOLOGICAL HAZARDS

- Asphyxia :

Most supercritical fluid equipment use CO₂ : non toxic, non flammable, it is particularly safe. However, CO₂ build-up in closed rooms could lead to people asphyxia. It is the reason why all possible CO₂ emissions (exit valves, safety valves, rupture disks,...) must be collected in a "over-dimensioned" vent line ensuring a good dispersion of the gas in the outside atmosphere. Moreover, it is highly recommended to install CO₂ detectors in the equipment room but also in any connex room, for action on high power fans and operators information. Anyway, it is preferable not to operate an equipment in rooms located over other rooms, especially underground cellars, where CO₂ that is heavier than air may accumulate.

- Chemical and biochemical toxicity :

Handling any co-solvent or raw material or fluid that presents a danger in terms of chemical toxicity or pathogenic agents must lead to drastic care as supercritical fluid equipments work at high pressure with possible leaks at any moment. It is to be noticed that fluid leakage often leads to aerosol formation (droplets of extract, co-solvent, fluid in the gas flux), that are easily absorbed when breathing. In particularly dangerous cases, it is necessary to isolate the equipment in a closed room with operation through a remote automation system. Moreover, in these cases, environment must be protected by liquid and gaseous effluent treatment and equipment cleaning and/or sterilization.

6. SOME FINAL ADVICES

As far as supercritical fluid equipments are concerned, safety must be taken into account at any moment : equipment design, building and installation, operation, inspection and maintenance,....

But we would stress on the fact that a key for a safe and reliable operation of a supercritical fluid equipment consists of a very cautious training of the operators, in close relation with the equipment designer and supplier.

Such training should avoid that they fall in various "traps" that could lead to accidents, among which we could cite :

- Never "over-screw" a leaking nut, as CO₂ leakage causes a very sharp temperature decrease and leak cure is not possible, with potential risk of nut break and metal piece ejection ;
- Be prudent after vessel decompression if exists a risk of plugging ; wait several minutes before opening a decompressed autoclave ;
- Verify the reliability of the instruments (especially pressure gauges) ; be prudent on instrument indications especially if "plugging" materials are handled ;
- Always check what could happen in case of electrical power or instrument air failure ; be sure that in case of electrical power/instrument air recovery, nothing hazardous will occur ;
- Never modify an equipment without the consent of the original manufacturer and never introduce "new" type of spare parts without his approval !

7. CONCLUSION

Supercritical fluid technology is potentially hazardous and should not be used by "beginners" is ; very often, home-designed and home-made equipments do not incorporate all the safety levels that are required, according to us ; moreover, it is extremely important that operators be trained by specialists prior to work on supercritical fluid equipments.

A detailed information exchange between the equipment supplier and user should be the key for a reliable and safe operation, both for lab/pilot scale versatile equipments and for large scale dedicated units.

REFERENCES

- [1] LI Z., PERRUT M., Chem. Eng. Comm., 117, 1992, p. 415.

This page intentionally left blank

Endurance Prediction of Thickwalled High Pressure Components under Corrosion Fatigue Conditions

G. Vetter, L. Depmeier

Lehrstuhl für Apparatechnik und Chemiemaschinenbau, Universität Erlangen-Nürnberg, Cauerstr. 4, D-91058 Erlangen

1. INTRODUCTION

In many high pressure applications for reaction or separation processes or when using high pressure as a tool for cleaning, cutting or deformation of parts, more or less corrosive liquids have to be pumped against pressures in the range of roughly 300 - 3000 bar. The high pressure components between the pump check valves - the pump cylinders or working chambers - are submitted to pulsating pressures resp. stresses of large amplitude. The usual features of thickwalled components are variable with application and production methods (Fig. 1a-c), which is in general connected with more or less large stress risers at the intersection locations of bores [1]. There are theoretical and experimental data available for the determination of approximate stress concentration factors (survey [2]) and in addition modern FEM computations is yielding the thickwalled components.

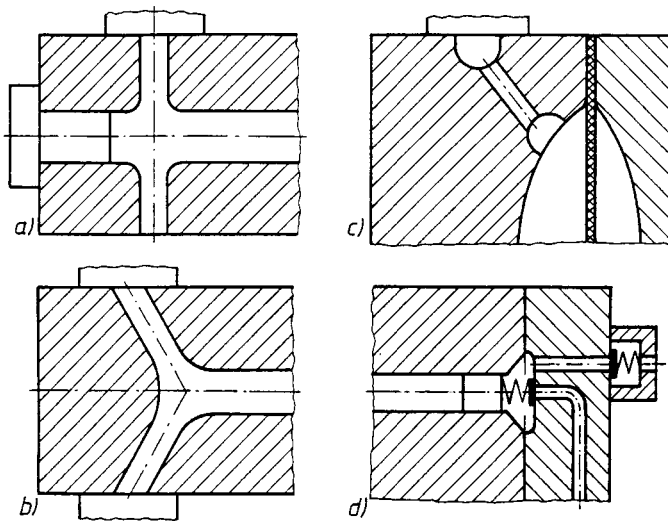


Fig. 1: Typical features of thick-walled high pressure components
 a) T-intersection b) Y-intersection
 c) ball/cylinder-intersection d) no intersection

The design of thickwalled components for pulsating pressure is based on the stress calculation with analytical or numerical methods and the determination of the maximum equivalent stress in relation to the admissible stresses at uniaxial conditions. The latter have to be extracted from Woehler-tests with specimen. If the stresses yield too large at load conditions including a safety factor, the design must be optimized by avoiding the major stress concentrations at bore intersections. The avoidance of T-intersections is reducing stresses by factor 2-3 (Fig. 1d).

Fatigue data of corrosion resistant steels and other relevant high strength materials are easy available for non-corrosive ambiance (air, oil). For the large variety of liquids applied in production processes the data have to be evaluated from special fatigue tests with corrosion cells. This paper answers the question if such uniaxial test results can be applied for the real component design in order to meet three-axial corrosion fatigue reality well.

material no.	name				Rp _{0.2} N/mm ²		Rm N/mm ²		A J	
1.4596 (HDV1)	X5CrNiMoCu 258				548		739		256 (DVM)	
1.4462	X2CrNiMoN 225				522		681		243 (ISO-V)	
	%C	Si	Mn	P	S	Cr	Mo	Ni	N	Cu
1.4596 (HDV1)	0.012	0.27	1.27	0.012	0.003	25.3	2.5	8.32	-	1.41
1.4462	0.021	0.54	1.7	0.021	0.004	22.12	2.95	5.34	0.0921	-

Table 1: Data of the test materials

2. METHODS AND TEST CONDITIONS

With regard to pump applications for high pressure processes two modern austenitic-ferritic (duplex) Chromium-Nickel steels (ESU quality) have been investigated (Table 1). All test specimen have been extracted from all-over forged bars (Fig. 2 and 3). The stress situation in pulsatingly loaded thickwalled pump components is simulated by the cross-bored pipe specimen (Fig. 3d). The uniaxial tests are carried out with bar specimen (Fig. 3a-c) for pulsating ($R = 0$) and reversed bending stress ($R = -1$). It should be pointed out, that the stress situation in cross-bored thickwalled pipes is triaxial and rather complex. At the relevant high pulsating pressures local plastification of the material must be expected [2] which is implementing autogeneous autofrettage effects.

A further speciality to mention is the test fluid (GM67): The pulsating pressure tests are carried out with a plunger pulsating machine (Fig. 4) [3], the plunger (Bridgman) seal of which requires a certain lubricity of the liquid. Therefore a corrosive mixture of Glycerol (67 %) and sea water (33 %) was chosen (artificial sea water: 28 g NaCl, 7 g MgSO₄ · 7 H₂O, 5 g MgCl₂ · 6 H₂O, 2,4 g CaCl₂ · 6 H₂O, 0,2 g NaHCO₃ and 985 ml distilled water).

All specimen are fully wetted (Fig. 5) by the corrosive test fluid (exception $R = -1$ probes which were only sprayed). The surface quality of the specimen - honed resp. polished - is well comparable to the finish of real pump components.

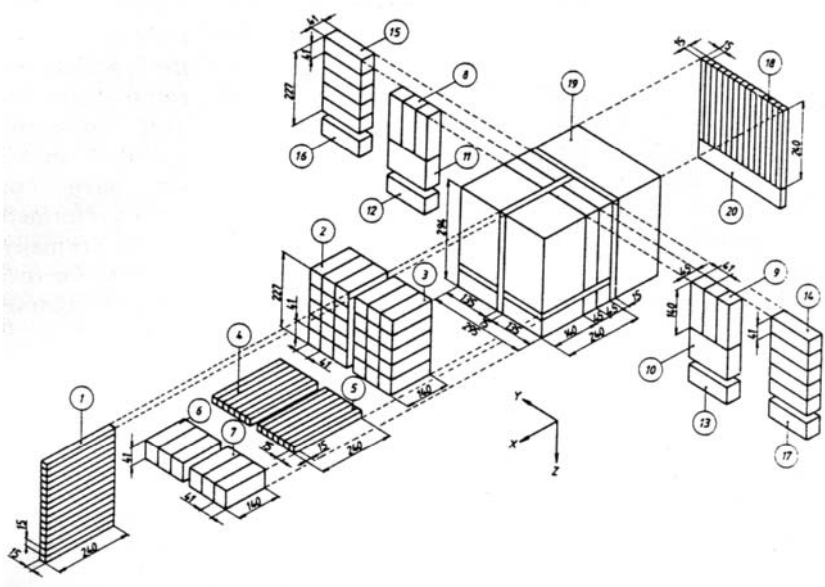


Fig. 2: Typical all-over forged bar for specimen extraction

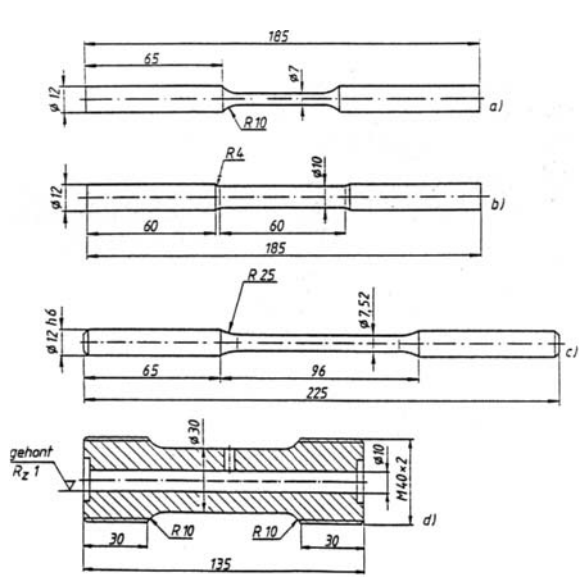


Fig. 3: Specimen
a) dynamic ($R = 0$), b) static,
c) dynamic ($R = -1$),
d) thickwalled crossbored pipe

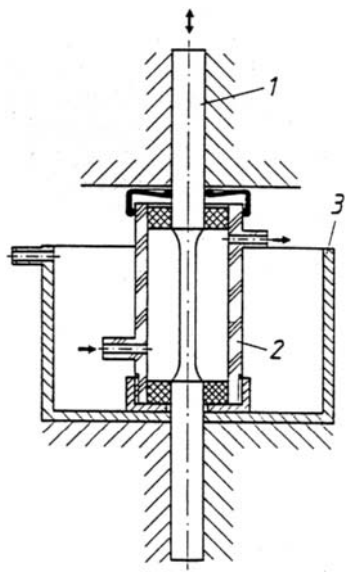
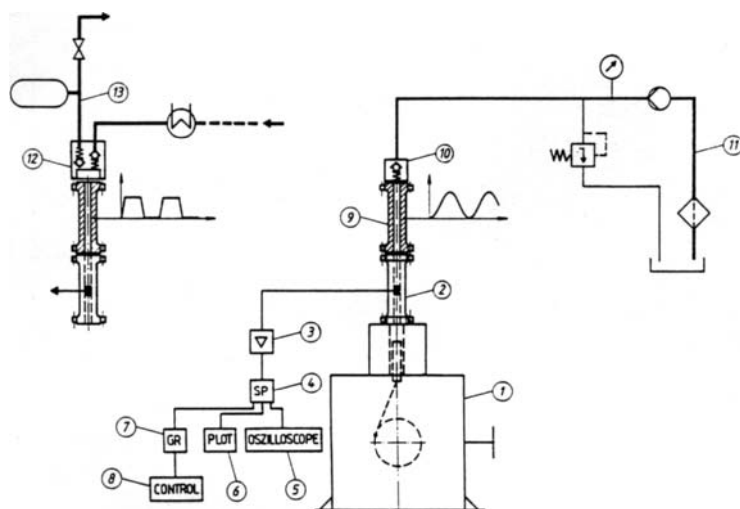


Fig. 5: Corrosion cell ($R = 0$)
1 specimen, 2/3 cell



Further characterizations of the specimen, as residual stresses and electrochemical analysis, have not been performed as it is normally the case for real pump components.

Fig. 4: Plunger pulsating machine
1-8 pulse machine, 9 pipe specimen,
10-11 reference pressure supply

3. RESULTS

3.1. Austenitic-ferritic Chromium-Nickel Steel X5CrNiMoCu255 (W.No. 1.4596)

The duplex steel obtains the corrosion resistance from Cr, Ni and Mo. The strength and toughness can be attributed to the interstitial carbon solution, the solid solution hardening and the fine grained austenitic phase.

The Cu contents promotes the generation of fine grained austenitic phase and the corrosion resistance.

The specimen ($R = 0$, $R = -1$) demonstrate clear effects of corrosion fatigue (Fig. 6 and 7). There evidently is a good correlation of the fatigue strength reduction between the pulsating stress ($R = 0$, uniaxial) and the pulsating pressure loaded pipe specimen (Fig. 8). The reversed bending probes ($R = -1$, uniaxial) exhibit some deviations.

It should be observed, that the comparison of the "fatigue strength" reduction is different for the probes: stress amplitudes for the uniaxial, pressure amplitudes for the pipe specimen.

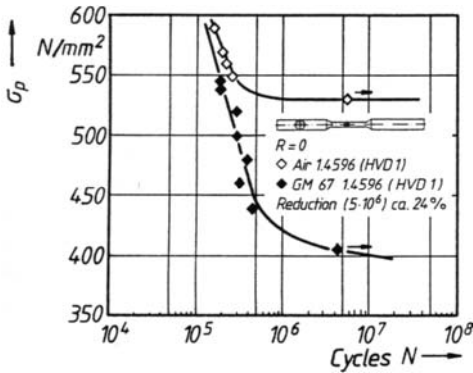
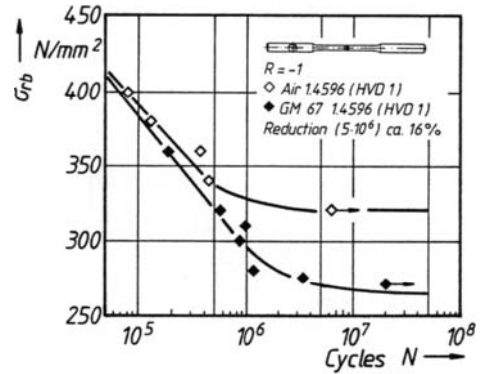
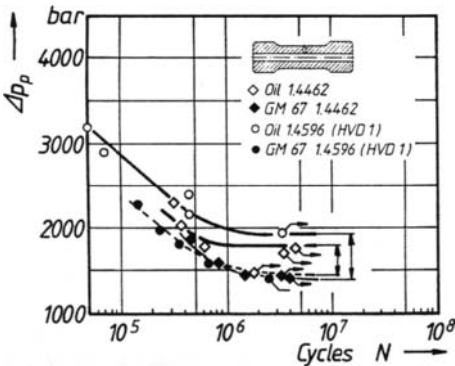
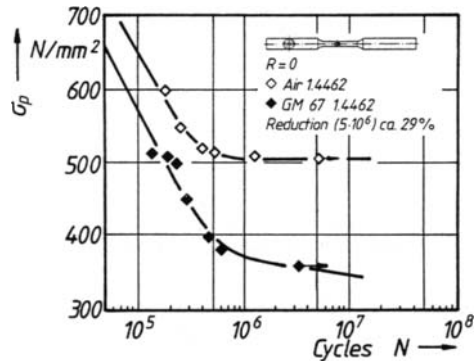
Fatigue strength reduction data ($5 \cdot 10^6$ cycles): $R = 0$: 24 %; $R = -1$: 16 %; Δp_p : 25 %.

3.2. Austenitic-ferritic Chromium-Nickel Steel X2CrNiMoN225 (W.No. 1.4462)

The material is a nitrogen alloyed duplex steel. The development has been continued to higher alloyed types (f.e. 1.4467 X3CrMnNiMoN2564)

The specimen (cross bored pipes and $R=0$) demonstrate the following fatigue reduction figures: $R = 0$: 29 %; Δp_p : 17 % (Fig. 9).

The quantitative correlation is not comparatively well as for previous tests, but still satisfactory.

Fig. 6: Fatigue strength 1.4596 ($R = 0$)Fig. 7: Fatigue strength 1.4596 ($R = -1$)Fig. 8: Fatigue pressure amplitudes Δp_p for pipe probesFig. 9: Fatigue strength 1.4462 ($R = 0$)

3.3. Failures of valve housings in a process diaphragm pump

The valve housing (1.4571 X6CrNiMoTi1810) demonstrated fatigue cracks (350 bar, Chlorine-Toluene/NaOH-mixture 1:1, 60 °C) starting predominantly from the spot K (Fig. 10, part 3) where the internal bushing (part 6) is located (1.4528).

The involved surface area exhibited small pittings, from where the fatigue cracks started (Fig. 11). Corrosion fatigue tests ($R = 0$) with uniaxial probes (1.4571) and narrow clearance rings (1.4528) in a corrosion cell yield an admissible pulsating stress of around 200-220 N/mm² at 10⁸ cycles (Fig. 13). The equivalent (v. Mises) stress in the valve housing was calculated to around 150 N/mm². The remaining difference between uniaxial probe and thickwalled pipe data by factor 1,3 - 1,5 can be attributed to stress risers by corrosion pittings and fatigue especially in the narrow clearance area. The problem was solved with a high strength duplex steel (1.4496 X5CrNiMoCu258).

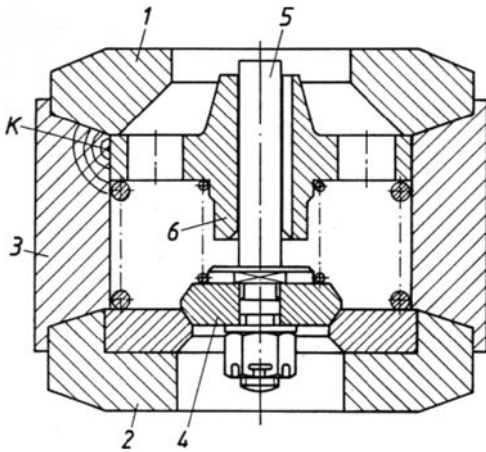


Fig. 10: Pump check valve

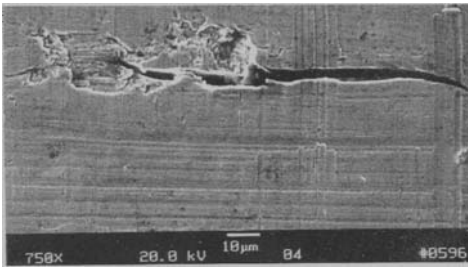
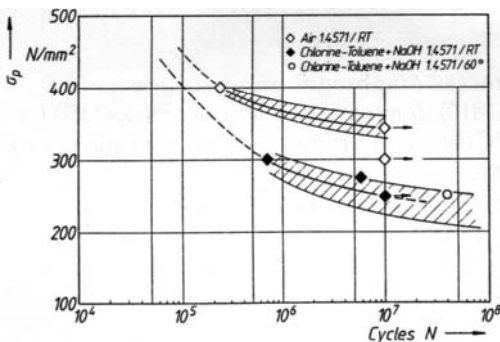


Fig. 11: Pittings and crack initiation

the application of corrosion fatigue data ($R = 0$) implement an additional safety factor. Applications for current failure analysis demonstrate the efficiency of the method.

Fig. 12: Fatigue strength 1.4571 ($R = 0$)

4. CONCLUSIONS

The corrosion fatigue data from uniaxial tests can be transmitted to the notched pulsating pressure loaded components quantitatively or with additional safety. The uniaxial pulsating stress yields to be the stricter criterion.

Differences in the correlation of the corrosion fatigue reduction data can be attributed to the residual stresses due to local plastification. The steel 1.4462 seems to develop more autogeneous autofrettage due to the lower strength.

Fatigue ruptures start with the uniaxial probes at any flaws, with the pipe probes very near to the cross-bore intersection (obviously influenced by the residual stress distribution). As a consequence the following design procedure can be recommended. If failures have already occurred, the improved material choice yields from uniaxial ($R = 0$) fatigue tests with the real liquid involved. For initial design purposes of thick-walled components uniaxial corrosion fatigue data ($R = 0$) can directly be applied. If the operational conditions or the component treatment involve autofrettage

5. REFERENCES

- [1] Vetter, G.; Karl, E: High Pressure Technolgy, Ullmann's Encyclopedia of Ind. Chemistry, vol 4, 1992, p. 587-625
- [2] Mischorr, G.: Dissertation Universität Erlangen-Nürnberg (Prof. G. Vetter)
- [3] Vetter, G.; Lambrecht, D., Mischorr, G.: Fatigue of Thick-walled Pipes from Soft-martensitic and Semi-austenitic Chromium-Nickel-Steels under Pulsating Pressure, Chem. Eng. Technol. 15 (1992) 300-312

Extrapolation from Pilot Plant to Industrial Scale SFE : a Case Study

J.Y. CLAVIER, W. MAJEWSKI, M. PERRUT.

SEPAREX, BP9, 54250 Champigneulle, France.

1. INTRODUCTION

Supercritical fluid extraction has now found a lot of applications in different fields (polymers, aromas and essential oils, fats, natural products, soil decontamination...) and several production units are operated in agroalimentary (coffee, hop...) and pharmaceutical industries. In order to estimate the economical interest of these applications, technical and economical extrapolation methods have been developed. These methods are dependent of the nature of the extraction and are based on experimental results obtained on pilot plant units. We describe here a general extrapolation procedure, and a case study is presented to illustrate an economical estimation of a supercritical fluid extraction.

2. TECHNICAL DESIGN OF AN INDUSTRIAL PLANT

The objective of this design is to determine operating conditions (pressure, temperature), but also what will be the optimal configuration of the plant, the dimension and the number of extractors, the capacity of the pump...

The design will always require some experimental data that have to be determined on a pilot plant unit.

The procedure of this design will be :

- to determine first the optimal physical conditions through a scanning of different pressures, temperatures, solvents...
- to obtain thermodynamic and kinetic data to design the industrial plant.

The extrapolation method will depend on the nature of the extraction and particularly on the mechanism controlling the extraction. Several mechanisms can be found :

- Some extractions are only limited by the solubility of the extract in the fluid. This is the case of the extraction of lipids when the access to the extract in the matrix is easy. This is for instance the case of extraction of beef tallow [1] or the extraction of fats from butter or cheese.
- Some extractions are only limited by diffusion and especially the internal diffusion. In certain cases like basil oil extraction or ginger extraction, the solubility of the extract in supercritical fluid is very high but the access in the matrix is more difficult, so that the concentration of

extract is the solvent is far below the solubility. In this case, the extraction can be represented only by diffusion and kinetic parameters [2,3].

- Most of the extractions are more complex and are limited by both solubility and diffusion. In a lot of cases, a fraction of the extract is extracted first and the extraction rate is function of the solubility of the extract in the fluid. The rest of the extract is extracted afterwards and the extraction is limited by diffusion [4,5]. This is the case in a lot of natural products extraction from seeds. The amount of "free" extract is usually dependent on the granulometry of the crushed seeds.

When several compounds can be extracted, the rate of extraction and the mechanism of extraction can be different for each of them.

Depending on the complexity and on the nature of the extraction, different extrapolation methods are available to design the production unit :

- A very simple way to extrapolate the experimental data obtained on a pilot plant is to keep the ratios U_s/M_f and M_s/M_f constant. (U_s is the solvent flowrate (in kg.h^{-1}), M_f is the feed mass in the extractor (kg), and M_s is the solvent mass required for the extraction (kg).

The ratio U_s/M_f is inversely proportional to residence time of the eluent in the extractor t_r (see equation 1), and this ratio will have to be conserved, especially for extraction limited by internal diffusion. These extractions are almost not dependent on the solvent flowrate, but the "contacting" time of the feed with the solvent is the determinant factor of plant design. Therefore, it will be necessary to use very large extractors or to use several extractors in series in order to maximize the contacting time of the solvent with the feed. On the other hand, it is possible to minimize the solvent flowrate and the energy consumption of the plant.

$$t_r = \varepsilon \cdot M_f / (U_s \cdot \rho_f) \quad (1)$$

with : ε : Void fraction of the bed

ρ_s : Specific gravity of the solvent

ρ_f : Specific gravity of the feed

M_f : Feed mass

U_s : Solvent flowrate

The ratio M_s/M_f corresponds to the amount of solvent needed to extract one kilogram of the feed. This ratio has to be maintained in the case of extraction limited by the solubility of the extract or by the thermodynamical equilibrium between the feed and the eluent. In these extraction the amount of solvent is the determinant factor of the plant design. So, for a given plant capacity, and therefore a given amount of solvent and energy consumption, it will be often possible to reduce the volume and the number of extractors as much as possible.

- In complex extractions, when both diffusion and thermodynamic are linked, or when the extract is a complex mixture of several components recovered at different rates, a numerical simulation software of the extraction can be very useful to estimate quickly any configuration and to optimize more precisely the industrial plant. A lot of different models have been proposed in the literature, and we built a versatile simulation software allowing to represent a lot of different systems [6].

Knowing the production requirements, the optimal configuration will be determined : the principal factors are :

- number of extractors,
- volume and number of shift/day of the extractors,
- pump and utilities capacities.

Traditional production units are composed of at least 2 extractors. One is discharged of solvent, the feed is replaced and the extractor is recompressed, when the other one is used for extraction. Three or more extractor configurations are often designed in order to optimize the extraction plant. One extractor is discharged and loaded when the others are operated in extraction. These extractors are connected in series, so that the feed and the solvent are contacted counter-currently. The last extractor of the series is the one with the previously unextracted feed and the first extractor of the series is the one which has been contacted the longest time with the eluent, and the next to be discharged. This "carrousel" implementation allows most of the time to reduce the amount of CO₂ required for a given extraction, and therefore, to reduce the energy consumption of the production plant. For a given production capacity, increasing the number of extractors will therefore decrease the energy consumption and the operating costs, but increase most of the time the investment costs, depending on the capacity of the extractors. The extractor volume will depend on the number of shift/day that can be operated. The more important is the number of shift/day, the less is the volume of the extractors, and the less is the investment cost. The economic estimation allows in each case to decide of the optimal configuration.

3. ECONOMICAL ESTIMATION OF AN INDUSTRIAL PLANT

The extraction of an economically interesting oil obtained from a natural seed is chosen to illustrate this estimation.

The characteristics of the raw material are the followings :

- Granulometry of the seed : 0.5 - 1.5 mm
- Moisture of the seed : $\approx 8\%$
- Apparent specific gravity : 550 kg.m⁻³
- Lipid in the feed : 3.8 % w/w

The extraction is performed at 250 bar and 40°C. The extract is recovered in 3 decompression/heating steps until 45 bar and 30°C.

Figure 1 represents 3 extractions curves obtained on a pilot plant at different flowrates U_s . The extractor volume is 1.5 l.

At the beginning of the runs, the extraction rate is approximately proportional to the amount of CO₂ pumped through the extractor, whatever the flowrate: the concentration of the extract in the fluid is therefore equal to the solubility which is in this case 0.9 g.kg⁻¹. At the end of the runs, the extraction is limited by diffusion, mainly inside the particles.

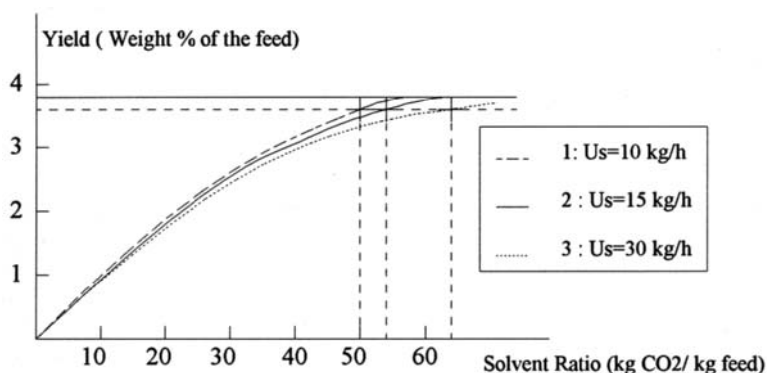


Figure 1

The industrial requirements are :

- A recovery yield of 95 % of the total extract (3.6% of the total mass)
- 2 capacities will be considered :
 - case a) 7 000 kg extract / year
 - case b) 10 700 kg extract /year

In case a) the plant will work 108 h/week and 48 weeks /year (5 200 h/year) with 3 operators working 3 x 8 h.

In case b) the plant will work 8 000 h/year with 4 operators working 4 x 8 h.

In both cases, the amount of seed to be treated is 37.1 kg.h⁻¹.

The economic calculation will be done in a 2 extractor configuration, one being in extraction mode while the other one is discharged, loaded, and compressed.

The extrapolation method consists here in keeping the ratios U_s/M_c and M_s/M_c constant. Table 1 resumes the extrapolation of the 3 curves obtained on the pilot plant.

Extraction	Batch length (h)	U_s/M_c	M_s/M_c	M_c (kg)	U_s (kg.h ⁻¹)	Extractor Volume (l)
1	4	12.5	50	160	2000	291
2	2.9	18.75	54	115	2160	209
3	1.7	37.5	64	68	2560	124

The economic estimation allows to decide which case is the most appropriate. The estimation in case 2 is detailed below :

Determination of production costs

Energy :

The CO₂ energy cycle encloses :

Pumping from liquid state 45 bar, 5°C to supercritical fluid 250 bar, 40°C : $\Delta H = 14 \text{ kcal.kg}^{-1}$

Expansion : from 250 bar, 40°C to 45 bar , 30 °C in three steps : $\Delta H = 46 \text{ kcal.kg}^{-1}$

Condensation : at 45 bar from 30°C to 5 °C : $\Delta H = 60 \text{ kcal.kg}^{-1}$

- Cooling utilities design:

60 kcal / kg CO₂ that is to say 130 000 kcal/h are required. In the case of an air refrigerated cooling device, the power of the cooling machine will be twice the required power. A buffer reservoir will be used to store the cooling glycol/water mixture and two pumps will pump the mixture to the process and to the cooling machine. The energy consumption of this system is evaluated at 120 kWh

- Hot utilities design:

A gas boiler is recommended. It provides hot water at 85 °C stored in a buffer and then sent to the process. The required power is 130 kcal/h, we will therefore plan a 200 T/h boiler, and the gas energy consumption taking into account heat losses is evaluated at 150 kWh.

- Pumps : The CO₂ pump consumption is estimated at 25 kWh. The other pumps and electric devices consumption (Air compressor, utilities....) are approximated at 15 kWh.

The total energy consumption is therefore evaluated at :

Electricity : 160 kWh

Gas : 150 kWh

CO₂ consumption

The 2 principal causes of solvent consumption are :

- Extract withdrawing : The optimization of an automated extract withdrawing system and the optimization of the extractor emptying and filling, allows to minimize the solvent consumption which is estimated at 0.5 kg CO₂/ kg extract.

- Extractor emptying : At each extractor shift, a 210 l extractor is vented from 45 bar, 20°C to atmospheric pressure which corresponds to a waste of 25 kg of CO₂ / shift.

The total CO₂ consumption is therefore evaluated at

- case A 50 : T/ year

- case B 75 : T/year

Labour work :

The whole unit is automated and we evaluate the labour work at :

- 1 operator working 3 x 8 (in case A)

- 1 operator working 4 x 8 (in case B)

- 1 maintenance technician

- Supervision/Management (25%)

- 1 more operator in the day is in charge of feed reception, storage, crushing...

Global economic evaluation :

Investment :

Process : 6 M FF (million of French Francs)

Utilities : 1 M FF

Feed preparation : 1 MFF

Total : 8 M FF

Operating costs:	case A (in M FF)	case B (in M FF)
Labour work	1.2	2.0
Energy	0.8	1.1
Maintenance	0.2	0.2
Insurance / taxes	0.2	0.2
General costs	0.6	0.9
Total	3.0	4.4

Considering a capital return of 25%, the annual cost is evaluated at 5 M FF/year in case A and 6.6 M FF in case B that corresponds to 25 FF/ kg feed in case A and 22 FF /kg feed in case B.

4. CONCLUSION

In front of the diversity and the complexity of supercritical fluid extraction, we dispose of all experimental and theoretical tools to compute and extrapolate pilot plant experimental data to an industrial unit. A lot of theoretical thermodynamic and kinetic data are now available, and experimental extractions carried out on pilot plants allow to build extrapolation models, from the very simple ones (like it is described in this case study) to the very sophisticated ones based on a numerical simulation software and taking into account hydrodynamic, thermodynamic and kinetic phenomena.

These extrapolation methods allow to determine what will be the best operating conditions, and the optimal system configuration of the production plant from a technical and economical point view. If the extrapolation and optimization methods describe above concerns only the "extraction step" of the process, it is also very important to optimize the other parts of the process : the optimization of the extract recovering and fractionation, the energetic process optimization, or the improvement of the extractor emptying and loading procedure are also some very important points that must be considered in the industrial process design.

REFERENCES :

1. CHAO R.R. , Supercritical fluids proceedings of food materials Eds Rizvi, (1994), ISBN 0-7514-01846, p 203-213.
2. REVERCHON E. , proceedings of the third international symposium on supercritical fluids, vol 2, (oct-1994), p189.
3. SANKAR K.U. , Supercritical fluids proceedings of food materials Eds Rizvi, (1994), ISBN 0-7514-01846, p 44.
4. GOTO M. , proceedings of the third international symposium on supercritical fluids ISBN 2-905267-23-8., vol 2, (oct-1994), p165-170.
5. SOVOVA H. , proceedings of the third international symposium on supercritical fluids, vol 2, (oct-1994), p131-136.
6. CLAVIER J. Y., MAJEWSKI W., PERRUT M., Atti del III congresso i fluidi supercritici e loro applicationni, Eds. Kikic. I. and Alesi P. (1995), p 107- 116.

Design Rules for the Wallcooled Hydrothermal Burner (WHB)

H. L. La Roche¹, M. Weber, Ch. Trepp, Institute of Process Engineering and Cryogenics,
Swiss Federal Institute of Technology, CH-8092 Zuerich, Switzerland

Keywords:

supercritical water oxidation (SCWO), hydrothermal oxidation (HTO), supercritical combustion, performance of reactor, reaction stability, wall compatibility

1. SUMMARY

SCWO reactors may be prone to rapid corrosion and plugging. Furthermore, the wall temperature is typically limited to about 900 K due to creep. To inhibit corrosion, prevent plugging, and overcome the temperature limit, the Wallcooled Hydrothermal Burner (WHB) is proposed as a generalized reactor concept. The WHB concept unifies several features of SCWO reactors which have been proposed in recent years.

The fundamental concept is to envelop the hot reaction zone with cool water which protects the wall from the hot, corrosive fluid while simultaneously dissolving salts, thus inhibiting the buildup of sticky solids at the wall. The reaction zone is stabilized by a recirculation zone with heat and mass transfer to the cold inflowing stream thus heating it to ignition temperature.

This concept was demonstrated at the Institute of Process Engineering and Cryogenics at ETH (Switzerland) during the last two years with the FilmCooled Hydrothermal Burner (FCHB). The FCHB operated at pressures of 25 MPa and temperatures up to 2000 K, cf. [1].

Experiments and detailed analysis led to the basic design approach for SCWO reactors discussed herein which is based on wall boundary layer control and internal recirculation.

In this paper, an overview of the important phenomena is given. The supercritical combustion process employed is also known to occur in liquid propellant rocket motors (e.g. in LOX/GH₂-motors), liquid propellant guns (LPG), advanced aviation gas turbines and, to a lesser extent, in internal combustion engines. Supercritical combustion is characterized by: (1) injection of at least one liquid state fuel component into a chamber which is thermodynamically in the supercritical state, (2) density ratios of fuel to oxidizer near one, (3) supercritical phase transitions of fluid-particles due to combustion, (4) non-ideal properties of the fluids. Additionally a short description of pertinent design criteria is given.

¹current address: General Atomics, P.O. Box 85608, San Diego, CA 92186-9784

2. INTRODUCTION

Supercritical water oxidation is an alternative to incineration or biological wastewater treatment for aqueous wastes, cf. [2]. The wastewater is pressurized to about 25 MPa and then mixed with air or oxygen. Heat is then added, and the organics are oxidized to harmless products such as carbon dioxide. Typical temperatures in a SCWO reactor are 670 to 920 K. The higher value imposed is a limit by the wallmaterial strength. The lower value is specified by the supercritical temperature where a homogeneous phase is formed. At these temperatures, most wastewaters are corrosive, and salts precipitate due to the low solubility of salts in supercritical water. The problems of corrosion and plugging are the main problems of SCWO and, consequently, they have influenced development patterns of reactor design. The first SCWO reactors were primarily tube reactors consisting of a preheat section, a reaction section, and a cooldown section. These were particularly prone to corrosion and plugging.

One approach to reduce corrosion and plugging is to cool the walls and to install a recirculation zone, which sustains the reaction via cold feed injection, i.e. the feed is injected at temperatures of 300 to 500 K. The MODAR Reverse Flow Reactor as proposed in [3] shows these features for the first time, although the reverse flow is primarily employed to separate solids.

Other reactor concepts show similar features (see [1] and [4]), which include boundary layer control and internal recirculation. Reference [5] proposes boundary layer control utilizing transpiration cooling.

These types of combustor-like reactors are unified by their overall design criteria, which include stability of reaction, wall compatibility, and performance. In the following, a description of the basic mechanism of the process and design rules for a reactor are provided.

2. BASIC MECHANISMS OF THE PROCESS

The process mechanism for SCWO in a WHB with cold feed injection (CFI) may include the following:

1. Feed is conditioned (e.g. pH) and pressurized.
2. Preheat to T_{wmax} , the maximum wall temperature T_w where no corrosion occurs (T_{wmax} is dependent on the corrosivity of the waste and is typically in the range of 400 to 500 K).
3. Mixing of oxidant and wastewater; formation of a dispersed, uniform spray.
4. Additional heatup to ignition temperature via recirculation.
5. Phase transition of the wastewater droplets to the supercritical state and mixing on the molecular scale.
6. Pyrolysis (may occur in unmixed regions).
7. Hydrolysis (water will react with hydrocarbons in the waste).
8. Oxidation.
9. Salt precipitation.
10. Salt and/or solid separation.
11. Cooling.
12. Expansion to ambient pressure.

Steps 3 to 9 take place simultaneously. Figure 1 shows the basic mechanism for steps 3 to 10.

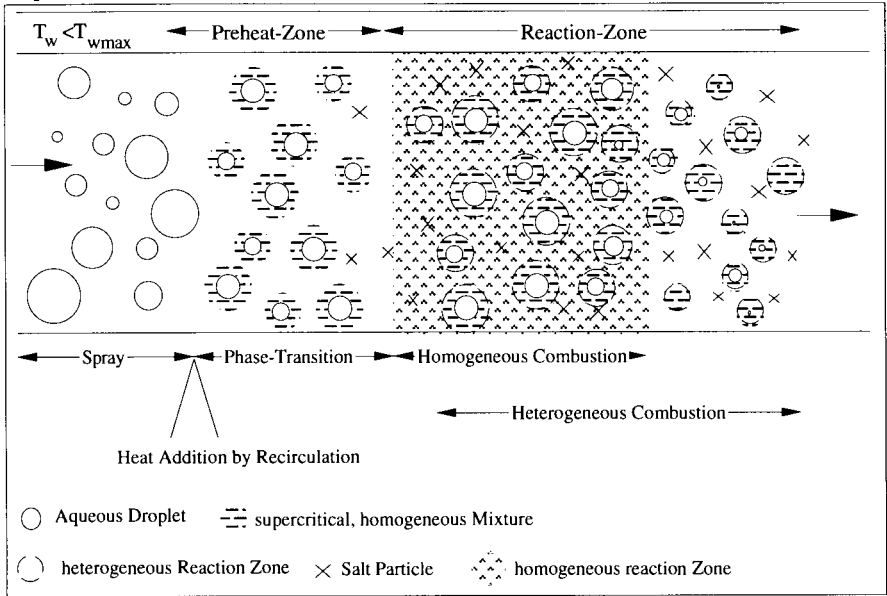


Fig. 1 : Basic process mechanism of SCWO in a WHB with cold feed injection (CFI)

For the process to work, the following three criteria must be met: (1) *performance*: Sufficient overall reaction rate at a specified temperature and pressure. (2) *stability*: Small disturbances in pressure and flow rate do not lead to extinction of combustion or to oscillations of state variables of the system. (3) *wall compatibility*: There are no thermal overloads, corrosive, abrasive or fouling interactions between the fluid in the system and the walls.

4. REACTOR DESIGN

There are four important elements in a combustor which interact and must be properly designed (see. Fig. 2):

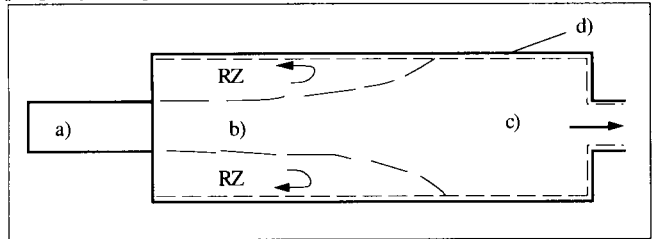


Fig. 2: Schematic of a combustor

a) The injector or burner which mixes and injects the oxidant and fuel in the reaction chamber.

- b) Recirculation Zones (RZ) which are separated flow zones that allow cold feed injection due to backmixing. RZ's behave almost like ideal stirred reactors.
 - c) Reaction zone with plug flow mixing characteristics.
 - d) Devices to control the wall boundary layer of the combustor.
- These four elements must be designed within the constraints of the specified performance, stability, and wall compatibility.

4.1. Injector

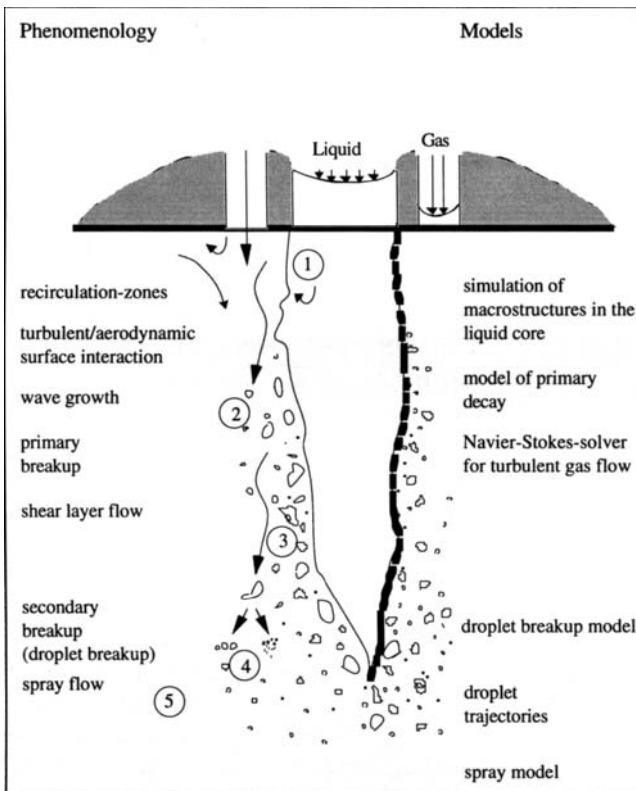


Fig. 3: Structure of coaxial mixing and atomization after [6]

At typical waste-water injection temperatures the oxidant (air or oxygen) will form a two-phase mixture with the wastewater. The injector must, therefore, be designed for two-phase flow. WHB-Injectors are characterized by a liquid to gas density ratio of 3 to 7, a liquid to gas mass flow ratio of 0.2 to 2. Injectors for such ratios are mainly used in liquid rocket motors. Figure 3 shows the phenomena and the attributed models for a coaxial injector.

At point 1, there is liquid flow in the core. The coaxial gas flow shears due to its higher velocity on the liquid core, thus breaking up the core (i.e. primary

break up). At point 2 is a region of dense spray with a high volume fraction of the denser fluid. At point 3, the fraction of dense fluid has decreased. Droplets are breaking up (secondary breakup) at point 4, while at point 5 there is homogeneous fluid flow. Depending on the feed properties of the wastewater and oxidant the injector has to be designed to achieve optimal mixing and atomization. The injector has to provide a uniform, dispersed, two-phase mixture, which leads to sufficient stability and performance.

4.2. Recirculation Zone (RZ)

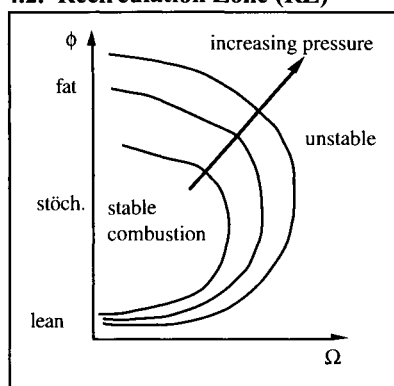
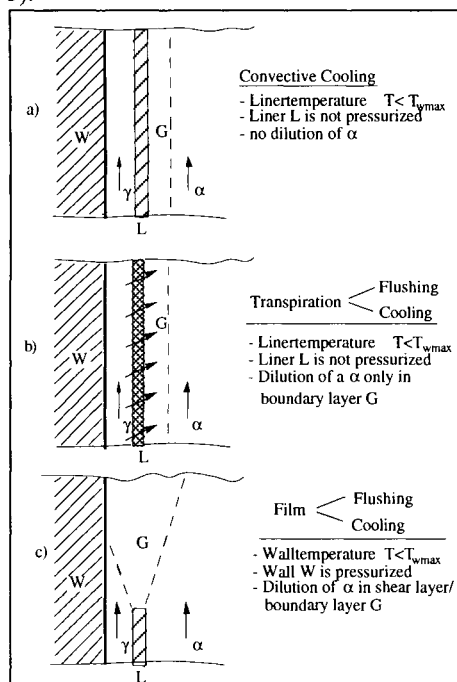


Fig. 4: Stability loop: ϕ = fuel to oxidant ratio, Ω = loading factor

To match the specified stability limits, the RZ's must be properly designed. Stability limits are described by stability loops (see Fig. 4), which show the region of stable combustion. ϕ is the fuel to oxidant ratio, Ω is a loading factor (e.g., velocity). RZ's are separated flows, which can be generated by various means, including bluff bodies or backward steps and vortex breakdown phenomena (see [1]). The interaction between the injector and RZ is essential. If the injection velocity is too high, stability decreases while mixing is enhanced. The RZ is also influenced by cool walls which cool the recirculating fluid. The RZ has to provide sufficient backmixing to provide the required stability and performance.

4.3. Wall boundary layer control

There are three typical methods to control boundary layers in combustors (see. Fig. 5):



a) Convective Cooling:

Liner L is cooled from the outside with cooling fluid γ which enforces a temperature drop in the wall boundary layer G, so that T_w can be kept below T_{wmax} .

b) Transpiration Cooling/Flushing:

The liner has a porous or near porous structure generating a uniformly distributed source of cooling or hot flushing fluid that keeps T_w of the liner cool or reduces the concentration of corrosive species in the wall boundary layer G.

c) Film Cooling/Flushing:

A wall jet γ is injected parallel to the reacting stream, which forms a turbulent shear layer G.

Fig. 5: Methods of wall boundary control to provide wall compatibility in combustors (Legend below)

Legend to Fig. 5: α : corrosive/hot, reacting fluid, γ : cooling/flushing fluid, L: Liner,

G: Boundary/shear layer, W: Wall of pressure vessel

The wall boundary layer control system must protect the walls, while the whole reactor must match the specified performance and stability.

4.4. Reaction chamber overall design

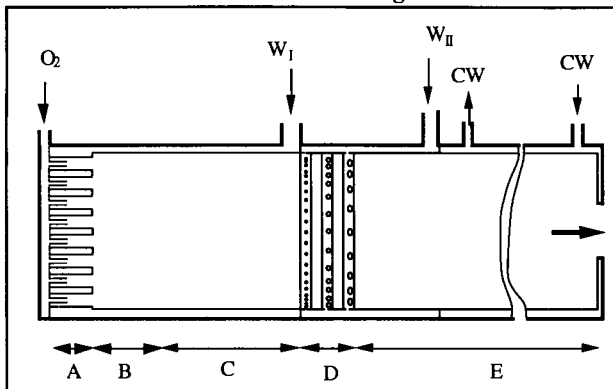


Fig. 6: WHB with staged wastewater injection: O_2 : oxygen flow, W_I high heat of combustion wastewater, W_{II} : low heat of combustion wastewater, CW : cooling water

Figure 6 shows an advanced WHB reactor concept which results from [1].

The reactor can be divided in 5 parts: A: injector face plate where multiple injectors mix the oxidant and wastewater (W_I).

B: Stabilizing region.

C: Primary reaction zone.

D: Radial injection of secondary wastewater (W_{II}).

E: Secondary reaction zone.

5. CONCLUSION

Development patterns of current SCWO reactor concepts generally follow combustor design rules. The basic process of *supercritical combustion* with aqueous feed has to be sustained in a reactor which matches required *performance*, *stability* and *wall compatibility*.

REFERENCES

1. H. L. La Roche, Wandgekuehlter Hydrothermal-Brenner (WHB) für die ueberkritische Nassoxidation, Dissertation ETH Nr. 11585, 1996
2. Tester J. W. et al., Supercritical water oxidation technology: A review of process development and fundamental research, 1991 ACS symposium series paper on emerging technologies for hazardous waste management, Atlanta, Georgia, oct. 1-3, 1991
3. Jacobs G. P. et al., Utilization of Phoenix in the design of the MODAR SCWO reactor, Presentation in session " Reactions in supercritical fluids", 1992 Annual AIChE Meeting, Miami Beach, FL, nov. 1992
4. McGuinness T. G., Developments in transpiring-wall SCWO reactor technology, 1st Intern. workshop on SCWO, Amelia Islands FL, Febr. 1995
5. Ahluwalia K. S. et al., Testing and application of a transpiring wall platelet reactor for SCWO of hazardous waste, 1st Intern. workshop on SCWO, Amelia Islands FL, Febr. 1995
6. Mayer W. O. H., Zur coaxialen Flüssigkeitszerstäubung im Hinblick auf die Treibstoffaufbereitung in Raketentriebwerken, Diss. Erlangen, 1993

High Pressure Cell Heaters for Diamond Synthesis

A.I.Borimsky, V.B.Volkov and P.A.Nagorny

Institute for Superhard Materials

National Academy of Sciences of Ukraine, 254074, Kiev, Avtozavodskaya str. 2, UKRAINE

Key words: high pressure and temperature apparatuses, reaction cell, heater, container, reaction mixture, synthetic diamond

INTRODUCTION

Diamond and other superhard material synthesis is the only technology widely used in industry for production of materials at highest pressures and temperatures. In particular, diamond synthesis is usually taking place at pressure more than 5 GPa and temperature more than 1200 °C in specially designed high pressure and temperature apparatuses [1,2,3]. Original components for diamond synthesis are graphite and carbon-soluble alloy which are inserted into the reaction cell of apparatus. As a rule, reaction cell has a form of cylindrical cavity in the apparatus container to be deformed.

During the diamond synthesis after developing of a high pressure in the apparatus the heating of reaction components are getting started for crystal growth initiation. Very important condition to be realized at this stage while synthesis is going on is to support and retain p-T parameters in the reaction cell during the whole cycle of synthesis process in predetermined fairly narrow range of values. One of the means to meet this condition is utilization of specially designed reaction cells and choice of most appropriate materials for cell and container construction.

METHODS

For developing of high temperature in reaction cell various heating schemes may be employed which must supply both minimum temperature drop in the cell body and maximum useful volume for reaction mixture deposition.

Due to the constructive peculiarities in the most of widely used high pressure and temperature apparatuses including both lens and belt type ones temperature field in reaction cell has axial symmetry. Thus, one has possibility to analyze temperature conditions in reaction cells of different design by means of finite element method calculation scheme [4]. Beneath we discuss the results and application of this kind of calculations of temperature fields for one possible type of lens-shaped high pressure apparatus [1].

RESULTS AND DISCUSSION

So the reaction mixture for diamond synthesis possesses fairly high electroconductivity it is possible to heat this mixture by passing electric current consequently through heaters and reaction mixture (the so called "direct heating"). While using this type of heating scheme, which is the most simple one from the view point of construction, one

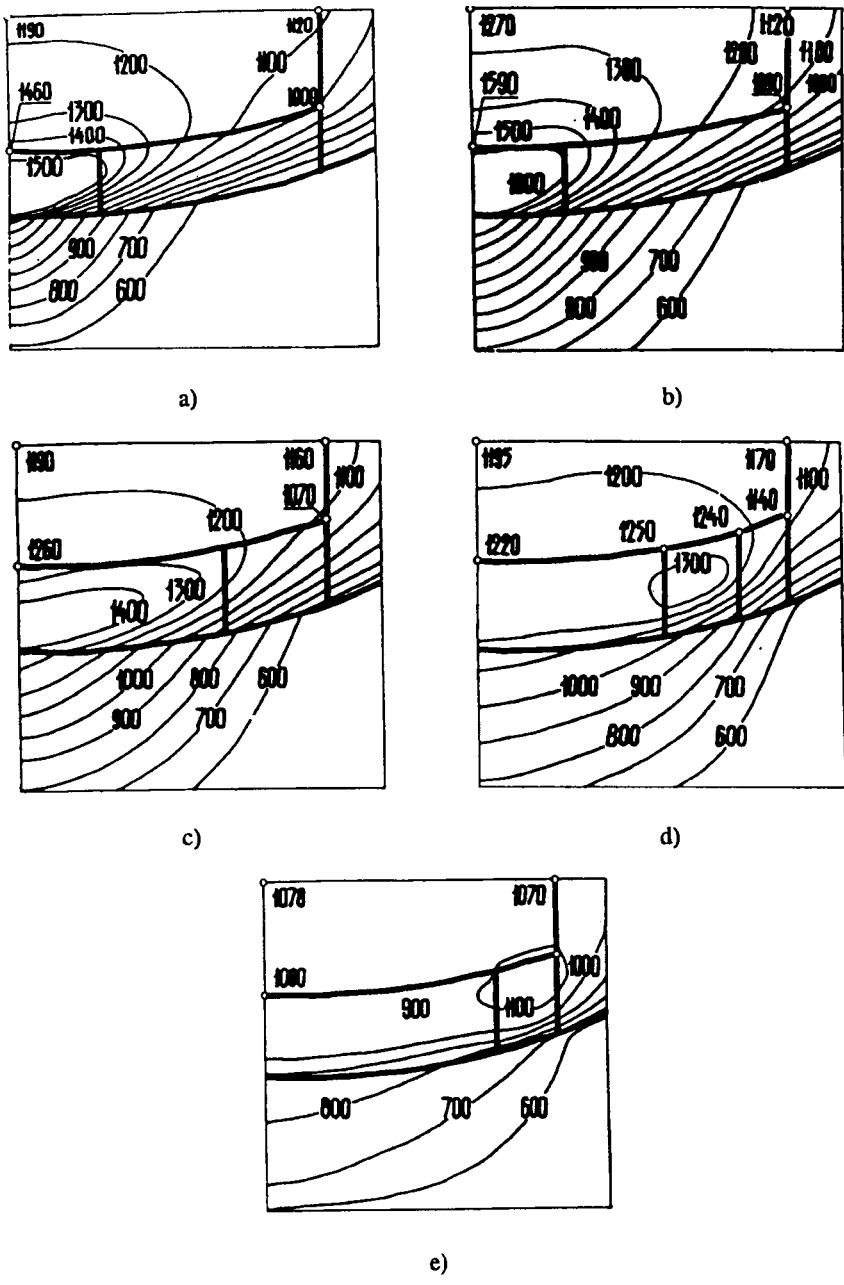
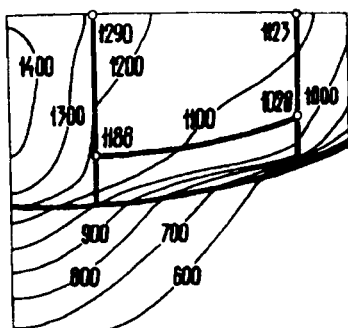
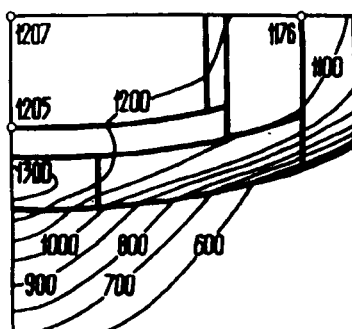


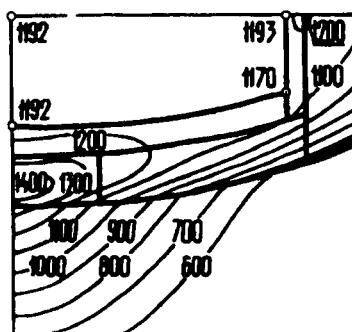
Fig. 1. Temperature field in reaction cells of the apparatus [1], equipped with end heaters in disk (a,b,c) and ring (d,e) shapes



a)



b)



c)

Fig. 2. Temperature fields in reaction cells of the apparatus [1], equipped with a rod-shaped heater (a) and with a complex heater (b, c)

gets rather high temperature drops in the reaction cell body.

For example, Fig.1 demonstrates temperature fields in reaction cells of apparatus with heaters of various shapes and sizes mounted in the container holes near the reaction cell ends. In the calculation scheme the dependence of thermo-physical characteristics of heated apparatus, container and cell details on temperature developed has been taken into account.

Influence of thermoconductivity of material used for apparatus details construction contacting with heaters on temperature field in reaction cell has been evaluated. It has been shown that when anvil was made of hard alloy the temperature gradient in the cell was more being compared with steel-made anvil because of lower thermoconductivity of steel.

Temperature drop in reaction cell decreases along with increasing of cylindrical heater diameter (Fig. 1b and 1c). Material for heaters of various size has been chosen in such a way as to increase its specific electric resistance and decrease the thermoconductivity along with heater diameter increase. On practice it may be accomplished, for example, by variation of heater components ratio [5].

Decrease of temperature drop in the cell in comparison with ones considered above may be achieved by using of end heaters in the form of rings, as shown in Fig. 1d and 1e. With the increase of diameter of ring heaters homogeneity of temperature field in reaction cell increases as well.

It is also possible to heat reaction cell by heaters isolated from reaction mixture (the so called "indirect heating"). Temperature fields for indirect heating of reaction mixture [1] are shown in Fig.2. Elements isolating heater details from reaction mixture are not shown in Fig.2 for bigger clarity of drawing.

The most simple variant of indirect heating includes rod-shaped heaters connecting opposite current inlet details of apparatus [5]. In this case the big temperature radial drop is observed in reaction cell (Fig.2a).

This temperature drop in the cell may be decreased by utilization of combined heater construction including end, plate and tube elements [6]. This type of heater construction gives possibility to achieve optimal temperature distribution field in the reaction cell body (Fig.2b and 2c).

CONCLUSION

The results of calculations performed demonstrate the possibility of wide range variations of temperature conditions in the reaction cells of high pressure and temperature apparatuses while employing heating devices of different design. The results obtained may be useful for development of heating schemes for apparatuses of different types because of general character of dependencies revealed.

Authors wish to acknowledge V.Yanchuk for support in temperature distribution field calculations.

REFERENCES

1. Patent 136 0281, Great Britain, CI B 01J 3/00
2. Patent 234 1248, USA, CI 18-16.5
3. Patent 296 8837, USA, CI 18-16.
4. A.S. 547 047, USSR, CI H 05B 3/14.
5. A.S. 902 801, USSR, CI B 01J 3/06.
6. A.S. 443 786, USSR, CI B 30b 11/32.

Interfacial Tension Measurements Between α -Tocopherol and Carbon Dioxide at High Pressures

M. Moser, W. Pietzonka and Ch. Trepp

Institute of Process Engineering and Cryogenics, Swiss Federal Institute of Technology,
ETH Zentrum, CH-8092 Zurich, Switzerland

1. SUMMARY

The interfacial tension of the binary system α -tocopherol/carbon dioxide was measured using the pendant drop method in the pressure range between 10 and 37 MPa at nine different temperatures: 313, 333, 343, 353, 363, 373, 383, 393 and 402 K. The interfacial tension decreases with rising pressure at a constant temperature and increases with increasing temperature at a constant pressure. The interfacial tension was found to be mainly a function of the mutual solubility of the two system components and of the density of pure carbon dioxide.

2. INTRODUCTION

Interfacial tension plays an important role in the modelling and design of both conventional and supercritical-fluid solvent extraction systems. The behaviour of fluid-fluid interfaces in the vicinity of the critical point is of fundamental importance. High pressure interfacial- and surface-tension phenomena are of particular relevance to phase separation and mass transfer. Factors determining the efficiency of mass transfer include drop diameter which is dependent on the interfacial tension. In order to design an extraction column operating in the region where one fluid is supercritical, there is the need for fundamental information on system physical properties including the interfacial tension.

A major chemical engineering task in supercritical fluid extraction is the optimisation of temperature and pressure. A thorough knowledge of physical properties, in particular phase equilibria, and of mass transfer as a function of pressure and temperature is required.

α -Tocopherol ($C_{29}H_{50}O_2$, $M = 430.7$) is an industrial product added increasingly to food and cosmetics products. Part of its synthesis can probably be carried out in dense gas solvents such as carbon dioxide.

While phase equilibria for the α -tocopherol/carbon dioxide system at high pressures have been studied by several authors [1-6], only a few measurements of dynamic viscosity [7], thermal conductivity [7] and mass transfer coefficients [3] were carried out. The present study of the interfacial tension in the α -tocopherol/carbon dioxide system at temperatures between 313 and 402 K and pressures from 10 to 37 MPa aims on the one hand at completing characterisation of this system and on the other at contributing to understanding interfacial phenomena in mass transfer processes.

3. EXPERIMENTAL

3.1. Materials

The carbon dioxide used in this study was purchased by PanGas, Schlieren, with a reported purity of 99.99% and recondensed from the gas phase. α -Tocopherol (98% reported purity) was supplied by Hoffmann-La Roche AG and used without further purification.

3.2. Method

The measurements of the interfacial tension were made with the pendant drop technique using the selected plane method as described by Andreas et al. [8]. This method was chosen because it is simple to use in high pressure systems.

The drop shape can be described by calculating the ratio S of two diameters at different horizontal planes:

$$S = \frac{d_s}{d_e} \quad (1)$$

The equatorial diameter d_e is erected vertically on the top apex of drop and defines the position of a selected plane with drop diameter d_s . The interfacial tension is then given by

$$\sigma = \frac{\Delta\rho \cdot g \cdot (d_e)^2}{H} \quad (2)$$

where $\Delta\rho$ is the density difference between the liquid and supercritical gas phase and g the acceleration due to gravity. The quantity $1/H$ is a function of S and has been calculated by several authors [9-12].

3.3. Apparatus and Procedure

A schematic representation of the experimental apparatus is shown in Figure 1. A cylindrical high pressure cell (6) with 30 ml volume was built with two sapphire windows with an optical width of 18 mm mounted in the central axis. To produce pendant drops, a narrow capillary was screwed vertically into the cell. The tip of the capillary could easily be replaced with tips of other sizes. The main components of the circulation equipment are a stirring autoclave (1) of 600 ml volume and a high pressure gear pump (2) to circulate the liquid or the supercritical gas phase depending on the position of the valves.

To form a pendant drop, the gear pump (2) was switched off and the air driven oscillating double piston pump (4) with 1.8 ml per stroke was used. This pump has the advantage of keeping the volume constant in the apparatus while pumping. The drop size was controlled by closing the metering valve (5).

To measure the densities of the two coexisting phases, a high pressure density measuring cell (3) (Paar DMA 512) was integrated in the system.

The desired drop parameters were determined using a digital image processing system. The images were taken with back-lighting from a CCD-b/w-camera (9) (Kappa CF-8) with 739(H) x 575(V) pixels resolution. The images were transferred to a computer (11) using a QuickCapture DT2255-50Hz frame grabber board (Data Translation Inc.) with 768(H) x 512(V) pixels resolution. The image analysis and the calculation of the drop parameters were done using the image application software NIH-Image v. 1.55 (National Institute of Health, U.S.A).

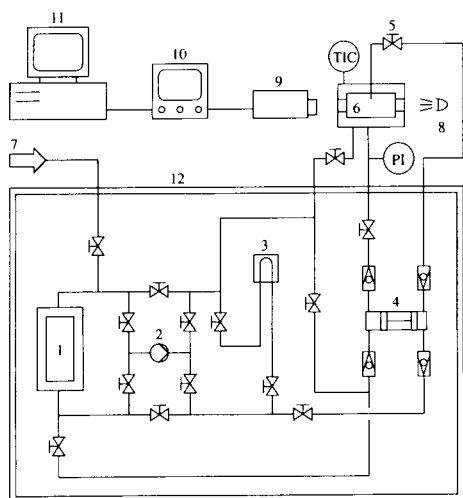


Figure 1. Schematic diagram of the apparatus for the measurement of the interfacial tension at high pressures.

(1) stirring autoclave, (2) circulation gear pump, (3) density measuring cell, (4) sample pump, (5) metering valve, (6) visual cell, (7) gas supply, (8) light source, (9) CCD-b/w-camera, (10) monitor, (11) computer with frame grabber card, (12) thermostated chamber.

After filling the autoclave (1) with α -tocopherol, carbon dioxide was pumped into the apparatus until the desired pressure was reached. The liquid phase was then stirred while the supercritical gas phase was circulated by the gear pump (2) until equilibrium was reached. Thereafter, a drop was formed by operating the sample pump (4) and the metering valve (5). The image of the pendant drop was recorded by the computer. After thresholding, the image was converted into a binary picture. Therefore the drop contour appeared black on a white background. After calibrating the image with the known diameter of the capillary, the equatorial diameter d_e and the diameter d_s of the selected plane were measured and the value of the interfacial tension calculated using eq. (2). For every value of the interfacial tension the arithmetic mean of twenty analysed drops was taken.

4. RESULTS AND DISCUSSION

Interfacial tensions between coexisting liquid and supercritical gas phases for the α -tocopherol/carbon dioxide system have been measured for different pressures at 313, 333, 343, 353, 363, 373, 383, 393 and 402 K. At each interfacial tension measurement the density of both the liquid and the supercritical gas phase was also determined as these values are essential in calculating interfacial tensions from the shape and size of drops. Densities of the system investigated have already been measured by other authors [4, 6, 7] and their results agree, within measurement accuracy, with those obtained in this work.

The results of the interfacial tension measurements are plotted in Figure 2. The interfacial tension decreases with increasing pressure at a constant temperature for all nine temperatures investigated. As the pressure increases both the concentration of carbon dioxide in the liquid phase (see Figure 4) and the density of supercritical carbon dioxide increases. Because of the increase in density the solvent power of carbon dioxide increases and the amount of α -tocopherol also increases as can be seen from Figure 5. The higher mutual solubility of the coexisting phases at higher pressures results in the physical properties of the phases becoming more similar. Also because of the larger amount of carbon dioxide in the liquid phase, the interaction forces between tocopherol molecules become weaker. For these reasons less en-

ergy is required to bring molecules from the bulk phase to the surface for the formation of new surface, therefore the interfacial tension decreases.

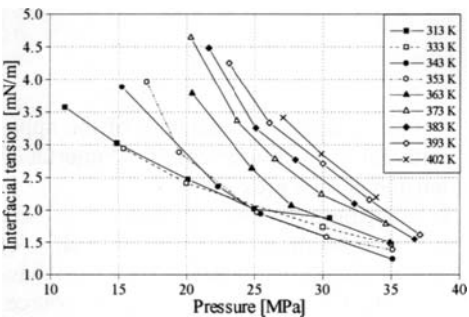


Figure 2. Interfacial tension as a function of pressure at all nine temperatures investigated.

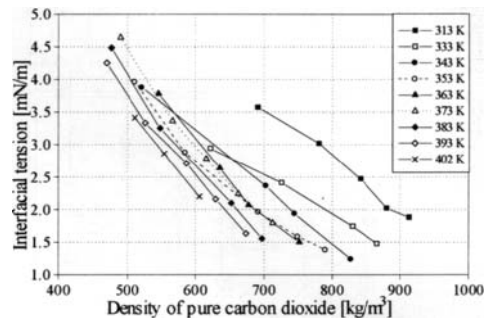


Figure 3. Interfacial tension as a function of density of pure carbon dioxide at all nine temperatures investigated.

Figure 4 plots equilibrium compositions of the liquid and respectively of the supercritical gas phase of the system α -tocopherol/carbon dioxide as a function of pressure. Compositions at 313 and 343 K were measured by Meier [4], at 333, 353, 373, 398 and 423 K by Hoffmann-La Roche AG in June 1995.

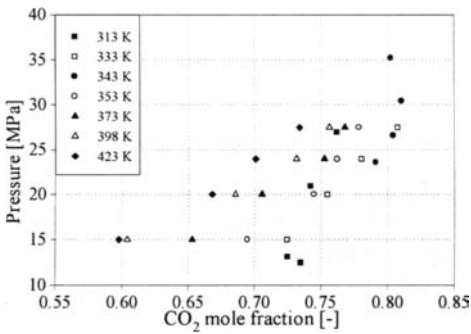
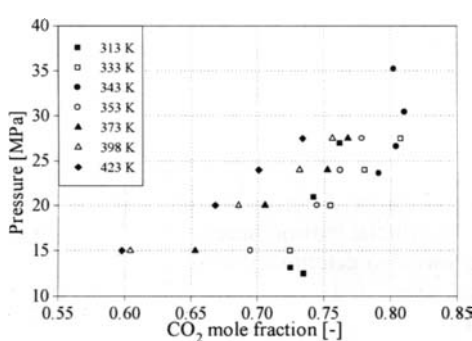


Figure 4. Equilibrium compositions of the system α -tocopherol/carbon dioxide as a function of pressure for different temperatures. On the left: liquid phase; on the right: supercritical gas phase.

Figure 5 shows the plots of the solubility of α -tocopherol in the supercritical gas phase as a function of the density of pure carbon dioxide, which has been calculated with the Bender equation of state.

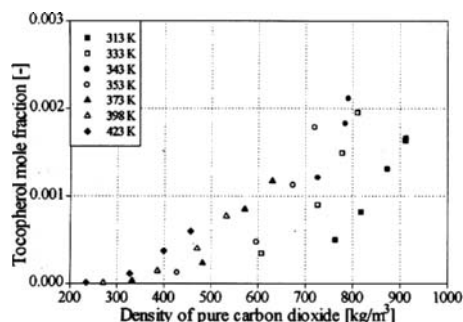


Figure 5. Supercritical gas phase solubility of α -tocopherol as a function of density of pure carbon dioxide.

From Figure 2, it can be seen that at temperatures higher than 353 K the interfacial tension clearly increases with rising temperature at a constant pressure. In the phase diagram shown in Figure 4, it is observed that there is a marked decrease in the mutual solubility of α -tocopherol and carbon dioxide with rising temperature above 343 K at a constant pressure. Therefore the coexisting liquid and supercritical gas phases become much more different. Furthermore, the interaction forces between the tocopherol molecules in the liquid phase become stronger, since the amount of carbon dioxide in it has decreased. More energy must then be spent on bringing molecules from the bulk phase to the surface and so the interfacial tension increases.

The values of the interfacial tension at 333 K are slightly below the ones at 313 K because of the higher mutual solubility of the two system components at 333 than 313 K. Measurements of interfacial tension at 343 K and at 353 K in the pressure range between 20 and 30 MPa give practically the same results, even though the amount of carbon dioxide in the liquid phase is lower at 353 K than at 343 K, as can be seen from Figure 4.

When the interfacial tension is plotted against the density of pure carbon dioxide as shown in Figure 3, the interfacial tension can be represented as a function of the solvent power of carbon dioxide. Its density has been calculated with the Bender equation of state and its solvent power has been represented in Figure 5. The interfacial tension decreases with rising temperature at a constant density of carbon dioxide, whereas the amount of tocopherol in the supercritical gas phase increases (Figure 5). There exists therefore a correlation between the interfacial tension and the concentration of tocopherol in the supercritical gas phase. The higher the supercritical gas phase solubility of tocopherol at a constant carbon dioxide density, the lower the interfacial tension. The crossover of the isotherm at 353 K with that at 373 K in Figure 3 is probably due to the fact that the amount of carbon dioxide in the liquid phase is larger at 353 K than at 373 K (see Figure 4).

The accuracy of the calculated interfacial tension values achieved in the experiments depends on two main factors. The first is the accuracy of the densimeter, which is estimated to be less than $\pm 3 \text{ kg/m}^3$ as is described by Meier [4]. The resulting error for the density difference is $\pm 4.2 \text{ kg/m}^3$, which leads to an increasing relative error for low density differences. The second influence is given by the accuracy of the measured diameters d_c and d_s . The diameters can be measured with an accuracy of 1 pixel. The effect of the inaccuracy of the diameters on the value of the interfacial tension is nearly constant. With these two effects an error of less than 3% is estimated for measured interfacial tensions with density differences of

more than 200 kg/m^3 . With decreasing density difference down to 100 kg/m^3 , the relative error increases to 5% and up to 9% for 50 kg/m^3 .

5. CONCLUSIONS

Both the mutual solubility of the coexisting liquid and supercritical gas phases and the density of carbon dioxide are the most important parameters in influencing interfacial tension in systems with both a non-volatile liquid and a supercritical component.

Due to the fact that interfacial tension becomes zero at the critical point of the mixture, above which complete miscibility occurs, the relatively high value of interfacial tension at 30.5 MPa and 313 K (1.88 mN/m) indicates that the system investigated in this work is still relatively far from its critical pressure. This observation is also valid for all nine temperatures investigated and agrees with the phase equilibrium measurements shown in Figure 4.

Meier et al. [13] assumed that above 353 K the upper critical solution temperature for the α -tocopherol/carbon dioxide system could be reached, above which the liquid and supercritical gas phase are completely soluble in each other. Measurements of phase equilibria carried out by Hoffmann-La Roche AG and our investigations contradict the assumption mentioned. Two coexisting phases are still present at 423 K and 27.5 MPa (see Figure 4).

ACKNOWLEDGEMENTS

This research was supported by the Emil Barell Foundation, Hoffmann-La Roche AG in Basel and the Swiss Federal Institute of Technology (ETH) Zurich.

REFERENCES

1. J. Chrastil, *J. Phys. Chem.*, 86 (1982) 3016.
2. K. Ohgaki, I. Tsukahara, K. Semba and T. Katayama, *Kag. Kog. Ronbunshu*, 13 (1987) 298.
3. B. Zehnder, Ph. D. Thesis, ETH Zurich, 1992.
4. U. Meier, Ph. D. Thesis, ETH Zurich, 1992.
5. P.J. Pereira, M. Gonçalves, B. Coto, E. Gomes de Azevedo and M. Nunes da Ponte, *Fluid Phase Equilib.*, 91 (1993) 133.
6. D. Schaffner, Ph. D. Thesis, ETH Zurich, 1993.
7. M. Meyer, Ph. D. Thesis, ETH Zurich, 1993.
8. J.M. Andreas, E.A. Hauser and W.B. Tucker, *J. Phys. Chem.*, 42 (1938) 1001.
9. S. Fordham, *Proc. Roy. Soc., (Serie A)* 194 (1948) 1.
10. O.S. Mills, *Brit. J. Appl. Phys.*, 4 (1953) 247.
11. C.E. Stauffer, *J. Phys. Chem.*, 69 (1965) 1933.
12. M.D. Misak, *J. Coll. Interf.*, 27 (1968) 141.
13. U. Meier, F. Gross and Ch. Trepp, *Fluid Phase Equilib.*, 92 (1994) 289.

Detection of nitroaromatic compounds dissolved in liquid and supercritical CO₂ by UV-VIS spectroscopy

S. Löbbecke*, G. Bunte, Th. Härdle, H. Krause

Fraunhofer-Institut für Chemische Technologie ICT,
P.O. Box 12 40, 76318 Pfinztal, Germany

Keywords:

supercritical carbon dioxide, UV-VIS spectroscopy, on-line analysis,
nitroaromatics (detection of), solvatochromism

ABSTRACT

A measuring device is presented which is capable for the detection of nitroaromatic compounds dissolved in sub- and supercritical carbon dioxide by UV-VIS spectroscopy. The specific spectroscopic behavior of these solutions at pressures up to 400 bar and temperatures up to 150 °C is described.

1 INTRODUCTION

Energetic materials like TNT or other nitroaromatic compounds are readily soluble in liquid and supercritical carbon dioxide (sc-CO₂). Extraction processes using sc-CO₂ as an extracting solvent (supercritical fluid extraction SFE) permit the discharging of TNT and its breakdown products out of contaminated soils or other matrices [1].

At present the analytical information about substances extracted by SFE is usually received by analytical methods following the extraction process. Therefore the development of on-line-analytics for SFE processes is highly required.

Main advantages of using such on-line-analytics are the direct identification and quantification of extracted substances during the extraction process. Hence, the monitoring and control of SFE processes would be possible.

In this work a measuring device is presented, which is capable for the simulation of UV-VIS spectroscopic on-line-analysis for SFE processes.

3 RESULTS

Systematic investigations into the UV-VIS spectroscopic properties of carbon dioxide at $p = 1 - 400$ bar and $T = 20 - 150$ °C showed that increasing CO_2 density effects a decrease in UV transparency (figure 3). This decrease is caused by a significant increase in the CO_2 refractive index (figure 4). Therefore changes in CO_2 pressure or temperature effect changes in CO_2 transparency. The detection of shortwave absorption bands, e.g., is limited at high CO_2 densities.

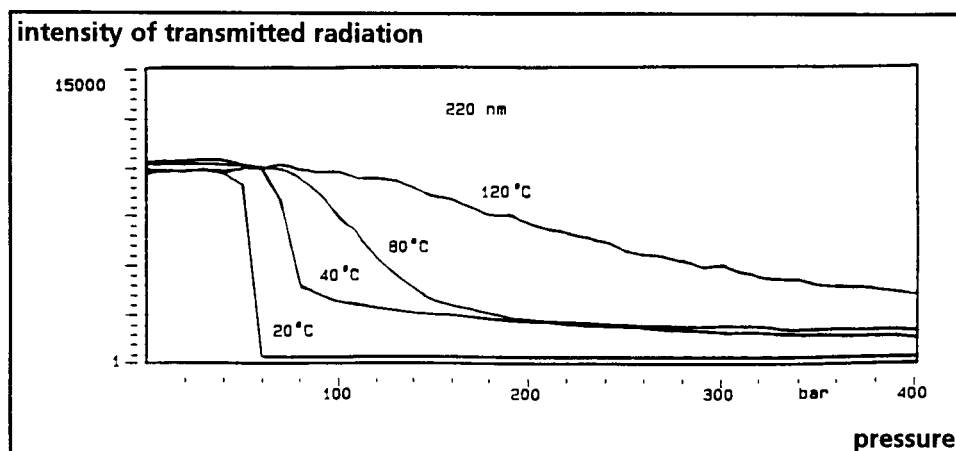


Fig. 3: CO_2 transparency at $\lambda = 220$ nm as a function of pressure and temperature

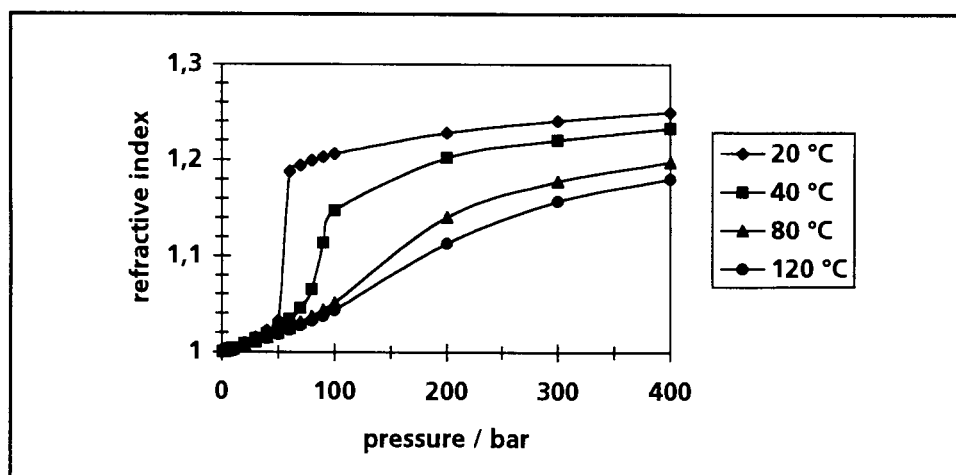


Fig. 4: CO_2 refractive index as a function of pressure at four different temperatures (calculated for $\lambda = 546$ nm, based on the Lorentz-Lorenz equation [2])

The on-line detection of TNT and some of its breakdown products during their sc-CO₂ extraction out of contaminated soils was simulated under different pressures and temperatures. The nitroaromatic compounds dissolved in sc-CO₂ were identified by their characteristic UV-VIS absorption bands. A quantification of the analytes was possible for concentrations lower than 1 ppm.

It is shown that the characteristic absorption bands of the substances dissolved in supercritical carbon dioxide were subjected to show intense hypsochromic shifts compared with conventional organic solvents. In addition, bathochromic shifts of the absorption bands were effected by increasing CO₂ density.

In figure 5 the observed solvatochromism is shown for the spectroscopic detection of the TNT breakdown product 4-amino-3-nitro-toluene. Increasing pressure (respectively density) effects an increasing solubility of 4-amino-3-nitro-toluene in sc-CO₂ and a bathochromic shift of the three absorption bands caused by increasing CO₂ polarity.

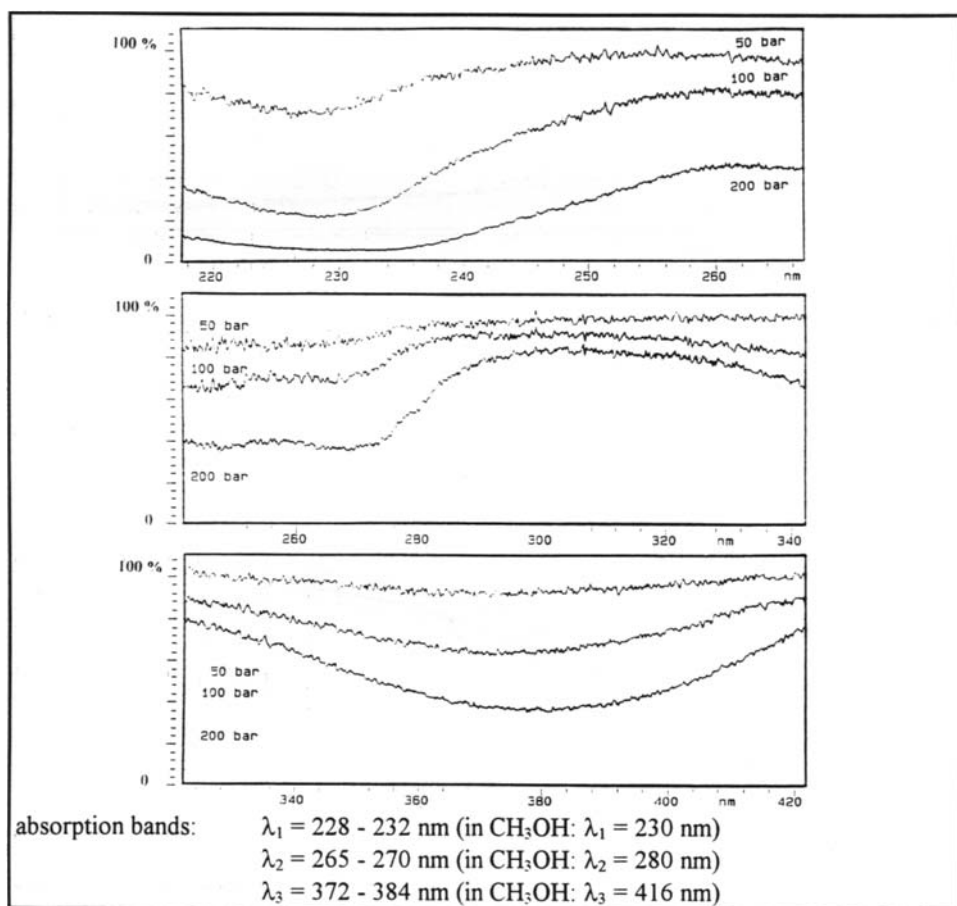


Fig. 5: Transmission spectra of the TNT breakdown product 4-amino-3-nitro-toluene dissolved in sub- and supercritical CO₂ at T = 80 °C and p = 50 - 200 bar

4 CONCLUSIONS

A measuring device was developed for the UV-VIS spectroscopic detection of nitroaromatic compounds dissolved in sub- and supercritical carbon dioxide.

It was shown that the spectroscopic detection is influenced by the varying optical properties of the solvent and by the solvatochromic behavior of the nitroaromatic compounds at different CO₂ densities. These specific effects have to be known for an accurate spectroscopic identification and quantification of analytes dissolved in sub- and supercritical carbon dioxide.

REFERENCES

- 1 G. Bunte, Th. Hirth, H. Krause, A. Kroll,
Extraktion von Explosivstoffen aus Böden mit überkritischem Kohlendioxid,
Proceedings of the 25th International Annual Conference of ICT, June 28 - July 1,
1994, Karlsruhe, Germany
- 2 E.P. Kholodov, N.I. Timashenko, A.L. Yaminov,
Determining the density and polarisability of CO₂ on the basis of experimental data
on the refractive index,
Therm. Eng. (Engl. Transl.) 19, 126 (1972)

This page intentionally left blank

PHASE TRANSITIONS REGISTRATION AT HIGH PRESSURES UP TO 30 GPa

V.V.Shchennikov^a, A.Yu.Derevskov^a, V.A.Smirnov^b

^a *Institute of Metals Physics Ural Branch RAS, 620219 Ekaterinburg, Russia*

^b *Ecological Centre of National Academy of Sciences of Ukraine 314000 Poltava, Ukraine*

The pressure apparatus, allowing to perform the simultaneous measurements of several parameters of sample under high pressure is described. The apparatus contains the microcontroller for the operation by the measurements and keeping the experimental data. The examples, comprised the volume, resistance and thermoelectric power jumps recording in HgSe, HgSeS and Ga₂Se₃ crystal during the pressure-induced phase transitions, are represented.

1 INTRODUCTION

Properties of substances, undergoing structural phase transitions at pressure P , are a complex functions of the extent of transformation [1]. In the region of the phase transformation the sample of volume V appear to be a mixture of phases with the concentrations $c_i = V_i/V$, where V_i – is the volume of i -phase ($\sum V_i = V$). In "effective medium" approximation the value of specific resistivity ρ of such mixture may be written as a normalized sum of the phases contributions [2]

$$\rho = \frac{\sum_i \rho_i c_i f_i(\rho)}{\sum_i c_i f_i(\rho)} \quad (1)$$

where configuration factor $f_i(\rho) = 3\rho/[A\rho + (3 - A)\rho_i]$, and A – is a constant. For the thermoconductivity λ the similar equation may be obtained by substitution $\rho, \rho_i \Rightarrow \lambda^{-1}, \lambda_i^{-1}$ in (1). The effective thermoelectric power S of phases mixture may be considered as a normalized sum of the phases thermoelectric voltages, depending on the configuration factors $f_i(\rho)$ [2]

$$S = \frac{\sum_i S_i c_i f_i(\rho) \lambda_i^{-1} f_i(\lambda)}{\sum_i c_i f_i(\rho) \lambda_i^{-1} f_i(\lambda)} \quad (2)$$

It was also taken into account, that the temperature gradients, and hence, the values of thermoelectric voltages are inversely proportional to the phases thermoconductivities and

depend on configuration factors $f_i(\lambda)$. When the constant A is equal 0 and 3, the Fig. 1, 2 exactly coincide with the cases of parallel and consequent electrical connections of phases, and at $A = 1$ – with the case of spherical shape of phases inclusions [3, 4]. So, the various values $0 < A < 1$ and $1 < A < 3$ correspond to the intermediate electrical connections (and sequentially intermediate shapes) of phase inclusions.

For the 2-phase systems Eq.1 reduces to a quadratic equation for ρ (or λ). From Eq.1,2 the clear relationship (independent on A) between ρ , S and λ can be derived [2]

$$\frac{S - S_2}{S_1 - S_2} = \frac{\rho\lambda - \rho_2\lambda_2}{\rho_1\lambda_1 - \rho_2\lambda_2}. \quad (3)$$

By Eq. 1 the abrupt change of ρ , relating to the phase transition, will occur near the concentration $c_i = A/3$ of the *conducting* phase. But as the values of ρ_1/ρ_2 , S_1/S_2 and λ_1/λ_2 are not identical, so according to Eq. 1 - Eq. 3. the "jumps" of entities V , ρ , S and λ during the phase transformation will occur at different concentrations of high pressure phase. Thus, the appropriate transition pressures will seem slightly various, that have been observed in experiment [1,2]. A rising of the accuracy of phase transition investigations may be achieved by a measurements of several kinetic effects of sample simultaneously, and also by using of various type high pressure chambers.

2 HIGH PRESSURE APPARATUS

The appropriate equipment, satisfied the above intention, was constructed by the authors of present paper. It includes the high pressure apparatus (fig. 1), the removable plungers (fig. 2), and recording block (fig. 3). At the table 1 of the apparatus, the lever

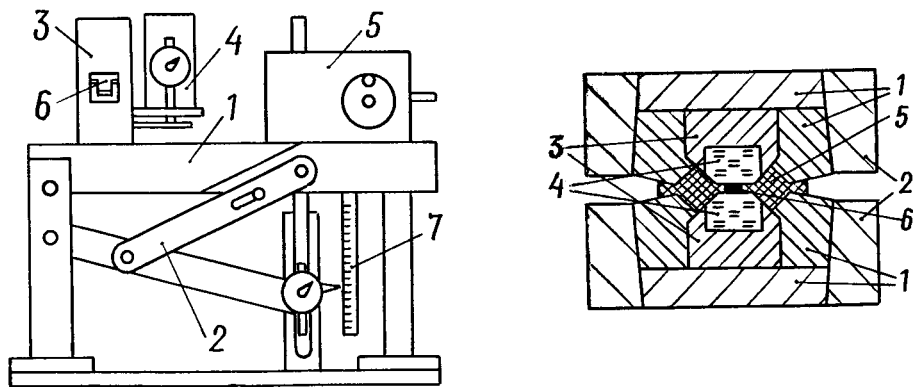


Figure 1: High pressure apparatus 1 - table, 2 - lever mechanism, 3 - pressure chamber, 4 - plunger displacement sensor, 5 - reduction gear with the electromotor drive, 6 - tips, 7 - lever displacement scale. Figure 2: The version of the high pressure plungers 1- complex tungsten carbide matrixes, 2 - supporting rings, 3 - two-layer tips, 4 - sintered diamond, 5 - the container of lithographic stone for the sample, 6 - sample.

mechanism 2 and the pressure chamber 3 are established, and the sensors of plunger displacement (X) 4, pressure P (stress F) and temperature T are set. The reduction gear by use of the hand- or the electromotor drive 5 creates the stress, transferred to the pressure cassette 6, containing the pressure plungers. The values of P were estimated from the acting stress F and tabulated dependence $P(F)$, recording in the apparatus [1].

The most parts of apparatus were made of titanium alloys. The removable high pressure cassette 6, inserting in the pressure chamber 3, contains the modified plungers of Bridgman anvils type [1,5], made of metal, tungsten carbide or synthetic diamonds for the pressure region up to 5, 10 and whole 30 GPa, respectively. As a sintered polycrystal diamond is known to be the most hard and high compression strength material for the pressure generation [5,6], we had prepared as diamond tips, and two-layer "sintered diamond-tungsten carbide" tips for our apparatus [7,8]. The construction of plungers is also crucial for its work. In our version of plungers (fig. 2) the diamond (or BN) tips were supporting by the external pressure up to 10 GPa, generated by tungsten carbide matrixes [7,8], as in F.P.Bandy apparatus [5]. So, the pressure range up to 30 GPa was available for the plungers with the sintered diamond tips.

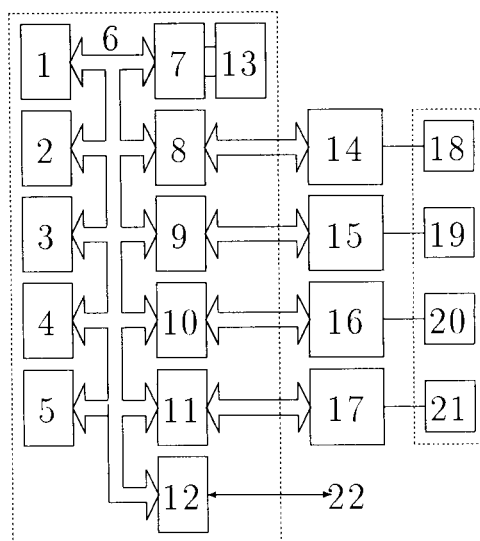


Figure 3: Functional scheme of recording block (microcontroller) 1- CPU, 2-ROM, 3-RAM, 4- timer, 5 - power supply, 6 - bus, 7-11 - PIA, 12 - serial interface , 13- keyboard/display, 14-17 - voltmeter, 18 - P-sensor, 19- T-sensor, 20- V-sensor, 21- sample, 22 - port RS-232S (communication with computer).

The recording block for the pressure device is shown at fig. 3. This block allowed to perform the simultaneous measurements of several parameters of sample during the phase transition. It contains the microprocessor 1, interfaces 8-11 for the connection the outputs of standart digital voltmeters 14-17, communicated with the T,P,X- sensors 18-20 and the sample electrical outputs 21. The experimental data are stored in the energy supply independent RAM, but may be transferred to IBM-PC by interface 12. The operation by measurements and choice the step of the ruling parameter (P, T, X, etc.) may be done by the keyboard 13, the results being read off from the indicator 13. The program of operation and testing is stored in ROM 2.

3 PHASE TRANSITION INVESTIGATION

3.1 Methods of measurements

By using of the high pressure apparatus, shown at fig. 1 – fig. 3, the pressure-induced phase transitions in some semiconductors were investigated up to 30 GPa [9,10]. The technique of S measurements supposedly will be in detail described in the special paper. Here we only outline the peculiar features of it.

The diamond anvils were the cooler and heater for producing the temperature gradient ΔT along the sample thickness "d" (fig. 2). Very high thermoconductivity λ of diamond (~ 2 –3 times higher, than λ of Cu) and extremely low λ of lithographic stone container tend to the considerable intensification of the heat flux density "q" in the sample, that results in the producing a sufficiently high $\Delta T = qd/\lambda_0$ [11]; a value of ΔT are estimated by measurements of T near the diamond tips [9,10]. The preliminary calculations of the temperature distribution, analogous to [12], showed, that when the λ_0 of the sample is essentially less, than the λ of the diamond, then the error of ΔT is'nt large, and it may be taken into account. Indeed, the majority results of S measurements by using the above technique [9,10] and the current ones at hydrostatic pressure up to 2–8 GPa [13,14] were in a good agreement. It's due to note, that in the alternative methods of S measurements at high pressures up to 30 GPa [15], where the heat flux is orientated perpendicular to the axes of the diamond plungers, it's hardly possible to produce the appreciable ΔT because of the high thermoconductivity of diamond.

3.2 Results

The following examples of phase transition investigations demonstrate the potentialities of the discussed equipment. In fig. 4 there is resistance vs pressure dependence for HgSe

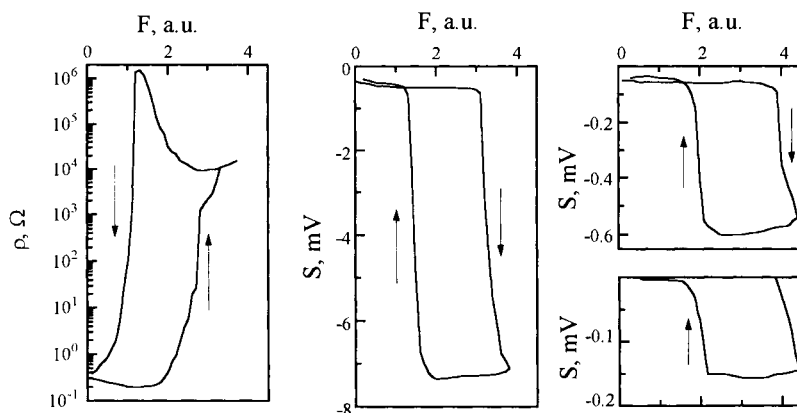


Figure 4: The dependence of resistance (left picture) and thermoelectric voltage of the HgSe sample on the stress F for the Gexanit (BN) plungers apparatus (fig. 2) at the constant gradient of T (middle picture) and at the progressive reduce of one in the "regular" thermal regime for consequent cycles of pressure increasing (right picture).

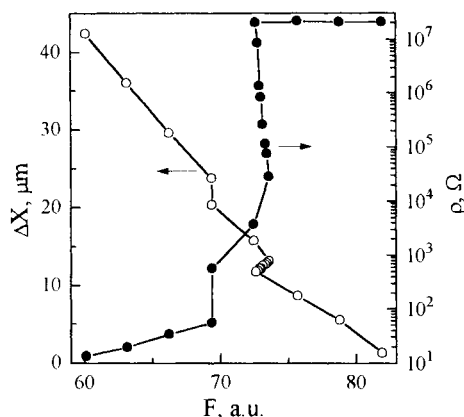


Figure 5: The data of synchronous measurements of plunger displacement X and resistance R of $\text{HgSe}_{0.4}\text{S}_{0.6}$ sample versus the stress F , driving by the tungsten-carbide plungers apparatus at $T=296$ K. The B3 \rightarrow B9 phase transition, beginning at $P=0.4$ GPa, can be seen.

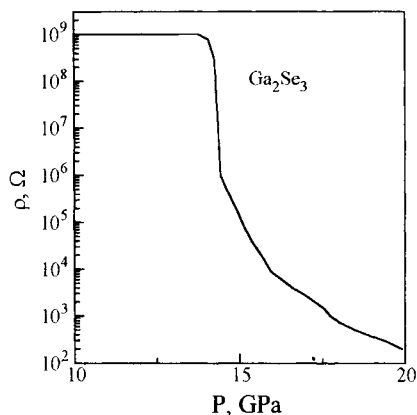


Figure 6: The resistance R vs pressure P for the Ga_2Se_3 sample, received in sintered diamond tipped plungers apparatus at $T=293$ K.

sample. The jump of R forestalls the appropriate jump of S during the semimetal – semiconductor phase transition ($B3 \rightarrow B9$), that accords well with the Eq.1–Eq.3. On contrary, during a semiconductor – metal transitions a change of S occurs before the relevant drop of resistance [2].

The method of the S research was described in [9,10]. A platinum-silver ribbons of $5 \mu\text{m}$ thickness were a potential electrical probes to a sample. The measurements were performed as at the constant gradient of T , and also at the progressive reducing of one, when the heat supply was cut off ("regular" thermal regime). As can be seen, the relative changes of S in the both cases are approximately the same; the exhibited data agrees well with the results of S measurements, received formerly [9, 14].

The results of the investigation of analogous phase transition in $\text{HgSe}_{0.4}\text{S}_{0.6}$ crystal [16] is shown at Fig. 5. The measurements were performed in the tungsten carbide plungers apparatus, the lithographic stone was the pressure-transmitting medium. There are two observed jumps of ρ and X within the width of transition. One can see, that the essential jump of plunger displacement X occurs before such a jump of resistance, as was mentioned above. The used equipment allows also to observe the small effect of pressure drop, resulting from the volume contraction of sample, during $B3 \rightarrow B9$ structural transition. The resemble effect of P reducing by $0.02\text{--}0.03$ GPa we observed at purely hydrostatic conditions in the same sample.

A new phase transitions were revealed in the semiconductor compounds HgTeS , HgSeS [16], Bi_2Te_3 , Ga_2Se_3 [17] etc. by using the discussed equipment. In fig. 6 such a new phase transition in Ga_2Se_3 crystal near $P=15$ GPa [17] is shown.

Acknowledgments

We are grateful to Mr.V.N.Neverov for his help in preparing the manuscript. Thus work was supported partly by the Russian Fundamental Research Foundation through Grant No 93-02-2832.

Reference

1. C.C. Bradley, High Pressure Methods in Solid State Research (London, Butterworths, 1969.)
2. V.V. Shchennikov, The Physics of Metals and Metallography **67** (1989) 93.
3. V.I. Odelevskii, Zhurnal Technicheskoi Fiziki **21** (1951) 667.
4. S.V. Airapetyants, Zhurnal Technicheskoi Fiziki **27** (1957) 478.
5. F.P. Bundy, Rev. Sci. Instruments **46** (1975) 1318.
6. W. Utsumi, N. Toyama, S. Endo, F.E. Fujita, O. Shimomura, J. Appl. Phys. **60** (1986) 2201.
7. V.V. Shchennikov, V.A. Smirnov, Ultrahigh pressure device, Rus. Patent No. 2050180 (1995).
8. V.V. Shchennikov, Ultrahigh pressure device, Rus. Patent No. 1762457 (1990).
9. I.M. Tsidil'kovskii, V.V. Shchennikov, N.G. Gluzman, Sov. Phys. Semiconductors **17** (1983) 604.
10. V.V. Shchennikov, Rasplavy **2** (1988) 33.
11. R.D. Barnard, Thermoelectricity in metals and alloys, Taylor & Francis LTD, London, 1972.
12. R.G. Munro, S. Block, G.J. Piermarini, and F.A. Mauer, J. Appl. Phys. **50** (1984) 4.
13. L.G. Khvostantsev, L.F. Vereshchagin, N.M. Uliyanitskaya, High Temp.-High Pressure **5** (1973) 261.
14. T.G. Ramesh, V. Shubha, J. Phys. C **15** (1982) 6193.
15. N. Sakai, K. Takemura, K. Tsuji, J. Phys. Soc. Japan **51** (1982) 1811.
16. V.V. Shchennikov, N.P. Gavaleshko, V.M. Frasunyak, Sov. Phys. Solid. State **35** (1993) 199.
17. K.V. Savchenko, V.V. Shchennikov, Can. J. Phys. **72** (1994) 681.

Design and Construction Criteria for Pressure Vessels under Constant and Cyclic Load

P. Körner and W. Hiller

UHDE GmbH, Hagen works, PO Box 4260, D-58089 Hagen, Germany

The design of pressure vessels is governed by the task of minimising manufacturing costs while fulfilling all predefined requirements, which represent a set of design and construction criteria.

These criteria basically come from three parties –the customer, the manufacturer and legislation– and focus on subjects such as operating conditions, dimensions, principles of construction, materials, applicable pressure vessel codes, closing systems and gaskets.

An overview of design criteria and the resulting pressure vessel types will be given for the high pressure range from 250 to 10,000 bars.

Two examples –one for static and one for cyclic load– will be reviewed from analysing customer needs to realising a modern pressure vessel design.

The first one is a hydrogenation autoclave for 250 bars and 350 °C with a completely encapsulated agitator, the second one a vessel for tobacco expansion with nitrogen, designed for a minimum of 140,000 cycles at 825 bars and 100 °C.

1. INTRODUCTION

High pressure vessels under static loading show substantial differences from low pressure vessels in terms of materials and fabrication method.

Additionally, in the pressure range from 250 bar to 10,000 bar a great number of batch processes can be found. This means, that the design of pressure vessels for these applications has to deal with cyclic loading and fatigue, considering far more severe conditions than at low pressure service.

Table 1 gives an overview of high pressure processes currently employed and their classification for batch / continuous service. The types of pressure vessels fabricated for these design conditions can be seen in table 2.

Table 1.
High pressure processes

	max. pressure	max. temperature	process type
Hydrogenation	250 bar	350°C	batch/cont.
Super Critical Fluid Dyeing (SCFD)	300 bar	300°C	batch
Extraction	550 bar	120°C	batch/cont.
Tobacco Expansion	825 bar	100°C	batch
Isostatic Pressing	4,000 bar	1,500°C*	batch
Low Density Polyethylene (LDPE)	4,000 bar	350°C	cont.
High Pressure Sterilisation	10,000 bar	-10°C/+50°C	batch

* requires a special cooling system for the pressure vessel

Table 2.
Types of high pressure vessels

	max. pressure	max. temperature	max. ID.
Welded vessels	600 bar	350°C	2000 mm
Forged vessels	2,000 bar	350°C	2000 mm
Autofrettaged forged vessels	4,000 bar	350°C	200 mm
Multi-Ring	6,000 bar	100°C	500 mm
Wire wound / plate wound	10,000 bar	-20°C / +50°C	500 mm

2. DESIGN CRITERIA FOR STATIC LOADING

From the customer point of view, the criteria for the design of a pressure vessel are determined in terms of costs (initial and subsequent) and output of a product (quantity and quality). While the initial cost of a pressure vessel is simply the price for purchasing and installation, subsequent costs are far more difficult to judge, because they depend on life time expectancy, reliability in service and effort for maintenance.

Since a container under internal pressure represents a risk for health and safety, extensive government regulations set minimum standards for the safe construction of a pressure vessel. These safety regulations not only focus on the design, they intend to procure a throughout quality approach for the fabrication of the vessel.

Regulated areas in the construction of a pressure vessel are (details depend upon the national code): design and calculation, permissible materials, quality control of materials, quality control of the fabrication processes (particularly welding), safety devices and -last but not least- full certification and documentation.

It remains the task of the manufacturer to fulfil the above mentioned requirements with the most suitable design principle and materials, aiming at a competitive price and low running costs for the operating of the vessel.

The dimensioning of vessel walls is generally controlled by the static failure mode "gross plastic deformation". Elastic stresses have to be kept below the limits according to the applicable stress category.

3. DESIGN CRITERIA FOR CYCLIC LOADING

When the pressure vessel is intended for batch service, particular attention often has to be paid on short opening / closing time of the closure system.

From the safety point of view, cyclic loading means that fatigue can occur at stress levels far below the limits for static strength.

Since fatigue always occurs at locations of stress concentrations or material imperfections, peak stresses and stresses at welding locations have to be calculated and evaluated.

Although the Finite Element Method is still not very common for calculating the static strength of a vessel, it became a standard tool for computation of peak stresses (Figure 1) for fatigue analysis.

The most common pressure vessel codes that include the evaluation of fatigue are the North-American "ASME Section VIII Division 2" [1] and the German "AD-Merkblatt S2" [2], the latter being the most detailed fatigue analysis currently available in pressure vessel codes.

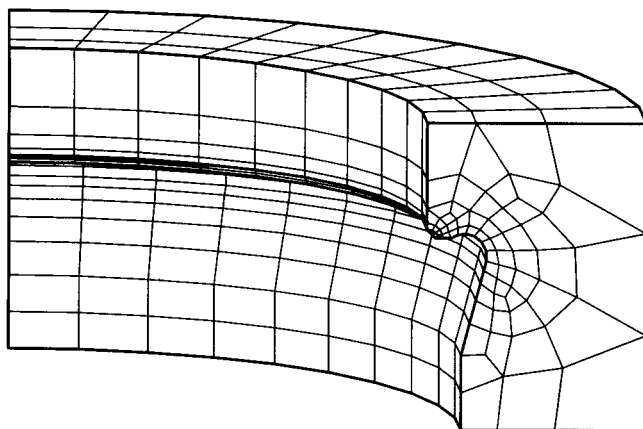


Figure 1. Finite Element model of a clamp closure for calculation of peak stresses

4. DESIGN EXAMPLES FOR STATIC AND CYCLIC LOADING

The following two pressure vessel types have been built for erection in France, hence the French pressure vessel code CODAP [3] has been followed.

4.1. HP-hydrogenation autoclave (figure 2)

For the design conditions 250 bar and 350°C an autoclave of 1800 litres equipped with a stirrer had to be designed. Further design criteria set by the customer were: austenitic stainless steel for all parts in contact with the medium, fast temperature control, extremely low leakage rate.

Since the duration of one batch cycle is about 1 day -which calculates to 7,000 cycles for 20 years- the design was governed basically by the static load.

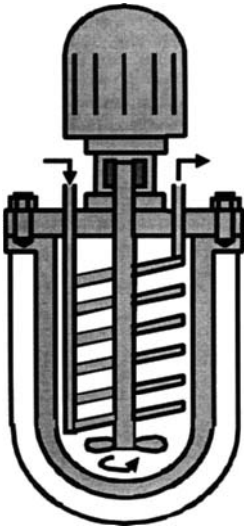


Figure 2. HP-hydrogenation autoclave

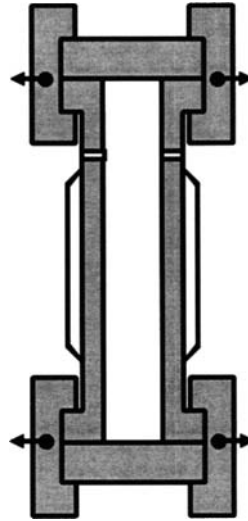


Figure 3. HP-tobacco expansion vessel

4.1.1. Selection of materials

In order to keep manufacturing costs low, a welded plate structure of medium strength fine-grained steels with good welding characteristics has been chosen. For an inner diameter of 1100 mm this is a much cheaper solution than a forging.

Because of the size and the pressure of the vessel, austenitic stainless steel could not be used throughout, but must be applied on the inner surfaces of the ferritic material. This has been done by explosion plating of a 4 mm cladding on the base material prior to rolling the cylinder and forming the hemispherical head. For the flat cover and the sealing faces weld-cladding was applied.

4.1.2. Sealing systems

Because of the high temperature encountered, a metallic gasket had to be used. In order to keep the bolt forces low (considering pressure and inner diameter), it was preferable not to choose flat gaskets with high pretensioning requirements, but instead a self-intensifying type like the Gray-type sealing (similar to double cone ring).

The sealing of a rotating shaft under low leakage conditions is extremely difficult, therefore the stirrer shaft was built completely encapsulated by austenitic material and the transmission of the torque was realised using a permanent magnetic coupling. The magnets were based on samarium-cobalt and are able to transmit a torque of 135 Nm.

4.1.3. Heating

A high heat transfer rate was guaranteed by the simultaneous use of a heating jacket and an internal coil; the heating medium was a thermal oil.

4.2. HP-tobacco expansion vessel (figure 3)

For a tobacco expansion plant several vessels had to be built for a process, in which rapid pressurising and depressurising takes place. The design conditions were 825 bar and 100°C with 2-3 cycles per hour, which means that the mechanical design of the vessels was governed by fatigue. Since the French pressure vessel code does not provide detailed fatigue rules, the customer agreed upon the German design rules for cyclic loading and a number of permissible cycles of 140,000 (based on the 1990 edition of AD-S2). It has to be pointed out, that after inspection of the vessel, it can be used for more than the initially permitted number of load cycles.

Further design requirements set by the customer were: Only stainless steel in contact with the tobacco, short opening and closing time, heating jacket.

4.2.1. Closure system and gasket

Because of the low design temperature of 100°C, an elastomer gasket material, which does not wear down the sealing surfaces too much, could be chosen. For two reasons it was advisable to use a self-intensifying type of gasket (lip seal): Firstly, the high pressure can be safely contained, and secondly, no pretensioning is necessary.

Having selected the gasket, a fast closure system for covers with sealings that needs no pretensioning is the clamp closure device (Figures 1 and 3). The design of the clamp is focused on keeping the peak stresses under the fatigue limit for the permissible number of cycles. From the static point of view the clamp is over-dimensioned, i.e. the allowable membrane and bending stresses are far below their limit. As an effective design tool for such a task, parametric 3-D Finite Element modelling and shape optimisation algorithms were used. The groove area of the clamp - as all locations of stress concentration - has been polished to a surface roughness $< 6\mu\text{m}$.

4.2.2. Selection of materials

For the pressure of 825 bar forgings of high strength ferritic-martensitic material have to be used. These steels are normally not suitable for welding. Because of special corrosion requirements and in order to avoid the use of liners, a martensitic precipitation-hardening stainless chromium steel was used for the cylinder and the covers. The clamps were made of a low alloy high strength steel.

The steels used for this pressure range are beyond the scope of the national codes and have been approved by an individual testing and certification procedure.

5. CONCLUSION

While the design of a pressure vessel for static loading is principally governed by dimensioning against gross plastic deformation of the vessel (bursting), the design for cyclic load can be -depending on the cycle time and design details- controlled by the fatigue failure mode. As a result, special attention has to be directed on a smooth geometry and good surface finish in the region of stress concentration.

The number of permissible load cycles, which results from the fatigue stress evaluation, does not necessarily determine the life time expectancy of the pressure vessel, but sets the intervals for fissure tests.

REFERENCES

1. ASME Boiler and Pressure Vessel Code, Edition 1995, Addenda 1995
2. AD-Merkblatt S2, VdTÜV Essen, 1990, 1995
3. CODAP, Syndicat National de la Chaudronnerie, de la Tôlerie et de la Tuyauterie Industrielle, 1990

Hydrodynamic Behaviour of Packed Column under High Pressure

B. Benadda, K. Kafoufi and M. Otterbein

LCPAE Bât.404, INSA 20 av. A. Einstein 69621 Villeurbanne FRANCE

The object of this study was to characterize the flow and to measure the hold-up and axial dispersion coefficients of the fluid phases (water-nitrogen) in a countercurrent gas-liquid packed column, operating under a pressure up to 1.5 MPa.

Determinations of Peclet number were carried out by comparison between experimental residence time distribution curves and the plug flow model with axial dispersion. Hold-up and axial dispersion coefficient, for the gas and liquid phases are then obtained as a function of pressure. In the range from 0.1-1.3 MPa, the obtained results show that the hydrodynamic behaviour of the liquid phase is independant of pressure. The influence of pressure on the axial dispersion coefficient in the gas phase is demonstrated for a constant gas flow velocity maintained at 0.037 m s.

1. INTRODUCTION

In industry, many installations operate under pressure for technical and/or economic reasons. Although many hydrodynamic studies have been reported for liquid-gas contactors at atmospheric pressure, there are few concerning elevated pressure. The aim of this study is to investigate the influence of pressure on fluid flow in a packed column operating with a gas-liquid countercurrent.

When a fluid passes through a packed column, the flow is divided due to the packing. Modelling of these phenomena is carried out by superimposing a dispersion, characterized by a coefficient D on the convective plug flow of velocity U . This is the model for an axial dispersion reactor. This model allows characterisation of a flow with intermediate properties between those of the plug flow reactor and those of a continuous stirred reactor.

The mathematical description of the global phenomenon leads to the general differential equation :

$$\frac{dC}{d\theta} = \frac{1}{Pe} \frac{d^2C}{dZ^2} - \frac{dC}{dZ} \quad (1)$$

In the case of a reactor open to dispersion, resolution of the equation is analytically possible and leads to the following solution :

$$E(\theta) = \frac{1}{2} \left[\frac{Pe}{\pi \cdot \theta} \right]^{1/2} \exp \left[-\frac{Pe(1-\theta)^2}{4\theta} \right] \quad (2)$$

From a practical point of view, it is possible to consider a closed-closed system as an open-open system and to apply the equation (2). In order to validate this hypothesis and to exploit the experimentally obtained curves of RTD (residence time distribution) Van Gelder *et al* [1] suggest ignoring the time spent by the tracer outside the reactor (before and after) in the obtained curves.

2. EXPERIMENTAL SET-UP AND PROCEDURE

The experimental study was carried out using the distribution of residence times, a method which can also be used under pressure. The use of a tracer allows simulation of the behaviour of fluids in the column during operation.

Figure 1 shows the experimental apparatus used. The glass column (1), of inner diameter 62 mm is packed to a height of 1 m with Berl saddles (6.4 mm). The column operates with a countercurrent at a pressure up to 1.5 MPa. The water is fed into the column from a tank (2) maintained at a higher pressure than the operating pressure. Nitrogen is fed into the bottom of the column from a gas cylinder (20.0 MPa).

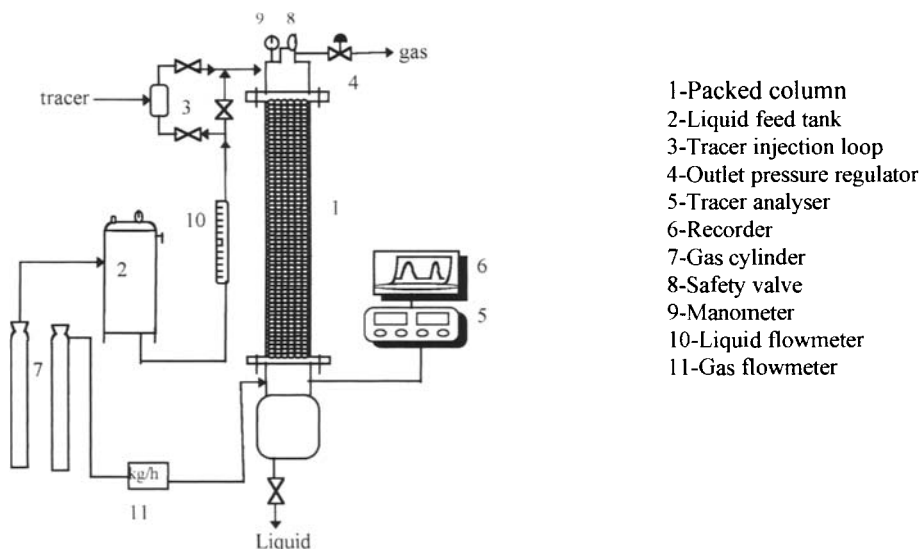


Figure 1. Flowsheet of the experimental apparatus.

Injection of liquid tracer (KCl at 3M) under pressure is achieved by a system of three electrovalves (3) and allows injection of the tracer with a Dirac type impulse. The tracer concentration is monitored in time using a conductimeter and a recorder. In order to

eliminate the time spent by the tracer outside the column from the curves, a second injection, identical to the first, is carried out at the column output.

For injection of gas tracer, a similar system was used with oxygen as tracer. The concentration of oxygen in the output gas was monitored with a paramagnetic analyser. The liquid phase (water) was first saturated with oxygen in the tank (2) before introduction into the column. Preliminary analyses of the feed gas and output gas have shown that absorption or desorption of the tracer was negligible up to a pressure of 1.3 MPa.

3. EXPERIMENTAL RESULTS

3.1. Gas phase

Figure 2 shows a typical example of response to the two injections impulse of tracer, carried out at the reactor input and output, with countercurrent gas-liquid flow at 0.7 MPa.

Identification of the experimental RTD curve by deconvolution of the two signals, to the plug flow model with axial dispersion Figure 3, allows access to residence time τ and the Peclet number.

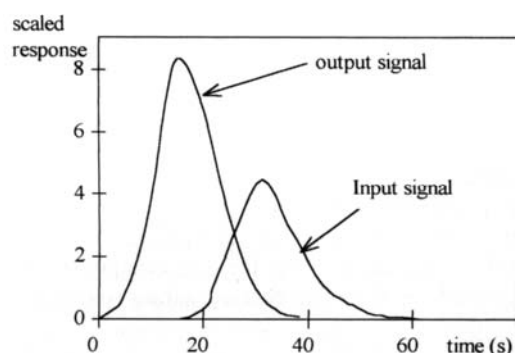


Figure 2. Response curve to injection impulse at reactor input and output under 0.7 MPa

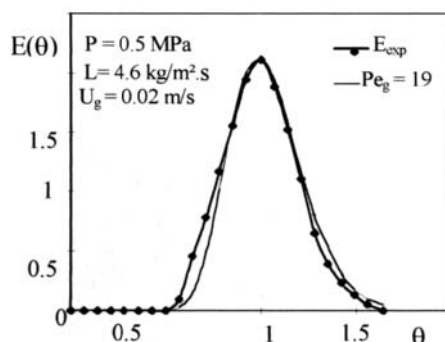


Figure 3. Application of the plug flow with axial dispersion in the gas phase

3.1.1. Axial dispersion

At atmospheric pressure, the axial dispersion coefficient $D_g = U_g H / Pe_g$ was determined for gas velocities ranging from 0.02 to 0.13 m/s and for a constant liquid flow rate of 4.63 kg/m²s. Figure 4 shows that the axial dispersion coefficient increases with the gas velocity. D_g increases from $0.5 \cdot 10^{-3}$ m²/s to $9.5 \cdot 10^{-3}$ m²/s when the gas velocity increases from 0.02 to 0.13 m/s which corresponds to Bodenstein's number Bo between 0.09 and 0.2. This result is very similar to that obtained by SATER *et al.*[2] who used Berl saddles of 12.7 mm.

Figure 5 shows the influence of pressure on the axial dispersion of the gas during diphasic flow. For a constant gas velocity, the axial dispersion coefficient increases significantly when the operating pressure increases from 0.1 to 1.3 MPa.

This result is unique as to our knowledge, no study has been published to date concerning the influence of pressure on this parameter and comparison with results in the literature is therefore impossible. To operate at constant gas velocity when the pressure

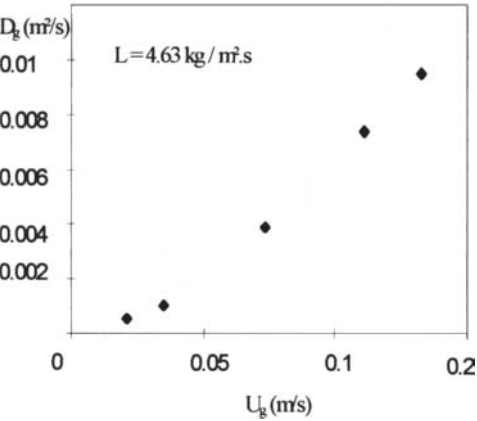


Figure 4. Influence of gas velocity on axial dispersion in the gas phase at atmospheric Pressure.

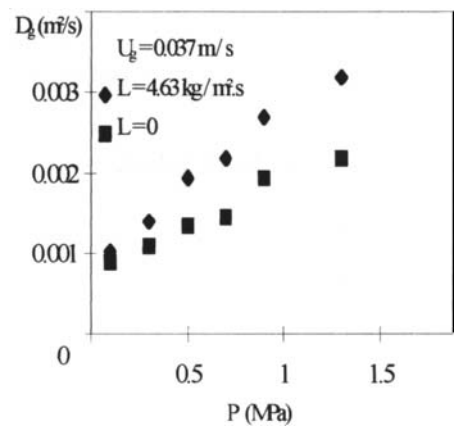


Figure 5. Influence of pressure on the axial dispersion coefficient in the gas phase.

increases, it is necessary to increase the gas mass flow to compensate for the increase in volumic density. One may think that this variation in gas mass flow could explain the influence of pressure on D_g . However, our results show that the gas residence time is independent of pressure despite the gas mass flow variations at constant gas velocity (table 1). One explanation, for a given liquid flow, may be related to the flow regimes (films or drops) and an interpenetration of fluids as we have recently reported during studies on interfacial areas under pressure [3].

Table 1 - Residence time τ in seconds according to pressure and $U_g=0.037$ m/s

Pressure (MPa)	0.1	0.3	0.5	0.7	0.9	1.3
U_L (m/s).						
0	17	19	16	16	16	16
$1.5 \cdot 10^{-3}$	10	11	11	10	10	10

3.1.2. Gas hold-up

The determination of the residence time of the gas phase τ by identification of the experimental RTD curves, allows us to obtain the total gas hold-up [4] by the equation :

$$\beta_g = \frac{U_g \cdot \tau}{H}$$

(3)

In the absence of liquid flow the gas hold-up is 0.58. This value is the porosity of the packing determined with a 10% error by a volumetric method. For constant gas velocity at 0.037 m/s measurement of the total hold-up in the gas phase have shown that the pressure had no effect on this hydrodynamic parameter in the range 0.1 to 1.3 MPa. This result can be explained by the fact that the hold-up only depends on the residence time, which is constant for a given gas velocity in the pressure range studied, as shown in table 1.

3.2 Liquid phase

As for the RTD study in the gas phase, we have used the method of two injections. The response of the conductimetric probe to the input and output injections, with a Dirac tracer impulse, is shown in figure 6. In order to model the liquid flow, several theoretical models were tested. The liquid flow corresponded to plug flow with axial dispersion as shown in figure 7.

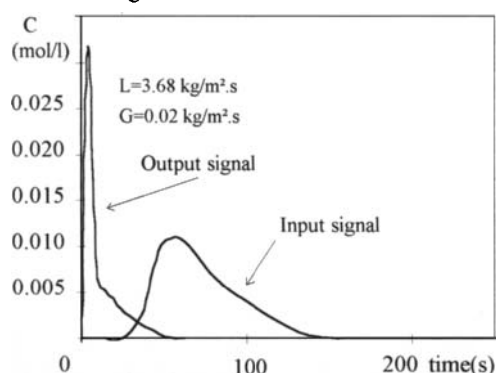


Figure 6. Response curve to injection impulse input and output at 0.5 MPa.

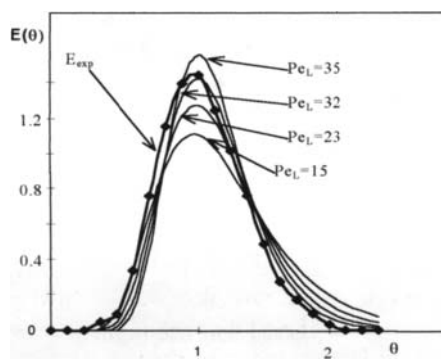


Figure 7. Identification of RTD curves by plug flow model with axial dispersion.

3.2.1. Axial dispersion

The parameter obtained after identification of the system as plug flow with axial dispersion, is the Peclet number defined from the packing height and the real fluid flow velocity :

$$Pe_L = \frac{U_L \cdot H}{D_L} \quad (4)$$

According to our results obtained up to 1.3 MPa, no effect of pressure on the Peclet number was observed. The dispersion coefficient D_L depends only on the liquid flow rate. Figure 8 shows an increase of D_L according to flow rate under atmospheric pressure. This result is in agreement with that obtained by Van Gelder *et al.* [1].

3.2.2. Liquid hold-up

As for the gas phase, the liquid hold-up was determined from identification of RTD curves. A series of experiments allowed us to study the variation in liquid hold-up according to liquid and gas flow rates in the pressure range 0.1 to 1.3 MPa.

Figure 9 shows that the liquid hold-up increases with liquid flow rate, when only the liquid is flowing.

The same result is obtained for countercurrent flow. The increase of gas flow rate from 0.02 to 0.19 kg/m²s has no influence on the liquid hold-up. At low gas flow rates, interaction between the two fluids is negligible and the texture of the liquid is identical to that of the liquid flow alone. This result has already been observed by Van Swaaij *et al.* [5] in a column packed with Raschig rings and operating with a countercurrent flow.

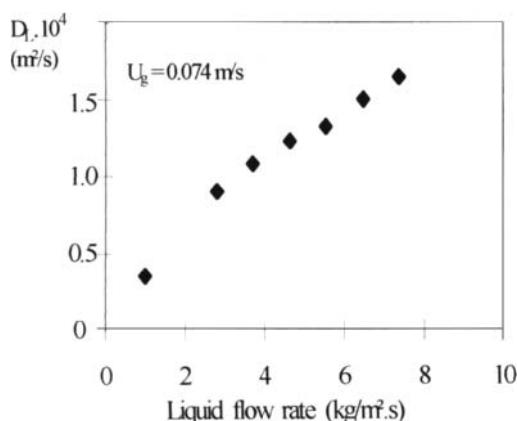


Figure 8. Influence of liquid flow rate on axial dispersion at atmospheric pressure.

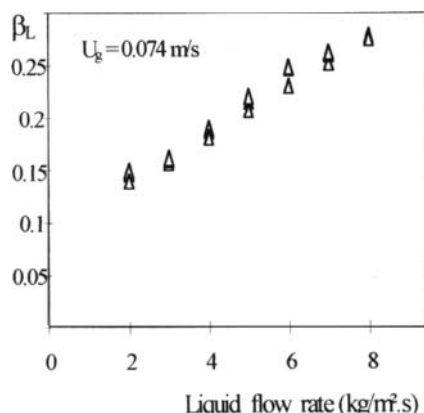


Figure 9. Influence of liquid flow rate on liquid hold-up at atmospheric pressure.

The study under pressure with countercurrent flow has shown that the operating pressure has no effect on hold-up. In fact for a liquid flow rate of 4.63 kg/m²s and constant gas velocity of 0.037 m/s, liquid hold-up is 0.21 for pressure ranging between 0.1 and 1.3 MPa. This result is in agreement with the conclusions of Van Gelder *et al.* [1] concerning the influence of pressure on liquid hold-up in a packed column operating with cocurrent flow. Larachi *et al.* [4] report the same observations in a fixed bed column with cocurrent flow.

4. Conclusion

This study, which contributes towards the understanding of hydrodynamic behaviour of gas-liquid reactors at elevated pressure, has shown the influence of pressure on the gas flow in a packed column through the axial dispersion coefficient. The gas flow diverges from plug flow when the pressure increases. As for the gas hold-up, an important parameter for the calculation of the reactional volume of a reactor, the pressure has no effect on this parameter in the studied range. This result allows to extrapolate gas hold-up values obtained

at atmospheric pressure to elevated pressure. No influence of pressure was found on liquid flow or liquid hold-up. These results seem obvious if we consider that the physical properties of the liquid are independent of pressure.

Notation

Bo	: Bodenstein number	$Bo = U \cdot d/D$
C	: tracer concentration	(mol/m^3)
d	: column diameter	(m)
D	: axial dispersion coefficient	(m^2/s)
$E(\theta)$: dimensionless residence time	
E_{exp}	: experimental curve	
G	: gas mass flow rate	$(\text{kg/m}^2 \cdot \text{s})$
H	: height of column	(m)
L	: liquid mass flow rate	$(\text{kg/m}^2 \cdot \text{s})$
P	: operating pressure	(MPa)
Pe	: Peclet number	
t	: time	(s)
U	: superficial fluid velocity	(m/s)

Greek symbols

β	: total hold-up
θ	: dimensionless time $\theta = t/\tau$
τ	: mean residence time (s)

Subscripts

g	: gas
L	: liquid

REFERENCES

1. K.B. Van Gelder and K.R. Westerterp, Residence time distribution and hold-up in a cocurrent upflow packed bed reactor at elevated pressure, Chem. Eng. Technol. N°13, 27 (1990).
2. V.E. Sater and O. Levenspiel, Two-phase flow in packed beds, I & EC Fundls. N°5, 86-92 (1966).
3. B. Benadda, K. Kafoufi, M. Prost. and Otterbein M, Influence of pressure on the gas-liquid area a and the coefficient $K_L a$ in a countercurrent packed column, Chem Eng. Process. forthcoming (1996).
4. F. Larachi, A. Laurent, N. Midoux and G. Wild, Experimental study of a trickle-bed reactor operating at high pressure : two-phase pressure drop and liquid saturation, Chem. Eng. Sci, N°46, 1233-1246 (1991).
5. W.P.M Van Swaaij, J.C. Charpentier and J. Villermaux, Residence distribution in liquid phase of trickle flow in packed column, Chem. Eng. Sci. N°24, 1083-1095 (1969).

This page intentionally left blank

Supercritical Adsorption and Desorption Measurements using a New Automated Apparatus

P. Alessi^a, A. Cortesi^a, I. Kikic^a and R. Kittel^b

^a Dept. of Chemical, Environmental and Raw Materials Engineering, DICAMP, Univ. of Trieste, P.le Europa, 1, 34127 Trieste, Italy.

^b Institut für Thermodynamik und Reaktionstechnik, TU Berlin, Strasse des 17. Juni 135, 10623 Berlin, Germany

1. ABSTRACT

A new equipment for adsorption and desorption measurements, similar to that suggested in a previous work, was assembled. With this apparatus experiments can be carried out at pressure up to 500 bar at water bath temperatures. The equipment consists of three parts: a high pressure pump, a water bath where the sample column is placed and a UV detector.

The apparatus, tested on the basis of literature data, has been used for adsorption and desorption measurements of a drug (nimesulide) in activated carbon.

2. INTRODUCTION

Many potential applications have been proposed which involve the desorption of solutes from matrix using SCF solvents at elevated pressure: these include activated carbon regeneration [1,2,3,4,5] and soil remediation [6,7,8] using supercritical carbon dioxide.

To design large scale supercritical desorption processes is necessary to understand in which way dynamic desorption is influenced by process variables as mass transfer effects and equilibrium considerations. The governing equilibrium in all desorption processes is the adsorption equilibrium and a description of this equilibrium is essential in all desorption models and design equations [3].

Several authors [2,3,9] have demonstrated that a complete knowledge of adsorption in certain cases is sufficient to accurately predict desorption behaviour.

For example, the local equilibrium theory combined with an accurate adsorption model (fitted to experimental adsorption equilibrium data) was successfully used to predict experimental desorption data [2,3].

In literature the existing experimental data base of supercritical adsorption equilibria is limited and most of the data have been modelled with one of three common adsorption isotherm models - the Langmuir, the Freundlich and the Toth. The models define adsorption isotherms with a similar shape and they have 2 or 3 adjustable parameters which allow an accurate correlation.

In supercritical adsorption processes the crucial problem encountered is that, summing up to fluid phase solute concentration, the adsorption equilibria is influenced by the system temperature and by the supercritical fluid density. So, the variation of the parameters in isotherm models as a function of both temperature and density limits the applicability of the equations when they are used for fitting experimental data. To date, due partly to insufficient data, the density and temperature dependence of the isotherm parameters has not been established.

The aim of this work is to investigate the adsorption and desorption of a pharmaceutical compound, taken as representative of a complex chemical molecule, on activated carbon.

Nimesulide is a non steroidal anti-inflammatory drug currently used in defeating respiratory tract infections.

Solubility data of nimesulide, which are essential when supercritical sorption is studied, were determined in a previous work by using a dynamic apparatus [10].

A new experimental sorption apparatus, based on previous experiences [3,9], was designed for this study. This apparatus is described and the first results of the study are presented. The adsorption apparatus was tested by determining the adsorption of salicylic acid on activated carbon from supercritical CO₂ as reported elsewhere [11].

3. EXPERIMENTAL

3.1. Materials

The CO₂ used in this study had food grade purity (99.98%) and was delivered in high pressure bombs by SIAD.

Nimesulide, 4-nitro-2-phenoxyethanesulfonamide, was provided by Helsinn and used in the delivered purity of 99.9% without further purification. Its molecular weight is 308.31.

Calgon Filtrasorb 400 activated carbon, for which some properties are listed in table 1, was used. It is originally designed for wastewater treatment, but it was found to be useful in adsorption/desorption studies.

Table 1
Properties of Filtrasorb 400

Property	Value
median surface area (N ₂ BET Method)	900-1100 m ² /g
Particle density	0.9 g/cm ³
Pore Volume	0.85-0.95 cm ³ /g
Particle size	0.55-0.75 mm

3.2. Sorption apparatus

Figure 1 gives a schematic overview of the whole adsorption equipment. With this apparatus adsorption/desorption experiments can be carried out up to 500 bar pressure at water bath temperatures. The equipment consists of three main sections: a high pressure pump, the water

bath containing the sample column and the UV Detector. The CO₂ is supplied by a high pressure bomb at 45-75 bar. The two cylinders (150ml volume each one) of the syringe-pump (SFC 300, Fisons Instruments) are cooled at 0°C by a cooling unit (Haake K, Haake N3). The cooling temperature was chosen in order to have pure CO₂ in the liquid phase. The pump provides a flow-stream up to 7000 ml/min at pressures up to 500 bar, where each cylinder supplies a stream to the system in the water bath.

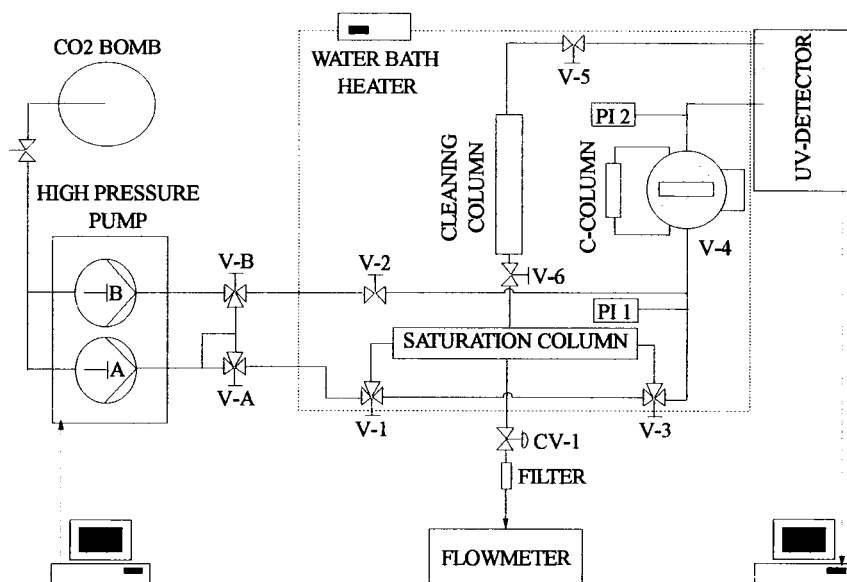


Figure 1. Sorption device.

A constant pressure or constant flow operating mode are assured by a personal computer (Fison Instr. software) so that either of these values is held constant by altering the other. The flow-meter in the pump registers the volume-flow of both cylinders, whereas the supply-ratio is set within the computer-program. If only one solvent flow is used, the pump can be programmed in constant operation, i.e. when one of the cylinders is exhausted, the other one overtakes operation and the first one is refilled automatically. In the water bath the sorption system is maintained at constant temperature by a heater (Fisons/Haake DC3) within $\pm 0.2^\circ\text{C}$. The supply stream of cylinder A leads to a saturation column (length 250 mm, inner diameter 9.3 mm) in which the solvent stream is saturated with the sorbate. This column can be bypassed by means of two 3-way valves (V-1, V-3). The first pressure transducer PI 1 (DS Europe, LP632) is located before the following mixing-tee-piece, where the saturated solvent flow of cylinder A and the pure solvent flow of cylinder B are mixed. Setting the supply-ratio of the cylinders, the concentration of the sorbate in the solvent can be altered. The mixed stream is forced to a 6-port switching valve (V-4; Valco), leading to the sample column which contains the adsorbent or bypassing it. This switching valve enables the gravimetric analysis of the sample column, without disturbing the other parts of the system. The sample column, in

which the activated carbon was packed, consists of stainless steel (length 30.7 mm, inner diameter 3.7 mm); the carbon is held in place using two 2 μm stainless steel chromatography filters in order to prevent loss of adsorbent. The column contains about 0.15 grams of activated carbon. After the 6-port valve a second pressure transducer PI 2 (same type as PI 1) is located, followed by the variable wavelength UV-Detector (UVIS 204, Linear Instruments). The detector cell is placed outside the bath, therefore the supply lines, as short as possible, are maintained at the same temperature of the bath. The UV-Signal is read out by the RS232-communication port to a personal computer, which records the values and the current time in desired periods (minimum 5s) in an ASCII-file. These files can be imported easily in other computer programs to perform all the calculations. The effluent stream is then lead through a cleaning column, which is filled with activated carbon to remove resident sorbate for preventing the following pressure-reducer-valve (CV-1) to be blocked up. This column can be shut off by valves V-5 and V-6. The solvent volume flow is then measured (Bronkhurst Hi-Tec, el-flow) under atmospheric conditions and the flow-meter signal processor (Bronkhurst, S200D) calculates the absolute volume of gas.

4. RESULTS AND DISCUSSION

The results of the adsorption experiments are presented in table 2. The equilibrium solubilities at the same conditions were determined and reported in a previous work [10]. The density values used were those of pure CO_2 [12] because nimesulide is only a trace component (max. solubility 0.0446 g/l at 22 MPa). As it can be seen, the sorbate capacity of activated carbon decreases with increasing pressure and density of CO_2 , regarding the values at similar concentrations as well as the total adsorption capacity at saturation concentrations. The higher solvent power of CO_2 at increasing pressure/density could be an explanation for the adsorption equilibrium shift in direction to lower coverage.

Furthermore, table 2 and figure 2 demonstrate the high affinity of the activated carbon surface for nimesulide. The equilibrium loadings at 10-20% of the saturation concentration are in the region of 80-90% of the final equilibrium loading at saturation concentration.

Carbon dioxide adsorption was not considered in these conditions according to the conclusions reported by King [13].

The best results to describe the adsorption isotherm by the selected isotherm equations were achieved by the Toth model. The Freundlich model showed in some cases a lack of flexibility in describing the region where the linear behaviour changed to saturation behaviour (22 MPa) and the Langmuir-model in some cases had difficulties in describing the region where the adsorbate is saturated (16 MPa).

At the same PT condition of adsorption three desorption runs were carried out.

In table 3 the desorption capacities of each experiment are presented. It can be seen that the desorption capacity (ratio between the desorbed and filled nimesulide) increases with increasing solubility of nimesulide in CO_2 . Due to the high affinity of the activated carbon surface to nimesulide the desorption capacity itself is very poor (max. value 38%). Since higher desorption capacity are related to higher solubilities, the addition of co-solvents to CO_2 , as proposed by Macnaughton et al. [9], can increase the solubility and therewith the desorption capacity.

Table 2
Experimental equilibrium adsorption loadings

T = 313.1 K					
Pressure [bar]	160.0	Pressure [bar]	190.0	Pressure [bar]	220.0
Density [g/cc]	0.79	Density [g/cc]	0.83	Density [g/cc]	0.86
Solubility [g/cc]	$1.77 \cdot 10^{-4}$	Solubility [g/cc]	$2.97 \cdot 10^{-4}$	Solubility [g/cc]	$4.46 \cdot 10^{-4}$
Concentr. [g/cc·10 ⁴]	Loading (g/gcarbon)	Concentr. [g/cc·10 ⁴]	Loading (g/gcarbon)	Concentr. [g/cc·10 ⁴]	Loading (g/gcarbon)
0.179	0.409	0.631	0.489	0.452	0.293
0.484	0.477	1.20	0.538	1.37	0.427
0.857	0.519	1.76	0.551	2.23	0.472
1.32	0.560	2.33	0.565	3.20	0.491
1.73	0.573	2.83	0.570	4.26	0.511

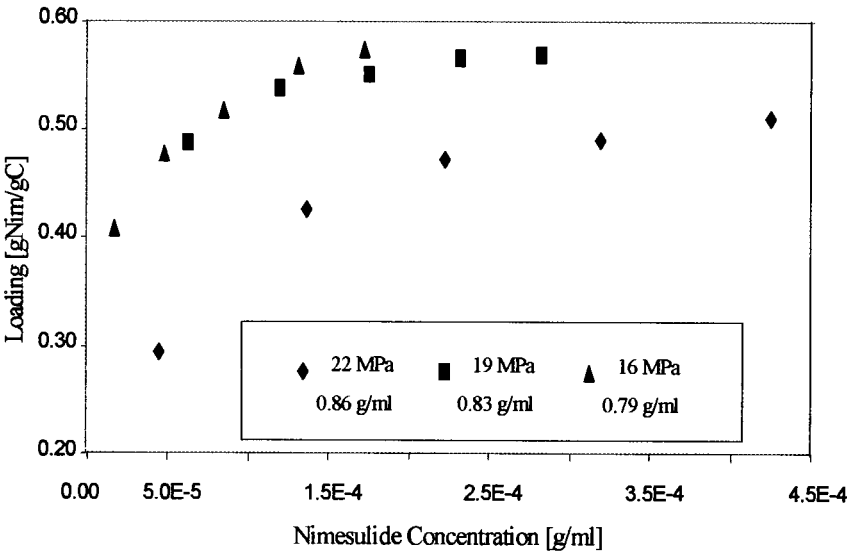


Figure 2. Adsorption isotherms.

The experimental desorption concentration profiles were obtained in the same way as the experimental adsorption profiles. However, using the local equilibrium model to describe the process, only qualitatively results can be obtained. Mass transfer resistance has stronger effect on desorption in comparison to adsorption so its importance cannot be neglected in the modeling.

Table 3
Desorption capacities

Pressure [MPa]	Sat. Solubility [g/cm ³]	Des. capacity %
22	4.46E-4	38
19	2.97E-4	30.7
16	1.77E-4	28

5. CONCLUSIONS

Adsorption and desorption measurements of nimesulide in supercritical carbon dioxide on activated carbon are determined at 313.1 K and in a pressure range of 160-220 bar.

The measured desorption capacities are too poor to design a separation process based on these materials. Further investigations could be made adding co-solvents to CO₂ to achieve a higher desorption potential.

The automated sorption apparatus developed can be useful for easy and rapid adsorption and desorption measurements of solutes in supercritical fluids.

ACKNOWLEDGEMENT

The authors acknowledge financial support from MURST and CNR.

REFERENCES

1. M.P. Srinivasan, J.M. Smith and B.J. McCoy, *Chem. Eng. Sci.*, 45 (1990) 1885.
2. G. Madras, C. Erkey, and A. Akgerman, *Ind. Eng. Chem. Res.* 32 (1993) 1163.
3. S.J. Macnaughton, and N.R. Foster, *Ind. Eng. Chem. Res.* 34 (1995) 275.
4. C-S. Tan and D-C. Liou, *Ind. Eng. Chem. Res.* 28 (1989) 1222.
5. C-S. Tan and D-C. Liou, *AIChE J.*, 35 (1989) 1029.
6. A.T. Andrews, R.C. Ahlert and D.S. Kosson, *Environ. Prog.*, 9 (1990) 204.
7. C. Erkey, G. Madras, M. Orejuela and A. Akgerman, *Environ. Sci. Technol.*, 27 (1993) 1225.
8. S. Kothandaraman, R.C. Ahlert, E.S. Venkataramani and A.T. Andrews, *Env. Progress*, 11 (1992) 220.
9. S.J. Macnaughton, N.R. Foster and I. Kikic, *Proc. 3rd Int. Symp. on Supercritical Fluids*, Tome 2, 1, France, Strasbourg, 1994.
10. S.J. Macnaughton, I. Kikic, N.R. Foster, P. Alessi and A. Cortesi, sent to JSF, 1996.
11. I. Kikic, P. Alessi, A. Cortesi, S.J. Macnaughton, N.R. Foster and B. Spicka, *Fluid Phase Equilibria*, in Press. 1996.
12. IUPAC Tables, *International Thermodynamic Tables of the fluid State Carbon Dioxide*, 1976, Pergamon Press, Oxford.
13. J.W. King, *ACS Symp. Series 329, Supercritical Fluids - Chemical and Engineering, Principles and Applications*, Squires and Paulaitis Editors, USA (Illinois), Chicago, 1985.

A Novel Microwave Autoclave for Automation of High Pressure Chemical Reaction Applications

W. Lautenschlaeger, W.G. Engelhart, M. Metzger, F. Visinoni - MLS/Milestone s.r.l. - Via Fatebenefratelli 1/5 - 24010 SORISOLE (BG) Italy.

Hundreds of laboratories currently utilize microwave systems to accelerate the preparation of samples for research purposes, quality control and process control analyses. Conventional microwave systems with multi-mode cavities and doors are designed for manual operation. A new microwave autoclave eliminates the impediments to automating microwave chemistry procedures. The ultraCLAVETM system combines microwave heating with high pressure vessel technology allowing chemical reactions to be conducted at pressures and temperatures up to 200 bar (2,900 psig) and 350°C. The system is specifically designed for semi-automated batch processing of multiple samples. Full automation is achieved by interfacing a laboratory robot arm to load/unload sample racks.

In operation containers constructed of microwave-transparent materials, (e.g. : quartz or fluoropolymers), are used to hold multiple samples inside the ultraCLAVETM. The interior of the stainless steel vessel is protected by a titanium nitride or multi-layer PTFE plasma coating for complete acid and chemical resistance. Sample containers may be open or covered by a lid. After the samples are loaded (manually or robotically) the ultraCLAVETM cover is lowered into place by an electric motor controlled from the system's PC. The vessel closure is engaged and secured in place to seal the ultraCLAVETM for high pressure operation.

Microwave heating and reaction parameters are selected and entered in the PC control software. Microwave power settings from 0 - 1000 watts may be selected. Continuous *unpulsed microwave energy* from the system's magnetron is introduced into the high pressure vessel through a special microwave-transparent port. Reaction pressure and temperature conditions are directly measured and controlled by the system PC. The system's compressor introduces pressurized nitrogen gas into the ultraCLAVETM. This high pressure nitrogen atmosphere greatly exceeds the vapor pressure developed inside the sample containers from microwave heating. Nitrogen pressure ensures that sample solutions are retained inside *open* or covered containers, with zero losses and absolutely no cross-contamination. When microwave emission is stopped at the conclusion of a run, microwave absorption and heating of the samples/reaction mixtures instantaneously ceases, minimizing by-product formation. With no further microwave absorption occurring vapor pressure from the heated sample solutions decreases to ambient conditions allowing a gradual release of nitrogen compensation pressure. When atmospheric pressure is reached inside the ultraCLAVETM the closure can be disengaged and cover lift mechanism operated to open the vessel for removal of samples.

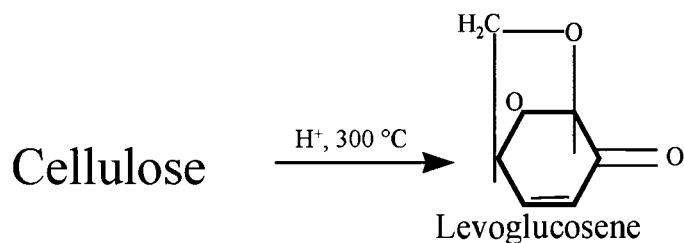
The unique operating principle of the ultraCLAVETM offers several major advantages for research involving combinatorial chemistry. Firstly, racks containing multiple samples and reaction mixtures can be run inside the vessel. Secondly, promising chemistries can be scaled up to from milliliters to > 2 liters. Thirdly, the ultraCLAVETM may be evacuated and purged so samples/reactions may be conducted in an oxygen free inert atmosphere of nitrogen to minimize oxidative degradation of reaction products.

Lastly, the semi-automated batch operating mode of the ultraCLAVETM facilitates high throughput reaction screening and full system automation is feasible.

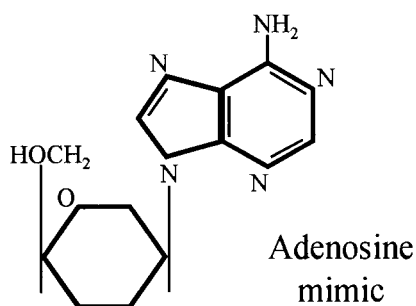
Related applications include : peptide/protein hydrolysis, heterogeneous catalysis reactions, acid digestion of samples, (e.g. : tissue, implants, catalysts, drugs, etc), for AA / ICP / ICP-MS analysis, solvent extractions, processing and/or destruction of toxic chemicals, chemotherapy and anti-neoplastic agents.

1. EXAMPLE OF A PHARMACEUTICAL INDUSTRY APPLICATION FOR THE ULTRACLAVETM

Acid digestion of cellulose yields chiral synthon ...



... used to produce nucleoside antiviral drugs



2. ULTRACLAVE™ ADVANTAGES FOR COMBINATORIAL CHEMISTRY

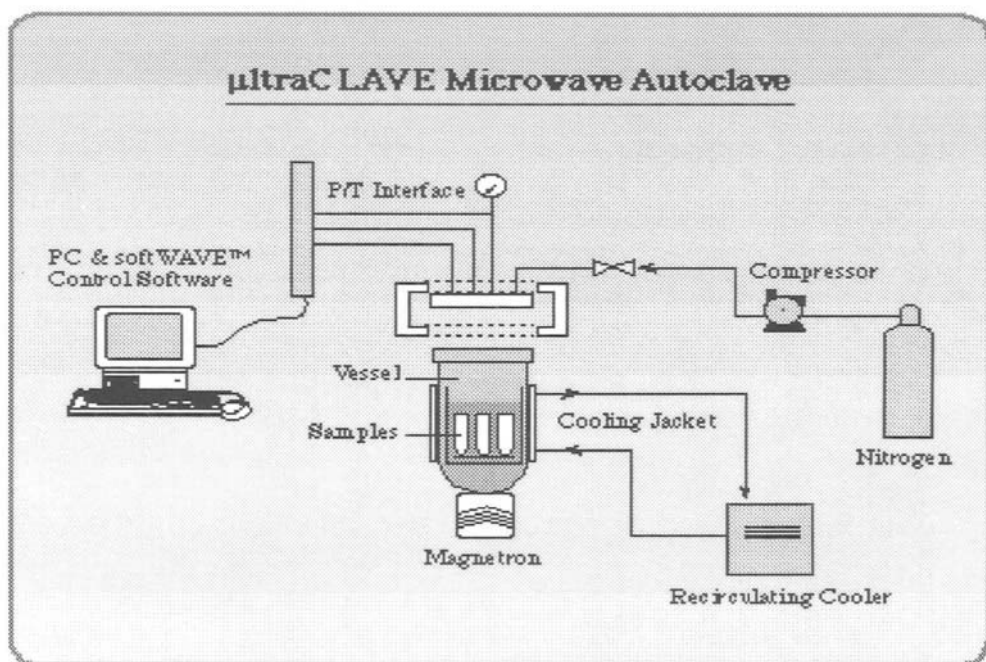
1. The system is specifically designed for semi-automated batch processing of samples. Full automation is possible by interfacing a laboratory robot to load/unload samples.
2. The 4.2 liter autoclave capacity accommodates a large number of samples for high throughput screening
3. All samples are processed under equivalent reaction conditions (P/T, MW power, etc)
4. Samples are processed in an inert atmosphere of nitrogen to prevent oxidative degradation of reaction products.
5. "Scale-up" of promising reactions from microliters to 2.5 liters can be accomplished in the same system
6. softWAVE™ PC control program documents reaction parameters from all runs in Paradox™ database for validation purposes
7. When microwave emission is stopped, microwave absorption by reactants and further heating of the reaction mixture instantaneously ceases, minimizing by-product formation and product degradation
8. Certain reactants, carrier solvents, catalysts and chemically active coatings applied to inert substrates directly absorb microwave energy.

3. ULTRACLAVE™ SPECIFICATIONS

Microwave Power:	0-1000 Watts (programmable in 1 Watt increment)
Microwave Emission:	continuous unpulsed
Magnetron Frequency:	2450 Mhz
Autoclave Design :	4.2 liter high pressure, stainless steel vessel with Titanium nitride coating
Pressure Vessel:	200 Bar (2,900 psig) M.A.W.P. - Maximum Allowable Working Pressure
Maximum Temperature:	350°C
Vessel Safety Certifications:	hydrostatically tested to 800 Bar (11,600 psig) for German TUV. Meets A.S.M.E Code criteria
Cover Lift Mechanism:	electronic motor for automatic raising/lowering
System Control:	via IBM-compatible PC with softWAVE™ Windows™ based control software

4. ULTRACLAVE™ OPERATING SEQUENCE

- Step 1. Load microwave-transparent sample containers manually/robotically
- Step 2. Vessel cover lowers automatically, engage closure mechanism and seal vessel for high pressure operation
- Step 3. Reaction Parameters (P/T, MW Power and Time) entered in PC control software
- Step 4. System compressor introduces pressurized nitrogen gas
- Step 5. Commence microwave heating cycle and reaction
- Step 6. At the end of the program, microwave emission ceases instantaneously stopping absorption of microwave energy by reactants and further heating
- Step 7. Control valve gradually releases N₂ gas to atmospheric pressure, vessel closure disengages and cover lift opens vessel for removal of samples



MILESTONE'S ULTRACLAVE HIGH PRESSURE MICROWAVE AUTOCLAVE

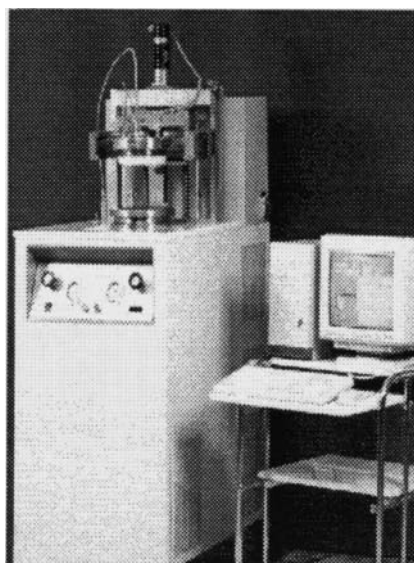
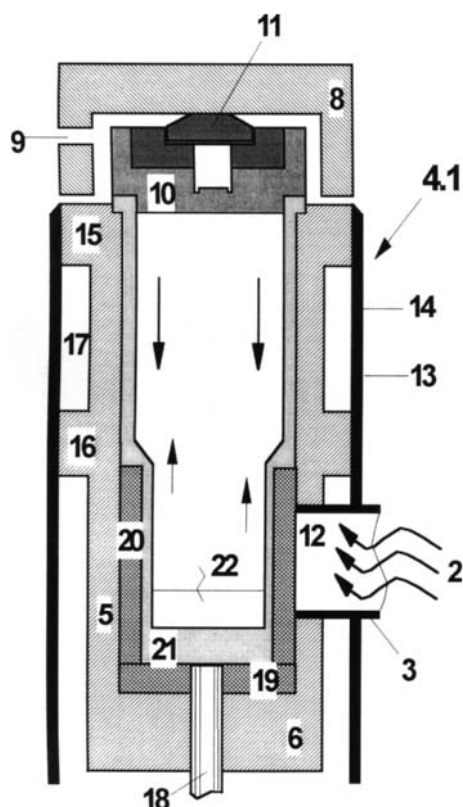
UNITED STATES PATENT (19) (11)
Lautenschlaeger (45)

Patent Number: 5,382,414
Date of Patent: Jan. 17, 1995

ABSTRACT

- (54) APPARATUS FOR
PERFORMING CHEMICAL AND
PHYSICAL PRESSURE
REACTIONS
- (75) Inventor: Werner Lautenschlaeger,
Leutkirch, Germany
- (73) Assignee: MLS Mikrowellen-Labor
Systeme GmbH, Leutkirch,
Germany

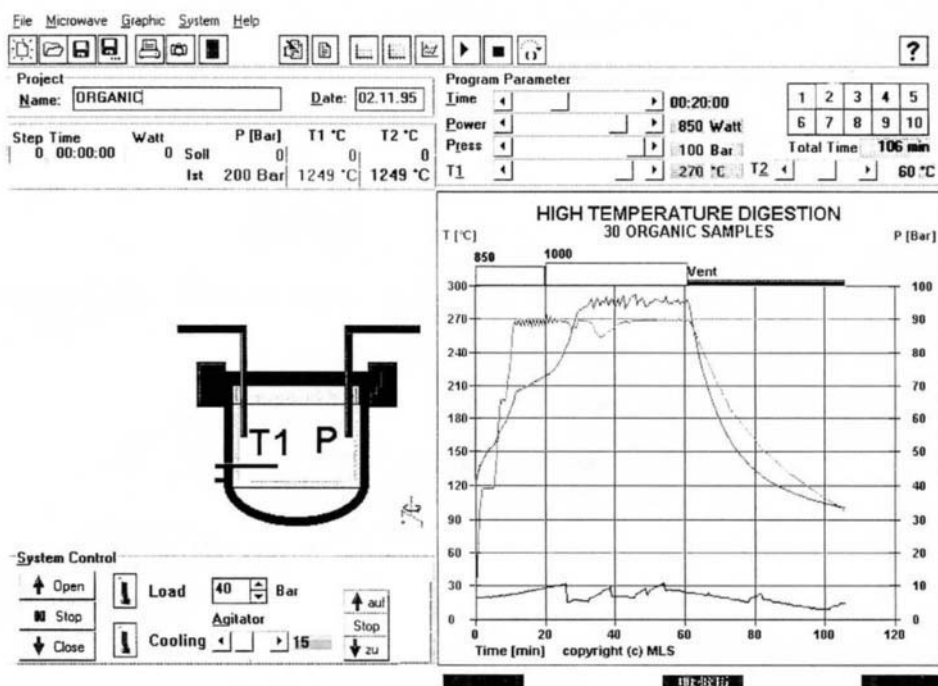
The invention relates to apparatus for performing chemical and physical pressure reactions on samples by the action of microwaves, having container inserts to receive the samples that are at least in part microwave-permeable and are arranged in a microwave-impermeable housing connected via at least one coupling opening to a microwave generator. To enable pressure reactions to be performed at higher pressures and more economically overall, it is proposed according to the invention that the housing include at least one pressure vessel (4) of high-pressure resistant material whose coupling opening (12) is microwave-permeable and closed in a high-pressure resistant manner, and that a single container insert is arranged in the pressure vessel (4) so as to fit closely against its inner surface.



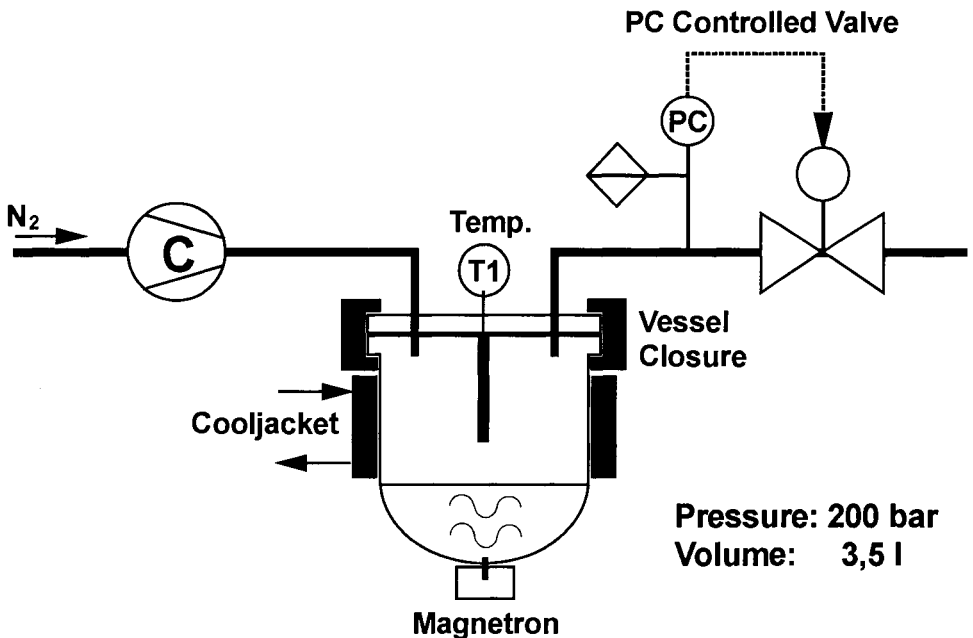
COMPARATIVE DIGESTION EFFICIENCIES (% SAMPLE DECOMPOSITION) AS DETERMINED BY RESIDUAL TOC-TOTAL ORGANIC CARBON MEASUREMENTS

Sample (weight)	ultraCLAVE microwave digestion 270°C/100 bar (1450 psig)	Standard microwave digestion 200°C/30 bar (435 psig)	High Pressure microwave digestion 280°C/80 bar (1160 psig)	High Pressure conventional "bomb" system 300°C/100 bar (1450 psig)
Pharmaceutical (0.600 g)	100% colorless/clear	88% light yellow	98% colorless	99% colorless
Organic Dye (0.500 g)	99.9% colorless/clear	65% brown-yellow	95% colorless light yellow	98% colorless
Plastic (0.400 g)	99.8% colorless/clear	incomplete digestion brown/cloudy	94% yellowish	97% light yellowish
Time	15 minutes (digestion) 25 minutes (total cycle time)	60 minutes	40 minutes	120 minutes *

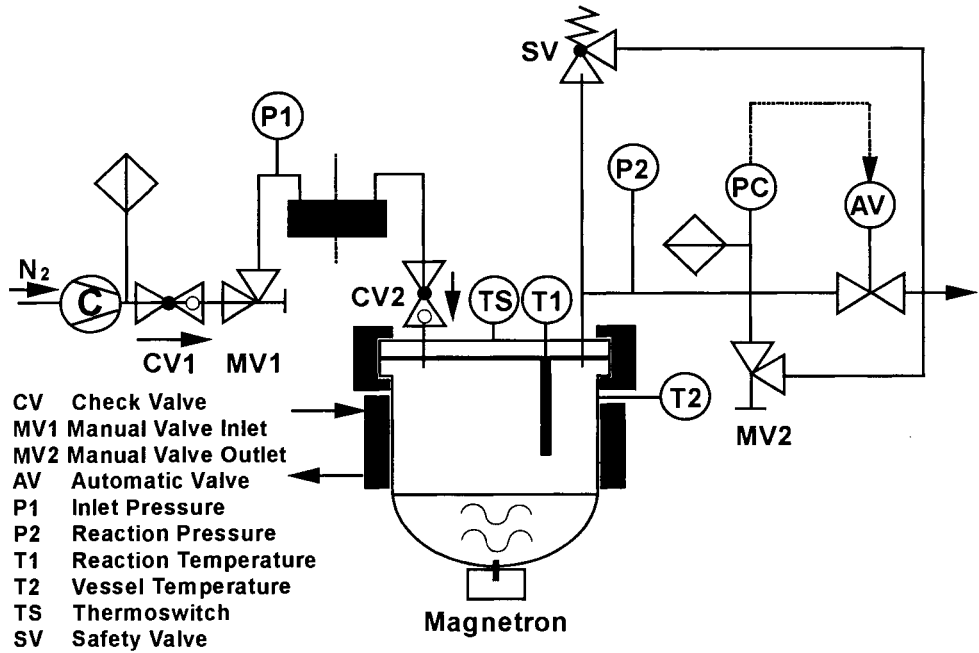
* (Time given is for heating/digestion only and does not include cool down time required before vessel can be opened. Total cycle time : 480 minutes)



ULTRACLAVE SCHEMATIC



ULTRACLAVE SAFETY SYSTEM



Author Index

A

Abeln J. 61, 157
 Adrian T. 241
 Adschiri T. 315
 Alessi P. 265, 687
 Anderson S.R.J. 309
 Andreyev A.V. 503
 Antranikian G. 127
 Arai K. 315
 Arlt W. 385, 519
 Atmaji P. 315

B

Bach E. 581
 Baiker A. 91, 139
 Balny C. 553
 Barna L. 469
 Barth D. 103, 423
 Bastos J. 399
 Bazan C. 509
 Becker O. 621
 Beirao da Costa M.L. 475
 Benadda B. 679
 Benedetti L. 217
 Bernard P. 103
 Bernardo-Gil M.G. 475, 525
 Berro C. 445, 469
 Bertoli C. 297
 Bertuccio A. 37, 217, 411
 Betts D.E. 23
 Bhaskar A.R. 297
 Bichari M. 169
 Blanchard J.-M. 469
 Bochechka A.A. 457
 Bocquet J.F. 133
 Bogatyreva G.P. 503
 Boguslawski S. 271
 Borimsky A.I. 651
 Brunner G. 127, 179, 277, 291
 Buback M. 175
 Bungert B. 519

Bunte G. 163, 345, 535, 661
 Busch M. 175

C

Caetano F.J. 475
 Calimli A. 463
 Carmelo P.J. 487
 Cassanello M. 493
 Cassel E. 379
 Catchpole O.J. 309
 Charbit F. 509
 Charbit G. 509
 Chhor K. 133
 Choi E.S. 531
 Choi Y.H. 531
 Clavier J.Y. 429, 627, 639
 Cleve E. 581
 Cocero M.J. 121
 Cortesi A. 265, 687
 Costa G.M.N. 351

D

d'Avila S.G. 185
 Dahmen N. 515
 Dariva C. 379
 de Simone J.M. 23
 de Sousa C.L. 525
 Debenedetti P. 49
 Deiters U.K. 405, 451
 Dennis A.J. 205
 Depmeier L. 633
 Derevskov A.Yu. 667
 Dietzsch H. 175
 Dohrn R. 277
 Dörfler W. 199
 Dröge T. 175

E

Ebukuro T. 97
 Eckl W. 559
 Eggert R. 247

Eisenreich N.	163, 559
Engelhart W.G.	693
Eshtiagi M.N.	271
Esquivel M.M.	525

F

Faizullin M.Z.	481
Fang, X.	441
Fekete J.	357
Fernandez-Polanco F.	121
Firus A.	179
Fogassy E.	393
Freese C.	55
Freund H.	211
Fröschl F.	339

G

Galla U.	31
Gamse T.	115, 339
Ganado O.	121
Gao Y.	151
Gargin V.G.	457
Garnier S.	265
Gehrig M.	333
George M.W.	67
Gerber P.	369
Ginosar D.M.	3
Goldacker H.	61
González R.	121
Goto M.	303
Gourinchas-Courtecuisse V.	133
Guarise G.B.	411
Gunnlaugsdottir H.	79
Guthmann O.	127
Güvenc A.	463
Gvyazdovskaya V.L.	503

H

Habulin M.	85
Hakuta Y.	315
Härdle Th.	535, 661
Härröd M.	43
Härtel G.	55
Hermann M.M.	559
Hethelyi E.	357
Hiller W.	673
Hirose T.	303
Hirth Th.	163

Hochmann S.	309
Hofmann H.	145
Horn W.	593
Howdle S.M.	67

I

Ivanov D.Yu.	389
-------------------	-----

J

Jaeger P.	247
Jähnke S.	163
Joachim J.	509

K

Kafoufi K.	679
Kang S.-P.	435
Kasche V.	127
Kautz C.B.	259
Kery A.	357
Keszei S.	393
Kikic I.	265, 687
Kim J.	531
King M.B.	399
Kittel R.	687
Kleintjens L.	541
Kluth M.	61
Knez Z.	85, 223
Knorr D.	271
Koda S.	97
Kodama A.	303
Kohlbruch J.	451
Köppel R.A.	91
Kornblatt J.A.	553
Kornblatt M.J.	553
Körner P.	673
Krämer R.	599
Krause H. .	163, 345, 369, 535, 661
Krmelj V.	85
Kröcher O.	91
Kruse A.	61

L

La Roche H.L.	645
Lack E.	253
Lange R.	553
Larachi F.	493
Larrayoz M.A.	363
Laurent A.	169, 493

Lautenschlaeger W.	693
Lee C.S.	385
Lee H.	435
Lee J.S.	531
Lee S.-H.	11
Leffrang U.	31
Lemberkovics E.	357
Lentz H.	541
Li C.-L.	441
Löbbecke S.	661
Lockemann C.A.	547
Lovas R.	393
Lovis K.	175
Lu T.	399
Luft G.	73

M

Magin P.	547
Magnan C.	509
Majewski W.	639
Mallat T.	139
Marioth E.	535
Marr R.	115, 339
Masuoka H.	235
Mathe I.	357
Maurer G.	241
Mc Clain J.B.	23
Mc Hugh M.A.	11
Mehmetoglu Ü.	463
Merz L.	373
Metzger M.	693
Michel U.	541
Michelfelder B.	559
Michor H.	115
Midoux N.	169, 493
Mierau B.D.	321
Minder B.	139
Miranda A.M.	417
Møller P.	43
Moser M.	655
Müller M.	199
Muth O.	373

N

Nagorny P.A.	651
Neau E.	265
Neumaier R.	599
Nicoud R.M.	429

Niehaus M.	345
Nieuwoudt I.	283
Niklos Cs.	393
Nitta T.	327
Niu F.	145
Noh M.J.	531
Noll B.	559
Notzon S.	575
Nunes da Ponte M.	417, 487

O

Oliveira J.V.	185, 379
Oshima Y.	97
Oszagyan M.	357
Otomo J.	97
Otterbein M.	679

P

Pallado P.	217, 411
Panster P.	17
Park E.J.	531
Pereira H.	417
Pereira P.J.	487
Perrut M.	429, 627, 639
Peter S.	55, 191
Petrich G.	157
Pfohl O.	277
Pietzonka W.	609, 655
Poliakoff M.	67
Pommier C.	133
Pongratz E.	55

R

Rauzy E.	445, 469
Rébufa C.	445
Recasens F.	363
Reis Machado A.S.	417
Reiss I.	229
Ribeiro M.A.	525
Riede Th.	547
Rieks A.	127
Riha V.	291
Rizvi S.S.H.	297
Robinson J.	205
Rocha S.R.P.	185
Roizard C.	169
Ronyai E.	357
Rusinova E.V.	499

S

Sablayrolles F.	445
Sadowski G.	519
Saldana J.-L.	553
Santos R.	399
Sato M.	303
Sawinsky J.	393
Schleussinger A.	229
Schlieper L.	399
Schlücker E.	593
Schmieder H.	31, 61, 157, 515
Schneider G.M.	259
Schollmeyer E.	581
Schön J.	515
Schulmeyr J.	333
Schulz S.	229
Schweppe R.	163
Schwerdtfeger R.	127
Sebald J.	333
Seidlitz H.	253
Shchennikov V.V.	667
Shi Y.-F.	151
Shigeta T.	327
Shin H.Y.	385
Shulzhenko A.A.	457
Siebenhofer M.	339
Sieber R.	587
Sievers U.	615
Simandi B.	357, 393
Simoës P.C.	487
Sims M.	205
Sivik B.	79
Skripov V. P.	481
Smirnov V.A.	667
Smith R.L. , Jr.	315
Soloviev A.V.	389
Soria J.L.	121
Steiner K.	291
Steiner R.	211, 223, 621
Stüber F.	363
Stute R.	271
Subra P.	49
Subramaniam B.	3
Sunol A.K.	109, 321
Sunol S.G.	109

T

Tacke Th.	17
Tanoue N.	303
Teipel U.	345, 369
Tiegs C.	291
Tippl R.	519
Tosyali Z.	109
Trepp Ch. .	199, 565, 609, 645, 655
Tufeu R.	389
Tuma D.	259

V

Vallée G.	423
Van Nhu N.	405
Verotti Filho C.	351
Vetter G.	633
Vieira de Melo S.A.B.	411
Visinoni F.	693
Volkov V.B.	651
Vshivkov S.A.	499

W

Wagner H.	247
Walisch T.	199
Weber M.	565, 645
Weidner E.	223, 621
Weindel M.	559
Weisweiler W.	345
Wiegand G.	61
Wieland S.	17
Wild G.	493
Wilde H.	515

Y

Yoo K.P.	385, 531
Yoo S.J.	385
Yoon J.-H.	435
Yuan W.-K.	151

Z

Zehnder B.	587
Zhang C.	441
Zhong C.	235
Zhu Z.-N.	151
Zwahlen A.G.	37

Keyword Index

A

abrasive ability 503
 activated carbon and
 zeolite 423
 active substance 509
 adsorption 229, 303, 503
 alkaloids 475
 alkane 283
 alkylation 151
 antisolvent 217
 aromatics 151
 Aspen 291
 autoclave 581, 693
 automated equipment 687
 axial dispersion 679

B

batch processing 693
 benzene 151
 bioassays 531
 biocatalysis 115
 biochemical reactions 85
 biocompatible polymers 217
 Bodenstein Number 191
 butyl acetate 423

C

cacao (-butter) 333
 caffeine 333
 canned motor centrifugal
 pumps 599
 capillare 541
 carbon dioxide 85, 91, 223, 241
 357, 393, 445, 463
 469, 475, 531, 615
 catalysis 67
 catalyst
 decoking 3
 design 109
 chemical 627
 reactions 67

circulation-type apparatus 411
 cis-chrysanthemic acid 393
 clathrate 435
 clean technology 67
 cloud point curves 175
 cobalt-base alloys 457
 cocoa butter 297
 coexisting phases 191
 coke precursor 151
 combustion cell 559
 compacting 457
 composed plastics 535
 computer modelling 565
 construction criteria 673
 container 651
 contaminated soils 363
 continuous
 extraction 205
 fixed bed catalysts 17
 flow reactor system 55
 thermodynamics 441
 copolymers 11
 coriolis flowmeter 575
 cork 417
 correlation 277
 corrosion simulation 633
 cosolvents 333
 counter current 283
 chromatography 429
 extraction 621
 critical
 region 241
 temperature 405
 crystallization 49
 cubic equations of state 241
 cyclic operation 303
 cytotoxicity 531

D

dampener 575
 decomposition 133

- decontamination of soil 179
- demixion 389
- density 655
- design 283
 - criteria 673
 - of experiments 379
- desorption process 423
- diamond
 - anvils 667
 - powder 457
- diaphragm pumps 593
- differential scanning
 - calorimetry (DSC) 297
- dimethylformamide 91
- dioxane 417
- distribution coefficient 327
- doping 503
- downward and upward flow 199
- drug delivery system 217
- drugs 509, 519
- dyeing machine 581
- dyestuffs 259
- dynamic simulation 157, 321
- E**
 - equation of state 235, 265, 277
351, 385, 445, 451
 - edible oils 309
 - electron disperse
 - spectroscopy (EDS) 109
 - enantioselective
 - hydrogenation 139
 - enantioselectivity 115, 127
 - energetic optimum 615
 - energy
 - consumption of waste
 - water treatment process 565
 - saving 599
 - enrichment of vitamins 609
 - environmental protection 599
 - enzymatic 103
 - enzyme 79, 127, 271
 - activities 553
 - equilibria 283, 435
 - essential oils 303, 309
 - esterification 85, 103
 - ethanol extraction 463
 - ethylene-acrylate
 - copolymerization 175
 - ethyleneglycol (ETG) 493
 - excess function 235, 445
 - expansion of supercritical
 - solution 49
 - experimental
 - data 277
 - separation 429
 - extract characterization 185
 - extraction 145, 179, 399
411, 417
 - column 191
 - kinetics 363
 - with carbon dioxide 333
 - extrapolation methods 639
- F**
 - fatigue conditions 633
 - fatty
 - acid ethyl esters (FAEE) 291
 - oil 357
 - FEM 633
 - fermentation 463
 - fine particle 369
 - fixed bed 525
 - catalyst 17, 37
 - flame
 - retardants 163, 535
 - stability 565
 - flow
 - field 559
 - in horizontal tubes 199
 - in vertical and tilted tubes 199
 - fractionation 283, 303
 - temperature 297
- G**
 - gas 547
 - anti-solvent 309
 - antisolvent process 519
 - large n-alkane systems 235
 - liquid mass transfer 493
 - liquid reactor 169
 - pressure 211
 - gradientless recycle reactor ... 145

group contribution 385
 contribution method 469

H

halogenated compounds 163
 hardening of fats and oils 17
 hazardous organics 61
 hazards 627
 heat transfer at constant
 wall temperature 199
 heater 651
 herbs 253, 399
 Herzberg states 97
 heterogeneous catalysis 91
 high
 level radioactive liquid
 waste stream 315
 power range 593
 high pressure 73, 85, 169, 277
 385, 441, 451, 457
 481, 519, 547, 559
 apparatus 651
 cleaning 633
 free-radical
 polymerization 175
 micronization 587
 nozzle 247
 spray drying 587
 systems 599
 wet oxidation 633
 high reliability 593
 safety 593
 temperature apparatus 651
 viscous systems 541
 hold-up 679
 hydrocarbon 179, 469
 hydrodynamics 679
 hydrogen 67
 peroxide 55
 hydrogenation 37, 43, 91
 hydrostatic pressure 127

I

imbibition 457
 impregnation 509
 indirect electrochemistry 31
 instabilities of a falling film .. 191

interfacial tension 247, 655
 internal
 mass transfer 103
 recycle reactor 37

K

kinetic study 133
 kinetics 37, 363

L

laser-induced oxidation 97
 lattice theory 385
 leakfree 593
 Leonnard-Jones
 potential model 327
 light scattering 389
 lipase 79, 85, 103
 lipid modification 79
 lipids 43
 low molecular weight
 compounds 49
 lupinus albus 475

M

manometric method 169
 mass
 balance 423
 transfer 169, 247, 487, 525
 medicinal plant 357, 531
 melt-crystallization 211, 297
 melting curve 211
 metallocene 73
 metallurgy 363
 methanol 445
 microorganism 271
 microwave energy 693
 mineral coal 185
 minimizing the
 manufacturing costs 673
 mixed convection 199
 mixing
 rule 235, 351
 theory 451
 mixtures 481
 model discrimination 379
 modelling 399, 469

- models of Anderson and Zemniak 315
- modification 373
- modifier 345
- Monte Carlo method 327
- multiphase equilibria 241
- multistage extraction
 - apparatus 609
- mutual solubility 655

- N**
- near critical fluids (NCF) 205
- nitroaromatics (detection of) 661
- nonpolar mixtures 405

- O**
- oils 487
- on-line
 - analysis 661
 - modelling 157
- operation 627
 - costs 615
- optimum conditions 531
- organum virens l. 525
- oxidation 61, 121, 157
 - of waste-water 55
- oxygen
 - atoms 97
 - states 97

- P**
- p-cresol 435
- packed
 - bed 363
 - column 679
- PAH 229
- particles 373
- pendant drop method 655
- performance 645
- petroleum fraction 441
- PGSS 223
- phase
 - behavior 11, 515
 - equilibria 223, 339, 379, 385, 411, 445, 451
 - separation 481
 - transition 499, 667
- phenol 435
- photochemistry 97
- pilot
 - plant 121, 639
 - units 587
- plant design 621
- PLC-8 185
- polar substances 345
- polyethyleneglycol 223
- polymer 373, 499, 519
 - mixtures 541
- polymerization 23, 67, 73
- porosity 503
- precipitation 519
- pressure
 - effect 679
 - modulation 429
 - vessels 673
- printed circuit boards 163
- process
 - optimization 615
 - simulation 429
- procritical fluid extraction 205
- production plant
 - characteristics 639
- propane 43
- protein 553
 - denaturation 271
- pulsation 575
- pulse tracer chromatography 321

- Q**
- quantum effects 451

- R**
- radiation modelling 559
- rapid expansion of
 - supercritical solutions (RESS-process) 369
- reaction 645
 - cell 651
 - engineering 79
 - mixture 651
- reactor 121
- reciprocating pumps 575
- regeneration 229

removal of xanthines 333
 resolution 393

S

scale-up 487, 581
 scanning electron
 microscopy (SEM) 109
 security 599
 semi-automated batch
 processing 693
 separation 31, 61, 435, 519
 of metals 315
 of multicomponent
 mixtures 291
 shear influence 499
 simulation 291, 487
 sol-gel method 109
 solid
 fat content (SFC) 297
 fluid phase equilibria 259
 solids 547
 solubility 339, 469, 515, 645
 solvation 553
 solvatochromism 661
 solvent effect 139
 sorption 547
 specific surface area 503
 spectroscopy 67, 553
 spices 253
 spray 223
 particles 247
 stability 127
 stabilizers 23
 stearin 297
 stereoselectivity 127
 suberin 417
 supercritical 43, 91, 217
 303, 417
 carbon dioxide 23, 37, 61
 79, 97, 103, 115
 229, 297, 373, 399
 411, 515, 535, 661
 carbon dioxide extraction .. 339
 combustion 645
 conditions 139
 extraction 475, 487, 525

supercritical
 fluid 31, 67, 145, 327
 351, 369, 389
 463, 509, 531
 fluid chromatography
 (SFC) 259
 fluid extraction (SFE) 185
 253, 345, 357, 393
 535, 587, 609, 615
 fluid reactions 587
 isopropanol 133
 reaction media 3
 solubility 265
 solvents 259
 sorption processes 687
 water 61, 121, 157, 179, 559
 water oxidation
 (SCWO) 163, 645
 wet oxidation (SCWO) 565
 surface
 chemical conditions 503
 energetic conditions 503
 surfactants 23
 swelling 547
 synthesis 31
 synthetic diamond 503, 651

T

technical oils 515
 temperature swing
 adsorption 321
 ternary systems 241
 terpenes 411
 test of packings 621
 theobromine 333
 theophylline 333
 thermodynamical 627
 thermoelectric power 667
 three phase flash 441
 thymus zygis 399
 titanium tetraisopropoxide
 decomposition 133
 toxic substances 55
 trans-fatty acids 43
 Trebble-Bishnoi-Salim
 equation (TBS) 405

trickle-bed reactors (TBR) 493
tube reactor 55

U

UNIFAC 235
upward and downward flow 199
UV/VIS
 biochemical spectroscopy .. 553
 spectroscopy 661

V

van der Waals equation 405
vapor
 liquid equilibria 235
 pressure 385
vegetables 271
VIS-spectroscopy 259
VLE 277
volatile oil 357

W

wall compatibility 645
waste
 destruction 31
 disposal 163
water 445
wettability 503

X

xylene 423

Z

zeolite 145, 151